Transactions of the ASME®

Technical Editor, LEON M. KEER (1993)

The Technological Institute
Northwestern University
Evanston, IL 60201

APPLIED MECHANICS DIVISION

Chairman, WILLIAM S. SARIC
Secretary, THOMAS A. CRUSE
Associate Technical Editors,
R. ABEYARATNE (1995)
R. K. AGARWAL (1994)
T. R. AKYLAS (1995)
S. A. BERGER (1995)
R. M. BOWEN (1994)
S. K. DATTA (1993)
G. J. DVORAK (1993)
M. E. FOURNEY (1994)
J. A. C. HUMPHREY (1994)
R. L. HUSTON (1991)
D. J. INMAN (1992)
J. T. C. LIU (1993)
X. MARKENSCOFF (1995)
R. M. McMEEKING (1991)
A. K. NOOR (1994)
J. W. RUDNICKI (1992)
C. F. SHIH (1993)
P. D. SPANOS (1992)
F. Y. M. WAN (1995)

BOARD ON COMMUNICATIONS
Chairman and Vice-President
R. E. NICKELL
Members-at-Large
W. BEGELL, T. F. CONRY, T. DEAR, R. L. KASTOR, J. KITTO, R. MATES, W. MORGAN, E. M. PATTON, R. E. REDER, A. VAN DER SLUYS, F. M. WHITE, B. ZIELS

President, N. H. HURT, JR.
Exec. Dir.
D. L. BELDEN
Treasurer, ROBERT A. BENNETT

PUBLISHING STAFF
Mng. Dir., Publ.,
CHARLES W. BEARDSLEY
Managing Editor,
CORNELIA MONAHAN
Production Editor, JUDY SIERANT
Prod. Asst., MARISOL ANDINO

Transactions of the ASME, Journal of Applied Mechanics (ISSN 0021-8936) is published quarterly (Mar., June, Sept., Dec.) for $160.00 per year by The American Society of Mechanical Engineers, 345 East 47th Street, New York, NY 10017. Second class postage paid at New York, NY and additional mailing offices. POSTMASTER: Send address changes to Transactions of the ASME, Journal of Applied Mechanics, c/o THE AMERICAN SOCIETY OF MECHANICAL ENGINEERS, 22 Law Drive, Box 2300, Fairfield, NJ 07007-2300.
CHANGES OF ADDRESS must be received at Society headquarters seven weeks before they are to be effective. Please send old label and new address.

PRICES: To members, $29.00, annually: to nonmembers, $160.00. Add $20.00 for postage to countries outside the United States and Canada.

INDEXED by Applied Mechanics Reviews and Engineering Information, Inc. Canadian Goods & Services Tax Registration #126148048.

Journal of Applied Mechanics

Published Quarterly by The American Society of Mechanical Engineers

VOLUME 58 • NUMBER 4 • DECEMBER 1991

TECHNICAL PAPERS

(Contents continued on Inside Back Cover)

BRIEF NOTES

BOOK REVIEWS

ERRATA

ANNOUNCEMENTS AND SPECIAL NOTES

Nicholas Zabaras[1]
Assistant Professor,
Department of Mechanical Engineering,
University of Minnesota,
Minneapolis, MN 55455
Assoc. Mem. ASME

Yimin Ruan
Research Engineer,
Assoc. Mem. ASME.

Owen Richmond
Corporate Fellow,
Mem. ASME.

Alcoa Laboratories,
Alcoa Center, PA 15069

On the Calculation of Deformations and Stresses During Axially Symmetric Solidification

In this paper finite element modeling of the deformation and stress development in solidifying bodies is presented. Emphasis is given to axially symmetric problems and especially to the accurate implementation of thermal and mechanical phenomena occurring at the freezing front. More specifically, the interface velocity and location are treated as primary variables of the heat transfer analysis, and the isostatic stress condition at the front is utilized as an initial condition in the stress analysis. A hypoelastic-viscoplastic constitutive model and a rate form of the principle of virtual work are involved to model the stresses and deformation. The mechanical and thermal properties are allowed to vary with temperature and strain rate in a realistic manner. Several examples of calculated residual stresses are shown for pure aluminum under axially symmetric geometries and realistic boundary conditions. The effects on the evolving deformations and stresses of the melt pressure, geometry, and cooling conditions are examined and reported.

Introduction

Study of the thermal stress and strain development in solidifying bodies can be an important tool for understanding the formation of cracks in the solid shell as well as geometrical distortions during solidification. It is the objective of this work to present a numerical methodology for the estimation of such stresses and strains for the solidification of pure aluminum in an ingot or continuous casting mold with axially symmetric geometry. Heat generated from inelastic deformation will be neglected so that the solution can be obtained in an uncoupled fashion, first involving the temperature field, and then the corresponding deformation and stresses.

Heat conduction boundary value problems with phase change have been examined extensively. The most important element of the heat transfer analysis is the proper modeling of the solid/liquid freezing front where an appropriate energy balance has to be met. Numerical techniques have been developed which track the front motion by using either transformed coordinates, a moving grid or the enthalpy transformation in a fixed domain (Crank, 1984).

The deformation part of the problem is more complicated than the heat transfer part. It requires a proper modeling of the mechanical conditions at the freezing front, integration of stiff constitutive models prescribing the inelastic deformation, temperature-dependent material properties, and coupling with the heat transfer part of the problem. A few references addressing one or more of these issues include Richmond and Tien (1971), Kristiansson (1982), Richmond (1982), Thomas et al. (1987), Smelser and Richmond (1988), and Zabaras et al. (1990).

The deformation of a solidifying material is very different from that of a standard fixed body. A solidifying body develops residual (initial) stresses immediately after solidification and is never in a state of zero stresses (stress-free state). It should be emphasized that this freezing interface condition is an initial rather than a boundary condition at the time of the solidification of a material point. It was first discussed by Richmond (1982) and implemented in one-dimensional solidification problems by Tien and Richmond (1982), Heinlein et al. (1986), and in two-dimensional plane stress applications by the authors (Zabaras et al., 1990).

This paper begins with a brief review of a front tracking analysis for the heat transfer part of the problem. A rate form of the principle of virtual work is then given, which together with a proper hypoelastic-viscoplastic constitutive model and a finite element implementation are used to calculate the deformation and stresses in an axially symmetric body. An accurate consideration of the freezing interface conditions is presented. Several cases of calculation of residual stresses are shown for plane strain and axially symmetric casting conditions. The effect of different cooling and melt pressure rates on the development of residual stresses are reported.

Thermal Analysis

Governing Equations. Consider liquid metal in an axially symmetric container (mold) at a uniform temperature $T_{in}(r, z)$ equal to or above the melting temperature T_m. Solidification

[1]Presently at the Sibley School of Mechanical and Aerospace Engineering, Cornell University, Ithaca, NY 14853.

Contributed by the Applied Mechanics Division of THE AMERICAN SOCIETY OF MECHANICAL ENGINEERS for publication in the JOURNAL OF APPLIED MECHANICS.

Discussion on this paper should be addressed to the Technical Editor, Prof. Leon M. Keer, The Technological Institute, Northwestern University, Evanston, IL 60208, and will be accepted until two months after final publication of the paper itself in the JOURNAL OF APPLIED MECHANICS. Manuscript received by the ASME Applied Mechanics Division, Oct. 25, 1989; final revision, Sept. 7, 1990.

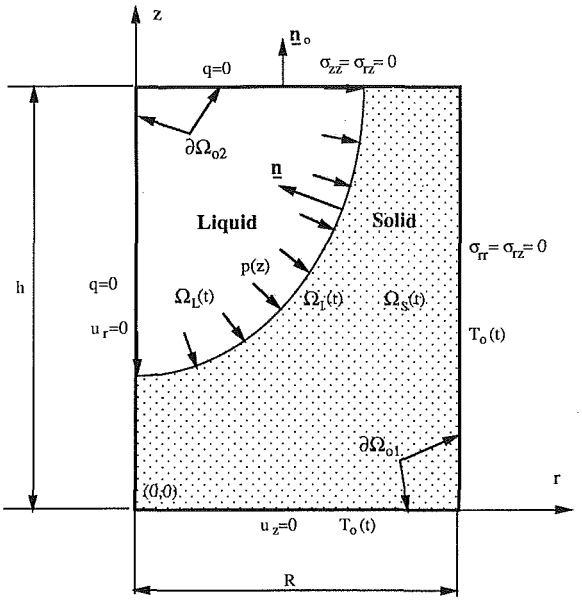

Fig. 1 Model section for the solidification problem

is assumed to start at time $t = 0$ when part of the boundary of the body is cooled down in an axially symmetric way to a temperature equal to or below T_m. Figure 1 shows, on the r-z plane, at time t, the two-dimensional model section Ω_o with boundary $\partial\Omega_o$. Let $\partial\Omega_I(t)$ be the isothermal freezing interface at time t, and $\Omega_s(t)$ and $\Omega_L(t)$ the regions occupied by the solid and liquid phases, respectively. In the absence of heat sources, the governing heat conduction equation for an axially symmetric solidification problem is given by Carslaw and Jaeger (1959) as

$$\rho c\frac{\partial T(r,z,t)}{\partial t}=\frac{1}{r}\frac{\partial}{\partial r}\left(Kr\frac{\partial T(r,z,t)}{\partial r}\right)+\frac{\partial}{\partial z}\left(K\frac{\partial T(r,z,t)}{\partial z}\right)\quad (r,z)\in\Omega_o \tag{1}$$

where ρ, c, and K are the density, specific heat, and conductivity, respectively, of the solid or liquid phase depending on $(r, z) \in \Omega_S(t)$ or $(r, z) \in \Omega_L(t)$ where the subscripts S and L are used to show quantities referred to the solid and liquid phases, respectively. Let also $T_o(r, z, t)$ be the prescribed temperature history on boundary $\partial\Omega_{o1}$ and $q_o(r, z, t)$ the prescribed normal heat flux on boundary $\partial\Omega_{o2}$ with $\partial\Omega_{o1} \cup \partial\Omega_{o2} = \partial\Omega_o$. Finally, the Stefan condition takes the form

$$K_S\frac{\partial T_S(r,z,t)}{\partial n}-K_L\frac{\partial T_L(r,z,t)}{\partial n}=\rho LV\cdot n\quad (r,z)\in\partial\Omega_I(t) \tag{2}$$

where n is a unit normal to the interface $\partial\Omega_I(t)$ at a point $(r, z) \in \partial\Omega_I(t)$ pointing away from the solid region, V is the interface velocity vector at the same point, and L denotes the latent heat of fusion.

Finite Element Modeling. Consider that the solid and liquid regions are discretized into a number of finite elements in such a way that no element crosses the solid/liquid interface. One way to account for the freezing front motion is to allow the element nodes to continuously move with time and update their positions according to the front motion. In this case, the temperature interpolation will take the form

$$T(r,z,t)=T_i^e(t)\Phi_i^e(r,z,t)\quad i=1,2,\ldots,M^e \tag{3}$$

where summation on i is implied over the number of nodes in an element M^e, $T_i^e(t)$ denote the nodal temperatures, and $\Phi_i^e(r, z, t)$ the element shape functions. Moving finite element formulations based on such an interpolation have been proposed earlier by Lynch (1982) and Zabaras and Ruan (1989, 1990). Each mesh point (r, z), at time t, is moving with nodal velocity $V(r, z, t) = (V_r, V_z)$ with V_r and V_z denoting the components of the velocity vector. This velocity can be easily calculated by using the isoparametric interpolation functions and assuming that the nodal velocities $(\dot{R}_i^e, \dot{Z}_i^e)$ are known. Usually these nodal velocities are calculated based on the velocities of the nodes at the freezing front and a rearrangement of the position of the internal nodes which preserves a uniform mesh (Zabaras and Ruan, (1990)). Applying a Galerkin type of weak formulation to Eq. (1), the following assembled system of equations is obtained

$$C_{IJ}\frac{dT_J}{dt}+(B_{IJ}+K_{IJ})T_J=F_I$$

$$I,J=1,2,\ldots,M\ (\text{sum on } J) \tag{4}$$

where **C**, **K**, and **F** are the familiar heat capacity matrix, stiffness matrix, and load vector, respectively, and the matrix **B** is resulting from the motion of the finite element nodal points and is given as

$$B_{IJ}=\sum_{e=1}^{E}B_{ij}^e=-\sum_{e=1}^{E}\int_{\Omega_e}\rho c\Phi_i^e(r,z,t)\times\left[\frac{\partial\Phi_j^e(r,z,t)}{\partial r}V_r(r,z,t)+\frac{\partial\Phi_j^e(r,z,t)}{\partial z}V_z(r,z,t)\right]d\Omega \tag{5}$$

where I and J denote the global nodal number corresponding to element nodes i and j, respectively, $(i, j = 1, 2, \ldots, M^e)$.

Denoting the nodal temperature vector at time $t = t_{n-1} + \Delta t$ with T^n, $n = 1, 2, \ldots$, where Δt is a time step, a stable integration scheme can be derived as

$$\left(\frac{\mathbf{C}_{n-1+\gamma}}{\Delta t}+\gamma(\mathbf{B}_{n-1+\gamma}+\mathbf{K}_{n-1+\gamma})\right)\mathbf{T}^n=\mathbf{F}_{n-1+\gamma}+\left(\frac{\mathbf{C}_{n-1+\gamma}}{\Delta t}-(1-\gamma)(\mathbf{B}_{n-1+\gamma}+\mathbf{K}_{n-1+\gamma})\right)\mathbf{T}^{n-1} \tag{6}$$

where the subscript $(n - 1 + \gamma)$ indicates the reference time $\hat{t}$ where $\hat{t} = (1 - \gamma)t_{n-1} + \gamma t_n$, for the calculation of the temperatures and material properties as well as of the freezing interface position and velocity.

To compute the front nodal velocities, Zabaras and Ruan (1990) have proposed a Galerkin type of weak formulation of the interface energy equation (2). In their approach, the velocity at the solid/liquid interface is approximated as

$$V=V_i^b\Psi_i^b(r,z,t)\quad i=1,2,\ldots,M_I^b \tag{7}$$

for each segment b of the interface where $\Psi_i^b(r, z, t)$ and $V_i^b = (\dot{r}_i, \dot{z}_i)$ are shape functions and interface nodal velocities at segment b, respectively, M_I^b are number of nodes in the segment b, and I is a number of boundary segments at the solid/liquid interface. The Galerkin type of weak formulation of Eq. (2) takes the form

$$\sum_{b=1}^{E_I}\int_{\partial\Omega_I^b}\rho LN^b\Psi_i^b\Psi_h^b d\Gamma\cdot V_h^b=\sum_{b=1}^{E_I}\int_{\partial\Omega_I^b}[K_S\nabla T_S-K_L\nabla T_L]\cdot N^b\Psi_i^b d\Gamma$$

$$i,h=1,2,\ldots,M_I^b\ (\text{sum on } h) \tag{8}$$

where E_I and M_I are the number of boundary segments and boundary nodes at the solid/liquid interface, respectively, N^b is the unit normal to the boundary segment b at the solid/liquid interface and points away from the solid region. In order to obtain a system of equations for the components of the nodal velocities, the tangential nodal interface velocities are taken as zero. This constraint, together with Eq. (8), provide

a system of algebraic equations for the components of the interface velocities in terms of the interface flux jump. The term on the right-hand side of Eq. (8) includes the normal flux jump at the solid/liquid interface $\partial\Omega_I$ and can be found directly using Eq. (6), after the temperature distribution is obtained. Indeed, these terms are the elements of the vector $\mathbf{F}_{n-1+\gamma}$ corresponding to the freezing front nodal points.

Here cases with $T_{in}(r, z) = T_m$ are considered for which one must analyze only the solid phase since the temperature in the liquid phase remains at all times at the melting point. For this work, only the solid elements connected to the solid/liquid interface are continuously moving, while the rest of the elements in the solid phase remain fixed. In other words, the solid region is partitioned into a fixed region and a moving region. The number of elements is changing with time since more elements are generated when the sizes of the deforming elements in the moving region become larger than prescribed values. Even though the most of the nodes are fixed, due to the motion of the front nodal points, the matrix **B** in equation (5) will not vanish. This special treatment of the finite element mesh is generally less expensive than the method of a fixed number of elements (Zabaras and Ruan, 1990), and it is also convenient for stress analysis.

To start the algorithm, a small initial finite solid region must be assumed. The initial interface velocities are arbitrary in general. In summary, by assuming initial front nodal velocities, one solves the system of Eqs. (6) to obtain the temperature distribution. Then the updated nodal velocities can be found by solving Eq. (8). Generally, an iterative procedure is required.

Table 1 Thermal properties of aluminum (after Heinlein et al., 1986)

Heat conductivity in solid	K_S	0.0548	kcal/m·s·°C
Heat conductivity in liquid	K_L	0.0548	kcal/m·s·°C
Heat capacity in solid	c_S	0.2526	kcal/kg·°C
Heat capacity in liquid	c_L	0.2526	kcal/kg·°C
Latent heat	L	94.44	kcal/kg
Density	ρ	2650	kg/m^3
Initial temperature	T_{in}	660	°C
Melting temperature	T_m	660	°C

Table 2 Mechanical properties of aluminum (after Heinlein et al., 1986)

a. Coefficients of constitutive law [equation (15)].

Coefficients	A	B	C	n
Values	0.382×10^{12} sec^{-1}	0.037 1/MPa	18849 °K	3.84

b. Thermal expansion coefficient a(T)§.

Temperature °C	25	300	400	660
a(T) m/m·°C	23.19×10^{-6}	27.86×10^{-6}	30.23×10^{-6}	38.355×10^{-6}

c. Poisson's ratio v=0.37.

d. Young's modulus E(T)=F-GT, where F=6.93×10^4 MPa and G=43.7152 MPa/°C

§ The variation of a(T) is assumed to be piecewise linear within the temperature intervals 25 – 300 °C, 300 – 400 °C and 400 – 660 °C.

Thermomechanical Analysis

Governing Equations. A quasi-static thermal stress theory as discussed by Boley and Weiner (1960) is employed, and attention is given only to the solid phase. Body forces and inertia forces are neglected, and the equilibrium equations in terms of the Cauchy stress σ have to be satisfied at any time t in a region which continuously changes (grows) with respect to time. As will be explained in the next section, the growth of the domain will be accounted for in the solution algorithm via a proper form of the constitutive equations. The shrinkage associated with the solid/liquid phase transformation, which can be substantial in metals like aluminum, is neglected.

It is assumed that the total strain-rate tensor $\dot{\epsilon} = [\dot{\epsilon}_{rr}\ \dot{\epsilon}_{zz}\ \dot{\epsilon}_{rz}\ \dot{\epsilon}_{\theta\theta}]^T$ is additively decomposed into an elastic, $\dot{\epsilon}^E$, a thermal, $\dot{\epsilon}^T$, and an inelastic, $\dot{\epsilon}^N$, part, respectively, i.e.,

$$\dot{\epsilon} = \dot{\epsilon}^E + \dot{\epsilon}^T + \dot{\epsilon}^N \tag{9}$$

where $\dot{\epsilon}$ can be expressed in terms of the rate of displacement field $[\dot{u}_r, \dot{u}_z]^T$. Dilatational thermal strains are assumed as

$$\epsilon^T_{rr}(T) = \epsilon^T_{zz}(T) = \epsilon^T_{\theta\theta}(T) = \int_{T_R}^{T} a(\nu)d\nu,\ \epsilon^T_{rz}(T) = 0 \tag{10}$$

where $a(T)$ is the temperature-dependent coefficient of thermal expansion and T_R is a reference temperature at which the thermal strains are zero, i.e., $T_R = T_m$. In addition to the above, one should specify proper traction $\hat{\tau}$ on $\partial\Omega_\sigma(t)$ and/or displacement $\hat{\mathbf{u}}$ on $\partial\Omega_u(t)$ where $\partial\Omega_u(t) \cup \partial\Omega_\sigma(t) = \partial\Omega_o(t)$.

Material Modeling. As already discussed in the Introduction, the static deformation problem in a solidifying body can be treated as an initial boundary value problem, since a solidifying body is never in a stress-free state. More specifically, the stress state of a material particle before solidification is exactly the same as that of the particle just after solidification, i.e., the stress state at the solid/liquid interface must always be purely isostatic, i.e.,

$$\sigma^o_{rr} = \sigma^o_{zz} = \sigma^o_{\theta\theta} = -p(z) = -\rho g(h - z(t)) \quad \sigma^o_{rz} = 0 \tag{11}$$

where $p(z)$ is the melt pressure at location z and h is the height of the melt. Note that to accurately account for such an interface behavior, one should interpret Eq. (11) as an initial rather than a boundary condition on $\partial\Omega_I(t)$. Apparently, a rate formulation of the involved equilibrium, kinematic, and constitutive equations must be involved. The evolution of stresses is prescribed with the following hypoelastic model:

$$\dot{\sigma} = \mathbf{D}\,\dot{\epsilon}^E \tag{12}$$

where $\dot{\sigma} = [\dot{\sigma}_{rr}\ \dot{\sigma}_{zz}\ \dot{\sigma}_{rz}\ \dot{\sigma}_{\theta\theta}]^T$, $\mathbf{D}$ are the temperature-dependent elastic constants, and where the superimposed dot denotes a time derivative. The "initial" residual stresses can now be treated as an integration constant arising when Eq. (12) is integrated in time.

The material used in this work is pure aluminum with thermal properties given in Table 1 and temperature-dependent mechanical properties reported by Heinlein et al. (1986) and given in Table 2. Finally, a viscoplastic constitutive model is needed to prescribe the inelastic deformation. Important effects such as rate sensitivity, strain hardening, and recovery should be included in a rather wide range of temperatures ranging from room temperature up to the melting point of the solidifying pure metal. The following unified form is usually assumed for such rate-dependent models

$$\dot{\epsilon}^N = \mathbf{f}(\sigma, \mathbf{q}^K, T) \tag{13}$$

where $\mathbf{q}^K$ denote properly defined state variables, if any, for which evolution equations of the following form are given

$$\dot{\mathbf{q}}^K = \mathbf{g}(\sigma, \mathbf{q}^L, T). \tag{14}$$

Several viscoplastic constitutive models fall in the above category (for example, Anand, 1982). In the simulations reported in this paper, a hyperbolic-sine constitutive law (Tien and Richmond, 1982; Heinlein et al., 1986) is used to prescribe the inelastic deformation. This constitutive law has the following form

$$\dot{\epsilon}^N = \frac{3}{2} A e^{-\frac{C}{T+273}} \frac{[\sinh B\bar{\sigma}]^n}{\bar{\sigma}}\,\mathbf{s} \tag{15}$$

where A, B, C, and n are material constants given in Table 2 for pure aluminum, $\bar{\sigma}$ is the effective stress defined as $\bar{\sigma} = \sqrt{\frac{3}{2}}\,\mathbf{s}\cdot\mathbf{s}$, and s denotes deviatoric stresses. The temperature T is in degrees Celsius and C in degrees Kelvin. The above constitutive model has been successfully used by Heinlein et al. (1986) for unidirectional solidification problems and by the authors (Zabaras et al., (1990)) for unidirectional and two-dimensional plane-stress calculations of deformation and residual stresses in solidifying bodies. Note that constitutive models with state variables can also be used here, but this is considered unnecessary for the high temperatures treated here since microstructural changes should be insignificant.

In summary, the major goal of this deformation analysis is to solve for the displacement field an initial-boundary value problem which is defined by the equilibrium equations, the kinematic strain-rate/displacement-rate relations, the mechanical boundary conditions on $\partial\Omega_o(t)$, the assumption (9), the initial conditions (11), and the constitutive Eqs. (12) and (15).

Finite Element Model. The finite element analysis of the stress problem is performed with the same discretization of the solid region as that used for the heat conduction analysis but the element type is different. In the stress analysis, eight-noded elements are used in order to improve accuracy. Let $\dot{\mathbf{u}}$ denote the vector of the nodal displacement rates in the solid phase. Then the field of displacement rate $\dot{d}$ can be approximated as $\dot{d} = \mathbf{N}\dot{\mathbf{u}}$, where $\mathbf{N}$ is the matrix of shape functions and the corresponding strain and stress rates are $\dot{\epsilon} = \mathbf{B}\dot{\mathbf{u}}$ and $\dot{\sigma} = \mathbf{DB}\dot{\mathbf{u}}$, respectively, where $\mathbf{B}$ is the standard matrix defined by differentiation of the shape functions in $\mathbf{N}$.

Assuming that time stepping is performed, one can write a weak statement of the equilibrium equation at time t_n as

$$\int_{\Omega_S(t_n)} \mathbf{B}^T\sigma_n d\Omega = \int_{\partial\Omega_S(t_n)} \mathbf{N}^T\tau_n d\Gamma \tag{16}$$

where σ_n the stress tensor (a vector form) at time t_n, the body forces have been neglected and $\tau = \hat{\tau}$ on $\partial\Omega_\sigma(t)$.

Let us assume that the stress state, σ_{n-1}, at t_{n-1} is known, then the stress state, σ_n, at current time t_n can be obtained using Euler's backward integration scheme as

$$\sigma_n = \dot{\sigma}_n \Delta t^* + \sigma_{n-1} \tag{17}$$

where $\dot{\sigma}_n$ denotes the stress rate at time t_n and Δt^* is the time step related to the arrival time of the freezing front at the material point under consideration. Note that the time integration of stresses is performed at material points and if the material point is solid at time $t = t_{n-1}$, Δt^* is equal to $\Delta t = t_n - t_{n-1}$, while if it is liquid at time $t = t_{n-1}$, Δt^* is defined as $\Delta t^* = t_n - t^*_{n-1}$, where t^*_{n-1} denotes the arrival time of the freezing front at the corresponding material point. Therefore, if the front arrival time at a point is later than t_{n-1}, the stress σ_{n-1} is equal to the melt hydrostatic stress state at arrival time and if the arrival time is earlier than t_{n-1}, it is the stress calculated at $t = t_{n-1}$.

Finally, using Eqs. (9), (12), (16), and (17), the following rate form of the principle of virtual work is obtained

$$\int_{\Omega_S(t_n)} \mathbf{B}^T\mathbf{DB}\Delta t^* d\Omega\dot{\mathbf{u}} = \int_{\partial\Omega_S(t_n)} \mathbf{N}^T\tau_n d\Gamma - \int_{\Omega_S(t_n)} \mathbf{B}^T\sigma_{n-1} d\Omega + \int_{\Omega_S(t_n)} \mathbf{B}^T\mathbf{D}(\dot{\epsilon}^T + \dot{\epsilon}^N)\Delta t^* d\Omega. \tag{18}$$

After the nodal displacement rates are found from Eq. (18), they are used to calculate stress rates at element Gauss points. For the nonmoving region, the stress rates are integrated at the Gauss points. For the moving region, in order to perform stress integration at Gauss points using Eq. (17), the stresses at the Gauss points at time t_{n-1}, σ_{n-1}, are transferred to the Gauss points at time t_n using a second-order polynomial approximation, i.e.,

$$\sigma = c_o + c_1 r + c_2 z + c_3 rz + c_4 r^2 + c_5 z^2 \tag{19}$$

where c_i are coefficients calculated through a least squares method, using the stresses at the old Gauss points and the hydrostatic stresses at the front nodal points.

The difference between the integrations of stress rates, $\dot{\sigma}_n$, and the time derivatives of temperature, $\dot{T}_n$, should be emphasized. In the stress problem, the primary unknowns are nodal displacement rates and the integration of stress rates is performed at material points. In the temperature problem, however, where the primary unknowns are nodal temperatures, the integration of the time derivative of temperature is performed at nodal points rather than at material points due to the time-dependent shape functions.

The solution procedure for the deformation part of the problem is as follows: (a) calculate the temperature field and front position as discussed in the section on thermal analysis and obtain the temperature distribution at Gauss integration points and (b) solve Eq. (18) iteratively to obtain displacement rates. Stresses can then be obtained using Eq. (17).

Numerical Results

The accuracy of the above algorithm was tested with a unidirectional plane-strain solidification example (Zabaras and Richmond, 1990). The calculated lateral stress history near the boundary where the shell is cooled was found to be two percent different from an approximate semi-analytical solution given by the senior author and co-workers (Heinlein et al., 1986).

In the examples reported here, solidification of a cylinder initially filled with liquid aluminum at melting temperature will be considered. The thermal and mechanical properties of aluminum are listed in Tables 1 and 2, respectively. Part of the boundary of the cylinder will be assumed to be cooled down as follows:

$$T_o(t) = T_a + (T_m - T_a)e^{-Qt} \tag{20}$$

where T_a is its final steady-state temperature, T_m is the melting temperature, and Q is a cooling rate parameter. In the following examples, T_a = 500 °C, Q = 0.1 sec^{-1} and T_m = 660 °C. Four-noded elements were used for the temperature analysis, while eight-noded quadrilateral elements were employed in the deformation part of the problem. The integration parameter γ in Eq. (6) is 0.85.

In the first example, it is assumed that the cylindrical body is insulated at the top and bottom and that the rest of its surface ($r = R$) is cooled with the temperature history depicted in Eq. (20). Plane-strain conditions with a traction-free outer surface were assumed. The geometrical parameters are assumed as h = 0.04 m and R = 0.018 m.

The front position and the temperature history at various locations are shown in Figs. 2 and 3, respectively. These results were compared with a one-dimensional deforming finite element implementation of the problem (Zabaras and Ruan, 1989), and they were found to coincide to within plotting accuracy. Figure 4 shows the residual stress distribution with the plane-strain assumption on the plane z = 0.002113 m, at the end of solidification, t = 8.32 secs. The stress history at location r = 0.017714 m and z = 0.002113 m (near the bottom and the surface $r = R$) is also shown in Fig. 5. As seen from these figures, the hoop stress at the outer surface $r = R$ is compressive, while near the center of the cylinder all the stresses are tensile. Generally, the residual stress in the axial direction is tensile, but it becomes slightly compressive in the region close to the surface $r = R$ near the end of solidification. In this example, as expected, the stresses were found not to significantly vary in the axial direction.

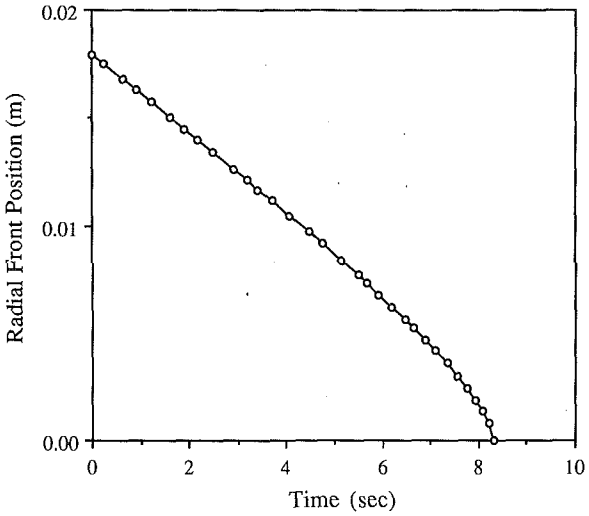

Fig. 2 Front position for solidification of a cylindrical body uniformly cooled at the surface $r = R$

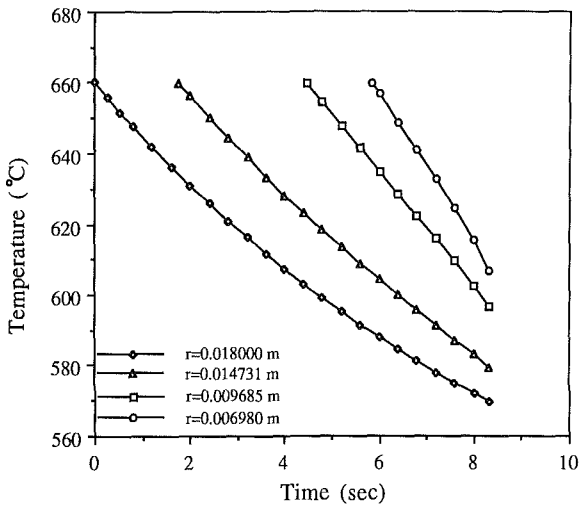

Fig. 3 Temperature history at various locations for solidification of a cylindrical body uniformly cooled at the surface $r = R$

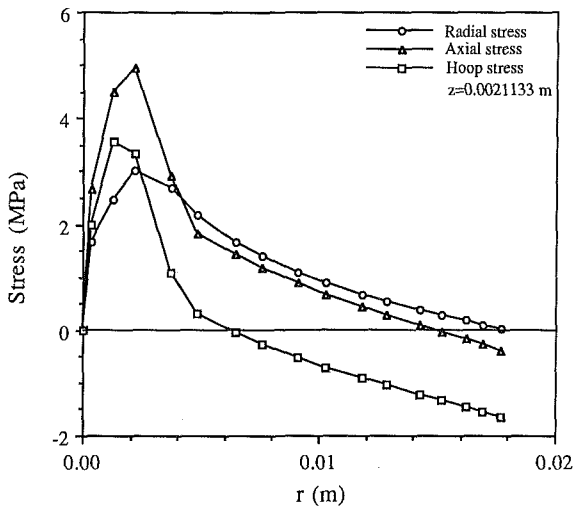

Fig. 4 Residual stress distribution in the radial direction at time 8.32 sec using a plane-strain assumption

In the second example, the geometry and the temperature boundary conditions are the same as those employed in the first example. It is assumed that the bottom is fixed in the axial direction, and traction-free conditions are applied to the top surface and to the outer surface, $r = R$. It was observed (Zabaras and Richmond, 1990) that the traction conditions at the top surface affect primarily the axial stress while leaving the radial and hoop stress almost the same for both free-top and plane-strain conditions. Large tensile residual axial stresses appear in the region close to the center of the cylinder. Figure 6 shows the residual stress variation in the axial direction at time $t = 8.3202$ sec and the stress history at location $r = 0.0177145$ m and $z = 0.0010566$ m (close to the bottom and $r = R$) is given in Fig. 7. The hoop and axial stress histories are almost the same, an assumption used before by Heinlein et al. (1986) to simplify a three-dimensional solidification problem to a unidirectional one.

To demonstrate the effect of melt pressure, a longer cylinder is considered with $h = 0.4$ m and other conditions are kept the same as those in the first example. In this case, the pressure at the bottom of the cylinder is about 0.0101 MPa. The displacements of three points at $r = R$ are given in Fig. 8, where it is shown that the surface $r = R$ near the bottom of the cylinder first expands before it starts contracting. Generally, the residual stress distribution is very close to that discussed in the first example; but at early time, the differences of the displacements at $r = R$ and the stress distribution between this and the first example are observable. Also, the hoop stress was found to have higher values at early time (Zabaras and Richmond, 1990). Therefore, as it is expected, one can conclude

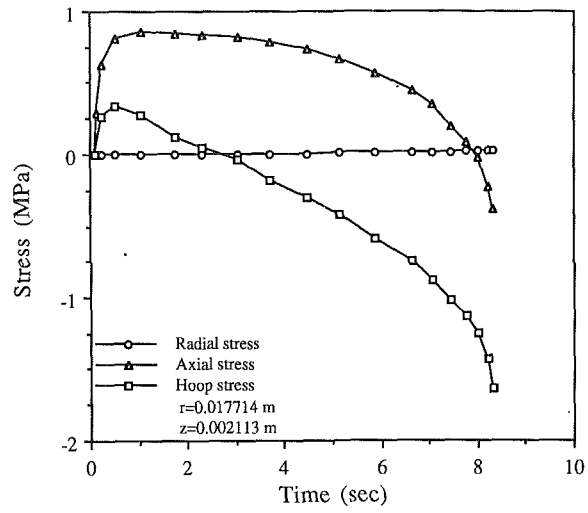

Fig. 5 Thermal stress history with a plane-strain assumption

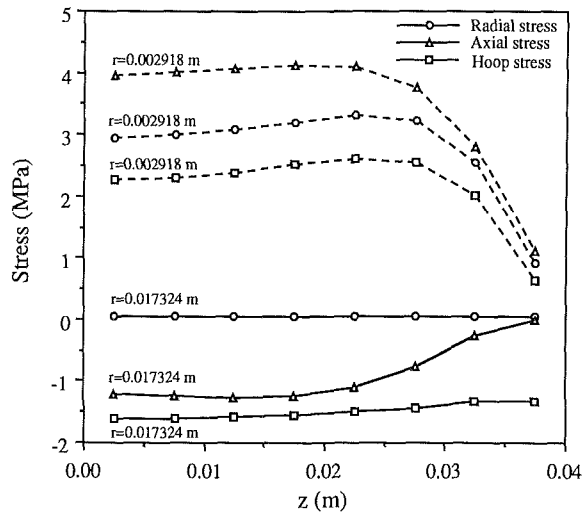

Fig. 6 Residual stress variation in the axial direction at time $t = 8.3202$ sec with a traction-free top surface

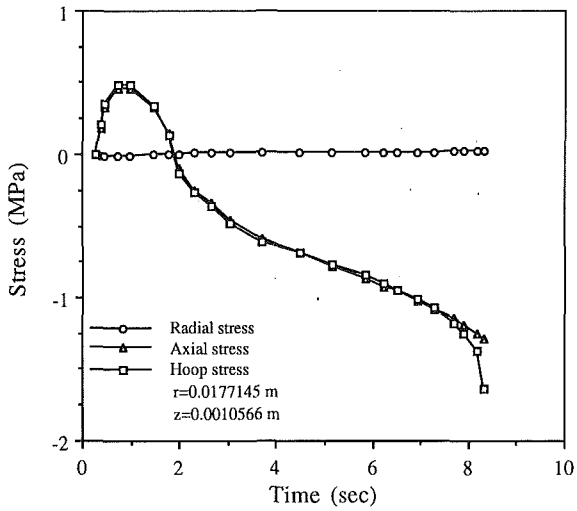

Fig. 7 Thermal stress history with a traction-free top surface

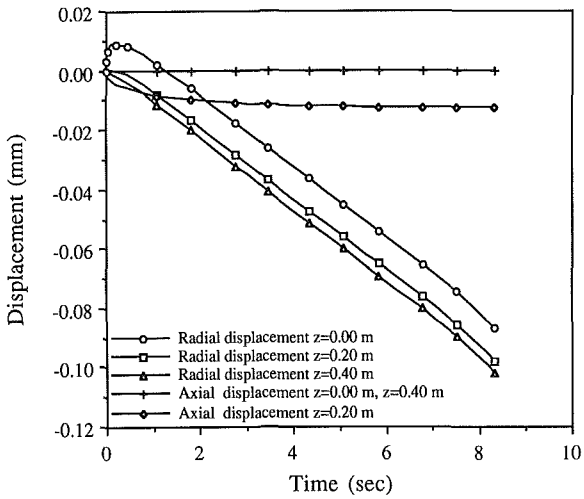

Fig. 8 Radial and axial displacements at the surface $r = R$ with a plane-strain assumption and large melt pressure

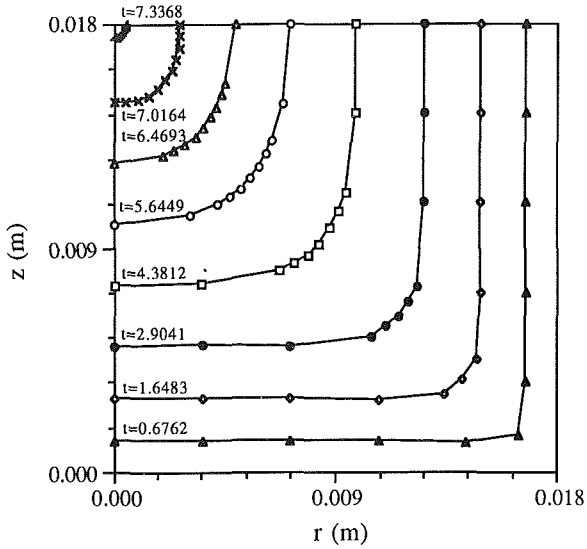

Fig. 9 Interface position at various times for the solidification problem shown in Fig. 1

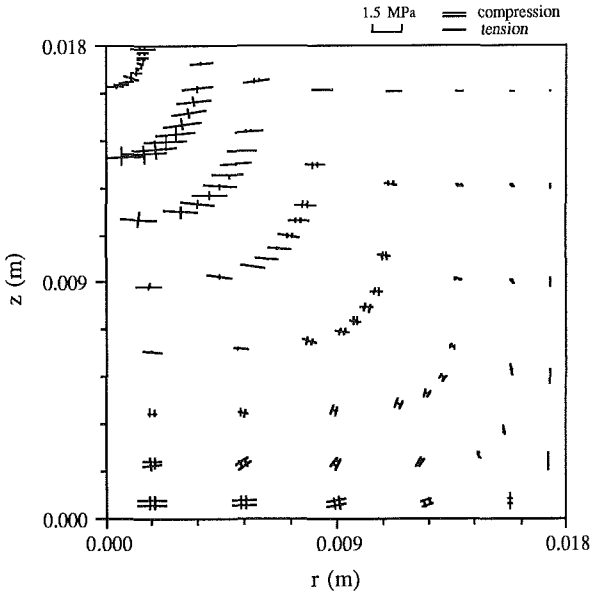

Fig. 10 Principle stresses in the r-z plane at time 7.3294 sec for the solidification problem shown in Fig. 1

that the melt pressure has a significant effect on the stresses at early time and it can play an important role in the location and time of formation of air-gaps in the solid shell/mold interface.

For cases with larger Q (high cooling rate), it was observed that the solidification process proceeds faster and that the calculated residual stresses obtained at the end of solidification are larger than those in the first example (Zabaras and Richmond, 1990).

In the final example, a cylinder with $R = h = 0.018$ m was cooled with the condition of Eq. (20) at both bottom surface and the surface $r = R$. The pattern of solidification is shown in Fig. 1. It is assumed that the outer surface, $r = R$, and the top surface are traction-free, while the bottom is fixed in the axial direction. The front position at various times is plotted in Fig. 9. Principle residual stresses in the r-z plane near the end of solidification are plotted in Fig. 10. Large tensile residual stresses appeared at the top around the center region, the stresses were small in the area close to the surface $r = R$, and the residual stresses were compressive at the bottom close to the center region. Further details on this example are also given by Zabaras and Richmond (1990).

Concluding Remarks

A general methodology has been presented for the calculation of realistic residual stresses and deformations in axially symmetric solidifying cylinders. For a cylinder cooled on its outer surface and insulated on the ends, the residual hoop stresses were compressive close to the outer surface, while tensile close to the axis of the cylinder. The radial stresses appear always tensile with their highest values close to the axis. Stress-free top conditions were found to affect primarily the axial residual stress. It was shown that for plane strain the axial stress is mostly tensile, while for stress-free top conditions the axial stress is tensile near the axis of the cylinder and compressive elsewhere. More involved residual stress patterns were obtained for more complex cooling conditions.

The liquid pressure was shown to significantly alter the stress pattern at early times of solidification, while it kept almost the same later stress pattern. This point emphasizes the importance of the melt pressure to the air-gap formation in the solid shell/mold interface. Finally, as expected, the residual stresses are very sensitive to the applied cooling rates.

The results presented here should be useful in the design of casting processes so that cracking and other defects induced by thermal stresses are avoided. This work is considered as the

first step in studying more complex and challenging casting problems including the formation of air-gaps and their effect on heat transfer and use of mixture theories to analyze the thermomechanical behavior of mushy regions.

Acknowledgments

The heat transfer part of this work was supported in part by a NSF (CBT-8802069) grant to the University of Minnesota. The computing time on Cray-2 was provided by the Minnesota Supercomputer Institute.

References

Anand, L., 1982, "Constitutive Equations For the Rate-Dependent Deformation of Metals at Elevated Temperatures," *ASME Journal of Engineering Materials and Technology*, Vol. 104, pp. 12–17.

Boley, B. A., and Weiner, J. H., 1960, *Theory of Thermal Stresses*, John Wiley and Sons, New York.

Crank, J., 1984, *Free and Moving Boundary Value Problems*, Clarendon Press, Oxford, U.K.

Carslaw, H. S., and Jaeger, J. C., 1959, *Conduction of Heat in Solids*, Oxford University Press, Oxford, U.K.

Heinlein, M., Mukherjee, S., and Richmond, O., 1986, "A Boundary Element Method Analysis of Temperature Fields and Stresses During Solidification," *Acta Mechanica*, Vol. 59, pp. 59–81.

Kristiansson, J. O., 1982, "Thermal Stresses in the Early Stage of Solidification," *Journal of Thermal Stresses*, Vol. 5, pp. 315–330.

Lynch, R. D., 1982, "Unified Approach to Simulation on Deforming Elements with Application To Phase Change Problems," *Journal of Computational Physics*, Vol. 47, pp. 387–411.

Richmond, O., and Tien, R., 1971, "Theory of Thermal Stress and Air-Gap Formation During the Early Stages of Solidification In a Rectangular Mold," *Journal of the Mechanics and Physics of Solids*, Vol. 19, pp. 273–284.

Richmond, O., 1982, "Models of Stresses and Deformations in Solidifying Bodies," *Modeling of Casting and Welding Processes*, AIME, New York, pp. 215–222.

Smelser, R. E., and Richmond, O., 1988, "Constitutive Model Effects on Stresses and Deformations in a Solidifying Circular Cylinder," *Proceedings of the Fourth Conference On Modeling of Casting and Welding Processes*, Palm Coast, Fla., Apr. 17–22.

Thomas, B. G., Samarasekera, I. V., and Brimacombe, J. K., 1987, "Mathematical Model of the Thermal Processing of Steel Ingots: Part II. Stress Model," *Metallurgical Transactions B*, Vol. 18B, pp. 131–147.

Tien, R., and Richmond, O., 1982, "Theory of Maximum Tensile Stresses in the Solidifying Shell of a Constrained Rectangular Casting," ASME JOURNAL OF APPLIED MECHANICS, Vol. 49, pp. 481–486.

Zabaras, N., and Ruan, Y., 1989, "A Deforming Finite Element Analysis of Inverse Stefan Problems," *International Journal for Numerical Methods for Engineering*, Vol. 28, pp. 295–313.

Zabaras, N., and Ruan, Y., 1990, "A Moving and Deforming Finite Element Simulation of Two Dimensional Stefan Problems," *Communications in Applied Numerical Methods*, Vol. 6, pp. 495–506.

Zabaras, N., and Richmond, O., 1990, "Analysis and Finite Element Approximations of Deformations and Thermal Stresses in Solidifying Bodies," *Computer Modeling and Simulation of Manufacturing Processes*, B. Singh and Y. T. Im, eds., ASME Winter Annual Meeting, Dallas, Texas.

Zabaras, N., Ruan, Y., and Richmond, O., 1990, "Front Tracking Thermomechanical Model for Hypoelastic-Viscoplastic Behavior in a Solidifying Body," *Computer Methods in Applied Mechanics and Engineering*, Vol. 81, pp. 333–364.

Steady Penetration of a Rigid Cone With a Rough Wall Into a Power-Law Viscous Solid

N. A. Fleck
University Engineering Department,
Cambridge University,
Cambridge, CB2 1PZ, U.K.

D. Durban
Faculty of Aerospace Engineering,
Technion-Israel Institute of Technology,
Haifa, 32000, Israel

Singular strain rate and stress fields are examined at the tip of a rigid conical indentor penetrating an incompressible viscous solid. Attention is focused on friction effects induced by wall roughness. The problem is formulated within the usual framework of eigenvalue analysis of locally singular fields. Some special cases are investigated further with emphasis on a boundary layer expansion for the rigid/perfectly plastic solid sliding along the perfectly rough wall. It has been found that the level of singularity increases as the cone becomes sharper and the wall friction decreases. Numerical results, presented for a variety of cases, suggest a boundary layer build up for sharp cones with rough walls.

1 Introduction

It is expected that steady penetration of sharp rigid indentors into viscoplastic media will give rise to singular stress fields near the tip of the indentor. For certain types of constitutive response (e.g., the family of power-law relations) it is possible to examine local singular fields using the method of eigenfunction analysis introduced by Hutchinson (1968) and Rice and Rosengren (1968) for nonlinear plane crack problems.

The present study has to do with a rigid cone, with a rough wall, that steadily penetrates an incompressible power-law viscous solid. The singular near-tip field is investigated with the aid of the corresponding local eigensolutions for stresses and strain rates. The emphasis here is on friction effects induced by the wall roughness. A simple friction factor m is assumed to be imposed along the wall within the bounds of $m = 0$ for a frictionless wall, and $m = 1$ for a perfectly rough wall (when the shear stress attains its highest possible value).

The framework of the analysis follows closely a recent paper by Fleck and Durban (1989)—henceforth referred to as (FD)—on asymptotic fields at tip of conical inhomogeneities embedded in power-law plastic solids. Accordingly, we begin, in the next section, with a recapitulation of the governing mathematical system derived in (FD).

Some special cases are considered next in Section 3. We show that, with the exception of a perfectly plastic solid, the creeping material sticks to the cone when the wall is perfectly rough. The perfectly plastic solid will slide along smoother walls of the indentor but an extra logarithmic singularity of the stress field is then needed to maintain equilibrium. In the extreme case where the indentor is perfectly rough and the medium is perfectly plastic, there is an intensive shear boundary layer near the wall. This is examined with the aid of a boundary layer expansion which is matched with the outer numerical solution. It is shown that the shear strain rate becomes unbounded as the wall is approached, and that the perfectly plastic solid does slide along the perfectly rough wall. Section 3 concludes with a simple analytical solution for possible non-singular strain-rate fields in a Newtonian fluid.

Sample numerical results are presented in the last section. The governing equations are solved with an available numerical procedure, and the dependence of the singularity level upon wall friction, cone angle, and strain-rate hardening parameter are examined in detail. The main finding is that the strain-rate singularity decreases with increasing friction and increasing cone angle. Characteristic contours of the effective strain rate are plotted along with a representative mapping of the stress profiles. A near-wall boundary layer build-up is observed as the cone becomes sharper as well as for increasing wall friction.

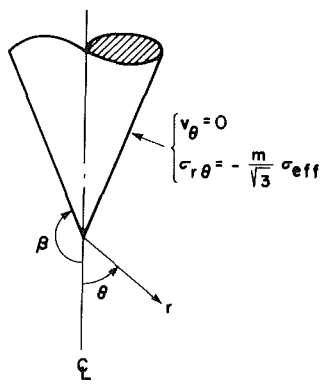

Fig. 1 Notation for steady penetration by a rigid cone. Wall friction is described by the friction factor m. A spherical-polar system (r, θ, ϕ) is attached to the apex (meridional angle ϕ is not shown).

Contributed by the Applied Mechanics Division of THE AMERICAN SOCIETY OF MECHANICAL ENGINEERS for publication in the JOURNAL OF APPLIED MECHANICS.

Discussion on this paper should be sent to the Technical Editor, Prof. Leon M. Keer, The Technological Institute, Northwestern University, Evanston, IL 60208, and will be accepted until two months after final publication of the paper itself in the JOURNAL OF APPLIED MECHANICS. Manuscript received by the ASME Applied Mechanics Division, Aug. 24, 1989; final revision, May 10, 1990.

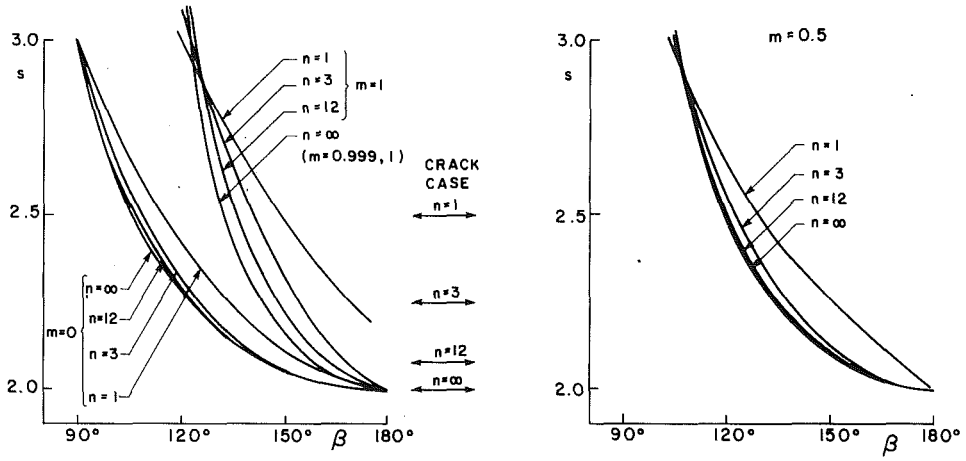

Fig. 2 Level of singularity s for different friction factors and for several values of the strain-rate hardening exponent. Also shown are the analogous crack singularities, $s = 3 - n/(n + 1)$, for a power-law plastic solid.

Our analysis aims at the investigation of slow steady penetration where it is certainly permissible to neglect inertia effects. Indentation creep experiments (Atkins et al., 1966; Matthews, 1980) have shown that creep properties measurements are beset by the influence of friction between the conical indentor and the material. The first step in analyzing indentation creep of materials is outlined in this paper; we determine the asymptotic field at the tip of an indenting cone as a function of cone angle, creep exponent of material, and wall friction.

2 Governing Equations

Consider an incompressible isotropic power-law viscous solid undergoing steady-state penetration by a rigid cone with rough walls. Attention is focused here on the singular stress field which is expected to develop near the tip of the conical indentor (Fig. 1).

Material behavior of the penetrated creeping medium is governed by the constitutive law

$$\mathbf{D}=\frac{3}{2}\left(\frac{\sigma_{\text{eff}}}{\sigma_o}\right)^n \frac{\mathbf{S}}{\sigma_{\text{eff}}} \tag{1}$$

where $\mathbf{D}$ is the Eulerian strain rate tensor, $\mathbf{S}$ is the Cauchy stress deviator tensor, $\sigma_{\text{eff}} = \left(\frac{3}{2}\mathbf{S}\cdot\cdot\mathbf{S}\right)^{1/2}$ is the effective stress, and (σ_o, n) are material constants. The Newtonian fluid is described by equation (1) with $n = 1$, while the rigid/perfectly plastic Mises solid is recovered at the limit of $n = \infty$.

Adopting an Eulerian frame of reference, with the origin of a spherical polar system (r, θ, ϕ) attached to the apex (Fig. 1), we find by symmetry that the velocity components, v_r, v_θ, depend only on (r, θ), while the circumferential component, v_ϕ, vanishes identically. The incompressibility constraint implied by equation (1) is satisfied if the velocities are derived from a stream function $\psi(r, \theta)$ by

$$v_r=\frac{\psi_{,\theta}}{r^2\sin\theta} \quad v_\theta=-\frac{\psi_{,r}}{r\sin\theta}. \tag{2}$$

Since the field equations are identical to those derived in (FD)—except the exchange of small strain displacements with finite velocities—we shall proceed with just a brief outline of the basic equations; the stream function is assumed to admit a separation of variables form, namely

$$\psi=r^s(\sin\theta)\phi(\theta) \tag{3}$$

where the eigenvalue s determines the stress singularity level

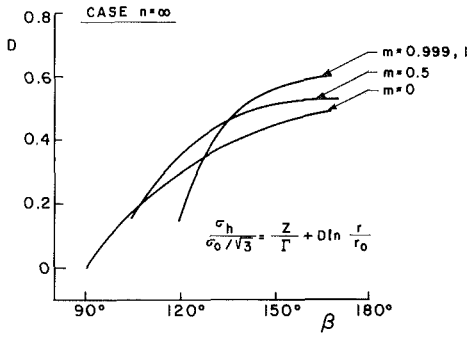

Fig. 3 Level of logarithmic singularity D of hydrostatic stress σ_h for $n = \infty$

and $\phi(\theta)$ is a function of θ. Inserting (3) in relations (2), we get the velocities in the form

$$v_r=r^{s-2}X \quad v_\theta=-sr^{s-2}\phi \tag{4}$$

with

$$X=\phi'+\phi\cot\theta \tag{5}$$

where the prime denotes differentiation with respect to θ.

The components of the Eulerian strain rate tensor $\mathbf{D}$, associated with (4), depend on the radial coordinate like $D_{ij} \sim r^{s-3}$; of particular interest here is the shear strain rate given by

$$D_{r\theta}=r^{s-3}Y(\theta) \tag{6}$$

where

$$Y=\frac{1}{2}[X'+s(3-s)\phi]. \tag{7}$$

Similarly, the effective strain rate can be expressed as

$$\epsilon_{\text{eff}}=\sqrt{\frac{2}{3}\mathbf{D}\cdot\cdot\mathbf{D}}=\frac{2}{\sqrt{3}}r^{s-3}\Gamma(\theta) \tag{8}$$

with the corresponding polar profile

$$\Gamma^2=(s^2-3s+3)X^2-s^2(X-\phi\cot\theta)\phi\cot\theta+Y^2. \tag{9}$$

The stress deviator components behave like $S_{ij} \sim r^{(s-3)/n}$ as exemplified by the shear stress component

$$\sigma_{r\theta}=\frac{\sigma_o}{\sqrt{3}}\left(\frac{2}{\sqrt{3}}\right)^{\frac{1}{n}}r^{\frac{s-3}{n}}\Gamma^{\frac{1-n}{n}}Y. \tag{10}$$

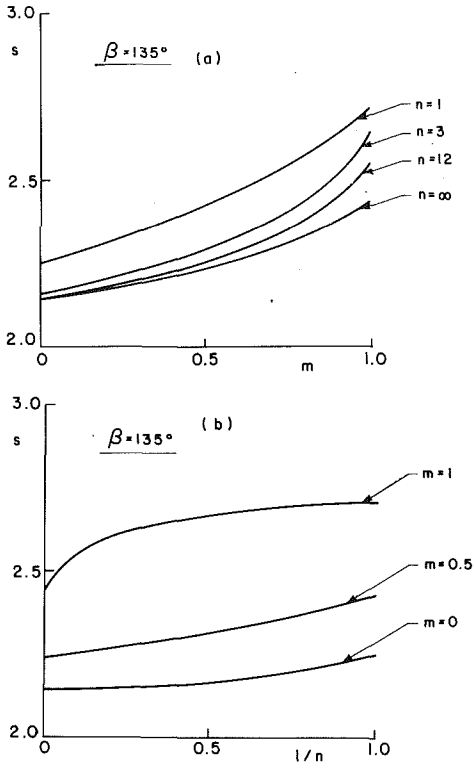

Fig. 4 Case of $\beta = 135$ deg; (*a*) variation of singularity level s with friction factor m for different values of n, (*b*) variation of singularity level s with strain-rate hardening for different values of m

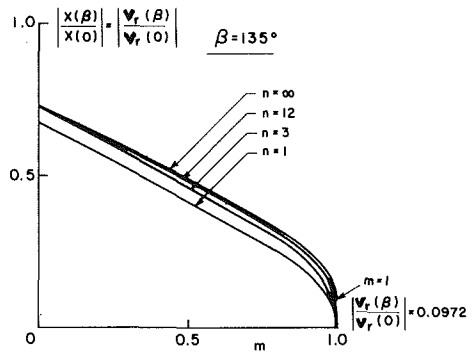

Fig. 5 Ratio of radial velocity at the wall $\theta = \beta$ and at the pole $\theta = 0$, for $\beta = 135$ deg. The creeping solid sticks to the wall for any finite n with $m = 1$, but sliding occurs at $\theta = \beta$ when $n = \infty$ and $m = 1$.

Likewise, the effective stress here takes the form

$$\sigma_{\text{eff}} = \sigma_o(\epsilon_{\text{eff}})^{\frac{1}{n}} = \sigma_o\left(\frac{2}{\sqrt{3}}\right)^{\frac{1}{n}} r^{\frac{s-3}{n}} \Gamma^{\frac{1}{n}}. \tag{11}$$

Turning to the equilibrium requirements, we have just two equations for the four active stress components (σ_{rr}, $\sigma_{\theta\theta}$, $\sigma_{\phi\phi}$, $\sigma_{r\theta}$). Substituting the stresses from (1) in the equilibrium equations results in the two ordinary differential equations

$$Y' - \left(\frac{n-1}{n}\right) Y \frac{\Gamma'}{\Gamma} + Y\cot\theta + (s-2)\left(3 + \frac{s-3}{n}\right) X + \left(\frac{s-3}{n}\right) Z + D\Gamma^{\frac{n-1}{n}} r^{\frac{3-s}{n}} = 0 \tag{12a}$$

$$Z' + (1-s)X' + s\phi'\cot\theta + \frac{1-n}{n}[Z + (1-s)X + s\phi\cot\theta]\frac{\Gamma'}{\Gamma} + s\phi(\cot^2\theta - 1) - sX\cot\theta + \left(\frac{s-3}{n} + 3\right) Y = 0 \tag{12b}$$

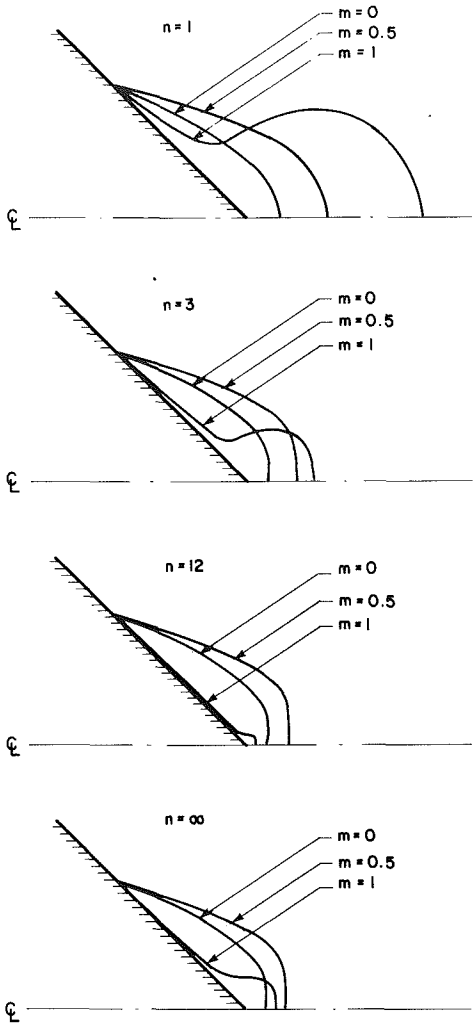

Fig. 6 Contours of constant ϵ_{eff} for different values of m and n; $\beta = 135$ deg

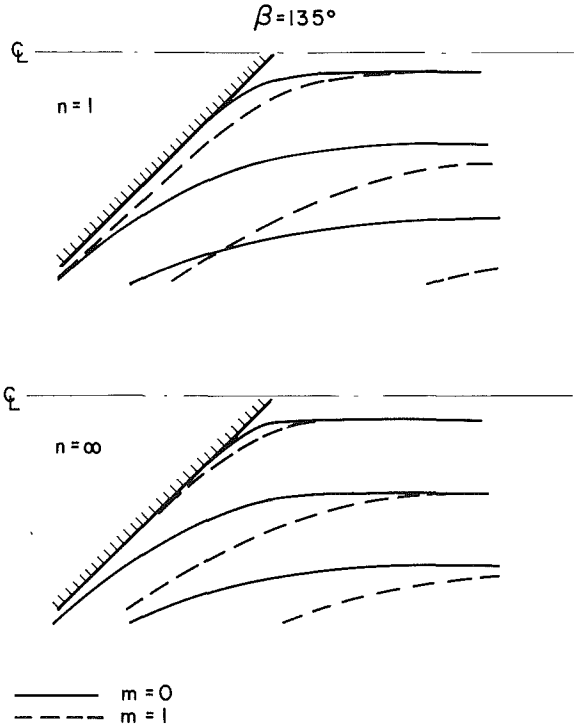

Fig. 7 Streamlines within the singular near-tip field; $\beta = 135$ deg

where $Z(\theta)$ is a function of θ (to be determined later) and D is a constant. As they stand, equations (12) present a restricted version of a more general form given in (FD equations (4.8)) which, however, will not be required in this study. The associated expression for the hydrostatic stress reads

$$\sigma_h = \frac{\sigma_o}{\sqrt{3}}\left(\frac{2}{\sqrt{3}}\right)^{\frac{1}{n}}\left(r^{\frac{s-3}{n}}\,\Gamma^{\frac{1-n}{n}}\,Z + D\ln\frac{r}{r_o}\right) \tag{13}$$

where r_o is a scaling factor. Constant D vanishes identically unless $n = \infty$ (the Mises solid) or $s = 3$ (r-independent strain rates and deviatoric stresses). For these cases, constant D forms an eigenvalue of the problem.

To sum up, we have four coupled nonlinear differential equations (5), (7), and (12a)-(12b) with four unknown functions ϕ, X, Y, Z. That system is supplemented by two boundary conditions along the wall; we assume $v_\theta = 0$ and $\sigma_{r\theta} = -\frac{m}{\sqrt{3}}\sigma_{\text{eff}}$ at $\theta = \beta$ or, in terms of the dependent variables

$$\phi(\beta) = 0 \tag{14a}$$

$$Y(\beta) = -m\Gamma(\beta) \qquad 0 \le m \le 1. \tag{14b}$$

The friction factor m serves as a measure of surface roughness ranging from $m = 0$ (for a smooth wall) to $m = 1$ for a perfectly rough wall. These bounds on the friction factor follow from the definition of the effective stress

$$\sigma_e^2 = \frac{3}{2}[(\sigma_r - \sigma_h)^2 + (\sigma_\theta - \sigma_h)^2 + (\sigma_\phi - \sigma_h)^2] + 3\sigma_{r\theta}^2. \tag{14c}$$

Additional "boundary" data can be extracted from symmetry requirements along the axis $\theta = 0$. Thus, with the same reasoning as in (FD) we obtain, for $n \neq \infty$ and $s \neq 3$, the following expansions near the pole

$$-\phi(\theta) = \theta + a_2\theta^3 + 0(\theta^5) \tag{15a}$$

$$-X(\theta) = 2 + \left(4a_2 - \frac{1}{3}\right)\theta^2 + 0(\theta^4) \tag{15b}$$

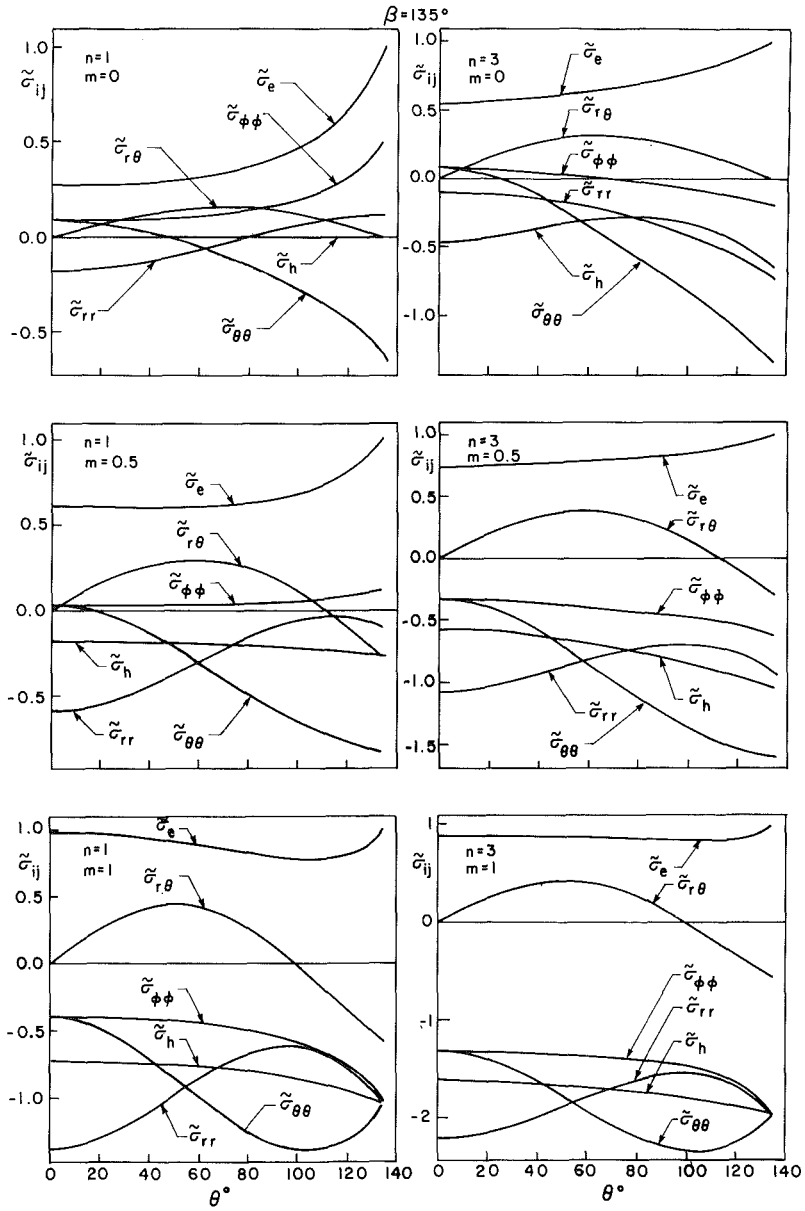

Fig. 8(*a*) Stress components $\tilde{\sigma}_{ij}(\theta)$ within the singular near-tip field; $\beta = 135$ deg, $n = 1, 3$

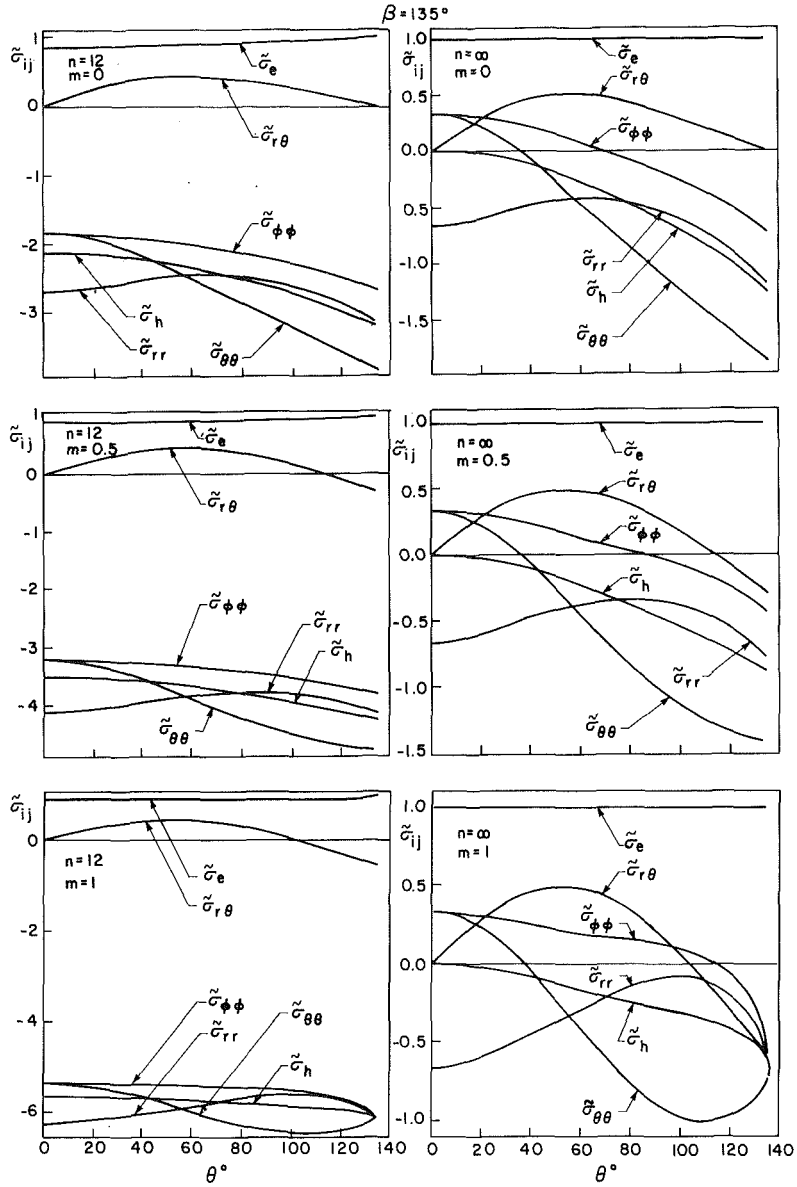

Fig. 8(*b*) Continued, $n = 12, \infty$; for $n = \infty$, $r = r_o$

$$-Y(\theta)=\left[\frac{s(3-s)}{2}+4a_2-\frac{1}{3}\right]\theta+0(\theta^3) \tag{15c}$$

$$-Z(\theta)=\frac{2n}{3-s}\left[4a_2-\frac{1}{3}+\frac{s(3-s)}{2}+(s-2)\left(3+\frac{s-3}{n}\right)\right]\theta+0(\theta^2), \tag{15d}$$

where a_2 is an unknown constant. Relations (15) are identical with (FD (4.13)) except for the minus sign on the left-hand side of (15), which is the appropriate form in the penetration problem since v_r is negative along $\theta = 0$. Note that expansions (15) have been arbitrarily scaled by putting the θ coefficient in (15*a*) as unity.

By now we have four unknown boundary parameters: a_2 and s at $\theta = 0$ and $X(\beta)$, $Z(\beta)$ at the wall. The resulting two-point boundary value problem consists, therefore, of four differential equations along with the four unknown parameters. That system has been solved numerically by integration of the differential equations using the Runge-Kutta-Merson method. Results for the eigenvalue s are shown in Fig. 2.

3 On Some Special Cases

I Case $m = 1, n < \infty$. The wall is now perfectly rough and conditions (14*a*)-(14*b*) imply that

$$X(\beta)=0. \tag{16}$$

It follows, via the first of (4), that $v_r(\theta = \beta) = 0$ and the viscous solid sticks to the rigid cone. The solution of this particular case is identical to the "rigid cone" solution in (FD) with zero displacements at the wall. Curves for the eigenvalue s are included here in Fig. 2, but for a complete discussion the reader is referred to (FD).

II Case $m < 1, n = \infty$. The material is perfectly plastic and the equilibrium equations (12) take the reduced form

$$Y'-Y\frac{\Gamma'}{\Gamma}+Y\cot\theta+3(s-2)X+D\Gamma=0 \tag{17a}$$

$$Z'+(1-s)X'+s(\phi\cot\theta)'-[Z+(1-s)X+s\phi\cot\theta]\frac{\Gamma'}{\Gamma}-s(X-2\phi\cot\theta)\cot\theta+3Y=0. \tag{17b}$$

A further simplification of (17b), with the aid of (5) and (7), results in

$$Z' - s(s-2)^2\phi - (2s-5)Y - [Z + (1-s)X + s\phi\cot\theta]\frac{\Gamma'}{\Gamma} = 0. \quad (18)$$

The governing system of equations consists now of (5), (7), (17a) and (18). Near the pole, expansions (15a)-(15c) remain valid but (15d) is now replaced by

$$-Z(\theta) = b_3\theta^2 + \ldots \quad (19)$$

where b_3 is a constant. Expansion (19), which follows directly from equation (18), shows that both Z and Z' vanish identically at $\theta = 0$. Inserting expansions (15a)-(15c) and (19) in equation (17a) we find a relation between constants D and a_2 namely

$$s(3-s) + 2\left(4a_2 - \frac{1}{3}\right) + 6(s-2) - \sqrt{3}(s-2)D = 0. \quad (20)$$

So again, we have a two-point boundary value problem with four unknown parameters: s, a_2, $X(\beta)$, and $Z(\beta)$. This may be solved using the same numerical routine as for the case with finite n. Results for the eigenvalue s are shown in Fig. 2. The level of singularity D of the hydrostatic stress (13) depends on both β and m as displayed in Fig. 3.

III Case $m = 1$, $n = \infty$. The extreme case where the wall is perfectly rough and the medium is perfectly plastic requires special attention. In this limit we enforce a state of pure plastic shear, at $\theta = \beta$, such that $\sigma_{r\theta} = -\sigma_o/\sqrt{3}$ where σ_o is now identified with the uniaxial tension yield stress. A solution is obtained by assuming that the radial velocity $v_r(\beta)$ at the wall is finite. That assumption is supported by near-wall boundary layer expansions along the following lines:

Introducing the local coordinate $\xi = \beta - \theta$ we seek a solution for small ξ, in the vicinity of the wall, such that

$$\phi \sim A\xi^t + B\xi \quad (21)$$

where A, B, and t remain to be found. Combining (21) with (5) and (7), we obtain

$$X \sim -B - At\xi^{t-1} + B(\cot\beta)\xi + \ldots \quad (22)$$

$$2Y \sim At(t-1)\xi^{t-2} - B\cot\beta + \ldots. \quad (23)$$

Since v_r is to remain finite at the wall ($\xi \to 0$), while v_θ vanishes, we find from (4) and (21)-(22) that $t > 1$. On the other hand, the pure plastic shear field at the wall together with the coaxiality of tensors **S** and **D** dictate an infinite shear strain rate at the wall. Thus, from (6) $Y \to \infty$ as $\xi \to 0$ leading, via (23), to the restriction $t < 2$.

A useful asymptotic expansion is now extracted from (9), with the aid of (21) and (22), in the form

$$\Gamma^2 - Y^2 \sim (s^2 - 3s + 3)(B^2 + 2ABt\xi^{t-1} + \ldots). \quad (24)$$

It remains to consider the equilibrium equations (17). The radial equation (17a) can be rewritten as

$$\frac{d}{d\xi}\left[\frac{Y}{\Gamma}\sin(\beta-\xi)\right] = \left[D + 3(s-2)\frac{X}{\Gamma}\right]\sin(\beta - \xi) \quad (25)$$

observing, however, from (22)-(24) that near the wall

$$\frac{X}{\Gamma} \sim \frac{2B}{At(t-1)}\xi^{2-t} + \ldots, \quad (26)$$

we can write the integral of (25) for small values of ξ as

$$\frac{Y}{\Gamma}\sin\beta \sim C + D\xi\sin\beta \quad (27)$$

where C is an integration constant. At the wall ($\xi = 0$) we have $Y = -\Gamma$; hence, $C = -\sin\beta$ and (27) is reduced to

$$Y \sim -\Gamma(1 - D\xi). \quad (28)$$

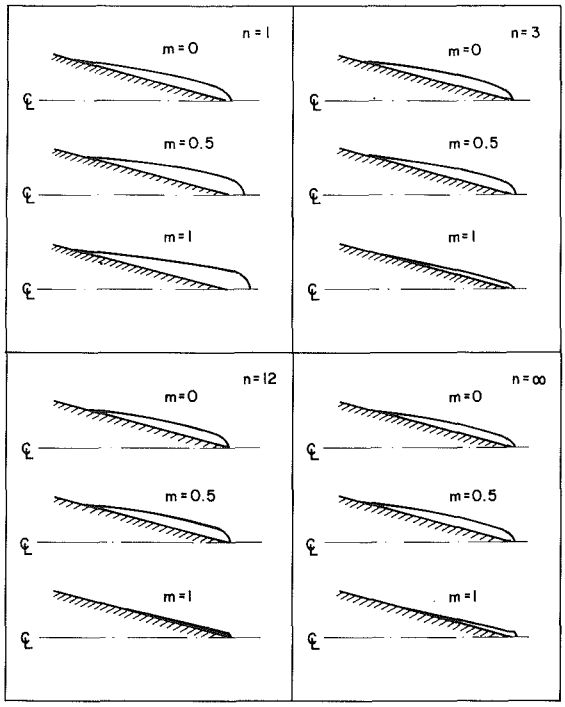

Fig. 9 Contours of constant $\epsilon_{\theta\text{eff}}$ for different values of m and n; β = 165 deg

Combining this with (23) gives

$$\Gamma^2 - Y^2 \sim 2D\left[\frac{A}{2}t(t-1)\right]^2\xi^{2t-3} + \ldots. \quad (29)$$

This should agree at the limit of small ξ with (24). Thus,

$$t = \frac{3}{2} \quad (30a)$$

and

$$\frac{9}{32}DA^2 = (s^2 - 3s + 3)B^2. \quad (30b)$$

Proceeding in a similar way, we obtain from equation (17b) the following expansion for $Z(\xi)$

$$Z \sim K\xi^{-\frac{1}{2}} + (1-s)B + \left(\frac{21-12s}{8}\right)A\xi^{\frac{1}{2}} + \ldots \quad (31)$$

where K is an integration constant.

All dependent variables have now been expanded in the vicinity of the wall. Both Y and Γ exhibit singular behavior of order $\xi^{-1/2}$ as $\xi \to 0$. This implies, by (6), an unbounded shear strain rate due to the "shear shock" at the wall. A similar solution cannot exist for $n < \infty$ as unbounded stresses at $\theta = \beta$ would give rise to an infinite force on the conical indentor. The present analysis also settles the question that was left open in (FD) in regard to the "rigid cone" with $m = 1$, $n = \infty$.

The numerical solution scheme is here straightforward with the unknown parameters s, a_2, B, $Z(\xi_o)$ where ξ_o is a fixed small value. Constant D is related to (a_2, s) by (20), and constant B is determined by (30b). Results for the eigenvalue s are included in Fig. 2, and the level of the logarithmic singularity of σ_h is shown in Fig. 3. The limit of integration was chosen to be $\xi_o = 1$ deg for $\beta \le 160$ deg; for $\beta > 160$ deg convergence problems were lessened by choosing $\xi_o = 5$ deg.

IV Case $n = 1$, $s = 3$. A simple analytical solution exists for a Newtonian fluid when the deviatoric stresses depend only on θ. This is a rather trivial case, but it serves, nevertheless, as further support to the numerical findings. The expression

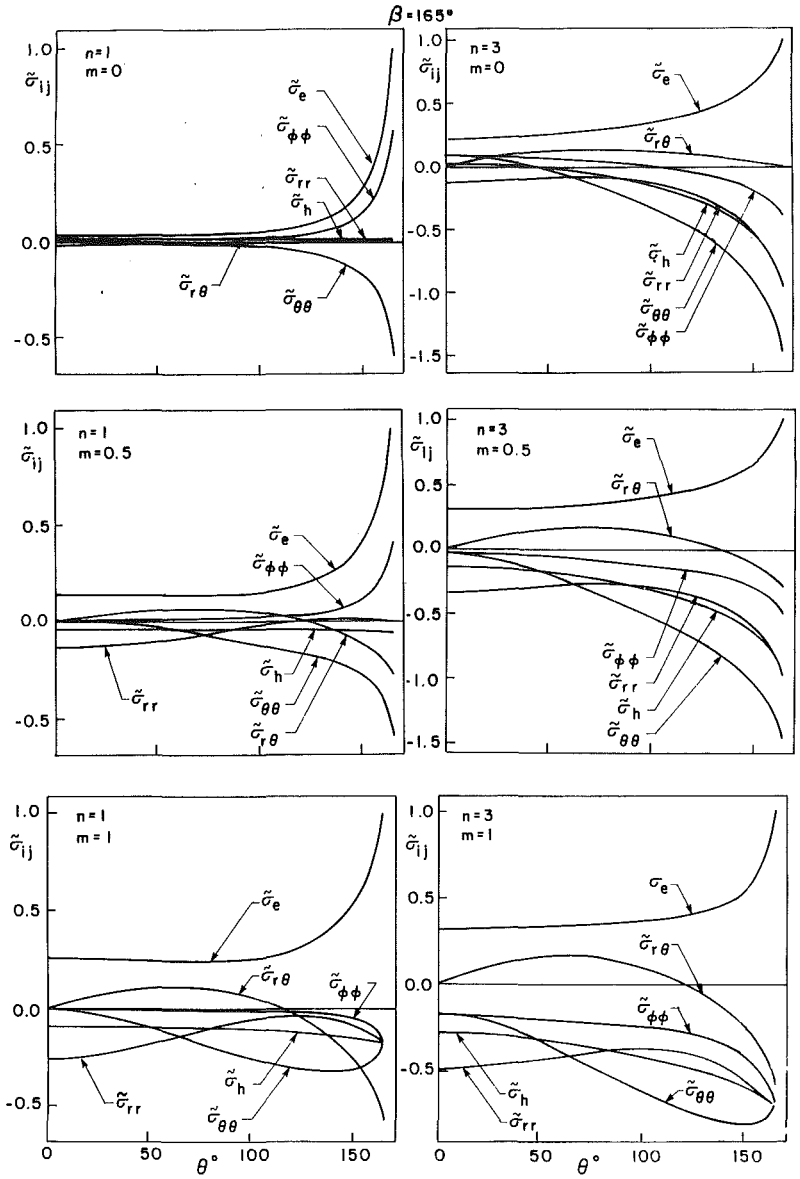

Fig. 10(*a*) Stress components $\tilde{\sigma}_{ij}(\theta)$ within the singular near-tip field; $\beta = 165$, $n = 1, 3$

for ϕ is identical with the corresponding linear elastic solution (FD), namely

$$\phi = C_1 \sin 2\theta + C_2 \tan\frac{\theta}{2}. \tag{32}$$

Inserting (32) in (5), (7), (9), and substituting in the boundary conditions (14) gives

$$\frac{m}{\sqrt{1-m^2}} = \left(\frac{\sqrt{3}}{2}\right)\frac{\sin 2\beta}{\cos 2\beta - \cos\beta}. \tag{33}$$

This relation determines the locus of pairs (m, β) for which $s = 3$. For a smooth wall ($m = 0$) we have $\beta = 90$ deg, while for a perfectly rough wall ($m = 1$), $\beta = 120$ deg. Numerical results (Fig. 2) are in complete agreement with (33). It is worth mentioning that while deviatoric stresses are r-independent, the hydrostatic stress admits a logarithmic singularity (13) given by

$$\sigma_h = -2C_2\sigma_o\left[2\ln\left(\cos\frac{\theta}{2}\right) + \ln\frac{r}{r_o}\right] \tag{34}$$

for all (m, β) of (33).

Equations (5), (7), and (12*a*)-(12*b*) remain well behaved for $s = 3$ with any value of n.

4 Numerical Results

The strain rates D_{ij} are of order r^{s-3} for small r near the tip of the cone. For all m and n, the near-tip field is singular ($s < 3$) for sufficiently large β. It is clear from Fig. 2 that the level of singularity inverses (i.e., s decreases) with increasing β and decreasing m. This is in agreement with common experience that sharper and smoother cones penetrate more easily. For sufficiently sharp cones ($\beta > 125$ deg), the strain rates become more singular with increasing n.

Consider the perfectly plastic case $n = \infty$. The level of logarithmic singularity in hydrostatic stress, D, increases with increasing β (Fig. 3). The variation of parameter D with friction factor m is complex; for $\beta > 130$, D increases with increasing m, whereas for smaller values of β, the dependence of D upon m is not monotonous.

It is worth mentioning that earlier studies (Lockett, 1963; Shield, 1955; Spencer, 1984) on conical flow of rigid/perfectly plastic solids used the Tresca model. The associated equations

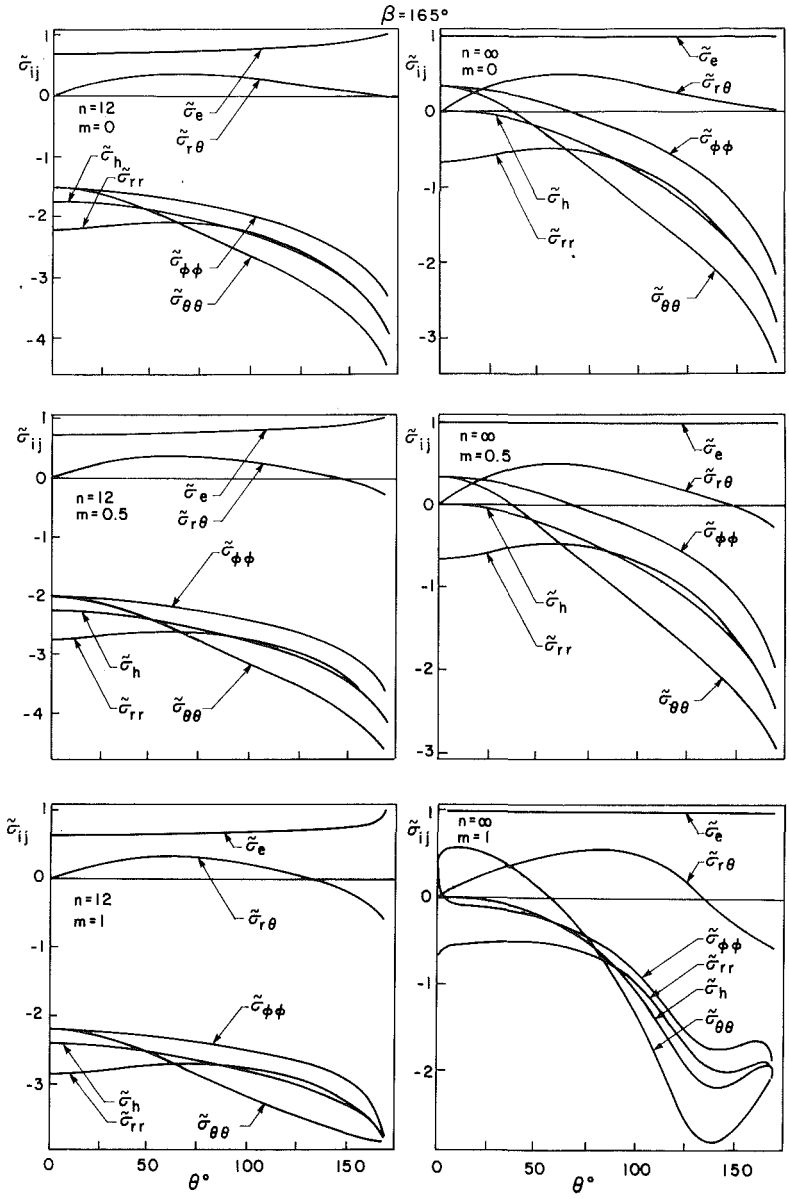

Fig. 10(*b*) Continued, $n = 12, \infty$; for $n = \infty$, $r = r_o$

are then hyperbolic while here, by contrast, the governing system remains elliptic for all n. It follows that the nature of the asymptotic fields obtained in the present work is uninfluenced by the remote field.

Typical results for $\beta = 135$ deg are shown in Figs. 4 and 5. For $0 \leq m \leq 1$, s decreases as n increases from $n = 1$ to $n = \infty$, (see Figs. 4(*a*)-4(*b*)). The ratio of radial velocity v_r at $\theta = \beta$ and at $\theta = 0$ is plotted in Fig. 5 against m. For $n \neq \infty$, as m is increased to unity the radial velocity falls to zero at the wall and the power-law viscous material sticks to the stationary cone. For the rigid/perfectly plastic case $n = \infty$, the deforming solid continues to slide past the cone along $\theta = \beta$ in the limit $m = 1$. This illustrates the special nature of the solution for $n = \infty$, $m = 1$.

Representative contours of constant ϵ_{eff} (normalized with respect to the magnitude at $\theta = \beta$) are shown in Fig. 6 for $\beta = 135$ deg. Samples of the associated streamline patterns are displayed in Fig. 7, and illustrative eigensolutions for the corresponding asymptotic stress fields are depicted in Figs. 8(*a*)-8(*b*). Results are shown for both smooth ($m = 0$) and perfectly rough ($m = 1$) indentors, and also for an intermediate value of $m = 0.5$.

For all m and n, the contour of constant ϵ_{eff} hugs the wall of the cone (Fig. 6). That contour projects ahead of the cone into the solid. Deepest penetration of the ϵ_{eff} contour occurs for $m = 1$. This is reflected in the shape of the streamlines, Fig. 7. Ahead of the cone tip the curvature of the streamlines increases with increasing m. There is also an obvious build-up of a boundary layer as both m and n increase (Fig. 6).

The stress profile $\tilde{\sigma}_{ij}(\theta)$ in Figs. 8(*a*)-8(*b*) have been normalized with respect to $\tilde{\sigma}_e(\beta)$. These figures include also the hydrostatic component $\tilde{\sigma}_h$; for the case $n = \infty$ (Fig. 8(*b*)) we have chosen to show the distribution of $\tilde{\sigma}_h$ over the circle $r = r_o$ so that the logarithmic term in (13) vanishes. A common feature, which may be concluded from these figures, is that the hoop strain rate $D_{\phi\phi}$ (which has the same sign as $\sigma_{\phi\phi} - \sigma_h$) is always positive except when it vanishes at the perfectly rough wall for $n < \infty$.

Similarly, the polar strain-rate $D_{\theta\theta}$ (which has the same sign as the deviatoric $\sigma_{\theta\theta} - \sigma_h$) is always positive along the tearing line $\theta = 0$, but becomes negative beyond a certain value of θ.

Analogous conclusions apply for the case of sharper cones with $\beta = 165$ deg. The contours of effective strain rate bear much resemblance to a boundary layer phenomenon (Fig. 9),

with relatively higher stress gradients near the wall (Figs. 10(*a*)–10(*b*)).

Acknowledgment

Part of this research was supported by the Seniel Ostrow Research Fund, Technion, Haifa.

References

Atkins, A. G., Silverio, A., and Tabor, D., 1966, "Indentation Hardness and the Creep of Solids," *J. Inst. Metals*, Vol. 94, pp. 369–378.

Fleck, N. A., and Durban, D., 1989, "Asymptotic Fields at Tip of Conical Notches and Inclusions in a Power Hardening Solid," *J. Mech. Phys. Solids*, Vol. 37, pp. 233–263.

Hutchinson, J. W., 1968, "Singular Behaviour at the End of a Tensile Crack in a Hardening Material," *J. Mech. Phys. Solids*, Vol. 16, pp. 13–31.

Lockett, F. J., 1963, "Indentation of a Rigid/Plastic Material by a Conical Indenter," *J. Mech. Phys. Solids*, Vol. 11, pp. 345–355.

Matthews, J. R., 1980, "Indentation Hardness and Hot Pressing," *Acta. Met.*, Vol. 28, pp. 311–318.

Rice, J. R., and Rosengren, G. F., 1968, "Plane Strain Deformation Near a Crack Tip in a Power-Law Hardening Material," *J. Mech. Phys. Solids*, Vol. 16, pp. 1–12.

Shield, R. T., 1955, "On the Plastic Flow of Metals Under Conditions of Axial Symmetry," *Proc. Roy. Soc., London*, Vol. A233, pp. 267–287.

Spencer, J. M., 1984, "Plastic Flow Past a Smooth Cone," *Acta Mechanica*, Vol. 54, pp. 63–74.

An Invariant-Based Flow Rule for Anisotropic Plasticity Applied to Composite Materials

Andrew C. Hansen
Department of Mechanical Engineering,
University of Wyoming,
Laramie, WY 82071
Assoc. Mem. ASME

Donald M. Blackketter
Department of Mechanical Engineering,
University of Idaho,
Moscow, ID 83843
Assoc. Mem. ASME

David E. Walrath
Department of Mechanical Engineering,
University of Wyoming,
Laramie, WY 82071
Assoc. Mem. ASME

In this paper we discuss some fundamental problems associated with incremental anisotropic plasticity theories when applied to unidirectional composite materials. In particular, we question the validity of an effective stress-strain relation for highly anisotropic materials of this nature. An effective stress-strain relation is conventionally used to determine a flow rule for plastic strain increments. It is our view that such a relation generally does not exist for many high-performance unidirectional composites. To alleviate the problem associated with defining an effective stress-strain curve we develop an anisotropic plasticity theory in which the flow rule does not requires such a relation. The proposed theory relies on developing an accurate expression for a scalar hardening parameter $g(\sigma)$. *The general form of* $g(\sigma)$ *is substantially reduced by invoking invariance requirements based on material symmetry. The general invariant-based theory developed herein is specialized to case of transverse isotropy and applied to the analysis of a nonlinear elastic-plastic unidirectional composite material. The invariant-based theory is shown to produce superior results over the traditional approach for a series of uniaxial and biaxial load cases predicted using finite element micromechanics.*

Introduction

The mathematical theory of plasticity is based on the existence of a plastic potential or yield function which demarcates the material behavior from elastic to plastic. The yield function is, in general, dependent on the stress state, and perhaps on an internal state vector which characterizes the plastic state of the material. The stress state must lie on the yield surface in order for plastic deformation to occur. Furthermore, one can show, using the energy arguments, that the increment in plastic strain must be normal to the yield surface. Therefore, a general form of an isotropic constitutive law for plastic strain increments assumes the form

$$d\epsilon_{ij}^p = d\lambda \frac{\partial \Phi}{\partial \sigma_{ij}}, \tag{1}$$

where Φ is the yield function. The scalar $d\lambda$ is normally determined by assuming there exists a unique effective stress-strain curve for the material such that the plastic work may be written as

$$dW^p = \bar{\sigma} d\bar{\epsilon}^p. \tag{2}$$

One can show the value of $d\lambda$ is a function of the tangent modulus of the effective stress-strain relation. The form of the effective stress-strain curve is determined experimentally using a specific load path and is then assumed to be valid for any multiaxial loading. This assumption is the foundation of isotropic plasticity and has generally been observed to be true for a wide variety of metals.

The constitutive law given by equation (1) has been extended to anisotropic materials by several investigators. Perhaps the most well known of these is attributable to Hill (1950) who developed an orthotropic plasticity theory for cold-rolled steels. The theory has its roots in the isotropic formulation and uses an effective stress-strain relation to determine the specific value of $d\lambda$. This approach has been specialized to the case of transversely isotropic materials to investigate the behavior of unidirectional composite materials (Griffin et al., 1981).

The theory developed by Hill (1950) is fundamentally sound and represents a major contribution to the theory of anisotropic plasticity. However, application of this theory to high-performance unidirectional composites must be questioned. In particular, we do not accept the concept of an effective stress-strain relation for highly anisotropic materials of this nature. The problem lies in the fact that the tangent modulus of the effective stress-strain relation is generally load-path dependent for this type of material. For instance, the behavior of many high-performance composites may be either linear elastic to failure or highly inelastic depending on the type of loading. The difference in behavior may be attributed to a variety of

Contributed by the Applied Mechanics Division of THE AMERICAN SOCIETY OF MECHANICAL ENGINEERS for publication in the JOURNAL OF APPLIED MECHANICS.

Discussion on this paper should be addressed to the Technical Editor, Prof. Leon M. Keer, The Technological Institute, Northwestern University, Evanston, IL 60208, and will be accepted until two months after final publication of the paper itself in the JOURNAL OF APPLIED MECHANICS. Manuscript received by the ASME Applied Mechanics Division, Mar. 3, 1989; final revision, June 30, 1990.

deformation mechanisms occurring on the microscale which are load-path dependent. Hence, the question arises as to what load path should be used to determine the tangent modulus, and hence $d\lambda$, when the material is under multiaxial loads.

The lack of a unique effective stress-strain relation for anisotropic materials has been noted by several previous investigators. Kenaga et al. (1987) developed a two-dimensional orthotropic plasticity theory to predict the plane stress behavior of unidirectional boron/aluminum composites. An optimum effective stress-strain relation was determined for the material using a trial and error analysis of off-axis tension test data. Sun and Chen (1988) extended the work of Kenaga et al. (1987) by reducing the number of coefficients needed for the effective stress-strain relation from three to one. A drawback to these works is that the parameters used to trial and error fit the effective stress-strain relation also directly influence the yield function. This is theoretically overly restrictive in the sense that the yield function should not be influenced by the effective stress-strain relation. Furthermore, the procedure for extending the theory to fully three-dimensional stress states is unclear.

Gotoh (1977) assumed a yield function that is fourth order in stress in his investigation of cold-rolled steels. While not directly applicable, he makes an important observation noting the tangent modulus of the "effective stress-strain" curve is in fact dependent on the type of loading, even though the curves should be intrinsically unique for a given material.

To alleviate problems associated with a flow rule for anisotropic plasticity we develop a plasticity theory in which the flow rule does not require an effective stress-strain relation. The constitutive law is cast in a form which sheds considerably more light on the specific nature of the flow rule. In particular, we reduce the problem to developing an accurate expression for a scalar-hardening parameter $g(\sigma)$. One significant aspect of this theory is that the explicit value of the scalar $g(\sigma)$ varies depending on the specific location of the stress state on the yield surface. This approach is in sharp contrast with the traditional approach of Hill in which $g(\sigma)$ is a constant everywhere on the yield surface. This is an implicit result of assuming the existence of an effective stress-strain curve.

The general form of $g(\sigma)$ can be substantially simplified by invoking invariance requirements on the material based on material symmetry. This is accomplished through the use of representation theorems for tensor functions. These theorems place valuable restrictions on the possible functional forms of tensor functions and are particularly useful when modeling anisotropic materials.

Two examples of the use of representation theorems for modeling anisotropic plasticity may be found in the work of Boehler (1987) and Spencer (1987). Boehler has developed an anisotropic-hardening theory for rolled sheet-steel whose macroscopic behavior is orthotropic. The constitutive law developed assumes the form

$$\mathbf{T} = \mathbf{F}(\mathbf{D}, \mathbf{P}, \mathbf{M}) \tag{3}$$

where $\mathbf{T}$, $\mathbf{D}$, and $\mathbf{P}$ are the stress, kinematic, and prestrain tensors, respectively. $\mathbf{M}$ is a structural tensor which characterizes the initial orthotropy of the material. Invariant-based yield criterion and hardening rules are then formulated based on an irreducible representation of equation (3) using representation theorems for tensor functions.

Spencer (1987) has also developed a plasticity theory for anisotropic materials based on representation theorems. In this work, plastic strain increments are defined in a manner analogous to equation (1). However, the current state of hardening is assumed to depend on the history of the strain rather than the current stress as proposed in this work. Hence, scalar invariants of the strain tensor are defined and general theories of "proportional hardening" and kinematic hardening are developed.

Problems Associated with Anisotropic Incremental Theories

Here we discuss some problems associated with incremental anisotropic theories when applied to unidirectional composite materials. We assume the composite may be modeled as a transversely isotropic material. In doing so, we specialize the orthotropic theory proposed by Hill (1950) to discuss these problems. However, these same problems associated with the Hill theory are present in many of the modified theories in which the yield surface is altered in some manner.

Hill proposed that the simplest yield criterion for an anisotropic material is one that reduces to the von Mises yield criterion when the anisotropy is vanishingly small. In the spirit of Hill, a quadratic form of the six components of stress is chosen for a transversely isotropic yield function as

$$\Phi = \phi - \bar{\phi}, \tag{4}$$

where

$$\phi = F(\sigma_{22}-\sigma_{33})^2 + G(\sigma_{33}-\sigma_{11})^2 + G(\sigma_{11}-\sigma_{22})^2 + (G+2F)(\sigma_{23}^2+\sigma_{32}^2) + M(\sigma_{13}^2+\sigma_{31}^2+\sigma_{12}^2+\sigma_{21}^2), \tag{5}$$

where the x_1-axis represents the axis of rotational symmetry. The value $\bar{\phi}$ represents the largest recorded value of ϕ. For initial yield, $\bar{\phi}$ is taken to be unity. This approach represents an isotropic hardening theory.

In the foregoing equations, F, G, and M are parameters characterizing the degree of anisotropy. These parameters remain unchanged during deformation, consistent with an isotropic hardening theory.

As is customary the yield function, Φ, defines the following material behavior:

$\Phi < 0$ – elastic behavior,
$\Phi = 0$ – the stress state lies on the yield surface, and
$\Phi > 0$ – inaccessible state.

Let σ_{ij}^y represent the initial yield stresses referenced to the orthogonal material coordinates. The parameters F, G, and M in equation (5) can be solved as

$$2F = \frac{2}{(\sigma_{22}^y)^2} - \frac{1}{(\sigma_{11}^y)^2},$$
$$2G = \frac{1}{(\sigma_{11}^y)^2},$$
$$2M = \frac{1}{(\sigma_{13}^y)^2}. \tag{6}$$

The yield stresses σ_{ij}^y must be known from experimental data or estimated analytically, e.g., using finite element micromechanics.

In order for plastic deformation to occur, the state of stress must lie on the yield surface, i.e., $\Phi = 0$. Following Martin (1975), the increment in plastic strain may be written as

$$d\epsilon_{ij}^p = g(\sigma)\left(\frac{\partial\Phi}{\partial\sigma_{rs}}d\sigma_{rs}\right)\frac{\partial\Phi}{\partial\sigma_{ij}}, \tag{7}$$

when

$$\frac{\partial\Phi}{\partial\sigma_{rs}}d\sigma_{rs} > 0 \quad \text{and} \quad \Phi(\sigma) = 0. \tag{8}$$

Comparing equations (1) and (7) we see that the scalar $d\lambda$ of equation (1) is given by

$$d\lambda = g(\sigma)\left(\frac{\partial\Phi}{\partial\sigma_{rs}}d\sigma_{rs}\right). \tag{9}$$

The significance of the latter term in the above becomes apparent by noting that $\partial\Phi/\partial\sigma_{rs}$ is a vector normal to the yield surface in stress hyperspace. Hence, $(\partial\Phi/\partial\sigma_{rs})d\sigma_{rs}$ is a measure of the component of the incremental stress normal to the yield

surface. The sign of this term determines the loading condition for the material as follows:

$(\partial\Phi/\partial\sigma_{rs})d\sigma_{rs}>0$ loading;

$(\partial\Phi/\partial\sigma_{rs})d\sigma_{rs}=0$ neutral loading;

$(\partial\Phi/\partial\sigma_{rs})d\sigma_{rs}<0$ unloading.

From equation (8), we see that plastic strain increments can only occur during loading.

To complete the theory one must develop a functional form for the scalar-hardening coefficient $g(\sigma)$. The simplest form of $g(\sigma)$ is to assume it has the same value at any point on a given yield surface. This is the approach taken in isotropic plasticity. For instance, for a von Mises yield surface we can write

$$\Phi=\frac{2}{3}(J_2-\bar{J}_2), \tag{10}$$

where J_2 represents the second invariant of the deviatoric stress and $\bar{J}_2$ represents the highest recorded value of J_2 beyond initial yield. A common form assumed for the scalar hardening parameter is given by

$$g(\sigma)=g(J_2). \tag{11}$$

The fact that g is only a function of the isotropic stress invariants is consistent with the representation theorems for a scalar function of a second-order tensor.

An experimental test for some particular load path is used to determine the specific functional form of $g(J_2)$. The normal convention is to determine $g(J_2)$ from a uniaxial tension test. For this case we arrive at a final form for $g(J_2)$ given by

$$g(J_2)=\frac{27}{16\,J_2}\left(\frac{1}{E^T(J_2)}-\frac{1}{E}\right), \tag{12}$$

where E and E^T are the elastic modulus and tangent modulus from the uniaxial stress strain curve. The assumption that the form of $g(J_2)$ as determined from a uniaxial test is valid for arbitrary load paths is central to the success of plasticity theory for isotropic materials. This in fact has been shown to be true for many materials; see, for example, Ivey's (1961) work on silicon-aluminum alloys. Furthermore, it is precisely this same assumption which leads to difficulties in modeling anisotropic material behavior.

Development of a functional form for the scalar-hardening coefficient in anisotropic plasticity follows the isotropic approach. For instance, the simplest approach is to assume $g(\sigma)$ is a function of the current yield surface ϕ. This is in fact the approach taken by Hill (1950). To demonstrate this we follow the work of Hill and write

$$d\epsilon_{ij}^p=d\lambda\frac{\partial\Phi}{\partial\sigma_{ij}}. \tag{13}$$

The increment in plastic work is then given by

$$dW^p=\sigma_{ij}d\epsilon_{ij}^p=\sigma_{ij}d\lambda\frac{\partial\Phi}{\partial\sigma_{ij}}. \tag{14}$$

Noting equations (4) and (5) and carrying out the required differentiation gives

$$dW^p=2d\lambda\phi. \tag{15}$$

To determine the constant $d\lambda$ we introduce the concept of an effective stress for the material which satisfies

$$dW^p=\bar{\sigma}d\bar{\epsilon}^p. \tag{16}$$

Following the work of Hill (1950), the specific choice taken for $\bar{\sigma}$ is

$$\bar{\sigma}=\frac{\sqrt{3}}{\sqrt{2}}\left(\frac{F(\sigma_{22}-\sigma_{33})^2+G(\sigma_{33}-\sigma_{11})^2+G(\sigma_{11}-\sigma_{22})^2}{F+2G}+\frac{2(G+2F)\sigma_{23}^2+2M\sigma_{13}^2+2M\sigma_{12}^2}{F+2G}\right)^{1/2}. \tag{17}$$

Comparing equations (5) and (17) it follows that

$$\bar{\sigma}^2=\frac{3}{2}\frac{\phi}{F+2G}. \tag{18}$$

The plastic work, as defined by equation (16), may be rewritten as

$$dW^p=\bar{\sigma}\frac{d\bar{\epsilon}^p}{d\bar{\sigma}}d\bar{\sigma}=\bar{\sigma}\,d\bar{\sigma}\frac{1}{H'}, \tag{19}$$

where

$$\frac{1}{H'}=\frac{d\bar{\epsilon}^p}{d\bar{\sigma}}. \tag{20}$$

Differentiating equation (18) and substituting into equation (19) it follows that

$$dW^p=\frac{3}{4(F+2G)}\frac{1}{H'}\frac{\partial\phi}{\partial\sigma_{rs}}d\sigma_{rs}. \tag{21}$$

Comparing equation (21) with equation (15), we obtain

$$d\lambda=\frac{3}{8\,\phi\,(F+2G)}\frac{1}{H'}\frac{\partial\phi}{\partial\sigma_{rs}}d\sigma_{rs}. \tag{22}$$

Finally, noting equation (9) we obtain a form for the scalar-hardening coefficient as a function of the yield surface given by

$$g(\phi)=\frac{3}{8\,\phi\,(F+2G)}\frac{1}{H'}. \tag{23}$$

The function $(1/H')$ is determined by considering a specific load path. For instance, consider a uniaxial tension test in the x_1 direction. For this case the effective stress is

$$\bar{\sigma}=\left(\frac{3G}{F+2G}\right)^{1/2}\sigma_{11}. \tag{24}$$

The effective strain is defined such that the increment in plastic work is energetically consistent with equation (14). Hence,

$$d\bar{\epsilon}=\left(\frac{F+2G}{3G}\right)^{1/2}d\epsilon_{11}. \tag{25}$$

Noting equation (20), the function $(1/H')$ is

$$\frac{1}{H'}=\left(\frac{1}{E_{11}^T}-\frac{1}{E_{11}}\right)\frac{F+2G}{3G}, \tag{26}$$

where E_{11} and E_{11}^T denote the modulus and the tangent modulus of the uniaxial stress-strain curve. Substituting equation (26) into equation (23), the scalar-hardening coefficient becomes

$$g(\phi)=\frac{1}{8\,\phi\,G}\left(\frac{1}{E_{11}^T(\phi)}-\frac{1}{E_{11}}\right). \tag{27}$$

Again, the fundamental assumption behind this approach is that the form for $g(\phi)$, determined from the uniaxial tension test, is valid for any multiaxial stress state. Herein lies a problem with the use of such a theory when applied to unidirectional composite materials in that the scalar-hardening coefficient is dependent on the specific location of the stress state on the yield surface. Hence, the assumption that the value of $g(\phi)$ is a constant for any given yield surface is overly restrictive. The specific behavior of the scalar-hardening coefficient for unidirectional composite materials will be examined using a finite element micromechanics analysis.

Finite element micromechanics has been extensively used to characterize the material behavior of unidirectional composites (Miller and Adams, 1977; Adams and Crane, 1984). This rep-

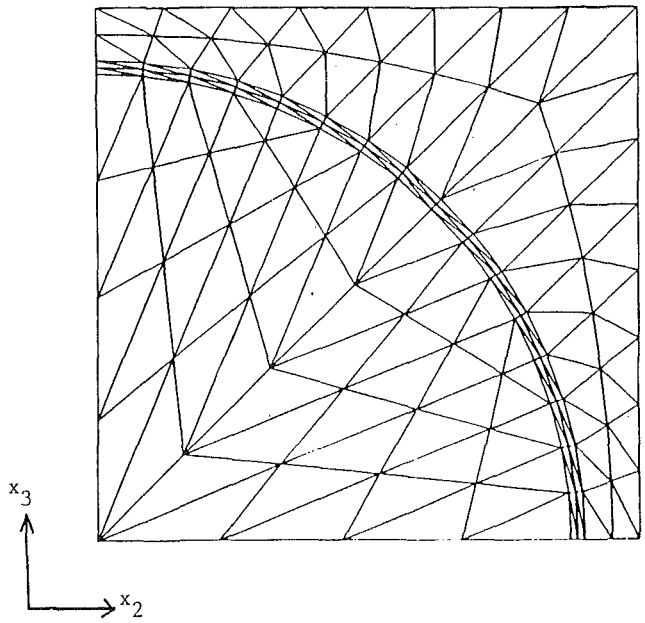

Fig. 1 Finite element mesh used for the fiber-matrix micromechanics model

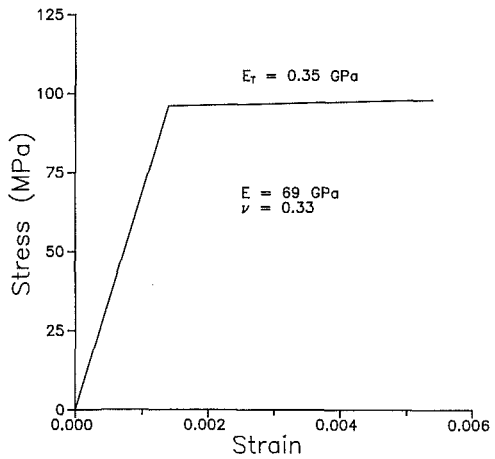

Fig. 2 Uniaxial tension stress-strain plot of a ductile matrix material

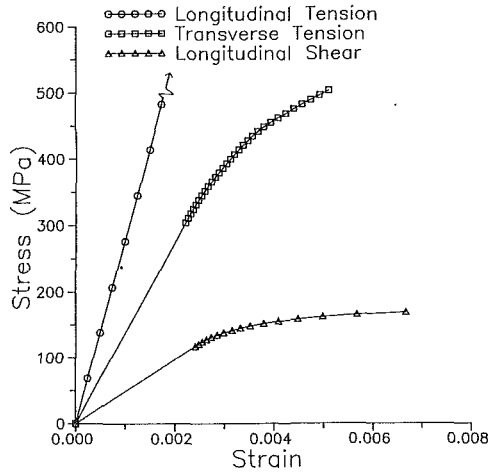

Fig. 3 Micromechanics generated stress-strain curves for longitudinal tension, transverse tension, and longitudinal shear loadings

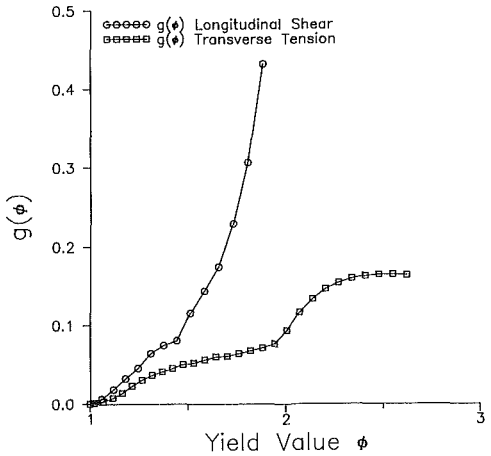

Fig. 4 Scalar-hardening coefficient plotted as a function of the yield surface for transverse tension and longitudinal shear load paths

resents a viable alternative to extensive experimental characterization of materials, particularly for multiaxial behavior. For instance, parametric studies involving different fiber volumes and constituent properties are readily carried out, thereby allowing one to characterize a wide variety of materials under various loading conditions.

The finite element micromechanics analysis used in this investigation is a generalized plane-strain analysis of a quarter fiber and surrounding matrix, representative of a continuous fiber unidirectional composite material, as shown in Fig. 1. The fiber direction is taken to be x_1. A square packing array is assumed for the fibers.

For example purposes, we choose to model the fiber as a stiff transversely isotropic material which is linear elastic to failure. The matrix material is softer than the fiber and is assumed to behave elastic plastically. The uniaxial stress-strain curve for the matrix constituent is taken to be bilinear as shown in Fig. 2. The specific elastic coefficients for the fiber are:

$$E_{11} = 417.0 \text{ GPa}, \; E_{22} = E_{33} = 208.5 \text{ GPa},$$

$$G_{12} = G_{13} = G_{23} = 83.4 \text{ GPa}, \; \nu_{11} = \nu_{13} = 0.2, \; \nu_{23} = 0.25.$$

The constituent behavior described above is not intended to model any specific material. Rather, the intent is to demonstrate the fundamental problems associated with modeling highly anisotropic materials of this nature. However, it should be noted that the ratios of the elastic moduli are typical of those found in many high performance composites such as boron/aluminum and silicon-carbide/titanium.

Figure 3 represents the behavior of the composite material as predicted by a micromechanics finite element analysis. The figure shows longitudinal tension (σ_{11}), transverse tension (σ_{22}), and longitudinal shear (σ_{12}) loadings. Note in Fig. 3 the longitudinal tension curve is not shown in its entirety since it is elastic to failure. The data clearly indicate the value for the scalar-hardening coefficient is strongly dependent on which loading is used to define $g(\phi)$. For instance, the longitudinal tension stress-strain curve is essentially linear elastic to failure resulting in no plastic strain. Hence, a value of $g(\phi) = 0$ is indicated. In contrast, the behavior of the same composite material subjected to shear loads is highly nonlinear, indicating a value $g(\phi) > 0$. Furthermore, the value of $g(\phi)$ is different for various loadings which exhibit plastic deformation. For instance, consider the longitudinal shear and transverse tension curves. Noting equation (23) the value of $g(\phi)$ may be determined for each load case as:

$$\sigma_{12}\text{: } g(\phi) = (1/G_{12}^T - 1/G_{12})/(8\,\phi M) \tag{28}$$

$$\sigma_{22}\text{: } g(\phi) = (1/E_{22}^T - 1/E_{22})/(4\,\phi\,(F+G)) \tag{29}$$

where G_{12} denotes the shear modulus and E_{22} represents the elastic modulus in the x_2-direction.

Figure 4 shows a plot of $g(\phi)$ for the transverse tension and longitudinal shear loadings as determined by equations (28) and (29). The figure clearly indicates a difference in the behavior of the scalar-hardening coefficient. This is also evidenced in Fig. 3 where it is seen that the longitudinal shear behavior is much more nonlinear than the transverse tension data. The question then arises as to what relation to use for $g(\phi)$ under multiaxial load cases.

An Invariant-Based Flow Rule

In this section we develop an advanced anisotropic plasticity theory in which the scalar-hardening coefficient is allowed to be load-path dependent. For comparison purposes, we assume a yield function identical to the one specified in equations (4) and (5). Furthermore, the plastic strain increments are assumed to be governed by equations (7) and (8), repeated for convenience as

$$d\epsilon_{ij}^p = g(\sigma)\left(\frac{\partial \Phi}{\partial \sigma_{rs}} d\sigma_{rs}\right)\frac{\partial \Phi}{\partial \sigma_{ij}}, \tag{30}$$

when

$$\frac{\partial \Phi}{\partial \sigma_{rs}} d\sigma_{rs} > 0 \quad \text{and} \quad \Phi(\sigma) = 0. \tag{31}$$

At this point we turn our attention to the scalar-hardening coefficient $g(\sigma)$. We note that g is a scalar function of a second-order tensor. The functional form of $g(\sigma)$ may be restricted by considering invariance properties of the material. For example, in modeling a unidirectional composite material, the usual approach is to assume the material is transversely isotropic. Under this assumption the functional form of $g(\sigma)$ must remain unchanged for arbitrary rotations about the axis of symmetry. Denoting this axis as x_1, the five transversely isotropic stress invariants for such coordinate rotations are given by Spencer (1971) as:

$$a_1 = \alpha_{11}, \quad a_2 = \sigma_{22} + \sigma_{33}, \quad a_3 = \sigma_{22}^2 + \sigma_{33}^2 + 2\sigma_{23}^2$$
$$a_4 = \sigma_{12}^2 + \sigma_{13}^2, \quad a_5 = \sigma_{22}\sigma_{12}^2 + \sigma_{33}\sigma_{13}^2 + 2\sigma_{12}\sigma_{13}\sigma_{23}. \tag{32}$$

A mathematically correct representation of $g(\sigma)$ must be of the form

$$g(\sigma) = g(a_1, a_2, a_3, a_4, a_5). \tag{33}$$

In order to further reduce equation (33), we must make some additional assumptions about the material behavior. First, we require the value of $g(\sigma)$ to remain unchanged when the signs of σ_{ij} are reversed. This implies that we must deal with quadratic forms for a_1, a_2, and a_5 as these invariants are odd functions of stress. We reject the fifth invariant for simplicity in that a_5^2 is sixth order in stress. A further simplification is achieved by rejecting the second invariant a_2. In doing so, we are restricting the nonlinear behavior of the model in the sense that the behavior of $g(\sigma)$ will be identical for both transverse tension and transverse shear load paths. The micromechanics analysis used in this paper was unable to verify this as a square packing geometry is not truly transversely isotropic. However, it should be noted that the invariant formulation is capable of modeling differences in these load paths simply by incorporating the second invariant in the function form of g. Therefore, a reduced form for $g(\sigma)$ is

$$g(\sigma) = g(a_1, a_3, a_4). \tag{34}$$

Finally, one may be tempted to eliminate the first invariant a_1 as the material is linear elastic to failure under uniaxial tension in the fiber direction. However, longitudinal tensile stresses do influence the nonlinear behavior of the material under multiaxial loads. This can only be accounted for by retaining a_1.

To complete the theory a specific functional form for $g(a_1, a_3, a_4)$ must be developed using experimental and/or micromechanics data. The specific form will be material dependent.

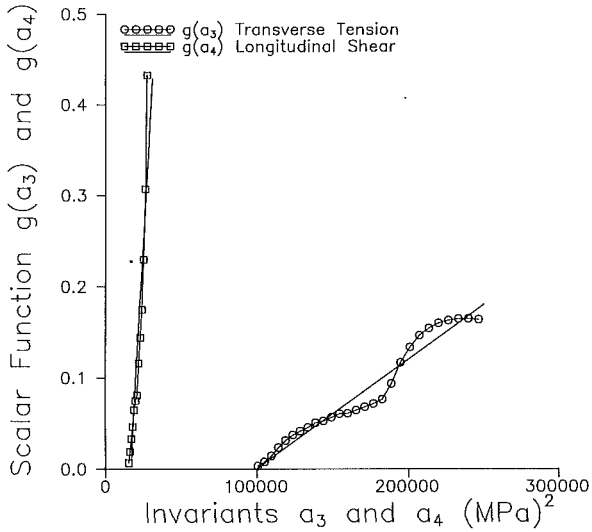

Fig. 5 Scalar-hardening coefficient plotted as a function of the stress invariants a_3 and a_4 for transverse tension and longitudinal shear load paths, respectively

To begin, we consider specific load paths in which the invariants a_3 and a_4 may be isolated. To study the effects of a_4 alone we consider a longitudinal shear test in which $\sigma_{12} \neq 0$ and all other $\sigma_{ij} = 0$. Rewriting equation (28) as a function of the fourth invariant gives

$$\sigma_{12}\text{: } g_4(a_4) = (1/G_{12}^T - 1/G_{12})/(16\, a_4 M^2). \tag{35}$$

The third invariant may be isolated by considering a transverse tension test in the x_2-direction. For this we can rewrite equation (29) to obtain

$$\sigma_{22}\text{: } g(a_3) = (1/E_{22}^T - 1/E_{22})/(4\, a_3\, (F+G)^2). \tag{36}$$

The behavior of the scalar-hardening coefficient as a function of the third and fourth invariants is shown in Fig. 5. A linear regression analysis of the data yielded the following forms for g_3 and g_4:

$$g_3 = 1.2\ (10^{-6})\ a_3 - 1.2\ (10^{-1})\ \text{MPa} \tag{37}$$

$$g_4 = 3.0\ (10^{-5})\ a_4 - 0.5\ \text{MPa}. \tag{38}$$

At this point one must assume a functional relationship for the scalar-hardening coefficient under multiaxial loads. The form chosen must reduce to the specific forms defined by equations (37) and (38) for the corresponding loading conditions. Furthermore, the influence of longitudinal stress on the nonlinear behavior must be incorporated. A negligible coupling effect between σ_{11} and σ_{22} was observed in biaxial micromechanics analyses. However, there was significant coupling between σ_{11} and σ_{12} in biaxial runs. Therefore, the final form for the scalar-hardening coefficient was taken as

$$g(a_1, a_3, a_4) = \frac{a_3}{a_3^*} g_3(a_3) + \frac{a_4}{a_4^*}(g_4(a_4) + g_1(a_1)) \tag{39}$$

where a_3^* and a_4^* are values of the stress invariants at the current yield surface as determined from a uniaxial transverse tension and a longitudinal shear load case, respectively. The influence of the first invariant was determined from a single biaxial micromechanics test in which $\sigma_{11} = 10\sigma_{12}$. The specific functional form taken for $g_1(a_1)$ is

$$g_1(a_1) = 6.5\ (10^{-8})\ a_1^2 - 0.5\ (10^{-14})\ a_1^4. \tag{40}$$

It should be noted that the coefficients of equation (40) are several orders of magnitude smaller than those of equation (38). This is consistent with the notion that longitudinal tension stresses do not have a major influence on the yielding of the material. However, the work performed here indicates that these stresses cannot be totally neglected.

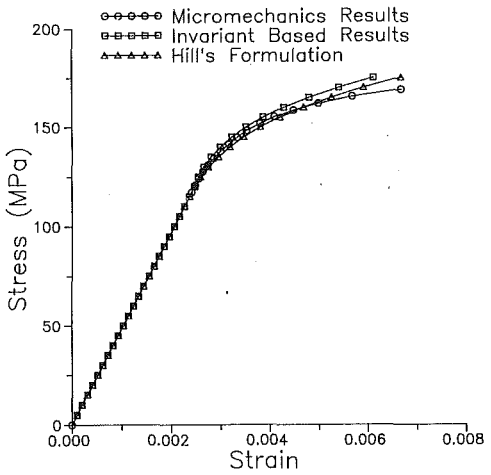

Fig. 6 Comparison of numerical micromechanics predictions with the invariant-based formulation and Hill's theory for a longitudinal shear loading, σ_{12}

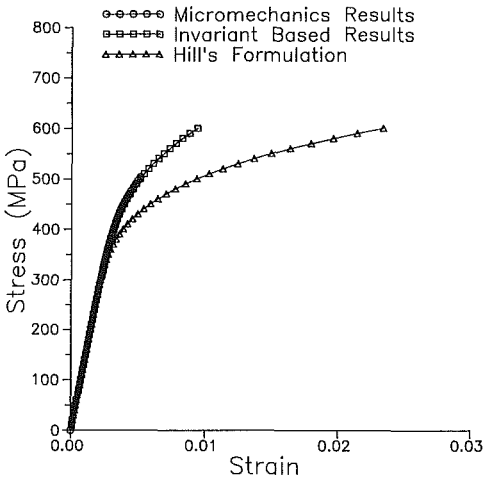

Fig. 7 Comparison of numerical micromechanics predictions with the invariant-based formulation and Hill's theory for a transverse tension loading, σ_{22}

The form of the scalar-hardening coefficients shown in equation (39) is now assumed to be valid for general three-dimensional loadings. While the approach used to determine a form for the scalar-hardening coefficient is not general, it does indicate the salient feature of the invariant based theory in that $g(\sigma)$ is allowed to vary on the yield surface. This may be contrasted with the classical theory in which $g(\sigma)$ is a constant everywhere on the yield surface.

Results

In this section we compare the invariant-based theory and the classical theory based on the work of Hill (1950) for a transversely isotropic material using a series of uniaxial and biaxial load cases predicted by finite element micromechanics. It should be noted that all shear stress-strain data is presented graphically using the engineering definition of strain as is customary. However, the equations developed in the previous section are based on the tensorial definition of shear strain to take full advantage of indicial notation.

To begin, one must choose a specific load path to determine the scalar-hardening coefficient $g(\phi)$ to be used in the Hill formulation. For example purposes, we shall determine $g(\phi)$ using the longitudinal shear data shown in Fig. 3. This is a reasonable approach in that σ_{12} is the stress for which the most pronounced nonlinearity is observed. To choose the longitudinal tension curve, as is traditional for isotropic plasticity theory, would indicate $g(\phi)$ as zero. This would suppress all plastic strains for any applied load path. This fact alone should cause one to question the validity of an effective stress-strain curve for anisotropic materials of this type. Finally, because the longitudinal tension behavior of the material is linear elastic to failure, the yield stress is defined as the ultimate stress for this loading.

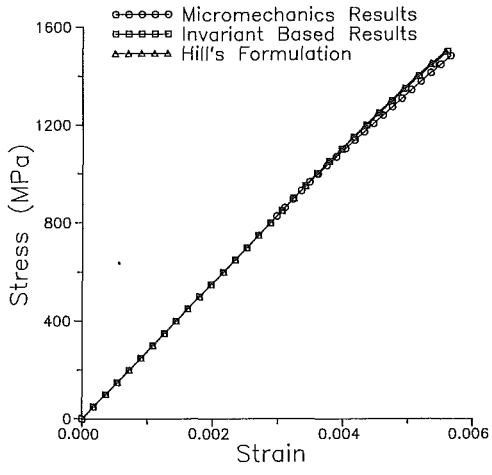

Fig. 8 Comparison of σ_{11}-ϵ_{11} stress-strain predictions for a combined longitudinal tension and longitudinal shear loading where $\sigma_{11} = 10\ \sigma_{12}$

One could argue that an optimum effective stress-strain curve could be chosen based on averaging all available data in order to minimize the error. This was the approach taken by Kenaga et al. (1987) for a biaxial test program. However, for fully multiaxial stress states such a procedure is unclear. Furthermore, as will be demonstrated, one can not totally eliminate the errors in this manner as the error is not consistent.

Figures 6 and 7 compare the longitudinal shear (σ_{12}) and uniaxial transverse tension (σ_{22}) numerical micromechanics predictions with the invariant-based theory and the classical formulation put forth by Hill. As expected, the two theories fall extremely close to the micromechanics prediction for longitudinal shear loading as shown in Fig. 6. However, the results are markedly different for transverse tension loading depicted in Fig. 7. For this case, the invariant-based theory tracks the micromechanics predictions while the Hill formulation predicts a much softer response. The discrepancy in the value predicted by the Hill formulation may be attributed to $g(\phi)$ being a constant for the entire yield surface.

A series of biaxial as opposed to uniaxial loadings were also modeled using finite element micromechanics to further compare the two plasticity theories. In each case the loading was assumed to be proportional and monotonically increasing. Figure 8 presents a $\sigma_{11} - \epsilon_{11}$ stress-strain curve for a combined longitudinal tension (σ_{11}) and longitudinal shear (σ_{12}) loading where $\sigma_{11} = 10\sigma_{12}$. The numerically predicted behavior of the material is near linear elastic. Both the invariant-based and Hill formulations agree quite well with the numerical results. The theory developed by Hill works well in predicting this behavior because the anisotropic yield parameter G is very small, tending to suppress incremental plastic strain values for this loading mode. Figure 9 shows the $\sigma_{12} - \gamma_{12}$ response for the same biaxial loading ($\sigma_{11} = 10\sigma_{12}$) case. Here, the invariant formulation performs slightly better than the Hill formulation although both theories are close to the micromechanics response. However, it is worth noting that the Hill formulation is conservative for this case, which is in sharp contrast to other biaxial cases. This is especially interesting in that $g(\phi)$ was determined from shear data showing the greatest degree of nonlinearity.

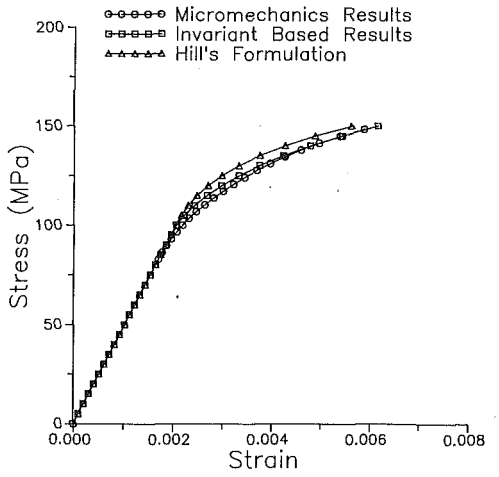

Fig. 9 Comparison of σ_{12}-γ_{12} stress-strain predictions for a combined longitudinal tension and longitudinal shear loading where $\sigma_{11} = 10\ \sigma_{12}$

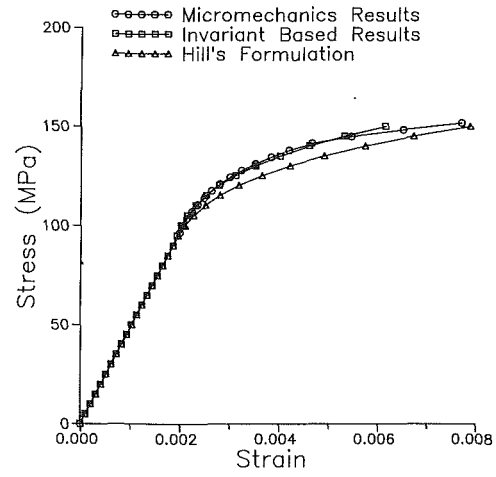

Fig. 12 Comparison of σ_{12}-γ_{12} stress-strain predictions for a combined transverse tension and longitudinal shear loading where $\sigma_{22} = 2\sigma_{12}$

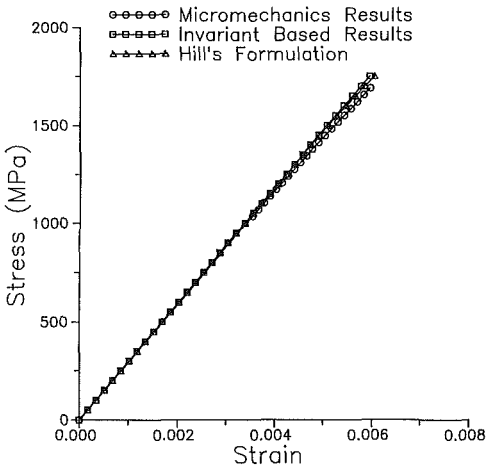

Fig. 10 Comparison of σ_{11}-ϵ_{11} stress-strain predictions for a combined longitudinal tension and transverse tension loading where $\sigma_{11} = 5\sigma_{22}$

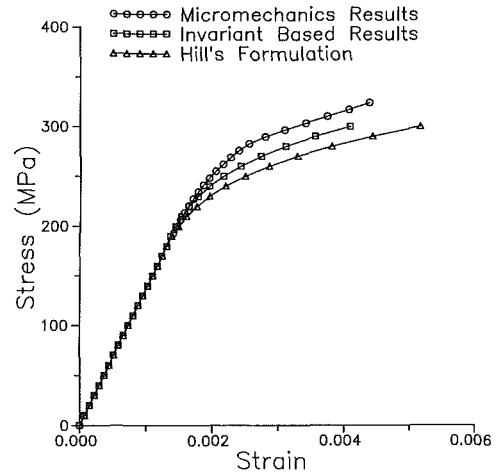

Fig. 13 Comparison of σ_{22}-ϵ_{22} stress-strain predictions for a combined transverse tension and longitudinal shear loading where $\sigma_{22} = 2\sigma_{12}$

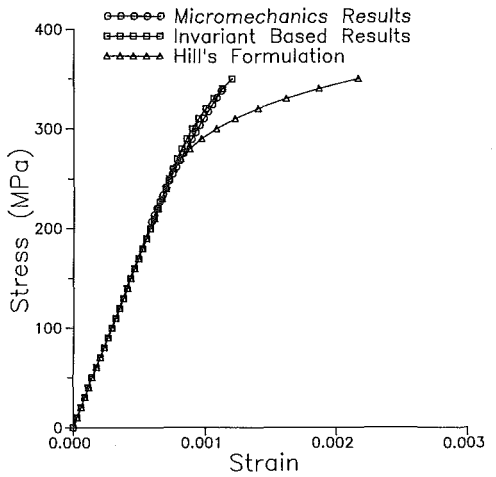

Fig. 11 Comparison of σ_{22}-ϵ_{22} stress-strain predictions for a combined longitudinal tension and transverse tension loading where $\sigma_{11} = 5\sigma_{22}$

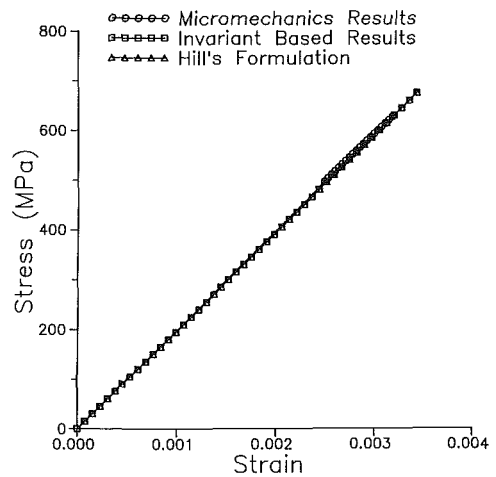

Fig. 14 Comparison of σ_{22}-ϵ_{22} stress-strain predictions for a biaxial loading given by $\sigma_{22} = \sigma_{33}$

Figures 10 and 11 compare the plasticity theories for a biaxial loading combining longitudinal tension (σ_{11}) and transverse tension (σ_{22}) where $\sigma_{11} = 5\sigma_{22}$. The longitudinal tension data shown in Fig. 10 again reflect a linear response for all three curves. However, the transverse tension stress-strain response, Fig. 11, shows the invariant formulation is superior to the classical theory in following the numerical micromechanics results.

Similar results were found for biaxial analyses involving transverse tension (σ_{22}) and longitudinal shear (σ_{12}) as shown in Figs. 12 and 13. The load path was taken to be $\sigma_{22} = 2\sigma_{12}$. For the longitudinal shear results plotted in Fig. 12, the in-

variant-based formulation tracks the micromechanics analysis while the Hill formulation is significantly softer. The transverse tension results plotted in Fig. 13 are interesting in that both theories show a softer response than that predicted by micromechanics. However, the invariant based theory represents a substantial improvement when compared to the Hill formulation.

Finally, Fig. 14 shows a comparison of the two theories with micromechanics for a biaxial plot where $\sigma_{22} = \sigma_{33}$. In this case both theories perform extremely well.

In summary, the correlation of the invariant-based formulation with the predicted micromechanics results is excellent. In contrast, the Hill formulation worked well for some load paths while breaking down for others. The improved results of the invariant based theory may be attributed to allowing the value of the scalar-hardening coefficient to vary over the yield surface. The results are particularly pleasing in that a relatively simple form of the scalar-hardening function was assumed.

Discussion

In this paper we have developed a generalized anisotropic plasticity theory using an invariant-based flow rule. In particular, we allow the value of the scalar-hardening coefficient to vary depending on the specific location of the stress state on the yield surface. The functional form of the scalar-hardening function is developed in terms of the stress invariants and without the assumption of an effective stress-strain relation. The specific form of $g(\sigma)$ may be significantly reduced by invoking invariance requirements on g based on material symmetry. This formulation permits more accurate modeling of uniaxial and multiaxial load cases without imposing the overly restrictive requirement of an effective stress-strain relation.

Development of an invariant-based flow rule has been slowed in the past by the specific requirement for an effective stress-strain relation. As has been demonstrated, such a relation generally does not exist for high performance, unidirectional composite materials. The assumed existence of an effective stress-strain relation implies the scalar-hardening coefficient is constant everywhere on the yield surface. Mathematically, this is an overly restrictive assumption in that $g(\sigma)$ is in general a function of the stress state. However, this fact is not immediately observable unless one casts the constitutive law in the form shown by equation (7).

Finally, we note that the invariant based theory developed here is based on an isotropic hardening model. For structures subjected to cyclic loading or significantly varying load paths it may be necessary to develop a kinematic hardening model. We refer to the excellent experimental work on metal matrix composites conducted by Dvorak et al. (1988) as an example.

Acknowledgments

This research was sponsored by the Honeywell Corporation, Defense Systems Division (A.C. Hansen) and Martin Marietta Corporation (D. M. Blackketter and D. E. Walrath).

References

Adams, D. F., and Crane, D. A., 1984, "Combined Loading Micromechanical Analysis of a Unidirectional Composite," *Composites*, Vol. 15, No. 3.

Boehler, J. P., 1987, *Anisotropic Hardening of Rolled Sheet-Steel* (CISM Courses and Lectures No. 292), J. P. Boehler, ed., Springer-Verlag, New York, pp. 123–139.

Dvorak, G. J., Bahei-El-Din, Y. A., Macheret, Y., and Liu, C. H., 1988, "An Experimental Study of Elastic-Plastic Behavior of a Fibrous Boron-Aluminum Composite," *J. Mech. Phys. Solids*, Vol. 36, pp. 655–687.

Gotoh, M., 1977, "A Theory of Plastic Anisotropy Based on a Yield Function of Fourth Order (Plane Stress State)—I," *International Journal of Mechanical Sciences*, Vol. 19, pp. 505–512.

Griffin, O. H., Kamat, M. P., and Herakovich, C. T., 1981, "Three-dimensional Inelastic Finite Element Analysis of Laminated Composites," *J. Composite Materials*, Vol. 5, pp. 543–560.

Hill, R., 1950, *The Mathematical Theory of Plasticity*, Oxford University Press, London, U.K.

Ivey, H. J., 1961, "Plastic Stress-Strain Relations and Yield Surfaces for Aluminum Alloys," *J. Mech. Eng. Sci.*, Vol. 3, No. 15.

Kenaga, D., Doyle, J. F., and Sun, C. T., 1987, "The Characterization of Boron/Aluminum Composite in the Nonlinear Range as an Orthotropic Elastic-Plastic Material," *Journal of Composite Materials*, Vol. 21, pp. 516–531.

Martin, J. B., 1975, *Plasticity: Fundamentals and General Results*, MIT Press, Cambridge, Mass.

Miller, A. K., and Adams, D. F., 1977, "Hydrothermal Microstresses in a Unidirectional Composite Exhibiting Inelastic Material Behavior," *Journal of Composite Materials*, Vol. 11, No. 3, pp. 285–299.

Spencer, A. J. M., 1974, *Continuum Physics I*, Part III, A. C. Eringen, ed., Academic Press, London, U.K.

Spencer, A. J. M., 1987, "Kinematic Constraints, Constitutive Equations and Failure Rules for Anisotropic Material," (CISM Courses and Lectures No. 292), J. P. Boehler, ed., Springer-Verlag, New York, pp. 187–201.

Sun, C. T., and Chen, J. L., 1988, "A Simple Flow Rule for Characterizing Nonlinear Behavior of Fiber Composites," *Proceedings of the International Conference on Composite Materials*, London, U.K.

Acoustic Emission From Single-Plate Martensitic Transformation

Xiangying Liu
Project Engineer,
Automated Analysis Corporation,
Peoria, IL 61615

Elijah Kannatey-Asibu, Jr.
Associate Professor,
Department of Mechanical Engineering and
Applied Mechanics,
The University of Michigan,
Ann Arbor, MI 48109
Assoc. Mem. ASME

Martensitic transformation occurs in a diffusionless manner at high velocity, with acoustic emission (AE) being generated during the process. The AE signal contains information about the dynamic process of martensitic transformation. In this analysis, a model is developed for the AE signal, or dynamic displacement, from the transformation strains and the growth process of martensitic transformation in an elastic half-space using Green's functions. The AE signal amplitude is found to be inversely proportional to the distance between the martensite source and the sensor, and to the duration of transformation. It also depends on the orientation of the martensite plate. The spectral bandwidth increases as the duration of plate formation decreases. In addition, raising the carbon content increases the fraction of plate martensite, and consequently the signal amplitude.

Introduction

Acoustic emission (AE) is defined as the high-frequency elastic waves from the rapid generation of strains (or stresses) in processes such as martensitic transformation, crack formation, and plastic deformation. Martensite may form during the welding of some alloy and high-carbon steels, and since it is a potential cold-crack former, it is desirable to monitor its formation. Some amount of work has been done in this regard.

Rice (1980) considered AE from damage processes such as slip microcracking. He gave general representation of the displacement field of an AE event in terms of the double-couple response to a distribution of "moment density tensor" in the source region. Simmons and Wadley (1984) developed an integral equation for the acoustic emission displacement field due to the formation of inhomogeneous inclusions during phase transformation. Their solution is elegant and general, but the growth process of martensitic transformation is not explicitly considered, and the result cannot be interpreted in detail. Kannatey-Asibu and Dong (1986) subsequently developed a simplified model for martensitic transformation using Gibbs free energy change, where a relationship between the RMS (root-mean-square) voltage of the AE signal, the transformation temperature, the cooling rate, and the transformed volume was obtained. Liu and Kannatey-Asibu (1990) extended this model for athermal martensitic transformation and verified it experimentally using AISI 4340, 1045, 1060, and 1075 steels. The intensity of the AE signal generated during transformation was found to be proportional to the cooling rate and the volume of specimen. The AE signal was also found to be related to the carbon content of the steel and the fraction of martensite.

In this study, the stress-free transformation strains for martensitic transformation and Green's functions are used to obtain the dynamic displacement at the epicenter. Solutions for the AE signal in the time and frequency domains for a double cone-shaped martensite plate are obtained.

Analysis

Let us define the martensite source as a region V inside an elastic isotropic and homogeneous medium D (Fig. 1); this region undergoes a spontaneous, uniform, nonelastic deformation strain or stress-free transformation strain $\epsilon^*_{mn}(\mathbf{x}', t')$ at position $\mathbf{x}'$ and time t', while constrained by the surrounding

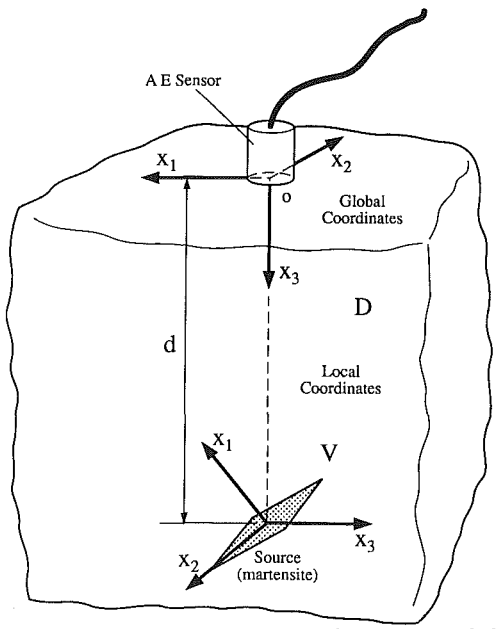

Fig. 1 A martensite plate inside an elastic homogeneous half-space

Contributed by the Applied Mechanics Division of THE AMERICAN SOCIETY OF MECHANICAL ENGINEERS for publication in the JOURNAL OF APPLIED MECHANICS.

Discussion on this paper should be addressed to the Technical Editor, Prof. Leon M. Keer, The Technological Institute, Northwestern University, Evanston, IL 60208, and will be accepted until two months after final publication of the paper itself in the JOURNAL OF APPLIED MECHANICS. Manuscript received by the ASME Applied Mechanics Division, Aug. 8, 1989; final revision, June 4, 1990.

material. If the boundary L of D is traction-free, then the resulting total displacement field at time t in the global coordinate system $\mathbf{x}$ is given (Willis, 1965; Mura, 1983) as

$$u_i(\mathbf{x},t) = -\int_V \int_{-\infty}^{+\infty} C_{jlmn}\epsilon^*_{mn}(\mathbf{x}',t')G_{ij,l}(\mathbf{x},\mathbf{x}',t-t')dt'dV \quad (1)$$

where

$u_i(\mathbf{x},t)$ = displacement in the x_i-direction at position $\mathbf{x}$ and time t;

C_{jlmn} = elastic constant, with $j,l,m,n = 1,2,3$;

$\epsilon^*_{mn}(\mathbf{x}',t')$ = stress-free transformation strain or eigenstrain at position $\mathbf{x}'$ and time t', with $m,n = 1,2,3$;

$G_{ij}(x,x',t-t')$ = Green's function or displacement component in the x_i-direction at sensor location $\mathbf{x}$ and time t due to a unit impulse force in the x_j-direction at $\mathbf{x}'$ and time t'; and

$G_{ij,l}(x,x',t-t') = \partial G_{ij}(x,x',t-t')/\partial x_l$.

The stress-free transformation strain or eigenstrain is the nonelastic strain such as thermal expansion, phase transformation, plastic, or misfit strain (Mura, 1983).

Considering the effect of martensite growth, we can write the stress-free transformation strain as

$$\epsilon^*_{mn}(\mathbf{x}',t') = \epsilon^*_{mn}H(t'-t_M) \quad (2)$$

where

ϵ^*_{mn} = magnitude of $\epsilon^*_{mn}(\mathbf{x}',t')$;

$H(t'-t_M)$ = the Heaviside unit step function; and

t_M = the martensite front propagation time, $0 \le t_M \le \tau$.

The transformation front is considered to be at position $\mathbf{x}'$ at time t_M. Thus, the stress-free transformation strain can be written as a function of t_M instead of $\mathbf{x}'$ in equation (2).

Since the stress-free transformation strain from the martensitic transformation is usually defined in the local coordinate system $\mathbf{X}$ (which is parallel to the crystallographic directions of the austenite matrix in this analysis) and the local coordinates X_1, X_2, X_3 of the martensite plate do not necessarily coincide with the global coordinates x_1, x_2, x_3, a transformation matrix $\mathbf{a}$ has to be applied to the stress-free transformation strain (Boresi and Chong, 1987):

$$\mathbf{a} = \begin{pmatrix} a_{11} & a_{12} & a_{13} \\ a_{21} & a_{22} & a_{23} \\ a_{31} & a_{32} & a_{33} \end{pmatrix}$$

where $a_{ij} = \cos(\phi_{ij})$ denotes the cosine of the angle between the x_i-axis and X_j-axis.

The strain in the global coordinate system $\mathbf{x}$ is thus rewritten as

$$\epsilon^*_{mn}(\mathbf{x}',t') = a_{\alpha m}a_{\beta n}\epsilon^*_{\alpha\beta}H(t'-t_M) \quad (3)$$

where $\epsilon^*_{\alpha\beta}$ is the strain magnitude in the coordinate system $\mathbf{X}$, and $\alpha,\beta = 1,2,3$. Substituting for $\epsilon^*_{mn}(\mathbf{x}',t')$ in equation (1) gives

$$u_i(\mathbf{x},t) = -C_{jlmn}a_{\alpha m}a_{\beta n}\epsilon^*_{\alpha\beta}\int_V \int_{-\infty}^{+\infty} H(t' - t_M)G_{ij,l}(\mathbf{x},\mathbf{x}',t-t')dt'dV. \quad (4)$$

Further expressing equation (4) in terms of Green's function for a step force input (Johnson, 1973), we have

$$u_i(\mathbf{x},t) = -C_{jlmn}a_{\alpha m}a_{\beta n}\epsilon^*_{\alpha\beta}\int_V \int_{-\infty}^{+\infty} (\partial H(t' - t_M)/\partial t')G^H_{ij,l}(\mathbf{x},\mathbf{x}',t-t')dt'dV \quad (5)$$

where $G^H_{ij,l}$ is the spatial derivative of Green's function for a step force input.

Since $\partial H(t'-t_M)/\partial t' = \delta(t'-t_M)$, we now have

$$u_i(\mathbf{x},t) = -C_{jlmn}a_{\alpha m}a_{\beta n}\epsilon^*_{\alpha\beta}\int_V \int_{-\infty}^{+\infty} \delta(t' - t_M)G^H_{ij,l}(\mathbf{x},\mathbf{x}',t-t')dt'dV \quad (6)$$

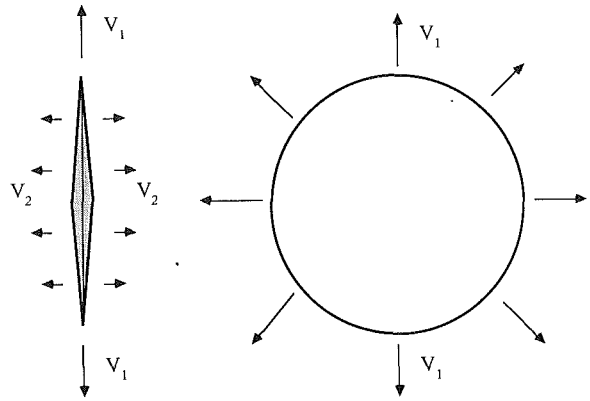

Fig. 2 Schematic of martensite growth

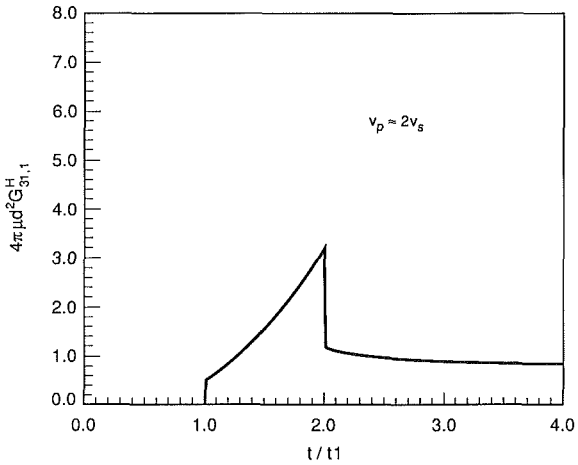

Fig. 3 Green's function $4\pi\mu d^2G^H_{31,1} = 4\pi\mu d^2G^H_{32,2}$

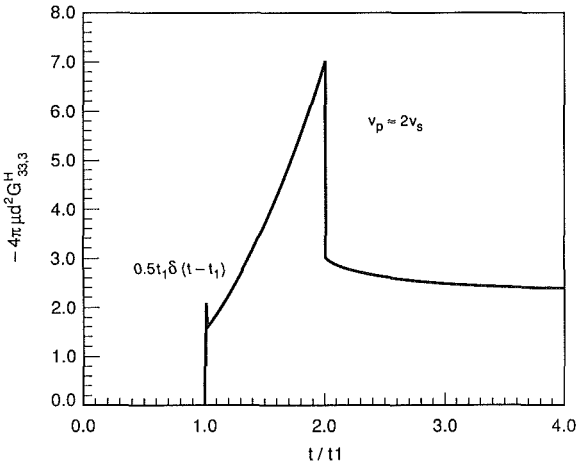

Fig. 4 Green's function $-4\pi\mu d^2G^H_{33,3}$

which further reduces to

$$u_i(\mathbf{x},t) = -C_{jlmn}a_{\alpha m}a_{\beta n}\epsilon^*_{\alpha\beta}\int_V G^H_{ij,l}(\mathbf{x},\mathbf{x}',t-t_M)dV. \quad (7)$$

Now consider a double cone-shaped martensite plate transforming at a radial velocity of v_1 and simultaneously thickening at velocity v_2 (Fig. 2). The midrib area at time t_M is

$$A(t_M) = \pi v_1^2 t_M^2$$

and the amount of martensite transformed during the interval dt_M is

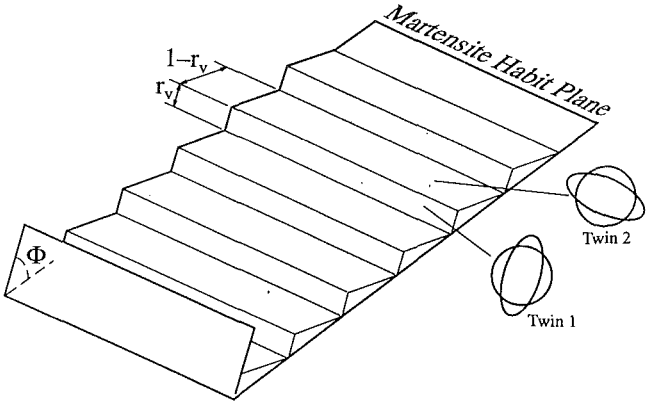

Fig. 5 Regions 1 and 2 for a twinned martensite plate (Porter and Easterling, 1981)

$$dV = 2A(t_M)v_2 dt_M = 2\pi v_1^2 v_2 t_M^2 dt_M. \tag{8}$$

Equation (7) can then be rewritten as

$$u_i(\mathbf{x},t) = -2\pi v_1^2 v_2 C_{jlmn} a_{\alpha m} a_{\beta n} \epsilon^*_{\alpha\beta} \int_0^\tau G^H_{ij,l}(\mathbf{x},\mathbf{x}',t-t_M) t_M^2 dt_M \tag{9}$$

where τ is the duration of transformation of a martensite plate.

Applying the Taylor expansion to $G^H_{ij,l}(\mathbf{x},\mathbf{x}',t-t_M)$ about the centroid of the martensite source $\mathbf{x}'_0$, we have

$$G^H_{ij,l}(\mathbf{x},\mathbf{x}',t-t_M) = G^H_{ij,l}(\mathbf{x},\mathbf{x}'_0,t-t_M) + G^H_{ij,lk}(\mathbf{x},\mathbf{x}'_0,t-t_M)\Delta\mathbf{x}'_k + \dots$$

where $\Delta\,\mathbf{x}'_k = \mathbf{x}'_k - \mathbf{x}'_0$. Considering a point source approximation, we can then neglect the higher-order terms:

$$u_i(\mathbf{x},t) = -2\pi v_1^2 v_2 C_{jlmn} a_{\alpha m} a_{\beta n} \epsilon^*_{\alpha\beta} \int_0^\tau G^H_{ij,l}(\mathbf{x},\mathbf{x}'_0,t-t_M) t_M^2 dt_M. \tag{10}$$

The approximation is valid if the size of the source (martensite) is much smaller than the distance d between the source and the sensor and the signal frequency information considered is not too high. (The errors introduced by the point source approximation are discussed by Simmons and Clough, 1981.) The displacement along direction x_3 (perpendicular to the sensor mounting plane) at sensor location (0, 0, 0) can thus be approximated as

$$u_3(t) = -2\pi v_1^2 v_2 C_{jlmn} a_{\alpha m} a_{\beta n} \epsilon^*_{\alpha\beta} \int_0^\tau G^H_{3j,l}(t-t_M) t_M^2 dt_M \tag{11}$$

where $G^H_{3j,l}(\mathbf{0},\mathbf{x}'_0,t-t_M)$ is simplified as $G^H_{3j,l}(t-t_M)$.

For a sensor located at the epicenter in an elastic half-space, all $G^H_{3j,l} = 0$, except $G^H_{31,1} = G^H_{32,2}$ (see Fig. 3) and $G^H_{33,3}$ (Fig. 4) (Sinclair, 1979). As a result, equation (11) becomes

$$u_3(t) = -2\pi v_1^2 v_2 C_{jjmn} a_{\alpha m} a_{\beta n} \epsilon^*_{\alpha\beta} \int_0^\tau G^H_{3j,j}(t-t_M) t_M^2 dt_M. \tag{12}$$

For isotropic materials, the nonzero C_{jlmn} are given by

$$C_{1111} = C_{2222} = C_{3333} = \lambda + 2\mu$$
$$C_{1122} = C_{1133} = C_{2233} = C_{2211} = C_{3311} = C_{3322} = \lambda$$
$$C_{2323} = C_{3232} = C_{3131} = C_{1313} = C_{1212} = C_{2121} = \mu.$$

For C_{jjmn}, the only nonzero terms are C_{jjmm}, where $j,m = 1,2,3$. Therefore, the displacement can be written as

$$u_3(t) = -2\pi v_1^2 v_2 C_{jjmm} a_{\alpha m} a_{\beta m} \epsilon^*_{\alpha\beta} \int_0^\tau G^H_{3j,j}(t-t_M) t_M^2 dt_M. \tag{13}$$

Figure 5 illustrates the twinned regions of a martensite plate. If the crystal lattice rearrangement is from f.c.c. to b.c.t. (as occurs in steels), then the stress-free transformation strains in the local coordinate system $\mathbf{X}$ are given in regions 1 and 2, respectively, by the tensors (Mura, 1983)

$$\epsilon^*(1) = \begin{bmatrix} \eta_1 & 0 & 0 \\ 0 & \eta_2 & 0 \\ 0 & 0 & \eta_1 \end{bmatrix}$$

and

$$\epsilon^*(2) = \begin{bmatrix} \eta_2 & 0 & 0 \\ 0 & \eta_1 & 0 \\ 0 & 0 & \eta_1 \end{bmatrix}.$$

Note that $\eta_1 = \dfrac{\sqrt{2}a - a_0}{a_0}$ and $\eta_2 = \dfrac{c - a_0}{a_0}$, where a and c are lattice parameters of the body-centered tetragonal structure, and a_0 is the lattice parameter of the face-centered cubic structure.

The overall strain for the plate is then given by

$$\epsilon^* = r_v\,\epsilon^*(1) + (1 - r_v)\epsilon^*(2)$$

where r_v is the volume ratio between regions 1 and 2 in a twinned martensite plate.

The necessary conditions for the overall strain to be an invariant plane strain is that one of its diagonal elements must vanish, i.e., $r_v\eta_1 + (1 - r_v)\eta_2 = 0$, giving $r_v = -\dfrac{\eta_2}{\eta_1 - \eta_2}$ (Khachaturyan, 1983). Substituting for r_v in the preceding equation yields

$$\epsilon^* = \begin{bmatrix} 0 & 0 & 0 \\ 0 & \eta_1 + \eta_2 & 0 \\ 0 & 0 & \eta_1 \end{bmatrix}. \tag{14}$$

From equation (14), $\epsilon^*_{\alpha\beta} = 0$, if $\alpha \neq \beta$. Equation (13) can then be written as

$$u_3(t) = -2\pi v_1^2 v_2 C_{jjmm} a^2_{\alpha m} \epsilon^*_{\alpha\alpha} \int_0^\tau G^H_{3j,j}(t-t_M) t_M^2 dt_M. \tag{15}$$

To compare signals from different martensite plates, we will use the same-sized reference. The total volume of the martensite plate is given by

$$V_M = \int_V dV = \int_0^\tau 2\pi v_1^2 v_2 t_M^2 dt_M = \frac{2}{3}\pi v_1^2 v_2 \tau^3. \tag{16}$$

The signals amplitude per unit volume of martensite thus becomes

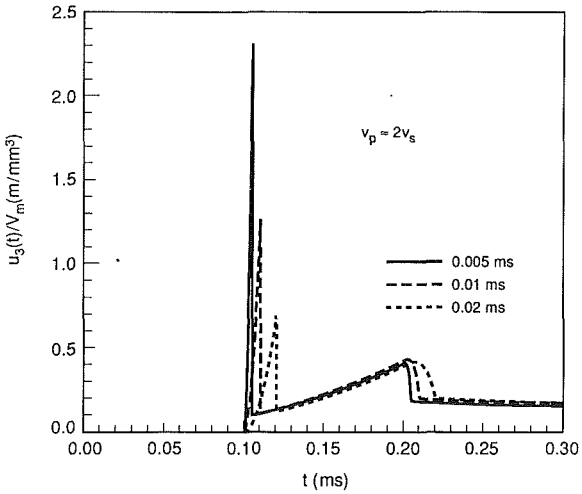

Fig. 6 Surface displacement for different durations of transformation τ

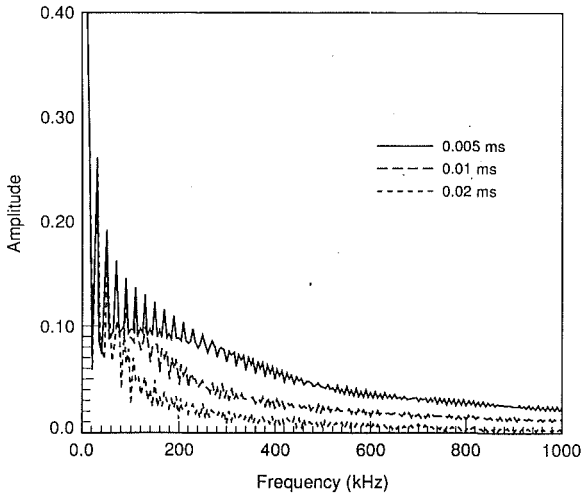

Fig. 7 Frequency response for different durations of transformation τ

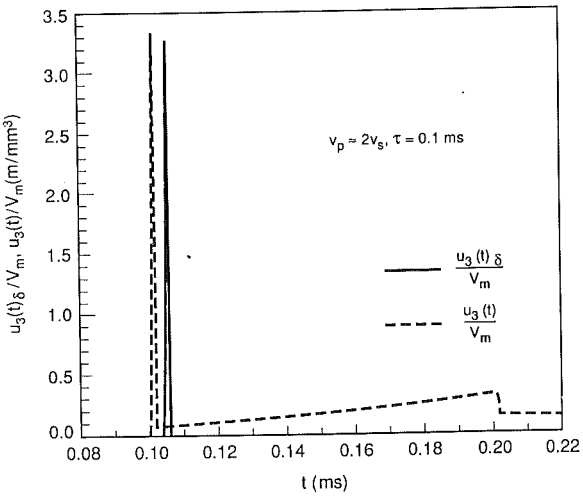

Fig. 8 AE signal from martensitic transformation

$$\frac{u_3(t)}{V_M} = -\frac{3}{\tau^3} C_{jjmm} a^2_{\alpha m} \epsilon^*_{\alpha\alpha} \int_0^\tau G^H_{3j,j}(t-t_M) t_M^2 dt_M. \qquad (17)$$

Figure 6 shows the displacement for different durations of the transformation τ. The displacement signals increase from zero at the longitudinal wave arrival time $t = t_1$ to a maximum at $t = t_1 + \tau$, with another peak occurring at the shear wave arrival time $t = 2t_1$. The first peak amplitude depends on the transformation period τ, increasing as the period decreases, while the second peak is nearly independent of the period. Both peaks, however, are delayed for longer transformations. The corresponding frequency responses obtained by the fast Fourier transform for different τ are illustrated in Fig. 7. Note that the frequency response contains periodic oscillations that result from truncation of the waveform.

As we can see from Figs. 3 and 4, there is an impulse at the longitudinal wave arrival time $t = t_1$ for $G^H_{33,3}$, but not for $G^H_{31,1}$ and $G^H_{32,2}$. The impulse has a dominant effect on the displacement $u_3(t)$ if $\frac{\tau}{t_1} \ll 1$. This can be shown as follows:

$$\frac{\int_0^\tau (G^H_{33,3})_\delta t_M^2 dt}{\int_0^\tau G^H_{33,3} t_M^2 dt} > \frac{\int_0^\tau 0.5 t_1 \delta(t-t_1-t_M) t_M^2 dt_M}{\int_0^\tau [0.5 t_1 \delta(t-t_1-t_M) + 7.2] t_M^2 dt_M} = \frac{(t-t_1)^2}{(t-t_1)^2 + 4.8\tau^2 \left(\frac{\tau}{t_1}\right)}$$

where $0.5\delta(t-t_1-t_M)$ is the impulse of the Green's function $-4\pi\mu d^2 G^H_{33,3}$ and 7.2 is its maximum amplitude. The above ratio is almost equal to unity, except when t is very close to t_1 ($u_3(t) = 0$ when $t = t_1$). Thus, the impulse has a dominant effect on $u_3(t)$. Similarly, we can show that the effects of $G^H_{31,1}$ and $G^H_{32,2}$ are also negligible. This is evident in Fig. 8 by comparing $u_3(t)_\delta$ and $u_3(t)$, where the $u_3(t)_\delta$ curve is shifted by 0.004 ms on the abscissa for clarity.

We thus rewrite equation (17) with $G^H_{33,3}(t-t_M)_\delta = -\frac{v_s^2}{2\pi\mu v_p^3 d}\delta(t-t_1-t_M)$ (Sinclair, 1979), and the signal amplitude per unit volume of martensite then becomes

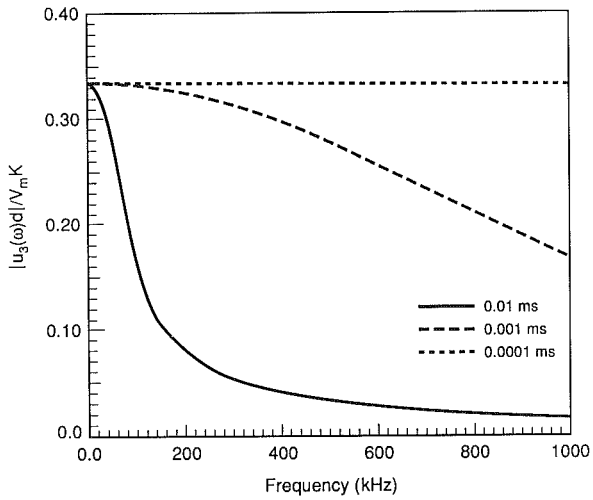

Fig. 9 Frequency response of AE signal from martensitic transformation

$$\frac{u_3(t)_\delta}{V_M} = \frac{3v_s^2}{2\pi\mu v_p^3 \tau^3 d} C_{33mm} a^2_{\alpha m} \epsilon^*_{\alpha\alpha} \int_0^\tau \delta(t-t_1-t_M) t_M^2 dt_M = \frac{3v_s^2}{2\pi\mu v_p^3 \tau^3 d} C_{33mm} a^2_{\alpha m} \epsilon^*_{\alpha\alpha} (t-t_1)^2, \; t_1 \le t \le t_1 + \tau \qquad (18)$$

or

$$\frac{u_3(t)_{\delta\max}}{V_M} = \frac{3v_s^2}{2\pi\mu v_p^3 \tau d} C_{33mm} a^2_{\alpha m} \epsilon^*_{\alpha\alpha} \qquad (19)$$

where

$t_1 = d/v_p$, = the longitudinal wave arrival time;
d = the distance between the sensor and martensite source; and
μ = the shear modulus.

Since the frequency response of the AE signal provides additional insight into the characteristics of the source, we also consider the analysis in the frequency domain. Taking the Fourier transform of equation (18), we get

$$\frac{u_3(\omega)_\delta}{V_M} = \int_{-\infty}^{+\infty} \frac{u_3(t)_\delta}{V_M} e^{-i\omega t} dt = \frac{3v_s^2}{2\pi\mu\tau^3 v_p^3 d} C_{33mm} a^2_{\alpha m} \epsilon^*_{\alpha\alpha} \int_{t_1}^{t_1+\tau} (t-t_1)^2 e^{-i\omega t} dt = \frac{K}{\omega^3 \tau^3 d} e^{-i\omega(t_1+\tau)} (2\omega\tau + i\omega^2\tau^2 + 2i(e^{i\omega\tau} - 1)) \qquad (20)$$

where $K=\frac{3v_s^2}{2\pi\mu v_p^3} C_{33mm}a_{\alpha m}^2\epsilon_{\alpha\alpha}^*$, and

$$\frac{|u_3(\omega)_\delta|}{V_M}=\frac{K}{\omega^3\tau^3 d}\sqrt{(2\omega\tau-2\sin(\omega\tau))^2+(\omega^2\tau^2-2+2\cos(\omega\tau))^2}. \tag{21}$$

The corresponding response is shown in Fig. 9. For very small $\omega\tau$, equation (21) can be further simplified by considering that $e^{i\omega\tau}-1\approx i\omega\tau-(\omega\tau)^2/2-i\omega^3\tau^3/6$. Thus,

$$\frac{u_3(\omega)_\delta}{V_M}\approx\frac{K}{3d}e^{-i\omega(t_1+\tau)} \tag{22}$$

and

$$\frac{|u_3(\omega)_\delta|}{V_M}\approx\frac{K}{3d}. \tag{23}$$

Discussion

To obtain the AE signals detected by an AE transducer, we must consider the response of the transducer and the instrumentation in the analysis. Assuming we have a transducer monitoring the process at position $\mathbf{x}=(0, 0, 0)$, we specify the response of the transducer and the instrumentation as $T_3(t-t')$. From equation (17), the voltage at time t due to martensite formation is then given by

$$\frac{V(t)_{AE}}{V_M}=-\frac{3}{\tau^3}C_{jjmm}a_{\alpha m}^2\epsilon_{\alpha\alpha}^*\int_{-\infty}^{\infty}\int_0^{\tau}T_3(t-t')G_{3j,j}^H(t'-t_M)t_M^2dt_Mdt' \tag{24}$$

or

$$\frac{V(\omega)_{AE}}{V_M}=\frac{-3}{\tau^3\omega^3}C_{jjmm}a_{\alpha m}^2\epsilon_{\alpha\alpha}^*T_3(\omega)G_{3j,j}^H(\omega)e^{-i\omega(t_1+\tau)}(2\omega\tau+i\omega^2\tau^2+2i(e^{i\omega\tau}-1)) \tag{25}$$

in the frequency domain.

For $\tau/t_1\ll 1$, equation (18) becomes

$$\frac{V(t)_{AE}}{V_M}=\frac{3v_s^2}{2\pi\mu v_p^3\tau^3 d}C_{33mm}a_{\alpha m}^2\epsilon_{\alpha\alpha}^*\int_{t_1}^{t_1+\tau}T_3(t-t')(t'-t_1)^2dt' \tag{26}$$

or

$$\frac{V(\omega)_{AE}}{V_M}=\frac{3v_s^2}{2\pi\mu v_p^3\tau^3 d\omega^3}C_{33mm}a_{\alpha m}^2\epsilon_{\alpha\alpha}^*T_3(\omega)e^{-i\omega(t_1+\tau)}(2\omega\tau+i\omega^2\tau^2+2i(e^{i\omega\tau}-1)) \tag{27}$$

in the frequency domain.

For an AE sensor sensitive only to displacement, the detected AE signal from martensitic transformation is a function of the resulting surface displacement. From equation (24), it is evident that the AE signal will depend on material properties such as C_{jjmm} or λ, μ. Thus, for a given set of conditions, different materials will result in different signal amplitudes. However, for a given material, say steel, these properties do not change very much; as a result, the AE signal will not be significantly affected. The results of the analysis further indicate that the amplitude of the AE displacement for a unit volume of material is inversely proportional to the distance between the source and sensor as well as the total time it takes to form a plate of martensite, as is evident from equation (19).

In carbon steels, there are two types of martensite morphology, i.e., lath martensite and plate martensite. Even though our analysis is based on a plate martensite we can make a qualitative comparison by first estimating the signals from both lath and plate martensites. Plate martensite in high-carbon steels transforms in about 10^{-6} to 10^{-7} s at a transformation velocity of about 1000 m/s (Bunshah and Mehl, 1953), while lath martensite has a much smaller velocity, the duration of formation being about 10^{-4} s (Liu, 1981). From Figs. 6 and 7, it is evident that the AE signal amplitude decreases as the duration of transformation increases. Thus, the intensity of the AE signal from the lath martensite is expected to be much smaller than that from plate martensite. As the carbon content increases, the fraction of plate martensite increases. Therefore, the AE signal is expected to increase in intensity. This explains why higher carbon steels generate signals of greater amplitudes (Speich and Fisher, 1972; Liu and Kannatey-Asibu, 1990).

Most commercial piezoelectric transducers have a frequency range of 50 KHz to 1 MHz, which cuts off the low and high-frequency information. Plots of the spectral characteristics of AE signals from martensitic transformation in this frequency range, in Figs. 7 and 9 show that the bandwidth of the AE frequency response increases as the duration of formation τ decreases. For the plate martensite in carbon steels, τ is about 10^{-6} to 10^{-7} s, resulting in an almost constant frequency response (Fig. 9). This means that the AE signal from plate martensitic transformation can be detected over a wider frequency range than that for lath martensite. If the process noise exceeds a certain frequency range and amplitude, then a resonant sensor can be used to minimize noise problems.

From the literature (Nishiyama, 1978) for tetragonal martensites in carbon steels, the lattice parameter $a_0=3.546+0.0467$ percent C, $c=2.8625+0.1176$ percent C, and the axial ratio $c/a=1.00+0.045$ percent C. Thus, for 0.4 percent C carbon steel, $\eta_1=0.134$, $\eta_2=-0.184$, and the non-zero terms in the overall strain matrix (equation (14)) become $\epsilon_{22}^*=-0.05$ and $\epsilon_{33}^*=0.134$, while for 0.8 percent C carbon steel, $\eta_1=0.126$, $\eta_2=-0.175$, $\epsilon_{22}^*=-0.049$, and $\epsilon_{33}^*=0.126$. The changes in ϵ_{22}^* and ϵ_{33}^* due to a 100 percent change in carbon content of the steel are less than 6 percent; consequently, the effect of variations in the stress-free transformation strain variation is not significant. A more pronounced effect is attributed to the duration of formation of a martensite plate. Thus, the increase in the AE signal amplitude with carbon content is due primarily to a larger fraction of plate martensite, which has a much higher transformation velocity, i.e., a much shorter duration of formation τ, than that of lath martensite.

Conclusions

In this study, the dynamic displacement that is detected as acoustic emission is obtained by considering the stress-free transformation strains for martensitic transformation. The solution is simplified by considering the martensite plate to be a point source with the sensor at the epicenter. Further simplification can be made by considering the impulse of the spatial derivatives of Green's function for a step-force input $G_{33,3}^H(t-t_M)_\delta$. Because the duration of transformation of a plate martensite is much shorter than that of a lath martensite and the fraction of plate martensite increases as the carbon content increases, the AE signal amplitude is found to increase with rise in carbon content. The signal in the frequency domain is found to increase in bandwidth as the duration of transformation for a single plate of martensite decreases.

Acknowledgment

The support of this work by the National Science Foundation under grant #MSM-8519980 is gratefully acknowledged.

References

Boresi, A. P., and Chong, K. P., 1987, "Tensor Character of Stress," *Elasticity in Engineering Mechanics*, Elsevier, New York, pp. 185–188.

Bunshah, R. F., and Mehl, R. F., 1953, "Rate of Propagation of Martensite," *Journal of Metals*, American Institute of Mining, Metallurgical and Petroleum Engineering, Vol. 5, pp. 1251–1258.

Johnson, L. R., 1973, "Green's Function for Lamb's Problem," *Geophysical*

Journal of the Royal Astronomical Society, Vol. 37, p. 127.

Kannatey-Asibu, Jr., E., and Dong, P., 1986, "Analysis of Acoustic Emission Signal Generation During Martensitic Transformation," *ASME Journal of Engineering for Industry*, Vol. 108, pp. 328–331.

Khachaturyan, A. G., 1983, "Morphology of Coherent Mixture of Cubic and Tetragonal Phases Controlled by Elastic Strain Effect," *Theory of Structural Transformation in Solids*, Johy Wiley and Sons, New York, pp. 377–380.

Liu, X., and Kannatey-Asibu, Jr., E., 1990, "Acoustic Emission During Athermal Martensitic Transformation in Steels," *ASME Journal of Engineering for Industry*, Vol. 112, pp. 84–91.

Liu, Y., 1981, "Morphology of Martensites," *Principle of Heat Treatment for Metals*, Mechanical Engineering Publisher, China, pp. 101–114.

Mura, T., 1983, *Micromechanics of Defects in Solids*, Martinus Nijhoff Publishers, pp. 1–2, 46–49, 194–203.

Nishiyama, Z., 1978, *Martensitic Transformation*, Academic Press, pp. 16–19.

Porter, D. A., and Easterling, K. E., 1981, "Diffusionless Transformations," *Phase Transformations in Metals and Alloys*, Van Nostrand Reinhold, New York, p. 395.

Rice, J. R., 1980, "Elastic Wave Emission from Damage Processes," *Journal of Nondestructive Evaluation*, Vol. 1, No. 4, pp. 215–224.

Simmons, J. A., and Wadley, H. N. G., 1984, "Theory of Acoustic Emission from Phase Transformation," *Journal of Research of the National Bureau of Standards*, Vol. 89, No. 1, pp. 55–64.

Simmons, J. A., and Clough, R. B., 1981, "Theory of Acoustic Emission," *Proceedings of the International Conference on Dislocation Modeling of Physical Systems*, J. Hirth, and M. Ashby, eds. Pergamon Press, pp. 464–497.

Speich, G. R., and Fisher, R. M., 1972, "Acoustic Emission During Martensite Formation," *Acoustic Emission*, ASTM STP 505, American Society for Testing and Materials, pp. 140–151.

Sinclair, J. E., 1979, "Epicentre Solutions for Point Multipole Sources in an Elastic Half-Space," *J. Phys. D: Appl. Phys.*, Vol. 12, pp. 1309–1315.

Willis, J. R., 1965, "Dislocation and Inclusions," *J. Mech. Phys. Solids*, Vol. 13, pp. 377–395.

Y.-Y. Wang

D. M. Parks
Mem. ASME

Department of Mechanical Engineering,
Massachusetts Institute of Technology,
Cambridge, MA 02139

W. R. Lloyd

W. G. Reuter

J. Epstein
Mem. ASME

Fracture and Dynamic Behavior Group,
Idaho National Engineering Laboratory,
Idaho Falls, ID 83415

Elastic-Plastic Deformation in Surface-Cracked Plates: Experiment and Numerical Analysis

Detailed three-dimensional nonlinear finite element (FE) analyses and experimental moire studies are performed on a plate containing a moderately deep part-through surface crack to establish limits of HRR-dominance. The plate is subjected to predominantly far-field tensile loading. The material under investigation is ASTM A710 steel, which was constitutively modeled by large deformation J_2 flow theory of plasticity. The FE mesh was carefully constructed to resolve both crack front fields *(such as J-integral and CTOD) and* global fields *(such as surface displacements, strains). By comparing the J-integral and CTOD results with an earlier HRR-dominance study using (small strain) deformation theory of plasticity, we found little effect of the different formulations on the crack front fields. The global deformation fields from the numerical simulation are in good agreement with our experimental results. The eventual loss of HRR-dominance is intimately related to the interaction of the global plastic flow fields with those of the crack front.*

Introduction

One of the major tasks of fracture mechanics is to establish similarity of crack-front fields between laboratory specimens and a structural component. Under certain conditions, existence of crack-front similarity ensures existence of *single parameter characterization*. Among those single parameters which make fracture mechanics practically feasible are the stress intensity factor K_I of linear elastic fracture mechanics (LEFM) and the J-integral of nonlinear (elastic) fracture mechanics (NLEFM).

A J-based approach has been found useful in correlating the initiation of ductile crack growth. Assuming that an elastic-plastic material has a power-law stress-strain relation as follows:

$$\epsilon/\epsilon_0 = \sigma/\sigma_0 + \alpha(\sigma/\sigma_0)^n, \tag{1}$$

where σ_0 is a reference stress (often chosen as the tensile yield stress, σ_y), $\epsilon_0 = \sigma_0/E$, where E is the Young's modulus, and n and α are material constants, with $n > 1$, this relation can be simplified as

$$\epsilon/\epsilon_0 \to \alpha(\sigma/\sigma_0)^n, \tag{2}$$

at any point near the crack tip by neglecting the elastic strain. Based on an isotropic, tensorial generalization of equation (2), Hutchinson (1968) and Rice and Rosengren (1968) defined the asymptotic field of a mathematically sharp crack under symmetrical loading (HRR fields). As r (local cylindrical coordinates centered at the crack tip are r, θ) approaches zero, the HRR singularity fields have the following form:

$$\sigma_{ij}(r, \theta) \to \sigma_0 \cdot [J/(\alpha\epsilon_0\sigma_0 I_n r)]^{\frac{1}{n+1}} \cdot \tilde{\sigma}_{ij}(\theta, n) \equiv \sigma_{ij}^{HRR}; \tag{3}$$

$$\epsilon_{ij}(r, \theta) \to \alpha\epsilon_0 \cdot [J/(\alpha\epsilon_0\sigma_0 I_n r)]^{\frac{1}{n+1}} \cdot \tilde{\epsilon}_{ij}(\theta, n) \equiv \epsilon_{ij}^{HRR}. \tag{4}$$

The normalizing factor $I_n(n)$ and the angular distribution of the dimensionless constants $\tilde{\sigma}_{ij}$ and $\tilde{\epsilon}_{ij}$ are functions of the strain-hardening exponent n, and of the state of stress, plane strain or plane stress. For certain material and loading conditions (those under which the HRR fields dominate the complete fields over regions large compared to fracture process zone size), J is the *single parameter* characterizing the crack-tip fields.

Under HRR-dominance, a unique relation exists between J and δ_t, the crack-tip opening displacement (CTOD). Using the ± 45 deg intercept definition of δ_t proposed by Rice (as discussed by Tracey, 1976), Shih (1981) obtained the explicit relation

$$\delta_t = d_n(\alpha\epsilon_0, n) \cdot \frac{J}{\sigma_0}. \tag{5}$$

Contributed by the Applied Mechanics Division of THE AMERICAN SOCIETY OF MECHANICAL ENGINEERS for presentation at the Joint Applied Mechanics/Bioengineering Conference, Ohio State University, Columbus, Ohio, June 16–19, 1991.

Discussion on this paper should be addressed to the Technical Editor, Prof. Leon M. Keer, The Technological Institute, Northwestern University, Evanston, IL 60208, and will be accepted until two months after final publication of the paper itself in the JOURNAL OF APPLIED MECHANICS. Manuscript received by the ASME Applied Mechanics Division, Nov. 21, 1989; final revision, June 22, 1990.

Paper No. 91-APM-37.

Shih (1983) has provided extensive tabular values of d_n, $\tilde{\sigma}_{ij}$, $\tilde{\epsilon}_{ij}$, etc. for essentially a complete range of n and $\alpha\epsilon_0$ for both plane strain and plane stress.

Two-dimensional study of HRR-dominance in plane strain is a relatively well-developed field. The pioneering work of McMeeking and Parks (1979) and Shih and German (1981) and, more recently, Shih (1985) and Al-Ani and Hancock (1991) are a few examples. However, understanding of crack-front HRR-dominance in a realistic three-dimensional crack configuration—for instance, a structure with a part-through surface crack—remains slight. The three-dimensional crack fields differ from those of either plane strain or plane stress in several aspects. The constraint at the crack tip of a surface crack is not only a function of loading and geometry, but is also varying along the crack front. Identifying critical points along the crack front and the stress and strain fields at these points is the basic, yet necessary condition for evaluating the fracture toughness of a surface-cracked plate. The line-spring model, first proposed by Rice and Levy (1972) and further developed by Parks (1981), Parks and White (1982), Shawki et al. (1989), and others, has proven to be an effective means in accurately and economically evaluating the J-integral of some surface-cracked plates. It may also be used to certain extent in providing indications of loss of HRR-dominance, as suggested by Parks (1981), Shawki et al. (1989), and our present research (Wang, 1991). However, a three-dimensional full-field characterization is necessary in resolving HRR-dominance at the present time. It may also provide some insights in further developing a simplified model, such as the line-spring model. Some three-dimensional finite element analyses have been performed with certain assessments of HRR-dominance; for instance, Brocks and Olschewski (1986), Delatte (1987), and Brocks and Noack (1988). The most comprehensive HRR-dominance study of plates with moderately deep surface cracks is by Parks and Wang (1988).

To date, most HRR-dominance studies have been performed by comparing detailed numerical solutions near the crack tip with the HRR singularity fields. Very little is known about the global deformation fields when a cracked structure loses HRR-dominance. Using a combination of surface replicating technique and surface interferometry, Francis, Davidson, and Forman (1972) studied a variety of semi-elliptical surface-cracked plates with various aspect ratios and depths. At high load, dimples were observed on the back surface and at crack tips on the free surface. They also found that those features could not be characterized by a local K_I field, or by simple extensions of two-dimensional plane-strain models. The strong three-dimensional nature of the deformation fields requires full three-dimensional analysis. Due to the complexity of the crack geometry and loading conditions, careful experimental verification of the analysis is necessary. However, until very recently, experimental techniques have not been able to resolve the very small displacement gradient on the free surface of a surface-cracked plate with sufficient precision (see, e.g., Rosakis et al., eds., 1988). The current joint project, combining extensive numerical analysis at M.I.T. and experimental study at I.N.E.L., is intended to investigate the HRR-constraints in this important class of engineering crack configurations, and hence, to begin assessment of parametric limits of applicability of J-based fracture mechanics approaches in predicting their structural integrity.

Back face topology would be a valuable source in evaluating the useful life of a component with a surface crack if the displacement fields could be related to the extent of crack penetration and the local loading conditions. Unfortunately, this relation is very difficult to establish for a general structure. However, valuable insights into the three-dimensional nature of plastic flow in a surface-cracked plate can be gained from the back face topology. Out-of-plane and in-plane displacements and their gradients are good indicators of the transition of the constraints from elastic to fully plastic conditions. In this study, using shadow moire and amplitude moire methods, the displacement fields on the back face immediately behind the crack front were continuously monitored as the specimen was loaded. However, the *global* deformation fields alone can not assess the degree of crack-front HRR constraint. Numerical simulation has to be performed to relate the global fields back to the crack front. The comparison of the crack-tip fields with the HRR singularity fields then determines the degree of HRR constraint. In addition to the global deformation fields, experimentally determined CTOD by metallurgical sectioning and fracture surface topography provide some indication of local fields. These values can be used to further verify the numerical simulation. The experimental study and the numerical simulation are mutually supportive, and the combined effort is essential for the assesment of HRR-dominance.

Procedures

Material. The material under study is an ASTM A710 Grade A steel. At room temperature, the material has following properties: Young's modulus of $E=206$ GPa, tensile yield

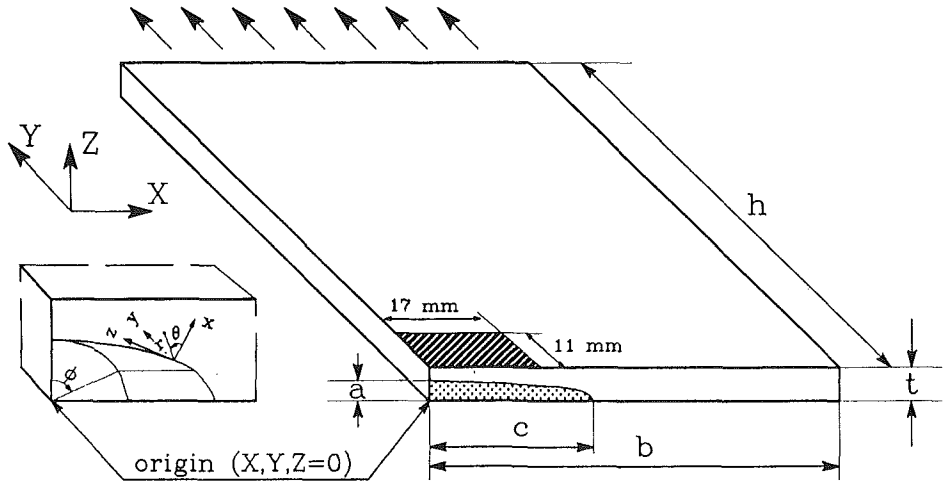

Fig. 1 Schematic of one-fourth of a surface-cracked plate. Back-face surface displacements are recorded in the cross-hatched region. The inset at left shows the local cartesian coordinate system (*x-y-z* system) with respect to global coordinate system (*X-Y-Z* system) and description of crack-front location parameter ϕ. NOTE: Drawing is not to scale.

stress of $\sigma_y = 480$ MPa, and ultimate tensile strength of 635 MPa. The experimental engineering stress-strain relation can be well characterized by equation (1) with material constants of $\sigma_0 = 480$ MPa, $\alpha = 1.0$, and $n = 12$.

Specimen Geometry and Finite Element Mesh. Figure 1 is a schematic of one-fourth of a surface-cracked plate. The experimental specimens were fabricated from as-rolled steel plates. The detailed specimen geometry can be found in Epstein et al. (1988). A triangular-crack starter notch was cut into the plate using EDM. The starter notch was then grown by bending fatigue cycling into the final configuration. The surface cracks had an aspect ratio a/c ranging from 0.20 to 0.24 and maximum penetration a/t ranging from 0.60 to 0.67. The variation in the aspect ratio and the penetration reflects natural variation in the pre-cracking process.

Due to the symmetry conditions, only one quarter of the specimen (as shown in Fig. 1) was modeled in the numerical simulation. The geometric ratios were $b/t = 8$ and $h/t = 16$. In the FE input data deck, the specimen thickness was taken as unity. Subsequently, all the results were appropriately normalized to the actual specimen thickness of $t = 6.35$ mm (0.25 in.). The aspect ratio a/c was taken as 0.24, and the maximum penetration was $a/t = 0.60$. Due to the variation of the surface crack geometry, data from those specimens with crack geometry closest to that of the finite element mesh was chosen for comparison with numerical simulations whenever possible. The finite element mesh was generated by an automatic mesh generator (Wang, 1988). Each of the 12 segments along the crack front consists of six focused rings of elements. Reduced integration ($2 \times 2 \times 2$ Gaussian) 20-node isoparametric brick elements are used. In the data post-processing, a local coordinate system (x-y-z system), as shown in Fig. 1 was used, to represent the local fields. Details of the mesh and the mesh generator (Wang, 1988). Each of the 12 segments along the crack front consisted of six focused rings of elements. Reduced integration ($2 \times 2 \times 2$ Gaussian) 20-node isoparametric brick elements were used. In the data post-processing, a local coordinate system (x-y-z system), as shown in Fig. 1 was used, to represent the local fields. Details of the mesh and the mesh generation are referred to Wang (1988). Extra care was taken to refine the mesh in the rectangular region on the back face behind the crack as shown in Fig. 1 by the cross-hatched area. ticity. Eight degenerated singular elements with independent nodes at the same point along the crack front were wrapped around each of the 12 crack-front segments. The final mesh has 1026 elements and 15711 degrees-of-freedom. Later, in a large geometry change (LGC) analysis, a new mesh was generated. The new mesh was essentially the same as that for the SGC analysis, except that the nodes along the crack front were not collapsed into a line, but kept in a small circular ring in space, forming a keyhole-like tube around the crack front. The radius of the keyhole was $0.006(t-a)$, or about 15 percent of the radial length of the first ring elements throughout the entire crack front. Subsequent analysis showed that the effect of the initial keyhole radius on both local and global quantities is slight.

Numerical Procedures. In simulating the loading condition in the experiment, uniform displacement, U_Y, at the remote boundary, $Y = h$, is applied. The symmetry conditions of $U_X = 0$ on $X = 0$ and $U_Y = 0$ on the ligament portion of plane $Y = 0$ are also imposed. The model is considered under uniform remote tension, although a very small through-thickness stress gradient exists. The remote load is characterized by an average remote stress, $\sigma^\infty/\sigma_0 = P/\sigma_0 bt$, where P is the Y-direction applied force on one-half of the specimen required to impose the remote displacement boundary condition.

The constitutive model used in the initial SGC formulation is J_2-deformation theory of plasticity based on the Ramberg-Osgood power-law form of equation (1). The three-dimensional generalized tensorial form was coded into a user-defined material subroutine UMAT of the ABAQUS (1987) finite element program, along with the Jacobian matrix. The material constants were taken as those previously determined values, which best fit the engineering stress-strain curve. In the numerical analysis, the Poisson's ratio, ν, was set to 0.3, while experimental measurement gave $\nu = 0.256$. This difference should be of only minor significance, especially at high loads.

The constitutive model used for the final LGC formulation was J_2 flow theory of plasticity with isotropic hypoelasticity based on the Jaumann rate of Kirchhoff stress. A true stress/logarithmic plastic strain curve was derived from the experimental engineering stress strain curve. This true stress/plastic strain curve was multilinearized for input into ABAQUS, along with the prior values of E and ν.

Computation was performed on an Alliant FX-8 multiprocessor computer using version 4-6-162 (1987) of the ABAQUS finite element program. One iteration took about 85 minutes on the single processor. For the SGC formulation with deformation theory plasticity, three iterations were generally required to reach convergence. It took nine load increments to reach about 95 percent of the *limit load* ($P_{\text{limit}} \equiv \sigma_0 bt$). The LGC formulation with flow theory plasticity required substantially more computation time. To reach the same level of remote load, it took 17 load increments with a total of 92 iterations.

Experimental Procedures. Tests of the surface-cracked specimens were performed on an Instron 1325 servohydraulic load frame (1000-kN capacity). The specimens were loaded through two 38.1-mm diameter pins. The amplitude (geometric) moire method was used to record the in-plane displacements. Detailed description of the method can be found in Parks (1986). Specimen surfaces were carefully prepared for optical observation. The area of interest on the specimens was coated with white polyurethane paint (thinned 1:4 with polyurethane thinner) using an air brush. The higher background reflectivity of the white paint, as compared with bare metal,improved contrast of the resultant experimental fringes. Linear amplitude gratings were replicated onto the front and back surfaces. These gratings were approximately 100-mm square with a pitch of 50.8 μm. A 20-power microscope was used to align the specimen grating, transfer side down, with either the crack plane or a reference line on the specimen surface. Cellulose tape was placed along one edge of the transfer grating to maintain alignment. The grating was then folded back and a liberal amount of cyanoacrylate adhesive was placed at the joint between grating and the specimen where they were taped together. A rubber-coated print roller was then used to press the grating into the adhesive, making sure not to trap air bubbles under the grating. After two or three minutes, the acetate backing on the transfer was peeled away, leaving the grating bonded to the painted surface. The master amplitude gratings, on glass photographic plates, were used to make flexible reference gratings on sheet film by contact printing with collimated light. Correct exposure of the print to obtain a 50/50 grating was obtained by making multiple exposures of different durations, developing, and inspecting the resulting film under a microscope. The reference gratings were placed over the specimen grating to obtain a null field, and cellulose tape was applied at two points along one edge to maintain alignment during the test.

High resolution (512×480 pixel) CCD video cameras were used to make real-time recordings of the optical data generated by geometric moire method. The video signals were recorded on Umatic format video recorders; a separate camera and recorder system were employed to record front and back surface displacement fringe patterns simultaneously. In addition, two 35-mm cameras with 105-mm macro lenses and power winders were used to collect data at discrete times during the

test. Full-field (spatially continuous) moire patterns representing surface displacements, U_Y, were collected on both the front and back surfaces of the specimen over areas extending approximately one-half the plate width above and below the crack plane (where uniform remote strain was observed). The 50.8-μm sensitivity proved ideal for measuring moderate plastic deformations at remote stress levels approaching yield; however, it became a limitation at stress levels below $\sigma^\infty/\sigma_0 = 0.75$.

The shadow moire method was used to record the out-of-plane displacement. Detailed description of the technique and the relevant equations can be found in Dykes (1971). Preparation of the specimens for shadow moire tests began by grit blasting the area of interest to produce a uniform matte surface. A small aluminum frame holding the reference grating with a 50.8-μm pitch was mounted on the specimen using spring clips. Small screws through the frame allowed adjustment of the reference grating to be parallel to the specimen's surface. A collimated monochromatic source (arc lamp) was used for illumination. Both video and film were used to record the fringe patterns. Data were collected on the back surface of several replicate specimens. Sensitivities ranged from 13 to 50 μm/fringe. The higher sensitivity provided good data in the elastic to elastic-plastic regimes, while the 50 μm/fringe sensitivity allowed data collection to extend well beyond net section yielding. Reference displacement points ($U_Z = 0$) were located at $X = \pm 50$ mm and $Y = \pm 50$ mm.

Results

A preliminary numerical analysis employed a SGC formulation and deformation theory of plasticity. The displacement fields on the back face were compared with experimental results. Though the in-plane displacement (U_Y) from this simulation agreed well with the experimental results, the out-of-phase displacement (U_Z) was much larger than the experimental values—by a factor of two. Careful examination of the displacement revealed that the remote plane (plane $Y = h$) had a quite significant through-thickness translation with respect to the cracked plane. At high load ($\sigma^\infty/\sigma_0 \to 1.0$), the through-thickness relative translation ΔU_Z between the remote plane ($Y = h$) and the cracked plane ($Y = 0$) was as large as half of the specimen thickness. The SGC formulation was thought to be inappropriate under these circumstances, since it did not take the global rotation into its global equilibrium calculation.

The analysis was then performed with a LGC formulation. Little difference was found in the in-plane displacement patterns at any load level, but the out-of-plane displacement was reduced to about half of the SGC result at high load. These results were in much better agreement with the experimental data. This formulation was considered more appropriate.

In the following sections, the crack-tip fields of the large geometry change formulation will be critically examined, in comparison with an earlier HRR-dominance study using SGC formulation (Parks and Wang, 1988). The correlation of global deformation features and the transition of the crack-tip HRR constraints will be established through both numerical and experimental results. Finally, the development of the plastic zone through the remaining ligament shows how the crack front loses HRR-dominance through the relaxation of constraints by global plastic flow.

***J*-integral.** The *J*-integral was evaluated in six domains using the virtual crack extension (VCE) method provided in ABAQUS. The method was first developed by Parks (1977). A modified version is used in ABAQUS version 4-6 which is based on the work of Li, Shih, and Needleman (1985) and Nakamura, Shih, and Freund (1989). The *J*-integral is domain dependent because of the (locally) nonproportional loading; this being in conjunction with the use of flow theory. McMeeking (1977) showed that, in plane strain small-scale yielding, the finite strain affects only a region not more than two

Table 1 Mean radii of various domains and *J* from those domains at $\sigma^\infty/\sigma_0 = 0.955$

domain level	1	2	3	4	5	6
$J_{\phi=0}/(\sigma_0\epsilon_0 t)$	8.776	11.94	13.17	13.85	14.32	14.82
$R/(J_6/\sigma_0)$	0.23	0.68	1.34	2.52	4.49	7.73

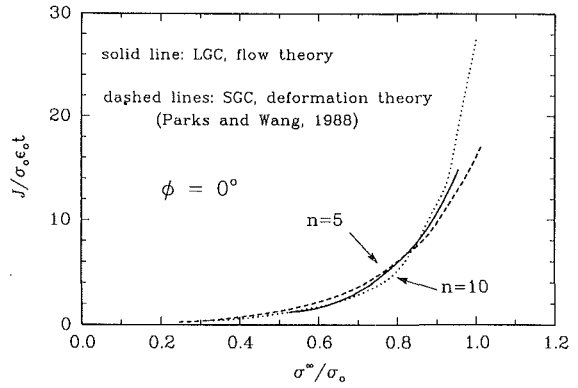

Fig. 2 Calculated *J* at center plane ($\phi = 0$), using LGC formulation, compared with the *J* of the SGC calculation, both as functions of applied load

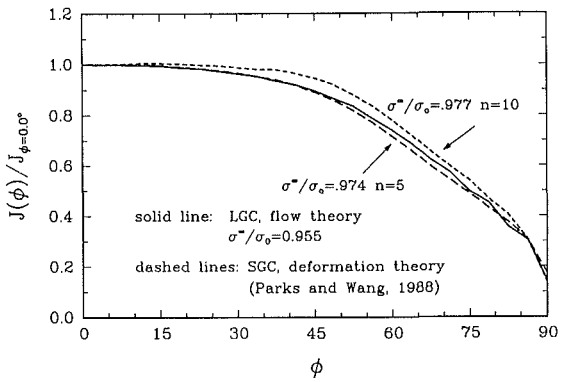

Fig. 3 Calculated *J*-distribution along the crack front using LGC formulation, compared with the *J*-distribution of SGC calculation

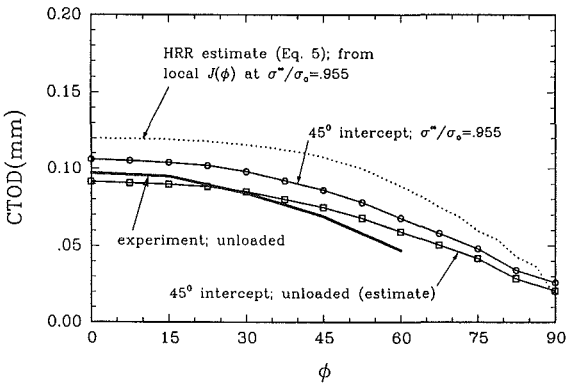

Fig. 4 CTOD from the numerical simulation and the estimated residual CTOD following Rice (1967). The HRR estimate is calculated from the local *J* using equation (5). The experimental CTOD is the residual CTOD after the specimen is unloaded from a peak load value of $\sigma^\infty/\sigma_0 = 0.95$.

to three CTODs from the crack tip. Recently, Moran, Ortiz, and Shih (1989) studied the effect of the crack-tip mesh on LGC solutions under small-scale yielding. Three crack-tip meshes, one with a finite radius notch, a second with crack-tip nodes collapsed into a point, and a third with a key-hole like tip, were used. The stress fields outside about two CTODs were independent of the details of the crack-tip finite element mesh. Here, the values of *J*-integral at center plane ($\phi = 0$) from all six domains at highest load attained (which shows the most path dependence) are listed in Table 1. The mean reference configuration radius of each domain, $\overline{R}$, normalized by

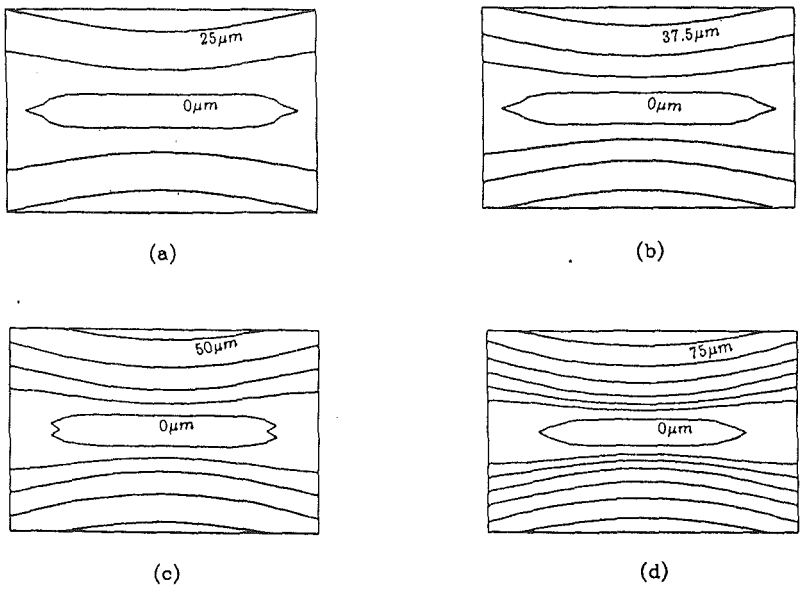

Fig. 5 Back-face in-plane displacement contours of numerical calculation at various load levels. The width of the areas shown is 34 mm. The gradient of the contours is 12.5μm. (*a*) $\sigma^\infty/\sigma_0 = 0.741$; (*b*) $\sigma^\infty/\sigma_0 = 0.821$; (*c*) $\sigma^\infty/\sigma_0 = 0.870$; (*d*) $\sigma^\infty/\sigma_0 = 0.955$.

the characteristic crack-tip opening displacement J_6/σ_0, is also listed in Table 1. Here, J_6 is the J-integral from the sixth (most remote) domain. The first three domains are clearly inside the finite deformation zone (the mean radius of domain three here corresponds to about three CTOD). The J-value varies significantly throughout this region. The last three domains are more or less out of the finite deformation zone, and the relative variation of J is limited. This is consistent with results of McMeeking (1979) and Moran et al. (1990). In the following sections, all the reported J-values will be taken from the sixth domain, which is considered to be most accurate.

Recalling that the numerical estimates of the global deformation fields can be significantly affected by different formulations, there is a need to check the effect of the formulations on the crack-tip fields, such as J-integral and CTOD. Figure 2 shows the center plane ($\phi = 0$ deg) normalized J at various load levels. Also shown are the results of a previous SGC HRR-dominance analysis (Parks and Wang, 1988). In normalizing the LGC data, the reference yield stress, σ_0, is taken as 480 MPa, and the reference yield strain, ϵ_0, is taken as $\sigma_0/E = .00233$. Little difference is seen between the two formulations, except that the J from the LGC formulation is slightly smaller than the SGC values for $n = 10$ (which represents the current material behavior more closely than the high strain-hardening of $n = 5$) at high load.

Another comparison of formulations is the J distribution along the crack front. Figure 3 shows $J(\phi)$, normalized by the J value at the center plane, at various crack-front locations (for parameter ϕ, see Fig. 1) at the highest load level. For comparison, the previous results (Parks and Wang, 1988) of SGC analysis are also shown. Again, very little difference is seen between the two formulations. The effect of the formulation on the crack-front J variation is slight at all load levels up to this magnitude.

CTOD. Figure 4 shows the crack-tip opening displacement (CTOD) along the crack front. The CTOD was obtained from the deformed crack-opening profiles using the 45 deg intercept definition. Also shown in Fig. 4 is the experimentally determined *residual* component of the CTOD along the crack front. These data were obtained by loading the specimen to $\sigma^\infty/\sigma_0 = 0.95$, unloading, cooling the specimen in liquid nitrogen and loading to failure by cleavage. Using fracture surface topography, the CTOD values are taken as the distance separating the tip of the fatigue precrack after blunting. Details of the procedures are found in Reuter and Lloyd (1990). The calculated CTOD distribution is very similar to the J distribution of Fig. 3, and it falls slightly below the HRR value of equation (5), which is also shown in Fig. 4. A tentative estimation of the *residual* CTOD of the numerical simulation is given, following the spirit of Rice's (1967) formula to estimate the elastic part of CTOD. The elastic part of the CTOD is obtained as $\Delta\delta_t = d_n(\alpha\epsilon_0, n) \cdot \Delta J^e/2\sigma_0$. The equation is similar to equation (5), except that the *effective flow strength* is taken as twice the yield stress, since the effective elastic stress range required to initiate reversed plasticity is $2\sigma_0$. The ΔJ^e is calculated as $\Delta J^e = -(\Delta K_I)^2/E'$ (E' is the plane-strain modulus) from the elastic K_I of the same surface crack, according to the results of Raju and Newman (1979). The *residual* CTOD shown in Fig. 4 is the difference between the total CTOD at $\sigma_\infty/\sigma_0 = 0.955$ and the unloading part, $\Delta\delta_t$. It is clear that the estimated *residual* CTOD is in good agreement with the experimental result.

The CTOD results are consistent with an earlier HRR-dom-

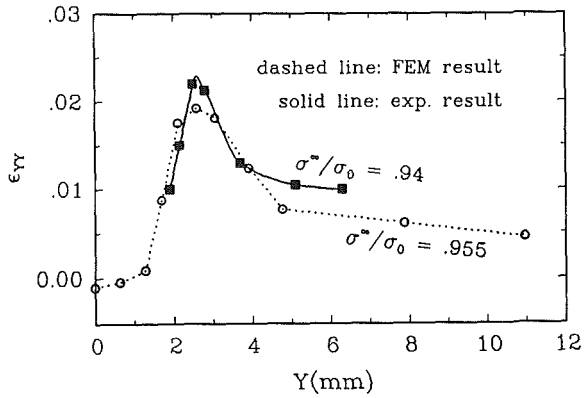

Fig. 6 Comparison of center line (line $X=0$, $Z=t$) normal strain (ϵ_{YY}) between the numerical and experimental results

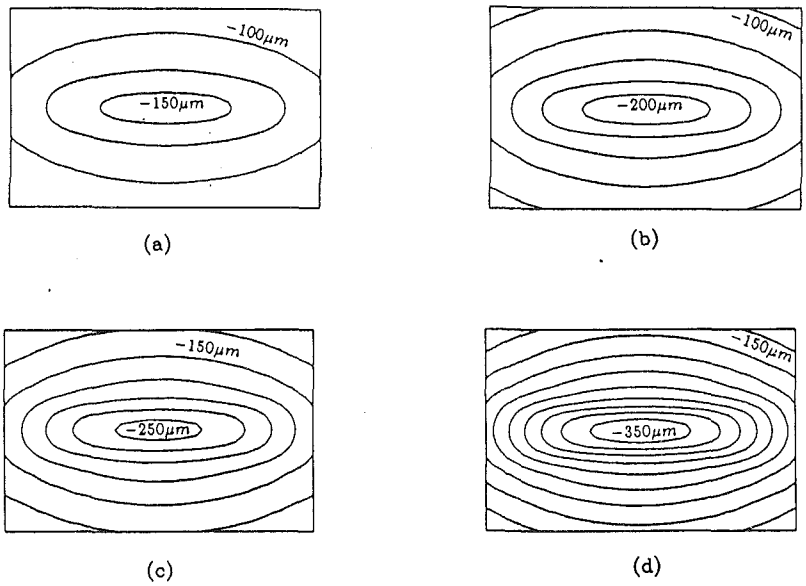

Fig. 7 Back-face out-of-plane displacement contours of numerical calculation at various load levels. The width of the areas shown is 34 mm. The gradient of the contours is 25.0μm. (*a*) $\sigma^\infty/\sigma_0 = 0.741$; (*b*) $\sigma^\infty/\sigma_0 = 0.821$; (*c*) $\sigma^\infty/\sigma_0 = 0.870$; (*d*) $\sigma^\infty/\sigma_0 = 0.955$.

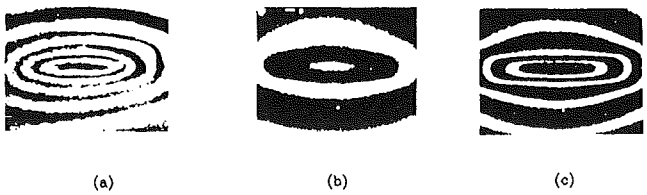

Fig. 8 Back-face out-of-plane displacement fringes of experiments by Epstein et al. (1988) at various load levels. The width of the areas shown is 39 mm. (*a*) $\sigma^\infty/\sigma_0 = 0.61$, 14.1μm/fringe; (*b*) $\sigma^\infty/\sigma_0 = 0.65$, 50.8μm/fringe; (*c*) $\sigma^\infty/\sigma_0 = 0.98$, 50.8μm/fringe.

inance study (Wang, 1988). Those SGC results showed that the CTOD versus the J-relation stays essentially unchanged from small-scale yielding to large-scale plastic yielding. Here, even at the highest load, the CTOD versus the J-relation is very close to that of a dominant HRR singular field, even though (as will be argued further below) no such dominant field exists at high loads. Delatte (1987) also found that the CTOD versus J-relation shows only slight deviation from equation (5) when a tensile-loaded plate with semi-circular surface crack loses HRR-dominance. All these surface crack results are in contrast with the early plane-strain study by McMeeking and Parks (1979), who noted appreciable differences in the terminal slope of CTOD versus J curves when comparing different specimen geometries. This implies that for a part-through surface crack, the closeness of the computed CTOD versus J relation to that of the HRR singularity field does not necessarily guarantee HRR-dominance.

In-plane Displacement and Strain. Computed contours of the in-plane displacement (U_Y) on the back face are shown in Fig. 5 at various load levels. The original ABAQUS output showed only one-quarter of the figure. A program developed by Stringfellow (1988) was used to mirror image the original plot to a full picture. The contour gradient was set to 12.5μm/contour for easy comparison with experimental results (see below). At stress levels, σ^∞/σ_0, below 0.741, the displacement gradients are very small. From the symmetry condition, the displacement on the symmetry plane $Y=0$ is zero ($U_Y=0$). Since the innermost contour shown is also a contour of zero displacement, the region bounded by $Y=0$ and the interior

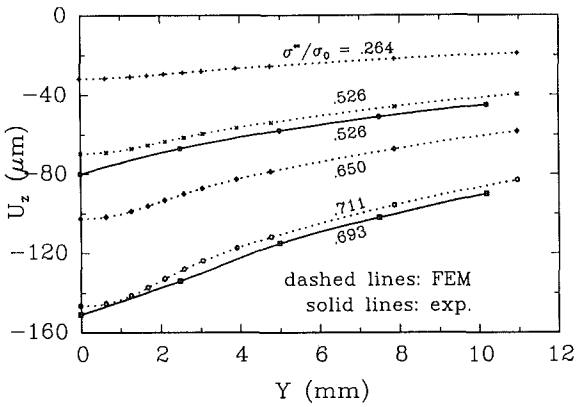

Fig. 9 Comparison of back-face center line (line $X=0$, $Z=t$) out-of-plane displacement between the numerical calculation and the experimental results

contour of $U_Y=0$ must have $U_Y<0$ (compressive strain) on the back face. At high loads, a large gradient is seen outside the compression zone. This high gradient is the surface manifestation of *shear zones* (see also Fig. 10). The higher the load level, the sharper the shear zones. The compressive zone generally shrinks with increasing load.

For a better examination of the quantitative agreement between the numerical and the experimental results, the in-plane normal strain, ϵ_{YY}, along the back-face center-line (line $X=0$, $Z=t$) is shown in Fig. 6 at the highest load level ($\sigma^\infty/\sigma_0 = 0.955$). Close agreement is seen in the overall pattern, although the numerical value is slightly smaller than the experimental value. The region with the highest strain is the zone of intense shearing. The peak corresponds to the shear zones observed in the displacement contours of Fig. 5. This peak is about 2.3 mm off the cracked plane. Considering that the remaining ligament at the deepest crack penetration is about 2.6 mm ($=0.4\times6.35$mm), the shear zone occurs at roughly ±45 deg lines from the crack front. A small region of negative strain is seen in a region near the center ($Y=0$). This is the compressive zone noted previously. Recent examination of moire patterns by Lloyd (1989) confirmed that there is a region of compression with a small strain of less than .002.

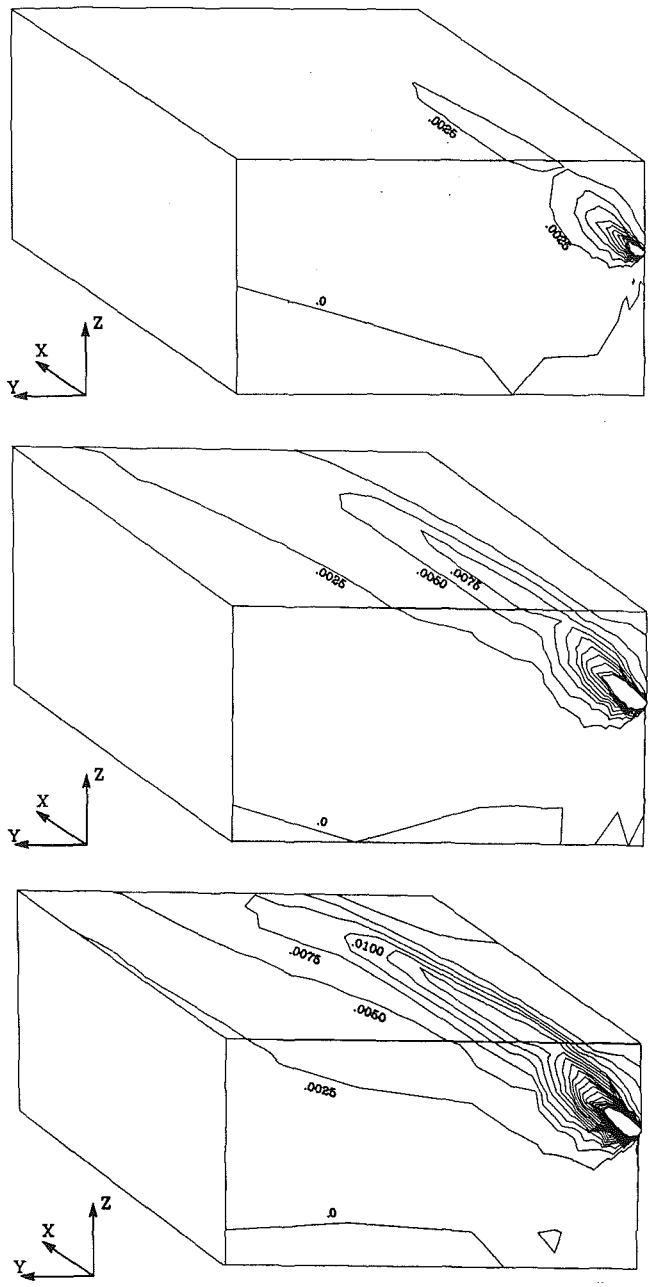

Fig. 10 Composite isometric contours of plastic strain on the center plane (plane $x=0$, facing reader) and on the back face (plane $Z=t$, on the top). The gradient of the contours is .0025. The dimensions of the region shown are: $\Delta Z=t$ ($t=6.35$ mm), $\Delta X=1.53t$, $\Delta Y=1.76t$. (*a*) $\sigma^{\infty}/\sigma_0=0.741$; (*b*) $\sigma^{\infty}/\sigma_0=0.870$; (*c*) $\sigma^{\infty}/\sigma_0=0.955$.

Out-of-Plane Displacement. The back-face out-of-plane displacement U_Z was monitored in the same region as the in-plane displacements throughout the loading. The computed out-of-plane displacement contours are shown in Fig. 7 at various load levels. The location of the reference ($U_Z=0$) displacement point was the same as the experiments. The displacement gradient was 25 μm/contour for easy comparison with experimental results. Again, at stress levels, σ^{∞}/σ_0, below about 0.74, the displacement gradients are almost uniform. At higher stresses, a high negative displacement zone encircled by some densely clustered contours is seen. This region is roughly similar to the compression zone seen in previous in-plane displacement contours. Physically, the material on the back face is sucked in (relatively) towards the crack front as the specimen is stretched. This is the phenomenon of dimpling.

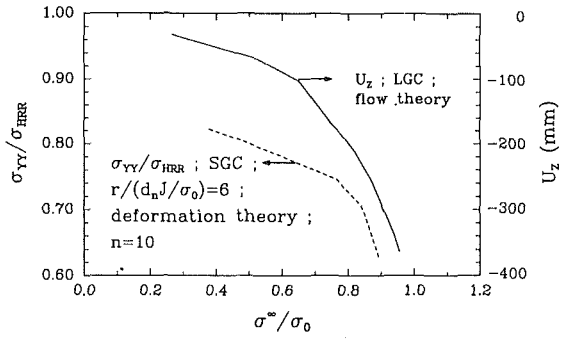

Fig. 11 Normalized near-tip crack-opening stress (σ_{YY}) at center plane ($X=0$) (read left), and the calculated out-of-plane displacement (U_Z) at the back-face center point ($X=0$, $Y=0$, $Z=t$) (read right), both versus load level. Local stress is calculated at a distance $r=6\ d_nJ/\sigma_0$ ahead of the crack front, and is normalized by the HRR stress at the same normalized distance. Stress calculations are from SGC solutions (Parks and Wang, 1988), while displacement calculations are from the current LGC solution.

Pronounced dimpling becomes apparent at the stress level $\sigma^{\infty}/\sigma_0=0.87$. It has been shown that this is also the load level at which the center plane ($\phi=0$) crack fields lose HRR-dominance (Parks and Wang, 1988). Figure 8 shows the experimental out-of-plane displacement moire pattern at various load levels. (Note: companion specimens were used to obtain back-face in-plane and out-of-plane moire data.) The close comparison we can make at high load level is between the $\sigma^{\infty}/\sigma_0=0.955$ contour of the numerical result and the $\sigma^{\infty}/\sigma_0=0.98$ moire pattern. From the numerical results, there are eight contours between the center point and the outermost contour in the observed region, a 200-μm displacement variation. Counting the size difference, the experimental moire pattern has roughly four contours, which also represents about 200 μm. This comparison is admittedly crude. More accurate comparison is made in Fig. 9 for the lower load levels. In this figure, the out-of-plane displacement along the center line (line $X=0$, $Z=t$ in Fig. 1) is plotted at various stress levels. The available experimental data at two close load levels are also drawn in the figure. The quantitative agreement is very good, although the numerical values are slightly smaller than those of the experiments.

Plastic Zone. Plastic zone is here defined as the region within which the equivalent plastic strain exceeds 0.25 percent. Plastic zone advance is monitored through the equivalent plastic strain contour on the center plane ($X=0$) and back face ($Z=t$) as shown in Fig. 10. Up to a stress level $\sigma^{\infty}/\sigma_0\cong 0.5$, the plastic zone is small relative to the remaining ligament. The plastic zone then gradually grows along the two ± 45 deg lines (only one side is shown) to the back face with the increase of load. At a stress level of about 0.8 (near that of Fig. 10(*a*)), the plastic zone reaches the back face and then spreads to the neighboring region at higher loads, while sharpening at the 45 deg location. At a load level of about 0.9 (near that of Fig. 10(*b*)), the remaining ligament becomes fully plastic. Note that, on the back face at the highest loads, the high-strain zones show curvature away from the cracked plane (plane $Y=0$) (Fig. 10(*c*)). The increasing distance from the shear zone to the cracked plane, with increasing distance from the center plane (plane $X=0$), reflects the corresponding increase in distance from the back face to the curved crack front.

Discussion

The comprehensive nonlinear finite element analysis presented here establishes that our early HRR-dominance study based on SGC formulation and deformation theory of plasticity is sound even though such formulation can not accurately

predict global out-of-plane deformation fields. Through a particular numerical analysis based on LGC formulation and using flow theory of plasticity, the limits of HRR dominance at the crack tip and the global deformation features associated with the loss of HRR-dominance are analyzed. The close agreement exhibited between the experimental results and the numerical simulation in the global deformation fields validates the numerical analysis, which in turn indicates that an earlier HRR-dominance study (Parks and Wang, 1988), using a different formulation, has its own merits. This joint experimental/computational effort illustrates how the often separated approaches can be synthesized to provide deeper understanding of complex engineering problems. It also emphasizes that the "rightness" of a numerical formulation is dependent upon the very purpose of the calculation.

Our LGC analysis shows that the load at which pronounced back-face dimpling in a tensile-loaded surface-cracked plate first appears roughly coincides with the load at which the crack-tip field rapidly begins to lose HRR-dominance. Intensive shearing becomes apparent at the load levels $\sigma^{\infty}/\sigma_0 \geq 0.8$. Figure 11 shows the variation of out-of-plane displacement at the center of the back face as the load increases (read right). The dimpling associated with the back-face penetration of the plastic zone accelerates once the load level exceeds about 0.7. Also shown in Fig. 11 is the variation of center plane ($\phi = 0$ deg) crack opening stress (σ_{YY}) at a distance $r = 6 \times (d_n J/\sigma_0)$ ahead of the crack front, normalized by the corresponding HRR stress, as the plate is loaded from small-scale yielding to fully plastic conditions (read left). By examining the *trend* of the stress deviation from HRR singularity field, it is obvious that the crack tip gradually (i.e., linearly with respect to the load level) loses HRR constraint below $\sigma^{\infty}/\sigma_0 \simeq 0.78$, and the stress rapidly deviates from the HRR stress once the load exceeds this value. Here we emphasize the *trend* of deviation from HRR field, rather than an absolute degree of agreement as used by some researchers (e.g., Shih and German, 1981), since the approach is less arbitrary. Recall the results of Fig. 10; it is apparent that there is an intrinsic correlation between the loss of crack-tip HRR-dominance and the growth of the global tensile plastic zone. It is seen that as long as some portion of the ligament remains elastic, the loss of HRR constraint is gradual. Once the ligament becomes fully plastic, the crack tip loses HRR constraint much more rapidly. This conclusion is likely applicable for a plate with a moderately deep crack ($a/t \geq .25$) under tension. Al-Ani and Hancock (1991) showed that in shallow plane-strain cracks ($a/t \leq 0.2$), the fully plastic field first reaches the front face (plane $Z = 0$ in Fig. 1) as the crack tip first gradually, then abruptly, loses HRR-dominance.

The calculated out-of-plane displacement and the in-plane strain are slightly smaller than those of the experimental values at the same load levels. One reason is that the cracked area of the numerical model is smaller than that of many of the experimental specimens. The experimental specimens generally have somewhat deeper (larger a/t) and longer (smaller a/c) surface cracks than the numerical model. The other reason could be that the remote boundary conditions applied in the experiments were slightly different from the mathematical model of the FE analysis. By any accounts, the differences are small, and the agreements should be considered satisfactory.

A logical extension of the analysis would be a stable crack growth of this class of crack configuration. With present knowledge and computational power, detailed continuum modeling of crack growth seems unfeasible. A simplified model, such as the line-spring, could be used to grow a crack up to several multiples of CTOD. Although the results of Shawki, Nakamura, and Parks (1989) give some encouragement, the task remains formidable.

Another remaining issue regarding the HRR-dominance in a surface-cracked plate is the effect of the ratio of bending to tension on HRR-dominance. This ratio affects the stress triaxiality at the crack tip. In fully plastic plane-strain analyses, Shih (1985) showed that the ratio of bending to tension in the remaining ligament of a deep edge-cracked bar had a strong effect on the attainment of HRR-dominance at the crack tip. This subject remains for future investigation.

Acknowledgments

This work was supported by the Office of Basic Energy Sciences, Department of Energy, under Grant #DE-FG02-85ER13331 to MIT and Contract #DE-AC07-76ID01670 with INEL. Computations were performed on an Alliant FX-8 computer obtained under D.A.R.P.A. Grant #N00014-86-K-0768 and on a Data General MV-10000 computer donated to MIT by the Data General Corporation. The ABAQUS finite element program was made available under academic license from Hibbitt, Karlsson, and Sorensen, Inc., Providence, R. I. Useful discussions with several of our colleagues, including T. Nakamura and F. A. McClintock, are acknowledged.

References

Al-Ani, A. M., and Hancock, J. W., 1989, "*J*-Dominance of Short Cracks in Tension and Bending," *Journal of Mechanics and Physics of Solids*, Vol. 39, pp. 23–43.

Brocks, W., and Noack, H.-D., 1988, "*J*-Integral and Stresses at an Inner Surface Flaw in a Pressure Vessel," *International Journal of Pressure Vessels and Piping*, Vol. 31, pp. 187–203.

Brocks, W., and Olschewski, J., 1986, "On *J*-dominance of Crack-tip Fields in Largely Yielded 3D Structures," *International Journal of Solids and Structures*, Vol. 22, No. 7, pp. 693–708.

Delatte, M. K., 1987, "Finite Element Studies of HRR-Dominance and Single Parameter Characterization of Crack-tip Fields for 3-Dimensional Cracks," M. Sc. Thesis, Department of Mechanical Engineering, Massachusetts Institute of Technology, Cambridge, Mass., May.

Dykes, B. C., 1971, "Analysis of Displacements in Large plates by the Grid-Shadow Moire Technique," *Experimental Stress Analysis and Its Influence on Design, Proceedings, 4th International Conference on Experimental Stress Analysis*, M. L. Meyer, ed., pp. 125–134.

Epstein, J. S., Lloyd, W. R., and Reuter, W. G., 1988, "Three-Dimensional Displacement Measurement of Elastic-Plastic Surface Flaws," *Analytical, Numerical, and Experimental Aspects of Three Dimensional Fracture Processes*, A. J. Rosakis, K. Ravi-Chandar, and Y. Rajapakse, eds., ASME AMD-Vol. 91, ASME, New York, pp. 33–50.

Francis, P. H., Davidson, D. L., and Forman, R. G., 1972, "An Experimental Investigation into the Mechanics of Deep Semi-elliptical Surface Cracks in Mode *I* Loading," *Engineering Fracture Mechanics*, Vol. 4, pp. 617–635.

Hibbitt, Karlsson, and Sorensen, Inc., 1987, *ABAQUS User's Manual*, Version 4-6-162, Hibbitt, Karlsson and Sorensen, Inc., Providence, R.I.

Hutchinson, J. W., 1968, "Singular Behavior at the End of a Tensile Crack in a Hardening Material," *Journal of the Mechanics and Physics of Solids*, Vol. 16, pp. 13–31.

Li, F. Z., Shih, C. F., and Needleman, A., 1985, "A Comparison of Methods for Calculating Energy Release Rate," *Engineering Fracture Mechanics*, Vol. 21, pp. 405–421.

Lloyd, W. R., 1989, private communication with D. M. Parks.

McMeeking, R. M., 1977, "Finite Deformation Analysis of Crack-Tip Opening in Elastic-Plastic Materials and Implications for Fracture," *Journal of the Mechanics and Physics of Solids*, Vol. 25, pp. 357–381.

McMeeking, R. M., and Parks, D. M., 1979, "On Criteria for *J*-Dominance of Crack-Tip Fields in Large-Scale Yielding," *Elastic-Plastic Fracture*, ASTM-STP 668, ASTM, Philadelphia, Penn., pp. 175–194.

Moran, B., Ortiz, M., and Shih, C. F., 1989 "Formulation of Implicit Finite Element Methods for Multiplicative Finite Deformation Plasticity," *International Journal for Numerical Methods in Engineering*, Vol. 29, pp. 483–514.

Nakamura, T., Shih, C. F., and Freund, L. B., 1989, "Three-Dimensional Transient Analysis of a Dynamically Loaded Three-Point-Bend Ductile Fracture Specimen," *Nonlinear Fracture Mechanics: Vol. I—Time-Dependent Fracture*, ASTM-STP 995, ASTM, Philadelphia, Penn., p. 217.

Parks, D. M., 1977, "The Virtual Crack Extension Method for Nonlinear Material Behavior," *Computer Methods in Applied Mechanics and Engineering*, Vol. 12, pp. 353–364.

Parks, D. M., 1981, "The Inelastic Line-Spring: Estimates of Elastic-Plastic Fracture Mechanics Parameters for Surface-Cracked Plates and Shells," *ASME Journal of Pressure Vessel Technology*, Vol. 103, pp. 246–254.

Parks, V. M., 1986, "Geometric Moire," *Handbook on Experimental Mechanics*, A. Kobayashi, ed., Society for Experimental Mechanics, Westport, Conn.

Parks, D. M., and White, C. S., 1982, "Elastic-Plastic Line-Spring Finite Elements for Surface-Cracked Plates and Shells," *ASME Journal of Pressure Vessel Technology*, Vol. 104, pp. 287–292.

Parks, D. M., and Wang, Y.-Y., 1988, "Elastic-Plastic Analysis of Part-Through Surface Cracks," *Analytical, Numerical, and Experimental Aspects*

of Three Dimensional Fracture Processes, A. J. Rosakis, K. Ravi-Chandar, and Y. Rajapakse, eds., ASME AMD-Vol. 91, ASME, New York, pp. 19–32.

Raju, I. S., and Newman, J. C., Jr., 1979, "Stress Intensity Factors for a Wide Range of Semi-Elliptical Surface Cracks in Finite-Thickness Plates," *Engineering Fracture Mechanics,* Vol. 11, pp. 817–829.

Reuter, W. G., and Lloyd, W. R., 1990, "Measurements of CTOD and CTOA Around Surface-Crack Perimeters and Relationships Between Elastic and Elastic-Plastic CTOD Values," *Surface-Crack Growth: Models, Experiments, and Structure,* ASTM-STP 1060, ASTM, Philadelphia, Penn.

Rice, J. R., 1967, "Mechanics of Crack Tip Deformation and Extension by Fatigue," *Fatigue Crack Propagation,* ASTM-STP 415, ASTM, Philadelphia, Penn., pp. 247–309.

Rice, J. R., and Rosengren, G. F., 1968, "Plane Strain Deformation Near a Crack Tip in a Power Law Hardening Material," *Journal of the Mechanics and Physics of Solids,* Vol. 16, pp. 1–12.

Rice, J. R., and Levy, N., 1972, "The Part-Through Surface Crack in an Elastic Plate," ASME JOURNAL OF APPLIED MECHANICS, Vol. 39, pp. 185–194.

Rosakis, A. J., Ravi-Chandar, K., and Rajapakse, Y., eds., 1988, *Analytical, Numerical, and Experimental Aspects of Three Dimensional Fracture Processes,* ASME AMD-Vol. 91, ASME, New York.

Shawki, T. G., Nakamura, T., and Parks, D. M., 1989, "Line-Spring Analysis of Surface Flawed Plates and Shells Using Deformation Theory," *International Journal of Fracture,* Vol. 41, pp. 23–38.

Shih, C. F., and German, M. D., 1981, "Requirements for a One Parameter Characterization of Crack Tip Fields by the HRR Singularity," *International Journal of Fracture,* Vol. 17, pp. 27–43.

Shih, C. F., 1981, "Relationship between the *J*-integral and the Crack Opening Displacement for Stationary and Extending Cracks," *Journal of the Mechanics and Physics of Solids,* Vol. 29, pp. 305–326.

Shih, C. F., 1983, "Tables of Hutchinson-Rice-Rosengren Singular Field Quantities," Division of Engineering, Brown University, Providence, R.I., June.

Shih, C. F., 1985, "*J*-Dominance Under Plane Strain Fully Plastic Conditions: The Edge Crack Panel Subject to Combined Tension and Bending," *International Journal of Fracture,* Vol. 29, pp. 73–84.

Stringfellow, R. G., 1988, private communication.

Tracey, D. M., 1976, "Finite Element Solutions for Crack-Tip Behavior in Small-Scale Yielding," *ASME Journal of Engineering Materials and Technology,* Vol. 98, pp. 146–151.

Wang, Y.-Y., 1988, "Analysis of Fracture Initiation in Surface-Cracked Plates," M. Sc. Thesis, Department of Mechanical Engineering, Massachusetts Institute of Technology, Cambridge, Mass., Sept.

Wang, Y.-Y., 1991, Ph.D. research under way, Department of Mechanical Engineering, Massachusetts Institute of Technology, Cambridge, Mass.

A Continuum Damage Model for Fracture of Brittle Solids Under Dynamic Loading

E. P. Fahrenthold
Department of Mechanical Engineering,
University of Texas,
Austin, TX 78712
Mem. ASME

A continuum damage mechanics description of elastic-brittle fracture provides an appropriate constitutive model for impact simulations involving ceramic, rock, or similar materials. For an orthotropically damaged solid, a complementary energy function may be derived from a mesomechanical description of three orthogonal arrays of coalescing cracks. Damage evolution equations suggested by dynamic fracture test measurements may be expressed in terms of tensor power functions which generalize classical one-dimensional analyses. Measured Weibull strength distributions may be employed to account for flaw size distribution effects on the damage accumulation rate. The resulting model avoids the introduction of effective stress assumptions or the use of specialized material property coefficients obtained from nonstandard mechanical tests.

Introduction

The effective use of general-purpose finite element codes in the dynamic analysis of fracture mechanics related problems, including for example impact dynamics simulations (Kawata and Shioiri, 1985; Anderson, 1987) and the design of wellbore fracturing treatments (Swenson and Taylor, 1983; Ang and Valliappan, 1988), is hindered by difficulties associated with continuum modeling of brittle fracture processes and resulting structural failures. Although materials science research has provided considerable insight into basic fracture mechanics mechanisms, incorporation of such knowledge into thermodynamically consistent three-dimensional models presents unusual geometric complications. Many numerical models have been dimensionally limited (Seaman et al., 1985) or have adopted strong fracture geometry assumptions (Mendelsohn, 1984a,b) which restrict their general utility. The continuum damage mechanics (Kachanov, 1986) approach to such problems aims at the development of intensive constitutive descriptions of fracture which can be easily incorporated into existing numerical codes. This paper describes a continuum damage mechanics model of elastic-brittle materials based on a three-dimensional mesomechanical (Haritos et al., 1988) description of elastic damage and a kinetic equation which accurately reflects the results of dynamic material property tests. The modeling methodology employs classical elasticity solutions to derive a complementary energy function for an orthotropically damaged elastic medium and a kinetic model (Murakami, 1987) to describe dynamic evolution of a second-order damage tensor. Weibull analysis of dynamic fracture tests provides a statistical description of flaw distributions which affect the damage accumulation rate under applied tensile loads. The resulting model incorporates a minimal number of measured material behavior coefficients, all of which may be determined using conventional test procedures. Implementation of the model as a constitutive augmentation of a structural finite element code provides for its application in impact dynamics simulations.

Contributed by the Applied Mechanics Division of THE AMERICAN SOCIETY OF MECHANICAL ENGINEERS for publication in the JOURNAL OF APPLIED MECHANICS.

Discussion on this paper should be addressed to the Technical Editor, Prof. Leon M. Keer, The Technological Institute, Northwestern University, Evanston, IL 60208, and will be accepted until two months after final publication of the paper itself in the JOURNAL OF APPLIED MECHANICS. Manuscript received by the ASME Applied Mechanics Division, Dec. 28, 1989; final revision, Aug. 17, 1990.

Elastic Damage Model

A thermodynamically consistent elastic damage model presumes the existence of a free energy function of a strain tensor **E** and a damage tensor **D**. The latter is assumed here to be of second order, allowing at most for orthotropic damage states but suitable for approximate analysis of many engineering applications. It is often found convenient to develop damage mechanics models in terms of a complementary energy function $\Omega(\mathbf{S}, \mathbf{D})$, with **S** the stress tensor, an approach used in the discussion which follows. The complementary energy function yields the constitutive relations

$$\mathbf{E} = \partial\Omega/\partial\mathbf{S}\,|_{\mathbf{D}}, \quad \mathbf{G} = \partial\Omega/\partial\mathbf{D}\,|_{\mathbf{S}} \qquad (1a,b)$$

where **G** is the intensive energy release rate tensor and only isothermal processes are considered. Equations (1) imply that the damage is in principle reversible, with thermally activated crack healing suggested by micromechanical thermodynamics (Krausz and Krausz, 1988). It is assumed here that a general state of orthotropic damage may be represented by three orthogonal arrays of penny-shaped cracks. The cracks may interact and coalesce, but the effects of three planar arrays of interacting cracks will be superposed to quantify the complementary energy Ω. This mesomechanical procedure (Atkinson, 1987) is an alternative to beginning with a postulated form for

a damage effect tensor (Chow and Wang, 1987a,b) based on triaxial or other material property tests. It should be noted that in the present context (excluding, e.g., electromagnetic effects), the complementary energy function is defined thermodynamically by static equilibrium states. Hence, this section employs static stress intensity factors in deriving an expression for Ω. Rate effects associated with dynamic crack propagation are imbedded in the formulation of the damage evolution equations discussed in the next section.

The complementary energy per unit volume of a uniaxially stressed elastic body containing a single penny-shaped crack of radius "a" is (Sneddon, 1946)

$$\Omega = \sigma^2/(2E) + [8(1-\nu^2)/(3E)]\sigma^2 a^3/V \tag{2a}$$

where E and ν are Young's modulus and Poisson's ratio for the isotropic solid, σ is the stress applied normal to the crack, and V is the bulk volume, with $V >> a^3$. In terms of the crack area ($A = \pi a^2$) and mode I stress intensity factor (K_∞), the associated extensive energy release rate (Hellan, 1984) is

$$G_{\text{ext}} = \partial\Omega/\partial A\,|_\sigma = (1-\nu^2)K_\infty^2/(VE),\quad K_\infty = 2\sigma(a/\pi)^{1/2}. \tag{2b,c}$$

In the case of a uniaxially stressed sphere of radius "b" containing the same crack, the stress intensity factor is increased to K_I (Tada, 1973), defined by

$$K_I^2 = cK_\infty^2(1-D^{1/2})/(1-D)^2,$$

$$D = A/(\pi b^2) = (a/b)^2,\quad c \approx 1 \tag{3a,b,c}$$

where the damage (D) has been introduced and the only restriction on the characteristic dimensions is $a \le b$. The associated intensive energy release rate is therefore

$$G_{\text{int}} = \partial\Omega/\partial D\,|_\sigma = (3/\pi)[(1-\nu^2)\sigma^2/E](D^{1/2}-D)/(1-D)^2 \tag{4a}$$

where $V = (4/3)\pi b^3$. Integration provides the complementary energy density

$$\Omega = \sigma^2/(2E) + (3/\pi)[(1-\nu^2)\sigma^2/E]f(D) \tag{4b}$$

where

$$f(D) = (D^{1/2}-D)/(1-D) - \ln(1+D^{1/2}) - (1/2)\ln(1-D). \tag{4c}$$

The effect of crack coalescence is quantified by the variation of the stress intensity factor reflected in $f(D)$.

Similarly, Segedin's (1950) expression for the change in complementary energy due to a penny-shaped crack in an elastic medium under a remote shearing stress τ parallel to the crack may be written

$$\Omega = (1+\nu)\tau^2/E + \{16(1-\nu^2)/[3(2-\nu)E]\}\tau^2(a^3/V). \tag{4d}$$

Recognizing the principal importance of mode I fracture in most engineering applications (Broek, 1987), if finite size corrections are neglected in considering shear stress effects, then

$$\Omega = (1+\nu)\tau^2/E + (4/\pi)\{(1-\nu^2)/[(2-\nu)E]\}\tau^2 D^{3/2}. \tag{4e}$$

Note that for small crack concentrations, Eqs. (2a) and (4d) lead to the same $D^{3/2}$ dependence of the added compliance on the damage for both normal and shear stress effects. Hence, the effect of finite crack concentrations on the added compliance in shear is assumed here to have the same damage dependence as in (4b), namely

$$\Omega = (1+\nu)\tau^2/E + (4/\pi)\{(1-\nu^2)/[(2-\nu)E]\}\tau^2 f(D). \tag{4f}$$

In terms of a six-dimensional stress vector expressed in the principal damage coordinate system (x, y, z),

$$\sigma^T = \{\sigma_1\sigma_2\sigma_3\sigma_4\sigma_5\sigma_6\} = \{\sigma_{xx}\sigma_{yy}\sigma_{zz}\sigma_{xy}\sigma_{yz}\sigma_{xz}\}, \tag{5}$$

the preceding results may be combined to obtain a general expression for $\Omega(\mathbf{S},\mathbf{D})$

$$\Omega = (1/2E)\{\sigma_1^2+\sigma_2^2+\sigma_3^2 - 2\nu(\sigma_1\sigma_2+\sigma_2\sigma_3+\sigma_1\sigma_3) + \alpha_1\sigma_1^2+\alpha_2\sigma_2^2+\alpha_3\sigma_3^2 + 2(1+\nu)[\sigma_4^2+\sigma_5^2+\sigma_6^2+\beta_1(\sigma_4^2+\sigma_6^2) + \beta_2(\sigma_4^2+\sigma_5^2)+\beta_3(\sigma_5^2+\sigma_6^2)]\} \tag{6a}$$

where

$$\alpha_i = (6/\pi)(1-\nu^2)f_i(D_i) \tag{6b}$$

$$f_i(D_i) = (D_i^{1/2}-D_i)/(1-D_i) - \ln(1+D_i^{1/2}) - (1/2)\ln(1-D_i) \tag{6c}$$

$$D_i = (\pi a_i^2)/(\pi b^2) = (a_i/b)^2 \tag{6d}$$

$$\beta_i = (4/\pi)[(1-\nu)/(2-\nu)]f_i(D_i) \tag{6e}$$

with $i = (1, 2, 3)$, no summation implied, and (D_1, D_2, D_3) the eigenvalues of the damage tensor. The stress-strain relations in the principal damage coordinate system are then

$$\epsilon_i = \partial\Omega/\partial\sigma_i\,|_{D_j};\quad i = 1, 2, \ldots 6;\ j = 1, 2, 3 \tag{7a}$$

where

$$\epsilon^T = \{\epsilon_1\epsilon_2\epsilon_3\epsilon_4\epsilon_5\epsilon_6\} = \{\epsilon_{xx}\epsilon_{yy}\epsilon_{zz}2\epsilon_{xy}2\epsilon_{yz}2\epsilon_{xz}\}. \tag{7b}$$

In matrix form, Eq. (6a) is

$$\Omega = (1/2E)\sigma^T\hat{\mathbf{C}}\sigma,\quad \hat{\mathbf{C}} = \mathbf{C} + \mathbf{M}(\mathbf{D}) \tag{7c}$$

where $\mathbf{C}$ represents the compliance of the undamaged solid and $\mathbf{M}$ is a damage effect matrix (Wang and Chow, 1989). In component form

$$\mathbf{C} = \begin{bmatrix} 1 & -\nu & -\nu & 0 & 0 & 0 \\ -\nu & 1 & -\nu & 0 & 0 & 0 \\ -\nu & -\nu & 1 & 0 & 0 & 0 \\ 0 & 0 & 0 & 2(1+\nu) & 0 & 0 \\ 0 & 0 & 0 & 0 & 2(1+\nu) & 0 \\ 0 & 0 & 0 & 0 & 0 & 2(1+\nu) \end{bmatrix} \tag{7d}$$

$$\mathbf{M} = \begin{bmatrix} \alpha_1 & 0 & 0 & 0 & 0 & 0 \\ 0 & \alpha_2 & 0 & 0 & 0 & 0 \\ 0 & 0 & \alpha_3 & 0 & 0 & 0 \\ 0 & 0 & 0 & 2(1+\nu)(\beta_1+\beta_2) & 0 & 0 \\ 0 & 0 & 0 & 0 & 2(1+\nu)(\beta_2+\beta_3) & 0 \\ 0 & 0 & 0 & 0 & 0 & 2(1+\nu)(\beta_1+\beta_3) \end{bmatrix}. \tag{7e}$$

Chow and Wang (1987a,b) have shown that such damage effect matrices can properly represent fourth-order tensor functions of a second-order damage tensor $\mathbf{D}$ and hence satisfy invariance requirements for the elastic constitutive relations.

Application of the preceding elastic-damage model to problems of dynamic fracture in brittle materials requires that several additional points be considered. In many finite element codes, convenient implementation of the derived constitutive model calls for use of the stress-strain relations (7a) in inverted form, namely

$$\sigma = \hat{\mathbf{K}}\epsilon,\quad \hat{\mathbf{K}} = \hat{\mathbf{C}}^{-1} \tag{7f,g}$$

where $\hat{\mathbf{K}}$ is the elastic modulus matrix for the damaged material. In addition, in the case of brittle materials, the preceding analysis must be modified to account for the fact that not all of the accumulated damage is active under all states of stress and strain (Ortiz, 1985 and Ju, 1989). Consistent with previous work (Ortiz, 1985) and considering the constitutive relations (7f), the components of the elastic modulus matrix $\hat{\mathbf{K}}$ are modified to account for brittle material response using

$$\alpha_i \rightarrow \alpha_i u(\sigma_i), \text{ (no sum)};\ \beta_i \rightarrow \beta_i u(\sigma_i), \text{ (no sum)};\ i=\{1,2,3\} \tag{7h}$$

where u is the unit step function. The effect of the substitutions (7*h*) is to cause only that portion of the total damage activated by tensile normal stresses to affect the stiffness matrix of damaged solid. Finally, a proper accounting for large rotation effects, important to impact modeling, requires that appropriate stress and strain measures be employed. Hence, the stress (**S**) and strain (**E**) tensors of the preceding discussion are defined to be the second Piola-Kirchoff and Lagrangian measures (Malvern, 1969).

$$\mathbf{S}=(\rho_o/\rho)\mathbf{F}^{-1}\mathbf{T}\mathbf{F}^{-T};\ \mathbf{E}=(1/2)(\mathbf{C}-\mathbf{I}),\ \mathbf{C}=\mathbf{F}^T\mathbf{F} \tag{7i,j}$$

where **T** is the Cauchy stress, **F** is the deformation gradient tensor, ρ is the density, and ρ_o is the density in the density in the reference (undeformed) configuration. These definitions imply that

$$\Omega=\rho_o\bar{\Omega} \tag{7k}$$

where $\bar{\Omega}$ is the complementary energy density per unit mass.

Damage Evolution Equations

The damage evolution equations may be written in the general form

$$\overset{\nabla}{\mathbf{D}}=\overset{\nabla}{\mathbf{D}}(\mathbf{S},\mathbf{D}) \tag{8a}$$

$$\overset{\nabla}{\mathbf{D}}=\dot{\mathbf{D}}-\mathbf{W}\mathbf{D}+\mathbf{D}\mathbf{W};\ \mathbf{W}=(1/2)(\mathbf{L}-\mathbf{L}^T);\ \mathbf{L}=\dot{\mathbf{F}}\mathbf{F}^{-1} \tag{8b,c,d}$$

where (8*b*) is the corotational rate of change of the damage. For example, one possible choice for the evolution relation, a special case of (8*a*) suggested by the infinitesimal deformation analysis of Ju (1989), is

$$\overset{\nabla}{\mathbf{D}}=\overset{\nabla}{\mathbf{D}}(\mathbf{G}). \tag{8e}$$

The evolution relation used in the present paper is motivated by the damage models of Cordebois and Sidoroff (1982) and reduces to Kachanov's classical evolution relation in one dimension (Kachanov, 1986). Here a power function of the tensile normal stress (Leckie and Onat, 1981) is used to describe the evolution of damage, but with a quotient factor introduced to account for the acceleration of the damage accumulation rate with reduction in the effective area under load (Kausch, 1987). The kinetic model proposed here

$$\overset{\nabla}{\mathbf{D}}=A[\mathbf{S}^{e+}]^k;\ \mathbf{S}^e=(\mathbf{I}-\mathbf{D})^{-1/2}\mathbf{S}(\mathbf{I}-\mathbf{D})^{-1/2} \tag{8f,g}$$

with A constant and k an integer, defines the corotational damage evolution rate as an objective isotropic function of the mesostress ($\mathbf{S}^e$) of Cordebois and Sidoroff (1982). The positive projection of the mesostress tensor ($\mathbf{S}^{e+}$) is that defined by Ortiz (1985)

$$\mathbf{S}^{e+}=\boldsymbol{P}^+\mathbf{S}^e=\sum_{i=1}^{3}u(\lambda_i)\mathbf{s}_i\otimes\mathbf{s}_i;\ |\mathbf{s}_i|=1 \tag{8h,i}$$

$$S^{e+}_{ij}=P^+_{ijkl}S^e_{kl};\ P^+_{ijkl}=Q^+_{ia}Q^+_{jb}Q_{ka}Q_{lb} \tag{8j,k}$$

$$\mathbf{Q}=\sum_{i=1}^{3}\mathbf{s}_i\otimes\mathbf{s}_i;\ \mathbf{Q}^+=\sum_{i=1}^{3}u(\lambda_i)\mathbf{s}_i\otimes\mathbf{s}_i \tag{8l,m}$$

where the λ_i and $\mathbf{s}_i$ are the eigenvalues and eigenvectors of $\mathbf{S}^e$ and $\boldsymbol{P}^+$ is a fourth-order projection tensor. The positive projection operator is introduced in order to stipulate that damage growth occurs only under tensile loading conditions.

The evolution Eqs. (8) may be evaluated by comparison with published experimental data (Davidge et al., 1973) describing the response of ceramic in constant load and constant loading rate tests. The cited three-point bending tests are analyzed here as uniaxial tension (Batdorf and Heinisch, 1978) applied to the reduced volume

$$V_r=V/[2(m+1)^2] \tag{9a}$$

where V is the sample volume and "m" is a Weibull modulus (Batdorf and Crose, 1974), to be discussed later. In uniaxial tension, the evolution Eqs. (8) reduce to

$$\dot{D}=A[\sigma/(1-D)]^k. \tag{9b}$$

For a constant load test (σ constant), Eq. (9*b*) reduces to

$$1-(1-D)^{k+1}=(k+1)A\sigma^k t \tag{10a}$$

where $D=0$ at time $t=0$. If sample fracture is defined by $D=D_c$ at $t=\tau$, the time to failure at any applied stress is

$$\tau=[1-(1-D_c)^{k+1}]/[(k+1)A\sigma^k]. \tag{10b}$$

The parameter D_c is the damage at fracture (see, e.g., Ju, 1989), with $0<D_c<1$. In general, results of a series of tests on identical samples would satisfy the similarity relation

$$\tau_1/\tau_2=(\sigma_2/\sigma_1)^k \tag{10c}$$

for different applied stress levels σ_1 and σ_2. Similarly, for constant loading rate tests ($\sigma=E\dot{\epsilon}t$ with $\dot{\epsilon}$ and E constant), Eq. (8) reduces to

$$1-(1-D)^{k+1}=A(E\dot{\epsilon})^k t^{k+1} \tag{11a}$$

with time to fracture

$$\tau=[1-(1-D_c)^{k+1}]/[A\sigma^k]. \tag{11b}$$

The variation of the failure stress with loading rate for identical samples would then satisfy

$$\dot{\epsilon}_1/\dot{\epsilon}_2=(\sigma_1/\sigma_2)^{k+1} \tag{11c}$$

for different strain rates $\dot{\epsilon}_1$ and $\dot{\epsilon}_2$. Consistency of the preceding damage description of constant load and constant loading rate tests requires that the time to failure (τ_{cs}) under a constant stress σ and the time to failure (τ_{cr}) at the same value of σ in a constant strain rate test be related by

$$\tau_{cs}=\tau_{cr}/(k+1) \tag{12}$$

for identical samples. Equations (10*c*), (11*c*), and (12) were derived by Davidge et al. (1973) based on a fracture mechanics analysis, and verified experimentally for alumina. Assuming that the experimental results generally represent the behavior of the material under study, the stochastic distribution of the parameters A and k may be estimated and kinetic equations of the form (8) used to describe damage accumulation under arbitrary stress histories. For the case in which k is an absolute constant, for any two samples tested at the same loading rate, Eq. (11*b*) implies

$$A_1/A_2=(\sigma_2/\sigma_1)^{k+1}. \tag{13a,b,c}$$

For the referenced experiments on alumina, it was found that the measured bending strengths at various strain rates were described by two-parameter Weibull distributions incorporating identical Weibull moduli (m) and differing only in their mean strengths (σ_m). A two-parameter Weibull model (Matsuo, 1981) estimates the probability of failure (F) of a ceramic part of volume V in uniaxial tension σ due to internal flaws as

$$F=1-\exp\{-V[1/(m+1/2)](\sigma/\sigma_o)^m\} \tag{14a}$$

where σ_o and m are determined experimentally. Since the measured strengths at any strain rate were described by

$$\ln\ln[1/(1-F)]=m\ln(\sigma)-m\ln(\sigma_o)+\ln\{V_r[1/(m+1/2)]\}, \tag{14b}$$

which is written in terms of the mean strength (σ_m) as

$$\ln\ln[1/(1-F)]-\ln\ln(2)=m\ln(\sigma)-m\ln(\sigma_m), \tag{14c}$$

then if Eqs. (13) and (14*c*) hold for any given strain rate, in general

$$A/A_m=\{\ln[1/(1-F)]/\ln(2)\}^{[(k+1)/m]}, \tag{14d}$$

where A_m is the value of A for the mean strength material

calculated using (11*b*). This provides a distribution of damage accumulation rate parameters A which lead to measured variations in material strength. Since the variable F in Eq. (14*d*) is a measure of material quality, the appropriate value for an A to be used in continuum simulations is

$$A = \int_0^1 A(F)\,dF = A_m \Gamma[(k+1)/m + 1]/\{\ln(2)^{[(k+1)/m]}\} \quad (14e)$$

where Γ is the gamma function. In summary, the measured Weibull parameters σ_o and m serve to represent the effect of a distribution of flaws in the material on the continuum damage accumulation rate. Note that in finite element implementations of the preceding damage evolution model, Eqs. (9*a*) and (14*a*), can be used to correct (at the element level) experimentally measured material properties in order to account for sample volume effects.

The quantities m, k, σ_o, and A_m calculated from the experiments of Davidge et al. (1973), with $D_c = 0.99$, provide appropriate values for 95 percent Al_2O_3:

$$m = 13.2;\ k = 22;\ \sigma_o = 120 \text{ MPa } (\text{m}^3)^{1/13.2} \quad (15a,b,c)$$

$$A_m = 2.09 \times 10^{-57} \text{MPa}^{-22} \text{sec}^{-1}. \quad (15d)$$

The cited experimental data used in calculating the preceding parameters was measured at strain rates between $1.8 \times 10^{-6}\text{sec}^{-1}$ and $1.8 \times 10^{-4}\text{sec}^{-1}$. In general, the measured parameters of Eqs. (15) will reflect the rate dependence of fracture processes in the material of interest (Williams and Knauss, 1985), such as are conventionally discussed in terms of crack velocity, dependent stress intensity factors (Hellan, 1984).

Finite Element Implementation

The material model described in the two preceding sections was implemented as a constitutive augmentation to the dynamic finite element code DYNA3D (Goudreau and Hallquist, 1982) for use in impact dynamics simulations. The implementation follows general guidelines for such augmentations (Hallquist, 1982) and employs EISPACK routines (Smith et al., 1976) for required eigenvalue calculations. The augmentation is vectorized consistent with the basic DYNA3D code, and incorporates as history (state) variables for each element the components of the symmetric damage tensor **D**. The kinetic equations and finite element implementation allow for independent evolution of the damage state in each element, with respect to both orientation of the damage eigenvectors and magnitude of the damage eigenvalues.

A one-step iteration procedure is used to integrate the evolution equations and update the stress at each time step. This procedure is similar to that employed in the basic DYNA3D code to update the pressure in materials whose equation of state is nonlinear in internal energy. Given current values for the strain ($E_{rs}^{(n+1)}$) and values of the damage and stress at the last time step ($D_{rs}^{(n)}$, $S_{rs}^{(n)}$), the components of the stress are first estimated as

$$S_{ij}^{(n+1)^*} = \hat{K}_{ijkl}(D_{rs}^{(n)}, S_{rs}^{(n)}) E_{kl}^{(n+1)}. \quad (16a)$$

These estimates are then used to update the damage and the stress in the form

$$D_{ij}^{(n+1)} = D_{ij}^{(n)} + \dot{D}_{ij}(D_{kl}^{(n)}, S_{rs}^{(n+1)^*})\Delta t \quad (16b)$$

$$S_{ij}^{(n+1)} = \hat{K}_{ijkl}(D_{rs}^{(n+1)}, S_{rs}^{(n+1)^*}) E_{kl}^{(n+1)} \quad (16c)$$

where Δt is the time step and the functions $\dot{D}_{ij}$ are defined by Eqs. (8). If the trial damage state of Eq. (16*b*) is inadmissible, based on the fracture criterion discussed in the next paragraph, a radial return algorithm (Hughes, 1984) is used to locate the fractured state in principal damage space. As in the case of the equation of state relations just mentioned, the outlined integration procedure is motivated by the nonlinear dependence of the stiffness matrix on the damage tensor and the relatively small time steps employed in the explicit DYNA3D code.

The stress-strain relations must be augmented by a brittle fracture criterion. Consistent with the damaged-based continuum approach used here, element fracture is defined by a minimum normal damage criterion

$$D_i = D_c;\ i = 1,\ 2,\ \text{or } 3. \quad (16d)$$

That is, damage is accumulated until an eigenvalue D_i reaches the critical damage value D_c, at which time the element is assumed to fracture along a plane normal to the ith eigenvector of the damage tensor. The fractured material is assumed to be unable to support any tensile normal stress or any shear stress component on the plane of fracture. Alternative fracture criteria could of course be adopted, but should be consistent with the evolutional equations employed, and be used in the experimental evaluation of damage accumulation coefficients. In order to avoid numerical instabilities associated with abrupt changes in element stiffness, evolution from the undamaged state to the fractured state is extended over a minimum of three time steps. This procedure is consistent with existing stress based element failure models included in the standard DYNA3D code.

Impact Simulations

The constitutive subroutine just described may be employed in the analysis of high-velocity impact experiments involving brittle solids. Tower et al. (1987) have used electromagnetic railguns to study the effect of low length to diameter ratio projectiles of various material types on steel plate targets at velocities as high as 7 km/sec. The behavior of ceramic projectiles in these experiments is anomalous, in that they exhibit a modest reduction in penetration efficiency with increased velocity, apparently due to "shattering" (Tower et al., 1987) of the projectile at sufficiently rapid loading rates. The constitutive subroutine developed here was applied to simulate the impact of spherical projectiles on steel plate, in order to estimate the effects of damage accumulation and brittle fracture on the penetration performance of ceramic. The numerical modeling incorporated plate thickness to sphere diameter and plate width to sphere diameter ratios of 1.1 and 5.6, respectively, and the following material properties: (1) for the alumina sphere, Young's modulus = 276 GPa, Poisson's ratio = 0.22, reference density = 3600 kg/m^3, $k = 22$, and $D_c = 0.99$, for various values of A; (2) for the steel target, Young's modulus = 207 GPa, Poisson's ratio = 0.30, and reference density = 7860 kg/m^3. The steel was assumed to be perfectly plastic, with a yield strength of 414 MPa, and to obey the Los Alamos equation of state (Reddy, 1976). Figures 1 and 2 show an oblique sectioned view of a typical three-dimensional impact simulation and a corresponding contour plot of the von Mises effective stress (Hallquist, 1982) in the projectile, at ten microseconds after impact for an initial velocity of 1 km/sec. Figure 3 shows the time variation of the depth of penetration (P, defined as the vertical displacement of the upper surface of the target centerline) for a damage accu-

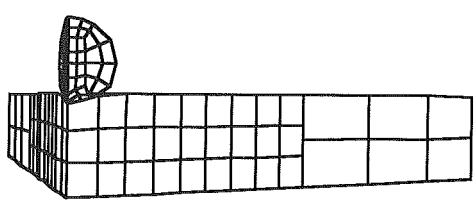

Fig. 1 Sectioned view of a 1-km/sec impact of a ceramic sphere on a steel plate ($t = 10$ μsec)

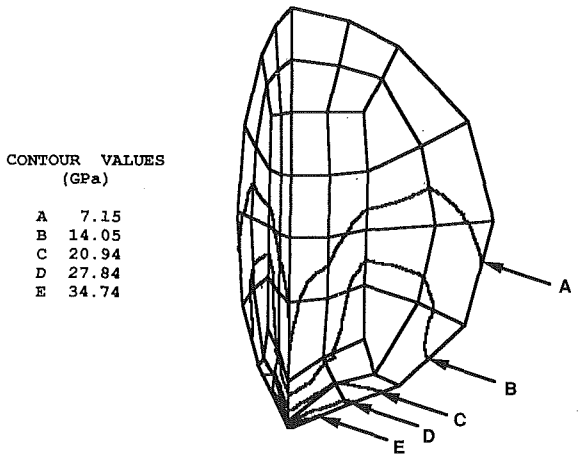

Fig. 2 Contour plot of the von Mises effective stress in a ceramic sphere impacting a steel plate at 1-km/sec ($t = 10$ μsec)

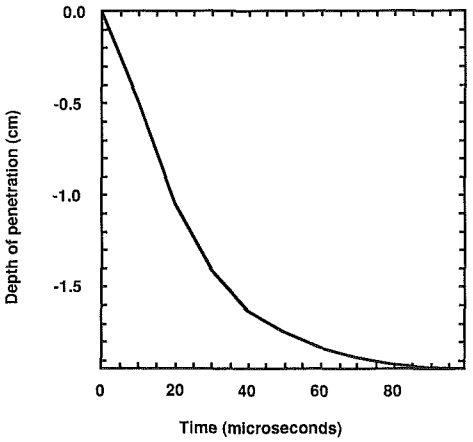

Fig. 3 Depth of penetration (cm) versus time (μsec) for a 1-km/sec impact of a ceramic sphere on a steel plate ($k = 22$, $A = 2.09 \times 10^{-57}$ $MPa^{-22}sec^{-1}$)

mulation parameter appropriate for mean strength ceramic. The dependence of the predicted dimensionless penetration depth (P/d, d = sphere diameter) on A is shown in Fig. 4 for impacts at 1 km/sec. The results are qualitatively as expected, with "weaker" ceramics, characterized by decreased mean fracture strength and increased values of A, leading to a reduction in predicted penetration depth at constant impact velocity. The difference between predicted penetration depths for perfectly elastic spheres and spheres exhibiting strength properties comparable to those measured in the Davidge et al. (1973) experiments is approximately 26 percent. The predicted value of $P/d = 0.43$ for high quality alumina, and a target thickness approximately equal to the sphere diameter, is generally consistent with the experimental data of Tower et al. (1987).

Conclusion

A complementary energy density-based approach to constitutive modeling of damaged elastic solids provides a mesomechanical description of the continuum stress-strain relations which need not invoke common effective stress assumptions, even in the case of finite crack concentrations. The algebraic form of the resulting material compliance matrix is analogous to that derived in simple one-dimensional cases (Broek, 1987), and differs significantly from those developed on the basis of effective area models (Murakami, 1987). Combining the complementary energy density function with tensor power function forms for the dissipative (evolutional) relations and an appropriate fracture criterion provides for the simulation of brittle fracture processes under large-rotation conditions characteristic of many impact dynamics problems. The use of measured Weibull strength parameters provides a simple accounting for flaw distribution effects described in tensorial form by Leckie and Onat (1981). Second-order tensor damage models of the type described here are the simplest of those used in three-dimensional analyses, and present few complications in finite element implementation beyond those associated with modeling of composites and other anisotropic materials. Nonetheless, the state variable storage requirements for such models are considerable, emphasizing the value of modeling simplicity, already motivated by the difficulties of obtaining application specific model parameters for a variety of dynamic analysis tasks (Zukas et al., 1982).

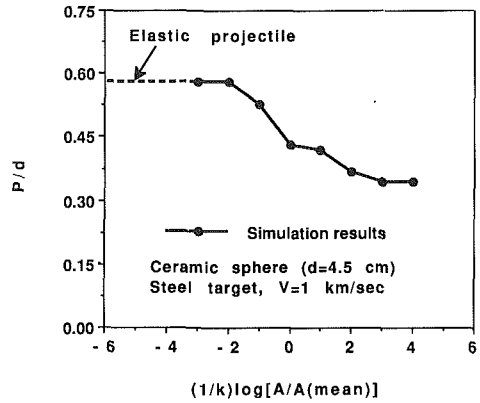

Fig. 4 Dependence of the dimensionless depth of penetration (P/d) on the continuum damage accumulation rate (A) for 1-km/sec impact of a ceramic sphere on a steel plate ($k = 22$, $A_m = 2.09 \times 10^{-57}$ $MPa^{-22}sec^{-1}$)

Acknowledgments

This work was supported by Cray Research, Inc. and by the Governor's Energy Management Center—State of Texas Energy Research in Applications Program under contract No. 5127. Computer time was provided by the University of Texas System Center for High Performance Computing.

References

Anderson, C. E., Jr., ed., 1987, "Hypervelocity Impact: Proceedings of the 1986 Symposium," *International Journal of Impact Engineering*, Vol. 5, No. 1-4.

Ang, K. K., and and Valliappan, S., 1988, "Pseudo-Plane Strain Analysis of Wave Propagation Problems Arising From Detonations of Explosives in Cylindrical Boreholes," *International Journal for Numerical and Analytical Methods in Geomechanics*, Vol. 12, pp. 301-322.

Atkinson, B. K., ed., 1987, *Fracture Mechanics of Rock*, Academic Press, New York.

Batdorf, S. B., and Crose, J. G., 1974, "A Statistical Theory for the Fracture of Brittle Structures Subjected to Nonuniform Polyaxial Stresses," ASME Journal of Applied Mechanics, June, pp. 459-464.

Batdorf, S. B., and Heinisch, H. L., Jr., 1978, "Weakest Link Theory Reformulated for Arbitrary Fracture Criterion," *Journal of the American Ceramic Society*, Vol. 61, No. 7, pp. 355-358.

Broek, D., 1987, *Elementary Engineering Fracture Mechanics*, Martinus Nijhoff, Boston.

Chow, C. L., and Wang, J., 1987a, "An Anisotropic Theory of Elasticity for Continuum Damage Mechanics," *International Journal of Fracture*, Vol. 33, pp. 3-16.

Chow, C. L., and Wang, J., 1987b, "An Anisotropic Theory of Continuum Damage Mechanics for Ductile Fracture," *Engineering Fracture Mechanics*, Vol. 27, No. 5, pp. 547-558.

Cordebois, J. P., and Sidoroff, F., 1982, "Damaged Induced Elastic Anisotropy," *Mechanical Behavior of Anisotropic Solids*, J.-P. Boehler, ed., Martinus Nijhoff, Boston, pp. 761-774.

Davidge, R. W., McLaren, J. R., and Tappin, G., 1973, "Strength-Probability-Time (SPT) Relationships in Ceramics," *Journal of Materials Science*, Vol. 8, pp. 1699-1705.

Goudreau, G. L., and Hallquist, J. O., 1982, "Recent Developments in Large-Scale Finite Element Lagrangian Hydrocode Technology," *Computer Methods in Applied Mechanics and Engineering*, Vol. 33, pp. 725-757.

Haritos, G. K., Hager, J. W., Amos, A. K., and Salkind, M. J., 1988,

"Mesomechanics: The Microstructure-Mechanics Connection," *International Journal of Solids and Structures*, Vol. 24, No. 11, pp. 1081–1096.

Hallquist, J. O., 1982, "Theoretical Manual for DYNA3D," Report No. UCID-19401, Lawrence Livermore National Laboratory, University of California.

Hellan, K., 1984, *Introduction to Fracture Mechanics*, McGraw-Hill, New York.

Hughes, T. J. R., 1984, "Numerical Implementation of Constitutive Models: Rate-Independent Deviatoric Plasticity," *Theoretical Foundation for Large-Scale Computations for Non-Linear Material Behavior*, S. Nemat-Nasser, R. J. Asaro, and G. A. Hegemeir, eds., Martinus Nijhoff, Dordrecht, pp. 29–57.

Ju, J. W., 1989, "On Energy-Based Coupled Elastoplastic Damage Theories: Constitutive Modeling and Computational Aspects," *International Journal of Solids and Structures*, Vol. 25, No. 7, pp. 803–833.

Kachanov, L. M., 1986, *Introduction to Continuum Damage Mechanics*, Martinus Nijhoff Publishers, Boston.

Kausch, H.-H., 1987, *Polymer Fracture*, Springer-Verlag, New York.

Kawata, K., and Shioiri, J., eds., 1985, *Macro- and Micro-Mechanics of High Velocity Deformation and Fracture*, Springer-Verlag, New York.

Krausz, A. S., and Krausz, K., 1988, *Fracture Kinetics of Crack Growth*, Kluwer, Boston.

Leckie, F. A., and Onat, E. T., 1981, "Tensorial Nature of Damage Measuring Internal State Variables," *Physical Non-Linearities in Structural Analysis*, Springer-Verlag, New York.

Malvern, L. E., 1969, *Introduction to the Mechanics of a Continuous Medium*, Prentice-Hall, Englewood Cliffs, N.J.

Matsuo, Y., 1981, "Statistical Fracture Theory for Multiaxial Stress States Using Weibull's Three Parameter Function," *Engineering Fracture Mechanics*, Vol. 14, pp. 527–538.

Mendelsohn, D. A., 1984a, "A Review of Hydraulic Fracture Modeling—Part II: General Concepts, 2D Models, Motivation for 3D Modeling," *Journal of Energy Resources Technology*, Sept., pp. 369–376.

Mendelsohn, D. A., 1984b, "A Review of Hydraulic Fracture Modeling—Part I: 3D Modeling and Vertical Growth in Layered Rock," *Journal of Energy Resources Technology*, Dec., pp. 543–553.

Murakami, S., 1987, "Anisotropic Aspects of Material Damage and Application of Continuum Damage Mechanics," *Continuum Damage Mechanics, Theory and Applications*, D. Krajcinovic and J. Lemaitre, eds., Springer-Verlag, New York.

Ortiz, M., 1985, "A Constitutive Theory for the Inelastic Behavior of Concrete," *Mechanics of Materials*, Vol. 4, pp. 67–93.

Reddy, J. N., 1976, "Finite Element Analysis of the Initial Stages of Hypervelocity Impact," *Computer Methods in Applied Mechanics and Engineering*, Vol. 9, pp. 47–63.

Seaman, L., Curran, D. R., and Murri, W. J., 1985, "A Continuum Model for Dynamic Tensile Microfracture and Fragmentation," ASME JOURNAL OF APPLIED MECHANICS, Vol. 52, pp. 593–600.

Segedin, C. M., 1950, "Note on a Penny-Shaped Crack Under Shear," *Proceedings of the Cambridge Philosophical Society*, Vol. 47, pp. 396–400.

Smith, B. T., Boyle, J. M., Dongarra, J. J., Garbow, S. S., Ikebe, Y., Klema, V. C., and Moler, C. B., 1976, *Matrix Eigensystem Routines—EISPACK Guide*, Springer-Verlag, New York.

Sneddon, I. N., 1946, "The Distribution of Stress in the Neighborhood of a Crack in an Elastic Solid," *Proceedings of the Royal Society of London*, Vol. A187, pp. 229–260.

Swenson, D. V., and Taylor, L. M., 1983, "A Finite Element Model for the Analysis of Tailored Pulse Stimulation of Boreholes," *International Journal for Numerical and Analytical Methods in Geomechanics*, Vol. 7, pp. 469–484.

Tada, H., Paris, P., and Irwin, G., 1973, *The Stress Analysis of Cracks Handbook*, Del Research Corporation, St. Louis, Mo.

Tower, M. M., Jackson, G. L., Farris, L. K., and Haight, C. H., 1987, "Hypervelocity Impact Testing Using an Electromagnetic Railgun Launcher," *International Journal of Impact Engineering*, Vol. 5, pp. 635–644.

Wang, J., and Chow, C. L., 1989, "Mixed Mode Ductile Fracture Studies With Nonproportional Loading Based on Continuum Damage Mechanics," *Journal of Engineering Materials and Technology*, Vol. 111, pp. 204–209.

Williams, M. L., and Knauss, W. G., eds., 1985, *Dynamic Fracture*, Martinus Nijhoff Publishers, Boston.

Zukas, J. A., Nicholas, T., Swift, H. F., Greszczuk, L. B., and Curran, D. R., 1982, *Impact Dynamics*, John Wiley and Sons, New York.

ERRATA

Errata on "Transient Thermal Stresses in Cylindrically Orthotropic Composite Tubes," ASME JOURNAL OF APPLIED MECHANICS, Vol. 56, June 1989, pp. 411–417, and on the follow-up paper, "The Initial Phase of Transient Thermal Stresses due to General Boundary Thermal Loads in Orthotropic Hollow Cylinders," ASME JOURNAL OF APPLIED MECHANICS, Vol. 57, Sept. 1990, pp. 719–724, both by G. A. Kardomateas.

The term q_2 was omitted in Eq. (14) of the 1989 paper and Eq. (11) of the 1990 paper, and this error carried through in the remaining of the equations, which otherwise are correct.

To account for this error, replace d_{4n} and d_{5n} in these equations (e.g., Eq. (14) of the 1989 paper and all equations thereafter that involve d_{4n} or d_{5n}) by $d_{4n}q_2$ and $d_{5n}q_2$, respectively, as well as replace q_1 by q_1/q_2 and q_3 by q_3/q_2.

Singular Fields in Plane-Strain Penetration

David Durban

Omri Rand

Faculty of Aerospace Engineering,
Technion-Israel Institute of Technology,
Haifa 32000, Israel

Local singular fields are investigated in the vicinity of the vertex of a sharp wedge that penetrates a viscous solid. Material behavior is modeled by the usual power-law constitutive relation. Wall friction is accounted for by imposing friction factors along the walls of the wedge. The case of a Newtonian fluid is investigated analytically, and sample numerical results are presented for nonlinear strain rate hardening. It is shown that the exponent of strain rate singularity increases as the wedge becomes sharper and smoother. Increasing the hardening parameter also results in a stronger strain rate singularity. High levels of wall friction induce an intensive shear boundary layer near the wall.

1 Introduction

Steady penetration of a rigid wedge into viscoplastic media will induce singular strain rate and stress fields in the neighborhood of the wedge tip. A start of such penetration studies has been presented recently by Fleck and Durban (1991) for a rigid conical cone with a rough wall that penetrates a power-law viscous solid. The present work addresses the plane-strain version of the penetration problem with the same material model, so that the near-tip singular field is governed by the HRR equation (Hutchinson, 1968; Rice and Rosengren, 1968). Frictional boundary conditions are accounted for along the walls of the wedge by assuming that wall roughness is measured by the friction factor. That factor determines the relative contribution of the shear stress at the wall to the effective plastic stress.

The study reveals the nature of the coupling between wall friction and the strain-rate hardening of the material within the singular zone. This could be helpful in analyzing experimental data of creep indentation where difficulties arise in measuring creep properties due to wall friction (Atkins et al., 1966; Matthews, 1980).

The governing equations for the stress function are given in the next section. We show that the mixed boundary data at each wall, that supplements the HRR equation, can be expressed in terms of the circumferential profile of the stress function. In Section 3, we consider in detail the special case of a Newtonian fluid. The field equation admits an exact solution which is used here for a simple illustration of the singular field characteristics for symmetric penetration modes. It is shown that the exponent of strain-rate singularity increases as the wedge becomes sharper and smoother. There is also a noticeable build-up of a near-wall boundary layer at high levels of friction. An interesting comparison is made between steady penetration of a rigid, perfectly rough knife (a wedge of zero thickness) in a Newtonian fluid and a stationary crack in an Hookean solid (modes I and II). Both fields have the same exponent of the singularity but entirely different stress profiles within the singular zone.

Finally, in Section 4 we show results of numerical calculations again for symmetric fields, but with different strain-rate hardening parameters. It is confirmed that the strain-rate components become less singular with increasing wall friction and wedge angle. Similarly, increasing the strain-rate hardening parameter results in an increasing strain-rate singularity. These results are in agreement with the findings reported by Fleck and Durban (1991) for the conical indentor. The near-wall boundary layer build-up is demonstrated for a number of cases. A similar boundary layer has been observed experimentally by Roth and Oxley (1972) in orthogonal machining. Comparison with available results for the analogous free-notch problem shows that below a certain level of wall friction the penetrating wedge induces a stronger singularity than the free notch.

The paper concludes with an example of asymmetric penetration where the wedge has one smooth wall while the other wall is of considerable roughness. Again, an intensive shear boundary layer is observed near the rough wall.

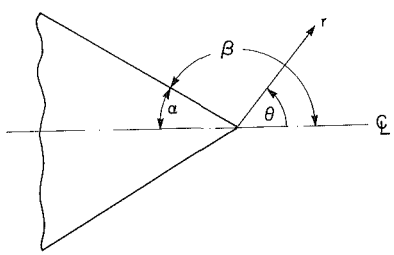

Fig. 1 Notation for steady penetration of a rigid wedge. A plane polar system (r,θ) is attached to the apex.

Contributed by the Applied Mechanics Division of THE AMERICAN SOCIETY OF MECHANICAL ENGINEERS for publication in the JOURNAL OF APPLIED MECHANICS.

Discussion on this paper should be addressed to the Technical Editor, Prof. Leon M. Keer, The Technological Institute, Northwestern University, Evanston, IL 60208, and will be accepted until two months after final publication of the paper itself in the JOURNAL OF APPLIED MECHANICS. Manuscript received by the ASME Applied Mechanics Division, Feb. 6, 1990; final revision, May 31, 1990.

2 Stress Function Formulation

A rigid wedge (Fig. 1) is steadily penetrating, under plane-strain conditions, an incompressible nonlinear viscous solid. The problem addressed here is that of determining the essential features of the near-tip singular field for given geometry, wall friction, and material response.

The rheological model of the medium is described by the pure power-law relation

$$\mathbf{D}=\frac{3}{2}\left(\frac{\sigma_e}{\sigma_o}\right)^{n-1}\frac{\mathbf{S}}{\sigma_o} \tag{1}$$

where (σ_o, n) are material parameters, $\mathbf{D}$ is the Eulerian strain rate, $\mathbf{S}$ is the stress deviator, and σ_e is the Mises effective stress. For our problem

$$\sigma_e^2=\frac{3}{4}(\sigma_r-\sigma_\theta)^2+3\tau_{r\theta}^2 \tag{2}$$

where $(\sigma_r, \sigma_\theta, \tau_{r\theta})$ denote, with the usual notation, the in-plane polar stress components.

Equilibrium requirements are satisfied if the stresses are derived from an Airy stress function $F(r, \theta)$ by

$$\sigma_r=\frac{1}{r}F_{,r}+\frac{1}{r^2}F_{,\theta\theta} \tag{3a}$$

$$\sigma_\theta=F_{,rr} \tag{3b}$$

$$\tau_{r\theta}=-\left(\frac{1}{r}F_{,\theta}\right)_{,r} \tag{3c}$$

Assuming that the near-tip singular field is governed by a separation of variables form, viz.

$$F=r^s\phi(\theta), \tag{4}$$

we find that the stresses (3) may be rewritten as

$$\sigma_r=r^{s-2}(\phi''+s\phi)=r^{s-2}\tilde{\sigma}_r \tag{5a}$$

$$\sigma_\theta=r^{s-2}s(s-1)\phi=r^{s-2}\tilde{\sigma}_\theta \tag{5b}$$

$$\tau_{r\theta}=r^{s-2}(1-s)\phi'=r^{s-2}\tilde{\tau}_{r\theta} \tag{5c}$$

where the prime denotes differentiation with respect to θ, and a tilde stands for the circumferential profile of the quantity. Similarly, the effective stress (2) becomes

$$\sigma_e=\frac{\sqrt{3}}{2}r^{s-2}\left\{[\phi''-s(s-2)\phi]^2+4(s-1)^2(\phi')^2\right\}^{1/2}=\frac{\sqrt{3}}{2}r^{s-2}\tilde{\sigma}_e. \tag{6}$$

Inserting relations (5)–(6) in the constitutive law (1) results in the strain-rate components

$$\epsilon_r=-\epsilon_\theta=\left(\frac{\sqrt{3}}{2}\right)^{n+1}\sigma_o^{-n}r^{n(s-2)}\tilde{\sigma}_e^{n-1}[\phi''-s(s-2)\phi]=kr^{n(s-2)}\tilde{\epsilon}_r \tag{7a}$$

$$\epsilon_{r\theta}=\left(\frac{\sqrt{3}}{2}\right)^{n+1}\sigma_o^{-n}r^{n(s-2)}\tilde{\sigma}_e^{n-1}[2(1-s)\phi']=kr^{n(s-2)}\tilde{\epsilon}_{r\theta} \tag{7b}$$

where

$$k=\left(\frac{\sqrt{3}}{2}\right)^{n+1}\sigma_o^{-n} \tag{7c}$$

is a suitable scaling coefficient.

Substituting (7a)–(7b) in the compatibility equation results in the r-independent equation,

$$\tilde{\epsilon}_r''-n(s-2)[n(s-2)+2]\tilde{\epsilon}_r-2[n(s-2)+1]\tilde{\epsilon}_{r\theta}'=0. \tag{8}$$

In terms of ϕ we have, in (8), a fourth-order nonlinear differential equation, due to Hutchinson (1968),

$$\left\{\frac{d^2}{d\theta^2}-n(s-2)[n(s-2)+2]\right\}\left\{\tilde{\sigma}_e^{n-1}[\phi''-s(s-2)\phi]\right\}+4(s-1)[n(s-2)+1](\tilde{\sigma}_e^{n-1}\phi')'=0 \tag{9}$$

where the circumferential profile of the effective stress $\tilde{\sigma}_e$ is defined by (6).

Equation (9) is supplemented by four boundary conditions, two at each wall of the wedge. Assuming that wall friction is imposed through the friction factor m, and expecting that the shear stresses along the wall oppose the direction of flow, we get, from (2), the boundary data

$$\sqrt{3}\tau_{r\theta}=\begin{Bmatrix}-m_1\\+m_2\end{Bmatrix}\sigma_e \quad \text{at} \quad \theta=\pm\beta \tag{10a}$$

or, with the aid of (5c)–(6),

$$2\tilde{\tau}_{r\theta}\begin{Bmatrix}+m_1\\-m_2\end{Bmatrix}\tilde{\sigma}_e=0 \quad \text{at} \quad \theta=\pm\beta. \tag{10b}$$

Employing the friction factor in viscoplastic flow problems is preferable to the use of the conventional Coulomb friction coefficient. This has been demonstrated in a number of studies by Durban (1979, 1980, 1983, 1984) on steady forming processes. The shear factor measures local surface roughness by stating the relative contribution of the shear stress along the wall to the total effective stress. This particular measure remains physically valid even in the absence of normal pressure. The values of the friction factors (m_1, m_2) vary from zero for a smooth wall to unity for a perfectly rough wall. Conditions (10) may be expressed in terms of the circumferential profiles of the strain rates (7a)–(7b) as

$$\begin{aligned}&\sqrt{1-m_1^2}\,\tilde{\epsilon}_{r\theta}+m_1\tilde{\epsilon}_r=0 \quad \text{at} \quad \theta=\beta\\&\sqrt{1-m_2^2}\,\tilde{\epsilon}_{r\theta}-m_2\tilde{\epsilon}_r=0 \quad \text{at} \quad \theta=-\beta.\end{aligned} \tag{11a}$$

This, in turn, can be further reduced to a form involving linear combinations of ϕ and its derivatives, namely

$$\begin{aligned}&2\sqrt{1-m_1^2}(1-s)\phi'+m_1[\phi''-s(s-2)\phi]=0 \quad \text{at} \quad \theta=\beta\\&2\sqrt{1-m_2^2}(1-s)\phi'-m_2[\phi''-s(s-2)\phi]=0 \quad \text{at} \quad \theta=-\beta\end{aligned} \tag{11b}$$

In passing, it is worth mentioning that while we have assumed so far that both friction factors (m_1, m_2) are positive, there exists the possibility of penetration eigenfields where one of the friction factors is negative. The near-tip velocity pattern would then resemble a local circulation as in classical hydrodynamics. No attempt has been made in this paper to investigate such rotational fields but their likelihood ought to be mentioned. Purely antisymmetric fields are not permissible for the penetration problem since normal pressure is expected to exist along both walls of the wedge.

In addition to (11) we have the obvious requirement that the circumferential velocity component has to vanish at the boundaries. To this end we denote the polar velocities components by (u, v) and integrate the radial kinematic relation $\epsilon_r=u_{,r}$ to obtain, with the aid of (7a),

$$u=kr^{n(s-2)+1}\frac{\tilde{\epsilon}_r}{n(s-2)+1}. \tag{12}$$

Now, take the shear strain-rate definition

$$\epsilon_{r\theta}=\frac{1}{2}\left(\frac{1}{r}u_{,\theta}+v_{,r}-\frac{v}{r}\right) \tag{13}$$

and combine it with (7b) and (12) to obtain the expression

$$v=kr^{n(s-2)+1}\frac{2[n(s-2)+1]\tilde{\epsilon}_{r\theta}-\tilde{\epsilon}_r'}{n(s-2)[n(s-2)+1]}. \tag{14}$$

Thus, at $\theta=\pm\beta$,

$$2[n(s-2)+1]\tilde{\epsilon}_{r\theta}-\tilde{\epsilon}_r'=0. \tag{15a}$$

Combining (15a) with (11a) gives, after some algebraic manipulations, the alternative form of (15a)

$$[n-(n-1)m_1^2][\phi'''-s(s-2)\phi'] - 2(1-s)\left\{m_1\sqrt{1-m_1^2}\,(n-1)\phi''+2[n(s-2)+1]\phi'\right\}=0 \quad \text{at } \theta=\beta \tag{15b}$$

with a similar condition at $\theta=-\beta$ except that m_1 is replaced by $(-m_2)$.

The four homogeneous boundary conditions, (11) and (15), provide the necessary data on ϕ and its derivatives along the walls. Equation (9), along with that boundary data, form an eigenvalue problem for the singularity measure s. Simple considerations show that s should be bounded within the range

$$\frac{2n}{n+1}<s<2 \tag{16}$$

where the upper bound assures a singular field and the lower bound guarantees finite power consumption near the wedge tip.

When $m_1=m_2=m$ the flow pattern may be expected to be symmetric with respect to the axis $\theta=0$. The conditions along the penetration line are then the same as for a smooth wall with $\tau_{r\theta}=0$ and $v=0$ or, in terms of ϕ,

$$\phi'=0 \quad \text{and} \quad \phi'''=0 \quad \text{at} \quad \theta=0. \tag{17}$$

At the other extreme, for a perfectly rough wall where the friction factor is equal to unity, we find from (11) that $\tilde{\epsilon}_r=0$ or, from (7a),

$$\phi''-s(s-2)\phi=0. \tag{18}$$

This gives, via (12), that

$$u=0, \tag{19}$$

implying a sticking condition along the wall. It is also worth noting that at a perfectly rough wall, condition (15) admits the simplified form

$$\phi'''-\{4(1-s)[n(s-2)+1]+s(s-2)\}\phi'=0. \tag{20}$$

3 The Newtonian Fluid ($n=1$)

It is instructive to consider first the case $n=1$ (Newtonian fluid) where equation (9) admits the simple solution (Karal and Karp, 1964)

$$\phi=C_1\sin(s-2)\theta+C_2\cos(s-2)\theta+C_3\sin s\theta+C_4\cos s\theta. \tag{21}$$

The same solution has been given by Rayleigh (1920) in discussing steady motion near corners. Subsequently, Dean and Montagnon (1949), Taylor (1960), and Moffatt (1964), have applied this solution to a variety of problems related to flow fields near corners. Limiting the discussion to symmetric fields ($C_1=C_3=0$, $m_1=m_2=m$) we obtain, from (11b) and (15b), the homogeneous system

$$C_2\sin(s-2)\beta+C_2\sin s\beta=0 \tag{22a}$$

$$(s-2)C_2[\sqrt{1-m^2}\sin(s-2)\beta-m\cos(s-2)\beta] + sC_4(\sqrt{1-m^2}\sin s\beta-m\cos s\beta)=0. \tag{22b}$$

The transcendental equation for the eigenvalues s follows as

$$2\sqrt{1-m^2}\sin s\beta\sin(s-2)\beta+m[(s-2)\sin s\beta\cos(s-2)\beta-s\cos s\beta\sin(s-2)\beta]=0. \tag{23}$$

The dependence of s on m and β, as evaluated from (23) is shown in Fig. 2. It can be clearly seen that the exponent of singularity increases, (i.e., s decreases) with decreasing friction and wedge angle; sharp and smooth wedges penetrate more easily. For frictionless walls ($m=0$) we have, from (23),

$$s=\frac{\pi}{\beta}. \tag{24}$$

Expanding the solution of (23) in powers of m gives, to the second order,

$$s\sim\frac{\pi}{\beta}\left[1+\left(\frac{m}{2\beta}\right)+\frac{\pi-2\beta+\tan 2\beta}{\tan 2\beta}\left(\frac{m}{2\beta}\right)^2\right]. \tag{25}$$

This expansion does not converge for very small wedge angles ($\beta\to\pi$), and for nearly flat wedges $\left(\beta\to\frac{\pi}{2}\right)$, but is nevertheless an excellent approximation (Fig. 2) to the exact results of (23) as long as $m^2\ll(2\beta)^2|\tan 2\beta|$.

At sufficiently large wedge angles and friction factors the near-tip field becomes nonsingular (Fig. 2). A simple yet fairly accurate estimation of those critical angles can be obtained at

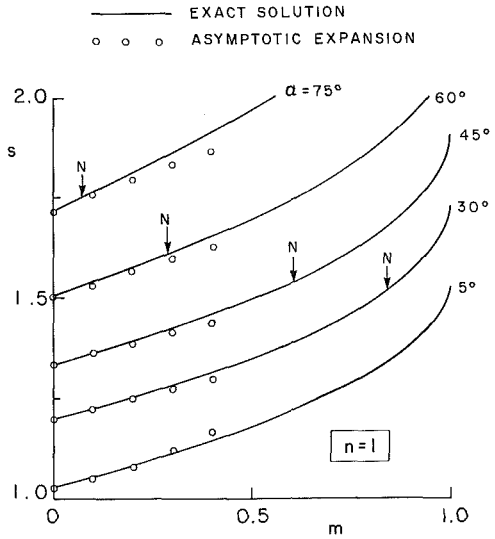

Fig. 2 Singularity exponent for different wedge angles and friction factors. Newtonian fluid, $n=1$. The corresponding free notch eigenvalue is indicated by an arrow.

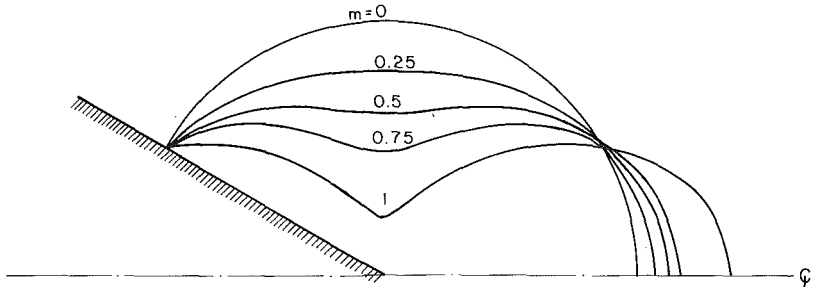

Fig. 3 Contours of constant effective stress for $\alpha=30$ deg and with different friction factors. Newtonian fluid, $n=1$. A boundary layer build-up is observed as m increases.

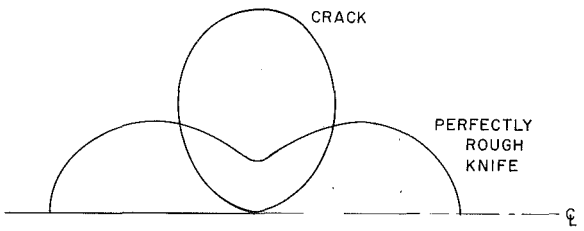

Fig. 4 Contours of constant effective stress for a perfectly rough knife penetrating a Newtonian fluid, and for a crack in a Hookean solid. The singularity exponent in both cases is $s = 3/2$.

low levels of friction, from the linear approximation of (25) along with the singularity requirement $s < 2$. This gives an upper bound on the wedge angle

$$2\alpha < \pi - m \tag{26}$$

ensuring singular near-tip behavior.

Contours of constant effective stress (6), nondimensionalized with respect to their value at the wall, are here determined by the relation

$$r = [1 - B(\cos 2\theta - \cos 2\beta)]^{\frac{1}{2(2-s)}} \tag{27}$$

with

$$B = \frac{2s(s-2)\sin s\beta \sin(s-2)\beta}{(s-2)^2\sin^2 s\beta + s^2\sin^2(s-2)\beta - 2s(s-2)\sin s\beta \sin(s-2)\beta\cos 2\beta}. \tag{28}$$

For a smooth wedge B vanishes identically, by (24), and (27) becomes the circle $r = 1$, regardless of the wedge angle.

Typical contours of constant effective stress are displayed in Fig. 3 with different values of the friction factor for a semi-wedge angle of $\alpha = 30$ deg. An obvious build-up of a friction boundary layer is clearly observed as the friction factor increases. This is accompanied by the development of a bulb-shaped singular zone ahead of the wedge.

In steady penetration of a rigid knife with zero thickness ($\beta = \pi$) we find, from (23),

$$s = 1 + \frac{1}{\pi}\arctan\frac{m}{\sqrt{1-m^2}}; \tag{29}$$

with the associated contour, from (27)–(28),

$$r = [1 - s(2-s)\sin^2\theta]^{\frac{1}{2(2-s)}}. \tag{30}$$

For a perfectly rough knife ($m = 1$, $s = 3/2$) the contour is given by $r = (1 + 3\cos^2\theta)/4$, indicating again the formation of a near-wall friction boundary layer (Fig. 4). The stresses admit here the same exponent of singularity ($r^{-1/2}$) as the crack-tip field in a Hookean solid. Contours of constant effective stress for the crack (nondimensionalized with respect to their value at $\theta = \pi/2$) are given by $r = \sin^2\theta$ and are shown for comparison in Fig. 4. It should be added that the hydrostatic stress in steady penetration of a rigid knife is negative

$$\sigma_h = -(\sqrt{3}/3)\left(\cos\frac{\theta}{2}\right)r^{-1/2}$$

while, in the near-tip field of a crack, the hydrostatic stress is in a state of tension

$$\sigma_h = 2(\sqrt{3}/3)\left(\cos\frac{\theta}{2}\right)r^{-1/2}.$$

The contour for a mode II crack in a Hookean solid is identical with that of the penetrating perfectly rough knife, but with a hydrostatic tension environment

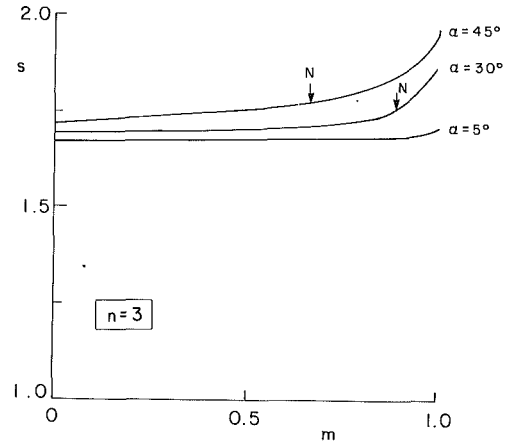

Fig. 5 Singularity exponent for different wedge angles and friction factors, $n = 3$. The corresponding free-notch eigenvalue is indicated by an arrow.

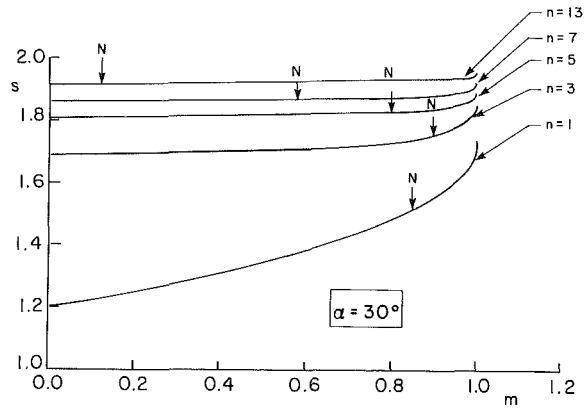

Fig. 6 Influence of the strain-rate hardening exponent on the eigenvalue s, $\alpha = 30$ deg. The corresponding free-notch eigenvalue is indicated by an arrow.

$$\sigma_h = (\sqrt{3}/3)\left(\sin\frac{\theta}{2}\right)r^{-1/2}.$$

4 Numerical Analysis for Nonlinear Strain-Rate Hardening ($n > 1$)

A special numerical scheme (Rand, 1988) has been employed to solve the differential equation (9) along with the associated boundary conditions (11) and (15). The function $\phi(\theta)$ is represented by a stationary vector $\mathbf{X}$, of dimension N, whose components are the corresponding coefficients of the truncated Fourier expansion

$$\phi(\theta) = X_1 + \sum_{i=3,5,\ldots}^{N}\left\{X_{i-1}\cos\left[(i-1)\frac{\theta}{2}\right] + X_i\sin\left[(i-1)\frac{\theta}{2}\right]\right\}. \tag{31}$$

Inserting (31) in equation (9) results in an expression which will be denoted by $G(\mathbf{X},\theta)$. Similarly, substitution of (31) in the boundary conditions (11b) and (15b) will give four expressions that will be referred to as $B_j(\mathbf{X})$ with $j = 1,\ldots,4$, respectively.

Now, we define an error functional $E(\mathbf{X})$ by

$$E(\mathbf{X}) = \int_{-\beta}^{\beta}[G(\mathbf{X},\theta)]^2 d\theta + \sum_{j=1}^{4}[B_j(\mathbf{X})]^2. \tag{32}$$

The solution method used here is based on minimizing the

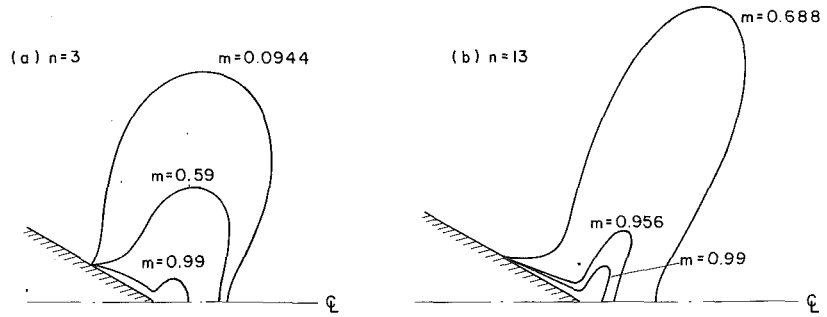

Fig. 7 Contours of constant effective stress, $\alpha = 30$ deg; (*a*) $n = 3$; (*b*) $n = 13$

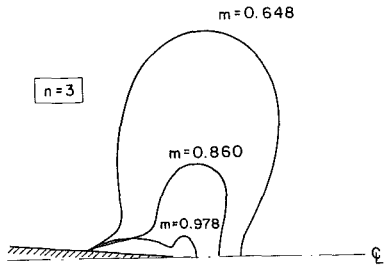

Fig. 8 Contours of constant effective stress for a sharp wedge with $\alpha = 5$ deg, $n = 3$

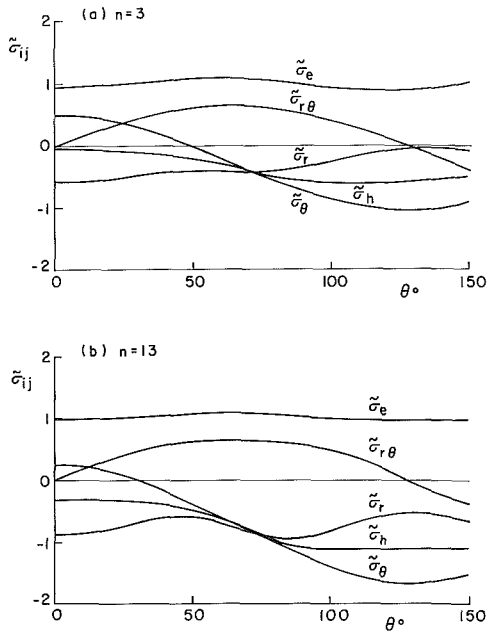

Fig. 9 Stress components $\tilde{\sigma}_{ij}$ profiles within the singular zone for $\alpha = 30$ deg and $m = 0.7$; (*a*) $n = 3$, (*b*) $n = 13$

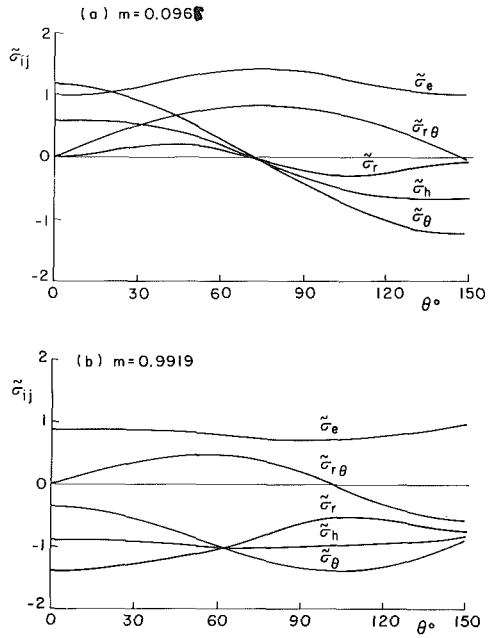

Fig. 10 Stress components $\tilde{\sigma}_{ij}$ profiles within the singular zone for $\alpha = 30$ and $n = 3$; (*a*) $m = 0.0965$, (*b*) $m = 0.09919$

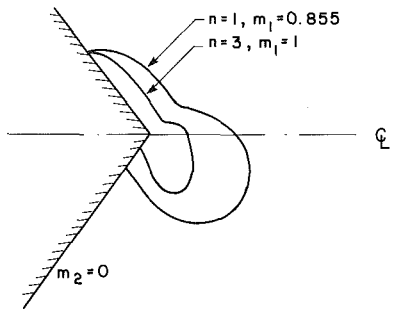

Fig. 11 Contours of constant effective stress in asymmetric penetration

error $E(\mathbf{X})$ over the vector $\mathbf{X}$. This is done through an iterative scheme whereby the Jacobian matrix is evaluated numerically at each step. The dimension N of vector $\mathbf{X}$ depends of course on the required accuracy. Simple measures have been defined for the maximum error, induced by truncating $\mathbf{X}$, in the differential equation and in the boundary conditions. The dimension of vector $\mathbf{X}$ is increased until the convergence requirements are met. This procedure can be further simplified, for symmetric fields, by choosing s and evaluating the corresponding value of m. Once the eigenfunction $\phi(\theta)$ has been determined, along with the associated eigenvalue, it is possible to construct the entire stress and strain-rate fields within the singular zone. For simplicity, most of the results reported below are for symmetric eigenfields with $m_1 = m_2 = m$.

Figure 5 illustrates the dependence of the singularity level on the friction factor m for $n = 3$ and with a few wedge angles. The variation of s with the strain-rate hardening parameter n is shown in Fig. 6, for $\alpha = 30$ deg, indicating that s increases with increasing n. This implies that the stress components—behaving like $\sigma_{ij} \sim r^{s-2}$—become less singular as n increases. On the other hand, the strain-rate components—behaving like $\epsilon_{ij} \sim r^{n(s-2)}$—become more singular as n increases; for example, with $\alpha = 30$ deg and $m = 0.7$ we have the eigenvalues $s = (1.20, 1.72, 1.93)$ for $n = (1, 3, 13)$, respectively. It follows that the corresponding levels of strain-rate singularity are $n(2-s) = (0.80, 0.85, 0.92)$. It should be added that the sen-

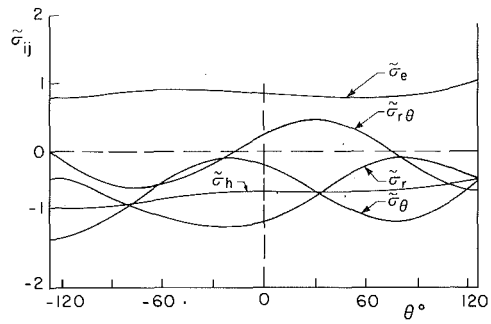

Fig. 12 Stress components $\tilde{\sigma}_{ij}$ profiles in asymmetric penetration with $\alpha = 53$ deg, $m_1 = 1$, $m_2 = 0$, $n = 3$

sitivity of s to α decreases considerably as n increases. Thus, the curve of Fig. 6 for $n = 13$ and $\alpha = 30$ will remain almost unchanged over a wide range of wedge angles. This trend can be observed also by comparing Figs. 2 and 5. By the same token, the dependence of s on the friction factor m becomes weaker with increasing n.

It is interesting to compare our results with those obtained by Kuang and Xu (1987) for HRR fields near the tip of sharp V-notches. Their results for the free-notch eigenvalues are indicated in Figs. 2, 5, and 6. It can be seen that, for given α and n, there is always a critical value of the friction factor below which the penetrating wedge induces a stronger singularity than the corresponding notch. That critical friction factor appears to decrease with α (Figs. 2, 5), but its dependence on n is more complex (Fig. 6). Other cases of plane-strain HRR fields with various boundary conditions have been considered recently by Alexandrov and Grishin (1987) and by Duva (1988). A review of available wedge III solutions for notches and wedges can be found in Ore and Durban (1988).

Typical contours of constant effective stress are shown in Figs. 7(*a*)-7(*b*) for a wedge with a semi-angle of 30 deg. These contours have been normalized with respect to their extent along the walls. An obvious boundary layer build-up can be observed as the friction factor m increases. It is also seen that for higher values of n the singular field becomes more tapered. Similar contours are shown in Fig. 8 for a sharper wedge with $\alpha = 5$ deg.

Representative stress profiles are shown in Figs. 9(*a*)-9(*b*) and 10(*a*)-10(*b*). All stress components are normalized with respect to the value of $\tilde{\sigma}_e$ at the walls. The first pair (Figs. 9(*a*)-9(*b*) illustrates the effect of n while the second pair (Figs. 10(*a*)-10(*b*) reflects the influence of m. The circumferential deviatoric component $(\tilde{\sigma}_\theta - \tilde{\sigma}_h)$ is always positive along the penetration line ($\theta = 0$ deg) implying, by (1), that the circumferential strain rate ϵ_θ is also positive ahead of the crack. Above a certain value of θ there is a sign reversal in ϵ_θ, so that the circumferential strain rate becomes negative for higher values of θ. That change of sign happens along a radius where $\sigma_r = \sigma_\theta$ with a state of simple radial shear at that particular angle. This further implies that the radial velocity u vanishes along that radius.

Finally, we show some sample figures for asymmetric penetration where each wall has a different friction factor. The lower wall ($\theta = -\beta$) is smooth while the upper wall is very rough. Again, the boundary layer near the rough wall is clearly seen (Fig. 11). The associated stress profiles are shown in Fig. 12 for the case where the upper wall is perfectly rough. The deviatoric $(\tilde{\sigma}_\theta - \tilde{\sigma}_h)$ is here positive only within a limited range of angles bounded by two radii along which the radial velocity vanishes.

Acknowledgment

The research was supported by Technion V.P.R. Fund—Seniel Ostrow Research Fund.

References

Alexandrov, V. M., and Grishin, S. A., 1987, "State of Stress and Strain of a Small Neighbourhood of the Apex of a Wedge for a Physical Non-linearity and Different Boundary Conditions," *PMM*, Vol. 51, pp. 509-515 (English translation).

Atkins, A. G., Silverio, A., and Tabor, D., 1966, "Indentation Hardness and the Creep of Solids," *J. Inst. Metals*, Vol. 94, pp. 369-378.

Dean, W. R., and Montagnon, P. E., 1949, "On the Steady Motion of Viscous Liquid in a Corner," *Proc. Camb. Phil. Soc.*, Vol. 45, pp. 389-394.

Durban, D., 1979, "Axially Symmetric Radial Flow of Rigid/Linear-Hardening Materials," ASME JOURNAL OF APPLIED MECHANICS, Vol. 46, pp. 322-328.

Durban, D., 1980, "Drawing of Tubes," ASME JOURNAL OF APPLIED MECHANICS, Vol. 47, pp. 736-740.

Durban, D., 1983, "Radial Flow Simulation of Drawing and Extrusion of Rigid/Hardening Materials," *Int. J. Mech. Sci.*, Vol. 25, pp. 27-39.

Durban, D., 1984, "Rate Effects in Steady Forming Processes of Plastic Materials," *Int. J. Mech. Sci.*, Vol. 26, pp. 293-304.

Duva, J. M., 1988, "The Singularity at the Apex of a Rigid Wedge Embedded in a Nonlinear Material," ASME JOURNAL OF APPLIED MECHANICS, Vol. 55, pp. 361-364.

Fleck, N. A., and Durban, D., 1991, "Steady Penetration of a Rigid Cone with a Rough Wall into a Power-Law Viscous Solid," ASME JOURNAL OF APPLIED MECHANICS, Vol. 58, pp. 872-880.

Hutchinson, J. W., 1968, "Singular Behavior at the End of a Tensile Crack in a Hardening Material," *J. Mech. Phys. Solids*, Vol. 16, pp. 13-31.

Karal, F. C., and Karp, S. N., 1964, "Stress Behavior in the Neighbourhood of Sharp Corners," *Geophysics*, Vol. 29, pp. 360-369.

Kuang, Z.-B., and Xu, X.-P., 1987, "Stress and Strain Fields at the Tip of a Sharp V-Notch in a Power-Hardening Material," *Int. J. Fracture*, Vol. 35, pp. 39-53.

Matthews, J. R., 1980, "Indentation Hardness and Hot Pressing," *Acta Met.*, Vol. 28, pp. 311-318.

Moffatt, H. K., 1964, "Viscous and Resistive Eddies Near a Sharp Corner," *J. Fluid Mech.*, Vol. 18, pp. 1-18.

Ore, E., and Durban, D., 1988, "Boundary Effects at a Notch Tip in Anti-Plane Shear," *Int. J. Fracture*, Vol. 38, pp. 15-24.

Rand, O., 1988, "Harmonic Variables—A New Approach to Nonlinear Periodic Problems," *J. Comp. Math. Appl.*, Vol. 15, pp. 953-961.

Rayleigh, Lord, 1920, Scientific Papers, Vol. VI, Cambridge University Press, pp. 18-21.

Rice, J. R., and Rosengren, G. F., 1968, "Plane Strain Deformation Near a Crack Tip in a Power-Law Hardening Material," *J. Mech. Phys. Solids*, Vol. 16, pp. 1-12.

Roth, R. N., and Oxley, P. L. B., 1972, "Slip-Line Field Analysis for Orthogonal Machining Based Upon Experimental Flow Fields," *J. Mech. Engng. Sci.*, Vol. 14, pp. 85-97.

Taylor, G. I., 1960, *Aeronautics and Astronautics*, Hoff and Vincenti, eds., Pergamon Press, pp. 21-28.

Measurement of Monotonic Biaxial Elastoplastic Stresses at Notch Roots

W. N. Sharpe, Jr.
Department of Mechanical Engineering,
The Johns Hopkins University,
Baltimore, MD 21218
Fellow ASME

Biaxial principal strains were measured at the roots of notches in aluminum specimens with a laser-based interferometric technique. Interference patterns from three tiny indentations spaced 150 or 200 micrometers apart in an orthogonal pattern were monitored with a microcomputer-controlled system. Elastoplastic strains up to one percent were measured in real time with a resolution of 25 microstrain. Procedures were developed for computing the two principal stresses from the incremental strain data using J_2-flow theory. The validity of the computations was checked by computing the stresses in smooth tensile specimens. Anisotropy in the thin sheet material leads to errors in the computed lateral stresses (which should be zero), but the maximum deviation of the computed effective stress from the uniaxial stress is only five percent. Three kinds of double-notched specimens were prepared to vary the amount of constraint at the notch root. These were tested under monotonic tensile loading and the biaxial notch-root strains recorded. There is considerable variation among the strains once the elastic limit is passed. This is due primarily to the local inhomogeneity of plastic strain, since the gage length of the measurement is only a few times larger than the grain size of the material. Local biaxial stresses were computed from the measured strains for the three cases. The nature of the material's stress-strain curve tends to smooth out the variations among tests, particularly when the effective stress is computed. It is discovered that the local stress predicted by the Neuber relation agrees very closely with the measured local effective stress.

1 Introduction

The prediction and measurement of stresses and strains at "stress concentrations" is an important problem in the field of solid mechanics. Given the long history of research into the elastic problem and the availability of sophisticated finite element codes, one can expect to get good agreement between predicted and measured elastic stresses and/or strains. However, the situation is not so favorable when the elastic limit of the materials has been exceeded—theories carry restrictive assumptions, computer predictions are cumbersome, and measurements can no longer be made on elastic models such as those used in photoelasticity. Local elastoplastic response at a discontinuity in a component or structure is still a rich area for research from an experimental, theoretical, and computational viewpoint.

The ability to predict stresses (as opposed to strains) is important from design considerations; one is much more likely to know the applied loads than the applied deformations. But of course one does not measure stress directly; one measures load on a simple geometry or measures strains on a complicated geometry. Conversion to stress occurs through the basic definition if load is measured and through the constitutive equations if strains are measured. This latter process is straightforward for elastic behavior, but less well developed for elastoplastic behavior. A major reason is the difficulty of measuring the elastoplastic strains in situations that are truly meaningful. Plasticity tends to initiate at stress concentrations, and in most cases these are relatively small which inhibits the use of the ubiquitous foil gages. Another difficulty with the study of elastoplastic behavior is that one cannot scale up the problem because the material's grain size is so important.

This paper reports the results of a series of experiments on three geometries of double-notched specimens of 2024 aluminum. These three cases were chosen to vary the amount of lateral constraint at the notch root. Longitudinal and lateral strains, ϵ_1 and ϵ_2, were measured at the notch roots with a laser-based technique having a gage length of either 150 μm and 200 μm—only a bit larger than the grain size of the material. These measured principal strains are then converted into stresses using the incremental version of the J_2 theory of plasticity. The material tested is not isotropic which the theory assumes, and this contributes to errors in the computed stresses;

Contributed by the ASME Applied Mechanics Division of THE AMERICAN SOCIETY OF MECHANICAL ENGINEERS for presentation at the Winter Annual Meeting, Atlanta, Georgia, Dec. 1-6, 1991.

Discussion on this paper should be addressed to the Technical Editor, Prof. Leon M. Keer, The Technological Institute, Northwestern University, Evanston, IL 60208, and will be accepted until two months after final publication of the paper itself in the JOURNAL OF APPLIED MECHANICS. Manuscript received by the ASME Applied Mechanics Division, Sept. 7, 1989; final revision, Nov. 26, 1990.

Paper No. 91-WA/APM-5.

however, it is very important technologically because the sheet material is widely used in the skins of aircraft.

The results reported here are part of a larger study of the elastoplastic behavior at notch roots under cyclic loading—the implications are obvious, one wants to be able to predict the initiation of cracks under low-cycle fatigue conditions. The discussion here focuses only the first monotonic part of the loading cycle. The Neuber relation (Neuber, 1961)

$$K_\sigma \times K_\epsilon = K_t^2 \tag{1}$$

(where K_σ is the stress concentration factor, K_ϵ is the strain concentration factor, and K_t is the elastic stress concentration factor) is widely used for predicting the stresses and strains at notch roots. It is generally regarded as satisfactory for plane stress loading, but not for loadings approaching plane strain. Another paper (Sharpe and Wang, 1991) explores this effect of constraint on the validity of a modified version of the Neuber relation for monotonic loading; the predicted strains were compared with the measured ones. The conclusion there is that a modification of the Neuber relation which makes it look more like a linear relation ($K_\epsilon = K_t$) is an improvement when constraints are present.

The development and application of the Neuber relation is reviewed in the Background section of Sharpe and Wang (1991) and will not be repeated here. Surprisingly, there have been few measurements of elastoplastic stresses in complicated geometries; those are reviewed in Section 2 of this paper. The local biaxial strains are measured with a laser-based interferometric technique that measures the relative displacements between three tiny indentations in the specimen surface. The computer-controlled version for measuring uniaxial strain has been described elsewhere (Guillot and Sharpe, 1983) but the important advance reported here is the extension of the system to biaxial measurements of the principal strains ϵ_1 and ϵ_2. The technique is described only briefly since this paper focuses more on the results than on the details of the measurement system.

The procedure for computing the stresses from the measured strains, which is a straightforward inversion of the equations of plasticity, is then presented. These procedures are applied to stress-strain data from smooth specimens (both ϵ_1 and ϵ_2 were measured) to validate the computational procedure and examine the effect of anisotropy.

At this point, one should have confidence in the stress measurements and can move on to the geometries in question. Measured biaxial notch-root strains room the three cases (ten different specimens were tested) are then presented; these serve as the input for the stress calculations. The measured stresses are presented as principal values σ_1 and σ_2. These are used to compute the effective stress σ_e which is compared to the stress predicted by the Neuber relation. Finally, conclusions are drawn as to the significance of the results.

2 Background

Theocaris (1962) wrote a paper in 1962 entitled "Experimental Solution of Elastic-Plastic Plane Problems" in which he presented procedures for computing stresses from strains measured by photoelastic coatings on specimens. He presents the equations for computing the change in stress components $d\sigma_x$, $d\sigma_y$, and $d\tau_{xy}$ from the measured strain increments $d\epsilon_x$, $d\epsilon_y$, and $d\gamma_{xy}$. The specimen was a thin steel sheet with large semicircular double notches to which a thin photoelastic coating was glued. The measurement of strains required analyses of patterns taken at normal and at oblique incidence and was tedious at best; however, it did give the strain field. The incremental theory of plasticity based on J_2 was used, but only seven increments were taken between the load corresponding to incipient plasticity at the notch root and the load corresponding to the spread of plasticity across the net section. McClintock (1963) praised the paper in a later discussion and compared the measured stress and strain concentrations to those predicted by the Neuber relation—showing that the predictions were accurate in the early stages of plastic deformation at the notch root.

A similar work was published shortly thereafter by Durelli and Sciammarella (1963) who measured strains by moiré techniques on a thin aluminum specimen with a central hole. Six load increments were used which required iteration of the stress increments to assure that the effective stress-strain curve was being followed. The stress field in the neighborhood of the hole was measured, and the stress and strain concentrations were compared to those from the classic experimental work by Griffith in 1948. Agreement was excellent, considering the slight difference in specimen materials.

Photoplastic materials with nonlinear behavior similar to that of metals are quite useful in gaining an understanding of the development of plasticity in a given geometry and in evaluating theories. An example of such a study is the fine work by Johnson (1976) in which he studied the plastic deformation of a circumferentially notched shaft subjected to torsion loading. He used a photoplastic material that has a stress-strain curve similar in shape to a medium-strength aluminum and the scattered light technique to measure the stresses on a plane down the center of the shaft. The material was calibrated in torsion, so he determined shear stresses directly from the fringe patterns. The stress and strain concentrations showed good agreement with the Neuber prediction for early stages of yielding; indeed, this geometry is the same as analyzed by Neuber.

One wonders why foil-resistance strain gages are not used to measure the necessary plastic strains; the larger post-yield ones have the capability of measuring strains to ten percent or more. One paper by Keil and Benning (1979) on their use appears in 1979. However, they use the deformation theory of plasticity instead of an incremental theory which, although requiring additional assumptions, is easier to apply. They work only with principal strains and provide nomographs from which one can obtain the stresses for a representative selection of materials. Given two strain measurements, one reads out the two principal stresses.

It appears that the paucity of research papers describing measurements of elastoplastic stresses is due more to the difficulty in measuring the strains than anything else. In fact, the *Handbook on Experimental Mechanics* (1987) presents the equations relating strain increments to stress increments on page 10, but there is no later reference to their actual use. Precedents have been set with the works of Theocaris and of Durelli and Sciammarella, and similar studies would be considerably easier with modern imaging and computational capabilities. However, these earlier works did not measure at the point of real interest—the root of the stress concentration where fatigue cracks initiate.

3 Strain Measurement Technique

The interferometric Strain/Displacement Gage (or ISDG) is a laser-based system that measures in-plane relative displacement between tiny reflective indentations in a specimen surface. The pyramidal-shaped indentations are oriented so that the light rays diffracted from their sides overlap to form interference patterns in space. When the distance between the indents changes, the fringe patterns move; in effect, one simply has an optical lever with a high ratio because of the interference phenomenon. A microcomputer-controlled system for measuring fractional fringe motion has been developed that has suitable resolution for elastoplastic strain measurement over gage lengths as short as 100 μm (Guillot and Sharpe, 1983). For more details about various applications of the technique, see Sharpe (1982).

Strains in two orthogonal directions can be measured if three indentations are placed in the specimen surface as shown in

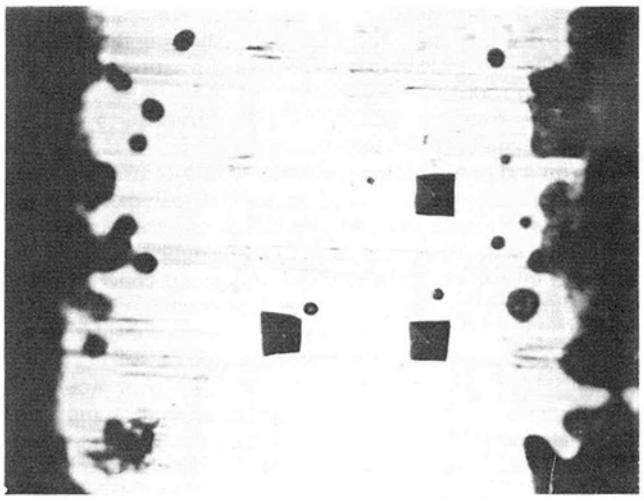

Fig. 1 Three indentations at the root of a notch. The spacing is 150 micrometers, and they are placed at the root of a notch with a 1-mm radius. The black areas on either side are paint that was applied to reduce stray reflections.

Fig. 1. That photomicrograph shows indentations at the root of a notch with a 1-mm radius; the spacing between them is 150 μm. Longitudinal strain is measured in the direct of loading, and lateral strain is measured in the perpendicular direction. The black areas at the sides of Fig. 1 are flat-black paint that was applied to limit stray reflections from the polished specimen surface.

Four fringe patterns are generated with the biaxial ISDG, and one must use four fringe sensors (scanning mirrors and photomultiplier tubes) to monitor the patterns and average out the rigid body motion of the specimen. A microcomputer system monitors the fringe motions, converts them to strains, stores the load and strains, and increments the load control signal to the test machine. The sampling rate is approximately ten points per second, and the least count of strain is approximately 35 microstrain for the 150-μm gage length. The relative uncertainty associated with the measurement of the relative displacement of the indentations is approximately $\pm$ three percent.

The effect of the indentations on the local strain field, especially in the plastic region, is a matter of concern. Unfortunately, there is no other experimental technique with a suitably short gage length, resolution, and range to permit a direct comparison at a notch root. The best that one can do is compare the ISDG with other techniques on smooth specimens, and this is quite good for longitudinal strains as will be seen in Fig. 3. Further, the reproducibility and reasonable behavior of the notch strain results that are presented here indicate that the ISDG is measuring elastoplastic strains with good fidelity.

4 Computation of Stresses

The computation of stresses from the measured strains are based on the incremental J_2-flow theory:

$$\dot{e}_{ij} = \dot{S}_{ij}/2G + f(\sigma_e)\,\dot{\sigma}_e S_{ij} \tag{2}$$

where "$\cdot$" denotes an increment in the applied stresses and strains. The deviator stresses and strains are defined by $S_{ij} = \sigma_{ij} - 1/3\ \sigma_{kk}\delta_{ij}$ and $e_{ij} = \epsilon_{ij} - 1/3\ \epsilon_{kk}\ \delta_{ij}$. σ_{ij} and ϵ_{ij} are the stress and total strain components, respectively. The effective stress, σ_e, is given by $(3/2\ S_{ij}S_{ij})^{1/2}$.

The function $f(\sigma_e)$ describes the deviation of the material's effective stress-strain behavior from linear elasticity, and is equal to $3/2\ (1/E_t - 1/E)/\sigma_e$. The modulus of elasticity is of course E, and E_t is the slope, $d\sigma_e/d\epsilon$, of the effective-stress versus total-strain, ϵ, curve of the point of interest (this stress-strain curve is obtained in a uniaxial stress test).

Equation (2) can be contracted with S_{ij} to permit one to solve for $\dot{\sigma}_e$ by noting that $2\sigma_e\dot{\sigma}_e = 3S_{ij}\dot{S}_{ij}$. The effective stress increment, $\dot{\sigma}_e$, can then be re-inserted into Eq. (2) to produce an equation relating $\dot{S}_{ij}$ to $\dot{e}_{ij}$.

$$\dot{S}_{ij} = 2G\dot{e}_{ij} - FS_{ij}S_{kl}\dot{e}_{kl} \tag{3}$$

where

$$F = \frac{6Gf(\sigma_e)}{\sigma_e/G + 2\sigma_e^2 f(\sigma_e)}.$$

The total strain is made up of elastic and plastic components; i.e., $\epsilon_{ij} = \epsilon^e_{ij} + \epsilon^p_{ij}$. By noting that $\dot{\epsilon}^p_{kk} = 0$, one can finally write

$$\dot{\sigma}_{ij} = \alpha\dot{\epsilon}_{ij} + \beta\dot{\epsilon}_{kk}\delta_{ij} - FS_{kl}\dot{\epsilon}_{klk}S_{ij}. \tag{4}$$

$\alpha = 2G$, and $\beta = K - 2G/3$ where G and K have the familiar definitions from elasticity of $E/2\ (1+\nu)$ and $E/3(1-2\nu)$, respectively. Equation (4) relates the increments of stress to the increments of strain and is the constitutive expression used to compute the stresses from the measured strains.

The stress and strain state of interest here is one of plane stress on the surface at the root of the notch. The measurements are in the principal directions because of the symmetry at the center of the notch root. The principal stresses and strains are therefore labelled σ_1, σ_2, ϵ_1, ϵ_2, and ϵ_3, respectively. ϵ_1 and ϵ_2 are the strains that are measured, and the three unknowns can be solved from the three equations of (4). The final version of the equations that is used becomes:

$$\Delta\epsilon_3 = \frac{(FS_1S_3 - \beta)\Delta\epsilon_1 + (FS_2S_3 - \beta)\Delta\epsilon_2}{\alpha + \beta - FS_3^2} \tag{5}$$

$$\Delta\sigma_1 = (\alpha + \beta - FS_1^2)\Delta\epsilon_1 + (\beta - FS_1S_2)\Delta\epsilon_2 + (\beta - FS_1S_3)\Delta\epsilon_3 \tag{6}$$

$$\Delta\sigma_2 = (\beta - FS_1S_2)\Delta\epsilon_1 + (\alpha + \beta - FS_2^2)\Delta\epsilon_2 + (\beta - FS_2S_3)\Delta\epsilon_3. \tag{7}$$

The principal stress, σ_1 and σ_2, are the sums of the stress increments as computed from the above three equations.

Implementation of Eqs. (5)–(7) is straightforward. One has the experimental record of applied load, P, ϵ_1, and ϵ_2 stored as discrete points in a data file. At a given P_n, the strain increments are taken as $\epsilon_{n+1} - \epsilon_n$. The two stress increments are then computed and added to the stress values (computed previously) corresponding to P_n. However, there are a couple of points to be considered.

First, σ_e appears in the denominator of F in Eq. (3) so the computations have to be started in some manner. They are started by computing elastic stresses directly from the measured strains. σ_e is computed at every increment, and when it exceeds a present value, the program switches to the incremental calculations of Eqs. (5)–(7). This present value must be below the proportional limit of the material, and in practice, is taken as approximately 25 percent of the yield stress.

Second, the computation of $f(\sigma_e)$ involves $1/E_t$ which equals $d\epsilon/d\sigma$. Two kinds of 2024 aluminum were tested—T3 and T351. The Ramberg-Osgood representation of the stress-strain curve, $\epsilon = \sigma_e/E + (\sigma_e/M)^{1/n}$, fits the T351 stress-strain curve quite well, and $d\epsilon/d\sigma_e$ is easily computed. However, a much better fit to the uniaxial stress-strain curve for the T3 material is obtained with a polynomial, $\sigma_e = g(\epsilon)$, where $\epsilon = \sigma_e/E + \epsilon^p$. The effective plastic strain, ϵ^p, is the sum of the plastic strain increments defined by

$$\Delta\epsilon^p = \sqrt{2}/3[(\Delta\epsilon_1^p - \Delta\epsilon_2^p)^2 + (\Delta\epsilon_2^p - \Delta\epsilon_3^p)^2 + (\Delta\epsilon_1^p - \Delta\epsilon_1^p)^2]^{1/2}. \tag{8}$$

After the stress increments have been computed for load P_n, they are used to compute increments of elastic strain which are subtracted from the measured strain increments, $\Delta\epsilon_1$ and $\Delta\epsilon_2$, and the computed strain increment, $\Delta\epsilon_3$, to give the three plastic strain increments needed in Eq. (8). The effective plastic strain increment, $\Delta\epsilon^p$, is added to the previously computed ϵ^p

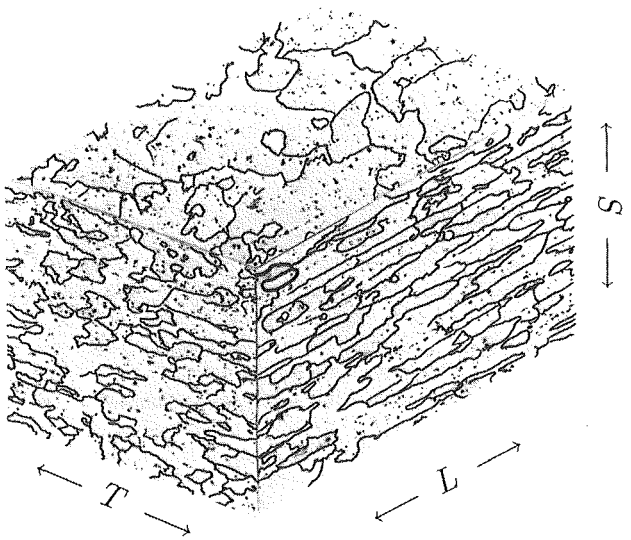

Fig. 2 Montage of photomicrographs of 2024 aluminum sheet—courtesy of Dr. J. C. Newman, Jr. The thickness of the grains in the S direction is approximately 25 micrometers. Grain boundaries have been highlighted.

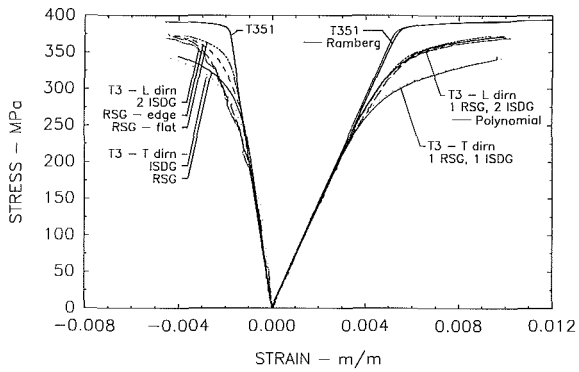

Fig. 3 Biaxial stress-strain curves from smooth specimens for the T3 and T351 materials. Measurements were made with the ISDG on the edge and with foil gages (RSG) on the flat side of the specimens. One lateral strain measurement was made on an edge with a RSG. The T3 material was tested both parallel (L) and perpendicular (T) to the rolling direction.

so that the proper value of ϵ is used for the calculation of E_t at P_{n+1}.

These computations are implemented in a short FORTRAN program on the same IBM-compatible microcomputer that was used for control of the experiments. Noise in the data does not appear to cause difficulties as will be seen in the next sections.

5 Material Response and Prediction for Smooth Specimens

This section presents the stresses and biaxial strains measured in uniaxial stress tests on smooth specimens. The purposes of these tests were to generate the constitutive equations needed for stress computation and to obtain biaxial strain data which could be used to check the computational procedures. One should be able to take the biaxial data, run it through the stress computation procedures, and get the result that $\sigma_1 = P/A$ and $\sigma_2 = 0$. As will be seen, the anisotropy of the material causes less than perfect agreement.

Figure 2 is a photomicrograph of 2024 sheet material showing the grain structure on the flat side of a sheet and on the edges; one edge parallel to the rolling direction, and one edge perpendicular to it. The nomenclature there is from ASTM E-399; "L" refers to the rolling direction, "T" to the width direction, and "S" to the edge direction. The grains have, in

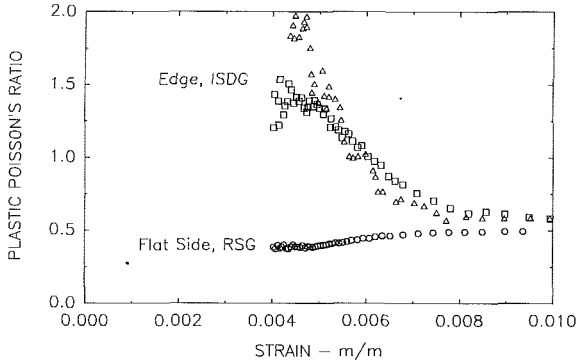

Fig. 4 The negative ratio of lateral and longitudinal plastic strain versus *longitudinal strain. The data presented are from* two smooth specimens that were instrumented with the biaxial ISDG on an edge and a smooth specimen with a biaxial RSG on the flat side.

general, the shape of elongated pancakes and are thinner in the direction perpendicular to the sheet.

Figure 3 shows the results from tests on three smooth specimens of 2024-T3 aluminum. One specimen was loaded in the L direction; it was instrumented with biaxial foil gages (RSGs) on the flat side and the biaxial ISDG on the edge. Another specimen was instrumented in the same way, but loaded in the T direction. A third specimen was loaded in the L direction, but used only the biaxial ISDG on the edge. In all cases, the agreement between the ISDG and the foil gage was excellent in the longitudinal direction (parallel to the load axis). But there is a significant difference between the lateral plastic strains measured on the flat side of a specimen with a foil gage and on the edge with the ISDG. That difference is greater when a specimen is loaded in the L direction than when one is loaded in the T direction.

It appears that the anisotropy of the material accounts for these differences in the lateral strains measured on the flat sides and edges of the smooth specimens. One might also argue that the indentations of the ISDG are influencing the plastic flow of the smaller grains on the edge. An argument against that hypothesis is that the agreement between the ISDG and the RSG lateral strains for the T-loaded specimen is actually fairly good. Also, if the indentations harden the specimen locally, one would expect smaller strains—not larger. Another test was run with a 0.79-mm long foil gage on the 2.5-mm thick edge of an L-loaded specimen. That result (RSG edge) is seen in Fig. 3 to lie between the edge lateral strains measured with the ISDG and the flat-side lateral strains. It therefore appears that the lateral ISDG-measured strains are reasonably accurate.

The 2024-T351 aluminum has the same general structure as the T3, but the grains are thicker in the S direction. The biaxial stress-strain curves, as measured with foil gages on the flat side and the edge of the smooth specimen, are nearly identical. One such curve is plotted in Fig. 3 and shows that this material is nearly elastic-perfectly plastic.

A representation of the uniaxial material behavior (actually the effective stress σ_e versus the total strain) is needed in order to evaluate $f(\sigma_e)$ in Eq. (3). The solid line through the "L" longitudinal strain data in Fig. 3 is a sixth-order polynomial fitted with the plotting package SIGMAPLOT from Jandel Scientific, Inc. Attempts to fit a Ramberg-Osgood equation to the data gave significant discrepancies either just after the proportional limit or at the maximum stress value and were abandoned. The equation describing the uniaxial stress-strain curve of 2024-T3 is:

$$\sigma = -0.4569 + 7.5004\times 10^4\epsilon - 5.5733\times 10^6\epsilon^2 + 3.6417\times 10^9\epsilon^3 - 1.0216\times 10^{12}\epsilon^4 + 1.0241\times 10^{14}\epsilon^5 - 3.4879\times 10^{15}\epsilon^6 \quad (9)$$

where σ is in MPa and ϵ is in m/m. The solid line fitted to the

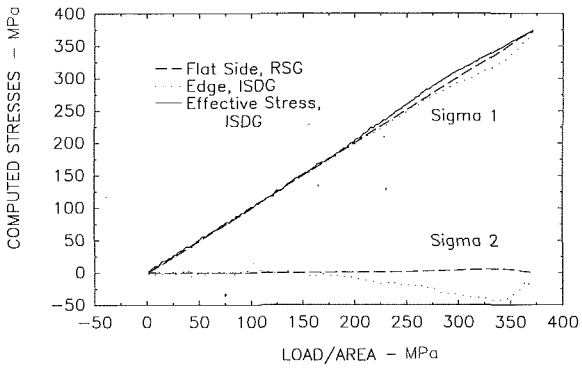

Fig. 5 Computed stresses for a smooth specimen versus the applied stress. The two principal stresses are computed from biaxial strains measured with foil gages on the flat side and the ISDG on the edge of the same specimen. The effective stress is computed only for the ISDG-measured stresses.

2024-T351 data is the Ramberg-Osgood equation with M = 414 MPa and n = 0.0094. This equation is much better at fitting a curve that has a sharper transition to plasticity.

The anisotropy considerations are important because J_2-flow theory assumes isotropy and that the plastic Poisson's ratio is 0.5. The anisotropy of the material is further illustrated in Fig. 4 which is a plot of the negative ratio of lateral to longitudinal plastic strain for the two specimens loaded in the L direction. The plastic strain was obtained by subtracting the computed elastic strain using $E = 71.8 \times 10^3$ MPa and $\nu = 0.325$. This subtraction and division generates noisy results at smaller strains, so the values are only plotted for longitudinal strains greater than 0.004 which corresponds roughly to the proportional limit of the material. The Poisson's ratio on the flat side of the specimen generally adheres to the assumption of the theory, but the edge results do not until later in the plastic yielding. Therefore, one cannot expect the computed stresses on the edge of the specimen to be accurate. However, the inaccuracy can be evaluated by using the biaxial strains measured on the smooth specimens—the data in Fig. 3—to compute the stresses σ_1 and σ_2. The result should of course be $\sigma_2 = P/A$ and $\sigma_2 = 0$.

The stresses computed using the data from the T3 specimen that was tested in the L direction and instrumented with both the foil gages and the ISDG are plotted in Fig. 5. The agreement is nearly perfect for the strains measured on the flat side of the specimen where the behavior is more isotropic; σ_1 is almost exactly equal to P/A, and σ_2 is nearly 0. Stresses computed from the edge data are noisier because of the coarser resolution of the ISDG, and σ_2 shows significant negative stresses. These clearly do not represent the physical situation; there are no compressive lateral forces in these long specimens to generate such a stress. The error in the computation comes from the deviation from isotropy in a direction perpendicular to the sheet material. Note that the computed edge stresses tend back toward perfect agreement at the higher stresses—the corresponding plastic Poisson's ratio of Fig. 4 tends toward 0.5 also.

In other words, the stresses computed from strains on the edge of the specimen (which are of greatest interest here) are simply incorrect. But, what is the effect of this error? The effective stress in this two-dimensional stress field is given by $(\sigma_1^2 - \sigma_1\sigma_2 + \sigma_2^2)^{1/2}$ which means that an error in σ_2 is suppressed. The effective stress computed from the edge stresses is plotted in Fig. 5 and agrees reasonably well with P/A; the maximum error is about five percent.

Based on these results, one can go ahead with the measurement of stresses at notch roots in this material with the understanding that the lateral stresses will be inaccurate, but the computed longitudinal stresses and the effective stresses will be accurate within ± five percent.

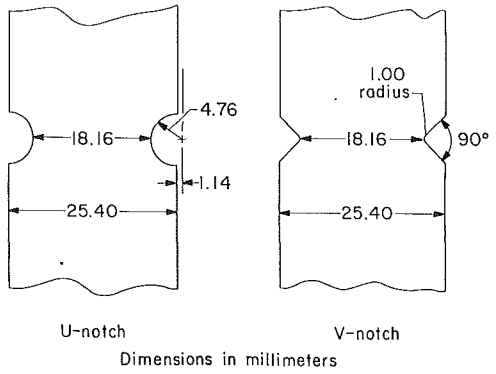

Fig. 6 Dimensions of the two types of notches

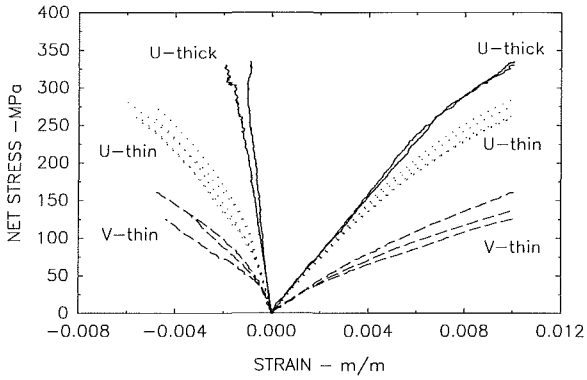

Fig. 7 Measured biaxial strains at the notch roots—longitudinal on the right and lateral on the left—for the three cases tested. The ordinate is the net stress applied to the specimen.

Table 1

Notch Thickness Shape	SCF Peterson	SCF FEM	SCF Measured	$(-\epsilon_x/\epsilon_y)_{el}$	Number of Tests
U-notch 2.5 mm	1.92	2.02	1.97	0.30	5
V-notch 2.5 mm	3.50	3.64	3.52	0.21	3
U-notch 25.4 mm	1.92	2.09	1.85	0.16	2

6 Biaxial Strain Results for Notched Specimens

Double-notched specimens were prepared with three different constraints at the notch root; i.e., three ratios of thickness to root radius. Two notch radii were used, and their dimensions are given in Fig. 6. Table 1 lists the three cases and their elastic stress concentration and constraint factors.

The "SCF Peterson" is a two-dimensional value from his handbook (Peterson, 1974). The "SCF FEM" are the results of a three-dimensional finite element analysis of the three geometries. The initial linear regions of the load versus longitudinal strain at the notch root were used to compute the "SCF Measured" value. Five tests were run for the thin U-notch geometry, and the variation of their initial slopes from the mean value was −2.4 percent + 5.7 percent which is an indicator of the fidelity of the ISDG measurement system.

The value $(-\epsilon_x/\epsilon_y)_{el}$ in Table 1 is the negative ratio of lateral to longitudinal elastic strain as calculated at the notch root in the finite element analysis. It should be the elastic Poisson's ratio of 0.325 for plane stress, and one sees that it is close to that value for the thin U-notch specimens. The sharper the stress concentration and the thicker the specimen, the smaller this value. It would be 0.0 for plane strain, but that would be very difficult to achieve without biaxial loading.

Figure 7 shows the results from ten different specimens for the three cases of Table 1. Each test was loaded in tension, and the testing program was set up so that when the longi-

tudinal strain reached a value of 0.01, the loading reversed. This value was chosen because cyclic loading over a range of ± 0.01 will produce microcracking at the notch root in a few hundred cycles. As mentioned earlier, the strain data used here is the monotonic part of a cyclic load sequence. The data sets ranged from 500 to 1000 points, but were reduced to around 150 for ease in plotting.

A notable feature of the data of Fig. 7 is the variation among the measured strains for a given case once the elastic limit has been passed. This is not at all surprising in view of the fact that the gage length is the same order of magnitude as the grain size of the aluminum. There is more variation among plastic strains for the V-notch specimens; the gage length there is 150 μm as opposed to 200 μm for the U-notch specimens. Part of this variation may come from local rotation of an indentation in a single grain or from plastic deformation of one of the faces of an indent. No matter what technique is used, measurement of plastic deformation over a few grains is likely to be inhomogeneous.

Figure 7 is the complete data set upon which the following stress computations are based. The variation among the plastic strains measured for supposedly identical specimens will of course show up in the computed stresses.

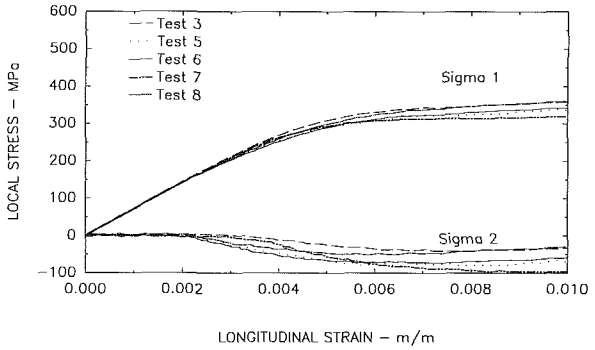

Fig. 8 Computed notch-root stresses for the thin U-notched specimens

7 Computed Notch-Root Stresses

Given the measured biaxial strains of Fig. 7 and Eqs. (5)–(7), the computation of the stresses is straightforward. The following three figures present the computed stresses for the three cases; they are plotted on the same scales. The abscissa is the measured longitudinal strain, ϵ_1; its upper limit of .01 was the same in all tests.

Figure 8 shows the stresses for the five U-thin specimens. The variation among the computed, σ_1 and σ_2 is similar to the variation among the measured ϵ_1 and measured ϵ_2, respectively. After all, ϵ_1 is the major contributor in the calculation of σ_1. The lateral stresses, σ_2, should be nearly zero in this thin specimen with a moderate stress concentration. They are negative—following the same pattern as the computed lateral stresses in the smooth specimens (see Fig. 5). This arises from the anisotropy of the material and again illustrates the point that the computed stresses are not completely correct.

The computed stresses for the V-thin specimens are shown in Fig. 9. The lateral stresses are approximately zero throughout the loading, but one can speculate that they should be a bit positive. That would be consistent with the increased level of constraint for this geometry as shown in Table 1.

The lateral stresses for the thick 2024-T351 specimens, as shown in Fig. 10, are always positive at the center of the notch root because of the greater constraint of the surrounding elastic material. The differences in the notch-root stresses for increasing constraint are clearly demonstrated in Figs. 8–10.

8 Comparison With the Neuber Prediction

The Neuber relation was derived using the deformation theory of plasticity for shear loading. Over the years, it has come to be used for cyclic loading of specimens or components

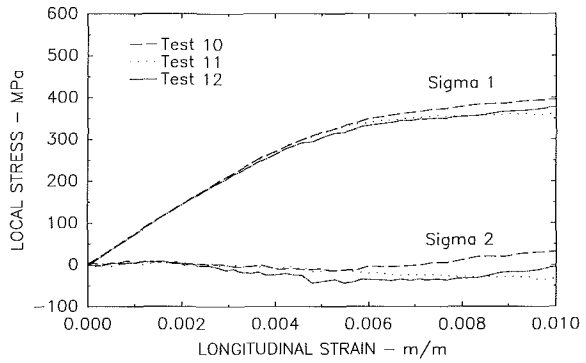

Fig. 9 Computed notch-root stresses for the thin V-notched specimens

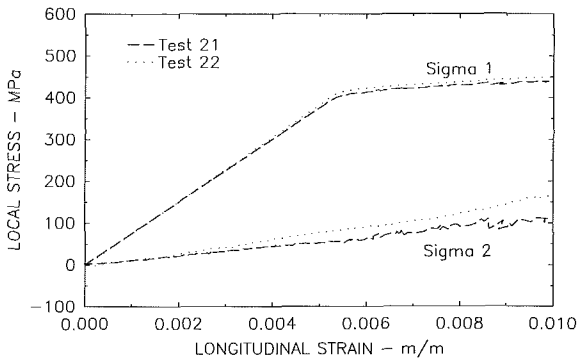

Fig. 10 Computed notch-root stresses for the thick U-notched specimens

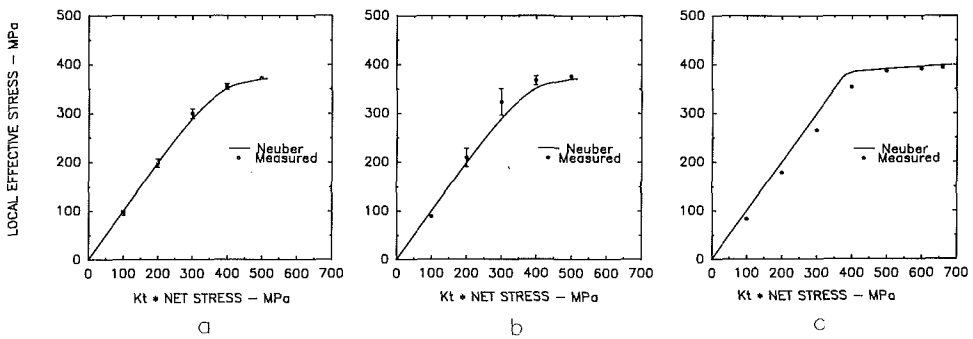

Fig. 11 Measured effective stresses at the notch root for the three cases and comparison with the predictions of the Neuber relation. (*a*) U-thin; (*b*) V-thin; (*c*) U-thick.

subjected to tensile or compressive loading. Certainly its simplicity has contributed to its popularity, but it is generally regarded to give accurate predictions of local stresses and strains only for plane-stress loading. The overall objective of the larger cyclic testing program (of which these monotonic results are a part) is to evaluate the Neuber relation for notched specimens with various amounts of constraint.

The computed stresses for the specimen with most constraint show significant positive lateral stresses at the notch root and lead one to use the effective stress, σ_e, as a measure of yielding. The Neuber relation does not recognize this; it predicts a single stress, σ_1, based on a uniaxial stress-strain curve (of course, this is σ_e if the stress at the notch root is truly uniaxial). It is therefore more appropriate to compare the measured effective stress with the Neuber-predicted stress, and this is done in Fig. 11.

Figure 11 is a plot of the local effective stress versus the product of the elastic stress concentration factor and the net stress; this latter quantity would be known by a designer seeking to predict the notch-root stresses. The Neuber prediction is a straightforward application of Eq. (1) and the appropriate constitutive equation. The experimental results shown were obtained by computing σ_e for each test at discrete values of $K_t \times \sigma_{net}$. Mean values were computed and are plotted as circles. The error bars represent the maximum and minimum values; not a statistical parameter. Where error bars are not visible, they were smaller than the size of the circle.

Figure 11 (a) shows near-perfect agreement between the predicted and measured effective stresses. This is for a moderate stress concentration factor and a thin specimen—nearly a purely plane-stress situation as shown in Table 1. Note that the agreement would not be as good if one used the measured σ_1. The average maximum value of σ_1 is 345 MPa (see Fig. 8), whereas the average maximum σ_e is 373 MPa—an eight percent difference. But, referring back to Fig. 5, σ_e is a better measure of the stress state in a smooth specimen. This result is nothing new; it was stated in the Introduction that the Neuber relation was generally valid for plane stress.

Figures 11 (b) and 11 (c) show a greater discrepancy as one moves toward more constraint, but in each case the peak σ_e agree very closely. It is also interesting to note that the scatter among the peak values of σ_e is very small for all three cases—in spite of the scatter in the measured strains and the computed stresses. The stress-strain curves flatten beyond the yield point, and therefore large strain errors produce only small stress errors.

9 Conclusions

There are three main conclusions from this work:

- Biaxial elastoplastic strain measurements are feasible over short gage lengths in materials and geometries that have practical significance. When applied to geometries that dictate the principal strains and materials that meet the assumptions of the theory, the addition of a second strain component enables one to compute stresses. Although the ISDG measurement system is somewhat sophisticated, once it is set up, testing becomes routine. The strain measurements demonstrate the needed for replication when plastic strains are measured over gage lengths on the order of the grain size. However, the variability among the strains is suppressed when they are used to compute effective stresses.
- Computation of elastoplastic stresses from measured strains is easy—given modern microcomputer-based measurement systems. The lack of accuracy lies more in the representation of the material's constitutive behavior than in the strain measurements and the computational procedures. Anisotropy of the material is important and leads to moderate errors in the longitudinal stress, σ_1, but large errors in the lateral stress, σ_2. That is not a fatal flaw because one is really more interested in the effective stress which suppresses the error in σ_2.
- The results show that the predicted peak stress from the Neuber relation agrees with the measured peak effective stress within the startling range of ± two percent! The Neuber relation is a good predictor of the effective stress at a notch root for monotonic loading regardless of the amount of constraint. This is important because a stress-based plasticity criterion should use the effective stress. However, it does not follow that the Neuber relation gives a good prediction of the strains; the shape of the upper portion of the stress-strain curve tends to dampen the variation of stresses. Low-cycle fatigue predictions are based on strain-life curves, so this point is important. However, for static design and monotonic loading, these results give one considerable confidence in the Neuber relation.

It is hoped that this presentation of the measured biaxial strains and the resulting computed stresses will contribute to a better understanding of the basic mechanics of notch-root behavior. The longer term goal is to gain a better understanding of the initiation phase of fatigue crack growth in order to improve life predictions.

Acknowledgments

The author appreciates the support of this research by the National Science Foundation under Grant MSM-8702110. It is part of a larger program to develop biaxial strain measurement techniques and use them to study cyclic plasticity under low-cycle fatigue conditions. The monotonic biaxial strain data is taken from the Ph.D. thesis of Dr. K. C. Wang; his careful work in measuring cyclic biaxial strains is an important contribution. Most of the preparation of this paper was done while the author was a Research Associate at NASA-Langley; the support of the National Research Council for that period is appreciated.

References

Durelli, A. J., and Sciammarella, C. A., 1963, "Elastoplastic Stress and Strain Distribution in a Finite Plate with a Circular Hole Subjected to Unidirectional Load," ASME Journal of Applied Mechanics, Vol. 30, pp. 115–121.

Griffith, G. E., 1948, "Experimental Investigation of the Effects of Plastic Flow in a Tension Panel with a Circular Hole," NACA-TN 1705.

Guillot, M. W., and Sharpe, Jr., W. N., 1983, "A Technique for Cyclic-plastic Notch-strain Measurement," *Experimental Mechanics*, Vol. 23, pp. 354–360.

Johnson, R. L., 1976, "Measurement of Elastic-Plastic Stresses by Scattered-light Photomechanics," *Experimental Mechanics*, Vol. 16, pp. 201–208.

Keil, S., and Benning, O., 1979, "On the Evaluation of Elasto-Plastic Strains Measured with Strain Gages," *Experimental Mechanics*, Vol. 19, pp. 265–270.

Kobayashi, A. S., ed., 1987, *Handbook on Experimental Mechanics*, Prentice-Hall, Englewood Cliffs, N.J., pp. 8–10.

McClintock, F. A., 1963, Discussion of "Experimental Solution of Elastic-Plastic Plane-Stress Problems," ASME Journal of Applied Mechanics, Vol. 30, pp. 631–634.

Neuber, H., 1961, "Theory of Stress Concentration for Shear-Strained Prismatical Bodies With Arbitrary Nonlinear Stress-Strain Law," ASME Journal of Applied Mechanics, Vol. 28, pp. 544–550.

Peterson, R. E., 1974, *Stress Concentration Factors*, John Wiley and Sons, New York.

Sharpe, W. N., Jr., and Wang, K. C., 1991, "Evaluation of a Modified Neuber Relation," *ASME Journal of Engineering Materials and Technology*, Vol. 113, pp. 1–8.

Sharpe, W. N., Jr., 1982, "Applications of the Interferometric Strain/Displacement Gage," *Optical Engineering*, Vol. 21, pp. 483–488.

Theocaris, P. S., 1962, "Experimental Solution of Elastic-Plastic Plane-Stress Problems," ASME Journal of Applied Mechanics, Vol. 29, pp. 735–743.

A Micromechanical Damage Model for Uniaxially Reinforced Composites Weakened by Interfacial Arc Microcracks

J. W. Ju
Assistant Professor,
Department of Civil Engineering and Operations Research,
Princeton University,
Princeton, NJ 08544
Mem. ASME

A micromechanical anisotropic damage model is presented for uniaxially reinforced (brittle matrix) composites weakened by an ensemble of (fiber/matrix) interfacial microcracks. All microcracks are assumed to occur along the fiber/matrix interfaces, and are modeled as arc *microcracks under "cleavage 1" deformation processes. Microcrack-induced strains and overall elastic-damage compliances are analytically derived based on micromechanical bimaterial (interfacial) arc-microcrack opening displacements and mesostructural probabilistic distributions. Both "*stationary*" and "*evolutionary*" damage models are given. In particular, microcrack kinetic equations are constructed based on micromechanical fracture criterion and mesostructural geometry in a representative volume element. Simple and efficient computational algorithms as well as some numerical uniaxial tension tests are also presented. Finally, it is noted that not a single arbitrary (fitted) "material constant" is employed in the present work.*

1 Introduction

Initiated by Kachanov (1958) and Rabotnov (1963) for one-dimensional creep damage of metals, continuum damage mechanics has been extensively explored and applied to various engineering materials by many researchers. Most of the existing works are classified as *phenomenological* damage models; see, e.g., Krajcinovic (1984, 1986, 1989) and Bazant (1986) for a comprehensive literature review. There are, however, some *micromechanical* "stationary" or "evolutionary" damage models proposed in the literature; see e.g., Budiansky and O'Connell (1976), Horii and Nemat-Nasser (1983, 1985), Kachanov (1987), Krajcinovic and Fanella (1986), Sumarac and Krajcinovic (1987), and Ju (1991).

In particular, interesting studies on damage mechanics in modern fibrous composite materials were presented by Weitsman (1987, 1988), Talreja (1985, 1986), and Allen et al. (1987) for distributed microcracks within the framework of *phenomenological* damage models. On the other hand, some noteworthy micromechanical (primarily "stationary") damage models for composites were proposed by, e.g., Wang et al. (1984), Laws et al. (1983), and Hashin (1985) for transverse (parallel) matrix crack systems, and Laws and Dvorak (1987) for aligned penny-shaped microcracks. It is noted that existing phenomenological damage models of Weitsman, Talreja, and Allen et al. employed either vector-valued or second-rank (symmetric or nonsymmetric) "damage tensors" (treated as internal state variables) to characterize the state of damage in composite materials. However, a vector or a second-rank damage tensor is inherently incapable of describing general anisotropy in composites. An appropriate description of anisotropic damage generally involves a *fourth-rank* (or even eighth-rank) damage tensor representation; see, Chaboche (1979), Cordebois and Sidoroff (1979), Ju (1989), and Krajcinovic (1989) for further remarks. In addition, in spite of attractive thermodynamic basis, specific functional forms of the Helmholtz or Gibbs free energy potentials in phenomenological damage models are to some extent *arbitrary* (heuristic). Therefore, the resulting overall stiffness-damage relationships and stress-strain laws are also somewhat arbitrary. Moreover, in order to have constitutive *predictive* capability, phenomenological damage models empirically postulate functional forms for damage "evolution equations." Consequently, in thermodynamic potentials and damage evolution equations existing phenomenological models rely on the use of many (perhaps up to 100) *fitted* "material constants." Thus, it becomes difficult to identify these fitted constants from actual experimental data of composites.

Hence, as pointed out by Krajcinovic and Fanella (1986) and Weitsman (1988), micromechanical damage theories for composites are warranted to incorporate mesostructural geometry, micromechanical deformations, and microcrack growth into the damage mechanics framework. Most of existing micromechanical damage models for composites focus on the effects of transverse *stationary* matrix cracks or aligned

Contributed by the Applied Mechanics Division of THE AMERICAN SOCIETY OF MECHANICAL ENGINEERS for publication in the JOURNAL OF APPLIED MECHANICS.

Discussion on this paper should be addressed to the Technical Editor, Prof. Leon M. Keer, The Technological Institute, Northwestern University, Evanston, IL 60208, and will be accepted until two months after final publication of the paper itself in the JOURNAL OF APPLIED MECHANICS. Manuscript received by the ASME Applied Mechanics Division, Jan. 17, 1990; final revision, Nov. 19, 1990.

penny-shaped microcracks (fiber breaks) on overall compliance tensors. The present paper, on the other hand, considers damage effects on uniaxially reinforced composites due to the *existence* and *growth* of many microcracks at the fiber/matrix *interfaces*. This circumstance corresponds to an ensemble of randomly distributed *arc microcracks* along the interfaces between cylindrical inclusions and extended exterior regions under *plane strain* and "cleavage 1" deformation processes. In the case of a single arc crack at the fiber/matrix interface subjected to remote tension field, solutions are available in England (1966), Perlman and Sih (1967), Toya (1974), and Piva (1982). In particular, Toya's solution is very suitable for damage mechanics formulation because it provides analytical expressions for arc microcrack opening displacements and fracture energy criteria.

An outline of this paper is as follows. The representation of the fourth-rank damage tensor and the thermodynamic basis for microcrack-weakened brittle composites are presented in Sec. 2. It is assumed that distributed arc microcrack concentration justified the use of effective continuum medium theory. Based on Toya's (1974) micromechanical solution of interface arc-crack opening displacements, damage-induced strains and compliances are systematically derived in Sec. 3 for an ensemble of *randomly* distributed and oriented (not necessarily periodically spaced) open arc microcracks. In Sec. 4, microcrack growth (evolution) is considered based on Toya's (1974) micromechanical fracture criterion for a single arc microcrack under uniaxial tension. The extension to account for biaxial tension loadings can be readily made. "Stable" and "unstable" domains are identified for stationary and propagating arc microcracks, respectively. As a consequence, a simple "evolutionary model" is rendered. It is emphasized that the present work does not employ any fitted "material constant." Simple and efficient computational algorithms are given in Sec. 5. In addition, some numerical uniaxial tension tests are presented to illustrate the potential capability of the proposed damage model for composites.

It is noted that the present work assumes an *interface* between a fiber and a matrix material. However, if there exists a third phase (such as a thin coated film) between a fiber and a matrix, an attractive choice is to use an *interphase* microcrack model; see Achenbach and Zhu (1989) for detailed discussions on the effects of an interphase and of fiber proximity. In Achenbach and Zhu (1989), the authors considered a simple one-dimensional linear elastic extensional and shear springs numerical model for periodically spaced fibers in a matrix material. Further investigation is needed to incorporate an interphase model (such as Achenbach and Zhu (1989)) into the present framework.

2 Thermodynamic Basis

We employ a fourth-rank anisotropic damage tensor to represent the state of damage in composite materials. It is worth mentioning that the fourth-rank damage tensor utilized has an appealing correspondence with the fourth-rank overall compliance tensor.

Within the framework of homogenization concept for inhomogeneous effective continuum medium, one may define the homogenized Gibbs free energy as

$$\chi \equiv \frac{1}{2}\,\sigma:[\mathbf{S}^o\cdot(\mathbf{I}+\mathbf{D})]:\sigma \tag{1}$$

where σ is the *volume-average* stress tensor, $\mathbf{S}^o$ is the undamaged (constant) linear elastic compliance of a composite material, $\mathbf{I}$ is the fourth-rank unit tensor, $\mathbf{D}$ denotes the fourth-rank damage tensor, and ":" denotes the tensor contraction operation. It is emphasized that $\mathbf{D}$ is an *evolving* tensorial state variable, not a constant tensor (see also Chaboche (1979), Krajcinovic (1984), and Ju (1989) for more thermodynamics details). By the Clausius-Duhem inequality for isothermal process, we have (ϵ = the volume-average strain)

$$\dot{\chi} - \dot{\sigma}:\epsilon \geq 0 \tag{2}$$

The standard Coleman's method then leads to the following macroscopic stress-strain law and overall elastic-damage compliance tensor $\mathbf{S}$:

$$\epsilon = \mathbf{S}:\sigma;\ \mathbf{S} \equiv [\mathbf{S}^o\cdot(\mathbf{I}+\mathbf{D})] \tag{3}$$

together with the damage dissipative inequality:

$$\frac{1}{2}\,\sigma:\dot{\mathbf{S}}:\sigma \geq 0,\ \text{or}\ \frac{1}{2}\,\sigma:[\mathbf{S}^o\cdot\dot{\mathbf{D}}]:\sigma \geq 0. \tag{4}$$

From Eq. (4), it is observed that the evolution $\dot{\mathbf{S}}$ (or $\dot{\mathbf{D}}$) plays an essential role in microcrack energy dissipation and growth. During a damage *loading* process, the total strain tensor ϵ is amenable to an additive decomposition: $\epsilon = \epsilon^e + \epsilon^*$, where ϵ^e and ϵ^* denote the elastic and damage-induced strains, respectively. The elastic-damage compliance tensor is also suitable for an additive decomposition: $\mathbf{S} = \mathbf{S}^o + \mathbf{S}^*$, where $\mathbf{S}^*$ signifies the damage-induced compliance. Clearly, the relationship between $\mathbf{S}^*$ and $\mathbf{D}$ can be formally expressed as $\mathbf{S}^* \equiv \mathbf{S}^o\cdot\mathbf{D}$. Therefore, if one can micromechanically *derive* the damage-induced compliance $\mathbf{S}^*$, then one can explicitly express the fourth-rank damage tensor $\mathbf{D}$ by means of micromechanics.

3 Microcrack-Induced Inelastic Strains and Overall Compliances

In this section, damage-induced strains and compliances are derived for an ensemble of randomly distributed fiber/matrix interfacial arc microcracks. Microcrack interactions are neglected at this stage of the development, and shall be subjects of future study. Accordingly, only "Taylor's model" is constructed here.

3.1 Microcrack-Induced Strains. In Toya's (1974) solution, the fiber and matrix are assumed to be homogeneous and isotropic, but with different linear elastic properties. Toya (1974) provided solutions for stresses, displacements, and debonding criteria for an *open* arc crack at the bimaterial interface under remote uniaxial and biaxial tension loadings. In what follows, for simplicity, we only consider the case of uniaxial tension loading.

As remarked by Toya (1974), both stresses and displacements *oscillate* violently at the immediate regions near the crack tips. This is quite typical for the mixed boundary value problem for interfacial cracks at bimaterial boundaries. However, the extent of the oscillating regions is very small under remote tension. Consequently, Toya (1974) concluded that his solutions provided a good approximation to the physical state of the body at the interface *except* in the immediate vicinity of the crack tips. Although some results of oscillation-free bimaterial stress and displacement analyses were reported in the literature, they were typically derived for line cracks at the interface of two dissimilar semi-infinite materials.

The global (unprimed) and local (primed) Cartesian coordinate systems as well as the local polar coordinate system (at a typical arc point) are shown in Fig. 1. In particular, α denotes the half-angle expanded by an arc microcrack, a denotes the radius of the fiber, ϕ denotes the angle between the x'-axis and y-axis, and $\psi(=\pi/2-\phi)$ signifies the angle between the y-axis and y'-axis. The uniaxial tension p is applied in the y-axis direction. Counterclockwise direction is taken as positive, and θ is measured from the x'-axis. In addition, $\mathbf{n}'$ and (u_r', u_θ') represent the outward unit normal vector and the polar coordinates at a typical point along the arc, respectively. The expressions for u_r' and u_θ' under remote uniaxial tension are given by Eq. (3.57) in Toya (1974) by means of a complex

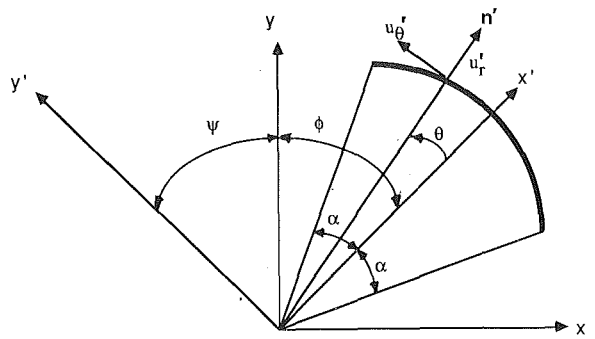

Fig. 1 The local (primed) and global Cartesian coordinates, as well as the polar coordinates at a typical arc point

variable form. Note that the real part is u_r' and the imaginary part is u_θ'. Let us first transform the local polar coordinates at a typical arc point to the local Cartesian coordinate defined at the *midpoint* of the arc:

$$u_x' = u_r' \cos\theta - u_\theta' \sin\theta \; ; \; u_y' = u_r' \sin\theta + u_\theta' \cos\theta. \quad (5)$$

Futhermore, the Cartesian components of the unit outward normal vector at a typical arc point are:

$$n_x' = \cos\theta \; ; \; n_y' = \sin\theta. \quad (6)$$

Under plane strain, the virgin (transversely isotropic) brittle composite material is isotropic. However, if the composite contains an ensemble of microcracks, it may become anisotropic, depending on microcrack sizes and orientations. First, the inelastic plane-strain components (in Voigt's notation) due to a *single* (kth) arc microcrack take the form:

$$\epsilon_1^{*(k)\prime} \equiv \epsilon_{xx}^{*(k)\prime} = \frac{a}{A}\int_{-\alpha}^{\alpha} u_x' \cos\theta \, d\theta = \frac{a}{A} \int_{-\alpha}^{\alpha} (u_r' \cos^2\theta - u_\theta' \sin\theta\cos\theta) d\theta \quad (7)$$

$$\epsilon_2^{*(k)\prime} \equiv \epsilon_{yy}^{*(k)\prime} = \frac{a}{A}\int_{-\alpha}^{\alpha} u_r' \sin d\theta = \frac{a}{A} \int_{-\alpha}^{\alpha} (u_r' \sin^2\theta + u_\theta' \sin\theta\cos\theta) d\theta \quad (8)$$

$$\epsilon_6^{*(k)\prime} \equiv 2\epsilon_{xy}^{*(k)\prime} = \frac{a}{A}\int_{-\alpha}^{\alpha} (u_x' \sin\theta + u_y' \cos\theta) d\theta = \frac{a}{A}\int_{-\alpha}^{\alpha} (u_r' \sin 2\theta - u_\theta' \cos 2\theta) d\theta \quad (9)$$

where A is the surface area of a representative volume element in two dimension.

In the above equations, it is implicitly assumed that the kth arc microcrack is entirely *open*; i.e., $u_r' > 0$. Therefore, there exist some restrictions on the arc microcrack size 2α and the orientation ϕ (Toya, 1974). For example, in the case of epoxy matrix (shear modulus μ_1 = 346 KSI or 2.39 GN/m^2, Poisson's ratio η_1 = 0.35) and glass fiber (shear modulus μ_2 = 6410 KSI or 44.2 GN/m^2, Poisson's ratio η_1 = 0.22) composite material, the range of "entirely open" arc microcracks is approximately defined by $|\phi| + \alpha \leq 65$ deg. See Fig. 2 in Toya (1974) for more information regarding allowable (ϕ, α) region.

The strains due to an ensemble of noninteracting arc microcracks can be evaluated by performing the following integration:

$$\epsilon_i^* = N \int_\Omega g_{ji}^{(k)} \epsilon_j^{*(k)\prime} \, P(\phi, \alpha) d\Omega \quad (10)$$

where N is the number of open (active) arc microcracks; i, j = 1, 2, 6; $P(\phi, \alpha)$ is a joint probability density function of

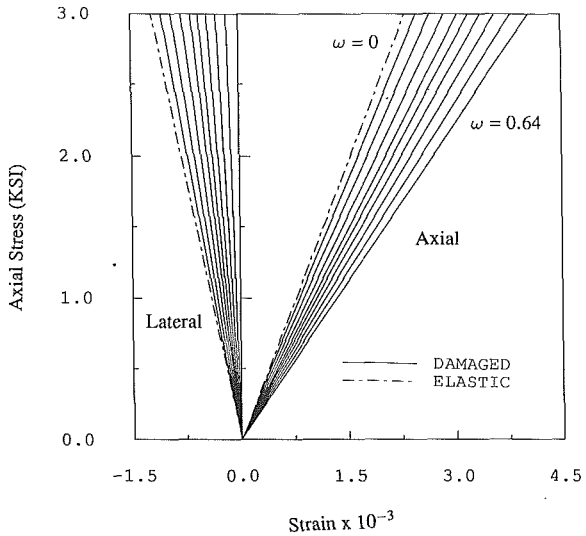

Fig. 2 The axial-stress versus the axial and lateral-strain under different microcrack concentrations ω (varying from 0 to 0.64). Note that $\omega \equiv N(a\alpha)^2/A$. The dotted lines are the undamaged elastic stress-strain responses.

randomly distributed (not necessarily periodically spaced) arc microcrack orientations and sizes; Ω is the domain of all open microcracks; and $g_{ji}^{(k)}$ is the component of the following local-global transformation matrix (Horii and Nemat-Nasser, 1983)

$$[\mathbf{g}^{(k)}] = \begin{bmatrix} \cos^2\psi & \sin^2\psi & \sin 2\psi \\ \sin^2\psi & \cos^2\psi & -\sin 2\psi \\ -\frac{1}{2}\sin 2\psi & \frac{1}{2}\sin 2\psi & \cos 2\psi \end{bmatrix}. \quad (11)$$

The total strain components can be obtained by adding ϵ_i^* to the elastic contributions ϵ_i^e, with ϵ_i^e expressed as: $\epsilon_i^e = S_{ij}^0 \sigma_j$.

Remark 3.1 In the case of *biaxial* tension loadings, ϵ^* can be obtained by the same procedure outlined above. The only modification required is to use Eq. (3.43) in Toya (1974) when integrating arc crack-opening displacements.

3.2 Overall Elastic-Damage Compliances. To derive the damage-induced compliance matrix $\mathbf{S}^*$, Eqs. (7)–(9) must be modified. The key step is to construct the strain-stress relationship ($\epsilon^{*(k)\prime}$ versus σ') in *local* Cartesian coordinates. However, this local relationship is not readily available from (3.57) in Toya (1974). The local stresses can be easily obtained as follows:

$$\sigma_1' \equiv \sigma_{xx}' = p\cos^2\phi \; ; \; \sigma_2' \equiv \sigma_{yy}' = p\sin^2\phi \; ; \; \sigma_6' \equiv \sigma_{xy}' = \frac{p}{2}\sin 2\phi. \quad (12)$$

After a lengthy derivation, Eqs. (7)–(9) can be recast as

$$\epsilon_1^{*(k)\prime} = \frac{a}{A}\left\{\sum_i \left[\int_{-\alpha}^{\alpha} (u_{ri}'\cos^2\theta - u_{\theta i}' \sin\theta\cos\theta) d\theta\right] \sigma_i'\right\} \quad (13)$$

$$\epsilon_2^{*(k)\prime} = \frac{a}{A}\left\{\sum_i \left[\int_{-\alpha}^{\alpha} (u_{ri}'\sin^2\theta + u_{\theta i}' \sin\theta\cos\theta) d\theta\right] \sigma_i'\right\} \quad (14)$$

$$\epsilon_6^{*(k)\prime} = \frac{a}{A}\left\{\sum_i \left[\int_{-\alpha}^{\alpha} (u_{ri}'\sin 2\theta - u_{\theta i}' \cos 2\theta) d\theta\right] \sigma_i'\right\} \quad (15)$$

where the summation is for i = 1, 2, 6, and the expressions for u_{ri}' and $u_{\theta i}'$ are

$$B_1 \equiv A_1 a \left[\sin \frac{1}{2}(\alpha-\theta) \sin \frac{1}{2}(\alpha+\theta) \right]^{1/2} e^{\lambda(\pi-\alpha)} \quad (16)$$

$$u'_{r1} = -B_1 \left\{ \left[\frac{1-(\cos\alpha+2\lambda\sin\alpha)e^{2\lambda(\pi-\alpha)}+(1-k)(1+4\lambda^2)\sin^2\alpha}{2-k-k(\cos\alpha+2\lambda\sin\alpha)e^{2\lambda(\pi-\alpha)}} - \frac{1}{k} - \frac{2(1-k)}{k} e^{2\lambda(\alpha-\pi)} \cos\theta \right] \cos\left(\frac{1}{2}\theta - \lambda \ln \left[\frac{\sin\frac{1}{2}(\alpha-\theta)}{\sin\frac{1}{2}(\alpha+\theta)} \right] \right) + \left[\frac{2(1-k)}{k} e^{2\lambda(\alpha-\pi)} \sin\theta \sin\left(\frac{1}{2}\theta - \lambda \ln \left[\frac{\sin\frac{1}{2}(\alpha-\theta)}{\sin\frac{1}{2}(\alpha+\theta)} \right] \right) \right] \right\} \quad (17)$$

$$u'_{\theta 1} = -B_1 \left\{ -\left[\frac{1-(\cos\alpha+2\lambda\sin\alpha)e^{2\lambda(\pi-\alpha)}+(1-k)(1+4\lambda^2)\sin^2\alpha}{2-k-k(\cos\alpha+2\lambda\sin\alpha)e^{2\lambda(\pi-\alpha)}} - \frac{1}{k} - \frac{2(1-k)}{k} e^{2\lambda(\alpha-\pi)} \cos\theta \right] \sin\left(\frac{1}{2}\theta - \lambda \ln \left[\frac{\sin\frac{1}{2}(\alpha-\theta)}{\sin\frac{1}{2}(\alpha+\theta)} \right] \right) + \left[\frac{2(1-k)}{k} e^{2\lambda(\alpha-\pi)} \sin\theta \cos\left(\frac{1}{2}\theta - \lambda \ln \left[\frac{\sin\frac{1}{2}(\alpha-\theta)}{\sin\frac{1}{2}(\alpha+\theta)} \right] \right) \right] \right\} \quad (18)$$

$$u'_{r2} = -B_1 \left\{ \left[\frac{1-(\cos\alpha+2\lambda\sin\alpha)e^{2\lambda(\pi-\alpha)}-(1-k(1+4\lambda^2)\sin^2\alpha}{2-k-k(\cos\alpha+2\lambda\sin\alpha)e^{2\lambda(\pi-\alpha)}} - \frac{1}{k} + \frac{2(1-k)}{k} e^{2\lambda(\alpha-\pi)} \cos\theta \right] \cos\left(\frac{1}{2}\theta - \lambda \ln \left[\frac{\sin\frac{1}{2}(\alpha-\theta)}{\sin\frac{1}{2}(\alpha+\theta)} \right] \right) - \left[\frac{2(1-k)}{k} e^{2\lambda(\alpha-\pi)} \sin\theta \sin\left(\frac{1}{2}\theta - \lambda \ln \left[\frac{\sin\frac{1}{2}(\alpha-\theta)}{\sin\frac{1}{2}(\alpha+\theta)} \right] \right) \right] \right\} \quad (19)$$

$$u'_{\theta 2} = -B_1 \left\{ -\left[\frac{1-(\cos\alpha+2\lambda\sin\alpha)e^{2\lambda(\pi-\alpha)}-(1-k)(1+4\lambda^2)\sin^2\alpha}{2-k-k(\cos\alpha+2\lambda\sin\alpha)e^{2\lambda(\pi-\alpha)}} - \frac{1}{k} + \frac{2(1-k)}{k} e^{2\lambda(\alpha-\pi)} \cos\theta \right] \sin\left(\frac{1}{2}\theta - \lambda \ln \left[\frac{\sin\frac{1}{2}(\alpha-\theta)}{\sin\frac{1}{2}(\alpha+\theta)} \right] \right) - \left[\frac{2(1-k)}{k} e^{2\lambda(\alpha-\pi)} \sin\theta \cos\left(\frac{1}{2}\theta - \lambda \ln \left[\frac{\sin\frac{1}{2}(\alpha-\theta)}{\sin\frac{1}{2}(\alpha+\theta)} \right] \right) \right] \right\} \quad (20)$$

$$u'_{r6} = -2B_1 \left\{ -\frac{2(1-k)}{k} e^{2\lambda(\alpha-\pi)} \times \sin\theta \cos\left(\frac{1}{2}\theta - \lambda \ln \left[\frac{\sin\frac{1}{2}(\alpha-\theta)}{\sin\frac{1}{2}(\alpha+\theta)} \right] \right) - \left[\frac{(1-k)(1+4\lambda^2)\sin^2\alpha}{k[1+(\cos\alpha+2\lambda\sin\alpha)e^{2\lambda(\pi-\alpha)}]} - \frac{2(1-k)}{k} e^{2\lambda(\alpha-\pi)} \cos\theta \right] \times \sin\left(\frac{1}{2}\theta - \lambda \ln \left[\frac{\sin\frac{1}{2}(\alpha-\theta)}{\sin\frac{1}{2}(\alpha+\theta)} \right] \right) \right\} \quad (21)$$

$$u'_{\theta 6} = -2B_1 \left\{ \frac{2(1-k)}{k} e^{2\lambda(\alpha-\pi)} \times \sin\theta \sin\left(\frac{1}{2}\theta - \lambda \ln \left[\frac{\sin\frac{1}{2}(\alpha-\theta)}{\sin\frac{1}{2}(\alpha+\theta)} \right] \right) - \left[\frac{(1-k)(1+4\lambda^2)\sin^2\alpha}{k[1+(\cos\alpha+2\lambda\sin\alpha)e^{2\lambda(\pi-\alpha)}]} - \frac{2(1-k)}{k} e^{2\lambda(\alpha-\pi)} \cos\theta \right] \times \cos\left(\frac{1}{2}\theta - \lambda \ln \left[\frac{\sin\frac{1}{2}(\alpha-\theta)}{\sin\frac{1}{2}(\alpha+\theta)} \right] \right) \right\}. \quad (22)$$

In the above equations, k, λ, and A_1 are given material properties defined as follows (Toya, 1974):

$$\kappa_1 \equiv 3-4\eta_1 \; ; \; \kappa_2 \equiv 3-4\eta_2 \quad (23)$$

$$\beta \equiv \frac{\mu_1(1+\kappa_2)}{(\mu_1+\kappa_1\mu_2)} \; ; \; \nu \equiv \frac{(\mu_2+\kappa_2\mu_1)}{(\mu_1+\kappa_1\mu_2)} \; ; \; k \equiv \frac{\beta}{1+\nu} \quad (24)$$

$$\lambda \equiv -\frac{\ln\nu}{2\pi} \; ; \; A_1 \equiv \frac{k}{4}\left[\frac{1+\kappa_1}{\mu_1} + \frac{1+\kappa_2}{\mu_2} \right]. \quad (25)$$

Therefore, Eqs. (13)–(15) can be rewritten as ($i, j = 1, 2, 6$)

$$\epsilon_i^{*(k)\prime} = S_{ij}^{*(k)\prime} \sigma'_j \quad (26)$$

where $S_{ij}^{*(k)\prime}$ are the local compliance components of the form:

$$S_{1i}^{*(k)\prime} = \frac{a}{A} \int_{-\alpha}^{\alpha} (u'_{ri}\cos^2\theta - u'_{\theta i}\sin\theta\cos\theta)d\theta \quad (27)$$

$$S_{2i}^{*(k)\prime} = \frac{a}{A} \int_{-\alpha}^{\alpha} (u'_{ri}\sin^2\theta + u'_{\theta i}\sin\theta\cos\theta)d\theta \quad (28)$$

$$S_{6i}^{*(k)\prime} = \frac{a}{A} \int_{-\alpha}^{\alpha} (u'_{ri}\sin 2\theta - u'_{\theta i}\cos 2\theta)d\theta. \quad (29)$$

It is noticed that the individual compliance matrix $\mathbf{S}^{*(k)\prime}$ is *nonsymmetric*; i.e. $S_{ij}^{*(k)\prime} \neq S_{ji}^{*(k)\prime}$ for $i \neq j$. In terms of global coordinates, $S_{ij}^{*(k)\prime}$ can be rephrased as (Eq. (11))

$$S_{ij}^{*(k)} = g_{mi}^{(k)} g_{nj}^{(k)} S_{mn}^{*(k)\prime}. \quad (30)$$

Consequently, the total compliance $\mathbf{S}^*$ due to an ensemble of randomly oriented interfacial arc microcracks can be expressed as

$$S_{ij}^* = N \int_{\Omega} S_{ij}^{*(k)} P(\phi,\alpha) d\Omega. \quad (31)$$

From Eqs. (27)–(31), it is observed that $\mathbf{S}^*$ is actually a *tensorial* function of the *mean* "arc microcrack density parameter" $\langle\omega\rangle$, with $\omega \equiv N(a\alpha)^2/A$. Finally, the overall elastic-damage compliance $\mathbf{S}$ is obtained simply by writing $\mathbf{S} = \mathbf{S}^o + \mathbf{S}^*$.

4 Microcrack Kinetic Equations

It is typical that brittle fibrous composites have some preexisting arc microcracks along the fiber/matrix interfaces even before specimens are first loaded. Some of these initial microcracks may grow (propagate) later upon application of loads. In this section, we transform the stationary damage model presented in Sec. 3 into an "evolutionary" model so that the model possesses a constitutive *predictive* capability. That is, "cleavage 1" microcrack *growth* and *evolution* of $\mathbf{S}^*$ are considered.

The present work is *not* restricted to monotonically increasing loads. In fact, loading/unloading sequences can be easily accommodated by computing and checking whether there is *undergoing* microcrack growth (excluding those previously propagating and currently arrested microcracks). If there is no (ϕ, α) region in which microcrack growth is now taking place, then the incremental load step is in an *unloading* state. Moreover, the damage-induced inelastic compliance $\mathbf{S}^*$ takes the form:

$$\mathbf{S}^* = \mathbf{S}_u^* + \mathbf{S}_i^* + \mathbf{S}_f^* \tag{32}$$

where $\mathbf{S}_u^*$ = the compliance contribution from undergoing microcrack growth, $\mathbf{S}_f^*$ = the contribution from stationary microcracks having *initial* sizes, and $\mathbf{S}_f^*$ = the contribution from arrested microcrack due to *previous* microcrack growth. In particular, if $\mathbf{S}_u^* = \mathbf{0}$, then the current load level, p is not high enough to cause further damage.

4.1 Interfacial Microcrack Fracture Criterion. The mixed-mode bimaterial fracture criterion was provided by Eqs. (4.7)–(4.8) in Toya (1974) for a single, entirely open arc microcrack along the fiber/matrix interface under biaxial and uniaxial tension. It is implicitly assumed that the bonding strength between the fiber and matrix is sufficiently *small* compared with the fracture toughness of the matrix, so that an existing arc microcrack grows along the bimaterial interface. Thus, microcrack kinking into the matrix is not considered here. Toya's fracture criterion for a *tip* of an arc microcrack under uniaxial tension reads:

$$\frac{1}{16} p^2 k a A_1 (1+4\lambda^2)\pi N_0 \bar{N}_0 \sin\alpha e^{2\lambda(\pi-\alpha)} = 2\gamma^{if} \tag{33}$$

where γ^{if} is the specific surface tension energy of the interface (i.e., critical energy release rate), and N_0 together with its complex conjugate $\bar{N}_0$ are functions of ϕ, α, and elastic material properties (see Eq. (4.9) in Toya, 1974). Note that one tip of a microcrack may reach the fracture criterion (33) before the other tip does. Hence, one tip may propagate while the other is stationary.

When the energy release rate reaches its critical value (or when tension reaches a critical value p_{cr}), an arc microcrack may grow in a stable or unstable fashion, according to Fig. 3 in Toya (1974). Within a limited range of the (ϕ, α) region, Eq. (33) may have two solutions for α and ϕ. Thus, one tip or both tips may actually grow in a *stable* manner. This implies that the *final* microcrack size α_f and orientation ϕ_f can be analytically obtained. However, for other ranges of (ϕ, α) region, there is only one solution for Eq. (33). Namely, an arc microcrack may grow in an *unstable* manner outside the limited two-solution (ϕ, α) domain. Moreover, with further increase of the tensile stress $p(>p_{cr})$, even an originally stable arc microcrack will grow continuously in an unstable manner.

In the case of many randomly distributed open arc microcracks, Eq. (33) is systematically checked for every permissible microcrack orientation ϕ and size α to numerically determine the domains of "growth zone" and "stationary zone" under a given tensile stress p and known elastic material properties.

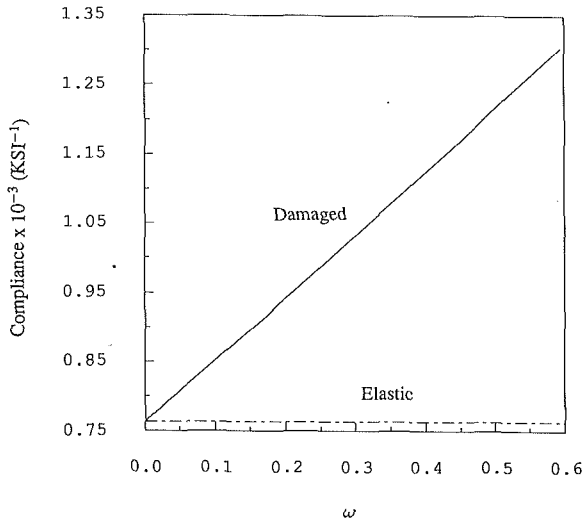

Fig. 3 The overall compliance S_{22} versus microcrack concentration ω for various stationary damage model simulations. The dotted line is the elastic response.

4.2 Microcrack Growth—A Simple Evolutionary Model. Since analytical solutions for mixed boundary value problems are not yet available for partially closed, entirely closed (mode II frictional sliding), or kinked arc microcracks, it is assumed here that all arc microcracks are entirely open and confined to the fiber/matrix interfaces. In view of the limiting range of "stable microcrack growth," it appears reasonable and practical to simplify the distributed microcrack kinetics as follows. If *one* tip of an arc microcrack reaches or exceeds the critical surface energy required to initiate microcrack growth, then *both* tips of the arc microcrack may grow continuously (generally in a nonsymmetric fashion) until the half-angle size reaches α_f and the central crack "orientation" $\phi_f \approx 0$ deg (i.e., approximately aligned with the applied tensile loading direction). In the case of the aforementioned epoxy-glass composite, $\alpha_f = 65$ deg is a reasonable value since it is the maximum allowable half-angle size for an arc microcrack to remain *open*. It is noted that the arc-microcrack central orientation indeed changes during microcrack growth.

In the case of many randomly distributed arc microcracks, Eq. (33) is used to numerically (iteratively) define *bounds* of (ϕ, α) regions undergoing microcrack growth for a *particular* tensile stress p. For simplicity, we shall assume that all arc microcracks are of *equal* initial size α_i and are such oriented that $|\phi_i| + \alpha_i \leq 65$ deg (opening) always holds. Thus, for a specified interface toughness γ^{if}, one can perform numerical iteration to obtain the minimum tension stress p_{cr} required to cause the first arc microcracks to propagate. The corresponding initial central microcrack orientations are denoted by $\pm\phi_{cr}$. The proposed microcrack kinetic sequence (for epoxy-glass composite) proceeds as follows.

(1) As $p < p_{cr}$, all arc microcracks are stable and of initial size α_i. Due to preferred initial microcrack orientations to ensure opening, the overall response is anisotropic even if virgin composite is isotropic (in plane strain). Although the overall response is currently linear and reversible, the material state is really *elastic-damage*.

(2) As $p = p_{cr}$, those microcracks with central orientations $\pm\phi_{cr}$ become unstable, and increase their lengths to $\alpha_f = 65$ deg as well as change their orientations to $\phi_f = 0$. The contributions from partially or entirely closed portions are neglected here.

(3) As $p \equiv p_1 > p_{cr}$, the unstable microcrack growth region increases. Therefore, microcracks in specific orientation do-

main Ω_{act} become activated and increase in size to $\alpha_f = 65$ deg as well as change their orientations to $\phi_f = 0$. It is noted that actual bounds of Ω_{act} depend on p_1, p_{cr}, α_i and γ^{if}, and can be obtained by numerical iteration. The compliance contributions $\mathbf{S}_u^*$ and $\mathbf{S}_f^*$ in Eq. (32) can be computed as follows:

$$\mathbf{S}_u^* = N \int_{\Omega_{act}} \mathbf{g}^{(k)T} \mathbf{S}^{*(k)\prime}(\phi, \alpha_f) \mathbf{g}^{(k)} P(\phi) d\phi \tag{34}$$

$$\mathbf{S}_f^* = N \int_{\Omega_{in}} \mathbf{g}^{(k)T} \mathbf{S}^{*(k)\prime}(\phi, \alpha_i) \mathbf{g}^{(k)} P(\phi) d\phi \tag{35}$$

where $P(\phi)$ is a probability density function of microcrack orientation, and Ω_{in} is the stable (no growth) domain.

(4) As $p_{cr} < p < p_1$, *unloading* takes place. There is no further microcrack growth and $\mathbf{S}_u^* = 0$. Hence, the elastic-damage compliance remains its previous value.

(5) As $p > p_1$, more microcracks are activated. The unstable growth domain can be computed similar to step (3). However, $\mathbf{S}_u^*$ in step (3) should now be replaced by the sum of $\mathbf{S}_u^*$ and $\mathbf{S}_f^*$.

(6) At some higher stress level $p = p_c$, the energy release rate reaches the critical value of the matrix energy barrier. Therefore, microcracks having size α_f will resume to propagate (kink) into the matrix, and eventually lead to final failure.

As was commented by Sumarac and Krajcinovic (1987), the above scheme implicitly assumes that ultimate failure prefers "runaway cracks" in comparison with "localization modes."

5 Computational Algorithms and Numerical Simulations

In this section, computational integration algorithms are given for the proposed micromechanical damage model. Furthermore, a number of uniaxial tension numerical simulations are presented. In the absence of suitable *plane-strain* experimental data at this stage, however, actual experimental validation is not included here. Experimental verification of the proposed model should be performed in the future once data become available.

5.1 Computational Integration Algorithms. The proposed micromechanical damage model does not include microcrack interaction effects, and therefore falls into the category of "Taylor's model." The computational schemes involved in the proposed stress-controlled micromechanical damage model proceed as follows. It is assumed that all initial arc microcracks are of equal size α_i and entirely open.

(1) For a given load level p, compute "unstable orientation bounds" $(-\phi_l, -\phi_h)$ and (ϕ_h, ϕ_l) according to the fracture criterion Eq. (33). For example, one may use the bisection method to locate the very *first* unstable microcrack orientations $\pm\phi_{cr}$, and later the *bounds* defining the microcrack growth domain. These "unstable orientation bounds" should be stored as *history variables* since they are irreversible.

(2) Obtain the individual and total damage-induced inelastic compliance $\mathbf{S}^{*(k)}$ and $\mathbf{S}^*$ by actually evaluating the double integral involved in Eq. (31). Numerical integration of Eq. (31) can be efficiently carried out by two double "Gauss quadratures"—one for stationary and the other for unstable regions. In particular, one needs to integrate compliance contributions from *every* θ-angle along an arc, and from *every* open microcrack. Here, we employ Gauss quadrature rule with 60 integration points for each single integral.

(3) Obtain updated overall elastic-damage compliance $\mathbf{S}$ by adding $\mathbf{S}^*$ to $\mathbf{S}^o$.

(4) Apply the next load p and go back to step (1).

5.2 Some Uniaxial Tension Tests. A number of mixed-mode *plane-strain* uniaxial tension tests are considered in this section for various fiber sizes a, microcrack concentrations ω and initial microcrack half-angle sizes α_i. Both *stationary* and *evolutionary* models are utilized. The composite material considered here is epoxy matrix/glass fiber; see Sec. 3.1 for elastic properties. The volume ratio of matrix and fiber constituents are 0.8 and 0.2, respectively. The overall Young's modulus and Poisson's ratio are found to be $E = 1151$ KSI (7.93 GN/m^2) and $\eta = 0.3481$, respectively. Therefore, the (plane-strain) elastic compliance matrix takes the form: (unit = KSI^{-1})

$$[\mathbf{S}^o] = \begin{bmatrix} 0.00076383 & -0.00040784 & 0 \\ -0.00040784 & 0.00076383 & 0 \\ 0 & 0 & 0.0023433 \end{bmatrix}. \tag{36}$$

Moreover, the interfacial specific surface tension energy (fracture toughness) $2\gamma^{if}$ is taken as 0.001 K/in. (0.175 KN/m). It is noted that all the figures presented in this section are under the *plane-strain* conditions.

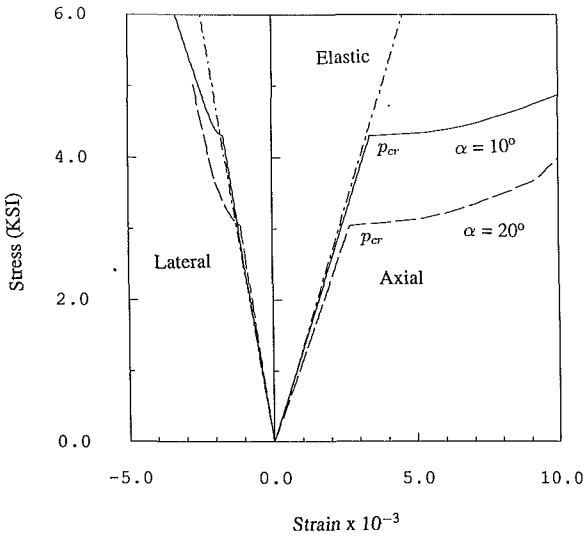

Fig. 4 The axial-stress versus the axial and lateral-strain for two different initial microcrack sizes: $\alpha_i = 10$ deg and $\alpha_i = 20$ deg. Note that $a = 0.1$ in. and $N/A = 100$.

First, we examine the effects of different initial microcrack concentrations ω on stress-strain responses and compliances of the uniaxially reinforced epoxy-glass composite. The initial microcrack concentration parameter ω increases gradually (with 256 increments) from 0 to 0.64. All microcracks are assumed to be stationary, open, and of half-angle size $\alpha_i = 10$ deg. In view of Fig. 2 in Toya (1974), $|\phi| + \alpha \leq 65$ deg is required for microcrack opening. Therefore, arc microcracks are assumed to be perfectly randomly oriented between $\phi = -55$ deg and $\phi = 55$ deg; i.e. the probability desnity of orientation is $P(\phi) = 0.521$. The uniaxial tension stress is applied in the 2-direction, and the lateral direction is denoted as the 1-direction. The axial-stress (KSI) versus the axial and lateral-strain curves are displayed in Fig. 2 for monotonically increasing values of ω. The elastic (undamaged) stress-strain response is also shown in Fig. 2 for comparison purpose. The elastic-damage compliance component S_{22} versus ω parameter is shown in Fig 3.

Next, we perform "process model" uniaxial tension tests. Let the fiber radius be $a = 0.1$ in. and microcrack number density be $N/A = 100$. Two initial half-angle sizes of arc microcracks are considered: $\alpha_i = 10$ deg and $\alpha_i = 20$ deg, respectively. The (plane-strain) axial-stress versus the axial and lateral-strain responses are recorded in Fig. 4. It is noted that before the load p reaches a certain critical value p_{cr}, the stress-strain response is *linear* (up to the *corner point* denoted by p_{cr}) for either $\alpha_i = 10$ or $\alpha_i = 20$ deg. This is due to the fact that all pre-existing microcracks are stationary. After the critical value p_{cr} (the corner point) is reached, more and more

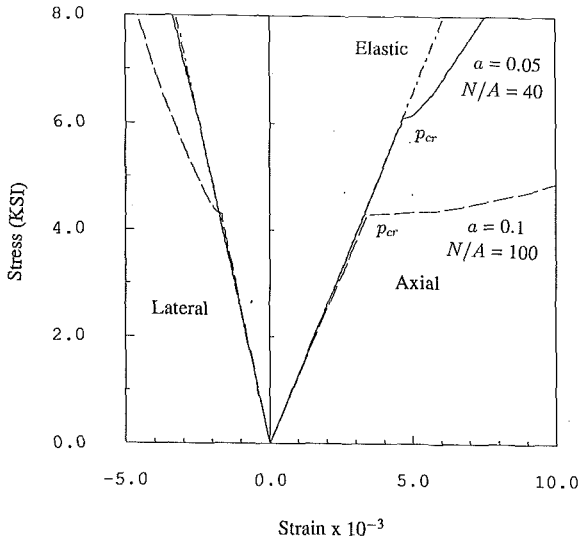

Fig. 5 The axial-stress versus the axial and lateral-strain for two different fiber sizes and microcrack number densities. Note that α_i = 10 deg.

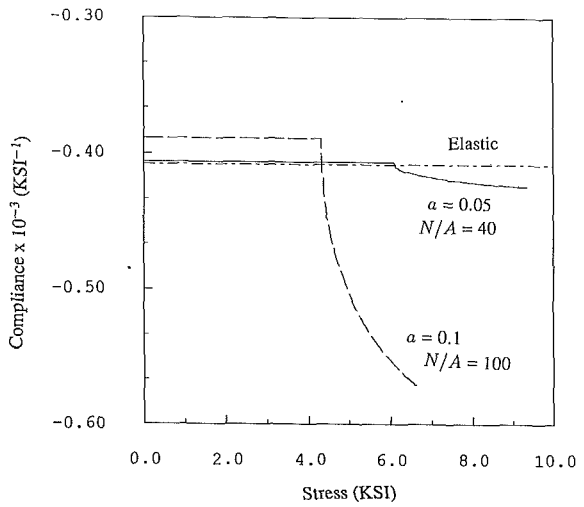

Fig. 7 The overall compliance S_{12} versus the axial stress p for two different sets of a and N/A values. Note that α_i = 10 deg.

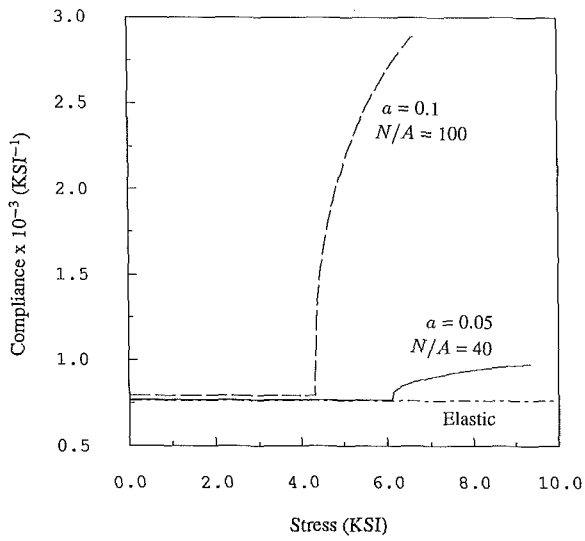

Fig. 6 The overall compliance S_{22} versus the axial stress p for two different sets of a and N/A values. Note that α_i = 10 deg.

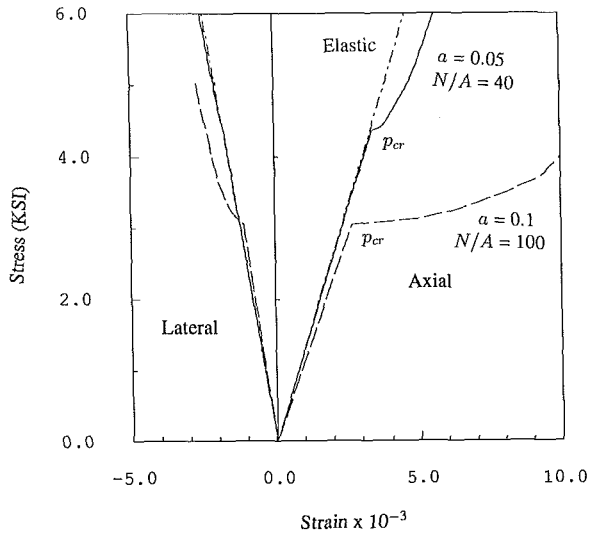

Fig. 8 The axial-stress versus the axial and lateral-strain for two different fiber sizes and microcrack number densities. Note that α_i = 20 deg.

microcracks become unstable and start to grow in size (cleavage 1 processes). Therefore, the overall stress-strain responses in Fig. 4 become *nonlinear* after the corner points. In the case of α_i = 10 deg, it is found (by numerical iteration) that the first microcracks to become unstable (propagating) are oriented in the direction ϕ_{cr} = 5.01. Later, as p increases, more "orientation fans" are enclosed within the unstable growth domain. In the case of α_i = 20 deg, on the other hand, it is found that ϕ_{cr} = 10.59 deg. It is also observed from Fig. 4 that larger initial microcrack size α_i = 20 results in lower critical load level p_{cr} for microcrack growth.

Let us now fix the initial microcrack size α_i = 10 deg and vary fiber sizes and microcrack number densities: (i) a = 0.05 in. and N/A = 40, and (ii) a = 0.1 in. and N/A = 100, respectively. The (plane-strain) axial-stress versus the axial and lateral-strain responses are shown in Fig. 5. Similar to Fig. 4, the stress-strain curves are *linear* up to the corner points (corresponding to critical threshold stresses for the first microcrack growth). The stress-strain curves subsequently become *nonlinear* after certain threshold stresses p_{cr} are reached at the corner points. The changes in overall elastic-damage compliances S_{22} and S_{12} versus axial stresses are plotted in Figs. 6 and 7. It is observed that S_{22} increases as tensile stress level p increases (after reaching critical threshold stresses p_{cr}). However, S_{12} is negative and decreases as the stress increases. The above uniaxial tension tests are repeated for fixed initial microcrack size α_i = 20 deg. The corresponding (plane-strain) axial-stress versus the axial and lateral-strain responses are shown in Fig. 8. The corresponding changes in overall elastic-damage compliances S_{22} and S_{12} versus axial stresses are qualitatively similar to those for α_i = 10 deg in Figs. 6 and 7, and are therefore not plotted here. From the above tests, it is observed that stress-strain curves and overall moduli deviate from their purely elastic (undamaged) counterparts even for *stationary* microcrack models. Moreover, results of *evolutionary* microcrack models are clearly different from those of *stationary* models due to growth of pre-existing arc microcracks. Finally, it is noted that the microcrack number density N/A is *fixed* and prescribed (e.g., based on results of scanning electron microscopy or computerized tomography, etc.) in each of the foregoing tests. That is, N/A is not a function of load. However, the average (mean) microcrack density parameter $\langle\omega\rangle$ ($\equiv \langle N(a\alpha)^2/A\rangle$) does increase with load due to microcrack growth (i.e., increase in α value).

6 Conclusion

A micromechanical damage model is presented for uniaxially reinforced brittle matrix fibrous composites, based on Toya's (1974) analytical solutions. All microcracks are assumed to occur along the fiber/matrix interfaces, and are modeled as *arc* microcracks under "cleavage 1" plane-strain deformation processes. Thermodynamic basis is rendered based on a fourth-rank damage tensor. Microcrack-induced strains and compliances are analytically derived. It is noted that the overall elastic-damage compliance matrix is *nonsymmetric*. Microcrack kinetic equations are given based on micromechanical fracture criterion and mesostructural geometry in a representative volume (area) element. Moreover, simple computational algorithms and a number of uniaxial tension tests are presented to illustrate the potential capability of the proposed micromechanical damage model. It is emphasized that the present work does not employ any arbitrary (fitted) "material constant." The proposed framework can be readily extended to account for biaxial tension loadings, as addressed in *Remark 3.1*. Issues related to the effects of an interphase (not interface), fiber proximity, microcrack interaction, closed microcracks, microcrack kinking, and microcrack nucleation mechanisms (cleavage 2) warrant further studies in the future to extend the proposed method.

Acknowledgments

This work was sponsored by the Air Force Office of Scientific Research, Directorate of Aerospace Sciences, under Grant No. AFOSR-89-0020. The author gratefully acknowledges this support and the interest of Lt. Colonel George K. Haritos. The author is indebted to Dr. Xiaogong Lee for valuable joint discussions and his numerical computations. Furthermore, the author is grateful to two anonymous reviewers for their valuable comments.

References

Achenbach, J. D., and Zhu, H., 1989, "Effects of Interfacial Zone on Mechanical Behavior and Failure of Fiber-Reinforced Composites," *J. Mech. Phys. Solids*, Vol. 37, No. 3, pp. 381–393.

Allen, D. H., Harris, C. E., and Groves, S. E., 1987, "Thermomechanical Constitutive Theory for Elastic Composites with Distributed Damage. Part I: Theoretical Development. Part II: Application to Matrix Cracking in Laminated Composites," *Int. J. Solids & Struct*, Vol. 23, No. 9, pp. 1301–1338.

Bazant, Z., 1986, "Mechanics of Distributed Cracking," ASME *Appl. Mech. Rev.*, Vol. 39, No. 5, pp. 675–705.

Budiansky, B., and O'Connell, R. J., 1976, "Elastic Moduli of a Cracked Solid," *Int. J. Solids & Struct.*, Vol. 12, pp. 81–97.

Chaboche, J. L., 1979, "Le Concept de Contrainte Effective Applique a L'elasticite et a la Viscoplasticite en Presence d'un Endommagement Anisotrope," *Mechanical Behavior of Anisotropic Solids*, Proc. Euromech Colloque 115, June, J. P. Boehler, ed., Martinus Nijhoff, pp. 737–760.

Cordebois, J. P., and Sidoroff, F., 1979, "Damage Induced Elastic Anisotropy," *Mechanical Behavior of Anisotropic Solids*, Proc. Euromech Colloque 115, June, J. P. Boehler, ed., Martinus Nijhoff, pp. 761–774.

England, A. H., 1966, "An Arc Crack Around a Circular Elastic Inclusion," ASME JOURNAL OF APPLIED MECHANICS, Vol. 33, pp. 637–640.

Hashin, Z., 1985, "Analysis of Cracked Laminates: A Variational Approach," *Mech. of Materials*, Vol. 4, pp. 121–136.

Horii, H.,and Nemat-Nasser, S., 1983, "Overall Moduli of Solids with Microcracks: Load Induced Anisotropy," *J. Mech. Phys. Solids*, Vol. 31, No. 2, pp. 155–171.

Horii, H., and Nemat-Nasser, S., 1985, "Elastic Fields of Interacting Inhomogeneities," *Int. J. Solids & Struct.*, Vol. 21, No. 7, pp. 731–745.

Ju, J. W., 1989, "On Energy-Based Coupled Elastoplastic Damage Theories: Constitutive Modeling and Computational Aspects," *Int. J. Solids & Struct.*, Vol. 25, No. 7, pp. 803–833.

Ju, J. W., 1991, "On Two-Dimensional Self-Consistent Micromechanical Damage Models for Brittle Solids," *Int. J. Solids & Struct.*, Vol. 27, No. 2, pp. 227–258.

Kachanov, L. M., 1958, "Time of the Rupture Process under Creep Conditions," *Izvestia Akademii Nauk*, USSR, Vol. 8, pp. 26–31.

Kachanov, M., 1987, "Elastic Solids with Many Cracks: A Simple Method of Analysis," *Int. J. Solids & Struct.*, Vol. 23, No. 1, pp. 23–43.

Krajcinovic, D., 1984, "Continuum Damage Mechanics," ASME *Appl. Mech. Rev.*, Vol. 37, pp. 1–6.

Krajcinovic, D., 1986, "Update to Continuum Damage Mechanics," *Appl. Mech. Update*, pp. 403–406.

Krajcinovic, D., 1989, "Damage Mechanics," *Mech. of Materials*, to appear.

Krajcinovic, D., and Fanella, D., 1986, "A Micromechanical Damage Model for Concrete," *Eng. Fract. Mech.*, Vol. 25, No. 5/6, pp. 585–596.

Laws, N., Dvorak, G. J., and Hejazi, M., 1983, "Stiffness Changes in Unidirectional Composites Caused by Crack Systems," *Mech. of Materials*, Vol. 2, pp. 123–137.

Laws, N., and Dvorak, G. J., 1987, "The Effect of Fiber Breaks and Aligned Penny-Shaped Cracks on the Stiffness and Energy Release Rates in Unidirectional Composites," *Int. J. Solids & Struct.*, Vol. 23, No. 9, pp. 1269–1283.

Perlman, A. B., and Sih, G. C., 1967, "Elastostatic Problems of Curvilinear Cracks in Bonded Dissimilar Materials," *Int. J. Eng. Sci.*, Vol. 5, pp. 845–867.

Piva, A., 1982, "Crack Along a Circular Interface Between Dissimilar Media," *Meccanica*, Vol. 17, pp. 85–90.

Rabotnov, I. N., 1963, "On the Equations of State for Creep," *Progress in Applied Mechanics—The Prager Anniversary Volume*, MacMillan, New York, pp. 307–315.

Sumarac, D., and Krajcinovic, D., 1987, "A Self-Consistent Model for Microcrack-Weakened Solids," *Mech. of Materials*, Vol. 6, pp. 39–52.

Talreja, R., 1985, "A Continuum Mechanics Characterization of Damage in Composite Materials," *Proc. R. Soc. London*, Vol. A399, pp. 195–216.

Talreja, R., 1986, "Stiffness Properties of Composite Laminates with Matrix cracking and Interior Delamination," *Eng. Fract. Mech.*, Vols. 5-6, pp. 751–762.

Toya, M., 1974, "A Crack Along the Interface of a Circular Inclusion Embedded in an Infinite Solid," *J. Mech. Phys. Solids*, Vol. 22, pp. 325–348.

Wang, A. S. D., Chou, P. C., and Lei, S. C., 1984, "A Stochastic Model for the Growth of Matrix Cracks in Composite Laminates," *J. Composite Mater.*, Vol. 18, May, pp. 239–254.

Weitsman, Y., 1987, "Coupled Damage and Moisture-Transport in Fiber-Reinforced, Polymeric Composites," *Int. J. Solids & Struct.*, Vol. 23, No. 7, pp. 1003–1025.

Weitsman, Y., 1988, "Damage Coupled with Heat Conduction in Uniaxially Reinforced Composites," ASME JOURNAL OF APPLIED MECHANICS, Vol. 55, pp. 641–647.

Weight Function Analysis of Interface Cracks: Mismatch Versus Oscillation

Huajian Gao
Division of Applied Mechanics,
Stanford University,
Stanford, CA 94305
Mem. ASME

This paper has two goals. First, it is aimed at providing a fundamental understanding of the oscillatory behavior of an interface crack between two dissimilar materials from the viewpoint of the interface mismatch that results from the cracking. Second, we extend the Bueckner-Rice weight function method to facilitate the interface crack analysis. Using properties of the surface Green's functions of a homogeneous solid and solutions obtained from weight function formulae, a mismatch analysis is carried out which indicates that the local mismatch near the crack tip results in the oscillatory near-tip field while the mismatch on the global scale leads to the corresponding stress intensity factors. For an oscillatory interface crack field, it is shown that, other than a few extra material constants, the interface weight function analysis is completely parallel to the well-developed homogeneous theory so that knowledge of one crack solution for a given bimaterial geometry is sufficient for determination of solutions under any other loading conditions.

Introduction

The problem to be discussed in this paper involves cracks along an interface between two dissimilar materials #1 and #2. When the two materials are isotropic, Williams (1959) discovered the so-called oscillatory behavior for the elastic field near the crack tip. In the coordinate system shown in Fig. 1(*a*), the crack-tip field has a universal structure for each given material pair with the normal stress σ_{yy} and shear stress σ_{yx} along the interface ahead of the crack tip given by

$$(\sigma_{yy}+i\sigma_{yx})_{\theta=0}=kr^{i\epsilon}/\sqrt{2\pi r} \tag{1}$$

where $i=\sqrt{-1}$. The complex constant k defines the stress intensity factor for an interface crack by Eq. (5) below and the "oscillation index" ϵ is related to the material constants by

$$\epsilon=(1/2\pi)\ln[(\kappa_1/\mu_1+1/\mu_2)/(\kappa_2/\mu_2+1/\mu_1)]. \tag{2}$$

Subscripts 1 and 2 refer to the materials #1 and #2, $\kappa=3-4\nu$ for plane strain and $\kappa=(3-\nu)/(1+\nu)$ for plane stress, ν = Poisson ratio, and μ = shear modulus. The complete near-tip stress field in the xy-plane can be written in the form (Rice et al., 1990)

$$\sigma_{ij}=\frac{1}{\sqrt{2\pi r}}\left[\mathrm{Re}(kr^{i\epsilon})\sum_{ij}^{I}(\theta)+\mathrm{Im}(kr^{i\epsilon})\sum_{ij}^{II}(\theta)\right] \quad (i,j=x,y). \tag{3}$$

In the sense of the crack-tip field structure expressed in (1) and (3), the angular functions $\Sigma_{ij}^{I}(\theta)$ and $\Sigma_{ij}^{II}(\theta)$ can be said to correspond to crack modes I and II that are inherently coupled together along the interface with a variable singularity strength $kr^{i\epsilon}$. The antiplane shear mode (mode III) involves no oscillation and will not be discussed in this paper.

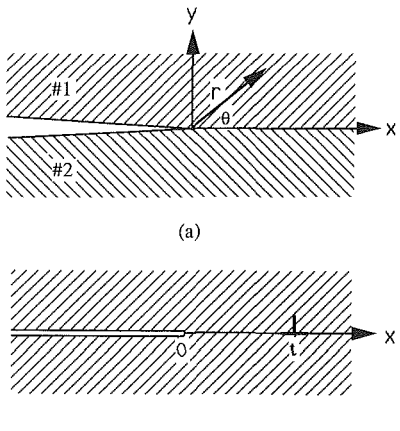

Fig. 1 *(a)* **A semi-infinite crack along a bimaterial interface with coordinates** *x, y* **and** *r, θ*; *(b)* **a semi-infinite crack in a homogeneous solid interacting with a dislocation**

Contributed by the ASME Applied Mechanics Division of THE AMERICAN SOCIETY OF MECHANICAL ENGINEERS for presentation at the Winter Annual Meeting, Atlanta, Ga., Dec. 1-6, 1991.

Discussion on this paper should be addressed to the Technical Editor, Prof. Leon M. Keer, The Technological Institute, Northwestern University, Evanston, IL 60208, and will be accepted until two months after final publication of the paper itself in the JOURNAL OF APPLIED MECHANICS. Manuscript received by the ASME Applied Mechanics Division, May 5, 1990; final revision, Mar. 4, 1991.

Paper No. 91-WA/APM-8.

The fracture analysis of interface cracks has been complicated by the oscillatory feature of the near-tip deformation field. For example, the oscillatory displacement field associated with (1, 3) is kinematically inconsistent in that it implies interpenetration of the crack faces behind the tip; this suggests that a small zone of nonlinear deformation (Knowles and Sternberg, 1983) and/or mechanical contact (Comninou, 1977) exists near the tip. Despite of these complications, Rice (1988) has argued that the oscillatory solution can still be used to characterize the interface crack field since the contact zone size is extremely small (e.g., subatomic) for a broad range of bimaterial and loading configurations of practical importance. For an absolute characterization of the interface stress intensity factor, Rice (1988) introduced a scaling length $\hat{r}$ so that Eq. (1) may be rewritten as

$$(\sigma_{yy}+i\sigma_{yx})_{\theta=0}=K(r/\hat{r})^{i\epsilon}/\sqrt{2\pi r} \tag{4}$$

where the coefficient $K=k\hat{r}^{i\epsilon}$ shall be defined as the stress intensity factor for the interface crack. As pointed out by Rice, the scaling length $\hat{r}$ may be chosen arbitrarily as long as it is held fixed when specimens of a given material pair but with different loading and geometry conditions are considered. Different values of $\hat{r}$ will not alter the magnitude of K but will change its phase angle. Since the oscillation index ϵ is typically very small, the variable quantity $(r/\hat{r})^{i\epsilon}=\exp[i\epsilon\ln(r/\hat{r})]$ has a very weak variation with r. Thus, it may sometimes be justified to choose $\hat{r}$ as a representative scale of the "fracture process zone" for a given bimaterial combination and define the "mode I and II" interface stress intensity factors K_I and K_{II} as

$$K=K_I+iK_{II}=k\hat{r}^{i\epsilon}. \tag{5}$$

It should be understood that the definition of (5) rigorously reduces to that of the classical mode I, II stress intensity factors only when $\epsilon=0$, but for simplicity we will use the same stress intensity factor notations (K_I, K_{II} and $K=K_I+iK_{II}$) for both homogeneous and interface cracks.

The stress intensity factor K defined in (5) can then be used to characterize the interface fracture toughness. Since interface fracture is inherently mixed mode with K being a complex number, the interface toughness in general cannot be given by a single material constant analogous to the K_{Ic} concept in homogeneous crack theory, rather the toughness is defined by a failure locus that gives the critical magnitude of K as a function of the phase angle of K (Cao and Evans, 1989; Wang and Suo, 1990).

Based upon the above definition and understanding for the interface stress intensity factor, the crack face relative displacements behind the crack tip $\Delta u_j=(u_j)_{\theta=\pi}-(u_j)_{\theta=-\pi}$ are found to be

$$\Delta u_y+i\Delta u_x=\frac{c_1+c_2}{2(1+2i\epsilon)\cosh(\pi\epsilon)}\left(\frac{r}{\hat{r}}\right)^{i\epsilon}K\sqrt{\frac{r}{2\pi}} \tag{6}$$

where the constant

$$c=(\kappa+1)/\mu=\begin{cases}8(1-\nu^2)/E & \text{for plane strain}\\ 8/E & \text{for plane stress}\end{cases} \tag{7}$$

(E = Young's modulus) with subscripts 1, 2 measures the compliance of each material. One can use the crack solutions provided in (1) and (6) to derive the Irwin-type energy release rate per unit length of crack extension along the interface, with the result giving

$$G=\frac{c_1+c_2}{16\cosh^2\pi\epsilon}(K_I^2+K_{II}^2). \tag{8}$$

An interesting special case occurs when the oscillation vanishes. Letting $\epsilon=0$ in Eq. (2) yields the so-called nonoscillation condition on the moduli:

$$[\![(\kappa-1)/\mu]\!]=(\kappa_2-1)/\mu_2-(\kappa_1-1)/\mu_1=0 \tag{9}$$

where $[\![f]\!]$ denotes the jump in f across the interface. Equation (9) can be alternatively written as $[\![(1-2\nu)/\mu]\!]=0$ for plane-strain conditions. The nonoscillation condition has been discussed recently by several authors for interface cracks in general anisotropic media (e.g., Ting, 1986; Bassani and Qu, 1989; Suo, 1990). Under the condition $\epsilon=0$, the following two important observations can be made by examining Eqs. (1), (6), (8): (i) The near-tip stress field decouples so that the ratio $\sigma_{yy}/\sigma_{yx}=K_I/K_{II}$ remains constant along the interface ahead of the crack tip; (ii) The crack face relative displacement Δu_j and the energy release rate G become the average of the corresponding homogeneous solutions for materials #1 and #2. For instance, letting $\epsilon=0$ in Eq. (8) results in

$$G=(\mathcal{G}_1+\mathcal{G}_2)/2, \tag{10}$$

where

$$\mathcal{G}=\frac{c}{8}(K_I^2+K_{II}^2) \tag{11}$$

with subscripts 1 or 2 denotes the familiar Irwin $G-K$ relation between the energy release rate and the stress intensity factors for cracks in the homogeneous solid #1 or #2, respectively.

This paper has two goals. First, it is aimed at providing a fundamental understanding of the crack-tip oscillation from the viewpoint of the interface mismatch that results from the cracking. Second, we extend the Bueckner-Rice weight function method (Bueckner, 1970, 1973; Rice, 1972) to facilitate the interface crack analysis. Using properties of the surface Green's functions of a homogeneous solid and solutions obtained from weight function formulae, a mismatch analysis is carried out which indicates that the local mismatch near the crack tip results in the oscillatory near-tip field structure while the mismatch on the global scale leads to the corresponding stress intensity factors. For oscillatory interface crack field, it is shown that, other than a few extra material constants, the weight function analysis for interface cracks is completely parallel to its homogeneous counterpart so that any one known crack solution is sufficient for determining solutions for the same bimaterial geometry under any other loading conditions. The reader is referred to Rice's (1989) review article for more references on the weight function development in homogeneous crack analyses. Sham and Bueckner (1988) has also attempted to use the weight function method to study a composite wedge under antiplane loading. Our result is significant in that it allows many well-established weight function applications to be directly extended to the interface crack analysis, such as those involving crack interaction with arbitrary forces, transformation strains and dislocations. The weight function approach is also important in devising finite element schemes (e.g., Sham, 1987) to compute stress intensity factors for arbitrary geometry.

Background

Muskhelishvili's Complex Variable Representation. The field of plane elastic deformation may be represented by the standard complex Kolosov-Muskhelishvili potentials $\phi(z)$, $\psi(z)$ where $z=x+iy$ (Muskhelishvili, 1953). For crack problems it is convenient to use an associated pair of potentials $\phi(z)$, $\Omega(z)$ where

$$\Omega(z)=z\phi'(z)+\psi(z). \tag{12}$$

The displacement field $u=u_x+iu_y$ is then expressed as

$$2\mu u=\kappa\phi(z)-\overline{\Omega(z)}+(\bar{z}-z)\overline{\phi'(z)} \tag{13}$$

where the overbar denotes complex conjugation. The stress components are derived from

$$\begin{aligned}\sigma_{xx}+\sigma_{yy}&=2[\phi'(z)+\overline{\phi'(z)}]\\ \sigma_{yy}+i\sigma_{xy}&=\overline{\phi'(z)}+\Omega'(z)-(z-\bar{z})\phi''(z).\end{aligned} \tag{14}$$

The solutions to two-dimensional crack problems can be fully

expressed in terms of $\phi(z)$, $\Omega(z)$. For example, the asymptotic crack-tip field in a homogeneous solid has a universal structure represented by

$$\phi(z)=\bar{\Omega}(z)=\bar{K}\sqrt{(z-l)/2\pi} \tag{15}$$

where the tip is assumed to be located at $x=l$ and $K=K_I+iK_{II}$ is the stress intensity factor. For a finite crack of length l subjected to the crack face traction $\sigma_\infty=\sigma_{yy}^\infty+i\sigma_{yx}^\infty$, corresponding to the reduced problem of remote loads, the solution is

$$\phi(z)=\bar{\Omega}(z)=\frac{1}{2}\,\overline{\sigma_\infty}\left[\sqrt{z(z-l)}-z\right]. \tag{16}$$

The stress field derived form (14), (16) results in the well-known stress intensity factor solution

$$K=\sigma^\infty\sqrt{\pi l/2}. \tag{17}$$

Weight Function Theory. The weight function $h_{\alpha j}(\mathbf{x};\ l)$ is defined as the mode α ($\alpha=I,\ II,\ III$) stress intensity factor at a crack tip located at $x=l$ due to a point force in j-direction at a position $\mathbf{x}$. If $h_{\alpha j}(\mathbf{x};\ l)$ is known, then the stress intensity factors are obtained by superposition as the weighted average of applied forces over the whole body. Using a reciprocal relation between the energetic force on a crack tip, which is just the energy release rate $\mathcal{G}$ given in (11), and a point force $\mathbf{P}$ acting at $\mathbf{x}$, Rice (1972) has shown that

$$\frac{\partial u_j}{\partial l}=\frac{\partial \mathcal{G}}{\partial P_j}=\frac{c}{4}\,(K_I\,h_{Ij}+K_{II}\,h_{IIj}). \tag{18}$$

It is convenient for us to define the complex valued weight function h_α as

$$h_\alpha=h_{\alpha x}+ih_{\alpha y}. \tag{19}$$

Using the displacement representation (13) and the fact that (18) must hold for any combinations of K_I and K_{II} leads to

$$\begin{aligned}2\mu h_I&=\kappa\phi_w(z)-\overline{\Omega_w(z)}+(\bar{z}-z)\overline{\phi_w'(z)}\\ 2\mu h_{II}&=\kappa[-i\phi_w(z)]-\overline{[i\Omega_w(z)]}+(\bar{z}-z)\overline{[-i\phi_w'(z)]}\end{aligned} \tag{20}$$

where ϕ_w, Ω_w are two "weight function potentials" which are related to the regular displacement potentials ϕ, Ω by

$$\frac{\partial\phi(z;\ l)}{\partial l}=\frac{c}{4}\,\bar{K}\phi_w(z;\ l),\quad \frac{\partial\Omega(z;\ l)}{\partial l}=\frac{c}{4}\,K\Omega_w(z;\ l). \tag{21}$$

The functional dependence on the crack-tip location l has been shown explicitly in the expressions of (21). Equations (20), (21) indicate that the weight function h_α may be treated as a special displacement field associated with stresses $2\mu U_{kl}^\alpha=C_{ijkl}h_{\alpha j,i}$, where C_{ijkl} is the elastic modulus tensor. The mode I stress quantities U_{kl}^I are represented by ϕ_w, Ω_w in the same manner as (14):

$$\begin{aligned}2\mu(U_{xx}^I+U_{yy}^I)&=2[\phi_w'(z)+\overline{\phi_w'(z)}]\\ 2\mu(U_{yy}^I+iU_{xy}^I)&=\overline{\phi_w'(z)}+\Omega_w'(z)-(z-\bar{z})\phi_w''(z).\end{aligned} \tag{22}$$

The mode II stress quantities U_{ij}^{II} are obtained from the same relations but using the potential pair $(-i\phi_w,\ i\Omega_w)$.

With the knowledge of h_α and U_{ij}^α, the following applications are possible:

(a) For a body force distribution f_j,

$$K_\alpha(l)=\int_{\text{body}} h_{\alpha j}(\mathbf{x};\ l)f_j(\mathbf{x})dA. \tag{23}$$

(b) For an arbitrary distribution of transformation strain ϵ_{kl}^T (Rice, 1985; Gao, 1989),

$$K_\alpha(l)=2\mu\int_{\text{body}} U_{kl}^\alpha(\mathbf{x};\ l)\epsilon_{kl}^T(\mathbf{x})dA. \tag{24}$$

(c) For a general Somigliana dislocation $\Delta\mathbf{u}=\mathbf{u}^+-\mathbf{u}^-$ on a dislocation cut surface d, having normal $\mathbf{N}$ pointing from the $(-)$ side to the $(+)$ side of d,

$$K_\alpha(l)=2\mu\int_d U_{kl}^\alpha(\mathbf{x};\ l)N_k(\mathbf{x})\Delta u_l(\mathbf{x})dL. \tag{25}$$

(d) For a dislocation at $s=x_d+iy_d$ with constant Burgers vector $b=b_x+ib_y$, the formula (25) can be simplified to

$$K=-i\bar{b}[\phi_w(z)+\overline{\Omega_w(z)}]_s^\infty-ib[(z-\bar{z})\phi_w'(z)]_s^\infty. \tag{26}$$

Using the basic weight function relations (21), a passage from one crack solution to any other solutions under the same geometry is established as follows: Starting with a known crack solution, deriving the weight function potential from the known solutions by (21) and calculating the stress intensity factors by (23)–(26), the full solution to any other loading system can then be obtained by integrating (21) with respect to the crack position parameter l. Thus, knowledge of one crack solution is sufficient for determining the solutions for the same geometry under any other loading conditions.

For a semi-infinite crack with crack tip located at $x=l$, differentiating the K-field potentials in (15) with respect to the crack-tip position l yields

$$\phi_w=\Omega_w=-\frac{2}{c\sqrt{2\pi(z-l)}}. \tag{27}$$

Similarly, potentials in Eqs. (16) and the K solution of (17) lead to ϕ_w, Ω_w for a finite crack of length l. At the right crack tip $x=l$, it may be shown that

$$\phi_w=\Omega_w=-\frac{2}{c\sqrt{2\pi l}}\sqrt{\frac{z}{z-l}}. \tag{28}$$

Using the weight function formulae, the solution to a semi-infinite crack interacting with a dislocation (Fig. 1(*b*)) may be easily obtained as

$$K=-\frac{4i\,\bar{b}}{c\sqrt{2\pi t}},\quad \phi'(z)=\bar{\Omega}'(z)=-\frac{ib}{\pi c(z-t)}\sqrt{\frac{t}{z}}. \tag{29}$$

Analysis of Interface Mismatch.

Surface Green's Functions. Observe that the interface crack problem shown in Fig. 1(*a*) may be viewed as interaction between two elastic half-planes #1 and #2 via forces along the interface plane $y=0$. We first consider the fundamental

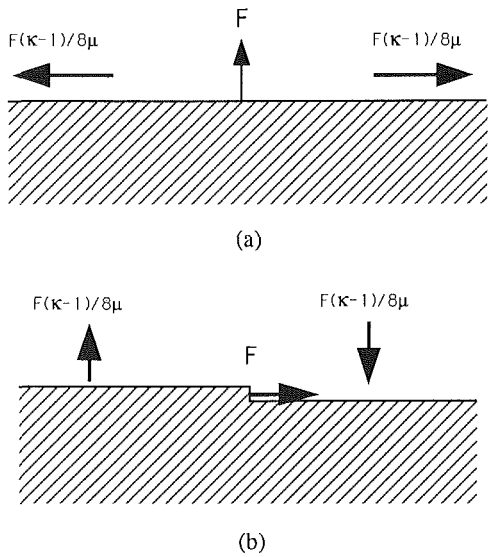

Fig. 2 Antisymmetric surface Green's functions of a homogeneous half-plane: (*a*) lateral expansion about a normal force; (*b*) antisymmetric warp about a shear force

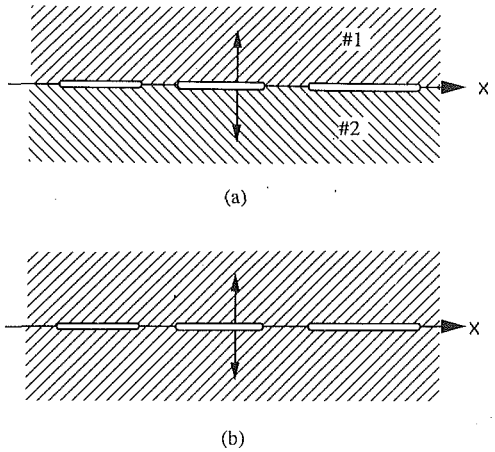

Fig. 3 (*a*) The basic interface crack problem considered in this paper, (*b*) the corresponding homogeneous configuration

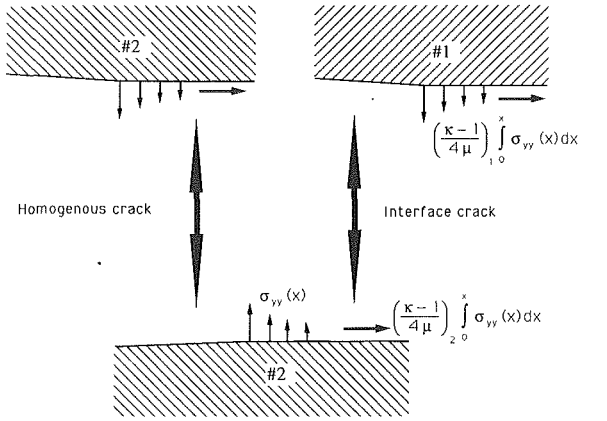

Fig. 4 The procedure of separating a homogeneous crack and forming an interface crack

Green's function problem of a homogeneous half-plane subjected to a concentrated surface force **F**. As schematically shown in Fig. 2, a fundamental result of contact mechanics indicates that a unit normal force F causes a uniform lateral expansion $F(\kappa-1)/8\mu$ along the surface. Similarly, a shear force causes an antisymmetric "warp" with the same magnitude. These surface deformations are represented by the "surface Green's function" (SGF) tensor **G** which allows one to use a simple superposition procedure to write the surface displacement vector $\mathbf{u}(x)$ due to an arbitrary distribution of surface traction $\mathbf{t}(x')$ in the convolution form

$$u_i(x)=\int_{-\infty}^{\infty} G_{ij}(x-x')t_j(x')dx' \tag{30}$$

Specifically, the Green's function component $G_{ij}(x-x')$ corresponds to the ith displacement at x due to a unit point force in the j-direction at x'. Standard two-dimensional elasticity solutions for **G** can be found in standard textbooks as (e.g., Muskhelishvili, 1953)

$$G_{xx}=G_{yy}=-\frac{c}{4\pi}\ln|x-x'|,$$

$$G_{xy}=-G_{yx}=\frac{\kappa-1}{8\mu}\,\mathrm{sgn}(x-x'). \tag{31}$$

The tensor **G** can be separated into a symmetric part $\mathbf{G}^S$ and an antisymmetric part $\mathbf{G}^A$, i.e.,

$$\mathbf{G}=\mathbf{G}^S+\mathbf{G}^A. \tag{32}$$

The symmetric part $\mathbf{G}^S$ is diagonal with components G_{xx}, G_{yy} while the antisymmetric part $\mathbf{G}^A$ has two off-diagonal components $G_{xy}=-G_{yx}$. Following (31), the matrix forms for $\mathbf{G}^S$ and $\mathbf{G}^A$ are

$$\mathbf{G}^S=-\frac{c}{4\pi}\begin{bmatrix}1&0\\0&1\end{bmatrix}\ln|x-x'|,$$

$$\mathbf{G}^A=\frac{\kappa-1}{8\mu}\begin{bmatrix}0&1\\-1&0\end{bmatrix}\mathrm{sgn}(x-x'). \tag{33}$$

The symmetric tensor $\mathbf{G}^S$ also represents symmetric displacement responses with respect to a force while the antisymmetric tensor $\mathbf{G}^A$ also represents the antisymmetric responses. The tensor $\mathbf{G}^A$ is of the same constant magnitude but opposite sign on both sides of the force, generating the lateral expansion with respect to a normal force and the antisymmetric warp with respect to a shear force, as shown in Fig. 2. The Green's function tensors of (33) satisfies Betti's reciprocal theorem

$$G_{ij}(x-x')=G_{ji}(x'-x). \tag{34}$$

The antisymmetry $G_{xy}(x-x')=-G_{yx}(x-x')$ is due to the fact that we have kept the same set of variables x, x', rather than interchanging them as in the reciprocal relation (34).

It is well known that under traction boundary conditions, stresses of a bimaterial interface may be expressed in terms of the two Dundurs mismatch constants (Dundurs, 1968)

$$\alpha=\frac{c_2-c_1}{c_2+c_1},\quad \beta=\frac{[\![(\kappa-1)/\mu]\!]}{c_2+c_1}. \tag{35}$$

In particular, the oscillation index ϵ defined in Eq. (2) is related to the parameter β by

$$\epsilon=\frac{1}{2\pi}\ln\frac{1-\beta}{1+\beta}=-\frac{\beta}{\pi}+0(\beta^3). \tag{36}$$

It is interesting to observe that α and β simply measure the dissimilarity of surface Green's function tensors $\mathbf{G}^S$ and $\mathbf{G}^A$ given in (33). By requiring $0<\nu<1/2$ and $\mu>0$, Dundurs showed that α and β are confined to a parallelogram in the (α,β) plane enclosed by $\alpha=\pm1$ and $\alpha-4\beta=\pm1$. Calculations by Suga et al. (1988) on more than a hundred material pairs suggest that the values of β are mostly restricted to $|\beta|<0.25$, implying that $|\epsilon|<0.08$. Hence, the oscillation index is a very small parameter for most of the bimaterial combinations of interest.

The Basic Interface Crack Problem. A general interface crack problem may involve complicated geometry and loading configurations. Without accounting for too much complications, we define the basic interface crack problem as a collinear crack array lying along an interface between two semi-infinite solids #1 and #2 and having a pair of unit point forces on the upper and lower crack faces as shown in Fig. 3(*a*). The solution to the basic problem can be used as the building block to construct the solutions to the given collinear crack problem with arbitrary crack-face traction, or to construct the solutions under general loading if the crack-face traction is equated to that would be induced at the crack site by the applied loadings in the absence of a crack.

Analysis of Interface Mismatch via SGF Tensor. To understand the basic interface crack problem, we consider the corresponding homogeneous cracks in Fig. 3(*b*). The case of a pair of wedge opening normal forces acting on the crack faces results in a mode I deformation field near the crack tips. Imagine that the body is separated without relaxation into two half-planes along the crack plane $y=0$, as shown in Fig. 4. Along the separated surface ahead of an arbitrarily chosen crack tip, a distribution of a normal traction $\sigma_{yy}(x)$ would be found which is independent of the material moduli in the present case of point force loading. Set the coordinate origin at the chosen crack tip. Then, by superposing on the Green's

function $\mathbf{G}^A$, the traction $\sigma_{yy}(x)$ results in a horizontal surface displacement

$$u_x(x) = \left(\frac{\kappa - 1}{4\mu}\right) \int_0^x \sigma_{yy}(x')dx' \tag{37}$$

relative to the crack tip. Since the vertical surface displacement ahead of the crack tip is identically zero by symmetry, the only interface mismatch arising in the process of joining an upper half-plane #1 with a lower half-plane #2 to form an interface crack is the difference in lateral displacements. Obviously, this lateral mismatch is given by

$$[\![u_x(x)]\!] = [\![(\kappa - 1)/4\mu]\!] \int_0^x \sigma_{yy}(x')dx' \tag{38}$$

($[\![u_y(x)]\!] = 0$). If the parameter $(\kappa - 1)/\mu$ is the same for no. 1 and no. 2, then there is no interface mismatch so that no extra forces shall be needed in forming the interface crack. But the compatibility condition $[\![(\kappa - 1)/\mu]\!] = 0$ is just the nonoscillation condition (9). Similar arguments may be applied to formation of interface cracks under mode II shear conditions with the same conclusion that there is no interface mismatch if the nonoscillatory condition is satisfied. Combining the mode I and II results, one finds that the interface mismatch may be represented by a continuous distribution of dislocations along the interface with density

$$\frac{\partial [\![u(x)]\!]}{\partial x} = [\![(\kappa - 1)/4\mu]\!] \overline{\sigma(x)} \tag{39}$$

where $u = u_x + iu_y$ and $\sigma = \sigma_{yy} + i\sigma_{yx}$. Equation (39) provides a relation between the traction and the mismatch along the interface between two semi-infinite solids. Thus, for the basic interface crack problem (Fig. 3(*a*)), when $\epsilon = 0$, there is no mismatch so that the stress state in each half plane #1 and #2 remains identical to that of the corresponding homogeneous cracks. This by superposition is also true for cracks under arbitrary crack-face traction. Given the fact that interface crack problems under general loading can be solved by the corresponding reduced problems involving crack-face tractions, it can be concluded that *the interface crack field for collinear cracks in an infinite bimaterial body will remain identical to that of the corresponding homogeneous crack if the induced crack-face traction is independent of the material moduli.* An obvious example is a finite crack or collinear cracks subjected to remote stresses in which case the stress solutions are identical to the corresponding homogeneous solutions. However, the induced traction in general will depend on the moduli of both materials so that the stress intensity factors will depend on the moduli of both materials while the structure of the stress field remains the same as that of the homogeneous cracks.

The nonoscillation condition for the interface crack fields can be given a more general interpretation as requiring the antisymmetric SGF tensor $\mathbf{G}^A$ to be continuous across the interface, i.e.,

$$[\![\mathbf{G}^A]\!] = 0. \tag{40}$$

The condition (40) also applies to more complex interface crack problems such as those involving anisotropic materials. Those problems will be considered in a separate paper (Gao et al., 1991).

The above SGF analysis indicates that for interface cracks in an infinite body subjected to prescribed crack-face traction, the oscillation and mismatch are equivalent in that the mismatch vanishes when oscillation does and vice versa. This is not true for interface cracks involving more complicated loadings and/or finite geometries such as thin films on a substrate. In those problems, there is also a strong dependence of the crack field on the other Dundurs parameter α. The reader is referred to Hutchinson (1990) for a review on some of the recent results of the stress intensity factors for various fracture specimens. Hutchinson and co-workers (e.g., Suo and Hutchinson, 1989; He and Hutchinson, 1989) have proposed to ignore the oscillation effects by setting $\epsilon = 0$ in many engineering applications, provided that in those cases the effect of ϵ (or β) is much less significant compared to that of α.

Weight Function Analysis of Nonoscillatory Interface Crack Fields

To understand the singularity nature of the oscillatory interface crack field, it is helpful to consider first the nonoscillatory case, i.e., when $\epsilon = 0$. In that case, the interface crack field has the same near-tip structure as homogeneous cracks and one may define the interface weight function $h_\alpha = h_{\alpha x} + ih_{\alpha y}$ in the same manner as the homogeneous case. The reciprocal relation (18) also holds for interface cracks if the homogeneous energy release rate $\mathcal{G}$ is replaced by the interface energy release rate G given by Eq. (8). Under the nonoscillation condition, $G = (\mathcal{G}_1 + \mathcal{G}_2)/2$ so that the fundamental weight function relation analogous to (18) may be written as

$$\frac{\partial u}{\partial l} = \frac{c_1 + c_2}{8} (K_I h_I + K_{II} h_{II}). \tag{41}$$

Similarly, the interface weight functions h_I, h_{II} can be represented by two weight function potentials ϕ_w, Ω_w. The analog of (21) is

$$\frac{\partial \phi(z; l)}{\partial l} = \frac{c_1 + c_2}{8} \overline{K}\, \phi_w(z; l),$$

$$\frac{\partial \Omega(z; l)}{\partial l} = \frac{c_1 + c_2}{8} K \Omega_w(z; l). \tag{42}$$

Equations (41), (42) are the basic weight function relations for the nonoscillatory interface crack fields. The weight function formulae (23)–(26) for crack interactions with arbitrary forces, transformation strains, and dislocations also apply for the interface cracks. It suffices to calculate one crack solution for a given material pair and geometry; all the other solutions can be developed from the weight function potentials ϕ_w, Ω_w following the same approach established in the homogeneous weight function theory.

For collinear cracks between two semi-infinite solids, one may conveniently choose u, ϕ, Ω, and K in (41), (42) as the solutions under remote stresses or prescribed crack face traction, in which case the deformation field in each material is identical to the corresponding homogeneous crack field. It is thus clear that for this special case the interface weight functions $h_{\alpha j}$ are related to the homogeneous weight functions by

$$h_\alpha = \begin{cases} [2c_1/(c_1 + c_2)](h_\alpha)_1 & \text{in \#1} \\ [2c_2/(c_1 + c_2)](h_\alpha)_2 & \text{in \#2} \end{cases} \tag{43}$$

where $(h_\alpha)_1$, $(h_\alpha)_2$ denote the homogeneous weight function field in material #1, #2, respectively. It can be shown that the continuity of h_α across the interface is guaranteed by the nonoscillation condition. Using the weight functions as the basic building block, one may further write the stress intensity factors for an interface crack between two semi-infinite solids in the following form

$$K = \frac{2c_1(K)_1 + 2c_2(K)_2}{c_1 + c_2} \tag{44}$$

where $(f)_1$, $(f)_2$ are the homogeneous solutions for the quantity f due to the loads lying, respectively, in material regions #1, #2. Similar relations also apply to complex potential functions; it may be shown that

$$\phi = \frac{2c_1(\phi)_1 + 2c_2(\phi)_2}{c_1 + c_2}, \quad \Omega = \frac{2c_1(\Omega)_1 + 2c_2(\Omega)_2}{c_1 + c_2}. \tag{45}$$

Therefore, under the nonoscillation condition, the stress intensity factor for the bimaterial case of Fig. 1(*b*), i.e., a semi-

infinite interface crack interacting with a dislocation ahead of the crack tip, can be directly derived from the corresponding homogeneous solutions (29) as

$$K=-\frac{8i\,\overline{b}}{(c_1+c_2)\sqrt{2\pi t}}. \tag{46}$$

The associated complex potential function is

$$\phi'(z)=\overline{\Omega}'(z)=-\frac{2i\,b}{\pi(c_1+c_2)(z-t)}\sqrt{\frac{t}{z}}. \tag{47}$$

Oscillatory Interface Crack Field Versus Interface Mismatch

Crack-Tip Oscillation Versus Local Mismatch. When the nonoscillation condition (9) is violated, oscillation at an interface crack tip would occur as a consequence of the interface mismatch. The oscillatory near-tip field expressed in (1), (3), (6) can be represented by the following potentials

$$\phi_1'(z)=\overline{\Omega}_2'(z)=\frac{\overline{K}e^{-\pi\epsilon}}{2\sqrt{2\pi(z-l)}\cosh(\pi\epsilon)}\left(\frac{\hat{r}}{z-l}\right)^{i\epsilon}$$

$$\Omega_1'(z)=\overline{\phi}_2'(z)=\frac{Ke^{\pi\epsilon}}{2\sqrt{2\pi(z-l)}\cosh(\pi\epsilon)}\left(\frac{\hat{r}}{z-l}\right)^{-i\epsilon} \tag{48}$$

where the subscripts refer to the two materials and the crack tip lies at $x=l$.

The relation (39) between the mismatch and traction along the interface can be used to form an iteration procedure that adjusts an initially assumed traction distribution $\sigma(x)$ to the oscillatory state. In that procedure, the mismatch due to the initial $\sigma(x)$ is represented by an array of dislocations with density given in (39), but the superposed effect of such mismatch dislocations will change the traction $\sigma(x)$ itself, forming a loop adjustment between the traction and mismatch along the interface. It will be shown below that this procedure leads to the oscillatory singularity field. Set up the coordinate origin at a chosen crack tip. The mismatch dislocation density along the interface ahead of the crack tip is related to the traction there by (39). Use the nonoscillatory field as the initial state in the loop adjustment procedure described above, so that the traction is taken as $\sigma(x)=K/\sqrt{2\pi x}$ and

$$\frac{\partial[\![u(x)]\!]}{\partial x}=[\![(\kappa-1)/4\mu]\!]\frac{\overline{K}}{\sqrt{2\pi x}}. \tag{49}$$

The superposed effect of such dislocations within the crack tip region characterized by $\hat{r}$ can be calculated from the single dislocation formula (47), which modifies, for example, the potential function $\phi'(z)$ in material #1 as

$$\phi_1'(z)=\frac{\overline{K}}{2\sqrt{2\pi z}}\left[1+\frac{4i\sqrt{2\pi z}}{\pi(c_1+c_2)\overline{K}}\int_0^{\hat{r}}\frac{1}{z-t}\sqrt{\frac{t}{z}}\left(\frac{\partial[\![u(t)]\!]}{\partial t}\right)dt\right]$$

$$=\frac{\overline{K}}{2\sqrt{2\pi z}}\left[1-i\epsilon\left(\ln\frac{z}{\hat{r}}-\pi i\right)+0(\epsilon^2)\right] \tag{50}$$

where the approximation $\epsilon=-\beta/\pi$ (correct to the second order in β) has been used and quantities of order $z/\hat{r}$ are ignored in the present "near-tip" calculation.

At a fixed position z, one may expand the exact solution of $\phi_1'(z)$, given by (48) for $l=0$, into a power series of ϵ as

$$\phi_1'(z)=\frac{\overline{K}}{2\sqrt{2\pi z}}\frac{e^{-\pi\epsilon}}{\cosh(\pi\epsilon)}\left(\frac{\hat{r}}{z}\right)^{i\epsilon}$$

$$=\frac{\overline{K}}{2\sqrt{2\pi z}}\left[1-i\epsilon\left(\ln\frac{z}{\hat{r}}-\pi i\right)-\frac{\epsilon^2}{2}\left(\ln\frac{z}{\hat{r}}\right)^2+0(\epsilon^3)\right]. \tag{51}$$

Thus, the results (50) of the first adjustment from the nonoscillatory state gives the first-order expansion in ϵ of the oscillatory field. Using the first-order potential given in (50) to update the traction distribution $\sigma(x)$ by (14) and repeating the above adjustment procedure result in the second-order expansion expression of $\phi_1'(z)$, as expressed in (51). Continuing the adjustment procedure leads to a Taylor expansion series in ϵ of the oscillatory field at any given material point. Summation of such Taylor expansion then constructs the full oscillatory near-tip field.

Global Mismatch Effect. The presence of interface mismatch not only alters the singularity nature at a crack tip as we have explored, but also changes the singularity strength of the oscillatory field. To understand how interface mismatch affects the stress intensity factor K, consider, for example, a semi-infinite crack subjected to a pair of crack-face forces $p=p_y+ip_x$ at a distance l behind the crack tip. In that case the exact solution is (e.g., Rice and Sih, 1965)

$$K=p\sqrt{\frac{2}{\pi l}}\cosh\pi\epsilon\left(\frac{\hat{r}}{l}\right)^{i\epsilon}. \tag{52}$$

Again, for a fixed $\hat{r}/l$, the above may be expanded into a Taylor power series of ϵ, giving

$$K=p\sqrt{\frac{2}{\pi l}}\left[1+i\epsilon\ln\frac{\hat{r}}{l}+0(\epsilon^2)\right] \tag{53}$$

where the zeroth-order term $p\sqrt{2/\pi l}$ corresponds to the nonoscillatory solution. The first-order term can be understood as the superposed effect of mismatch dislocations given by (39) with traction $\sigma(x)$ taken as the $\epsilon=0$ result, i.e.,

$$\frac{\partial[\![u(x)]\!]}{\partial x}=[\![(\kappa-1/4\mu]\!]\frac{\overline{p}}{\pi(x+l)}\sqrt{\frac{l}{x}}. \tag{54}$$

Since the above dislocation density is of order ϵ, it may be justified to use the nonoscillatory crack-dislocation formula (46) in the superposition procedure. Thus, the mismatch dislocations outside the crack-tip region characterized by $\hat{r}$ give the first-order term in (53):

$$K=\frac{8i}{(c_1+c_2)\sqrt{2\pi}}\int_{\hat{r}}^{\infty}\frac{1}{\sqrt{x}}\left(\frac{\partial[\![u(x)]\!]}{\partial x}\right)dx$$

$$=\left(p\sqrt{\frac{2}{\pi l}}\right)i\epsilon\ln\frac{\hat{r}}{l}. \tag{55}$$

As explained before, the traction and mismatch along the interface will adjust themselves to the oscillatory state via the loop procedure based on (39), eventually resulting in the full Taylor expansion of the exact K-solution (52). Clearly, the scaling length $\hat{r}$ is acting here as a characteristic distance at the crack tip where the global information of geometry and loading is transmitted to the fracture process zone.

A Finite Interface Crack. As the corresponding reduced problem of that shown in Fig. 5, a crack along the interface subjected to uniform crack-face traction $\sigma_\infty=\sigma_{yy}^\infty+i\sigma_{yx}^\infty$ has the following potential function solution (e.g., England, 1965; Rice and Sih, 1965)

$$\phi_1(z)=\overline{\Omega}_2(z)=\frac{e^{-\pi\epsilon}\overline{\sigma_\infty}}{2\cosh(\pi\epsilon)}\left[\sqrt{z(z-l)}\left(\frac{z}{z-l}\right)^{i\epsilon}-z\right]$$

$$\phi_2(z)=\overline{\Omega}_1(z)=\frac{e^{\pi\epsilon}\sigma_\infty}{2\cosh(\pi\epsilon)}\left[\sqrt{z(z-l)}\left(\frac{z}{z-l}\right)^{i\epsilon}-z\right]. \tag{56}$$

Substituting this into (14) and using the stress intensity factor definition given in (4), one finds that

$$K=(1+2i\epsilon)(\hat{r}/l)^{i\epsilon}\sigma_\infty\sqrt{\pi l/2}. \tag{57}$$

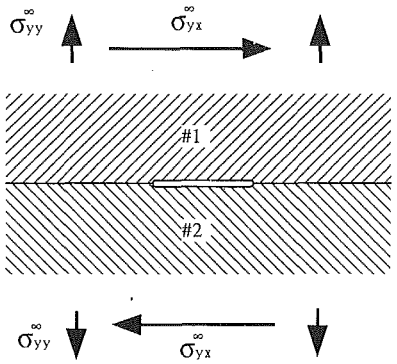

Fig. 5 A finite interface crack under remote loading

When $\epsilon = 0$, the K of (57) reduces to the corresponding homogeneous solution (17) since the interface mismatch also vanishes in the present case (of infinite geometry).

Weight Function Method for Oscillatory Interface Crack Fields

In general, an interface crack will have an oscillatory near-tip field due to the existing interface mismatch. Since the oscillatory field predicts crack-face interpenetration behind the crack tip, the forms given in (1), (3), (6) for the near-tip stress and displacement field must be wrong on a sufficiently small scale. However, the near-tip contact zone size estimated by several authors (Comninou, 1977; Rice, 1988; Rice et al., 1989) is found to be negligible (e.g., subatomic) for a broad range of crack-tip loading configuration. Thus, Rice (1988) pointed out that the stress intensity factor K as defined in (5) does characterize the severity of the near-tip loading when the size of the fracture process zone involving crack-face contact, material nonlinearity (plasticity, microcracking, transformation) and/or the discreteness of material microstructure (e.g., fiber distance in a composite globally treated as a continuum) is much smaller than characteristic macroscale dimensions such as crack length or a film thickness. When such a size restriction is met, the value and history of K uniquely characterize the crack-tip state. With this understanding, we extend the weight function method to the general interface crack analysis, for determination of the oscillatory field solutions such as the stress intensity factors.

In terms of the crack mode designation displayed in $K = k\hat{r}^{i\epsilon} = K_I + iK_{II}$, we may define the weight function h_α for interface cracks in exactly the same manner as the homogeneous case. We note that the reciprocal relation (18) still holds for the oscillatory interface crack field if the homogeneous energy release rate $\mathcal{G}$ is replaced by the interface energy release rate G given by (8). Therefore, the basic weight function relation for interface cracks analogous to (18) is

$$\frac{\partial u}{\partial l} = \frac{c_1 + c_2}{8\cosh^2(\pi\epsilon)}(K_I h_I + K_{II} h_{II}). \tag{58}$$

Similarly, two weight function potentials ϕ_w and Ω_w can be used to represent h_α by (20), with (21) becoming

$$\frac{\partial \phi(z; l)}{\partial l} = \frac{c_1 + c_2}{8\cosh^2(\pi\epsilon)} \overline{K}\, \phi_w(z; l),$$

$$\frac{\partial \Omega(z; l)}{\partial l} = \frac{c_1 + c_2}{8\cosh^2(\pi\epsilon)} K \Omega_w(z; l). \tag{59}$$

The above relations may be used to determine the weight function field by differentiating any known crack solution with respect to the crack-tip position l, or to determine the full-field potentials ϕ, Ω by integration with respect to l from given solutions of ϕ_w, Ω_w, and K. Therefore, other than a few material constants, the interface weight function formulation is completely parallel to its homogeneous counterpart developed by Bueckner (1970) and Rice (1972) as presented in Eqs. (18)–(26). The important conclusion is that knowledge of any one crack solution leads to the determination of crack solutions for the same geometry under any other loading conditions. The crack interaction with arbitrary forces, transformation strains, and dislocation can be studied by the same formulae (23)–(26), now with the understanding that K represents the near-tip stress field in the sense of (1)–(5).

For a semi-infinite crack with crack tip located at $x = l$, differentiating the crack-tip potentials in (48), with respect to the crack-tip position l according to (59), yields the interface weight function potentials as

$$\epsilon^{\pi\epsilon}\phi_{w1}(z) = e^{-\pi\epsilon}\overline{\Omega_{w1}}(z) = -\frac{4\cosh(\pi\epsilon)}{c_1 + c_2}\frac{1}{\sqrt{2\pi(z-l)}}\left(\frac{\hat{r}}{z-l}\right)^{i\epsilon} \tag{60}$$

in material #1. The potential functions in material #2 are obtained from $\phi_{w2}(z) = \overline{\Omega_{w1}}(z)$ and $\Omega_{w2}(z) = \overline{\phi_{w1}}(z)$. Also, potentials in Eqs. (56) and K in (57) lead to ϕ_w, Ω_w for a finite crack of length l. At the right crack tip $x = l$, it may be shown that

$$e^{\pi\epsilon}\phi_{w1}(z) = e^{-\pi\epsilon}\overline{\Omega_{w1}}(z) = -\frac{4\cosh(\pi\epsilon)}{c_1 + c_2}\frac{1}{\sqrt{2\pi l}}\left(\frac{z}{z-l}\right)^{1/2+i\epsilon}\left(\frac{\hat{r}}{l}\right)^{i\epsilon} \tag{61}$$

Similarly, $\phi_{w2}(z) = \overline{\Omega_{w1}}(z)$ and $\Omega_{w2}(z) = \overline{\phi_{w1}}(z)$. The complete weight function field derived from the above potentials via (20), (22) can be used to compute the interface stress intensity factors due to arbitrary forces, dislocations, and transformation strains according to formulae given in (23)–(26).

For example, when a dislocation at $s = x_d + iy_d$ in #2 interacts with a finite interface crack lying along (0, l) of the x-axis, substituting (61) into (26) immediately gives the K result

$$K = -\frac{4i\cosh(\pi\epsilon)}{(c_1 + c_2)\sqrt{2\pi l}}\left(\frac{\hat{r}}{l}\right)^{i\epsilon}\left\{\bar{b}\left[e^{-\pi\epsilon}\left(\frac{\bar{s}}{\bar{s}-l}\right)^{1/2+i\epsilon} - 2\cosh(\pi\epsilon) + e^{\pi\epsilon}\left(\frac{s}{s-l}\right)^{1/2+i\epsilon}\right] - (1/2 + i\epsilon)be^{\pi\epsilon}[(s-\bar{s})s^{-1/2+i\epsilon}(s-l)^{-3/2-i\epsilon}l]\right\}. \tag{62}$$

In the limit of a semi-infinite crack with crack tip at the coordinate origin, (62) reduces to

$$K = -\frac{4i\cosh(\pi\epsilon)}{(c_1 + c_2)\sqrt{2\pi}}\{\bar{b}(e^{-\pi\epsilon}(\hat{r}/\bar{s})^{i\epsilon}/\sqrt{\bar{s}} + e^{\pi\epsilon}(\hat{r}/s)^{i\epsilon}/\sqrt{s}) - (1/2 + i\epsilon)be^{\pi\epsilon}[(s-\bar{s})s^{-3/2}(\hat{r}/s)^{i\epsilon}]\}. \tag{63}$$

These results are consistent with those derived by Suo (1989) from a different approach.

Conclusions

We have accomplished the following in this paper: First, it is shown that the near-tip oscillation of an interface crack may be understood from the viewpoint of the interface mismatch that results from the cracking. Our study indicates that the local mismatch near the crack tip results in the oscillatory near-tip field structure, while the mismatch on the global scale leads to the corresponding stress intensity factors. The study also reveals that the scaling length $\hat{r}$ introduced by Rice (1988) in defining the interface stress intensity factor defines a characteristic distance at the crack tip where global information of geometry and loading is transmitted into the fracture process zone. Second, we have extended the Bueckner-Rice weight function method to the interface crack analysis, showing that,

other than a few extra material constants, the interface weight function analysis is completely parallel to its homogeneous counterpart so that all the well established formulae such as those given in (23)–(26) concerning crack interaction with transformation strains and dislocations can be directly applied to the interface crack problems.

The interface weight function method presented here follows Rice's (1972) notion of reciprocal relations among energetic forces on a crack tip and other interacting defects. An alternative approach can be formulated following that of Bueckner (1970) in searching for a fundamental field whose potential functions behave as $z^{-1/2\pm i\epsilon}$ near a crack tip. Apparently unaware of Bueckner's work, Stern and coworkers (e.g., Stern, 1978; Hong and Stern, 1978) developed a concept of "complementary elastic state" for interface cracks which is essentially the same as the fundamental field of Bueckner (1970). However, the analysis by Stern and coworkers is cumbersome and much less transparent than our present formulation given in (58), (59). In recent years, the weight function method has been intensively developed for both two and three-dimensional crack analysis in homogeneous materials, as reviewed by Rice (1989). Finite element schemes have also been devised to compute the two and three-dimensional weight functions (e.g., Parks and Kamenetzky, 1979; Sham, 1987) for arbitrary geometry. Use of these existing techniques in the same vein of the present work will greatly facilitate the interface fracture analysis.

Acknowledgment

The work reported was supported by the NSF-MRL program through the Center for Material Research at Stanford University. The author is indebted to Prof. J. R. Rice for critical comments on the initial manuscript. I am also grateful to Profs. D. M. Barnett, J. W. Hutchinson, and Z. Suo for numerous discussions in the course of this work.

References

Bassani, J. L., and Qu, J., 1989, "Finite Crack on Bimaterial and Bicrystal Interfaces," *Journal of the Mechanics and Physics of Solids*, Vol. 37, pp. 434–453.

Bueckner, H. F., 1973, "Field Singularities and Related Integral Representtions," *Mechanics of Fracture 1: Methods of Analysis and Solution of Crack Problems*, G. C. Sih, ed., Noordhoff, Leyden, pp. 239–314.

Bueckner, H. F., 1970, "A Novel Principle for the Computation of Stress Intensity Factors," *Zeitschrift fuer angewandte Mathematik und Mechanik*, Vol. 50, pp. 529–546.

Cao, H. C., and Evans, A. G., 1989, "An Experimental Study of the Fracture Resistance of Bimaterial Interfaces," *Mechanics of Materials*, Vol. 7, pp. 295–304.

Comninou, M., 1977, "Interfacial Crack With Friction in the Contact Zone," ASME JOURNAL OF APPLIED MECHANICS, Vol. 44, pp. 780–781.

Dundurs, J., 1968, "Elastic Interactions of Dislocations with Inhomogeneities," *Mathematical Theory of Dislocations*, ASME, New York, pp. 70–115.

England, A. H., 1965, "A Crack Between Dissimilar Media," ASME JOURNAL OF APPLIED MECHANICS, Vol. 32, pp. 400–402.

Eshelby, J. D., 1957, "The Determination of the Elastic Field of an Ellipsoidal Inclusion, and Related Problems," *Proc. Roy. Soc., London*, Vol. A241, pp. 376–396.

Hong, C., and Stern, M., 1978, "The Computation of Stress Intensity Factors in Dissimilar Materials," *Journal of Elasticity*, Vol. 8, pp. 21–34.

Gao, H., 1989, "Application of 3-D Weight Functions—I. Formulations of Problems of Crack Interaction with Transformation Strains and Dislocations," *Journal of the Mechanics and Physics of Solids*, Vol. 37, pp. 133–153.

Gao, H., Abbudi, M., and Barnett, D. M., 1991, "On Interfacial Crack-Tip Field in Anisotropic Elastic Solids," *Journal of the Mechanics and Physics of Solids*, in press.

He, M-Y., and Hutchinson, J. W., 1989, "Kinking of a Crack Out of an Interface," ASME JOURNAL OF APPLIED MECHANICS, Vol. 56, pp. 270–278.

Hong, C. C., and Stern, M., 1978, "The Computation of Stress Intensity Factors in Dissimilar Materials," *Journal of Elasticity*, Vol. 8, pp. 21–34.

Hutchinson, J. W., 1990, "Mixed Mode Fracture Mechanics of Interfaces," to appear in *Scripta Metallurgica*.

Knowles, J. K., and Sternberg, E., 1983, "Large Deformation Near a Tip of an Interface Crack Between Two Neo-Hookean Sheets," *Journal of Elasticity*, Vol. 13, pp. 257–293.

Muskhelishvili, N. I., 1953, *Some Basic Problems of the Mathematical Theory of Elasticity*, Noordhoff, Groningen-Holland.

Parks, D. M., and Kamenetzky, E. A., 1979, "Weight Functions from Virtual Crack Extensions," *International Journal of Numerical Methods in Engineering*, Vol. 14, pp. 1693–1706.

Rice, J. R., Suo, Z., and Wang, J. S., 1990, "Mechanics and Thermodynamics of Brittle Interfacial Failure in Bimaterial Systems," *Metal-Ceramic Interfaces*, M. Ruhle, A. G. Evans, M. F. Ashby, and J. P. Hirth, eds., Pergamon Press, New York, pp. 269–294.

Rice, J. R., 1989, "Weight Function Theory For Three-Dimensional Elastic Crack Analysis," *Fracture Mechanics: Perspectives and Directions* (Twentieth Symposium), ASTM-STP-1020, R. P. Wei and R. P. Gangloff, eds., American Society for Testing and Materials, Philadelphia, pp. 29–57.

Rice, J. R., 1988, "Elastic Fracture Mechanics Concepts for Interfacial Cracks," ASME JOURNAL OF APPLIED MECHANICS, Vol. 55, pp. 98–103.

Rice, J. R., 1985, "Three Dimensional Elastic Crack Tip Interactions with Transformation Strains and Dislocations," *International Journal of Solids and Structures*, Vol. 21, pp. 781–791.

Rice, J. R., 1972, "Some Remarks on Elastic Crack Tip Stress Fields," *International Journal of Solids and Structures*, Vol. 8, pp. 751–758.

Rice, J. R., 1968, "Mathematical Analysis in the Mechanics of Fracture," *Fracture: An Advanced Treatise*, H. Liebowitz, ed., Vol. 2, pp. 191–311.

Rice, J. R., and Sih, G. C., 1965, "Plane Problems of Cracks in Dissimilar Media," ASME JOURNAL OF APPLIED MECHANICS, Vol. 32, pp. 418–423.

Sham, T. L., 1987, "A Unified Finite Element Method for Determining Weight Functions in Two and Three Dimensions," *International Journal of Solids and Structures*, Vol. 23, pp. 1357–1372.

Sham, T. L., and Bueckner, H. F., 1988, "The Weight Function Theory for Piecewise Homogeneous Isotropic Notches in Antiplane Strain," ASME JOURNAL OF APPLIED MECHANICS, Vol. 55, pp. 596–603.

Stern, M., 1979, "The Numerical Calculation of Thermally Induced Stress Intensity Factors," *Journal of Elasticity*, Vol. 9, pp. 91–95.

Suga, T., Elssner, G., and Schmauder, J., 1988, "Composite Parameters and Mechanical Compatibility of Material Joints," *Journal of Composite Materials*, pp. 917–934.

Suo, Z., and Hutchinson, J. W., 1989, "Sandwich Specimens for Measuring Interface Crack Toughness," *J. Mat. Sci. Engng.*, Vol. A107, pp. 135–143.

Suo, Z., 1989, "Singularities Interacting with Interfaces and Cracks," *Int. J. Solids Struct.*, Vol. 25, pp. 1133–1142.

Suo, Z., 1990, "Singularities, Interfaces and Cracks in Dissimilar Anisotropic Media," *Proc. Roy. Soc. London*, Vol. A427, pp. 331–358.

Ting, T. C. T., 1986, "Explicit Solution and Invariance of Singularities at an Interface Crack in Anisotropic Composites," *International Journal of Solids and Structures*, Vol. 22, pp. 965–983.

Wang, J. S., and Suo, Z., 1990, "Experimental Determination of Interfacial Toughness Curves Using Brazil Nut Sandwiches," *Acta Metall. Mater*, Vol. 38, pp. 1279–1290.

Williams, M. L., 1959, "The Stresses Around a Fault or Crack in Dissimilar Materials," *Bull. Seis. Soc. Am.*, Vol. 49, pp. 199–204.

Willis, J. R., 1971, "Fracture Mechanics of Interfacial Cracks," *Journal of Mechanics and Physics of Solids*, Vol. 19, pp. 353–368.

Three-Dimensional Stress Fields of Elastic Interface Cracks

T. Nakamura
Department of Mechanical Engineering,
State University of New York
at Stony Brook,
Stony Brook, NY 11794
Assoc. Mem. ASME

Various aspects of stress fields near an interface crack in three-dimensional bimaterial plates are investigated. Due to the nature of the resulting deformation field, three-dimensional effects are more critical in a bimaterial plate than in a homogeneous plate. In the close vicinity of the crack front, the stress field is characterized by the asymptotic bimaterial K*-field, and its domain size is a very small fraction of a plate thickness. Unlike a homogeneous case, the asymptotic field always consists all three modes of fracture, and an interface crack must propagate under mixed-mode conditions. Furthermore, computational results have shown that the two phase angles representing the relative magnitudes of the three modes strongly depend on the bimaterial properties. It has been also observed that a significant antiplane (Mode III) deformation exists along the crack front, especially near the free surface. Since experimental investigations have shown that critical energy release rate* $\mathcal{G}_c$ *is highly dependent on the phase angles, accurate prediction of the interface fracture behavior requires not only the* $\mathcal{G}$ *distribution but also the variations of phase angles along the crack front.*

1 Introduction

With the rapidly increasing use of composite materials for engineering structures, a great deal of interest in the interface crack has been generated. During the past few years, comprehensive analyses have been carried out, and many questions regarding the mechanics of interface fracture has been answered. However, progress has been generally restricted to understanding of the two-dimensional idealization of an interface crack, and limited work has been conducted on the three-dimensional aspect of interface fracture. This is in part due to the extreme complexity of such problems and the very large computational efforts required for their numerical analysis. However, given the material mismatch along the interface boundary, it is expected that the three-dimensional effects play a more significant role in a bimaterial structure than in a homogeneous structure.

In this study, detailed three-dimensional finite element computations are performed to investigate the complete stress field near the interface crack front. A large, finite thickness, bimaterial plate containing a finite length crack along the interface under remote tensile load is considered. The purposes of the analysis are to assess the zone of three-dimensionality and to determine characteristic features of the deformation field, including the variations of energy release rate and mixed-mode stress intensity factors along the crack front. Accurate determinations of these parameters are essential in predicting fracture behavior along the bimaterial crack front.

We also examine the field very close to the crack front to determine the existence and size of the asymptotic bimaterial *K*-field. In addition, the presence of bimaterial corner field near the intersection of the crack front and free surface is investigated. Near the free surface or in the corner field region where the three-dimensional effects are large, variations of stress intensity factors along the crack front are expected to be significant. The behavior of these fracture parameters are studied from a very detailed finite element model in conjunction with the bimaterial corner solutions.

2 Crack-Tip Field at Bimaterial Interfaces

2.1 Singular Stress Field. In an elastic bimaterial body containing a crack along the interface, the stress field very close to the crack front should correspond to the asymptotic field based on the two-dimensional (plane strain and antiplane) solutions (Williams, 1959). The form of the bimaterial *K*-field given by Rice, Suo, and Wang (1990) (with an addition of Mode III) is,

$$\sigma_{ij}=\frac{1}{\sqrt{2\pi r}}\{\mathrm{Re}[\mathbf{K}r^{i\epsilon}]\,\tilde{\sigma}^{\mathrm{I}}_{ij}(\theta;\epsilon)+\mathrm{Im}[\mathbf{K}r^{i\epsilon}]\,\tilde{\sigma}^{\mathrm{II}}_{ij}(\theta;\epsilon)+K_{\mathrm{III}}\,\tilde{\sigma}^{\mathrm{III}}_{ij}(\theta)\}, \quad (1)$$

where r and θ are the in-plane coordinates of the plane normal to the crack front, $\mathbf{K}$ is defined as the complex stress intensity factor for the in-plane modes, $K_{\mathrm{I}}+iK_{\mathrm{II}}$, and $\tilde{\sigma}_{ij}$ are the angular variations of stress components for each mode. The oscillatory index ϵ is

Contributed by the ASME Applied Mechanics Division of THE AMERICAN SOCIETY OF MECHANICAL ENGINEERS for publication in the JOURNAL OF APPLIED MECHANICS.

Discussion on this paper should be addressed to the Technical Editor, Leon M. Keer, The Technological Institute, Northwestern University, Evanston, IL 60208, and will be accepted until two months after final publication of the paper itself in the JOURNAL OF APPLIED MECHANICS. Manuscript received by the ASME Applied Mechanics Division, June 13, 1990; final revision, Nov. 6, 1990.

$$\epsilon=\frac{1}{2\pi}\ln\left[\frac{\kappa_1\mu_2+\mu_1}{\kappa_2\mu_1+\mu_2}\right]=\frac{1}{2\pi}\ln\left[\frac{1-\beta}{1+\beta}\right]. \quad (2)$$

Here, $\kappa_\alpha = 3 - 4\nu_\alpha$ for plane strain and $\kappa_\alpha = (3 - \nu_\alpha)/(1 + \nu_\alpha)$ for plane stress, μ_α is the shear modulus, ν_α is the Poisson ratio and the subscripts $\alpha = 1$ and 2 refer to the materials above and below the crack plane, respectively. Furthermore, β is one of Dundurs' parameters. In two-dimensional problems, the solutions can be characterized by the two Dundurs' parameters, and they are defined as (Dundurs, 1969),

$$\alpha=\frac{\mu_1(\kappa_2+1)-\mu_2(\kappa_1+1)}{\mu_2(\kappa_1+1)+\mu_1(\kappa_2+1)},\ \beta=\frac{\mu_1(\kappa_2-1)-\mu_2(\kappa_1-1)}{\mu_2(\kappa_1+1)+\mu_1(\kappa_2+1)}. \quad (3)$$

Unlike two-dimensional cases, the above parameters are not sufficient to characterize the full-field deformation of three-dimensional boundary value problems. However, for any bimaterial combinations of $\beta = 0$ (under plane strain), the oscillatory index ϵ vanishes, and the asymptotic stress field along the three-dimensional crack front coincides with the homogeneous material solution. Note, a bimaterial combination yields different Dundurs' parameters under plane-strain and plane-stress conditions.

2.2 Three-Dimensional Energy Release Rate. Based on energy release arguments, the relationship between the *energy release rate* $\mathcal{G}$ (or the equivalent J-integral in the case of an elastic medium) and the stress intensity factors of an interface crack is,

$$\mathcal{G}=\frac{1}{E^*\cosh^2(\pi\epsilon)}\left[K_{\mathrm{I}}^2+K_{\mathrm{II}}^2\right]+\frac{1}{2\mu^*}K_{\mathrm{III}}^2. \quad (4)$$

Here, E^* and μ^* are the average/effective plane-strain tensile modulus and shear modulus of two materials, respectively, and they are

$$\frac{1}{E^*}=\frac{1}{2}\left(\frac{1-\nu_1^2}{E_1}+\frac{1-\nu_2^2}{E_2}\right),\ \frac{1}{\mu^*}=\frac{1}{2}\left(\frac{1}{\mu_1}+\frac{1}{\mu_2}\right). \quad (5)$$

The local energy release rate $\mathcal{G}$ along the crack front advancing in the x_1-direction (i.e., along the interface boundary) can be expressed in terms of near-tip fields for three-dimensional bodies as,

$$\mathcal{G}^{\mathrm{local}}(s)=\lim_{\Gamma\to 0}\int_{\Gamma(s)}\left(Wn_1-\sigma_{ij}n_j\frac{\partial u_i}{\partial x_1}\right)d\Gamma. \quad (6)$$

Here, the superscript "local" emphasizes that $\mathcal{G}^{\mathrm{local}}$ is a *pointwise* energy release rate along a three-dimensional crack front. Also, s represents the location/arc length of the crack tip on the crack front measured from any reference point (e.g., corner point), W is the strain energy density and n_i are the components of a unit vector normal to Γ, which surrounds the crack front at s.

2.3 Three-Dimensional Interaction Integrals. For elastic interface cracks where the field is mixed mode, an effective method was introduced to extract each stress intensity factor by considering an auxiliary (pseudo) field that is the solution to a crack problem under some arbitrary loads (Shih and Asaro, 1988). Here their formulation is extended to the general three-dimensional case. We begin by superimposing an auxiliary field to the actual field (the three-dimensional interface crack boundary value problem) and introducing a local interaction energy release rate as

$$I(s)=\lim_{\Gamma\to 0}\int_{\Gamma(s)}\left[\sigma_{ij}\epsilon_{ij}^{\mathrm{aux}}n_1-\sigma_{ij}\frac{\partial u_i^{\mathrm{aux}}}{\partial x_1}n_j-\sigma_{ij}^{\mathrm{aux}}\frac{\partial u_i}{\partial x_1}n_j\right]d\Gamma. \quad (7)$$

The variables with the superscript "aux" are the solutions of the auxiliary field. The above integral is a conservation integral as long as the limit ($\Gamma \to 0$) is preserved. Additionally, $I(s)$ along the crack front relates to local K at a point s by

$$I(s)=\frac{2}{E^*\cosh^2(\pi\epsilon)}\left[K_{\mathrm{I}}K_{\mathrm{I}}^{\mathrm{aux}}+K_{\mathrm{II}}K_{\mathrm{II}}^{\mathrm{aux}}\right]+\frac{1}{\mu^*}K_{\mathrm{III}}K_{III}^{\mathrm{aux}}, \quad (8)$$

where $K_{\mathrm{I}}^{\mathrm{aux}}$, $K_{\mathrm{II}}^{\mathrm{aux}}$ and $K_{\mathrm{III}}^{\mathrm{aux}}$ are local stress intensity factors for the auxiliary field at a point s. To extract K_{I}, we choose the auxiliary field to be the known interface K-field shown in equation (1) and the values of its stress intensity factors be $K_{\mathrm{I}}^{\mathrm{aux}} = 1$, $K_{\mathrm{II}}^{\mathrm{aux}} = K_{\mathrm{III}}^{\mathrm{aux}} = 0$. Next, we calculate the interaction energy (7) from both the actual and the auxiliary field solutions. Finally, the Mode I component of stress intensity factor, K_{I}, at a point s on the crack front can be deduced from $I(s)$ through (8) as

$$K_{\mathrm{I}}(s)=\frac{E^*\cosh^2(\pi\epsilon)}{2}I(s). \quad (9)$$

This procedure can be repeated for extracting K_{II} and K_{III} by choosing the corresponding auxiliary fields to be the Mode II and III singular field solutions, respectively, and using (8) after each $I(s)$ is evaluated through (7). To obtain the complete variations of local K along the crack front, the calculation must be carried out over the entire crack front.

From a discrete computational point of view, the expressions (6) and (7) are not suitable for evaluating values of $\mathcal{G}^{\mathrm{local}}(s)$ and $I(s)$ since a precise numerical evaluation of limiting fields along the crack front is difficult. An accurate procedure based on the "domain integral method" exists for obtaining three-dimensional $\mathcal{G}$ and K. A detailed description of the domain integral method for the similar three-dimensional mixed-mode field is given by Nakamura and Parks (1989).

2.4 Phase Angles. The relative value of each stress intensity factor along the crack front plays an important role in the initiation and direction (e.g., kinking) of interface crack growth. It is convenient to define their relative magnitude in terms of nondimensional phase angles. The first phase angle has been defined and employed in earlier two-dimensional studies as

$$\psi(L)=\tan^{-1}\left\{\frac{\mathrm{Im}[\mathbf{K}L^{i\epsilon}]}{\mathrm{Re}[\mathbf{K}L^{i\epsilon}]}\right\}. \quad (10)$$

Here, L is the reference/characteristic length and $\mathbf{K}$ is the previously defined complex stress intensity factor for the in-plane models. For nonzero ϵ, this phase angle is a function of L. However, for a small ϵ, the phase angle essentially represents the relative strengths between K_{I} and K_{II}.

In three-dimensional situations, K_{III} is generally nonzero, and an additional phase angle is necessary to express the relative strength of antiplane deformation. The second phase angle may be introduced as

$$\phi=\cos^{-1}\left\{\frac{K_{\mathrm{III}}}{\sqrt{\frac{2\mu^*}{E^*\cosh^2(\pi\epsilon)}\left[K_{\mathrm{I}}^2+K_{\mathrm{II}}^2\right]+K_{\mathrm{III}}^2}}\right\}=\cos^{-1}\left\{\frac{K_{\mathrm{III}}}{\sqrt{2\mu^*\mathcal{G}}}\right\}. \quad (11)$$

The above form of the second phase angle is consistent with the relationship between $\mathcal{G}$ and stress intensity factors given in (4). Suppose we imagine a coordinate system formed by three othogonal axes: $\mathrm{Re}[\mathbf{K}L^{i\epsilon}]/\sqrt{E^*\cosh^2(\pi\epsilon)}$, $\mathrm{Im}[\mathbf{K}L^{i\epsilon}]/\sqrt{E^*\cosh^2(\pi\epsilon)}$ and $K_{\mathrm{III}}/\sqrt{2\mu^*}$. Then the length of a vector from the origin to a point in such a coordinate space equals $\sqrt{\mathcal{G}}$. Thus, ψ and ϕ are the standard spherical angles representing the directions of the vector in such a coordinate system. Unlike the first phase angle, the second phase angle ϕ is always *independent* of the characteristic length. This phase angle de-

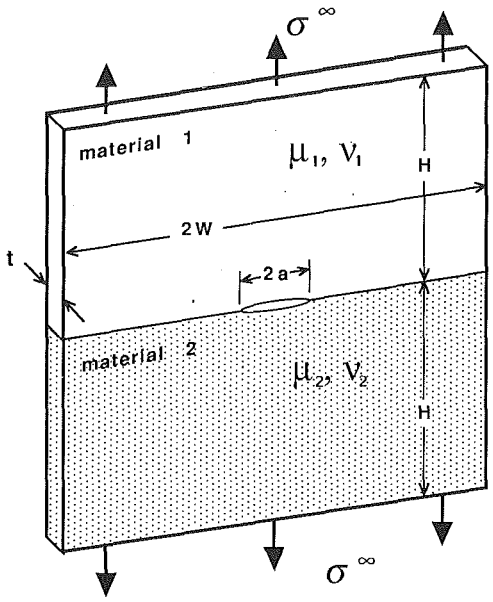

Fig. 1 Schematic of three-dimensional bimaterial plate with an interface crack along the boundary under tensile load

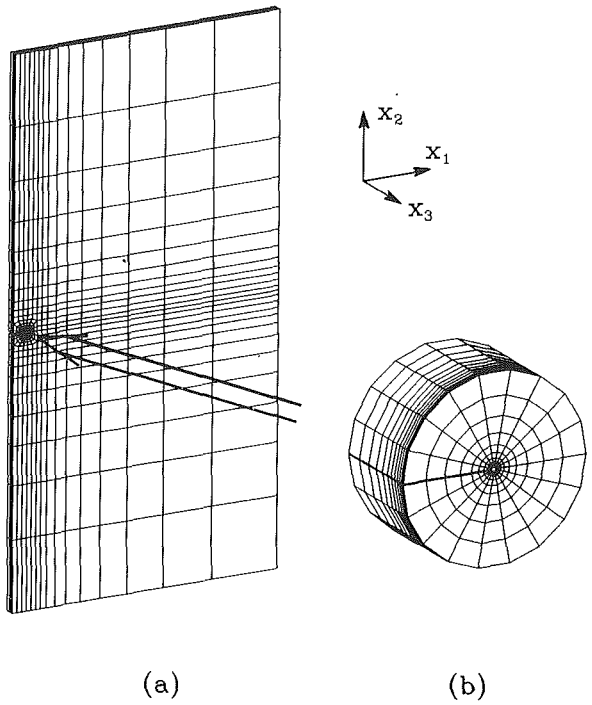

Fig. 2 Typical finite element meshes for (*a*) a quarter of bimaterial plate, (*b*) near crack front region. The front plane corresponds to the free surface.

creases for increasing relative magnitude of K_{III}. In a bimaterial combination of $\epsilon = 0$, the phase angles under pure Mode I, II, III conditions are $(\psi, \phi) = \left(0, \frac{\pi}{2}\right), \left(\frac{\pi}{2}, \frac{\pi}{2}\right), (*, 0)$, respectively. (Under pure Mode III, ψ is undefined.)

3 An Interface Crack in a Large Plate Under Tension

3.1 Computational Model. For the three-dimensional study, a large bimaterial plate (thickness t) containing a through crack on the interface is considered. This Griffith-type crack is assumed to be under remote tensile stress σ^∞ as shown in Fig. 1. In the model, the height and width of the plate are chosen to be 30 times the crack length ($W/a = 30$, $H/a = 30$). These dimensions are large enough so that the geometry represents essentially a finite length crack in an infinite (in-plane) plate. We have selected this geometry for the analysis since the only characteristic dimensions are the crack length and the thickness. The computations are performed for various plate thicknesses ranging from $t/a = 0.001$ to $t/a = 1.0$.

In order to minimize the complexity of the present three-dimensional bimaterial study, the Poisson's ratio of the upper half plate is kept at $\nu_1 = 0.2$. Moreover, the material properties of the lower half plate are selected so that the bimaterial combinations yield $\epsilon = 0$ (and $\beta = 0$) under plane-strain conditions (except for the elastic-rigid substrate plate). The three sets of material properties employed in the analysis are; (1) $\nu_2 = 0.2$, $\mu_1/\mu_2 = 1.0$ (homogeneous case), (2) $\nu_2 = 0.3$, $\mu_1/\mu_2 = 1.5$, and (3) $\nu_2 = 0.4$, $\mu_1/\mu_2 = 3.0$. With these combinations, the oscillatory behavior in the asymptotic stress and deformation fields disappear and the stress intensity factors in (1) are well defined. Here, the extent of bimaterial mismatch can be measured by the other Dundurs' parameter ($\alpha = 0, 0.1351, 0.3846$ for each case).

In constructing the finite element mesh, we have used the symmetry conditions across the center plane ($x_1 = 0$) and the midplane ($x_3 = 0$) to model a quarter of the plate. Zero displacement boundary conditions in the x_1-direction are prescribed on the right and left planes of the model and also in the x_3-direction on the $x_3 = 0$ plane. The finite element mesh of this geometry is constructed with 8-node trilinear hexahedron (brick) elements. In carrying out the analyses, two finite element meshes are employed for each bimaterial combination. The first mesh, shown in Fig. 2(*a*), models the entire plate while the finer second mesh is cylindrically shaped and models only the near crack front region. This finer mesh, shown in Fig. 2(*b*), is used to obtain more accurate solutions close to the crack front. In order to prescribe the boundry condition on the outer perimeter of the finer mesh, the computed displacements from the first mesh are interpolated to the boundary nodal points of the second mesh. The first (coarser) mesh has a total of 6048 elements (8 layers through half-thickness). The second (finer) mesh has 4860 elements (15 layers through half-thickness). The outer most nodes of the second mesh have a radial extent of 0.014 a, its crack-tip elements have a radial extent of 10^{-5} a, and the thickness of the element layer adjoining the free surface is 10^{-3} t.

3.2 Three-Dimensionality in a Bimaterial Plate. In a homogeneous plate with sufficiently small thickness (as compared to in-plane dimensions), a three-dimensional region exists only near the crack front. From various experimental and numerical investigations it has been determined that such a region extends to the radial distance of about a plate thickness from the crack tip. Due to the mismatch in the material moduli along the interface, the size of the three-dimensional region in a bimaterial plate is expected to be substantially different from the one in a homogeneous plate. Here the extent of three dimensionality is quantitatively determined from the difference between the stress fields in a three-dimensional plate and the corresponding plane-stress plate. For given in-plane coordinates (x_1, x_2), the average difference through thickness is calculated as

$$D^{\text{ave}}(x_1, x_2) = \frac{1}{\sigma^\infty t} \int_{-t/2}^{t/2} \| \sigma_{ij}(x_1, x_2, x_3) - \sigma_{ij}^{\text{pl.stress}}(x_1, x_2) \| dx_3, \quad (12)$$

where σ_{ij} are components of the three-dimensional stress field, $\sigma_{ij}^{\text{pl.stress}}$ are the plane-stress solutions of the same bimaterial crack plate subjected to remote tension, and $\| \cdot \|$ is a spectral matrix norm. This coordinate invariant parameter D^{ave} ap-

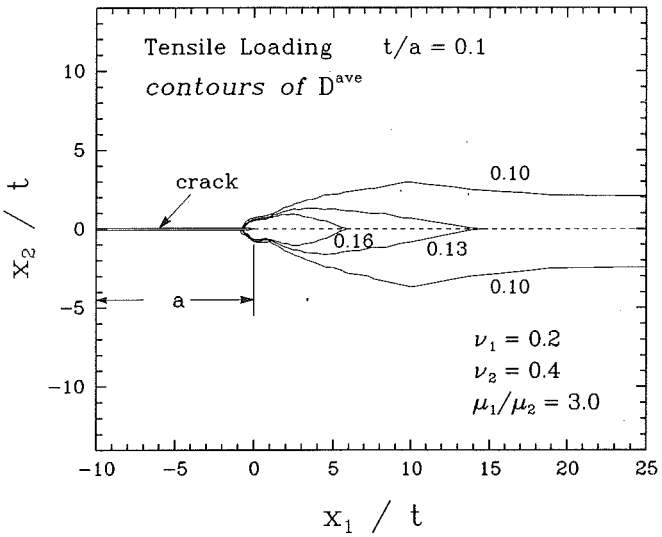

Fig. 3 Thee-dimensional regions in a bimaterial plate (t/a = 0.1) with ν_2 = 0.4, μ_1/μ_2 = 3.0 are indicated through the contours of D^{ave}

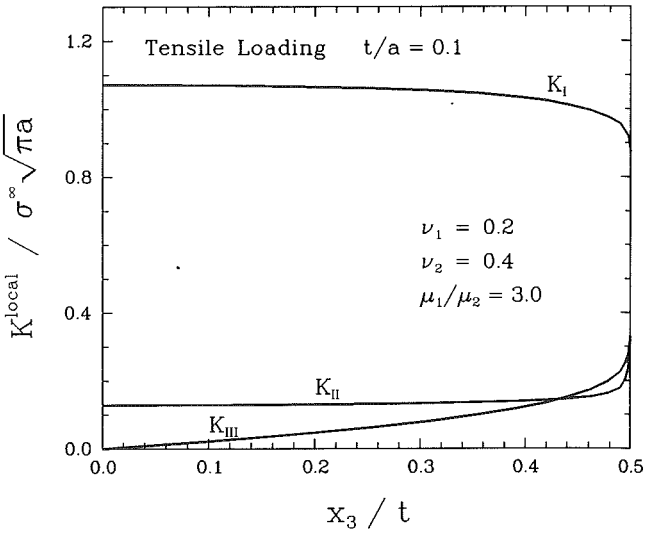

Fig. 5 Normalized local stress intensity factor components along the half-crack front in t/a = 0.1 plate with ν_2 = 0.4, μ_1/μ_2 = 3.0

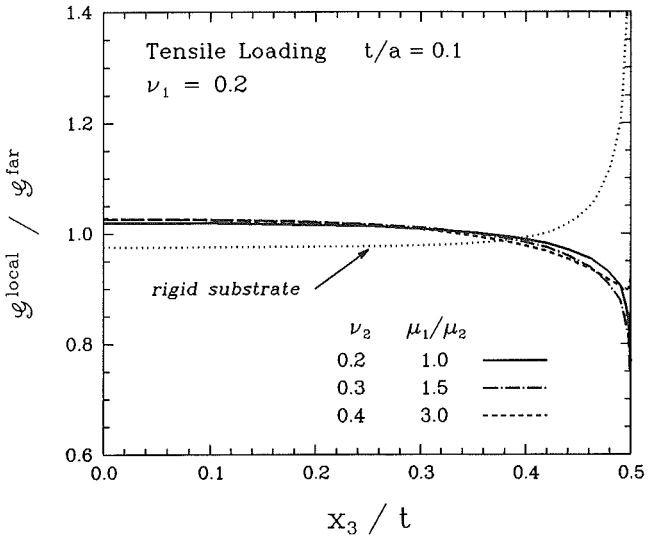

Fig. 4 Normalized local $\mathcal{G}$ along the half-crack front for t/a = 0.1 with various bimaterial combinations. (Note zero suppression of ordinate axis.)

proaches zero for closer agreement with the plane-stress solution, becoming zero if and only if σ_{ij} is *identical* to $\sigma_{ij}^{pl.stress}$ throughout the thickness.

This parameter is calculated over the x_1-x_2 plane of a relatively thin bimaterial plate with t/a = 0.1, and the contours of D^{ave} = 0.10, 0.13, 0.16 are plotted in Fig. 3. As in the case of a homogeneous material plate (now shown here), these results indicate a strong three-dimensional effect near the crack-tip (x_1 = 0, x_2 = 0) region. However, due to the modulus mismatch, the three-dimensional zone extends ahead of the crack and continues along the bimaterial boundary. The width of this zone is nearly constant ($\sim 4t$) for $x_1/t > 10$ (or $x_1/a > 1$) where the influence of the crack-tip field becomes negligible. In fact, this is the extent of three-dimensional zone along the interface boundary in a bimaterial plate without a crack.

3.3 Energy Release Rate and Stress Intensity Factors. The energy release rate along the crack front is obtained using the domain integral method. In Fig. 4, the local $\mathcal{G}$ along the crack front are shown for plates (t/a = 0.1) with various bimaterial properties. In the figure, the $\mathcal{G}^{local}$ are normalized by $\mathcal{G}^{far}$ which is the energy release rate of a *plane-stress* plate under tension, $\mathcal{G}^{far} = |\mathbf{K}|^2/[E^*\cosh^2(\pi\epsilon)]$ where $|\mathbf{K}| = \sigma^\infty\sqrt{(1+4\epsilon^2)\pi a}$. (Here, ϵ is from the plane-stress conversion in (2)). Since the plane-stress condition essentially exists far away from the crack front in the current model (as shown by Fig. 3), this value must be close to the average value for $\mathcal{G}$ along the entire crack front. Our computed average $\mathcal{G}$ over the entire crack front is within one percent of the plane-stress solution, $\mathcal{G}^{far}$.

The $\mathcal{G}^{local}$ variations through-thickness of all cases are nearly identical. The highest value is at the midplane (x_3/t = 0), and $\mathcal{G}^{local}$ continuously decreases away from the midplane except very near the free surface (x_3/t = 0.5). In the same figure, the distribution of $\mathcal{G}^{local}$ along the crack front of an elastic-rigid substrate model (ν_1 = 0.2) is also shown. The oscillatory index for this model is ϵ = 0.1255, and it is the worst possible mismatch in a bimaterial plate. Contrary to the other cases, $\mathcal{G}^{local}$ *increases* towards the free surface. This behavior is attributed to the much greater level of shearing condition affecting the crack-tip field. The results from the homogeneous plate (Nakamura and Parks, 1989) have shown that the behavior of $\mathcal{G}$ along the crack front is directly related to the amount of in-plane and antiplane shear in the crack front surrounding region. In a bimaterial plate, even in absence of any remote shear loading, the antisymmetrical conditions are induced by the material mismatch along the interface. The magnitude of shear increases with a larger mismatch, and when a sufficient bimaterial mismatch exists, a higher $\mathcal{G}^{local}$ prevails near the free surface as shown by the elastic-rigid substrate result.

Each mode of stress intensity factor is computed along the crack front via the interaction integral. Figure 5 shows K_I^{local}, K_{II}^{local}, and K_{III}^{local} along the crack front of the plate with ν_2 = 0.4, μ_1/μ_2 = 3.0. Each stress intensity factor is normalized by $\sigma^\infty\sqrt{\pi a}$, which is the amplitude of stress intensity factor under plane-strain condition. In a plane-strain plate under tensile loading, K_{II} and K_{III} are zero as long as ϵ = 0. However, in three-dimensional tensile plates, this condition (ϵ = 0) does not insure the symmetrical loading in the crack front region. In fact, the stress field near the crack front is mixed mode. Due to the relatively small bimaterial mismatch in this plate (α = 0.3846, β = 0), the tensile force is still dominant and values of K_{II} and K_{III} are relatively small along the crack front. Near the free surface, the amplitudes of both antisymmetrical modes increase while K_I decreases near the free surface (see the discussion on the corner field in Section 4.3).

In order to study the relative strength of each mode effec-

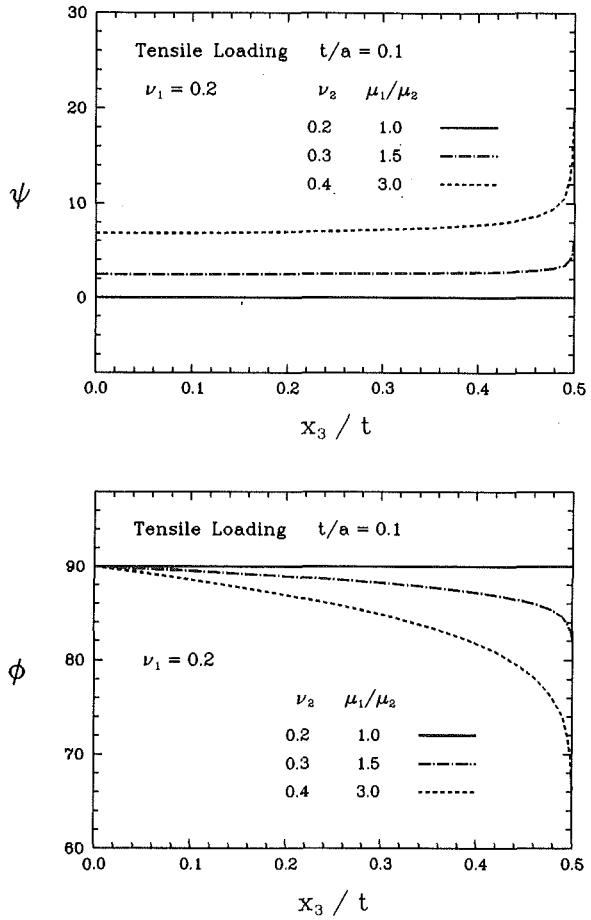

Fig. 6 Phase angles along the half-crack front in t/a = 0.1 plate with various bimaterial combinations, (*a*) first-phase angle ψ, (*b*) second-phase angle ϕ

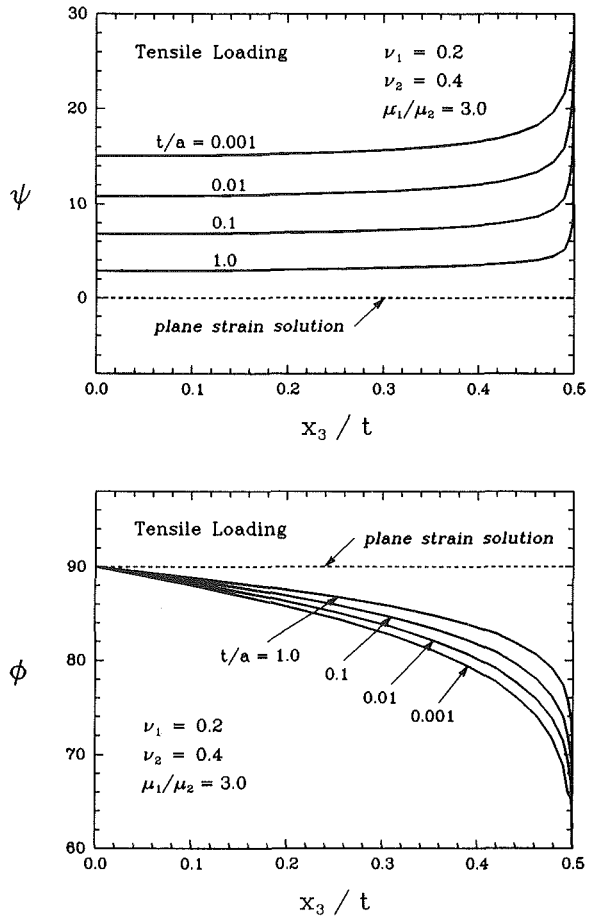

Fig. 7 Phase angles along the half-crack front in plates with various thickness with ν_2 = 0.4, μ_1/μ_2 = 3.0, (*a*) first-phase angle ψ, (*b*) second-phase angle ϕ. The corresponding plane strain results are also indicated.

tively, the two phase angles described in the Section 2.4 are plotted in Fig. 6. In the homogeneous plate (ν_2 = 0.2, μ_1/μ_2 = 1.0), the only nonzero stress intensity factor is K_I, and the phase angles are always ψ = 0 deg and ϕ = 90 deg along the crack front. In the two bimaterial plates, the first phase angle ψ remains nearly constant along the crack front except very near the free surface. The results imply that the ratio of K_I and K_{II} is essentially uniform throughout the crack front (see also Fig. 5). The second phase angle ϕ decreases from the midplane, reflecting the rising Mode III deformation near the free surface. These results clearly show a higher mixed-mode state near the free surface, and also larger in-plane and anti-plane shear deformation in a plate with greater material mismatch.

3.4 Effect of Thickness. The effect of thickness is shown by the variation of the phase angles along the crack front in Fig. 7. The results are given for the plate thickness, t/a = 1.0, 0.1, 0.01, 0.001, with the bimaterial properties ν_1 = 0.2, ν_2 = 0.4, μ_1/μ_2 = 3.0. In all cases, the relative strength of Mode II remains nearly constant along most of the crack front, as shown by ψ in Fig. 7(*a*). Similar results for ϕ in various plates are shown in Fig. 7(*b*). Both Mode II and Mode III deformations increase for the thinner plates.

Corresponding solutions from the plane-strain plate (limiting case of $t/a \to \infty$) are also shown in the figures. As the plate thickness increases, both ψ and ϕ approach the plane-strain limits (ψ = 0 deg, ϕ = 90 deg). Except near the free surface, there is a very small difference in ψ between the results for the t/a = 1.0 plate and the plane-strain limit. However, a significant difference remains between the same plate and the plane-strain solutions for ϕ. These results indicate that while the in-plane shear is small in a thick tensile plate, the antiplane shear is not negligible and may play an influential role in the fracture initiation.

3.5 Near Crack-Front Field. In order to use $\mathcal{G}$ and K as the fracture parameters in three-dimensional structures, one must substantiate the asymptotic bimaterial K-field along the crack front. A basic requirement for the existence of K-field is a sufficient plane-strain constraint near the tip. The amount of constraint can be measured by the parameter, $\sigma_{33}/(\sigma_{11} + \sigma_{22})$. Under plane-strain conditions, this parameter equals ν_1 and ν_2 above and below the crack plane, respectively. The angular variations of this parameter at various radial distances away from the crack front near the midplane are plotted in Fig. 8. The parameter indeed approaches the plane-strain limit as $r/t \to 0$, and the discontinuity jump at θ = 0 is accurately illustrated in the figure. At about r/t = 0.005, there is already a sufficient constraint in both upper and lower half of the plate.

The complete stress field very near the crack tip (r/t = 0.001) is plotted in Fig. 9. The components of computed stress are normalized by the $\sigma^\infty \sqrt{\pi a}/\sqrt{2\pi r}$ to obtained the dimensionless angular variations over $-\pi < \theta < \pi$. The solution from the K-field (1), $\tilde{\sigma}_{ij}^{I}$, $\tilde{\sigma}_{ij}^{II}$, $\tilde{\sigma}_{ij}^{III}$, are also shown with dashed lines. Since the field is a mixture of all modes, as shown in Fig. 5, these functions are weighted by respective local stress intensity factors ($K^{local}/\sigma^\infty \sqrt{\pi a}$ = 1.08, 0.13, 0.01, for Modes I, II, III, respectively at x_3/t = 0.05). The figure shows an excellent agreement between the computed stress components and the asymptotic solutions, and these results confirm the existence

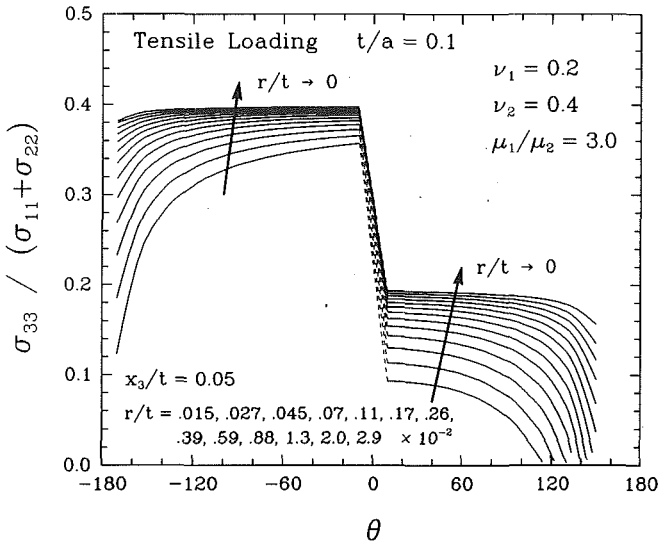

Fig. 8 Angular variations of constraint parameter on the plane x_3/t = .05 at various r/t in t/a = 0.1 plate with ν_2 = 0.4, μ_1/μ_2 = 3.0

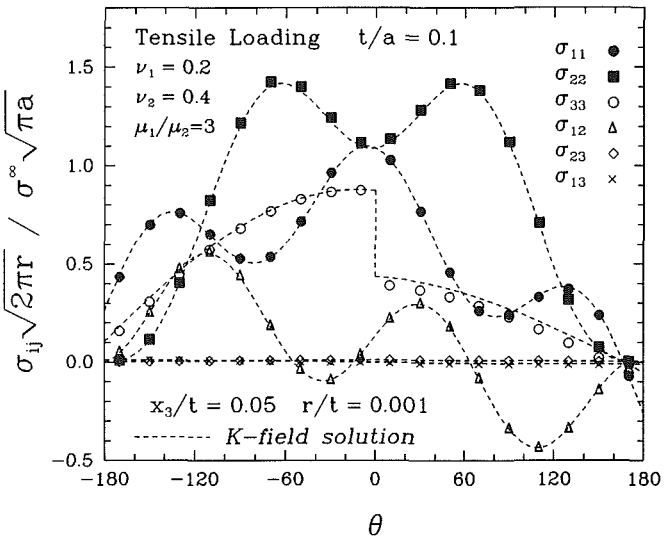

Fig. 9 Angular distributions of normalized stress components very near crack front on the plane x_3/t = .05 at r/t = 0.001 in t/a = 0.1 plate with ν_2 = 0.4, μ_1/μ_2 = 3.0. Appropriately weighted K-field solutions are shown with dashed lines for comparison.

of the K-field in three-dimensional bimaterial plates. We have also compared the near-tip stresses with the corresponding mixed-mode K-field solutions on a plane closer to the free surface at the same radial location. The agreement of each stress component is as good as that of the midplane results except for the σ_{33} component. The worsened result of σ_{33} is explained by a lesser constraint near the free surface.

The agreement with the K-field solution deteriorates as the radial distance from the crack front increases. Based on the results from individual stress components and the constraint parameter, we conclude that the K-field exists within the radius of about 0.5 percent of plate thickness near the midplane for a plate with $t/a \leq 1.0$.

4 A Thin Plate Under Mixed-Mode Loading

4.1 Computational Model. For the investigation of the stress field near the corner a different model is constructed. It has been established in Section 3.2 that if the plate thickness is sufficiently small, a nearly plane-stress field exists outside the crack-front region (except the narrow band of three-dimensional zone ahead of crack). By taking the thickness to be very small ($t/a \to 0$), one could assume an existence of annular region where the field is essentially characterized by the plane-stress K-field. An advantage for using such a thin plate model with a surrounding plane-stress K-field is that the characteristic dimension is reduced to the plate thickness alone.

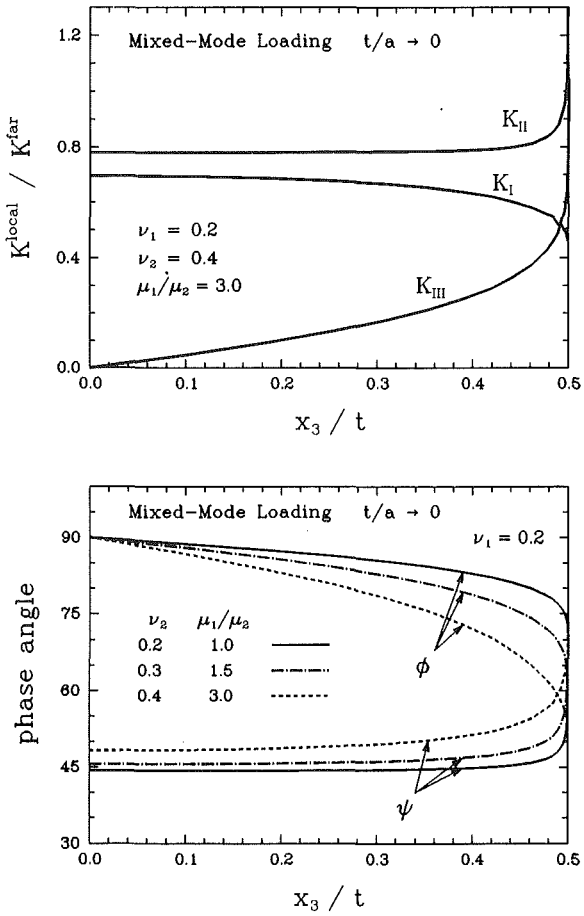

Fig. 10(*a*) Normalized local stress intensity factor components along the half-crack front in a very thin plate ($t/a \to 0$) with ν_2 = 0.4, μ_1/μ_2 = 3.0. (*b*) Phase angles along the half-crack front in a thin plate with various bimaterial combinations.

For the computational model, a mesh with similar shape and element arrangement as shown in Fig. 1(*b*) is constructed. The maximum radial extent of a disk-shaped mesh is chosen to be 100 times the thickness, which should be large enough to contain any three-dimensional effects along the interface to minimum. The external strip of boundary is subjected to the traction of *plane-stress* mixed-mode bimaterial K-field. A detailed description of a similar mesh is given in Nakamura and Parks (1991). The amplitudes of far-field stress intensity factors are chosen as $K_I^{far} = 1$ and $K_{II}^{far} = 1$. This combination is selected so that the resulting field along the crack front is strongly mixed mode, and any numerical errors which may arise from calculating smaller stress intensity factors are minimized. For the material properties, the same sets of Poisson's ratios and shear moduli as in the previous analysis are used.

4.2 Stress Intensity Factors. The stress intensity factors along the crack front are computed by the interaction integrals and normalized by the magnitude of applied load, $K^{far} = K_I^{far} + K_{II}^{far}$ and the results are shown in Fig. 10(*a*). The two in-plane stress intensity factors K_I^{local} and K_{II}^{local} are nearly identical along the crack front except near the free surface where K_I^{local} decreases while K_{II}^{local} increases. As in the previous model, the antiplane K_{III}^{local} rises from the symmetry plane ($x_3/t = 0$) toward the free surface.

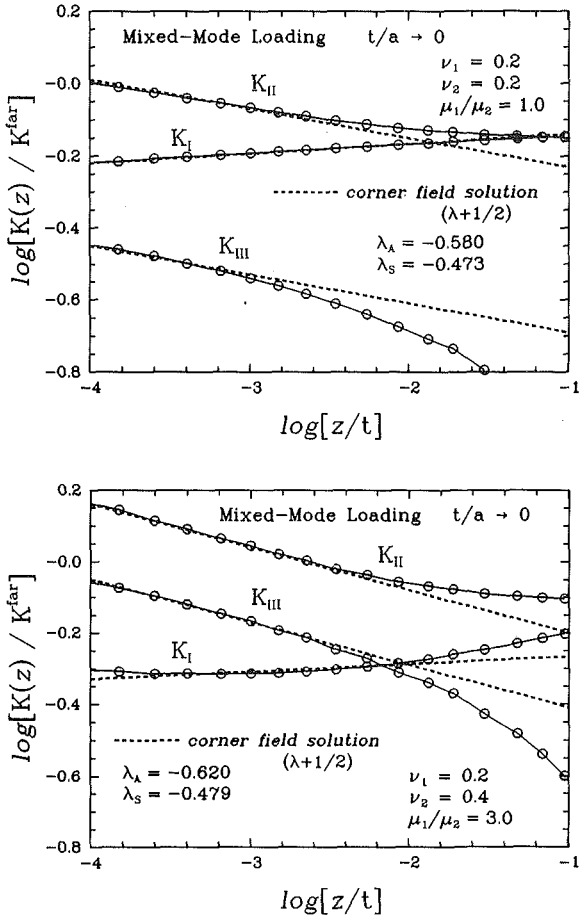

Fig. 11 Normalized stress intensity factors plotted against normalized distance from the intersection on a log-log scale. Small circles represent the midlocations of element layers along crack front. Also, slopes of straight lines correspond to the corner singularity field solutions; (*a*) homogeneous plate ($\nu = 0.2$), (*b*) bimaterial plate ($\nu_2 = 0.4$, $\mu_1/\mu_2 = 3.0$).

In Fig. 10(*b*), the phase angles of various bimaterial properties are plotted. The trends are similar for all cases: increasing antisymmetrical deformation near the free surface as shown by increasing ψ and decreasing ϕ. Again, the levels of shear deformation are greater in the plates with larger bimaterial mismatch.

4.3 Corner Singularity Field. At a point sufficiently close to the normal intersection of a crack front and a free surface, the asymptotic deformation field can be characterized by the corner singularity field of a quarter-infinite crack plane in a half space. Such a corner field has an interesting implication toward crack growth since the stress singularity on the free surface is *different* from the usual $1/\sqrt{r}$ singularity. The corner field in the homogeneous material has been extensively investigated by Benthem (1977, 1979) and Bazant and Estenssoro (1979). Recently, Barsoum and Chen (1989) and Ghahremani and Shih (1991) have computed eigenvalues corresponding to the singularities of corner fields in various interface cracks.

For many bimaterial combinations, the first two eigenvalues are real, and the stress near the intersection of a homogeneous solid may be expressed in terms of dominant *symmetrical* and *antisymmetrical* elastic corner singularities as shown in a homogeneous material (Nakamura and Parks, 1989),

$$\sigma_{ij}(\rho,\theta,\phi) = \frac{1}{\sqrt{2\pi}} [\mathfrak{B}_S \rho^{\lambda_S} g_{ij}^S(\theta,\phi;\lambda_S) + \mathfrak{B}_A \rho^{\lambda_A} g_{ij}^A(\theta,\phi;\lambda_A)]. \tag{13}$$

Here, $\mathfrak{B}_S$ and $\mathfrak{B}_A$ are the corner stress intensity factors, and g_{ij}^S and g_{ij}^A are angular functions corresponding to the dominant symmetrical and antisymmetrical fields, respectively. The spherical coordinates, ρ, θ, and ϕ, are centered at the corner, and in the present model they are

$$\rho = \sqrt{r^2+z^2},\ \phi = \tan^{-1}\left(\frac{r}{z}\right),\ z = \frac{t}{2} - x_3. \tag{14}$$

Also, λ_S is the eigenvalue for symmetrical fields, and λ_A is the eigenvalue for antisymmetrical fields. Typically, $\lambda_S > -0.5$ and $\lambda_A < -0.5$ for many bimaterial solids (Ghahremani and Shih, 1991). On the free surface we have $\rho = r$, and thus these values of λ suggest that the second term in (13) dominates as $r \to 0$ and the stress singularity is more severe than the usual $1/\sqrt{r}$ singularity.

The general relationship between the bimaterial K-field and the corner field is complex. However, for solids with $\epsilon = 0$, a relationship between the stress intensity factors and the corner stress intensity factors can be expressed as,

$$\begin{aligned} K_I^{\text{local}}(z) &= \mathfrak{B}_S z^{\lambda_S + 1/2} \\ K_{II}^{\text{local}}(z) &= \mathfrak{B}_A z^{\lambda_A + 1/2} \qquad \text{for } z \to 0. \\ K_{III}^{\text{local}}(z) &= R(\lambda_A)\mathfrak{B}_A z^{\lambda_A + 1/2} \end{aligned} \tag{15}$$

Here, $R(\lambda_A)$ is a dimensionless factor equivalent to the ratio of K_{III}^{local} to K_{II}^{local}, and it is a function of *only* λ_A and independent of loading conditions. Equations (15) suggest that the local stress intensity factor tends to zero in a symmetrical field (Mode I) and tends to infinity in an antisymmetrical field (Modes II, III) for small z. Furthermore, since the corner field is always mixed mode in a bimaterial plate, the energy release rate increases to infinity near the free surface.

In order to determine the dominance of such corner singularity fields in a finite thickness plate, all three modes of K^{local} are plotted in a log-log scale in Fig. 11. The small circles in the figure indicate K^{local} at the midlocations of element layers along the crack front. Also plotted in the figure are the straight lines whose slopes are $(\lambda_S + 1/2)$ for K_I, $(\lambda_A + 1/2)$ for K_{II} and K_{III}. The values of λ_S and λ_A indicated in the figures are given by Ghahremani and Shih (1991). The curves are nearly straight for $z/t < .003$, and the agreements with the corner field solutions are very good for both the homogeneous and bimaterial plates shown in Fig. 11. Similar results are also obtained with $\nu_2 = 0.3$, $\mu_1/\mu_2 = 1.5$. Based on the behaviors of K^{local} near a corner as shown in Fig. 11, we tentatively conclude that the corner singularity field in a thin plate dominates within the spherical radius of $\rho/t \simeq .003$ from the intersection in a thin bimaterial plate.

5 Discussions

The present analysis has shown that three-dimensional effects are more complex in a bimaterial plate than in a homogeneous plate with similar dimensions. It has been observed that a large Mode III deformation exists along the crack front, even in a relatively thick plate. Furthermore, the bimaterial properties are found to play an important role in the state of mixed mode. In view of determining fracture behavior, these effects are very critical since they influence not only the variations of energy release rate but also all three stress intensity factors along the crack front.

The manner which $\mathcal{G}$ varies along the crack front is directly dependent on the relative magnitude of shear in the near crack-front region. The rise of $\mathcal{G}$ near the free surface occurs when there are sufficient shear loads. This phenomena is consistent with the $\mathcal{G}$ variation observed in a homogeneous plate under a remote shear loading (Nakamura and Parks, 1989). In a bimaterial tensile plate, the shearing condition near the crack front is caused by the material mismatch, and as a consequence,

the behavior of $\mathcal{G}$ along the crack front is affected. The extent of shearing increases with greater material mismatch in a plate, and the most severe case occurs in an elastic-rigid substrate plate. Certainly, any remotely applied antisymmetrical loadings enhance the shear deformation near the crack front, and hence promote the increase of $\mathcal{G}$ near the free surface.

Recently, Cao and Evans (1989) showed experimentally that the critical energy release rate $\mathcal{G}_c$ of a propagating interface crack depends on the phase angle ψ, and that $\mathcal{G}_c$ increases for larger ψ. The increase of $\mathcal{G}_c$ is explained by the shielding of the crack tip from the large stress by rubbing/contact of crack surfaces under a large in-plane shear deformation (high ψ). A similar mechanism is expected to operate under antiplane shear, and the critical energy release rate should increase when the relative magnitude of K_{III} is high (small ϕ). Thus, the critical energy release is a function of both ψ and ϕ as

$$\mathcal{G}_c = \mathcal{G}_c(\psi, \phi). \tag{16}$$

Based on the above argument, to predict the location of a crack growth initiation with an available $\mathcal{G}_c$ (ψ, ϕ), one must know the $\mathcal{G}$ variation (e.g., Fig. 4) as well as the complete phase angle distributions (e.g., Fig. 6). In the near free-surface region, the driving force $\mathcal{G}$ is generally high due to the mixed-mode corner field. At the same time, there are greater shear deformation (high ψ, low ϕ) in the region, which may lead to more fracture resistance condition. These two effects compete during the initiation, and they must be considered carefully when one tries to estimate the steady state angle made by the propagating crack front and the free surface.

Acknowledgments

We appreciate Dr. Ghahremani for providing us with the corner singularities of various bimaterial combinations reported here. The computations were performed on VAX station 3500 in State University of New York at Stony Brook. The finite element analysis was carried out with the ABAQUS code which was made available under academic license from Hibbit, Karlsson, and Sorensen, Inc., Providence, R.I.

References

Barsoum, R. S., and Chen, T. K., 1989, "Three Dimensional Surface Singularity of an Interface Crack," presented at the ASME Summer Meeting at San Diego.

Bazant, Z. P., and Estenssoro, L. F., 1979, "Surface Singularity and Crack Propagation," *International Journal of Solids and Structures*, Vol. 15, pp. 405–426.

Benthem, J. P., 1977, "State of Stress at the Vertex of a Quarter-Infinite Crack in a Half-Space," *International Journal of Solids and Structures*, Vol. 13, pp. 479–492.

Benthem, J. P., 1980, "The Quarter-Infinite Crack in a Half Space; Alternative and Additional Solutions," *International Journal of Solids and Structures*, Vol. 16, pp. 119–130.

Cao, H. C., and Evans, A. G., 1989, "An Experimental Study of the Fracture Resistance of Bimaterial Interfaces," *Mechanics of Materials*, Vol. 7, pp. 295–301.

Dundurs, J., 1969, "Edge-Bonded Dissimilar Orthogonal Elastic Wedges Under Normal and Shear Loading," ASME JOURNAL OF APPLIED MECHANICS, Vol. 36, pp. 650–652.

Ghahremani, F., and Shih, C. F., 1991, "Corner Singularities of Three-Dimensional Planar Interface Cracks," to appear on ASME JOURNAL OF APPLIED MECHANICS.

Nakamura, T., and Parks, D. M., 1989, "Anti-Symmetrical 3D Stress Field Near the Crack Front of a Thin Elastic Plate," *International Journal of Solids and Structures*, Vol. 25, pp. 1411–1426.

Nakamura, T., and Parks, D. M., 1991, "Three-Dimensional Crack Front Field in a Thin Ductile Plate," to appear on *Journal of the Mechanics and Physics of Solids*, Vol. 58, pp. 787–812.

Rice, J. R., Suo, Z., and Wang, J. S., 1990, "Mechanics and Thermodynamics of Brittle Interfacial Failure in Bimaterial Systems," *Metal-Ceramics Interfaces*, M. Ruhle, et al., eds., Pergamon Press, pp. 269–294.

Shih, C. F., and Asaro, R. J., 1988, "Elastic-Plastic Analysis of Cracks on Bimaterial Interfaces; Part I: Small Scale Yielding," ASME JOURNAL OF APPLIED MECHANICS, Vol. 55, pp. 299–316.

Williams, M. L., 1959, "The Stress Around a Fault or Crack in Dissimilar Media," *Bulletin of the Seismological Society of America*, Vol. 49, pp. 199–204.

Nonaxisymmetric Annular Punch Problem

V. I. Fabrikant
Department of Mechanical Engineering,
Concordia University,
Montreal, Quebec H3G 1M8, Canada

A general formulation is given for the first time to the title problem. The method is based on the new results in potential theory obtained by the author earlier. The problem is reduced to a two-dimensional integral equation with an elementary kernel. Several specific examples are considered.

Introduction

It is impossible even to mention all the publications related to the Dirichlet problem for a flat circular annulus, a particular case of which is the annular punch problem. Their number is awesome. One can find many references related to a contact problem in Barber (1983). Other references related to the equivalent electrostatic problem can be found in Love (1976). Why is there any need for yet another paper on the subject? The main reason is that the majority of publications is devoted to the simplest, flat, centrally loaded, annular punch problem. A very small number of publications treat nonflat but still axisymmetric problems (Barber, 1976, 1983). An important problem of circular sliding contact was considered by Keer and Mowry (1979). The zone of contact was split in two: circular and annular, with a complete adhesion applied at the first one and Coulomb friction law at the other. Two interesting problems involving annular crack, externally cracked body and a penny-shaped crack were considered by Selvadurai (1985, 1987). The case of an elastic plate on a half-space was solved by Rajapakse (1988). Some more complicated dynamical problems were considered by Veletsos (1987, 1988).

Though some results related to consideration of specific harmonics have been published (Williams, 1963; Cooke, 1963), no general solution to the problem has been attempted as yet. This kind of solution is now possible due to the new results in potential theory obtained by the author (Fabrikant, 1989). The problem is reduced to a two-dimensional Fredholm integral equation with an elementary kernel which can be solved numerically. Flat inclined and centrally loaded annular punches are considered as examples. Asymptotic formulae are derived for the case of a very narrow annulus.

Theory

Consider a rigid annular punch $b \le \rho \le a$ penetrating a transversely isotropic elastic half-space $z > 0$. Neglecting the shear stress under the punch base, the boundary conditions for the problem can be formulated as follows:

$$w(\rho,\phi)=\delta-s(\rho,\phi), \text{ for } b<\rho<a,\ 0\le\phi<2\pi;$$
$$\sigma_z=0, \text{ for } \rho<b \text{ or } \rho>a,\ 0\le\phi<2\pi;$$
$$\tau_{yz}=\tau_{zx}=0, \text{ for } 0\le\rho<\infty,\ 0\le\phi<2\pi. \quad (1)$$

Here, δ is the maximum punch penetration and s describes the shape of the punch base. It is well known (Fabrikant, 1989) that the problem can be reduced to the governing integral equation

$$H\int_0^{2\pi}\int_b^a \frac{\sigma(\rho_0,\phi_0)\rho_0 d\rho_0 d\phi_0}{\sqrt{\rho^2+\rho_0^2-2\rho\rho_0\cos(\phi-\phi_0)}}=w(\rho,\phi). \quad (2)$$

Here, H is the elastic constant (see Fabrikant, 1989), w is the known function (1), and $\sigma = -\sigma_z$ is the yet unknown function. The following integral representation for the reciprocal of the distance between two points can be found in (Fabrikant, 1989)

$$\frac{1}{R}=\frac{1}{\sqrt{\rho^2+\rho_0^2-2\rho\rho_0\cos(\phi-\phi_0)}}$$
$$=\frac{2}{\pi}\int_0^{\min(\rho_0,\rho)}\frac{\lambda\left(\dfrac{x^2}{\rho\rho_0},\ \phi-\phi_0\right)dx}{\sqrt{\rho^2-x^2}\sqrt{\rho_0^2-x^2}}. \quad (3)$$

Here,

$$\lambda(k,\psi)=\frac{1-k^2}{1-2k\cos\psi+k^2}. \quad (4)$$

Substitution of (3) in (2) leads to the governing integral equation

$$4\int_b^\rho \frac{dx}{\sqrt{\rho^2-x^2}}\int_x^a \frac{\rho_0 d\rho_0}{\sqrt{\rho_0^2-x^2}}\,\mathfrak{L}\left(\frac{x^2}{\rho\rho_0}\right)\sigma(\rho_0,\phi)$$
$$+4\int_0^b \frac{dx}{\sqrt{\rho^2-x^2}}\int_b^a \frac{\rho_0 d\rho_0}{\sqrt{\rho_0^2-x^2}}\,\mathfrak{L}\left(\frac{x^2}{\rho\rho_0}\right)\sigma(\rho_0,\phi)=\frac{w(\rho,\phi)}{H}. \quad (5)$$

In Fabrikant (1989) the $\mathfrak{L}$-operator was introduced as follows:

Contributed by the ASME Applied Mechanics Division of The American Society of Mechanical Engineers for presentation at the Winter Annual Meeting, Atlanta, Ga., Dec. 1–6, 1991.

Discussion on this paper should be addressed to the Technical Editor, Prof. Leon M. Keer, The Technological Institute, Northwestern University, Evanston, IL 60208, and will be accepted until two months after final publication of the paper itself in the Journal of Applied Mechanics. Manuscript received by the ASME Applied Mechanics Division, Aug. 1, 1990; final revision, Mar. 4, 1991.
Paper No. 91-WA/APM-10.

$$\mathfrak{L}(k)f(\rho,\phi)=\frac{1}{2\pi}\int_0^{2\pi}\lambda(k,\phi-\phi_0)f(\rho,\phi_0)d\phi_0$$
$$=\frac{1}{2\pi}\sum_{n=-\infty}^{\infty}k^{|n|}e^{in\phi}\int_0^{2\pi}e^{-in\phi_0}f(\rho,\phi_0)d\phi_0$$
$$=\sum_{n=-\infty}^{\infty}k^{|n|}f_n(\rho)e^{in\phi}. \quad (6)$$

Here, f_n is the nth Fourier coefficient of the function f. Application of the operator

$$\mathfrak{L}\left(\frac{1}{r}\right)\frac{d}{dr}\int_b^r\frac{\rho d\rho}{\sqrt{r^2-\rho^2}}\mathfrak{L}(\rho)$$

to both sides of (5) yields

$$2\pi\int_r^a\frac{\rho_0 d\rho_0}{\sqrt{\rho_0^2-r^2}}\mathfrak{L}\left(\frac{r}{\rho_0}\right)\sigma(\rho_0,\phi)$$
$$+\frac{4r}{\sqrt{r^2-b^2}}\int_0^b\frac{\sqrt{b^2-x^2}dx}{r^2-x^2}\int_b^a\frac{\rho_0 d\rho_0}{\sqrt{\rho_0^2-x^2}}\mathfrak{L}\left(\frac{x^2}{r\rho_0}\right)\sigma(\rho_0,\phi)$$
$$=\frac{1}{H}\mathfrak{L}\left(\frac{1}{r}\right)\frac{d}{dr}\int_b^r\frac{\rho d\rho}{\sqrt{r^2-\rho^2}}\mathfrak{L}(\rho)w(\rho,\phi). \quad (7)$$

We introduce a new unknown function

$$\chi(r,\phi)=\int_r^a\frac{\rho_0 d\rho_0}{\sqrt{\rho_0^2-r^2}}\mathfrak{L}\left(\frac{r}{\rho_0}\right)\sigma(\rho_0,\phi). \quad (8)$$

The inverse of (8) is readily available, and is

$$\sigma(\rho,\phi)=-\frac{2}{\pi}\frac{\mathfrak{L}(\rho)}{\rho}\frac{d}{d\rho}\int_\rho^a\frac{rdr}{\sqrt{r^2-\rho^2}}\mathfrak{L}\left(\frac{1}{r}\right)\chi(r,\phi). \quad (9)$$

Substitution of (8) in (7) gives

$$2\pi\chi(r,\phi)+\frac{8}{\pi}\frac{r}{\sqrt{r^2-b^2}}\int_0^b\frac{b^2-x^2}{r^2-x^2}dx$$
$$\times\int_b^a\frac{ydy}{\sqrt{y^2-b^2}(y^2-x^2)}\mathfrak{L}\left(\frac{x^2}{yr}\right)\chi(y,\phi)$$
$$=\frac{1}{H}\mathfrak{L}\left(\frac{1}{r}\right)\frac{d}{dr}\int_b^r\frac{\rho d\rho}{\sqrt{r^2-\rho^2}}\mathfrak{L}(\rho)w(\rho,\phi). \quad (10)$$

One can interchange the order of integration in the second term of (10) and perform the integration with respect to x. The result is

$$\chi(r,\phi)+\frac{1}{\pi^3}\int_0^{2\pi}\int_b^a\frac{K(y,r,\phi-\phi_0)-K(r,y,\phi-\phi_0)}{y^2-r^2}\chi(y,\phi_0)dyd\phi_0$$
$$=\frac{1}{2\pi H}\mathfrak{L}\left(\frac{1}{r}\right)\frac{d}{dr}\int_b^r\frac{\rho d\rho}{\sqrt{r^2-\rho^2}}\mathfrak{L}(\rho)w(\rho,\phi). \quad (11)$$

The kernel of (11) can be expressed in terms of elementary functions as follows:

$$K(y,r,\phi-\phi_0)=ry\left(\frac{r^2-b^2}{y^2-b^2}\right)^{1/2}\left\{-\lambda\left(\frac{r}{y},\phi-\phi_0\right)\frac{1}{r}\ln\left(\frac{r+b}{r-b}\right)\right.$$
$$\left.+2\Re\left[\frac{1}{\xi\left(1-\frac{r}{y}e^{-i(\phi-\phi_0)}\right)}\ln\frac{\xi+b}{\xi-b}\right]\right\}, \quad (12)$$

where

$$\xi=\sqrt{yre^{i(\phi-\phi_0)}}. \quad (13)$$

Here, $\Re$ denotes the real part of the expression to follow. Thus, the general problem of annular punch has been reduced to a Fredholm integral Eq. (11) with an elementary kernel which can be solved numerically. It is noteworthy that the governing equation for each specific harmonic will also have an elementary kernel. For example, the equation corresponding to the zero harmonic is

$$\chi_0(r)+\frac{2}{\pi^2}\int_b^a\frac{K_0(y,r)-K_0(r,y)}{y^2-r^2}\chi_0(y)dy$$
$$=\frac{1}{2\pi H}\frac{d}{dr}\int_b^r\frac{w_0(\rho)\rho d\rho}{\sqrt{r^2-\rho^2}}, \quad (14)$$

with

$$K_0(y,r)=r\left(\frac{y^2-b^2}{r^2-b^2}\right)^{1/2}\ln\frac{y+b}{y-b}. \quad (15)$$

There have been so many variations of the governing integral equation published for the case of axial symmetry, that there is no doubt that Eq. (14) coincides with some known result, though we have difficulty to pinpoint exactly which one. The governing integral equation for the first harmonic will take the form

$$\chi_1(r)+\frac{2}{\pi^2}\int_b^a\frac{K_1(y,r)-K_1(r,y)}{y^2-r^2}\chi_1(y)dy$$
$$=\frac{1}{2\pi H}\frac{1}{r}\frac{d}{dr}\int_b^r\frac{w_1(\rho)\rho^2 d\rho}{\sqrt{r^2-\rho^2}}, \quad (16)$$

with

$$K_1(y,r)=\left(\frac{y^2-b^2}{r^2-b^2}\right)^{1/2}\left[y\ln\frac{y+b}{y-b}-2b\right]. \quad (17)$$

There is no need to compute the stress distribution σ if one is interested in the integral characteristics only. Indeed, both the resultant force P and the tilting moment M can be expressed through the new unknown function χ as follows:

$$P=\frac{2}{\pi}\int_0^{2\pi}\int_b^a\frac{\chi(\rho,\phi)\rho d\rho d\phi}{\sqrt{\rho^2-b^2}}=4\int_b^a\frac{\chi_0(\rho)\rho d\rho}{\sqrt{\rho^2-b^2}}, \quad (18)$$

$$M=-\frac{2}{\pi}\int_0^{2\pi}\int_b^a\frac{(2\rho^2-b^2)\chi(\rho,\phi)\cos\phi d\rho d\phi}{\sqrt{\rho^2-b^2}}$$
$$=-2\int_b^a\frac{(2\rho^2-b^2)\chi_1(\rho)d\rho}{\sqrt{\rho^2-b^2}}. \quad (19)$$

We note also that the kernels in (14) and (16) are finite at the point $y = r$. The following limits can be computed

$$\lim_{y\to r}\frac{K_0(y,r)-K_0(r,y)}{y^2-r^2}=\frac{1}{r^2-b^2}\left[\frac{r^2+b^2}{2r}\ln\frac{r+b}{r-b}-b\right],$$
$$\lim_{y\to r}\frac{K_1(y,r)-K_1(r,y)}{y^2-r^2}=\frac{1}{r^2-b^2}\left[\frac{3r^2-b^2}{2r}\ln\frac{r+b}{r-b}-3b\right]. \quad (20)$$

Equations (11), (12), (18), and (19) are the main new results of this article.

Description of the Numerical Procedure

Consider the following integral equation:

$$h(r)f(r)+\int_b^a\mathcal{K}(r,x)f(x)dx=g(r). \quad (21)$$

Here, h and g are known functions, $\mathcal{K}$ is the kernel, and f is the as yet unknown function. The procedure which is usually used may be described as follows. We divide the interval $[b, a]$ into $n - 1$ equal subintervals of length $\Delta = (a - b)/(n$

-1). The points of division are called x_k, $k = 1, 2, \ldots, n$. Assume the unknown function f to be piecewise *constant* on each of the subintervals and equal to f_k on the subinterval number k. Introduce a set of points $r_k = (x_k + x_{k+1})/2$, for $k = 1, 2, \ldots, n-1$. These assumptions allow us to reduce the integral Eq. (21) to a set of $n-1$ linear algebraic equations

$$h(r_k)f(r_k) + \sum_{i=1}^{n-1} \kappa_i(r_k)f_i = g(r_k),$$

$$\text{for } k = 1, 2, \ldots, n-1. \quad (22)$$

Here,

$$\kappa_i(r_k) = \int_{x_i}^{x_{i+1}} \mathcal{K}(r_k, x)\,dx. \quad (23)$$

The second method to be used here is somewhat different from that above. We consider the unknown function f to be piecewise *linear*. Assuming $f_k = f(x_k)$, for $k = 1, 2, \ldots, n$, this implies that at the kth subinterval the function f can be expressed as follows:

$$f(x) = f_k + (f_{k+1} - f_k)\left(\frac{x-b}{\Delta} - k\right), \text{ for } x_k < x < x_{k+1}. \quad (24)$$

Substitution of (24) in (21) leads to a set of n linear algebraic equations

$$h(r_l)f_l + f_1\left[\kappa_1(r_l) - \frac{\theta_1(r_l)}{\Delta}\right] + \sum_{i=2}^{n-1} f_i\left[ik_i(r_l) - (i-2)\kappa_{i-1}(r_l) - \frac{\theta_i(r_l) - \theta_{i-1}(r_l)}{\Delta}\right] + f_n\left[\frac{\theta_{n-1}(r_l)}{\Delta} - (n-2)\kappa_{n-1}(r_l)\right] = g(r_l),\ r_l = x_l, \text{ for } l = 1, 2, \ldots, n. \quad (25)$$

Here,

$$\theta_i(r_l) = \int_{x_i}^{x_{i+1}} \mathcal{K}(r_l, x)\,(x-b)\,dx. \quad (26)$$

Since the piecewise linear function follows the real function more close than the piecewise constant one, we should expect the set of Eqs. (25) to give a more accurate solution than (22).

Examples

Flat, Centrally Loaded, Annular Punch. In this case $w_0 =$ const., and the governing integral Eq. (14) will take the form

$$\chi_0(r) + \frac{2}{\pi^2}\int_b^a \frac{K_0(y,r) - K_0(r,y)}{y^2 - r^2}\chi_0(y)\,dy = \frac{w_0}{2\pi H}\frac{r}{\sqrt{r^2 - b^2}}. \quad (27)$$

It is well known that the stress distribution σ has square root singularities at $\rho = a$ and at $\rho = b$. We can then conclude from (8) that function χ_0 will have a logarithmic singularity at the point $\rho = b$. In order to obtain an effective numerical solution of (27) we have to eliminate singularities whenever possible. We introduce a new unknown function

$$f(r) = \frac{\chi_0(r)}{\ln\dfrac{r+b}{r-b}}, \quad (28)$$

which will have no singularities and will be limited on the $[b, a]$. Substitution of (28) in (27) allows us to rewrite it as follows:

$$\frac{\sqrt{r^2-b^2}}{r}\ln\frac{r+b}{r-b}f(r) + \frac{2}{\pi^2}\frac{\sqrt{r^2-b^2}}{r} \times \int_b^a \frac{K_0(y,r) - K_0(r,y)}{y^2 - r^2} f(y)\ln\left(\frac{y+b}{y-b}\right)dy = \frac{w_0}{2\pi H}. \quad (29)$$

Note that in the limiting case of $r \to b$ Eq. (29) yields

$$\int_b^a \ln^2\left(\frac{y+b}{y-b}\right)\frac{f(y)\,dy}{\sqrt{y^2-b^2}} = \frac{\pi w_0}{4H}. \quad (30)$$

The problem was solved numerically by using both methods from the previous section. The value of the total force P was computed in the first method according to the formula (18) as follows:

$$P = 4\sum_{i=1}^{n-1} f_i \int_{x_i}^{x_{i+1}} \ln\left(\frac{\rho+b}{\rho-b}\right)\frac{\rho\,d\rho}{\sqrt{\rho^2-b^2}}. \quad (31)$$

The resultant force in the case of the second numerical method was computed as

$$P = 4\sum_{i=1}^{n-1}\left\{\left[\left(i + \frac{b}{\Delta}\right)f_i - \left(i + \frac{b}{\Delta} - 1\right)f_{i+1}\right]\int_{x_i}^{x_{i+1}} \ln\left(\frac{\rho+b}{\rho-b}\right)\frac{\rho\,d\rho}{\sqrt{\rho^2-b^2}} + \frac{f_{i+1} - f_i}{\Delta}\int_{x_i}^{x_{i+1}} \ln\left(\frac{\rho+b}{\rho-b}\right)\frac{\rho^2\,d\rho}{\sqrt{\rho^2-b^2}}\right\}. \quad (32)$$

The integrals in (31) and (32) can be computed exactly in terms of elementary functions or it can be computed numerically.

Numerical computations were performed according to both methods for different values of n and various ratios b/a. The dimensionless quantity $f^* = Hf/w_0$ is plotted on Fig. 1 against the dimensionless argument $\rho^* = (\rho - b)/\Delta + 1$. The argument of each plot was scaled in such a way that it stretch over the same interval. The pattern of each curve consists of three long dashes and a certain number of dots which corresponds to a specific ratio b/a defined by Table 1. For example, five dots in the pattern correspond to the fifth line in Table 1, with $b/a = 0.9$. The dimensionless resultant force $P^* = P/P_0$ is presented in the Table 1. The quantity $P_0 = 2w_0a/(\pi H)$ corresponds to the resultant force producing normal displacement w_0 when applied to a circular punch of radius a (see Fabrikant, 1989, p. 342). The column denoted as exact was computed independently according to the formula derived in (Love, 1976). This formula in our notation reads

$$P^* = 1 - \sum_{n=1}^{\infty} k\int_0^k \left\{\int_0^k K_L^n(u,t)\,\frac{dt}{t}\right\}^2 du. \quad (33)$$

Here, $k = \sqrt{b/a}$, and K_L^n is the nth iteration of the kernel

$$K_L(u,t) = \frac{2}{\pi}\frac{ut}{1-u^2t^2}. \quad (34)$$

Let us point out some interesting features of the numerical results in Table 1. First of all, two different methods lead to different results, but the discrepancy between them decreases as n increases, and in such a way that their average changes very little being very close to the exact value. The second conclusion is that each of the methods gives either upper or lower bound for the computed quantity. This feature is extremely important since it allows us to estimate the error of computation. As we expected, the second method is everywhere more accurate than the first one.

An asymptotic solution for a very narrow annulus can be found by using the analogy with a two-dimensional contact problem. The stress distribution can be taken in the form

$$\sigma(\rho) = \frac{\sigma_0}{\sqrt{c^2 - (\rho - r_0)^2}}. \quad (35)$$

Here, σ_0 is the as yet unknown constant,

$$c = (a-b)/2,\ r_0 = (a+b)/2. \quad (36)$$

Substitution of (35) in (8) yields

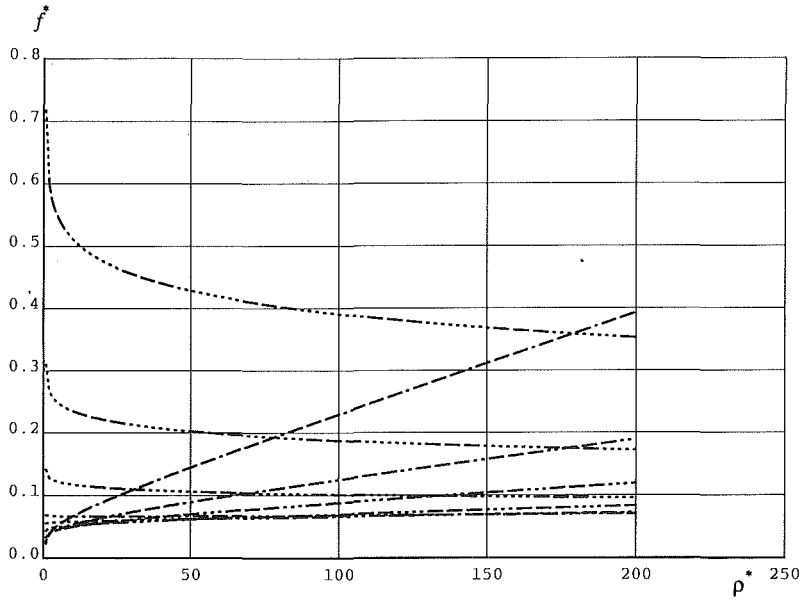

Fig. 1 The dimensionless stress function f^*

Table 1

n	b/a	Method 1 P^*	Method 2 P^*	Average P^*	Exact P^*
10	0.20000	1.0325	0.9855	1.0090	0.9989
	0.40000	1.0117	0.9807	0.9962	0.9907
	0.60000	0.9776	0.9587	0.9682	0.9651
	0.80000	0.9027	0.8950	0.8988	0.8976
	0.90000	0.8224	0.8204	0.8214	0.8210
	0.95000	0.7473	0.7483	0.7478	0.7478
	0.99500	0.5598	0.5632	0.5615	0.5618
	0.99950	0.4440	0.4471	0.4456	0.4458
	0.99995	0.3676	0.3702	0.3689	0.3691
20	0.20000	1.0119	0.9924	1.0022	0.9989
	0.40000	0.9993	0.9859	0.9926	0.9907
	0.60000	0.9704	0.9620	0.9662	0.9651
	0.80000	0.8998	0.8964	0.8981	0.8976
	0.90000	0.8216	0.8207	0.8212	0.8210
	0.95000	0.7475	0.7481	0.7478	0.7478
	0.99500	0.5608	0.5625	0.5617	0.5618
	0.99950	0.4449	0.4465	0.4457	0.4458
	0.99995	0.3684	0.3697	0.3690	0.3691
30	0.20000	1.0066	0.9946	1.0006	0.9989
	0.40000	0.9959	0.9876	0.9918	0.9907
	0.60000	0.9684	0.9631	0.9657	0.9651
	0.80000	0.8990	0.8968	0.8979	0.8976
	0.90000	0.8214	0.8208	0.8211	0.8210
	0.95000	0.7476	0.7480	0.7478	0.7478
	0.99500	0.5612	0.5623	0.5617	0.5618
	0.99950	0.4452	0.4463	0.4457	0.4458
	0.99995	0.3686	0.3695	0.3691	0.3691
40	0.20000	1.0043	0.9958	1.0000	0.9989
	0.40000	0.9944	0.9884	0.9914	0.9907
	0.60000	0.9674	0.9636	0.9655	0.9651
	0.80000	0.8986	0.8970	0.8978	0.8976
	0.90000	0.8213	0.8209	0.8211	0.8210
	0.95000	0.7477	0.7479	0.7478	0.7478
	0.99500	0.5613	0.5622	0.5618	0.5618
	0.99950	0.4454	0.4462	0.4458	0.4458
	0.99995	0.3687	0.3694	0.3691	0.3691

$$\chi(t) \approx \sigma_0 \frac{\sqrt{r_0}}{\sqrt{2}} \int_t^c \frac{dx}{\sqrt{c^2-x^2}\sqrt{x-t}}. \tag{37}$$

Here the following new variables were introduced

$$\rho_0 = r_0 + x, \; r = r_0 + t, \tag{38}$$

and the small quantities of the order of c/r_0, x/r_0, and t/r_0 were neglected. The same procedure applied to (18) and (30) yields, respectively,

$$P = 2\sigma_0\sqrt{2r_0} \int_{-c}^{c} \frac{\chi(t)dt}{\sqrt{t+c}}, \tag{39}$$

$$w_0 = \frac{2\sqrt{2}\sigma_0}{\pi H\sqrt{r_0}} \int_{-c}^{c} \ln\left(\frac{2r_0}{t+c}\right) \frac{x(t)dt}{\sqrt{t+c}}. \tag{40}$$

Substitution of (37) in (39) and (40), interchange of the order of integration and subsequent integration yield

$$P = 2\pi^2 r_0 \sigma_0, \tag{41}$$

$$w_0 = 2\pi H \sigma_0 \ln\left(\frac{16r_0}{c}\right). \tag{42}$$

Here the following integral was used

$$\int_{-c}^{x} \ln\left(\frac{2r_0}{t+c}\right) \frac{dt}{\sqrt{t+c}\sqrt{x-t}} = \pi \ln\left(\frac{8r_0}{x+c}\right). \tag{43}$$

We may now deduce from (41) and (42) that

$$P = \frac{\pi w_0 r_0}{H \ln\left(\frac{16r_0}{c}\right)}, \tag{44}$$

$$\sigma_0 = \frac{P}{2\pi^2 r_0} = \frac{w_0}{2\pi H \ln\left(\frac{16r_0}{c}\right)}, \tag{45}$$

$$P^* = \frac{\pi^2}{2\ln\left(\frac{16(a+b)}{a-b}\right)}. \tag{46}$$

The last result is in agreement with that of Smythe (1951) and Collins (1963).

Flat Inclined Annular Punch. Assume that the punch is tilted about axis Oy in the positive direction, and that the angle of rotation is α. The normal displacements under the punch can be expressed as

$$w(\rho,\phi) = -\alpha\rho\cos\phi. \tag{47}$$

Substitution of (47) in (16) leads to the governing integral equation

$$\chi_1(r) + \frac{2}{\pi^2} \int_b^a \frac{K_1(y,r) - K_1(r,y)}{y^2 - r^2} \chi_1(y)dy = -\frac{\alpha}{2\pi H} \frac{2r^2 - b^2}{\sqrt{r^2 - b^2}}. \tag{48}$$

It is reminded that the kernel K_1 is defined by (17). We may conclude once again that since the stress distribution is singular

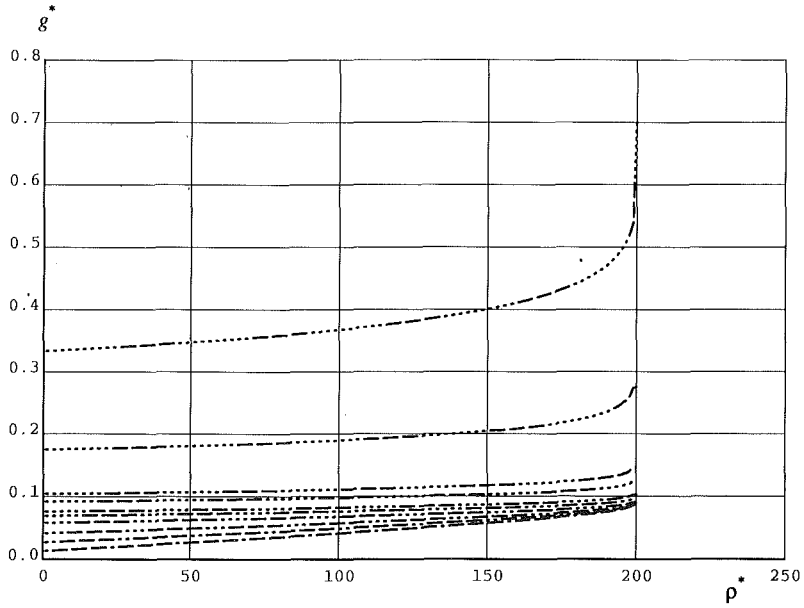

Fig. 2 The dimensionless stress function g^*

at the edges $\rho = b$ and $\rho = a$, the function χ_1 will have a logarithmic singularity at the point $\rho = b$. Introducing a new unknown function q as

$$q(r) = \frac{\chi_1(r)}{\ln\dfrac{r+b}{r-b}}, \tag{49}$$

we may rewrite (48) in the form

$$\frac{\sqrt{r^2-b^2}}{2r^2-b^2}\ln\frac{r+b}{r-b}\,q(r) + \frac{2}{\pi^2}\frac{\sqrt{r^2-b^2}}{2r^2-b^2}\int_b^a \frac{K_1(y,r)-K_1(r,y)}{y^2-r^2} \times q(y)\ln\left(\frac{y+b}{y-b}\right)dy = -\frac{\alpha}{2\pi H}. \tag{50}$$

The problem was solved numerically by using both methods from the previous section. The value of the tilting moment M was computed in the first method according to the formula (19) as follows:

$$M = -2\sum_{i=1}^{n-1} q_i \int_{x_i}^{x_{i+1}} \ln\left(\frac{\rho+b}{\rho-b}\right)\frac{(2\rho^2-b^2)d\rho}{\sqrt{\rho^2-b^2}}. \tag{51}$$

The following formula was used in the second numerical method

$$M = -2\sum_{i=1}^{n-1}\left\{\left[q_i\left(i+\frac{b}{\Delta}\right) - q_{i+1}\left(i+\frac{b}{\Delta}-1\right)\right]\int_{x_i}^{x_{i+1}}\ln\left(\frac{\rho+b}{\rho-b}\right)\frac{(2\rho^2-b^2)d\rho}{\sqrt{\rho^2-b^2}} + \frac{q_{i+1}-q_i}{\Delta}\int_{x_i}^{x_{i+1}}\ln\left(\frac{\rho+b}{\rho-b}\right)\frac{(2\rho^2-b^2)\rho d\rho}{\sqrt{\rho^2-b^2}}\right\}. \tag{52}$$

The integrals in (51) and (52) can be computed in terms of elementary functions, namely,

$$\int \ln\left(\frac{\rho+b}{\rho-b}\right)\frac{(2\rho^2-b^2)d\rho}{\sqrt{\rho^2-b^2}} = \sqrt{\rho^2-b^2}\left[2b+\rho\ln\left(\frac{\rho+b}{\rho-b}\right)\right],$$

$$\int \ln\left(\frac{\rho+b}{\rho-b}\right)\frac{(2\rho^2-b^2)\rho d\rho}{\sqrt{\rho^2-b^2}} = \frac{1}{3}(2\rho^2+b^2)\sqrt{\rho^2-b^2}\ln\left(\frac{\rho+b}{\rho-b}\right) + \frac{2}{3}b(\rho\sqrt{\rho^2-b^2}+2b^2\ln(\rho+\sqrt{\rho^2-b^2}).$$

Table 2

n	b/a	Method 1 M^*	Method 2 M^*	Average M^*	Exact M^*
10	0.2000	1.0028	1.0017	1.0023	0.99996
	0.4000	1.0079	0.9959	1.0019	0.99878
	0.6000	1.0012	0.9839	0.9925	0.98930
	0.8000	0.9491	0.9368	0.9429	0.94084
	0.9000	0.8658	0.8609	0.8633	0.86243
	0.9400	0.7991	0.7982	0.7986	0.79830
	0.9800	0.6677	0.6707	0.6692	0.66942
	0.9900	0.5989	0.6027	0.6008	0.60115
	0.9990	0.4392	0.4429	0.4411	0.44138
	0.9999	0.3449	0.3479	0.3464	0.34661
20	0.2000	1.0012	1.0000	1.0006	0.99996
	0.4000	1.0024	0.9971	0.9997	0.99878
	0.6000	0.9941	0.9866	0.9904	0.98930
	0.8000	0.9443	0.9389	0.9416	0.94084
	0.9000	0.8638	0.8617	0.8627	0.86243
	0.9400	0.7986	0.7982	0.7984	0.79830
	0.9800	0.6685	0.6701	0.6693	0.66942
	0.9900	0.6000	0.6020	0.6010	0.60115
	0.9990	0.4403	0.4422	0.4412	0.44138
	0.9999	0.3458	0.3473	0.3465	0.34661
30	0.2000	1.0007	0.9998	1.0003	0.99996
	0.4000	1.0010	0.9976	0.9993	0.99878
	0.6000	0.9923	0.9875	0.9899	0.98930
	0.8000	0.9430	0.9396	0.9413	0.94084
	0.9000	0.8633	0.8620	0.8626	0.86243
	0.9400	0.7984	0.7983	0.7983	0.79830
	0.9800	0.6688	0.6699	0.6693	0.66942
	0.9900	0.6004	0.6017	0.6010	0.60115
	0.9990	0.4407	0.4419	0.4413	0.44138
	0.9999	0.3461	0.3471	0.3466	0.34661
40	0.2000	1.0005	0.9998	1.0002	0.99996
	0.4000	1.0003	0.9979	0.9991	0.99878
	0.6000	0.9914	0.9880	0.9897	0.98930
	0.8000	0.9424	0.9399	0.9411	0.94084
	0.9000	0.8630	0.8621	0.8625	0.86243
	0.9400	0.7984	0.7983	0.7983	0.79830
	0.9800	0.6690	0.6697	0.6694	0.66942
	0.9900	0.6006	0.6016	0.6011	0.60115
	0.9990	0.4408	0.4418	0.4413	0.44138
	0.9999	0.3462	0.3470	0.3466	0.34661

Numerical computations were performed according to both methods for different values of n and various ratios b/a. The dimensionless quantity $q^* = H|q|/(a\alpha)$ is plotted on Fig. 2. The conventions are the same as with Fig. 1 except for the curve identification which is now related to Table 2. For example, six dots in the curve pattern now correspond to $b/a = 0.94$. The dimensionless tilting moment $M^* = M/M_0$ is presented in the Table 2. The quantity $M_0 = 4a^3\alpha/(3\pi H)$ corresponds to the tilting moment producing angular displacement α when applied to a circular punch of radius a. Here we no longer have that peculiar property that each method gives either

upper or lower bound for the solution. It does not hold for $b/a = 0.2$, though it appears to be valid for $b/a \geq 0.4$. All the numerical results presented in this article are in excellent agreement with similar data received in personal communication from Professor Mastrojannis.

An asymptotic solution for a very narrow $[(a - b)/a] \ll 1$ annulus can be attempted as above. Assume

$$\sigma(\rho,\phi)=\frac{\sigma_1\cos\phi}{\sqrt{c^2-(\rho-r_0)^2}}. \tag{53}$$

Here, as before, $2c$ is the annulus thickness and r_0 is its average radius as defined in (36). Substitution of (53) in (8) yields

$$\chi_1(t)\approx\sigma_1\frac{\sqrt{r_0}}{\sqrt{2}}\int_t^c\frac{dx}{\sqrt{c^2-x^2}\sqrt{x-t}}. \tag{54}$$

Here the new variables were introduced in the manner similar to (38). In the limiting case of $r \to b$ we can deduce from (50) that

$$\alpha=-\frac{4H}{\pi b^2}\int_b^a\left[y\ln\left(\frac{y+b}{y-b}\right)-2b\right]\frac{\chi_1(y)dy}{\sqrt{y^2-b^2}}$$
$$\approx-\frac{2\sqrt{2}H}{\pi b^2\sqrt{r_0}}\int_{-c}^c\left[r_0\ln\left(\frac{2r_0}{t+c}\right)-2b\right]\frac{\chi_1(t)dt}{\sqrt{t+c}}. \tag{55}$$

Substitution of (54) in (55) yields after interchanging the order of integration and subsequent integration

$$\alpha=-\frac{2\pi H\sigma_1}{r_0}\left[\ln\left(\frac{16r_0}{c}\right)-2\right]. \tag{56}$$

A similar procedure performed on (19) gives

$$M=-\pi^2r_0^2\sigma_1. \tag{57}$$

We may now deduce from (56) and (57) that

$$\sigma_1=-\frac{M}{\pi^2r_0^2}, \tag{58}$$

$$\alpha=\frac{2HM}{\pi r_0^3}\left[\ln\left(\frac{16(a+b)}{a-b}\right)-2\right]. \tag{59}$$

Taking into consideration that for a circular punch of radius a we have

$$M_0=\frac{4a^3\alpha}{3\pi H}, \tag{60}$$

the following expression for the dimensionless moment can be written

$$M^*=\frac{M}{M_0}=\frac{3\pi^2(a+b)^3}{64a^3\left[\ln\left(\frac{16(a+b)}{a-b}\right)-2\right]}. \tag{61}$$

We are unaware of a similar result published elsewhere.

Discussion

An attempt can be made to obtain an approximate analytical solution. We can multiply both sides of (27) by $4rdr/\sqrt{r^2-b^2}$ and integrate with respect to r from $b + \epsilon$ to a. The result is

$$4\int_{b+\epsilon}^a\frac{\chi_0(r)rdr}{\sqrt{r^2-b^2}}+\frac{4}{\pi^2}\int_b^a\frac{1}{\sqrt{y^2-b^2}}$$
$$\times\left\{\ln\left(\frac{y+b}{y-b}\right)\left[y\ln\frac{(y-b)(a+y)}{(y+b)(a-y)}-b\ln\frac{(a+b)\epsilon}{(a-b)2b}\right.\right.$$
$$\left.\left.-y\int_b^a\ln\left(\frac{x+b}{x-b}\right)\frac{xdx}{y^2-x^2}\right\}\chi_0(y)dy\right.$$
$$=\frac{2w_0}{\pi H}\left[a-b-\frac{b}{2}\ln\frac{(a+b)\epsilon}{(a-b)2b}\right]. \tag{62}$$

By using indentity (30), the limiting case of $\epsilon \to 0$ can be computed

$$P+\frac{4}{\pi^2}\int_b^a T(y)\frac{\chi_0(y)ydy}{\sqrt{y^2-b^2}}=\frac{2w_0(a-b)}{\pi H}, \tag{63}$$

with

$$T(y)=\ln\left(\frac{y+b}{y-b}\right)\ln\left(\frac{(a+y)(y-b)}{(a-y)(y+b)}\right)$$
$$-\int_b^a\ln\left(\frac{x+b}{x-b}\right)\frac{xdx}{y^2-x^2}. \tag{64}$$

Taking into consideration that χ_0 does not change sign in the interval $[b, a]$, we can use the mean value theorem and to rewrite (63) as

$$P\left[1+\frac{1}{\pi^2}T(Y)\right]=\frac{2w_0(a-b)}{\pi H},$$

with an immediate consequence

$$P=\frac{2w_0(a-b)}{\pi H\left(1+\frac{1}{\pi^2}T(Y)\right)}. \tag{65}$$

We know about the value of Y only that it is located somewhere in the interval $[b, a]$. This condition allows infinite variation of T, thus making (65) of little practical value. On the other hand, formula (65) is exact in two limiting cases, namely for $b \to 0$ and $b \to a$. This means that an additional investigation can reveal an optimal value of Y, making (65) useful.

Yet another solution can be deduced from (18) and (30) which can be rewritten as

$$\int_b^a\ln\left(\frac{y+b}{y-b}\right)\frac{\chi_0(y)dy}{\sqrt{y^2-b^2}}=\frac{\pi w_0}{4H}. \tag{66}$$

Taking into consideration that λ_0 does not change sign in the $[b, a]$, we can apply the mean value theorem to (66), with the result

$$\frac{1}{Y}\ln\left(\frac{Y+b}{Y-b}\right)\int_b^a\frac{\chi_0(y)ydy}{\sqrt{y^2-b^2}}=\frac{\pi w_0}{4H}. \tag{67}$$

Comparison of (67) with (18) yields

$$P=\frac{\pi w_0 Y}{H\ln\left(\frac{Y+b}{Y-b}\right)}. \tag{68}$$

Again, the main problem with (68) is the fact that we know about the value of Y only that it is located somewhere between b and a, which allows infinite variation. This does not preclude, however, from finding some optimal value for Y which would make (68) useful. This investigation is beyond the scope of this paper.

The complete solution, namely, the explicit expressions for the field of stresses and displacements in the elastic half-space due to the annular punch indentation, can be derived in terms of the function χ. Indeed, in order to obtain the field of normal displacements, one has to compute the integral

$$I(\rho,\phi,z)=\int_0^{2\pi}\int_b^a\frac{\sigma(\rho_0,\phi_0)\rho_0d\rho_0d\phi_0}{\sqrt{\rho^2+\rho_0^2-2\rho\rho_0\cos(\phi-\phi_0)+z^2}}. \tag{69}$$

Substitution of (9) in (69) yields, after interchanging the order of integration and subsequent integration,

$$I(\rho,\phi,z)=\frac{2}{\pi}\int_0^{2\pi}\int_b^a \frac{\sqrt{l_2^2(x)-x^2}\chi(x,\phi_0)dxd\phi_0}{\rho^2+x^2-2\rho x\cos(\phi-\phi_0)+z^2}$$

$$+\frac{8}{\pi}\int_b^a\left\{\int_0^{l_1(b)}\mathfrak{L}\left(\frac{x^2}{\rho y}\right)\frac{\sqrt{b^2-g^2(x)}dx}{[y^2-g^2(x)]\sqrt{\rho^2-x^2}}\right\}\frac{\chi(y,\phi)ydy}{\sqrt{y^2-b^2}}. \tag{70}$$

Here

$$l_1(x)=\frac{1}{2}\{\sqrt{(\rho+x)^2+z^2}-\sqrt{(\rho-x)^2+z^2}\},$$

$$l_2(x)=\frac{1}{2}\{\sqrt{(\rho+x)^2+z^2}+\sqrt{(\rho-x)^2+z^2}\},$$

$$g(x)=x\left[1+\frac{z^2}{\rho^2-x^2}\right]^{1/2} \tag{71}$$

Note that function g is inverse to both l_1 and l_2. The method of integration is described in (Fabrikant, 1989). The complete solution is to be published separately.

Acknowledgment

The author is grateful to Professor Mastrojannis for making his numerical results available. The reported research was supported by a grant from NSERC of Canada.

References

Barber, J. R., 1983, "A Four-Part Boundary Value Problem in Elasticity—Indentation by a Discontinuously Concave Punch," *Applied Scientific Research*, Vol. 40, pp. 159–167.

Barber, J. R., 1976, "Indentation of a Semi-Infinite Elastic Solid by a Concave Rigid Punch," *Journal of Elasticity*, Vol. 2, pp. 149–159.

Collins, W. D., 1963, "On the Solution of Some Axisymmetric Boundary Value Problems by Means of Integral Equations: VIII. Potential Problems for a Circular Annulus," *Proc. Edinburgh Math. Soc.*, Vol. 13, pp. 235–246.

Cooke, J. C., 1963, "Some Further Triple Integral Equations," *Proc. Edinburgh Math. Soc.*, Vol. 13, pp. 193–203.

Fabrikant, V. I., 1989, *Applications of Potential Theory in Mechanics: Selection of New Results*. Kluwer Academic.

Love, E. R., 1976, "Inequalities for the Capacity of an Electrified Conducting Annular Disk," *Proc. Roy. Soc. of Edinbourgh*, Vol. 74A, 1974–1975, pp. 257–270.

Rajapakse, R. K. N. D., 1988, "Interaction between a Circular Elastic Plate and a Transversely Isotropic Elastic Half-Space," *Int. J. for Numer. and Anal. Methods in Geomech.*, Vol. 12, pp. 419–436.

Selvadurai, A. P. S., 1985, "Annular Crack Problem for an Isotropic Elastic Solid," *Quart. J. of Appl. Math. and Mech.*, Vol. 38, pp. 233–243.

Selvadurai, A. P. S., 1987, "Axisymmetric Problem for an Externally Cracked Elastic Solid. II. Effect of a Penny-Shaped Inclusion," *Int. J. of Engng. Sci.*, Vol. 25, pp. 1477–1490.

Smythe, W. R., 1951, "The Capacitance of a Circular Annulus," *Journal of Applied Physics*, Vol. 22, pp. 1499–1501.

Veletsos, A. S., 1988, "Vertical and Torsional Vibrations of Foundations in Non-Homogeneous media," *J. of Geotechnical Engng.*, Vol. 114, pp. 1002–1021.

Veletsos, A. S., 1987, "Rocking Vibration Rigid Ring Foundation," *J. of Geotechnical Engng.*, Vol. 113, pp. 1019–1032.

Williams, W. E., 1963, "Integral Equation Formulation of Some Three-Part Boundary Value Problem," *Proc. Edinburgh Math. Soc.*, Vol. 13, pp. 317–323.

R. E. Worden

L. M. Keer
Fellow ASME.

Department of Civil Engineering,
Northwestern University,
Evanston, IL 60208

Green's Functions for a Point Load and Dislocation in an Annular Region

This paper contains an analysis of a two-dimensional annular region whose inner boundary is that of either a hole or a perfectly bonded, rigid inclusion. Fast-converging Green's functions for a point load or a dislocation on the annulus are determined using analytic continuation across the boundaries of the annulus.

1 Introduction

Problems of annular regions have applications to many different engineered structures such as pressure vessels, rollers, and toughness test specimens, and their solutions have occupied mathematicians and engineers for many years. In the first book published on the theory of elasticity, Lamé (1852) included the solution for the stresses in a pressure vessel under uniform external or internal pressure (Timoshenko, 1953). The general solution for the annulus was given by Michell (1899) in his landmark paper on planar elasticity. The Michell solution determines the Airy stress function for the annulus from the Fourier expansions of the boundary stresses, given that the solution is nondislocational (see Timoshenko and Goodier, 1970). Michell also showed that the stresses in the annulus are independent of the elastic constants provided that the resultants of the tractions on the inner and outer boundaries are zero. An analysis of a ring test specimen loaded by diametrically opposed compressive point loads was undertaken by Ripperger and Davids (1947). Stresses at critical points in the loaded annulus were determined by solving what was essentially the Fourier series of the Michell solution. Modern analyses of the annulus containing a crack includes the finite element method (Ahmad and Ashbaugh, 1982) and the boundary collocation method (Bowie and Freese, 1972).

Delale and Erdogan (1982) solved for the Green's function for a dislocation on the annulus with a Burgurs vector normal to the boundaries of the annulus. This solution was used to determine an integral equation for a crack on the annulus. By solving the integral equation subject to the condition that the normal and shear stresses along the crack are zero, the crack opening displacement and stress intensity factors for the crack were found.

This work derives the Green's functions for a point load or a dislocation in an annular region. Two types of annular regions are examined: that of the annulus whose inner boundary is a hole and that of the annulus whose inner boundary is a perfectly bonded, rigid inclusion. Thus two boundary value problems are examined for the inner boundary: that of the stress-free boundary, and that of the rigidly displaced boundary. For the outer boundary, only the stress-free condition is examined; however, the method is easily extended to solve for the displacement free boundary.

Since the Green's functions considered here are derived for a finite body, the Green's function for the point load must be for a system that is in equilibrium. This condition is not necessary for the displacement free outer boundary, and the two problems, while similar, cannot be formulated together as for the case of the inner boundary.

2 Formulation

The method of solution used here is that of analytic continuation across the boundaries of the annulus (Milne-Thompson, 1968). The complex variable method of Muskehelishvili (1954) is used to define the stresses and displacements in the elastic plane in terms of the Kolosov potentials, $\phi(z)$ and $\psi(z)$:

$$\sigma_{xx}+\sigma_{yy}=4\ \mathrm{Re}\ \{\Phi\ (z)\}, \tag{1}$$

$$\sigma_{yy}-\sigma_{xx}+2i\sigma_{xy}=2\{\bar{z}\Phi'(z)+\Psi(z)\}, \tag{2}$$

$$2\mu(u+iv)=\kappa\phi(z)-z\overline{\varphi'(z)}-\overline{\psi(z)}, \tag{3}$$

where σ_{xx}, σ_{yy}, and σ_{xy} are the stresses and u and v are the displacements in the x-y plane, $\kappa=3-4\nu$ for plane strain and $\kappa=(3-\nu)/(1+\nu)$ for plane stress where ν is the Poisson's ratio, μ is the shear modulus, z is the complex coordinate: $z=x+iy$ where $i=\sqrt{-1}$, the bars denote complex conjugation, Re denotes the real part of the function, and, following the common notation, $\Phi(z)=\phi'(z)$ and $\Psi(z)=\psi'(z)$.

The polar form of the stresses is:

$$\sigma_{rr}+\sigma_{r\theta}=4\ \mathrm{Re}\ \{\Phi(z)\}, \tag{4}$$

$$\sigma_{\theta\theta}-\sigma_{rr}+2i\sigma_{r\theta}=2e^{2i\theta}\{\bar{z}\Phi'(z)+\Psi(z)\}, \tag{5}$$

where θ is the rotation of the stresses. If θ is measured from the origin, then $z=re^{i\theta}$, where r is the modulus of z, and $e^{2i\theta}=z/\bar{z}$.

[1]Presently at the Boeing Aircraft Company, Seattle, WA 98124.

Contributed by the Applied Mechanics Division of THE AMERICAN SOCIETY OF MECHANICAL ENGINEERS for publication in the JOURNAL OF APPLIED MECHANICS.

Discussion on this paper should be addressed to the Technical Editor, Prof. Leon M. Keer, The Technological Institute, Northwestern University, Evanston, IL 60208, and will be accepted until two months after final publication of the paper itself in the JOURNAL OF APPLIED MECHANICS. Manuscript received by the ASME Applied Mechanics Division, Jan. 31, 1990; final revision, Nov. 19, 1991.

The annulus is pictured in Fig. 1; the center region contains either a hole or perfectly bonded, rigid inclusion. The boundary condition on the inner boundary of the annulus containing the inclusion is

$$2\mu(u+iv)=\kappa\phi(t)-t\overline{\phi}'\left(\frac{a^2}{t}\right)-\overline{\psi}\left(\frac{a^2}{t}\right)=2\mu(\delta+i\omega t) \quad (6)$$

where $t=ae^{i\theta}$, δ is complex and represents a rigid body translation, and ω is real and represents a rigid body rotation. Taking derivatives with respect to t, Eq. (6) becomes

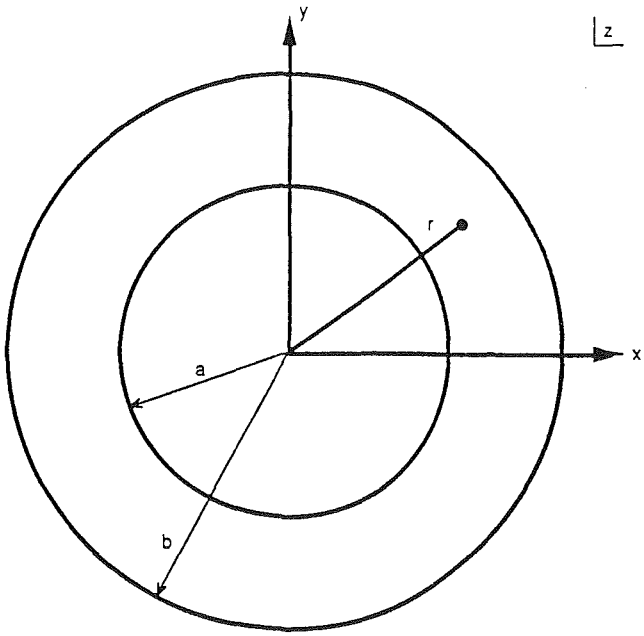

Fig. 1 Problem configuration for the annulus

$$\kappa\Phi(t)-\overline{\Phi}\left(\frac{a^2}{t}\right)+\frac{a^2}{t}\overline{\Phi}'\left(\frac{a^2}{t}\right)+\frac{a^2}{t^2}\overline{\Psi}\left(\frac{a^2}{t}\right)-2\mu i\omega=0. \quad (7)$$

Also, for the annulus containing a hole, we have at the inner boundary

$$\sigma_{rr}+i\sigma_{r\theta}=\Phi(t)+\overline{\Phi}\left(\frac{a^2}{t}\right)-\frac{a^2}{t}\overline{\Phi}'\left(\frac{a^2}{t}\right)-\frac{a^2}{t^2}\overline{\Psi}\left(\frac{a^2}{t}\right)=f(t) \quad (8)$$

where $f(t)$ is the complex sum of the normal and shear stresses on the inner boundary at the point t. Equations (7) and (8) can be combined into one boundary condition for both the hole and the inclusion,

$$\alpha\Phi(t)+\overline{\Phi}\left(\frac{a^2}{t}\right)-\frac{a^2}{t}\Phi'\left(\frac{a^2}{t}\right)-\frac{a^2}{t^2}\overline{\Psi}\left(\frac{a^2}{t}\right)+i\Omega=\frac{\alpha+\kappa}{\kappa+1}f(t), \quad (9)$$

where $\alpha=1$ for the hole, $\alpha=-\kappa$ for the inclusion and $\Omega=-(\alpha-1)2\mu\omega/(\kappa+1)$.

Similarly, the boundary condition on the outer boundary is

$$\Phi(t)+\overline{\Phi}\left(\frac{b^2}{t}\right)-\frac{b^2}{t}\overline{\Phi}'\left(\frac{b^2}{t^2}\right)-\frac{b^2}{t^2}\overline{\Psi}\left(\frac{b^2}{t}\right)=0, \quad (10)$$

where, in this case, $t=be^{i\theta}$.

A Green's function solution is sought for the annulus of Fig. 1 for $a\le r\le b$. Since the strength of the singularity in the Green's function is known, define

$$\Phi(z)=\Phi_0(z)+\Phi_1(z)+\Phi_2(z), \quad (11)$$

$$\Psi(z)=\Psi_0(z)+\Psi_1(z)+\Psi_2(z), \quad (12)$$

where $\Phi_1(z)$ and $\Psi_1(z)$ are the potentials for the known singular solution for the point load or dislocation at the point ζ in the infinite plane, $\Phi_0(z)$ and $\Psi_0(z)$ contain reactive singular sources at the origin, and $\Phi_2(z)$ and $\Psi_2(z)$ are nonsingular and are determined so that the boundary conditions are satisfied. Then (9) and (10) become

$$\alpha\Phi_2(z)+\overline{\Phi}_2\left(\frac{a^2}{t}\right)-\frac{a^2}{t}\overline{\Phi}_2'\left(\frac{a^2}{t}\right)-\frac{a^2}{t^2}\overline{\Psi}_2\left(\frac{a^2}{t}\right)=G_a(t), \quad (13)$$

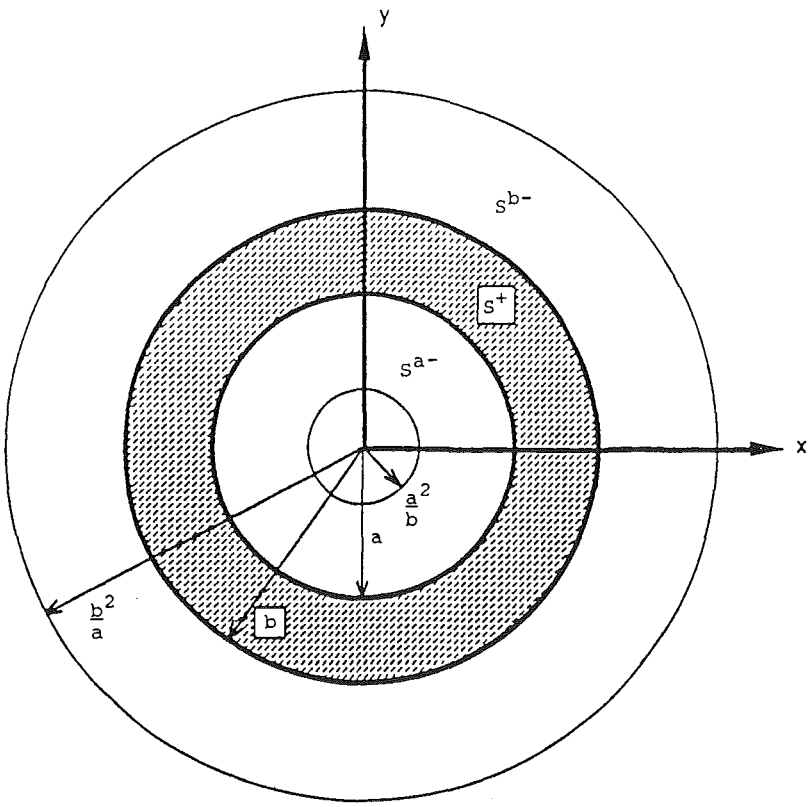

Fig. 2 Analytic regions of the annulus

$$\Phi_2(z)+\overline{\Phi}_2\left(\frac{b_2}{t}\right)-\frac{b^2}{t}\overline{\Phi}_2'\left(\frac{b^2}{t}\right)-\frac{b^2}{t^2}\overline{\Psi}_2\left(\frac{b^2}{t}\right)=G_b(t), \quad (14)$$

where

$$G_a(t)=-\alpha\Phi_1(z)-\overline{\Phi}_1\left(\frac{a^2}{t}\right)+\frac{a^2}{t}\overline{\Phi}_1'\left(\frac{a^2}{t}\right)+\frac{a^2}{t^2}\overline{\Psi}_1\left(\frac{a^2}{t}\right)$$
$$-\alpha\Phi_0(z)-\overline{\Phi}_0\left(\frac{a^2}{t}\right)+\frac{a^2}{t}\overline{\Phi}_0'\left(\frac{a^2}{t}\right)+\frac{a^2}{t^2}\overline{\Psi}_0\left(\frac{a^2}{t}\right)$$
$$-i\Omega+\frac{\alpha+\kappa}{\kappa+1}f(t) \quad (15)$$

and

$$G_b(t)=-\Phi_1(z)-\overline{\Phi}_1\left(\frac{b^2}{t}\right)+\frac{b^2}{t}\overline{\Phi}_1'\left(\frac{b^2}{t}\right)+\frac{b^2}{t^2}\overline{\Psi}_1\left(\frac{b^2}{t}\right)$$
$$-\Phi_0(z)-\overline{\Phi}_0\left(\frac{b^2}{t}\right)+\frac{b^2}{t}\overline{\Phi}_0'\left(\frac{b^2}{t}\right)+\frac{b^2}{t^2}\overline{\Psi}_0\left(\frac{b^2}{t}\right). \quad (16)$$

The function Φ_2 is analytically continued into the regions S^{a-} and S^{b-} shown in Fig. 2 by defining

$$\Phi_2(z)=\begin{cases}\Phi_2^{a-}(z) & z\in S^{a-}\\ \Phi_2^{+}(z) & z\in S^{+}\\ \Phi_2^{b-}(z) & z\in S^{b-}\end{cases} \quad (17)$$

so that $\overline{\Phi_2^{a-}(a^2/\bar{z})}$ and $\overline{\Phi_2^{b-}(b^2/\bar{z})}$ are analytic in S^+. Also, unless otherwise stated, $\Phi_2(z)=\Phi_2^+(z)$ since the solution is in the region S^+. If the definition for $\Psi_2(z)$ is chosen:

$$\Psi_2(z)=\frac{a^2}{z^2}\left\{\overline{\Phi_2^{a-}}\left(\frac{a^2}{z}\right)+\Phi_2(z)-z\Phi_2'(z)\right\}, \quad (18)$$

then (13) reduces to

$$\alpha\Phi_2^+(t)-\Phi_2^{a-}(t)=G_a(t). \quad (19)$$

Again, $\Psi_2(z)$ may be defined so as to determine a solution on the outer boundary.

$$\Psi_2(z)=\frac{b^2}{z^2}\left\{\overline{\Phi_2^{b-}}\left(\frac{b^2}{z}\right)+\Phi_2(z)-z\Phi_2'(z)\right\}, \quad (20)$$

and (13) becomes

$$\Phi_2^+(t)-\Phi_2^{b-}(t)=G_b(t). \quad (21)$$

Equations (19) and (21) can be solved by considerations of the Plemelj formula:

$$\Phi_2^+(z)=-\frac{1}{2\pi i}\oint_{C_a}\frac{G_a(t)/\alpha}{t-z}dt+\frac{1}{2\pi i}\oint_{C_b}\frac{G_b(t)}{t-z}dt$$
$$+F(z)+P(z)+p_0+p_1z, \quad (22)$$

where C_a is the contour $r=a$ and C_b is the contour $r=b$, both integrals are taken in the counterclockwise sense, $F(z)$ and $P(z)$ are analytic functions in $S^{a-}\cup S^{+}\cup S^{b-}$. The function $P(z)$ has the form

$$P(z)=\sum_{n=2}^{\infty}p_nz^n+p_{-n}z^{-n}. \quad (23)$$

The function $F(z)$ is arbitrary; it is chosen so that a more convergent form of $P(z)$ is obtained. The potentials $\Phi_2^{a-}(z)$ and $\Phi_2^{b-}(z)$ are determined from (19) and (21). Next, Eqs. (18) and (20) are set equal to each other to obtain the compatibility condition of Milne-Thompson (1968)

$$(b^2-a^2)\{\Phi_2(z)-z\Phi_2'(z)\}-b^2\overline{\Phi_2^{b-}}\left(\frac{b^2}{z}\right)$$
$$+a^2\overline{\Phi_2^{a-}}\left(\frac{a^2}{z}\right)=0. \quad (24)$$

By expanding the terms in (24) into a Laurent series, a solution for $P(z)$ can be found depending on the choice of $F(z)$. Consequently, a first choice of $F(z)=0$ is best used to determine the initial coefficients of $P(z)$. By inspection, less convergent coefficients can be deleted by choosing appropriate functions for $F(z)$. The final step of the solution is to determine $\Psi_2(z)$ from (18) or (20).

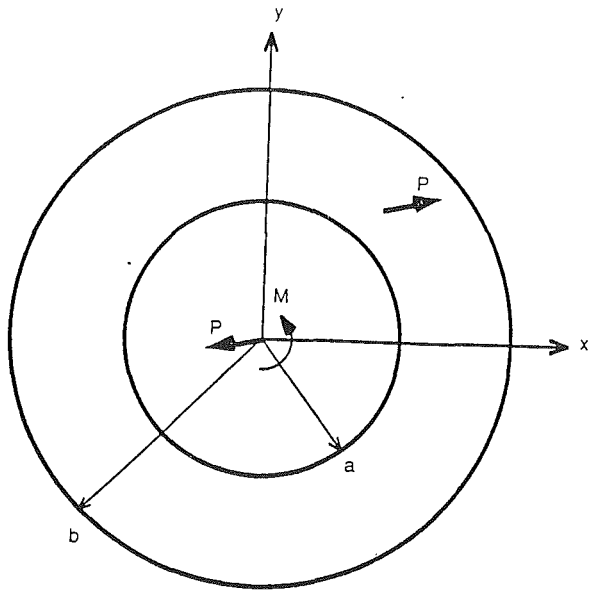

Fig. 3 Equilibrating loads for the point load on the annulus

The constant $i\Omega$ in Eq. (9) does not directly affect the solution; it can be seen from (1) and (2) that $\Phi(z)$ can have an additive imaginary constant without changing the distribution of stresses in the body. However, when the compatibility condition is applied, only the real part of p_0 can be determined; the imaginary part depends on the choice of Ω. If a consistent choice of the two constants is made and then used when solving for $\Psi_2(z)$, no spurious moments will be added to the solution and boundary conditions will be satisfied. When the final result is found, any imaginary constants in $\Phi(z)$ can be deleted, particularly those that are inversely proportional to the inner radius of the annulus.

3 Solutions

The singular potentials for the point load or for the dislocation at the point ζ in the infinite plane are (Muskhelishvili, 1954):

$$\Phi_1(z)=\frac{A}{z-\zeta}, \quad (25)$$

$$\Psi_1(z)=\frac{\beta\overline{A}}{z-\zeta}+\frac{A\bar{\zeta}}{(z-\zeta)^2}, \quad (26)$$

where

$$A=\begin{cases}-\dfrac{P_x+iP_y}{2\pi(\kappa+1)} & \text{for the point load}\\ \dfrac{b_x+ib_y}{2\pi i(\kappa+1)} & \text{for the dislocation}\end{cases} \quad (27)$$

and

$$\beta=\begin{cases}-\kappa & \text{for the point load}\\ 1 & \text{for the dislocation.}\end{cases} \quad (28)$$

Here, P_x and P_y are the point loads and b_x and b_y are the dislocations; the relation between these two solutions was pointed out by Dundurs (1968).

3.1 Point Load Solution. The applied loads on a finite

body must be in equilibrium if a solution is to be found. Therefore, the point load Green's function for the annulus must be for a system of point loads that are in equilibrium. Equilibrating loads are most conveniently placed at the center of the annulus to counter the action of the applied point load at the point ζ. This choice will not leave any extraneous loads when a Green's function is used to determine the stresses in an annulus under applied boundary tractions. Since the tractions must be in equilibrium, in the overall solution the loads at the center will cancel.

For equilibrium, the following complex point load and moment are applied at the center of the annulus as shown in Fig. 3:

$$P = -(P_x + iP_y), \tag{29}$$

$$M = P_x \cdot \mathrm{Im}(\zeta) - P_y \cdot \mathrm{Re}(\zeta). \tag{30}$$

The potentials for these loads are (Muskhelishvili, 1954)

$$\Phi_0(z) = -\frac{A}{z}, \tag{31}$$

$$\Psi_0(z) = \frac{\kappa\overline{A}}{z} - \frac{iM}{2\pi}\frac{1}{z^2}, \tag{32}$$

where A is defined in Eq. (27) for the point load. In the case of the annulus with a hole, boundary tractions are applied on the inner boundary such that a net force and moment are exerted on the annulus equal to the point loads applied to the center. The function $f(t)$ chosen for the solution here is

$$f(t) = \Phi_0(t) + \overline{\Phi}_0\left(\frac{a^2}{t}\right) - \frac{a^2}{t}\overline{\Phi}_o'\left(\frac{a^2}{t}\right) - \frac{a^2}{t^2}\overline{\Psi}_o\left(\frac{a^2}{t}\right) \tag{33}$$

so that

$$f(t) = (\kappa+1)A\left\{\frac{1}{t} + \frac{\bar{\zeta}}{2a^2}\right\} - \overline{A}\left\{\frac{2t}{a^2} - (\kappa+1)\frac{\zeta}{2a^2}\right\}. \tag{34}$$

This simple solution has a sinusoidal distribution of normal and shear tractions for the point loads and a constant distribution of shear tractions for the moment. This result is similar to one previously obtained by Dundurs (1963). In determining the Green's function for a point load and moment in an elastic embedded disk, he obtained the same distribution of tractions for the limiting case of a disk with a free boundary. He concluded his solution was a convenient Green's function for the disk as the tractions vanish for any problem where the applied loads are in equilibrium.

The total solution for the equilibrated point load on the annulus is given in the Appendix. The best convergence for $P(z)$ was achieved when the function $F(z)$ in Eq. (22) was chosen as

$$F(z) = A\left\{\frac{1}{\alpha}\left[\frac{1}{z - a^2\zeta/b^2} - \frac{1}{z}\right] - \frac{a^2(b^2-a^2)}{\alpha b^6}\zeta^2\left(\bar{\zeta} - \frac{b^2}{\zeta}\right)\frac{3z - a^2\zeta/b^2}{(z - a^2\zeta/b^2)^3}\right\}$$
$$+\overline{A}\left\{-\frac{\beta}{\alpha}\frac{a^2(b^2-a^2)}{b^6}\zeta^2\left(\bar{\zeta} - \frac{b^2}{\zeta}\right)\frac{1}{(z - a^2\zeta/b^2)^3}\right\}. \tag{35}$$

Note that when $a = 0$ or $b \to \infty$, $P(z) = F(z) = 0$.

3.2 Dislocation Solution. The dislocation Green's function is derived in the same manner as the point load Green's function. There is only one consideration to make: When the Green's function is used for an edge crack on a hole, displacement continuity must be satisfied on a contour that encloses the edge crack and the hole. This is done by using an appropriate Green's function. By adding the solution for a dislocation at the origin that is opposite in sign to the dislocation at the point ζ, a Green's function that enforces displacement continuity is obtained (Comminou and Chang, 1985). The solution for the dislocation at the center of the annulus with free boundaries is:

$$\Phi_0(z) = -A\frac{1}{z} + 2\overline{A}\frac{z}{b^2 + a^2} \tag{36}$$

$$\Psi_0(z) = -2A\frac{a^2b^2}{b^2 + a^2}\frac{1}{z^3} - \overline{A}\frac{1}{z}. \tag{37}$$

When the Green's function is used for the edge crack on a hole, the potentials for the dislocation at the center are added to the already determined potentials for the dislocation at the point ζ in the annulus. The entire solution is given in the Appendix.

4 Conclusion

Green's functions for an annulus whose inner boundary is a free surface or a rigid, perfectly bonded inclusion have been obtained using the complex variable method of Muskhelishvili (1954). Be carefully defining the analytic regions for an annulus, the potentials describing an equilibrated point load and a dislocation were found in the form of functions plus an infinite series. By taking functions that are singular outside of the analytic regions of the annulus and expanding them in a Laurent series for the annulus, less convergent terms in the infinite series were cancelled by adding and subtracting the nonsingular functions from the function part and the infinite series part of the potentials. The convergence of the infinite series is dependent on the ratio a/b; this method is not appropriate for analyzing thin-walled annuli. For problems concerning thin-walled members, the reader is referred to Cheng and Finnie (1989).

The resulting Green's functions can be used to solve problems of an annulus with applied tractions on its free boundaries that contains a crack. Future work will consider curved crack propagation in an annulus acted on by concentric point loads.

Acknowledgment

The authors are grateful for support given by the Chrysler Motors Corporation. Discussions with J. M. Corwin, Program Manager, are gratefully acknowledged.

References

Ahmad, J., and Ashbaugh, N. E., 1982, "Constant K_I Crack Propagation Test Specimens," *International Journal of Fracture*, Vol. 19, pp. 115–129.

Bowie, O. L., and Freese, C. E., 1972, "Elastic Analysis for a Radial Crack in a Circular Ring," *Engineering Fracture Mechanics*, Vol. 4, pp. 315–321.

Cheng, W., and Finnie, I., 1989, "Stress Intensity Factors for Radial Cracks in Circular Cylinders and Other Simply Closed Cylindrical Bodies," *Engineering Fracture Mechanics*, Vol. 32, pp. 767–774.

Cominou, M., and Chang, F.-K., 1985, "Effects of Partial Closure and Friction on a Radial Crack Emanating From a Circular Hole," *International Journal of Fracture*, Vol. 28, pp. 29–36.

Delale, F., and Erdogan, F., 1982, "Stress Intensity Factors in a Hollow Cylinder Containing a Radial Crack," *International Journal of Fracture*, Vol. 20, pp. 251–265.

Dundurs, J., 1963, "Concentrated Force in an Elastically Embedded Disk," ASME Journal of Applied Mechanics, Vol. 30, pp. 568–570.

Dundurs, J., 1968, "Analogy Between Concentrated Forces and Edge Dislocations," *Journal of Applied Physics*, Vol. 39, pp. 4152–4156.

Lamé, G., 1852, *Lecons sur la Théorie Mathématique de l'Élasticité des Corps Solides*, Gauthier-Villars, Paris.

Michell, J. H., 1899, "On the Direct Determination of Stress in an Elastic Solid," *Proceedings of the London Mathematical Society*, Vol. 31, pp. 100–124.

Milne-Thompson, L. M., 1968, *Plane Elastic Systems*, Springer-Verlag, Heildelberg.

Muskhelishvili, N. I., 1954, *Some Basic Problems of the Mathematical Theory of Elasticity*, 4th ed., P. Noordhoff, Groningen, The Netherlands.

Ripperger, E. A., and Davis, N., 1947, "Critical Stresses in a Circular Ring," *ASCE Transactions*, Vol. 112, pp. 619–628.

Timoshenko, S. P., 1953, *History of Strength of Materials*, McGraw-Hill Book Company, New York.

Timoshenko, S. P., and Goodier, J. N., 1970, *Theory of Elasticity*, 3rd ed., McGraw-Hill Book Company, New York.

APPENDIX

Potentials for the Point Load and Dislocation

The Kolosov potentials for the point load are:

$$\Phi(z)=A\left\{\frac{1}{z-\zeta}-\frac{1}{z}+\frac{\kappa}{\alpha}\left[\frac{1}{z-a^2/\bar{\zeta}}-\frac{1}{z}\right]+\frac{1}{\alpha}\left[\frac{1}{z-a^2\zeta/b^2}-\frac{1}{z}\right]\right.$$
$$+\frac{\kappa}{z-b^2/\bar{\zeta}}-\frac{a^2(b^2-a^2)}{\alpha b^6}\zeta^2\left(\bar{\zeta}-\frac{b^2}{\zeta}\right)\frac{3z-a^2\zeta/b^2}{(z-a^2\zeta/b^2)^3}$$
$$\left.+(\kappa+1)\left[\frac{1}{b^2}-\frac{1}{2b^2-(\alpha+1)a^2}\right]\bar{\zeta}-\frac{\alpha a^4}{b^4(b^4-\alpha a^4)}\left(\kappa\bar{\zeta}^2+\frac{b^4}{\zeta^2}\right)z\right\}$$
$$+\overline{A}\left\{\frac{1}{\alpha}\frac{a^2}{\bar{\zeta}^2}\left(\zeta-\frac{a^2}{\bar{\zeta}}\right)\frac{1}{(z-a^2/\bar{\zeta})^2}+\frac{\kappa}{\alpha}\frac{a^2(b^2-a^2)}{b^6}\zeta^3\frac{1}{(z-a^2\zeta/b^2)^2}\right.$$
$$+\frac{b^2}{\bar{\zeta}^2}\left(\zeta-\frac{b^2}{\bar{\zeta}}\right)\frac{1}{(z-b^2/\bar{\zeta})^2}-2\frac{b^2-(\alpha+1)a^2}{2b^2-(\alpha+1)a^2}\frac{1}{b^2}\left(\zeta-\frac{b^2}{\bar{\zeta}}\right)$$
$$\left.+\frac{2}{b^4-\alpha a^4}\left[b^2+\frac{\alpha-1}{\kappa+1}a^2+\frac{\alpha a^4}{b^4}\bar{\zeta}\left(\zeta-\frac{b^2}{\bar{\zeta}}\right)\right]z\right\}+P(z) \quad \text{(A1)}$$

$$\Psi(z)=A\left\{\frac{\bar{\zeta}}{(z-\zeta)^2}+\kappa\frac{\bar{\zeta}}{(z-b^2/\bar{\zeta})^2}\right.$$
$$+\frac{\kappa}{\alpha}\frac{\bar{\zeta}}{(z-a^2/\bar{\zeta})^2}+\frac{1}{\alpha}\frac{b^2/\zeta}{(z-a^2\zeta/b^2)^2}$$
$$+\alpha\frac{a^2}{b^2}\left(\bar{\zeta}-\frac{b^2}{\zeta}\right)\frac{1}{(z-a^2\zeta/b^2)^2}$$
$$+\frac{b^2-a^2}{\alpha b^2}\left(\bar{\zeta}-\frac{b^2}{\zeta}\right)\frac{z^2-4(a^2\zeta/b^2)z-3(a^2\zeta/b^2)^2}{(z-a^2\zeta/b^2)^4}$$
$$+\left[-(\kappa+1)\left(\frac{1}{\alpha}+\frac{b^2}{2b^2-(\alpha+1)a^2}\right)\bar{\zeta}\right.$$
$$\left.+(\alpha+1)\left(\frac{1}{\alpha}-\frac{b^2-(\alpha+1)a^2}{2b^2-(\alpha+1)a^2}\right)\frac{a^2}{b^2}\left(\bar{\zeta}-\frac{b^2}{\zeta}\right)\right]\frac{1}{z^2}$$
$$+2\left[-\frac{\kappa+1}{\alpha}a^2+\frac{b^4}{b^2-\alpha a^4}\frac{\alpha-1}{\kappa+1}a^2\right.$$
$$\left.\left.+\frac{\alpha a^4}{b^4-\alpha a^4}\left(b^2+\frac{\alpha a^4}{b^4}\zeta\left(\bar{\zeta}-\frac{b^2}{\zeta}\right)\right)\right]\frac{1}{z^3}\right\}$$
$$+\overline{A}\left\{-\frac{\kappa}{z-\zeta}+\frac{\kappa}{z}-\frac{1}{z-b^2/\bar{\zeta}}-\alpha\left[\frac{1}{z-a^2/\bar{\zeta}}-\frac{1}{z}\right]\right.$$
$$-\alpha\kappa\left[\frac{1}{z-a^2\zeta/b^2}-\frac{1}{z}\right]-\frac{1}{\alpha}\left(\zeta-\frac{a^2}{\bar{\zeta}}\right)\frac{z-3a^2/\zeta}{(z-a^2/\bar{\zeta})^3}$$
$$-\frac{\kappa}{\alpha}\frac{b^2-a^2}{b^2}\zeta\frac{z-3a^2\zeta/b^2}{(z-a^2\zeta/b^3)^2}-\left(\zeta-\frac{b^2}{\bar{\zeta}}\right)\frac{z-3b^2/\bar{\zeta}}{(z-b^2/\bar{\zeta})^3}$$
$$+\left[(\kappa+1)\left(\alpha\frac{a^2}{b^2}+\frac{b^2-a^2}{\alpha b^2}+\frac{b^2-(\alpha+1)a^2}{2b^2-(\alpha+1)a^2}\right)\zeta\right.$$
$$\left.+(\alpha+1)\left(\frac{1}{\alpha}-\frac{b^2-(\alpha+1)a^2}{2b^2-(\alpha+1)a^2}\right)\frac{a^2}{b^2}\left(\zeta-\frac{b^2}{\bar{\zeta}}\right)\right]\frac{1}{z^2}$$
$$\left.-\frac{(\alpha a^4)^2}{b^4(b^4-\alpha a^4)}\left(\kappa\zeta^2+\frac{b^4}{\bar{\zeta}^2}\right)\frac{1}{z^3}\right\}\frac{a^2}{z^2}Q(z). \quad \text{(A2)}$$

The Kolosov potentials for the dislocation are:

$$\Phi(z)=A\left\{\frac{1}{z-\zeta}-\frac{1}{\alpha}\left[\frac{1}{z-a^2/\bar{\zeta}}-\frac{1}{z-a^2\zeta/b^2}\right]-\frac{1}{z-b^2\bar{\zeta}}\right.$$
$$\left.-\frac{a^2(b^2-a^2)}{\alpha b^6}\zeta^2\left(\bar{\zeta}-\frac{b^2}{\zeta}\right)\frac{3z-a^2\zeta/b^2}{(z-a^2\zeta/b^2)^3}\right.$$
$$\left.+\frac{\alpha a^4}{b^4(b^4-\alpha a^4)}\left(\bar{\zeta}^2-\frac{b^4}{\zeta^2}\right)z\right\}$$
$$+\overline{A}\left\{\frac{1}{\alpha}\frac{a^2}{\bar{\zeta}^2}\left(\zeta-\frac{a^2}{\bar{\zeta}}\right)\frac{1}{(z-a^2/\bar{\zeta}^2)^2}-\frac{1}{\alpha}\frac{a^2(b^2-a^2)}{b^6}\zeta^3\frac{1}{(z-a^2\zeta/b^2)^2}\right.$$
$$+\frac{b^2}{\bar{\zeta}^2}\left(\zeta-\frac{b^2}{\bar{\zeta}}\right)\frac{1}{(z-b^2/\bar{\zeta})^2}-2\frac{b^2-(\alpha+1)a^2}{2b^2-(\alpha+1)a^2}\frac{1}{b^2}\left(\zeta-\frac{b^2}{\bar{\zeta}}\right)$$
$$\left.+\frac{2\alpha a^4}{b^4(b^4-\alpha a^4)}\bar{\zeta}\left(\zeta-\frac{b^2}{\bar{\zeta}}\right)z\right\}+P(z) \quad \text{(A3)}$$

and

$$\Psi(z)=A\left\{\frac{\bar{\zeta}}{(z-\zeta)^2}-\frac{\bar{\zeta}}{(z-b^2/\bar{\zeta})^2}-\frac{1}{\alpha}\left[\frac{\bar{\zeta}}{(z-a^2/\bar{\zeta})^2}-\right.\right.$$
$$\left.\frac{b^2/\zeta}{(z-a^2\zeta/b^2)^2}\right]+\alpha\frac{a^2}{b^2}\left(\bar{\zeta}-\frac{b^2}{\zeta}\right)\frac{1}{(z-a^2\zeta/b^2)^2}$$
$$+\frac{b^2-a^2}{\alpha b^2}\left(\bar{\zeta}-\frac{b^2}{\zeta}\right)\frac{z^2-4(a^2\zeta/b^2)z-3(a^2\zeta/b^2)^2}{(z-a^2\zeta/b^2)^4}$$
$$-(\alpha+1)\left(\frac{\alpha-1}{\alpha}-\frac{b^2}{2b^2+(\kappa-1)a^2}\right)\frac{a^2}{b^2}\left(\bar{\zeta}-\frac{b^2}{\zeta}\right)\frac{1}{z^2}$$
$$\left.+\frac{2(\alpha a^4)^2}{b^4(b^4-\alpha a^4)}\zeta\left(\bar{\zeta}-\frac{b^2}{\zeta}\right)\frac{1}{z^3}\right\}$$
$$+\overline{A}\left\{-\frac{1}{z-\zeta}-\frac{1}{z-b^2/\bar{\zeta}}-\alpha\left[\frac{1}{z-a^2/\bar{\zeta}}-\frac{1}{z-a^2\zeta/b^2}\right]\right.$$
$$-\frac{1}{\alpha}\left(\zeta-\frac{a^2}{\bar{\zeta}}\right)\frac{z-3a^2\bar{\zeta}}{(z-a^2/\bar{\zeta})^3}+\frac{b^2-a^2}{\alpha b^2}\zeta\frac{z-3a^2\zeta/b^2}{(z-a^2\zeta/b^2)^3}$$
$$-\left(\zeta-\frac{b^2}{\bar{\zeta}}\right)\frac{z-3b^2/\bar{\zeta}}{(z-b^2/\bar{\zeta})^2}$$
$$-(\alpha+1)\left(\frac{a^2-1}{\alpha}-\frac{b^2}{2b^2+(\kappa-1)a^2}\right)\frac{a^2}{b^2}\left(\zeta-\frac{b^2}{\bar{\zeta}}\right)\frac{1}{z^2}$$
$$\left.+\frac{(\alpha a^4)^2}{b^4(b^4-\alpha a^4)}\left(\zeta^2-\frac{b^4}{\bar{\zeta}^2}\right)\frac{1}{z^3}\right\}+\frac{a^2}{z^2}Q(z), \quad \text{(A4)}$$

where a is the inner radius and b is the outer radius of the annulus, ζ is the point at which the point load or dislocation is applied, z is the point where the stresses are measured, and A is defined for the point load or the dislocation in Eq. (3). The functions $P(z)$ and $Q(z)$ are Laurent series in z and are defined as follows,

$$P(z)=\sum_{n=2}^{\infty}p_n z^n+p_{-n}z^{-n} \quad \text{(A5)}$$

and

$$Q(z)=\sum_{n=2}^{\infty}q_n z^n+q_{-n}z^{-n} \quad \text{(A6)}$$

where

$$p_n=\frac{A}{D}\left\{-(n^2-1)f_1\left(\bar{\zeta}-\frac{a^2}{\zeta}\right)\frac{1}{\zeta^n}-f_2\frac{a^2}{\zeta}\frac{1}{\zeta^n}+\beta f_4\bar{\zeta}\left(\frac{\bar{\zeta}}{b^2}\right)^n\right\}$$
$$+\frac{\overline{A}}{D}(n+1)\left\{f_4\left(\zeta-\frac{b^2}{\bar{\zeta}}\right)\left(\frac{\bar{\zeta}}{b^2}\right)^n-f_1\frac{b^2}{\zeta}\left(\frac{\bar{\zeta}}{b^2}\right)^n+\beta f_1\zeta\frac{1}{\zeta^n}\right\}, \quad \text{(A7)}$$

$$p_{-n}=\frac{A}{D}\Bigg\{-(n^2-1)f_6\left(\bar{\zeta}-\frac{b^2}{\zeta}\right)\left(\frac{a^2}{b^2}\zeta\right)^n f_5\frac{b^2}{\zeta}\left(\frac{a^2}{b^2}\zeta\right)^n - \beta f_5\bar{\zeta}\left(\frac{a^2}{\bar{\zeta}}\right)^n\Bigg\}+\frac{\overline{A}}{D}(n-1)\Bigg\{f_5\left(\zeta-\frac{a^2}{\bar{\zeta}}\right)\left(\frac{a^2}{\bar{\zeta}}\right)^n + \alpha f_1\frac{a^2}{\bar{\zeta}}\left(\frac{a^2}{\bar{\zeta}}\right)^n-\beta f_6\zeta^n\left(\frac{a^2}{b^2}\zeta\right)^n\Bigg\}, \quad \text{(A8)}$$

$$q_n=\frac{A}{D}(n-1)\Bigg\{f_7\left(\bar{\zeta}-\frac{a^2}{\zeta}\right)\frac{1}{\zeta^n}+f_8\frac{a^2}{\zeta}\frac{1}{\zeta^n}-\beta f_9\bar{\zeta}\left(\frac{\bar{\zeta}}{b^2}\right)^n\Bigg\} + \frac{\overline{A}}{D}\Bigg\{-(n^2-1)f_9\left(\zeta-\frac{b^2}{\bar{\zeta}}\right)\left(\frac{\bar{\zeta}}{b^2}\right)^n+f_7\frac{b^2}{\bar{\zeta}}\left(\frac{\bar{\zeta}}{b^2}\right)^n-\beta f_7\zeta\frac{1}{\zeta^n}\Bigg\}, \quad \text{(A9)}$$

and

$$q_{-n}=\frac{A}{D}(n+1)\Bigg\{-f_{12}\left(\bar{\zeta}-\frac{b^2}{\zeta}\right)\left(\frac{a^2}{b^2}\zeta\right)^n + f_{10}\frac{b^2}{\zeta}\left(\frac{a^2}{b^2}\zeta\right)^n-\beta f_{10}\bar{\zeta}\left(\frac{a^2}{\bar{\zeta}}\right)^n\Bigg\}+\frac{\overline{A}}{D}\Bigg\{(n^2-1)f_{10}\left(\zeta-\frac{a^2}{\bar{\zeta}}\right)\left(\frac{a^2}{\bar{\zeta}}\right)^n + f_{11}\frac{a^2}{\bar{\zeta}}\left(\frac{a^2}{\bar{\zeta}}\right)^n-\beta f_{12}\zeta\left(\frac{a^2}{b^2}\zeta\right)^n\Bigg\}, \quad \text{(A10)}$$

where

$$D=(b^2b^{2n}-\alpha a^2a^{2n})(\alpha a^2b^{2n}b^2a^{2n}) - (n^2-1)a^{2n}b^{2n}(b^2-a^2), \quad \text{(A11)}$$

$$f_1=a^{2n}b^{2n}(b^2-a^2), \quad \text{(A12)}$$

$$f_2=\alpha a^{2n}(\alpha a^2b^{2n}-b^2a^{2n}), \quad \text{(A13)}$$

$$f_3=a^{2n}(b^2b^{2n}-\alpha a^2a^{2n}), \quad \text{(A14)}$$

$$f_4=(n^2-1)\rho f_1+\frac{a^2}{b^2}f_2, \quad \text{(A15)}$$

$$f_5=\frac{b^2}{\alpha a^2}\left((n^2-1)\rho f_1+f_3\right), \quad \text{(A16)}$$

$$f_6=\rho f_5+\frac{\alpha a^2}{b^2}f_1, \quad \text{(A17)}$$

$$f_7=\frac{b^2}{a^2}\left((n^2-1)f_1+f_3\right), \quad \text{(A18)}$$

$$f_8=\alpha b^2a^{2n}(\alpha b^{2n}-a^{2n}), \quad \text{(A19)}$$

$$f_9=\rho f_7+\frac{a^2}{b^2}f_8, \quad \text{(A20)}$$

$$f_{10}=f_5-\alpha f_1, \quad \text{(A21)}$$

$$f_{11}=\alpha\left((n^2-1)f_1-f_2\right), \quad \text{(A22)}$$

$$f_{12}=(n^2-1)\rho f_{10}+\frac{a^2}{b^2}f_{11}, \quad \text{(A23)}$$

and

$$\rho=\frac{b^2-a^2}{b^2}. \quad \text{(A24)}$$

V. M. Gharpuray
Department of Bioengineering,
Clemson University,
Clemson, SC 29634-0905

J. Dundurs
Fellow ASME.

L. M. Keer
Fellow ASME.

Departments of Civil and Mechanical Engineering,
Northwestern University,
Evanston, IL 60208

A Crack Terminating at a Slipping Interface Between Two Materials

The paper investigates an edge crack that terminates at a slipping interface with a different material. The formulation is reduced to a singular integral equation. The integral equation is solved and the stress intensity factor extracted using a numerical method. Moreover, the asymptotic nature of the stresses at the open tip of the crack is studied.

Introduction

It is often observed in experiments dealing with bone implants that the bond at an interface breaks before the formation of cracks (Gharpuray et al., 1990). This may happen either on the bone side or the implant side of the material used to provide adhesion. Moreover, the subsequent cracks appear to emanate from the interfaces that, after debonding, allow slip. This suggests that it is worthwhile to analyze the interaction of an edge crack with a slipping interface.

The problem is formulated using a continuous distribution of dislocations which leads to a singular integral equation. The singularity at the open end of the crack that touches the interface is studied using the Williams technique. The integral equation is solved and the stress intensity factor extracted using a numerical method.

Formulation of the Problem

As shown in Fig. 1, let region 1 with shear modulus μ_1 and Poisson's ratio ν_1 be the half plane containing the crack and region 2 with shear modulus μ_2 and Poisson's ratio ν_2 be the half plane without the crack. The crack of length c emanates from the frictionless interface at an angle θ to the positive x-axis. The half plane 1 is loaded by a constant tensile stress T at infinity, as shown in Fig. 1, while the two half planes are pressed together normal to the interface. The boundary conditions to be satisfied in this problem are:

On the interface ($x = 0$),

$$u_x^{(1)}(0, y) = u_x^{(2)}(0, y)$$

$$\sigma_{xx}^{(1)}(0, y) = \sigma_{xx}^{(2)}(0, y)$$

$$\sigma_{xy}^{(1)}(0, y) = \sigma_{xy}^{(2)}(0, y) = 0. \tag{1}$$

Along the crack ($0 < r < c$),

$$\sigma_{r\theta}^{(1)}(r,\theta) = 0$$

$$\sigma_{\theta\theta}^{(1)}(r,\theta) = 0. \tag{2}$$

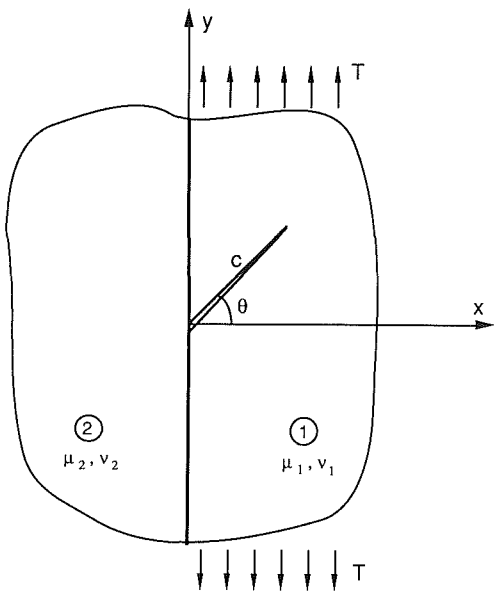

Fig. 1 Geometry of the problem for a finite crack

Contributed by the Applied Mechanics Division of THE AMERICAN SOCIETY OF MECHANICAL ENGINEERS for presentation at the Winter Annual Meeting, Atlanta, Ga., Dec. 1-6, 1991.

Discussion on this paper should be addressed to the Technical Editor, Prof. Leon M. Keer, The Technological Institute, Northwestern University, Evanston, IL 60208, and will be accepted until two months after final publication of the paper itself in the JOURNAL OF APPLIED MECHANICS. Manuscript received by the ASME Applied Mechanics Division, Feb. 9, 1990; final revision, Oct. 29, 1990.
Paper No. 91-WA/APM-3.

The crack is represented as an unknown continuous distribution of edge dislocations. This is most easily formulated in terms of the complex potentials $\phi(z)$ and $\psi(z)$, as defined by Muskhelishvili (1953), so that

$$\sigma_{rr}+\sigma_{\theta\theta}=2[\phi'(z)+\overline{\phi'(z)}]$$
$$\sigma_{\theta\theta}-\sigma_{rr}+2i\sigma_{r\theta}=2e^{2i\theta}[\bar{z}\phi''(z)+\psi'(z)]$$
$$2\mu(u_x+iu_y)=\kappa\phi(z)-z\overline{\phi'(z)}-\overline{\psi(z)} \quad (3)$$

where $z = x + iy = re^{i\theta}$, and $\kappa = 3 - 4\nu$ for plane strain, $\kappa = (3 - \nu)/(1 + \nu)$ for plane stress, with ν denoting Poisson's ratio.

The potentials for the discrete edge dislocation in the vicinity of a slipping interface between two half planes can be obtained from the concentrated force solution given by Dundurs (1962) and the correspondence between concentrated forces and edge dislocations (Dundurs 1968), and may be written as

$$\phi_1(z)=b\log(z-z_o)-(1-D)b\log(z+\bar{z}_o)-D\bar{b}\log(z+\bar{z}_o)-(1-D)\frac{\bar{b}(z_o+\bar{z}_o)}{z+\bar{z}_o}$$

$$\psi_1(z)=\bar{b}\log(z-z_o)-\frac{b\bar{z}_o}{z-z_o}-(1-D)\bar{b}\log(z+\bar{z}_o)-Db\log(z+\bar{z}_o)+(1-D)\frac{b\bar{z}_o}{z+\bar{z}_o}+(1-D)\frac{\bar{b}(z_o+\bar{z}_o)}{z+\bar{z}_o}-D\frac{\bar{b}z_o}{z+\bar{z}_o}-(1-D)\frac{b\bar{z}_o(z_o+\bar{z}_o)}{(z+\bar{z}_o)^2} \quad (4)$$

$$\phi_2(z)=D(b-\bar{b})\log(z-z_o)+D\frac{b(z_o+\bar{z}_o)}{z-z_o}$$

$$\psi_2(z)=D(\bar{b}-b)\log(z-z_o)-D\frac{b(z_o+2\bar{z}_o)}{z-z_o}-D\frac{\bar{b}z_o}{z-z_o}-D\frac{bz_o(z_o+\bar{z}_o)}{(z-z_o)^2} \quad (5)$$

where z_o specifies the position of the discrete dislocation in region 1, and with b_r and b_θ denoting the components of the Burgers vector,

$$b=\frac{\mu_1(b_\theta-ib_r)e^{i\theta}}{\pi(\kappa_1+1)}$$

$$D=\frac{\mu_2(\kappa_1+1)}{\mu_2(\kappa_1+1)+\mu_1(\kappa_2+1)}.$$

The subscripts 1 and 2 denote regions 1 and 2, respectively.

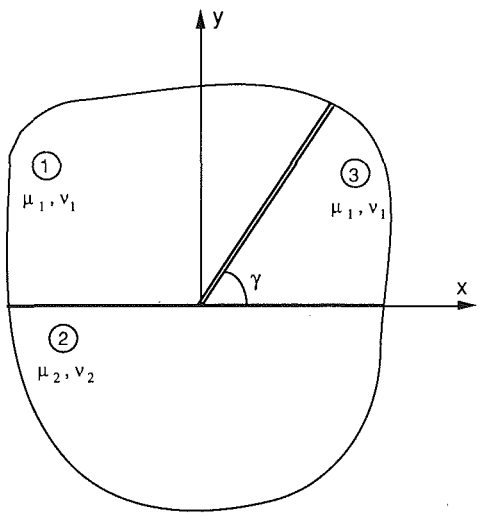

Fig. 2 Geometry of the problem for an infinite crack

By enforcing the condition of traction-free crack faces, a singular integral equation of the Cauchy type is obtained as

$$\int_0^c\left\{\frac{2\bar{B}(r)e^{i\theta}}{q-r}+B(r)K_1(q,r)+\bar{B}(r)K_2(q,r)\right\}dr+f(q)=0$$
$$0\le q\le c \quad (6)$$

where B_r and B_θ are now the unknown dislocation densities and $K_1(q, r)$, K_2 (q, r) are given in the Appendix. For the specific loading condition investigated in this paper,

$$f(q)=\frac{1}{2}T(1+e^{2i\theta}). \quad (7)$$

Equation (6) can be separated into its real and imaginary parts to obtain two coupled singular integral equations which must be solved for the unknown real-valued dislocation densities B_r and B_θ. These equations can be written as

$$\frac{1}{\pi}\int_0^c\frac{B_\theta(r)}{r-q}dr-\frac{1}{2\pi}\int_0^c\{B_\theta(r)\mathrm{Re}\,[K_1+K_2]+B_r(r)\mathrm{Im}\,[K_1-K_2]\}dr=\frac{\kappa_1+1}{2\mu_1}\mathrm{Re}\,[f(q)] \quad (8)$$

$$\frac{1}{\pi}\int_0^c\frac{B_r(r)}{r-q}dr+\frac{1}{2\pi}\int_0^c\{B_r(r)\mathrm{Re}\,[K_1-K_2]+B_\theta(r)\mathrm{Im}\,[K_1+K_2]\}dr=\frac{\kappa_1+1}{2\mu_1}\mathrm{Im}\,[f(q)]. \quad (9)$$

Since the crack terminates at an interface, the singularity at the crack tip touching the interface may not be of order $-1/2$. Hence, the crack-tip singularity should be determined before the numerical solution of (8) and (9) is attempted.

Stress Field Singularities at the Crack Tip

The length c of the crack in the problem indicated in Fig. 1 does not affect the nature of the stress singularity at the interface, and hence in the singularity investigation the crack can be viewed as of infinite length. The half plane with the crack can then be treated as two wedges pressed against the other half plane as shown in Fig. 2. Let 1 and 3 denote the two wedges that make up the cracked half plane, with μ_1 and ν_1 being their elastic constants, and let 2 denote the uncracked half plane with μ_2 and ν_2 being its elastic constants. The boundary conditions that must be satisfied for the three regions are

$$u_\theta^{(1)}(r,-\pi)=u_\theta^{(2)}(r,-\pi)$$
$$\sigma_{r\theta}^{(1)}(r,-\pi)=\sigma_{r\theta}^{(2)}(r,-\pi)=0$$
$$\sigma_{\theta\theta}^{(1)}(r,-\pi)=\sigma_{\theta\theta}^{(2)}(r,-\pi) \quad (10)$$
$$\sigma_{r\theta}^{(1)}(r,\gamma-2\pi)=0$$
$$\sigma_{\theta\theta}^{(1)}(r,\gamma-2\pi)=0 \quad (11)$$
$$\sigma_{r\theta}^{(3)}(r,\gamma)=0$$
$$\sigma_{\theta\theta}^{(3)}(r,\gamma)=0 \quad (12)$$
$$u_\theta^{(3)}(r,0)=u_\theta^{(2)}(r,0)$$
$$\sigma_{r\theta}^{(3)}(r,0)=\sigma_{r\theta}^{(2)}(r,0)=0$$
$$\sigma_{\theta\theta}^{(3)}(r,0)=\sigma_{\theta\theta}^{(2)}(r,0). \quad (13)$$

The nature of the singularity can be determined by employing the Mellin transform, as explained by Bogy (1971), or by simply using the Williams (1959) technique. Convenient for the latter approach are the elastic fields tabulated by Comninou (1977).

The results of the asymptotic analysis are as follows: The

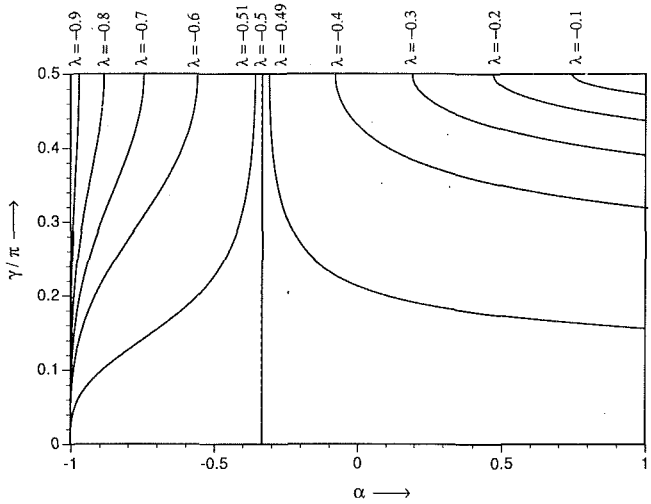

Fig. 3 Roots of $\Delta(\lambda;\alpha,\gamma)$ for $-1<\lambda<0$

stresses in the vicinity of the crack tip touching the interface are of the form

$$\sigma_{ij}=r^{\lambda}f_{ij}(\theta), \quad r\to 0. \tag{14}$$

The exponent λ is determined by the condition that the determinant of the homogeneous system that follows from the boundary conditions (10)–(13) vanishes. Omitting the multiplier $2[\mu_2(\kappa_1+1)+\mu_1(\kappa_2+1)]\sin^2(\lambda\pi)$, the determinant is

$$\begin{aligned}\Delta(\lambda;\alpha,\gamma)=&\,2\lambda(2+\lambda)(1-\alpha)^2\sin^2\gamma\,[\lambda(2+\lambda)\sin^2\gamma-\cos 2\gamma]\\&+2\lambda(2+\lambda)(1+\alpha)^2\sin^2\gamma\cos^2\gamma\\&+2\lambda(2+\lambda)(1-\alpha)\sin^2\gamma\,\{\cos[2(1+\lambda)\gamma]\\&+\cos[2\lambda\pi-2(1+\lambda)\gamma]\}\\&+\lambda(1+\alpha)\sin 2\gamma\,\{\sin[2(1+\lambda)\gamma]\\&-\sin[2\lambda\pi-2(1+\lambda)\gamma]\}\\&-4\sin[(2+\lambda)\gamma]\sin[\lambda\pi-(2+\lambda)\gamma]\,\{\cos\lambda\pi\\&+\cos[\lambda(\pi-2\gamma)]\}\end{aligned} \tag{15}$$

where γ is the angle the crack makes with the interface, and

$$\alpha=\frac{\mu_2(\kappa_1+1)-\mu_1(\kappa_2+1)}{\mu_2(\kappa_1+1)+\mu_1(\kappa_2+1)}.$$

The first observation that can be made is that Δ depends on the single composite parameter α. This is not a coincidence, but rather follows from some general properties of frictionless contact along a straight interface (Dundurs, 1975). Although complicated in λ and γ, it is seen from (15) that the expression for Δ is a simple quadratic in α. Thus, it is easy to obtain the loci of λ = constant in the α, γ plane by selecting the values of λ and γ and computing the corresponding value of α. The results of the computation are shown in Fig. 3 for $-1<\mathrm{Re}(\lambda)<0$. The question of complex roots is left open since the study of real roots in this range appears of greater concern.

The computations reveal that only a single real root $-1<\lambda<0$ exists in the physical range $(0<\gamma<\pi,\ -1\le\alpha\le 1)$ of the problem. Thus, there is no singularity at the crack tip for the mode when the crack faces move in a direction parallel to the interface while for the mode perpendicular to the interface, the stress singularity has the order shown in Fig. 3.

It may be of interest to note that the singularity at the open end of the crack is not directly related to the singularities of two wedges that are pressed against a surface. If two wedges with angles that add to π are a finite distance apart, the orders of the two singularities at the vertices are those given by Dundurs and Lee (1972) and are generally different. As the two wedges are allowed to approach each other, we have what might be called an interaction between two geometric singularities, the apparent result being that the resulting common singularity is associated with an entirely different value of λ even in the case of $\gamma=\pi/2$.

For the special case when the crack is perpendicular to the interface, or $\gamma=\pi/2$, $\Delta(\lambda;\alpha,\pi/2)$ factors as

$$\cdot\Delta(\lambda;\alpha,\pi/2)=\Delta_1(\lambda;\alpha)\cdot\Delta_2(\lambda;\alpha) \tag{16}$$

where

$$\begin{aligned}\Delta_1(\lambda;\alpha)&=\cos(\lambda\pi)+\alpha-2(1-\alpha)\lambda-(1-\alpha)\lambda^2\\ \Delta_2(\lambda;\alpha)&=\cos(\lambda\pi)-1-2(1-\alpha)\lambda-(1-\alpha)\lambda^2.\end{aligned}$$

The roots of Δ_1 correspond to crack-tip singularities for the symmetric or mode I crack, and those of Δ_2 correspond to crack-tip singularities for the antisymmetric or mode II crack. It is found that Δ_2 has roots for $-1<\lambda<0$, whereas Δ_1 does not, which means that the mode I crack for $\gamma=\pi/2$ has no singularity at the crack tip touching the interface.

It is of interest to note here that when $\gamma=\pi/2$ (or $\theta=0$ as in Fig. 1), the two coupled equations in B_θ and B_r, (8) and (9), decouple to two equations, one each in B_θ and B_r. Employing the method used by Erdogan and Biricikoglu (1973) to find the singularity at the crack tip at the interface gives the same result as obtained from (15). From the equation for B_θ,

$$\Delta_1(\lambda;\alpha)=0 \tag{17}$$

and from the equation for B_r,

$$\Delta_2(\lambda;\alpha)=0. \tag{18}$$

The same result is also obtained in the study by Dempsey and Sinclair (1981).

Stresses Near the Crack Tip and Stress Intensity Factors

Once the zeros of Δ are obtained, stresses near the crack tip at the interface are obtained in a straightforward manner in terms of a free constant by back substituting into the simultaneous equations previously obtained. The normal stresses across the interface are found to be always positive on one side of the crack and negative on the order; thus, the crack will always cause separation of the interface. The only exception to this rule is for the symmetric mode I crack normal to the interface where normal stresses across the interface are always compressive if the free constant is chosen to be negative. Separation at the interface is not considered here, and hence stress intensity factors are given only for the special case of the symmetric mode I crack.

Once the crack is assumed to be a mode I crack normal to the interface, equation (9) becomes trivial and equation (8) gives the Cauchy singular equation to be solved as

$$\frac{1}{\pi}\int_0^c\left\{\frac{1}{q-r}-\frac{1}{q+r}-2(1-D)\frac{r(q-r)}{(q+r)^3}\right\}B_y(r)dr+\frac{\kappa_1+1}{2\mu_1}T=0$$

$$0\le q\le c. \tag{19}$$

This equation is solved numerically using the method described by Gerasoulis (1982). At first the limits of integration are changed to $(-1, 1)$ by the substitution

$$q=\frac{1}{2}c(s+1), \quad r=\frac{1}{2}c(t+1). \tag{20}$$

Then, assuming square root singularities at both ends of the crack, the unknown dislocation density may be expressed as

$$B_y(t)=g(t)(1-t^2)^{-1/2}, \tag{21}$$

where $g(t)$ is regular in $(-1, 1)$. The function $g(t)$ is then approximated by piecewise quadratic polynomials and the re-

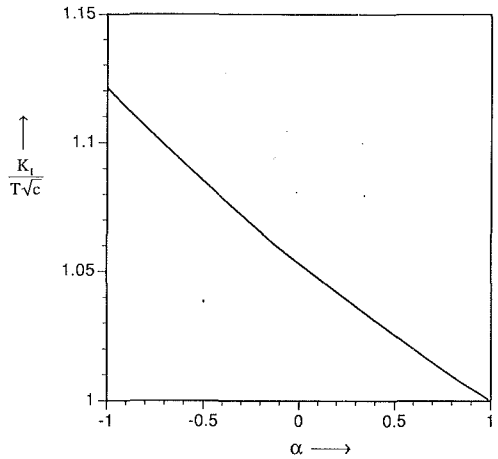

Fig. 4 Stress intensity factors for a crack normal to a slipping interface for different combinations of materials

sulting system of linear simultaneous equations is solved to get $g(t)$ at selected collocation points in the interval $(-1, 1)$. However, an additional condition is required to solve the singular integral equation. This is taken as

$$g(-1)=0 \tag{22}$$

in order to remove the square root singularity at the tip of the crack touching the interface.

Once equation (19) is solved for the unknown dislocation density $B_y(t)$, stress intensity factors are calculated from the expressions given by Erdogan (1983) as

$$K_I=\frac{2\mu_1}{\kappa_1+1}\lim_{r\to c}[2(c-r)]^{1/2}B_y(r). \tag{23}$$

On substitution for $B_y(r)$, (23) becomes

$$\frac{K_I}{T\sqrt{c}}=\frac{g(t=1)}{\sqrt{2}}. \tag{24}$$

The resulting mode I stress intensity factors for different values of material constants are shown in Fig. 4. It can be seen that for $\alpha = -1$ (i.e., $\mu_2/\mu_1 = 0$ or the edge crack in a half plane), the expected value of $K_I = 1.12$ (Paris and Sih, 1965) is obtained. For the case of $\alpha = 1$ (i.e., $\mu_2/\mu_1 = \infty$ or when the half plane not containing the crack is rigid), the stress intensity factor obtained is 1. This is as expected since the full rigidity of the abutting half plane causes normal displacements to vanish, and the problem reduces to that of a Griffith crack due to symmetry.

Acknowledgment

Two of the authors (LMK and VMG) were supported by the National Science Foundation.

References

Comninou, M., 1977, "The Interface Crack," ASME JOURNAL OF APPLIED MECHANICS, Vol. 44, pp. 631-636.

Dempsey, J. P., and Sinclair, G. B., 1981, "On the Singular Behavior at the Vertex of a Bi-material Wedge," *Journal of Elasticity*, Vol. 11, pp. 317-327.

Dundurs, J., 1962, "Force in Smoothly Joined Elastic Half-Planes," *Journal of the Engineering Mechanics Division, Proceedings of the ASCE*, Vol. 88, pp. 25-40.

Dundurs, J., 1968, "Analogy between Concentrated Forces and Edge Dislocations," *Journal of Applied Physics*, Vol. 39, pp. 4152-4156.

Dundurs, J., 1975, "Properties of Elastic Bodies in Contact," *The Mechanics of the Contact Between Deformable Bodies*, A. D. de Pater and J. J. Kalker, eds., Delft University Press.

Dundurs, J., and Lee M.-S., 1972, "Stress Concentration at a Sharp Edge in Contact Problems," *Journal of Elasticity*, Vol. 2, pp. 109-112.

Erdogan, F., 1983, "Stress Intensity Factors," ASME JOURNAL OF APPLIED MECHANICS, Vol. 50, pp. 992-1002.

Erdogan, F., and Biricikoglu, V., 1973, "Two Bonded Half Planes with a Crack Going Through the Interface," *International Journal of Engineering Science*, Vol. 11, pp. 745-766.

Gerasoulis, A., 1982, "The Use of Piecewise Quadratic Polynomials for the Solution of Singular Integral Equations of the Cauchy Type," *Computers and Mathematics with Applications*, Vol. 8, pp. 15-22.

Gharpuray, V. M., Keer, L. M., and Lewis, J. L., 1990, "Crack Emanating from Circular Voids or Elastic Inclusions in PMMA Near a Bone-Implant Interface," *ASME Journal of Biomechanical Engineering*, Vol. 112, pp. 22-28.

Muskhelishvili, N. I., 1954, *Some Basic Problems of the Mathematical Theory of Elasticity*, 4th ed., Noordhoff.

Paris, P. C., and Sih., G. C., 1965, "Stress Analysis of Cracks," *ASTM STP*, Vol. 391, pp. 38-81.

Williams, M. L., 1959, "The Stress Around a Fault or Crack in Dissimilar Media," *Bulletin of the Seismological Society of America*, Vol. 49, pp. 199-204.

APPENDIX

$$K_1(q,r)=-(1-D)\frac{1}{z+\bar{z}_o}-D\frac{1}{\bar{z}+z_o}+(1-D)\frac{z_o+\bar{z}_o}{(z+\bar{z}_o)^2}+(1-D)\frac{\bar{z}\,e^{2i\theta}}{(z+\bar{z}_o)^2}-D\frac{e^{2i\theta}}{z+\bar{z}_o}-(1-D)\frac{\bar{z}_o e^{2i\theta}}{(z+\bar{z}_o)^2} \tag{A1}$$

$$K_2(q,r)=-D\frac{1}{z+\bar{z}_o}+(1-D)\frac{z_o+\bar{z}_o}{(z+\bar{z}_o)^2}-(1-D)\frac{1}{\bar{z}+z_o}+D\frac{\bar{z}e^{2i\theta}}{(z+\bar{z}_o)^2}-2(1-D)\frac{(z_o+\bar{z}_o)\,\bar{z}e^{2i\theta}}{(z+\bar{z}_o)^3}-(1-D)\frac{e^{2i\theta}}{z+\bar{z}_o}+D\frac{z_o e^{2i\theta}}{(z+\bar{z}_o)^2}-(1-D)\frac{(z_o+\bar{z}_o)e^{2i\theta}}{(z+\bar{z}_o)^2}+2(1-D)\frac{(z_o+\bar{z}_o)\bar{z}_o e^{2i\theta}}{(z+\bar{z}_o)^3} \tag{A2}$$

A Micromechanics Analysis of Cracks in Unidirectional Fiber Composites

Jalees Ahmad
Battelle Memorial Institute,
Columbus, OH 43201-2963

The elastic problem of a crack normal to a bimaterial interface is addressed in the context of unidirectional fiber composites. The structure of asymptotic crack-tip stress fields is obtained numerically. The numerical results are then analyzed to formulate criteria for assessing cracking normal to the fiber, interface splitting, and fiber pull-out.

Introduction

Failure in fiber composites is often a result of damage which starts close to an existing notch or a crack. The objective of the present work is to investigate how the concepts of linear elastic fracture mechanics (LEFM) of homogeneous materials can be exploited in characterizing crack-tip damage in (non-homogeneous) fiber composite materials. Specifically, the plane-strain problem of a crack with its tip at or close to a bimaterial interface is considered. The crack resides entirely in one material (designated as material 2 in Fig. 1) and is normal to the interface. Both materials 1 and 2 are assumed to be elastic and isotropic.

The problem depicted in Fig. 1 (*a*) has been addressed in a number of articles. For example, see Zak and Williams (1963), Bogy (1971), Fenner (1976), and Cook and Erdogan (1972). Using the eigenfunction expansion method and Mellin transform, these articles provide the form of the crack-tip stress and deformation fields as $r \to o$. The key result of these investigations is that as the crack tip is approached, the stress field under opening mode (Mode I) loading is of the following form:

$$\sigma_{ij} = Q_I (r)^{\lambda - 1} g_{ij}(\theta, \alpha, \beta) \tag{1}$$

in which α and β are the bimaterial constants of Dundurs (1969) and $o \leq \lambda(\alpha, \beta) \leq 1$ is the smallest real root of the following equation:

$$2\lambda^2(\alpha - \beta)(\beta + 1) - \alpha + \beta^2 + (1 - \beta^2)\cos(\lambda\pi) = 0. \tag{2}$$

The functions g_{ij} are unobtainable in closed form (unlike in the homogeneous case), but can be found numerically. Q_I, the intensity of the singular crack-tip stress field, is determined using the boundary conditions for a specific problem. Note that Q_I would be called the Mode I stress intensity factor (K_I) of LEFM if the two materials were the same. In that case, both α and β would be zero and λ would be equal to 1/2.

Values of K_I for specific boundary value problems of a crack whose tip is close to the interface (Fig. 1 (*b*)) have been given by Cook and Erdogan (1972), Isida (1970), and Erdogan and Bakioglu (1976). In this case, the crack-tip stress field is exactly the same as for a crack in a homogeneous solid (Williams, 1972), that is

$$\sigma_{ij} = K_I \cdot r^{-1/2} \cdot G_{ij}(\theta). \tag{3}$$

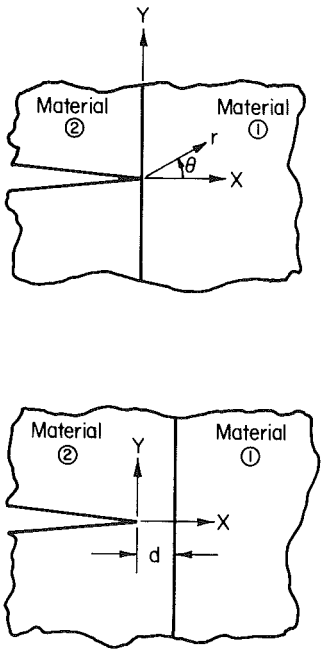

Fig. 1 The plane problem of a crack normal to a bimaterial interface with crack tip (*a*) at the interface, and (*b*) close to the interface

Contributed by the ASME Applied Mechancis Division of THE AMERICAN SOCIETY OF MECHANICAL ENGINEERS for presentation at the Winter Annual Meeting, Atlanta, Ga., Dec. 1-6, 1991.

Discussion on this paper should be addressed to the Technical Editor, Prof. Leon M. Keer, The Technological Institute, Northwestern University, Evanston, IL 60208, and will be accepted until two months after final publication of the paper itself in the JOURNAL OF APPLIED MECHANICS. Manuscript received by the ASME Applied Mechanics Division, Nov. 1, 1989; final revision, Sept. 7, 1990.

Paper No. 91-WA/APM-6.

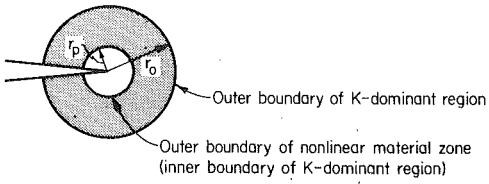

Fig. 2 The *K*-dominant region (shaded)

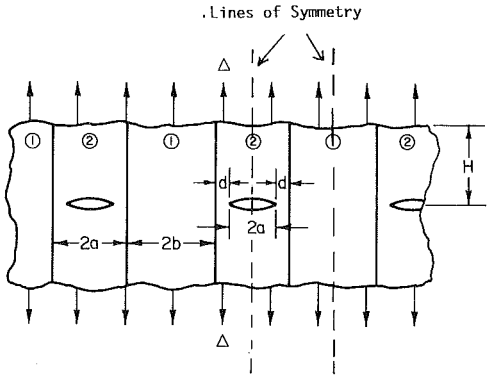

Fig. 3 The boundary value problem solved by finite element method (FEM) with $d = 0.0$ (Problem A) and $d \ll a$ (Problem B) and zero normal displacement at $X = \pm\infty$

In fracture mechanics, a macroscopic characteristic length must always be associated with the asymptotic crack-tip fields. This characteristic length (c) is the shortest of the nonzero distances from the crack tip to any of the boundaries of the solid containing the crack, and to the nearest point of load application. In a bimaterial system, the nearest boundary could be the bimaterial interface. For a given boundary value problem, the length c may be used to scale the intensity (Q_I or K_I) of the crack-tip stress fields. But more generally, c helps define a radial distance $r_o \ll c$ beyond which Eqs. (1) and (3) no longer accurately represent stress fields. For the homogeneous material case, r_o (Fig. 2) is often referred to as the outer boundary of K-dominant region. The validity of Eqs. (1) and (2) prevails over an annular region which encompasses the fracture process zone of dimension L_m and the inevitably present zone of inelastic deformation, r_p (Fig. 2). As long as r_o is large compared to smaller scale heterogeneities (e.g., interface thickness, interface irregularities, and grain sizes of materials), the condition for the validity of Eqs. (1) and (2) may be stated as: $(r_o - r_p) \gg L_m$. Later in this paper these concepts are called upon to discuss relevance of the numerical results.

In the present paper, we investigate the efficacy of Q_I for analyzing the behavior of cracks in bimaterial systems. We first focus on finding the outer boundary of Q-dominant region for the specific boundary value problem shown in Fig. 3 using the finite element method (FEM). Then, the results are generalized to other geometrical configurations by normalizing the r_o for various material combinations by a characteristic length (c). Next, the numerical results are used to assess the relative tendencies of cracks to propagate in self-similar fashion, cause splitting of the interface, or cause fiber pull-out.

Numerical Study

Numerical solutions for both Problem A and Problem B (Fig. 3) were obtained by the displacement finite element method. Eight-node isoparametric elements of general quadrilateral shape were employed. The quadratic shape functions for these elements can be found on page 131 of Bathe (1976). The elements contain four corner and four midside nodes. Element stiffness matrices were generated using 3×3 Gaussian quadrature and assuming plane-strain condition. The global stiffness equation was solved using the Gauss elimination method. The finite element discretization domain is bounded by the dashed lines shown in Fig. 3.

Table 1 Summary of numerical results

Case	α	β	λ	$\bar{f}$	$\bar{Q}$	r_o/c	$\frac{\mu_1/\mu_2}{(\nu=0.3)}$
A-1	0.00000	0.00000	0.5000	3.128	1.2650	10^{-1}	1.000
A-2	-0.81818	-0.23377	0.6672	4.420	0.0712	10^{-4}	10.000
A-3	-0.98020	-0.28006	0.7061	29.750	0.0010	10^{-10}	100.000
A-4	0.81818	0.23377	0.2464	14.340	4.3915	0.6	0.100
A-5	0.98020	0.28006	0.0852	119.800	7.1271	0.8	0.010
A-6	0.72843	0.20812	0.2942	9.854	3.7362	0.5	0.157
A-7	-0.72843	-0.20812	0.6471	3.473	0.1452	10^{-3}	6.365
B-1	-0.72843	-0.20812	0.5	3.128	0.9366	0.1	6.365
B-2	-0.72843	-0.20812	0.5	3.128	0.6557	0.1	6.365

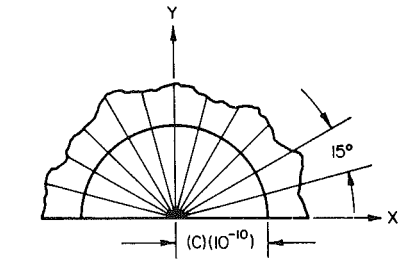

4a.

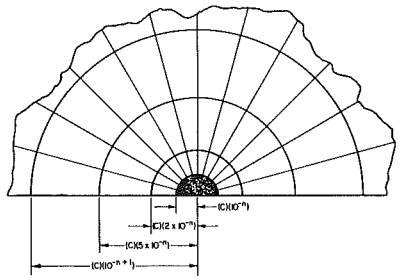

4b.

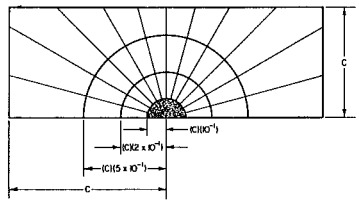

4c.

Fig. 4 Finite element mesh close to the crack tip

For Problem A, solutions were obtained for the seven different material combinations designated (A-1 to A-7) in Table 1. In each case, the crack length (a) was taken to be equal to the material 1 width (b). Uniform displacement (Δ) was applied at a distance of 10 times b ($H/b = 10.0$). The material combinations in Table 1 are given in terms of Dundurs' parameters, defined as:

$$\alpha = \frac{\mu_2 m_1 - \mu_1 m_2}{\mu_1 m_2 + \mu_2 m_1} \tag{4}$$

$$\beta = \frac{\mu_2(m_1 - 2) - \mu_1(m_2 - 2)}{\mu_1 m_2 + \mu_2 m_1} \tag{5}$$

where, for plane strain $m_i = 4\ (1 - \nu_i)$, and for plane stress $m_i = 4/(1 + \nu_i)$. μ and ν represent the shear modulus and the Poisson's ratio with the subscripts indicating the material. Note that in all cases the crack is taken to be in material 2. Figure 4(*a*) shows the finite element discretization around the crack tip. The wedge-shaped elements were formed by collapsing the eight-node general quadrilateral elements. No attempt was made to enforce crack-tip stress singularly by relocating the midside nodes. The radial dimension of the crack-tip elements was taken to be 10^{-10} times the characteristic length (c), which for Problem A is the same as the dimension b. As seen later, this degree of mesh refinement is sufficient to accurately model the crack-tip stress and deformation fields.

Surrounding the crack-tip elements are rings of elements, with each consecutive group of three rings representing a decade of radial dimension (Fig. 4(*b*)). The radial dimension of each successive ring within a group is 2, 6, and 10 times the outer dimension of the previous group of rings. This mesh design allows for smooth element size transition from the crack-tip region to the outer domain while maintaining a maximum element aspect ratio of 4. The outermost ring group culminates with its outer boundary shaped as a rectangle (Fig. 4(*c*)) of dimension $c \times 2c$, and fits into the far-field mesh which contains a uniform grid of elements of size ($b \times b/3$). Overall, the mesh contains 426 elements with 1383 nodes, each with two degrees-of-freedom.

For uniform remote stress (σ), the Irwin (1957) exact solution for colinear cracks (with $H \to \infty$) gives $K_I = 1.12838\ \sigma\sqrt{\pi a}$. Using the computed crack opening displacement, $v(r, \pi)$, at $r/c = 10^{-6}$ obtained by FEM corresponding to uniform applied stress along the edge and same material constants, $K_I = 1.13244\ \sqrt{\pi a}$. The 0.36 percent difference from the exact solution is attributable to numerical error and to the fact that the FEM result is for a large but finite $H/(a + b)$. The problem with uniform applied stress (rather than displacement) was analyzed primarily to assess the accuracy of the FEM solutions of the other cases in Table 1 using the discretization shown in Figs. 4(*a*) through 4(*c*).

For cases (A-1) to (A-7), one can define dimensionless quantities $\bar{Q}$ and $\bar{f}$ as follows:

$$\bar{Q} = Q_I \cdot \frac{m_1^2 \mu_2}{4\mu_1(m_1\mu_2 + m_2\mu_1)} \cdot \frac{H}{\Delta\pi^{1/2}(a)^{1-\lambda}} \tag{6a}$$

where

$$Q_I = \sigma_{yy}(r, o)\,(r)^{1-\lambda}(2\pi)^{1/2} \tag{6b}$$

$$\bar{f} = (\mu_1 m_2 + \mu_2 m_1)\,\frac{v(r,\pi)}{Q_I(r)^{\lambda}} \tag{7a}$$

where

$$\frac{v(r,\pi)}{Q_I(r)^{\lambda}} = \frac{\left(\frac{\mu_1}{\mu_2} + m_1 - 1\right)\left(\frac{\mu_2}{\mu_1} + m_2 - 1\right)}{2\lambda\sqrt{2\pi}(1 - 2\lambda\beta)(\mu_1 m_2 + \mu_2 m_1)} \cdot \sin(\pi\lambda). \tag{7b}$$

Both the stress normal to the crack line, $\sigma_{yy}(r, o)$, and half the crack opening displacement, $v(r, \pi)$, are, of course, limiting values as $r \to o$. Equations (6*b*) and (7*b*) provide the means to obtain Q_I values using the FEM integration point stress and nodal displacement solutions, respectively. The value of λ used in these equations can be found by either solving Eq. (2) or by using near-tip FEM stress versus r solutions. The difference between numerically determined and the exact value of λ was found to be within 0.2 percent.

The λ, $\bar{f}$, and $\bar{Q}$ solutions for cases (A-1) through (A-7) are given in Table 1. If the Poisson's ratio for the two materials is taken to be the same and equal to 0.3, Cases (A-2) to (A-5) then represent materials with modulus ratio (μ_1/μ_2) of 10.0, 100.0, and 0.1, and 0.01, respectively, as indicated in Table 1. Cases (A-6) and (A-7) represent cracks in a metal matrix composite with silicon carbide (SiC) fibers ($E = 413.7$ GPa, $\nu = 0.3$) and titanium aluminide (Ti-24Al11MO) matrix ($E = 65$ GPa, $\nu = 0.3$). In Case (A-6) the cracks reside in the fiber and in Case (A-7) the cracks are in the matrix with fibers intact. The results in Table 1 can also be obtained using the method of Erdogan and Bakioglu (1976).

Figure 5 shows numerically obtained values of the functions g_{ij} of Eq. (1) for Case (A-1). Since this is the homogeneous material case, the functions are also available in closed form. The difference between the exact and the numerically computed values is less than 0.5 percent. Figure 6 shows the variation of the logarithm of normalized stress component ($\bar{\sigma}$) with the logarithm of normalized distance from the crack tip ($\bar{r}$) along $\theta = 1.7$ deg. The deviation from linearity close to the crack tip is because the numerical value of crack-tip stress in the FEM analysis must remain finite. The departure from linearity at $\bar{r} \simeq 0.1$ for Case (A-1) is because of loss of Q (or, K) dominance. Thus, the outer boundary of the dominant region (r_o) for (Case A-1) is 0.1 times the characteristic length. In determining r_o, ~5 percent deviation between computed and

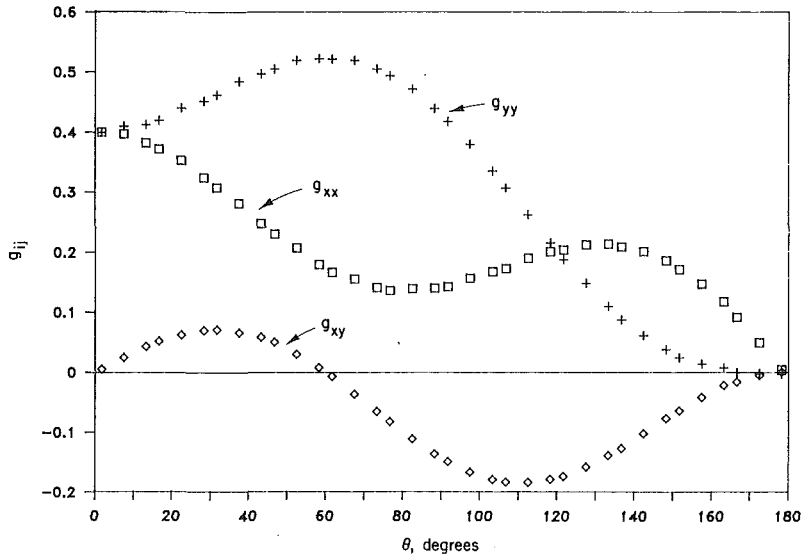

Fig. 5 Angular variation of crack-tip stresses for Case A-1

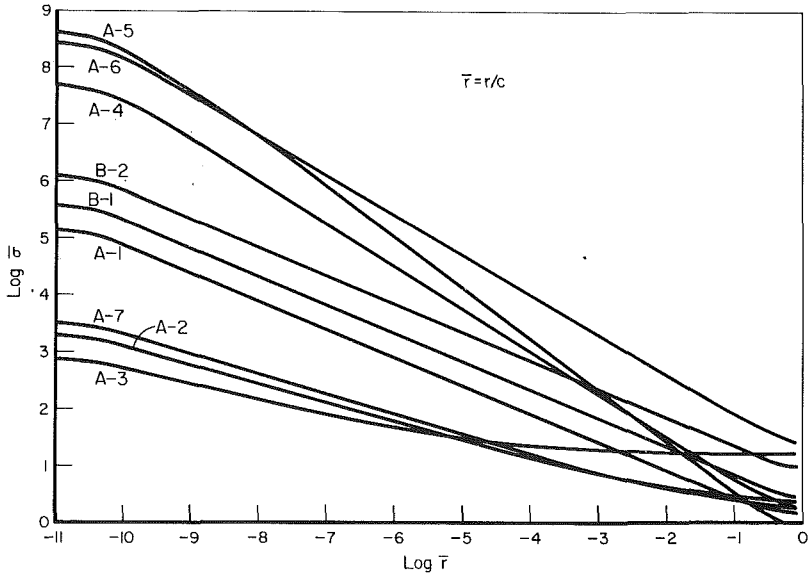

Fig. 6 Radial variation of crack-tip stress normal to crack plane

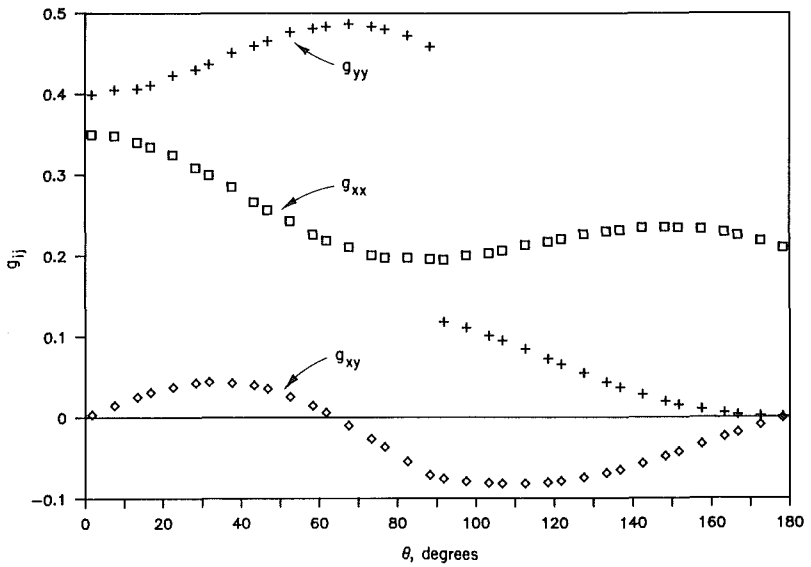

Fig. 7 Angular variation of crack-tip stresses for Case A-2

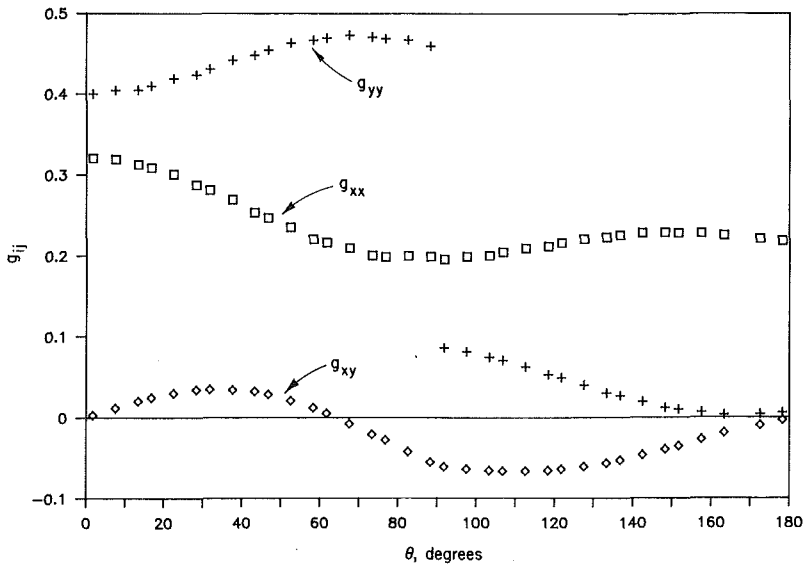

Fig. 8 Angular variation of crack-tip stresses for Case A-3

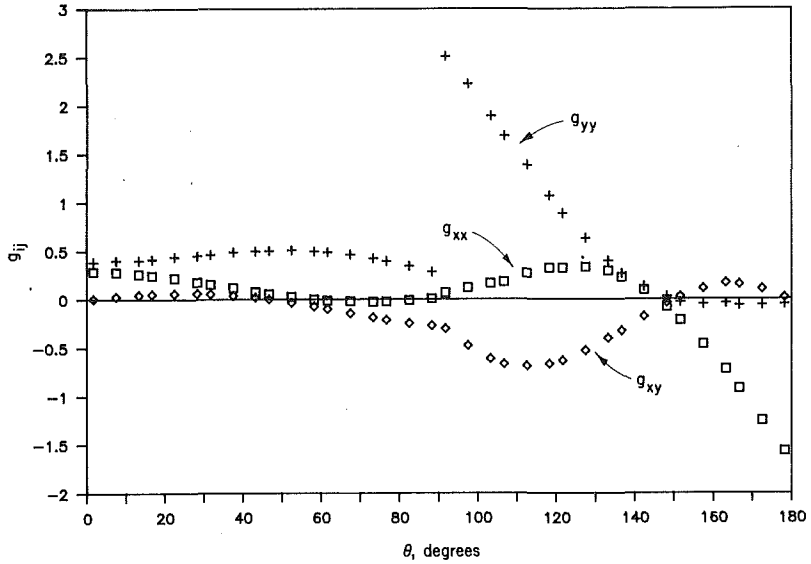

Fig. 9 Angular variation of crack-tip stresses for Case A-4

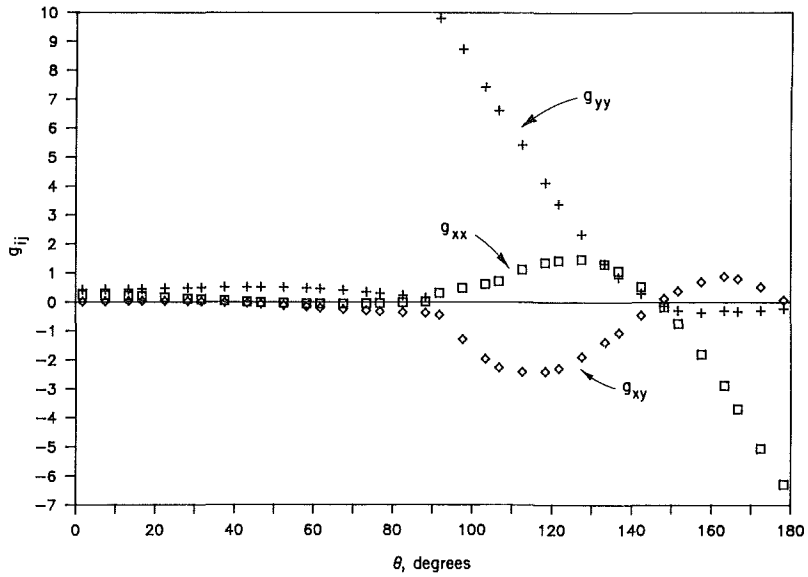

Fig. 10 Angular variation of crack-tip stresses for Case A-5

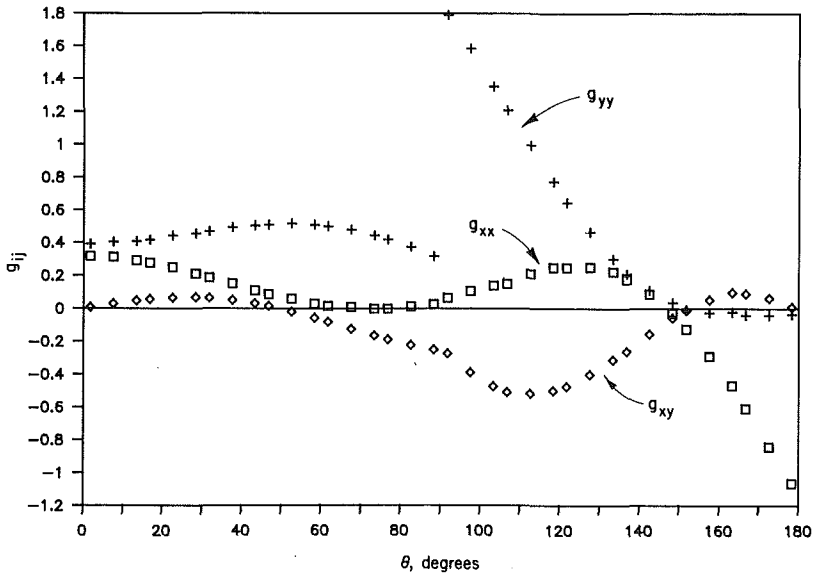

Fig. 11 Angular variation of crack-tip stresses for Case A-6

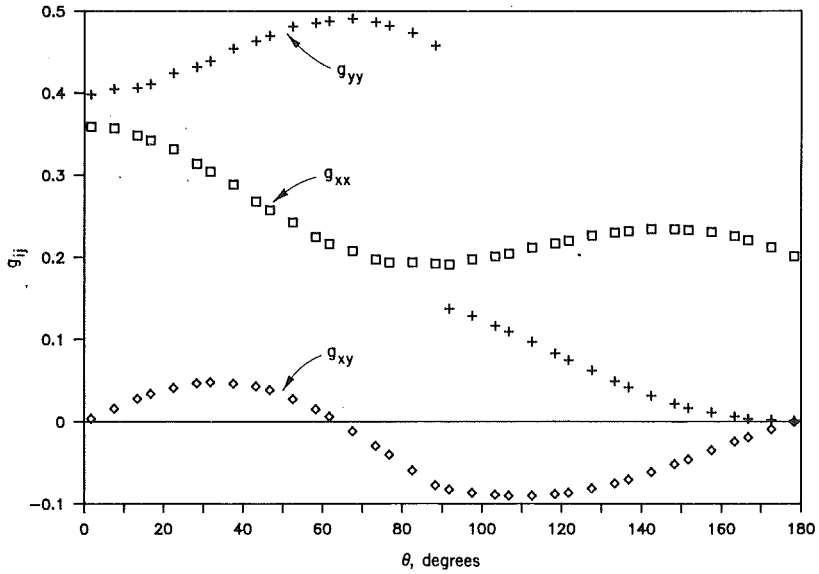

Fig. 12 Angular variation of crack-tip stresses for Case A-7

exact stress solutions was allowed. Recall that for this case, Q and K are synonymous.

The crack-tip stress field structures for the bimaterial cases are shown in Figs. 7 to 12. As expected, the g_{yy} function, corresponding to the σ_{yy} stress of Eq. (1), is discontinuous at the bimaterial interface ($\theta = 90$ deg). The g_{xx} and g_{xy} functions are continuous, and thus satisfy the condition of continuity of traction normal to the interface. As they should be, g_{xy} and g_{yy} are zero at the crack surface ($\theta = 180$ deg) and g_{xy} is zero along the symmetry line ($\theta = 0$ deg). The variations of $\bar{\sigma}$ with $\bar{r}$ for Cases (A-2) to (A-7) are shown in Fig. 6 and the r_o values are given in Table 1.

The finite element mesh design for Problem B is similar to that of Problem A. Figures 4(a), 4(b), and 4(c) show the mesh in the crack-tip region. The characteristic length c now represents the distance d (Fig. 3) between the crack tip and the interface. The smallest element size around the crack tip for Problem B is 10^{-10} times the distance d. For Case (B-1), the mesh contains 471 elements with 1522 nodes. The mesh for case (B-2) consists of 579 elements with 1864 nodes.

In both Cases (B-1) and (B-2), the crack lies entirely within material 2. Thus, the crack-tip stress fields are expected to be the same as for a crack in a homogeneous solid (see Eq. (3)). The finite element results agree with Eq. (3) to within 0.5 percent. For both Cases (B-1) and (B-2), the extent of the K-dominant zone (r_o) is found to be 0.1 times the characteristic length (see Fig. 6). Note that the characteristic length for case (B-1) is 10 times that for Case (B-2). Also, the characteristic length for Case (A-1) is 10 times that for Case (B-1). Thus, as long as the entire crack lies within the same material, the ratio of the K-dominant zone size (r_o) to the characteristic length (c) remains unchanged.

Summary of results for Cases (B-1) and (B-2) is included in Table 1. The symbols $\bar{f}$ and $\bar{Q}$ are retained only for consistency with Problem A results. These values were calculated by using $m_1 = m_2$, $\mu_1 = \mu_2$, $\lambda = 0.5$ and $\beta = 0.0$ in Eqs. (6) and (7). The Q_I ($\equiv K_I$) values were found using Eq. (7b) together with the finite element results for crack opening displacement.

Analysis of Numerical Results

The solutions of Problem B (crack tip close to the interface) indicate that stresses at any point on the interface are not uniquely characterized by the stress intensity factor (K_I). The outer boundary of the K-dominant zone, defined by r_o, is limited to ~10 percent of the distance between the crack tip and the interface. Thus, when the crack tip reaches the interface, r_o becomes zero and K_I no longer exists. As expected, for the same remote strain, K_I for a given geometry decreases sharply as a crack residing in the more compliant material approaches the interface with a less compliant material (see results for Cases (B-1), (B-2), and (A-7)). The K_I would increase sharply if the crack was approaching an interface with a more compliant material. But, in either circumstance, the loss of K-dominance is gradual and K_I ceases to exist when the distance between the crack tip and the interface becomes zero. Also, in both circumstances, the stresses at the intersection of interface and the plane of an approaching crack increase monotonically, becoming infinite when the crack front intersects the interface. A single parameter (K_I) cannot uniquely characterize stresses at the interface as a function of distance from the crack tip. But, full-field solutions (such as those obtained

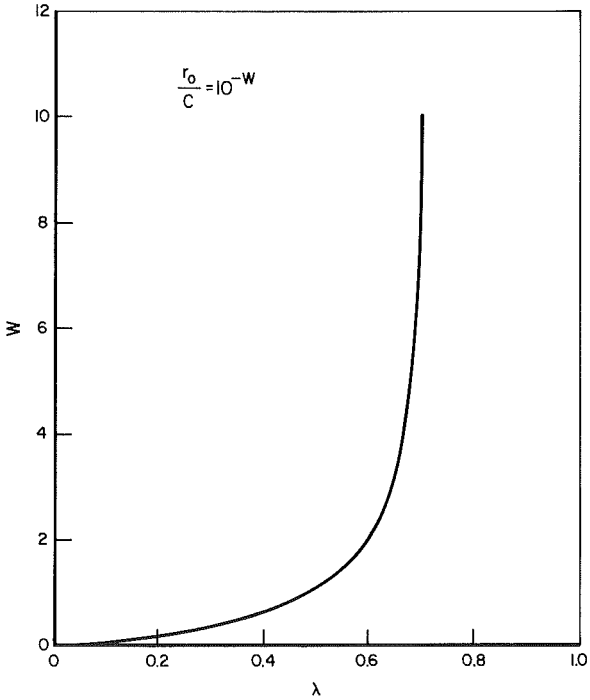

Fig. 13 Variation of normalized Q-dominant zone size with λ

by the finite element method in the present work) can be used to determine the stresses at the interface.

For a given bimaterial pair, when the crack tip is at the interface (Problem A), the stresses within the Q-dominant zone (including those at the interface) can be uniquely characterized by a single parameter (Q_I). But, even for a crack propagating through a bimaterial system, such as an idealized unidirectionally fiber-reinforced composite, a single parameter (Q_I or K_I) cannot characterize crack-tip behavior for all crack-tip locations. A unified crack-tip characterization would require establishing a connection between K_I and Q_I-dominated stress fields. A pragmatic way to accomplish this is discussed in later paragraphs. But first, it is worthwhile to comment on the remarkable dependence of the size of the Q-dominant zone (r_o) on the elastic properties mismatch between the two materials and crack location, as shown in Fig. 13. The size of the Q-dominant zone (normalized by characteristic length) diminishes sharply with increasing λ (crack about to enter a less compliant material), and increases relatively slowly with decreasing λ (crack about to enter a more compliant material). As the end values of λ (0 and 1) are approached, r_o approaches the characteristic length (c) and zero, respectively.

In addition to the size of Q-dominant zone, structure of the crack-tip stress fields (characterized by g_{xx}, g_{yy}, and g_{xy}) changes dramatically with elastic property mismatch, as seen by comparing Figs. 5 and 7 to 12. For instance, the remarkably different structure of crack-tip stress fields in Figs. 10 and 11 corresponds to the same material pair (Ti-24Al11MO SiC) with the crack located in titanium aluminide in one case and in silicon carbide in the other. The only nontrivial similarity among the various cases is that g_{yy} directly ahead of the crack ($\theta = 0$) remains unchanged at $1.0/\sqrt{2\pi}$. The most noticeable difference among the various cases may be the relative size of the jump in g_{yy} at the interface ($\theta = 90$ deg).

Enforcing the strain (ϵ_{yy}) and σ_{xx} and σ_{xy} continuity at the interface, one gets:

$$\left(\frac{\sigma_{yy}(r,90+)}{\sigma_{yy}(r,90-)}-1\right)\frac{\mu_1 m_2}{\mu_1 m_2+\mu_2 m_1}=\alpha+(2\beta-\alpha)\frac{\sigma_{xx}(r,90)}{\sigma_{yy}(r,90-)} \tag{8}$$

where the (+) and (−) signs indicate the material 2 (with crack) and material 1 (no crack) sides at the interface, respectively. For the homogeneous case ($\alpha = \beta = 0$), Eq. (8) yields the continuity of σ_{yy} at $\theta = 90$ deg. Within the Q-dominant region, the stress components in Eq. (8) may be replaced by the corresponding functions g_{ij} (θ, α, β). Then,

$$g_{xx}=\frac{\mu_1 m_2 g_{yy}(90+,\alpha,\beta)-\mu_2 m_1 g_{yy}(90-,\alpha,\beta)}{\mu_2(m_1-4)-\mu_1(m_2-4)}. \tag{9}$$

Equations (8) and (9) may be found useful in assessing the effect of thermal expansion coefficient mismatch between the two materials giving rise to readily calculable σ_{yy} stresses at the interface.

The fact that g_{yy} at $\theta = 0$ is independent of elastic properties of the materials yields the following two potentially useful asymptotic relations:

$$Q_I=(2\pi)^{1/2}\cdot\sigma_{yy}(r,o)\cdot(r)^{1-\lambda} \tag{10}$$

and

$$Q_I=(2\pi)^{1/2}\cdot\epsilon_{yy}(r,o)\cdot(r)^{1-\lambda}\cdot\Phi \tag{11}$$

where

$$\Phi(\bar{g})=\frac{8\mu_1}{m_1-(4-m_1)\cdot\bar{g}} \tag{12}$$

and

$$\bar{g}=\frac{g_{xx}(0,\alpha,\beta)}{g_{yy}(0,\alpha,\beta)}=(2\pi)^{1/2}\cdot g_{xx}(0,\alpha,\beta) \tag{13}$$

and ϵ_{yy} is the Y-component of strain. In the following paragraphs, significance of the above observations is presented first in the context of cracking normal to fiber direction, then in the context of interface failure.

Cracking. Recall that Q_I represents the propensity for Mode I crack extension, or crack driving "force," only for a crack normally intersecting the interface of a given bimaterial system. Therefore, it has the undesirable feature that the same numerical value of Q_I corresponding to different bimaterial systems does not imply the same crack driving force. It is worthwhile to investigate if a more useful representation of crack driving force can be found. If one hypothesizes that the propensity for crack extension by cleavage is governed by an "average" value of the first invariant (I_1) of the stress tensor over the Q-dominant region along $\theta = 0$, an interesting result is obtained. The choice of I_1 (instead of, for example, σ_{yy}) is to acknowledge the fact that there is more triaxial stress constraint ahead of the crack tip in the homogeneous case than in the bimaterial case. The value of g_{yy} at $\theta = 0$ being material independent, I_1 includes a representation for hydrostatic stress. Specifically, consider the average first invariant defined as follows:

$$I_a=\frac{1}{2(r_o-r_p)}\int_{r_p}^{r_o} I_1(r,o)\,dr \tag{14}$$

where

$$I_1(r,o)=\sigma_{xx}(r,o)+\sigma_{yy}(r,o)+\sigma_{zz}(r,o). \tag{15}$$

The radial distances r_o and r_p are the same as in Fig. 2. Using Eq. (1), Eq. (14) may be expressed as follows:

$$I_a=\frac{Q_I(r_o^{\lambda}-r_p^{\lambda})}{2\lambda\sqrt{2\pi}(r_o-r_p)}(1+\bar{g})\left[1+\frac{n\cdot(4-m_1)}{4}\right] \tag{16}$$

where n has the value 1 for plane strain and 0 for plane stress. In deriving Eq. (16) from Eq. (14), the material independent value $1/\sqrt{2\pi}$ for g_{yy} at $\theta = 0$ has been used.

Following the hypothesis that equal I_a in different bimaterial systems means equal propensity for crack extension, one can express the relative propensity of a bimaterial crack to that of a crack in a homogeneous solid of material 1 as follows:

$$C_r=\frac{Q_I}{K_I}\cdot C_o \tag{17}$$

where

$$C_o=\frac{1+\bar{g}}{4\lambda}\cdot\frac{r_m-r_h}{r_m-r_p}\cdot\frac{r_m^{\lambda}-r_p^{\lambda}}{r_m^{0.5}-r_h^{0.5}}. \tag{18}$$

Table 2 Summary of results for cracking

Case	F	$\bar{g}$	$\bar{F}$	C_r
A-1	1.1332	1.00	1.0000	1.0000
A-2	0.3510	0.88	0.3097	0.6463
A-3	0.0482	0.80	0.0425	0.5542
A-4	3.6186	0.73	3.1932	1.4597
A-5	12.3878	0.52	10.9315	3.2878
A-6	2.8099	0.81	2.4796	1.3301
A-7	0.4765	0.90	0.4205	0.6828
B-1	0.7382	1.00	0.6515	1.0000
B-2	0.5409	1.00	0.4773	1.0000

The distance r_m represents the smaller of the r_o (outer dimension of Q-dominant zone) for the bimaterial crack and for the homogeneous case. The stress intensity factor (K_I) in Eq. (17) is for the same geometry (including crack length) and boundary conditions as for Q_I, but in a homogeneous solid with elastic properties that of material 1 (the material without a crack). The nonlinear zone size (r_p) corresponds to material 1 of the bimaterial system and must be small compared to r_m. For the corresponding homogeneous case, the nonlinear zone size is r_h, which must also be small compared to r_m. Since r_o in homogeneous material is 0.1 times the characteristic length (c), and because c must be the same for the bimaterial and the corresponding homogeneous material problems, r_m must always be less than or equal to 0.1 times c. So that Q_I and K_I correspond to the same remote strain, one can use Eqs. (11) to (13) to define the following normalizing parameter (Q_o):

$$Q_o = \Phi \cdot \epsilon_{yy}^{\infty} (a)^{1-\lambda} \sqrt{\pi/2} \tag{19}$$

which for the homogeneous case becomes K_o, and is given as:

$$K_o = \frac{4\mu_1}{(m_1 - 2)\sqrt{2}} \epsilon_{yy}^{\infty} (\pi a)^{1/2}. \tag{20}$$

In Eqs. (19) and (20), ϵ_{yy}^{∞} represents remotely applied normal strain. Then, one can express Q_I and K_I in terms of dimensionless functions $F(a/b, H/b, \alpha, \beta)$ as follows:

$$Q_I = F(a/b, H/b, \alpha, \beta) \cdot Q_o \tag{21}$$

and

$$K_I = F(a/b, H/b, 0.0, 0.0) \cdot K_o. \tag{22}$$

Substituting Eqs. (19) to (22) in Eq. (17), the following expression for the relative propensity is found:

$$C_r = C_o \cdot (a)^{0.5-\lambda} \cdot \frac{2 \cdot (m_1 - 2)}{m_1 - (4 - m_1)\bar{g}} \cdot \frac{F(a/H, b/H, \alpha, \beta)}{F(a/H, b/H, 0.0, 0.0)}. \tag{23}$$

Using the finite element analysis results presented earlier, the values of the functions F and $\bar{g}$ in Eq. (23) are given in Table 2. To evaluate C_o, one needs (in addition to Table 1) r_p and r_h.

If the nonlinear zone sizes r_p and r_h are interpreted to be due to plastic deformation, small-scale yielding estimates of these can be found using the following relation based on the von Mises yield criterion at $\theta = 0$:

$$r_p^{1-\lambda} = \frac{Q_I}{\sigma_{01}\sqrt{2\pi}} \left[1 + \bar{g}^2 - \bar{g} - \frac{n}{16} \cdot m_1 \cdot (4 - m_1)(\bar{g} + 1) \right]^{1/2} \tag{24}$$

where $\bar{g}$ and n have been defined in the context of Eqs. (13) and (16) earlier, and σ_{01} is the yield strength in uniaxial tension of material 1. The plastic zone (r_h) for the homogeneous case is found by using $\lambda = 0.5$, $g = 1.0$ and substituting Q_I by K_I.

In the limit as the nonlinear zone size goes to zero, Eq. (18) reduces to:

$$C_o = \frac{1 + \bar{g}}{4\lambda} r_m^{\lambda - 0.5}. \tag{25}$$

Substituting Eq. (25) into (23), one gets

$$C_r = \bar{C}_r \cdot \bar{F} \bar{a}^{0.5-\lambda} \tag{26}$$

where

$$\bar{C}_r = \frac{1 + g}{2\lambda} \frac{\bar{m}_1 - 2}{m_1 - (4 - m_1)\bar{g}} \tag{27}$$

$$\bar{F} = \frac{F(a/H, b/H, \alpha, \beta)}{F(a/H, b/H, 0, 0)}, \tag{28}$$

and

$$\bar{a} = \frac{a}{r_m}. \tag{29}$$

Equations (23) and (26) are relevant for a crack normally intersecting a bimaterial interface. For a crack approaching the interface, one gets the trivial result, $C_r = \bar{F}$.

As an example, to analyze a crack traversing through the titanium aluminide-silicon carbide composite considered earlier, r_m would be 10^{-3} times the smaller of the fiber radius and half the fiber spacing. That is, the smaller of the r_o for Cases (A-6) and (A-7). The geometry-independent parameter $\bar{C}_r$ would range between 0.683 (Case (A-7)) and 1.333 (Case (A-6)), its value being unity for the homogeneous case. The function $\bar{F}$ would of course depend on geometry and (depending on crack-tip location) on α and β. The values of $\bar{F}$ and $\bar{C}_r$ for the cases considered in the present work are given in Table 2.

In a global sense, one may define a pseudo-elastic stress intensity factor (K_I^p) for a given unidirectional fiber composite with crack normal to fiber direction as

$$K_I^p = C_r K_I \tag{30}$$

which, using Eqs. (20), (22), (27), and (28) gives

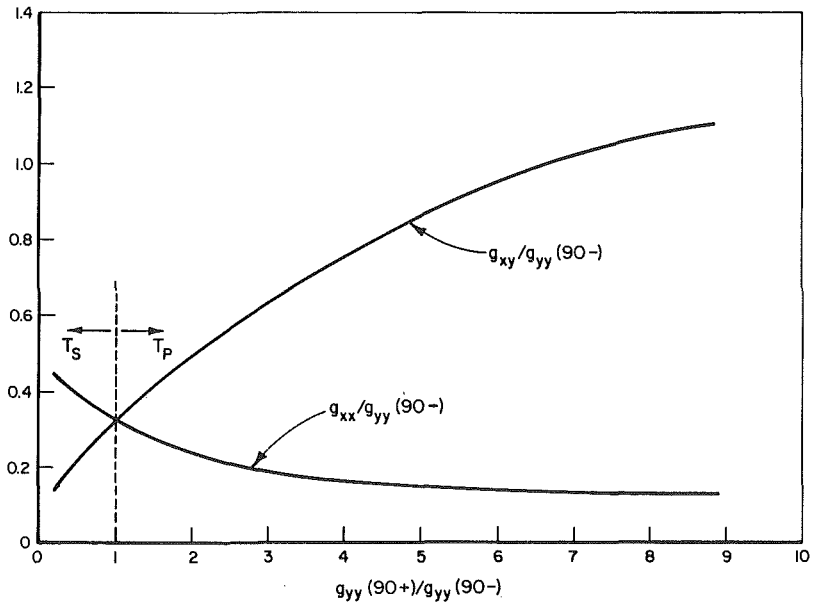

Fig. 14 Variation of interfacial shear and normal stresses

$$K_I^p = \frac{\mu_1(1+\bar{g})\sqrt{2}}{\lambda[m_1-(4-m_1)\bar{g}]} \cdot \left(\frac{a}{r_m}\right)^{0.5-\lambda} \cdot F(a/H,b/H,\alpha,\beta)\cdot\epsilon_{yy}^{\infty}(\pi a)^{1/2} \quad (31)$$

in which all material constants (μ_1, m_1, g, α, β, and λ) are dependent on crack-tip location. Depending on the crack-tip location, r_m is a fraction of either the fiber diameter (D) or the fiber spacing (s). For a crack in a homogeneous material, K_I^p does reduce to K_I of Eq. (22).

Interface Failure. The stress state at the interface cannot be described by the asymptotic stress field of Eq. (3) corresponding to a crack approaching the interface. The dominance of this field is limited to ~10 percent of the distance between the crack tip and the interface. However, the asymptotic stress field of Eq. (1) can be useful in studying the interface stresses close to the crack tip. In this context, the following observations are offered. First, the asymptotic stress field along the interface (θ = 90 deg) is not always shear dominated. When the crack is in the more compliant of the two materials (Cases (A-2), (A-3), and (A-7)), g_{xy} along the interface is the lowest of the g_{ij}. When the crack is in the less compliant of the two materials (Cases (A-4), (A-5), and (A-6)), g_{xy} along the interface is higher than g_{xx}, comparable to g_{yy} in the more compliant material, and smaller than g_{yy} in the less compliant material. It is also observed that along the interface, both g_{xx} and g_{xy} show a weak dependence on λ except in the neighborhood of λ = 0.5. What does change with λ more significantly is the ratio of g_{yy} in one material to the other at the interface. As seen from Eq. (8), for a given bimaterial system this ratio is uniquely related to the ratio of g_{xx} and g_{yy} at the interface.

Analysis of the numerical results for Cases (A-1) to (A-7) also indicates that within the Q-dominant region, the directions of both the maximum J_2 (second invariant of the deviatoric stress tensor) and the maximum shear stress remain essentially unchanged compared to the homogeneous case. The maximum shear in all cases occurs along the interface (θ = 90 deg). The magnitude of maximum shear stress at the interface decreases monotonically as λ increases. Assuming the Poisson's ratio to be 0.3 for both materials, the maximum J_2 in plane strain occurs at θ = 87 deg for the homogeneous case (λ = 0.5) and when $\lambda > 0.5$. For $\lambda < 0.5$, maximum J_2 occurs along the interface. Thus, the directions of maximum J_2 and maximum shear stress do not provide a particularly discriminatory basis to study interface failure.

Based on the above observations, it may be deduced that the tendency for shear failure of the interface (fiber pull-out) is higher when the crack resides in the less compliant of the two materials. The tendency for interface separation (splitting) is higher when the crack resides in the more compliant material. One may postulate that the tendency for splitting is directly proportional to g_{xx} and the tendency for pull-out is proportional to g_{xy} at the interface. However, as discussed earlier in the context of cracking, the degree of hydrostatic tension at the interface may also play an important role in determining the interfacial failure mode. A quantity that provides a smooth and monotonic variation of the degree of hydrostatic tension over the entire range of λ is the ratio of the two g_{yy} values along the interface. Figure 14 shows the variation of this quantity with interfacial shear and normal stresses. Accordingly, one may postulate that the tendencies for the intersecting crack should be addressed in formulating criteria for self-similar crack extension.

The finding that the Q-dominant zone becomes smaller with increasing λ suggests that for $\lambda > 0.5$, direct consideration of nonlinear deformation field around the crack tip may be necessary for accurate assessment of cracking and interface failure. Also, for composite systems which show evidence of reaction or diffusion zones in the interfacial region (whose width cannot be considered small in comparison to D and s), direct consideration of interfacial region properties may be warranted.

Acknowledgments

The author wishes to thank Dr. T. Nicholas of WRDC, Wright Patterson Air Force Base and Dr. N. E. Ashbaugh of University of Dayton Research Institute for their encouragement and support. The author also wishes to thank Prof. C. F. Shih of Brown University for helpful comments.

References

Bathe, K. J., and Wilson, E. W., 1976, *Numerical Methods in Finite Element Analysis*, Prentice-Hall, Englewood Cliffs, N.J.

Bogy, D. B., 1971, "On the Plane Elastostatic Problem of a Loaded Crack Terminating at a Material Interface," ASME JOURNAL OF APPLIED MECHANICS, Vol. 38, pp. 911–918.

Cook, T. S., and Erdogan, F., 1972, "Stresses in Bonded Materials with a Crack Perpendicular to the Interface," *Internal Journal of Engineering Science*, Vol. 10, pp. 677–697.

Dundurs, J., 1969, Discussion, ASME JOURNAL OF APPLIED MECHANICS, Vol. 36, pp. 650–652.

Erodogan, F., and Bakioglu, M., 1976, "Fracture of Plates Which Consist of Periodic Dissimilar Strips," *International Journal of Fracture*, Vol. 12, No. 1, pp. 71–84.

Fenner, D. N., 1976, "Stress Singularities in Composite Materials with an Arbitrarily Oriented Crack Meeting an Interface," *International Journal of Fracture*, Vol. 12, No. 5, pp. 705–721.

Irwin, G. R., 1957, "Analysis of Stresses and Strains Near the End of a Crack Traversing a Plate," ASME JOURNAL OF APPLIED MECHANICS, Vol. 24, p. 361.

Isida, M., 1970, "On the Determination of Stress Intensity Factors for Some Common Structural Problems," *Engineering Fracture Mechanics*, Vol. 2, pp. 61–79.

Williams, M. L., 1957, "On the Stress at the Base of a Stationary Crack," ASME JOURNAL OF APPLIED MECHANICS, Vol. 24, pp. 109–114.

Zak, A. R., and Williams, M. L., 1963, "Crack Point Stress Singularities at a Bimaterial Interface," ASME JOURNAL OF APPLIED MECHANICS, Vol. 30, pp. 142–143.

Conditionally Averaged Response Formulations for Two-Phase Random Mixtures

John J. McCoy
School of Engineering and Architecture,
The Catholic University of America,
Washington, DC 20064
Fellow ASME

A technique known as a projection or a smoothing, which has been used successfully to derive formulations on the mean (or unconditionally averaged) field response of specimens with a random substructure, is extended to obtain formulations on conditionally averaged response measures for two-phase mixtures. The condition in the averaging refers to the location of the field point, in one or the other of the phases. The obtained formulation has the structure of a theory for interacting mixtures of nonlocal continua. The formulations are then investigated in a two-scale microscale/macroscale limit; specifically we determine the conditions necessary for the obtained formulations to reduce to local formulations which can be interpreted to provide bases for physical theories. It is argued that for weakly coupled, two-phase mixtures for which both phases are connected over distances that are measured on the macroscale, the mixture theory-type formulation is local in the limit whereas the mean-field formulation is not. In the presence of strong coupling, or for mixtures in which one of the phases is connected only for distances measured on the microscale, both type formulations are local in the two-scale limit.

Introduction

In a series of papers, Beran and McCoy (1970a,b) and McCoy (1972a, 1973) presented formulations expressed in the mean, ensemble averaged, field responses for material specimens which on one scale of observation—a microscale—are modeled as classical, linear continua with property measures described by stochastic processes. By classical continua are meant those expressed by local balance and constitutive laws. The derivations were formal, using a procedure that may be termed a projection. The obtained formulations were identified with the same local balance laws as apply on the microscale and with nonlocal *effective* constitutive laws. Details were presented for the cases of the statical response of linearly elastic solids, (Beran and McCoy, 1970a) for electrical conduction, (Beran and McCoy, 1970b) and for the propagation of elastic waves in one (McCoy, 1972a) and three (McCoy, 1973) dimensions.

For specimens with geometries which are observable on a second scale, much larger than the microscale, one can argue, using the prescriptions provided for calculating parameters in the effective constitutive laws, that these parameters are independent of the specimen geometries and of the details of any specimen forcings. This independence allows for the determination of the parameters through canonical experiments in which only mean-field responses are to be measured. The formulations can thus be interpreted to provide *physical theories* expressed in the mean response measures. Further arguments, this time that the range of the nonlocality of the constitutive laws are observable on the length scale defined by the heterogeneity, can be used for the two-length scale experiments to approximate the effective constitutive laws with ones that are local. The results of this approximation are intuitively satisfying *effective modulus* formulations. The mean-field response, which varies on the macroscale, is now interpreted to be a spatially averaged response. The formulation has affected a separation of length scales in which the smaller scale material heterogeneity appears in a formulation of a response measure which varies on the larger scale of the specimen geometry, via parameters which are canonical in not depending on any experiment description which applied to the larger length scale. This separation of length scales is crucial for the development of computationally useful predictive algorithms of the response of composite materials, for example.

For specimens which are weakly heterogeneous, the infinite series prescriptions for calculating the parameters of the effective constitutive laws can be truncated giving theories that are specific; i.e., require only a limited number of specific statistics of the microstructure heterogeneity. For these specimens the arguments that the range of nonlocality of the effective constitutive laws is measured on the microscale was explicitly demonstrated and, moreover, it was shown that the microscale length is made precise by two-point correlation functions defined on the material heterogeneity (Beran and

Contributed by the Applied Mechanics Division of THE AMERICAN SOCIETY OF MECHANICAL ENGINEERS for presentation at the Winter Annual Meeting, Atlanta, GA, Dec. 1-6, 1991.

Discussion on this paper should be addressed to the Technical Editor, Prof. Leon M. Keer, The Technological Institute, Northwestern University, Evanston, IL 60208, and will be accepted until two months after final publication of the paper itself in the JOURNAL OF APPLIED MECHANICS. Manuscript received by the ASME Applied Mechanics Division, Dec. 12, 1989; final revision, Mar. 4, 1991.
Paper No. 91-WA/APM-7.

McCoy, 1970a,b). Using these specific formulations it was possible to investigate the nature of the physics described by them. Thus, for example, Beran and McCoy (1970c) demonstrated that a strain gradient theory did not represent a consistent generalization of the classical theory of linear elasticity for materials with weakly heterogeneous random substructures. As another example, McCoy (1972b) demonstrated that elastic solids with weakly heterogeneous random structures would not support "optical branches" of waves of lengths measured on the macroscale. The conclusion of McCoy (1972a, 1973), however, that the concept of a dynamical effective modulus theory applied only for long wavelength—low frequency propagation and that the proper dynamical effective moduli and mass density are equal to the statical effective moduli and the averaged mass density, respectively, are not dependent on a weakly heterogeneous assumption.

In this paper we return to a number of issues related to the macroscale response of material specimens with a randomly heterogeneous microstructure. This time we restrict the microscale heterogeneity to a mixture of two phases and extend the projection procedure to obtain formulations expressed in conditionally averaged response measures, the condition being that the observation point lies in one or the other of the two phases. Reflecting the formal nature of the derivation procedure, which depends only on the algebraic structure of the underlying field equations, the formulations are accomplished using an abstract operator notation. Once completed, however, the abstract formulation is considered in the context of a specific application to make it more intuitive. In this way one can identify it with theories of mixtures of nonlocal continua.

With the abstract formulation expressed in conditionally averaged response measures in hand, we next demonstrate the recovery of the unconditionally averaged response measure formulation obtained by the projection procedure, as usually applied. The demonstration follows from the recognition that the projection to obtain the unconditionally averaged response refers to a space with fewer degrees-of-freedom than does the projection to obtain conditionally averaged responses. Thus, the formulation expressed in the unconditionally averaged response can be achieved by a further projection of that required to obtain the formulation in the conditionally averaged response. Turning this statement around, the formulation in terms of the conditional averages can be said to be more complete. If not for the fact that this more complete formulation is also more complex, the suggestion might be to eschew the formulation in terms of the unconditional average and always first obtain the conditionally averaged measures to subsequently calculate the unconditionally averaged response if this is desired. That one does not do so is simply a matter of computational convenience.

The derivation of the formulation expressed in conditional averages and the recovery, therefrom, of the earlier result is independent of any questions of length scales. Questions of length scales were introduced in the earlier studies when considering the *interpretation* of the formulation on the mean-field response as a physical theory, which required that it be self-contained. It is the possibility that one can ignore the prescription for calculating the parameters in the effective constitutive laws and elect instead to obtain them by accomplishing physical experiments requiring the measuring of the mean-field responses only, which is central to the step by which a mathematical formulation can also be interpreted as a physical formulation. The existence of two widely separated length scales and its consequence, that the parameters in the effective constitutive laws are canonical in not depending on specimen measures which are observable on the larger scale, provided this possibility for the earlier formulation. We, therefore, introduce the questions of length scales in the context of the formulation expressed in the conditional averages and of the recovery of that expressed in the unconditional average. An interesting conclusion obtained is a possibility of locality in the two-scale mixture formulation limit, while the formulation expressed in the unconditional average remains nonlocal. Since nonlocal formulations are in general less convenient for computing than are local formulations, the formulation in terms of conditional averages might be the more convenient one even if one is interested in ultimately predicting the unconditionally averaged response. More fundamental than convenience, the possibility exists that the mixture theory formulation could be interpreted as a physical theory while the effective constitutive law formulation might not.

For what type two-phase microstructures would the mixture theory formulation become local in the two-length scale limit while the effective constitutive law theory remains nonlocal? The answer to this is first in the strength of the coupling of the described physics for each of the two phases, and then in the definition of length scales on the heterogeneity. Thus, to retain nonlocality in the effective constitutive law theory in the two-length scale limit requires *weak coupling* in the described physics which implies strong heterogeneity in the material parameters. Assuming weak coupling, the questions of length scales and how they are defined arise. Thus, one can distinguish between *geometric* length scales and *connectivity* or topologic length scales. As discussed in the paper, it is possible for these two type lengths to differ widely. For weakly coupled two-phase microstructures for which the topologic lengths for both phases are measured on the macroscale; i.e., the scale determined by the specimen geometry and forcing, while the geometric lengths define the microscale, the mixture theory formulation is local and the effective constitutive theory formulation nonlocal in the two-length scale limit. The reason is the conditions for which a nonlocal effective constitutive theory obtains in the two-length scale limit are just the conditions required for two coupled, but identifiable, solution *modes*. The mixture theory formulation has a structure that enables description of the two modes in a local context. The effective constitutive theory can only describe them in a nonlocal formulation. For strongly coupled two-phase microstructures or weakly coupled microstructures for which the topologic lengths of one of the phases and the geometric lengths are measured on the microscale, both formulations could be local in the two-length scale limit. "Could be" because for such microstructures there remains a possibility of a "tunnelling" which could result in a nonlocal effective constitutive law theory.

The lack of connectivity of one of the phases over distances that are larger than a microscale length, essentially blocks or *localizes* the solution mode that is primarily associated with this phase. The phenomenon is related to the localization of the response of a dynamical system comprised of weakly coupled subsystems. In the present context, localization of the response is not achieved since the connectivity of one of the phases, and hence of a solution mode associated with it, is assumed to extend over macroscale lengths. Thus, only one solution mode is blocked and the local effective modulus theory describes the unblocked mode. The localization of the response of weakly coupled dynamical systems is of current interest in a number of studies of structural acoustics (Hodges and Woodhouse, 1983; Pierre and Dowell, 1987). In these studies the localization is interpreted to a classical mechanics analog of an Anderson localization (Anderson, 1958).

Since the projection procedure and the extension presented herein do not have the status of rigorous mathematics, the arguments presented and the conclusions obtained therefrom require further investigation. In a study to be reported subsequently, Gillette (1991) has considered the issues raised in the context of a two-phase mixture of acoustic media using asymptotic and computational analyses. This more specific study is correspondingly less formal. The advantage of the formal study is in the suggestion of generality of a derivation

procedure which uses only the algebraic structure of the underlying formulation. The objectives of asymptotic, numeric, and/or rigorous analyses which might follow would be to explore the limits of validity of the formally obtained results.

The structure of the paper is as follows: In the next section we briefly review the projection method to obtain a mathematical formulation expressed in the unconditionally averaged response field. Then, in the following section, we introduce the restriction to a two-phase microstructure and extend the projection method to obtain mathematical formulations expressed in conditional averages. A demonstration that the mathematical formulations are consistent and that those expressed in conditional averages are simply more complete follows next, followed by a section treating the two-scale limit and the interpretation of the derived formulations as physical theories. A final section of remarks on the studies required to add a degree of mathematical rigor to the formal results of the present study concludes the paper.

A Formulation on the Averaged Response Field

Restricting consideration to a linear system and introducing the notion of a reference material, we assume that the point-by-point response of the material specimen on one scale of observation, which we term a microscale, is governed by the symbolic equation

$$u = u_0 + G_0 \delta C u. \tag{1}$$

Here, u denotes the response field; u_0 denotes the response field in the reference material assumed to be deterministic; δC denotes a local operator that represents the "interaction" of the response field and material heterogeneity; and G_0 denotes a nonlocal operator that describes the "propagation" of the effects of the local interaction due to material heterogeneity, to points removed from the center of interaction. The "forcing" of the problem appears via u_0, the response field in the reference material. The G_0 operator is also defined for the reference material; algorithmically it is described by a Green's function and hence incorporates homogeneous boundary conditions applied to the material specimen. Randomness enters the formulation through the local interaction operator, δC.

The tensorial rank of the response field, the nature of the local interaction operator, and the dimensions of the space on which the formulation applies all depend on the application. As an example, we make reference to determining the response of a randomly heterogeneous, linearly elastic solid. The governing equations are obtained from the requirements of equilibrium, compatibility, and a generalized Hooke's law. Neglecting inertia effects and employing a dyadic notation we write,

$$\nabla \cdot \tau(\mathbf{x}) = \mathbf{f}(\mathbf{x}), \tag{2a}$$

$$\nabla \times \epsilon(\mathbf{x}) \times \nabla = 0, \tag{2b}$$

and

$$\tau(\mathbf{x}) = \boldsymbol{C}(\mathbf{x}) : \epsilon(\mathbf{x}). \tag{2c}$$

These equations are to be solved subject to prescribed conditions on the boundary of the specimen. Equivalent integral and integro-differential equation formulations can be obtained on introducing a (homogeneous) reference material, by writing

$$\boldsymbol{C}(\mathbf{x}) = \boldsymbol{C}_0 + \delta \boldsymbol{C}(\mathbf{x}), \tag{3}$$

and on defining a dyadic Green's function, $\boldsymbol{G}_0(\mathbf{x}, \mathbf{x}')$. This function gives the displacement $\mathbf{u}$ at the field point $\mathbf{x}$, that results from an arbitrarily directed point force acting at the source point $\mathbf{x}'$.

The Green's function is to satisfy homogeneous boundary conditions, as dictated by the original problem specification. Using this Green's function, the following integro-differential equation can be directly written on the displacement field of the specimen

$$\mathbf{u}(\mathbf{x}) = \mathbf{u}_0(\mathbf{x}) - \int_V \boldsymbol{G}_0(\mathbf{x}, \mathbf{x}') : (\nabla_0' \cdot (\delta \boldsymbol{C}(\mathbf{x}') : \epsilon(\mathbf{x}')))d\mathbf{x}', \tag{4a}$$

where

$$\epsilon = \frac{1}{2}(\nabla \mathbf{u} + \mathbf{u} \nabla). \tag{4b}$$

In this equation, $\mathbf{u}_0(\mathbf{x})$ is the displacement field that would exist in the specimen made from the reference material; the forcing of the specimen is described by $\mathbf{u}_0$. The integration is over the region of the specimen.

An integral equation formulation written on the strain field is obtained from Eq. (4*a*) on taking a symmetric derivative on both sides and on accomplishing an integration by parts. We write this equation as

$$\epsilon(\mathbf{x}) = \epsilon_0(\mathbf{x}) + \int_V \boldsymbol{G}_0^{(4)}(\mathbf{x}, \mathbf{x}') : (\delta \boldsymbol{C}(\mathbf{x}') : \epsilon(\mathbf{x}'))d\mathbf{x}', \tag{5}$$

where $\epsilon_0(\mathbf{x})$ is the strain field in the reference specimen and $\boldsymbol{G}_0^{(4)}(\mathbf{x}, \mathbf{x}')$ is a two-point quartic field, obtained from the dyadic Green's function $\boldsymbol{G}_0(\mathbf{x}, \mathbf{x}')$. For a precise definition of $\boldsymbol{G}_0^{(4)}(\mathbf{x}, \mathbf{x}')$ in terms of $\boldsymbol{G}(\mathbf{x}, \mathbf{x})$ the reader is referred to McCoy (1981), for example. We note that $\boldsymbol{G}_0^4(\mathbf{x}, \mathbf{x})$ must be understood in a generalized function sense. A comparison of the specific Eq. (5) and the symbolic Eq. (1) shows the algebraic structure of the two equations to be the same. We shall carry out the manipulations to be accomplished on the level of the symbolic equation since it is only the algebraic structure of the underlying formulation that enters these manipulations.

A formulation on the average of the field response across an ensemble of random materials specimens can be obtained from Eq. (1) by a technique that can be termed a projection (Fishman and McCoy, 1980, 1981; Keller, 1962, 1964).

To proceed we first average, or project, Eq. (1) and write

$$\begin{aligned} \langle u \rangle &= u_0 + G_0 \langle \delta C u \rangle \\ &= u_0 + G_0 \langle \delta C \rangle \langle u \rangle + G_0 \langle \delta C' u' \rangle, \end{aligned} \tag{6}$$

where the angular brackets denote the averaging and a prime denotes the fluctuating part of the indicated quantity. We can write, for example,

$$\langle u \rangle = Pu$$

and

$$u' = (I - P)u, \tag{7}$$

where P denotes the projection operator and I the identity operator. Equation (6) is not a closed equation on $\langle u \rangle$, presenting the familiar closure problem of all statistical continuum calculations. In the projection method this problem is solved by first operating on Eq. (1) using $(I - P)$, to obtain

$$u' = G_0 \delta C' \langle u \rangle + G_0 \langle \delta C \rangle u' + G_0 (I - P) \delta C' u', \tag{8}$$

which we interpret as an equation on the fluctuating, u', response field. The forcing in this equation is the $G_0 \delta C' \langle u \rangle$ term. Solving Eq. (8) would give u' in terms of $\langle u \rangle$ which can then be used to form $\langle \delta C' u' \rangle$ in Eq. (6). The result of these operations is the desired closed equation on $\langle u \rangle$.

Accomplishing this program we write

$$u' = N G_0 \delta C' \langle u \rangle, \tag{9}$$

where the N operator is defined as

$$N = (I - G_0 \langle \delta C \rangle - G_0 (I - P) \delta C')^{-1}. \tag{10}$$

Next, we form

$$\langle \delta C' u' \rangle = \langle \delta C' N G_0 \delta C' \rangle \langle u \rangle, \tag{11}$$

and finally write for the equation on

$$\langle u \rangle = u_0 + G_0 M \langle u \rangle, \tag{12}$$

where the M operator is defined as

$$M = \langle \delta C \rangle + \langle \delta C' N G_0 \delta C' \rangle. \tag{13}$$

To be noted is the obvious conclusion that, in general, the M operator will be nonlocal. In the context of a randomly heterogeneous, linearly elastic solid assumed to be governing on the subscale, Eq. (12) has the following explicit form,

$$\langle \epsilon(\mathbf{x}) \rangle = \epsilon_0(\mathbf{x}) + \int \boldsymbol{G}_0^{(4)}(\mathbf{x}, \mathbf{x}'): \times \left(\int \boldsymbol{C}^{(4)}(\mathbf{x}_1, \mathbf{x}_2): \langle \epsilon(x_2) \rangle d\mathbf{x}_2 \right) d\mathbf{x}_1, \quad (14)$$

where $\boldsymbol{C}^{(4)}(\mathbf{x}_1, \mathbf{x}_2)$ is a two-point quartic field. By association with Eqs. (2) and (5), it is clear that this equation is equivalent to the following formulation,

$$\nabla \cdot \langle \tau(\mathbf{x}) \rangle = \mathbf{f}(\mathbf{x}), \quad (15a)$$

$$\nabla \times \langle \epsilon(x) \rangle \times \nabla = 0, \quad (15b)$$

and

$$\langle \tau(\mathbf{x}) \rangle = \int \boldsymbol{C}^{(4)}(\mathbf{x}_1, \mathbf{x}_2): \langle \epsilon(\mathbf{x}_1) \rangle d\mathbf{x}_1. \quad (15c)$$

Equations (15) are readily identified with the equations governing a nonlocal, linearly elastic solid.

In the more general context, a comparison of Eqs. (1) and (12) allows the further conclusion that the equations that govern the averaged response field for a material with a random substructure differ from those that govern the random response field only in that a random, local, interaction operator is to be replaced by a deterministic, nonlocal, interaction operator. It is natural then to term M operator in Eq. (12) an effective interaction operator, and to term the formulation an effective interaction formulation. The term effective constitutive law also applies to the formulation.

It is obvious that the derivation of the effective interaction formulation is formal. Any attempt at a strict mathematical justification on the manipulations involved would necessitate statements as to the nature of the operators that describe the underlying physical process. Referring to Eq. (10), the presence of the projection operator would seem to make clear that N can only be made explicit in certain asymptotic regimes. Still, the result of the derivation is physically suggestive of a nonlocal continuum formulation expressed in the averaged field response. We accept the derived Eq. (12) to provide a microstructural basis for physical theories of nonlocal continua.

Formulations on Conditionally Averaged Response Fields

In the formulation of the last section no specific reference was made to the fact that the material of interest is a mixture of two homogeneous component phases. Further, the formulation is expressed in terms of the unconditionally averaged response field. In this section we consider a formulation suitable for a two-phase mixture, expressed in terms of conditionally averaged response field measures that incorporate restrictions that the observation point is located in one or the other of the two component phases.

To accomplish the restriction to a two-phase material we introduce two functions of position, denoted by $g_i(x)$; $i=1$, 2, and defined to equal unity if the point located by the position coordinate x is in the i phase and equal to zero if the point is not in the i phase. The restriction to a two-phase material is incorporated by expressing the local interaction operation, δC, as

$$\delta C = \sum_{i=1}^{2} \delta C_i g_i(x). \quad (16)$$

We introduce this expression in a rewrite of Eq. (1), in a slightly expanded form. Thus,

$$u(x) = u_0(x) + G_0(x, x_1) \sum_{i=1}^{2} \delta C_i g_i(x_1) u(x_1). \quad (17)$$

We next emphasize a distinction that the observation point for evaluating the response field measure is in one, or the other of the two phases by introducing a subscript to u. Equation (17) then is equivalent to the following pair of equations[1]

$$u_i(x) = u_0(x) + G_0(x, x_1) \sum_{j=1}^{2} \delta C_j g_j(x_1) u_j(x_1); \; x \subset i. \quad (18)$$

The notation $x \subset i$ denotes that the observation point x is to be located in the i phase. For any single manifestation of the ensemble of mixtures, $u_1(x)$ and $u_2(x)$ are defined only over disjoint portions of the total space covered by the mixtures. Note that according to Eq. (18), the values of $u_i(x)$ for x points that do not lie in the portion of space for which $u_i(x)$ is defined do not enter the formulation. Our objective in this section is to derive a formulation expressed in

$$\langle u_i(x) \rangle = \langle u_i(x) \rangle_{x \subset i} = \langle u(x) \rangle_{x \subset i}, \quad (19)$$

conditional averages of the response field taken over subensembles that have the observation point in the appropriate single phase. The conditions that apply in a particular average will be indicated by a subscript to the variable being averaged, unless otherwise indicated. While for any single manifestation a particular $u_i(x)$ is defined only over a portion of the total space covered by the mixtures, the average of $u_i(x)$ is defined over the total space.

Taking conditional averages of Eq. (18), we write

$$\langle u_i(x) \rangle = u_0(x) + G_0(x, x_1) \sum_{j=1}^{2} \delta C_j \langle g_j(x_1) u_j(x_1) \rangle_{x \subset i}. \quad (20)$$

Equation (20), one for each i, apply for all points covered by the mixtures. Note the condition for averaging the interaction terms at the point, x_1, is that the observation point, x, be in one or the other of the two phases[2] On writing

$$u_j(x_1) = \langle u_j(x_1) \rangle + u_j'(x_1) \quad (21)$$

where the average here is conditional on $x_1 \subset j$, Eq. (20) becomes

$$\langle u_i(x) \rangle = u_0(x) + G_0(x, x_1) \sum_{j=1}^{2} \delta C_j (\langle g_j(x_1) \rangle_{x \subset i} \langle u_j(x_1) \rangle + \langle g_j(x_1) u_j'(x_1) \rangle_{x \subset i}). \quad (22)$$

The two-point average $\langle g_j(x_1) \rangle_{x \subset i}$, can be identified with the conditional probability that the interaction point, x_1, is in the j phase given that the observation point, x, is in the i phase. Equations (22) are the analog of Eq. (6) of the last section. They do not constitute a closed system on $\langle u_i(x) \rangle$ due to the presence of $\langle g_j(x_1) u_j'(x_1) \rangle_{x \subset i}$. Accordingly, we proceed as before and derive equations that govern $u_i'(x)$, the fluctuating component of the single-phase response measures.

Subtracting Eq. (22) from Eq. (18), we obtain

$$u_i'(x) = G_0(x, x_1) \sum_{j=1}^{2} \delta C_j (g_j'(x_1 | x \subset i) \langle u_j(x_1) \rangle + (I - P_{x \subset i}) g_j(x_1) u_j'(x_1)); \; x \subset i, \quad (23)$$

where

$$g_j'(x_1 | x \subset i) = g_j(x_1) - \langle g_j(x_1) \rangle_{x \subset i} \quad (24)$$

and the projection operation is an averaging that incorporates

[1] A subscript could be introduced to the $G_0(x, x_1)$ operator allowing for the possibility of a different reference material depending on the phase in which the observation point is to be located. This added flexibility might have some utility in future calculations, but does not appear to add anything to our treatment.

[2] The average $\langle g_j(x_1) u_j(x_1) \rangle_{x \subset i}$ is a two-point probability measure. To emphasize this we can write

$$\langle g_j(x_1) \mu_j(x_1) \rangle_{x \subset i} = \langle g_i(x) g_j(x_1) u_j(x) \rangle_{x \subset i} = \langle g_i \rangle^{-1} \langle g_i(x) g_j(x_1) u_j(x_1) \rangle,$$

where the averages on the right-hand side of the last equality are unconditional.

the condition that the observation point be in the i phase. Equations (23) are to be interpreted as an equation to determine the $u_i'(x)$, each defined in the appropriate phase, in terms of the "known" forcing,

$$F(x) = G_0(x, x_1) \sum_{j=1}^{2} \delta C_j g_j'(x, |x \subset i) \langle u_j(x_1) \rangle. \quad (25)$$

The forcing is defined for all points covered by the mixture, in any single manifestation. The functional expression for $F(x)$ depends on the phase in which the field point, x, is located.

The solution of Eq. (24) is formally accomplished by a pair of operators that are the analog of the N operator of the last section. We write

$$u_i'(x) = N_i(x, x_1) F(x_1); \; x \subset i, \quad (26)$$

emphasizing in our expanded notation that the N_i are nonlocal, in general. Using Eqs. (20) and (26), we form

$$\langle g_j(x_1) u_j'(x_1) \rangle_{x \subset i} = \sum_{k=1}^{2} \delta C_k \langle g_j(x_1) N_j(x_1, x_2) G_0(x_2, x_3) g_k'(x_3 | x_2 \subset j) \rangle_{x \subset i} \langle u_k(x_3) \rangle, \quad (27)$$

to substitute in Eqs. (22). The closed system of equations expressed in $\langle u_i(x) \rangle$ is written

$$\langle u_i(x) \rangle = u_0(x) + G_0(x, x_1) \sum_{j=1}^{2} \delta C_j M_{ij}(x_1, x_2; x) \langle u_j(x_2) \rangle, \quad (28)$$

where

$$M_{ij}(x_1, x_2; x) = \langle g_j(x_1) \rangle_{x \subset i} \delta(x_1 - x_2) + \sum_{k=1}^{2} \delta C_k \langle g_k(x_1) N_k(x_1, x_3) G_0(x_3, x_2) g_j'(x_2 | x_3 \subset k) \rangle_{x \subset i}, \quad (29)$$

where $\delta(x)$ is the Dirac distribution. The coordinate denoted by x_3 in Eqs. (29) is a dummy variable. The nonlocal operator, $M_{ij}(x_1, x_2; x)$, is a mapping of a function $\langle u_j(x_2) \rangle$ to a function of x_1; the mapping depends on the location of the point pair x_1, x_2 relative to the field point x. There is no counterpart of this dependence in the formulation expressed in $\langle u(x) \rangle$, the unconditionally averaged field response. We shall return to this difference presently.

Equations (28) are a significant new result of this paper. These demonstrate that for a two-phase mixture one can obtain a closed formulation expressed in conditionally averaged response fields in much the same manner as earlier demonstrations that one can obtain a formulation expressed in the unconditionally averaged response field. Moreover, the formulation obtained can be recognized to have the "structure" of that for a mixture of "interacting continua," (Bedford and Drumheller, 1983) a recognition that is possibly more transparent in the context of a specific application.

In the context of a randomly heterogeneous, linearly elastic solid assumed to be governing on the subscale, Eqs. (28) have the following explicit form

$$\langle \epsilon_i(\mathbf{x}) \rangle = \epsilon_0 + \int \boldsymbol{G}_0^{(4)}(\mathbf{x}, \mathbf{x}_1) : \sum_{j=1}^{2} \int \boldsymbol{C}_{ij}^{(4)}(\mathbf{x}_1, \mathbf{x}_2; \mathbf{x}) \langle \epsilon_j(\mathbf{x}_2) \rangle d\mathbf{x}_2; \quad i = 1, 2, \quad (30)$$

where the $\boldsymbol{C}_{ij}^{(4)}(\mathbf{x}_1, \mathbf{x}_2; \mathbf{x})$ are three-point quartic fields. The presence of the observation point $\mathbf{x}$, along with the dummy source points $\mathbf{x}_1$ and $\mathbf{x}_2$ introduces a complication to a direct identification of Eqs. (30) with a continuum theory formulation. To eliminate this problem we average, or smooth, the equations over a localized region of $\mathbf{x}$. This is suggested by an observation that the dependence of the quartics on the precise location $\mathbf{x}$, relative to $\mathbf{x}_1$, $\mathbf{x}_2$, is limited to $|\mathbf{x}|$ values that are within a correlation length of these points. This observation follows from their definitions and the footnote following Eq. (20). Assuming, then, the remaining terms in Eq. (30) vary slowly with changes in $\mathbf{x}$ on this scale, the quartics can be replaced by their local averaged values which are independent of $\mathbf{x}$. The smoothed equations can then be seen to be equivalent to the following formulation

$$\nabla \cdot \langle \tau_1(\mathbf{x}) \rangle = f(\mathbf{x}) - \nabla \cdot \int \boldsymbol{C}_{12}^{(4)}(\mathbf{x}, \mathbf{x}_1) : (\langle \epsilon_2(\mathbf{x}_1) \rangle - \langle \epsilon_1(\mathbf{x}_1) \rangle) d\mathbf{x}_1,$$

$$\nabla \cdot \langle \tau_2(\mathbf{x}) \rangle = f(\mathbf{x}) - \nabla \cdot \int \boldsymbol{C}_{21}^{(4)}(\mathbf{x}, \mathbf{x}_1) : (\langle \epsilon_2(\mathbf{x}_1) \rangle - \langle \epsilon_1(\mathbf{x}_1) \rangle) d\mathbf{x}_1, \quad (30a)$$

$$\nabla \langle \epsilon_1(\mathbf{x}) \rangle \times \nabla = 0,$$

$$\nabla \langle \epsilon_2(\mathbf{x}) \rangle \times \nabla = 0, \quad (30b)$$

and

$$\langle \tau_1(\mathbf{x}) \rangle = \int (\boldsymbol{C}_{11}^{(4)}(\mathbf{x}, \mathbf{x}_1) + \boldsymbol{C}_{12}^{(4)}(\mathbf{x}, \mathbf{x}_1)) : \langle \epsilon_1(\mathbf{x}_1) \rangle d\mathbf{x}_1,$$

$$\langle \tau_2(\mathbf{x}) \rangle = \int (\boldsymbol{C}_{22}^{(4)}(\mathbf{x}, \mathbf{x}_1) + \boldsymbol{C}_{21}^{(4)}(\mathbf{x}, \mathbf{x}_1)) : \langle \epsilon_2(\mathbf{x}_1) \rangle d\mathbf{x}_1. \quad (30c)$$

Equations (30a) have the interpretation of momentum balance laws for two "interacting," linearly elastic continua. Equations (30b) and (30c) have the interpretation of compatibility and effective constitutive laws for the two continua. It is clear that nonlocal operators are necessary to describe both the interaction of the continua and the effective constitutive laws. We note that the coupling terms in Eqs. (30a) are in the ratio of the volume fractions of the component phases, i.e., $\langle g_1 \rangle$. This can be concluded either directly from the definitions of $\boldsymbol{C}_{12}^{(4)}$ and $\boldsymbol{C}_{21}^{(4)}$ or from multiplying the first of Eqs. (30a) by $\langle g_1 \rangle$, the second by $\langle g_2 \rangle$ and by adding. Comparing the result with Eq. (15a) shows that for consistency, the coupling terms must vanish in this sum.

A condition on the location of the field point in one or the other of the two phases is not the only one that might be imagined in defining partial response field measures. Thus, for example, one might also investigate a class of experiments in which the forcing of the two-phase mixture is a singular, or point, forcing. The response field $u(x, x_s)$ can, then, be interpreted as a function of both the source and the field points. Conditional averages based on either, or both, of these points being in one or the other of the two phases can be discussed. We write,

$$\langle u^{(i)}(x, x_s) \rangle = \langle u(x, x_s) \rangle_{x \subset i}, \quad (31a)$$

and

$$\langle u_i^{(j)}(x, x_s) \rangle = \langle u(x, x_s) \rangle_{\substack{x \subset i \\ x_s \subset j}} \quad (31b)$$

as additional partial response field measures. Deriving deterministic equations that these measures satisfy is rather trivial, in view of Eqs. (12) and (28), since the source point location enters the calculations only as a parameter. Thus, we immediately write

$$\langle u^{(j)}(x, x_s) \rangle = u_0(x, x_s) + G_0(x, x_1) M^{(j)}(x_1, x_2; x_s) \langle u^{(j)}(x, x_s) \rangle, \quad (32a)$$

and

$$\langle u_i^{(j)}(x, x_s) \rangle = u_0(x, x_s) + G_0(x, x_1) \sum_{k=1}^{2} \delta C_k M_{ik}^{(j)}(x_1, x_2; x, x_s) \langle u_k^{(j)}(x_2, x_s) \rangle. \quad (32b)$$

The $M^{(j)}$ and $M_{ik}^{(j)}$ operators are obvious extensions of the M and M_{ik} operators of Eqs. (12) and (28), respectively. We note that there is no coupling across the j index, the one indicating the source point phase. We also note that the nonlocal mappings described by $M^{(j)}(x_1, x_2; x_s)$ and $M_{ik}^{(j)}(x_1, x_2; x, x_s)$ depend on x_s and x, as well as on the dummy locations x_1, x_2.

Recovery of Unconditionally Averaged Response Field Formulation

The projections that resulted in formulations on conditionally averaged response measures can be termed incomplete, where that on the unconditionally averaged $\langle u \rangle$ is complete. We consider, next, completing the projections of the formulations on the conditionally averaged response measures to obtain that governing $\langle u \rangle$. Two such developments are considered; one starting with Eqs. (28), written on the $\langle u_i(x) \rangle$, and one starting with Eqs. (32*a*), written on the $\langle u^{(i)}(x, x_s) \rangle$. The developments are different since there is a coupling between the equations governing the $\langle u_i \rangle$, and not between those governing the $\langle u^{(i)} \rangle$.

The manipulations to obtain a formulation expressed in $\langle u(x) \rangle$ starting with Eqs. (28) are similar to the developments of the last two sections. Thus, the projection operation expressed in the equation

$$\langle u(x) \rangle = \sum_{i=1}^{2} \langle g_i(x) \rangle \langle u_i(x) \rangle, \tag{33}$$

is applied to Eqs. (28) to obtain

$$\langle u(x) \rangle = u_0(x) + G_0(x, x_1) \sum_{j=1}^{2} \delta C_j \overline{M}_j(x_1, x_2) \langle u_j(x_2) \rangle, \tag{34}$$

where

$$\overline{M}_j(x_1, x_2) = \sum_{i=1}^{2} \langle g_i(x) \rangle M_{ij}(x_1, x_2; x). \tag{35}$$

The presence of the $\langle u_j(x) \rangle$ term in Eq. (34) presents the familiar closure problem, which we address in the same manner as previously. Thus, we write

$$\langle u_j(x) \rangle = \langle u(x) \rangle + u_j'(x) \tag{36}$$

and subtract Eq. (34) from Eqs. (28) to obtain

$$u_i'(x) = G_0(x, x_1) \sum_{j=1}^{2} \delta C_j M_{ij}'(x_1, x_2; x) [\langle u(x_2) \rangle + u_j'(x_2)], \tag{37}$$

where

$$M_{ij}'(x_1, x_2; x) = M_{ij}(x_1, x_2; x) - \overline{M}_j(x_1, x_2). \tag{38}$$

Equations (37) are now interpreted to determine $u_j'(x)$ in terms of $\langle u(x) \rangle$; to be used in Eqs. (36) to determine $\langle u_j(x) \rangle$ in terms of $\langle u(x) \rangle$; to be used in Eq. (34) to obtain the closed equation on $\langle u(x) \rangle$. The result is an equation with the algebraic structure of Eq. (12) with the following expression for the effective interaction operator contained therein:

$$M(x_1, x_2) = \sum_{j=1}^{2} \delta C_j \overline{M}_j(x_1, x_4) \left[\delta(x_4 - x_2) + \sum_{k=1}^{2} \sum_{i=1}^{2} N_{jk}(x_4, x_3) G_0(x_3, x_2) \delta C_i M_{ki}'(x_3, x_2; x) \right]. \tag{39}$$

In this equation, N_{jk} is the operator that inverts Eqs. (37) to determine u_j' in terms of $\langle u \rangle$.

It is clear the Eqs. (37) might not provide for a unique prescription for u_j', anymore than Eq. (8) might not provide for a unique prescription for u', in the projection method as usually applied. This point is not an issue, however. What is an issue is whether the formulism expressed in $\langle u \rangle$, which results, does provide for a unique prescription for it. To answer this question one must look to the resulting formulism as obtained in the context of a specific application. McCoy (1971) considered one investigation in the context of the equations of linear elastostatics. We shall not address this question further in this study, and simply assume that lack of uniqueness is not an issue.

The manipulations to obtain a formulation expressed in $\langle u(x, x_s) \rangle$ starting with Eqs. (32*a*) follow a different route, since the equations on the $\langle u^{(i)}(x, x_s) \rangle$ are uncoupled. Thus, we first formally invert Eqs. (32*a*) to write

$$\langle u^{(i)}(x, x_s) \rangle = (I - G_0 M^{(i)})^{-1} u_0(x, x_s). \tag{40}$$

The projection operation

$$\langle u(x, x_s) \rangle = \sum_{i=1}^{2} \langle g_i(x_s) \rangle \langle u^{(i)}(x, x_s) \rangle \tag{41}$$

is now applied to Eqs. (40) to obtain an equation to govern $\langle u(x, x_s) \rangle$ of the same algebraic structure as the formal inverse of Eq. (12), i.e.,

$$\langle u(x, x_s) \rangle = (I - G_0 M)^{-1} u_0(x, x_s). \tag{42}$$

Equating the two we obtain an operator equation to determine the effective interaction operator

$$(I - G_0 M)^{-1} = \sum_{i=1}^{2} \langle g_i(x_s) \rangle (I - G_0 M^{(i)}(x_1, x_2; x_s))^{-1}. \tag{43}$$

In the next section we consider this derivation of the formulation on the mean-field response, $\langle u(x) \rangle$, via intermediate formulations on conditionally averaged responses in a two-length scale limit. The objective there is to gain insight as to the properties of the effective interaction operator and their dependence on the configuration statistics of the two-phase mixture. We close this section by considering the further projection of Eqs. (32*b*) on the conditionally averaged $\langle u_i^{(j)}(x, x_s) \rangle$, to obtain a formulation with the algebraic structure of Eqs. (28) on the conditionally averaged $\langle u_i(x) \rangle$. The manipulations directly follow those above, and we obtain the following operator equations to determine the $M_{ij}(x_1, x_2; x)$,

$$\left(I - G_0 \sum_{j=1}^{2} \delta C_j M_{ij} \right)^{-1} = \sum_{k=1}^{2} \langle g_k(x_s) \rangle \left(I - G_0 \sum_{j=1}^{2} \delta C_j M_{ij}^{(k)}(x_1, x_2; x, x_s) \right)^{-1}. \tag{44}$$

A Two-Scale Limit and the Interpretation of Derived Formulations as Continuum Theories

An asymptotic regime of important technological interest applies for a two-length-scale scenario in which the scale for measuring variations in δC is small when compared to the scale for measuring the specimen geometry and variations in the specimen forcing. In this section we investigate the derived formulations in this regime. Our principal interest is the behavior of the effective interaction operators in the two-scale limit—how do they simplify and on what do they depend—and in what sense can we interpret the obtained formulations as bases for continuum theories.

The issue of interpreting the obtained formulations as bases for continuum theories represents a change in perspective, which warrants comment. To this point in our treatment the objective of the calculations presented can be characterized to be the solution of a well-defined mathematical problem; determine the average (conditional or not) response of an ensemble of two-phase material specimens. The solution procedure is in two steps. The first step was to derive from a stochastic description of the equations governing the response in each manifestation of the ensemble, a deterministic description of equations governing the averaged response of the ensemble. The second step would be to solve the formulations derived in the context of a particular physical experiment. To make the derived formulations specific requires one to invert certain stochastic field equations. The solutions of these equations determine the effective interaction operators that appear

in the formulations that govern the averaged response. The change in perspective is now to eschew the stochastic field equations in terms of which the effective interaction operators are defined. Instead, we now seek to determine these operators—or actually to determine the values of the constants that make a suitable parameterized representation of these specific—"experimentally" by matching physical data with predictions of the formulations that govern the averaged response. It is to the extent to which this perspective can be validated that allows the formulations on the averaged response to be interpreted in terms of physical theories.

The efficacy of this new interpretation will depend on the class of physical experiments over which the effective interaction operators are invariant and on the ease with which these operators can be parameterized. Thus, with reference to Eq. (12) as a basis for a continuum theory on the unconditionally averaged response field, its derivation suggests that the M operator is invariant under changes of the specimen forcing, u_0, but depends on the specimen geometry, through G_0. Actually, the M operator also depends on the nature of any forcing that is applied at the boundary, through G_0. While the lack of dependence on M on the specimen forcing would allow for some predictive capability of Eq. (12) interpreted as a theory, a conclusion that the effective interaction operator changes along with a change in the specimen geometry certainly is very restrictive. Fortunately, it can be argued that this dependence is unimportant for many experiments in the two-scale asymptotic regime. The key to these arguments is in an assumption (Beran and McCoy, 1970a,b) that the range of the nonlocality of the M operator is to be measured on the smaller, i.e., microscale on which variations in δC are measured. Then, the argument is that the dependence of the M operator on specimen geometry will only be significant within a layer of the specimen boundary surface which is also to be measured on the microscale. Ignoring this layer, M depends only on the material properties of the constituent phases and on the microstructure geometry. The operator can truly be termed a "material" operator. We note that the two-length-scale condition can also be used to argue an ergodicity that equates the statistical average of the response field with a spatial average, thereby obtaining a completely deterministic interpretation. We also note that to zeroth order in this asymptotic limit, the effective interaction operator is local. The interpretation of M as a material operator and its approximation as a local operator are thus closely tied.

A direct demonstration that the nonlocality range of M is to be measured on the microscale requires an explicit representation of the operator. In earlier studies (Beran and McCoy, 1970a,b; McCoy, 1972a, 1973) this was considered by writing Eq. (10) as

$$N=(I-G_0\langle\delta C\rangle)^{-1}(I-(I-G_0\langle\delta C\rangle)^{-1}G_0(I-P)\delta C')^{-1}, \tag{45}$$

which formally can be written

$$N=(I-G_0\langle\delta C\rangle)^{-1}\sum_{n=0}^{\infty}((I-G_0\langle\delta C\rangle)^{-1}G_0(I-P)\delta C')^n. \tag{46}$$

Using Eq. (46) in Eq. (13) results in the desired explicit representation as an infinite series in which the substructure geometry appears via multipoint moments of all orders, defined on the variations in $\delta C'$. Moreover, the series collects terms in powers of the strength in the variations in $\delta C'$, enabling its truncation for weakly inhomogeneous substructures. While the entire analysis suffers from lack of mathematical rigor, it can be used to suggest the validity of some general conclusions in the limit of weak homogeneity. The conclusions reached in the earlier studies were in agreement with the desired intuitive arguments, and, moreover, provided a precise method for determining the length of the microscale. Thus, the statistical moments, or correlation functions, defined on $\delta C'$ served to define it.

The results of the last section can provide for an indirect investigation of the nonlocality range of M, which is not limited to the asymptotic regime of weak inhomogeneity. Consider the derivation of the formulation on the unconditionally averaged response for an ensemble of specimens subjected to a point forcing based on formulations on the conditionally averaged responses for two subensembles of specimens in which the point forcing is located in one or the other of the two phases. Equation (43) provides the prescription for obtaining the effective interaction operator for the unconditionally averaged formulation in terms of the effective interaction operators for the conditionally averaged formulations. The question we pose is the following: Assuming that conditions apply such that the effective interaction operator for the conditionally averaged formulations can be approximated as local in the two-scale limit, does it necessarily follow that the effective interaction operator for the unconditionally averaged formulation can also be approximated as local? Clearly the answer to this question must be no. Indeed, the prescription of Eq. (43) would appear to require that it is necessary that the effective interaction operators in the conditionally averaged formulations be approximately equal to each other as well as be approximated by local operators for the effective interaction operator for the unconditionally averaged formulation to be approximated by a local operator.

One can speculate on two-type microstructures for which this would be so. One would be a two-phase mixture in which one of the two phases can be identified as inclusions dispersed throughout the second-phase matrix. At distances sufficiently removed from the point forcing, it is intuitive that the response in any specimen in the ensemble will not depend on the forcing location phase. In the two-scale limit, the response of the single inclusion in which any point forcing is located itself will result in what would appear, at a sufficiently large distance, to be a point force acting in the matrix. This scenario implicitly accepts that the above-referenced, sufficiently large distance is to be measured on a scale of the size of the inclusions, and assumes a sufficiently large separation distance between inclusions so as to exclude the effects of what might be termed a tunnelling. Sufficiently large, in this last reference, is to be measured on a different, much smaller scale than that determined by inclusion size.

The second type microstructure for which the effective interactions in the conditionally averaged formulations would be approximately equal would be one in which the two phases are strongly coupled. By a strongly coupled two-phase mixture is meant one in which the transport, of whatever flux quantity is being modeled, across the interface separating the two phases is of the same order as the transport across a surface within either of the two phases. A weakly inhomogenous two-phase mixture would be strongly coupled by this definition. Thus, the properties of a weakly coupled two-phase mixture cannot be addressed by investigating the explicit series representation for M which follows from the representation in Eq. (46).

However, for weakly coupled two-phase mixtures for which both phases are *connected* for separation distances that are measured on the scale of the specimen, the effective interaction operators for the conditionally averaged formulations can differ greatly according to the phase in which the forcing point is located. By a connected phase over some distance is meant that two points in the phase separated by the distance can be joined by a continuous curve that lies completely in the phase. For weakly coupled mixtures of two phases which are connected over distances which are measured on the scale of the specimen, then the effective interaction operator for the unconditionally averaged response can be expected to remain nonlocal in the two-scale limit.

Left to be investigated is whether the mixture theory-type formulation, which applied for conditional averages based on the location of the observation point and for an arbitrary forcing, contains nonlocal effective interaction operators in the two-scale limit for weakly coupled, two-phase mixtures of connected phases. We can investigate this issue indirectly by considering the projection of the formulation for the conditionally averaged response to a point forcing where the condition requires the phases of both the forcing and observation points to obtain the formulation for the conditionally averaged response where the condition requires only the phase of the observation point. The investigation follows a reasoning similar to the above, but concentrating on Eq. (44) instead of Eq. (43). A conclusion that locality in the formulation for both the forcing and observation point phases specified implies locality in the formulation for only the observation point phase specified, *for the two-phase mixture of interest*, follows from the stated restriction to a weak coupling. The weak coupling limit implies that the important flux paths connecting the forcing point and the receiving point are to continuously lie in a single phase. Thus, the off-diagonal $M_{ij}^{(k)}$ and M_{ij} operators are to be far less significant than are the operators with identical indices. Thus, in the presence of weak coupling of phases, locality in those $M_{ij}^{(k)}$ operators that significantly influence the transport of flux through the specimen in the two-scale limit implies locality in those M_{ij} operators that have a significant influence.

The nonlocality identified with reference to Eq. (12) in reducing from an extended formulation in which the forcing phase is specified is not significant with reference to Eq. (28). The reason is that the nonlocality identified with reference to Eq. (12) required a mixture for which the coupling terms in Eq. (28) are necessarily weak. Moreover, the operators in the *direct* terms in Eq. (28) do not contain the nonlocality identified with reference to that in Eq. (12). Referring to Eq. (39), there is a nonlocality introduced in the infinite series sum that is in addition to any contained in the various M operators that appear therein.

The fact that a weakly coupled local mixture theory applies for the conditionally averaged response in the two-scale limit, whereas the formulation on the unconditionally averaged response must remain nonlocal for the identified conditions, is a significant conclusion of this paper. Not only can a mixture theory formulation be obtained from projecting a more fundamental description on the microscale, its importance as a predictive model can be argued even for experiments in which the partial response fields, i.e., the conditionally averaged fields, are not directly measurable. The importance is in the convenience of the formulation, i.e., weak coupling and local, when compared to the nonlocal formulation required for the full-response field, i.e., the unconditionally averaged field. Possibly more important than convenience, however, are the questions to be raised when interpreting the obtained formulations as bases for physical theories. We refer back to the discussion of the tie between locality of an effective interaction operator and its interpretation as a "material" property.

What about the significance, or utility, of a strongly coupled, local mixture theory? As a predictive model for partial response field measures for an experiment in which local balance and constitutive laws apply on a microscale, this formulation can be useful. If, however, there is no interest in the partial response field measures themselves, but only as an intermediate step to obtaining an estimate of the full-field response, the utility is less. This is because the condition of a strong coupling implies locality is a properly obtained formulation to govern the full-field response.

Concluding Remarks

The mathematical arguments presented have been formal, and none of the resulting formulations have the status of rigorously derived mathematical results. Providing such a status would clearly require more detailed statements of both the underlying physical process to be modeled and the nature of the heterogeneity. Again, we make reference to Gillette (1991). Although to my knowledge a mathematically rigorous approach to the questions addressed has not been attempted, the foundation for this would appear to be available.

Homogenization deals with the partial differential equations encountered in studying the physics of heterogeneous materials with a periodic structure, in the limit of the characteristic length of the period vanishing. The subject has a long history, tracing back at least to Poisson (1822). Modern treatments are given by Babuska (1976), Bensoussan et al. (1978), and Sanchez-Palencia (1980). These treatments are applicable to heterogeneity that is deterministic, as well as periodic. Keller (1977) is generally credited with suggesting the application of two-scale asymptotic analysis to heterogeneity that is described by stochastic processes. A specific recent application of this type analysis to a heterogeneity that need not be deterministic is the derivation of Biot's equations of poroelasticity (Biot, 1956), by Burridge and Keller (1981). Like the present paper, the above-referenced applications of two-scale asymptotic analysis to random heterogeneity does not address questions of the nature of the convergence of the approximations introduced. It is in answering these questions that the derivations would be elevated from an exercise in formal mathematics to rigorous analysis.

Elevation of an homogenization to the status of rigorous analysis would begin with a precise identification of two widely different length scales. While this step may be relatively straightforward in the context of material heterogeneity which is deterministic and periodic, the identification of the microscale is far less certain for material heterogeneity which is stochastic. Further with regard to a stochastic homogenization, our ability to identify the microscale would appear to be greater for experiments in which material heterogeneity results from a dynamic process. The dispersion of an additive by the small-scale structure of a turbulent flow field would be an example of such an experiment.

For material heterogeneity which is stochastic and for which the identification of an underlying dynamic process is not possible, the situation is much more problematic. Transport processes in composite materials, or through porous media, would fall in this category. In the context of such experiments, it would be necessary to determine whether the microscale lengths are properly identified with the geometric properties of material heterogeneity, or with the topologic properties, or with both. Characteristic lengths given by multipoint moments or multipoint probability functions would be useful measure of the former, but not the latter. Consider, for example, one such characteristic length to be the separation distance between two points, in a two-scale medium, required for the events defined on the phases of the two points to be statistically independent. Denote this length by l. For a reasonably well-mixed composite material, l would most properly be identified with the size of the inclusion phase; for a porous medium it would be most properly identified with a pore size. Thus, l is a geometric length. Now consider another characteristic length to be the separation distance between two points such that there is a vanishingly small probability of connecting any two points in the neighborhoods, of dimension l, of the two specified points by a line that remains entirely in one or the other of the two phases. This would be a topologic length, and it is hard to see it determined from any multipoint probalibity function.

The calculations and arguments presented in this paper suggest that for a certain class of two-phase materials, the proper structure of the homogenized equations would depend on whether the topologic lengths of one or of both phases can be described as macroscale lengths.

We can cite two experimental studies by Plona (1980) and Johnson and Plona (1982) that relate to the calculations presented in this paper. First, Plona demonstrated the existence of two compressional modes of momentum transport in a water-saturated porous solid composed of sintered, fused, glass beads. The second compressional mode observed by Plona confirmed a prediction of the above-referenced theory of Biot (1956). In the second study, the experiment was repeated both for the case in which the glass beads were fused and for the case in which they were not. Only one compressional mode was observed in the absence of fusing, with a wave speed that corresponds to neither of the two wave speeds that corresponded to neither of the two wave speeds observed for the fused beads. Further, no shear mode was observed when the beads were not fused. Superficially these results would appear to be in agreement with the arguments presented. Thus, the fluid contained in the pores of the manufactured medium is singly connected, independent of the fusing of the beads, and would provide for a mode of momentum transport by compressional waves. The singly connected solid frame formed by fusing the glass beads would provide for two possible modes of momentum transport, by compressional waves and by shear waves. Thus, the three modes observed when the beads are fused are to be expected. In the absence of the fusing, the beads are, in principle, not connected, which might be argued to eliminate the modes of transport which are primarily through this phase. Since the volume fraction of the beads was 38 percent, however, which is typical for a dense packing of spheres, it would appear to be unlikely that the solid phase cannot support any momentum transport by itself. Rather, the reason for observing the second compressional mode and the shear mode probably is a result of the "interface" between the water bath and the "porous material" sample. That is, the reason for not observing the waves is probably not because the waves cannot be supported in the absence of the fusing; it is because the experimental arrangement did not excite them. This does not explain the strong dependence of the wave speed of the single wave observed on the fact that the beads were fused, however.

Acknowledgment

The study, a part of which is reported herein, is being accomplished with the support of the Office of Naval Research (N00014-88-K-0314 and N00014-89-J-3136). I thank Dr. Albert Tucker for his encouragement and for recognizing the importance of some of the issues addressed in the context of structural acoustics for highly complex systems.

References

Anderson, P. W., 1958, "Absence of Diffusion in Certain Random Lattices," *Physical Review*, Vol. 109, pp. 1492–1505.

Babuska, I., 1976, "Homogenization and Its Application: Mathematical and Computational Problems," *Numerical Solution of Partial Differential Equations—III*, B. Hubbard, ed., Academic Press, pp. 89–116.

Bedford, A., and Drumheller, D. S., 1983, "Theories of Immiscible and Structured Mixtures," *Int. J. Engr. Sci.*, Vol. 21, No. 8, pp. 863–960.

Bensoussan, A., Lions, J. L., and Papanicolaou, G., 1978, *Asymptotic Analysis for Periodic Structures*, North-Holland, Amsterdam.

Beran, M. J., and McCoy, J. J., 1970a, "Mean Field Variations in a Statistical Sample of Heterogeneous Linearly Elastic Solids," *Int. J. Solids Struct.*, Vol. 6, pp. 1035–1054.

Beran, M. J., and McCoy, J. J., 1970b, "Mean Field Variations in a Random Medium," *Quart. Appl. Math.*, Vol. 28, No. 2, pp. 245–258.

Beran, M. J., and McCoy, J. J., 1970c, "The Use of Strain Gradient Theory for Analysis of Random Media," *Int. J. Solids Struct.*, Vol. 6, pp. 1035–1054.

Biot, M. A., 1956, "Theory of Propagation of Elastic Waves in a Fluid-Saturated Porous Solid, I: Low-Frequency Range," *J. Acoust. Soc. Am.*, Vol. 28, No. 2, pp. 168–178.

Burridge, R., and Keller, J. B., 1981, "Poroelasticity Equations Derived From Microstructure," *J. Acoust. Soc. Am.*, Vol. 70, No. 4, pp. 1140–1146.

Fishman, L., and McCoy, J. J., 1980, "Homogenization and Smoothing: A Unified View of Two Derivations of Effective Property Theories and Extensions," ASME JOURNAL OF APPLIED MECHANICS, Vol. 47, pp. 679–682.

Fishman, L., and McCoy, J. J., 1981, "A Unified View of Bulk Property Theories for Stochastic and Periodic Media," *ZAMP*, Vol. 32, pp. 45–61.

Gillette, G., 1991 "Coupled Perturbation Series for Disparate Mixtures," *J. Acoust. Soc. Am.*, Vol. 89, pp. 2084–2092.

Hodges, C. H., and Woodhouse, J., 1983, "Vibration Isolation From Irregularity in a Nearly Periodic Structure: Theory and Measurements," *J. Acoust. Soc. Am.*, Vol. 74, pp. 894–905.

Johnson, D. L., and Plona, T. J., 1982, "Acoustics Slow Waves and the Consolidation Transition," *J. Acoust. Soc. Am.*, Vol. 72, No. 2, pp. 556–565.

Keller, J. B., 1962, "Wave Propagation in Random Media," *Proc. Symp. Appl. Math.*, Vol. 13, American Mathematical Society, Providence, R. I., pp. 227–246.

Keller, J. B., 1964, "Stochastic Equations and Wave Propagation in Random Media," *Proc. Symp. Appl. Math.*, Vol. 16, American Mathematical Society, Providence, R. I., pp. 145–170.

Keller, J. B., 1977, "Effective Behavior of Heterogeneous Media," *Statistical Mechanics and Statistical Methods in Theory and Applications,* R. Landman, ed., Plenum Press, pp. 631–644.

McCoy, J. J., 1971, "Statistical Average Response of a Bounded Linearly Elastic Solid," *Proc. 1st Int. Conf. of Struct. Mech. in Reactor Tech.*, Vol. 6M, Berlin, pp. 539–553.

McCoy, J. J., 1972a, "Pressure Signals in Random Linearly Elastic Rods," *Int. J. Solids Struct.*, Vol. 8, pp. 877–894.

McCoy, J. J., 1972b, "A Note on the Mean Field Dispersion Spectrum for Media with Disordered Substructures," ASME JOURNAL OF APPLIED MECHANICS, Vol. 39, pp. 1155–1156.

McCoy, J. J., 1973, "On the Dynamic Response of Disordered Composites," ASME JOURNAL OF APPLIED MECHANICS, Vol. 40, Series E, pp. 511–517.

McCoy, J. J., 1981, "Macroscopic Response of Continua with Random Microstructures," *Mechanics Today*, Vol. 6, S. Nemat-Nasser, ed., Pergamon Press, pp. 1–40.

Pierre, C., and Dowell, E. H., 1987, "Localization of Vibrations by Structural Irregularity," *J. Sound and Vibration*, Vol. 114, pp. 549–564.

Plona, T. J., 1980, "Observation of a Second Bulk Compressional Wave in a Porous Medium at Ultrasonic Frequencies," *Appl. Phys. Lett.*, Vol. 36, No. 4, pp. 259–261.

Poisson, S. D., 1822, "Second Mém sur la Théorie de Magnétisme," *Med. de L'Acad de France*, Vol. 5.

Sanchez-Palencia, E., 1980, *Non-homogeneous Media and Vibration Theory* (Lecture Notes in Physics, Vol. 127), Springer-Verlag, New York.

Elastodynamic Local Fields for a Crack Running in an Orthotropic Medium

A. Piva
Assistant Professor,
Department of Physics,
University of Bologna,
40126 Bologna, Italy

E. Radi
Istituto di Scienza delle Construzioni,
University of Bologna,
40136, Bologna, Italy

The dynamic stress and displacement fields in the neighborhood of the tip of a crack propagating in an orthotropic medium are obtained. The approach deals with the methods of linear algebra to transform the equations of motion into a first-order elliptic system whose solution is sought under the assumption that the local displacement field may be represented under a scheme of separated variables. The analytical approach has enabled the distinction between two kinds of orthotropic materials for which explicit espressions of the near-tip stress fields are obtained. Some results are presented graphically also in order to compare them with the numerical solution given in a quoted reference.

1 Introduction

A number of powerful analytical approaches for the solution of a propagating crack problem in an anisotropic elastic medium are available.

Among the most notable of these there is the Stroh's formulation (1962) which provides an elegant method of treating steady-state problems in anisotropic elasticity.

A modified version of the Stroh's method has been applied by Atkinson (1964) and by Atkinson and Head (1966) to develop the steady-state model of a propagating crack in an anisotropic medium.

One of the most general features, common to plane elastodynamic solutions for moving cracks through an elastic solid, is the representation of the spatial dependence of the elastic fields in the neighborhood of the crack tip, under a scheme of separated variables.

This result has been well established by Freund and Clifton (1974) in the case of a crack moving nonuniformly in an isotropic medium.

A work that directly relates to the present analysis is that of Achenbach and Bažant (1975) in which the above representation has been used to obtain elastodynamic near-tip fields for traction-free cracks running in isotropic and orthotropic materials. For the case of isotropic materials they found the closed-form solution for the spatial dependence of the elastic fields, whereas a numerical approach was used for the orthotropic case.

In the present paper the problem of a crack propagating at a time-dependent velocity in an orthotropic medium is revisited to obtain closed-form expressions for the near-tip elastic fields.

In solving the problem, use is made of an approach recently proposed by Piva (1987) and by Piva and Viola (1988) to transform the equations of motion into a first-order elliptic system which is then solved following the initiative of the previously cited authors.

In addition, the method of solution allows to distinguish between two kinds of orthotropic materials for which significant differences on the near-tip stress field are pointed out.

2 Mathematical Preliminaries

Consider an infinite orthotropic elastic body and a crack moving with a time-dependent speed $c(t)$ along the x-axis of a Cartesian coordinate system $O(x, y, z)$ whose axes are of elastic symmetry. By referring to coordinates (x, y) attached to the moving crack tip and following the considerations reported by Achenbach and Bažant (1975), the system of equations governing the elastodynamic displacement field in a deleted neighborhood of the crack tip may be written as

$$\frac{\partial^2 u}{\partial x^2}+2\beta\frac{\partial^2 v}{\partial x\partial y}+\alpha\frac{\partial^2 u}{\partial y^2}=0, \tag{1a}$$

$$\frac{\partial^2 v}{\partial x^2}+2\beta_1\frac{\partial^2 u}{\partial x\partial y}+\alpha_1\frac{\partial^2 v}{\partial y^2}=0, \tag{1b}$$

where $u = u(x, y, t)$ and $v = v(x, y, t)$ are the displacement components and

$$2\beta=\frac{c_{12}+c_{66}}{c_{11}(1-M_1^2)},\quad \alpha=\frac{c_{66}}{c_{11}(1-M_1^2)},$$

$$2\beta_1=\frac{c_{12}+c_{66}}{c_{66}(1-M_2^2)},\quad \alpha_1=\frac{c_{22}}{c_{66}(1-M_2^2)}.$$

The coefficients c_{ij} are parameters related to the elastic costants, $M_1^2 = c^2(t)/v_1^2$, $M_2^2 = c^2(t)/v_2^2$, $v_1^2 = c_{11}/\rho$, $v_2^2 = c_{66}/\rho$, and ρ is the mass density.

The stress-strain equations for an orthotropic elastic body are

Contributed by the Applied Mechanics Division of THE AMERICAN SOCIETY OF MECHANICAL ENGINEERS for publication in the JOURNAL OF APPLIED MECHANICS.

Discussion on this paper should be addressed to the Technical Editor, Prof. Leon M. Keer, The Technological Institute, Northwestern University, Evanston, IL 60208, and will be accepted until two months after final publication of the paper itself in the JOURNAL OF APPLIED MECHANICS. Manuscript received by the ASME Applied Mechanics Division, June 12, 1989; final revision, July 30, 1990.

$$\sigma_{xx}=c_{11}\frac{\partial u}{\partial x}+c_{12}\frac{\partial v}{\partial y},$$

$$\sigma_{yy}=c_{12}\frac{\partial u}{\partial x}+c_{22}\frac{\partial v}{\partial y}, \qquad (2a,b,c)$$

$$\sigma_{xy}=c_{66}\left(\frac{\partial u}{\partial y}+\frac{\partial v}{\partial x}\right),$$

in which σ_{xx}, σ_{yy}, and σ_{xy} are Cartesian stress components. According to a previous paper (Piva, 1987), the system of equations (1*a*,*b*) may be rewritten as

$$I\frac{\partial \Phi}{\partial x}+A\frac{\partial \Phi}{\partial y}=0, \qquad (3)$$

where I is the 4 × 4 identity matrix, Φ is a 4 × 1 matrix valued function with real entries Φ_k (k = 1, 2, 3, 4) (which are related to the displacement components as follows):

$$\Phi=\begin{pmatrix}\Phi_1\\ \Phi_2\\ \Phi_3\\ \Phi_4\end{pmatrix}\equiv\left(\frac{\partial u}{\partial x},\frac{\partial u}{\partial y},\frac{\partial v}{\partial x},\frac{\partial v}{\partial y}\right)^T, \qquad (4)$$

and A is a 4 × 4 constant matrix, given by

$$A=\begin{pmatrix}0 & \alpha & 2\beta & 0\\ -1 & 0 & 0 & 0\\ 2\beta_1 & 0 & 0 & \alpha_1\\ 0 & 0 & -1 & 0\end{pmatrix} \qquad (5)$$

The characteristic equation of (5) is

$$m^4+2a_1m^2+a_2=0 \qquad (6)$$

in which

$$2a_1=\alpha+\alpha_1-4\beta\beta_1,\ a_2=\alpha\alpha_1.$$

In the subsonic case, Eq. (6) provides four distinct (either complex or purely imaginary) eigenvalues which occur in conjugate pairs.

In order for all roots of (6) to be purely imaginary, the orthotropic material must satisfy the conditions

$$a_2>0,\ a_1>\sqrt{a_2},$$

and two eigenvalues $m_1 = ip_1$ and $m_2 = ip_2$ can be chosen with

$$p_1=[a_1-(a_1^2-a_2)^{1/2}]^{1/2},\ p_2=[a_1+(a_1^2-a_2)^{1/2}]^{1/2},$$

positive constants.

In this case, Eq. (3) may be transformed to (Piva, 1987)

$$\mathrm{I}\frac{\partial \Psi}{\partial x}+\mathrm{B}\frac{\partial \Psi}{\partial y}=0, \qquad (7)$$

where

$$\Psi=P^{-1}\Phi,\ B=P^{-1}AP=\begin{pmatrix}0 & -p_1 & 0 & 0\\ p_1 & 0 & 0 & 0\\ 0 & 0 & 0 & -p_2\\ 0 & 0 & p_2 & 0\end{pmatrix}, \qquad (8a,b)$$

and

$$P=\begin{pmatrix}0 & \dfrac{2\beta p_1^2}{\alpha-p_1^2} & 0 & \dfrac{2\beta p_2^2}{\alpha-p_2^2}\\ \dfrac{2\beta p_1}{\alpha-p_1^2} & 0 & \dfrac{2\beta p_2}{\alpha-p_2^2} & 0\\ -p_1 & 0 & -p_2 & 0\\ 0 & 1 & 0 & 1\end{pmatrix}. \qquad (9)$$

When the elastic properties of the material are such that

$$a_2>0,\ |a_1|<\sqrt{a_2},$$

Eq. (6) has complex roots. Without loss of generality, it is always possible to choose the eigenvalues

$$m_1=\gamma_1+i\gamma_2,\ m_2=-\overline{m}_1,\ \gamma_2>0$$

where a bar denotes complex conjugation, with

$$\gamma_1=[(\sqrt{a_2}+a_1)/2]^{1/2},\ \gamma_2=[(\sqrt{a_2}-a_1)/2]^{1/2}.$$

In this case, Eq. (3) may be rewritten as

$$I\frac{\partial \Psi}{\partial x}+C\frac{\partial \Psi}{\partial y}=0, \qquad (10)$$

with

$$\Psi=R^{-1}\Phi,\ C=R^{-1}AR=\begin{pmatrix}\gamma_1 & -\gamma_2 & 0 & 0\\ \gamma_2 & \gamma_1 & 0 & 0\\ 0 & 0 & -\gamma_1 & -\gamma_2\\ 0 & 0 & \gamma_2 & -\gamma_1\end{pmatrix}. \qquad (11a,b)$$

The matrix R, which enters into (11*a*,*b*), is

$$R=\begin{pmatrix}-2\beta q_4 & -2\beta q_3 & 2\beta q_4 & -2\beta q_3\\ 2\beta q_2 & 2\beta q_1 & 2\beta q_2 & -2\beta q_1\\ -\gamma_2 & -\gamma_1 & -\gamma_2 & \gamma_1\\ 0 & 1 & 0 & 1\end{pmatrix}, \qquad (12)$$

where the following contractions have been used:

$$q_1+iq_2=\frac{m_1}{\alpha+m_1^2},\ q_3+iq_4=m_1(q_1+iq_2).$$

In what follows, the integration of Eqs. (7) and (10) will be performed by referring to a system of moving polar coordinates (r, θ) attached to the crack tip and assuming, as suggested by Achenbach and Bažant (1975), that the local displacement field may be represented as

$$u(r,\vartheta,t)=r^\gamma T(t)U(\vartheta),v(r,\vartheta,t)=r^\gamma T(t)V(\vartheta), \qquad (13a,b)$$

in which γ, $U(\theta)$, and $V(\theta)$ are the unknowns.

The solutions will be sought under traction-free conditions on the surface $\theta = \pm\pi$ of the crack—and symmetry or skew-symmetry conditions for the displacement field accordingly, as mode I or mode II fracture are respectively studied.

3 Purely Imaginary Eigenvalues

Substituting (13) into (4), and using the chain rule of differentiation with respect to polar coordinates, leads to

$$\Phi=r^{\gamma-1}T(t)f(\vartheta), \qquad (14)$$

where

$$f(\vartheta)=\begin{pmatrix}\gamma\cos\vartheta\ U(\vartheta)-\sin\vartheta\ U'(\vartheta)\\ \gamma\sin\vartheta\ U(\vartheta)+cos\ \vartheta\ U'(\vartheta)\\ \gamma\sin\vartheta\ V(\vartheta)-\sin\vartheta\ V'(\vartheta)\\ \gamma\sin\vartheta\ V(\vartheta)+\cos\vartheta\ V'(\vartheta)\end{pmatrix}, \qquad (15)$$

in which a prime denotes differentiation with respect to the argument. Hence, from (8*a*) it follows that

$$\Psi=r^{\gamma-1}T(t)h(\vartheta),\ h(\vartheta)=P^{-1}f(\vartheta). \qquad (16)$$

The system (7) may be decomposed into two independent systems

$$\frac{\partial \Psi^{(i)}}{\partial x}+B_i\frac{\partial \Psi^{(i)}}{\partial y}=0,\ i=1,2, \qquad (17)$$

where

$$\Psi^{(1)}\equiv\begin{pmatrix}\Psi_1\\ \Psi_2\end{pmatrix},\ \Psi^{(2)}\equiv\begin{pmatrix}\Psi_3\\ \Psi_4\end{pmatrix},\ B_i=\begin{pmatrix}0 & -p_i\\ p_i & 0\end{pmatrix}.$$

The general solution to (17) is obtained by introducing new variables

$$r_i = r[g_i(\vartheta)]^{1/2},\ \vartheta_i = tg^{-1}\left(\frac{tg\ \vartheta}{p_i}\right),\ i = 1, 2, \quad (18a,b)$$

with

$$g_i(\vartheta) = \cos^2\vartheta + (\sin^2\vartheta)/p_i^2. \quad (19)$$

In view of (18*a*,*b*) and (19) the functions $\Psi^{(i)}(x,y)$ defined above become

$$\Psi^{(i)}(r_i, \vartheta_i) = r_i^{\gamma-1}T(t)H^{(i)}(\vartheta_i),\ i=1, 2, \quad (20)$$

where

$$H^{(i)}(\vartheta_i) = \{g_i[\vartheta(\vartheta_i)]\}^{\frac{(1-\gamma)}{2}}\cdot h^{(i)}[\vartheta(\vartheta_i)], \quad (21)$$

and $h^{(i)}[\theta(\theta_i)]$ follows from (16*b*).

Using the chain rule of differentiation, one obtains

$$\frac{\partial\Psi^{(i)}}{\partial x} = \cos\vartheta_i\frac{\partial\Psi^{(i)}}{\partial r_i} - \frac{\sin\vartheta_i}{r_i}\frac{\partial\Psi^{(i)}}{\partial\vartheta_i}, \quad (22a,b)$$

$$\frac{\partial\Psi^{(i)}}{\partial y} = \frac{\sin\vartheta_i}{p_i}\frac{\partial\Psi^{(i)}}{\partial r_i} + \frac{\cos\vartheta_i}{r_i p_i}\frac{\partial\Psi^{(i)}}{\partial\vartheta_i}.$$

Inserting (20) into (22*a*,*b*), substituting into (17), multiplying the result by $r_i^{2-\gamma}$, and considering the limit as $r \to 0$, gives

$$R_1^{(i)}\frac{dH^{(i)}}{d\vartheta_i} = (\gamma-1)R_2^{(i)}H^{(i)}(\vartheta_i),\ i = 1, 2, \quad (23)$$

where $R_1^{(i)}$ and $R_2^{(i)}$ are the following orthogonal matrices

$$R_1^{(i)} = \begin{pmatrix}\sin\vartheta_i & \cos\vartheta_i\\ -\cos\vartheta_i & \sin\vartheta_i\end{pmatrix},\ R_2^{(i)} = \begin{pmatrix}\cos\vartheta_i & -\sin\vartheta_i\\ \sin\vartheta_i & \cos\vartheta_i\end{pmatrix}. \quad (24a,b)$$

In view of (24*a*,*b*), the system (23) reduces to

$$\frac{dH^{(i)}}{d\vartheta_i} = (\gamma-1)I_1H^{(i)},\ I_1 = \begin{pmatrix}0 & -1\\ 1 & 0\end{pmatrix},$$

whose solution can be represented as

$$H^{(i)}(\vartheta_i) = \begin{pmatrix}H_{01}^{(i)} & -H_{02}^{(i)}\\ H_{02}^{(i)} & H_{01}^{(i)}\end{pmatrix}\begin{pmatrix}\cos(\gamma-1)\vartheta_i\\ \sin(\gamma-1)\vartheta_i\end{pmatrix}. \quad (25)$$

The constants of integration $H_{0j}^{(i)} = H_j^{(i)}(0), j = 1, 2$, will be determined in order to satisfy the appropriate boundary conditions. Combining (15) with (16*b*) and (21), the expressions for the functions $U(\theta)$ and $V(\theta)$ introduced in Eqs. (13*a*,*b*), as well as for their derivatives, are obtained as follows:

$$U(\vartheta) = \frac{2\beta p_1 g_1^{\frac{\gamma-1}{2}}(\vartheta)}{\gamma(\alpha-p_1^2)}[H_1^{(1)}(\vartheta)\sin\vartheta + p_1H_2^{(1)}(\vartheta)\cos\vartheta] + \frac{2\beta p_2 g_2^{\frac{\gamma-1}{2}}(\vartheta)}{\gamma(\alpha-p_2^2)}[H_1^{(2)}(\vartheta)\sin\vartheta + p_2H_2^{(2)}(\vartheta)\cos\vartheta], \quad (26)$$

$$U'(\vartheta) = \frac{2\beta p_1 g_1^{\frac{\gamma-1}{2}}}{\alpha-p_1^2}[H_1^{(1)}(\vartheta)\cos\vartheta - p_1H_2^{(1)}(\vartheta)\sin\vartheta] + \frac{2\beta p_2 g_2^{\frac{\gamma-1}{2}}(\vartheta)}{\alpha-p_2^2}[H_1^{(2)}(\vartheta)\cos\vartheta - p_2H_2^{(2)}(\vartheta)\sin\vartheta], \quad (27)$$

$$V(\vartheta) = \frac{g_1^{\frac{\gamma-1}{2}}(\vartheta)}{\gamma}[H_2^{(1)}(\vartheta)\sin\vartheta - p_1H_1^{(1)}(\vartheta)\cos\vartheta] + \frac{g_2^{\frac{\gamma-1}{2}}(\vartheta)}{\gamma}[H_2^{(2)}(\vartheta)\sin\vartheta - p_2H_1^{(2)}(\vartheta)\cos\vartheta], \quad (28)$$

$$V'(\vartheta) = g_1^{\frac{\gamma-1}{2}}(\vartheta)[p_1H_1^{(1)}(\vartheta)\sin\vartheta + H_2^{(1)}\cos\vartheta] + g_2^{\frac{\gamma-1}{2}}(\vartheta)[p_2H_1^{(2)}(\vartheta)\sin\vartheta + H_2^{(2)}\cos\vartheta]. \quad (29)$$

In order for the solutions (25) to satisfy the symmetry conditions

$$U'(0) = V(0) = 0, \quad (30)$$

for the mode I fracture or the skew symmetry conditions

$$U(0) = V'(0) = 0, \quad (31)$$

for the mode II, it has to be valid that $H_{01}^{(1)} = H_{01}^{(2)} = 0$ or $H_{02}^{(1)} = H_{02}^{(2)} = 0$, respectively.

In order to apply the traction-free conditions on the surface of the crack, the relevant stress components are obtained by combining (20) with (8*a*) and putting into (2*b*,*c*). The result is

$$\sigma_{yy} = c_{66}r^{\gamma-1}T(t)[l_2g_1^{\frac{\gamma-1}{2}}(\vartheta)H_2^{(1)}(\vartheta) + l_4g_2^{\frac{\gamma-1}{2}}(\vartheta)H_2^{(2)}(\vartheta)], \quad (32)$$

$$\sigma_{xy} = c_{66}r^{\gamma-1}T(t)[l_1g_1^{\frac{\gamma-1}{2}}(\vartheta)H_1^{(1)}(\vartheta) + l_3g_2^{\frac{\gamma-1}{2}}(\vartheta)H_1^{(2)}(\vartheta)], \quad (33)$$

in which

$$l_1 = p_1\left(\frac{2\beta}{\alpha-p_1^2}-1\right),\ l_2 = \frac{c_{22}}{c_{66}} + \frac{c_{12}}{c_{66}}\left(\frac{2\beta p_1^2}{\alpha-p_1^2}\right),$$

$$l_3 = p_2\left(\frac{2\beta}{\alpha-p_2^2}-1\right),\ l_4 = \frac{c_{22}}{c_{66}} + \frac{c_{12}}{c_{66}}\left(\frac{2\beta p_2^2}{\alpha-p_2^2}\right).$$

The traction-free conditions $\sigma_{yy}(\pm\pi) = \sigma_{xy}(\pm\pi) = 0$ on the surface of the crack yield a system of homogeneous equations for the unknown costants $H_{02}^{(1)}$ and $H_{02}^{(2)}$ or $H_{01}^{(1)}$ and $H_{01}^{(2)}$, for the mode I or mode II, respectively. The necessary and sufficient condition to avoid the trivial solution is

$$D(M_2)\sin 2\gamma\pi = 0, \quad (34)$$

where $D(M_2) = l_1l_4 - l_2l_3$ is the Rayleigh function for the orthotropic medium. When the crack velocity is subsonic and smaller than the Rayleigh wave velocity, the smallest root of (34), allowing the strain energy density to be integrable in a neighborhood of the crack tip, is $\gamma = 1/2$.

The constants of integration are then determined, up to an arbitrary multiplier, and satisfy the following relations

$$\frac{H_{02}^{(2)}}{H_{02}^{(1)}} = -\frac{l_1}{l_3},\ \frac{H_{01}^{(2)}}{H_{01}^{(1)}} = -\frac{l_2}{l_4}, \quad (35a,b)$$

for mode I and mode II, respectively.

Hence, the asymptotic expressions of the relevant stress components (32) and (33) become

$$\sigma_{yy} = \frac{K_I(t)}{\sqrt{2\pi r}D(M_2)}\left[l_2l_3g_1^{-1/4}(\vartheta)\cos\frac{\vartheta_1}{2} - l_1l_4g_2^{-1/4}(\vartheta)\cos\frac{\vartheta_2}{2}\right], \quad (36)$$

$$\sigma_{xy} = \frac{l_1l_3K_I(t)}{\sqrt{2\pi r}D(M_2)}\left[g_1^{-1/4}(\vartheta)\sin\frac{\vartheta_1}{2} - g_2^{-1/4}(\vartheta)\sin\frac{\vartheta_2}{2}\right], \quad (37)$$

for mode I fracture and

$$\sigma_{yy} = \frac{l_2l_4K_{II}(t)}{\sqrt{2\pi r}D(M_2)}\left[g_1^{-1/4}(\vartheta)\sin\frac{\vartheta_1}{2} - g_2^{-1/4}(\vartheta)\sin\frac{\vartheta_2}{2}\right], \quad (38)$$

$$\sigma_{xy} = \frac{K_{II}(t)}{\sqrt{2\pi r}D(M_2)}\left[l_2l_3g_2^{-1/4}(\vartheta)\cos\frac{\vartheta_2}{2} - l_1l_4g_1^{-1/4}(\vartheta)\cos\frac{\vartheta_1}{2}\right], \quad (39)$$

for mode II, where the usual definitions of the stress intensity factors $K_I(t)$ and $K_{II}(t)$ have been assumed. The expressions

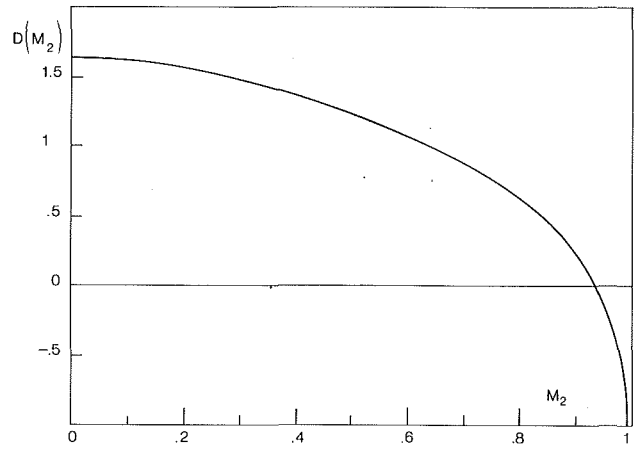

Fig. 1 Variation of $D(M_2)$ for steel aluminium

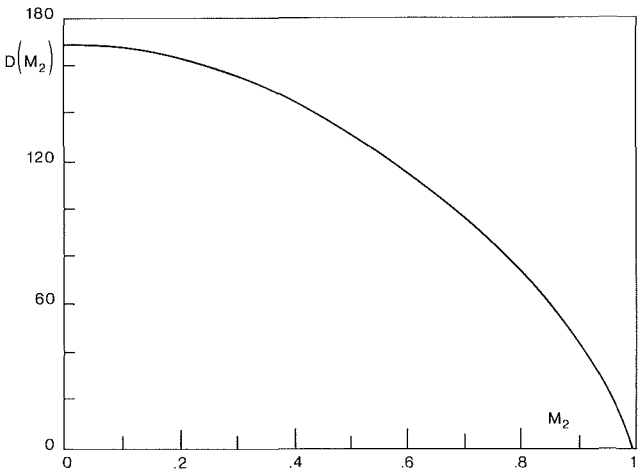

Fig. 2 Variation of $D(M_2)$ for graphite epoxy.

for the displacement components may be obtained through (26) and (28) with appropriate values of the functions $H_j^{(i)}(\theta)$, $i, j = 1, 2$.

It is worth noting that the asymptotic expressions (36)–(39) are highly influenced by the behavior of the Rayleigh function $D(M_2)$. In Fig. 1, this function is represented for a steel-aluminium composite whose elastic coefficients, under plane-strain conditions, are

$$\frac{c_{11}}{c_{66}} = 3.952, \quad \frac{c_{22}}{c_{66}} = 4.155, \quad \frac{c_{12}}{c_{66}} = 1.959.$$

In Fig. 2, the above function is represented for a distinctly orthotropic material, i.e., for a graphite-epoxy composite for which

$$\frac{c_{11}}{c_{66}} = 3.504, \quad \frac{c_{22}}{c_{66}} = 29.822, \quad \frac{c_{12}}{c_{66}} = 1.723.$$

It should be noted also that the trends are similar; an increase of orthotropy reflects into a remarkable increase of the values of the Rayleigh function.

In order to compare the above obtained analytical results with the numerical solution given by Achenbach and Bažant (1975), the stress component σ_{xx} was derived and combined with Eqs. (36), (37) and (38), (39) to get the polar stress components $\sigma_{\theta\theta}$ and $\sigma_{r\theta}$ for mode I and mode II fracture, respectively.

The quantities $\sigma_{\theta\theta}(r/c_{66}\gamma_0)^{1/2}$ and $\sigma_{r\theta}(r/c_{66}\gamma_0)^{1/2}$ have been graphically represented in Figs. 3–4 versus the angle θ, for two values of M_2^2 in mode I and mode II fracture.

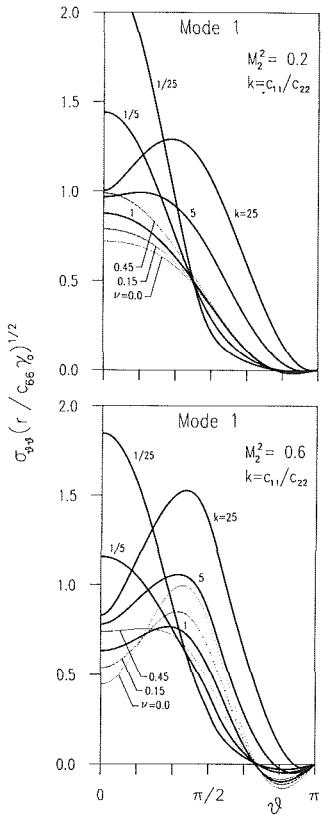

Fig. 3 Angular variation of $\sigma_{\theta\theta}$ in mode I fracture (according with Fig. 2 in Achenbach and Bažant, 1975)

The constant γ_o, one half of the specific energy of crack extension, was obtained (see Eq. (47) of Achenbach and Bazănt, 1975) as follows:

$$\gamma_o = \begin{cases} \dfrac{(p_1 l_3 - p_2 l_1)}{4\, c_{66} D(M_2)} K_I^2(t) & , \text{ mode I} \\ \dfrac{\beta}{2\, c_{66} D(M_2)} \left[\dfrac{l_2 p_2^2}{\alpha - p_2^2} - \dfrac{l_4 p_1^2}{\alpha - p_1^2} \right] K_{II}^2(t), & \text{mode II.} \end{cases}$$

According to the nomenclature of the quoted paper, the curves have been represented for several values of the ratio $k = E_{xx}/E_{yy} = c_{11}/c_{22}$. Taking $E = \min\{c_{11}, c_{22}\}$, the values of $G_{xy}/E = c_{66}/E$ and $E_{xy}/E = c_{12}/E$ were chosen as those for an isotropic material; i.e., as $(1 - 2\nu)/2(1 - \nu)$ and $\nu/(1 - \nu)$, respectively, where ν is the Poisson ratio. Solid lines have been plotted for $\nu = 0.3$ and dotted lines, corresponding to the isotropic case ($k = 1$), have been represented for several values of the Poisson ratio. It appears that the results are in accordance with the corresponding ones reported in Figs. 2–3 of the above-mentioned paper.

The effects due to the increase of material anisotropy are shown also in Figs. 4–5, which refer to graphite-epoxy and steel-aluminum composites. The dimensionless stress components $\sigma_{\theta\theta}(2\pi r)^{1/2}/K(t)$ and $\sigma_{r\theta}(2\pi r)^{1/2}/K(t)$ have been represented versus the angle θ for several values of M_2^2 in mode I (solid lines, $K(t) = K_I(t)$) and mode II fracture (dotted lines, $K(t) = K_{II}(t)$).

4 Complex Eigenvalues

The system (10) can be decomposed as

$$\frac{\partial \Psi^{(i)}}{\partial x} + C_i(\gamma_1, \gamma_2) \frac{\partial \Psi^{(i)}}{\partial y} = 0, \quad i = 1, 2, \tag{40}$$

in which

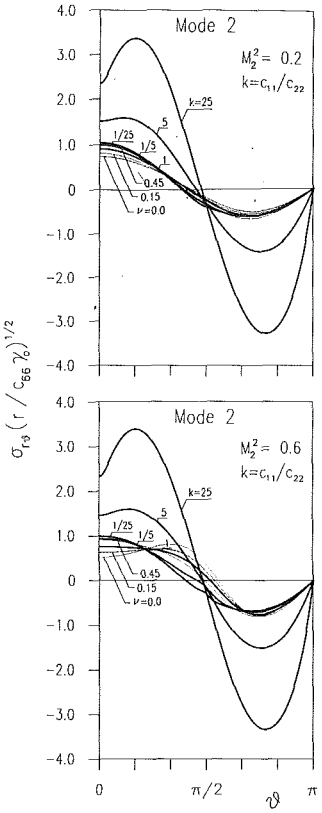

Fig. 4 Angular variation of $\sigma_{r\vartheta}$ in mode II fracture (according to Fig. 3 in Achenbach and Bažant, 1975)

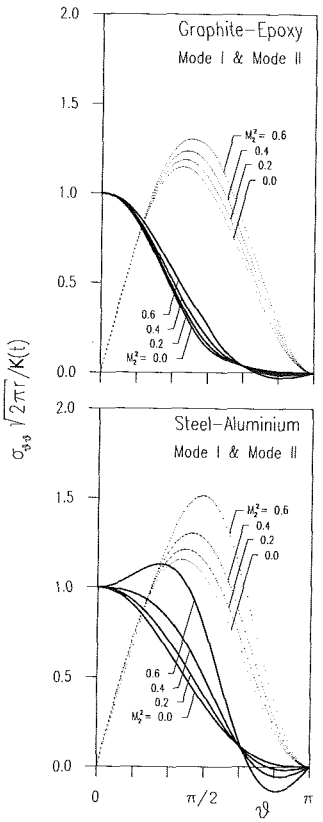

Fig. 5 Angular variation of $\sigma_{\vartheta\vartheta}$ in mode I and mode II fracture for graphite-epoxy and steel-aluminum composites

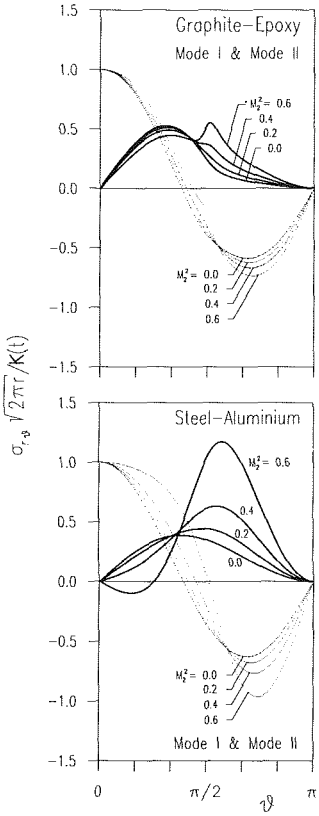

Fig. 6 Angular variation of $\sigma_{r\vartheta}$ in mode I and mode II fracture for graphite-epoxy and steel-aluminium composites

$$\Psi^{(1)} \equiv \begin{pmatrix} \psi_1 \\ \psi_2 \end{pmatrix}, \ \Psi^{(2)} \equiv \begin{pmatrix} \psi_3 \\ \psi_4 \end{pmatrix}, \ C_1(\gamma_1, \gamma_2) = \begin{pmatrix} \gamma_1 & -\gamma_2 \\ \gamma_2 & \gamma_1 \end{pmatrix},$$

and $C_2(\gamma_1, \gamma_2) = C_1(-\gamma_1, \gamma_2)$.

The general solution to (40) is obtained by introducing new variables

$$r_i = r[g_i(\vartheta)]^{1/2}, \ \vartheta_i = tg^{-1}[f_i(\vartheta)], \ i = 1, 2, \tag{41}$$

where

$$g_i(\vartheta) = (\cos^2 \vartheta + l^2 \sin^2 \vartheta + \epsilon_i \gamma r_1 l^2 \sin^2 \vartheta), \ f_i(\vartheta) = \frac{\gamma_2 l^2 \sin \vartheta}{\cos\vartheta + \epsilon_i \gamma_1 l^2 \sin \vartheta} \tag{42}$$

with

$$\epsilon_i = \begin{cases} -1, & i=1 \\ 1, & i=2 \end{cases}, \ l^2 = (\gamma_1^2 + \gamma_2^2)^{-1}.$$

Combining (11*a*) and (14) with (41*a*,*b*) and (42*a*,*b*) gives the following local representation

$$\Psi^{(i)}(r_i, \vartheta_i) = r_i^{\gamma - 1} T(t) G^{(i)}(\vartheta_i). \tag{43}$$

Using again the chain rule of differentiation, the system (40) becomes

$$\frac{dG^{(i)}}{d\vartheta_i} = (\gamma - 1) I_1 G^{(i)}, \tag{44}$$

whose solution may be expressed as

$$G^{(i)}(\vartheta_i) = \begin{pmatrix} G_{01}^{(i)} - G_{02}^{(i)} \\ G_{02}^{(i)} \ \ G_{01}^{(i)} \end{pmatrix} \begin{pmatrix} \cos(\gamma - 1)\vartheta_i \\ \sin(\gamma - 1)\vartheta_i \end{pmatrix}, \ i = 1, 2. \tag{45}$$

By referring to the matrix of transformation (12), the expressions for the displacement functions $U(\theta)$ and $V(\theta)$, as well as for the derivatives, may be obtained in the same way as in the case of imaginary eigenvalues.

The expressions (2*b*,*c*) for the relevant stress components become

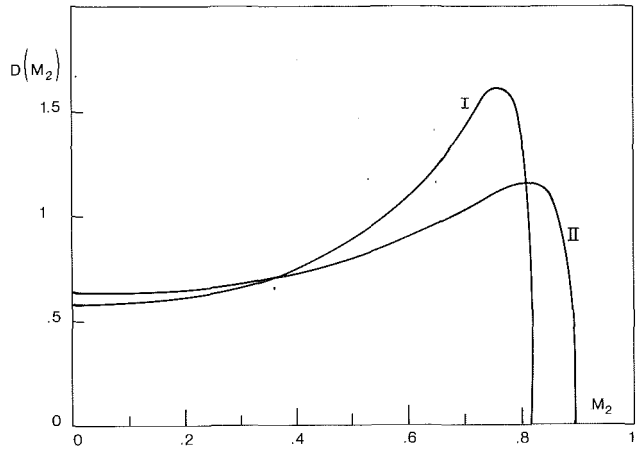

Fig. 7 Variation of $D_1(M_2)$ for materials I and II

$$\sigma_{yy}=c_{66}r^{\gamma-1}T(t)\left\{g_2^{\frac{\gamma-1}{2}}(\vartheta)[d_1G_1^{(2)}(\vartheta)+d_2G_2^{(2)}(\vartheta)]-g_1^{\frac{\gamma-1}{2}}(\vartheta)[d_1G_1^{(1)}(\vartheta)-d_2G_2^{(1)}(\vartheta)]\right\}, \quad (46)$$

$$\sigma_{xy}=c_{66}r^{\gamma-1}T(t)\left\{g_2^{\frac{\gamma-1}{2}}(\vartheta)[d_3G_1^{(2)}(\vartheta)-d_4G_2^{(2)}(\vartheta)]+g_1^{\frac{\gamma-1}{2}}(\vartheta)[d_3G_1^{(1)}(\vartheta)+d_4G_2^{(1)}(\vartheta)]\right\}, \quad (47)$$

with

$$d_1=2\beta q_4\frac{c_{12}}{c_{66}},\ d_2=\frac{c_{22}}{c_{66}}-2\beta q_3\frac{c_{12}}{c_{66}},$$

and

$$d_3=2\beta q_2-\gamma_2,\ d_4=2\beta q_1-\gamma_1.$$

In view of the traction-free conditions on the surface of the crack, the solutions (45) are nontrivial if and only if

$$D_1(M_2)\sin 2\gamma\pi=0, \quad (48)$$

where $D_1(M_1) = d_1d_3 - d_2d_4$ may be thought again as the Rayleigh function for the orthotropic medium. Similarly, to the previous section, the appropriate solution to (48) is $\gamma = 1/2$ and the following relations hold

$$G_{02}^{(1)}=\frac{d_4}{d_3}G_{01}^{(1)},\ G_{02}^{(1)}=-\frac{d_2}{d_1}G_{01}^{(1)},$$

for mode I and mode II, respectively.

Equations (46) and (47) then take the following explicit forms

$$\sigma_{yy}=\frac{K_I(t)}{2\sqrt{2\pi r}D_1(M_2)}\left\{g_1^{-1/4}(\vartheta)\left[D_1(M_2)\cos\frac{\vartheta_1}{2}+(d_1d_4+d_2d_3)\sin\frac{\vartheta_1}{2}\right]+g_2^{-1/4}(\vartheta)\left[D_1(M_2)\cos\frac{\vartheta_2}{2}-(d_1d_4+d_2d_3)\sin\frac{\vartheta_2}{2}\right]\right\}, \quad (49)$$

$$\sigma_{xy}=\frac{K_I(t)(d_3^2+d_4^2)}{2\sqrt{2\pi r}D_1(M_2)}\left[g_2^{-1/4}(\vartheta)\cos\frac{\vartheta_2}{2}-g_1^{-1/4}(\vartheta)\cos\frac{\vartheta_1}{2}\right], \quad (50)$$

Table 1

	c_{11}/c_{66}	c_{22}/c_{66}	c_{12}/c_{66}
Material I	2.0	1.5	1.0
Material II	3.0	3.0	2.0

for mode I fracture and

$$\sigma_{yy}=\frac{K_{II}(t)(d_1^2+d_2^2)}{2\sqrt{2\pi r}D_1(M_2)}\left[g_2^{-1/4}(\vartheta)\cos\frac{\vartheta_2}{2}-g_1^{-1/4}(\vartheta)\cos\frac{\vartheta_1}{2}\right], \quad (51)$$

$$\sigma_{xy}=\frac{K_{II}(t)}{2\sqrt{2\pi r}D_1(M_2)}\left\{g_1^{-1/4}(\vartheta)\left[D_1(M_2)\cos\frac{\vartheta_1}{2}-(d_1d_4+d_2d_3)\sin\frac{\vartheta_1}{2}\right]+g_2^{-1/4}(\vartheta)\left[D_1(M_2)\cos\frac{\vartheta_2}{2}+(d_1d_4+d_2d_3)\sin\frac{\vartheta_2}{2}\right]\right\}, \quad (52)$$

for mode II fracture.

It should be remarked that the angular variation of the above stress components differ substantially from those shown in (36)–(39). The Rayleigh function $D_1(M_2)$ is shown in Fig. 7 for two kinds of orthotropic materials whose elastic coefficients are such that the eigenvalues of Eq. (6) are complex conjugate. Due to the difficulty of finding experimental results concerning such materials, fictitious elastic parameters, which allow the condition $|a_1| < \sqrt{a_2}$ to be satisfied, have been taken as in Table 1.

It is evident the different behavior of the function $D_1(M_2)$ with respect to that shown by the function $D(M_2)$ in Figs. 1–2.

Acknowledgment

This work was performed under the auspices of the G.N.F.M. (C.N.R.) and supported by the M.P.I.

References

Achenbach, J. D., and Bažant, Z. P., 1975, "Elastodynamic Near-Tip Stress and Displacement Fields for Rapidly Propagating Cracks in Orthotropic Materials," JOURNAL OF APPLIED MECHANICS, Vol. 42, pp. 183–189.

Atkinson, C., 1964, "The Propagation of Fracture in Aeolotropic Materials," *Int. Journal of Fract. Mech.*, Vol. 1, pp. 47–55.

Atkinson, C., and Head, A. K., 1966, "The Influence of Elastic Anisotropy on the Propagation of Fracture," *Int. Journal of Fract.*, Vol. 2, pp. 489–505.

Freund, L. B., and Clifton, R., 1974, "On the Uniqueness of Plane Elastodynamic Solutions for Running Cracks," *Journal of Elasticity*, Vol. 4, pp. 293–299.

Piva, A., 1987, "An Alternative Approach to Elastodynamic Crack Problems in an Orthotropic Medium," *Quarterly of Applied Mathematics*, Vol. 45, pp. 97–104.

Piva, A., and Viola, E., 1988, "Crack Propagation in an Orthotropic Medium," *Engineering Fracture Mechanics*, Vol. 29, pp. 535–548.

Stroh, A. N., 1962, "Steady State Problems in Anisotropic Elasticity," *Journal of Math. and Phys.*, Vol. 61, pp. 77–103.

M. R. Karim
Research Assistant.

T. Kundu
Assoc. Professor,
Mem. ASME.

Department of Civil Engineering and
Engineering Mechanics,
University of Arizona,
Tucson, AZ 85721

Dynamic Response of an Orthotropic Half-Space With a Subsurface Crack: In-Plane Case

Scattering of elastic waves by a subsurface crack in an orthotropic half-space subjected to a surface line load of arbitrary angle of inclination is studied. Green's functions are developed and used along with the representation theorem to reduce the problem to a set of simultaneous singular integral equations in the Fourier transformed domain. Solution to these equations is then obtained by expanding the unknown crack opening displacement (COD) in terms of Chebyshev polynomials. Numerical results are given for specific examples involving orthotropic materials.

1 Introduction

Scattering of elastic waves by subsurface cracks has been the subject of intensive study in the recent years because of its importance in seismology and nondestructive evaluation (NDE) applications. Achenbach and Brind (1981a,b) studied the response of the crack normal to the free surface in an isotropic half-space. Achenbach and his co-workers (1983, 1984a,b) later extended their previous studies to obtain the stress intensity factor and resonance effects for cracks parallel and inclined to the free surface. Yang and Bogy (1985) studied the response of an interface crack in a layered half-space. Gracewski and Bogy (1986a,b) extended the work of Yang and Bogy (1985) to obtain the response of an interface crack in a layered half-space submerged in water. In most of these studies response due to continuous surface loads was considered; only Gracewski and Bogy (1986b) considered the response due to arbitrary wavefronts and Gaussian beams. Corresponding problems of surface-breaking cracks also received due attention (Datta (1979), Mendelson et al. (1980), Stone et al. (1980), Kundu and Mal (1981)). Antiplane problems, because of their relative mathematical simplicity, have been the subject of intensive investigation (Boström (1987), Kundu (1987a) and references therein). Problems of subsurface multiple cracks have also been investigated mostly numerically in the recent years (Zhang and Achenbach (1988) and references therein).

Although most of the attention of the investigators have been devoted to the isotropic materials only, recent widespread use of composite materials warrant the investigation of the response of orthotropic or anisotropic materials with cracks. Helmholtz decomposition, which simplifies the two-dimensional problems for isotropic materials, is not valid for composite materials. Although for static problems involving orthotropic materials a parallel decomposition was developed (Georgiadis and Papadopaulos (1987)), no such simplifying decomposition has been developed for dynamic problems yet. So these problems have to be solved in terms of displacements in the frequency domain. Kassir and Bandyopadhyay (1983) studied the response of a central crack in an infinite orthotropic medium. Kuo (1984a,b) studied the response of cracks at the interface of two dissimilar orthotropic or anisotropic half-spaces. Ang (1988) solved the problem of a crack in an orthotropic layer sandwiched between two orthotropic half-spaces. In all these studies the external loads were applied only at the crack surfaces.

Traditionally, internal cracks are considered to be open so that it does not transmit any traction. Although analytically we can solve a problem assuming a relation between tractions and displacements across the crack plane (Achenbach and Norris (1982), Thompson and Fiedler (1984)), finding such relations experimentally for a particular problem can be very difficult or even impossible.

In the present paper, response of a subsurface crack parallel to the free surface in an orthotropic half-space is considered. The incident wave field is generated by a line load on the surface acting at an arbitrary angle. Crack surfaces are considered to be smooth and stress-free—in other words, contact and transmission of stresses across the crack is neglected. A corresponding antiplane problem was solved by Karim and Kundu (1989). The solution to this in-plane problem will help us understand the ultrasonic nondestructive evaluation of nonisotropic materials and composites which are becoming increasingly more common. This solution can act as a Green's function for computing the acoustic material signature (AMS) of an orthotropic solid with crack. Comparing AMS of cracked and uncracked composites, internal cracks may be detected. This application is currently under investigation.

In the analytical formulation a coupled set of integral equations are obtained from the frequency domain representation theorem (Mal (1972)). Alternatively, these relations can be obtained by using Betti's reciprocal theorem (Neerhoff (1979)).

Contributed by the Applied Mechanics Division of THE AMERICAN SOCIETY OF MECHANICAL ENGINEERS for publication in the JOURNAL OF APPLIED MECHANICS.

Discussion on this paper should be addressed to the Technical Editor, Prof. Leon M. Keer, The Technological Institute, Northwestern University, Evanston, IL 60208, and will be accepted until two months after final publication of the paper itself in the JOURNAL OF APPLIED MECHANICS. Manuscript received by the ASME Applied Mechanics Division, Aug. 8, 1988; final revision, June 1, 1989.

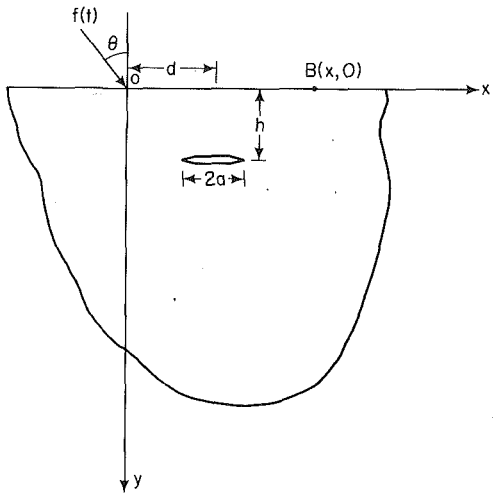

Fig. 1 Geometry of the problem; an orthotropic half-space containing a subsurface crack

In these integral equations, unknown COD's are expanded in a complete set of Chebychev polynomials. The unknown coefficients of these expansions are obtained by satisfying the stress-free boundary conditions at the crack surfaces. As a sample problem, the surface response of a cracked half-space at different points is studied.

Surface response computation for a line load excitation is computationally more difficult. This is due to the fact that unlike a plane wavefront, in this case, the incident field is expressed as an infinite integral over the wave number.

2 Problem Formulation

A homogeneous, orthotropic, linearly elastic solid, which occupies the half-plane $y > 0$, contains a subsurface crack parallel to the free surface as shown in Fig. 1. The crack with traction-free surfaces, having a length of $2a$, is located at a depth h. The in-plane line load, $T = \delta(x)f(t)$, is applied at the origin of the xy-coordinate system as shown in the figure. The applied load makes an angle θ with the vertical direction. The Fourier transform of $f(t)$ is given by $F(\omega)$.

To solve this problem of our interest we need to solve two fundamental problems (1) a flawless half-space subjected to a line load at the boundary, and (2) the Green's functions corresponding to internal unit loads in x and y-directions. The representation theorem is then used along with the Green's function to obtain scattered displacement field.

2.1 Flawless Half-Space Subjected to a Line Load at the Boundary. The geometry of this problem is very similar to Fig. 1, the only difference is that there is no crack. The time-harmonic in-plane stress field of time dependence, $e^{-i\omega t}$, acts as a line load at an angle of inclination, θ, at the origin.

Constitutive equations of the material can be written in the reduced matrix notation as

$$\sigma_k = C_{kj}\epsilon_j \quad (k, j = 1, 2, 6) \tag{1}$$

where a repeated subscript indicates summation and C_{kj} is the stiffness tensor. For orthotropic materials, C_{16}, C_{26}, C_{61}, and C_{62} are equal to zero. The engineering strains, ϵ_j, in Eq. (1) are defined by

$$\epsilon_1 = u_{,x}, \quad \epsilon_2 = v_{,y}, \quad \epsilon_6 = u_{,y} + v_{,x} \tag{2}$$

where u and v are displacement components in the x and y directions, respectively, and a comma (,) indicates partial derivative. Equations of motion of the problem are given by

$$C_{11}u_{,xx} + C_{66}u_{,yy} + (C_{12} + C_{66})v_{,xy} = \rho u_{,tt} \tag{3a}$$

$$C_{22}v_{,yy} + C_{66}v_{,xx} + (C_{12} + C_{66})u_{,xy} = \rho v_{,tt} \tag{3b}$$

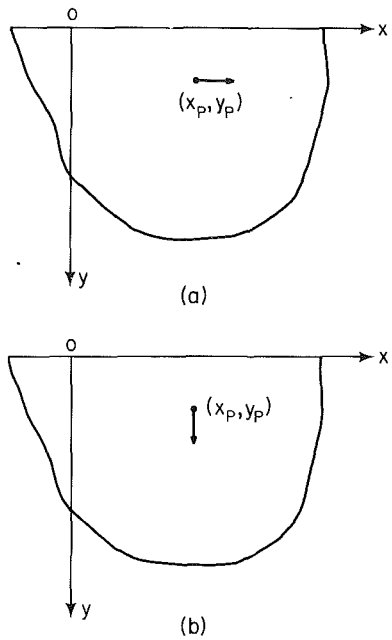

Fig. 2 A line load in a half-space: (a) line load in horizontal direction, (b) line load in vertical direction

where ρ is the density of the elastic material.

Solutions of these coupled equations in the Fourier transformed domain (ω) can be written as

$$U(x,y) = \frac{1}{2\pi}\int_{-\infty}^{\infty}\sum_{j=1}^{2} A_j e^{p_j y + ikx}dk \tag{4a}$$

$$V(x,y) = \frac{1}{2\pi}\int_{-\infty}^{\infty}\sum_{j=1}^{2} A_j S_j e^{p_j y + ikx}dk \tag{4b}$$

where p_j is the jth root with negative real part and/or positive imaginary part of the following equation

$$C_{22}C_{66}p^4 + p^2(k^2C_{12}^2 + 2C_{12}C_{66}k^2 + C_{22}\rho\omega^2 - k^2C_{11}C_{22} + C_{66}\rho\omega^2) + (\rho^2\omega^4 - k^2C_{66}\rho\omega^2 - k^2C_{11}\rho\omega^2 + k^4C_{11}C_{66}) = 0. \tag{5}$$

A_j are the unknown functions of k and ω. They are determined by using boundary conditions and are given in the Appendix, and

$$S_j = \frac{k^2C_{11} - p_j^2C_{66} - \rho\omega^2}{ikp_j(C_{12} + C_{66})} \text{ (no summation on } j). \tag{6}$$

2.2 Green's Function: A Line Load in a Flawless Half-Space. A number of Green's functions are available in the literature (Xu and Mal (1987) and references therein) for isotropic materials, in terms of displacement potentials. But none of these can be used for orthotropic materials directly. So, in this section, two new Green's functions are developed for unit load in the x and y-directions.

The geometry of this problem is shown in Fig. 2. A time-harmonic line load is acting at a point $P(x_p, y_p)$ as shown in the figure. Unit loads along the x and y-directions can be considered as a body force corresponding to a delta function $\delta(x - x_p, y - y_p, t)$. Equations of motion for this problem should be the same as Eqs. (3), with the additional body force term in Eq. (3a) for a unit load in the x-direction and in (3b) for a unit load in the y-direction. Solution to these equations can be written as

$$U_\alpha^G(x,y) = \frac{1}{2\pi}\int_{-\infty}^{\infty}\left\{B_\alpha^{\pm}e^{p_1|y-y_p|} + C_\alpha^{\pm}e^{p_2|y-y_p|} + \sum_{j=1}^{2} D_j^\alpha e^{p_j y}\right\}e^{ik(x-x_p)}dk \tag{7a}$$

$$V_\alpha^G(x,y)=\frac{1}{2\pi}\int_{-\infty}^{\infty}\left\{B_\alpha^{\pm}S_1^{\pm}e^{p_1|y-y_p|}+C_\alpha^{\pm}S_2^{\pm}e^{p_2|y-y_p|}+\sum_{j=1}^{2}D_j^\alpha S_j e^{p_j y}\right\}e^{ik(x-x_p)}dk \quad (7b)$$

where $\alpha = 1$ for a unit load in the x-direction and 2 for a unit load in the y-direction and

$$S_j^{\pm}=\pm S_j \quad j=1,\ 2$$

$$B_1^{\pm}=-\frac{p_1p_2a_1(C_{12}+C_{66})}{2C_{66}(a_1a_6-a_2a_5)}$$

$$C_1^{\pm}=\frac{p_1p_2a_2(C_{12}+C_{66})}{2C_{66}(a_1a_6-a_2a_5)}$$

$$B_2^{\pm}=C_2^{\mp}=\mp\frac{a_4}{2a_3} \quad (8)$$

with "+" for $y > y_p$ and "−" for $y < y_p$. Expressions of a_1 through a_6 are given in the Appendix. $B_\alpha^{\pm}$, $C_\alpha^{\pm}$ are obtained by using the fact that for a unit load in the x-direction, there will be a unit jump in σ_6^G while U^G, V^G, and σ_2^G, are continuous across the $y = y_p$ plane. Similarly, for a unit load in the y-direction there will be a jump in σ_2^G, while U^G, V^G, and σ_6^G are continuous. These conditions give rise to two 4×4 matrices which are then inverted to obtain $B_\alpha^{\pm}$, $C_\alpha^{\pm}$. Constants D_j^α (α, $j = 1, 2$) can be obtained from the boundary conditions and are given in the Appendix. Superscript G in U, V and σ indicates that displacements and stresses correspond to the Green's functions.

2.3 Application of Representation Theorem. From the frequency domain representation theorem (Mal (1972)) one can obtain the scattered displacement field ($U^s(x_p, y_p)$, $V^s(x_p, y_p)$) in the form

$$U^s(x_p,y_p)=\int_{d-a}^{d+a}[\phi(x-d)\sigma_6^1|_{y=h}+\psi(x-d)\sigma_2^1|_{y=h}]dx \quad (9a)$$

$$V^s(x_p,y_p)=\int_{d-a}^{d+a}[\phi(x-d)\sigma_6^2|_{y=h}+\psi(x-d)\sigma_2^2|_{y=h}]dx \quad (9b)$$

where σ_2^α, σ_6^α ($\alpha = 1, 2$) are the stress fields corresponding to a unit load acting in the α-direction; in other words, they are stress fields corresponding to the Green's functions obtained from (7*a*) and (7*b*). $\phi(x - d)$ and $\psi(x - d)$ are crack opening displacements (COD) along the x and y-directions, respectively, and are defined as

$$\begin{aligned}\phi(x-d)&=U(x-d,h^+)-U(x-d,h^-)\\ \psi(x-d)&=V(x-d,h^+)-V(x-d,h^-).\end{aligned} \quad (10)$$

Combining Eqs. (1), (7), and (9) and after some simplifications one can write

$$U^s(x_p,y_p)=\frac{1}{2\pi}\int_{d-a}^{d+a}\phi(x-d)\int_{-\infty}^{\infty}F_1(k)|_{y=h}e^{ik(x-x_p)}dkdx+\frac{1}{2\pi}\int_{d-a}^{d+a}\psi(x-d)\int_{-\infty}^{\infty}F_2(k)|_{y=h}e^{ik(x-x_p)}dkdx \quad (11a)$$

$$V^s(x_p,y_p)=\frac{1}{2\pi}\int_{d-a}^{d+a}\phi(x-d)\int_{-\infty}^{\infty}F_3(k)|_{y=h}e^{ik(x-x_p)}dkdx+\frac{1}{2\pi}\int_{d-a}^{d+a}\psi(x-d)\int_{-\infty}^{\infty}F_4(k)|_{y=h}e^{ik(x-x_p)}dkdx \quad (11b)$$

expressions of functions $F_j(k)$, $j = 1, 2, 3, 4$ are given in the Appendix.

The scattered stress field can be obtained from the displacement field of Eq. (11). To satisfy the stress-free boundary conditions this stress field should be equal to the negative of the incident stress field that can be obtained from Eq. (4). Hence,

$$\begin{aligned}&-iC_{21}\int_{-\infty}^{\infty}kF_1(k)|_{y=y_p=h}\int_{-a}^{a}\phi(x)e^{ik(x-x_p)+ikd}dxdk\\&-iC_{21}\int_{-\infty}^{\infty}kF_2(k)|_{y=y_p=h}\int_{-a}^{a}\psi(x)e^{ik(x-x_p)+ikd}dxdk\\&+C_{22}\int_{-\infty}^{\infty}\frac{\partial F_3(k)}{\partial y_p}\bigg|_{y=y_p=h}\int_{-a}^{a}\phi(x)e^{ik(x-x_p)+ikd}dxdk\\&+C_{22}\int_{-\infty}^{\infty}\frac{\partial F_4(k)}{\partial y_p}\bigg|_{y=y_p=h}\int_{-a}^{a}\psi(x)e^{ik(x-x_p)+ikd}dxdk\\&=-\int_{-\infty}^{\infty}\{A_1(ikC_{21}+C_{22}S_1p_1)e^{p_1h}+A_2(ikC_{21}+C_{22}S_2p_2)e^{p_2h}\}e^{ikx_p}dk\end{aligned} \quad (12a)$$

$$\begin{aligned}&C_{66}\int_{-\infty}^{\infty}\frac{\partial F_1(k)}{\partial y_p}\bigg|_{y=y_p=h}\int_{-a}^{a}\phi(x)e^{ik(x-x_p)+ikd}dxdk\\&+C_{66}\int_{-\infty}^{\infty}\frac{\partial F_2(k)}{\partial y_p}\bigg|_{y=y_p=h}\int_{-a}^{a}\psi(x)e^{ik(x-x_p)+ikd}dxdk\\&-iC_{66}\int_{-\infty}^{\infty}kF_3(k)|_{y=y_p=h}\int_{-a}^{a}\phi(x)e^{ik(x-x_p)+ikd}dxdk\\&-iC_{66}\int_{-\infty}^{\infty}kF_4(k)|_{y=y_p=h}\int_{-a}^{a}\psi(x)e^{ik(x-x_p)+ikd}dxdk\\&=-\int_{-\infty}^{\infty}\{A_1C_{66}(p_1+ikS_1)e^{p_1h}+A_2C_{66}(p_2+ikS_2)e^{p_2h}\}e^{ikx_p}dk.\end{aligned} \quad (12b)$$

In the above equations the only unknowns are the crack opening displacements ϕ and ψ, which are obtained in the next section.

3 Computation of the Crack Opening Displacement Functions

In order to evaluate the crack opening displacements, $\phi(x)$ and $\psi(x)$ are expanded in a complete set of Chebyshev polynomials,

$$\phi(x)=\sum_{n=0}^{\infty}\left[\frac{\alpha_{2n}}{2n}\phi_{2n}(x)+i\frac{\alpha_{2n+1}}{2n+1}\phi_{2n+1}(x)\right]$$

$$\psi(x)=\sum_{n=0}^{\infty}\left[\frac{\gamma_{2n}}{2n}\psi_{2n}(x)+i\frac{\gamma_{2n+1}}{2n+1}\psi_{2n+1}(x)\right] \quad (13)$$

where

$$\begin{aligned}\phi_{2n}(x)&=\sin\{2n\ \arcsin(x/a)\}\\ \psi_{2n}(x)&=\sin\{2n\ \arcsin(x/a)\}\\ \phi_{2n+1}(x)&=\cos\{(2n+1)\arcsin(x/a)\}\\ \psi_{2n+1}(x)&=\cos\{(2n+1)\arcsin(x/a)\}.\end{aligned} \quad (14)$$

To obtain the unknown coefficients α_n and γ_n, both sides of Eq. (12*a*) are multiplied by $\phi_m(x_p)$ then integrated from $x_p = -a$ to $x_p = a$, and both sides of Eq. (12*b*) are multiplied by $\psi_m(x_p)$ then integrated from $x_p = -a$ to $x_p = a$. After some algebraic manipulation an infinite set of linear equations is obtained to solve for α_n and γ_n.

$$\sum_{n=1}^{\infty}(K_{mn}\alpha_n+L_{mn}\gamma_n)=f_1(k)$$

$$\sum_{n=1}^{\infty}(M_{mn}\alpha_n+N_{mn}\gamma_n)=f_2(k) \tag{15}$$

where

$$f_1(k)=l_m\int_{-\infty}^{\infty}\{A_1(ikC_{21}+C_{22}S_1p_1)e^{p_1h}+A_2(ikC_{21}+C_{22}S_2p_2)e^{p_2h}\}\frac{J_m(ka)}{k}e^{ikd}dk$$

$$f_2(k)=l_m\int_{-\infty}^{\infty}\{A_1C_{66}(p_1+ikS_1)e^{p_1h}+A_2C_{66}(p_2+ikS_2)e^{p_2h}\}\frac{J_m(ka)}{k}e^{ikd}dk \tag{16}$$

$$K_{mn}=\int_{-\infty}^{\infty}\left[-C_{21}i\pi\frac{F_1(k)}{k}\bigg|_{y=y_p=h}+\frac{\pi}{k^2}C_{22}\frac{\partial F_3(k)}{\partial y_p}\bigg|_{y=y_p=h}\right]J_m(ka)J_n(ka)dk$$

$$L_{mn}=\int_{-\infty}^{\infty}\left[-C_{21}i\pi\frac{F_2(k)}{k}\bigg|_{y=y_p=h}+\frac{\pi}{k^2}C_{22}\frac{\partial F_4(k)}{\partial y_p}\bigg|_{y=y_p=h}\right]J_m(ka)J_n(ka)dk$$

$$M_{mn}=\int_{-\infty}^{\infty}\left[C_{66}\frac{\pi}{k^2}\frac{\partial F_1(k)}{\partial y_p}\bigg|_{y=y_p=h}-C_{66}\,i\pi\frac{F_3(k)}{k}\bigg|_{y=y_p=h}\right]J_m(ka)J_n(ka)dk$$

$$N_{mn}=\int_{-\infty}^{\infty}\left[C_{66}\frac{\pi}{k^2}\frac{\partial F_2(k)}{\partial y_p}\bigg|_{y=y_p=h}-C_{66}i\pi\frac{F_4(k)}{k}\bigg|_{y=y_p=h}\right]J_m(ka)J_n(ka)dk \tag{17}$$

and J_m is the Bessel function of first kind of order m, and

$$l_m=\begin{cases} i & \text{for odd } m\\ -i & \text{for even } m.\end{cases}$$

Matrices K, L, M, and N are all symmetric. In addition, when $(m+n)$ is even, then $K_{mn}=N_{mn}=0$, and when $(m+n)$ is odd, then $L_{mn}=M_{mn}=0$.

Equations (15) have an infinite series in their expressions. However, they can be terminated after a finite number of terms without introducing any significant error (Kundu (1985)). Then α_n, γ_n can be obtained from a finite set of linear equations.

3.1 Computation of Surface Displacements. The total displacement components U and V are given by

$$U=U^i+U^s$$

$$V=V^i+V^s \tag{18}$$

in which U^i and V^i are displacement components in absence of any crack given by Eq. (4), whereas the scattered field components U^s and V^s represent the change in U^i and V^i due to the presence of the crack. U^s and V^s are given by Eqs. (9*a*) and (9*b*), respectively. After some mathematical simplifications one can write the displacement components U and V at any point $B(x, 0)$ on the surface in the following manner

$$U^i(x,0)=\frac{1}{2\pi}\int_{-\infty}^{\infty}(A_1+A_2)e^{ikx}dk \tag{19a}$$

$$V^i(x,0)=\frac{1}{2\pi}\int_{-\infty}^{\infty}A_jS_je^{ikx}dk\quad(j=1,2) \tag{19b}$$

and

$$U^s(x,0)=i\int_0^{\infty}\frac{F_1(k)}{k}\bigg|_{y=h,y_p=0}\cos(kd-kx)\times\sum_{n=\text{odd}}^{\infty}\{\alpha_nJ_n(ka)\}dk-\int_0^{\infty}\frac{F_1(k)}{k}\bigg|_{y=h,y_p=0}\sin(kd-kx)\times\sum_{n=\text{even}}^{\infty}\{\alpha_nJ_n(ka)\}dk-\int_0^{\infty}\frac{F_2(k)}{k}\bigg|_{y=h,y_p=0}\sin(kd-kx)\times\sum_{n=\text{odd}}^{\infty}\{\gamma_nJ_n(ka)\}dk+i\int_0^{\infty}\frac{F_2(k)}{k}\bigg|_{y=h,y_p=0}\cos(kd-kx)\times\sum_{n=\text{even}}^{\infty}\{\gamma_nJ_n(ka)\}dk \tag{20a}$$

$$V^s(x,0)=-\int_0^{\infty}\frac{F_3(k)}{k}\bigg|_{y=h,y_p=0}\sin(kd-kx)\times\sum_{n=\text{odd}}^{\infty}\{\alpha_nJ_n(ka)\}dk+i\int_0^{\infty}\frac{F_3(k)}{k}\bigg|_{y=h,y_p=0}\cos(kd-kx)\times\sum_{n=\text{even}}^{\infty}\{\alpha_nJ_n(ka)\}dk+i\int_0^{\infty}\frac{F_4(k)}{k}\bigg|_{y=h,y_p=0}\cos(kd-kx)\times\sum_{n=\text{odd}}^{\infty}\{\gamma_nJ_n(ka)\}dk-\int_0^{\infty}\frac{F_4(k)}{k}\bigg|_{y=h,y_p=0}\sin(kd-kx)\times\sum_{n=\text{even}}^{\infty}\{\gamma_nJ_n(ka)\}dk. \tag{20b}$$

Then Eqs. (19) and (20) are added to obtain the total surface displacement.

3.2 Computational Aspects. The next task is to compute the integral expressions in Eqs. (16), (17), (19), and (20). Numerical techniques to obtain such integrals and methods used to verify convergence and accuracy of the computer programs were discussed in several previous papers by the authors (Kundu and Mal (1985), Kundu (1986), Kundu (1987b), Karim and Kundu (1988)).

4 Results and Discussions

The method discussed above has been implemented in a FORTRAN program. Results are given for a graphite-epoxy composite specimen which is used widely in aircraft industries. Response of the cracked half-space to different impact loadings are shown in Figs. 3 through 8. The following function is considered as the loading function:

$$f(t)=\begin{cases}16Pt^2(t-\tau)^2\tau^{-4} & 0\le t\le\tau\\ 0 & t\ge\tau\end{cases} \tag{21}$$

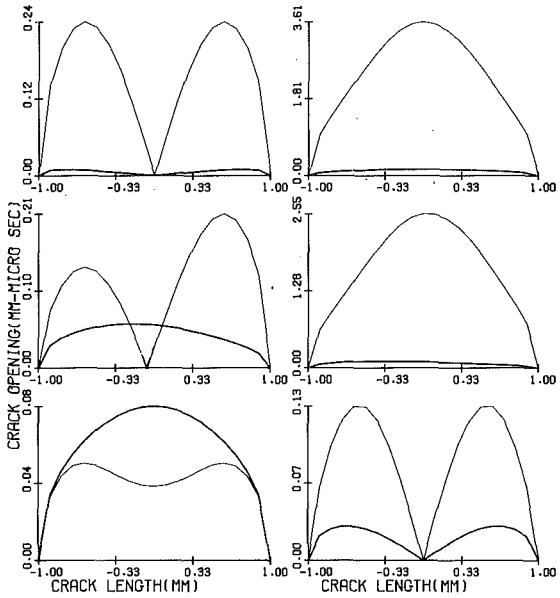

Fig. 3 Spectral amplitude (in mm-μsec) of crack opening displacements at a frequency 0.04 MHz for F(ω) equal to 10. Left and right columns show the displacements along the x and y-directions, respectively. Thin and thick curves are for d = 0 mm and 2 mm, respectively, (see Fig. 1).

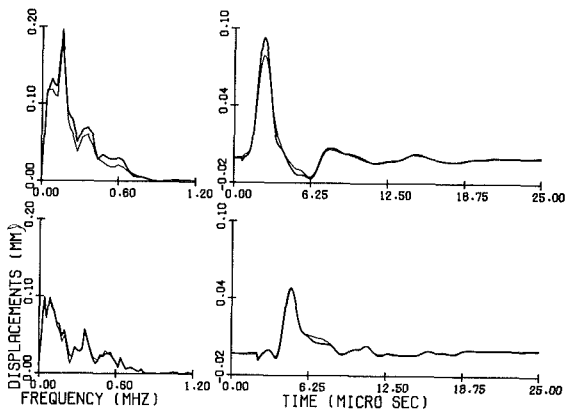

Fig. 4 Surface displacements along the x-direction in an orthotropic half-space. The half-space is excited by a line load at d = 2 mm with an angle of inclination, θ = 45 deg and pulse duration time τ = 2 μsec. The top and bottom rows show the surface displacements at x = 5 and 15 mm, respectively (see Fig. 1). Left and right columns give spectra and time histories, respectively. The thick curves show displacements in presence of the crack while thin curves are for a flawless half-space

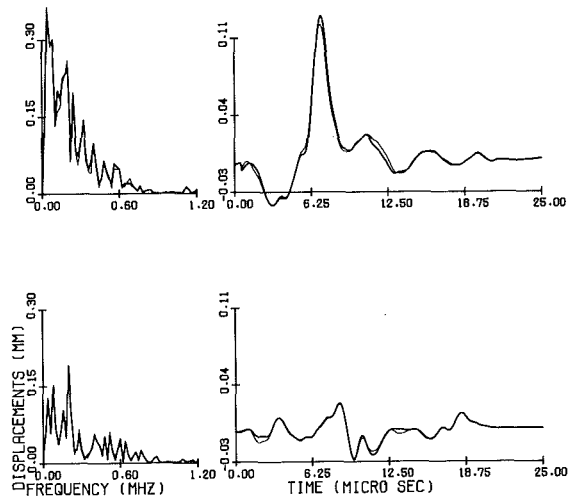

Fig. 5 Same as Fig. 4, but computed displacements are along the y-direction

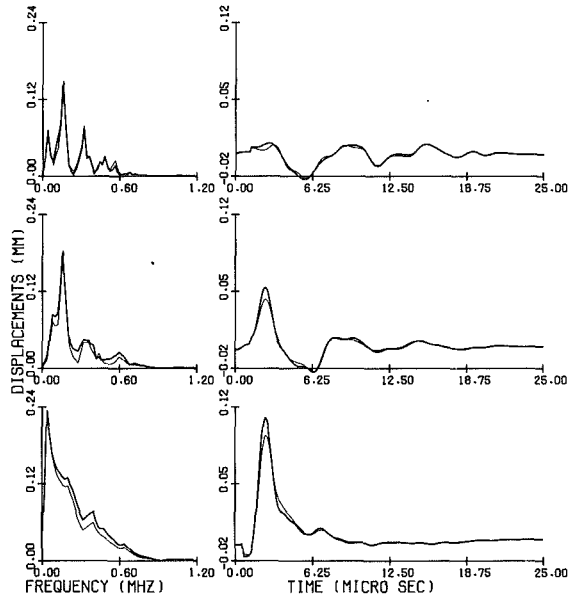

Fig. 6 Surface displacements along the x-direction for a load applied at d = 2 mm, with the pulse duration time τ = 2 μsec. Top, middle, and bottom rows are for angles of inclination equal to 0 deg, 30 deg and 90 deg, respectively. Left and right columns give spectral amplitudes and time histories, respectively. Thick curves are for the cracked half-space and thin curves are for the flawless half-space.

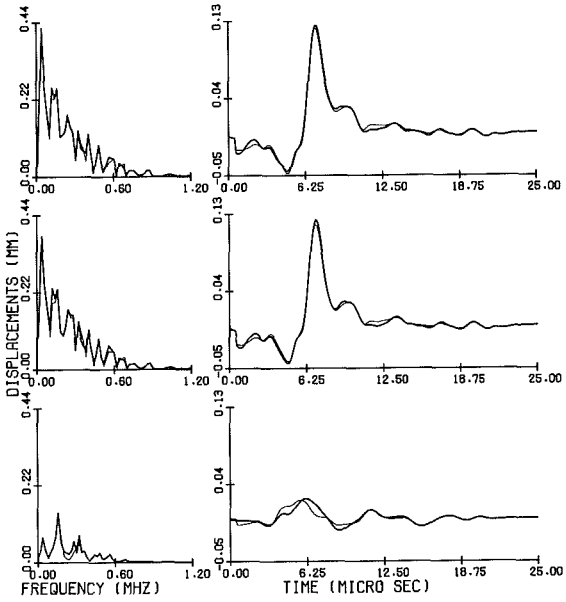

Fig. 7 Same as Fig. 6, but computed displacements are along the y-direction

whose Fourier transform is given by

$$F(\omega)=\frac{32P}{\tau^4\omega^3}\left[\left\{-\frac{6\tau}{\omega}+i\left(\tau^2-\frac{12}{\omega^2}\right)\right\}e^{i\omega\tau}-\left\{\frac{6\tau}{\omega}+i\left(\tau^2-\frac{12}{\omega^2}\right)\right\}\right]. \quad (22)$$

In the above equations, P defines the peak value of the plate surface excitation load. In subsequent calculations, Figs. 4 through 8, P is set equal to 10. τ is the duration of the impact load. Sharpness of the impact time history can be increased by either decreasing τ or increasing P. Results are given for τ = 2 micro seconds. The following material properties of the graphite-epoxy composite (Kuo (1984a)) are used for all subsequent analyses:

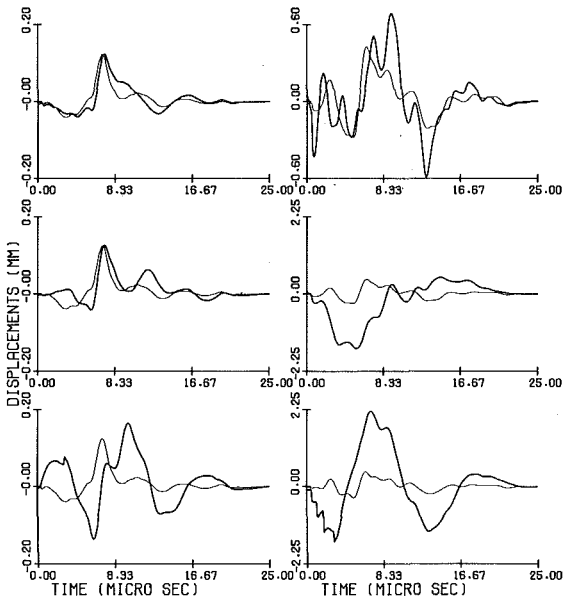

Fig. 8 Vertical displacements of $x = 5$ mm at the surface of an orthotropic half-space (left column) and an isotropic half-space (right column). For all plots $d = 0$ mm and $\theta = 45$ deg. The top row is for $a = 1$ mm, $h = 0.5$ mm, the middle row is for $a = 2$ mm, $h = 0.5$ mm, and for the bottom row $a = 1$ mm, $h = 0.25$ mm. Thick curves are for the cracked half-space and thin curves are for the flawless half-space.

$$C_{11} = 138.4408 \text{ GPa}$$

$$C_{22} = 14.5365 \text{ GPa}$$

$$C_{12} = 3.0530 \text{ GPa}$$

$$C_{66} = 5.8565 \text{ GPa}$$

$$\rho = 7.44 \text{ gm/cm}^3. \tag{23}$$

For the sample problem considered in Figs. 4–7, the half-crack length is taken as 1 mm, depth of crack h is taken as 0.5 mm, and distance of the crack center from the point of application of the load is taken as 2 mm. These dimensions are of the same order of magnitude as generally obtained in impact tests (Joshi and Sun (1985)).

It is shown in Figs. 4–7 that spectral values of surface displacements become very small after 1-MHz frequency for the excitation load considered here. So numerical computations are carried out up to 1.2-MHz frequency at an interval of 0.04MHz. The crack opening displacement (COD) along the crack length is shown in Fig. 3 for 0.04-MHz frequency and $F(\omega)$ equal to 10. For any other value of $F(\omega)$, all graphs in Fig. 3 should be appropriately scaled. $F(\omega)$ is set equal to 10 only to make sure that COD values along the y-axis are not too small and the computer doesn't use any scaling factor along the y-axis while plotting these curves.

The left column shows the variation of displacement along the x-direction (U) while the right column shows the same in the y-direction (V). Three rows correspond to three angles of inclination (θ), which are 0 deg (top row), 45 deg (middle row), and 90 deg (bottom row). In each plot two curves are drawn, the thick curve shows the COD of the sample problem described above, while the thin curve is for a similar problem where the load is shifted horizontally just above the center of the crack ($d = 0$ mm). From the problem geometry and the direction of applied load it is obvious that for $d = 0$, the problem is symmetric for $\theta = 0$ deg and antisymmetric for $\theta = 90$ deg. Hence, for $\theta = 0$ deg, one should expect symmetric V and antisymmetric U, whereas for $\theta = 90$ deg, V and U should be antisymmetric and symmetric, respectively. This is what we get in our computation also. However, in the COD plots (thin curves of Fig. 3), both U and V appear to be symmetric for $\theta = 0$ deg (top row) and $\theta = 90$ deg (bottom row). This is because the modulus or absolute value of COD amplitudes are plotted in these figures; hence, both symmetric and antisymmetric curves appear to be symmetric in the figure. For a 45 deg inclination (middle row) and other angles of inclination (not shown), COD plots are neither symmetric nor antisymmetric.

In a few more words let us explain clearly what is meant by antisymmetric U and V. If the horizontal displacement is positive (towards right) at a point $(+x, 0)$ and negative (towards left) but of the same magnitude at another point $(-x, 0)$, then we call it an antisymmetric U. So antisymmetric U really means a horizontal motion of the half-space which is symmetric about the y-axis. Hence, we get antisymmetric U for the symmetric loading ($\theta = 0$, $d = 0$). Since U displacements are parallel to the crack faces, the problem of overlapping or penetration of crack faces does not arise for symmetric or antisymmetric U. However, for antisymmetric V, this problem definitely comes. This is due to the fact that for an antisymmetric V, if the vertical component (V) of the crack opening displacement is positive for, say $x > 0$, then for $x < 0$, V should be negative, meaning penetration of crack faces one into another. However, as mentioned in the next section, under Concluding Remarks, if the crack has some nonzero width, the crack faces may go through antisymmetric vertical displacements without touching each other. Similar types of symmetric and antisymmetric COD plots are obtained at other frequencies as well, but because of the page limitation, those plots are not presented in this paper.

In Figs. 4 through 7, thick and thin curves indicate the surface response of an orthotropic half-space with and without cracks, respectively. Left and right columns give spectral amplitudes and time histories, respectively. In Figs. 4 and 5, variations of u and v on the surface of the half-space are shown. Top and bottom rows indicate the displacements at x equal to 5 and 15 mm, respectively (see Fig. 1). It should be noted here that for both Figs. 4 and 5, the percentage difference between the peak values of surface displacements with and without the subsurface crack is more at $x = 5$ mm than that at $x = 15$ mm. Intuitively also one should expect it, since the effect of crack decays as the distance from the crack increases.

Horizontal (u) and vertical (v) displacements at $x = 5$ mm are plotted in Figs. 6 and 7 for three different angles of inclination θ, which are 0 deg (top row), 30 deg (middle row) and 90 deg (bottom row). It can be seen in these two figures that as the external load changes its orientation from vertical ($\theta = 0$ deg, top row) to horizontal position ($\theta = 90$ deg, bottom row) u increases and v decreases. Qualitatively, we can justify these results since a horizontal force should produce more horizontal displacement, whereas a vertical force should produce more vertical displacement as long as the Poisson's ratio of the material is less than unity.

It should also be noted here that the peak displacement increases with the presence of the crack. This is because a cracked half-space is more flexible than an uncracked half-space; hence, a cracked half-space gives larger displacement. In Figs. 4 through 7, the difference between surface motions of cracked and uncracked composites is found to be very small. However, this difference can be significantly increased for a smaller value of h and a larger value of a as shown in Fig. 8.

To investigate the effect of the crack length ($2a$) and depth (h) on the surface motion, the vertical component of the surface displacement at $x = 5$ mm is plotted in Fig. 8 for $\theta = 45$ deg and $d = 0$. The top row is for $a = 1$ mm and $h = 0.5$ mm, the middle row is for $a = 2$ mm and $h = 0.5$ mm, and the bottom row is for $a = 1$ mm and $h = 0.25$ mm. The left column shows the surface displacements for an orthotropic half-space whose material properties are given in Eq. (23), and the right column shows surface motions in an isotropic (epoxy) half-space. Material properties of epoxy are taken as follows:

$$C_{11} = 5.81 \text{ GPa}$$

$$C_{22} = 5.81 \text{ GPa}$$

$$C_{12} = 2.90 \text{ GPa}$$

$$C_{66} = 1.45 \text{ GPa}$$

$$\rho = 1.20 \text{ gm/cm}^3. \quad (24)$$

It can be seen in this figure that increase in the crack length (middle row), as well as decrease in the crack depth (bottom row), increases the difference between the surface motions of cracked and uncracked half-spaces. A comparison between the left and right columns shows that a crack in an isotropic solid (right column) alters the surface motion comparatively more than a crack along the fiber direction in a composite solid (left column). So it is relatively easier to detect a crack in an isotropic solid. Intuitively, one can explain this observation in the following manner: A crack in an isotropic material makes it anisotropic, since due to the presence of a crack, the gross stiffness of the material perpendicular to the crack length decreases, whereas its stiffness along the crack length remains unchanged. Similarly, in a fiber-reinforced composite solid, a crack which is parallel to the fibers does not change its stiffness along the fiber direction, but reduces its gross stiffness in the perpendicular direction. So the stronger direction (the fiber direction) remains equally strong but the weaker direction (perpendicular to the fiber) becomes more weak after the crack is introduced. Since elastic waves propagate more quickly and easily along the fiber direction, material properties in that direction should have a stronger effect on the surface motion. So a slight change in stiffness in the direction perpendicular to the fiber does not have much effect on the surface motion as can be seen in Figs. 3 through 7. However, when cracks are too big or too close to the surface, their effects can be clearly observed as in the middle and bottom rows of Fig. 8.

5 Concluding Remarks

In this paper the surface displacement of a cracked orthotropic half-space is computed when it is excited by an impact load of arbitrary inclination at a point on the surface. The nature of computed results qualitatively agrees with the expected form. However, we could not compare our results with any other published result since no analytical or numerical results are available in the literature for any problem with geometry and loading similar to this one.

In this analysis traction-free crack surfaces are considered; in other words it is assumed that the crack surfaces do not come in contact with each other. However, under dynamic loading the crack surfaces should come in contact with each other and introduce nonlinearity in the problem. Under certain situations these crack surface tractions may significantly alter the surface displacements computed here. However, under some other real situation, such as a subsurface crack of nonzero width being excited dynamically by an ultrasonic signal, the crack surfaces may vibrate and yet may not come in contact with each other. The assumption of stress-free crack surfaces is justified under such situations. Then the response computed with this simplifying assumption should be close to the actual response.

In most of the results presented in this paper the difference between cracked and uncracked half-space response is found to be very small. The possible reason behind it has been qualitatively explained at the end of the previous section. However, this difference significantly increases if the crack length is increased or the depth of embedment of the crack is decreased. It is also observed in this paper that the effect of the crack is relatively stronger in an isotropic solid.

Acknowledgment

This research was partially supported by the National Science Foundation under Contract DMC-8807661.

References

Achenbach, J. D., and Brind, R. J., 1981a, "Elastodynamic Stress Intensity Factor for a Crack Near a Free Surface," ASME JOURNAL OF APPLIED MECHANICS, Vol. 48, pp. 539–542.

Achenbach, J. D., and Brind, R. J., 1981b, "Scattering of Surface Waves by a Sub-Surface Crack," *J. of Sound and Vibrations*, Vol. 76, pp. 43–56.

Achenbach, J. D., Lin, W., and Keer, L. M., 1983, "Surface Waves Due to Scattering by a Near-surface Parallel Crack," *IEEE Trans. Sonics and Ultrasonics*, Vol. SU-30 4, pp. 270–276.

Achenbach, J. D., and Norris, A. N., 1982, "Loss of Specular Reflection Due to Nonlinear Crack-Face Interaction," *Journal of Nondestructive Evaluation*, Vol. 3, pp. 229–239.

Ang, W. T., 1988, "A Crack in an Anisotropic Layered Material Under the Action of Impact Loading," ASME JOURNAL OF APPLIED MECHANICS, Vol. 55, pp. 120–125.

Boström, A., 1987, "Elastic Wave Scattering from an Interface Crack: Antiplane Strain," ASME JOURNAL OF APPLIED MECHANICS, Vol. 54, pp. 503–508.

Datta, S. K., 1979, "Diffraction of SH-wave by an Edge Crack," ASME JOURNAL OF APPLIED MECHANICS, Vol. 46, pp. 101–106.

Georgiadis, H. G., and Papadopoulos, G. A., 1987, "Determination of SIF in a Cracked Plane Orthotropic Strip by the Weiner-Hopf Technique," *International Journal of Fracture*, Vol. 34, pp. 57–64.

Gracewski, S. M., and Bogy, D. B., 1986a, "Elastic Wave Scattering from an Interface Crack in a Layered Half Space Submerged in Water: Part 1—Applied Traction at the Liquid-Solid Interface," ASME JOURNAL OF APPLIED MECHANICS, Vol. 53, pp. 326–332.

Gracewski, S. M., and Bogy, D. B., 1986b, "Elastic Wave Scattering from an Interface Crack in a Layered Half Space Submerged in Water: Part 2—Incident Plane Waves and Bounded Beams," ASME JOURNAL OF APPLIED MECHANICS, Vol. 53, pp. 323–338.

Joshi, S. P., and Sun, C. T., 1985, "Impact Induced Fracture in Laminated Composite," *Journal of Composite Materials*, Vol. 19, pp. 51–56.

Karim, M. R., and Kundu, T., 1989, "Transient Response of Three Layered Composites with Two Interface Cracks Due to a Line Load," *Acta Mechanica*, Vol. 76, pp. 53–72.

Karim, M. R., and Kundu, T., 1988, "Transient Surface Response of Layered Isotropic and Anisotropic Half-Spaces with Interface Cracks: SH Case," *International Journal of Fracture*, Vol. 37, pp. 245–262.

Kassir, M. K., and Bandyopadhyay, K. K., 1983, "Impact Response of a Cracked Orthotropic Medium," ASME JOURNAL OF APPLIED MECHANICS, Vol. 50, pp. 630–636.

Keer, L. M., Lin, W., and Achenbach, J. D., 1984a, "Resonance Effect for a Crack Near a Free Surface," ASME JOURNAL OF APPLIED MECHANICS, Vol. 51, pp. 65–70.

Kundu, T., 1987a, "Dynamic Interaction Between Two Interface Cracks in a Three Layered Plate," *International Journal of Solids and Structures*, Vol. 24, pp. 27–39.

Kundu, T., 1987b, "The Transient Response of Two Cracks at the Interface of a Layered Half-Space," *International Journal of Engineering Science*, Vol. 25, pp. 1427–1439.

Kundu, T., 1986, "Transient Response of an Interface-Crack in a Layered Plate," ASME JOURNAL OF APPLIED MECHANICS, Vol. 53, pp. 579–586.

Kundu, T., and Mal, A. K., 1985, "Elastic Waves in a Multilayered Solid Due to a Dislocation Source," *Wave Motion*, Vol. 7, pp. 459–471.

Kundu, T., and Mal, A. K., 1981, "Diffraction of Elastic Waves by a Surface Crack on a Plate," ASME JOURNAL OF APPLIED MECHANICS, Vol. 48, pp. 507–576.

Kuo, A.-Y., 1984a, "Transient Stress Intensity Factors of an Interfacial Crack Between Two Dissimilar Anisotropic Half-Spaces: Part 1—Orthotropic Materials," ASME JOURNAL OF APPLIED MECHANICS, Vol. 51, pp. 71–76.

Kuo, A.-Y., 1984b, "Transient Stress Intensity Factors of an Interfacial Crack Between Two Dissimilar Anisotropic Half-Spaces: Part 2 Fully Anisotropic Materials," ASME JOURNAL OF APPLIED MECHANICS, Vol. 51, pp. 780–786.

Lin, W., Keer, L. M., and Achenbach, J. D., 1984b, "Dynamic Stress Intensity Factor for an Inclined Sub-surface Crack," ASME JOURNAL OF APPLIED MECHANICS, Vol. 51, pp. 773–779.

Mal, A. K., 1972, "Rayleigh Waves from a Moving Thrust Fault," *Bulletin of the Seismological Society of America*, Vol. 62, pp. 751–762.

Mendelson, D. A., Achenbach, J. D., and Keer, L. M., 1980, "Scattering of Elastic Waves by a Surface-Breaking Crack," *Wave Motion*, Vol. 2, pp. 277–292.

Neerhoff, F. L., 1979, "Diffraction of Love Waves by a Stress-Free Crack of Finite Width in the Plane Interface of a Layered Composite," *Applied Scientific Research*, Vol. 35, pp. 265–315.

Stone, S. F., Gosh, M. L., and Mal, A. K., 1980, "Diffraction of Antiplane Shear Waves by an Edge Crack," ASME JOURNAL OF APPLIED MECHANICS, Vol. 47, pp. 359–362.

Thompson, R. B., and Fiedler, C. J., 1984, *The Effect of Crack Closure on Ultrasonic Measurements* (Review of Progress in QNDE, 3A), D. O. Thompson, and D. E. Chimenti, eds., Plenum, New York, pp. 207–215.

Xu, P.-C., and Mal, A. K., 1987, "Calculation of Green's Functions for a Layered Viscoelastic Solid," *Bulletin of the Seismological Society of America*, Vol. 77, pp. 1823–1837.

Yang, H. J., and Bogy, D. B., 1985, "Elastic Wave Scattering from an Interface Crack in a Layered Half-Space," ASME JOURNAL OF APPLIED MECHANICS, Vol. 52, pp. 42–50.

Zhang, Ch., and Achenbach, J. D., 1988, "Scattering by Multiple Crack Configurations," ASME JOURNAL OF APPLIED MECHANICS, Vol. 55, pp. 104–110.

APPENDIX

Expressions of A_j, D_j^α, (α, j = 1, 2), (j = 1 to 6) in Eqs. (4), (7), and (8) are given in this section. Values of functions $F_j(k)$, (k = 1 to 4) in Eq. (11) are also defined here.

$$A_1 = \frac{-a_{22}F(\omega)\cos\theta + a_{21}F(\omega)\sin\theta}{a_{11}a_{22} - a_{12}a_{21}}$$

$$A_2 = \frac{+a_{21}F(\omega)\cos\theta - a_{11}F(\omega)\sin\theta}{a_{11}a_{22} - a_{12}a_{21}} \tag{A1}$$

where

$$\begin{aligned} a_{11} &= ikC_{21} + C_{22}S_1p_1 \\ a_{12} &= ikC_{21} + C_{22}S_2p_2 \\ a_{21} &= C_{66}(p_1 + ikS_1) \\ a_{22} &= C_{66}(p_2 + ikS_2) \end{aligned} \tag{A2}$$

and

$$D_1^1 = \frac{a_{22}R_1 - a_{12}R_2}{a_{11}a_{22} - a_{12}a_{21}}$$

$$D_2^1 = \frac{-a_{21}R_1 + a_{11}R_2}{a_{11}a_{22} - a_{12}a_{21}}$$

$$D_1^2 = \frac{a_{22}R_3 - a_{12}R_4}{a_{11}a_{22} - a_{12}a_{21}}$$

$$D_2^2 = \frac{-a_{21}R_3 + a_{11}R_4}{a_{11}a_{22} - a_{12}a_{21}} \tag{A3}$$

where

$$\begin{aligned} R_1 &= -B_1^- e^{p_1y_p}a_{11} - C_1^- e^{p_2y_p}a_{12} \\ R_2 &= B_1^- e^{p_1y_p}a_{21} + C_1^- e^{p_2y_p}a_{22} \\ R_3 &= -B_2^- e^{p_1y_p}a_{11} - C_2^- e^{p_2y_p}a_{12} \\ R_4 &= B_2^- e^{p_1y_p}a_{21} + C_2^- e^{p_2y_p}a_{22} \end{aligned} \tag{A4}$$

$$\begin{aligned} a_1 &= p_1(k^2C_{11} - C_{66}p_2^2 - \rho\omega^2) \\ a_2 &= p_2(k^2C_{11} - C_{66}p_1^2 - \rho\omega^2) \\ a_3 &= C_{22}C_{66}(p_1^2 - p_2^2) \\ a_4 &= -ik(C_{12} + C_{66}) \\ a_5 &= p_1(p_2^2C_{12} + k^2C_{11} - \rho\omega^2) \\ a_6 &= p_2(p_1^2C_{12} + k^2C_{11} - \rho\omega^2) \end{aligned} \tag{A5}$$

$$\begin{aligned} F_1(k) &= C_{66}(B_1^+ p_1 e^{p_1|y-y_p|} + p_2C_1^+ e^{p_2|y-y_p|} + D_1^1p_1e^{p_1y} \\ &\quad + D_2^1p_2e^{p_2y}) + ikC_{66}(B_1^+S_1e^{p_1|y-y_p|} + C_1^+S_2e^{p_2|y-y_p|} \\ &\quad + D_1^1S_1e^{p_1y} + D_2^1S_2e^{p_2y}) \\ F_2(k) &= ikC_{21}(B_1^+e^{p_1|y-y_p|} + C_1^+e^{p_2|y-y_p|} + D_1^1e^{p_1y} \\ &\quad + D_2^1e^{p_2y}) + C_{22}(B_1^+S_1p_1e^{p_1|y-y_p|} + C_1^+S_2p_2e^{p_2|y-y_p|} \\ &\quad + D_1^1S_1p_1e^{p_1y} + D_2^1S_2p_2e^{p_2y}) \\ F_3(k) &= C_{66}(B_2^+ p_1 e^{p_1|y-y_p|} + p_2C_2^+ e^{p_2|y-y_p|} + D_1^2p_1e^{p_1y} \\ &\quad + D_2^2p_2e^{p_2y}) + ikC_{66}(B_2^+S_1e^{p_1|y-y_p|} + C_2^+S_2e^{p_2|y-y_p|} \\ &\quad + D_1^2S_1e^{p_1y} + D_2^2S_2e^{p_2y}) \\ F_4(k) &= ikC_{21}(B_2^+e^{p_1|y-y_p|} + C_2^+e^{p_2|y-y_p|} + D_1^2e^{p_1y} + D_2^2e^{p_2y}) \\ &\quad + C_{22}(B_2^+S_1p_1e^{p_1|y-y_p|} + C_2^+S_2p_2e^{p_2|y-y_p|} \\ &\quad + D_1^2S_1p_1e^{p_1y} + D_2^2S_2p_2e^{p_2y}). \end{aligned} \tag{A6}$$

A Solution of the Mixed Boundary Value Problem for an Infinite Plate With a Hole Under Uniform Heat Flux

Norio Hasebe

Hideaki Irikura

Takuji Nakamura

Department of Civil Engineering,
Nagoya Institute of Technology,
Gokisocho, Showaku, Nagoya 466, Japan

A general solution of the mixed boundary value problem with displacements and external forces given on the boundary is obtained for an infinite plate with a hole subjected to uniform heat flux. Complex stress functions, a rational mapping function, and the dislocation method are used for the analysis. The stress function is obtained in a closed form and the first derivative is given by such a form that does not contain the integral term. The mapping function is represented in the form of a sum of fractional expressions. A problem is solved for a crack initiating from a point of a circular hole on which the displacement is rigidly stiffened. Stress distributions and stress intensity factors are calculated.

Introduction

Florence and Goodier (1960) analyzed thermal stresses due to uniform heat flux for an infinite plate with a hole of ovaloid form by using the dislocation method. The writers analyzed thermal stresses due to a uniform heat flux for an infinite plate with a kinked crack (Hasebe et al., 1986) and a circular hole with a crack (Hasebe et al., 1988a) by using a rational mapping function and the dislocation method. Further, a solution of the displacement boundary value problem under uniform heat flux was given by Hasebe et al. (1989).

The first purpose of the present paper is to obtain a general solution of the mixed boundary value problem for thermal stresses in an infinite plate with a hole due to uniform heat flux. Without losing generality, the boundary condition is given for the situation that a part of the boundary is free from external forces and the rest of the boundary is constrained by vanishing displacements. Complex stress functions and a rational mapping function represented in the form of a sum of fractional expressions are used for the analysis. A strict solution can be obtained in closed form for the shape represented by the rational mapping function. The mixed boundary value problem for the thermal stress is more difficult to solve compared to the boundary value problem for the external force or the displacement. It seems that a general solution of this problem has not been obtained.

The second purpose is to solve a problem for a crack initiating from a point on a circular hole where displacements are constrained. This problem is a model of a crack initiating from a point on a rigid stiffening ring or a circular rigid inclusion. It is assumed that the heat flux does not flow through the surface of the rigid ring and crack. The case without a stiffening ring is the same problem as for a crack initiating from a circular hole (Hasebe et al., 1988a), which is an extreme state where the rigidity of the ring is equal to zero. Another extreme state is the case when the ring is rigid. The stress state for an elastic ring must be intermediate to these two states.

The stress distributions and the stress intensity factors are obtained for the heat flux in an arbitrary direction. The distributions of temperature and heat flux are the same as those in Hasebe et al. (1988a).

Mapping Function and Temperature Analysis

The infinite region with a circular hole and a crack as shown in Fig. 1 is analyzed. The conformal function that maps the infinite region to the outside region of the unit circle is expressed as follows (Bowie 1956):

$$z=\frac{1}{2\sin^2\gamma}\left\{\zeta+\frac{1}{\zeta}+\cos 2\gamma+(\zeta+1)\times\left(1+\frac{e^{2i\gamma}}{\zeta}\right)^{0.5}\left(1+\frac{e^{-2i\gamma}}{\zeta}\right)^{0.5}\right\}. \quad (1)$$

In Fig. 1 and Eq. (1), a is the radius of the circular hole, c is the crack length, γ is a parameter with regard to the crack length, and $c/a=\cos\gamma/(1-\cos\gamma)$. The rational mapping function is formulated as follows (Hasebe et al., 1987; Hasebe and Ueda, 1980):

Contributed by the Applied Mechanics Division of THE AMERICAN SOCIETY OF MECHANICAL ENGINEERS for publication in the JOURNAL OF APPLIED MECHANICS.

Discussion on this paper should be addressed to the Technical Editor, Prof. Leon M. Keer, The Technological Institute, Northwestern University, Evanston, IL 60208, and will be accepted until two months after final publication of the paper itself in the JOURNAL OF APPLIED MECHANICS. Manuscript received by the ASME Applied Mechanics Division, Dec. 7, 1989; final revision, Mar. 15, 1991.

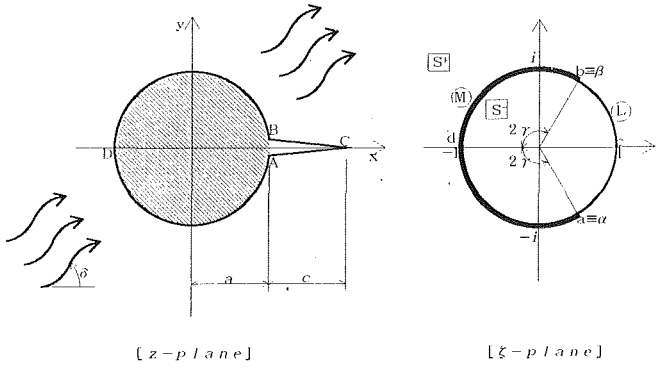

Fig. 1 Analyzed region under heat flux and the associated unit circle

$$z=\omega(\zeta)=E_0\zeta+\frac{E_{25}}{\zeta}+\sum_{k=1}^{N}\frac{E_k}{\zeta_k-\zeta}+E_{-1} \tag{2}$$

where $E_{25}=E_0/2$, and $N=24$. The heat flux and the temperature are expressed by the complex temperature function $\psi(\zeta)$ (Hasebe et al., 1986, 1988a),

$$q_x-iq_y=-k\frac{\psi'(\zeta)}{\omega'(\zeta)},\qquad q_r-iq_\theta=\frac{\zeta\omega'(\zeta)}{|\zeta\omega'(\zeta)|}(q_x-iq_y)$$

$$\Theta(\zeta,\bar{\zeta})=\frac{1}{2}[\psi(\zeta)+\overline{\psi(\zeta)}] \tag{3}$$

where k is the thermal conductivity; q_x and q_y are components of the heat flux in the x and y-directions; q_r and q_θ are components of the heat flux in the orthogonal curvilinear coordinates expressed by $\omega(\zeta)$; $\Theta(\zeta,\bar{\zeta})$ is the temperature. For the uniform heat flux q through the unit area, $\psi(\zeta)$ is given as follows:

$$\psi(\zeta)=-\frac{q}{k}\left(E_0\zeta e^{-i\delta}+\frac{\overline{E_0}}{\zeta}e^{i\delta}\right) \tag{4}$$

where δ is the angle between the direction of heat flux and the x-axis (see Fig. 1).

Method of Analysis

Using the complex stress functions $\phi(\zeta)$ and $\psi(\zeta)$ which are regular in the region S^+ outside the unit circle, the stress components are expressed as (Muskhelishvili 1963)

$$\begin{aligned}&\sigma_x+\sigma_y=4\mathrm{Re}\left[\frac{\phi'(\zeta)}{\omega'(\zeta)}\right]\\&\sigma_y-\sigma_x+2i\tau_{xy}=2\frac{\overline{\omega(\zeta)}\left\{\dfrac{\phi'(\zeta)}{\omega'(\zeta)}\right\}'+\psi'(\zeta)}{\omega'(\zeta)}\\&\sigma_\theta+\sigma_r=\sigma_x+\sigma_y\\&\sigma_\theta-\sigma_r+2i\tau_{r\theta}=\frac{\zeta^2\omega'(\zeta)}{|\zeta|^2\overline{\omega'(\zeta)}}(\sigma_y-\sigma_x+2i\tau_{xy}).\end{aligned} \tag{5}$$

The boundaries on which the external forces and the displacements are applied are denoted by L and M, respectively. The boundary conditions on L and M are given by

$$\phi(\sigma)+\frac{\omega(\sigma)}{\omega'(\sigma)}\overline{\phi'(\sigma)}+\overline{\psi(\sigma)}=i\int(p_x+ip_y)ds\qquad\text{on } L \tag{6}$$

$$\kappa\phi(\sigma)-\frac{\omega(\sigma)}{\overline{\omega'(\sigma)}}\overline{\phi'(\sigma)}-\overline{\psi(\sigma)}=2G(u+iv)-2G\alpha'\int\psi(\zeta)\omega'(\zeta)d\zeta\qquad\text{on } M \tag{7}$$

where σ is ζ on the unit circle; p_x and p_y are external forces in the x and y-directions, respectively; ds is an increment of the integration contour along the boundary; u and v are the x and y-components of the displacement, respectively; G is the shear modulus. Using Poisson's ratio ν and the coefficient of thermal expansion α_0, κ, and α' are expressed as follows:

$$\begin{aligned}&\kappa=3-4\nu,\quad \alpha'=(1+\nu)\alpha_0\qquad\text{for plane strain}\\&\kappa=(3-\nu)/(1+\nu),\quad \alpha'=\alpha_0\qquad\text{for generalized plane stress.}\end{aligned} \tag{8}$$

The second term in the right-hand side of (7) gives the displacement due to uniform heat flux. The mixed boundary value problem where p_x, p_y, u and v are given (Hasebe, 1979; Hasebe et al., 1988b) and the problem for thermal stress can be analyzed separately. Hence, without losing generality, $p_x=p_y=0$ and $u=v=0$ may be given in (6) and (7). Since a traction-free boundary exists, $\psi(\zeta)$ is given by analytic continuation as follows:

$$\psi(\zeta)=-\overline{\phi(1/\bar{\zeta})}-\frac{\overline{\omega(1/\bar{\zeta})}}{\omega'(\zeta)}\phi'(\zeta). \tag{9}$$

Substituting (2) and (4) into the second term of the right-hand side in (7), and integrating it, the term $\log\zeta$ will be obtained as a part of the result. This $\log\zeta$ is the dislocation of displacement. To remove this dislocation, the following functions are considered (Florence and Goodier, 1960):

$$\phi_1(\zeta)=A\log\zeta,\qquad \phi_1(\zeta)=B\log\zeta \tag{10}$$

where $B=\overline{A}$, because the dislocation of the resultant must be removed when (10) is substituted into (6). The value A required to remove the dislocation of displacement is (Hasebe et al., 1986, 1988a),

$$A=\frac{\alpha_0 qGR}{2k}E_0\left(\sum_{k=1}^{N}E_k e^{-i\delta}+\overline{E_0}e^{i\delta}-E_{25}e^{-i\delta}\right) \tag{11}$$

where

$$\begin{aligned}&R=(1+\nu)/(1-\nu)\qquad\text{for plane strain}\\&R=1+\nu\qquad\text{for generalized plane stress.}\end{aligned} \tag{12}$$

The stress functions to be obtained are expressed as

$$\phi(\zeta)=\phi_1(\zeta)+\phi_2(\zeta),\quad \psi(\zeta)=\psi_1(\zeta)+\psi_2(\zeta). \tag{13}$$

From (6), (9), (10), and (13), the boundary condition on L is

$$\phi_2^+(\sigma)-\phi_2^-(\sigma)=0 \tag{14}$$

because $p_x=p_y=0$; in (14), the superscripts + and − indicate the values of $\phi_2(\zeta)$ on the unit circle approached from the region S^+ and S^-, respectively (see Fig. 1). From (7), (9), (10), and (13),

$$\begin{aligned}\kappa\phi_2^+(\sigma)+\phi_2^-(\sigma)&=-(1+\kappa)A\log\sigma-2G\alpha'\int\psi(\sigma)\omega'(\sigma)d\sigma\\&=-\frac{\alpha_0 qGR}{2k}(1+\kappa)\left[\frac{E_0^2}{2}e^{-i\delta}\sigma^2+\frac{E_0\overline{E_{25}}}{2}e^{i\delta}\frac{1}{\sigma^2}\right.\\&\quad+\sum_{k=1}^{N}\left(E_0e^{-i\delta}\zeta_k+\frac{\overline{E_0}}{\zeta_k}e^{i\delta}\right)\frac{E_k}{\zeta_k-\sigma}\\&\quad\left.-\sum_{k=1}^{N}\left(E_0e^{-i\delta}-\frac{\overline{E_0}}{\zeta_k^2}e^{i\delta}\right)E_k\{\log\sigma-\log(\zeta_k-\sigma)\}\right]+\text{const.}\end{aligned} \tag{15}$$

Therefore, a Riemann-Hilbert problem for (14) on L and (15) on M is obtained and its solution is (Muskhelishvili, 1963)

$$\phi_2(\zeta)=\frac{\chi(\zeta)}{2\pi i}\int_M\frac{H(\sigma)}{\chi(\sigma)(\sigma-\zeta)}d\sigma+Q(\zeta)\chi(\zeta), \tag{16}$$

in which $H(\sigma)$ represents the right-hand side of both (14) on L and (15) on M. However, since the right-hand side in (14) is zero, the integral in (16) is carried out on M. The function

$Q(\zeta)$ is an unknown rational function and the Plemelj function $\chi(\zeta)$ is expressed by

$$\chi(\zeta)=(\zeta-\alpha)^m(\zeta-\beta)^{1-m} \tag{17}$$

where α and β are the coordinates corresponding to the junctures of L and M (see Fig. 1); $m=0.5-i(\log\kappa)/(2\pi)$ where the index 0.5 was determined from the condition of continuity for displacements and discontinuity for stresses at the junctures of L and M. The branch of $\chi(\zeta)$ is chosen so that $\chi(\zeta)/\zeta\to 1$ for $\zeta\to\infty$. The integral in (16) is described in Appendix A.

The function $Q(\zeta)$ is determined from the regular condition in S^+ for $\psi(\zeta)$ in (9). Substituting (10), (13), and (16) into (9), the irregular terms in S^+ can be written out as

$$\psi(\zeta)=-\frac{\overline{\omega}(1/\zeta)}{\omega'(\zeta)}\frac{A}{\zeta}-\frac{\overline{\omega}(1/\zeta)}{\omega'(\zeta)}\phi_2'(\zeta)$$

$$-\overline{\chi}(1/\zeta)\overline{Q}(1/\zeta)+\text{regular term}=-\sum_{k=1}^{N}\frac{A\overline{B}_k\zeta}{\zeta\overline{\zeta}_k-1}-\sum_{k=1}^{N}\frac{A_k\overline{B}_k\zeta}{\zeta\overline{\zeta}_k-1}$$

$$-\overline{\chi}(1/\zeta)\overline{Q}(1/\zeta)+\text{regular term} \tag{18}$$

where $B_k=E_k/\overline{\omega'(\zeta_k')}$; $\zeta_k'=1/\overline{\zeta}_k$; $A_k=\phi_2'(\zeta_k')$ (Hasebe, 1984; Hasebe et al., 1988b). The function $Q(\zeta)$ is determined so as to cancel out the first and second terms of the right-hand side in (18), i.e.,

$$Q(\zeta)=-\sum_{k=1}^{N}\frac{(\overline{A}\zeta_k+\overline{A}_k)B_k}{\chi(\zeta_k)(\zeta_k-\zeta)}. \tag{19}$$

Finally, $\phi(\zeta)$ is obtained by using the results in Appendix A with (19) to give

$$\phi(\zeta)=A\log\zeta-\chi(\zeta)\sum_{k=1}^{N}\frac{(\overline{A}_k+\overline{A}\zeta_k)B_k}{\chi(\zeta_k)(\zeta_k-\zeta)}$$

$$+\frac{\alpha_0 qGR}{2k}\left[\frac{E_0^2}{2}e^{-i\delta}\{\zeta^2-\chi(\zeta)(\zeta+m\alpha+(1-m)\beta)\}\right.$$

$$-\sum_{k=1}^{N}\left(E_0e^{-i\delta}\zeta_k+\frac{\overline{E_0}}{\zeta_k}e^{i\delta}\right)\frac{E_k}{\zeta_k-\zeta}\left(\frac{\chi(\zeta)}{\chi(\zeta_k)}-1\right)$$

$$+\frac{E_0\overline{E_{25}}}{2}e^{i\delta}\frac{1}{\zeta^2}\left\{1+\chi(\zeta)\frac{\chi'(0)\zeta-\chi(0)}{\chi(0)^2}\right\}$$

$$-\sum_{k=1}^{N}\left(E_0e^{-i\delta}-\frac{\overline{E_0}}{\zeta_k^2}e^{i\delta}\right)E_k\left\{\log\zeta-\log(\zeta-\zeta_k)\right.$$

$$\left.\left.+\chi(\zeta)\int_0^{\zeta_k}\frac{d\sigma}{\chi(\sigma)(\sigma-\zeta)}\right\}\right]. \tag{20}$$

Since the first derivative of the integral term in (20) is given by (35) in Appendix B, the first derivative of $\phi(\zeta)$ is expressed in a form that does not contain an integral term. Using $A_k=\phi_2'(\zeta_k')$ $(k=1, 2, \ldots N)$, and solving $2N$ simultaneous equations with respect to the real and imaginary parts of A_k, the unknown constants A_k are determined. Since the first and second derivatives of $\phi(\zeta)$ are obtained, the stress components are obtained without numerical integration. However, in order to obtain the displacement, the numerical integration for the integral term in (20) is required. From (20), a solution of the boundary value problem subjected to external forces only is given by $\alpha\to\beta$ (Hasebe et al., 1986, 1988a). A solution of the displacement boundary value problem is given by $\alpha\to\beta$, $\chi(\zeta_k)\to-\kappa\chi(\zeta_k)$, $\chi(0)\to-\kappa\chi(0)$ and $\chi'(0)\to-\kappa\chi'(0)$ (Hasebe et al., 1989). A solution for the elliptical rigid inclusion with a debond can be obtained by substituting $E_k=0$, $\zeta_k=0$ $(k=1, 2, \ldots N)$, $E_0=(a+b)/2$ and $E_{25}=(a-b)/2$ into (2) and (20), where a and b are the semi-axes of the ellipse.

Stress Distribution

Since it is assumed that the heat flux does not pass through the boundary, the distributions of the temperature and the heat flux are the same as those in Hasebe et al. (1988a), in which examples of the temperature and heat flux were shown for the crack length $c/a=1$. In the present paper, the stress distribution is also shown for $c/a=1$ and $\kappa=2$.

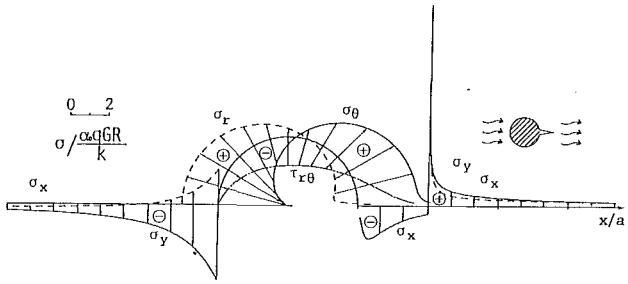

Fig. 2 Stress distribution: $\kappa=2$, $c/a=1.0$, $\delta=0$ deg

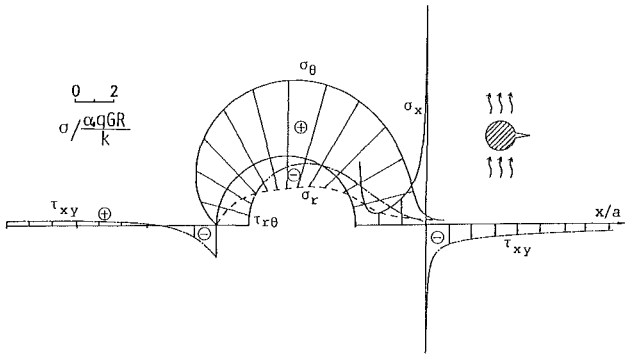

Fig. 3 Stress distribution: $\kappa=2$, $c/a=1.0$, $\delta=90$ deg

Figure 2 shows normal stress σ_r, tangential stress σ_θ, and shearing stress $\tau_{r\theta}$ on the boundary, as well as σ_x and σ_y on the x-axis for $\delta=0$ deg. The normal stress σ_r attains a maximum at point D for $\sigma_r>0$, and so a debonding initiates at this point if it occurs. On the other hand, a crack possibly initiates and grows in the x-axis for $x>0$ due to $\sigma_y>0$. Figure 3 shows the stress distribution for $\delta=90$ deg and $\sigma_x=\sigma_y=0$ in the x-axis due to antisymmetry. The stress distribution for the heat flux in an arbitrary direction can be obtained by superposition of the stresses for $\delta=0$ deg and 90 deg.

Stress Intensity Factor

The stress intensity factors (S.I.F.) K_I and K_{II} are obtained by using the complex stress function $\phi(\zeta)$ and the mapping function $\omega(\zeta)$ as follows:

$$K_I-iK_{II}=\frac{2\sqrt{\pi}\,e^{-\frac{i}{2}\lambda}\phi'(\zeta_0)}{\sqrt{\omega''(\zeta_0)}} \tag{21}$$

where λ is the angle between a crack and the x-axis; ζ_0 is the coordinate at the crack tip. In the present case, $\lambda=0$ and $\zeta_0=1$. The following nondimensional S.I.F. are used:

$$F_I+iF_{II}=\frac{k}{\alpha_0 qGR}\frac{K_I+iK_{II}}{\sqrt{\pi(C'/2)^3}} \tag{22}$$

where $C'=(2a+c)/2$.

Figure 4 and Table 1 contain the values of F_I for $\delta=0$ deg and $F_{II}=0$ due to symmetry. The values of c/a and a/c are plotted as the abscissa, and thus, S.I.F. are shown for the crack length a, where $0\le a\le\infty$. When $\delta=0$ deg, $F_I>0$ and so the crack possibly grows. From Fig. 4, the influence of κ on the nondimensional S.I.F. is known. Since S.I.F. takes the

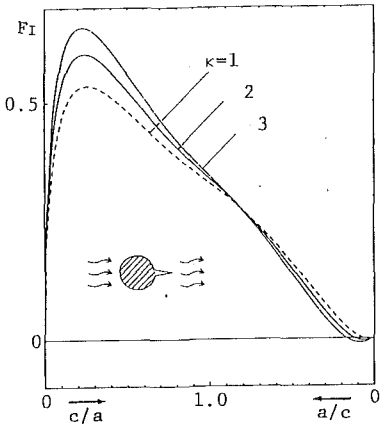

Fig. 4 Nondimensional stress intensity factor F_I: $\delta = 0$ deg

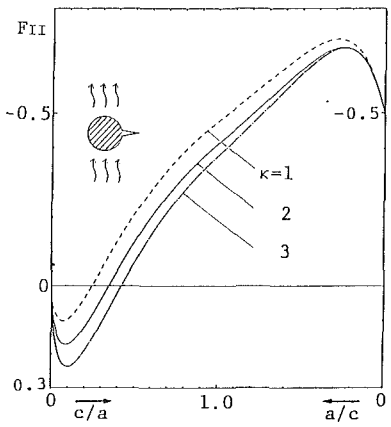

Fig. 5 Nondimensional stress intensity factor F_{II}: $\delta = 90$ deg

Table 1 Nondimensional stress intensity factors F_I for $\delta = 0$ deg and F_{II} for $\delta = 90$ deg for $\kappa = 1.0$, 2.0, and 3.0

		F_I ($\delta = 0°$)			F_{II} ($\delta = 90°$)		
		$\kappa = 1.0$	$\kappa = 2.0$	$\kappa = 3.0$	$\kappa = 1.0$	$\kappa = 2.0$	$\kappa = 3.0$
	0.01	0.1796	0.2091	0.2333	0.0580	0.0877	0.1145
	0.02	0.2493	0.2896	0.3227	0.0767	0.1178	0.1549
	0.04	0.3364	0.3895	0.4332	0.0954	0.1507	0.2003
	0.05	0.3663	0.4235	0.4705	0.0991	0.1586	0.2119
	0.10	0.4630	0.5313	0.5875	0.0958	0.1710	0.2374
	0.20	0.5293	0.5991	0.6564	0.0334	0.1185	0.1903
c/a	0.30	0.5326	0.5951	0.6461	-0.0491	0.0374	0.1070
	0.40	0.5120	0.5650	0.6078	-0.1319	-0.0474	0.0169
	0.50	0.4821	0.5256	0.5603	-0.2086	-0.1273	-0.0688
	0.60	0.4494	0.4842	0.5115	-0.2776	-0.1997	-0.1470
	0.70	0.4168	0.4439	0.4646	-0.3383	-0.2640	-0.2166
	0.80	0.3856	0.4060	0.4211	-0.3911	-0.3203	-0.2777
	0.90	0.3565	0.3711	0.3814	-0.4368	-0.3695	-0.3311
	1.00	0.3295	0.3393	0.3454	-0.4763	-0.4121	-0.3776
	0.90	0.3022	0.3074	0.3097	-0.5137	-0.4529	-0.4222
	0.80	0.2718	0.2723	0.2707	-0.5527	-0.4957	-0.4691
	0.70	0.2380	0.2339	0.2284	-0.5924	-0.5399	-0.5176
	0.60	0.2008	0.1923	0.1833	-0.6314	-0.5842	-0.5664
	0.50	0.1604	0.1482	0.1361	-0.6675	-0.6263	-0.6132
	0.40	0.1176	0.1027	0.0886	-0.6964	-0.6622	-0.6538
a/c	0.30	0.0743	0.0586	0.0441	-0.7112	-0.6850	-0.6810
	0.20	0.0342	0.0207	0.0083	-0.6999	-0.6828	-0.6822
	0.10	0.0053	-0.0023	-0.0091	-0.6419	-0.6342	-0.6354
	0.05	-0.0010	-0.0044	-0.0074	-0.5847	-0.5814	-0.5824
	0.04	-0.0013	-0.0039	-0.0061	-0.5703	-0.5677	-0.5686
	0.02	-0.0011	-0.0021	-0.0029	-0.5378	-0.5366	-0.5371
	0.01	-0.0005	-0.0009	-0.0012	-0.5196	-0.5190	-0.5193
	0.00	0.0000	0.0000	0.0000	-0.5000	-0.5000	-0.5000

extreme value, the crack growth is arrested in a certain length. If the fracture toughness value of a material is larger than the maximum value, then the crack does not grow. Negative values of F_I change to positive values when the direction of heat flux becomes reversed, i.e., $\delta = 180$ deg. Figure 5 and Table 1 contain the values of F_{II} for $\delta = 90$ deg and $F_I = 0$ due to symmetry. When $a/c = 0$, the value of F_{II} converges to -0.5 and this value corresponds to the value of F_{II} for a crack only (Sih, 1962). S.I.F. for the heat flux in an arbitrary direction can be obtained by superposition of F_I and F_{II} for $\delta = 0$ deg and 90 deg.

Conclusions

The complex stress functions $\phi(\zeta)$ and $\psi(\zeta)$ for the mixed boundary value problem are given by (20) and (9), respectively. Since the first derivative of the integral term in (20) is given by (35), $\phi'(\zeta)$ is given by the form without integral term. Therefore, the numerical integration is not required for the calculation of stress components. Substituting $E_k = \zeta_k = 0$ $(k = 1, 2, \ldots, N)$, $E_0 = (a+b)/2$ and $E_{25} = (a-b)/2$ into (20), the solution is obtained for an elliptical hole with the semi-axes a and b. The solution of free or clamped boundary value problems can also be obtained by a limiting operation for (20). Shifting the coordinates of the junctures α and β in (20), the position of clamped ends can be changed freely. Thus, both a crack and a debonding initiated from a circular rigid inclusion can be analyzed. Changing the coefficients of the mapping function in (2), other shapes can be also analyzed. For example, the case of a crack initiated from a rectangular hole is analyzed by using the mapping function in Hasebe and Ueda (1980). A mapping function of a comparatively arbitrary shape can be found in the form of (2). The stress distributions and the stress intensity factors for the heat flux in an arbitrary direction are obtained by superposition of the results for $\delta = 0$ deg and 90 deg. In this paper, the stress intensity factor K_I is produced by the heat flux for $\delta = 0$ deg. Since K_I has the maximum value and $K_I \to 0$ as $c \to \infty$, a crack is arrested at a certain length. If the fracture toughness value of a material is larger than the maximum value of K_I, then a crack does not grow. However, if the fracture toughness value depends on temperature, then the information of temperature distribution is necessary for the crack growth. From the stress state before the crack initiation, a debonding occurs on the side that the heat flux meets $(x/a = -1)$ and a crack initiates on the opposite side $(x/a = 1)$.

References

Bowie, O. L., 1956, "Analysis of an Infinite Plate Containing Radial Cracks Originating at the Boundary of an Internal Circular Hole," *Journal of Mathematics Physics*, Vol. 35, pp. 60–71.

Florence, A. L., and Goodier, J. N., 1960, "Thermal Stresses due to Disturbance of Uniform Heat FLow by an Insulated Ovaloid Hole," ASME JOURNAL OF APPLIED MECHANICS, Vol. 27, pp. 635–639.

Hasebe, N., 1979, "Uniform Tension of a Semi-Infinite Plate with a Crack at an End of a Stiffened Edge," *Ingenieur-Archiv*, Vol. 48, pp. 129–141.

Hasebe, N., and Ueda, M., 1980, "Crack Originating from a Corner of a Square Hole," *Engineering Fracture Mechanics*, Vol. 13, pp. 913–923.

Hasebe, N., 1984, "Mixed Boundary Value Problem of Plate with Crack," *Journal of Engineering Mechanics*, Vol. 110, pp. 37–48.

Hasebe, N., Tamai, K., and Nakamura,T., 1986, "Analysis of a Kinked Crack under Uniform Heat Flow," *Journal of Engineering Mechanics*, Vol. 112, pp. 31–42.

Hasebe, N., Okumura, M., and Nakamura, T., 1987, "Stress Analysis of a Debonding and a Crack around a Circular Rigid Inclusion," *International Journal of Fracture*, Vol. 32, pp. 169–183.

Hasebe, N., Tomida, A., and Nakamura, T., 1988a, "Thermal Stresses of a Cracked Circular Hole due to Uniform Heat Flux," *Journal of Thermal Stresses*, Vol. 11, pp. 381–391.

Hasebe, N., Tsutsui, S., and Nakamura, T., 1988b, "Debondings at a Semielliptic Rigid Inclusion on the Rim of a Half Plane," ASME JOURNAL OF APPLIED MECHANICS, Vol. 55, pp. 574–579.

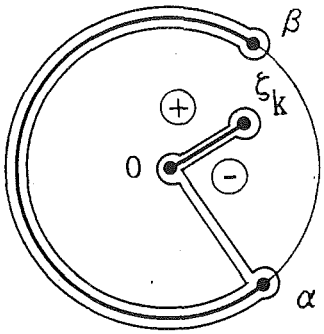

Fig. 6 Contour integral around the branch lines $\alpha\beta$ and $0\zeta_k$

Hasebe, N., Tomida, A., and Nakamura, T., 1989, "Solution of Displacement Boundary Value Problem under Uniform Heat Flux," *Journal of Thermal Stresses*, Vol. 12, pp. 71–81.

Muskhelishvili, N. I., 1963, *Some Basic Problems of Mathematical Theory of Elasticity*, 4th ed., Noordhoff, The Netherlands.

Sih, G. C., 1962, "On the Singular Character of Thermal Stresses Near a Crack Tip," ASME JOURNAL OF APPLIED MECHANICS, Vol. 29, pp. 587–589.

APPENDIX A

Integral of Equation (16)

Substituting the right-hand side of (15) into $H(\sigma)$ in (16), changing the integral on M into the contour integral around M, and using the residue theorem, the integral of each term is obtained as (Muskhelishvili, 1963)

$$\frac{1}{2\pi i}\int_\alpha^\beta \frac{d\sigma}{\chi^+(\sigma)(\sigma-\zeta)(\zeta_k-\sigma)} = \frac{\kappa}{(1+\kappa)(\zeta_k-\zeta)}\left(\frac{1}{\chi(\zeta)}-\frac{1}{\chi(\zeta_k)}\right) \quad (23)$$

$$\frac{1}{2\pi i}\int_\alpha^\beta \frac{\sigma^2 d\sigma}{\chi(\sigma)(\sigma-\zeta)} = \frac{\kappa}{1+\kappa}\left[\frac{\zeta^2}{\chi(\zeta)} - \{\zeta + m\alpha + (1-m)\beta\}\right] \quad (24)$$

$$\frac{1}{2\pi i}\int_\alpha^\beta \frac{d\sigma}{\chi(\sigma)(\sigma-\zeta)\sigma^2} = \frac{\kappa}{1+\kappa}\left\{\frac{1}{\zeta^2\chi(\zeta)} + \frac{\chi'(0)\zeta+\chi(0)}{\zeta^2\chi^2(0)}\right\} \quad (25)$$

where the following relation on M is used:

$$\chi^-(\sigma) = -\kappa\chi^+(\sigma). \quad (26)$$

The integral containing the logarithmic function is carried out in the following manner. As shown in Fig. 6, considering the contour integral around the branch lines $\alpha\beta$ and $0\zeta_k$,

$$\int_\alpha^\beta \frac{\log\sigma - \log(\sigma-\zeta_k)}{\chi^+(\sigma)(\sigma-\zeta)}\,d\sigma + \int_\beta^\alpha \frac{\log\sigma-\log(\sigma-\zeta_k)}{\chi^-(\sigma)(\sigma-\zeta)}\,d\sigma + \int_0^{\zeta_k} \frac{[\log\sigma-\log(\sigma-\zeta_k)]^+}{\chi(\sigma)(\sigma-\zeta)}\,d\sigma + \int_{\zeta_k}^0 \frac{[\log\sigma-\log(\sigma-\zeta_k)]^-}{\chi(\sigma)(\sigma-\zeta)}\,d\sigma = \oint \frac{\log\sigma-\log(\sigma-\zeta_k)}{\chi(\sigma)(\sigma-\zeta)}\,d\sigma, \quad (27)$$

where the integral between the contour 0α and $\alpha 0$ is omitted because they cancel each other. The superscript + refers to the integral for $0\zeta_k$ and − does for $\zeta_k 0$. In this case,

$$[\log\sigma - \log(\sigma-\zeta_k)]^+ + 2\pi i = [\log\sigma - \log(\sigma-\zeta_k)]^-. \quad (28)$$

Arranging (27) by (26) and (28), the following expression is obtained:

$$\frac{1+\kappa}{\kappa}\int_\alpha^\beta \frac{\log\sigma-\log(\sigma-\zeta_k)}{\chi^+(\sigma)(\sigma-\zeta)}\,d\sigma - 2\pi i\int_0^{\zeta_k}\frac{d\sigma}{\chi(\sigma)(\sigma-\zeta)} = \frac{2\pi i}{\chi(\zeta)}[\log\zeta - \log(\zeta-\zeta_k)]. \quad (29)$$

The integral of the right-hand side in (16) becomes the right-hand side in (20) except the first and second terms by using (23), (24), (25), and (29).

APPENDIX B

First Derivative of Integral Term in Equation (20)

The following differentiation is considered:

$$\frac{d}{d\sigma}\left[\frac{1}{y(\sigma)(\sigma-\zeta)}\right] = \frac{1}{\sigma-\zeta}\left[\frac{1}{y(\sigma)}\right]' - \frac{1}{y(\sigma)(\sigma-\zeta)^2} = -\frac{(\zeta-\alpha)(\zeta-\beta)}{\chi(\sigma)(\sigma-\zeta)^2} + \frac{\alpha-m(\alpha-\beta)-\zeta}{\chi(\sigma)(\sigma-\zeta)} \quad (30)$$

where $(\zeta-\alpha)(\zeta-\beta)/\chi(\zeta) \equiv 1/y(\zeta)$. If (30) is integrated with respect to σ from a and b and arranged by using the following expression,

$$\int_a^b \frac{d\sigma}{\chi(\sigma)(\sigma-\zeta)} \equiv f(\zeta), \quad (31)$$

then

$$f'(\zeta) + H(\zeta)f(\zeta) + G(\zeta) = 0 \quad (32)$$

where

$$H(\zeta) = \frac{m}{\zeta-\alpha} + \frac{1-m}{\zeta-\beta}$$
$$G(\zeta) = \left[\frac{1}{y(b)(b-\zeta)} - \frac{1}{y(a)(a-\zeta)}\right]\frac{1}{(\zeta-\alpha)(\zeta-\beta)}. \quad (33)$$

The solution of the differential equation (32) is

$$\exp\{\int H(\zeta)d\zeta\}f(\zeta) + \int G(\zeta)\exp\{\int H(\zeta)d\zeta\}d\zeta = C_1 \quad (34)$$

where C_1 is an integration constant. Noting that $\exp[\int H(\zeta)d\zeta] = C_2\chi(\zeta)$ (C_2 is an integration constant) and differentiating both sides in (34) with respect to ζ, the following equation is obtained:

$$\frac{d}{d\zeta}[\chi(\zeta)f(\zeta)] = -\chi(\zeta)G(\zeta). \quad (35)$$

Through (31), (33), and (35), the first derivative of the integral term in (20) is obtained for $a=0$ and $b=\zeta_k$.

R. L. Yuan
Professor,
Department of Civil Engineering
and Engineering Mechanics,
The University of Texas at Arlington,
Arlington, TX 76019

L. S. Wang
Associate Professor,
Department of Mechanics,
Hohai University,
Nanjing, China

Generalized Variational Principle of Plates on Elastic Foundation

The theory of variational principle is enhanced by using the Lagrange multiplier to establish a generalized variational principle for plates on an elastic foundation. In the first part of this paper, the principle of minimum potential energy is introduced in which the integral equation is employed as the variational constrained condition. In the second part, it is shown that the generalized variational principle with two variational functions can be established. This represents, to the authors' knowledge, the first treatment of the variational principle with these types of equations.

1 Introduction

The behavior of beams and slabs on elastic foundations have been of great interest to structural and geotechnical engineers for many years due to their extensive application in the analysis and design of foundations. The majority of analytical work in this area has been done by using the classical Winkler model, such as Hetenyi (1946) and Westergaard (1948), where the coefficient k, called subgrade reaction of the foundation, is employed. Vlasov and Leont'ev (1966) developed a unique two-parameter model using a variational approach; the mode required an estimation of the parameter γ, which controls the decay of stress distribution within the foundation. Jones (1977) established a relationship between γ and the displacement characteristics. Vallabhan and Das (1988) made further study on the determination of γ for various loading conditions.

In this paper, plates on elastic foundations are investigated by using the Lagrange multiplier to establish a generalized variational principle with two variational functions: deflection w and foundation reaction p. The functional stationary values, expressed in terms of a group of differential-integral equations, are equivalent to the basic equations and boundary conditions. The variational principle approach with these types of equations has not been shown in the publications by Washizu (1975), Shames and Dym (1985), or Landau and Lifshitz (1986).

In the first part of this paper, the principle of minimum potential energy for plates on elastic foundations is introduced, and the integral equation is employed as the variational constrained condition; in the second part, it is shown how the generalized variational principle with two variational functions can be established.

2 Basic Equations and Boundary Conditions

As we all know, the basic equations of Kirchhoff's thin plates on elastic foundations are expressed as follows:

$$D\nabla^2\nabla^2 w(x,y) - q(x,y) + p(x,y) = 0 \tag{1}$$

$$w(x,y) = \int_s\int p(\xi,\eta)k(x,y;\xi,\eta)d\xi d\eta \tag{2}$$

where p is the foundation reaction, k is the displacement function at point (x, y) when a concentrated load is applied at point (ξ, η), and S is the surface area of the plate under investigation. The plate boundary is $C = C_1 + C_2 + C_3$, where C_1 represents built-in edge, C_2 represents simply-supported edge, and C_3 represents free edge.

The corresponding boundary conditions are:

at built-in edge C_1: $$w = \overline{w},\ \frac{\partial w}{\partial n} = \frac{\partial \overline{w}}{\partial n}, \tag{3}$$

at simply-supported edge C_2: $$w = \overline{w},\ M_n = \overline{M}_n, \tag{4}$$

at free edge C_3: $$M_n = \overline{M}_n,\ V_n = \overline{V}_n = \overline{Q}_n + \frac{\partial \overline{M}_{ns}}{\partial s}, \tag{5}$$

and at the corner: $$R_n = \overline{R}_n \tag{6}$$

where $\overline{w}$ is the plate deflection along the boundary, $\overline{Q}_n$ is the shearing force on the normal surface on the boundary, $\overline{M}_n$ and $\overline{M}_{ns}$ are the bending and twisting moments, $\overline{V}_n$ is the summation of shearing forces $\overline{Q}_n$ and $\frac{\partial \overline{M}_{ns}}{\partial s}$, and $\overline{R}_n$ is the concentrated force at the corner point on the boundary.

3 Undetermined Variational Functions

The minimum potential energy of a plate on an elastic foundation with two undetermined variables w and p can be expressed as

$$\Pi_w = \frac{1}{2}\int_s\int D\left\{(\nabla^2 w)^2 - 2(1-\mu)\left[\frac{\partial^2 w}{\partial x^2}\cdot\frac{\partial^2 w}{\partial y^2} - \left(\frac{\partial^2 w}{\partial x \partial y}\right)^2\right]\right\} dx\, dy$$

Contributed by the Applied Mechanics Division of THE AMERICAN SOCIETY OF MECHANICAL ENGINEERS for publication in the JOURNAL OF APPLIED MECHANICS.

Discussion on this paper should be addressed to the Technical Editor, Prof. Leon M. Keer, The Technological Institute, Northwestern University, Evanston, IL 60208, and will be accepted until two months after final publication of the paper itself in the JOURNAL OF APPLIED MECHANICS. Manuscript received by the ASME Applied Mechanics Division, Apr. 11, 1990; final revision, Aug. 13, 1990.

$$-\int_s\int qw\,dx\,dy+\frac{1}{2}\int_s\int pw\,dx\,dy+\oint_{c_2+c_3}\overline{M}_n\frac{\partial w}{\partial n}\,ds$$
$$-\oint_{c_3}\overline{V}_n\,w\,ds-\sum_{k=1}^{i}\overline{R}_{n,k}\cdot w_k. \quad (7)$$

In Eq. (7), w and p must satisfy the variational constrained condition, i.e., Eq. (2). By applying variation to the fundamental Π_w in Eq. (7), the functional variation may be represented in the following form:

$$\delta\Pi_w=\int_s\int(D\nabla^2\nabla^2w-q)\delta w\,dx\,dy$$
$$+\frac{1}{2}\int_s\int(p\delta w+w\delta p)dx\,dy+\mu D\oint_c\nabla^2w\frac{\partial}{\partial n}\delta w\,ds$$
$$-D\oint_c\frac{\partial}{\partial n}\nabla^2w\,\delta w\,ds+(1-\mu)D\oint_c\left\{\left[\cos^2\alpha\frac{\partial^2w}{\partial x^2}\right.\right.$$
$$\left.+2\cos\alpha\sin\alpha\frac{\partial^2w}{\partial x\partial y}+\sin^2\alpha\frac{\partial^2w}{\partial y^2}\right]\frac{\partial}{\partial n}\delta w$$
$$+\left[-\cos\alpha\sin\alpha\left(\frac{\partial^2w}{\partial x^2}-\frac{\partial^2w}{\partial y^2}\right)\right.$$
$$\left.\left.+(\cos^2\alpha-\sin^2\alpha)\frac{\partial^2w}{\partial x\partial y}\right]\frac{\partial}{\partial s}\delta w\right\}ds$$
$$+\oint_{c_2+c_3}\overline{M}_n\frac{\partial}{\partial n}\delta w\,ds-\oint_{c_3}\overline{V}_n\,\delta w\,ds-\sum_{k=1}^{i}\overline{R}_{n,k}\delta w_k$$

rearranging and collecting terms,

$$\delta\Pi_w=\int_S\int(D\nabla^2\nabla^2w-q)\delta w\,dx\,dy$$
$$+\frac{1}{2}\int_s\int(p\delta w+w\delta p)dx\,dy$$
$$+\oint_{c_2+c_3}\left\{\overline{M}_n+D\left[\mu\nabla^2w+(1-\mu)\frac{\partial^2w}{\partial n^2}\right]\right\}\delta\left(\frac{\partial w}{\partial n}\right)ds$$
$$-\oint_{c_3}\left\{\overline{V}_n+D\left[\frac{\partial}{\partial n}\nabla^2w+(1-\mu)\frac{\partial}{\partial s}\left(\frac{\partial^2w}{\partial s\partial n}-\frac{1}{\rho_s}\frac{\partial w}{\partial s}\right)\right]\right\}\delta w\,ds$$
$$-(1-\mu)D\int_c\frac{\partial}{\partial s}\left[\left(\frac{\partial^2w}{\partial s\partial n}-\frac{1}{\rho_s}\frac{\partial w}{\partial s}\right)\delta w\right]ds-\sum_{k=1}^{i}\overline{R}_{n,k}\delta w_k$$
$$=\int_s\int(D\nabla^2\nabla^2w-q)\delta w\,dx\,dy+\frac{1}{2}\int_s\int(p\delta w+w\delta p)dx\,dy$$
$$+\oint_{c_2+c_3}\left\{\overline{M}_n+D\left[\mu\nabla^2w+(1-\mu)\frac{\partial^2w}{\partial n^2}\right]\right\}\delta\left(\frac{\partial w}{\partial n}\right)ds$$
$$-\oint_{c_3}\left\{\overline{V}_n+D\left[\frac{\partial}{\partial n}\nabla^2w\right.\right.$$
$$\left.\left.+(1-\mu)\frac{\partial}{\partial s}\left(\frac{\partial^2w}{\partial s\partial n}-\frac{1}{\rho_s}\frac{\partial w}{\partial s}\right)\right]\right\}\delta w\,ds$$
$$-\sum_{k=1}^{i}\left\{(1-\mu)D\Delta\left(\frac{\partial^2w}{\partial s\partial n}-\frac{1}{\rho_s}\frac{\partial w}{\partial s}\right)_k+\overline{R}_{n,k}\right\}\delta w_k \quad (8)$$

where $\frac{1}{\rho_s}=\frac{\partial\alpha}{\partial s}$, α is the angle between the normal to the periphery and the x-axis as shown in Fig. 1,
and

$$\sum_{k=1}^{i}\Delta\left(\frac{\partial^2w}{\partial s\partial n}-\frac{1}{\rho_s}\frac{\partial w}{\partial s}\right)_k\delta w_k=\oint\frac{\partial}{\partial s}\left[\left(\frac{\partial^2w}{\partial s\partial n}-\frac{1}{\rho_s}\frac{\partial w}{\partial s}\right)\delta w\right]ds$$

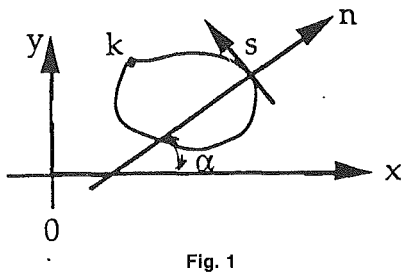

Fig. 1

where $\Delta\left(\frac{\partial^2w}{\partial s\partial n}-\frac{1}{\rho_s}\frac{\partial w}{\partial s}\right)_k$ represents the increment of $\left(\frac{\partial^2w}{\partial s\partial n}-\frac{1}{\rho_s}\frac{\partial w}{\partial s}\right)$ at the corner point k on the boundary C. It is assumed here that there are i number of discontinuous corner points, and δw_k is the value of δw at corner point k. From the expressions $\overline{V}_n$, $\overline{R}_n$, we can see that $-(1-\mu)D\left(\frac{\partial^2w}{\partial s\partial n}-\frac{1}{\rho_s}\frac{\partial w}{\partial s}\right)=M_{ns}$, and that ΔM_{ns} is the increment of twisting moment which is also equal to the concentrated force at the corner point of the plate.

In order to simplify Eq. (8), we use the following relation:

$$\frac{1}{2}\int_s\int w\,\delta p\,dx\,dy=\frac{1}{2}\int_s\int p\,\delta w\,dx\,dy. \quad (9)$$

Equation (9) can be proven in the following.

Substituting w from Eq. (2) in Eq. (9) where w must satisfy the variational constraint condition, the left-hand side of Eq. (9) becomes

$$\frac{1}{2}\int_s\int\left[\int_s\int p(\xi,\eta)k(x,y;\xi,\eta)d\xi d\eta\right]\delta p\ (x,y)dx\,dy.$$

Since the definite integration and the variables are not related, the above term can be expressed as

$$\frac{1}{2}\int_s\int\left[\int_s\int p(x,y)k(\xi,\eta;x,y))dx\,dy\right]\delta p(\xi,\eta)d\xi\,d\eta.$$

Since $k(x,y;\xi,\eta)=k(\xi,\eta;x,y)$, the above term can be further expressed as

$$\frac{1}{2}\int_s\int\left[\int_s\int p(x,y)k(x,y;\xi,\eta)dx\,dy\right]\delta p(\xi,\eta)d\xi\,d\eta.$$

Exchanging the order of integration, the left-hand side of Eq. (9) finally becomes

$$\frac{1}{2}\int_s\int\left[\int_s\int\delta p(\xi,\eta)k(x,y;\xi,\eta)d\xi\,d\eta\right]p(x,y)dx\,dy. \quad (10)$$

Now, substitute the variation of Eq. (2) with

$$\delta w(x,y)=\int_s\int\delta p(\xi,\eta)k(x,y;\xi,\eta)d\xi\,d\eta$$

on the right-hand side of Eq. (9), which is equal to Eq. (11). Thus, Eq. (9) is proved.

Now, substituting Eq. (9) in Eq. (8), we get

$$\delta\Pi_w=\int_s\int(D\nabla^2\nabla^2w-q+p)\delta w\,dx\,dy$$
$$+\int_{c_2+c_3}\left\{\overline{M}_n+D\left[\mu\nabla^2w+(1-\mu)\frac{\partial^2w}{\partial n^2}\right]\right\}\delta\left(\frac{\partial w}{\partial n}\right)ds$$
$$-\oint_{c_3}\left\{\overline{V}_n+D\left[\frac{\partial}{\partial n}\nabla^2w\right.\right.$$

$$+(1-\mu)\frac{\partial}{\partial s}\left(\frac{\partial^2 w}{\partial s\partial n}-\frac{1}{\rho_s}\frac{\partial w}{\partial s}\right)\Bigg]\Bigg\}\delta w\, ds$$
$$-\sum_{k=1}^{i}\left[(1-\mu)D\Delta\left(\frac{\partial^2 w}{\partial s\partial n}-\frac{1}{\rho_s}\frac{\partial w}{\partial s}\right)_k+\overline{R}_{n,k}\right]\delta w_k. \quad (11)$$

Since δw is arbitrary, Eq. (8) is equivalent to

$$D\nabla^2\nabla^2 w-q+p=0;$$

on the boundary C_1

$$\overline{M}_n=-D\left[\mu\nabla^2 w+(1-\mu)\frac{\partial^2 w}{\partial n^2}\right]$$

$$\overline{V}_n=-D\left[\frac{\partial}{\partial n}\nabla^2 w+(1-\mu)\frac{\partial}{\partial s}\left(\frac{\partial^2 w}{\partial s\partial n}-\frac{1}{\rho_s}\frac{\partial}{\partial s}\right)\right],$$

on the boundary C_3

$$\overline{M}_n=-D\left[\mu\nabla^2 w+(1-\mu)\frac{\partial^2 w}{\partial n^2}\right], \text{ and}$$

at the corner point k

$$\overline{R}_n=-(1-\mu)D\Delta\left(\frac{\partial^2 w}{\partial s\partial n}-\frac{1}{\rho_s}\frac{\partial w}{\partial s}\right).$$

In the foregoing equations, w and p must satisfy Eq. (2).

Now we are able to derive the undetermined variables for the generalized variational principle with two variational functions w and p. The functional of the principle can be expressed in the following form:

$$\Pi_{w,p}=\Pi_w+\frac{1}{2}\int_s\int\left[w(x,y)-\int_s\int p(\xi,\eta)k(x,y;\xi,\eta)d\xi d\eta\right]\lambda(x,y)dx\,dy \quad (12)$$

where $\lambda(x, y)$ is the undetermined Lagrange multiplier and is a function of the variables x and y; it is not a constant independent of x and y. From Eq. (2), after the variational constraint is released, the integral equation is still a functional constraint condition. Actually, Eq. (2) can be written as

$$G(x,y)=w(x,y)-\int_s\int p(\xi,\eta)k(x,y;\xi,\eta)d\xi d\eta=0.$$

Thus, according to the variational principle, the use of the Lagrange multiplier $\lambda(x, y)$ is appropriate.

The variation of Eq. (12) can be written in the following form:

$$\delta\Pi_{w,p}=\delta\Pi_w+\frac{1}{2}\int_s\int\lambda(x,y)\delta w\,dx\,dy$$
$$-\frac{1}{2}\int_s\int\left[\int_s\int\delta p(\xi,\eta)k(x,y;\xi,\eta)d\xi\,d\eta\right]\lambda(x,y)dx\,dy$$
$$+\frac{1}{2}\int_s\int\left[w-\int_s\int p(\xi,\eta)k(x,y;\xi,\eta)d\xi\,d\eta\right]\delta\lambda(x,y)dx\,dy \quad (13)$$

where $\delta\Pi_w$ in Eq. (13) is the same as shown in Eq. (8), except the functions w and p are independent and do not satisfy Eq. (2).

Considering the third term on the right-hand side of Eq. (13) and using the same analogy in Eq. (11), we have

$$\frac{1}{2}\int_s\int\left[\int_s\int\delta p(\xi,\eta)k(x,y;\xi,\eta)d\xi\,d\eta\right]\lambda(x,y)dx\,dy$$
$$=\frac{1}{2}\int_s\int\left[\int_s\int\lambda(\xi,\eta)k(x,y;\xi,\eta)d\xi\,d\eta\right]\delta p(x,y)dx\,dy. \quad (14)$$

Substituting Eq. (14) in Eq. (13) and following Eq. (8), we have

$$\delta\Pi_{w,p}=\int_s\int\left[D\nabla^2\nabla^2 w-q+\frac{1}{2}(p+\lambda)\right]\delta w\,dx\,dy$$
$$+\frac{1}{2}\int_s\int\left[w-\int_s\int p(\xi,\eta)k(x,y;\xi,\eta)d\xi d\eta\right]\delta\lambda(x,y)dx\,dy$$
$$+\frac{1}{2}\int_s\int\left[w-\int_s\int\lambda(\xi,\eta)k(x,y;\xi,\eta)d\xi d\eta\right]\delta p(x,y)dx\,dy$$
$$+\oint_{c_2+c_3}\left\{\overline{M}_n+D\left[\mu\nabla^2 w+(1-\mu)\frac{\partial^2 w}{\partial n^2}\right]\right\}\delta\left(\frac{\partial w}{\partial n}\right)ds$$
$$-\oint_{c_3}\left\{\overline{V}_n+D\left[\frac{\partial}{\partial n}\nabla^2 w+(1-\mu)\frac{\partial}{\partial s}\left(\frac{\partial^2 w}{\partial s\partial n}-\frac{1}{\rho_s}\frac{\partial w}{\partial s}\right)\right]\right\}\delta w\,ds$$
$$-\sum_{k=1}^{i}\left\{(1-\mu)D\Delta\left(\frac{\partial^2 w}{\partial s\partial n}-\frac{1}{\rho_s}\frac{\partial w}{\partial s}\right)_k+\overline{R}_{n,k}\right\}\delta w_k=0. \quad (15)$$

In Eq. (15), δw, δp, and $\delta\lambda$ are independent, thus, $\delta\Pi_{w,p}=0$ is equivalent to

$$D\nabla^2\nabla^2 w-q+\frac{1}{2}(p+\lambda)=0 \quad (16)$$

$$w-\int_s\int p(\xi,\eta)k(x,y;\xi,\eta)d\xi d\eta=0 \quad (17)$$

$$w-\int_s\int\lambda(\xi,\eta)k(x,y;\xi,\eta)d\xi d\eta=0 \quad (18)$$

and

$$\overline{M}_n=-D\left[\mu\nabla^2 w+(1-\mu)\frac{\partial^2 w}{\partial n^2}\right]$$
$$\overline{V}_n=-D\left[\frac{\partial}{\partial n}\nabla^2 w+(1-\mu)\frac{\partial}{\partial s}\left(\frac{\partial^2 w}{\partial s\partial n}-\frac{1}{\rho_s}\frac{\partial w}{\partial s}\right)\right] \quad (19)$$
$$\overline{R}_{n,k}=-D(1-\mu)\Delta\left(\frac{\partial^2 w}{\partial s\partial n}-\frac{1}{\rho_s}\frac{\partial w}{\partial s}\right)_k \quad (20)$$

Comparing Eqs. (17) and (18), with respect to any point (x, y), it can be shown

$$\int_s\int[p(\xi,\eta)-\lambda(\xi,\eta)]k(x,y;\xi,\eta)d\xi\,d\eta=0 \quad (21)$$

and we have

$$\lambda(\xi,\eta)=p(\xi,\eta) \text{ or } \lambda(x,y)=p(x,y). \quad (22)$$

Substituting Eq. (22) in Eq. (12)

$$\Pi_{w,p}=\Pi_w+\frac{1}{2}\int_s\int\left[w-\int\int_s p(\xi,\eta)k(x,y;\xi,\eta)d\xi d\eta\right]\times p(x,y)dx\,dy \quad (23)$$

or

$$\Pi_{w,p}=\frac{1}{2}\int_s\int D\left\{(\nabla^2 w)^2-2(1-\mu)\left[\frac{\partial^2 w}{\partial x^2}\frac{\partial^2 x}{\partial y^2}-\left(\frac{\partial^2 w}{\partial x\partial y}\right)^2\right]\right\}dx\,dy$$
$$-\int_s\int qw\,dx\,dy+\int_s\int pw\,dx\,dy-\frac{1}{2}\int_s\int\left[\int_s\int p(\xi,\eta)k(x,y;\xi,\eta)d\xi\,d\eta\right]p(x,y)dx\,dy+\int_{c_2+c_3}\overline{M}_n\frac{\partial w}{\partial n}ds$$
$$-\int_{c_3}\overline{V}_n w\,ds-\sum_{k=1}^{i}\overline{R}_{n,k}w_k. \quad (24)$$

Equation (24) is the functional of the generalized variational principle for plates on an elastic foundation with two unde-

termined variables w and p. The application of Eq. (24) can be illustrated by using an example shown in the publication of Cheung and Zienkiewicz (1965). Based upon the foundation flexibility matrix $[f_f]$, reaction column matrix $\{p\}$, plate deflection column matrix $\{w\}$, and the plate stiffness matrix $[K]$ in the publication, we are able to establish the generalized variational principle with two variational functions in the following form

$$\Pi_{w,p}=\frac{1}{2}\{w\}^T[K]\{w\}-\{q\}^T\{\omega\} + \{p\}^T\{w\}-\frac{1}{2}\{p\}^T[f_f]\{p\}. \quad (25)$$

From $\delta\Pi_{wp} = 0$, the corresponding governing equations for the finite element analysis can be obtained.

4 Summary and Conclusions

The theory of variational principle is further enhanced by introducing the functional of the generalized variational principle for plates on an elastic foundation. In practical application, it can be shown that, using Eq. (24) and interpolation functions of deflection w and reaction p, the corresponding governing equations can be established based upon the ordinary variational procedure. The authors have found that it is very convenient for finite element analysis of plates on an elastic foundation.

In addition, the corner conditions for plates have also been given in terms of deflections. This presentation has not been shown in any of the previous publications.

References

Cheung, Y. K., and Zienkiewicz, O. C., 1965, "Plates and Tanks on Elastic Foundations—An Application of Finite Element Method," *Int. J. Solids Structures*, Vol. 1, pp. 451–461.

Hetenyi, M., 1946, *Beams on Elastic Foundation*, University of Michigan Press, Ann Arbor, Mich.

Jones, R., 1977, "The Vlasov Foundation Model," *Int. J. Mech. Sci.*, Pergamon Press, Elmsford, N.Y.

Landau, L. D., and Lifshitz, E. M., 1986, *Theory of Elasticity*, Pergamon Press, Elmsford, N.Y.

Shames, I. H., and Dym, C. L., 1985, *Energy and Finite Element Methods in Structural Mechanics*, Hemisphere Publishing Corporation.

Vallabhan, C. V. G., and Das, Y. C., 1988, "Parametric Study of Beams on Elastic Foundations," *J. Engrg. Mech.*, Vol. 114, No. 12.

Vlasov, V. Z., and Leont'ev, N. N., 1966, *Beams, Plates and Shells on Elastic Foundations*, (Translated from the Russian by Israel Program for Scientific Translations, NTIS Accession No. N67-1428).

Washizu, K., 1975, *Variation Methods in Elasticity and Plasticity*, Pergamon Press, Elmsford, N.Y.

Westergaard, H. M., 1948, "New Formulas for Stresses in Concrete Pavements of Airfield," *Trans., ASCE*, p. 113.

Stability Analysis for the Head-Disk Interface in a Flexible Disk Drive

Kyosuke Ono[1]

Jen-San Chen

D. B. Bogy
Mem. ASME

Computer Mechanics Laboratory,
Department of Mechanical Engineering,
University of California,
Berkeley, CA 94720

This paper describes the modeling, theoretical formulation, and eigenvalue analysis for a combined system of a spinning flexible disk and a pair of head and suspension systems that contact the disk at opposing points on its two sides. In the analytical model a constant friction force between the sliders and disk and the slider pitch motion, as well as its transverse motion, are taken into account. From the eigenvalue analysis it is found that pitch stiffness and moment of inertia of the heads induce instability above the critical rotation speed similarly to the transverse stiffness and mass. This instability can be effectively stabilized by increasing the external damping which is spinning with the disk. It is also found that the friction force makes all forward modes unstable over the entire rotational speed range. The friction induced instability can be effectively suppressed by increasing the transverse stiffness and mass and it can be stabilized by the pitch damping and the external damping. The characteristics of instability due to the friction force qualitatively agree well with experimental results reported previously.

Introduction

Flexible disk storage systems have been widely used as convenient input/output devices in data processing systems, especially in small personal computers. To meet user demand for convenient removable media, smaller size and larger capacity flexible disk drives have been developed in the past 20 years. Recent progress in the performance-to-cost ratio in computers and hard disk drives increases the need for development of a high speed and large capacity flexible disk storage system with more than ten megabytes.

The most difficult problem encountered in developing a new flexible disk drive is to obtain a stable and reliable scanning condition between the medium and recording head. The disk and head suspension often exhibit vibrations which cause not only malfunctions in the read/write signal but also a remarkable reduction of recording medium life. Until now this vibration has been suppressed through trial and error by changing the tribological characteristics of the medium, the slider contour and its suspension system. Therefore, efforts to understand the mechanism of vibration related to the head and flexible disk interface through analysis and to find a stable scanning condition has recently become of great concern for many researchers.

Vibrations of a spinning flexible disk induced by a point contact stationary head was investigated by Benson and Bogy (1978), Ono et al. (1986), and Ono and Maeno (1987). Benson and Bogy (1978) discussed different stationary deflection patterns of a spinning flexible disk depending on its thickness and the position of the head. Ono et al. (1986) analyzed stationary disk deflections associated with critical speeds for 8, 5.25, and 3.5-in. flexible disks, but they found qualitative discrepancies between theory and experiment. Ono and Maeno (1987) found that the steady deflection and vibrations of a 3.5-in. flexible disk induced by a point contact head can be qualitatively predicted by taking into account a residual compressible stress in the circumferential direction and an initial deflection of the disk.

As for the vibration of a coupled system of a spinning flexible disk with a head and suspension, Iwan and Moeller (1976) analyzed the instability of a spinning disk due to coupling effects of a translational mass, spring, and damper. They found three different instability regions above the critical speed due to the attached mass, spring, and damper, respectively. For the investigation of unstable head vibrations, Good and Lowery (1985) used finite element modeling and free vibration analysis of an actual disk and head assembly system. They included head pitch and roll motion as well as transverse motion and could get good agreement with experiment for the dominant mode frequencies, but they did not analyze the instability. A comprehensive experimental study of unstable vibration of an actual 5.25-in. flexible disk and head was reported by Kohno et al. (1989). Since the unstable vibration observed by them is related to the head pitch motion and appears to

[1]On sabbatical leave from the Tokyo Institute of Technology, Department of Mechanical Engineering, Meguro-ku, Tokyo, Japan.

Contributed by the Applied Mechanics Division of THE AMERICAN SOCIETY OF MECHANICAL ENGINEERS for presentation at the Joint Applied Mechanics/Bioengineering Conference, Ohio State University, Columbus, Ohio, June 16–19, 1991.

Discussion of this paper should be addressed to the Technical Editor, Prof. Leon M. Keer, The Technological Institute, Northwestern University, Evanston, IL 60208, and will be accepted until two months after final publication of the paper itself in the JOURNAL OF APPLIED MECHANICS. Manuscript received by the ASME Applied Mechanics Division, June 4, 1990; final revision, Aug. 16, 1990.

Paper No. 91-APM-31.

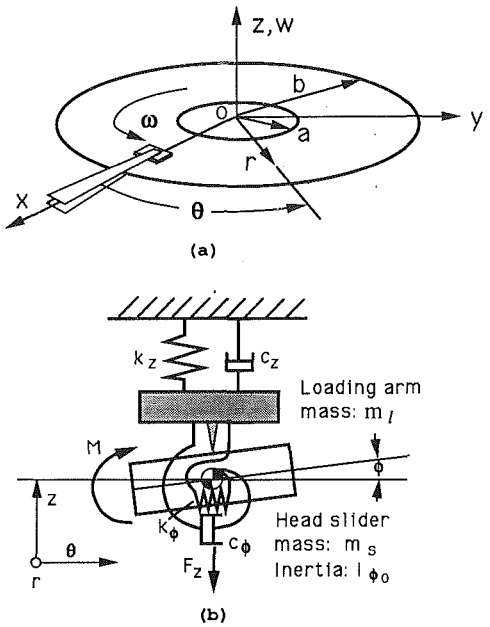

Fig. 1 Model of flexible disk and head assembly system; (*a*) Spinning flexible disk, head assemblies, and fixed coordinate system; (*b*) Model of upper and lower head assemblies

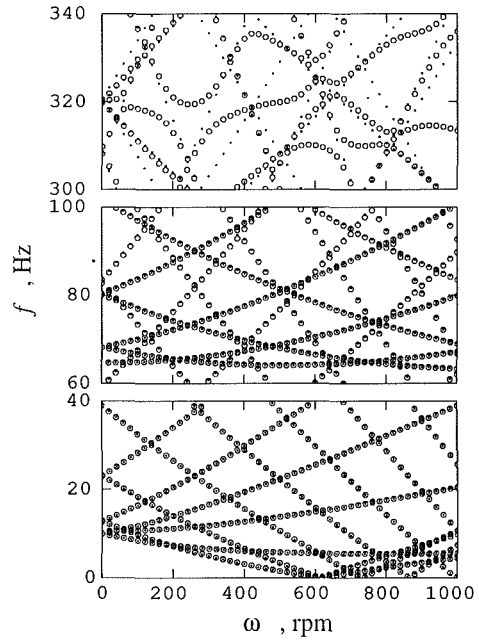

Fig. 2 The pitch moment of inertia and small pitch stiffness effects on the natural frequency ($I_\phi = I_{\phi 0}$, $k_\phi = 10 \times k_{\phi 0}$ [f_ϕ = 31.6 Hz])

occur far below the lowest critical speed, it appears to be unrelated to the instability phenomena predicted by Iwan and Moeller (1976). Jiang and Chonan (1989) theoretically obtained many unstable regions below the lowest critical speed for a coupled system of a flexible disk and a translational mass and spring. However, the unstable vibrations observed by Kohno et al. cannot be explained by the results obtained by Jiang and Chonan, because the relationship between unstable frequency and rotational speed is qualitatively different in the two studies. In addition, the pitch motion of the head was not considered in their analysis. Moreover, the unstable regions below the critical speed in Jiang and Chonan appear to result from mistreatment in their theoretical formulation of a stationary force applied to the spinning disk by the head.

In view of the discrepancy between theory and experiment for the unstable vibration related to head-to-medium interface as stated above, an effort is made here to develop a more accurate model of a flexible disk and head assembly system which has the potential to eliminate this discrepancy. This paper presents the theoretical formulation and eigenvalue analysis for an extended model where the pitch motion of the head and friction force between the heads and medium are taken into account. Although an actual head-to-medium interface and suspension system are more complex than the present model, it is hoped that this work will contribute to a better physical insight into unstable vibrations in the head-to-medium interface in flexible disk systems.

Analytical Model and Theoretical Formulation

Figure 1 portrays an analytical model of a coupled system of a spinning flexible disk and upper and lower head assemblies, together with the fixed coordinate systems *O-xyz*, *O-rθz* and physical parameters considered in this model. In order to simplify the analytical model while not losing important factors relevant to the instability phenomena, the following assumptions are made with respect to the head-to-medium interface and head assemblies.

1 Identical upper and lower heads are sliding on the disk with equal and opposite static loads F_{z0} and with no initial static disk deflection.

2 The upper and lower head sliders move together as a rigid body in the transverse and pitch directions in contact with the disk. The lower head slider is stiffly supported in the transverse direction, whereas the upper one is loaded on the disk by a flexible spring through a suspension arm. Thus, the effective transverse mass m_z is the sum of the two slider masses m_s and the mass of the loading arm m_l in a normal operating condition. The pitch moment of inertia I_ϕ is related to the two head sliders whose mass center G is in the middle plane of the disk. The head sliders are not allowed to move in the direction parallel to the disk surface. The roll motion of the head slider about an axis in the circumferential direction is not coupled to other motions and can be omitted for the stability analysis.

3 The suspension system of the two head assemblies is modeled as a simple transverse spring with stiffness coefficient k_z and damper with damping coefficient c_z together with a pitch moment spring k_ϕ and damper c_ϕ. They are uncoupled from each other.

4 The acting and reacting forces and moment between the disk and a pair of head sliders are transverse force F_z, friction force F_θ and pitch moment M. They are concentrated at the mass center G of the two head sliders.

5 The friction force F_θ is constant and given by $2\mu F_{z0}$, where μ is the friction coefficient.

Even when the disk is rotating in air without any constraint such as a liner, the surrounding air has some inertia and damping effects on the disk vibration, especially in the high-frequency region. Estimation of these effects is not easy and is itself a subject to be studied. The mass effect of the surrounding air may be equivalently understood not only as an additional spinning mass of the disk, but also as a stationary mass which is attached to the disk like the two heads. However, because of the difficulty of its qualitative estimation, the mass effect of the surrounding air is neglected here. Although the estimation of the damping effect of the surrounding air is also difficult, we simply regard it as two kinds of homogeneous external damping; one of them is spinning with the disk (c_1) and another is stationary (c_2).

From the infinitesimal analysis, the equation of motion of the disk can be written in terms of transverse displacement w and with respect to the stationary coordinate system (r, θ), as

$$\rho H\left(\frac{\partial}{\partial t}+\omega\frac{\partial}{\partial \theta}\right)^2 w + c_1\left(\frac{\partial}{\partial t}+\omega\frac{\partial}{\partial \theta}\right)w + c_2\frac{\partial w}{\partial t}$$

$$+D\nabla^4 w - H\frac{\partial}{r\partial r}\left(\sigma_r r\frac{\partial w}{\partial r}\right) - H\frac{\sigma_\theta}{r^2}\frac{\partial^2 w}{\partial\theta^2}$$

$$=\frac{1}{r}\left(F_z + F_\theta\frac{\partial w}{r\partial\theta}\right)\delta(r-\xi)\delta(\theta) - \frac{1}{r^2}\frac{\partial}{\partial\theta}[M\delta(\theta)]\delta(r-\xi) \quad (1)$$

where

$$D=\frac{EH^3}{12(1-\nu^2)}, \quad \nabla^2=\left(\frac{\partial^2}{\partial r^2}+\frac{1}{r}\frac{\partial}{\partial r}+\frac{1}{r^2}\frac{\partial^2}{\partial\theta^2}\right).$$

The parameters ρ, H, E, and ν are the density, thickness, Young's modulus, and Poisson's ratio of the disk. $\delta(:)$ is the Dirac delta function. The coupling position between heads and disk is assumed to be $r = \xi$ and $\theta = 0$. When the spinning disk is clamped at the inner radius $r = a$ and free at the outer radius $r = b$, the in-plane stresses σ_r and σ_θ due to the centrifugal effect are given by

$$\left.\begin{aligned}
&\sigma_r = C_1 + \frac{C_2}{r^2} + C_3 r^2, \ \sigma_\theta = C_1 - \frac{C_2}{r^2} + C_4 r^2\\
&C_1 = \frac{1+\nu}{8}\rho\omega^2\frac{(\nu-1)a^4-(3+\nu)b^4}{(\nu-1)a^2-(1+\nu)b^2}\\
&C_2 = \frac{1-\nu}{8}\rho\omega^2 a^2 b^2\frac{(1+\nu)a^2-(3+\nu)b^2}{(\nu-1)a^2-(1+\nu)b^2}\\
&C_3 = -\frac{3+\nu}{8}\rho\omega^2, \ C_4 = -\frac{1+3\nu}{8}\rho\omega^2
\end{aligned}\right\} \quad (2)$$

From Fig. 1(*b*), the dynamic transverse force F_z and pitching moment M are, respectively, given by

$$F_z = -m_z\frac{\partial^2 w}{\partial t^2} - c_z\frac{\partial w}{\partial t} - k_z w \quad (3)$$

$$M = -I_\phi\frac{\partial^2}{\partial t^2}\left(\frac{\partial w}{r\partial\theta}\right) - c_\phi\frac{\partial}{\partial t}\left(\frac{\partial w}{r\partial\theta}\right) - k_\phi\frac{\partial w}{r\partial\theta}. \quad (4)$$

Equation (1) looks like an inhomogeneous equation but becomes a homogeneous equation after substitution of equations (3) and (4) into equation (1).

A particular solution of the disk deflection for this homogeneous system is assumed in the form of a Fourier sine and cosine series expansion as follows:

$$w=\sum_{l=0}^{L}(G_l(r,t)\cos l\theta + K_l(r,t)\sin l\theta). \quad (5)$$

In the case of a freely spinning disk, the sine and cosine functions represent circumferential eigenmodes. In the case of the coupled system of the disk and head assembly, each eigenmode deviates from a harmonic function, but can be approximately expressed as a linear combination of harmonic functions. Regarding the mode functions' dependence on r, G_l, and K_l are obtained by the finite element method as described in a previous paper (Ono et al., 1986). This implies that the radial mode functions, which are decomposed into harmonic functions, are assumed to be approximately represented in the third-order polynomial function space within the region of each element.

Substituting the disk deflection (5) into the basic equations (1), (2), (3), and (4), we can get a set of partial differential equations for $G_l(r,t)$ and $K_l(r,t)$. Based on the finite element method, we next transform these differential equations with respect to r into matrix algebraic equations for the state vector at the nodes of the finite number of elements. When the element number in the r direction is denoted by N and the harmonic functions are taken into account up to $l = L$, the degrees-of-freedom of the final matrix equation for this coupled system becomes $2(1 + 2L)N$. Since the coefficient matrices of this second-order time-derivative equation are asymmetrical, the eigenvalue analysis was carried out by using an available library program of generalized eigenvalue analysis.

For the purpose of comparison with the theoretical and experimental works published previously, a 5.25-in. flexible disk is chosen for computer calculation, although the calculated data of the most prevailing 3.5-in. disk will be more interesting than for the 5.25-in. disk from a technical point of view. For the physical parameters of the disk, the following values are used in the calculation: $E = 4.9\times10^9$ N/m^2, $\nu = 0.3$, $\rho = 1.3\times10^3$ kg/m^3, $H = 0.078$ mm, $a = 17.5$ mm, $b = 65.0$ mm, and $\xi/b = 0.75$.

As for the head and suspension parameters, the mass m_s and pitching moment of inertia I_ϕ of the two sliders are estimated as 4.0×10^{-4} kg and 1.60×10^{-9} kg m^2, respectively. The effective transverse mass m_z including both slider mass m_s and the loading arm mass m_l are estimated as 4.0×10^{-3} kg; ten times larger than m_s. Then, 4.0×10^{-3} kg and 1.60×10^{-9} kg m^2 are, respectively, considered to be representative transverse mass and pitch moment of inertia, which we denote henceforth by m_{z0} and $I_{\phi0}$. Since the transverse mass m_z and pitch moment of inertia I_ϕ are not easily changed, their nominal values, m_{z0} and $I_{\phi0}$, are usually used in the following calculations.

On the other hand, the stiffness and damping of the suspension cannot be definitely estimated, since different manufacturers may choose quite different values. Especially, the stiffness can be changed so easily that its value may be selected from the view point of stability. Therefore, the effects of stiffness on the eigenvalues were investigated by using several different values in the calculation. In order to get better physical insight into the frequency characteristics of the coupled system, we first note the natural frequencies of the different subsystems. The lowest values of the transverse stiffness k_{z0} and pitch stiffness $k_{\phi0}$ are chosen to be 15.8 N/m and 6.32×10^{-6} Nm/rad, respectively, so that the transverse natural frequency f_z ($\equiv\sqrt{k_{z0}/m_z}/2\pi$) and the pitch natural frequency f_ϕ ($\equiv\sqrt{k_{\phi0}/I_\phi}/2\pi$) of the two head assemblies both become 10 Hz, when m_z is equal to m_{z0} ($= 4.0\times10^{-3}$ kg) and I_ϕ is equal to $I_{\phi0}$ ($= 1.60\times10^{-9}$ kg m^2), respectively.

The effect of the suspension damping is one of the most important concerns in this study, because it is well known that the singing noise has been often stabilized by the addition of some damping material to the suspension. Since it is not easy to increase the damping factor by a large amount, the effects of transverse and pitch damping are examined with the nondimensional damping ratio having the value 0.1. The effects of the external damping c_1 and c_2 are also investigated by choosing their values properly.

From the viewpoints of both computing efficiency and accuracy, the maximum number L of the order of the harmonic functions and the finite element number N is chosen to be 15 and 5, respectively. Eigenvalues are generally expressed in the form $\alpha \pm 2\pi fj$, where $j = \sqrt{-1}$. The real part α and the frequency f are plotted and discussed. The notation (n,l) represents the nth nodal circle and lth nodal diameter mode. Its forward and backward travelling components are expressed by the subscripts f and b, respectively.

Calculated Results and Discussion

(1) Pitch Moment of Inertia and Stiffness Effects. The coupling effects of a spinning disk and a pitch vibration system have not been investigated previously, and the effects of the pitch parameters in the real head assemblies are weak compared with those of the transverse parameters. Therefore, a coupled system, which includes only pitch moment of inertia and stiffness, is discussed first. Figure 2 shows the natural frequencies f of the coupled system (open circles) where the pitch moment of inertia I_ϕ is equal to $I_{\phi0}$ and the pitch stiffness k_ϕ is equal to $10\times k_{\phi0}$. Since the pitch frequency of the head and suspension system f_ϕ is 31.6 Hz in this case, the amount of k_ϕ is regarded as fairly small compared with actual cases. For com-

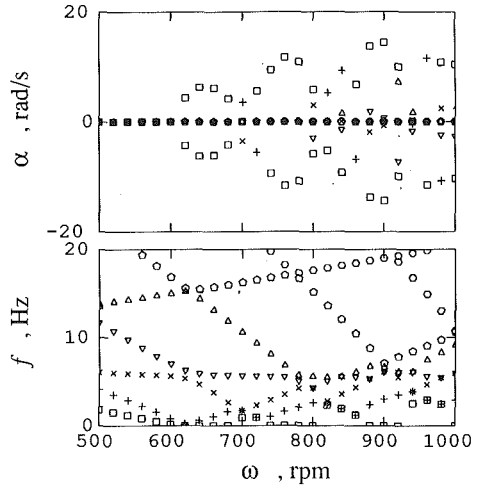

Fig. 3 Instability due to large pitch stiffness ($I_\phi = I_{\phi 0}$, $k_\phi = 10^3 \times k_{\phi 0}$ [f_ϕ = 316 Hz])

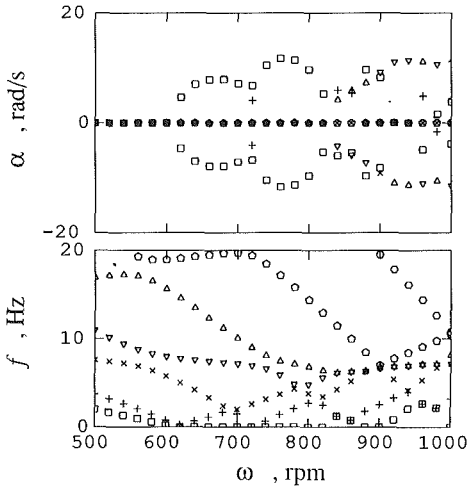

Fig. 5 Instability due to transverse mass and large transverse stiffness ($m_z = m_{z0}$, $k_z = 10^4 \times k_{z0}$ [f_z = 1.0 kHz])

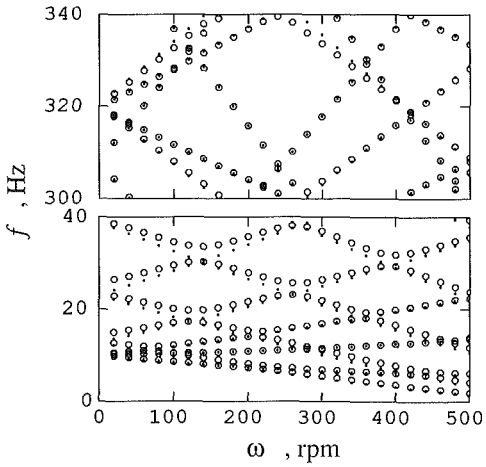

Fig. 4 The pitch moment of inertia and large pitch stiffness effects on the natural frequency ($I_\phi = I_{\phi 0}$, $k_\phi = 10^3 \times k_{\phi 0}$ [f_ϕ = 316 Hz])

parison the natural frequency of a free disk is indicated in Fig. 2 with small black dots. Since the real part of the eigenvalue is almost zero in this case, the α value is not shown here.

It is seen from this figure that a nonrotating 5.25-in. flexible disk has the lowest natural frequencies for the zero nodal circle modes (0,0) and (0,1) at about 10 Hz, while the lowest one nodal circle mode, i.e., the (1,0) mode, starts from about 64 Hz. Although not illustrated in Fig. 2, it was found that the lowest two nodal circle mode (2,0) starts from about 190 Hz and the lowest three nodal circle mode (3,0) from about 370 Hz. The frequencies of the backward traveling $(0,2)_b$ and $(0,3)_b$ modes become zero just above 600 rpm. This rotational speed corresponds to the critical speeds of the associated modes. The $(0,4)_b$, $(0,5)_b$, and $(0,6)_b$ modes undergo critical speeds at about 730, 860, and 1000 rpm, respectively. No apparent instability can be observed above the critical speeds in this case.

As seen in this figure, the deviation of the natural frequencies from those of the free disk is negligible in the low and middle frequency ranges. However, a remarkable change of frequency is noted in the high-frequency range. From additional calculations to investigate the effects of I_ϕ and k_ϕ separately, it was found that a k_ϕ of this amount does not change the frequency from that of the free disk. Therefore, the change of the natural frequency from that of the free disk in the high-frequency range is caused by the I_ϕ only. As seen in Fig. 2, the change of frequency from the free disk can be noted from around 100 Hz, which is above the original natural frequency of the pitch vibration system f_ϕ. The effect of I_ϕ on the frequency becomes stronger for higher nodal-diameter modes. From a detailed examination of the frequency change above 100 Hz, it was found that the frequency change due to I_ϕ occurs in such a way that the top corner and the two upper-side frequency lines of each diamond or upper triangle shift downward, keeping the two side corners at the initial crossing points for the free disk. As seen from the high-frequency range in Fig. 2, all frequency lines always pass through the original crossing points of different mode lines, as pointed out by Schajer (1984).

If the pitch stiffness k_ϕ increases by 100 times from the case of Fig. 2, instability regions appear above the critical speeds as shown in Fig. 3. In this figure, the same symbols in the frequency f and the real part α represent the corresponding imaginary and real parts of a pair of complex conjugate eigenvalues. Except for the case of zero frequency, each single symbol in f corresponds to a conjugate pair of pure imaginary eigenvalues, since the corresponding α value is zero. At the rotational speed ω where f decreases to zero, the eigenvalues become a pair of positive and negative reals with the same absolute value. This implies that one of the modes with zero frequency becomes unstable. Since the zero-frequency mode is a stationary mode, this type of instability is termed here as a "stationary-type instability." The overlapped symbols in f also correspond to positive and negative reals with the same absolute value in α. This means that two modes have the same frequency, and that one of them is unstable. At this point the frequency curves of the two different modes are merged into one. Thus, this type of instability is termed here as a "merged-type instability."

Each stationary-type instability appears to start from near the critical speed described above. The rule that determines the onset of a merged-type instability is more complex. The merged-type instability apparently takes place when a reflected increasing frequency line and a decreasing frequency line meet in the neighborhood of a third line. As seen in the range 800–1000 rpm in Fig. 3, more than one instability of different types, or the same type, can occur at the same rotational speed.

From the calculated results for the case where only large pitch moment of inertia of $I_\phi = 10^2 \times I_{\phi 0}$ is included, it was found that the merged-type instabilities are also induced. However, its illustration and detail discussion are omitted here, because the characteristics of this instability are qualitatively similar to those due to the transverse mass which will be discussed later.

Small frequency changes from those for the free disk, such as a veering feature (Schajer, 1984), can be noted at crossing points between different mode lines in Fig. 3. Therefore, it is

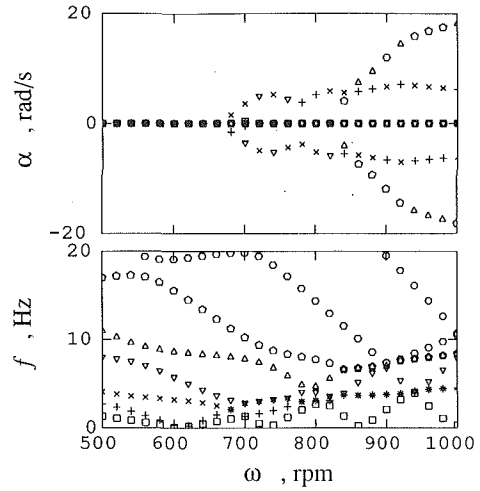

Fig. 6 Instability due to transverse mass only ($m_z = m_{z0}$)

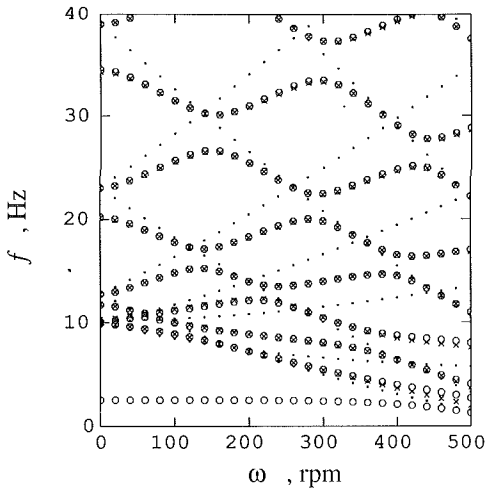

Fig. 7 The frequency change due to transverse mass and large transverse stiffness (o: transverse mass only [$m_z = m_{z0}$]; ×: transverse stiffness only [$k_z = 10^4 \times k_{z0}$]; •: freely spinning disk)

also interesting to examine the effect of increased pitch stiffness on natural frequency. For this purpose, the low and high-frequency ranges in the rotational speed range less than 500 rpm are depicted in Fig. 4 for the same parameters as in Fig. 3. From the comparison between Figs. 4 and 2, it is noted that the large deviation of f in the high-frequency range caused by moment of inertia is thoroughly suppressed by the increased pitch stiffness. Since the stiffness effect becomes predominant over the mass effect in the low-frequency range, all frequencies increase from the free disk values except for the (0,0) mode and the original crossing points of different modes. Compared with the frequency change due to moment of inertia, the frequency change due to stiffness takes place in the opposite direction such that the bottom corner and the lower two-side frequency lines of each diamond or the bottom-side frequency line of each upper triangle move upward, keeping the two side corners fixed at the initial crossing points for the free disk.

Moreover, it is interesting and worth noting that all frequencies above about 320 Hz decrease from the free disk values. Considering that the pitch vibration system attached to the disk has the natural frequency of 316 Hz in this case, we found that a general rule of frequency change due to the combination of pitch moment of inertia and pitch stiffness can be explained as follows: The inertia effect to decrease frequency and the stiffness effect to increase frequency are competitive with each other and the two effects are canceled just at the natural frequency f_ϕ of the pitch vibration system attached to the disk. The frequency of the disk below f_ϕ increases due to the dominance of the stiffness effect, while the frequency of the disk above f_ϕ decreases due to the dominance of the inertia effect. The degree of frequency deviation from the free disk values in the regions below and above f_ϕ increases with an increase in the pitch stiffness and inertia. Since the original $(n,0)$ mode motions have no pitch component, their frequencies are never affected by the pitch parameters, as seen in Fig. 4.

Although not illustrated, it was found from the additional parameter studies where large amounts of I_ϕ and k_ϕ are taken into account separately, that the frequencies asymptotically approach certain limiting values with an increase in pitch inertia, and these limiting frequency values are the same as are obtained with an increase in pitch stiffness, except the lowest natural frequency. The lowest natural frequency tend to zero with an increase in pitch inertia. These behaviors will be discussed in more detail in the case of transverse mass and stiffness effects.

(2) Transverse Mass and Stiffness Effects. Next, the transverse mass and stiffness effects on the eigenvalues are investigated. Figure 5 shows the destabilized eigenvalues due to a transverse mass of m_{z0} and a large transverse stiffness of $10^4 \times k_{z0}$. These values are regarded as close to the effective mass and stiffness of an actual head assembly in normal operating conditions. The natural frequency of the transverse mass and stiffness system f_z is 1.0 kHz in this case.

It is seen from Fig. 5 that this combination of m_z and k_z is large enough to cause instability after the critical speed. From additional calculated data for the cases where only m_z or k_z is taken into account separately, it was found that the eigenvalues in the presence of k_z only are the same as in Fig. 5 in all frequency ranges less than 400 Hz, and therefore the stiffness effect is predominant in these ranges. The eigenvalues in the presence of m_z only are found to be different from Fig. 5 in the low-frequency range, and are depicted in Fig. 6 for comparison.

As seen in Fig. 5, both stationary and merged-type instabilities again appear due to the transverse stiffness. By comparison of Fig. 5 with Fig. 3, one can note that the instability regions due to transverse stiffness only or dominant stiffness are fairly similar to those due to pitch stiffness. On the other hand, transverse mass gives rise to only the merged-type instability, as seen in Fig. 6. The reason why transverse mass and pitch inertia do not induce the stationary-type instability is that the inertia effects always vanish at zero frequency. If a large number of modes are taken into account, the unstable speed region caused by the transverse mass appears to be bounded differently from the Iwan and Moeller (1976) results where a few modes were taken into account.

It is worth noting that the frequencies f in Figs. 5 and 6 have the same values except in the low-frequency region where the merged-type instabilities take place. This suggests that f approaches a limiting value with an increase in stiffness only, and that this limiting value is the same as the one which f approaches with an increase in mass only, except in the low-frequency region associated with instability.

For a more detailed examination of the changes in frequency due to transverse mass and stiffness, the natural frequencies for the two cases which include transverse mass of $10 \times m_{z0}$ or transverse stiffness of $10^4 \times k_{z0}$ separately are plotted in Fig. 7 with circle and cross symbols, respectively, in the low-frequency and low rotational speed ranges. For comparison the natural frequencies of the free disk are also shown with small dots. It is found from this figure that the natural frequencies are almost equal in both cases except for the lowest frequency line of the case with transverse mass only.

Regarding the mass effect on frequency, it was found from this figure and additionally calculated data that the lowest

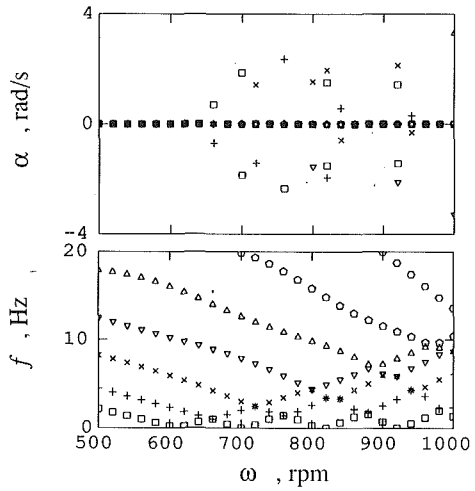

Fig. 8 Combination effect of I_ϕ, k_ϕ, m_z and k_z ($I_\phi = I_{\phi 0}$, $k_\phi = 10^3 \times k_{\phi 0}$ [f_ϕ = 316 Hz], $m_z = m_{z0}$, $k_z = 10^4 \times k_{z0}$ [f_z = 1.0 kHz]

frequency curve is reduced toward zero frequency as the transverse mass increases. At the same time the other frequencies decrease and approach asymptotic values in such a way that the top corner and two-side frequency lines of each diamond or triangle go down, keeping the two side corners at their original crossing points, similarly to the high-frequency region in Fig. 2. In the case where $m_z = m_{z0}$, the f value has not approached the asymptotic value, because the lowest frequency has not become zero and the f values with circles are slightly larger than the ones with cross symbols, as seen from Fig. 7. When the spinning disk is constrained by only transverse stiffness, on the other hand, the bottom corner and two-side frequency lines of each diamond or the bottom side of each triangle rise up from the free disk lines, keeping the two side corners at the same positions. As the transverse stiffness increases, the natural frequencies approach asymptotic values. In the case of Fig. 7, the transverse stiffness is so large that the natural frequency indicated by cross symbols is almost in the asymptotic state. It is seen from Fig. 7 that these limiting frequencies are equal except for the lowest frequency. However, it should be noticed that when both the mass and stiffness are combined together, the frequency changes can cancel each other near the natural frequency f_z of the attached mass and spring system, because the same asymptotic state is obtained by the decrease or increase of f depending on the mass or stiffness effect. From these results it can be said that the combination effects of the transverse mass and stiffness on the eigenvalues is also competitive rather than additive similarly to the combination effect of the pitch inertia and stiffness.

As mentioned before, the same behaviors as are described above for the transverse parameters can be obtained for the pitch parameters, although the limiting frequency values are different and the $(n,0)$ modes are not affected by pitch parameters.

(3) Combination Effect of Pitch and Transverse Parameters. An actual spinning disk in a floppy disk drive system is coupled with not only pitch moment of inertia and stiffness but also transverse mass and stiffness. So the next interest is to investigate the combined effects of the pitch and transverse parameters. Figure 8 shows the eigenvalues related to instability above the critical speed when the pitch parameters in Fig. 3 and the transverse parameters in Fig. 5 are taken into account at the same time.

It is worth noting that the unstable speed regions and the strength of the instability are markedly reduced by one fifth, as compared with Figs. 3 and 5. From the calculated data for the cases where only transverse and pitch stiffnesses are included, it was found that the instability characteristics are the same as shown in Fig. 8. This seems to imply that large pitch stiffness and large transverse stiffness can mutually suppress the strong instability tendencies indicated in Figs. 3 and 5. From the calculated results for the several cases where k_ϕ or k_z are further increased from the case in Fig. 8, it was found that the α values associated with instability change slightly but that the instability regions can neither be completely eliminated nor can they be increased again as in Fig. 3 or Fig. 5 by increasing k_ϕ or k_z. This implies that the combination effect of pitch and transverse stiffness on instability is neither additive nor competitive, but may be called a suppression effect.

From the additional parameter study where only I_ϕ and m_z are included, it was found that the instability characteristics above the critical speeds are governed by either I_ϕ or m_z, depending on their relative amounts. In other words, the combination effect of the pitch inertia and transverse mass is

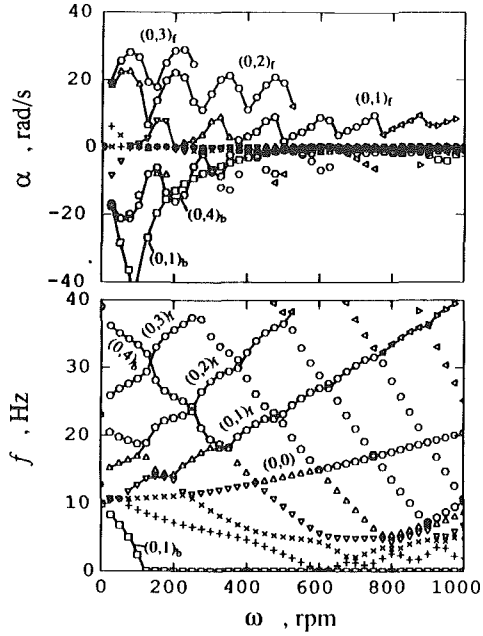

(a) Low frequency range

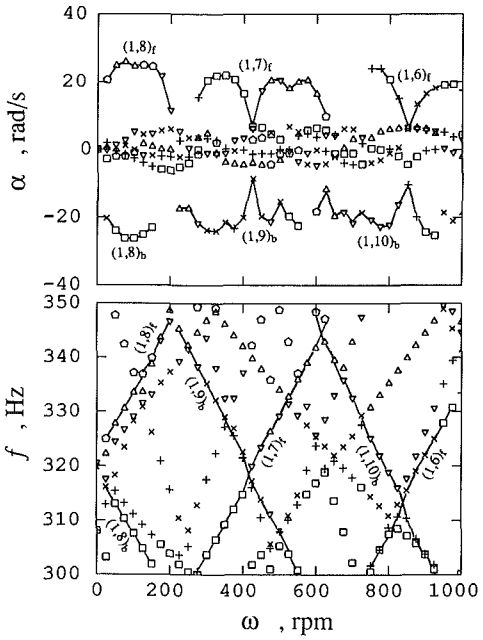

(b) High frequency range

Fig. 9 Friction effects on eigenvalues

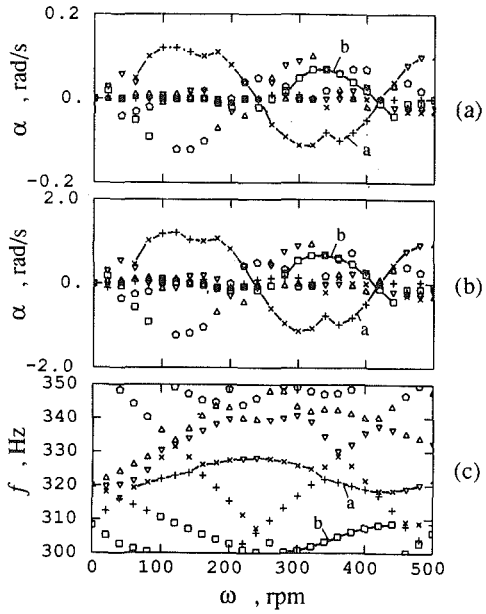

Fig. 10 Combination effect of friction force and other parameters on eigenvalues ($l_\phi = l_{\phi 0}$, $k_\phi = 10^3 \times k_{\phi 0}$, $k_z = k_{z0}$, $F_\theta = 0.32$ N); (*a*) real part values when $m_z = m_{z0}$; (*b*) real part values when $m_z = 0.1 \times m_{z0}$; (*c*) frequency when $m_z = m_{z0}$ or $0.1 \times m_{z0}$

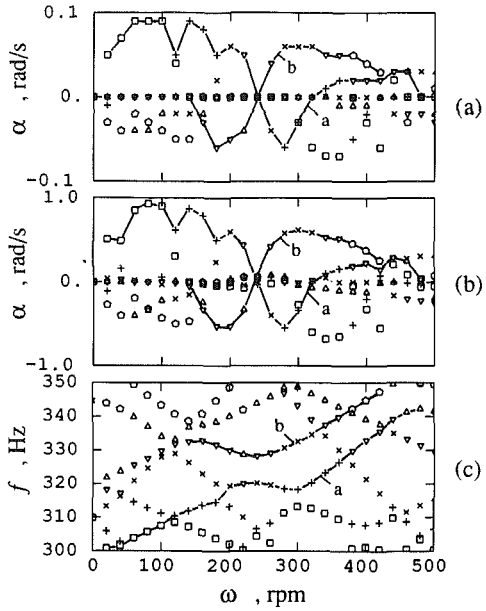

Fig. 11 Combination effect of friction force and other parameters on eigenvalues ($l_\phi = l_{\phi 0}$, $k_\phi = 10^2 \times k_{\phi 0}$, $k_z = k_{z0}$, $F_\theta = 0.32$ N); (*a*) real part values when $m_z = m_{z0}$; (*b*) real part values when $m_z = 0.1 \times m_{z0}$; (*c*) frequency when $m_z = m_{z0}$ or $0.1 \times m_{z0}$

competitive and any suppression effect as shown in Fig. 8 cannot be obtained. Therefore, a combination of two of the four parameters I_ϕ, k_ϕ, m_z and k_z usually affects the instability competitively except for the combination of k_ϕ and k_z.

The suppression effect due to the combination of k_ϕ and k_z may be hypothetically interpreted as follows: Modes destabilized by large pitch stiffness are possibly allowed to move only in the transverse direction, like a symmetrical deflection mode with respect to the coupling point. On the other hand, modes destabilized by large transverse stiffness are allowed to rotate about the coupling point, like a skew symmetrical deflection mode. Therefore, the former unstable modes may be suppressed by the addition of a transverse stiffness constraint, while the latter modes may be suppressed by a pitch stiffness constraint.

Since the values of pitch and transverse parameters considered in Fig. 8 are regarded as equivalent to those of an actual flexible disk drive in the normal operating condition, it can be said that the instability tendency above critical speeds can be largely removed by the constraints of pitch and transverse stiffnesses. However, the residual instability tendency cannot be eliminated without employing some other stabilizing means, such as a damping, as will be discussed later.

(4) Friction Effect. Next we investigate the instability effect of the head-disk friction force. In the following calculation, the static head load F_{z0} is assumed to be 0.4 N. The friction coefficient is considered as relatively large and is taken as 0.4. Then the tangential friction force F_θ is 0.32 N. Figures 9(*a*) and (*b*) show the eigenvalues in the low and high-frequency ranges, respectively, for the case where only the friction force is applied to the coupling point.

From the comparison of f values in Figs. 9(*a*) and (*b*) with those of the free disk in Fig. 2, it is found that the friction has an effect to change the frequencies from those of the free disk except for the $(n,0)$ modes. The reason for no change in the $(n,0)$ mode frequencies is that they have zero derivative in the circumferential direction so the static friction force effect vanishes as seen from the friction term in equation (1). The change of the frequencies from the free disk values and the veering feature near the crossing points are relatively stronger in the low-frequency range than in the high-frequency range. In particular, the $(0,1)_b$ mode frequency drops markedly and remains at zero above about 100 rpm.

As seen from the α values of Figs. 9(*a*) and (*b*), the instabilities are induced by constant friction force in the entire frequency range. Since the interaction between different original modes due to friction is not so strong, the notation of the corresponding original mode number is indicated for the typical increasing and decreasing frequency components for convenience. From comparison between the α and f values in Fig. 9, it is found that the forward, or increasing frequency, modes generally become unstable, while the backward, or decreasing, frequency modes remain stable. Near the crossing or veering points, the α values generally tend to zero. The steepness of the increasing or decreasing lines does not always result in a large absolute value of α. The largest positive α value appears in the $(0,3)_f$ mode in the low-frequency range, although the eigenvalues for higher-order modes are not illustrated in Fig. 9(*a*). In the high-frequency range between 300 and 350 Hz, on the other hand, the $(1,6)_f$, $(1,7)_f$, and $(1,8)_f$ mode lines have relatively large positive α values, while the $(1,8)_b$, $(1,9)_b$ and $(1,10)_b$ mode lines have relatively large negative α values. It is interesting to note in Fig. 9(*a*) that all the backward modes have small negative α values for frequency below the $(0,1)_f$ mode line, even above their critical speeds. The $(0,1)_b$ mode has a particularly large negative α value. From the rotational speeds above which the f values for the $(0,1)_b$ mode becomes zero, this conjugate eigenvalue changes to two negative values.

In an actual floppy disk drive, the static friction force is imposed on the disk together with pitch and transverse parameters. Therefore, we next calculated the combination effect of the friction force and the large pitch and transverse parameters which were used for the case in Fig. 8. The calculated result was found to be the same as in Fig. 8 in the entire speed range up to 1000 rpm and in the frequency range up to 400 Hz. The absolute value of α for any mode is reduced to less than 0.02 rad/s except the ones which are related to stationary (zero frequency) and merged-type instabilities. This means that the destabilizing effect of friction force is completely suppressed by the combination effects of large pitch and transverse stiffnesses.

Although the present analytical model may be still much simpler than the actual experimental set up used by Khono

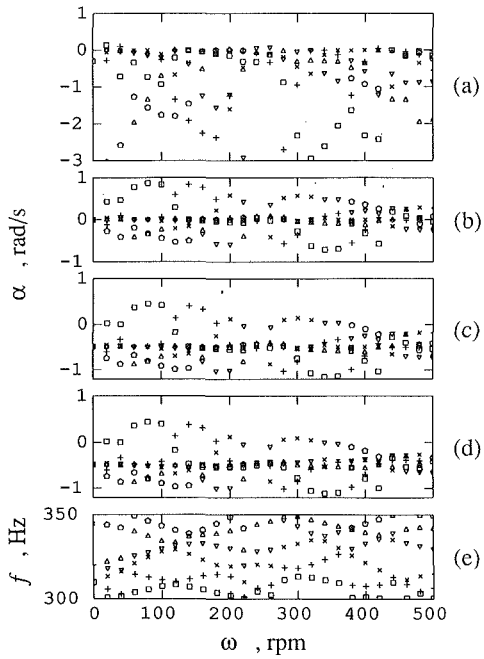

Fig. 12 Effect of damping factors c_ϕ, c_z, c_1, and c_2 on eigenvalues ($I_\phi = I_{\phi 0}$, $k_\phi = 10^2 \times k_{\phi 0}$, $k_z = k_{z0}$, $F_\theta = 0.32$ N); (*a*) $c_\phi = 2.01 \times 10^{-7}$ Nms/rad ($= 0.2\sqrt{I_\phi k_\phi}$); (*b*) $c_z = 1.59 \times 10^{-2}$ Ns/m ($= 0.2\sqrt{m_z k_z}$); (*c*) $c_1 = 0.1$ Ns/m; (*d*) $c_2 = 0.1$ Ns/m; (*e*) frequency for the cases (*a*), (*b*), (*c*), and (*d*)

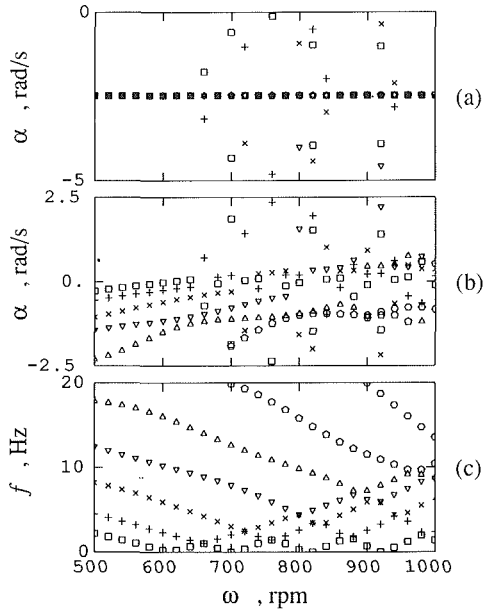

Fig. 13 Effect of damping factors c_1 and c_2 on instability above critical speeds ($I_\phi = I_{\phi 0}$, $k_\phi = 10^3 \times k_{\phi 0}$ [$f_\phi = 316$ Hz], $m_z = m_{z0}$, $k_z = 10^4 \times k_{z0}$ [$f_z = 1.0$ kHz]); (*a*) real part values for $c_1 = 0.5$ Ns/m; (*b*) real part values for $c_2 = 0.5$ Ns/m; (*c*) frequency for $c_2 = 0.5$ Ns/m

and et al. (1989), it is interesting to compare their observed characteristics of unstable vibration in the flexible disk and head assembly system with the calculated results obtained from the present model. According to their observation, typical features of unstable vibration are that the instability occurs in a certain rotational speed range and its frequency increases with increase in rotational speed. These features agree well with the characteristics of unstable vibration caused by friction force only, as shown in Figs. 9(*a*) and (*b*). In the normal operating condition, however, the transverse stiffness is so high, because of the fixed lower head, that the instability due to friction force can be thoroughly suppressed, as stated above. Therefore, if we imagine that the leading and trailing disk supporters used in their experiment have no function to stabilize a particular mode, and that the lift of the leading disk supporter functions to weaken the suppressing effect of mass and stiffness, then one of the interesting modes can possibly become unstable in a certain rotational speed region whose terminations correspond to veering points; for example, the $(1,7)_f$ mode becomes unstable between 425 and 600 rpm and the frequency may change from 320 to 347 Hz with increase in the rotational speed, as seen from Fig. 9(*b*). According to their description, the unstable vibration may have nodes near the disk supporters and may be regarded as a higher-order mode like the $(1,7)_f$ mode. Accordingly, it is reasonable to consider that the lift of the leading-side disk supporter induces some reduction in the transverse stiffness. For example, strong air-bearing effects may be developed between the lower head slider and the disk. If the loading arm and slider are decoupled, the effective mass of m_{z0} ($= 10m_s$) may be reduced to the slider mass m_s.

In order to investigate the possibility of friction instability under such abnormal conditions with reduced values of stiffness and mass parameters as described above, the eigenvalue analysis was further carried out for the four cases which include friction force as in Fig. 9 and the decreased pitch and transverse parameter values. If the transverse stiffness decreases to k_{z0}, the α values increase to more than 10 rad/s in the low-frequency range, but still remain less than 0.2 rad/s in the high-frequency range. In order to increase the α values in the high-frequency range, it is also necessary to decrease the transverse mass. The parameter study was done for the following four cases: (1) $k_z = k_{z0}$ with the other parameters having the same values as in Fig. 8, (2) $k_z = k_{z0}$, $m_z = 0.1 \times m_{z0}$ and the other parameters the same as in Fig. 8, (3) $k_z = k_{z0}$, $k_\phi = 10^2 \times k_{\phi 0}$ and the other parameters the same as in Fig. 8, and (4) $k_z = k_{z0}$, $m_z = 0.1 \times m_{z0}$, $k_\phi = 10^2 \times k_{\phi 0}$ and the other parameters the same as in Fig. 8.

If we confine our discussions only to the characteristics of eigenvalues in the high-frequency range, it was found that cases (1) and (2) have the same f values but different α values, and that cases (3) and (4) have the same f values but different α values. Thus, the α values for the cases (1) and (2) and their identical frequency f in the high-frequency range are shown in Figs. 10(*a*), (*b*), and (*c*), respectively. Similarly, Figs. 11(*a*), (*b*), and (*c*) show the corresponding quantities for the cases (3) and (4).

It is seen from these figures that the α values decrease almost inversely proportional to the increase in m_z in both Figs. 10 and 11 and that the f values in the high-frequency range depend not on m_z but on k_ϕ in these ranges of parameter values. The reason why m_z does not apparently change the f values, while changing the α values, is considered to be as follows: Since f_z is 31.6 Hz at most in these cases, the m_z effect is predominant over the k_z effect in the high-frequency range and the eigenvalues in Figs. 10 and 11 are close to the limiting state, in terms of the transverse mass effect, where the α values are zero.

For better understanding, the α and f lines of typical eigenvalues with relatively large α values are indicated with the same letters. Along the lines denoted by (*a*) and (*b*) in both Figs. 10 and 11, the same relationship between the slope of f and the sign of α as observed in Fig. 8 still holds. However, the increasing frequency regions with relatively large α values of the lines (*a*) and (*b*) in Fig. 10(*c*) are remarkably reduced compared with those in Fig. 11(*c*). As seen in Fig. 11, the mode indicated with (*a*) becomes unstable in the rotational speed region from 325 to 473 rpm. In this unstable region the unstable vibration frequency increases from 320 to 340 Hz, with an increase in the rotational speed. Similarly, the mode denoted by (*b*) becomes unstable in the rotational speed region from 240 to 440 rpm and the frequency increases from 330 to 350 Hz. It can be said that these results are in good qualitative

agreement with the experimental ones observed by Kohno et al. (1989).

From these parameter studies it is obvious that the instability caused by friction force can be suppressed by increasing the transverse stiffness and mass. From additional parameter studies it was also found that the friction instability can be suppressed by increasing the pitch moment of inertia and stiffness. The reason why the α values with $k_\phi = 10^3 \times k_{\phi 0}$ in Fig. 10 are larger than those with $k_\phi = 10^2 \times k_{\phi 0}$ in Fig. 11 is that the effect of I_ϕ and k_ϕ on the eigenvalues is almost canceled near 316 Hz, because $f_\phi = 316$ Hz in Fig. 10.

(5) Damping Effects. Lastly, we discuss the damping effects on the instability. To examine the effects of damping factors on the high-frequency instability caused by the friction force, we chose the abnormal case in Fig. 11(b) and (c), where $I_\phi = I_{\phi 0}$, $k_\phi = 10^2 \times k_{\phi 0}$ ($f_\phi = 100$ Hz), $m_z = 0.1 \times m_{m0}$ ($= m_s$), $k_z = k_{z0}$ ($f_z = 31.6$ Hz) and $F_\theta = 0.32$ N. The values of the damping coefficients c_ϕ and c_z are chosen to be 2.01×10^{-7} Nms/rad and 1.59×10^{-2} Ns/m, which correspond to 0.1 nondimensional damping ratios. Although the c_1 and c_2 values are not known, they both are chosen to be 0.1 Ns/m.

Figure 12 shows the α values for each case where only one damping factor described above is additionally taken into account. Since damping factors of this amount have no visible effect on frequency, the f values shown in Fig. 12(e) are common for the four cases. Similarly to the previous figures, the same symbols for α and f belong to a conjugate pair of eigenvalues. From Fig. 12(a) and (b) it is noted that c_ϕ has a strong stabilizing effect on the instability caused by friction force, whereas c_z has little stabilizing effect. However, this superiority of c_ϕ to c_z does not hold in the low-frequency range (not shown) where c_z has a rather stronger stabilizing effect than c_ϕ. It should be also noted from Fig. 12(a) that the α which originally had larger absolute values without c_ϕ move downward by a greater amount due to the addition of c_ϕ.

On the other hand, the damping factors c_1 and c_2 have different stabilizing effects such that all α values are shifted in the negative direction by the same amount, as seen from Figs. 12(c) and (d). Strictly speaking, some slight deviation from the uniform shift rule can be noted in Fig. 12(d) in the higher rotational speed region. It is obvious that this difference in the deviation of the α value with c_1 from that with c_2 results from the lack of the convective term of c_2 in equation (1).

From the additional parameter studies for the combination effects of these damping factors, it was found that they affect the α value under a simple principle of superposition, while keeping the f values unchanged, in the ranges of parameter values used here. It can be said from these results that the instability with high frequency caused by friction force can be effectively stabilized by the addition of a pitch damping to the suspension and some external damping to the disk.

Although not illustrated, it was found from the calculated results for the same parameters as in Fig. 11(b), but with damping, that the positive α values become more than 10 rad/s in the low-frequency range and these unstable vibrations of the lower-order modes cannot be stabilized by the four kinds of damping factors of this amount. In order to change the positive α value to negative, the amounts of c_ϕ, c_z, c_1, and c_2 should be increased by more than 20 times from those in Fig. 12. In an actual system, however, those lower-order modes would be practically suppressed by a disk liner, even if the transverse stiffness happens to be small.

In order to develop a high-speed flexible disk drive, on the other hand, it is well known that we should develop some means of increasing the external damping, for example, such as a Bernoulli plate. Therefore it is interesting to investigate the effect of strong surrounding air damping c_1 and c_2 on the instability in the high rotational speed region above the critical speeds. For the purpose of this parameter study, we chose three different combinations of the transverse and pitch parameters, as have already been treated in the above discussion. The first is the same as in Fig. 5 (large transverse mass and stiffness). The second is the same as in Fig. 8 (small pitch inertia and large pitch stiffness together with large transverse mass and stiffness). The third is the case having the same parameters as in Fig. 11(b) excluding the friction force (small pitch and transverse parameter values). Currently available high rotational speed flexible disk drives with a fixed recording head and some stabilizing plate may be modeled as the one with parameter values between the first and second cases. If a pair of flying head sliders are employed, similarly to those rigid disk drives, the head and suspension system is modeled as the third case. In high-speed flexible disk drive, the friction force should be decreased to be negligible value in any case. For each case described above, the external damping effects were examined by calculating three cases where $c_1 = 0.5$ Ns/m, $c_2 = 0.5$ Ns/m and $c_1 = c_2 = 0.5$ Ns/m are added separately.

Since it was found that the external damping effects on the eigenvalues are essentially equivalent for all three cases of different combinations of the pitch and transverse parameters, the c_1 and c_2 effects on the f and α values in the second case are representatively shown in Fig. 13. Figure 13(a) portrays the α values in the case where only c_1 is included. The corresponding f values are just the same as shown in Fig. 8. From the comparison between the α values in Fig. 8 and those in Fig. 13(a), it is seen that the α values for all modes uniformly shift to the negative direction and almost all unstable modes are stabilized except for the one which emerges at 1000 rpm (α value is off the graph). As seen from the comparison between Fig. 12(c) and Fig. 13(a), the amount of negative shift in the α values due to c_1 is proportional to the c_1 value. Therefore, it can be said that all unstable modes can be stabilized by the addition of the necessary amount of the spinning external damping factor c_1.

Figures 13(b) and (c), respectively, show the α and f values when only $c_2 = 0.5$ Ns/m is included. From careful comparison of the f values in Fig. 13(c) with those in Fig. 8, it is found that some of the merged frequencies in Fig. 8 separate by small amounts due to the c_2 effect in Fig. 13(c). Even though the two frequencies are not merged, the original pair of positive and negative α values remain unchanged excluding a few exceptions such as the pairs observed at 840 and 940 rpm. From Fig. 13(b) it is found that the α value of every backward mode increases from the same negative value as is obtained by the same amount of c_1 and becomes positive just above the corresponding critical speed, as the rotational speed increases. The eigenvalues of the stationary-type instability modes are not affected by the addition of c_2. As the rotational speed increases further, the increasing frequency lines which reflect back at the critical speeds cross the decreasing frequency lines of the other backward modes, and the α values of the two crossing modes become a large positive and negative pair near the crossing points, even if the two frequencies do not merge into one. By careful inspection to the correspondency between the α in Fig. 13(b) and the f in Fig. 13(c) near the crossing point, it is noted that the α value of the decreasing frequency line jumps to the negative value of the pair, while that of the increasing frequency line jumps to its positive value. On the whole, it is found that the stationary external damping factor c_2 has no effect to stabilize the instability above the critical speed caused by the pitch and transverse inertias and stiffnesses. On the contrary, all backward modes become unstable, although the amounts of the positive α values remain small.

From the calculated results for the case where both c_1 and c_2 are included, it was also found that the α values are equal to the sum of the two cases where c_1 and c_2 are separately

included and that the f values are nearly equal to the ones where only c_2 is included.

Conclusions

A new modeling and theoretical formulation is presented including friction force and pitch motion of a head slider as well as its transverse motion. The results of an eigenvalue analysis for a 5.25-in. flexible disk drive system with various values of the related parameters can be summarized as follows:

1 Large pitch moment of inertia and large pitch stiffness have destabilizing effects on the backward travelling modes above their critical speed similarly to transverse mass and stiffness.

2 Large pitch and transverse stiffness induce two kinds of instability above critical speeds; stationary (zero frequency)-type instability and merged-type instability. Every unstable speed region is bounded.

3 Large pitch moment of inertia and transverse mass causes only the merged-type instability above critical speeds. The unstable speed region is also bounded.

4 Pitch moment of inertia and transverse mass attached to the disk shift downward the original free-disk frequency lines, except for the crossing points of two different frequency lines. On the other hand, the pitch and transverse stiffness shift upward the original frequency lines, excluding the crossing points. In case of pitch parameters, the eigenvalues of the original zero-nodal diameter modes do not change.

5 With an increase in transverse mass, the frequency lines approach certain limiting lines which are the same as the frequency lines approach with increase in transverse stiffness, with the exception of the lowest frequency line. The lowest frequency line tends to zero with an increase in the transverse mass. The same situation occurs in the relation between the pitch moment of inertia and stiffness. The limiting frequency lines are different for the transverse and pitch parameters.

6 The combination effects of pitch inertia and stiffness or transverse mass and stiffness on eigenvalues are competitive. The two effects are canceled at the mass-stiffness natural frequencies, above which the inertia or mass effect becomes predominant and below which the stiffness effect becomes predominant.

7 The positive real part values of the unstable modes caused by the pitch stiffness and transverse stiffness separately can be largely reduced by the combination of the pitch and transverse stiffnesses. This suppression effect of instability cannot be observed in the combination of the pitch moment of inertia and transverse mass.

8 A constant friction force makes every increasing frequency mode unstable and every decreasing frequency mode stable over the entire rotational speed region, except the original zero-nodal diameter mode. Near the crossing points between the increasing and decreasing frequency lines, the real part values tend to be zero. This result shows good correlation with prior experimental ones.

9 The instability due to the friction force can be suppressed by increasing the transverse mass and stiffness and pitch stiffness. In the normal operating condition of an actual flexible disk drive with a lower fixed head, the friction instability is regarded as completely suppressed due to large transverse stiffness and large effective transverse mass. However, if the constraints due to the large transverse stiffness and mass are accidentally released, the instability due to the friction force may appear.

10 The unstable vibration with high frequency caused by the friction force can be effectively stabilized by the pitch damping of the head suspension. The transverse damping of the head suspension has little stabilizing effect on the high-frequency unstable modes. The external rotating and stationary dampings also have a stabilizing effect on the friction instability. The degrees of the stabilizing effects are proportional to the amount of each damping factor and the combination effect of different damping factors is additive.

11 The instability caused by pitch stiffness and transverse mass and stiffness above the critical speed can be stabilized by increasing the effect of spinning external damping. The stationary external damping has no stabilizing effect on the instability of this kind. In addition, the stationary external damping has a small destabilizing effect on all backward modes above the critical speeds.

References

Benson, R. C., and Bogy, D. B., 1978, "Deflection of a Very Flexible Spinning Disk due to a Stationary Transverse Load," ASME JOURNAL OF APPLIED MECHANICS, Vol. 45, pp. 636–642.

Good, J. K., and Lowery, R. L., 1985, "The Finite Element Modeling of the Free Vibration of a Read/Write Head Floppy Disk System," ASME *Journal of Vibration, Acoustics, Stress, and Reliability in Design*, Vol. 107, pp. 329–333.

Iwan, W. D., and Moeller, T. L., 1976, "The Stability of a Spinning Elastic Disk With a Transverse Load System," ASME JOURNAL OF APPLIED MECHANICS, Vol. 43, pp. 485–490.

Jiang, Z. W., and Chonan, S., 1989, "Optimum Design of a Read/Write Head Floppy Disk System," *Proc. Int. Conf. Advanced Mechatronics*, Tokyo, pp. 325–330.

Kohno, T., Matsushita, O., Terayama, T., and Nemoto, Y., 1989, "Unstable Vibration of Head Assembly in Flexible Disk Drive Unit," *Proc. Int. Conf. Advanced Mechatronics*, Tokyo, pp. 319–324.

Ono, K., Maeno, T., and Ebihara, T., 1986, "Study on Mechanical Interface Between Head and Media in Flexible Disk Drive (2nd Report, Dynamic Response Characteristics due to a Concentrated Force)," *Bulletin of the JSME*, Vol. 29, No. 255, pp. 3109–3115.

Ono, K., and Maeno, T., 1987, "Theoretical and Experimental Investigation on Dynamic Characteristics of a 3.5-Inch Flexible Disk due to a Point Contact Head," *Tribology and Mechanics of Magnetic Storage Systems*, Vol. 3, SP.21 (STLE), pp. 144–151.

Schajer, G. S., 1984, "The Vibration of a Rotating Circular String Subject to a Fixed Elastic Restraint," *Journal of Sound and Vibration*, Vol. 92, No. 1, pp. 11–19.

Christopher D. Pionke
Graduate Student.

Gerald Wempner
Professor,
Fellow ASME.

Engineering Science and
Mechanics Program,
School of Civil Engineering,
Georgia Institute of Technology,
Atlanta, GA 30332

The Various Approximations of the Bimetallic Thermostatic Strip

A thin strip, formed by bonding two dissimilar materials, constitutes a simple thermostatic element. If edge effects are neglected, then the strip is reduced to a uniform beam, or plate, with two degrees-of-freedom. The flexure occurs only because of the bond and interfacial shear which is also accompanied by transverse normal stress. These latter stresses are very localized at the end and edges. Here, the elementary approximations, and refinements via finite elements, are presented and compared. Deflections are given with reasonable accuracy by the simple approximations, but the severe interfacial stresses are revealed only by the refinements.

Introduction

A thin strip, formed by bonding two hookean, homogeneous, but dissimilar materials, constitutes a simple thermostatic element (Fig. 1). It provides an interesting study in mechanics and approximations. If end and edge effects are neglected, and the Bernoilli assumptions are invoked, then the strip is reduced to a model with two degrees-of-freedom (Timoshenko, 1925). By acknowledging the edge effects in the y direction and treating the element as a plate under the Kirchhoff assumption, the element is likewise reduced to two degrees-of-freedom (Timoshenko, 1925). Either model provides a prediction of the interior behavior and deflections, but the latter gives a better description of normal stresses upon a cross-section.

Of course, the flexure caused by heating occurs only because of the bond and the essential interfacial shear stress which is also accompanied by transverse normal stress. These effects are very localized near the ends and edges. Some indication of these effects are obtained by approximating each layer as a separate beam and enforcing interfacial continuity and interactions, as well as appropriate end conditions. This constitutes a one-dimensional "bonded-beam" approach which has been adopted and reported by Suhir (1986, 1989), Grimado (1978), Chang (1983), and others. Unfortunately, a beam theory can not accurately predict effects which occur in an edge zone, equal or smaller in magnitude than the thickness.

Finite elements can give more accurate descriptions of the stresses near the edges and ends (Gerstle and Chambers, 1987; Suganuma et al., 1984). This can be employed in the context of either a plane-stress (two-dimensional) or a general (three-dimensional) model. However, neither can accurately describe the singularity which is apparent in the interfacial normal stress (Dundurs, 1967, 1969; Bogy, 1968, 1970).

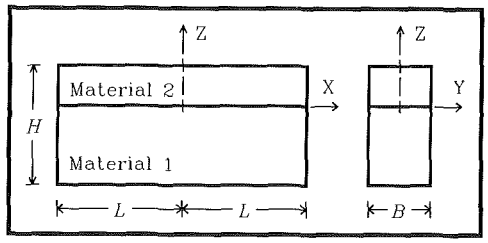

Fig. 1 Thermostat geometry

In this paper, the authors present derivations of both the simple beam and simple plate approximations first outlined by Timoshenko (1925). To validate these simple approximations, and to gain a deeper understanding of the interfacial stresses, we also examine this problem using both plane-stress (two-dimensional) and general (three-dimensional) finite elements previously developed by Wempner (1982, 1983). (The procedure for the FEM calculations was interactive; the mesh was progressively altered and refined as successive results indicated the very severe gradients near the end and edges.) In comparison, a summary of earlier works using both the bonded-beam approach and other (different) plane-stress (two-dimensional) finite elements are also presented.

Our purpose is to display the very interesting results and differences obtained by the various elementary theories and the more refined models of the finite element method. Though the predictions of stresses differ in the various approximations, similar predictions of the deflection of the tip are given by all. The effectiveness of employing a simple element (Wempner, 1982, 1983) for this study is also evident, since all numerical results were obtained using a personal computer. Finally, the results provide a graphic example of St.-Venant's principle.

A First Approximation—a Simple Beam

For the simplest approximation first described by Timoshenko, the assumption is made that $L \gg B > H$. Therefore, all stresses in the y and z directions are neglected. If end effects are also neglected by invoking St.-Venant's principle, the only nonzero stresses are the longitudinal normal stresses in each material. By the Bernoulli assumption, plane sections remain plane, and the normal stresses follow:

Contributed by the Applied Mechanics Division of THE AMERICAN SOCIETY OF MECHANICAL ENGINEERS for presentation at the Winter Annual Meeting, Atlanta, Ga., Dec. 1-6, 1991.

Discussion on this paper should be addressed to the Technical Editor, Prof. Leon M. Keer, The Technological Institute, Northwestern University, Evanston, IL 60208, and will be accepted until two months after final publication of the paper itself in the JOURNAL OF APPLIED MECHANICS. Manuscript received by the ASME Applied Mechanics Division, Aug. 15, 1990; final revision, Mar. 4, 1991.
Paper No. 91-WA/APM-11.

$$\sigma_{x_i} = E_i\epsilon^0 - E_i\kappa z - E_i\alpha_i\Delta T \quad \text{where } i = 1, 2. \tag{1}$$

Here, ϵ^0 and κ are the extensional strain and curvature of the x axis; they are obtained by enforcing equilibrium; viz., force and couple vanish:

$$F = \int \sigma_x dA = B\int \sigma_x dz = 0 \quad M = \int z\sigma_x dA = B\int z\sigma_x dz = 0. \tag{2}$$

In accordance with (1), Eqs. (2) are expressed in ϵ^0 and κ:

$$\left(1 + \frac{E_2}{E_2}\frac{H_2}{H_1}\right)\epsilon^0 + \frac{1}{2}\left(1 - \frac{E_2}{E_1}\frac{H_2^2}{H_1^2}\right)\kappa H_1 = \left(1 + \frac{E_2}{E_1}\frac{H_2}{H_1}\frac{\alpha_2}{\alpha_1}\right)\alpha_1\Delta T \tag{3a}$$

$$\left(1 - \frac{E_2}{E_2}\frac{H_2^2}{H_1^2}\right)\epsilon^0 + \frac{2}{3}\left(1 + \frac{E_2}{E_1}\frac{H_2^3}{H_1^3}\right)\kappa H_1 = \left(1 - \frac{E_2}{E_1}\frac{H_2^2}{H_1^2}\frac{\alpha_2}{\alpha_1}\right)\alpha_1\Delta T. \tag{3b}$$

The small deflection of the tip follows:

$$w = \frac{\kappa}{2}L^2. \tag{4}$$

By the above approximations, the only nonzero stresses depend on the transverse position in the strip, and the entire system is reduced to one with two degrees-of-freedom (ϵ^0 and κ).

This approximation was also given by Gerstle and Chambers (1987), but was derived in a different manner.

A Better Approximation—a Simple Plate

For most real thermostats, the geometry of the bimetallic strip corresponds to $L > B > H$ or $L > B \gg H$. Then stresses on z surfaces might be neglected, but on y sections, a better approximation is obtained if only the resultants are required to vanish, as on x sections. In effect, the strip is viewed as a simple Kirchhoff plate, wherein the interfacial strains (ϵ_x^0, ϵ_y^0) and curvatures (κ_x, κ_y) are constants. This plane stress approximation follows ($i = 1, 2$):

$$\sigma_{x_i} = \frac{E_i}{1-\nu_i^2}(\epsilon_x^0 + \nu_i\epsilon_y^0) - \frac{E_i}{1-\nu_i^2}(\kappa_x + \nu_i\kappa_y)z - \frac{1+\nu_i}{1-\nu_i^2}E_i\alpha_i\Delta T \tag{5a}$$

$$\sigma_{y_i} = \frac{E_i}{1-\nu_i^2}(\epsilon_y^0 + \nu_i\epsilon_x^0) - \frac{E_i}{1-\nu_i^2}(\kappa_y + \nu_i\kappa_x)z - \frac{1+\nu_i}{1-\nu_i^2}E_i\alpha_i\Delta T. \tag{5b}$$

The values for the four unknown constants ϵ_x^0, ϵ_y^0, κ_x, and κ_y are found by enforcing the conditions of vanishing force and couple on x and y sections:

$$F_x = \int \sigma_x dA = B\int \sigma_x dz = 0 \quad M_y = \int z\sigma_x dA = B\int z\sigma_x dz = 0 \tag{6a}$$

$$F_y = \int \sigma_y dA = L\int \sigma_y dz = 0 \quad M_x = \int z\sigma_y dA = L\int z\sigma_y dz = 0. \tag{6b}$$

The strains and the curvatures are the same in both the x and y directions, i.e., $\epsilon_x^0 = \epsilon_y^0 = \epsilon^0$ and $\kappa_x = \kappa_y = \kappa$:

$$\sigma_{x_1} = \sigma_{y_1} = \bar{E}_1\bar{\epsilon} - \bar{E}_1\bar{\kappa}z - \bar{E}_1\bar{\alpha}_1\Delta T \tag{7a}$$

$$\sigma_{x_2} = \sigma_{y_2} = \bar{E}_2\bar{\epsilon} - \bar{E}_2\bar{\kappa}z - \bar{E}_2\bar{\alpha}_2\Delta T \tag{7b}$$

where

$$\bar{\kappa} = (1+\nu)\kappa \quad \bar{\epsilon} = (1+\nu)\epsilon^0 \quad \bar{E} = \frac{E}{1-\nu^2} \quad \bar{\alpha} = (1+\nu)\alpha. \tag{8}$$

The two equations governing $\bar{\epsilon}$ and $\bar{\kappa}$ are similar to (3a,b) viz.:

$$\left(1 + \frac{\bar{E}_2}{\bar{E}_1}\frac{H_2}{H_1}\right)\bar{\epsilon} + \frac{1}{2}\left(1 - \frac{\bar{E}_2}{\bar{E}_1}\frac{H_2^2}{H_1^2}\right)\bar{\kappa}H_1 = \left(1 + \frac{\bar{E}_2}{\bar{E}_1}\frac{H_2}{H_1}\frac{\bar{\alpha}_2}{\bar{\alpha}_1}\right)\bar{\alpha}_1\Delta T \tag{9a}$$

$$\left(1 - \frac{\bar{E}_2}{\bar{E}_1}\frac{H_2^2}{H_1^2}\right)\bar{\epsilon} + \frac{2}{3}\left(1 + \frac{\bar{E}_2}{\bar{E}_1}\frac{H_2^3}{H_1^3}\right)\bar{\kappa}H_1 = \left(1 - \frac{\bar{E}_2}{\bar{E}_1}\frac{H_2^2}{H_1^2}\frac{\bar{\alpha}_2}{\bar{\alpha}_1}\right)\bar{\alpha}_1\Delta T. \tag{9b}$$

By this approximation, the small deflection along the centerline at the tip is again given by Eq. (4).

As in the simple beam approximation, the only nonzero stresses depend on the transverse position in the strip, and the entire system is reduced to one with two degrees-of-freedom ($\bar{\epsilon}$ and $\bar{\kappa}$). In fact, Timoshenko (1925) showed that the simple plate approximation can be obtained from the simple beam approximation by making the following substitutions:

$$E_1 = \frac{E_1}{1-\nu_1} \quad E_2 = \frac{E_2}{1-\nu_2} \tag{10}$$

In addition, if $\nu_1 = \nu_2 = \nu$, the stresses predicted by the simple plate approximation are just $1/(1-\nu)$ times the stresses predicted by the simple beam approximation.

Approximation as Two Bonded Beams

Both of the preceding approximations provide ready calculation of the stresses in the interior of the strip. However, neither solution provides any information about the interfacial shear and normal stresses. These interfacial stresses are negligible in the interior of the strip, but are significant near the end of the strip as first noted by Timoshenko.

Two-dimensional elasticity solutions of infinite quarter-planes by Dundurs (1967, 1969) and Bogy (1968, 1970) indicate that there is a singularity in the interfacial normal stress at the end and edges of the strip. Because of this singularity, there is also a severe gradient in the interfacial shear stress near the end and edges of the strip. However, an investigation of these interfacial stresses for the exact geometry of a real thermostat by either a two or three-dimensional elasticity solution would be exceedingly difficult, if not impossible.

In an effort to develop simplified calculations for the interfacial stresses, several authors such as Suhir (1986, 1989), Grimado (1978), Chang (1983), and others have analyzed bimaterial strips by beam theory. Although their approaches differ slightly, all of these authors model each material as a separate beam or long narrow plate. Equilibrium for each beam is enforced, as well as the boundary conditions at the interface of the two beams and at the end of the strip. This "bonded-beam" method can be subdivided into two types; bonded beam I (Suhir, 1986 and Grimado, 1978) enforces a zero shear *force* at the end; while bonded beam II (Suhir, 1989, and Chang, 1983) enforces a zero shear *stress* at the end. As an example of this method, the general results from Suhir's (1986, 1989) work will be presented.

For the bonded-beam I approximation, the interfacial shear and normal stresses are given by:

$$\tau_{xz} = \frac{\Delta T(\alpha_1 - \alpha_2)}{A_1}\sinh(\mu_1 x) \tag{11a}$$

$$\sigma_z = \frac{\Delta T(\alpha_1 - \alpha_2)}{A_1 A_2}\cosh(\mu_1 x) \tag{11b}$$

Likewise, for the bonded-beam II approximation, the interfacial shear and normal stresses are given by:

$$\tau_{xz} = C_1\sinh(\beta_1 x) + C_2\cosh(\beta_2 x)\sin(\beta_3 x) + C_3\sinh(\beta_2 x)\cos(\beta_3 x) \tag{12a}$$

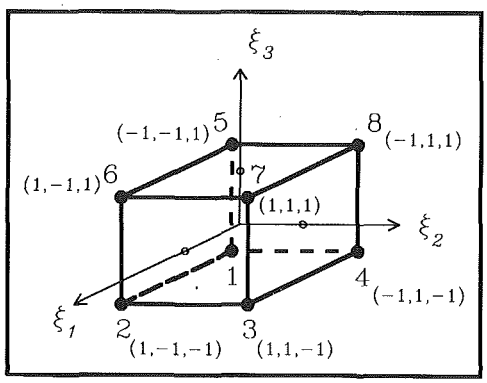

Fig. 2 Finite element geometry

$$\sigma_z = C_4\cosh(\beta_1 x) + C_5\cosh(\beta_2 x)\cos(\beta_3 x) + C_6\sinh(\beta_2 x)\sin(\beta_3 x). \quad (12b)$$

All of the constants in (11*a*) through (12*b*) depend on the geometry of the strip and the properties of the two materials.

For both bonded-beam approximations, the deflection at the tip of the strip is:

$$w = \frac{3HL^2(\alpha_1-\alpha_2)\Delta T}{H_1^2+H_2^2+3H^2+\left[\frac{E_2H_2^3(1-\nu_1^2)}{E_1H_1(1-\nu_2^2)}\right]+\left[\frac{E_1H_1^3(1-\nu_2^2)}{E_2H_2(1-\nu_1^2)}\right]}. \quad (13)$$

Although these approximations lead to reasonably simple closed-form solutions for the interfacial stresses, all suffer from some fundamental errors. First, all of the solutions ignore the effects of stresses and strains in the y direction and, therefore, ignore equilibrium in that same direction. Second, all of them predict finite values for the transverse interfacial normal stress at the end of the strip, as opposed to the singularity indicated by the solutions of elasticity. In fact, certain combinations of properties and thicknesses predict zero normal stress, e.g., from Suhir:

$$\frac{E_1H_1^2(1-\nu_2^2)}{E_2H_2^2(1-\nu_1^2)} = 1. \quad (14)$$

Previous Finite Element Approaches

In an effort to probe the nature of the interfacial stresses for real geometries of thermostats and similar structures, Gerstle and Chambers (1987), Suganuma et al. (1984), and others have employed the finite element method (FEM). These previous studies used two-dimensional elements, wherein the direction of zero stress is again taken as the y direction (the width). However, as already shown for real geometries of thermostats, $B>H$. Therefore, if the singularity at the tip is ignored, a model using plane-stress elements with zero stress in the z direction (the height) is also a valid model.

Present Approach

In this paper, the authors employ both two-dimensional and three-dimensional finite elements (Fig. 2). Both types of elements were derived using the Hu-Washizu (1955) functional. This functional was chosen as a basis for development of finite elements for two reasons. First, it allows independent approximations for the displacements, strains, and stresses. Second, elements based on the Hu-Washizu functional avoid the problem of "shear locking" when the thickness of the element decreases, (Wempner, 1968, 1982, 1983).

The first element is a plane-stress plate (i.e., the normal stress in the transverse direction is ignored). This element has trilinear approximations for the in-plane displacements, bilinear approximations for the transverse displacements and the in-plane normal strains and stresses, as well as linear approximations for all three shear strains and stresses. In view of the approximations, i.e., suppression of the transverse normal stress, this model has the attributes of a (two-dimensional) shear deformable plate.

Since the normal stress in the transverse direction is neglected, the extensions of the normals in the transverse direction are also neglected. Let ξ_i ($i=1, 2, 3$) denote the local normalized coordinates which originate at the center of the element. Nodal values are $\xi_i^j = \pm 1$, where $j = 1, 2, \ldots 8$ signify node numbers. Also, the nodal displacements are denoted by u_i^j. Then the plane-stress displacement approximation is given by:

$$u_i = \frac{1}{8}\sum_{j=1}^{8} N_j u_i^j \ (i=1, 2) \qquad u_3 = \frac{1}{4}\sum_{k=1}^{4} N_k u_3^k \quad (15a)$$

where

$$N_j = (1+\xi_1^j\xi_1)(1+\xi_2^j\xi_2)(1+\xi_3^j\xi_3)$$
$$N_k = (1+\xi_1^k\xi_1)(1+\xi_2^k\xi_2). \quad (15b)$$

The strain approximations are:

$$\epsilon_1 = \mu_1 + \mu_2\xi_2 + \mu_3\xi_3 + \mu_4\xi_2\xi_3$$
$$\epsilon_2 = \mu_5 + \mu_6\xi_1 + \mu_7\xi_3 + \mu_8\xi_1\xi_3$$
$$\gamma_{12} = \mu_9 + \mu_{10}\xi_3$$
$$\gamma_{13} = \mu_{11} + \mu_{12}\xi_2$$
$$\gamma_{23} = \mu_{13} + \mu_{14}\xi_1. \quad (15c)$$

Likewise, the stress approximations are:

$$\sigma_1 = \beta_1 + \beta_2\xi_2 + \beta_3\xi_3 + \beta_4\xi_2\xi_3$$
$$\sigma_2 = \beta_5 + \beta_6\xi_1 + \beta_7\xi_3 + \beta_8\xi_1\xi_3$$
$$\tau_{12} = \beta_9 + \beta_{10}\xi_3$$
$$\tau_{13} = \beta_{11} + \beta_{12}\xi_2$$
$$\tau_{23} = \beta_{13} + \beta_{14}\xi_1. \quad (15d)$$

The second element is a three-dimensional brick. This element has a trilinear approximation for all three displacements, bilinear approximations for all three normal strains and stresses, and linear approximations for all three shear strains and stresses.

The displacement approximation is given by:

$$u_i = \frac{1}{8}\sum_{j=1}^{8} N_j u_i^j \quad (i=1, 2, 3) \quad (16a)$$

where N_j is defined in (15*b*).

Now, in addition to the strains (15*c*) and the stresses (15*d*), one also has:

$$\epsilon_2 = \mu_{15} + \mu_{16}\xi_1 + \mu_{17}\xi_2 + \mu_{18}\xi_1\xi_2$$
$$\sigma_3 = \beta_{15} + \beta_{16}\xi_1 + \beta_{17}\xi_2 + \beta_{18}\xi_1\xi_2. \quad (16b)$$

In both elements, the strain approximations are the simplest polynomials that inhibit all zero energy or "hour glass" modes of deformation (Wempner, 1982, 1983).

Finite Element Models

Our numerical examples employ the following material and geometrical properties: $E_1 = 15.0\times10^6$ psi, $E_2 = 30.0\times10^6$ psi, $\nu_1 = 0.300$, $\nu_2 = 0.300$, $\alpha_1 = 13.0\times10^{-6}/°\text{F}$, $\alpha_2 = 6.50\times10^{-6}/°\text{F}$, $L = 2.000$ in., $B = 0.200$ in., $H_1 = 0.060$ in., $H_2 = 0.015$ in., $\Delta T = 400°\text{F}$. These properties were chosen to provide a realistic example. The much thinner layer might be ferrous alloy with greater strength; the thicker layer a cuprous alloy. Of course, the relatively thin layer aggravates the computational problem; in particular, the normal stress gradient must be severe to vanish at the nearby surface.

Table 1 Summary of FEM models

FEM MODEL NUMBER	DESCRIPTION
1	X-Y Plane-Stress Y Continuity Not Enforced
2	X-Y Plane-Stress Y Continuity Enforced
3	X-Z Plane-Stress
4	3-D

Table 2 Comparison of tip deflections

APPROXIMATION	DEFLECTION (in./L)
Simple Beam	0.0418
Simple Plate	0.0418
Bonded Beam I & II	0.0418
FEM 1: X-Y Plane-Stress Y Continuity Relaxed	0.0418
FEM 2: X-Y Plane-Stress Y Continuity Enforced	0.0418
FEM 3: X-Z Plane-Stress	0.0416
FEM 4: General 3-D	0.0411

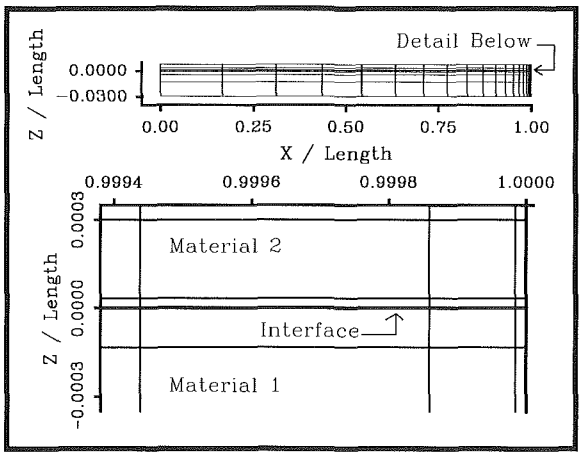

Fig. 3 Finite element mesh

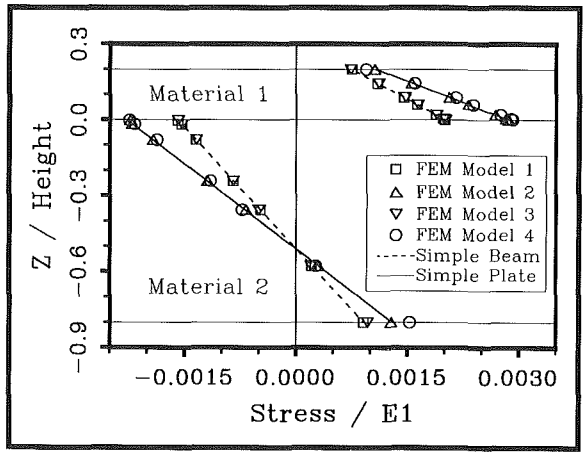

Fig. 4 Longitudinal normal stress

In view of the symmetry, only one-fourth of the strip was modeled. Because the interfacial stresses are highly localized and have sharp gradients, iterations were made with various mesh configurations, and element sizes until a $29 \times 4 \times 10$ (length $\times$ width $\times$ height) mesh was chosen for use in all computations. This mesh has progressively smaller elements near the end, edges, and material interface (Fig. 3). Utilizing this mesh, computations were made with four different combinations of elements and interfacial continuity (Table 1).

The first and second models use the plane-stress element with the z direction taken as the direction of zero stress (i.e., an x-y plane-stress model). For comparison with the simple beam, model 1 relaxes interfacial continuity in the y direction (i.e., differences in anticlastic strain and curvature are ignored). In model 2 interfacial continuity is enforced; this corresponds to the (better) simple plate.

For comparison with the previous finite element studies of Gerstle and Chambers (1987), and Suganuma et al. (1984), model 3 uses the plane-stress element, but the y direction is taken as the direction of zero stress (i.e., an x-z plane-stress model). This model also corresponds to the simple beam for the longitudinal normal stresses since the difference in anticlastic strain and curvature are again ignored.

Finally, model 4 uses the general (three-dimensional) element. This model provides a benchmark with which to compare the other FEM models and the elementary approximations.

Results

The predicted displacements of the tip of the strip are shown in Table 2. Since the values differ by less than two percent, the simple beam is entirely adequate for predicting deflections.

The predicted longitudinal normal stresses for an interior region are shown in Fig. 4. The simple beam and simple plate have a similar linear distribution but different values. Since both materials in our model have the same value of ν, the stresses for the simple plate are exactly $1/(1-\nu)$ times the values for the simple beam.

Also, from Fig. 4, a summary of the predicted values of longitudinal normal stresses are as follows:

FEM model 1 $\approx$ simple beam

FEM model 2 $\approx$ simple plate

FEM model 3 $\approx$ simple beam

FEM model 4 $\approx$ simple plate.

The results for FEM models 1, 2, and 3 were expected since the basis of FEM models 1 and 3, as well as the simple beam ignore the effects of the strains and curvatures in the y direction (the width); while these effects are accounted for in FEM model 2 and the simple plate. The results for model 4 indicate that the simple plate is entirely adequate for predicting the interior stresses.

The interfacial shear stresses for the two x-y plane-stress

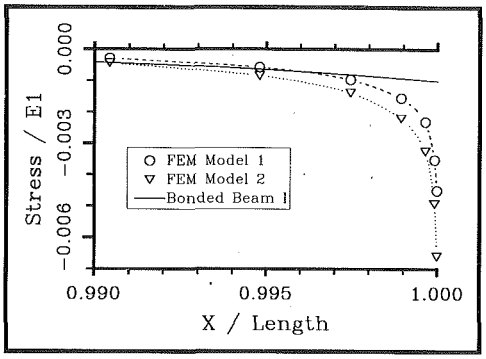

Fig. 5 Interfacial stress σ_{xz}—material 2—graph 1

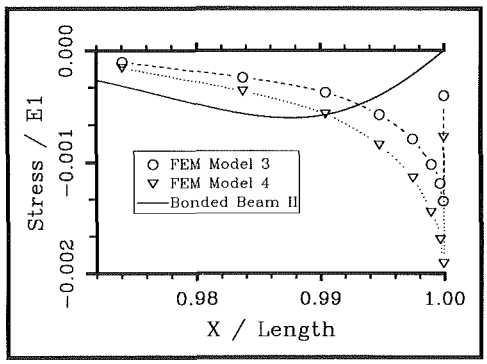

Fig. 6 Interfacial stress σ_{xz}—material 2—graph 2

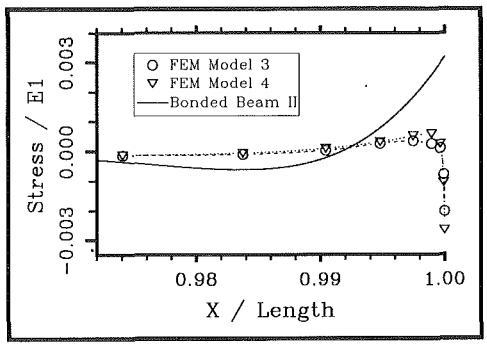

Fig. 7 Interfacial stress σ_z—material 2

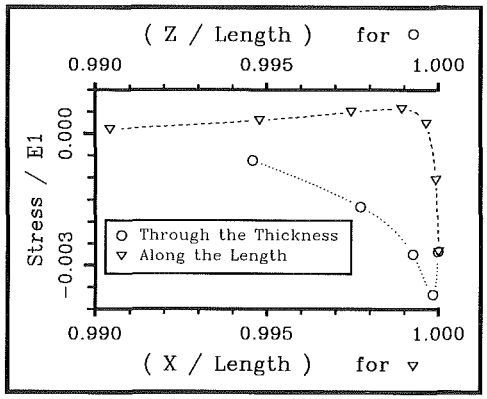

Fig. 8 Stress σ_z decay—material 2

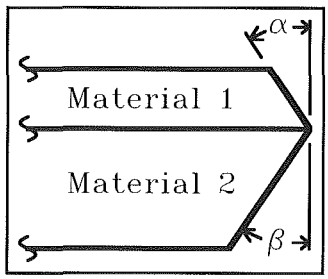

Fig. 9 Beveling of material faces

finite element models (models 1 and 2), and the bonded beam I are shown in Fig. 5. (Note, for all plots of interfacial stresses, only the results for material 2 are shown since it is thinner, and therefore it exhibits higher values and sharper gradients.) The two FEM models indicate higher absolute values of stress, but all three approximations indicate continuously increasing values of shear as the end of the strip is approached. However, this violates the boundary condition of vanishing shear stress at the end. As noted, the bonded beam I enforces the condition of zero shear *force* at the end of the strip, not zero shear *stress*. Also, since $L > B$, the two x-y plane-stress FEM models behave like a beam model.

The predicted values of the interfacial shear stresses for the three-dimensional (model 4) as well as the x-z plane stress (model 3) FEM models are shown in Fig. 6, while the predicted values of the transverse interfacial normal stress are shown in Fig. 7 and Fig. 8. Also plotted in these figures are the stresses according to the bonded beam II.

These three approximations correctly predict a zero shear stress at the end of the strip, and the signs for all three are the same. But, the two FEM models again predict much higher absolute values of stress. Also, the bonded beam II indicates a more gradual transition from zero to peak and back to zero, while the FEM models indicate a much steeper gradient in shear with an abrupt reversal to zero in a zone much closer to the end of the strip.

For the interfacial normal or "peeling" stress, the absolute values of the stresses are similar for FEM models 3 and 4, and the bonded beam II, but there is a marked difference in the direction of the stress predicted by the bonded beam II. The FEM models predict a compressive stress at the end of the strip, while the bonded beam II predicts a tensile stress. Again, the bonded beam II indicates a more gradual transition of stress from zero to a finite peak value, while the FEM models indicate extremely sharp gradients and reversals of peeling stress at the very tip of the strip. These reversals and extremely sharp gradients are an indication of the singularity in the peeling stress at the tip. Also, though material 2 is extremely thin, the gradient of the peeling stress is greater along its interface than through its thickness (Fig. 8).

Finally, as was the case for longitudinal normal stresses, the values of shear stress for model 2 are approximately $1/(1-\nu)$ greater than the values of model 1; while the values of both the shear and peeling stresses for model 4 are approximately $1/(1-\nu)$ greater than the values of model 3. The differences are again attributed to the effects of the strains and curvatures in the y direction which are continuous in models 2 and 4, but not in models 1 and 3.

Conclusions

The behavior of a simply bimetallic thermostatic strip provides an interesting study in the effectiveness of various approximations.

The simple beam (two degrees-of-freedom) is adequate for the prediction of deflections, while the simple plate (again, two degrees-of-freedom) is adequate for the prediction of stresses at interior points.

Though these simple approximations are useful in predicting the deflections and interior stresses, they provide no information about the interfacial shear and normal stresses that appear near the end and edges of the strip. The theory of bonded beams demonstrates that these stresses are highly lo-

calized in a small region near the edges and end of the strip. However, it failed to predict the magnitude, the severity of the gradients, and in some cases the correct sign of these stresses. This is not unexpected since beam theory can not predict behavior in a region, equal or smaller than the thickness of the beam.

To probe the nature of the interfacial shear and normal stresses, previous studies were performed using plane-stress finite elements with the y direction (the width) taken as the direction of zero normal stress. Those studies predicted the general character of the interfacial stresses, indicating that a singularity exists in the peeling stress. However, since those previous studies did not account for the strains and curvatures in the y direction, the values of the stresses are in error by a factor of $1/(1-\nu)$.

The effectiveness of a simplified quadrilateral element has been demonstrated since all the numerical results were obtained on a personal computer with no computational difficulty, or "shear locking," though the interface and end elements were extremely thin.

Finally, since the simple plate describes the deflection *and all* non-negligible stresses in 95 percent of the strip, it provides a graphic example of St.-Venant's principle.

Practical Comment

The large normal stress at the end and edges can be eliminated if the faces of the layers are beveled as illustrated in Fig. 9 (Lukasiewicz).

Acknowledgment

The authors gratefully acknowledge support from the National Science Foundation through award MSM-8720394 under auspices of the Division of Mechanical Systems administered by Dr. Ken Chong.

References

Bogy, D. B., 1968, "Edge-Bonded Dissimilar Orthogonal Elastic Wedges Under Normal and Shear Loading," ASME JOURNAL OF APPLIED MECHANICS, Vol. 35, pp. 460–466.

Bogy, D. B., 1970, "On the Problem of Edge-Bonded Elastic Quarter-Planes Loaded at the Boundary," *Int. J. Solid Structures*, Vol. 6, Pergamon Press, pp. 1287–1313.

Chang, Fo-van, 1983, "Thermal Contact Stresses of Bi-Metal Strip Thermostat," *Appl. Math. and Mech.*, Vol. 4, No. 3, Tsing-hua Univ., Beijing, China, pp. 363–376.

Dundurs, J., 1967, "Effect of Elastic Constants on Stress in a Composite Under Plane Deformation," *J. Composite Materials*, Vol. 1, pp. 310–322.

Dundurs, J., 1969, discussion of D. B. Bogy's "Edge-Bonded Dissimilar Orthogonal Elastic Wedges Under Normal and Shear Loading," ASME JOURNAL OF APPLIED MECHANICS, Vol. 36, pp. 650–652.

Gerstle, Jr. F. P., and Chambers, R. S., 1987, "Analysis of End Stresses in Glass-Metal Bimaterial Strips," ASME WAM, Boston, Mass., Dec. 1987.

Grimado, P. B., 1978, "Interlaminar Thermoelastic Stresses in Layered Beams," *J. Thermal Stresses*, No. 1, pp. 75–86.

Hu, H. C., 1955, "On Some Variational Principles in the Theory of Elasticity and Plasticity," *Scientia Sinica*, Vol. 4.

Lukasiewicz, S., private discussions with Professor Lukasiewicz of the University of Calgary.

Suganuma, K., Okamoto, T., Koizumi, M., and Shimada, M., 1984, "Effect of Interlayers in Ceramic-Metal Joints with Thermal Expansion Mismatches," *J. Am. Cer. Soc.*, Vol. 67, No. 12, pp. C256–C257.

Suhir, E., 1986, "Stresses in Bi-Metal Thermostats," ASME JOURNAL OF APPLIED MECHANICS, Vol. 53, pp. 657–660.

Suhir, E., 1989, "Interfacial Stresses in Bimetal Thermostats," ASME JOURNAL OF APPLIED MECHANICS, Vol. 56, pp. 595–600.

Timoshenko, S. P., 1925, "Analysis of Bi-Metal Thermostats," *J. Opt. Soc. of Am.*, Vol. 11, pp. 233–255.

Washizu, K., 1955, "On the Variational Principles of Elasticity and Plasticity," *Technical Report No. 25–18, Mass. Inst. of Tech.*

Wempner, G. A., 1968, "New Concepts for Finite Elements of Shells," *ZAMM*, pp. T174–T176.

Wempner, G. A., Talaslidis, D., and Hwang, C.-M., 1982, "A Simple and Efficient Approximation of Shells via Finite Quadrilateral Elements," ASME JOURNAL OF APPLIED MECHANICS, Vol. 49, pp. 115–120.

Wemper, G. A., 1983, "Finite Element Modeling of Solids Via the Hu-Washizu Functional," *CIME*, Sept. 1983, pp. 67–75.1

Surot Thangjitham
Associate Professor.

Hyung Jip Choi
Graduate Student.

Department of Engineering Science
and Mechanics,
Virginia Polytechnic Institute
and State University,
Blacksburg, VA 24061

Thermal Stresses in a Multilayered Anisotropic Medium

A steady-state thermoelasticity problem of a multilayered anisotropic medium under the state of generalized plane deformation is considered in this paper. By utilizing the Fourier transform technique, the general solutions of thermoelasticity for layers with transversely isotropic, orthotropic, and monoclinic properties are derived. The complete solution of the entire layered medium is then obtained through introducing the thermal and mechanical boundary and layer interface conditions. This is accomplished via the flexibility/stiffness matrix method. As a numerical illustration, the distributions of temperature and thermal stresses in a laminated anisotropic slab subjected to a uniform surface temperature rise are presented for various stacking sequences of fiber-reinforced layers.

1 Introduction

The use of fiber-reinforced composite materials in a wide variety of modern engineering applications has been rapidly increasing over the past few decades. The advantages of composites over traditional materials are well known (Jones, 1975). The inherent heterogeneous and anisotropic nature of layered composites, however, makes the analysis of such materials become more involved than that of homogeneous and isotropic counterpart (Lekhnitskii, 1981). For the thermoelastic analysis, the problem becomes even more complicated. In this case, solutions to both the heat conduction and thermoelasticity problems for all layers are required. These solutions are also to satisfy the thermal and mechanical boundary and interface conditions. As a result, the conventional procedure for thermal stress analysis of a multilayered medium results in having to solve two systems of simultaneous equations for a large number of unknown constants as evidenced from the previous work by Padovan (1975, 1976), Tauchert (1980), and Tanigawa et al. (1989). Specifically, based on the method of complex series expansion together with the use of complex adjoint differential operators, Padovan (1975, 1976) examined the effects of material anisotropy on the stationary thermoelastic fields of generally laminated slabs and cylinders subjected to spatially periodic thermal loadings. Tauchert (1980) obtained the solution of thermoelasticity for a simply-supported orthotropically laminated slab via the method of displacement potential and compared the results with those by the bending theory. On the other hand, Tanigawa et al. (1989) performed the transient thermal stress analysis of laminated beam composed of dissimilar isotropic layers.

To provide an efficient approach to stress analysis of a multilayered medium, various alternative solution procedures have been proposed. Among them is the transfer matrix method originally developed for isothermal elasticity problem by Bufler (1971) and Bahar (1972) and later extended to thermoelasticity problems by Bahar and Hetnarski (1980). In terms of the vectors containing the appropriate state variables of the layer, this approach recasts the boundary value problem in the form of an equivalent initial value problem. The state vector of any given layer is then related to the initial state vector of layers with known boundary conditions via successive multiplications of the transfer matrices of the intermediate layers. This process amounts to applying the interface continuity conditions for the state variables of any two adjacent layers.

Another matrix approach is the flexibility/stiffness matrix method. In this approach, a local matrix equation is constructed in terms of the unknowns representing the value of selected field variables (stresses for flexibility formulation and displacements for stiffness formulation) evaluated at the layer interfaces. The global matrix equation is assembled from the local matrices through the applications of boundary and layer interface conditions. The unknowns are then obtained by solving the global matrix equation. In terms of the resulting interfacial values, the required unknown constants for the general solution of the elasticity problem are readily evaluated. Consequently, by dividing the solution procedure into two steps, this matrix formulation results, in comparison with the conventional formulation, in a significant reduction in the number of equations that must be solved simultaneously. Small and Booker (1984) and Kausel and Seale (1987) applied, respectively, the flexibility matrix and stiffness matrix formulations to the elasticity problem of a layered isotropic medium resting on a halfspace. More recently, Choi and Thangjitham (1991a,b) performed the stress analysis of a multilayered anisotropic medium based on the stiffness matrix formulation. The foregoing studies are, however, limited to an isothermal condition.

Contributed by the ASME Applied Mechanics Division of THE AMERICAN SOCIETY OF MECHANICAL ENGINEERS for presentation at the Winter Annual Meeting, Atlanta, Ga., Dec. 1–6, 1991.

Discussion on this paper should be addressed to the Technical Editor, Prof. Leon M. Keer, The Technological Institute, Northwestern University, Evanston, IL 60208, and will be accepted until two months after final publication of the paper itself in the JOURNAL OF APPLIED MECHANICS. Manuscript received by the ASME Applied Mechanics Division, June 13, 1990; final revision, Mar. 4, 1991.
Paper No. 91-WA/APM-9.

The objective of this study is to extend the flexibility/stiffness matrix method to the thermoelasticity problem of a multilayered anisotropic medium under the state of generalized plane deformation. By utilizing the Fourier transform technique, the general solutions to heat conduction and thermoelasticity problems for layers with transversely isotropic, orthotropic, and monoclinic properties are first derived. The flexibility/stiffness matrix method is then employed to obtain the specific solution which satisfied the thermal and mechanical boundary and layer interface conditions. As an illustrative example, the thermoelastic response of a multilayered fiber-reinforced slab to a uniform surface temperature rise is examined for various layers stacking sequences.

2 Governing Equations and General Solutions

A layered slab (Fig. 1) composed of N fiber-reinforced layers is considered in this study. The fiber angle, θ, is measured counterclockwise from the positive x-axis to the fiber direction. The external thermal and mechanical loads are assumed to be applied such that all field variables are functions of x and z. Due to the presence of off-axis monoclinic layers, the state of generalized plane deformation for thermoelasticity as discussed by Lekhnitskii (1981) is assumed such that

$$T \equiv T(x,z), \quad u \equiv u(x,z), \quad v \equiv v(x,z), \quad w \equiv w(x,z) \tag{1a,b,c,d}$$

where T is the temperature field measured from the reference stress-free temperature, and u, v, and w are the displacement components in the x, y, and z-directions, respectively. For the case of on-axis transversely isotropic and orthotropic layers, the generalized plane deformation is equivalent to the pure plane deformation.

2.1 Layers With Monoclinic Properties. For the off-axis monoclinic layers with the plane of material symmetry normal to the z-axis, the temperature field satisfies the steady-state heat conduction equation (Nowinski, 1978)

$$\tilde{\kappa}_{11}\frac{\partial^2 T}{\partial x^2}+\tilde{\kappa}_{33}\frac{\partial^2 T}{\partial z^2}=0 \tag{2}$$

where $\tilde{\kappa}_{ij}$, $i,j=1,2,3$, are the coefficients of thermal conductivity in the structural coordinates of the medium (Fig. 1) which can be written in terms of those, κ_{ll}, $l=1,2,3$, (in this paper, repeated indices do not imply summation) in the material coordinates of the layer and of the fiber angle, θ (Jones, 1975). The material coordinates of the layer refer to the directions parallel, transverse, and normal to the fibers.

The corresponding heat fluxes are given as

$$q_x=-\tilde{\kappa}_{11}\frac{\partial T}{\partial x}, \quad q_y=-\tilde{\kappa}_{12}\frac{\partial T}{\partial x}, \quad q_z=-\tilde{\kappa}_{33}\frac{\partial T}{\partial z} \tag{3a,b,c}$$

where $q_j(x,z)$, $j=x,y,z$, are the heat flux components in the x, y, and z-directions, respectively.

The Duhamel-Neumann constitutive equations under the state of generalized plane deformation are written as (Nowinski, 1978)

$$\sigma_{xx}=\tilde{C}_{11}\frac{\partial u}{\partial x}+\tilde{C}_{13}\frac{\partial w}{\partial z}+\tilde{C}_{16}\frac{\partial v}{\partial x}-\beta_1 T \tag{4a}$$

$$\sigma_{yy}=\tilde{C}_{12}\frac{\partial u}{\partial x}+\tilde{C}_{23}\frac{\partial w}{\partial z}+\tilde{C}_{26}\frac{\partial v}{\partial x}-\beta_2 T \tag{4b}$$

$$\sigma_{zz}=\tilde{C}_{13}\frac{\partial u}{\partial x}+\tilde{C}_{33}\frac{\partial w}{\partial z}+\tilde{C}_{36}\frac{\partial v}{\partial x}-\beta_3 T \tag{4c}$$

$$\tau_{xy}=\tilde{C}_{16}\frac{\partial u}{\partial x}+\tilde{C}_{36}\frac{\partial w}{\partial z}+\tilde{C}_{66}\frac{\partial v}{\partial x}-\beta_6 T \tag{4d}$$

$$\tau_{yz}=\tilde{C}_{44}\frac{\partial v}{\partial z}+\tilde{C}_{45}\left(\frac{\partial u}{\partial z}+\frac{\partial w}{\partial x}\right) \tag{4e}$$

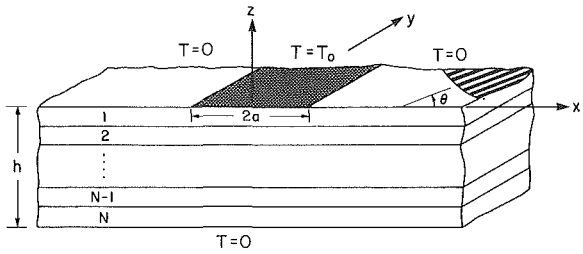

Fig. 1 Configuration of the N-layer anisotropic medium

$$\tau_{xz}=\tilde{C}_{45}\frac{\partial v}{\partial z}+\tilde{C}_{55}\left(\frac{\partial u}{\partial z}+\frac{\partial w}{\partial x}\right) \tag{4f}$$

where $\sigma_{ii}(x,z)$ and $\tau_{ij}(x,z)$, $i,j=x,y,z$, are the normal stress in the i-direction and the shear stress in the i-j plane, respectively, and $\tilde{C}_{ij}$, $i,j=1,2,\ldots,6$, are the elastic stiffness constants in the coordinates of the medium which are functions of the stiffness constants, C_{ij}, $i,j=1,2,\ldots,6$, in the layer coordinates and of the fiber angle, θ. The thermal moduli, β_j, $j=1,2,3,6$, are defined as

$$\beta_1=\tilde{C}_{11}\tilde{\alpha}_{11}+\tilde{C}_{12}\tilde{\alpha}_{22}+\tilde{C}_{13}\tilde{\alpha}_{33}+\tilde{C}_{16}\tilde{\alpha}_{12} \tag{5a}$$

$$\beta_2=\tilde{C}_{12}\tilde{\alpha}_{11}+\tilde{C}_{22}\tilde{\alpha}_{22}+\tilde{C}_{23}\tilde{\alpha}_{33}+\tilde{C}_{26}\tilde{\alpha}_{12} \tag{5b}$$

$$\beta_3=\tilde{C}_{13}\tilde{\alpha}_{11}+\tilde{C}_{23}\tilde{\alpha}_{22}+\tilde{C}_{33}\tilde{\alpha}_{33}+\tilde{C}_{36}\tilde{\alpha}_{12} \tag{5c}$$

$$\beta_6=\tilde{C}_{16}\tilde{\alpha}_{11}+\tilde{C}_{26}\tilde{\alpha}_{22}+\tilde{C}_{36}\tilde{\alpha}_{33}+\tilde{C}_{66}\tilde{\alpha}_{12} \tag{5d}$$

in which $\tilde{\alpha}_{ij}$, $i,j=1,2,3$, are the thermal expansion coefficients in the coordinates of the medium which are again functions of those, α_{ll}, $l=1,2,3$, in the layer coordinates and of the fiber angle, θ.

In the absence of body forces, the governing equations for the plane thermoelasticity of a given monoclinic layer expressed in terms of the displacement components are written as

$$\tilde{C}_{11}\frac{\partial^2 u}{\partial x^2}+\tilde{C}_{55}\frac{\partial^2 u}{\partial z^2}+\tilde{C}_{16}\frac{\partial^2 v}{\partial x^2}+\tilde{C}_{45}\frac{\partial^2 v}{\partial z^2}+(\tilde{C}_{13}+\tilde{C}_{55})\frac{\partial^2 w}{\partial x\partial z}=\beta_1\frac{\partial T}{\partial x} \tag{6a}$$

$$\tilde{C}_{16}\frac{\partial^2 u}{\partial x^2}+\tilde{C}_{45}\frac{\partial^2 u}{\partial z^2}+\tilde{C}_{66}\frac{\partial^2 v}{\partial x^2}+\tilde{C}_{44}\frac{\partial^2 v}{\partial z^2}+(\tilde{C}_{36}+\tilde{C}_{45})\frac{\partial^2 w}{\partial x\partial z}=\beta_6\frac{\partial T}{\partial x} \tag{6b}$$

$$(\tilde{C}_{13}+\tilde{C}_{55})\frac{\partial^2 u}{\partial x\partial z}+(\tilde{C}_{36}+\tilde{C}_{45})\frac{\partial^2 v}{\partial x\partial z}+\tilde{C}_{55}\frac{\partial^2 w}{\partial x^2}+\tilde{C}_{33}\frac{\partial^2 w}{\partial z^2}=\beta_3\frac{\partial T}{\partial z} \tag{6c}$$

where Eqs. (6a)-(6c) constitute a system of nonhomogeneous partial differential equations.

To solve the field Eqs. (2) and (6a)-(6c), the Fourier transform is applied over the variable x. The transform pair for an arbitrary function $g(x)$ is defined as (Sneddon, 1951)

$$\bar{g}(s)=\int_{-\infty}^{\infty} g(x)e^{isx}dx, \quad g(x)=\frac{1}{2\pi}\int_{-\infty}^{\infty}\bar{g}(s)e^{-isx}ds \tag{7a,b}$$

where an overbar denotes the transformed quantity, s is the transform variable, and $i=\sqrt{-1}$.

Under the condition that the field variables and their first derivatives with respect to x vanish as $x\to\pm\infty$, the heat conduction Eq. (2), is readily solved to give the temperature field, $\bar{T}(s,z)$, in the transformed domain as

$$\bar{T}=H_1\cosh s\kappa z+H_2\sinh s\kappa z \tag{8}$$

where $H_j(s)$, $j=1,2$, are the unknown constants to be evaluated from the proper boundary conditions and $\kappa=\sqrt{\tilde{\kappa}_{11}/\tilde{\kappa}_{33}}$. It is

noted that the variable s in the above equation is regarded as a parameter. The transformed heat fluxes are then obtained by taking the Fourier transform of Eqs. (3*a*)–(3*c*) and using Eq. (8).

In the Fourier transformed domain, the governing equations for thermoelasticity, Eqs. (6*a*)–(6*c*), are reduced to the following system of nonhomogeneous ordinary differential equations

$$M_1\frac{d^2\bar{\mathbf{u}}}{dz^2}+M_2\frac{d\bar{\mathbf{u}}}{dz}+M_3\bar{\mathbf{u}}=\bar{\mathbf{u}}_0 \tag{9}$$

where $\bar{\mathbf{u}}(s,z)=\{\bar{u}(sz),\bar{v}(sz),\bar{w}(sz)\}$ is the displacement vector of length three, $M_j(s)$, $j=1,2,3$, are the 3×3 symmetric matrices defined as

$$M_1=\begin{bmatrix}\tilde{C}_{55} & \tilde{C}_{45} & 0\\ \tilde{C}_{45} & \tilde{C}_{44} & 0\\ 0 & 0 & \tilde{C}_{33}\end{bmatrix},$$

$$M_2=\begin{bmatrix}0 & 0 & -is(\tilde{C}_{13}+\tilde{C}_{55})\\ 0 & 0 & -is(\tilde{C}_{36}+\tilde{C}_{45})\\ -is(\tilde{C}_{13}+\tilde{C}_{55}) & -is(\tilde{C}_{36}+\tilde{C}_{45}) & 0\end{bmatrix},$$

$$M_3=\begin{bmatrix}-s^2\tilde{C}_{11} & -s^2\tilde{C}_{16} & 0\\ -s^2\tilde{C}_{16} & -s^2\tilde{C}_{66} & 0\\ 0 & 0 & -s^2\tilde{C}_{55}\end{bmatrix}, \tag{10a,b,c}$$

and the right-hand side vector, $\bar{\mathbf{u}}_0(s,z)$, is given as

$$\bar{\mathbf{u}}_0=\{-is\beta_1\bar{T}\quad -is\beta_6\bar{T}\quad \beta_3\bar{T}'\} \tag{10d}$$

in which the prime denotes differentiation with respect to z.

To obtain the particular solutions corresponding to the nonhomogeneous part of Eq. (9), the method of undetermined coefficients (Hildebrand, 1976) is employed rather than that of displacement potentials. This is due to the fact that, unlike the problems of orthotropic (Tauchert, 1980) and transversely isotropic (Sharma, 1958) media, the use of such potentials for monoclinic media leads to a noncanonic form of the governing equations as depicted by Padovan (1974, 1975). Supplemented by the complementary solutions of the homogeneous part of Eq. (9) (Choi and Thangjitham, 1991b), the general solutions for displacements are obtained as

$$\bar{u}=\sum_{j=1}^{3}(A_j\cosh s\lambda_j z+B_j\sinh s\lambda_j z)+i\frac{\eta_1}{s}(H_1\cosh s\kappa z+H_2\sinh s\kappa z) \tag{11}$$

$$\bar{v}=\sum_{j=1}^{3}(A_j\cosh s\lambda_j z+B_j\sinh s\lambda_j z)L_j+i\frac{\eta_2}{s}(H_1\cosh s\kappa z+H_2\sinh s\kappa z) \tag{12}$$

$$\bar{w}=\sum_{j=1}^{3}i(A_j\sinh s\lambda_j z+B_j\cosh s\lambda_j z)R_j+\frac{\eta_3}{s}(H_1\sinh s\kappa z+H_2\cosh s\kappa z) \tag{13}$$

where $A_j(s)$ and $B_j(s)$, $j=1,2,3$, are the unknown constants to be evaluated by applying the proper boundary conditions and λ_j, $j=1,2,3$, are the roots of the characteristic equation

$$\det\Delta=0 \tag{14}$$

in which Δ is a 3×3 symmetric matrix whose elements are given as

$$\begin{aligned}&\Delta_{11}=\tilde{C}_{55}\lambda_j^2-\tilde{C}_{11},\quad \Delta_{12}=\Delta_{21}=\tilde{C}_{45}\lambda_j^2-\tilde{C}_{16},\\ &\Delta_{13}=\Delta_{31}=-i(\tilde{C}_{13}+\tilde{C}_{55})\lambda_j,\quad \Delta_{22}=\tilde{C}_{44}\lambda_j^2-\tilde{C}_{66},\\ &\Delta_{23}=\Delta_{32}=-i(\tilde{C}_{36}+\tilde{C}_{45})\lambda_j,\quad \Delta_{33}=\tilde{C}_{33}\lambda_j^2-\tilde{C}_{55}.\end{aligned} \tag{15}$$

The constants L_j and R_j, $j=1,2,3$, for each root λ_j in Eqs. (12) and (13) are obtained as

$$L_j=\frac{\Delta_{12}\Delta_{13}-\Delta_{11}\Delta_{23}}{\Delta_{12}\Delta_{23}-\Delta_{22}\Delta_{13}},\quad R_j=\frac{i(\Delta_{j2}^2-\Delta_{11}\Delta_{22})}{\Delta_{12}\Delta_{23}-\Delta_{22}\Delta_{13}} \tag{16a,b}$$

and the constants η_j, $j=1,2,3$, are given as

$$\eta_1=\frac{(\beta_1a_4-\beta_6a_2)+\eta_3(a_3a_4-a_2a_6)}{a_2^2-a_1a_4} \tag{17a}$$

$$\eta_2=\frac{(\beta_6a_1-\beta_1a_2)+\eta_3(a_1a_6-a_2a_3)}{a_2^2-a_1a_4} \tag{17b}$$

$$\eta_3=\frac{\beta_1(a_3a_4-a_2a_6)+\beta_6(a_1a_6-a_2a_3)+\beta_3\kappa(a_2^2-a_1a_4)}{a_6(2a_2a_3-a_1a_6)+a_5(a_2^2-a_1a_4)-a_3^2a_4} \tag{17c}$$

in which a_j, $j=1,2,\ldots,6$, are defined as

$$\begin{aligned}&a_1=\kappa^2\tilde{C}_{55}-\tilde{C}_{11},\quad a_2=\kappa^2\tilde{C}_{45}-\tilde{C}_{16},\quad a_3=-\kappa(\tilde{C}_{13}+\tilde{C}_{55})\\ &a_4=\kappa^2\tilde{C}_{44}-\tilde{C}_{66},\quad a_5=\kappa^2\tilde{C}_{33}-\tilde{C}_{55},\quad a_6=-\kappa(\tilde{C}_{36}+\tilde{C}_{45}).\end{aligned} \tag{18}$$

It is noted that the quadratic roots λ_j^2 of Eq. (14) are positive, real, and distinct (Pagano, 1970).

By taking the Fourier transform of Eqs. (4*a*)–(4*f*) and using the displacement expressions, Eqs. (11)–(13), the stress components are obtained as

$$\bar{\sigma}_m=\sum_{j=1}^{3}is(\tilde{C}_{m3}\lambda_jR_j-\tilde{C}_{1m}-\tilde{C}_{m6}L_j)(A_j\cosh s\lambda_jz+B_j\sinh s\lambda_jz)+(\tilde{C}_{1m}\eta_1+\tilde{C}_{m6}\eta_2+\tilde{C}_{m3}\eta_3\kappa-\beta_m)(H_1\cosh s\kappa z+H_2\sinh s\kappa z),\quad m=1,2,3,6 \tag{19}$$

$$\bar{\sigma}_m=\sum_{j=1}^{3}s[\tilde{C}_{4m}\lambda_jL_j+\tilde{C}_{m5}(R_j+\lambda_j)](A_j\sinh s\lambda_jz+B_j\cosh s\lambda_jz)+i[\tilde{C}_{4m}\eta_2\kappa+\tilde{C}_{m5}(\eta_1\kappa-\eta_3)](H_1\sinh s\kappa z+H_2\cosh s\kappa z),\quad m=4,5 \tag{20}$$

where $\bar{\sigma}_m(s,z)$, $m=1,2,\ldots6$, are the contracted notation for $\bar{\sigma}_{xx}$, $\bar{\sigma}_{yy}$, $\bar{\sigma}_{zz}$, $\bar{\tau}_{yz}$, $\bar{\tau}_{xz}$, $\bar{\tau}_{xy}$, respectively.

2.2 Layers With Orthotropic Properties. For the case of on-axis orthotropic layers with fibers aligned in the x-direction ($\theta=0$ deg), there exists three mutually orthogonal planes of material symmetry. In this case, the elastic stiffness constants $\tilde{C}_{ij}=C_{ij}$ with $\tilde{C}_{45}=0$ and $\tilde{C}_{m6}=0$, $m=1,2,3$. The thermal expansion coefficient causing the shearing thermal strain, $\tilde{\alpha}_{12}$, is also zero. As a result, the displacement v in the governing Eqs. (6*a*)–(6*c*) is decoupled from the remaining components, u and w. Consequently, the complementary part of the transformed displacements, Eqs. (11)–(13), and stresses, Eqs. (19)–(20), is no longer valid. By following the similar solution procedure, the expressions for the transformed displacements of orthotropic layers are obtained as

$$\bar{u}=\sum_{j=1}^{2}(A_j\cosh s\lambda_jz+B_j\sinh s\lambda_jz)+i\frac{\eta_1}{s}(H_1\cosh s\kappa z+H_2\sinh s\kappa z) \tag{21}$$

$$\bar{w}=\sum_{j=1}^{2}i(A_j\sinh s\lambda_jz+B_j\cosh s\lambda_jz)R_j+\frac{\eta_3}{s}(H_1\sinh s\kappa z+H_2\cosh s\kappa z) \tag{22}$$

$$\bar{v}=A_3\cosh s\lambda_0z+B_3\sinh s\lambda_0z \tag{23}$$

where $\lambda_0=\sqrt{\tilde{C}_{66}/\tilde{C}_{44}}$ and λ_j, $j=1,2$, are the roots of the characteristic equation

$$\tilde{C}_{33}\tilde{C}_{55}\lambda^4+[(\tilde{C}_{13}+\tilde{C}_{55})^2-\tilde{C}_{11}\tilde{C}_{33}-\tilde{C}_{55}^2]\lambda^2+\tilde{C}_{11}\tilde{C}_{55}=0 \tag{24}$$

and the constants R_j, $j=1,2$, are given as

$$R_j = \frac{\tilde{C}_{11} - \tilde{C}_{55}\lambda_j^2}{(\tilde{C}_{13} + \tilde{C}_{55})\lambda_j}. \quad (25)$$

It should be noted that the particular solutions of Eq. (9) for orthotropic layers can be obtained from those for monoclinic layers by substituting the corresponding thermal and mechanical properties. The quadratic roots λ_j^2 in Eq. (24) are also positive, real, and distinct.

The transformed stresses for the case of orthotropic layers are obtained as

$$\bar{\sigma}_m = \sum_{j=1}^{2} is(\tilde{C}_{m3}\lambda_j R_j - \tilde{C}_{1m})(A_j \cosh s\lambda_j z + B_j \sinh s\lambda_j z) + (\tilde{C}_{1m}\eta_1 + \tilde{C}_{m3}\eta_3\kappa - \beta_m)(H_1 \cosh s\kappa z + H_2 \sinh s\kappa z), \quad m = 1,2,3 \quad (26)$$

$$\bar{\tau}_{xz} = \sum_{j=1}^{2} s\tilde{C}_{55}(R_j + \lambda_j)(A_j \sinh s\lambda_j z + B_j \cosh s\lambda_j z) + i\tilde{C}_{55}(\eta_1\kappa - \eta_3)(H_1 \sinh s\kappa z + H_2 \cosh s\kappa z) \quad (27)$$

$$\bar{\tau}_{yz} = s\lambda_0 \tilde{C}_{44}(A_3 \sinh s\lambda_0 z + B_3 \cosh s\lambda_0 z) \quad (28)$$

$$\bar{\tau}_{xy} = -is\tilde{C}_{66}(A_3 \cosh s\lambda_0 z + B_3 \sinh s\lambda_0 z) \quad (29)$$

where $\bar{\sigma}_m$, $m = 1,2,3$, refer to $\bar{\sigma}_{xx}$, $\bar{\sigma}_{yy}$, $\bar{\sigma}_{zz}$, respectively.

2.3 Layers With Transversely Isotropic Properties. Another case of interest arises when the material properties of layers are transversely isotropic in the x-z plane. This condition occurs when the material properties in all directions perpendicular to the fibers are the same and the fibers are aligned in the y-direction ($\theta = 90$ deg). In addition to $\tilde{C}_{45} = 0$, $\tilde{C}_{m6} = 0$, $m = 1,2,3$, and $\tilde{\alpha}_{12} = 0$ as for the case of orthotropic layers, the thermal and mechanical properties of the transversely isotropic layers are further simplified such that $\tilde{C}_{11} = \tilde{C}_{33}$, $\tilde{C}_{12} = \tilde{C}_{23}$, $\tilde{C}_{44} = \tilde{C}_{66}$, $\tilde{C}_{55} = (\tilde{C}_{11} - \tilde{C}_{13})/2$, $\tilde{\alpha}_{11} = \tilde{\alpha}_{33}$ and $\tilde{\kappa}_{11} = \tilde{\kappa}_{33}$. In this case, the quadratic roots of the characteristic Eq. (24), are repeated and equal to unity. Consequently, the expressions for the transformed displacements are obtained as

$$\bar{u} = (A_1 + A_2 z)\cosh sz + (B_1 + B_2 z)\sinh sz - i\frac{\beta_1 z}{2\tilde{C}_{11}}(H_1 \sinh sz + H_2 \cosh sz) \quad (30)$$

$$\bar{w} = i\left[\left(B_1 + B_2 z + A_2\frac{R}{s}\right)\cosh sz + \left(A_1 + A_2 z + B_2\frac{R}{s}\right)\sinh sz\right] + \frac{\beta_1}{2\tilde{C}_{11}}\left[\left(\frac{H_2}{s} + H_1 z\right)\cosh sz + \left(\frac{H_1}{s} + H_2 z\right)\sinh sz\right] \quad (31)$$

$$\bar{v} = A_3 \cosh sz + B_3 \sinh sz \quad (32)$$

where the constant R is given as

$$R = -\frac{\tilde{C}_{13} + 3\tilde{C}_{55}}{\tilde{C}_{13} + \tilde{C}_{55}}. \quad (33)$$

The corresponding transformed stresses are obtained as

$$\bar{\sigma}_{xx} = i[\tilde{C}_{13}(1+R)B_2 - 2s\tilde{C}_{55}(A_1 + A_2 z)]\cosh sz + i[\tilde{C}_{13}(1+R)A_2 - 2s\tilde{C}_{55}(B_1 + B_2 z)]\sinh sz - \frac{2\tilde{C}_{55}\beta_1}{\tilde{C}_{11}}\left[\left(\frac{H_2 s}{2}z + H_1\right)\cosh sz + \left(\frac{H_1 s}{2}z + H_2\right)\sinh sz\right] \quad (34)$$

$$\bar{\sigma}_{zz} = i[\tilde{C}_{11}(1+R)B_2 + 2s\tilde{C}_{55}(A_1 + A_2 z)]\cosh sz + i[\tilde{C}_{11}(1+R)A_2 + 2s\tilde{C}_{55}(B_1 + B_2 z)]\sinh sz + \frac{\tilde{C}_{55}\beta_1}{\tilde{C}_{11}}(H_1 sz \sinh sz + H_2 sz \cosh sz) \quad (35)$$

$$\bar{\tau}_{xz} = \tilde{C}_{55}[(1+R)A_2 + 2s(B_1 + B_2 z)]\cosh sz + \tilde{C}_{55}[(1+R)B_2 + 2s(A_1 + A_2 z)]\sinh sz - i\frac{\tilde{C}_{55}\beta_1}{\tilde{C}_{11}}[(H_1 sz + H_2)\cosh sz + (H_2 sz + H_1)\sinh sz] \quad (36)$$

$$\bar{\sigma}_{yy} = i\tilde{C}_{12}(1+R)(A_2 \sinh sz + B_2 \cosh sz) + \left(\frac{\tilde{C}_{12}\beta_1}{\tilde{C}_{11}} - \beta_2\right)(H_1 \cosh sz + H_2 \sinh sz) \quad (37)$$

$$\bar{\tau}_{xy} = -is\tilde{C}_{44}(A_3 \cosh sz + B_3 \sinh sz) \quad (38)$$

$$\bar{\tau}_{yz} = s\tilde{C}_{44}(A_3 \sinh sz + B_3 \cosh sz). \quad (39)$$

3 Flexibility/Stiffness Matrix Method

The next step of the solution procedure is to determine the temperature, displacement, and stress fields for all layers by solving the specific boundary value problem. For the foregoing sections, it is seen that, for each layer, there are two unknown constants, H_j, $j = 1,2$, and six unknown constants, A_j and B_j, $j = 1,2,3$, for heat conduction and thermoelasticity problems, respectively. Consequently, for an N-layer medium, a total of $8N$ unknown constants must be evaluated from a set of $8N$ appropriate boundary and interface conditions. For laminated composites which, in general, contain a large number of layers, the conventional procedure results in having to solve two systems of simultaneous equations for a large number of unknown constants. To circumvent these difficulties, the flexibility matrix and stiffness matrix formulations are employed for the heat conduction and thermoelasticity problems, respectively.

3.1 Flexibility Matrix Formulation for Heat Conduction Analysis. In the flexibility matrix formulation of heat conduction problem, the transformed temperature, $\bar{T}_k^{\pm}(s)$, and transverse heat fluxes, $\bar{q}_k^{\pm}(s) \equiv (\bar{q}_z)_k^{\pm}$, at the upper (+) and lower (−) surfaces of the kth layer are expressed in terms of the unknown constants, H_j^k, $j = 1,2$, as

$$\begin{Bmatrix} \bar{T}_k^+ \\ -\bar{T}_k^- \end{Bmatrix} = \begin{bmatrix} C_k & S_k \\ -C_k & S_k \end{bmatrix} \begin{Bmatrix} H_1^k \\ H_2^k \end{Bmatrix} \quad (40)$$

$$\begin{Bmatrix} \bar{q}_k^+ \\ \bar{q}_k^- \end{Bmatrix} = -s\sqrt{\tilde{\kappa}_{11}^k \tilde{\kappa}_{33}^k} \begin{bmatrix} S_k & C_k \\ -S_k & C_k \end{bmatrix} \begin{Bmatrix} H_1^k \\ H_2^k \end{Bmatrix} \quad (41)$$

where $C_k = \cosh s\kappa_k h_k/2$ and $S_k = \sinh s\kappa_k h_k/2$ for which h_k is the thickness of the layer.

Upon eliminating the constants, H_j^k, from Eqs. (40)–(41), the relations for the surface temperature and transverse heat fluxes of the layer are obtained as

$$\begin{Bmatrix} \bar{T}_k^+ \\ -\bar{T}_k^- \end{Bmatrix} = \begin{bmatrix} F_{11}^k & F_{12}^k \\ F_{12}^k & F_{22}^k \end{bmatrix} \begin{Bmatrix} \bar{q}_k^+ \\ \bar{q}_k^- \end{Bmatrix} \quad (42)$$

where $F_{ij}^k(s)$, $i,j = 1,2$, are the elements of the local flexibility matrix of the kth layer defined as

$$\begin{bmatrix} F_{11}^k & F_{12}^k \\ F_{12}^k & F_{22}^k \end{bmatrix} = -\frac{1}{s\sqrt{\tilde{\kappa}_{11}^k \tilde{\kappa}_{33}^k}} \begin{bmatrix} C_k & S_k \\ -C_k & S_k \end{bmatrix} \begin{bmatrix} S_k & C_k \\ -S_k & C_k \end{bmatrix}^{-1} \quad (43)$$

in which the 2×2 local flexibility matrix, F_k, is symmetric.

For a perfectly bonded N-layer medium subjected to arbitrary temperature variations on the bounding surfaces, the following thermal boundary and interface continuity conditions are applied

$$\bar{T}_1^+ = \bar{t}^+ \quad (44a)$$

$$\bar{T}_k^- = \bar{T}_{k+1}^+, \quad \bar{q}_k^- = \bar{q}_{k+1}^+, \quad k = 1,2,\ldots,(N-1) \quad (44b,c)$$

$$\bar{T}_N^- = \bar{t}^- \quad (44d)$$

where $\bar{t}^{\pm}(s)$ signify the transformed temperatures on the upper (+) and lower (−) surfaces of the medium, respectively.

By denoting $\bar{q}_1 = \bar{q}_1^+$ and $\bar{q}_{N+1} = \bar{q}_N^-$ the transverse heat fluxes on the upper and lower bounding surfaces of the medium, respectively, and $\bar{q}_{k+1} = \bar{q}_k^- = \bar{q}_{k+1}^+$, $k = 1,2,\ldots,(N-1)$, the common interfacial transverse heat fluxes between the kth and $(k+1)$th layers, the successive applications of the conditions in Eqs. (44a)–(44d) lead to the global flexibility equations for the N-layer medium written as

$$F_{11}^1\bar{q}_1+F_{12}^1\bar{q}_2=\bar{t}^+ \tag{45a}$$

$$F_{12}^k\bar{q}_k+(F_{22}^k+F_{11}^{k+1})\bar{q}_{k+1}+F_{12}^{k+1}\bar{q}_{k+2}=0,$$
$$k=1,2,\ldots,(N-1) \tag{45b}$$

$$F_{12}^N\bar{q}_N+F_{22}^N\bar{q}_{N+1}=-\bar{t}^- \tag{45c}$$

In matrix form, the above system of algebraic equations can be expressed as

$$F\bar{\mathbf{q}}=\bar{\mathbf{t}} \tag{46}$$

where $F(s)$ is the $(N+1)\times(N+1)$ banded and symmetric global flexibility matrix, $\bar{\mathbf{q}}(s)$ is the global vector containing the unknown interfacial transverse heat fluxes, i.e., $\{\bar{q}_1\ \bar{q}_2\ldots\bar{q}_{N+1}\}$, and $\bar{\mathbf{t}}(s)$ is the vector containing the transformed surface temperature and zero elements. It is noted that the half-bandwidth of F is two.

3.2 Stiffness Matrix Formulation for Thermal Stress Analysis. To utilize the stiffness matrix formulation for the thermal stress analysis of a multilayered medium, the following vectors for the kth layer are defined as

$$\bar{\mathbf{d}}_k=\{-i\bar{w}_k\quad \bar{u}_k\quad \bar{v}_k\},\ \bar{\sigma}_k=\{-i\bar{\sigma}_{zz}^k\quad \bar{\tau}_{xz}^k\quad \bar{\tau}_{yz}^k\} \tag{47a,b}$$

$$\mathbf{a}_k=\{A_1^k\quad A_2^k\quad A_3^k\},\quad \mathbf{b}_k=\{B_1^k\quad B_2^k\quad B_3^k\} \tag{47c,d}$$

where $\bar{\mathbf{d}}_k(s,z)$ and $\bar{\sigma}_k(s,z)$ are the vectors for the transformed displacements and tractions, respectively, and $\mathbf{a}_k(s)$ and $\mathbf{b}_k(s)$ are the vectors for the unknown constants.

In terms of $\mathbf{a}_k$ and $\mathbf{b}_k$, the vectors containing the surface values of displacements, $\bar{\mathbf{d}}_k^{\pm}(s)$, and tractions, $\bar{\sigma}_k^{\pm}(s)$, of the layer can be written as

$$\begin{Bmatrix}\bar{\mathbf{d}}_k^+\\ \bar{\mathbf{d}}_k^-\end{Bmatrix}=\begin{bmatrix}P_{11}^k & P_{12}^k\\ P_{21}^k & P_{22}^k\end{bmatrix}\begin{Bmatrix}\mathbf{a}_k\\ \mathbf{b}_k\end{Bmatrix}-i\begin{Bmatrix}(\bar{\mathbf{d}}_k^+)_T\\ (\bar{\mathbf{d}}_k^-)_T\end{Bmatrix} \tag{48}$$

$$\begin{Bmatrix}\bar{\sigma}_k^+\\ -\bar{\sigma}_k^-\end{Bmatrix}=\begin{bmatrix}Q_{11}^k & Q_{12}^k\\ Q_{21}^k & Q_{22}^k\end{bmatrix}\begin{Bmatrix}\mathbf{a}_k\\ \mathbf{b}_k\end{Bmatrix}-i\begin{Bmatrix}(\bar{\sigma}_k^+)_T\\ -(\bar{\sigma}_k^-)_T\end{Bmatrix} \tag{49}$$

where $P_{ij}^k(s)$ and $Q_{ij}^k(s)$, $i,j=1,2$, are the 3×3 real submatrices and $(\bar{\mathbf{d}}_k^{\pm})_T$ and $(\bar{\sigma}_k^{\pm})_T$ are, respectively, the vectors containing surface displacements and tractions of the layer corresponding to the nonhomogeneous part of the governing Eqs. (6*a*)–(6*c*).

The elimination of the unknown vectors, $\mathbf{a}_k$ and $\mathbf{b}_k$, from Eqs. (48) and (49) yields the relations for the surface tractions and displacements of the layer as follows

$$\begin{Bmatrix}\bar{\sigma}_k^+\\ -\bar{\sigma}_k^-\end{Bmatrix}=\begin{bmatrix}K_{11}^k & K_{12}^k\\ K_{21}^k & K_{22}^k\end{bmatrix}\begin{Bmatrix}\bar{\mathbf{d}}_k^+\\ \bar{\mathbf{d}}_k^-\end{Bmatrix}-i\begin{Bmatrix}\bar{\mathbf{r}}_k^+\\ \bar{\mathbf{r}}_k^-\end{Bmatrix} \tag{50}$$

where $K_{ij}^k(s)$, $i,j=1,2$, are the 3×3 real submatrices defined as

$$\begin{bmatrix}K_{11}^k & K_{12}^k\\ K_{21}^k & K_{22}^k\end{bmatrix}=\begin{bmatrix}Q_{11}^k & Q_{12}^k\\ Q_{21}^k & Q_{22}^k\end{bmatrix}\begin{bmatrix}P_{11}^k & P_{12}^k\\ P_{21}^k & P_{22}^k\end{bmatrix}^{-1} \tag{51}$$

in which the matrix on the left-hand side is the 6×6 real and symmetric local stiffness matrix, K_k, of the kth layer. This matrix is fully populated for layers with monoclinic properties. The thermal effects represented by the vectors $\bar{\mathbf{r}}_k^{\pm}(s)$ are expressed in terms of K_k as

$$\begin{Bmatrix}\bar{\mathbf{r}}_k^+\\ \bar{\mathbf{r}}_k^-\end{Bmatrix}=\begin{Bmatrix}(\bar{\sigma}_k^+)_T\\ -(\bar{\sigma}_k^-)_T\end{Bmatrix}-\begin{bmatrix}K_{11}^k & K_{12}^k\\ K_{21}^k & K_{22}^k\end{bmatrix}\begin{Bmatrix}(\bar{\mathbf{d}}_k^+)_T\\ (\bar{\mathbf{d}}_k^-)_T\end{Bmatrix} \tag{52}$$

For an N-layer medium subjected to applied tractions on the bounding surfaces, the mechanical boundary and layer interface continuity conditions are imposed such that

$$\bar{\sigma}_1^+=\bar{\mathbf{f}}^+ \tag{53a}$$

$$\bar{\mathbf{d}}_k^-=\bar{\mathbf{d}}_{k+1}^+,\ \bar{\sigma}_k^-=\bar{\sigma}_{k+1}^+,\ k=1,2,\ldots,(N-1) \tag{53b,c}$$

$$\bar{\sigma}_N^-=\bar{\mathbf{f}}^- \tag{53d}$$

where $\bar{\mathbf{f}}^{\pm}(s)$ denote the transformed self-equilibrating tractions applied on the upper $(+)$ and lower $(-)$ surfaces of the laminated medium, respectively.

By defining $\bar{\boldsymbol{\delta}}_{k+1}=\bar{\mathbf{d}}_k^-=\bar{\mathbf{d}}_{k+1}^+$, $k=1,2,\ldots,(N-1)$ as the vector for the values of interfacial displacements common to the kth and $(k+1)$th layers, and $\bar{\boldsymbol{\delta}}_1=\bar{\mathbf{d}}_1^+$ and $\bar{\boldsymbol{\delta}}_{N+1}=\bar{\mathbf{d}}_N^+$, the following global stiffness equations for the N-layer medium are obtained through the successive applications of the conditions in Eqs. tions (53*a*)–(53*d*)

$$K_{11}^1\bar{\boldsymbol{\delta}}_1+K_{12}^1\bar{\boldsymbol{\delta}}_2=\bar{\mathbf{f}}^+ +i\bar{\mathbf{r}}_1^+ \tag{54a}$$

$$K_{21}^k\bar{\boldsymbol{\delta}}_k+(K_{22}^k+K_{11}^{k+1})\bar{\boldsymbol{\delta}}_{k+1}+K_{12}^{k+1}\bar{\boldsymbol{\delta}}_{k+2}=i(\bar{\mathbf{r}}_k^- +\bar{\mathbf{r}}_{k+1}^+),$$
$$k=1,2,\ldots,(N-1) \tag{54b}$$

$$K_{21}^N\bar{\boldsymbol{\delta}}_N+K_{22}^N\bar{\boldsymbol{\delta}}_{N+1}=-\bar{\mathbf{f}}^- +i\bar{\mathbf{r}}_N^- \tag{54c}$$

The above system of algebraic equations can be written in matrix notation as

$$K\bar{\boldsymbol{\delta}}=\bar{\mathbf{f}}+\bar{\mathbf{r}} \tag{55}$$

where $K(s)$ is the $3(N+1)\times3(N+1)$ banded and symmetric global stiffness matrix, $\bar{\boldsymbol{\delta}}(s)$ is the global vector for the unknown interfacial displacements, i.e., $\{\bar{\boldsymbol{\delta}}_1\ \bar{\boldsymbol{\delta}}_2\ldots\bar{\boldsymbol{\delta}}_{N+1}\}$, $\bar{\mathbf{f}}(s)$ is the vector containing the transformed surface tractions and zero elements, and $\bar{\mathbf{r}}(s)$ is the vector containing the effects of thermal loadings. The half-bandwidth of K is six.

In contrast to the conventional procedure which yields, respectively, a system of $2N$ and $6N$ simultaneous equations for heat conduction and thermoelasticity problems, the current matrix approach offers fifty percent reduction in the number of equations that must be solved. With the foregoing remarks in mind, the general solution procedure for thermal stress analysis by the matrix formulations can be divided into the following steps.

- First, the global interfacial heat flux vector, $\bar{\mathbf{q}}$, is obtained by solving the global flexibility matrix Eq. (46).
- The unknown constants of the kth layer, H_j^k, are then evaluated from Eq. (41) in terms of the corresponding local interfacial heat fluxes, $\mathbf{q}_k$ and $\bar{\mathbf{q}}_{k+1}$.
- The constants H_j^k are substituted into Eq. (52) to evaluate the thermal effects, $\bar{\mathbf{r}}_k^{\pm}$, of the layer which will be used in the local stiffness matrix Eq. (50).
- With the vectors $\bar{\mathbf{r}}_k^{\pm}$, $k=1,2,\ldots,N$, determined, the global stiffness matrix Eq. (55) is assembled to be solved for the global interfacial displacement vector, $\bar{\boldsymbol{\delta}}$.
- Similar to the second step, the vectors for the unknown constants of the kth layer, $\mathbf{a}_k$ and $\mathbf{b}_k$, are evaluated from Eq. (48) in terms of the corresponding local interfacial displacements, $\bar{\boldsymbol{\delta}}_k$, $\bar{\boldsymbol{\delta}}_{k+1}$, and $(\bar{\mathbf{d}}_k^{\pm})_T$.
- As a final step, the inter and intralaminar displacements and stresses within the medium are calculated by taking the inverse Fourier transform of the appropriate expressions.

4 Numerical Examples and Discussions

As a numerical example a [0 deg/90 deg/θ/$-\theta$]$_s$ balanced symmetrically laminated slab is considered. Specifically, the following thermal and mechanical boundary conditions are applied.

$$T_1^+(x)=\begin{cases}T_0; & |x|\le a\\ 0; & \text{otherwise}\end{cases} \tag{56a}$$

$$T_N^-(x)=0;\ |x|<\infty \tag{56b}$$

$$\sigma_{zz}^{1+}(x)=\tau_{xz}^{1+}(x)=\tau_{yz}^{1+}(x)=0;\ |x|<\infty \tag{56c}$$

$$\sigma_{zz}^{N-}(x)=\tau_{xz}^{N-}(x)=\tau_{yz}^{N-}(x)=0;\ |x|<\infty \tag{56d}$$

where T_0 is a temperature rise in a region of $2a$ on the top surface of the laminated slab (Fig. 1).

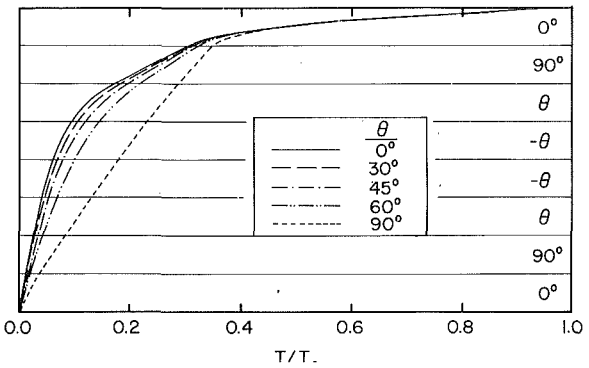

Fig. 2 Temperature distribution at $x=0$ for a [0 deg/90 deg/θ/ $-\theta$]$_s$ laminated slab

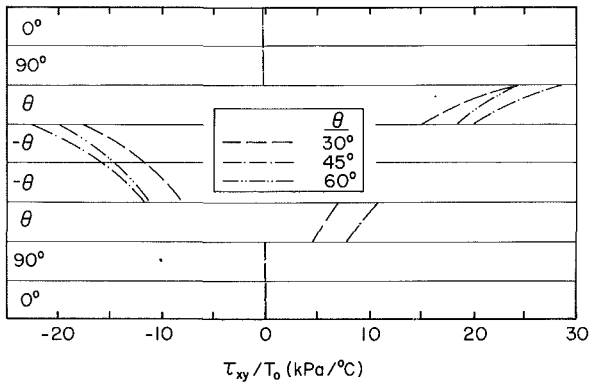

Fig. 5 Distribution of σ_{yy} at $x=0$ for a [0 deg/90 deg/θ/ $-\theta$]$_s$ laminated slab

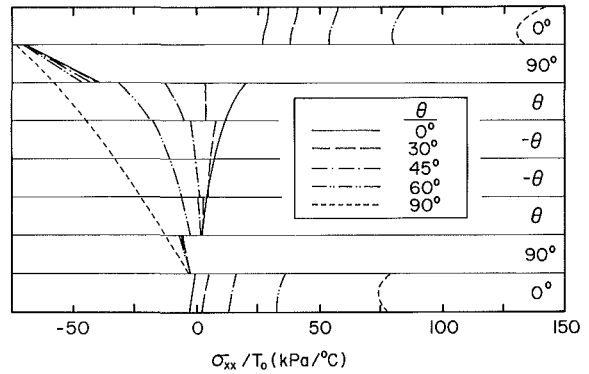

Fig. 3 Distribution of σ_{xx} at $x=0$ for a [0 deg/90 deg/θ/ $-\theta$]$_s$ laminated slab

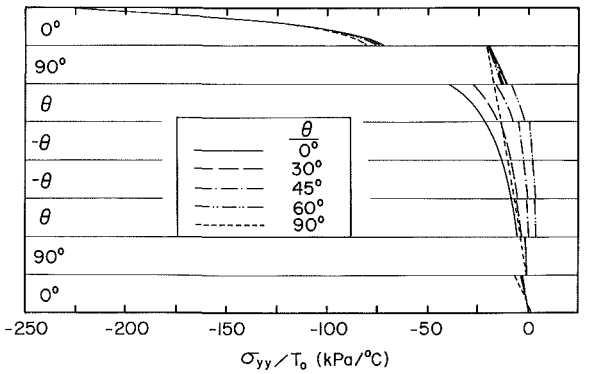

Fig. 6 Distribution of τ_{xy} at $x=0$ for a [0 deg/90 deg/θ/ $-\theta$]$_s$ laminated slab

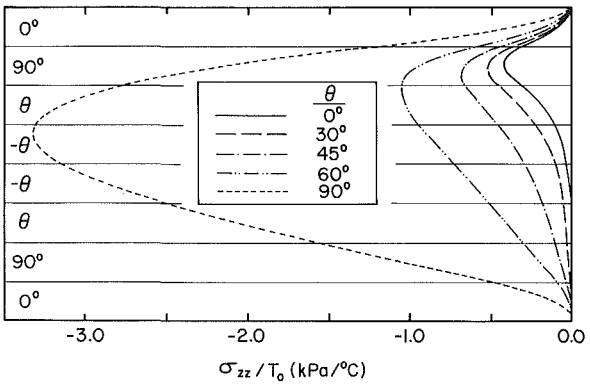

Fig. 4 Distribution of σ_{zz} at $x=0$ for a [0 deg/90 deg/θ/ $-\theta$]$_s$ laminated slab

In addition, the unidirectionally fiber-reinforced constituting layers are assumed to have the following fiber (T300) graphite) and matrix (epoxy) thermoelastic properties (Chamis, 1984)

$$E_f^1 = 220.6 \text{ GPa},\ \nu_f^1 = 0.2,\ G_f^1 = 8.9 \text{ GPa},\ \kappa_f^1 = 84 \text{ W/m•K},$$
$$\alpha_f^1 = -0.98\times10^{-6} \text{ cm/cm/K},\ E_f^2 = 13.8 \text{ GPa},\ \nu_f^2 = 0.25,$$
$$G_f^2 = 4.8 \text{ GPa},\ \kappa_f^2 = 8.4 \text{ W/m•K},\ \sigma_f^2 = 10\times10^{-6} \text{ cm/cm/K},$$
$$E_m = 3.45 \text{ GPa},\ \nu_m = 0.35,\ G_m = 1.28 \text{ GPa},$$
$$\kappa_m = 0.18 \text{ W/m•K},\ \alpha_m = 64.3\times10^{-6} \text{ cm/cm/K}$$

where E, ν, G, κ, and α are Young's moduli, Poisson's ratios, shear moduli, thermal conductivities, and coefficients of thermal expansion, respectively. The subscripts f and m refer to the fiber and matrix phases, while the superscripts 1 and 2 denote the longitudinal and transverse properties of the fiber, respectively.

Regarding each layer as being homogeneous and anisotropic, the corresponding gross elastic stiffness constants, C_{ij}, and thermal properties, κ_{ll} and α_{ll}, in the material coordinates of the layer are evaluated using the composite micromechanics equations by Chamis (1984). For a specific fiber volume fraction $V_f = 0.5$, the gross thermoelastic properties are obtained as

$$C_{11} = 114 \text{ GPa},\ C_{22} = C_{33} = 8.7 \text{ GPa},\ C_{12} = C_{13} = 3.3 \text{ GPa}$$
$$C_{23} = 3.4 \text{ GPa},\ C_{44} = 2.7 \text{ GPa},\ C_{55} = C_{66} = 3.2 \text{ GPa}$$
$$\kappa_{11} = 42.1 \text{ W/m•K},\ \kappa_{22} = \kappa_{22} = 0.466 \text{ W/m•K}$$
$$\alpha_{11} = 0.025\times10^{-6} \text{ cm/cm/K},$$
$$\alpha_{22} = \alpha_{33} = 32.4\times10^{-6} \text{ cm/cm/K}$$

from which the gross properties in the structural coordinates for a given fiber orientation θ of the layer can be determined via the tensor transformation equations (Jones, 1975).

The numerical results are obtained for the layer thicknesses $h_k = 1.25$ mm, $k = 1,2,\ldots,8$, and for the fiber angles $\theta = 0$ deg, 30 deg, 45 deg, 60 deg, and 90 deg. In this study, the heated area in Fig. 1 is taken as $2a = h$ where h is the thickness of the slab. The resulting through-the-thickness variations of the temperature, T, and the stresses, σ_{xx}, σ_{zz}, σ_{yy}, and τ_{xy}, at $x=0$ are shown in Figs. 2-6, respectively.

In Fig. 2, while the temperature field close to the heated area is almost invariant with respect to the change of fiber angle θ, the temperature field away from the heated area is observed to decrease with decreasing fiber angle. This is due to the fact that, for layers with the smaller values of fiber angle, the increased thermal conductivity in the longitudinal (x) direction renders the heat flow in that direction more easily. For the case of $\theta = 90$ deg, however, which corresponds to the layers with transversely isotropic properties, the considerable heat flow occurs in both the longitudinal and transverse (z)

directions. Nonetheless, for all fiber angles θ considered herein, the extreme temperature gradients, $\partial T/\partial z$, which occur at the heated area are shown to have the identical value.

Figure 3 shows the distributions of σ_{xx} which are discontinuous across the layer interfaces owing to the mismatch of thermal and mechanical properties arising from the difference in fiber angles between adjacent layers. For all cases under consideration, the most severe discontinuity of σ_{xx} is observed to occur at the first interface when $\theta = 90$ deg. It is also noted that, in contrast to the case of homogeneous, anisotropic slab (Tauchert and Aköz, 1975), the maximum absolute value of σ_{xx} does not necessarily occur at the location where the temperature gradient is the greatest. Additionally, in the region of nearly linear temperature distributions, as illustrated for the case of $\theta = 90$ deg, the significant values (compressive) of σ_{xx} are found.

The transverse normal stress σ_{zz} shown in Fig. 4 is observed to yield the increasing values (compressive) for the increasing fiber angle θ. The magnitude of σ_{zz} is, however, insignificant when compared with that of σ_{xx}. In Fig. 5, the distributions of σ_{yy} component are also found to be discontinuous across the layer interfaces. The degree of discontinuity is rather attenuated relative to that of σ_{xx}. It is noted, however, that the maximum values (compressive) of this out-of-plane normal stress occur at the heated area, where the slab is experiencing the greatest temperature gradients. Because of the distributions of τ_{xy} component are identically zero for the case of orthotropic laminates ($\theta = 0$ deg, 90 deg), only those corresponding to $\theta = 30$ deg, 45 deg, 60 deg are illustrated in Fig. 6. Similarly, the distributions of τ_{xy} exhibit discontinuities at the layer interfaces, except for the first and the last interfaces. The slab with $\theta = 45$ deg is shown to have the larger values of τ_{xy} than those with $\theta = 30$ deg and 60 deg. The other shear stress components, τ_{xz} and $\tau_y x_z$, are zero at $x = 0$ regardless of the fiber orientations of the laminates.

5 Concluding Remarks

The flexibility/stiffness matrix method is presented for the heat conduction and thermoelasticity problems of a multilayered anisotropic medium subjected to arbitrary thermal and mechanical loadings applied on the bounding surfaces. Along with the explicit expressions for the displacement and stress fields for layers with transversely isotropic, orthotropic, and monoclinic properties, a general solution procedure is provided such that it can be uniformly applied to media with any given number of layers and layer properties. In contrast to the conventional solution procedure, a significant reduction in the number of equations that must be solved simultaneously for the required unknown constants is achieved without provoking any approximations. Based on this fact, the flexibility/stiffness matrix method is suitable for the accurate thermal stress analysis of composite materials which, in general, contain a large number of anisotropic layers.

References

Bahar, L. Y., 1972, "Transfer Matrix Approach to Layered Systems," *ASCE Journal of Engineering Mechanics Division*, Vol. 98, pp. 1159–1172.

Bahar, L. Y., and Hetnarski, R. B., 1980, "Coupled Thermoelasticity of a Layered Medium," *Journal of Thermal Stresses*, Vol. 3, pp. 141–152.

Bufler, H., 1971, "Theory of Elasticity of a Multilayered Medium," *Journal of Elasticity*, Vol. 1, pp. 125–143.

Chamis, C. C., 1984, "Simplified Composite Micromechanics Equations for Hygral, Thermal, and Mechanical Properties," *SAMPE Quarterly*, Apr., pp. 14–23.

Choi, H. J., and Thangjitham, S., 1991a, "Micro- and Macromechanical Stress and Failure Analyses of Laminated Composites," *Composites Science Technology*, Vol. 40, pp. 289–305.

Choi, H. J., and Thangjitham, S., 1991b, "Stress Analysis of Multilayered Anisotropic Elastic Media," ASME JOURNAL OF APPLIED MECHANICS, Vol. 58, pp. 382–387.

Hildebrand, F. B., 1976, *Advanced Calculus for Applications*, 2nd ed., Prentice-Hall, Englewood Cliffs, N.J.

Jones, R. M., 1975, *Mechanics of Composite Materials*, McGraw-Hill, New York.

Kausel, E., and Seale, S. H., 1987, "Static Loads in Layered Halfspaces," ASME JOURNAL OF APPLIED MECHANICS, Vol. 54, pp. 403–408.

Lekhnitskii, S. G., 1981, *Theory of Elasticity of an Anisotropic Body*, Mir Pub., Moscow.

Nowinski, J. L., 1978, *Theory of Thermoelasticity with Applications*, Sijthoff and Noordhoff Int. Pub., The Netherlands.

Padovan, J., 1974, "Thermoelasticity of an Anisotropic Half Space," ASME JOURNAL OF APPLIED MECHANICS, Vol. 41, pp. 935–940.

Padovan, J., 1975, "Thermoelasticity of Anisotropic Generally Laminated Slabs Subject to Spatially Periodic Thermal Loads," ASME JOURNAL OF APPLIED MECHANICS, Vol. 42, pp. 341–346.

Padovan, J., 1976, "Thermoelasticity of Cylindrically Anisotropic Generally Laminated Cylinders," ASME JOURNAL OF APPLIED MECHANICS, Vol. 43, pp. 124–130.

Pagano, N. J., 1970, "Influence of Shear Coupling in Cylindrical Bending of Anisotropic Laminates," *Journal of Composite Materials*, Vol. 4, pp. 330–343.

Sharma, B., 1958, "Thermal Stresses in Transversely Isotropic Semi-Infinite Elastic Solids," ASME JOURNAL OF APPLIED MECHANICS. Vol. 25, pp. 86–88.

Small, J. C., and Booker, J. R., 1984, "Finite Layer Analysis of Layered Elastic Materials Using a Flexibility Approach. Part 1-Strip Loadings," *International Journal for Numerical Methods in Engineering*, Vol. 20, pp. 1025–1037.

Sneddon, I. N., 1951, *Fourier Transforms*, McGraw-Hill, New York.

Tanigawa, Y., Murakami, H., and Ootao, Y., 1989, "Transient Thermal Stress Analysis of a Laminated Composite Beam," *Journal of Thermal Stresses*, Vol. 12, pp. 25–39.

Tauchert, T. R., and Aköz, A. Y., 1975, "Stationary Temperature and Stress Fields in an Anisotropic Elastic Slab," ASME JOURNAL OF APPLIED MECHANICS, Vol. 42, pp. 647–650.

Tauchert, T. R., 1980, "Thermoelastic Analysis of Laminated Orthotropic Slabs," *Journal of Thermal Stresses*, Vol. 3, pp. 117–132.

W. Karunasena
Graduate Student.

A. H. Shah
Professor.

Department of Civil Engineering,
University of Manitoba,
Winnipeg, R3T 2N2, Canada

S. K. Datta
Professor,
Department of Mechanical Engineering,
University of Colorado,
Boulder, CO 80309-0427
Fellow ASME

Wave Propagation in a Multilayered Laminated Cross-Ply Composite Plate

Dispersion of guided waves in a cross-ply laminated plate has been studied here using a stiffness method and an exact method. It is shown that number of laminae strongly influences the dispersion behavior. Further, it is found that when the number of laminae is sufficiently large, then the dispersion behavior can be predicted by treating the plate as homogeneous with six stiffness constants obtained by using an effective modulus method.

Introduction

Guided Lamb waves in laminated composite plates have been receiving considerable attention in recent years. The interest in this subject arises from the need to develop effective nondestructive evaluation techniques to characterize defects in, and mechanical properties of, composite structures. Ultrasonic waves provide such a technique. But in order for this to become a practical tool, a considerable amount of work is needed in both analysis and experiment of the characteristics of guided waves in anisotropic layered structures. The present study focuses on the effect of layering on free guided wave propagation in a laminated plate.

Propagation of free guided waves (Lamb waves) in an anisotropic homogeneous plate has been studied in detail recently by Nayfeh and Chimenti (1989) and Li and Thompson (1990). These studies provide an interesting picture of the rich dispersion characteristics of these Lamb waves. They also contain a comprehensive survey of the literature on guided waves in homogeneous anisotropic plates. A comprehensive review of current work (theoretical and experimental) can also be found in the edited volumes of Mal and Ting (1988) and Datta, Achenbach, and Rajapakse (1990). Among the theoretical works, mention may be made of those by Kaul and Mindlin (1962), Abubakar (1962), Solie and Auld (1973), Baylis and Green (1986), Mal (1988), Datta et al. (1988), Bratton et al. (1989, 1990), and Dayal and Kinra (1989).

In the studies mentioned above, attention was focused on free Lamb waves. The effect of fluid loading on ultrasonic guided waves in composite plates has also been investigated by several authors. References to these can be found in the two edited volumes mentioned above and in the works by Nayfeh and Chimenti (1988a,b) and Mal and Bar-Cohen (1989).

Guided waves in layered (laminated) composite plates have also received attention. For references the reader is referred to the edited volumes mentioned previously and to the papers by Dong and Nelson (1972), Mal (1988), Datta et al. (1988), Dayal and Kinra (1989), and Chimenti and Nayfeh (1990). In none of these works, however, has a *systematic* investigation of the effect of increasing number of laminae on the dispersion of free guided waves in a laminated plate been reported. Since in many structural applications there are usually many laminae in a composite plate (shell), it is of interest to investigate the effect of the number of layers on the dispersion behavior. This is the subject of the present study.

Although in principle it is possible to obtain, using a propagator matrix approach, an exact dispersion equation governing guided waves in layered anisotropic plate, finding roots of this transcendental determinantal equation is quite cumbersome and time consuming, especially when the number of layers is quite large. Also, addition of each layer involves a new equation and a new search. Additional complications arise when it is necessary to obtain not only the propagating modes, but also the evanescent modes (complex roots). The latter are needed to study scattering by defects or reflections at edges. For reasons of numerical efficacy an alternative procedure has been used in this paper to obtain the dispersive modes in a multilayered plate. This is a stiffness method originally proposed by Dong and Nelson (1972). In this approach each lamina is divided into several sublayers. The variation of the displacement through the thickness of each sublayer is approximated by quadratic interpolation polynomials in a thickness variable with coefficients that are the unknown displacements at the top, middle, and bottom of the sublayer. Then applying Ham-

Contributed by the ASME Applied Mechanics Division of THE AMERICAN SOCIETY OF MECHANICAL ENGINEERS for presentation at the Winter Annual Meeting, Atlanta, Ga., Dec. 1-6, 1991.

Discussion on this paper should be addressed to the Technical Editor, Prof. Leon M. Keer, The Technological Institute, Northwestern University, Evanston, IL 60208, and will be accepted until two months after final publication of the paper itself in the JOURNAL OF APPLIED MECHANICS. Manuscript received by the ASME Applied Mechanics Division, Sept. 18, 1990; final revision, May 3, 1991.

Paper No. 91-WA/APM-41.

ilton's principle, the dispersion equation is obtained as a standard algebraic eigenvalue problem. Eigenvalues and eigenvectors of this equation yield the propagating and evanescent modes and the associated displacements at the nodes. Earlier, Datta et al. (1988) and Karunasena et al. (1990) used a higher order discretization in which the displacements were approximated by cubic interpolation polynomials that involved the displacements and tractions at the interfaces between the adjacent sublayers. It was found that this approach led to better accuracies at high frequencies. Since the interest in this paper is an analysis of the effect of layering at low and moderately high frequencies, the simpler quadratic interpolation functions have been used. As will be shown, this leads to predictions that agree well with exact solutions in the frequency range considered.

Formulation and Solution

Consider a cross-ply laminated plate, which is composed of alternate layers of continuous fiber-reinforced material of equal thickness, h. Although the stiffness method used applies to arbitrary lay-ups, for simplicity it is assumed that fibers are oriented at 90 deg to one another in adjacent layers and that the configuration is symmetric in the plate. A global Cartesian coordinates system with origin on the midplane of the middle layer is chosen. X-axis is chosen along the fibers in the middle layer, Y-axis is in the mid-plane, and Z-axis perpendicular to the plane.

Stiffness Method

Since we are concerned with a large and varying number of layers, it will be convenient to resort to a numerical technique in which the number and properties of the layers can be arbitrarily varied without substantially changing the solution procedure. Such a technique was proposed earlier (Dong and Nelson, 1972), where the authors presented a stiffness method in which the thickness variations of the displacements were approximated by quadratic functions of a thickness variable. The generalized coordinates in this representation are the displacements at the top, middle, and bottom of each layer. An alternative higher-order polynomial representation was proposed (Datta et al., 1988) where generalized coordinates were the displacements and tractions at the top and bottom of each layer. Thus, in this approach continuity of both displacements and tractions were maintained at the interfaces between the adjacent layers. This was found to give better results at high frequencies. However, because both displacements and tractions were involved, it entailed more cumbersome algebra than the scheme using quadratic interpolation polynomials. In this paper we have used this simpler scheme.

Since we will consider waves propagating in a direction making an arbitrary angle with the symmetry axis of a lamina the motion will be three-dimensional, having particle displacement components u_x, u_y, and u_z. In order to achieve numerical accuracy, each lamina is divided into several sublayers. A local coordinate system $(x^{(k)}, y^{(k)}, z^{(k)})$ is chosen in the kth sublayer with the origin in the midplane of the sublayer, and $x^{(k)}$ axis making an angle α with the X-axis. It will be assumed that the waves are propagating in a direction making an angle α with the X-axis. The strain displacement relations in each sublayer are,

$$\epsilon_{xx}^{(k)} = u_{x,x}^{(k)},\ \epsilon_{yy}^{(k)} = u_{y,y}^{(k)},\ \epsilon_{zz}^{(k)} = u_{z,z}^{(k)}$$

$$\epsilon_{xz}^{(k)} = \frac{1}{2}\gamma_{xz}^{(k)} = \frac{1}{2}(u_{x,z}^{(k)} + u_{z,x}^{(k)}),\ \epsilon_{yz}^{(k)} = \frac{1}{2}\gamma_{yz}^{(k)} = \frac{1}{2}(u_{y,z}^{(k)} + u_{z,y}^{(k)}),$$

$$\epsilon_{xy}^{(k)} = \frac{1}{2}\gamma_{yx}^{(k)} = \frac{1}{2}(u_{x,y}^{(k)} + u_{y,x}^{(k)}) \quad (1)$$

where a comma denotes differentiation. The stress-strain relation in this sublayer is

$$\{\sigma\} = [c^{(k)}][\epsilon] \quad (2)$$

where

$$\{\sigma\}^T = [\sigma_{xx}\ \sigma_{yy}\ \sigma_{zz}\ \sigma_{yz}\sigma_{zx}\ \sigma_{xy}] \quad (3)$$

$$\{\epsilon\}^T = [\epsilon_{xx}\ \epsilon_{yy}\ \epsilon_{zz}\epsilon_{yz}\ \epsilon_{zx}\ \epsilon_{xy}] \quad (4)$$

$$[c^{(k)}] = \begin{bmatrix} c_{11}^{(k)} & c_{12}^{(k)} & c_{13}^{(k)} & 0 & 0 & c_{16}^{(k)} \\ c_{12}^{(k)} & c_{22}^{(k)} & c_{23}^{(k)} & 0 & 0 & c_{26}^{(k)} \\ c_{13}^{(k)} & c_{23}^{(k)} & c_{33}^{(k)} & 0 & 0 & c_{36}^{(k)} \\ 0 & 0 & 0 & c_{44}^{(k)} & c_{45}^{(k)} & 0 \\ 0 & 0 & 0 & c_{45}^{(k)} & c_{55}^{(k)} & 0 \\ c_{16}^{(k)} & c_{26}^{(k)} & c_{36}^{(k)} & 0 & 0 & c_{66}^{(k)} \end{bmatrix}. \quad (5)$$

For convenience, the superscript (k) on u, σ, and ϵ has been dropped above and in the subsequent development. Using the interpolation polynomials in the z-direction, the displacement components are approximated as,

$$\{U\} = [N]\{q\} \quad (6)$$

where

$$\{U\}^T = [u_x\ u_y\ u_z] \quad (7)$$

$$\{q\}^T = [u_x^b,\ u_y^b,\ u_z^b,\ u_x^m,\ u_y^m,\ u_z^m,\ u_x^f,\ u_y^f,\ u_z^f] \quad (8)$$

$$[N] = \begin{bmatrix} n_1 & 0 & 0 & n_2 & 0 & 0 & n_3 & 0 & 0 \\ 0 & n_1 & 0 & 0 & n_2 & 0 & 0 & n_3 & 0 \\ 0 & 0 & n_1 & 0 & 0 & n_2 & 0 & 0 & n_3 \end{bmatrix}. \quad (9)$$

In Eqs. (7)–(9) the generalized displacements u^b, u^m, u^f are taken at the back, middle, and front (top) nodal surfaces of the sublayer. The interpolation polynomials n_i are quadratic functions given by

$$n_1 = -\hat{z} + 2\hat{z}^2,\ n_2 = 1 - 4\hat{z}^2,\ n_3 = 2\hat{z}^2 + \hat{z} \quad (10)$$

when $\hat{z} = z^{(k)}/h^{(k)}$, $h^{(k)}$ being the thickness of the sublayer.

Using Hamilton's principle the governing equation for the entire plate is found to be

$$[K_1]\{Q\}'' + [K_2^*]\{Q\}' - [K_3]\{Q\} - [M]\{Q\} = 0. \quad (11)$$

Here, $[K_1]$, $[K_3]$, and $[M]$ are symmetric and $[K_2^*]$ is skew symmetric. Primes and dots denote differentiation with respect to x and t, respectively. $\{Q\}$ is the vector of all nodal displacements. For wave propagation in the x-direction, $\{Q\}$ is assumed of the form

$$\{Q\} = \{Q_0\}e^{j(kx-\omega t)}. \quad (12)$$

Substituting (12) in (11) we get the eigenvalue problem

$$[-K_1k^2 + K_2^*jk - K_3 + M\omega^2]\{Q_0\} = 0. \quad (13)$$

For nontrivial solution $\{Q_0\}$, the determinant of the matrix formed by the square brackets in the above equation must be zero. This equation can be solved directly to find ω for a k or to find k when ω is known. Some numerical results are discussed later.

Analytical Method

The analytical solution is presented for the case where each layer has transversely isotropic material properties with the symmetry axis lying in the plane of the plate. As in the case of stiffness method, we start with dividing each layer into several sublayers. It should be noted at this stage that division into sublayers is not required to obtain the exact frequency spectrum, but is required to calculate exact wave functions (discrete eigenvectors). The stress-strain relation within the ith sublayer is given by Eq. (14) in the global X, Y, Z coordinate system. Let U, V, W be the displacement components in the

X, Y, Z directions, respectively. The stress and strain are related by dropping the superscript i for the sublayer

$$\begin{Bmatrix}\sigma_{XX}\\ \sigma_{YY}\\ \sigma_{ZZ}\\ \sigma_{YZ}\\ \sigma_{ZX}\\ \sigma_{XY}\end{Bmatrix}=\begin{bmatrix}C_{11} & C_{12} & C_{13} & 0 & 0 & 0\\ C_{12} & C_{22} & C_{23} & 0 & 0 & 0\\ C_{13} & C_{23} & C_{33} & 0 & 0 & 0\\ 0 & 0 & 0 & C_{44} & 0 & 0\\ 0 & 0 & 0 & 0 & C_{55} & 0\\ 0 & 0 & 0 & 0 & 0 & C_{66}\end{bmatrix}\begin{Bmatrix}\epsilon_{XX}\\ \epsilon_{YY}\\ \epsilon_{ZZ}\\ \gamma_{YZ}\\ \gamma_{ZX}\\ \gamma_{XY}\end{Bmatrix} \tag{14}$$

where σ_{IJ} and ϵ_{IJ} are the stress and strain components, respectively, and $\gamma_{IJ}=2\epsilon_{IJ}$. C_{IJ} are the elements of constitutive matrix for the sublayer. Note that $C_{22}=C_{33}$, $C_{55}=C_{66}$, $C_{12}=C_{13}$, and $C_{44}=(C_{22}-C_{23})/2$. Let θ be the angle between the global X-axis and the local x-axis measured counterclockwise from the global X-axis. For wave propagation in the x-direction the appropriate forms for U, V, and W, that satisfy the equations of motion, can be written as (see Mal, 1988; Karunasena et al., 1990)

$$U=jk(\Omega_1^+ + B\Omega_2^+)\exp(j\psi), \tag{15}$$

$$V=[jL(A\Omega_1^+ + \Omega_2^+) - \zeta\Omega_3^+]\exp(j\psi), \tag{16}$$

$$W=[Ar_1\Omega_1^- + r_2\Omega_2^- - jL\Omega_3^-]\exp(j\psi), \tag{17}$$

where

$$\begin{aligned}\psi &= KX+LY-\omega t,\\ \Omega_1^+ &= A_{11}\cos(r_1Z)+A_{12}\sin(r_1Z),\\ \Omega_1^- &= A_{12}\cos(r_1Z)-A_{11}\sin(r_1Z),\\ \Omega_2^+ &= A_{21}\cos(r_2Z)+A_{22}\sin(r_2Z),\\ \Omega_1^- &= A_{22}\cos(r_2Z)-A_{21}\sin(r_2Z),\\ \Omega_3^+ &= A_{31}\cos(\zeta Z)+A_{32}\sin(\zeta Z),\\ \Omega_3^- &= A_{32}\cos(\zeta Z)-A_{31}\sin(\zeta Z),\\ A &= [k_2^2-\lambda K^2-(r_1^2+L^2)]/[\delta(r_1^2+L^2)],\\ B &= [k_2^2-K^2-\beta(r_2^2+L^2)]/[\delta K^2],\end{aligned} \tag{18}$$

and

$$\zeta=[(k_2^2-K^2-\epsilon L^2)/\epsilon]^{1/2}, \tag{19}$$

$$\lambda=\frac{C_{11}}{C_{55}};\ \beta=\frac{C_{33}}{C_{55}};\ \epsilon=\frac{C_{44}}{C_{55}};\ k_2=\sqrt{\frac{\rho\omega^2}{C_{55}}};\ \delta=1+\frac{C_{13}}{C_{55}}, \tag{20}$$

$K=k\cos\theta$, $L=k\sin\theta$. r_1 and r_2 are the roots of the following equation with positive imaginary parts.

$$\begin{vmatrix} r^2+L^2+\lambda K^2-k_2^2 & \delta(r^2+L^2)\\ \delta K^2 & K^2-k_2^2+\beta(r^2+L^2)\end{vmatrix}=0 \tag{21}$$

A_{11}, A_{12}, A_{21}, A_{22}, A_{31}, and A_{32} are arbitrary constants for the sublayer. Stress and displacement components in the sublayer can be expressed in terms of these six unknown constants. After evaluating the stresses and displacements at $z=z_i$ and $z=z_{i+1}$, after some manipulations, the following relation can be obtained,

$$\{B_{i+1}\}=[P_i]\{B_i\} \tag{22}$$

where

$$\{B_i\}^T=[U_i\ V_i\ \sigma_{zzi}\ \sigma_{zxi}\ \sigma_{yzi}\ W_i]. \tag{23}$$

The vector quantity $\{B_i\}$, which is still unknown, is independent of X and t, and it represents the displacement and stress components at $z=z_i$. $[P_i]$ is the propagator matrix in the ith sublayer. The elements of $[P_i]$ are defined in the Appendix.

Repeated application of Eq. (22) results in

$$\{B_{N+1}\}=[P]\{B_1\}, \tag{24}$$

where

$$[P]=[P_n][P_{N-1}].....[P_2][P_1]. \tag{25}$$

The repeated application of Eq. (22) ensures the continuity of displacements and tractions at the interfaces. Let us denote the elements of the 6×6 matrix $[P]$ by P_{mn} ($m=1$ to 6, $n=1$ to 6). Invoking the zero-traction conditions at interfaces 1 and $(N+1)$, we obtain, from Eq. (24),

$$\begin{bmatrix}P_{31} & P_{32} & P_{36}\\ P_{41} & P_{42} & P_{46}\\ P_{51} & P_{52} & P_{56}\end{bmatrix}\begin{Bmatrix}U\\ V\\ W\end{Bmatrix}=\begin{Bmatrix}0\\ 0\\ 0\end{Bmatrix}. \tag{26}$$

The exact dispersion relation for the plate is obtained by setting the determinant of the coefficient matrix to zero as

$$\begin{aligned}f(\omega,k)=P_{31}(P_{42}P_{56}-P_{46}P_{52})-P_{32}(P_{41}P_{56}-P_{46}P_{51})\\ +P_{36}(P_{41}P_{52}-P_{42}P_{51})=0.\end{aligned} \tag{27}$$

Equation (27) can be solved for k given ω, or alternatively, it can be solved for ω for given k.

For a fixed value of either ω or k, Eq. (27) is a transcendental function of either k or ω, respectively. It is possible to find the roots of this transcendental equation by some search method (see Press et al., 1988). This approach will be computationally formidable since the roots are sparsely scattered. Herein Muller's method is employed to recover the exact roots. Approximate roots obtained from the stiffness method described earlier are used as initial guesses in the Muller's method. If the roots are required over a range of k (or ω), approximate roots from the stiffness method are required only at the first step to use as initial guesses. At the next step, k (or ω) is changed by a small amount, and Eq. (23) is solved taking the exact roots from the previous step as initial guesses for the current step. The process is repeated until the range of interest is scanned. Once the exact roots are determined, the exact wave functions can be computed as discrete eigenvectors using Eq. (22) at successive interfaces.

If the problem under consideration is symmetric or antisymmetric, it is possible to model only the half-thickness of the plate in the analysis. In this case, the boundary conditions at the middle surface of the plate, $z=H/2$; are

$$W=0;\ \sigma_{zx}=0;\ \sigma_{yz}=0, \text{ for symmetric problems,}$$

$$U=0;\ V=0;\ \sigma_{zz}=0, \text{ for antisymmetric problems.} \tag{28}$$

Applying these boundary conditions in Eq. (24) appropriate dispersion relations and eigenvectors can be obtained. The boundary conditions given in Eq. (28) are applicable to the stiffness method also, if the problem is symmetric or antisymmetric.

Numerical Results and Discussion

The stiffness method outlined above was used to study the effect of increasing number of layers on the dispersion of guided waves in a laminated plate. For this purpose a cross-ply graphite fiber reinforced composite plate was considered with the symmetric lay-ups, 90 deg/0 deg/... 0 deg/90 deg. Thus, in this case the symmetric and antisymmetric modes were uncoupled. The elastic constants of the middle lamina in the global coordinate system are, in units of 10^{11} N/m^2, $C_{11}=1.6073$, $C_{33}=0.1392$, $C_{13}=0.0644$, $C_{44}=0.0350$, and $C_{55}=0.0707$. The number of laminae varied from 3 to 39. In order to ascertain the accuracy of the results obtained using the stiffness method the results were compared with the exact solutions for plates with different numbers of laminae for propagation at 45 deg with the X-axis. This was chosen because of the strong coupling of the P—SV and SH modes in this case. The number of sublayers used in each lamina was varied to get close agreement with the exact solution. Figure 1 shows the comparison of the results for a plate with 35 laminae. The number of sublayers used in each lamina was 2. Agreement is found to be excellent in the range of the phase velocity-fre-

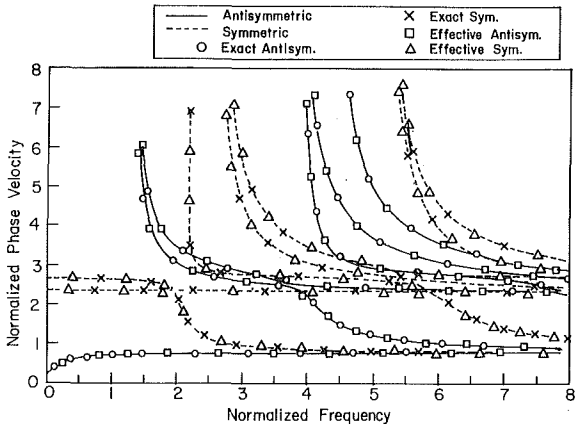

Fig. 1 Dispersion of guided waves in a 35-layered cross-ply plate. Lines at the predictions of stiffness method; , × — predictions of exact equation; ,— predictions of the effective modulus model.

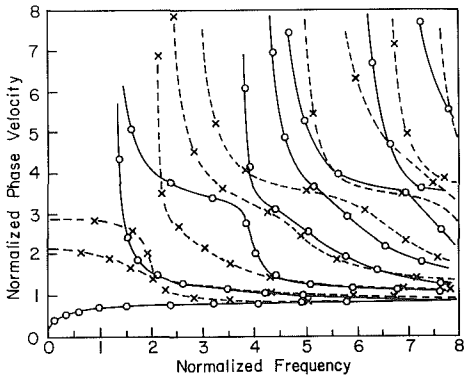

Fig. 2 Results for a 3-layered cross-ply plate. Symbols are as in Fig. 1.

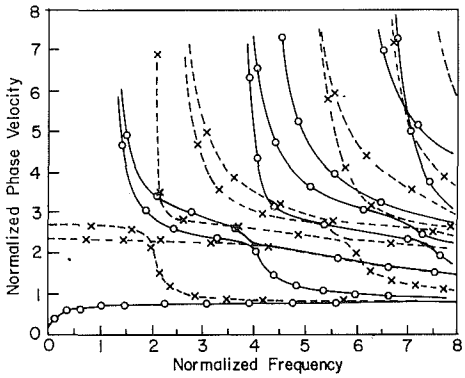

Fig. 3 Results for a 11-layered cross-ply plate. Symbols are the same as in Fig. 1.

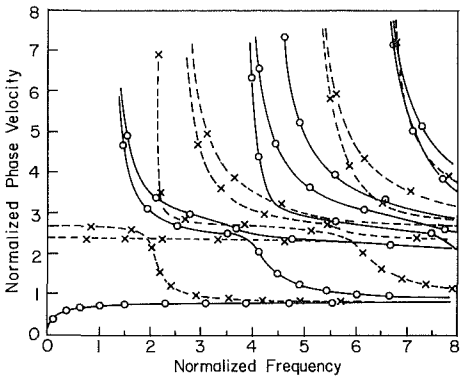

Fig. 4 Same as in Fig. 3 for a 19-layered plate

quency considered. In all the figures shown, the nondimensional frequency and phase velocity are defined as, $\Omega = \omega H/2\sqrt{C_{55}/\rho}$ and $C = \omega/k\sqrt{C_{55}/\rho}$.

The effect of the increasing number of laminae on the dispersion behavior is illustrated in Figs. 2–4 for propagation at 45 deg to the X-axis in plates with 3, 11, and 19 laminae, respectively. Comparison of Figs. 2 and 3 show considerable differences. Notable among them are: significantly different behaviors of the first symmetric quasi-longitudinal and quasi-SH modes in the two cases (curves labeled S_0 and SH_0); strong tendency (seen in Fig. 3) of the higher modes to become asymptotic to straight lines in certain bands of frequency; lowering of the phase velocities of some modes. As the number of laminae is increased further, it is seen that (Figs. 4 and 1) the dispersion curves for the third and higher modes tend to have three plateaus: first the long wavelength velocity of the quasi-S_0 mode, then at the long wavelength phase velocity of the quasi-SH_0 mode, and finally the quasi-shear velocity in the plane of propagation. At these plateaus, velocities are constant when the number of layers is sufficiently large. As seen from Figs. 1 and 4, the dispersion curves for the first few modes are nearly identical and there are differences for the higher modes. It was found that for the lay-ups and material properties the dispersion curves did not change within the frequency range considered when the number of layers was increased beyond 35. This suggested that the guided wave dispersion in this plate could be predicted by an effective modulus model. In fact, this is seen from Fig. 1, which shows the results for a homogeneous plate with (static) effective moduli calculated in the manner presented by Postma (1955) for periodic isotropic layers and generalized to orthotropic plates by Yeo (1983). The fact that the plate with a sufficiently large number of laminae can be modeled as homogeneous with certain effective properties is not unexpected. The important conclusion of this systematic study is that even though the dispersion of the first two modes can be predicted by the effective medium approximation for a plate with only a few layers, for this approximation to be valid for higher modes the plate must have a minimum number of layers. For the particular system considered, this number was found to be ≈ 35. Note that the (static) effective moduli of a cross-ply plate are given by the following equations. Let c_{ij} be the stiffness of the 0-deg lamina. Then for a periodic 90 deg/0 deg/... laminate the effective moduli are:

$$\bar{c}_{11} = \frac{2c_{33}(c_{11}+c_{33}) - (c_{13}-c_{23})^2}{4c_{33}} = \bar{c}_{22}$$

$$\bar{c}_{13} = \frac{1}{2}(c_{23}+c_{13}) = \bar{c}_{23}$$

$$\bar{c}_{33} = c_{33}$$

$$\bar{c}_{12} = \frac{4c_{11}c_{33} + (c_{13}-c_{23})^2}{4c_{33}}$$

$$\bar{c}_{66} = c_{66},\ \bar{c}_{44} = \bar{c}_{55} = \frac{2c_{44}c_{55}}{c_{44}+c_{55}}. \tag{29}$$

Thus, using the particular properties considered here, the effective moduli of the plate are:

$$\bar{c}_{11} = 0.8732,\ \bar{c}_{13} = 0.0668,\ \bar{c}_{12} = 0.0644$$
$$\bar{c} = 0.1392,\ \bar{c}_{44} = 0.0468,\ \bar{c}_{66} = 0.0707. \tag{30}$$

Conclusion

Guided wave propagation in a multilayered laminated plate

has been studied here using a stiffness method, and the predicted dispersion has been shown to agree well with exact solution. The solution of the exact dispersion equation is facilitated by using the predictions of the stiffness method. It is shown that the number of laminae has a strong influence on the dispersion behavior when there are only a few laminae. As the number of laminae increases, however, the plate can be modeled as homogeneous. To limit the length of the paper, results for propagation in the 45 deg direction are shown here. However, the agreement between the results of the layered and effective modulus models was found to hold for other propagation directions also.

Acknowledgment

The work here was supported by grants from the Office of Naval Research (#N00014-86-K-0280; Scientific Officer Dr. Y. Rajapakse), from NASA (#NAGW-1388), and from the Natural Science and Engineering Research Council of Canada (#OGP007988).

References

Abubakar, I., 1962, "Free Vibrations of a Transversely Isotropic Plate," *Quarterly Journal of Mechanics and Applied Mathematics*, Vol. 15, pp. 129–136.

Baylis, E. R., and Green, W. A., 1986, "Flexural Waves in Fiber Reinforced Laminated Plates," *Journal of Sound and Vibration*, Vol. 110, pp. 1–26.

Bratton, R. L., Datta, S. K., and Shah, A. H., 1989, "Anisotropy Effects on Lamb Waves in Composite Plates," *Review of Progress in Quantitative Nondestructive Evaluation*, Vol. 8A, D. O. Thompson and D. E. Chimenti, eds., Plenum Press, New York, pp. 197–204.

Bratton, R. L., Datta, S. K., and Shah, A. H., 1990, *Propagation and Scattering of Lamb Waves in a Fiber-Reinforced Composite Plate*, CSC Report 90-1, Center for Space Construction, University of Colorado, Boulder, Colo.

Chimenti, D., and Nayfeh, A. H., 1990, "Ultrasonic Reflection and Guided Wave Propagation in Biaxially Laminated Composite Plates," *Journal of the Acoustical Society of America*, Vol. 87, pp. 1409–1415.

Datta, S. K., Shah, A. H., Bratton, R. L., and Chakraborty, T., 1988, "Wave Propagation in Laminated Composite Plates," *Journal of the Acoustical Society of America*, Vol. 83, pp. 2020–2026.

Datta, S. K., Achenbach, J. D., and Rajapakse, Y. S., eds., 1990, *Elastic Waves and Ultrasonic Nondestructive Evaluation*, North-Holland, Amsterdam.

Dayal, V., and Kinra, V. K., 1989, "Leaky Lamb Waves in an Anisotropic Plate. I: An Exact Solution and Experiments," *Journal of the Acoustical Society of America*, Vol. 00, pp. 2268–2276.

Dong, S. B., and Nelson, R. B., 1972, "On Natural Vibrations and Waves in Laminated Orthotropic Plates," ASME JOURNAL OF APPLIED MECHANICS, Vol. 39, pp. 739–745.

Karunasena, W. M., Bratton, R. L., Datta, S. K., and Shah, A. H., 1990, "Elastic Wave Propagation in Laminated Composite Plates," ASME *Journal of Engineering Materials and Technology*, Vol. 113, pp. 411–418.

Kaul, R. K.,and Mindlin, R. D., 1962, "Frequency Spectrum of a Monoclinic Crystal Plate," *Journal of the Acoustical Society of America*, Vol. 34, pp. 1902–1910.

Li, Y., and Thompson, R. B., 1990, "Influence of Anisotropy on the Dispersion Characteristics of Guided Ultrasonic Plate Modes," *Journal of the Acoustical Society of America*, Vol. 87, pp. 1911–1931.

Mal, A. K., and Ting, T. C. T., eds., 1988, *Wave Propagation in Structural Composites*, ASME, New York.

Mal, A. K., 1988, "Wave Propagation in Layered Composite Laminates Under Periodic Surface Loads," *Wave Motion*, Vol. 10, pp. 257–266.

Mal, A. K., and Bar-Cohen, Y., 1989, "Ultrasonic NDE of Thick Composite Laminates," *Review of Progress in Quantitative Nondestructive Evaluation*, Vol. 8B, D. O. Thompson and D. E. Chimenti, eds., Plenum Press, New York, pp. 1551–1558.

Nayfeh, A. H., and Chimenti, D., 1988a, "Ultrasonic Wave Reflection from Liquid-Coupled Orthotropic Plates with Application to Fibrous Composites," ASME JOURNAL OF APPLIED MECHANICS, Vol. 55, pp. 863–870.

Nayfeh, A. H., and Chimenti, D., 1988b, "Propagation of Guided Waves in Fluid-Coupled Plates of Fiber-Reinforced Composite," *Journal of the Acoustical Society of America*, Vol. 83, pp. 1736–1743.

Postma, G. W., 1955, "Wave Propagation in a Stratified Medium," *Geophysics*, Vol. 20, pp. 780–806.

Press, W. H., Flannery, B. P., Teukolsky, S. A., and Wetterling, W. T., 1988, *Numerical Recipes*, Cambridge University Press.

Solie, L. P., and Auld, B. A., 1973, "Elastic Waves in Free Anisotropic Plates," *Journal of the Acoustical Society of America*, Vol. 54, pp. 50–65.

Yeo, J. K. T., 1983, "Three Dimensional Analysis of Harmonic Waves in a Peridically Laminated Medium," M. S. Thesis, Department of Manitoba, Winnipeg, Canada.

APPENDIX

The propagator matrix $[P_l]$, appearing in Eq. (22), is given by

$$[P_l] = [E][T_1][H]$$

where

$$[T_1] = \begin{bmatrix} \cos(2hr_1) & 0 & 0 & \sin(2hr_1) & 0 & 0 \\ 0 & \cos(2hr_2) & 0 & 0 & \sin(2hr_2) & 0 \\ 0 & 0 & \cos(2h\zeta) & 0 & 0 & \sin(2h\zeta) \\ -\sin(2hr_1) & 0 & 0 & \cos(2hr_1) & 0 & 0 \\ 0 & -\sin(2hr_2) & 0 & 0 & \cos(2hr_2) & 0 \\ 0 & 0 & -\sin(2h\zeta) & 0 & 0 & \cos(2h\zeta) \end{bmatrix},$$

$$[E] = \begin{bmatrix} [[T_2][R]] & [0] \\ [0] & [[T_2][S]] \end{bmatrix},$$

$$[H] = \begin{bmatrix} [[T_2][R]]^{-1} & [0] \\ [0] & [[T_2][S]]^{-1} \end{bmatrix},$$

$$[T_2] = \begin{bmatrix} m & n & 0 \\ -n & m & 0 \\ 0 & 0 & 1 \end{bmatrix},$$

$$[S] = \begin{bmatrix} C_{55}jKr_1(1+A) & C_{55}jKr_1(1+B) & C_{55}KL \\ 2C_{55}\epsilon jLr_1A & 2C_{55}\epsilon jLr_2 & C_{55}\epsilon(L^2-\zeta^2) \\ r_1A & r_2 & -jL \end{bmatrix},$$

$$[R] = \begin{bmatrix} jk & jkB & 0 \\ jkA & jL & -\zeta \\ R_{31} & R_{32} & 2C_{55}\epsilon jL\zeta \end{bmatrix},$$

$$R_{31} = C_{55}[(1-\delta)K^2 - A\beta(r_1^2+L^2) + 2A\epsilon L^2],$$

$$R_{32} = C_{55}[(1-\delta)K^3B - \beta(r_2^2+L^2) + 2\epsilon L^2].$$

Here, $m = \cos\theta$ and $n = \sin\theta$.

Nonlinear Response of Infinitely Long Circular Cylindrical Shells to Subharmonic Radial Loads

Ali H. Nayfeh
University Distinguished Professor, Mem. ASME

Raouf A. Raouf[1]
Assoc. Mem. ASME

Jamal F. Nayfeh
Graduate Research Assistant, Assoc. Mem. ASME

Department of Engineering Science and Mechanics, Virginia Polytechnic Institute and State University, Blacksburg, VA 24061

The method of multiple scales is used to analyze the nonlinear response of infinitely long, circular cylindrical shells (thin circular rings) in the presence of a two-to-one internal (autoparametric) resonance to a subharmonic excitation of order one-half of the higher mode. Four autonomous first-order ordinary differential equations are derived for the modulation of the amplitudes and phases of the interacting modes. These modulation equations are used to determine the fixed points and their stability. The fixed points correspond to periodic oscillations of the shell, whereas the limit-cycle solutions of the modulation equations correspond to amplitude and phase-modulated oscillations of the shell. The force response curves exhibit saturation, jumps, and Hopf bifurcations. Moreover, the frequency response curves exhibit Hopf bifurcations. For certain parameters and excitation frequencies between the Hopf values, limit-cycle solutions of the modulation equations are found. As the excitation frequency changes, all limit cycles deform and lose stability through either pitchfork or cyclic-fold (saddle-node) bifurcations. Some of these saddle-node bifurcations cause a transition to chaos. The pitchfork bifurcations break the symmetry of the limit cycles.

Introduction

Although single-mode analyses can provide some insight into the problem of nonlinear dynamics, the interesting behavior results from modal interactions; see Nayfeh and Mook (1979) for a comprehensive literature review. Such a phenomenon may occur when the linear natural frequencies are commensurate or nearly commensurate.

The first studies of modal interactions in the response of shells were initiated by McIvor (1962, 1966), Goodier and McIvor (1964), McIvor and Sonstegard (1966), and McIvor and Lovell (1968). They analyzed the response of cylindrical and spherical shells to radial and nearly radial impulses, taking into account the coupling of the breathing mode and a flexural mode when their frequencies are in the ratio of two-to-one (i.e., a two-to-one internal or autoparametric resonance). Integrating numerically the governing ordinary differential equations, they found that the energy is continuously exchanged between the internally resonant modes. Bieniek, Fan, and Lackman (1966) and Mente (1973) are also among the first to study modal interactions in the dynamic response of shells.

Evensen (1966) conducted a pioneering experimental and theoretical study in shell dynamics; he studied the case of one-to-one internal resonance of thin circular rings. He showed that the response involves either a single or two coupled bending modes. He reported experimental observations of regions in the frequency response curve where nonsteady vibrations were found. He verified his results by analog-computer simulations. Chen and Babcock (1975) investigated analytically and experimentally the nonlinear response of cylindrical shells to a harmonic excitation. They studied both the driven as well as the companion mode and their interaction. They reported experimental observations of "nonstationary" responses "in which the amplitude drifts from one value to another." Maewal (1986) numerically integrated Miles' evolution equations for axisymmetric shells in the presence of primary and internal resonances. He showed that for certain ranges of the excitation frequency, the response is chaotically modulated.

Yasuda and Kushida (1984) studied theoretically and experimentally the axisymmetric response of shallow spherical shells. They studied the case of primary resonance of the higher mode in the presence and absence of a two-to-one internal resonance. They analyzed the stability of the periodic solutions and verified their analysis experimentally. They also observed aperiodic motions.

Moganty and Bickford (1987) used the method of multiple scales to study the nonlinear free vibrations of circular rings in the presence of internal resonances between an in-plane and an out-of-plane bending mode. They found a continuous exchange of energy between the coupled modes.

[1]Currently at GWU-NASA Langley Research Center.

Contributed by the Applied Mechanics Division of THE AMERICAN SOCIETY OF MECHANICAL ENGINEERS for publication in the JOURNAL OF APPLIED MECHANICS.

Discussion on this paper should be addressed to the Technical Editor, Prof. Leon M. Keer, The Technological Institute, Northwestern University, Evanston, IL 60208, and will be accepted until two months after final publication of the paper itself in the JOURNAL OF APPLIED MECHANICS. Manuscript received by the ASME Applied Mechanics Division, July 13, 1988; final revision, Aug. 25, 1989.

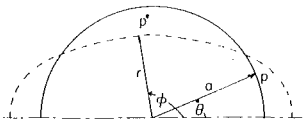

Fig. 1 Polar coordinates of a point on the shell which was initially at p and is at p^* at time t^*

Nayfeh and Raouf (1986, 1987a) analyzed the nonlinear inextensional response of an infinitely long, circular cylindrical shell to a harmonic excitation having the frequency Ω when the frequency ω_o of the breathing mode is approximately twice the frequency of a flexural mode ω_f. They used the method of multiple scales (Nayfeh, 1973, 1981) to fully account for the nonlinear interaction, including the influence of the flexural mode on the breathing mode. They demonstrated the existence of the saturation phenomenon in the response when $\Omega \approx \omega_o$. They also showed that the response exhibits a Hopf bifurcation. Between the Hopf bifurcation points, the modulation equations possess limit-cycle solutions, which undergo a cascade of period-doubling bifurcations that culminates in a chaotic motion. Nayfeh and Raouf (1987b) extended their analysis to the case where the excitation frequency is near the frequency of the flexural mode (i.e., $\Omega \approx \omega_f$). They showed that the system exhibits a Hopf bifurcation resulting in amplitude and phase-modulated motions.

In this paper we study the response of infinitely long circular cylindrical shells to subharmonic radial excitations of order one-half (i.e., $\Omega \approx 2\omega_o$) in the presence of a two-to-one internal resonance (i.e., $\omega_o \approx 2\omega_f$). We demonstrate the existence of a Hopf bifurcation, leading to amplitude and phase-modulated rather than periodic oscillations of the shell. These amplitude and phase-modulated oscillations correspond to limit-cycle solutions of the modulation equations. All limit cycles deform as the excitation frequency changes between the Hopf bifurcation points. Some undergo symmetry-breaking bifurcations and some undergo cyclic-fold bifurcations. Some cyclic folds result in a transition to chaos.

2 Problem Formulation

Following McIvor (1962) and Goodier and McIvor (1964), we consider the case in which the strain parallel to the generators of the shell is everywhere zero. Thus, the deformation of the shell is identical in every plane perpendicular to the shell axis, and the shell can be considered as being in plane motion. In such a plane, we consider a point p on the undeformed shell midsurface with the polar coordinates (a, θ), which after a time t^* moves to p^* with the polar coordinates (r, ϕ), as shown in Fig. 1. We introduce the dimensionless displacement w and time t defined by

$$w = \frac{a-r}{a}, \quad t = \frac{ct^*}{a} \tag{1}$$

where t^* is the dimensional time, $c^2 = E/\rho(1-\nu^2)$, E is Young's modulus, ν is Poisson's ratio, and ρ is the mass density of the shell per unit width. Moreover, we let

$$\psi = \phi - \theta. \tag{2}$$

Then, to second order in the displacements w and ψ, the governing equations are (Goodier and McIvor, 1964; Raouf, 1985; Nayfeh and Raouf, 1986)

$$\ddot{w} + \alpha^2(w^{iv} + 2w'' + w) - \psi' + w = w''(\psi' - w) - \dot{\psi}^2 + \psi'^2 - 2w\psi' + w'\psi'' - \frac{1}{2}w'^2 + \frac{a(1-\nu^2)}{Eh}P(1+\psi'-w) + \text{cubic terms in } w \text{ and } \psi \tag{3}$$

and

$$\ddot{\psi} - \psi'' + w' = w'w'' - 2w'\psi' + 2\dot{w}\dot{\psi} + \frac{a(1-\nu^2)}{Eh}w'P + \text{cubic terms in } w \text{ and } \psi \tag{4}$$

where the dot indicates the partial derivative with respect to t, the prime indicates the partial derivative with respect to θ, and P is the applied radial pressure load. Here,

$$\alpha^2 = h^2/12a^2 \tag{5}$$

where h and a are the thickness and initial radius of the shell, respectively.

In this paper, we consider the case of a two-to-one internal resonance (i.e., $\omega_o \approx 2\omega_f$) when the frequency Ω of the radial load is approximately twice the frequency ω_o of the breathing mode; that is, $\Omega \approx 2\omega_o$, subharmonic resonance of order one half.

3 Perturbation Solution

We use the method of multiple scales (Nayfeh, 1973, 1981) to determine a second-order uniform expansion of the solutions of equations (3) and (4) for small but finite amplitudes when P is given by

$$\frac{a(1-\nu^2)}{Eh}P = \epsilon F\cos\Omega t \tag{6}$$

where ϵ is a small dimensionless quantity. Thus, we seek expansions in the form

$$w(\theta,t;\epsilon) = \epsilon w_1(\theta,T_o,T_1) + \epsilon^2 w_2(\theta,T_o,T_1) + \ldots \tag{7}$$

$$\psi(\theta,t;\epsilon) = \epsilon\psi_1(\theta,T_o,T_1) + \epsilon^2\psi_2(\theta,T_o,T_1) + \ldots \tag{8}$$

where $T_o = t$, a fast scale characterizing motions with the natural and excitation frequencies, and $T_1 = \epsilon t$, a slow scale characterizing the modulation of the amplitudes and phases of the modes with damping, nonlinearity, and any possible resonances. Substituting equations (6)–(8) into equations (3) and (4) and equating coefficients of like powers of ϵ, we obtain:

Order ϵ

$$D_o^2 w_1 + \alpha^2(w_1^{iv} + 2w_1'' + w_1) - \psi_1' + w_1 = F\cos\Omega T_o \tag{9}$$

$$D_o^2\psi_1 - \psi_1'' + w_1' = 0. \tag{10}$$

Order ϵ^2

$$D_o^2 w_2 + \alpha^2(w_2^{iv} + 2w_2'' + w_2) - \psi_2' + w_2 = -2D_oD_1w_1 + w_1''(\psi_1' - w_1) - (D_o\psi_1)^2 + \psi_1'^2 - 2w_1\psi_1' + w_1'\psi_1'' - \frac{1}{2}w_1'^2 + F(\psi_1' - w_1)\cos\Omega T_o \tag{11}$$

$$D_o^2\psi_2 - \psi_2'' + w_2' = -2D_oD_1\psi_1 + w_1'w_1'' - 2w_1'\psi_1' + 2(D_ow_1)(D_o\psi_1) + Fw_1'\cos\Omega T_o \tag{12}$$

where $D_n = \partial/\partial T_n$.

It turns out that, in the presence of structural or viscous damping, all modes that are not directly or indirectly excited vanish in the steady state (Nayfeh and Mook, 1979). Consequently, in the case of internal resonance between the breathing and nth flexural modes, we express the solution of the first-order problem as

$$w_1 = p_1(T_1)\cos\left(\frac{1}{2}\Omega T_o\right) + q_1(T_1)\sin\left(\frac{1}{2}\Omega T_o\right) + \left[p_2(T_1)\cos\left(\frac{1}{4}\Omega T_o\right) + q_2(T_1)\sin\left(\frac{1}{4}\Omega T_o\right)\right]\cos n\theta + \left[p_3(T_1)\cos\left(\frac{1}{4}\Omega T_o\right) + q_3(T_1)\sin\left(\frac{1}{4}\Omega T_o\right)\right]\sin n\theta + F(1+\alpha^2-\Omega^2)^{-1}\cos(\Omega T_o) \tag{13}$$

$$\psi_1 = \Gamma_n\left[p_2(T_1)\cos\left(\frac{1}{4}\,\Omega T_o\right) + q_2(T_1)\sin\left(\frac{1}{4}\,\Omega T_o\right)\right]\sin n\theta$$

$$-\Gamma_n\left[p_3(T_1)\cos\left(\frac{1}{4}\,\Omega T_o\right) + q_3(T_1)\sin\left(\frac{1}{4}\,\Omega T_o\right)\right]\cos n\theta \quad (14)$$

where

$$\Gamma_n = \frac{1}{n}\,[1+\alpha^2(n^2-1)^2-\omega_n^2]$$

$$\nu_1 = \frac{1}{2}\,\sigma_1 + \frac{1}{4}\,\sigma_2,\ \nu_2 = \frac{1}{2}\,\sigma_2 \quad (15)$$

and σ_1 and σ_2 are detuning parameters defined as

$$\Omega = 2\omega_o + \epsilon\sigma_2 \text{ and } \omega_o = 2\omega_n + \epsilon\sigma_1. \quad (16)$$

We note that the problem is degenerate because there are two orthogonal modes (i.e., $\cos n\theta$ and $\sin n\theta$) corresponding to the same flexural frequency ω_n. This degeneracy can be removed by an imperfection, or the nonlinearity, or initial conditions. To remove the degeneracy by the nonlinearity, we need to carry out the expansion to another order. Hence, the level of excitation needed to remove the degeneracy is an order of magnitude higher than that needed to activate the two-to-one autoparametric resonance being considered. In this paper, we study the case of a perfect circular shell, excitation levels that do not activate the one-to-one autoparametric resonance, and initial conditions that produce $p_3 = q_3 = 0$.

Substituting equations (13) and (14) with $p_3 = q_3 = 0$ into equations (11) and (12), using equations (16), and eliminating the secular terms, we obtain the following modulation equations:

$$p_1' = -\nu_2 q_1 - \mu_0 p_1 - 2\Lambda_1 p_2 q_2 - f q_1 \quad (17)$$

$$q_1' = \nu_2 p_1 - \mu_0 q_1 + \Lambda_1(p_2^2 - q_2^2) - f p_1 \quad (18)$$

$$p_2' = -\nu_1 q_2 - \mu_n p_2 - \Lambda_2(q_1 p_2 - q_2 p_1) \quad (19)$$

$$q_2' = \nu_1 p_2 - \mu_n q_2 + \Lambda_2(p_1 p_2 + q_1 q_2) \quad (20)$$

where

$$4\omega_o\Lambda_1 = \frac{1}{4}\,n^2 + \frac{1}{2}\,(\omega_n^2 + n^2)\Gamma_n^2 - n\Gamma_n \quad (21)$$

$$4\omega_o(1+\Gamma_n^2)\Lambda_2 = n^2 - 2n\Gamma_n + 2\omega_o\omega_n\Gamma_n^2 \quad (22)$$

$$F = 4\omega_o f. \quad (23)$$

Modal damping has been incorporated into equations (17)–(20) with μ_o being the damping coefficient of the breathing mode and μ_n being the damping coefficient of the nth flexural mode.

The fixed-point solutions of equations (17)–(20) correspond to $p_i' = q_i' = 0$. There are two possibilities. First,

$$p_i = q_i = 0 \quad \text{for} \quad i = 1 \text{ and } 2 \quad (24)$$

which is the trivial solution. Second,

$$p_1 = a_o\cos\frac{1}{2}\,\gamma_2,\ q_1 = a_o\sin\frac{1}{2}\,\gamma_2 \quad (25)$$

$$p_2 = a_n\cos\left(\frac{1}{2}\,\gamma_1 + \frac{1}{4}\,\gamma_2\right),\ q_2 = a_n\sin\left(\frac{1}{2}\,\gamma_1 + \frac{1}{4}\,\gamma_2\right) \quad (26)$$

where

$$a_o = a_o^* = \Lambda_2^{-1}\left[\mu_n^2 + \frac{1}{4}\left(\frac{1}{2}\,\sigma_2 + \sigma_1\right)^2\right]^{1/2} \quad (27)$$

$$a_n^2 = -\chi_1 \pm \left(\frac{f^2 a_o^2}{\Lambda_1^2} - \chi_2^2\right)^{1/2} \quad (28)$$

$$\tan\gamma_1 = -2\mu_1/\left(\sigma_1 + \frac{1}{2}\,\sigma_1\right) \quad (29)$$

$$\tan\gamma_2 = -[\mu_0\Lambda_2 a_o^2 + \mu_n\Lambda_1 a_n^2]/\left[\frac{1}{2}\,\sigma_2\Lambda_2 a_o^2 - \frac{1}{2}\left(\sigma_1 + \frac{1}{2}\,\sigma_2\right)\Lambda_1 a_n^2\right] \quad (30)$$

$$\chi_1 = \left[4\mu_o\mu_n - \sigma_2\left(\frac{1}{2}\,\sigma_2 + \sigma_1\right)\right]/4\Lambda_1\Lambda_2 \quad (31)$$

$$\chi_2 = [\mu_o(\sigma_2 + 2\sigma_1) + 2\sigma_2\mu_n]/4\Lambda_1\Lambda_2. \quad (32)$$

The stability of a fixed point to a perturbation proportional to $\exp(\lambda T_1)$ is determined by the zeros of the characteristic equation

$$\begin{vmatrix} \lambda+\mu_0 & f+\nu_2 & 2\Lambda_1 q_2 & 2\Lambda_1 p_2 \\ f-\nu_2 & \lambda+\mu_o & -2\Lambda_1 p_2 & 2\Lambda_1 q_2 \\ -\Lambda_2 q_2 & \Lambda_2 p_2 & \lambda+\mu_n+\Lambda_2 q_1 & \nu_1-\Lambda_2 p_1 \\ -\Lambda_2 p_2 & -\Lambda_2 q_2 & -\nu_1-\Lambda_2 p_1 & \lambda+\mu_n-\Lambda_2 q_1 \end{vmatrix} = 0. \quad (33)$$

To investigate the stability of the trivial fixed points given by equation (24), we put $p_n = q_n = 0$ in equation (33) and obtain

$$\lambda = -\mu_o \pm (f^2 - \nu_2^2)^{1/2},\ -\mu_n \pm i\nu_1. \quad (34)$$

Thus, a trivial fixed point is stable if

$$f < (\mu_o^2 + \nu_2^2)^{1/2} \quad (35a)$$

and unstable if

$$f > (\mu_o^2 + \nu_2^2)^{1/2}. \quad (35b)$$

When $f = (\mu_o^2 + \nu_2^2)^{1/2}$, a nonlinear analysis is needed to determine the stability of the trivial fixed point. To analyze the stability of the nontrivial fixed points, we use equations (25)–(30) in equation (33) and obtain

$$\lambda^4 + 2(\mu_o+\mu_n)\lambda^3 + [\mu_o^2 + 4\mu_o\mu_n + \nu_2^2 - f^2 + 4\Lambda_1\Lambda_2 a_n^2]\lambda^2$$
$$+ [2\mu_n\mu_o^2 + 2\mu_n\nu_2^2 - 2\mu_n f^2 + 4\Lambda_1\Lambda_2(\mu_o+\mu_n)a_n^2]\lambda$$
$$+ 8\Lambda_1\Lambda_2 a_n^2[\Lambda_1\Lambda_2 a_n^2 + \mu_o\mu_n - \nu_1\nu_2] = 0. \quad (36)$$

Consequently, a given nontrivial fixed point is stable if the real part of each root of equation (36) is negative. It follows from equations (21) and (22) that $\Lambda_1\Lambda_2 < 0$, and hence equation (36) has real positive roots if and only if

$$\Lambda_1\Lambda_2 a_n^2 + \mu_o\mu_n - \nu_1\nu_2 < 0 \quad (37)$$

which, in conjunction with equations (27) and (28), implies that the fixed point corresponding to the positive sign in equation (28) is stable and that corresponding to the negative sign is unstable. Moreover, equation (36) has a pair of complex conjugate roots with a positive real part if

$$r_3(r_1 r_2 - r_3) - r_1^2 r_4 < 0 \quad (38)$$

where r_1, r_2, r_3, and r_4 are, respectively, the coefficients of λ^3, λ^2, λ, and λ^o in equation (36).

4 Numerical Results

Next we present numerical results for the case $h/a = 0.028$, which yields $\omega_o = 1.00033$ and $\omega_8 = 0.50528$ so that $\omega_o \simeq 2\omega_8$; that is, $n = 8$. In this case, $\Lambda_1 = 3.87539$, $\Lambda_2 = 15.2611$, and $\epsilon\sigma_1 = -0.01023$. We let $\epsilon = 1.40137 \times 10^{-2}$, and $\hat{\mu}_{0,8} = \Lambda_2^{-1/2}\,\mu_{0,8} = 0.02$; then $\hat{\sigma}_1 = \Lambda_2^{-1/2}\,\sigma_1 = -0.73$. For such a high flexural mode number (i.e., 8), Simmonds (1979) showed that adding the cubic terms in equations (3) and (4) does not have any significant effects. Calculations are performed on the autonomous modulation equations (17)–(20) rather than on the original equations of motion. A fixed point of the modulation equations corresponds to a periodic motion of the shell, whereas a periodic solution of the modulation equations corresponds to a two-period quasi-periodic motion of the shell.

All numerical integrations are performed using a sixth-order Runge-Kutta algorithm and the results are confirmed by changing the step-size of the integration. Either the detuning pa-

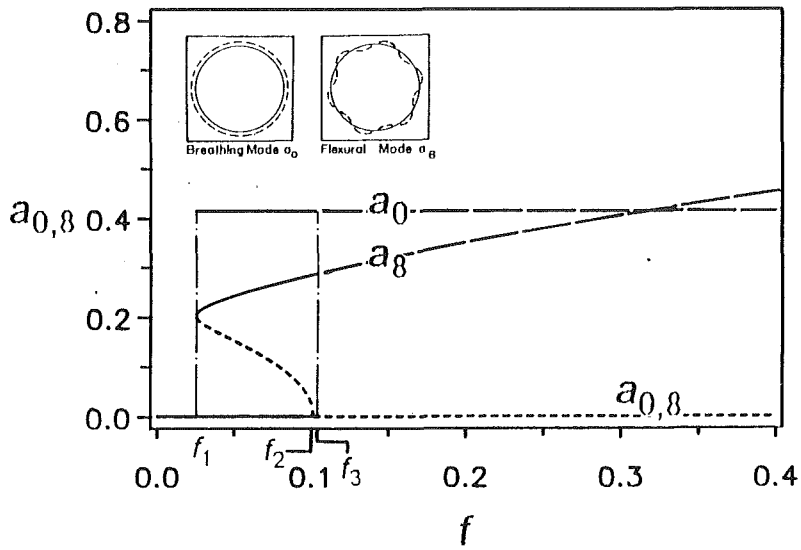

Fig. 2 Variation of amplitude of the response with the amplitude of the excitation for $\chi_1 < 0$, $\mu_{0,8} = 0.02$ and $\hat{\sigma}_2 = -0.2$: $a_o = \sqrt{p_1^2 + q_2^2}$ and $a_8 = \sqrt{p_2^2 + q_2^2}$ are the amplitudes of the breathing and eighth flexural modes, respectively

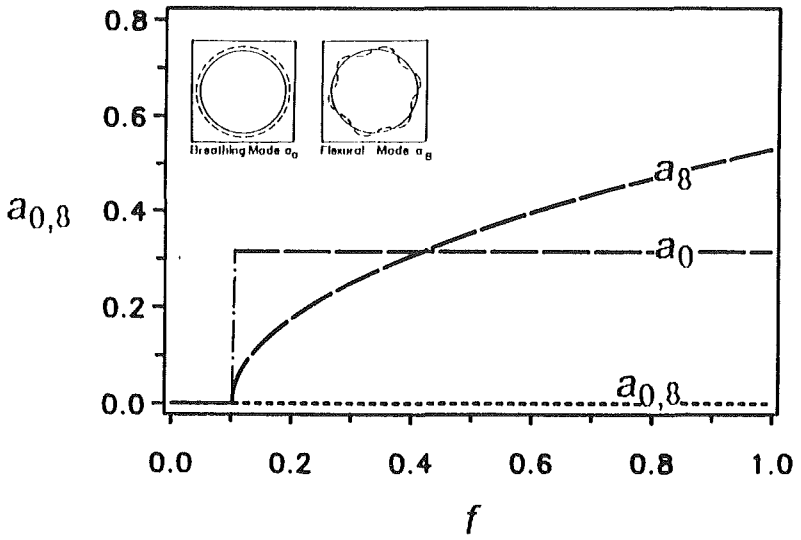

Fig. 3 Variation of amplitude of the response with the amplitude of the excitation for $\chi_1 > 0$, $\mu_{0,8} = 0.02$ and $\hat{\sigma}_2 = 0.2$: $a_o = \sqrt{p_1^2 + q_1^2}$ and $a_8 = \sqrt{p_2^2 + q_2^2}$ are the amplitudes of the breathing and eighth flexural modes, respectively

rameter $\hat{\sigma}_2 = \Lambda_2^{-1/2}\sigma_2$ or the excitation amplitude f is used as a bifurcation parameter, all others being held fixed. The fixed points are determined from equations (25)–(32). The stability of the fixed points is determined by numerically calculating the eigenvalues of the Jacobi matrix from either equation (33) or equation (36).

In Fig. 2, we show the force-response curves for $\chi_1 < 0$. This figure shows the saturation and jump phenomena (Nayfeh and Mook, 1979) and its exhibits a Hopf bifurcation. Hopf bifurcation occurs when two complex-conjugate eigenvalues of the Jacobi matrix cross the imaginary axis transversely with nonzero speed into the right half of the complex plane. When $f < f_1 = 0.025$, only trivial fixed points are possible; they are stable. Hence, it follows from equations (13) and (14) that the response of the shell is linear and periodic. When $f_1 < f < f_2 = 0.101$, there are three possible fixed-point solutions: the trivial solution, which is stable, and two nontrivial solutions, the larger of which is stable and the other is unstable with a real eigenvalue being positive. When $f_2 < f < f_3 = 0.104$, there are two fixed-point solutions: the trivial solution, which is unstable with a real eigenvalue being positive, and a nontrivial solution, which is stable. When $f > f_3$, there are two fixed-point solutions: the trivial solution, which is unstable with a real eigenvalue being positive, and a nontrivial solution, which is unstable with a pair of complex conjugate eigenvalues having a positive real part. As f increases beyond f_3, the nontrivial fixed point with both breathing and flexural components loses its stability with two complex conjugate eigenvalues crossing the imaginary axis transversely from the left half to the right half of the complex plane. Consequently, $f = f_3$ is a Hopf bifurcation value.

As the forcing amplitude f increases slowly from zero, the trivial fixed point (i.e., $a_o = a_8 = 0$) is the only steady-state solution until a threshold is reached at $f = f_2$. As pointed out by one of the referees, when $f = f_2$, there exists another family of fixed points described by

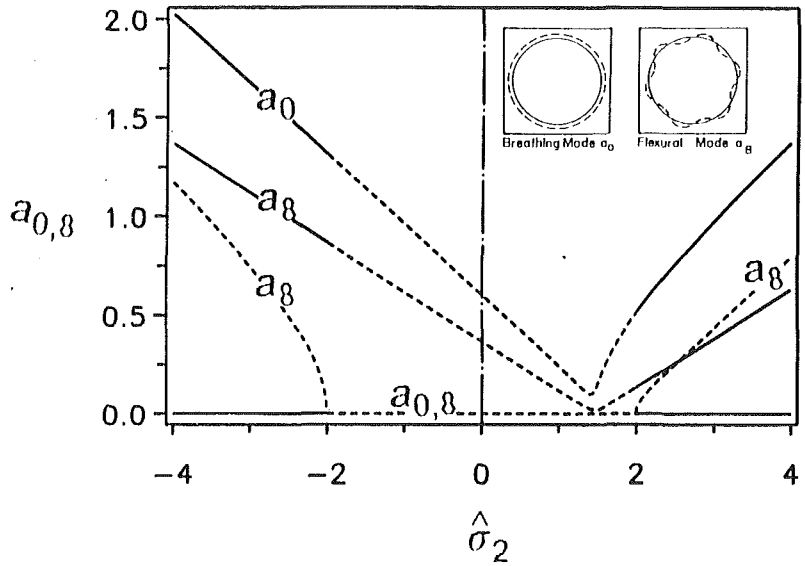

Fig. 4 Frequency response curves for $f = 1.0$

$$p_1 = -\gamma(\nu_2+f_2)/\mu_o,\ q_1=\gamma,\ p_2=0,\ q_2=0 \qquad (39)$$

for any γ. This is a nongeneric bifurcation. As f increases beyond f_2, the trivial fixed point becomes unstable and the flow jumps to a nontrivial solution. As f increases further, the amplitude a_o of the breathing mode remains constant (i.e., saturates) and spills over the extra input energy into the coupled eighth flexural mode, which responds nonlinearly causing a large amplitude wrinkling of the shell. At $f = f_3$, the nontrivial fixed point with both breathing and flexural components undergoes a Hopf bifurcation. For values of f near f_3, the modulation equations (17)–(20) possess limit-cycle solutions, and hence the response of the shell is an amplitude and phase-modulated oscillation.

As f decreases slowly below f_3, a_o remains constant and a_8 decreases slowly until f reaches the critical value $f = f_1$, where the nontrivial stable and unstable fixed points of the flexural mode collide in a fold (saddle-node) bifurcation. As f decreases below f_1, both a_8 and a_o jump down to zero. In the region $f_1 < f < f_2$, an unstable fixed point separates two stable fixed points of the flexural mode. In this interval, the flow tends to one of the stable fixed points depending on their basins of attraction. Consequently, the response of the shell consists of either the breathing mode only or a combination of the breathing and eighth flexural modes, depending on the initial conditions.

Figure 3 shows a force response curve for $\chi_1 > 0$. In this case, no fold bifurcation takes place and the jump occurs only in the breathing mode response at $f = 0.102$.

Figure 4 shows frequency curves for $f = 1.0$. Whereas a_o is a single-valued function of $\hat{\sigma}_2$, a_8 can be a multivalued function of $\hat{\sigma}_2$. Moreover, Fig. 4 exhibits a jump phenomenon at $\hat{\sigma}_2 = -1.9996$. It shows a Hopf bifurcation at $\hat{\sigma}_2 = -1.9987$ and 1.9981. The nontrivial fixed point becomes unstable as $\hat{\sigma}_2$ increases beyond -1.9987 or decreases below 1.9981 and limit cycles are observed.

The stability of the limit cycles is determined by using Floquet theory. The modulation equations (17)–(20) have the general form

$$x' = f(x) \qquad (40)$$

where the prime indicates the derivative with respect to T_1. The stability of a T-periodic solution $X(T_1) = X(T_1+T)$ of equations (40) is determined by the linear variational equation

$$\xi' = \nabla f(X)\xi \qquad (41)$$

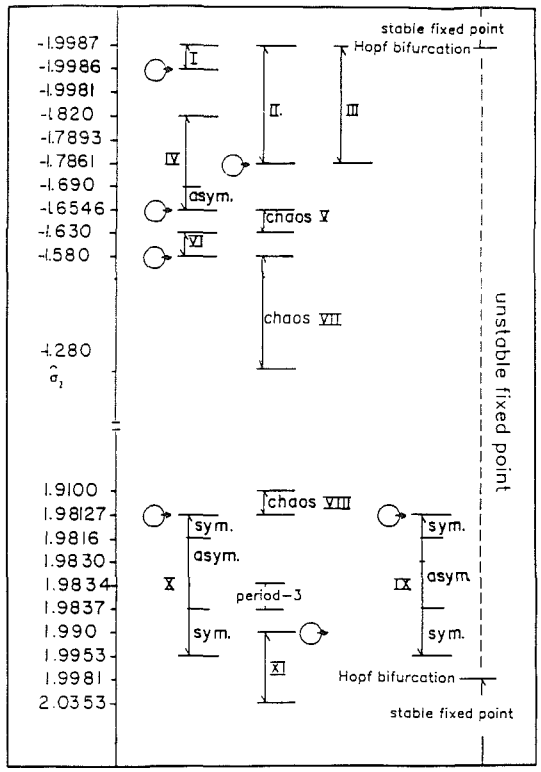

Fig. 5 Schematic for the behavior of the system for $\hat{\sigma}_2 \in (-1.9987, 2.0353)$

where $\nabla f(X)$ is a 4×4 T-periodic matrix. Let $\Phi = \Phi(T_1)$ be a solution satisfying

$$\Phi' = \nabla f(X)\Phi \quad \Phi(0) = I \qquad (42)$$

where I is the identity matrix. The Floquet multipliers are the eigenvalues of the monodromy matrix $\Phi(T)$ whose columns are the solution vectors of equation (42) evaluated at $T_1 = T$. The monodromy matrix is calculated by numerically integrating equation (42) from $T_1 = 0$ to $T_1 = T$ four times. The positions of the Floquet multipliers relative to the unit circle in the complex plane determine the stability of the limit cycle. Because equations (17)–(22) are autonomous, one of the Floquet multipliers is always +1 (Hale, 1963; Urabe, 1967; Hirsch and Smale, 1974). If the modulus of one of the other multipliers

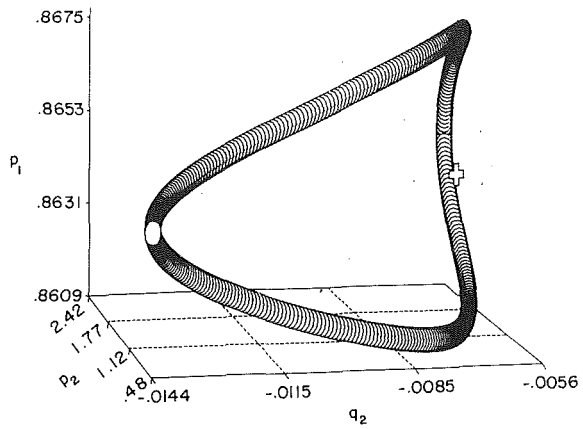

Fig. 6(a)

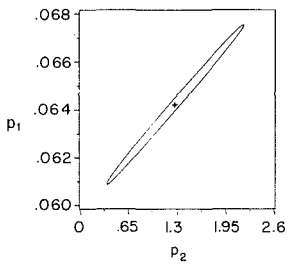

Fig. 6(b)

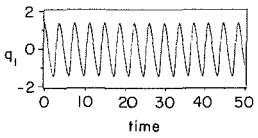

Fig. 6(c)

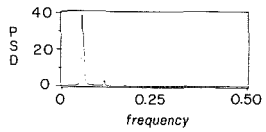

Fig. 6(d)

Fig. 6 Limit cycle I: (*a*) projection of phase space on the three-dimensional space spanned by p_1, p_2, and q_2; "balloons" represent points on limit cycle, (*b*) projection of phase space on the two-dimensional plane spanned by p_1 and p_2, (c) waveform of q_1, and (*d*) power spectral density (PSD) of q_1 signal

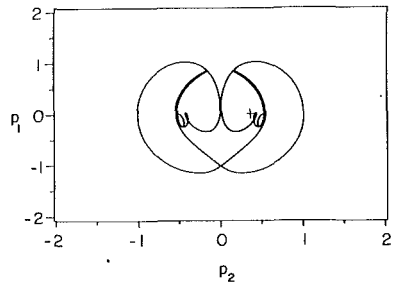

Fig. 7(a)

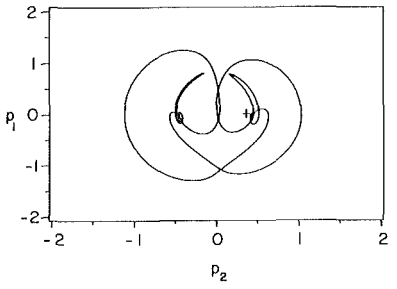

Fig. 7(b)

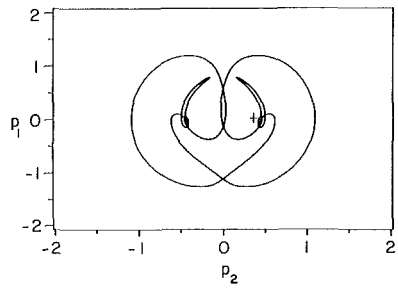

Fig. 7(c)

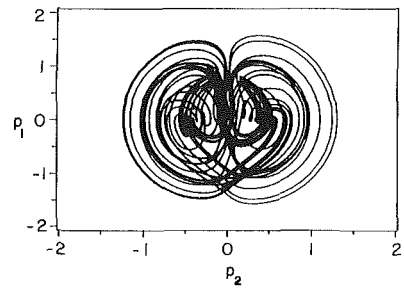

Fig. 7(d)

Fig. 7 Deformation of attractor X as a function of $\hat{\sigma}_2$: (*a*) $\hat{\sigma}_2 = 1.9840$, (*b*) $\hat{\sigma}_2 = 1.9820$, (*c*) $\hat{\sigma}_2 = 1.9815$, and (*d*) $\hat{\sigma}_2 = 1.9800$

is greater than one, the limit cycle is unstable; otherwise it is stable. A bifurcation occurs when a multiplier leaves the unit circle. The type of bifurcation depends on the way a multiplier leaves the unit circle. In our study, we observe cyclic-fold and pitchfork bifurcations associated with a multiplier leaving the unit circle through $+1$. The cycle-fold bifurcations result in cyclic jumps where the flow jumps to another limit cycle or to a chaotic attractor. A symmetry breaking is observed when a multiplier touches $+1$ from within the unit circle.

To calculate the limit cycles, we use an algorithm originally proposed by Aprille and Trick (1972) to eliminate transient responses, thereby latching onto a limit cycle and calculating its period. It uses a combination of a numerical integration scheme and a Newton-Raphson iteration procedure. This algorithm proved efficient in reducing the computation time but is sensitive to the initial guesses and the step size of the integration because of the coexistence of attractors. Using different step sizes and with the same initial guesses, we found that the algorithm sometimes may land on different orbits for the same $\hat{\sigma}_2$. The results of the algorithm were verified by long-time numerical integration.

To compute the power spectrum we use the fast Fourier transform algorithm developed by Cooley and Tukey (1965) and implemented by Singleton (1968). Different techniques are used to identify chaos: the broadening of the power spectrum, the fractal structure of the Poincaré section, capacity or fractal dimension, and the existence of a positive Lyapunov exponent of the attractor. A positive Lyapunov exponent indicates an exponential divergence of neighboring trajectories, confirming chaos. Lyapunov exponents are calculated using the algorithm proposed by Wolf et al. (1985). The Lyapunov dimension d_L of the attractor is also calculated using the following relation proposed by Frederickson et al. (1983):

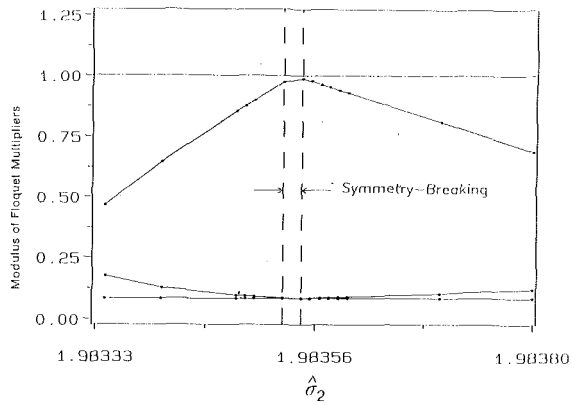

Fig. 8 Floquet multipliers for limit cycle X around the symmetry breaking frequency ($\hat{\sigma}_2 \approx 1.9837$). The fourth multiplier is +1.

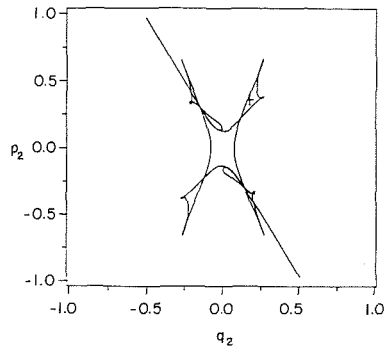

Fig. 9(*a*)

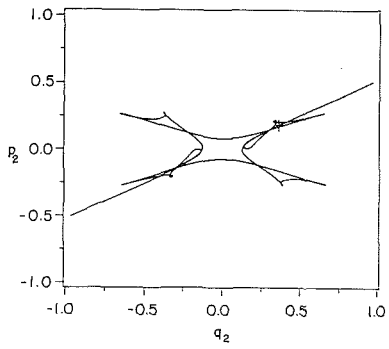

Fig. 9(*b*)

Fig. 9 Projection of phase space on the $p_2 - q_2$ plane for $\hat{\sigma}_2 = 1.984$: (*a*) limit cycle IX and (*b*) limit cycle X.

$$d_L = j + \sum_{i=1}^{j} \sigma_i / |\sigma_{j+1}| \tag{43}$$

where σ_j is the jth Lyapunov exponent and j is defined as

$$\sum_{i=1}^{j} \sigma_i > 0, \quad \sum_{i=1}^{j+1} \sigma_i < 0. \tag{44}$$

The Lyapunov exponents are ordered in the usual way

$$\sigma_1 > \sigma_2 > \sigma_3 > \ldots > \sigma_N. \tag{45}$$

The Lyapunov dimension is actually the information dimension, which is bounded from above by the capacity or fractal dimension d_f (Lichtenberg and Lieberman, 1983; Farmer, 1982). On the other hand, the phase space has a negative divergence, thus it is volume contracting. Accordingly, the capacity d_f is bounded from above by the phase dimension, and hence $d_f < 4$. Consequently,

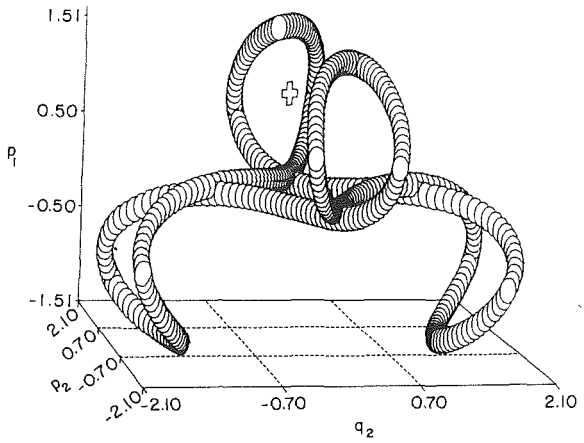

Fig. 10(*a*)

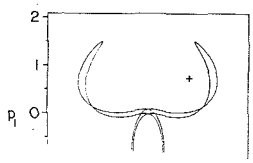

Fig. 10(*b*)

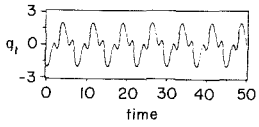

Fig. 10(*c*)

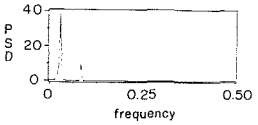

Fig. 10(*d*)

Fig. 10 Limit cycle III (unstable): (*a*) projection of phase space on the three-dimensional space spanned by p_1, p_2, and q_2 ("balloons" represent points on limit cycle), (*b*) projection of phase space on the $p_1 - p_2$ plane, (*c*) waveform of q_1, and (*d*) power spectral density (PSD) of q_1 signal

$$d_L < d_f < 4. \tag{46}$$

For $\hat{\sigma}_2 < -1.9987$ and $\hat{\sigma}_2 < 2.0353$, limit cycles do not exist and the flow asymptotically approaches a fixed point as $t \to \infty$. The behavior of the flow within the above internal is summarized in Fig. 5. Here we note the following:

(1) There always exists an unstable fixed-point solution for $-1.9987 < \hat{\sigma}_2 < 1.9981$. This fixed point is indicated by a plus sign in the two-dimensional projections and a cross in the three-dimensional projections (e.g., Fig. 6(*a*), (*b*)).

(2) All periodic limit cycles start symmetric (i.e., there exists a group of symmetries which maps the limit cycle to itself, see item 5 below) and lose stability through either a pitchfork or a cyclic-fold bifurcation.

(3)Deformation of limit cycles: all cycles undergo deformation as $\hat{\sigma}_2$ changes. Interesting behaviors are observed in the following:

(*a*) Limit cycle IV starts at $\hat{\sigma}_2 = -1.8200$ as a symmetric one and loses its symmetry just before collision, then the flow jumps onto a chaotic attractor.

(*b*) Limit cycles IX and X are born at $\hat{\sigma}_2 = 1.9953$ as symmetric ones, lose symmetry but regain it before their saddle-

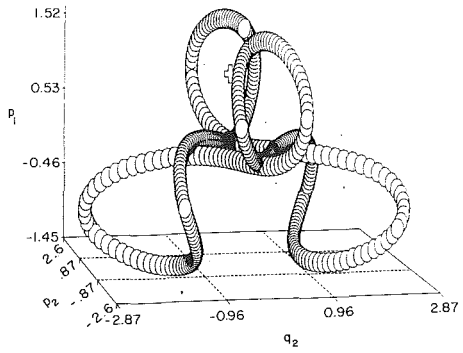

Fig. 11(*a*)

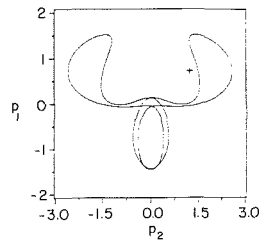

Fig. 11(*b*)

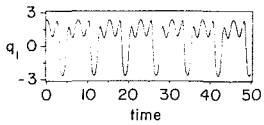

Fig. 11(*c*)

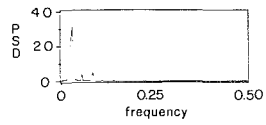

Fig. 11(*d*)

Fig. 11 Limit cycle II: (*a*) projection of phase space on the three-dimensional space spanned by p_1, p_2, and q_2 ("balloons" represent points on limit cycle), (*b*) projection of phase space on the $p_1 - p_2$ plane, (*c*) waveform of q_1, and (*d*) power spectral density (PSD) of q_1 signal

node bifurcations. Figures 7(*a*)-(*d*) show the deformation of limit cycle X.

(4) The loss of symmetry is associated with a Floquet multiplier touching +1 from within the unit circle. Figure 8 shows the behavior of the multipliers for limit cycle X around the symmetry breaking frequency.

(5) The modulation equations (17)-(22) exhibit a symmetry apparent in the phase trajectories. The equations are invariant under the transformation

$$T: \quad p_1 \rightarrow -p_1,\ q_1 \rightarrow -q_1,\ p_2 \rightarrow q_2,\ q_2 \rightarrow -p_2. \tag{47}$$

Equations (47) show the possibility of a mirror image reflection around $p_1 = 0$ and $q_1 = 0$ and a rotation of $\frac{1}{2}\pi$ in the $p_2 - q_2$ plane. Consider, for example, Fig. 9, which shows the projection of the limit cycles IX and X onto the $p_2 - q_2$ plane. It is obvious by inspection that there is a rotation of $\frac{1}{2}\pi$ between (a) and (b).

(6) For $-1.9987 < \hat{\sigma}_2 < -1.7861$, the unstable limit cycle III coexists with the stable fixed point and the stable limit cycle II. Limit cycle I exists for $-1.9987 < \hat{\sigma}_2 \leq -1.9986$. As $t \rightarrow \infty$, the flow tends to one of the stable states depending on their domains of attraction. The unstable orbit III was achieved by changing the size of the integration step in the Aprille and Trick algorithm and by a short time integration (Fig. 10).

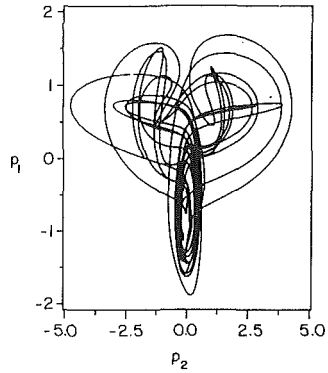

Fig. 12(*a*)

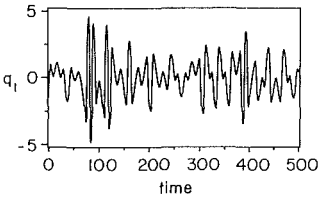

Fig. 12(*b*)

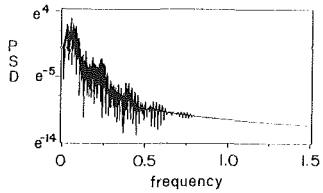

Fig. 12(*c*)

Fig. 12 Chaotic attractor VII at $\hat{\sigma}_2 = -1.55$: (*a*) two-dimensional projection of phase space on the $p_1 - p_2$ plane, (*b*) waveform of q_1, and (*c*) power spectral density (PSD) of q_1 signal

Figure 11 shows its accompanying stable orbit II. The two limit cycles collide and annihilate each other at $\hat{\sigma}_2 = -1.7861$.

(7) The broadening of the power spectrum at $\hat{\sigma}_2 = -1.55$ of the time history of the component q_1 (Fig. 12(*c*)) compared with the spectra of the limit cycles in Fig. 6(*d*), 10(*d*), and 11(*d*) and the fractal nature of the Poincaré section (Fig. 13) indicate the chaotic nature of the attractor which exists for $\hat{\sigma}_2 \in (-1.58, -1.28)$. The Poincaré section is the set of all points at which the trajectories on the chaotic attractor intersect the hyperplane defined by $q_2 = 0$. Although this was constructed by long-time numerical integration, it still contains some transients as evident from the presence of the isolated points. To confirm the chaotic nature of this attractor, we calculate its Lyapunov exponents and fractal dimension d_f. At $\hat{\sigma}_2 = -1.55$ (chaotic region VII), the Lyapunov exponents are (0.566, 0.000, -0.057, -0.624) and the Lyapunov dimension $d_L \simeq 3.8$. Thus, $3.8 < d_f < 4.0$ and the attractor has a fractal dimension.

(8) Period-three motion is found over a very narrow range of $\hat{\sigma}_2$ (see Fig. 5). Figure 14 shows a projection of this limit cycle (compare with Fig. 7). Because it has three revolutions (as compared with Fig. 7(*a*)-(*c*)), it is called a period-three motion.

5 Conclusions

The modulation equations for the nonlinear oscillations of cylindrical shells subject to a radial subharmonic excitation are obtained. The case of a two-to-one internal resonance between the breathing mode and a flexural mode is considered. The stability of the fixed points and limit cycles of these equations is presented.

As the bifurcation parameter $\hat{\sigma}_2$ (the frequency detuning of the subharmonic excitation) varies, the flow exhibits a Hopf bifurcation, in which fixed points lose stability and limit cycles

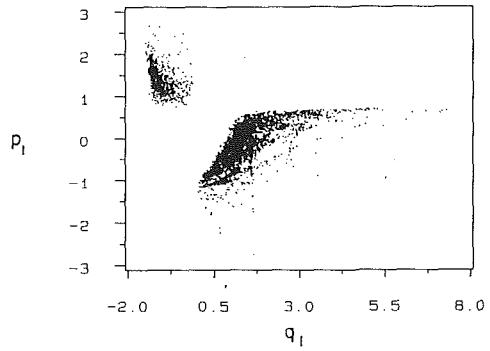

Fig. 13(*a*)

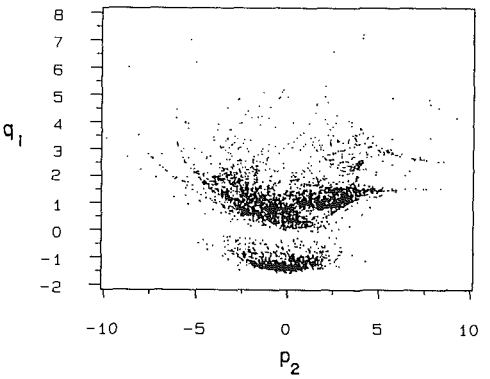

Fig. 13(*b*)

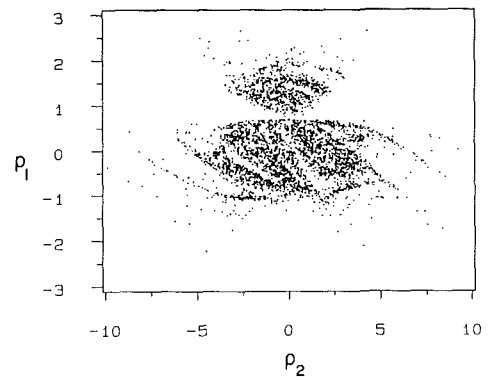

Fig. 13(*c*)

Fig. 13 Poincaré sections of chaotic attractor VII at $\hat{\sigma}_2 = -1.55$

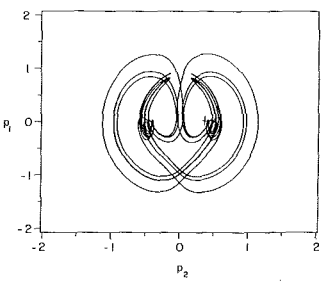

Fig. 14 Limit cycle XII (period-three motion): projection of phase space on the $p_1 - p_2$ plane

are created. Multiple limit cycles coexist over some ranges of $\hat{\sigma}_2$. Some limit cycles undergo a symmetry breaking bifurcation. Period-three motions are observed over a narrow range of excitation frequencies. Cyclic-fold bifurcations are observed. They are accompanied by cyclic jumps. Numerical integration suggests that some of these jumps cause a transition to chaos.

Acknowledgment

This work was supported by the National Science Foundation under Grant # MSM-8521748 and the Air Force Office of Scientific Research under Grant # AFOSR-86-0090.

References

Aprille, T. J., Jr., and Trick, T. N., 1972, "A Computer Algorithm to Determine the Steady-State Response of Nonlinear Oscillators," *IEEE Transactions on Circuit Theory*, Vol. CT-19, pp. 354–360.

Bieniek, M. P., Fan, T. C., and Lackman, L. M., 1966, "Dynamic Stability of Cylindrical Shells," *AIAA Journal*, Vol. 4, pp. 495–500.

Chen, J. C., and Babcock, C. D., 1975, "Nonlinear Vibration of Cylindrical Shells," *AIAA Journal*, Vol. 13, pp. 868–876.

Cooley, J. W., and Tukey, J W., 1965, "An Algorithm for the Machine Computation of Complex Fourier Series," *Math. Computation*, Vol. 19, pp. 297–301.

Evensen, D. A., 1966, "Nonlinear Flexural Vibrations of Thin Circular Rings," ASME JOURNAL OF APPLIED MECHANICS, Vol. 33, pp. 553–560.

Farmer, J. D., 1982, "Chaotic Attractors of an Infinite-Dimensional Dynamical System," *Physica D*, Vol. 4, pp. 366–393.

Frederickson, P., Kaplan, J. L., Yorke, E. D., and Yorke, J. A., 1983, "The Lyapunov Dimension of Strange Attractors," *Journal of Differential Equations*, Vol. 49, pp. 185–207.

Goodier, J. N., and McIvor, I. K., 1964, "The Elastic Cylindrical Shell under Nearly Uniform Radial Impulse," ASME JOURNAL OF APPLIED MECHANICS, Vol. 31, pp. 259–266.

Hale, J. K., 1963, *Oscillations in Nonlinear Systems*, McGraw-Hill Book Co., New York.

Hirsch, M. W., and Smale, S., 1974, *Differential Equations, Dynamical Systems and Linear Algebra*, Academic Press, New York.

Lichtenberg, A. J., and Lieberman, M. A., 1983, *Regular and Stochastic Motion*, Springer-Verlag, New York.

Maewal, A., 1986, "Miles' Evolution Equations for Axisymmetric Shells: Simple Strange Attractors in Structural Dynamics," *Int. J. Non-Linear Mechanics*, Vol. 21, pp. 433–438.

McIvor, I. K., 1962, "Dynamic Stability and Nonlinear Oscillations of Cylindrical Shells (Plane Strain) Subjected to Impulsive Pressure," Ph.D. Dissertation, Stanford University, Stanford, Calif.

McIvor, I. K., 1966, "The Elastic Cylindrical Shell Under Radial Impulse," ASME JOURNAL OF APPLIED MECHANICS, Vol. 33, pp. 831–837.

McIvor, I. K., and Songstegard, D. A., 1966, "Axisymmetric Response of a Closed Spherical Shell to a Nearly Uniform Radial Impulse," *The Journal of the Acoustical Society of America*, Vol. 40, pp. 1540–1547.

McIvor, I. K., and Lovell, E. G., 1968, "Dynamic Response of Finite-Length Cylindrical Shells to Nearly Uniform Radical Impulse," *AIAA Journal*, Vol. 6, pp. 2346–2351.

Mente, L. J., 1973, "Dynamic Nonlinear Response of Cylindrical Shells to Asymmetric Pressure Loading," *AIAA Journal*, Vol. 11, pp. 793–800.

Moganty, S. P., and Bickford, W. B., 1987, "Large Amplitude Oscillations of Thin Circular Rings," ASME JOURNAL OF APPLIED MECHANICS, Vol. 54, pp. 315–322.

Nayfeh, A. H., 1973, *Perturbation Methods*, John Wiley and Sons, New York.

Nayfeh, A. H., and Mook, D. T., 1979, *Nonlinear Oscillations*, John Wiley and Sons, New York.

Nayfeh, A. H., 1981, *Introduction to Perturbation Techniques*, John Wiley and Sons, New York.

Nayfeh, A. H., and Raouf, R. A., 1986, "Nonlinear Forced Response of Circular Cylindrical Shells," *ASME Design and Analysis of Plates and Shells*, Vol. 105, pp. 145–155.

Nayfeh, A. H,. and Raouf, R. A., 1987a, "Nonlinear Forced Response of Infinitely Long Circular Shells," ASME JOURNAL OF APPLIED MECHANICS, Vol. 109, pp. 571–577.

Nayfeh, A. H., and Raouf, R. A., 1987b, "Non-Linear Oscillation of Circular Cylindrical Shells," *International Journal of Solids and Structures*, Vol. 23, pp. 1625–1638.

Raouf, R. A., 1985, "Nonlinear Forced Response of Circular Cylindrical Shells," Thesis, Department of Engineering Science and Mechanics, Virginia Polytechnic Institute and State University, Blacksburg, Va.

Simmonds, J. G., 1979, "Accurate Nonlinear Equations and a Perturbation Solution for the Free Vibrations of a Circular Elastic Ring," ASME JOURNAL OF APPLIED MECHANICS, Vol. 46, pp. 156–160.

Singleton, R. C., 1969, "An Algorithm for Computing the Mixed Radix Fast Fourier Transform," *IEEE Transactions of Audio and Electroacoustics*, Vol. AU-17, pp. 93–103.

Urabe, M., 1967, *Nonlinear Autonomous Oscillations*, Academic Press, New York.

Wolf, A., Swift, J. B., Swinney, H. L., and Vastano, J. A., 1985, "Determining Lyapunov Exponents from a Time Series," *Physica D*, Vol. 16, pp. 285–317.

Yasuda, K., and Kushida, G., 1984, "Nonlinear Forced Oscillations of a Shallow Spherical Shell," *Bulletin of JSME*, Vol. 27, pp. 2233–2240.

H. Cohen
Department of Applied Mathematics,
University of Manitoba,
Winnipeg, Manitoba R3T 2N2 Canada

G. P. Mac Sithigh
Department of Mechanical and Aerospace
Engineering and Engineering Mechanics,
University of Missouri-Rolla,
Rolla, MO 65401-0249
Mem. ASME

Impulsive Motions of Elastic Pseudo-Rigid Bodies

We develop the formalism for treating impact problems in the theory of pseudo-rigid bodies developed by Cohen and Muncaster. Our treatment is general enough to include the effect of kinematical constraints.

1 Introduction

The theory of pseudo-rigid bodies was introduced by Cohen (1981) and Muncaster (1984). It is a dynamical theory which in a certain sense approximates the theory of finite elasticity. The monograph of Cohen and Muncaster (1988) gives a detailed exposition of the theory, with some applications.

The theory is useful as a practical model in situations in which the motion is approximately homogeneous, or, more generally, in which only spatial averages of stress and strain are required. In particular, the theory has been suggested as a simplified model of deformable satellites.

In this paper we develop the formalism for impulsive motions of pseudo-rigid bodies. Our development parallels that for rigid bodies as presented in McMillan (1960) or Goldsmith (1960). The impact is modeled as consisting of a deformation phase and a restitution phase. The impact is characterized by impulsive point loads of deformation and restitution, and by their ratio, the coefficient of restitution. As in the rigid case, this treatment amounts to coarse modeling of phenomena which, strictly speaking, lie outside the scope of the theory being used. In the pseudo-rigid case, the phenomena in question are *inhomogeneous* deformations and inelastic effects. (In the rigid case they are deformation and inelastic effects.)

The theory of impulsive motions of *rigid* bodies is still a matter of current research. Brach (1981) has argued that, in general, impulsive couples at the impact site must be included. He has also (1984, 1989) discussed the status of the tangential impulse in impacts. Keller (1986) has given a careful analysis of ambiguous situations that can arise in impacts with friction.

The impact of linearly elastic bodies is sometimes modeled by the Hertz approximation (Goldsmith, 1960, Chapter 4). The local nature of this analysis and the various approximations involved make it difficult to meaningfully compare its results with those of the present work.

In Section 2 of this paper, we establish notation and recall some essential facts from the theory of pseudo-rigid bodies. In Section 3 we present a detailed analysis of the impact for the case of two pseudo-rigid bodies, each subject to two independent constraints.

In Section 4, we develop the equations governing the impact of an incompressible pseudo-rigid body on a rigid wall. We apply these to the study of the details of pre-impact and post-impact motions for a specific example.

2 Notation and Preliminaries

In this section we establish the notational scheme of the work and recall some essential facts from the theory of pseudo-rigid bodies.

In this work we shall adhere to the summation convention for repeated indices. Lower case roman indices will range from 1 to 3, lower case Greek indices from 1 to 2.

The equations governing the smooth $(\bar{\mathbf{r}}(t), \mathbf{F}(t))$ of a pseudo-rigid body are

$$m\ddot{\bar{\mathbf{r}}} = \mathbf{f}_{\text{ext}},$$

and

$$\ddot{\mathbf{F}}\,\mathbf{E}\,\mathbf{F}^T = \mathbf{M}_{\text{ext}} - \boldsymbol{\Sigma}. \tag{1}$$

Here, $\bar{\mathbf{r}}$ denotes the position vector of the body's mass center, $\mathbf{F}$ the deformation gradient tensor, m the mass and $\mathbf{E}$ the Euler (inertia) tensor of the body.

If the body is acted upon only by a system of N concentrated loads $\mathbf{f}_p$, $1 \le p \le N$, applied at points whose current position vectors relative to the mass center are $\mathbf{r}_p$, $1 \le p \le N$, then we have

$$\mathbf{f}_{\text{ext}} = \sum_{p=1}^{N} \mathbf{f}_p,$$

$$\mathbf{M}_{\text{ext}} = \sum_{p=1}^{N} \mathbf{f}_p \otimes \mathbf{r}_p. \tag{2}$$

If the body is composed of an elastic material with stored-energy function per unit mass $W(\cdot)$ and subject to the kinematical constraints $g^\alpha(\mathbf{F}) \equiv 0$, the internal force moment is given by

$$\boldsymbol{\Sigma} = mW_F(\mathbf{F})\mathbf{F}^T + \Gamma_\alpha g^\alpha_F(\mathbf{F})\mathbf{F}^T, \tag{3}$$

Contributed by the Applied Mechanics Division of THE AMERICAN SOCIETY OF MECHANICAL ENGINEERS for publication in the JOURNAL OF APPLIED MECHANICS.

Discussion on this paper should be addressed to the Technical Editor, Prof. Leon M. Keer, The Technological Institute, Northwestern University, Evanston, IL 60208, and will be accepted until two months after final publication of the paper itself in the JOURNAL OF APPLIED MECHANICS. Manuscript received by the ASME Applied Mechanics Division, Mar. 2, 1990; final revision, June 18, 1990.

the Γ_α, as usual, denoting constitutively indeterminate constraint reactions.

We may recover the appropriate expressions for the case of one or of no constraints by setting one or both of the Γ_α equal to zero in Eq. (3).

In this paper we shall sometimes be concerned with the collision of two such bodies. We shall carry over as much as possible of the foregoing notational scheme to this situation by simply indexing quantities to distinguish between bodies 1 and 2. Thus, the meaning of expressions such as m_1, $\bar{\mathbf{r}}_1$, $\mathbf{F}_2$, $\mathbf{E}_2$, $W^1(\cdot)$, are fairly obvious; $g^{12}(\mathbf{F}_1)$ denotes the second constraint on body 1, Γ_{12} is the corresponding constraint reaction, and so on.

As in our previous paper (1989), we shall often be concerned with pseudo-rigid *membranes* rather than three-dimensional bodies. The only modification to the foregoing development is that now $\mathbf{F}$ denotes a nonsingular tensor on a two-dimensional space.

We recall from the results of the above-mentioned paper the fact that in a *plane* motion in the plane normal to $\mathbf{i}_3$, $\mathbf{F}$ has the representation

$$\mathbf{F}=\lambda\mathbf{e}_1(\phi)\otimes\mathbf{e}_1(\psi)+\mu\mathbf{e}_2(\phi)\otimes\mathbf{e}_2(\psi)+\upsilon\mathbf{i}_3\otimes\mathbf{i}_3 \tag{4}$$

where

$$\mathbf{e}_1(\zeta) := \cos\zeta\,\mathbf{i}_1+\sin\zeta\,\mathbf{i}_2,$$

$$\mathbf{e}_2(\zeta) := -\sin\zeta\,\mathbf{i}_1+\cos\zeta\,\mathbf{i}_2.$$

In the next section we shall develop in detail the formalism for the mutual impact of two pseudo-rigid bodies each subject to two independent general constraints.

3 The Collision of Two Generally Biconstrained Bodies

In this section, we consider the impact of two pseudo-rigid bodies. We shall model the impact process as involving jumps in $\dot{\mathbf{F}}_\alpha$, $\dot{\bar{\mathbf{r}}}_\alpha$ while $\mathbf{F}_\alpha$ $\bar{\mathbf{r}}_\alpha$ remain fixed. We regard the impact process as consisting of a deformation phase and a restitution phase. During the deformation phase, an impulse $\hat{P}\mathbf{e}$ acts at the point of impact; during the restitution phase an impulse $\hat{R}\mathbf{e}$ acts at the point of impact. Moreover,

$$\hat{R}=k\hat{P}, \tag{5}$$

k being the coefficient of restitution for the impact. During the deformation phase, the constraint reactions suffer an impulse $\hat{\Gamma}_{\alpha\beta}$, while during the restitution phase, they undergo an impulse $\hat{\Gamma}'_{\alpha\beta}$. We shall impose on the constraints $g^{\alpha\beta}(\cdot)$ the mild restriction that

(i) $g_{\mathbf{F}}^{\alpha\beta}(\mathbf{F})\neq 0$ for $\mathbf{F}$ non-singular,

(ii) $g_{\mathbf{F}}^{\alpha 1}(\mathbf{F})$ and $g_{\mathbf{F}}^{\alpha 2}(\mathbf{F})$ are linearly independent for $\mathbf{F}$ nonsingular.

In our previous work (1989), we considered three types of kinematical constraint, namely, incompressibility, inextensibility, and unshearability. It is easy to see that any pair of these will satisfy both of these conditions.

We shall denote by $\mathbf{R}_\alpha$ the position vector of the impact point on body α and introduce the notation

$$\mathbf{r}_\alpha=\mathbf{R}_\alpha-\bar{\mathbf{r}}_\alpha. \tag{6}$$

We denote, by $\mathbf{n}$, the common normal vector at impact pointing from body 2 into body 1. If μ_k is the coefficient of kinetic friction for the surfaces of the two bodies, then the vector $\mathbf{e}$ has the orthogonal decomposition

$$\mathbf{e}=e_n\mathbf{n}+\mathbf{e}' \tag{7}$$

where

$$\frac{|\mathbf{e}'|}{e_n}=\mu_k. \tag{8}$$

We shall denote pre-impact quantities by a superscript $(-)$, post-impact quantities by a superscript $(+)$, and quantities at the transition between deformation and restitution by a superscript (i).

The final ingredient in our model of the impact process is the requirement that at the transition from deformation to restitution, the relative normal velocity of the impact points should be zero, thus

$$\mathbf{n}\cdot\dot{\mathbf{R}}_1^{(i)}=\mathbf{n}\cdot\dot{\mathbf{R}}_2^{(i)},$$

or, more explicitly,

$$\mathbf{n}\cdot\dot{\bar{\mathbf{r}}}_1^{(i)}+\mathbf{n}\cdot\dot{\mathbf{F}}_1^{(i)}\mathbf{F}_1^{-1}\mathbf{r}_1=\mathbf{n}\dot{\bar{\mathbf{r}}}_2^{(i)}+\mathbf{n}\cdot\dot{\mathbf{F}}_2^{(i)}\mathbf{F}_2^{-1}\mathbf{r}_2. \tag{9}$$

Granted those preliminaries, the equations governing the impact process are

$$m_1\dot{\bar{\mathbf{r}}}_1^{(i)}-m_1\dot{\bar{\mathbf{r}}}_1^{(-)}=\hat{P}\mathbf{e}, \tag{10a}$$

$$m_1\dot{\bar{\mathbf{r}}}_1^{(+)}-m_1\dot{\bar{\mathbf{r}}}_1^{(i)}=k\hat{P}\mathbf{e}, \tag{10b}$$

$$m_2\dot{\bar{\mathbf{r}}}_2^{(i)}-m_2\dot{\bar{\mathbf{r}}}_2^{(-)}=-\hat{P}\mathbf{e}, \tag{10c}$$

$$m_2\dot{\bar{\mathbf{r}}}_2^{(+)}-m_2\dot{\bar{\mathbf{r}}}_2^{(i)}=-k\hat{P}\mathbf{e} \tag{10d}$$

$$\dot{\mathbf{F}}_1^{(i)}\mathbf{E}_1-\dot{\mathbf{F}}_1^{(-)}\mathbf{E}_1=\hat{P}\mathbf{e}\otimes\mathbf{F}_1^{-1}\mathbf{r}_1-\hat{\Gamma}_{1\alpha}g_{\mathbf{F}}^{1\alpha}(\mathbf{F}_1), \tag{10e}$$

$$\dot{\mathbf{F}}_1^{(+)}\mathbf{E}_1-\dot{\mathbf{F}}_1^{(i)}\mathbf{E}_1=k\hat{P}\mathbf{e}\otimes\mathbf{F}_1^{-1}\mathbf{r}_1-\hat{\Gamma}'_{1\alpha}g_{\mathbf{F}}^{1\alpha}(\mathbf{F}_1), \tag{10f}$$

$$\dot{\mathbf{F}}_2^{(i)}\mathbf{E}_2-\dot{\mathbf{F}}_2^{(-)}\mathbf{E}_2=-\hat{P}\mathbf{e}\otimes\mathbf{F}_2^{-1}\mathbf{r}_2-\hat{\Gamma}_{2\alpha}g_{\mathbf{F}}^{2\alpha}(\mathbf{F}_2), \tag{10g}$$

$$\dot{\mathbf{F}}_2^{(+)}\mathbf{E}_2-\dot{\mathbf{F}}_2^{(i)}\mathbf{E}_2=-k\hat{P}\mathbf{e}\otimes\mathbf{F}_2^{-1}\mathbf{r}_2-\hat{\Gamma}'_{2\alpha}g_{\mathbf{F}}^{2\alpha}(\mathbf{F}_2). \tag{10h}$$

We note the fact that since the constraints are identically satisfied by $\mathbf{F}_\alpha$, we must have

$$g_{\mathbf{F}}^{1\alpha}(\mathbf{F}_1)\cdot\dot{\mathbf{F}}_1=g_{\mathbf{F}}^{2\alpha}(\mathbf{F}_2)\cdot\dot{\mathbf{F}}_2=0 \quad \text{each } \alpha. \tag{11}$$

Moreover, it follows from (10e)–(10h) that

$$\dot{\mathbf{F}}_1^{(+)}+k\dot{\mathbf{F}}_1^{(-)}-[1+k]\dot{\mathbf{F}}_1^{(i)}=-[\hat{\Gamma}'_{1\alpha}-k\hat{\Gamma}_{1\alpha}]g_{\mathbf{F}}^{1\alpha}(\mathbf{F}_1)\mathbf{E}_1^{-1}, \tag{12a}$$

$$\dot{\mathbf{F}}_2^{(+)}+k\dot{\mathbf{F}}_2^{(-)}-[1+k]\dot{\mathbf{F}}_2^{(i)}=-[\hat{\Gamma}'_{2\alpha}-k\hat{\Gamma}_{2\alpha}]g_{\mathbf{F}}^{2\alpha}(\mathbf{F}_2)\mathbf{E}_2^{-1}. \tag{12b}$$

We define tensors $\mathbf{K}^{1\alpha}$, $\mathbf{K}^{2\alpha}$ by

$$\mathbf{K}^{1\alpha}(\mathbf{F}_1):=g_{\mathbf{F}}^{1\alpha}(\mathbf{F}_1)\mathbf{E}_1^{-1/2},$$

$$\mathbf{K}^{2\alpha}(\mathbf{F}_2):=g_{\mathbf{F}}^{2\alpha}(\mathbf{F}_2)\mathbf{E}_2^{-1/2}. \tag{13}$$

If we operate on (12a), (12b) with $g_{\mathbf{F}}^{1\alpha}(\mathbf{F}_1)$, $g_{\mathbf{F}}^{1\alpha}(\mathbf{F}_2)$, respectively, the left-hand side vanishes by (11) and we are left with the identities

$$\{\mathbf{K}^{1\alpha}(\mathbf{F}_1)\cdot\mathbf{K}^{1\beta}(\mathbf{F}_1)\}\{\hat{\Gamma}'_{1\beta}-k\hat{\Gamma}_{1\beta}\}=0, \tag{14a}$$

$$\{\mathbf{K}^{2\alpha}(\mathbf{F}_2)\cdot\mathbf{K}^{2\beta}(\mathbf{F}_2)\}\{\hat{\Gamma}'_{2\beta}-k\hat{\Gamma}_{2\beta}\}=0. \tag{14b}$$

The symmetric 2×2 matrix, whose entries are $\{\mathbf{K}^{1\alpha}(\mathbf{F}_1)\cdot\mathbf{K}^{1\beta}(\mathbf{F}_1)\}$, is nonsingular precisely if

$$|\mathbf{K}^{11}(\mathbf{F}_1)\cdot\mathbf{K}^{12}(\mathbf{F}_1)|\neq|\mathbf{K}^{11}(\mathbf{F}_1)||\mathbf{K}^{12}(\mathbf{F}_1)|. \tag{15}$$

But this follows from the Cauchy-Schwarz inequality and the fact that the $\mathbf{K}^{1\alpha}$ are linearly independent. Hence, (14b) implies

$$\hat{\Gamma}'_{1\alpha}=k\hat{\Gamma}_{1\alpha}. \tag{16}$$

Similarly, we see that

$$\hat{\Gamma}'_{2\alpha}=k\hat{\Gamma}_{2\alpha}. \tag{17}$$

We next exploit (11) to develop relationships between the $\hat{\Gamma}_{\alpha\beta}$ and $\hat{P}$. It follows from (10e) that

$$\dot{\mathbf{F}}_1^{(i)}-\dot{\mathbf{F}}_1^{(-)}=\hat{P}\mathbf{e}\otimes\mathbf{E}_1^{-1}\mathbf{F}_1^{-1}\mathbf{r}_1+\hat{\Gamma}_{1\alpha}g_{\mathbf{F}}^{1\alpha}(\mathbf{F}_1)\mathbf{E}_1^{-1}. \tag{18}$$

Operation on (18) with $g_{\mathbf{F}}^{1\beta}(\mathbf{F}_1)$ implies, in view of (11) that

$$\{\mathbf{K}^{1\beta}(\mathbf{F}_1)\cdot\mathbf{K}^{1\alpha}(\mathbf{F}_1)\}\hat{\Gamma}_{1\alpha}=\hat{P}\mathbf{e}\cdot\mathbf{K}^{1\beta}(\mathbf{F}_1)\mathbf{E}_1^{-1/2}\mathbf{F}_1^{-1}\mathbf{r}_1. \tag{19}$$

Similarly, from (10g) and (11) we get

$$\{\mathbf{K}^{2\beta}(\mathbf{F}_2)\cdot\mathbf{K}^{2\alpha}(\mathbf{F}_2)\}\hat{\Gamma}_{2\alpha}=-\hat{P}\mathbf{e}\cdot\mathbf{K}^{2\beta}(\mathbf{F}_2)\mathbf{E}_2^{-1/2}\mathbf{F}_2^{-1}\mathbf{r}_2. \tag{20}$$

Since the matrices on the left-hand sides of (19) and (20) are nonsingular, we may rewrite these equations in the form

$$\hat{\Gamma}_{1\alpha} = \Lambda_{1\alpha}(\mathbf{F}_1)\hat{P}, \quad \hat{\Gamma}_{2\alpha} = \Lambda_{2\alpha}(\mathbf{F}_2)\hat{P}, \tag{21}$$

for known functions $\Lambda_{\alpha\beta}(\cdot)$.

Our next step is to use the impact condition (9) to determine the impulse $\hat{P}$ in terms of pre-impact quantities. We introduce the notation

$$\mathbf{H}_\alpha := \mathbf{F}_\alpha^{-T}\mathbf{E}_\alpha^{-1}\mathbf{F}_\alpha^{-1} \quad (\alpha \text{ no sum}) \tag{22}$$

The left-hand side of (9) now takes the form

$$\begin{aligned}\mathbf{n}\cdot\dot{\mathbf{R}}^{(i)} &= \mathbf{n}\cdot\{\dot{\bar{\mathbf{r}}}^{(-)} + \dot{\mathbf{F}}_1^{(-)}\mathbf{F}_1^{-1}\mathbf{r}_1\} + \hat{P}\{(\mathbf{n}\cdot\mathbf{e})[m_1^{-1} \\ &\quad + (\mathbf{r}_1\cdot\mathbf{H}_1\mathbf{r}_1)] - \Lambda_{1\alpha}(\mathbf{F}_1)\mathbf{n}\cdot\mathbf{K}^{1\alpha}(\mathbf{F}_1)\mathbf{E}_1^{-1/2}\mathbf{F}_1^{-1}\mathbf{r}_1\} \\ &= \mathbf{n}\cdot\dot{\mathbf{R}}_1^{(-)} + \hat{P}\{(\mathbf{n}\cdot\mathbf{e})[m_1^{-1} + \mathbf{r}_1\mathbf{H}_1\mathbf{r}_1] \\ &\quad - \Lambda_{1\alpha}(\mathbf{F}_1)\mathbf{n}\cdot\mathbf{K}^{1\alpha}(\mathbf{F}_1)\mathbf{E}_1^{-1/2}\mathbf{F}_1^{-1}\mathbf{r}_1\}. \end{aligned} \tag{23}$$

Similarly, the right-hand side of (9) becomes

$$\begin{aligned}\mathbf{n}\cdot\dot{\mathbf{R}}_2^{(i)} &= \mathbf{n}\cdot\dot{\mathbf{R}}_2^{(-)} - \hat{P}\{(\mathbf{n}\cdot\mathbf{e})[m_2^{-1} + \mathbf{r}_2\mathbf{H}_2\mathbf{r}_2] \\ &\quad - \Lambda_{2\alpha}(\mathbf{F}_2)\mathbf{n}\cdot\mathbf{K}^{2\alpha}(\mathbf{F}_2)\mathbf{E}^{-1/2}{}_2\mathbf{F}_2^{-}\mathbf{r}_2\}. \end{aligned} \tag{24}$$

Thus, (9) takes the final form

$$\begin{aligned}\mathbf{n}\cdot(\dot{\mathbf{R}}_1^{(-)} - \dot{\mathbf{R}}_2^{(-)}) = -\hat{P}\Bigg\{&(\mathbf{n}\cdot\mathbf{e})\left[\frac{m_1+m_2}{m_1m_2} + \mathbf{r}_1\cdot\mathbf{H}_1\mathbf{r}_1 + \mathbf{r}_2\cdot\mathbf{H}_2\mathbf{r}_2\right] \\ &- \Lambda_{1\alpha}(\mathbf{F}_1)\mathbf{n}\cdot\mathbf{K}^{1\alpha}(\mathbf{F}_1)\mathbf{E}_1^{-1/2}\mathbf{F}_1^{-1}\mathbf{r}_1 \\ &- \Lambda_{2\alpha}(\mathbf{F}_2)\mathbf{n}\cdot\mathbf{K}^{2\alpha}(\mathbf{F}_2)\mathbf{E}_2^{-1/2}\mathbf{F}_2^{-1}\mathbf{r}_2\Bigg\}. \end{aligned} \tag{25}$$

Equation (25) relates $\hat{P}$ to the relative normal velocity of the impact points before impact, the $\mathbf{F}_\alpha$, and the inertial and constraint properties of the two bodies. Our final task, now that $\hat{P}$ has been determined as a function of pre-impact quantities, is to develop the initial conditions for the subsequent motion, that is $\dot{\bar{\mathbf{r}}}_\alpha^{(+)}$, $\dot{\mathbf{F}}_\alpha^{(+)}$. It follows from (10), (16), (17), and (21) that

$$\dot{\bar{\mathbf{r}}}_1^{(+)} = \dot{\bar{\mathbf{r}}}_1^{(-)} + m_1^{-1}(1+k)\hat{P}\mathbf{e}, \tag{26a}$$

$$\dot{\bar{\mathbf{r}}}_2^{(+)} = \dot{\bar{\mathbf{r}}}_2^{(-)} - m_2^{-1}(1+k)\hat{P}\mathbf{e}, \tag{26b}$$

$$\begin{aligned}\dot{\mathbf{F}}_1^{(+)} &= \dot{\mathbf{F}}_1^{(-)} + (1+k)\hat{P}\{\mathbf{e}\otimes\mathbf{E}_1^{-1}\mathbf{F}_1^{-1}\mathbf{r}_1 \\ &\quad - \Lambda_{1\alpha}(\mathbf{F}_1)\mathbf{K}^{1\alpha}(\mathbf{F}_1)\mathbf{E}_1^{-1/2}\} \end{aligned} \tag{26c}$$

$$\begin{aligned}\dot{\mathbf{F}}_2^{(+)} &= \dot{\mathbf{F}}_2^{(-)} - (1+k)\hat{P}\{\mathbf{e}\otimes\mathbf{E}_2^{-1}\mathbf{F}_2^{-1}\mathbf{r}_2 \\ &\quad - \Lambda_{2\alpha}(\mathbf{F}_2)\mathbf{K}^{2\alpha}(\mathbf{F}_2)\mathbf{E}_2^{-1/2}\}. \end{aligned} \tag{26d}$$

These equations determine $\dot{\bar{\mathbf{r}}}_\alpha^{(+)}$, $\dot{\mathbf{F}}_\alpha^{(+)}$ in terms of pre-impact quantities.

Several remarks are in order. First, the foregoing treatment assumes that the tangential relative velocity of the impact points does not change direction in the course of the impact, i.e., that

$$\begin{aligned}&\mathbf{e}'\cdot(\dot{\mathbf{R}}_1^{(-)} - \dot{\mathbf{R}}_2^{(-)}) < 0, \quad \mathbf{e}'\cdot(\dot{\mathbf{R}}_1^{(i)} - \dot{\mathbf{R}}_2^{(i)}) < 0, \\ &\qquad\qquad \mathbf{e}'\cdot(\dot{\mathbf{R}}_1^{(+)} - \dot{\mathbf{R}}_2^{(+)}) < 0. \end{aligned} \tag{27}$$

Should the second or third of these conditions fail, the foregoing analysis will yield physically incorrect results. For the analogous situation in *rigid* body mechanics, the subtleties of such cases have been discussed by Brach (1984; 1989), and Keller (1986). It would be straightforward to adapt the techniques of these works to the pseudo-rigid case, and we intend to do this in a future paper.

A second observation is that the governing equations for an assortment of simpler cases may be extracted from the above analysis without further labor. For instance, the equation governing the collision of two unconstrained bodies are obtainable from (10) simply by setting the $\hat{\Gamma}_{\alpha\beta}$ and $\hat{\Gamma}'_{\alpha\beta}$ equal to zero. If body 1 is subject to only one constraint, the system (14*a*) is replaced by a single equation, as is the system (19). The case in which a pseudo-rigid body impacts a rigid plane with outer unit normal $\mathbf{n}$ has governing equations (10*a*), (10*b*), (10*e*), (10*f*) with impact condition

$$\mathbf{n}\cdot\dot{\mathbf{R}}^{(i)} = 0 \tag{28}$$

replacing (9).

In Section 4 we shall present the results for the impact of an incompressible pseudo-rigid body on a rigid plane and apply these to the detailed study of an explicit example.

4 An Explicit Example

In this section, we shall study the free motion on a smooth horizontal plane of an incompressible, isotropic, pseudo-rigid disk before and after impact with a rigid, vertical wall. We begin by developing the relevant equations.

For the constraint of incompressibility, the constraint function $g(\cdot)$ is given by

$$g(\mathbf{F}) \equiv 1 - \det\mathbf{F}, \tag{29}$$

and the internal force moment by

$$\Sigma = mW_{\mathbf{F}}(\mathbf{F})\mathbf{F}^T - p\mathbf{1}. \tag{30}$$

If such a body collides with a rigid wall with normal $\mathbf{n}$, the impulse of deformation $\hat{P}$ is

$$\begin{aligned}\hat{P} = -\{&(\mathbf{n}\cdot\mathbf{e})\mathrm{tr}\mathbf{H}[m^{-1} + \mathbf{r}\cdot\mathbf{H}\mathbf{r}] \\ &- (\mathbf{n}\cdot\mathbf{H}\mathbf{r})(\mathbf{e}\cdot\mathbf{H}\mathbf{r}\}^{-1}\,\mathrm{tr}\mathbf{H}(\mathbf{n}\cdot\dot{\mathbf{R}}^{(-)}). \end{aligned} \tag{31}$$

The corresponding impulse to the constraint reaction p is

$$\hat{p} = -(\mathrm{tr}\mathbf{H})^{-1}\mathbf{e}\cdot\mathbf{H}\mathbf{r}\hat{P}. \tag{32}$$

The initial conditions for the subsequent motion of the body are

$$\dot{\bar{\mathbf{r}}}^{(+)} = \dot{\bar{\mathbf{r}}}^{(-)} + m^{-1}(1+k)\hat{P}\mathbf{e}, \tag{33a}$$

$$\dot{\mathbf{F}}^{(+)} = \dot{\mathbf{F}}^{(-)} + (1+k)\{\hat{P}\mathbf{e}\otimes\mathbf{E}^{-1}\mathbf{F}^{-1}\mathbf{r} + \hat{p}\mathbf{F}^{-T}\mathbf{E}^{-1}\}. \tag{33b}$$

Recall that the kinetic energy of a pseudo-rigid body is defined as

$$T := \frac{1}{2}m\dot{\bar{\mathbf{r}}}\cdot\dot{\bar{\mathbf{r}}} + \frac{1}{2}\mathrm{tr}\{\dot{\mathbf{F}}\,\mathbf{E}\,\dot{\mathbf{F}}^T\}. \tag{34}$$

A simple calculation using (31)–(33) yields

$$T^{(+)} - T^{(-)} := \Delta T$$

$$\begin{aligned}\Delta T = \{&(\mathbf{n}\cdot\mathbf{e})\mathrm{tr}\,\mathbf{H}[m^{-1} + \mathbf{r}\cdot\mathbf{H}\mathbf{r}] - (\mathbf{n}\cdot\mathbf{H}\mathbf{r})(\mathbf{e}\cdot\mathbf{H}\mathbf{r})\}^{-1}(1+k)\hat{P} \\ &\times\Bigg\{\mathrm{tr}\,\mathbf{H}[m^{-1} + \mathbf{r}\cdot\mathbf{H}\mathbf{r}]\left[(\mathbf{n}\cdot\mathbf{e})(\mathbf{e}\cdot\dot{\mathbf{R}}^{(-)}) - \frac{1}{2}(1+k)(\mathbf{n}\cdot\dot{\mathbf{R}}^{(-)})\right] \\ &+ (\mathbf{e}\cdot\mathbf{H}\mathbf{r})\left[\frac{1}{2}(1+k)(\mathbf{e}\cdot\mathbf{H}\mathbf{r})(\mathbf{n}\cdot\dot{\mathbf{R}}^{(-)}) - (\mathbf{n}\cdot\mathbf{H}\mathbf{r})(\mathbf{e}\cdot\dot{\mathbf{R}}^{(-)})\right]\Bigg\}, \end{aligned} \tag{35}$$

for the change in kinetic energy due to the impact. Notice that in the absence of friction ($\mathbf{e} = \mathbf{n}$), $\Delta T = 0$ precisely if $k = 1$. We now turn to our specific example.

In our previous paper (1989), we considered the free motion of a circular incompressible, isotropic pseudo-rigid membrane on a smooth horizonal plane. The center of mass has constant velocity $\dot{\bar{\mathbf{r}}}$, the deformation gradient tensor is given by

$$\mathbf{F} = \lambda\mathbf{e}_1(\phi)\otimes\mathbf{e}_1(\psi) + \lambda^{-1}\mathbf{e}_2(\phi)\otimes\mathbf{e}_2(\psi) \tag{36}$$

and the stored energy function is given by

$$W(\mathbf{F}) = \tilde{W}(\lambda,\lambda^{-1}). \tag{37}$$

As we established in the above-mentioned work, this motion has three first integrals, namely

$$(\lambda - \lambda^{-1})^2[\dot{\phi} + \dot{\psi}] = K \quad (\text{const}), \tag{38a}$$

$$(\lambda + \lambda^{-1})^2[\dot{\phi} - \dot{\psi}] = L \quad (\text{const}), \tag{38b}$$

and

$$\begin{aligned}\frac{r^2}{8}\left\{\frac{\lambda^4+1}{\lambda^4}\dot{\lambda}^2 + \frac{K^2\lambda^2}{2(\lambda^2-1)^2} + \frac{L^2\lambda^2}{2(\lambda^2+1)^2}\right\} \\ + \tilde{W}(\lambda,\lambda^{-1}) = E \ (\text{const}). \end{aligned} \tag{38c}$$

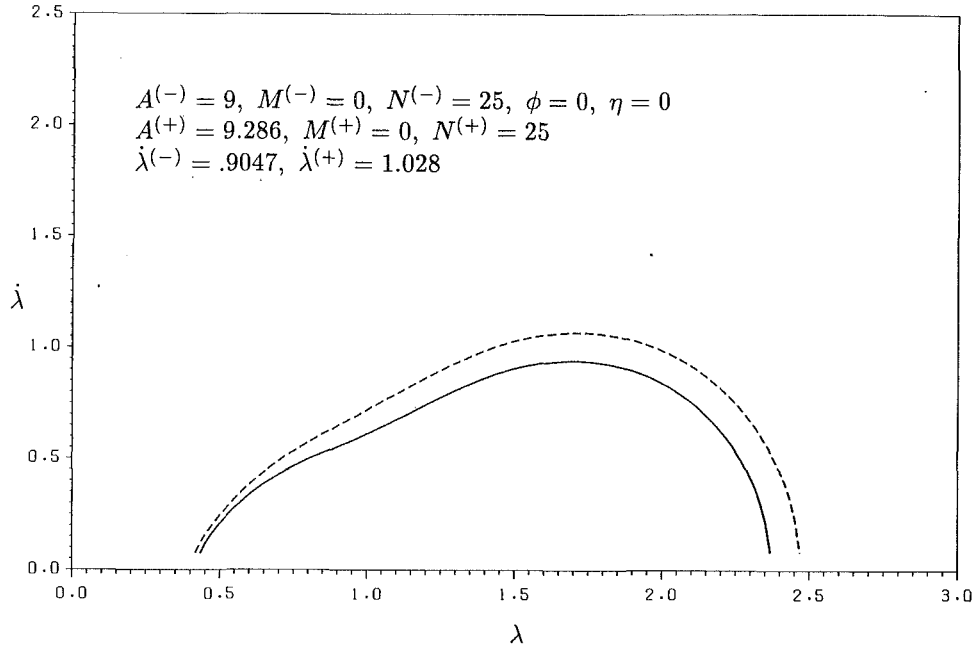

Fig. 1

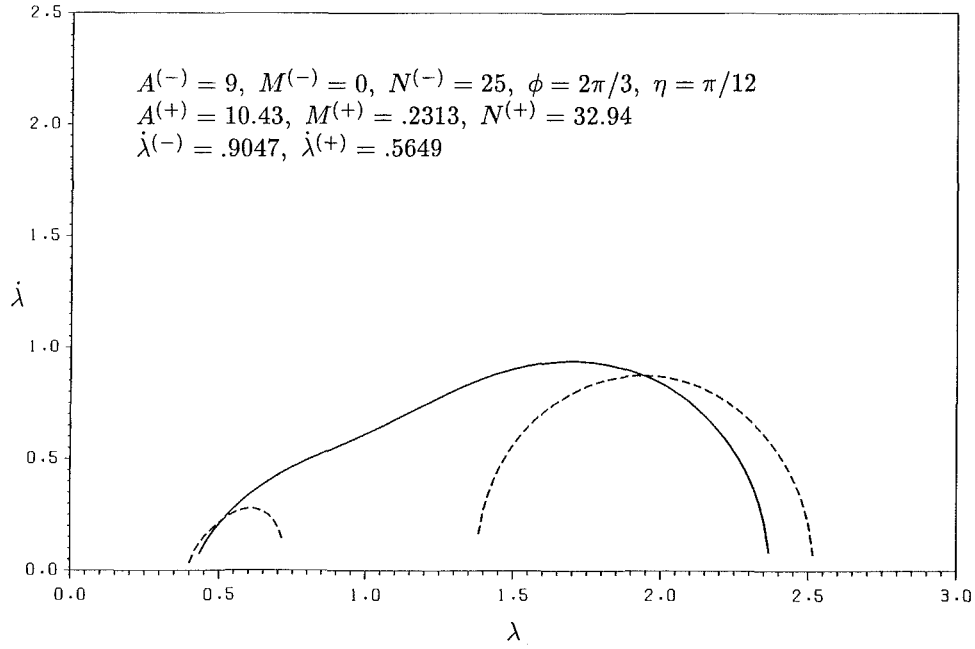

Fig. 2

Here, E is the total energy less the (constant) kinetic energy of translation and r is the undeformed radius of the disk. Equation (38c) forms the basis for a phase-plane analysis which will determine the qualitative behavior of λ. Equations (38a), (38b) then enable one to find ϕ and ψ as functions of t. The tensor $\dot{\mathbf{F}}$ is given by

$$\dot{\mathbf{F}} = \dot{\lambda}[\mathbf{e}_1(\phi)\otimes\mathbf{e}_1(\psi) - \lambda^{-2}\mathbf{e}_2(\phi)\otimes\mathbf{e}_2(\psi)] + \frac{K\lambda}{2(\lambda^2-1)}[\mathbf{e}_1(\phi)\otimes\mathbf{e}_2(\psi) + \mathbf{e}_2(\phi)\otimes\mathbf{e}_1(\psi)] + \frac{L\lambda}{2(\lambda^2+1)}[\mathbf{e}_2(\phi)\otimes\mathbf{e}_1(\psi) - \mathbf{e}_1(\phi)\otimes\mathbf{e}_2(\psi)]. \quad (39)$$

Here we study the situation in which a disk undergoing such a motion collides with a rigid wall whose outer normal vector is $\mathbf{i}_2$. Thus, we have $\mathbf{n} = \mathbf{i}_2$ and

$$\mathbf{e} = \{\mu_k^2 + 1\}^{-1/2}\{-\mu_k \text{sgn}(\mathbf{i}_1 \cdot \dot{\mathbf{R}}^{(-)})\mathbf{i}_1 + \mathbf{i}_2\} : = \sin\eta\ \mathbf{i}_1 + \cos\eta\ \mathbf{i}_2. \quad (40)$$

The inertia tensor $\mathbf{E}$ is given by $\mathbf{E} = mr^2/4\ \mathbf{1}$, and the tensor $\mathbf{H}$ has the form

$$\mathbf{H} = 4(mr^2)^{-1}[\lambda^{-2}\mathbf{e}_1(\phi)\otimes\mathbf{e}_1(\phi) + \lambda^2\mathbf{e}_2(\phi)\otimes\mathbf{e}_2(\phi)]. \quad (41)$$

It follows from the kinematical analysis of our earlier work (1989) that

$$\mathbf{r} = -r\{\lambda^2\sin^2(\phi) + \lambda^{-2}\cos^2\phi\}^{-1/2}\{\lambda^2\sin\phi\ \mathbf{e}_1(\phi) + \lambda^{-2}\cos\phi\ \mathbf{e}_2(\phi)\}. \quad (42)$$

We shall use Eqs. (31)–(33) to analyze this impact. We note that, in this case,

$$\mathbf{n}\cdot\mathbf{e} = \cos\eta,$$

$$\text{tr}\mathbf{H} = 4(mr^2)^{-1}(\lambda^2 + \lambda^{-2}),$$

$$\mathbf{Hr} = -4(mr)^{-1}\{\lambda^2\sin^2\phi + \lambda^{-2}\cos^2\phi\}^{-1/2}\mathbf{i}_2, \quad (43)$$

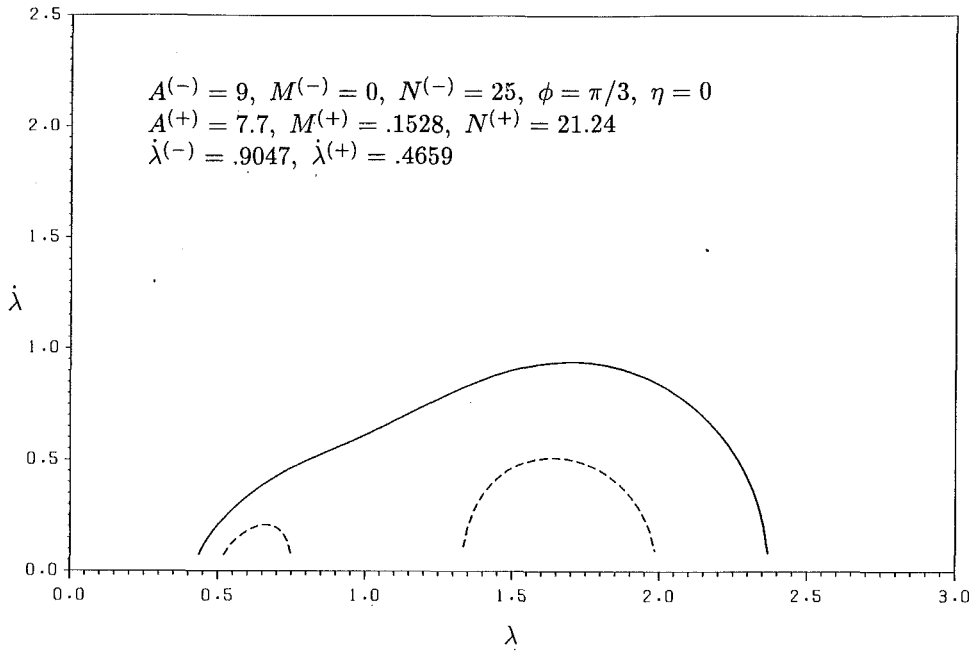

Fig. 3

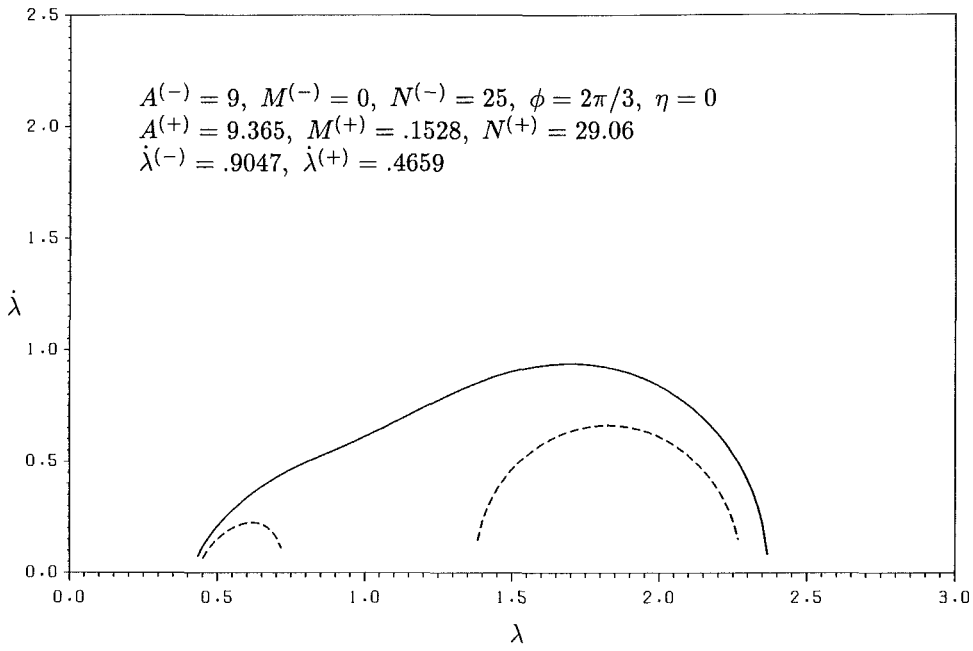

Fig. 4

so that

$$\begin{aligned}\mathbf{r}\cdot\mathbf{Hr} &= 4m^{-1},\\ \mathbf{n}\cdot\mathbf{Hr} &= -4(mr)^{-1}\{\lambda^2\sin^2\phi+\lambda^{-2}\cos^2\phi\}^{-1/2},\\ \mathbf{e}\cdot\mathbf{Hr} &= -4(mr)^{-1}\{\lambda^2\sin^2\phi+\lambda^{-2}\cos^2\phi\}^{-1/2}\cos\eta.\end{aligned}\tag{44}$$

Substituting these into Eq. (31), we find

$$\hat{P} = -m(\cos\eta)^{-1}\{5\lambda^8\sin^2\phi+\lambda^4+5\cos^2\phi\}^{-1}\{\lambda^8\sin^2\phi + \lambda^4+\cos^2\phi\}(\mathbf{i}_2\cdot\dot{\mathbf{R}}^{(-)}),\tag{45}$$

and, from (32), that

$$\hat{p} = r\{\lambda^4+1\}^{-1}[\lambda^2\sin^2\phi+\lambda^{-2}\cos^2\phi]^{-1/2}\lambda^2\cos\eta\,\hat{P}.\tag{46}$$

We consider (33b) in the form

$$\dot{\mathbf{F}}^{(+)}\mathbf{F}^{-1} = \dot{\mathbf{F}}^{(-)}\mathbf{F}^{-1} + (1+k)\hat{P}\mathbf{e}\otimes\mathbf{Hr} + (1+k)\hat{p}\mathbf{H}.\tag{47}$$

Expressing this in components with respect to the basis $\{\mathbf{e}_\alpha(\phi)\}$ we find, upon introducing the notation

$$S := 4(mr)^{-1}\{\lambda^2\sin^2\phi+\lambda^{-2}\cos^2\phi\}^{-1/2}(1+k)\hat{P},\tag{48}$$

that

$$\begin{aligned}\dot{\lambda}^{(+)} &= \dot{\lambda}^{(-)} + S\lambda(\lambda^4-1)^{-1}\{\cos\phi\cos(\phi+\eta) - \lambda^4\sin\phi\sin(\phi+\eta)\},\\ (\lambda^2+1)[K^{(+)}-K^{(-)}] + (\lambda^2-1)[L^{(+)}-L^{(-)}] &= -2S(\lambda^4-1)\sin\phi\cos(\phi+\eta),\\ (\lambda^2+1)[K^{(+)}-K^{(-)}] - (\lambda^2-1)[L^{(+)}-L^{(-)}] &= -2S(\lambda^2-\lambda^{-2})\cos\phi\sin(\phi+\eta).\end{aligned}\tag{49}$$

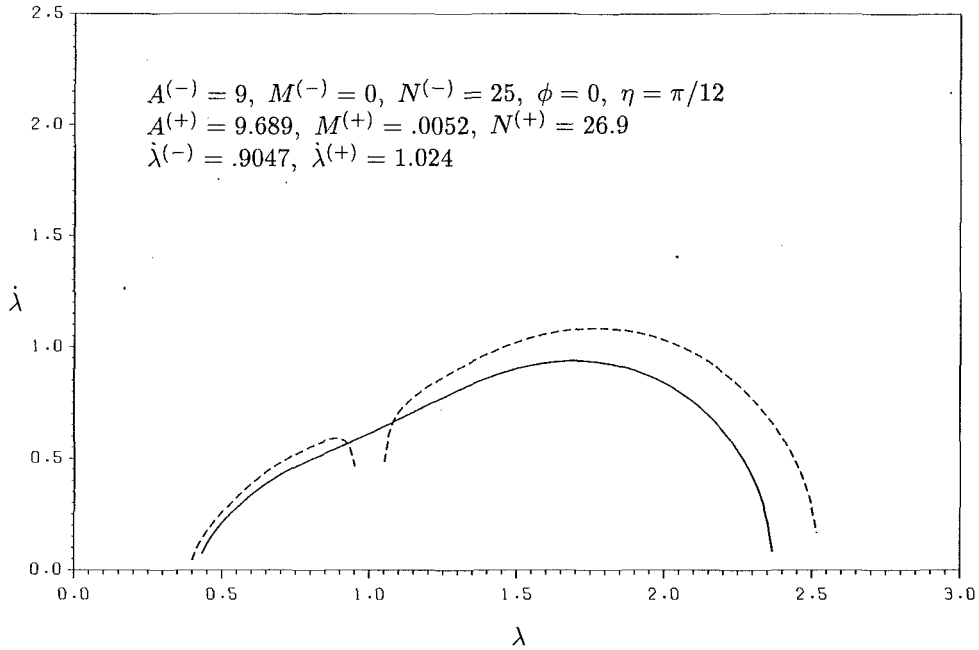

Fig. 5

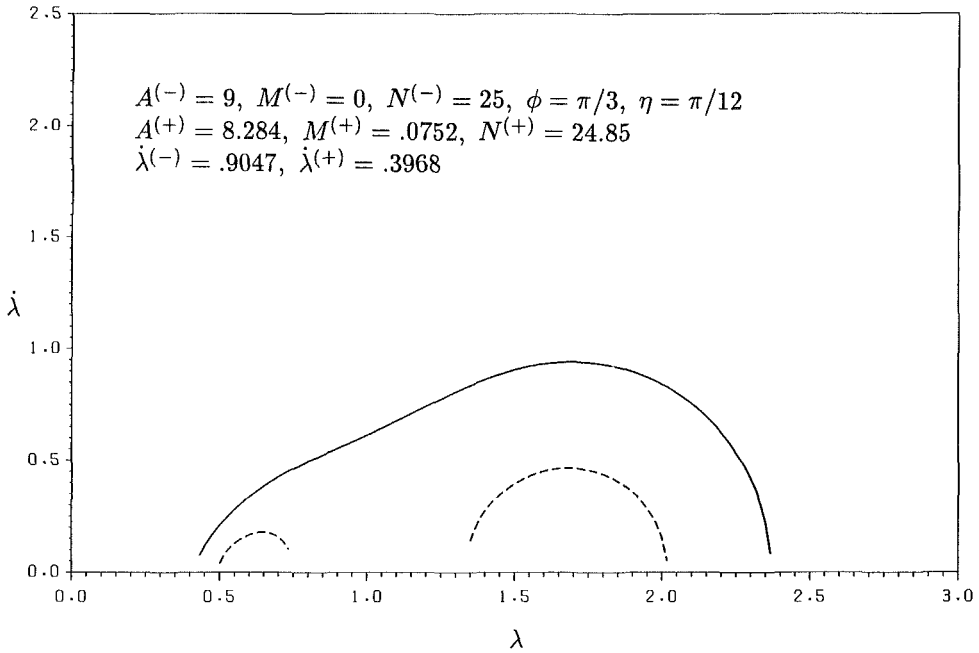

Fig. 6

It follows that

$$K^{(+)} = K^{(-)} - S(\lambda^2 - 1)\{\sin\phi\cos(\phi+\eta) + \lambda^{-2}\cos\phi\sin(\phi+\eta)\},$$
$$L^{(+)} = L^{(-)} - S(\lambda^2 + 1)\{\sin\phi\cos(\phi+\eta) - \lambda^{-2}\cos\phi\sin(\phi+\eta)\}, \quad (50)$$

We may substitute these post-impact values of $\dot{\lambda}$, K, and L into (38c) to determine $E^{(+)}$, the post-impact value of E.

We now consider, as we did in (1989), the specific material model for which

$$\tilde{W}(\lambda,\lambda^{-1}) = C[\lambda^2 + \lambda^{-2} - 2]. \quad (51)$$

For this particular motion and material, the phase portraits for λ are governed by the relationship

$$\dot{\lambda}^2 = 8C\,r^{-2}(1+\lambda^{-4})^{-1}\{A - M(\lambda-\lambda^{-1})^{-2} - N(\lambda+\lambda^{-1})^{-2} - \lambda^2 - \lambda^{-2}\} \quad (52)$$

with

$$A := 2 + C^{-1}E, \quad M := \frac{1}{16}C^{-1}K^2r^2, \quad N := \frac{1}{16}C^{-1}L^2r^2. \quad (53)$$

Here, M and N may be regarded as measures of that portion of the nontranslational energy which resides in spin rather than in elastic stored energy or kinetic energy of stretching. Recall from the results of our earlier work (1989) that in the case $M = 0$, different qualitative behaviors are possible, depending on the value of N. For values of N less than 16, all trajectories pass through the value $\lambda = 1$, while for values of N greater

than 16, only those associated with sufficiently large values of A do so. For $M \neq 0$, λ never passes through the value 1; it would require an infinite amount of energy to do so.

We have computed the pre-impact and post-impact trajectories for a selection of these. We take $S = 0.5$ in all of the examples shown. We rescale our time units so that $8Cr^{-2} = 1$. We take as our initial values

$$A^{(-)}=9, \quad M^{(-)}=0, \quad N^{(-)}=25 \tag{54}$$

so that $\dot{\lambda}^{(-)} = 0.9047$. In all of the phase-plane diagrams shown, the solid line represents the situation before impact and the dotted line that after impact. Impact occurs at $\lambda = 1.5$.

Figure 1 corresponds to the case in which $\phi = 0$ and $\eta = 0$. Thus, the point of impact lies on the semi-major axis of the deformed state, and no friction acts. Notice that the impact involves a direct conversion of translational kinetic energy into kinetic energy of stretching; A and $\dot{\lambda}$ increases through the impact, while the values of M and N are unchanged.

Figure 2 depicts the case $\phi = \pi/3$, $\eta = 0$. This time A, N, and $\dot{\lambda}$ decrease through the impact, while M increases. The post-impact behavior of λ is radically different than that before impact. Nontranslational kinetic energy has been redistributed to accommodate a nonzero value of M and has undergone a net decrease. If $k < 1$, some of this energy is dissipated due to inelastic effects. The rest is converted to kinetic energy of translation. If $k = 1$, all of it is so converted.

Figure 3 shows the case $\phi = 2\pi/3$, $\eta = 0$. Now, A, N, and M increase due to the impact, while $\dot{\lambda}$ decreases. Physically, this corresponds to a conversion of kinetic energy of translation and kinetic energy of stretching into kinetic energy of spinning.

Figures 4, 5, and 6 refer to the case $(\phi, \eta) = (0, \pi/12)$, $(\pi/3, \pi/12)$, $(2\pi/3, \pi/12)$, respectively. Comparison with Figs. 1, 2, and 3 indicate the effect of friction on the impact process. Figure 4 shows an impact in which A increases at the expense of translational energy. (Total energy decreases due to frictional and possible inelastic dissipation.) In contrast with Fig. 1, this increase in nontranslational energy is shared between stretching and spinning modes. The reader can readily interpret Figs. 5 and 6.

Thus, we see that even in this simple example rather complex behavior is possible.

5 Discussion

The mechanics of pseudo-rigid bodies involves degrees-of-freedom of stretch and shear in addition to those of rotation and translation associated with a rigid motion. These extra degrees-of-freedom contribute to both kinetic and elastic potential energy. In an impact, there will, in general, be a net loss of kinetic energy due to friction and bulk inelastic effects. In addition, kinetic energy will, in general, be redistributed among these various modes by an impact. The foregoing example illustrates this process.

Analyses such as that of Hunter (1957) have attempted to study permanent transfer of energy from translation to vibration, within the framework of the Hertz approximation. These studies find that such effects are negligible. Since the Hertz analysis assumes that the effect of impact is a *local* indentation of the impacting body, and, moreover, neglects material inertia in the indented region, these results are to be expected.

The developments of this paper, on the other hand, speak to a situation in which the impact produces gross deformation of the impacting body. Thus, it is no surprise that the implications of the model are so different from those of the Hertz treatment.

Acknowledgment

The authors wish to gratefully acknowledge the support, in part, by the Natural Sciences and Engineering Research Council of Canada.

References

Brach, R. M., 1981, "Moments Between Impacting Bodies," ASME *Journal of Mechanical Design*, Vol. 103, pp. 812–817.

Brach, R. M., 1984, "Friction Restitution and Energy Loss in Planar Collisions," ASME JOURNAL OF APPLIED MECHANICS, Vol. 51, pp. 164–170.

Brach, R. M., 1989, "Rigid Body Collisions," ASME JOURNAL OF APPLIED MECHANICS, Vol. 56, pp. 133–138.

Cohen, H., 1981, "Pseudo-Rigid Bodies," *Utilitas Mathematica*, Vol. 20, pp. 221–247.

Cohen, H., and Mac Sithigh, G. P., 1989, "Plane Motions of Elastic Pseudo-Rigid Bodies," *J. Elasticity*, Vol. 21, pp. 193–226.

Cohen, H., and Muncaster, R. G., 1988, *The Theory of Pseudo-Rigid Bodies*, (Springer Tracts in Natural Philosophy, 33), Spring-Verlag, New York.

Goldsmith, W., 1960, *Impact*, Edward Arnold.

Hunter, S. C., 1957, "Energy Absorbed by Elastic Waves During Impact," *J. Mech. Phys. Solids*, Vol. 5, pp. 162–171.

Keller, J. B., 1986, "Impact with Friction," ASME JOURNAL OF APPLIED MECHANICS, Vol. 53, pp. 1–4.

McMillan, W. D., 1960, *Dynamics of Rigid Bodies*, Dover.

Muncaster, R. G., 1984, "Invariant Manifolds in Mechanics II: Zero-Dimensional Elastic Bodies with Directors," *Arch. Rat. Mech. Anal.*, Vol. 84, pp. 375–392.

Unraveling Paradoxical Theories for Rigid Body Collisions

W. J. Stronge
Department of Engineering,
University of Cambridge,
Cambridge, CB2 1PZ, U.K.
Mem. ASME

A collision between two rigid bodies has a normal impulsive reaction at the contact point (CP). *If the bodies are slightly rough and the contact points have a relative tangential velocity* (*slip*), *there is also a frictional force that opposes slip. Small initial slip can halt before contact terminates; when slip halts the frictional force changes and the collision process is separated into periods before and after halting. An energetically consistent theory for collisions with slip that halts is based on the work done by normal* (*nonfrictional*) *forces during restitution and compression phases. This theory clearly separates dissipation due to frictional forces from that due to internal irreversible deformation. With this theory, both normal and tangential components of the impulsive reaction always dissipate energy during collisions. In contrast, Newton's impact law results in calculations of paradoxical increases in energy for collisions where slip reverses. This law relates normal components of relative velocity for the CP at separation and incidence by a constant* (*the coefficient of restitution* e). *Newton's impact law is a kinematic definition for* e *that generally depends on the slip process and friction; consequently it has limited applicability.*

Colliding bodies are effectively rigid during collision if there is negligible deformation outside the contact region and if the contact region remains negligibly small in comparison with the size of the bodies. Collisions between topologically smooth bodies occur at a contact point (*CP*) where the bodies have a common tangent plane and a common normal direction $\mathbf{n}$. The dynamics of rigid body collisions are a limiting case for a time-dependent process of local deformation; in this process active forces are present at the contact point only during the collision. Since the total collision period is very small, this process has changes in momenta without changes in configuration.

Most collisions between rigid bodies can be considered as this limiting case where equal but opposed impulses act on the bodies at an instant of contact. The relative velocities for the *CP*s at incidence $\mathbf{v}_o$ and separation $\mathbf{v}_f$ have normal components that are related by the coefficient of restitution e where $0 \le e \le 1$. Bounds $e = 1$ and $e = 0$ denote elastic and completely inelastic collisions, respectively.

The "impact law" defines e as a simple proportionality of relative velocity components at incidence and rebound, $\mathbf{v}_f \cdot \mathbf{n} = -e\,\mathbf{v}_o \cdot \mathbf{n}$[1]. This definition expresses a velocity constraint; in contrast, an alternative definition relates e to normal components of impulse for restitution and compression periods of collision (Poisson, 1817). Newton's impact law and Poisson's hypothesis are equivalent if the collision is collinear (i.e., both colliding bodies have centers of mass on the common normal through *CP*) or if friction is negligible.

During a collision the relative velocity $\mathbf{v}(t)$ for the *CP*s can also have a tangential component $\mathbf{v} - (\mathbf{v}\cdot\mathbf{n})\mathbf{n}$ called slip. Friction acts at the *CP* of a body in a direction that opposes slip. Friction complicates the collision process by introducing dynamic constraints on relative motion at the *CP*; if slip is initially small, the reaction can stop slip during collision. Rigid body collisions with friction and slip that terminates before contact ceases have confounded theoreticians for more than a century (Poisson, 1817; Kane, 1984; Brach, 1989).

Stronge (1991) has shown that when slip stops or reverses, the time-dependent nature of the collision process cannot be neglected. If there is friction and the collision is noncollinear the normal reaction force on each *CP* changes when slip stops during a collision; consequently, analyses of collision dynamics must be separated into periods before and after stopping. Taking this separation into account, Keller (1986) used Poisson's hypothesis to describe the analysis of collisions with slip reversal. This analysis did not examine energy dissipation by separate components of impulse however, so it failed to recognize that Poisson's hypothesis can yield nonfrictional energy dissipation that does not vanish if the collision is elastic, $e = 1$. Both the impact law and Poisson's hypothesis are energetically inconsistent in this regard if the collision is noncollinear and there is friction with slip that stops.

A new definition of coefficient of restitution was proposed by Stronge (1990) that always satisfies dissipation constraints for the normal compressive reaction. This definition relates e to inelastic deformation of colliding bodies; it is independent of friction and slip. With this definition the ratio of separation and incident velocities explicitly depends on both e and the

[1]Newton first expressed this velocity constraint; the expression generalizes analytical results by J. Wallis (1670) regarding conservation of momentum for inelastic and elastic particle collisions.

Contributed by the Applied Mechanics Division of THE AMERICAN SOCIETY OF MECHANICAL ENGINEERS for publication in the JOURNAL OF APPLIED MECHANICS.

Discussion on this paper should be addressed to the Technical Editor, Prof. Leon M. Keer, The Technological Institute, Northwestern University, Evanston, IL 60208, and will be accepted until two months after final publication of the paper itself in the JOURNAL OF APPLIED MECHANICS. Manuscript received by the ASME Applied Mechanics Division, Mar. 30, 1990; final revision, Aug. 22, 1990.

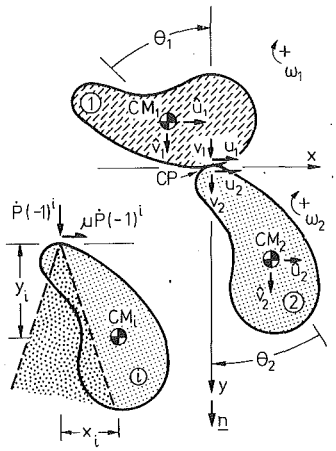

Fig. 1 Planar collision of two bodies at *CP*. At collision, the direction to CM_i from *CP* is inclined at angle θ_i relative to the common normal direction *n*; $\theta_i = \tan^{-1}(x_i/y_i)$. The normal reaction force $\hat{P}$ acts at *CP*.

process of slip at *CP*. The complexity of including friction in the collision process is unravelled by examining impulse-dependent velocity changes during separate phases of collision representing compression, restitution, and slip in each direction.

Planar Collisions With Slip

Changes in velocity during collision depend on differences between velocities of contact points. The dynamics of collision are most transparent in terms of velocities relative to a reference frame that moves with the common tangent plane at the instant when compression ceases; let this reference frame move steadily in direction **n** during each phase of slip.

Suppose rigid laminae labeled 1 and 2 with masses M_i, $i = 1, 2$ collide at *CP* as shown Fig. 1. We acknowledge that the colliding bodies are only relatively rigid by considering an infinitesimally small deformable element between the *CP*s that admits only infinitesimal deformation in direction **n**; i.e., this deformable element is assumed to have negligible tangential compliance. The contact point of each body CP_i has changing velocity $\mathbf{v}_i(t)$ relative to the steadily moving reference frame. During the compression period $t<t_c$, $\mathbf{v}_1\cdot\mathbf{n}>0>\mathbf{v}_2\cdot\mathbf{n}$. Let the centers of mass (CM_i) have velocities $\hat{\mathbf{v}}_i(t) = (\hat{v}_i, \hat{u}_i)$ where $\hat{v}_i$ and $\hat{u}_i$ are the normal and tangential components relative to the steadily moving reference frame. Each laminae has an angular velocity $\omega_i(t)$. Velocities for CP_i and CM_i are related by $\mathbf{v}_i(t) = \hat{\mathbf{v}}_i - \omega_i \times \mathbf{r}_i = (\hat{v}_i - x_i\omega_i, \hat{u}_i + y_i\omega_i)$ where $\mathbf{r}_i = (x_i, y_i)$ is the position vector of CM_i from CP_i. During collision the contact points have a difference in velocity $\mathbf{v}(t) = \mathbf{v}_1 - \mathbf{v}_2 = (v, u)$ with both normal and tangential components; the tangential component is termed slip. Equal but opposed reaction forces $\mathbf{P}_i = (P, \mu P \operatorname{sgn}(u))(-1)^i$ act at coincident points of contact that are slipping; these forces have normal components P, tangential components $\mu P \operatorname{sgn}(u)$, and change sign according to $(-1)^i$. The tangential force on each body acts in a direction opposed to slip; while there is slip the tangential force has a magnitude that is proportional to the normal component of force $\dot{P} = dP/dt$ where $P(t)$ is the normal component of impulse. The limiting friction coefficient μ prescribes this proportionality. We assume that μ is a constant although in practice, μ can vary with $\mathbf{v}(t_o)$ due to surface indentation.

The initial difference in velocity at *CP* can be separated into initial velocities for CP_i relative to the steadily moving reference frame, $\mathbf{v}_1(t_o) = (v_o, u_o)$ and $\mathbf{v}_2(t_o) = (-\eta v_o, -\xi u_o)$ where η, ξ are constants. (It is convenient to make η proportional to the relative rate of change for the normal component of velocity of CP_i during compression.) Hence, at the *CP* there is an initial difference in velocity $\mathbf{v}_1(t_o) - \mathbf{v}_2(t_o) = ((1+\eta)v_o, (1+\xi)u_o)$ when collision commences. Each body also has an initial angular velocity $\omega_i(t_o)$.

Although the total collision period is very small, changes in motion during a collision can be separated into an initial phase of compression followed immediately by a phase of restitution. The notion of this separation was originally due to Poisson (1817): here it is used to consider changes in motion for colliding rigid bodies as a function of the normal component of impulse. In this analysis, impulses for separate phases of the collision process are determined in comparison with the compression phase impulse for unidirectional slip in the initial slip direction. The direction of initial slip relative to the inclination of the colliding bodies turns out to be an important discriminator for different possible slip processes.

Initial Slip $u_1(t_o)>u_2(t_o)$: Labeling the bodies such that $u_1(t_o)>u_2(t_o)$, the changes in velocity components $\hat{v}_i$, $\hat{u}_i$, ω_i for laminae $i = 1, 2$ depend on the normal component of impulse $P(t) = \int_{t_o}^{t} \dot{P}dt'$:

$$\hat{v}_i(t) - \hat{v}_i(t_o) = (-1)^i P/M_i$$
$$\hat{u}_i(t) - \hat{u}_i(t_o) = (-1)^i \mu P/M_i$$
$$\omega_i(t) - \omega_i(t_o) = (-1)^i(\mu y_i - x_i)P/M_i k_i^2 \qquad (1)$$

where k_i is the radius of gyration of body i for CM_i. Corresponding changes in velocity components at the contact points CP_i can be expressed as:

$$v_i(t) = v_i(t_o) + (-1)^i P/m_i$$
$$u_i(t) = u_i(t_o) + (-1)^i \mu P/n_i \qquad (2)$$

where effective masses m_i and n_i for normal and tangential accelerations of CP_i are defined as:

$$m_i = M_i k_i^2[k_i^2 + x_i^2 - \mu x_i y_i]^{-1},\ n_i = M_i k_i^2[k_i^2 + y_i^2 - x_i y_i/\mu]^{-1} \qquad (3)$$

for $u_1(t_o) > u_2(t_o)$. The rates of change for velocity components at CP_i are proportional to m_i^{-1} and n_i^{-1}; notice that the sign of each effective mass depends on the orientation of the body and the coefficient of friction μ. Effective mass n_i can be negative if friction is small; this indicates that slip speed increases despite small friction.

We define a characteristic normal impulse for compression $\overline{P}$ and a ratio η for rate of change of velocity of CP_i that bring normal components of relative velocity for contact points of both bodies to a common speed at the end of the compression period, $v_1(t_c) = v_2(t_c)$. The relative rate of approach η for the initial phase of slip yields $v_i(t_c) = 0$ if slip does not stop during compression; hence, during any initial period of slip,

$$\overline{P} = \frac{v_o(1+\eta)}{m_1^{-1} + m_2^{-1}},\quad \eta = m_1/m_2, \qquad \text{for } u_1 > u_2 \qquad (4)$$

and $\overline{P} = m_1 v_o$. The characteristic reaction $\overline{P}$ and the effective masses m_i, n_i all depend on the sense of slip at *CP*.

Reversed Slip $u_2(t)>u_1(t)$ After Slip Stops $t>t_s$: If slip of one *CP* relative to the other has the opposite sense, the previous expressions for effective masses and characteristic normal compression impulse are altered by changing the sign of μ. Hence, the effective masses m_{i*}, n_{i*} after reversal are:

$$m_{i*} = M_i k_i^2[k_i^2 + x_i^2 + \mu x_i y_i]^{-1},\ n_{i*} = M_i k_i^2[k_i^2 + y_i^2 + x_i y_i/\mu]^{-1} \qquad (5)$$

while the characteristic normal impulse $\overline{P}_*$ is given by:

$$\overline{P}_* = \frac{v_o(1+\eta)}{m_{1*}^{-1} + m_{2*}^{-1}},\ \text{for } u_2 > u_1. \qquad (6)$$

If there is friction and CM_i is not on the common normal,

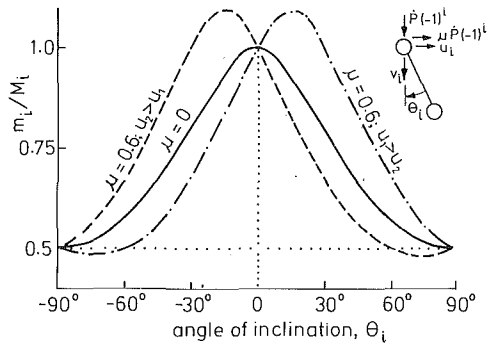

Fig. 2(*a*)

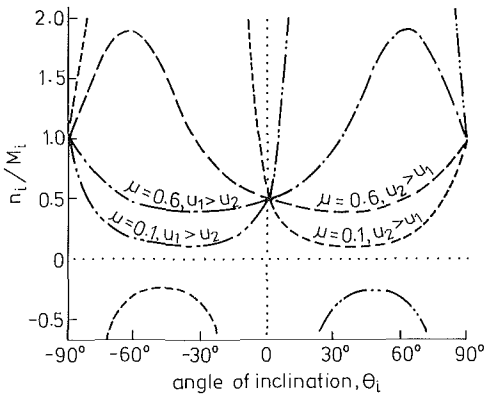

Fig. 2(*b*)

Fig. 2 Normal and tangential effective masses for the mass distribution of dumbbell ($k_i^2 = x_i^2 + y_i^2$) depend on angle of inclination, friction, and direction of slip

$\mu x_i y_i \neq 0$ so effective masses depend on the direction of slip. Figure 2 illustrates the effect of slip direction on effective masses for a simple body with a large radius of gyration k_i.

With these characteristic impulses, the velocity components (1) and (2) can be expressed as functions of impulse ratio $P/\bar{P}$ rather than time; e.g., the contact velocity components during the period before slip stops are given by,

$$\frac{v_i}{v_o} = (-1)^{i-1}\frac{m_1}{m_i}\left(1-\frac{P}{\bar{P}}\right)$$

$$\frac{u_i}{v_o} = \frac{u_i(0)}{v_o} + (-1)^i \frac{\mu m_1}{n_i}\frac{P}{\bar{P}} \tag{7}$$

These changes in velocity for contact points CP_i are succinctly illustrated in Fig. 3. In this diagram the impulse ratio on the abscissa changes with the direction of slip; hence, the normal velocity components for CP_i are simply lines that intersect where compression terminates at either $P/\bar{P} = 1$ or $P/\bar{P}_* = 1 - \gamma + \gamma\, \bar{P}/\bar{P}_*$ depending on whether slip stops during restitution or compression. These lines kink at the impulse that stops slip if $\bar{P}_* \neq \bar{P}$ but this does not alter the rate of convergence. This scaling of impulse ratio $P/\bar{P}_j$ results in the same rate of change of relative velocity $v_1 - v_2$ before and after slip reverses. Note that initially $P/\bar{P} = 0$. By using impulse ratio as an independent variable rather than time, details associated with compliance at CP_i have been eliminated.

Slip Stops at Impulse Ratio $\gamma = P(t_s)/\bar{P}$: We calculate slip $u(P/\bar{P})$ of CP_1 relative to CP_2 when compression terminates by supposing for a moment that initial slip does not stop during compression:

$$u(1) = u_1(1) - u_2(1) = u_o(1+\xi) - \mu v_o m_1(n_1^{-1}+n_2^{-1}). \tag{8}$$

The impulse ratio γ stops slip; this impulse ratio can be determined by recognizing that slip is a linear function of $P/\bar{P}$

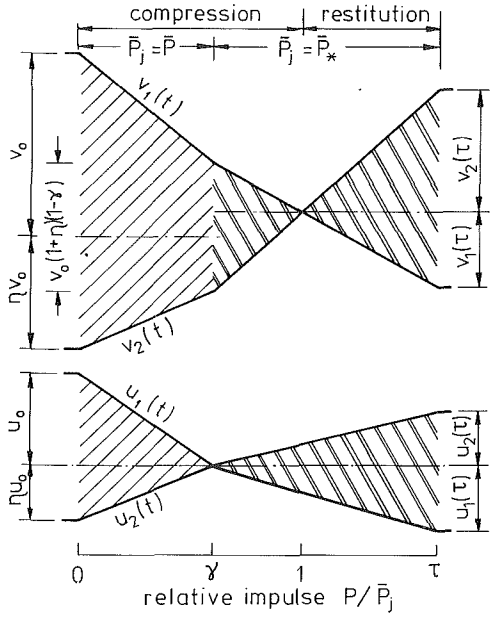

Fig. 3 Variation of normal and tangential relative velocity components for *CP*s during collision with slip reversal at relative impulse γ during compression. The characteristic impulse $\bar{P}_j$ changes with slip direction.

before slip stops. Hence, independent of whether slip stops during restitution or compression,

$$\gamma = \frac{u(0)}{u(0)-u(1)} = \frac{u_o(1+\xi)}{\mu v_o m_1(n_1^{-1}+n_2^{-1})}. \tag{9}$$

The impulse ratio γ is a key parameter for identifying collision processes. We find that slip only reverses if it stops during compression (i.e., $0<\gamma<1$) so stopping and reversal depend on the orientation of the bodies when collision commences.

During the initial phase of slip, the ratio ξ for rate of change of slip speed for CP_2 compared with CP_1 is established by requiring that γ is symmetric; i.e., independent of the designation of the bodies. Hence,

$$\xi = \eta = m_1/m_2. \tag{10}$$

Note that relative changes in speed for the two bodies η, ξ depend on the sense of slip and the angles of inclination for CM_i during the collision. These relative changes in speed at CP are translated directly to the centers of mass only if $x_i = 0$ or $y_i = 0$ for normal or tangential components, respectively; i.e., if changes in motion induced by normal and tangential components of impulse are not coupled. If the collision is noncollinear with friction, the center of mass is generally not stationary in the reference frame where $v_i(\bar{P}) = 0$.

After impulse γ, when slip stops the velocity components at CM_i are:

$$\frac{\hat{v}_1(\gamma)}{v_o} = 1 + \frac{x_1\omega_1(0)}{v_o} - \frac{\gamma(1+\eta)}{M_1(m_1^{-1}+m_2^{-1})},$$

$$\frac{\hat{u}_1(\gamma)}{v_o} = \frac{u_o}{v_o} - \frac{y_1\omega_1(0)}{v_o} - \frac{\gamma\mu(1+\eta)}{M_1(m_1^{-1}+m_2^{-1})}$$

$$\frac{k_1\omega_1(\gamma)}{v_o} = \frac{k_1\omega_1(0)}{v_o} + \frac{\gamma(x_1-\mu y_1)(1+\eta)}{k_1 M_1(m_1^{-1}+m_2^{-1})} \tag{11}$$

$$\frac{\hat{v}_2(\gamma)}{v_o} = -\eta + \frac{x_2\omega_2(0)}{v_o} + \frac{\gamma(1+\eta)}{M_2(m_1^{-1}+m_2^{-1})},$$

$$\frac{\hat{u}_2(\gamma)}{v_o} = -\xi\frac{u_o}{v_o} - \frac{y_2\omega_2(0)}{v_o} + \frac{\gamma\mu(1+\eta)}{M_2(m_1^{-1}+m_2^{-1})}$$

$$\frac{k_2\omega_2(\gamma)}{v_o} = \frac{k_2\omega_2(0)}{v_o} - \frac{\gamma(x_2-\mu y_2)(1+\eta)}{k_2 M_2(m_1^{-1}+m_2^{-1})} \tag{12}$$

$$u(\tau)=u_1(\tau)-u_2(\tau)=\begin{cases}-\mu v_o(1+\eta)(\tau-\gamma)(n_{1*}^{-1}+n_{2*}^{-1})/(m_{1*}^{-1}+m_{2*}^{-1}), & 0<\gamma<1\\ 0, & 1<\gamma<\tau\\ u_o(1+\xi)-\mu v_o(1+\eta)\tau(n_1^{-1}+n_2^{-1})/(m_1^{-1}+m_2^{-1}), & \tau<\gamma\end{cases} \tag{20}$$

Reversal of Slip Direction

After slip stops the direction of slip for CP_i can reverse. Slip reversal introduces changes in the effective masses m_i, n_i and changes in the characteristic normal component of impulse for the compression period $\overline{P}$. The ratio of characteristic impulses for periods after and before slip reversal can be expressed as a ratio of effective masses m_i;

$$\overline{P}_*/\overline{P}=(m_1^{-1}+m_2^{-1})/(m_{1*}^{-1}+m_{2*}^{-1}) \tag{13}$$

This ratio depends upon masses M_i and angles of inclination θ_i for both bodies and also friction μ. The ratio describes a change at reversal in the rate that impulse is applied to the colliding bodies. It will be shown that if slip reverses, this characteristic impulse ratio is larger than unity.

For each body, all velocity changes are linear functions of the reaction impulse during each phase of slip. Although reaction forces change when slip reverses, the changes in velocity are always directly proportional to either $P/\overline{P}$ or $(P-\gamma\overline{P})/\overline{P}_*$ depending on the direction of slip. If slip stops the tangential velocity components show a change in slope at γ since $m_i/n_i \neq m_{i*}/n_{i*}$.

Final Velocities at Terminal Impulse P_f: If slip stops ($0<\gamma<\tau$), the terminal impulse P_f is the sum of impulses during periods before and after slip stops; $P_f=\gamma\overline{P}+(\tau-\gamma)\overline{P}_*$ where $\tau\geq 1$. In this case the final velocities for CM_i can be expressed in terms of effective masses m_i, m_{i*} for each phase of collision.

$$\frac{\hat{v}_1(\tau)}{v_o}=1+\frac{x_1\omega_1(0)}{v_o}-\frac{\gamma(1+\eta)}{M_1(m_1^{-1}+m_2^{-1})}-\frac{(\tau-\gamma)(1+\eta)}{M_1(m_{1*}^{-1}+m_{2*}^{-1})} \tag{14}$$

$$\frac{\hat{v}_2(\tau)}{v_o}=-\eta+\frac{x_2\omega_2(0)}{v_o}+\frac{\gamma(1+\eta)}{M_2(m_1^{-1}+m_2^{-1})}+\frac{(\tau-\gamma)(1+\eta)}{M_2(m_{1*}^{-1}+m_{2*}^{-1})} \tag{15}$$

$$\frac{\hat{u}_1(\tau)}{v_o}=\frac{u_o}{v_o}-\frac{y_1\omega_1(0)}{v_o}-\frac{\gamma\mu(1+\eta)}{M_1(m_1^{-1}+m_2^{-1})}+\frac{\mu(\tau-\gamma)(1+\eta)}{M_1(m_{1*}^{-1}+m_{2*}^{-1})} \tag{16}$$

$$\frac{\hat{u}_2(\tau)}{v_o}=-\xi\frac{u_o}{v_o}-\frac{y_2\omega_2(0)}{v_o}+\frac{\gamma\mu(1+\eta)}{M_2(m_1^{-1}+m_2^{-1})}-\frac{\mu(\tau-\gamma)(1+\eta)}{M_2(m_{1*}^{-1}+m_{2*}^{-1})} \tag{17}$$

$$\frac{k_1\omega_1(\tau)}{v_o}=\frac{k_1\omega_1(0)}{v_o}+\frac{\gamma(x_1-\mu y_1)(1+\eta)}{k_1M_1(m_1^{-1}+m_2^{-1})}+\frac{(\tau-\gamma)(x_1+\mu y_1)(1+\eta)}{k_1M_1(m_{1*}^{-1}+m_{2*}^{-1})} \tag{18}$$

$$\frac{k_2\omega_2(\tau)}{v_o}=\frac{k_2\omega_2(0)}{v_o}-\frac{\gamma(x_2-\mu y_2)(1+\eta)}{k_2M_2(m_1^{-1}+m_2^{-1})}-\frac{(\tau-\gamma)(x_2+\mu y_2)(1+\eta)}{k_2M_2(m_{1*}^{-1}+m_{2*}^{-1})}. \tag{19}$$

The corresponding final normal relative velocities for CP_i at impulse ratio τ when collision terminates are:

$$v_i(\tau)=v_i(0)+\frac{(-1)^i(1+\eta)m_i^{-1}v_o\gamma}{m_1^{-1}+m_2^{-1}}+\frac{(-1)^i(1+\eta)m_{i*}^{-1}v_o(\tau-\gamma)}{m_{1*}^{-1}+m_{2*}^{-1}}.$$

When collision terminates, this results in the following separation velocity components at CP.

$$v(\tau)=v_1(\tau)-v_2(\tau)=-v_o(1+\eta)(\tau-1)$$

The negative sign for expressions on the right indicates that the sense of both components of relative velocity has changed during collision if $(n_{1*}^{-1}+n_{2*}^{-1})>0$. In (20), the three ranges of γ correspond to slip reversal, slip stick, and unidirectional slip, respectively.

Dissipation During Collision: Dissipation is the negative of work done by contact forces during a collision, and it can be evaluated by integrating the rate-of-work by impulse during $0<P<P_f$. Dissipation naturally separates into compressive and frictional parts; if tangential compliance is negligible, these parts are equivalent to the product of the appropriate characteristic impulse $\overline{P}$ (or $\overline{P}_*$) and the area in Fig. 3 between lines representing components of contact velocity for the two bodies (Stronge, 1990). The irreversible deformation dissipation D_n and frictional dissipation D_t for slip that reverses at relative impulse $0<\gamma<1$ are given by:

$$D_n=\overline{P}v_o(1+\eta)\gamma(2-\gamma)/2+\overline{P}_*v_o(1+\eta)[(1-\gamma)^2-(\tau-1)^2]/2$$

$$D_t=\mu\overline{P}u_o(1+\xi)\gamma/2-\mu\overline{P}_*u_f(\tau-\gamma)/2 \tag{21}$$

where $u_f=u(\tau)$ is evaluated from (20)[2]. If (9) yields $\gamma<0$ or $\gamma>1+e$, this indicates that slip does not stop during collision. In this case,

$$D_n=\overline{P}v_o(1+\eta)[1-(\tau-1)^2]/2$$
$$D_t=\mu\overline{P}[u_o(1+\xi)+u_f]\tau/2. \tag{22}$$

Total dissipation D is equivalent to the change in kinetic energy during collision, $D=D_n+D_t=K_o-K_f$.

Consistent and Inconsistent Collision Theories

At this point it is necessary to introduce a hypothesis that relates restitution and compression reactions. The hypothesis determines the relative durations of restitution and compression phases of collision. Since the dynamics of colliding bodies are linear relations between impulse and rates-of-change for velocity components, the normal dissipation D_n associated with internal irreversible deformation during restitution and compression phases is also directly determined by this hypothesis. In a consistent theory, this part of energy dissipation during restitution cannot be larger than the corresponding part during compression. Also we require $D_n=0$ for elastic collisions. Theories that do not satisfy these constraints are termed inconsistent.

One consistent collision theory has been proposed. Stronge (1990) formulated a theory based on the normal dissipation D_n. This proposition and the corresponding terminal impulse ratio τ are given below:

(a) Internal Dissipation Hypothesis: The square of coefficient of restitution e^2 is the ratio of elastic strain energy released at CP during restitution to the energy absorbed by internal deformation during compression.

For negligible tangential compliance, an equivalent form of this hypothesis expresses that negative work by the normal

[2]These expressions are obtained also from a theorem for energy loss in collisions (Stronge, 1987). The theorem must be applied separately to each phase of motion if slip stops or reverses.

component of reaction entirely represents nonfrictional dissipative effects. Hence, e^2 equals work of the normal component of reaction during restitution divided by negative work of the normal component of reaction during compression.

For slip reversal, $u_1(0)>0>u_1(\tau)$:

$$\gamma<1: \quad e^2=\frac{(\tau-1)^2}{(1-\gamma)^2+\gamma(2-\gamma)\overline{P}/\overline{P}_*}$$

$$\leftrightarrow \tau=1+e[(1-\gamma)^2+\gamma(2-\gamma)\overline{P}/\overline{P}_*]^{1/2} \quad (23)$$

$$1<\gamma<1+e: \quad e^2=\frac{(\tau-1)^2-(\gamma-1)^2(1-\overline{P}/\overline{P}_*)}{\overline{P}/\overline{P}_*}$$

$$\leftrightarrow \tau=1+\{(\gamma-1)^2(1-\overline{P}/\overline{P}_*)+e^2\overline{P}/\overline{P}_*\}^{1/2}. \quad (24)$$

For unidirectional slip, $u_1(0)>u_1(\tau)>0$:

$$1+e<\gamma: \quad e^2=(\tau-1)^2 \leftrightarrow \tau=1+e. \quad (25)$$

For a coefficient of restitution $e=1$, the internal dissipation hypothesis equates D_n for compression and restitution. In Fig. 3, this represents a balance of the areas on either side of the impulse that terminates compression if the area after slip reversal is weighted by the characteristic impulse ratio $\overline{P}_*/\overline{P}$.

There are at least two inconsistent collision theories.

(b) Impulse Hypothesis: The coefficient of restitution e is the normal reaction impulse during restitution divided by normal reaction impulse during compression.

For slip reversal, $u_1(0)>0>u_1(\tau)$:

$$\gamma<1: \quad e=\frac{(\tau-1)}{(1-\gamma)+\gamma\overline{P}/\overline{P}_*}$$

$$\leftrightarrow \tau=1+e(1-\gamma+\gamma\overline{P}/\overline{P}_*) \quad (26)$$

$$1<\gamma<1+e: \; e=\frac{(\tau-\gamma)+(\gamma-1)\overline{P}/\overline{P}_*}{\overline{P}/\overline{P}_*}$$

$$\leftrightarrow \tau=\gamma+(1+e-\gamma)\overline{P}/\overline{P}_*. \quad (27)$$

For unidirectional slip, $u_1(0)>u_1(\tau)>0$:

$$1+e<\gamma: \; e=\tau-1, \leftrightarrow \tau=1+e. \quad (28)$$

Poisson proposed this hypothesis which yields the usual impact law for collinear collisions or unidirectional slip. However, if the bodies are noncollinear and slip stops, $\overline{P}_* \neq \overline{P}$, and this theory yields predictions of normal dissipation D_n that do not vanish for elastic collisions.

Newton's impact law also results in an inconsistent theory.

(c) Kinematic Hypothesis: The coefficient of restitution e is the negative of normal component of relative velocity between contact points CP_i at separation divided by normal component of relative velocity at incidence.

For all slip conditions:

$$e=\tau-1 \leftrightarrow \tau=1+e. \quad (29)$$

With this hypothesis, Eq. (20) yields a simple proportionality between normal components of contact velocity for incidence and separation (Newton's impact law). However, if e and μ are presumed to be independent, hypothesis (c) yields normal dissipation D_n recovered during restitution that can exceed the normal dissipation during compression if slip stops and $\overline{P}_*>\overline{P}$ as a consequence of the collision configuration; i.e., this theory is energetically inconsistent. The inconsistency is an indication that with the hypothesis, e depends on friction and the slip process. Consequently, this hypothesis and the impact law are not useful for noncollinear collisions with friction if initial slip stops or reverses during the collision.

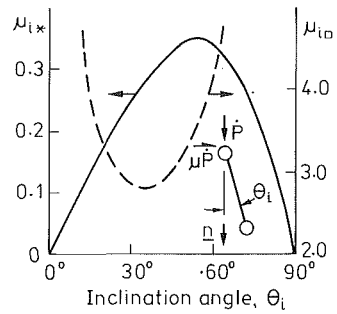

Fig. 4 Friction bounds for slip stick μ_{i*} and jamb $\mu_{i\square}$ of body with dumbbell mass distribution ($k_i^2 = x_i^2 + y_i^2$)

The three theories have the same terminal impulse τ if slip does not stop during collision or if the collision is collinear so $\overline{P}_* = \overline{P}$. If slip stops and $\overline{P}_* \neq \overline{P}$, the dissipation and impulse theories have a slightly smaller relative impulse during restitution $\tau-1$ than is specified by hypothesis (c); i.e., they have $\tau - 1<e$. The terminal impulse ratios for the three theories are ordered as follows:

$$1 \leq \tau(\text{Impulse}) \leq \tau(\text{Dissipation}) \leq \tau(\text{Impact Law}) = 1+e.$$

Collision Processes With Friction

There are several possible scenarios for collision processes if friction retards slip. During collision the slip can either continue without stopping, stop and stick, or stop and then reverse depending on the magnitudes of coefficient of friction μ and initial slip speed u_o/v_o. The dynamics equations are used to find the boundaries of regions where these slip processes occur. In addition to friction and slip speed, the processes depend on the angle-of-inclination $\theta_i = \tan^{-1}(x_i/y_i)$ for CM_i relative to the common normal. Conditions that identify these processes are:

(i) initial slip slows only if $(n_1^{-1} + n_2^{-1})/(m_1^{-1}+m_2^{-1})>0$;
(ii) slip stops after impulse $\gamma\overline{P}$ if:

$$0<\gamma=\frac{u_o(1+\xi)}{\mu v_o(1+\eta)}\frac{(m_1^{-1}+m_2^{-1})}{(n_1^{-1}+n_2^{-1})}<\tau;$$

(iii) if slip stops, it reverses only if $(n_{1*}^{-1} + n_{2*}^{-1})/(m_{1*}^{-1}+m_{2*}^{-1})>0$;
(iv) otherwise, slip that stops then sticks.

Bounds on slip processes are most apparent if the impulse when slip stops γ and the final slip velocity $u(\tau)$ are expressed in terms of two friction parameters related to slip processes. If the coefficient of friction is large enough to prevent slip reversal, the contact points can only roll after slip stops. This collision process wherein slip vanishes before contact ceases is termed slip stick. Even larger friction can prevent slip altogether; i.e., the contact points jamb. The process of jamb results in discontinuous relative velocities for CP_i at initial contact. Jamb is present if the characteristic impulse in (4) is indefinitely large due to $m_1^{-1} + m_2^{-1} \leq 0$; this process is equivalent to a dynamic constraint on sliding of rough bodies (Lötstedt, 1981). Each body has friction bounds for stick μ_{i*} and jamb $\mu_{i\square}$ that depend on the angle of inclination.

$$\mu_{i*}=x_iy_i/(k_i^2+y_i^2), \; \mu_{i\square}=(k_i^2+x_i^2)/x_iy_i \quad (30)$$

These bounds are illustrated in Fig. 4 for a simple body. The effective masses (3) can be expressed in terms of the bounds,

$$m_i/M_i=[(1+y_i^2/k_i^2)\mu_{i*}(\mu_{i\square}-\mu)]^{-1}$$
$$n_i/M_i=[(1+y_i^2/k_i^2)(1-\mu_{i*}/\mu)]^{-1} \quad (31)$$

where μ_{i*} and $\mu_{i\square}$ have the same sign as the angle of inclination, θ_i. Examples of slip processes are now determined for three orientations of colliding bodies with $M_1k_1^2/(k_1^2 + y_1^2) = M_2k_2^2/(k_2^2 + y_2^2)$.

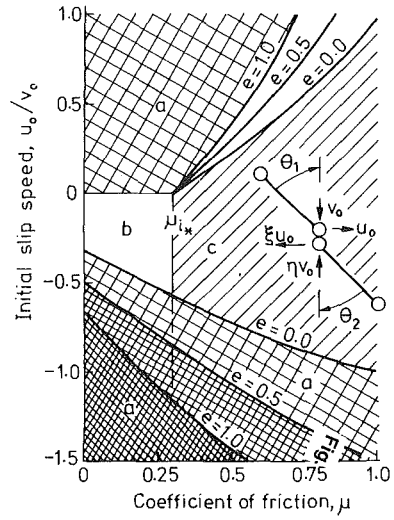

Fig. 5(*a*)

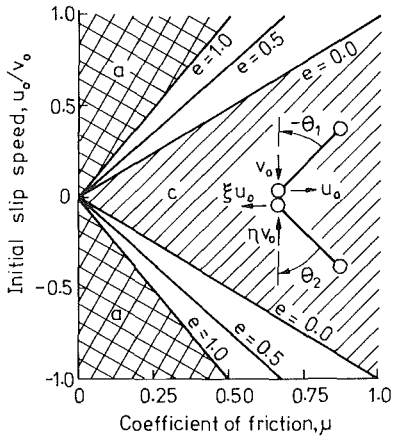

Fig. 5(*b*)

Fig. 5 Active regions for each slip process depend on collision parameters and initial conditions: (*a*) antisymmetric configuration, $\theta_1 = \theta_2 = \pi/4$; (*b*) symmetric configuration, $-\theta_1 = \theta_2 = \pi/4$. Collisions between two identical dumbbells exhibit the following processes: (*a*) continuous slip in initial direction, (*b*) slip with reversal during contact, and (*c*) slip stick.

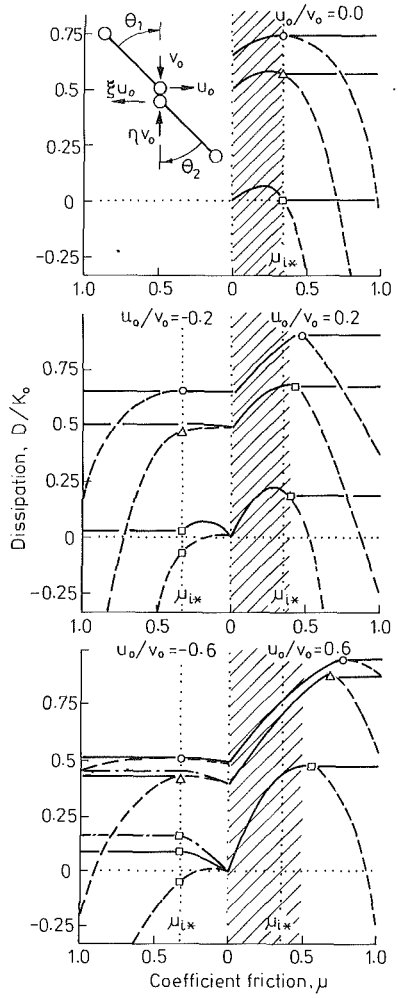

Fig. 6 Dissipation of initial energy for antisymmetric collision between two dumbbells with $\omega_i(t_o) = 0$, $\theta_1 = \theta_2 = \pi/4$. The impact law, impulse hypothesis, and internal dissipation hypothesis are given by the dashed curve, chained curve, and continuous curve, respectively. Shaded region has continuous slip during collision. The coefficient of restitution is designated as follows: *o*, $e = 0$; Δ, $e = 0.5$, and □, $e = 1.0$.

Case 1, $\theta_1 < 0$, $\theta_2 < 0 \rightarrow n_i > m_i > 0$ if $\mu > 0$: In this configuration the initial slip of CP_i is in the direction of a component of $\mathbf{r}_i$; i.e., initial slip of CP_i is towards CM_i. Changes in contact point velocities for this case are illustrated in Fig. 3. Equations (9) and (10) show that slip stops at impulse ratio γ,

$$\gamma = \frac{S[\mu_{1*}(\mu_{1\square} - \mu) + \mu_{2*}(\mu_{2\square} - \mu)]}{2\mu - \mu_{1*} - \mu_{2*}}$$

where $\mu_{i*} < 0$, $\mu_{i\square} < 0$ and $S = u_o(1+\xi)/v_o(1+\eta)$. To stop slip, friction must be large enough to overcome μ_{i*} and the initial momentum during collision;

$$\mu > \frac{(\mu_{1*} + \mu_{2*})\tau + (\mu_{1*}\mu_{1\square} + \mu_{2*}\mu_{2\square})S}{2\tau + (\mu_{1*} + \mu_{2*})S}. \tag{32}$$

Slip that stops does so during compression if $\mu < \mu_{i*}$ and during restitution if $\mu > \mu_{i*}$. After slip stops it reverses if $\mu_i < |\mu_{i*}|$ since $m_{i*} > 0$ and $n_{i*} > 0$; i.e., from (20),

$$u(\tau) = -\mu v_o(1+\eta)(\tau - \gamma)(n_{1*}^{-1} + n_{2*}^{-1})/(m_{1*}^{-1} + m_{2*}^{-1}) < 0. \tag{33}$$

Thus, if μ is sufficiently large so $n_{1*}^{-1} + n_{2*}^{-1} \le 0$, slip stops and sticks[3]. On the other hand if the initial slip speed is large,

$$S > \tau(2\mu - \mu_{1*} - \mu_{2*})/[\mu_{1*}\mu_{1\square} + \mu_{2*}\mu_{2\square} - \mu(\mu_{1*} + \mu_{2*})],$$

then unidirectional slip continues without stopping. Figure 5(*a*) shows slip processes for this case.

Case 2, $\theta_1 < 0 < \theta_2 \rightarrow n_1 > 0 > n_2$, $m_2 > m_1 > 0$ if $0 < \mu < \mu_{1\square}$: In this case the rate of change for the tangential velocity of CP_2 is negative. Hence, the limiting friction that stops slip is the same as that of the previous case (33). After slip stops it reverses if and only if $n_{1*}^{-1} + n_{2*}^{-1} > 0$. Otherwise, slip stops and sticks. Slip processes for this case are shown in Fig. 5(*b*).

Case 3, $\theta_1 > 0$, $\theta_2 > 0 \rightarrow n_i > m_i > 0$ if $\mu_{i*} < \mu < \mu_{i\square}$: This configuration has initial slip of each contact point away from the corresponding CM_i. If $\mu < \mu_{i*}$, $n_i < 0 < m_i$; hence, the initial slip speed increases and does not stop. If $\mu > \mu_{i*}$ slip stops during restitution, $1 < \gamma < \tau$. The maximum initial slip speed that stops during collision only stops at separation:

$$S = \frac{\tau(2\mu - \mu_{1*} - \mu_{2*})}{\mu_{1*}\mu_{1\square} + \mu_{2*}\mu_{2\square} - \mu(\mu_{1*} + \mu_{2*})}. \tag{34}$$

After slip stops the effective masses satisfy inequalities $n_{i*} < 0 < m_{i*}$ so there is no reversal; i.e., in this case slip stops and sticks if and only if

$\mu_{1*} + \mu_{2*} < 2\mu < \mu_{1\square} + \mu_{2\square}$ and

[3]If one body is massive in comparison with the other only n_{i*} of the light body determines whether slip reverses or sticks after stopping.

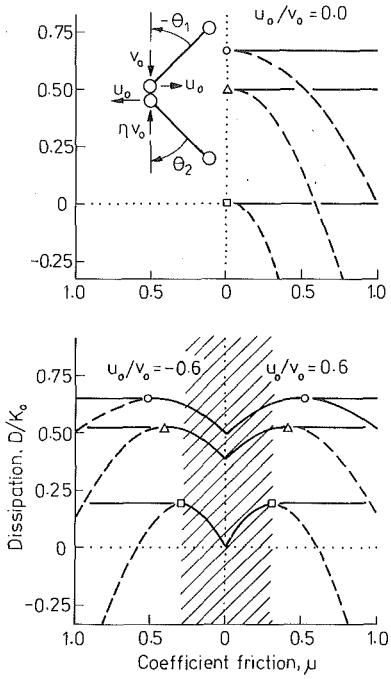

Fig. 7 Dissipation of initial energy for symmetric collision between two dumbbells with $\omega_i(t_o) = 0$, $-\theta_1 = \theta_2 = \pi/4$. The impact law, impulse hypothesis, and internal dissipation hypothesis are given by the dashed curve, chained curve, and continuous curve, respectively. Shaded region has continuous slip and outer bands have slip stick behavior. The coefficient of restitution is designated as follows: o, $e = 0$; Δ, $e = 0.5$ and □, $e = 1.0$.

$$\frac{u_0(1+\xi)}{v_o(1+\eta)} < \frac{\tau(2\mu - \mu_{1*} - \mu_{2*})}{\mu_{1*}\mu_{1\square} + \mu_{2*}\mu_{2\square} - \mu(\mu_{1*} + \mu_{2*})}.$$

Active regions for each slip process are shown in Fig. 5 for antisymmetric and symmetric configurations at collision of identical symmetric bodies. In this figure, positive and negative initial tangential velocities u_o/v_o correspond to the illustrated configuration and its mirror image (reflected about the common normal), respectively. Identical bodies that collide in an antisymmetric configuration $\theta_1 = \theta_2$ have equal but opposite accelerations for each body during collision; hence, contact forces on each body are equivalent to those in a collision with a very massive body.

Comparison of Consistent and Inconsistent Theories

Energy dissipation during collision is the scalar measure of collision dynamics that has pointed to an inherent defect in Newton's impact law. Both Kane (1984) and Brach (1989) examined dissipation during collisions between inclined elongated bodies and commented on paradoxical energy gains which occurred with friction and small initial slip that is halted during collision. This effect is observable in Fig. 6 which shows dissipation during a collision between two identical inclined dumbbells for a range of friction and initial slip speed. This figure shows that the impact law yields negative dissipation if friction is large, the collision is at least partially elastic, and we presume that e is independent of friction. Energy dissipation obtained with the impulse and internal dissipation hypotheses are never smaller than that of the restitution period hypothesis; more important, dissipation obtained with the internal dissipation theory is *always* positive.

Figures 6 and 7 show that the three theories are identical if slip does not halt during collision (the cross-hatched region). If slip stops but friction then prevents reversal, (slip-stick) frictional dissipation ceases before collision terminates. Slip that reverses after stopping is present only if the configuration is not symmetric with respect to the common tangent plane (Fig. 6) and initial slip of CP_i is towards CM_i; i.e., $u_o/v_o < 0$. With reversal there is a difference between the results of the impulse and internal dissipation hypotheses if $e > 0$. This difference is only obvious in this example if the collision is nearly elastic and slip reversal occurs near the transition from compression to restitution.

The example of a symmetric collision configuration illustrated in Fig. 7 stops and sticks if there is sufficient friction; the slip direction cannot reverse. Velocity changes for this configuration are not symmetric because of friction.

Conclusion

The impact law is an empirical relation for normal components of incident and rebound velocities at CP. The law provides a kinematic definition of coefficient of restitution e; however, if the collision is noncollinear then this definition results in a coefficient e that depends on friction and slip processes. This dependence results from coupling between the effects of normal and tangential contact forces. Consequently, if slip reverses during collision the kinematic definition of coefficient of restitution is not useful; any measurement of this coefficient is only applicable in a vanishingly small range of incident velocities. Furthermore, it is energetically inconsistent to assume that this definition yields a coefficient e that is independent of friction; this assumption leads to paradoxical calculations of increases in energy during impact.

A dynamic collision theory proposed by Stronge (1990) determines energy losses from the work done by contact *forces*; moreover, it imposes no constraints on slip. This *internal dissipation hypothesis* defines a coefficient of restitution that is *independent of friction*; for partly elastic collisions ($e < 1$) this theory always dissipates energy. It produces a kinetic energy loss due to irreversible internal deformation that is proportional to $1 - e^2$ irrespective of slip. If the contact point slips, there is also an energy loss due to friction. The internal dissipation hypothesis, the impact law, and Poisson's hypothesis are equivalent if slip does not halt during collision or if both CM_i are on the common normal line through CP (i.e, collinear). However, the theories are distinct for rough bodies if at least one center of mass is noncollinear and there is small initial slip that halts during collision; in this case only the internal dissipation hypothesis is energetically consistent.

Acknowledgment

The author gratefully acknowledges stimulating discussions on this topic with Profs. C. Calladine, K. L. Johnson, and M. Hubbard.

References

Brach, R. M., 1989, "Rigid Body Collisions," ASME JOURNAL OF APPLIED MECHANICS, Vol. 56, pp. 133–138.

Kane, T. R., 1984, "A Dynamics Puzzle," Stanford Mech. Alumni Club Newsletter.

Keller, J. B., 1986, "Impact With Friction," ASME JOURNAL OF APPLIED MECHANICS, Vol. 53, pp. 1–4.

Lötstedt, P., 1981, "Coulomb Friction in Two-Dimensional Rigid Body Systems," *Z.A.M.M*, Vol. 61, pp. 605–615.

Poisson, S. D., 1817, *Mechanics*, Vol. II, Trans. H. H. Harte, Longman, London.

Stronge, W. J., 1987, "The Domino Effect: A Wave of Destabilizing Collisions," *Proc. Roy. Soc. Lond.*, A409, pp. 199–208.

Stronge, W. J., 1990, "Rigid Body Collisions With Friction," *Proc. Roy. Soc. Lond.*, Vol. A431, pp. 169–181.

Stronge, W. J., 1991, "Friction in Collisions: Resolution of a Paradox," *J. Applied Physics*, Vol. 69, pp. 610–612.

Wallis, J., 1670, *Mechanica, sive De Motu, Tractatus Geometricus*, London.

Abd Alla El-Marhomy

Department of Engineering, Mathematics, and Physics,
Ain Shams University
Cairo, Egypt

A. L. Schlack, Jr.

Department of Engineering Mechanics,
University of Wisconsin-Madison,
Madison, WI 53706

Dynamic Stability of Elastic Rotor-Bearing Systems via Liapunov's Direct Method

A general method of analysis based on Liapunov's direct method is presented for studying the dynamic stability of elastic rotor-bearing systems. A model comprised of a continuous elastic shaft mounted on two 8-coefficient bearings is used to develop closed-form (series) stability criteria involving system stiffness and damping parameters. It is quantitatively shown by means of graphs how the instability regions are reduced by (a) increasing the shaft dimensionless stiffness parameters, (b) increasing the bearing direct stiffness and damping parameters, and (c) decreasing the bearing cross-coupling stiffness and damping parameters.

Introduction

The dynamics of rotors has been the subject of investigations for over a century. More recently, a new interest in this subject has emerged because of the trend toward ultra-high speeds in rotating machinery and the instability problems caused by the inherent flexibility of rotor-bearing systems. A considerable amount of research has been devoted to the dynamics and stability of rotating flexible shaft-appendage systems. However, all of these investigations either ignore the bearing support flexibility or oversimplify the bearing model. Typical studies are by Chivens and Nelson (1975), Klompas (1974), Kuo (1975), Masoom (1980), and Wilgen and Schlack (1977, 1979). Modeling the bearing support as a single spring and dashpot is frequently not adequate because, in many cases, the anisotropy of bearing supports must also be considered, as demonstrated by such authors as Gunter (1966), Klompas (1974), Moore (1972), Nelson and McVaugh (1976), and Parkinson (1965).

The asymmetric bearing model, however, is still not a completely satisfactory model, especially for large flexible rotors which are usually supported by journal bearings. The journal bearing actually acts as a nonisotropic spring and dashpot system with cross-coupling between the vertical and horizontal directions. The vast majority of investigations found in the literature neglect the cross-coupling stiffness and damping coefficients of the bearing support to simplify the mathematical model. Among the few authors who used an appropriate bearing support model (i.e., taking into account the anisotropic and cross-coupling coefficients by using an 8-coefficient bearing model) are Adams (1980, 1983), Adams and Padovan (1981), Doyle (1971), Gunter (1966), Rao (1985), and Stanway and Burrows (1981). However, due to the complexity of the problem when an 8-coefficient bearing model is adopted none of these studies treat the rotating shaft as a continuous elastic model.

Although Liapunov's direct method is a powerful tool for analyzing stability of linear and nonlinear dynamical systems and has frequently been applied successfully in examining attitude stability of elastic satellites, only a very few investigations (Grobov and Kantemir (1978) and Wilgen and Schlack (1977, 1978)) are found in the literature that adopt this technique to the study of rotor dynamics. Moreover, they focus mainly on the effect of appendage flexibility on shaft whirl stability, ignoring completely the flexibility of the two end-bearing supports.

The main objective of this paper is to gain a comprehensive insight into the effects of the various end support parameters coupled with the rotor flexibility parameters on the whirling stability of rotor-bearing systems. This is done by modeling the system as a continuous elastic rotor mounted on two dissimilar 8-coefficient bearings. Series expansions are used for describing the elastic rotor deflections. By mathematical induction, a general closed-form (series) set of sufficient conditions for stability is derived which leads to an easy assessment of truncation error.

Problem Formulation

The model consists of a rotor of mass m treated as a continuous elastic shaft of length L supported at its ends by two dissimilar 8-coefficient bearings shown schematically in Fig. 1. The shaft is initially straight, balanced, uniform, and with a slenderness ratio sufficiently small that the Euler-Bernoulli theory of bending may be used for small displacements. It is assumed that extensional and torsional deformations are negligible and aerodynamic effects are not included.

Consider that in the dynamic equilibrium configuration of

Contributed by the Applied Mechanics Division of THE AMERICAN SOCIETY OF MECHANICAL ENGINEERS for publication in the JOURNAL OF APPLIED MECHANICS.

Discussion on this paper should be addressed to the Technical Editor, Prof. Leon M. Keer, The Technological Institute, Northwestern University, Evanston, IL 60208, and will be accepted until two months after final publication of the paper itself in the JOURNAL OF APPLIED MECHANICS. Manuscript received by the ASME Applied Mechanics Division, Feb. 23, 1990; final revision, July 25, 1990.

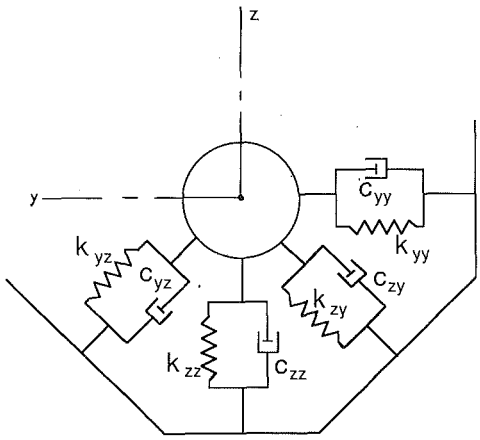

Fig. 1 8-coefficient bearing model

the rotor-bearing system the undeformed shaft is along the x-direction of an inertial x, y, z coordinate system. Denoting the deflection of the center of the left bearing by $\mathbf{r}_1 = y_1\mathbf{j} + z_1\mathbf{k}$ and that of the right bearing by $\mathbf{r} = y_2\mathbf{j} + z_2\mathbf{k}$, we can describe the displacement of an arbitrary element of the undeformed shaft axis at a distance x from the left bearing as

$$\mathbf{r}_s(x, t) = y(x, t)\mathbf{j} + z(x, t)\mathbf{k} = (y_1 + x\theta)\mathbf{j} + (z_1 + x\phi)\mathbf{k} \quad (1)$$

where, for small angles and small displacements, we have approximately,

$$\theta = \frac{y_2 - y_1}{L} \text{ and } \phi = \frac{z_2 - z_1}{L}. \quad (2)$$

Also, the resultant angular velocity of the shaft which rotates at a speed Ω about its bearing axis can be written as

$$\omega = \Omega\mathbf{i} + (\dot{\phi} + \theta\Omega)\mathbf{j} + (\dot{\theta} + \phi\Omega)\mathbf{k}. \quad (3)$$

Adopting the assumed mode approach the elastic shaft deflections can be expressed as

$$v(x, t) = \sum_{n=1}^{N} a_n(t) \sin\frac{n\pi x}{L} \quad w(x, t) = \sum_{n=1}^{N} b_n(t) \sin\frac{n\pi x}{L} \quad (4)$$

where $a_n(t)$ and $b_n(t)$ are time-dependent generalized coordinates and N denotes the number of terms in the truncated series expansion. Therefore, the position vector $\mathbf{r}(x, t)$ of a typical differential element at a distance x along the shaft is

$$\mathbf{r}(x,t) = [y(r,t) + v(x,t)]\mathbf{j} + [z(x,t) + w(x,t)]\mathbf{k} \quad (5)$$

where $y(x, t)$ and $z(x, t)$ are the rigid body displacements and $v(x, t)$ and $w(x, t)$ are the elastic displacements of the differential element. Differentiating $\mathbf{r}(x, t)$ with respect to time, the velocity vector is

$$\dot{\mathbf{r}}(x, t) = [(z + w)(\dot{\phi} + \theta\Omega) - (y + v)(\dot{\theta} + \phi\Omega)]\mathbf{i} + [(\dot{y} + \dot{v}) - \Omega(z + w)]\mathbf{j} + [(\dot{z} + \dot{w}) + \Omega(y + v)]\mathbf{k}. \quad (6)$$

The kinetic energy of the shaft is

$$T = \frac{1}{2}\rho\int_0^L \dot{\mathbf{r}}\cdot\dot{\mathbf{r}}\,dx = \frac{1}{2}\rho\int_0^L \{(\dot{y} + \dot{v})^2 + (\dot{z} + \dot{w})^2 + \dot{\theta}^2(y + v)^2 + \dot{\phi}^2(z + w)^2 - 2\dot{\theta}\dot{\phi}(y + v)(z + w)] + 2\Omega[(y + v)(\dot{z} + \dot{w}) - (z + w)(\dot{y} + \dot{v}) + \phi\dot{\theta}(y + v)^2 + \theta\dot{\phi}(z + w)^2 - (\theta\dot{\theta} + \phi\dot{\phi})(y + v)(z + w)] + \Omega^2[(y + v)^2(1 + \phi^2) + (z + w)^2(1 + \theta^2) - 2(y + v)(z + w)\theta\phi]\}dx. \quad (7)$$

Note that, in general, the kinetic energy T can be rewritten as $T = T_2 + T_1 + T_0$ where the subscript refers to the algebraic degree in the generalized velocity variables.

The strain energy expression for the bearing system under consideration is

$$V_b = \frac{1}{2}\sum_i\sum_j k_{ij}q_iq_j = \frac{1}{2}(k_{y_1y_1}y_1^2 + k_{y_1z_1}y_1z_1 + k_{z_1z_1}z_1^2 + k_{z_1y_1}z_1y_1 + k_{y_2y_2}y_2^2 + k_{y_2z_2}y_2z_2 + k_{z_2z_2}z_2^2 + k_{z_2y_2}z_2y_2) \quad (8)$$

where the subscript 1 refers to the left bearing and 2 to the right bearing. The strain energy expression for the shaft is

$$V_s = \frac{1}{2}EI\int_0^L \left[\left(\frac{\partial^2 v(x,t)}{\partial x^2}\right)^2 + \left(\frac{\partial^2 w(x,t)}{\partial x^2}\right)^2\right]dx. \quad (9)$$

The strain energy of the system is thus given by

$$V = V_b + V_s. \quad (10)$$

The energy dissipation function of the system is

$$D = \frac{1}{2}\sum_i\sum_j C_{ij}\dot{q}_i\dot{q}_j = \frac{1}{2}(C_{y_1y_1}\dot{y}_1^2 + C_{y_1z_1}\dot{y}_1\dot{z}_1 + C_{z_1z_1}\dot{z}_1^2 + C_{z_1y_1}\dot{z}_1\dot{y}_1 + C_{y_2y_2}\dot{y}_2^2 + C_{y_2z_2}\dot{y}_2\dot{z}_2 + C_{z_2z_2}\dot{z}_2^2 + C_{z_2y_2}\dot{z}_2\dot{y}_2). \quad (11)$$

The state of motion of the mechanical system under consideration is thus completely defined by the functions $v(x, t)$ and $w(x, t)$ plus the four state variables y_1, z_1, y_2, and z_2 which can be alternatively taken as y_1, z_1, θ and ϕ. Thus, this mechanical system can be completely defined by $2N + 4$ generalized coordinates given by y_1, z_1, θ, ϕ and a_n, b_n for $n = 1, 2, \ldots N$.

Stability Analysis

The nature of stability in the neighborhood of the equilibrium configuration, identified by $q_i = \dot{q}_i = 0$, is determined using Liapunov's direct method (Meirovitch, 1970). If damping is neglected, the Hamiltonian H is constant and is a suitable Liapunov function. In the presence of damping, the total time derivative of H can be shown to be

$$\dot{H} = \sum_{i=1}^{n} Q_i\dot{q}_i, \quad (12)$$

which indicates that the sign definiteness of $\dot{H}$ depends on the nature of the nonconservative force, Q_i. Since Q_i comprises damping forces representing either complete damping or pervasive damping, it does not alter the nature of equilibrium in a meaningful way. That is to say, a stable system becomes asymptotically stable, whereas an unstable one remains unstable.

The system Hamiltonian function can be written as

$$H = T_2 - T_o + V. \quad (13)$$

Since the terms T_2 is automatically positive definite, the positive definiteness of a function U called the dynamic potential given by

$$U = V - T_o \quad (14)$$

ensures the positiveness of H. Therefore, introducing expressions for V and T_0 into Eq. (14), the dynamic potential U after algebraic manipulations and integration of Eqs. (7)–(10) can be written as

$$U = \frac{1}{2}\{k_{y_1y_1}y_1^2 + k_{z_1z_1}z_1^2 + (k_{y_1z_1} + k_{z_1y_1})y_1z_1 + k_{y_2y_2}(y_1 + L\theta)^2 + k_{z_2z_2}(z_1 + L\phi)^2 + (k_{y_2z_2} + k_{z_2y_2})(y_1 + L\theta)(z_1 + L\phi)\} + \frac{1}{4}k_s\sum_{n=1}^{N} n^4(a_n^2 + b_n^2) - \frac{1}{2}m\Omega^2\{y_1^2(1 + \phi^2) + z_1^2(1 + \theta^2) - 2y_1z_1\theta\phi + L[y_1\theta(1 + \phi^2) + z_1\phi(1 + \theta^2) - (y_1\phi + z_1\theta)\theta\phi]$$

$$+\frac{1}{3}L^2(\theta^2+\phi^2)+\sum_{n=1}^{N}\left\{\frac{1}{2}[a_n^2(1+\phi^2)+b_n^2(1+\theta^2)-2a_nb_n\theta\phi]\right.$$

$$-2\frac{(-1)^n-1}{n\pi}[y_1a_n(1+\phi^2)+z_1b_n(1+\theta^2)-(y_1b_n+z_1a_n)\theta\phi]$$

$$\left.-2\frac{(-1)^n}{n\pi}L[a_n\theta(1+\phi^2)+b_n\phi(1+\theta^2)-(a_n\phi+b_n\theta)\theta\phi)]\right\} \tag{15}$$

where k_s = shaft stiffness parameter = $EIL(\pi/L)^4$.

Using Euler's theorem on homogeneous functions, it can be shown that Eq. (12) becomes

$$\dot{H}=-2D. \tag{16}$$

Thus, a positive definite D leads to a negative definite $\dot{H}$. Therefore, due to Liapunov stability theory, if for such a system H is positive definite (which can be guaranteed by the positive definiteness of U), then the system is asymptotically stable and if H can assume negative values in the neighborhood of the equilibrium point, then the system is unstable. Thus, the problem simplifies to testing for (a) the positive definiteness of U to achieve stability in the undamped case and (b) the positive definiteness of both U and D in order to achieve asymptotic stability of the damped system. Testing for the positive definiteness of U and D can be accomplished by applying Sylvester's theorem to the Hessian matrices of U and D (evaluated at the equilibrium position) given by

$$U_{ij}=\left.\frac{\partial^2 U}{\partial q_i \partial q_j}\right|_E$$

and (17)

$$D_{ij}=\left.\frac{\partial^2 D}{\partial \dot{q}_i \partial \dot{q}_j}\right|_E.$$

To demonstrate the general method of analysis, similar bearings are adopted to simplify the complexity of the stability calculations and resulting conditions. Stability conditions for dissimilar bearings have been developed by El-Marhomy (1987), but they will not be reproduced in this paper due to their length.

Dividing U by $m\Omega^2$, evaluating the second partial derivatives at the equilibrium position, letting $k_{i_1j_1} = k_{i_2j_2} = \frac{1}{2}k_{ij}$ for similar bearings and making appropriate algebraic manipulations the Hessian matrix, denoted by $U_{ij}^{(N)}$, can be written in the form given by Eq. (18). The shaft stiffness parameter $\alpha = \frac{EI}{\rho\Omega^2}\left(\frac{\pi}{L}\right)^4$ and the bearing cross-coupling stiffness parameter $\beta=\frac{1}{2\Omega^2}(\omega_{yz}^2+\omega_{zy}^2)$ where $\omega_{ij}^2=\frac{k_{ij}}{m}$.

Equation (18) is the Hessian matrix of the system with N modal terms included in the series expressing the shaft elastic deflections. It is a square matrix of order $2N + 4$. The first four rows and columns represent the Hessian matrix for the rigid body case (rigid rotor on elastic bearings) for which the generalized coordinates are y_1, z_1, θ, and ϕ.

$$U_{ij}^{(N)}=\begin{bmatrix}
\left(\frac{\omega_{yy}^2}{\Omega^2}-1\right) & \beta & \frac{1}{2}L\left(\frac{\omega_{yy}^2}{\Omega^2}-1\right) & \frac{1}{2}L\beta & -\frac{2}{\pi} & 0 & \cdots & -\frac{2}{N\pi} & 0 & 0 & \cdots & 0 \\
\beta & \left(\frac{\omega_{zz}^2}{\Omega^2}-1\right) & \frac{1}{2}L\beta & \frac{1}{2}L\left(\frac{\omega_{zz}^2}{\Omega^2}-1\right) & 0 & 0 & \cdots & 0 & -\frac{2}{\pi} & 0 & \cdots & -\frac{2}{N\pi} \\
\frac{1}{2}L\left(\frac{\omega_{yy}^2}{\Omega^2}-1\right) & \frac{1}{2}L\beta & L^2\left(\frac{1}{2}\frac{\omega_{yy}^2}{\Omega^2}-\frac{1}{3}\right) & \frac{1}{2}L^2\beta & -\frac{L}{\pi} & \frac{L}{2\pi} & \cdots & -\frac{L}{N\pi} & 0 & 0 & \cdots & 0 \\
\frac{1}{2}L\beta & \frac{1}{2}L\left(\frac{\omega_{zz}^2}{\Omega^2}-1\right) & \frac{1}{2}L^2\beta & L^2\left(\frac{1}{2}\frac{\omega_{zz}^2}{\Omega^2}-\frac{1}{3}\right) & 0 & 0 & \cdots & 0 & -\frac{L}{\pi} & \frac{L}{2\pi} & \cdots & -\frac{L}{N\pi} \\
-\frac{2}{\pi} & 0 & -\frac{L}{\pi} & 0 & \frac{1}{2}(\alpha-1) & 0 & \cdots & 0 & 0 & 0 & \cdots & 0 \\
0 & 0 & \frac{L}{2\pi} & 0 & 0 & \frac{1}{2}(16\alpha-1) & \cdots & 0 & 0 & 0 & \cdots & 0 \\
\vdots & \vdots & \vdots & \vdots & \vdots & \vdots & \vdots & \vdots & \vdots & \vdots & \vdots & \vdots \\
-\frac{2}{N\pi} & 0 & -\frac{L}{N\pi} & 0 & 0 & 0 & \cdots & \frac{1}{2}(N^4\alpha-1) & 0 & 0 & \cdots & 0 \\
0 & -\frac{2}{\pi} & 0 & -\frac{L}{\pi} & 0 & 0 & \cdots & 0 & \frac{1}{2}(\alpha-1) & 0 & \cdots & 0 \\
0 & 0 & 0 & \frac{L}{2\pi} & 0 & 0 & \cdots & 0 & 0 & \frac{1}{2}(16\alpha-1) & \cdots & 0 \\
\vdots & \vdots & \vdots & \vdots & \vdots & \vdots & \vdots & \vdots & \vdots & \vdots & \vdots & \vdots \\
0 & -\frac{2}{N\pi} & 0 & -\frac{L}{N\pi} & 0 & 0 & \cdots & 0 & 0 & 0 & \cdots & \frac{1}{2}(N^2\alpha-1)
\end{bmatrix} \tag{18}$$

According to Sylvester's theorem, the positive definiteness of $U_{ij}^{(N)}$ requires the positive definiteness of all its principal minors. However, it has been proved by El-Marhomy (1987, pp. 177–179) that the greatest principal minor $\Delta_{2N+4} = |U_{ij}^{(N)}|$ is the relevant principal minor that makes the other principal minors trivially positive provided that it is positive. In other words, it is only the $|U_{ij}^{(N)}|$ that must be tested each time a term is added to the series expansion in order to understand the pattern of stability conditions as one successively increases the value of N. Each additional term in the pair of series expansions describing the shaft's deflections corresponds to an additional pair of rows and columns in the system's Hessian matrix leading to two new stability conditions. A consistent pattern of stability conditions is obtained for successively increased values of N by performing a certain series of elementary row operations on each Δ_{2N+4} such that its form reduces to a unified structure. Therefore, the expansion of $|U_{ij}^{(N)}|$ for any number N of terms included in the series expressing the shaft's elastic deflections can be developed by mathematical induction.

It can be shown by performing the row operations

$$R_1 \leftrightarrow R_1-\frac{2}{L}R_3+\frac{4}{\pi}\sum_{n\ \text{even}}^{r\le N}[n(n^4\alpha-1)]^{-1}R_{n+4},$$

$$R_2 \mapsto R_2 - \frac{2}{L} R_4 + \frac{4}{\pi} \sum_{n\ \text{even}}^{r \le N} \frac{1}{n(n^4\alpha - 1)} R_{N+n+4},$$

$$R_3 \mapsto R_3 + \frac{2L}{\pi} \sum_{n=1}^{N} \frac{(-1)^{n+1}}{n(n^4\alpha - 1)} R_{n+4}$$

and

$$R_4 \mapsto R_4 + \frac{2L}{\pi} \sum_{n=1}^{N} \frac{(-1)^{n+1}}{n(n^4\alpha - 1)} R_{N+n+4} \tag{19}$$

$$U_{ij}^{(N)} = \begin{bmatrix}
0 & 0 & A_N & -\frac{1}{2}L\beta & 0 & 0 & 0 & 0 & 0 & 0 & 0 & 0 \\
0 & 0 & -\frac{1}{2}L\beta & B_N & 0 & 0 & 0 & 0 & 0 & 0 & 0 & 0 \\
C_N & \frac{1}{2}L\beta & H_N & \frac{1}{2}L^2\beta & 0 & 0 & 0 & 0 & 0 & 0 & 0 & 0 \\
\frac{1}{2}L\beta & D_N & \frac{1}{2}L^2\beta & E_N & 0 & 0 & 0 & 0 & 0 & 0 & 0 & 0 \\
-\frac{2}{\pi} & 0 & -\frac{L}{\pi} & 0 & \frac{1}{2}(\alpha-1) & 0 & 0 & 0 & 0 & 0 & 0 & 0 \\
0 & 0 & \frac{L}{2\pi} & 0 & 0 & \frac{1}{2}(16\alpha-1) & 0 & 0 & 0 & 0 & 0 & 0 \\
-\frac{2}{3\pi} & 0 & -\frac{L}{3\pi} & 0 & 0 & 0 & \frac{1}{2}(81\alpha-1) & 0 & 0 & 0 & 0 & 0 \\
\vdots & \vdots & \vdots & \vdots & \vdots & \vdots & \vdots & \vdots & \vdots & \vdots & \vdots & \vdots \\
-\frac{2}{N\pi} & 0 & -\frac{L}{N\pi} & 0 & 0 & 0 & 0 & \frac{1}{2}(N^4\alpha-1) & 0 & 0 & 0 & 0 \\
0 & -\frac{2}{\pi e} & 0 & -\frac{L}{\pi} & 0 & 0 & 0 & 0 & \frac{1}{2}(\alpha-1) & 0 & 0 & 0 \\
0 & 0 & 0 & \frac{L}{2\pi} & 0 & 0 & 0 & 0 & 0 & \frac{1}{2}(16\alpha-1) & 0 & 0 \\
0 & -\frac{2}{3\pi} & 0 & -\frac{L}{3\pi} & 0 & 0 & 0 & 0 & 0 & 0 & \frac{1}{2}(81\alpha-1) & 0 \\
\vdots & \vdots & \vdots & \vdots & \vdots & \vdots & \vdots & \vdots & \vdots & \vdots & \vdots & \vdots \\
0 & -\frac{2}{N\pi} & 0 & -\frac{L}{N\pi} & 0 & 0 & 0 & 0 & 0 & 0 & 0 & \frac{1}{2}(N^4\alpha-1)
\end{bmatrix} \tag{20}$$

that the determinant $|U_{ij}^{(N)}|$ reduces to the unified form given by Eq. (20), where R_i refers to row i, $R_i \mapsto k R_i + sR_j$ means to change R_i to $kR_i + sR_j$, and r is the largest even integer $r \le N$. The coefficients A_N, B_N, C_N, D_N, E_N, and H_N used in Eq. (20) are defined by

$$A_N = -L\left[\frac{1}{2}\left(\frac{\omega_{yy}^2}{\Omega^2} - \frac{1}{3}\right) - \frac{4}{\pi^2}\sum_{n\ \text{even}}^{r \le N} \frac{1}{n^2(n^4\alpha - 1)}\right]$$

$$B_N = -L\left[\frac{1}{2}\left(\frac{\omega_{zz}^2}{\Omega^2} - \frac{1}{3}\right) - \frac{4}{\pi^2}\sum_{n\ \text{even}}^{r \le N} \frac{1}{n^2(n^4\alpha - 1)}\right]$$

$$C_N = L\left[\frac{1}{2}\left(\frac{\omega_{yy}^2}{\Omega^2} - 1\right) - \frac{4}{\pi^2}\sum_{n\ \text{odd}}^{q \le N} \frac{1}{n^2(n^4\alpha - 1)}\right]$$

$$D_N = L\left[\frac{1}{2}\left(\frac{\omega_{zz}^2}{\Omega^2} - 1\right) - \frac{4}{\pi^2}\sum_{n\ \text{odd}}^{q \le N} \frac{1}{n^2(n^4\alpha - 1)}\right]$$

$$E_N = L^2\left[\left(\frac{1}{2}\frac{\omega_{zz}^2}{\Omega^2} - \frac{1}{3}\right) - \frac{2}{\pi^2}\sum_{n=1}^{N} \frac{1}{n^2(n^4\alpha - 1)}\right]$$

$$H_N = L^2\left[\left(\frac{1}{2}\frac{\omega_{yy}^2}{\Omega^2} - \frac{1}{3}\right) - \frac{2}{\pi^2}\sum_{n=1}^{N} \frac{1}{n^2(n^4\alpha - 1)}\right]$$

where q is the largest odd integer $q \le N$.

Therefore, $|U_{ij}^{(N)}|$ can be written in the following form after various algebraic manipulations:

$$|U_{ij}^{(N)}| = \left[\frac{L^4}{2^{2N}}\prod_{n=1}^{N}(n^4\alpha - 1)^2\right]\left\{\left[\frac{1}{2}\left(\frac{w_{yy}^2}{\Omega^2} - 1\right) - \frac{4}{\pi^2}\sum_{n\ \text{odd}}^{q \le N} \frac{1}{n^2(n^4\alpha - 1)}\right]\left[\frac{1}{2}\left(\frac{\omega_{zz}^2}{\Omega^2} - 1\right) - \frac{4}{\pi^2}\sum_{n\ \text{odd}}^{q \le N} \frac{1}{n^2(n^4\alpha - 1)}\right] - \frac{1}{4}\beta^2\right\}\left\{\left[\frac{1}{2}\left(\frac{w_{yy}^2}{\Omega^2} - \frac{1}{3}\right) - \frac{4}{\pi^2}\sum_{n\ \text{even}}^{r \le N} \frac{1}{n^2(n^4\alpha - 1)}\right]\left[\frac{1}{2}\left(\frac{\omega_{zz}^2}{\Omega^2} - \frac{1}{3}\right) - \frac{4}{\pi^2}\sum_{n\ \text{even}}^{r \le N} \frac{1}{n^2(n^4\alpha - 1)}\right] - \frac{1}{4}\beta^2\right\}. \tag{21}$$

Presenting the expansion of $|U_{ij}^{(N)}|$ in this closed-form series leads to general closed-form conditions for system stability. Thus, for positive definiteness of $U_{ij}^{(N)}$, $|U_{ij}^{(N)}|$ must be positive definite, i.e., $|U_{ij}^{(N)}| > 0$ which results in the following non-trivial sufficient conditions for system stability:

$$(\alpha - 1) > 0,$$

$$\left(\frac{\omega_{yy}^2}{\Omega^2} - 1\right) > \frac{8}{\pi^2}\sum_{n\ \text{odd}}^{q \le N} \frac{1}{n^2(n^4\alpha - 1)},$$

$$\left[\left(\frac{\omega_{yy}^2}{\Omega^2} - 1\right) - \frac{8}{\pi^2}\sum_{n\ \text{odd}}^{q \le N} \frac{1}{n^2(n^4\alpha - 1)}\right]\left[\left(\frac{\omega_{zz}^2}{\Omega^2} - 1\right) - \frac{8}{\pi^2}\sum_{n\ \text{odd}}^{q \le N} \frac{1}{n^2(n^4\alpha - 1)}\right] > \beta^2. \tag{22}$$

Discussion of Results

Examining the foregoing conditions, the following observations are made:

1 Equations (22) represent general closed-form sufficient conditions for whirling stability of elastic rotors mounted on elastic bearings possessing both anisotropic and cross-coupling stiffnesses. Note that only the odd terms in the series expansions affect the stability boundaries.

2 The series in Eqs. (22) can be shown to rapidly converge. In fact, they are asymptotic to the highly convergent series $\sum_n \frac{1}{n^6}$.

3 In the limiting case $\alpha \to \infty$ (rigid rotor case), Eqs. (22) reduce to

$$\left(\frac{\omega_{yy}^2}{\Omega^2}-1\right)>0$$

and

$$\left(\frac{\omega_{yy}^2}{\Omega^2}-1\right)\left(\frac{\omega_{zz}^2}{\Omega^2}-1\right)>\beta^2 \tag{23}$$

where the reader may recall that β is the nondimensional cross-coupling stiffness parameter.

4 In the other limiting case $\frac{\omega_{yy}^2}{\Omega^2}=\frac{\omega^2{}_{zz}}{\Omega^2}=\infty$ (rigid bearing case), the second and third of Eqs. (22) are trivially satisfied. Therefore, conditions for whirl stability of an elastic rotating shaft on rigid bearings simplifies to

$$(\alpha-1)>0, \tag{24}$$

which is the same result reached by Wilgen and Schlack (1979) and others.

The Hessian matrix of an elastic rotating shaft on rigid bearings is obtained from $U_{ij}^{(N)}$ by deleting its first four rows and columns. Therefore, applying Sylvester's theorem to test positive definiteness in this case yields

$$\prod_{n=1}^{N}(n^4\alpha-1)>0, \tag{25}$$

which results in the nontrivial condition (24). It is worthwhile noting here that if the inequality sign in condition (25) is changed into an equality sign, the condition is transformed to the system characteristic equation (frequency equation) given by

$$\prod_{n=1}^{N}(n^4\alpha_{cr}-1)=0. \tag{26}$$

The roots of Eq. (26) give the well-known critical speeds of the system (elastic rotating shaft on rigid bearings) as

$$\Omega_{cr}=\omega_s,\ 4\omega_s,\ 9\omega_s,\ \ldots,\ N^2\omega_s;\quad \text{for } \omega_s=\sqrt{\frac{k_s}{m}}. \tag{27}$$

5 In the special case of isotropic bearings where the bearing elasticity can be represented by a single spring of constant k_b by letting $\omega_{yy}^2=\omega_{zz}^2=\omega_b^2=\frac{k_b}{m}$ and $\beta=0$ in conditions (22), we get the following sufficient conditions for stability:

$$(\alpha-1)>0$$

and

$$\left(\frac{\omega_b^2}{\Omega^2}-1\right)>\frac{8}{\pi^2}\sum_{n\ \text{odd}}^{q\le N}\frac{1}{n^2(n^4\alpha-1)} \tag{28}$$

6 The stability criteria in Eqs. (22) functionally show the effects of the system's nondimensional parameters α, β, $\frac{\omega_{yy}^2}{\Omega^2}$, and $\frac{\omega_{zz}^2}{\Omega^2}$ and the number of series term N on the whirling stability of the elastic rotor bearing system under investigation. The effects of these factors on the stability regions of the system based on Eqs. (22) are presented graphically in Figs. 2 through 7.

Although the graphs are not included herein, it has been shown by El-Marhomy (1987) that the stability boundaries are not appreciably affected by increasing the number N of series terms above the fundamental term $N = 1$. The difference is so indistinguishable that the stability curves for all N lie on top of one another when plotted by typical software programs. Mathematically, this is attributed to the fact that the first term in the highly convergent $\sum_{n=1}^{\infty}\frac{1}{(2n-1)[(2n-1)^4\alpha-1]}$ is the dominant term that leaves the others trivially small with respect to it.

Figures 2, 3, and 4 show the influence of rotor elasticity on the system stability. It is easy to see that the curves with higher values of $\alpha=\frac{EI}{\rho\Omega^2}(\pi/L)^4$ contain larger stable regions. It is also obvious that the stability boundaries change dramatically

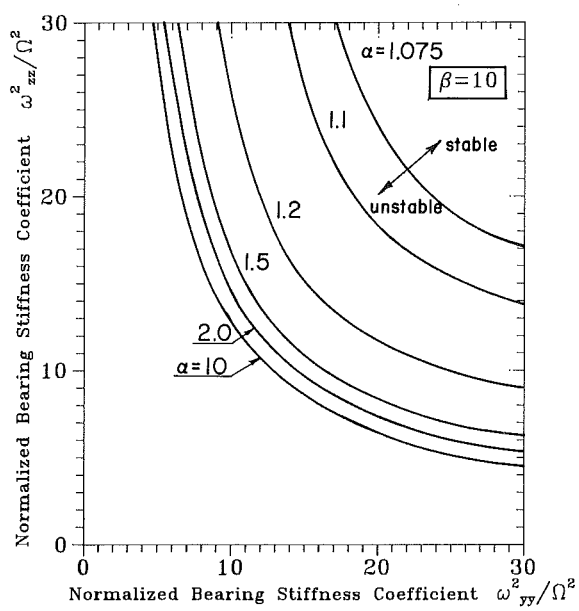

Fig. 2 Stability regions with α as a parameter for $\beta = 10$

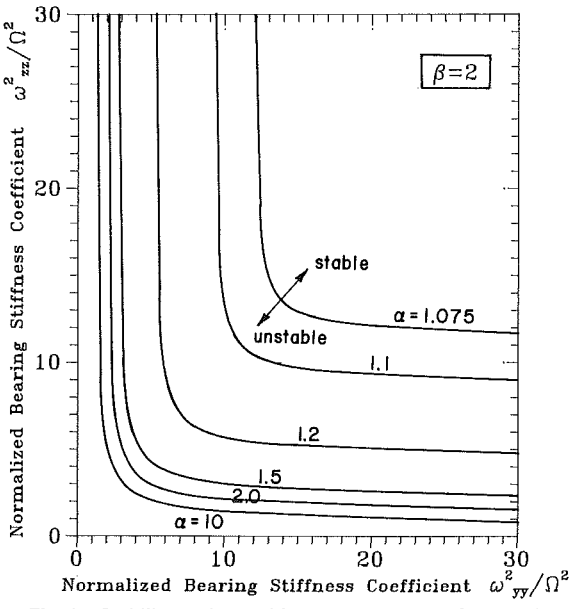

Fig. 3 Stability regions with α as a parameter for $\beta = 2$

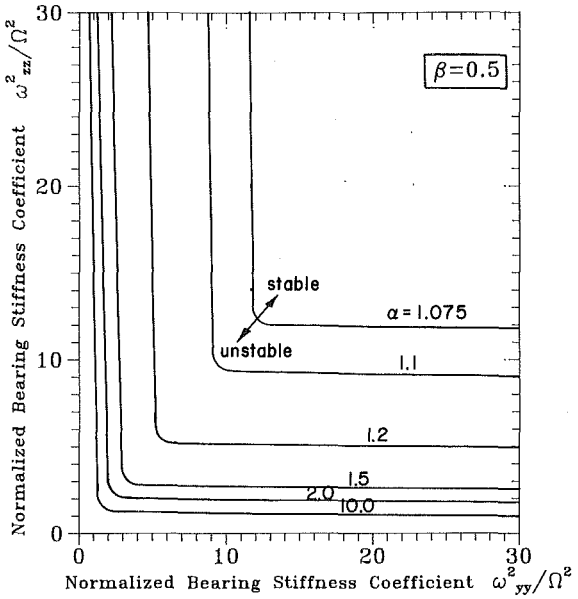

Fig. 4 Stability regions with α as a parameter for β = 0.5

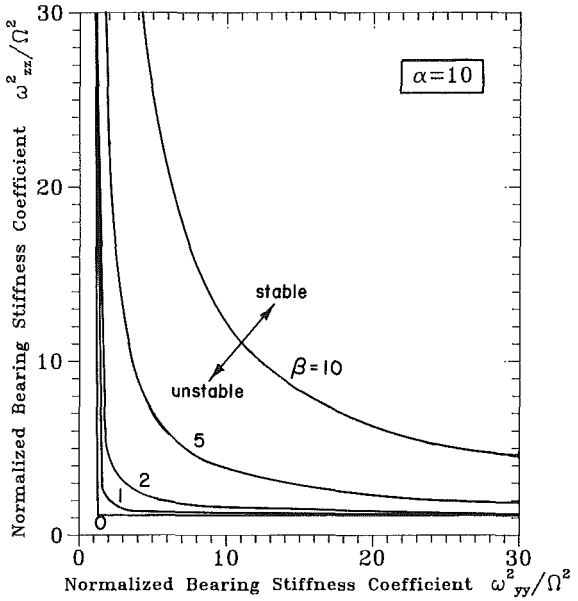

Fig. 5 Stability regions with β as a parameter for α = 10

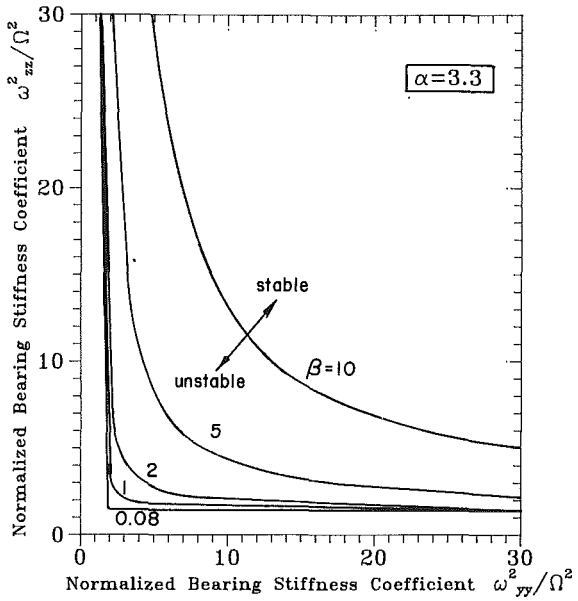

Fig. 6 Stability regions with β as a parameter for α = 3.3

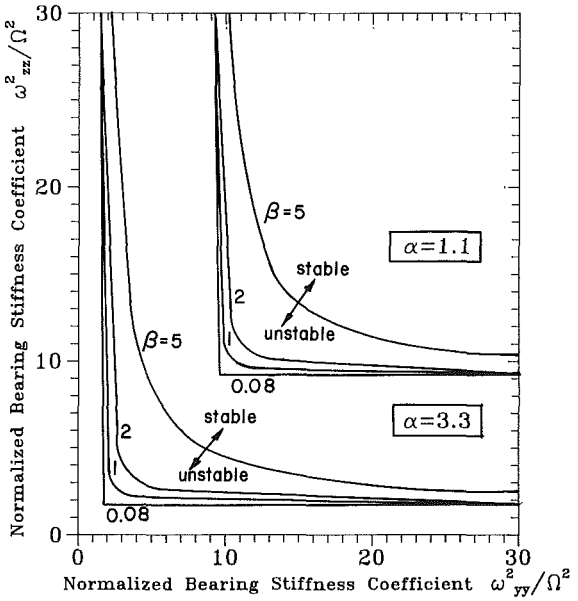

Fig. 7 Combined effect of α and β on stability regions

as α approaches the critical value $\alpha = 1$. The stability curves drawn in Figs. 5, 6, and 7 demonstrate the effect of the bearing cross-coupling parameters β on the stability of the system, where greater values of β lead to smaller stability regions for a given value of α. This points out the important role played by the bearing cross-coupling stiffness coefficients which can be a significant source of instability. Figure 7 also illustrates the combined effect of α and β on the stability boundaries where it is clear that the stability regions grow with increasing α and decreasing β. All figures from 2 through 7 share the common characteristic that the values of the normalized bearing stiffness coefficients $\frac{\omega_{yy}^2}{\Omega^2}$ or $\frac{\omega_{zz}^2}{\Omega^2}$ must be greater than their critical value $1 + \frac{8}{\pi^2} \sum_{n \text{ odd}}^{q \le N} \frac{1}{n(n^4\alpha - 1)}$ in order to ensure stability.

Effect of Damping

Concerning the damped system, it is necessary to test for the positive definiteness of D in order to study asymptotic stability in the sense of Liapunov. Therefore, letting $C_{i_1 j_1} = C_{i_2 j_2} = \frac{1}{2} C_{ij}$ in Eq. (11) for similar bearings and evaluating the second partial derivatives of D at the equilibrium position, the Hessian matrix D_{ij} takes the form

$$D_{ij} = \begin{bmatrix} C_{yy} & \gamma & \frac{1}{2}LC_{yy} & L\gamma \\ & C_{zz} & L\gamma & \frac{1}{2}LC_{zz} \\ \text{Symmetry} & & \frac{1}{2}L^2C_{yy} & \\ & & & \frac{1}{2}L^2C_{zz} \end{bmatrix} \tag{29}$$

where the bearing cross-coupling damping parameter $\gamma = \frac{1}{2}(C_{yz} + C_{zy})$.

Applying Sylvester's theorem to test the positive definiteness

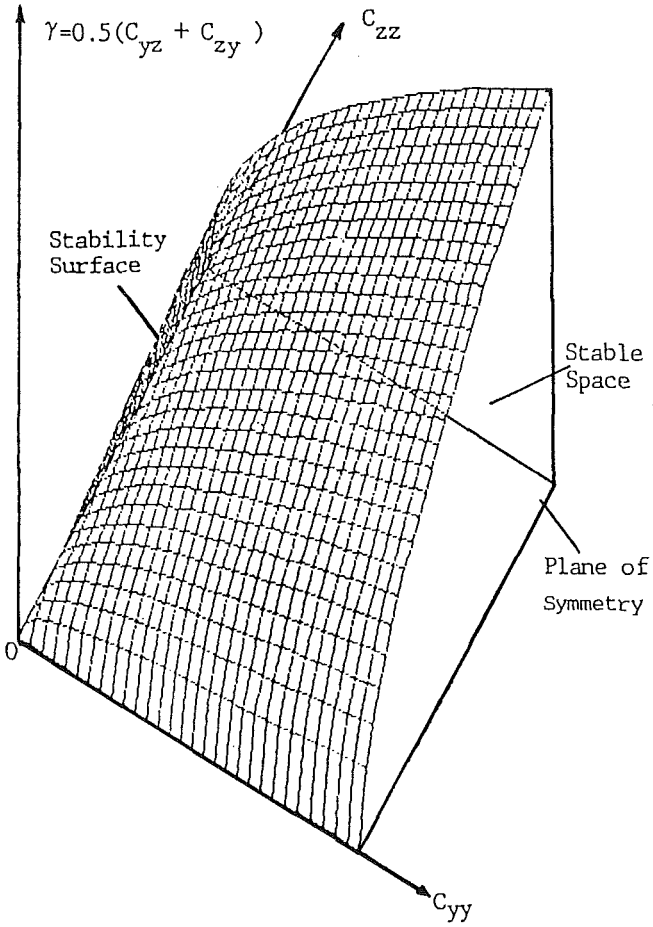

Fig. 8 Subspace of stable bearing damping coefficients

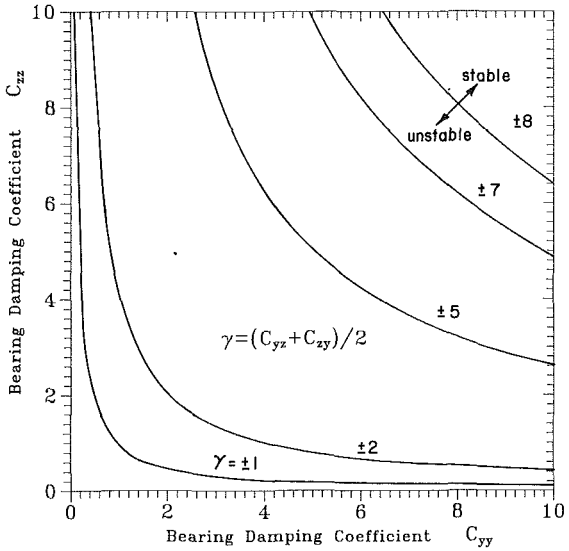

Fig. 9 Effect of damping cross-coupling parameter γ on stability regions

of D_{ij} yields the following nontrivial conditions for an asymptotically stable rotating system:

$$C_{yy}>0$$

and

$$C_{yy}C_{zz}>\gamma^2. \tag{30}$$

These conditions can be geometrically visualized by constructing a three-dimensional space for the bearing damping coefficients with C_{yy}, C_{zz} and γ as a basis for this space. Accordingly, the subspace of asymptotically stable bearing damping coefficients based on Eqs. (30) is the spatial region inside the parabolic hypberoloid shown in Fig. 8. This indicates that all possible values of bearing damping coefficients that result in asymptotically stable motion are located inside this stability surface. The cross-sections of the stability surface in Fig. 8 formed by planes perpendicular to either C_{yy} or C_{zz} is a family of parabolas. Thus, the stability regions grow with the increase of the principal damping coefficients C_{yy} and C_{zz}. It can also be shown that if the stability surface is cut by planes perpendicular to the γ-axis, then the cross-sections are rectangular hyperbolas representing the stability boundaries in terms of γ as shown in Fig. 9. The area inside each hyperbola decreases with the increase of γ which indicates that the stability regions decrease with the increase of γ. This clearly demonstrates the fact that the bearing damping cross-coupling parameter γ can have a significant influence on the nature of the system's stability.

Summary and Conclusion

This paper presents a general method of analysis for investigating the effect of the various end-support parameters coupled with the rotor's flexibility parameters on the whirling stability of rotor bearing systems modeled as a continuous elastic rotating shaft mounted on two dissimilar 8-coefficient bearings. Presentation of a closed-form (series) stability criterion for N terms included in the series expansions provides a systematic method for investigating the effects of modal series truncation on the accuracy of the stability boundaries. Thus, truncation error, which has been pointed out by several authors to be an open question in a variety of applications, can be analytically studied in mathematically similar problems by the techniques demonstrated in this paper. The results of this paper show that stability predictions obtained from a severely truncated series expansion can be very accurate. Realizing that the rotor-bearing system discussed in this paper is a very complex system, it is noteworthy that the fundamental term provides such a close approximation to the exact stability boundaries.

The stability boundaries drawn in terms of the bearing cross-coupling parameters β and γ show that the instability regions grow as the values of these parameters increase. It has also been shown that the instability regions grow with the decrease of the shaft stiffness parameter α, increasing dramatically as α approaches its critical value of unity. The stability criteria have been shown to reduce to the special cases of (a) an elastic rotor on rigid bearings as k_{yy} and k_{zz} tend to infinity, (b) isotropic bearings as $k_{yy} = k_{zz} = k_b$ and $\beta = 0$, and (c) a rigid rotor on elastic bearings as α tends to infinity.

All possible values of bearing damping coefficients which result in asymptotically stable motion have been shown to be located inside a stability surface in the shape of a parabolic hyperboloid. Several graphs demonstrating parametrically the influence of the shaft's stiffness and the bearings' direct and cross-coupled stiffness and damping coefficients on critical speeds are presented. These graphs are typical examples of the types of design information available to engineers through the equations provided in this paper.

References

Adams, M. L., 1980, "Nonlinear Dynamics of Flexible Multibearing Rotors," *J. Sound and Vib.*, Vol. 71, pp. 129–144.

Adams, M. L., and Padovan, J., 1981, "Insights into Linearized Rotor Dynamics," *J. Sound and Vib.*, Vol. 76, pp. 129–142.

Adams, M. L., 1983, "A Note on Rotor-Bearing Stability," *J. Sound Vib.*, Vol. 86, pp. 435–438.

Chivens, D. R., and Nelson, H. D., 1975, "The Natural Frequencies and Critical Speeds of a Rotating Flexible Shaft-disk System," *ASME Journal of Engineering for Industry*, Vol. 97, pp. 881–885.

Doyle, R. E., 1971, "A Generalized Matrix Solution for Elliptic Whirling of

Elastic Rotors," Ph.D. Thesis, Dept. of Engineering Mechanics, University of Wisconsin, Madison, WI.

El-Marhomy, A. M., 1987, "Dynamic Stability of Elastic Rotor-bearing Systems via Liapunov's Direct Method," Ph.D. Thesis, Dept. of Engineering Mechanics, University of Wisconsin, Madison, WI.

Grobov, A. A., and Kantemir, I. I., 1978, "Stability of the Steady Motions of a Free Solid Body with a Rotor Mounted on an Elastic Shaft," *Prikladnaia Mekhanika*, Vol. 14, pp. 85–93.

Gunter, G. J., Jr., 1966, "Dynamic Stability of Rotor-Bearing Systems," NASA SP-113.

Klompas, N., 1974, "Theory of Rotor Dynamics with Coupling of Disk and Blade Flexibility and Support Structure Asymmetry," ASME Paper No. 74-GT-159, ASME Gas Turbine Conf., Zurich, Mar.

Kuo, P. S., 1975, "Finite Element Approach to the Vibration Analysis of Elastic Disks on a Flexible Shaft," ASME Paper 75-G7-57.

Masoom, A. K. M., 1980, "Effect of Disk Flexibility on the Whirling Frequencies of a Shaft-disc System," M.Sc. Thesis, Carlton Univ., Ontario, Canada.

Meirovitch, L., 1970, *Methods of Analytical Dynamics*, McGraw-Hill, New York.

Moore, L. S., 1972, "The Significance of Anisotropy of Support Conditions with Balancing Very Large Flexible Rotors," *The Inst. of Mech. Engr. Conf. on Vib. in Rotating Systems*, London, pp. 86–95.

Nelson, H. D., and McVaugh, J. M., 1976, "The Dynamics of Rotor-Bearing Systems Using Finite Elements," *ASME Journal of Engineering for Industry*, Vol. 98, pp. 593–600.

Parkinson, A. G., 1965, "The Vibration and Balancing of Shafts Rotating in Asymmetric Bearings," *J. Sound Vib.*, Vol. 2, p. 477.

Rao, J. S., 1985, "Instability of Rotors in Fluid Film Bearings with a Negative Cross-Coupled Stiffness Coefficient," *Mechanism and Machine Theory*, Vol. 20, pp. 181–187.

Rao, J. S., 1983, *Rotor Dynamics*, Halsted Press, New York.

Stanway, R., and Burrows, C. R., 1981, "Active Vibration Control of a Flexible Rotor on Flexibly-mounted Journal Bearings," ASME *Journal of Dynamic Systems, Measurement and Control*, Vol. 103, pp. 383–388.

Wilgen, F. J., and Schlack, A. L., Jr., 1977, "Effect of Radial Appendage Flexibility on Shaft Whirl Stability," *AIAA Journal*, Vol. 15, pp. 1531–1533.

Wilgen, F. J., and Schlack, A. L., Jr., 1979, "Effect of Disk Flexibility on Shaft Whirl Stability," *ASME Journal of Mechanical Design*, Vol. 101, pp. 298–303.

Vertical Autorotation of a Single-Winged Samara

A. Rosen

D. Seter

Faculty of Aerospace Engineering,
Technion-Israel Institute of Technology,
Haifa 32000, Israel

A derivation of a theoretical model for the vertical autorotation of a samara wing is presented. The dynamic effects are treated in an accurate manner. The aerodynamic effects are calculated by using the blade element/momentum theory. Because of basic differences between the mode of operation of a samara wing and other rotary wings, the model differs from existing rotary wing models. An experimental setup, aimed at verifying the theoretical model, is also described. Comparison between theoretical and experimental results are presented.

1 Introduction

Autorotation is a well-known aerodynamic/dynamic phenomenon that refers to a rotational motion of a body due to aerodynamic loads acting on it. This phenomenon can be divided into different groups, as explained in a survey by Lugt (1983).

One of the most interesting kinds of autorotation involves a single wing with a concentrate mass at its root that spins while descending. This phenomenon is very common in nature and this wing is usually referred to as samara. The functional significance of the samara is to reduce the falling speed of the seed, thus increasing the distance it may be transported by horizontal winds. From the way the samara functions, it is obvious that its occurrence is restricted to tall plants where some height can be spent on a rapid initial fall before entering autorotation. In Fig. 1 a samara in vertical descent is shown. Usually the motion is comprised of a vertical descent (no horizontal wind) and a spin about a vertical axis. Certain samara, as they spin about the vertical axis, also roll about their longitudinal axis, a few times each revolution.

As early as 1808, the samara of the Sycamore had been the object of a close study by the founding father of aeronautics, Sir George Cayley. An entry from his notebook is quoted by Ward-Smith (1984).

Most of the research on the samara was reported by botanists, who were usually interested in the dispersal characteristics and flight path of different samaras, as a function of their morphological details. A representative work of this kind is McCutchen (1973). The author presented an experimental comparison between samaras that roll about their longitudinal axis, and those that don't. He concluded that those that roll about their longitudinal axis descent faster, but they are very stable. A theoretical analysis was not presented in this study.

Another similar study was presented by Green (1980). He photographed over 200 samaras from seven species of trees. The data that were gathered included: rate of descent, angular velocity, orientation, and other parameters. These data were then used to compare the aerodynamic behavior of samaras, helicopters, and theoretically ideal rotors. The rate of descent showed high correlation with the square root of the samara's wing loading. Again, the difference between the samaras that roll about their longitudinal axis, and those that don't, was presented.

A thorough detailed investigation was presented by Norberg (1973). The author presented a simplified approximate aerodynamic analysis of the samara motion, based on the momentum theory. His analysis included vertical descent and descent with side slip. Qualitative discussion of the stability of the autorotation was also presented, as well as the problem of the entrance into autorotation. Norberg also presented new experimental results for two kinds of samara, and some theoretical calculations for these specimens.

Burrows (1975) and Ward-Smith (1984) presented surveys on the subject of airborne dispersal of fruits and seeds. Among different flight techniques, they mentioned the autorotation

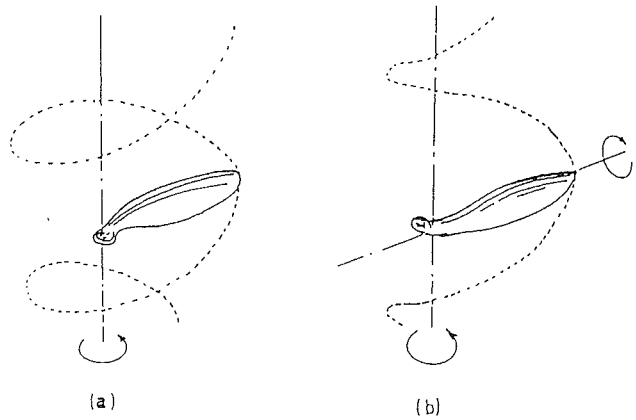

Fig. 1 A samara in vertical descent; (*a*) without roll about the longitudinal axis, (*b*) with roll about the longitudinal axis

Contributed by the Applied Mechanics Division of THE AMERICAN SOCIETY OF MECHANICAL ENGINEERS for presentation at the Joint Applied Mechanics/Bioengineering Conference, Ohio State University, Columbus, Ohio, June 16–19, 1991.

Discussion on this paper should be addressed to the Technical Editor, Prof. Leon M. Keer, The Technological Institute, Northwestern University, Evanston, IL 60208, and will be accepted until two months after final publication of the paper itself in the JOURNAL OF APPLIED MECHANICS. Manuscript received by the ASME Applied Mechanics Division, Jan. 4, 1990; final revision, Oct. 16, 1990.

Paper No. 91-APM-32.

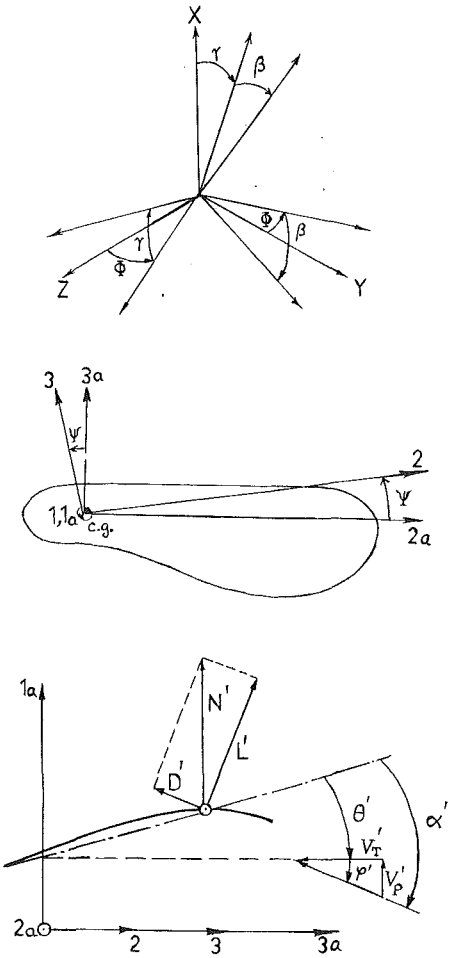

Fig. 2 The systems of coordinates and the flow description at the cross-section

of the samara as one of the more efficient. The theoretical background in these surveys was very limited and mainly qualitative.

Autorotation has been successfully used in different engineering devices. Analysis of the steady-state characteristics of a samara wing decelerator was presented by Crimi (1988). The decelerator was different from the common samara geometry in two main aspects: It had a relatively large center body, and the wing was flexible, depending on centrifugal forces for rigidity. Thus, basic flight mechanics of this device seem to differ from the "classical" samara. The system was modeled with 11 degrees-of-freedom. The inertia and aerodynamic contributions were treated in detail. Numerical results were in good agreement with test data for different configurations.

The purpose of the present paper is to present a derivation of a theoretical model that describes the vertical descent of a "classical" samara wing, namely: a single flat, rigid wing with a concentrate mass at its root. The model will not include spin about the spanwise axis. The derivation will deal in detail with the inertial and aerodynamic contributions. The method of solution will also be discussed. Then an experimental program for testing samara wing models in vertical descent will be described. Comparisons between theoretical and experimental results will be presented.

2 The Equations of Motion

In order to describe the wing motion, two coordinate systems are defined. The X, Y, Z system is fixed with respect to the earth, and for the present purposes is considered an inertial system. X is pointing upward in the negative gravity direction. $\hat{e}_x$, $\hat{e}_y$, $\hat{e}_z$ are unit vectors in the X, Y, and Z directions, respectively. The system (1, 2, 3) is attached to the wing, with the origin at the wing's center of mass. Since the mass is concentrated at the root, the origin always lies in the root region. $\hat{e}_1$, $\hat{e}_2$, and $\hat{e}_3$ are unit vectors in 1, 2 and 3 directions, respectively.

The transformation from the inertial system directions to those of the body system is described by three Euler angles (see Fig. 2). The order of rotation is as follows: a rotation Φ about the X-axis, followed by a "pitch" rotation, γ, about the new y-axis, followed by a conning rotation, β, about the 3-axis. All the rotations are carried out according to the right-hand law. It should be noted that a positive β, according to the present notation, refers to a negative conning in the common literature.

The transformation matrix will be:

$$\begin{Bmatrix}\hat{e}_x\\ \hat{e}_y\\ \hat{e}_z\end{Bmatrix} = \begin{pmatrix} \cos\gamma\cos\beta & -\cos\gamma\sin\beta & \sin\gamma \\ [\cos\Phi\sin\beta + & [\cos\Phi\cos\beta - & \\ \sin\Phi\sin\gamma\cos\beta] & \sin\Phi\sin\gamma\sin\beta] & -\sin\Phi\cos\gamma \\ [\sin\Phi\sin\beta - & [\sin\Phi\cos\beta + & \\ \cos\Phi\sin\gamma\cos\beta] & \cos\Phi\sin\gamma\sin\beta] & \cos\Phi\cos\gamma \end{pmatrix} \cdot \begin{Bmatrix}\hat{e}_1\\ \hat{e}_2\\ \hat{e}_3\end{Bmatrix} \cdot \quad (1)$$

For the sake of convenience, the 1, 2, 3 system will be chosen so that it coincides with the principal axes of inertia. Thus, the only nonzero components of the inertia tensor are: I_{11}, I_{22}, and I_{33}.

The absolute velocity of the center of mass of the wing, $\mathbf{U}$, is described by its components in the body coordinates directions:

$$\mathbf{U} = u_1\,\hat{e}_1 + u_2\hat{e}_2 + u_3\hat{e}_3. \quad (2)$$

It can be shown that the angular velocity of the wing, λ, is:

$$\lambda = \lambda_1\hat{e}_1 + \lambda_2\hat{e}_2 + \lambda_3\hat{e}_3 \quad (3a)$$

$$\begin{Bmatrix}\lambda_1\\ \lambda_2\\ \lambda_3\end{Bmatrix} = \begin{pmatrix} \cos\gamma\cos\beta & \sin\beta & 0 \\ -\cos\gamma\sin\beta & \cos\beta & 0 \\ \sin\gamma & 0 & 1 \end{pmatrix} \begin{Bmatrix}\dot{\Phi}\\ \dot{\gamma}\\ \dot{\beta}\end{Bmatrix} \quad (3b)$$

The external loads acting on the wing include the weight and aerodynamic loads.The aerodynamic loads include a force $\mathbf{F}_A$ and a moment $\mathbf{T}_A$ about the center of mass.

$$\mathbf{F}_A = F_{1A}\hat{e}_1 + F_{2A}\hat{e}_2 + F_{3A}\hat{e}_3 \quad (4a)$$

$$\mathbf{T}_A = T_{1A}\hat{e}_1 + T_{2A}\hat{e}_2 + T_{3A}\hat{e}_3 \quad (4b)$$

By applying standard techniques, the six equations of motion become:

$$m[\dot{u}_1 + u_3\,(\cos\beta\dot{\gamma} - \dot{\Phi}\cos\gamma\sin\beta) - (\dot{\Phi}\sin\gamma + \dot{\beta})u_2] = F_{1A} - mg\cos\beta\cos\gamma \quad (5a)$$

$$m[\dot{u}_2 + u_1\,(\dot{\Phi}\sin\gamma + \dot{\beta}) - u_3\,(\dot{\Phi}\cos\gamma\cos\beta + \sin\beta\dot{\gamma})] = F_{2A} + mg\cos\gamma\sin\beta \quad (5b)$$

$$m[\dot{u}_3 + u_2\,(\dot{\Phi}\cos\gamma\cos\beta + \sin\beta\dot{\gamma}) - u_1\,(\cos\beta\dot{\gamma} - \dot{\Phi}\cos\gamma\sin\beta)] = F_{3A} - mg\sin\gamma \quad (5c)$$

$$I_{11}\,[\ddot{\Phi}\cos\gamma\cos\beta - \dot{\Phi}\,(\sin\gamma\cos\beta\dot{\gamma} + \cos\gamma\sin\beta\dot{\beta}) + \ddot{\gamma}\sin\beta + \dot{\gamma}\cos\beta\dot{\beta}] + (I_{33} - I_{22})\,(\dot{\beta} + \sin\gamma\dot{\Phi})\,(\cos\beta\dot{\gamma} - \cos\gamma\sin\beta\dot{\Phi}) = T_{1A} \quad (5d)$$

$$I_{22}\,[\ddot{\gamma}\cos\beta - \ddot{\Phi}\cos\gamma\sin\beta + \dot{\Phi}\,(\sin\gamma\sin\beta\dot{\gamma} - \cos\gamma\cos\beta\dot{\beta}) - \dot{\gamma}\,\dot{\beta}\sin\beta] + (I_{11} - I_{33})\,(\cos\gamma\cos\beta\dot{\Phi} + \sin\beta\dot{\gamma})\,(\sin\gamma\dot{\Phi} + \dot{\beta}) = T_{2A} \quad (5e)$$

$$I_{33}\,[\ddot{\Phi}\sin\gamma + \dot{\Phi}\cos\gamma\dot{\gamma} + \ddot{\beta}] + (I_{22} - I_{11})\,(\cos\gamma\cos\beta\dot{\Phi} + \sin\beta\dot{\gamma}) \times (\cos\beta\dot{\gamma} - \cos\gamma\sin\beta\dot{\Phi}) = T_{3A}. \quad (5f)$$

m is the mass of the wing, g is the gravity acceleration, and the upper dot indicates differentiation with respect to time.

3 Aerodynamic Contributions

3.1 Blade Element Theory. The aerodynamic contributions will be calculated using the aerodynamic system of coordinates $1a$, $2a$, $3a$. The axes $2a$ and $3a$ form the reference aerodynamic plane. While the axis $2a$ defines the spanwise direction, the axes $1a$ and $3a$ define the wing's cross-sections. The origin of the aerodynamic system coincides with the origin of the body system (see Fig. 2). Since the derivation will be confined to relatively flat wings, the aerodynamic system is chosen in such a manner that the axes 1 and $1a$ coincide. If $\hat{e}_{1a}$, $\hat{e}_{2a}$, and $\hat{e}_{3a}$ are unit vectors in the directions of the aerodynamic coordinates, then:

$$\begin{Bmatrix} \hat{e}_1 \\ \hat{e}_2 \\ \hat{e}_3 \end{Bmatrix} = \begin{pmatrix} 1 & 0 & 0 \\ 0 & \cos\Psi & \sin\Psi \\ 0 & -\sin\Psi & \cos\Psi \end{pmatrix} \begin{Bmatrix} \hat{e}_{1a} \\ \hat{e}_{2a} \\ \hat{e}_{3a} \end{Bmatrix}. \tag{6}$$

The aerodynamic loads will be calculated by using the blade element/momentum theory (see Glauert, 1943), which is very useful in dealing with rotary wings. According to this method the cross-sections of the wing can be looked upon as a cross-section in a two-dimensional flow. The correction for the fact that the phenomenon is three-dimensional is achieved by introducing the induced flow, which is calculated based on momentum considerations. As will be shown later, the aerodynamic analysis in the case of a samara wing is more complicated than the usual application of the blade element/momentum theory to helicopter rotors or propellers. One of the main reasons is the fact that many aerodynamic angles, which are small in most of the practical cases of rotary wings, are not small in this case. Thus, it is not possible to apply the small angles assumption which may simplify the analysis significantly. Because of these differences the expressions that have been used in different previous analyses cannot be used here, and therefore the detailed new expressions will be presented in what follows.

A cross-section of the wing is shown in Fig.2. The cross-sectional resultant force per unit length is N'. The notation $(\,)'$ indicates parameters associated with a certain cross-section. N' is assumed to act at the quarter chord point of the cross-section, which also will be considered as the representative aerodynamic point of the cross-section. The position vector of this representative point is:

$$\mathbf{r}_{c/4} = r_{1a}\hat{e}_{1a} + r_{2a}\hat{e}_{2a} + r_{3a}\hat{e}_{3a}. \tag{7}$$

r_{2a} defines the specific cross-section. r_{1a} and r_{3a} depend on the wing's geometry and as such they are in general functions of r_{2a}.

The relative velocity between the wing and the air, as seen by an observer on the wing, is described by its components in the directions of the aerodynamic system. According to the assumptions of the blade element theory, the spanwise component does not have any influence on the aerodynamic loads (see a correction later). The resultant incoming velocity in the cross-section is V', where V'_T and V'_p are its tangential and perpendicular components, respectively. From Fig. 2 it is clear that:

$$V' = \sqrt{V'^2_p + V'^2_T} \tag{8a}$$

$$\varphi' = \tan^{-1}(V'_p/V'_T) \tag{8b}$$

where φ' is usually referred to as the local inflow angle. θ' is the local pitch angle of the wing. In the case of a flat wing, $\theta' = 0$. The cross-sectional effective angle of attack, α', is defined as the angle between the zero lift line of the profile and the cross-sectional incoming flow. From Fig. 2 it is clear that:

$$\alpha' = \theta' + \varphi'. \tag{9}$$

The aerodynamic loads include a lift L' and a drag D' per unit length, and in addition an aerodynamic moment M'_{2a} (per unit length) about the quarter chord point (positive when it tends to increase the angle of attack). These loads are described in the following usual manner:

$$L' = \frac{1}{2}\rho V'^2\, C'_L C' \tag{10a}$$

$$D' = \frac{1}{2}\rho V'^2\, C'_D C' \tag{10b}$$

$$M'_{2a} = \frac{1}{2}\rho V'^2\, C'_m C'^2. \tag{10c}$$

ρ is the air mass density, C' is the local chord, and C'_L, C'_D, C'_m are the lift, drag, and moment coefficients. The last three coefficients are functions of the cross-sectional angle of attack, Reynolds number, and Mach number. In the present investigation the velocities are relatively small and therefore an incompressible flow is assumed.

Based on the above equations, the resultant aerodynamic force and moment, acting on the wing, are obtained after an integration over the wing:

$$F_{1A} = \frac{1}{2}\rho \int_l V'^2 C'\,(C'_L\cos\varphi' + C'_D\sin\varphi')dr_{2a} \tag{11a}$$

$$F_{2A} = \frac{1}{2}\rho \left\{ \int_l V'^2 C'\,(C'_L\sin\varphi' - C'_D\cos\varphi')dr_{2a} \right\} \sin\Psi \tag{11b}$$

$$F_{3A} = \frac{1}{2}\rho \left\{ \int_l V'^2 C'\,(C'_L\sin\varphi' - C'_D\cos\varphi')dr_{2a} \right\} \cos\Psi \tag{11c}$$

$$T_{1A} = \frac{1}{2}\rho \int_l V'^2 C'\,(C'_L\sin\varphi' - C'_D\cos\varphi')(r_{2a}dr_{2a} \tag{11d}$$

$$T_{2A} = \frac{1}{2}\rho \int_l V'^2 C'\,(C'_L\cos\varphi' + C'_D\sin\varphi')r_{3a}\cos\Psi - r_{2a}\sin\Psi)dr_{2a} + \frac{1}{2}\rho \left\{ \int_l V'^2 C'^2 C'_m dr_{2a} \right\} \cos\Psi \tag{11e}$$

$$T_{3A} = -\frac{1}{2}\rho \int_l V'^2 C'\,(C'_L\cos\varphi' + C'_D\sin\varphi')(r_{3a}\sin\Psi + r_{2a}\cos\Psi)dr_{2a} - \frac{1}{2}\rho \left\{ \int_l V'^2 C'^2 C'_m dr_{2a} \right\} \sin\Psi. \tag{11f}$$

dr_{2a} is a length element in the r_{2a}-direction. The integral sign $\int_l$ indicates integration along the wing. The specific limits of the integration will be discussed later.

In equation (11*e*) a term $(C'_L\sin\varphi' - C'_D\cos\varphi')r_{1a}$ has been neglected compared to $(C'_L\cos\varphi' + C'_D\sin\varphi')r_{3a}$. This is justified since the present derivation deals with flat wings, where $r_{3a} \gg r_{1a}$ and usually $(C'_L\cos\varphi' + C'_D\sin\varphi') \gg (C'_L\sin\varphi' - C'_D\cos\varphi')$.

In order to calculate the loads it is necessary to know the components V'_p and V'_T of the cross-sectional incoming flow. These components are the result of two main contributions:

(*a*) the "dynamic component" due to the sinking speed and rotation of the wing and

(*b*) the induced velocity due to the interaction between the wing and the surrounding fluid.

In the next two subsections these two contributions will be presented in detail.

3.2 The "Dynamic Component" of the Cross-Sectional Incoming Flow. The absolute velocity of the representative quarter chord point of the cross-section is $\mathbf{V}'_D$:

$$\mathbf{V}'_D = \mathbf{U} + \boldsymbol{\lambda} \times \mathbf{r}_{c/4}. \tag{12}$$

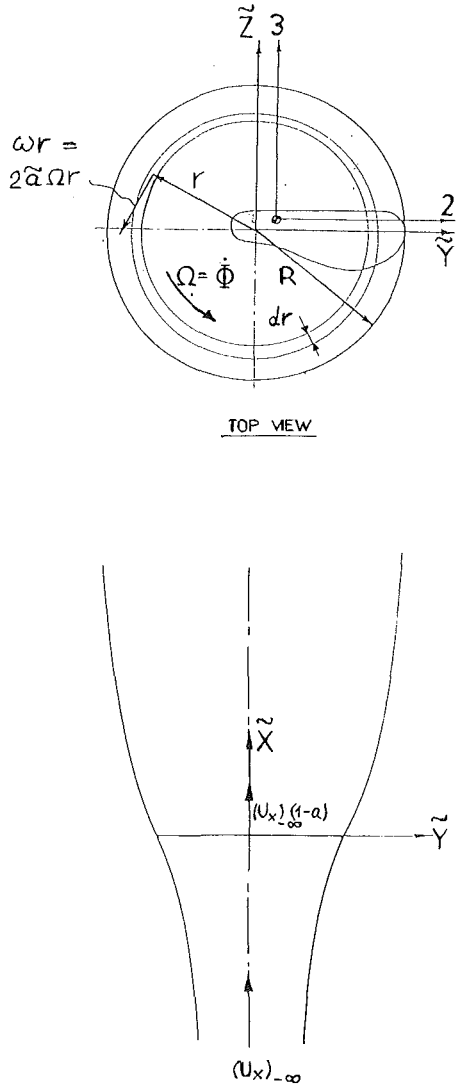

Fig. 3 The actuator disk and induced velocities

Substitution of equations (2), (3*a*), (3*b*), and (7) into the last equation, and using equation (6), result in:

$$\mathbf{V}'_D = V'_{D1a}\,\hat{e}_{1a} + V'_{D2a}\hat{e}_{2a} + V'_{D3a}\hat{e}_{3a} \tag{13}$$

where:

$$V'_{D1a} = [u_1 + (\dot{\gamma}\cos\beta - \dot{\Phi}\cos\gamma\sin\beta)r_3 - (\dot{\Phi}\sin\gamma + \dot{\beta})r_2] \tag{14a}$$

$$V'_{D2a} = [u_2 + (\dot{\Phi}\sin\gamma + \dot{\beta})r_1 - (\dot{\Phi}\cos\gamma\cos\beta + \dot{\gamma}\sin\beta)r_3]\cos\Psi - [u_3 + (\dot{\Phi}\cos\gamma\cos\beta + \dot{\gamma}\sin\beta)r_2 - (\dot{\gamma}\cos\beta - \dot{\Phi}\cos\gamma\sin\beta)r_1]\sin\Psi \tag{14b}$$

$$V'_{D3a} = [u_3 + (\dot{\Phi}\cos\gamma\cos\beta + \dot{\gamma}\sin\beta)r_2 + (\dot{\Phi}\cos\gamma\sin\beta - \dot{\gamma}\cos\beta)r_1]\cos\Psi + [u_2 + (\dot{\Phi}\sin\gamma + \dot{\beta})r_1 - (\dot{\Phi}\cos\gamma\cos\beta + \dot{\gamma}\sin\beta)r_3]\sin\Psi. \tag{14c}$$

For the aerodynamic calculations the incoming velocity, as seen by an observer on the wing, U'_D, is used (see Fig. 2)

$$\mathbf{U}'_D = -\mathbf{V}'_D = -V'_{D1a}\hat{e}_{1a} - V'_{D2a}\hat{e}_{2a} - V'_{D3a}\hat{e}_{3a}. \tag{15}$$

3.3 The Induced Velocity. The general momentum theory is applied in order to calculate the induced velocity. According to this theory the rotary wing is replaced by a disk. The radius of this disk is equal to the radius of rotation of the rotor tip. The details of the theory may be found in Glauert (1943). Here only the main equations, which are necessary for the completeness of the paper, are presented.

The induced flow through the disk is axisymmetric, namely, the induced velocities are functions of the radial distance, r, from the disk center. If the sinking velocity of the disk is $(U_x)_{-\infty}$, then the axial velocity through the disk will be $(U_x)_{-\infty}(1-a)$ (see Fig. 3), where a is the axial induced-velocity coefficient. As indicated above, "a" is in general a function of r. The fluid under the disk does not have any tangential (circumferential) velocity. After passing through the disk and applying an aerodynamic torque on the wing, the fluid in return (according to Newton's third law) develops a rotation in the opposite direction. It is convenient to express this component as ωr (see Fig. 3), where ω is the "angular velocity" of the fluid. It is further convenient to describe ω itself as:

$$\omega = 2\tilde{a}\Omega. \tag{16}$$

Ω is the angular velocity of the wing (see the positive direction in Fig. 3), while $\tilde{a}$ is the tangential induced-velocity coefficient which is in general a function of r.

According to the momentum theory, an annular element of the disk will be considered (see Fig. 3). This element has a radius r and a thickness dr. Expressions for the vertical force dT, that is applied on the annular element by the fluid passing through it, are obtained by applying conservation laws of: axial momentum, angular momentum, and energy. According to the general momentum theory of Glauert (1943):

$$dT = 4\pi\rho(U_x)_{-\infty}^2(1-a)aFrdr \tag{17}$$

$$dT = 4\pi\rho\Omega^2\tilde{a}(1+\tilde{a})Fr^3dr. \tag{18}$$

F is a tip (effect) factor that accounts for the fact that there is a finite number of blades and not really a disk. According to Prandtle (see Glauert, 1943, p. 263), for the case of a single blade:

$$F = (2/\pi)\cos^{-1}(e^{-f}) \tag{19a}$$

$$f = (\sqrt{1+\mu^2}/2\mu)(1-r/R) \tag{19b}$$

$$\mu = (U_x)_{-\infty}(1-a)/(\Omega R). \tag{19c}$$

If can be seen that, as expected, the aerodynamic load drops to zero toward the tip.

By comparing equations (17) and (18), the following relation between the axial and tangential induced velocities is obtained:

$$(U_x)^2_{-\infty}(1-a)a = \Omega^2r^2(1+\tilde{a})\tilde{a}. \tag{20}$$

If we consider equations (17) and (20), we have three unknowns (dT, a, $\tilde{a}$). Thus, in order to solve for the induced velocity, a third equation is required. This equation is the axial force dT, as obtained by using the blade element calculations. Since the blade element calculations in Subsection 3.1 were carried out using the aerodynamic system of coordinates, in order to be able to work with these three equations it is necessary to write the momentum relations (equations (17) and (20)) using the aerodynamic coordinates. Namely: $(U_x)_{-\infty}$, Ω, r, dr, and consequently dT, should be expressed as functions of (r_{1a}, r_{2a}, r_{3a}). In order to do that a new rotating system of coordinates is defined: $\tilde{X}$, $\tilde{Y}$, $\tilde{Z}$. $\tilde{X}$ is parallel to X and is the axis of rotation of the wing. The system $\tilde{X}$, $\tilde{Y}$, $\tilde{Z}$ rotates about $\tilde{X}$ with the same angular velocity as the wing itself, Ω, where:

$$\Omega = \dot{\Phi}. \tag{21}$$

The rate of descent of the wing, $(U_x)_{-\infty}$, is the component of $\mathbf{U}$ (equation (2)) in the $(-\hat{e}_x)$ direction. After using equation (1), the following expression is obtained:

$$(U_x)_{-\infty} = -u_1\cos\gamma\cos\beta + u_2\cos\gamma\sin\beta - u_3\sin\gamma. \tag{22}$$

In the case of helicopter or propeller blades, where γ and β

are small angles and u_2 and u_3 (in axial flight) are negligible compared to u_1, $(u_x)_{-\infty}$ is approximately equal to $-u_1$. In the present case such an assumption may lead to increasing errors. Thus, equation (22) should be used in spite of the nonlinearities it introduces.

Since the system $\tilde{X}$, $\tilde{Y}$, $\tilde{Z}$, rotates at the same rate as the wing, it is clear that the orientation of the wing system (1, 2, 3), relative to $\tilde{X}$, $\tilde{Y}$, $\tilde{Z}$, is not changing with time (in the present case of "steady" vertical descent). Without losing any generality, we may choose, $\tilde{X}$, $\tilde{Y}$, $\tilde{Z}$ in such a manner that the azimuth angle of the axes $\tilde{Y}$ and $\tilde{Z}$, relative to the axes Y and Z, respectively, is equal to Φ. It can be shown that in this case r, which is the radial distance from the axis $\tilde{X}$ to a point r_{2a} along the wing axis, is given by (see Fig. 3):

$$r=(r_{\tilde{y}}^2+r_{\tilde{z}}^2)^{1/2} \tag{23a}$$

$$r_{\tilde{Y}}=\tilde{Y}_m+r_{2a}\cos\beta\cos\Psi \tag{23b}$$

$$r_{\tilde{z}}=\tilde{Z}_m+r_{2a}(\sin\gamma\sin\beta\cos\Psi-\cos\gamma\sin\Psi) \tag{23c}$$

$\tilde{Y}_m$ and $\tilde{Z}_m$ are the $\tilde{Y}$ and $\tilde{Z}$ coordinates, respectively, of the center of mass of the wing, and are given by:

$$\tilde{Y}_m=[-u_1\sin\gamma\cos\beta+u_2\sin\gamma\sin\beta+u_3\cos\gamma]/\dot{\Phi} \tag{24a}$$

$$\tilde{Z}_m=-(u_1\sin\beta+u_2\cos\beta)/\dot{\Phi}. \tag{24b}$$

By differentiating equation (23*a*) and using equations (23*b*), (23*c*), we obtain:

$$\frac{dr}{dr_{2a}}=\frac{1}{r}[r_{\tilde{y}}\cos\beta\cos\Psi+r_{\tilde{z}}(\sin\gamma\sin\beta\cos\Psi-\cos\gamma\sin\Psi)]. \tag{25}$$

If Ω, $(U_x)_{-\infty}$, r, and dr in equations (17) and (20) are replaced by equations (21), (22), (23), and (25), then two equations with respect to the aerodynamic system (1_a, 2_a, 3_a) are obtained. As already mentioned above, the third equation will be the expression for dT according to the blade element theory (see Subsection 3.1). Based on the definitions of Section 2, it can be shown that:

$$dT=[(L'\cos\varphi'+D'\sin\varphi')\cos\gamma\cos\beta+(L'\sin\varphi'-D'\cos\varphi')(\sin\gamma\cos\Psi-\cos\gamma\sin\beta\sin\Psi)]dr_{2a}. \tag{26}$$

From the three equations, dT, a, and $\tilde{a}$ can be calculated.

The induced velocity is given relative to the system $\tilde{X}$, $\tilde{Y}$, $\tilde{Z}$. If $\hat{e}_{\tilde{x}}$, $\hat{e}_{\tilde{y}}$ and $\hat{e}_{\tilde{z}}$ are unit vectors in these coordinates directions, respectively, then the vector of induced velocity, $\mathbf{v}$, will be:

$$\mathbf{v}=(u_{\tilde{x}})a\hat{e}_{\tilde{x}}+\Omega\tilde{a}(r_{\tilde{z}}\hat{e}_{\tilde{y}}-r_{\tilde{y}}\hat{e}_{\tilde{z}}). \tag{27}$$

For the aerodynamic calculations the induced velocity should be expressed relative to the aerodynamic system of coordinates. Using the transformations between the different systems of coordinates, we obtain:

$$\mathbf{v}'=v_{1a}'\hat{e}_{1a}+v_{2a}'\hat{e}_{2a}+v_{3a}'\hat{e}_{3a} \tag{28}$$

where:

$$v_{1a}'=-(U_x)_{-\infty}a\cos\gamma\cos\beta+\underline{\Omega\tilde{a}(r_{\tilde{z}}\sin\beta+r_{\tilde{y}}\sin\gamma\cos\beta)} \tag{29a}$$

$$v_{2a}'=(U_x)_{-\infty}a(\cos\gamma\sin\beta\cos\Psi+\sin\gamma\sin\Psi)+\Omega\tilde{a}[r_{\tilde{z}}\cos\beta\cos\Psi-r_{\tilde{y}}(\sin\gamma\sin\beta\cos\Psi-\cos\gamma\sin\Psi)] \tag{29b}$$

$$v_{3a}'=\underline{(U_x)_{-\infty}a(\cos\gamma\sin\beta\sin\Psi-\sin\gamma\cos\Psi)}+\Omega\tilde{a}[r_{\tilde{z}}\cos\beta\sin\Psi-r_{\tilde{y}}(\sin\gamma\sin\beta\sin\Psi+\cos\gamma\cos\Psi)]. \tag{29c}$$

The small underlined terms in the last equations, which present the influence of the axial and tangential components of the induced velocity, on the tangential and axial cross-sectional components of the incoming flow, respectively, are negligible in most of the rotary wing applications. Yet, these terms will be retained in the present derivation since, as already mentioned above, the angles β and γ are much larger in the present case than in regular rotary wing applications.

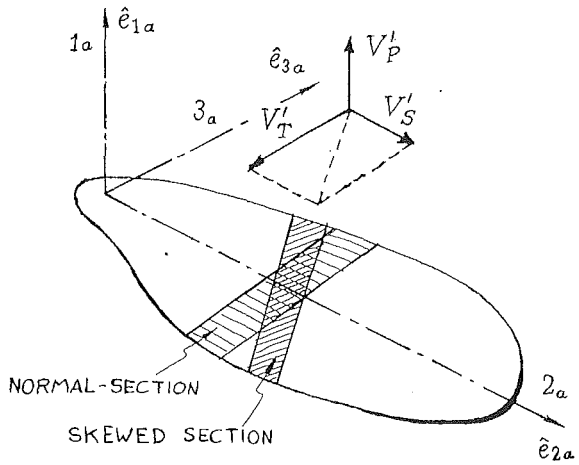

Fig. 4 The influence of the spanwise component of the flow

3.4 The Resultant Incoming Flow. The resultant incoming flow velocity, as seen by an observer on the wing, is $\mathbf{V}'$. This velocity is the sum of the dynamic contribution $\mathbf{U}'_D$ as defined by equation (15), and the induced velocity $\mathbf{v}'$ as defined by equation (28). Thus, we may write (see Fig. 2):

$$\mathbf{V}'=\mathbf{U}_D'+\mathbf{v}'=V_P'\hat{e}_{1a}+V_S'\hat{e}_{2a}-V_T'\hat{e}_{3a} \tag{30}$$

where, according to equations (15) and (28),

$$V_P'=-V_{D1a}'+v_{1a}' \tag{31a}$$

$$V_S'=-V_{D2a}'+v_{2a}' \tag{31b}$$

$$V_T'=V_{D3a}'-v_{3a}'. \tag{31c}$$

The components V_{D1a}', V_{D2a}', V_{D3a}' are given by equations (14*a*)–(14*c*), while v_{1a}, v_{2a}, v_{3a} are given by equations (29*a*)–(29*c*).

3.5 The Effect of the Spanwise Velocity Component. As indicated above, the spanwise component of the incoming velocity does not have any influence within the context of the classical blade element theory. Yet, due to the presence of a relatively large conning angle (much larger than in most other rotary wings applications), the spanwise component in the present case is more significant. Thus, it has been decided to include a correction for this effect. This correction is based on replacing the classical cross-section of the wing (see Fig. 2), which is perpendicular to the wing axis, by a skewed cross-section, as shown in Fig. 4. The skewed cross-section lies in the direction of the flow resultant in the plane $2a$–$3a$. Thus, it is clear that the direction of this cross-section is varied along the wing.

A linear two-dimensional aerodynamic analysis shows that the lift that will be obtained based on skewed cross-section calculations will be identical to the lift as obtained by calculations based on the perpendicular cross-section (see Rosen and Rand, 1985). On the other hand, there will be a change in the drag force calculations. If it is assumed that the drag force acts in the resultant velocity direction, then a spanwise drag component will appear. If it is assumed that in the important regions of the wing $V_S'^2 \ll V_T'^2$, then the spanwise component of the aerodynamic force per unit length of the wing can be approximated as:

$$F_S'=\frac{1}{2}\rho V' V_S' C_D' C'. \tag{32}$$

Integration of this force over the wing yields a resultant aerodynamic force in the spanwise direction.

3.6 The Procedure of Calculating the Aerodynamic Loads. When entering the aerodynamic calculations, the val-

ues of u_1, u_2, u_3, β, γ, and Φ are assumed to be known. The aerodynamic calculations can be divided into two main stages: The first stage includes an iterative procedure which is repeated at a few cross-sections along the wing. After this stage is accomplished, the second stage of calculating all the loads along the wing and integrating them to obtain the resultant force and moment components, is carried out.

The first stage includes the following steps:

(*a*) A cross-section r_{2a} is chosen such that $R_o < r_{2a} < R_T$. R_T is the tip radius of the wing. R_o is the root radius and its choice will be discussed in what follows.

(*b*) Initial values of a and $\tilde{a}$ are chosen.

(*c*) Ω, $(U_x)_{-\infty}$, r, $r_{\bar{y}}$, $r_{\bar{z}}$, and dr are calculated as functions of Φ, u_1, u_2, u_3, β, γ, r_{2a}, and dr_{2a}, according to equations (21), (22), (23*a*)–(23*c*), (24*a*)–(24*b*), and (25). F is calculated by using equations (19*a*)–(19*c*).

(*d*) The components V'_{D1a}, V'_{D2a}, and V'_{D3a} are calculated using equations (14*a*)–(14*c*) and the induced-velocity components v'_{1a}, v'_{2a}, v'_{3a} are calculated using equations (29*a*)–(29*c*). Then, the resultant incoming velocity components V'_P, V'_S, and V'_T are calculated according to equations (31*a*)–(31*c*).

(*e*) The cross-sectional resultant velocity V', the inflow angle φ', and the angle of attack α' are calculated using equations (8*a*), (8*b*), and (9), respectively.

(*f*) The lift and drag forces per unit length are calculated using equations (10*a*), (10*b*).

(*g*) The axial force dT is obtained from equation (26).

(*h*) Another expression for the axial force dT is obtained after substituting the expressions for $(U_x)_{-\infty}$, F, r, and dr, as obtained in (*c*), into equation (17).

(*i*) The two expressions for dT (*g*, *h*) and equation (20), are used to solve for a and $\tilde{a}$.

(*j*) The new results for a and $\tilde{a}$ are compared with the values of a and $\tilde{a}$ that were assumed at the beginning of the iteration. If convergence has been achieved, then the cross-sectional iterative procedure is terminated. Otherwise, new values of a and $\tilde{a}$ are assumed and the procedure is repeated again from (*c*).

After convergence is achieved at all the cross-sections, the resultant aerodynamic forces and moments are calculated by using equations (11*a*)–(11*f*). The influence of the spanwise aerodynamic force is added according to equation (32).

4 Solution of the Steady Vertical Descent

4.1 General Scheme. In a steady vertical descent u_1, u_2, u_3, γ, β, and Φ are constant. In this case, equations (5*a*)–(5*f*) are reduced to a system of nonlinear coupled algebraic equations in the above six parameters. For a certain known wing (geometry, mass distribution, and aerodynamic properties are given), the nonlinear system is solved by the Powell algorithm (Moré, Jore, 1980) which is an improved version of Newton's method.

4.2 The Lift and Drag Coefficients. The lift and drag coefficients determine the aerodynamic forces. In the case of samara wings in nature, or the experimental model that will be described in what follows, the determination of the lift and drag coefficients is problematic because of the following three aspects:

(*a*) The cross-sections of samara wings operate at Reynolds numbers in the range $\mathrm{Re} = 10^3 - 10^5$. This range is very low compared to helicopter rotors or propellers. This range is typical to birds or airplane models, and especially insects' wings.

(*b*) As will be shown later, and as indicated by previous researchers, large regions of the samara wing are characterized by relatively high local angles of attack, beyond the stall limit. Such angles of attack are not typical to airplane models, but are common in insects' and birds' flight.

(*c*) The cross-sections of samara are not smooth as typical aeronautical profiles. Instead they are corrugated, have a concentration of ribs at the leading edge, and a rough surface. These characteristics are also typical to the cross-sections of insect and bird wings.

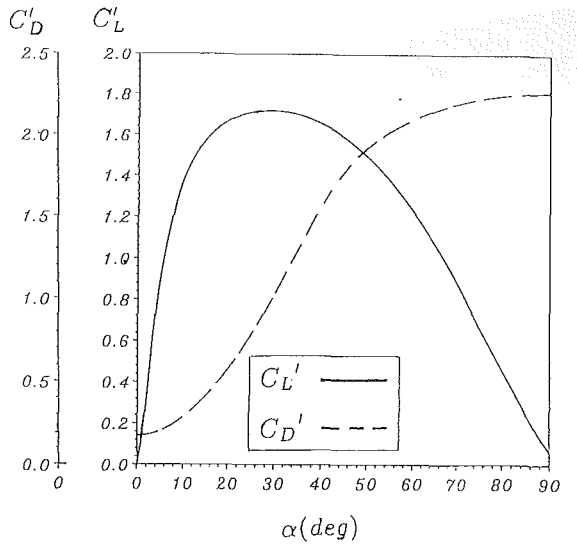

Fig. 5 The lift and drag coefficients as functions of the angles of attack

All the above aspects and examination of the relevant material in the existing literature indicate that probably the best way to determine the lift and drag coefficients in such cases is through direct experiments with the samara wings in carefully controlled wind tunnel tests. Unfortunately, such measurements are fairly complicated, require special instrumentation that was not available, and therefore were beyond the scope of the research. Instead, it was decided to determine the C_L and C_D characteristics based on the data that exist in the literature for insects' and birds' wings.

A detailed literature survey which was described by Seter (1989) led to the C_L and C_D plots which are shown in Fig. 5. Since it was not possible to find a single source that could give the entire spectrum of information, these plots represent an accumulation of information from different sources. Few of these sources include: Nachtigall (1981), Rees (1975), Vogel (1967), and Withers (1981).

It is clear that the inaccuracy associated with the aerodynamic coefficients can be quite large. Therefore, in a sequel to this paper the sensitivity of the solution to changes in the C_L and C_D plots will be presented.

4.3 The Aerodynamic Moment About the Quarter Chord Point. The cross-sections are considered as two-dimensional flat-plates. According to the classical theory, there is no aerodynamic moment about the quarter chord point in this case. Bradford (1954) showed that practically there is an aerodynamic moment about the quarter chord point, which is a function of the local angle of attack. Norberg (1973) considered this effect as the mechanism that stabilizes the wing in pitch. Thus, because of the importance that this effect may have (according to Norberg), its influence on the steady vertical descent will be investigated. The calculations will be based on the data that were presented graphically by Bradford (1954).

4.4 The Root Region. At the root region of the wing the velocities are relatively small, and the angles of attack fairly high. Therefore, in this region the blade element momentum theory is not applicable. Instead, since in this region the flow is approximately normal to the surface, it can be treated as a

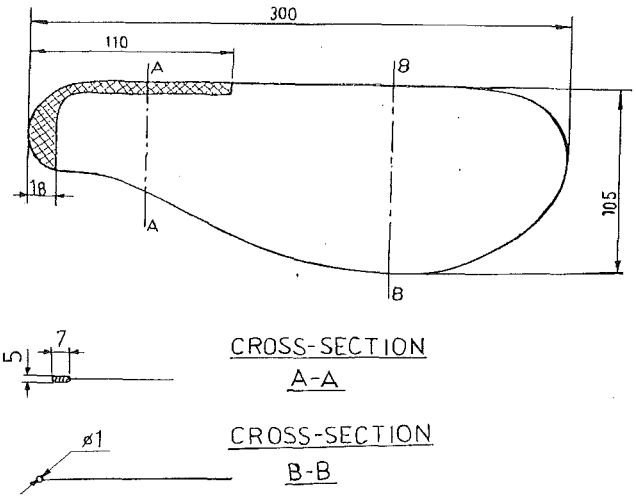

Fig. 6 The experimental model; all dimensions in mm

flat-plate in normal flow. Thus, it is assumed that a drag force D_{root} is acting on this region in the $\tilde{X}$ direction. This force is given by:

$$D_{\text{root}} = \frac{1}{2}\rho U_{\dot{x}}^2 C_{D\text{root}} S_{\text{root}}. \tag{33}$$

S_{root} is the root region area, while $C_{D\text{root}}$ is the drag coefficient of this region, which because of the analogy to a flat-plate in normal flow (two-dimensional) will be taken as $C_{D\text{root}} = 2.25$ (Bradford, 1945).

5 The Experimental Setup

The research included also relatively simple experiments that yielded fairly good results for verification purposes.

The samara models were made up of cardboard. These models were not simple scale-up models of samara wings in nature. Instead, a trial and error procedure led to models that exhibited stable and relatively efficient autorotation. The model that will be used in the paper is shown in Fig. 6. The thickness of the cardboard was 0.35 mm. An aluminum wire of 1-mm diameter was used to strengthen the leading edge of the wing, and the trailing edge at the tip. This wire also simulates the concentration of ribs along the leading edge, that exists in most of the samara wings in nature.

The mass concentration at the root is obtained by placing a plasticine (putty) there (see Fig. 6). This technique is very convenient since it allows quick and simple variations of the mass at the root. The total mass of the model was 17.3 g, where the root mass accounted for 60 percent of the total mass, as compared to a typical 85 percent in samara wings in nature.

The wing was painted black with the root region white. White strips were also painted at: the leading and trailing edges, along the spanwise coordinate on both sides of the wing, and the midchord on one side. All these white strips were helpful in analyzing the photographs of the wing (taken while it sank vertically) and determining the orientation of the wing in space.

A variety of devices were used to photograph the experiments. Polaroid and video cameras were used to obtain immediate pictures and synchronize the instruments. Then, in order to obtain higher quality pictures, a super 8-mm movie camera, and stills camera with a special winder for quick shots, were used.

The experiments were carried out in a closed room in order to avoid any winds. The initial tests indicated that it took the wing between six to ten meters to enter a steady-state autorotation after it was released from rest. This left a relatively short distance to investigate the steady motion. Therefore, it was decided to give the wing an initial rotation while releasing it. In this case it entered steady autorotation after falling a distance of two meters only.

Based on the techniques used for the measurements of the different variables, the maximum errors are estimated as follows: 5 percent in the sinking rate, 25 percent in the conning angle, and 15 percent in the angular rate.

Table 1 Comparison between calculated and measured results

Parameter	Calculated Results	Experimental Results	Percentage of Deviation
	EXPERIMENTAL MODEL		
$U_{\tilde{x}}\left(\frac{m}{s}\right)$	-2.17	-2.	8.5
$\dot{\Phi}\left(\frac{rad}{s}\right)$	21.23	18.	17.9
β(deg)	-18.	-24.	25.
$u_1\left(\frac{m}{s}\right)$	-1.9	-	-
$u_2\left(\frac{m}{s}\right)$	-0.63	-	-
$u_3\left(\frac{m}{s}\right)$	0.69	-	-
γ(deg)	-16.26	-	-
$\tilde{Y}_m$(m)	4×10^{-3}	-	-
$\tilde{Z}_m$(m)	9×10^{-4}	-	-
	SAMARA: *ACER PLATENOIDS*		
$U_{\tilde{x}}\left(\frac{m}{s}\right)$	-1.29	-0.9	43.3
$\dot{\Phi}\left(\frac{rad}{s}\right)$	82.39	81.6	0.9
β(deg)	-16.5	-21.0	21.4
$u_1\left(\frac{m}{s}\right)$	-1.25	-	-
$u_2\left(\frac{m}{s}\right)$	-0.27	-	-
$u_3\left(\frac{m}{s}\right)$	0.53	-	-
γ(deg)	-21.8	-	-
$\tilde{Y}_m$(m)	3.2×10^{-4}	-	-
$\tilde{Z}_m$(m)	6.19×10^{-6}	-	-

6 Comparison Between Theoretical and Experimental Results

Calculations were carried out for the experimental model that was described in Fig. 6 which will be denoted EM in what follows. Calculations were also carried out for a Norway Maple (*Acer platenoides*) winged seed that will be denoted AP. Experimental results for the AP were presented by Norberg (1973).

The experiments in both cases included measurements of the: sinking rate $U_{\dot{x}}$, angular rate $\dot{\Phi}$, and the conning angle β. In Table 1 the experimental results for these three variables are compared with theoretical results. It can be seen that a fair agreement is presented for the EM, if one recalls the uncertainty in the aerodynamic coefficients. It can be shown that relatively small changes in the coefficient (which are all within the range of the possible inaccuracies), may lead to changes in the results which are in the range of the deviations presented in the Table. In the case of the EM the largest deviation between the measurements and the calculations appears in the case of the conning angle (25 percent). In the case of the AP the deviation in the sinking rate exceeds 43 percent. The larger errors in the case of the AP can be the result of incomplete information concerning the mass distribution, which requires certain assumptions that, if not accurate, may result in increasing deviations. The reader should note the relatively high values of the conning

angles in both cases as compared to other rotary wing applications (usually less than 10 deg). These high conning angles are one of the reasons for the differences between the model of a samara wing and other rotary wings.

Table 1 also presents the rest of the variables which were calculated, but not measured experimentally.One should note the relatively high spanwise velocity component u_2, and the high negative value of the pitch angle γ. These values are much higher than the same variables in other cases of rotary wings. $\tilde{Y}_m$ and $\tilde{Z}_m$ define the location of the center of mass relative to the rotation center. The calculations in both cases predict that the center of rotation is very close to the center of mass of the wing, and thus still within the wing itself. While for the case of the AP also the experiments indicated a rotation center which is very close to the center of mass, in the EM case the observation was that the center of rotation was outside the wing and thus much further from the center of mass than the theoretical predictions.

7 Conclusions

A theoretical model of a samara wing in vertical descent has been developed. This model is more accurate and complete than all the models that have been used previously for this purpose. The inertial effects are dealt with in an accurate manner. The blade element/momentum theory is used to model the aerodynamic contributions.

The aerodynamic behavior of typical samara wings is different in many aspects from helicopter blades or other rotary wings. This involves higher conning and attack angles (beyond stall), low Reynolds numbers, etc. These differences required a derivation of a theoretical model which is different from existing models. Thus, for example, the present model includes corrections for the spanwise aerodynamic force, which is usually ignored.

The obtained model is highly nonlinear and requires a complex iterative solution procedure.

In order to verify the model an experimental investigation was also carried out. Quite good agreement was presented between the theoretical and experimental results involving the present experiments with a cardboard model, and previous experimental results for a winged seed. Deviations may be the result of lack of accurate information concerning the two-dimensional aerodynamic properties of the wing cross-sections.

8 Acknowledgment

The authors would like to thank Mr. S. Nachmani and Mr. A. Greenwald for their assistance in carrying out the experiment. Thanks are also given to Mrs. A. Goodman for typing the manuscript.

References

Bradford, H. W., 1954, "Study of the Subsonic Forces and Moments on an Inclined Plate of Infinite Span," NACA TN 3221.

Burrows, F. M., 1975, "Wing-Borne Seeds and Fruit Movement," *New Phytol.*, Vol. 75, pp. 405–418.

Crimi, P., 1988, "Analysis of a Samara-Wing Decelerator Steady State Characteristics," *Journal of Aircraft*, Vol. 25, No. 1, pp. 41–47.

Glauert, H., 1943, "Airplanes Propellers," *Aerodynamic Theory*, W. F. Durand, Durand Reprinting Committee, Vol. IV, pp. 191–230.

Green, S. D., 1980, "The Terminal Velocity and Dispersal of Spinning Samaras," *Amer. J. Bot.*, Vol. 67, No. 8, pp. 1218–1224.

McCutchen, C. W., 1977, "The Spinning Rotation of Ash and Tulip Tree Samaras," *Science*, Vol. 197, pp. 691–692.

Moré, Jorge, Garbow, Burton, Hillstorm, and Kenneth, 1980, "User Guide for MINPACK-1," Argonne National Laboratory, Report ANL-80-74, Argonne, Ill., Subroutine HYBRD1.

Nachtigall, W., 1977, "Die Aerodynamische Polare des Tipula-Flügels und Eine Einrichtung zur Halbautomatischen Polarenaufnahme," *The Physiology of Movement Biomechanics*, W. Nachtigall, ed., Fischer, Stuttgart, pp. 347–352.

Norberg, R. Åke, 1973, "Autorotation, Self-Stability and Structure of Single-Winged Fruits and Seeds (Samaras) with Comparative Remarks on Animal Flight," *Biol. Rev.*, Vol. 48, pp. 561–596.

Rees, J. C., 1975, "Aerodynamic Properties of Insect Wing Section and a Smooth Aerofoil Compared," *Nature*, Vol. 258, pp. 1411–1412.

Rosen, A., and Rand, O., 1985, "The Aerodynamic Behavior of Infinite Swept Wings—Another Point of View," *Journal of Aircraft*, Vol. 22, No. 1, pp. 83–85.

Seter, D., 1989, "Investigation of the Autorotation of a Free Rotor," M.Sc. Thesis, Faculty of Aerospace Engineering, Technion—Israel Institute of Technology, Haifa, Israel.

Vogel, S., 1967, "Flight in Drosophila: III—Aerodynamic Characteristics of Fly Wing and Wing Models," *J. Exp. Biol.*, Vol. 46, pp. 431–443.

Ward-Smith, A. J., 1984, *Biophysical Aerodynamics and the Natural Environment*, John Wiley and Sons, New York, pp. 53–70.

Withers, P. C., 1981, "An Aerodynamic Analysis of Bird Wings as Fixed Aerofoils," *J. Exp. Biol.*, Vol. 90, pp. 143–162.

Vibration Localization by Disorder in Assemblies of Monocoupled, Multimode Component Systems

Philip D. Cha[1]
Graduate Research Assistant.

Christophe Pierre
Assistant Professor,
Mem. ASME

Department of Mechanical Engineering and Applied Mechanics,
The University of Michigan,
Ann Arbor, MI 48109-2125

Disorder in nominally periodic engineering structures results in the localization of the mode shapes to small geometric regions and in the attenuation of waves, even in the passbands of the corresponding perfectly periodic system. This paper investigates, via probabilistic methods, the transmission of steady-state harmonic vibration from a local source of excitation in nearly periodic assemblies of monocoupled, multicomponent mode substructures. A transfer matrix formulation is used to derive analytical expressions for the localization factor (the rate of exponential decay of the vibration amplitude) in the limiting cases of strong and weak modal coupling. The degree of localization is shown to increase with the ratio of disorder strength to modal coupling. The increase is nearly parabolic for small values of this ratio, and logarithmic for large values. Furthermore, the localization factor increases very rapidly with the passband number. Typically, the transition from weak to strong localization occurs from one passband to the next, and severe vibration confinement is unavoidable at high frequencies, even for very small disorder.

1 Introduction

The dynamic analysis of repetitive engineering structures is greatly simplified by assuming perfect periodicity. However, unavoidable manufacturing and material tolerances destroy this mathematical idealization. Typical examples of often-assumed-periodic structures are bladed disk assemblies and large space structures.

Unfortunately for the designer and analyst confronted with repetitive structures, slight disruption in their periodicity may alter drastically the dynamic response from the assumed-periodic predictions. For example, under conditions of weak internal coupling, the extended mode shapes of the periodic structure become localized to a small geometric region when small disorder (or mistuning) is introduced. This phenomenon, known as normal mode localization, was first evidenced by Hodges (1982) in structural dynamics.

The motivation for studying localization is threefold. First, the occurrence of localization may severely reduce the effectiveness of structural models, associated control schemes, and identification techniques that assume perfect periodicity. For example, a control strategy based upon the erroneous extended modes of a perfectly periodic structure would be unpredictable. Second, localized vibrations increase amplitudes and stresses locally and may result in severe damage. For instance, single-blade failure in turbomachinery rotors is a plausible result of blade mistuning. Third, when localization occurs, irregularities exhibit a damping-like effect that could be used as a passive control of vibration transmission. This has applications in flexible and lightly damped structures such as truss beams in space. However, although disorder and dissipation both result in a spatial decay of the amplitude, the localization and damping mechanisms are intrinsically distinct: For localization the vibrational energy is *confined* near the source of excitation by disorder, while for damping the energy is *dissipated* as it propagates.

Research on localization in structural dynamics has been limited mostly to *deterministic* analyses of the free modes of disordered one-dimensional structures. Here we cite several representative studies. Pierre and Dowell (1987) investigated mode localization by perturbation methods for a chain of coupled oscillators. Other works by Bendiksen (1987), Cornwell and Bendiksen (1989a), and Wei and Pierre (1988) examined localization in mistuned cyclic periodic structures such as large space reflectors and blade assemblies. Pierre and Cha (1989) tackled localization analytically in assemblies of *multimode* subsystems and showed that confinement effects increase rapidly with frequency. This result was confirmed recently by Cornwell and Bendiksen (1989b), who examined a similar (but cyclic) structure by defining a deterministic localization length scale.

Considerably fewer *probabilistic* studies of localization have been conducted. Hodges and Woodhouse (1983) formulated a statistical treatment of the transmission of harmonic forced vibrations from a local excitation source. They applied the

[1]Presently Senior Research Engineer, Ford Motor Company.

Contributed by the Applied Mechanics Division of THE AMERICAN SOCIETY OF MECHANICAL ENGINEERS for presentation at the Joint Applied Mechanics/Bioengineering Conference, Ohio State University, Columbus, Ohio, June 16-19, 1991.

Discussion on this paper should be addressed to the Technical Editor, Leon M. Keer, The Technological Institute, Northwestern University, Evanston, IL 60208, and will be accepted until two months after final publication of the paper itself in the JOURNAL OF APPLIED MECHANICS. Manuscript received by the ASME Applied Mechanics Division, Sept. 14, 1989; final revision, Mar 13, 1990.

Paper No. 91-APM-27.

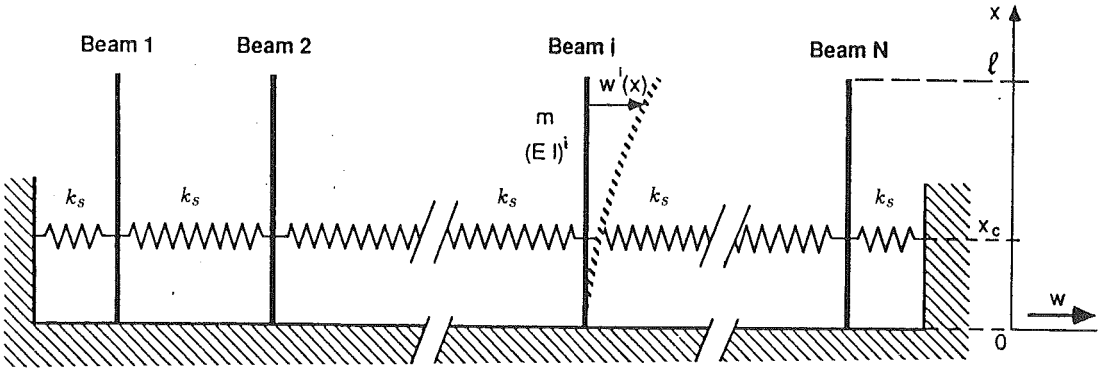

Fig. 1 Assembly of coupled, component systems (cantilevered beams)

work of Herbert and Jones (1971) to calculate localization factors (the exponential spatial decay rate of the amplitude) for a simple model of a stretched string with irregularly spaced masses attached. Their work exhibited two types of localization—*weak* and *strong*—depending on the magnitude of internal coupling in the structure. Recently, Kissel (1987, 1988) chose the wave description of Ishii (1973) to calculate localization factors for several one-dimensional structures. He studied systematically the dependence of the localization factor on frequency in the limiting case of weak disorder. However, the models he chose did not allow him to vary the relative magnitudes of internal coupling and disorder, thereby restricting his findings to *weak* localization effects. Recently, Pierre (1989) utilized stochastic perturbation methods to calculate localization factors in terms of frequency, coupling, and disorder strength. He evidenced both *weak* and *strong* localization regimes. His study, however, was restricted to chains of *single-mode* subsystems.

This paper investigates weak and strong confinement effects of random disorder in assemblies of *multimode* component systems. To highlight the effects of disorder, we do not include damping in the model. A *statistical* treatment of the structural irregularities is chosen. Special attention is paid to the dependence of the degree of localization on frequency, both inside a passband (or, equivalently, for a group of modes) and from passband to passband. The transmission of vibration from a local excitation source and the propagation of incident waves are studied by techniques that are reviewed in Section 2. The frequency stopbands and passbands of the ordered assembly are discussed in Section 3. Statistical perturbative techniques are used to derive the localization factors in the two limiting cases of strong and weak modal coupling in Section 4, and these analytical results are verified by Monte Carlo simulations in Section 5. In Section 6, the dependence of localization effects on disorder strength, modal coupling, and passband number is investigated. Finally, the relevance of the localization phenomenon to structural dynamics applications is illustrated.

The contributions of this study are twofold. First, analytical results of general significance to the theory of localization in engineering structures are presented. For example, the dependence of localization effects on frequency and disorder strength is examined for both weak and strong localization regimes. Second, it is shown that, for assemblies of multimode subsystems, confinement effects at high frequencies are severe, and unavoidable even if the internal coupling is very large and the disorder very small. This has important consequences for structural dynamics applications.

2 Calculation of Localization Factors

2.1 Equations of Motion. Consider an undamped assembly of N, monocoupled, one-dimensional, almost identical

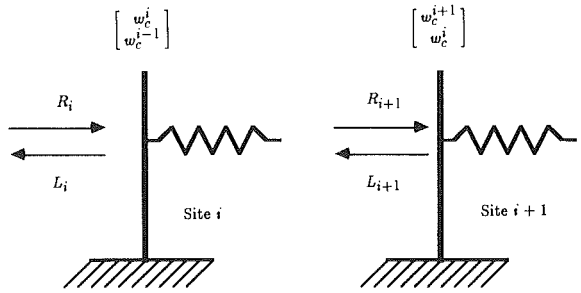

Fig. 2 Site representation for wave formulation

component systems (see Fig. 1). Each subsystem is coupled to its nearest neighbors through linear springs of stiffness k_s located at $x=x_c$ along each component structure. To study vibration transmission, the system is excited at its left end by a simple harmonic force of frequency, ω, and the steady-state response of the right-end component is examined. Applying component mode analysis (Dowell, 1972), the nominal component system is represented by its modal representation, $(\lambda_p, \phi_p(x))_{p=1,\ldots,M}$, where M is the number of component modes, λ_p the pth eigenvalue (the square of the pth natural frequency), and $\phi_p(x)$ the corresponding mode shape. In the presence of disorder, the modes of the ith (uncoupled) component system are slightly perturbed, becoming

$$\begin{cases} \lambda_p^i = \lambda_p(1+d\lambda_p^i),\ p=1,\ \ldots,\ M,\ i=1,\ \ldots,\ N \\ \phi_p^i(x) = \phi_p(x)(1+d\phi_p^i(x)),\ p=1,\ \ldots,\ M,\ i=1,\ \ldots,\ N, \end{cases} \tag{1}$$

where p denotes the component mode number, and i the component system number.

For simplicity, we assume no component mode shape perturbation due to disorder, as well as constant modal mistuning;[2] thus, $\phi_p^i(x) \equiv \phi_p(x)$ and $d\lambda_p^i \equiv d\lambda^i$. Furthermore, denoting the pth modal mass of a subsystem by M_p, we choose them to be identical for all component modes;[3] thus, $M_p \equiv \mathfrak{M}$. These assumptions allow for all the important localization effects to be captured in a relatively straightforward analysis. For harmonic motion the deflection amplitude of the ith component system is expanded as

$$w^i(x) = \sum_{p=1}^{M} \phi_p(x)\theta_p^i \quad ,i=1,\ \ldots,\ N, \tag{2}$$

where θ_p^i is the pth normal coordinate amplitude for the ith subsystem. Applying Lagrange's equations gives (see the derivation in (Pierre and Cha, 1989))

[2]This is exact for Euler-Bernoulli beams with random flexural rigidities. In general, we found that the effect of mode shape disorder is small compared to that of frequency (or diagonal) disorder (Pierre and Cha, 1989).

[3]This is the case if the modes are normalized consistently.

$$R\begin{bmatrix} \ddots & \ddots & [0] & \cdots & [0] \\ \ddots & \ddots & \ddots & \ddots & \vdots \\ [0] & -[A] & [B^i] & -[A] & [0] \\ \vdots & \ddots & \ddots & \ddots & \ddots \\ [0] & \cdots & [0] & \ddots & \ddots \end{bmatrix}\begin{bmatrix} \boldsymbol{\Theta}^1 \\ \boldsymbol{\Theta}^2 \\ \vdots \\ \boldsymbol{\Theta}^i \\ \vdots \\ \boldsymbol{\Theta}^N \end{bmatrix} = \begin{bmatrix} \frac{F}{\mathfrak{M}}\boldsymbol{\Phi}_f \\ \mathbf{0} \\ \vdots \\ \mathbf{0} \\ \vdots \\ \mathbf{0} \end{bmatrix}, \tag{3}$$

where

$$[A] = \boldsymbol{\Phi}_c\boldsymbol{\Phi}_c^T,$$
$$[B^i] = \frac{1}{R}\left([\Lambda](1+d\lambda^i) + 2R\boldsymbol{\Phi}_c\boldsymbol{\Phi}_c^T - \omega^2[I]\right) \tag{4}$$

and $\boldsymbol{\Theta}^i = [\ldots, \theta_p^i, \ldots]^T$ is the M-vector of amplitudes for the ith component system, F the forcing amplitude, $\mathfrak{M}$ the modal mass, $\boldsymbol{\Phi}_f = [\ldots, \phi_p(x_f), \ldots]^T$ the M-vector of modal deflections at the forcing location, $R = k_s/\mathfrak{M}$ can be regarded as a coupling frequency squared, $[\Lambda] = [\text{diag}(\lambda_p)]$ is the $M \times M$ diagonal matrix of the eigenvalues of the nominal subsystem, $[I]$ the $M \times M$ identity matrix, and $\boldsymbol{\Phi}_c$ is the M-vector of modal deflections at the constraint location, x_c.

While the theoretical results derived in this paper hold for a generic assembly of component systems, numerical calculations are performed on an assembly of clamped-free Euler-Bernoulli beams (see Fig. 1). We assume there is no domain perturbation and that disorder originates from discrepancies among the flexural rigidities $(EI)^i$ of the beams. Thus, the modal mass is $\mathfrak{M} = ml$, the component modes, $\phi_p(x)$, are the modes of a clamped-free beam (see the expression in Pierre and Cha, 1989), and the equations of motion (3) are divided by EI/ml^4 to introduce the dimensionless parameters $\overline{R} = k_s/(EI/l^3)$, $\overline{\lambda}_p = \lambda_p/(EI/ml^4)$, $\overline{\omega}^2 = \omega^2/(EI/ml^4)$, and $\overline{F} = F/(EI/l^3)$, where EI is the flexural rigidity of the nominal beam.

2.2 Wave Formulation. We choose a traveling wave perspective to examine the spatial decay of the vibration amplitude. Since the assembly in Fig. 1 is monocoupled, it carries a single pair of waves and thus can be modeled by 2×2 transfer matrices. We choose the ith bay to consist of the ith component system and the coupling spring to its right, as shown in Fig. 2. Defining the state vector of normal coordinates at the ith site by $[\boldsymbol{\Theta}^i, \boldsymbol{\Theta}^{i-1}]^T$, a $2M \times 2M$ normal coordinate transfer matrix that relates the states at adjacent sites is obtained from equation (3):

$$\begin{bmatrix} [A] & [0] \\ [0] & [A] \end{bmatrix}\begin{bmatrix} \boldsymbol{\Theta}^{i+1} \\ \boldsymbol{\Theta}^i \end{bmatrix} = \begin{bmatrix} [B^i] & -[A] \\ [A] & [0] \end{bmatrix}\begin{bmatrix} \boldsymbol{\Theta}^i \\ \boldsymbol{\Theta}^{i-1} \end{bmatrix}. \tag{5}$$

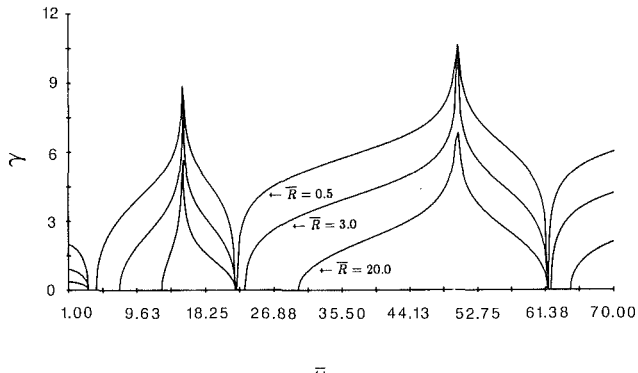

Fig. 3 Real part of propagation constant versus frequency in the first three passbands of an ordered system. Coupling is at the tip.

Next, we note that the deflection of the ith subsystem at the constraint location, $w^i(x_c) \equiv w_c^i$, is the coupling coordinate between subsystems. It can be expressed in terms of the normal coordinate amplitudes as

$$w_c^i = \boldsymbol{\Phi}_c^T\boldsymbol{\Theta}^i. \tag{6}$$

Combining equations (5) and (6), we obtain the 2×2 displacement transfer matrix[4] for the ith bay, which relates the constraint deflections at adjacent sites:

$$\begin{bmatrix} w_c^{i+1} \\ w_c^i \end{bmatrix} = [T^i]\begin{bmatrix} w_c^i \\ w_c^{i-1} \end{bmatrix} \text{ with } [T^i] = \begin{bmatrix} \beta^i & -1 \\ 1 & 0 \end{bmatrix}, \tag{7}$$

where β^i is given in Appendix A. For a disordered system the $[T^i]$'s are random transfer matrices, their average matrix being that of the ordered structure,

$$[T^o] = \begin{bmatrix} \beta^o & -1 \\ 1 & 0 \end{bmatrix}, \tag{8}$$

where β^o is obtained as β^i with $d\lambda^i = 0$.

The displacement amplitudes are expressed in terms of the right and left-traveling wave amplitudes by the transformation (Brillouin, 1953; Kissel, 1988)

$$\begin{bmatrix} w_c^i \\ w_c^{i-1} \end{bmatrix} = [X]\begin{bmatrix} L^i \\ R^i \end{bmatrix} \text{ with } [X] = \begin{bmatrix} 1 & 1 \\ e^{-jk} & e^{jk} \end{bmatrix} \tag{9}$$

where the columns of $[X]$ are the eigenvectors of the ordered transfer matrix $[T^o]$ and k is a (complex) wave number related to the frequency, ω, by the dispersion relation. Substituting equation (9) into equation (7) leads to a wave transfer matrix that relates the wave amplitudes at sites i and $i+1$,

$$\begin{bmatrix} L^{i+1} \\ R^{i+1} \end{bmatrix} = [W^i]\begin{bmatrix} L^i \\ R^i \end{bmatrix}, \quad \text{with} \quad [W^i] = [X]^{-1}[T^i][X]. \tag{10}$$

One can show, for real wave number k,

$$[W^i] = \begin{bmatrix} 1/t^i & -r^i/t^i \\ -(r^i)^*/(t^i)^* & 1/(t^i)^* \end{bmatrix}, \tag{11}$$

where* denotes a complex conjugate, and t^i and r^i are the complex transmission and reflection coefficients for the ith bay.

For an ordered site, the wave transfer matrix is diagonal consisting of the eigenvalues of $[T^o]$, and there is no reflection ($r^i = 0$). For frequencies such that k is real, there is no attenuation, and such frequencies define a passband. For k not real, there is attenuation, and the frequency belongs to a stopband. For a disordered site, $[X]$ does not diagonalize $[T^i]$, and thus there is reflection ($r^i \neq 0$). This scattering from the random sites leads to localization.

We now consider the transmission of a wave of amplitude a, incident from the left, through an N-site disordered system ($i = 1, \ldots, N$) embedded in an otherwise ordered infinite system. The wave transfer matrix for the disordered segment relates the wave amplitudes entering and leaving it. For frequencies in a passband:

$$\begin{bmatrix} L^{N+1} \\ R^{N+1} \end{bmatrix} = [\mathfrak{W}^N]\begin{bmatrix} L^1 \\ R^1 \end{bmatrix},$$

$$[\mathfrak{W}^N] = \left(\prod_{i=N}^{1}[W^i]\right) = \begin{bmatrix} 1/\tau^N & -\rho^N/\tau^N \\ -(\rho^N)^*/(\tau^N)^* & 1/(\tau^N)^* \end{bmatrix}, \tag{12}$$

where τ^N and ρ^N are the transmission and reflection coefficients for the disordered segment. Since there is no reflection for the tuned sites, $R^1 = a$ and $L^{N+1} = 0$. It follows that the ratio of

[4] An exact formulation for the displacement transfer matrix is possible for an assembly of cantilevered Euler-Bernoulli beams. This was used to check the convergence of the component mode analysis. In all cases excellent agreement was observed.

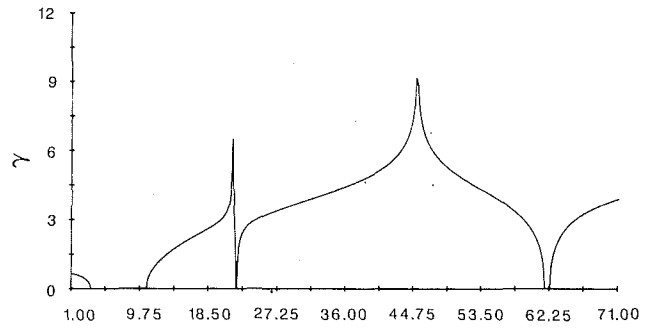

Fig. 4(*a*)

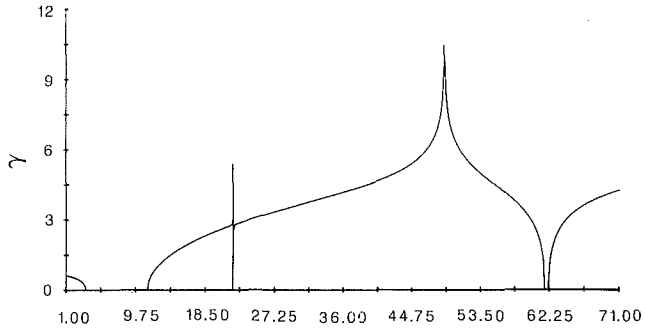

Fig. 4(*b*)

Fig. 4 Real part of propagation constant versus frequency for an ordered system with $x_c = 0.75$; (*a*) and $x_c = 0.78$ (*b*). The dimensionless coupling is $\bar{R} = 15.0$ The node of the nominal beam's second mode is at $x = 0.7844$.

the amplitude transmitted through the disordered segment (R^{N+1}) to the incident amplitude (a) is the transmission coefficient, τ^N. Thus, the rate of exponential decay of the transmitted wave amplitude is, for an infinite assembly,

$$\gamma = \lim_{N\to\infty} -\frac{1}{N} \ln|\tau^N|, \tag{13}$$

which is determined by the (1,1) term in the overall wave transfer matrix. Equation (13) means that, asymptotically, the transmission coefficient decays exponentially with N at the rate γ. For $\gamma > 0$, the energy is *confined* near the excitation source. For an ordered system γ is the real part of the propagation constant (Mead, 1975). For a disordered system it is called the localization factor.

2.3 Modal Formulation. The vibration amplitude transmitted to the right end of the assembly due to a left-end excitation can be calculated by applying the modal analysis technique developed by Herbert and Jones (1971) and used by Hodges and Woodhouse (1983) and Pierre (1989). This formulation was not retained for the analytical evaluation of localization factors because the wave approach leads to simpler calculations, but it was used in some of the Monte Carlo simulations when the wave approach failed to provide satisfactory results. From equations (2) and (3), the steady-state response amplitude of the Nth component system at the constraint location is

$$\left| \frac{w_c^N}{F/\mathfrak{M}} \right| = |\Phi_c^T [F_{1N}] \Phi_f|, \tag{14}$$

where $[F_{1N}]$ is the $(1,N)$th $M \times M$ submatrix of $([K] - \omega^2[I])^{-1}$, which can be obtained recursively by exploiting tridiagonality. This yields, assuming exponential decay of the vibration amplitude,

$$\gamma = \lim_{N\to\infty} -\frac{1}{N} \ln|\Phi_c^T [F_{1N}] \Phi_f|. \tag{15}$$

3 Passbands and Stopbands of the Ordered System

The real part of the propagation constant is calculated for an infinite ordered assembly over the entire frequency spectrum by the wave formulation.

3.1 Propagation Constant. For the ordered system, the eigenvalues of the transfer matrix $[T^o]$ in equation (8) are

$$\lambda_{1,2} = \frac{\beta^o}{2} \pm \sqrt{\left(\frac{\beta^o}{2}\right)^2 - 1}, \tag{16}$$

such that $\lambda_1 \lambda_2 = 1$ and β^o is a function of ω. The modal and wave transfer matrices are

$$[X] = \begin{bmatrix} 1 & 1 \\ 1/\lambda_1 & 1/\lambda_2 \end{bmatrix} \quad [W^o] = \begin{bmatrix} \lambda_1 & 0 \\ 0 & \lambda_2 \end{bmatrix}. \tag{17}$$

For the ordered assembly the decay is identical for all sites; thus, from equation (13), $\gamma = \ln|\lambda_1|$. Several cases are considered.

- For $|\beta^o(\omega)/2| < 1$, λ_1 and λ_2 are complex conjugates of modulus 1. Letting $\beta^o/2 = \cos k (0 < k < \pi)$, we have $\lambda_{1,2} = \exp(\pm jk)$, where k is the real wave number. This readily yields $\gamma = 0$, and the corresponding frequencies define the *passbands*. It can be shown that for a given wave number k, $(\beta^o(\omega^2) - 2\cos k)$ has M zeros, defining M frequency bands.
- For $|\beta^o(\omega)/2| > 1$, λ_1 and λ_2 are real. The wave number is complex and γ is positive, leading to attenuation. The corresponding frequencies define the *stopbands*.
- For $|\beta^o(\omega)/2| = 1$, there is a double eigenvalue $\lambda_1 = \lambda_2 = 1$ or -1. Thus, $\gamma = 0$, and the corresponding frequencies define the *passband-stopband edges*. The M zeros of $(\beta^o(\omega^2) - 2)$ give the lower limits of the passbands, $(\omega^2_{p_l})_{p=1,\ldots,M}$, while the zeros of $(\beta^o(\omega^2) + 2)$ give the upper limits, $(\omega^2_{p_u})_{p=1,\ldots,M}$. For an exact representation of the assembly ($M \to \infty$), the number of passbands is infinite.

3.2 Results. Figure 3 illustrates the alternating bands of attenuation and propagation for an assembly of Euler-Bernoulli beams. The first band is a stopband, where γ decreases to zero as the frequency increases to reach the first passband. In the second and higher stopbands, γ becomes large and tends to infinity at some particular frequencies (these peaks are probably due to the poles of $\beta^o(\omega^2)$). The effect of spring stiffness is clearly illustrated in Fig. 3: An increase in coupling between the subsystems results in smaller values of the propagation constant and in a widening of the passbands. This is because vibration transmission is easier for larger coupling. Also, the width of the passbands diminishes rapidly with increasing passband number. This is because an increase in the component mode number, p, results in a decrease in the dynamic coupling, R/λ_p (the square of the ratio of the coupling frequency to the pth component frequency). Thus, propagation becomes more difficult as the dynamic coupling decreases, or as p increases.

The effect of constraint location on the propagation constant is displayed in Fig. 4. Here, the static coupling is strong, and the constraint is near the node of the second mode of a component beam. Note the severe narrowing of the second passband accompanied by the shifting of the stopband peak toward the left edge of the second passband. As the coupling constraint moves closer to the node, the peak of the stopband practically superposes onto the second passband and the corresponding frequency bandwidth becomes negligible. Thus, positioning the coupling constraint very close to the node of a component mode practically eliminates the corresponding passband.

The bounding frequencies of the passbands are of importance. The lower limits are independent of the coupling and the constraint location (see Fig. 3), and simply equal the pth frequency of the nominal subsystem. As a check, we obtained the passband-stopband edges by considering the free vibration

natural frequencies of the tuned assembly. For an infinite assembly ($N\to\infty$), these frequencies lie densely in the pass bands, with the lowest and highest frequencies in each cluster corresponding to the edges (Mead, 1975). In all cases, the passband edges obtained by the wave formulation were found to be identical to the bounding free vibration frequencies obtained by Cha and Pierre (1989).

4 Localization Factors of the Disordered System

In general, localization factors cannot be calculated in closed form, and one must resort to numerical evaluations. However, analytical approximations can be obtained in the two limiting cases of strong and weak modal coupling. This is presented here with the aid of probabilistic perturbation methods. Since strong attenuation already occurs in the tuned system's stopbands, we focus on disorder effects in the passbands. The mistunings $d\lambda^i$ are assumed to be independent and identically distributed random variables of mean zero and standard deviation σ.

4.1 Small Disorder To Coupling Ratio. Here we assume that the elements of $R\Phi_c\Phi_c^T$ are much larger than those of $d\lambda^i[\Lambda]$. Thus, $O(\sigma/(R\phi_p^2/\lambda_p)<1$, $p=1,\ldots,M$, where $O(\cdot)$ denotes the order of the argument and $R\phi_p^2/\lambda_p$ is the "modal" coupling in the pth component mode. Since disorder is small, it implies that the modal coupling is finite or large. A classical perturbation method (CPM) that treats disorder as the perturbation is applied to derive the localization factor.

For frequencies inside the pth passband, it is convenient to rewrite the (1,1) term of the transfer matrix as

$$\beta^i=\frac{\lambda_p}{R\phi_p^2}\,(E_p^i-\mathbf{F}_p^{iT}[G_p^i]^{-1}\mathbf{F}_p^i)\quad(p=1,\ldots,M). \tag{18}$$

Although equation (18) holds for all values of p and all frequencies, it is preferable to use the pth representation of β^i for frequencies in the pth band. Equation (18) is justified in Appendix B.

The random transfer matrix for the ith site is written as,

$$[T^i]=\begin{bmatrix}\beta^o & -1\\ 1 & 0\end{bmatrix}+\begin{bmatrix}\delta\beta^i & 0\\ 0 & 0\end{bmatrix}=[T^o]+[\delta T^i], \tag{19}$$

where β^o and $\delta\beta^i$ are given in Appendix B. In a passband, the wave transfer matrix for the ith site is $[W^i]=[W^o]+[\delta W^i]$ where, from equation (10),

$$\begin{cases}[W^o]=\begin{bmatrix}e^{jk} & 0\\ 0 & e^{-jk}\end{bmatrix}\\ [\delta W^i]\simeq -j\left(\dfrac{d\lambda^i}{2\sin k}\right)\left(\dfrac{\lambda_p\alpha_p}{R\phi_p^2}\right)\begin{bmatrix}e^{jk} & e^{jk}\\ -e^{-jk} & -e^{-jk}\end{bmatrix}.\end{cases} \tag{20}$$

The wave transfer matrix for an N-site disordered segment is, to the first order in the disorder to coupling ratio, from equations (12) and (20),

$$[\mathfrak{W}^N]\simeq[W^o]^N+\sum_{l=1}^{N}[W^o]^{l-1}[\delta W^{N-l+1}][W^o]^{N-l}+O'\left(\frac{\sigma^2\lambda_p^2}{R^2\phi_p^4}\right) \tag{21}$$

where $O'(\cdot)$ consists of terms $d\lambda^l d\lambda^m$ for $l\neq m$. We take the modulus of the (1,1) term in equation (21) to calculate the localization factor:

$$\gamma=\lim_{N\to\infty}\frac{1}{2N}\ln\left|1+\frac{\alpha_p^2\lambda_p^2}{4R^2\phi_p^4\sin^2k}\left(\sum_{l=1}^{N}d\lambda^l\right)\left(\sum_{m=1}^{N}d\lambda^m\right)+O'\left(\frac{\sigma^2\lambda_p^2}{R^2\phi_p^4}\right)\right|. \tag{22}$$

Next, we approximate $\ln|1+z|$ by z. Since the mistunings are uncorrelated and identically distributed, all terms for $l\neq m$ vanish, which justifies retaining only the first-order terms. We obtain

$$\gamma=\frac{\sigma^2\lambda_p^2\alpha_p^2}{8R^2\phi_p^4\sin^2k}+O\left(\frac{\sigma^4\lambda_p^4}{R^4\phi_p^8}\right). \tag{23}$$

Using the dispersion relation $\beta^o(\omega)=2\cos k$ gives γ in terms of frequency:

$$\gamma^{(c)}(\omega)=\frac{\sigma^2\lambda_p^2\alpha_p^2(\omega)}{2R^2\phi_p^4(4-\beta^{o2}(\omega))} \tag{24}$$

where $\gamma^{(c)}$ denotes the *classical* approximation of the localization factor, which holds for strong modal coupling. The pth representation of γ is preferred for frequencies in the pth passband, as it exhibits the dependence of γ on modal coupling.

If the pth component mode contributes largely to the motion, we can use a *single-mode* approximation. Then $\beta^o=(\lambda_p+2R\phi_p^2-\omega^2)/(R\phi_p^2)$, $\alpha_p=1$, and the wave number is related to frequency by

$$\omega_p^2=\lambda_p+4R\phi_p^2\sin^2\frac{k}{2},\ 0\le k\le\pi,\quad p=1,\ldots,M, \tag{25}$$

where λ_p and $(\lambda_p+4R\phi_p^2)$ are the pth passband edges, and ω_p lies in the pth passband. The one-mode approximation of the localization factor is

$$\gamma^{(c)}(\omega_p)\simeq\frac{\sigma^2}{2\left(\dfrac{\omega_p^2}{\lambda_p}-1\right)\left(1+4\dfrac{R\phi_p^2}{\lambda_p}-\dfrac{\omega_p^2}{\lambda_p}\right)}. \tag{26}$$

We can make some observations about the localization factor. First, in the pth passband, the classical approximation is only valid for small values of $\sigma/(R\phi_p^2/\lambda_p)$, the ratio of mistuning to modal coupling. Second, $\gamma^{(c)}$ goes to infinity at the passband-stopband edges. Thus, we expect the approximation to deteriorate near the stopbands. Finally, $\gamma^{(c)}$ is primarily a function of the ratio of mistuning to modal coupling, the same that governs the strong localization of the free modes (Pierre and Cha, 1989). Equation (26) shows that this is exact for a one-mode analysis.

4.2 Large Disorder To Coupling Ratio. Here we assume that the elements of $d\lambda^i[\Lambda]$ are much larger than those of $R\Phi_c\Phi_c^T$. Thus, $O(\sigma/(R\phi_p^2/\lambda_p))>1$. Since disorder is small, this implies that modal coupling is weak. Note that even for arbitrarily large static coupling, weak modal coupling inevitably occurs at high frequencies, because λ_p increases with the passband number. Here we use a modified perturbation method (MPM) which treats coupling as the perturbation, while including disorder in the unperturbed system to avoid degeneracy (Pierre and Dowell, 1987). This yields

$$[T^i]=\begin{bmatrix}\beta^i & 0\\ 0 & 0\end{bmatrix}+\begin{bmatrix}0 & -1\\ 1 & 0\end{bmatrix}=[T^{oi}]+[\delta T] \tag{27}$$

where, in this weak coupling case, $|\beta^i|\gg 1$. Since the unperturbed matrix is diagonal, no transformation is needed to obtain the wave transfer matrix; thus, $[W^i]\equiv[T^i]$. Note that the modified perturbation scheme is valid in both passbands and stopbands. To the first order in the modal coupling to disorder ratio, the wave transfer matrix for an assembly of size N is

$$[\mathfrak{W}^N]\simeq\prod_{i=N}^{1}[T^{oi}]+\sum_{l=1}^{N}\left(\left(\prod_{i=N}^{l+1}[T^{oi}]\right)[\delta T]\left(\prod_{i=l-1}^{1}[T^{oi}]\right)\right). \tag{28}$$

A little algebra shows that the first-order terms in equation (28) do not contribute to $[\mathfrak{W}^N]$. Thus, from equation (13),

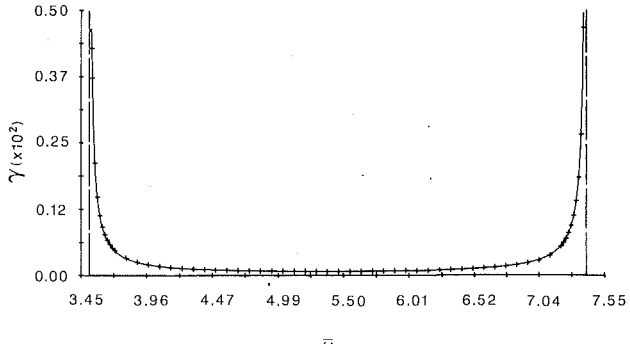

Fig. 5(*a*) First passband

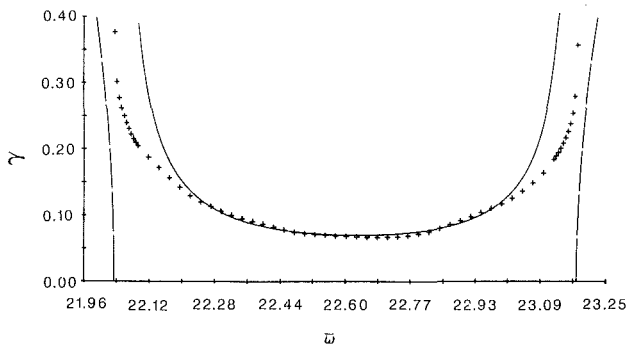

Fig. 5(*b*) Second passband

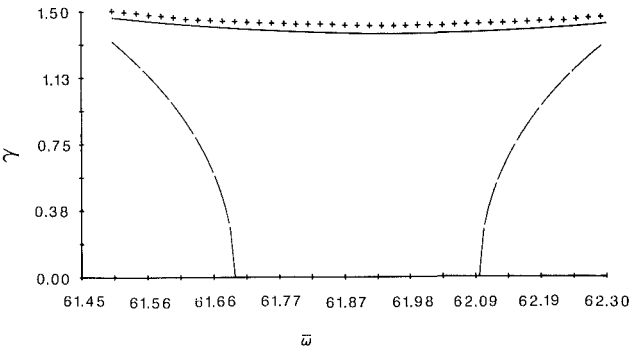

Fig. 5(*c*) Third passband

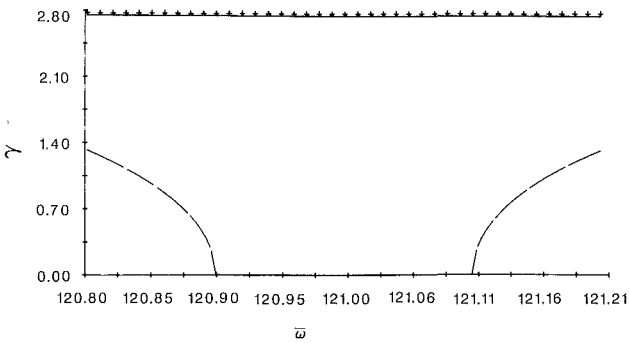

Fig. 5(*d*) Fourth passband

Fig. 5 Localization factor in the first four frequency passbands, for $x_c = 1.0$, $\bar{R} = 3.0$ and $\sigma = 2.0$ percent (—— ——) ordered system; (+) Monte Carlo simulation; (——) classical and modified perturbations in first two and last two passbands, respectively.

$$\gamma^{(m)}(\omega) = \lim_{N\to\infty} \frac{1}{N} \sum_{i=1}^{N} \ln|\beta^i|, \tag{29}$$

where $\gamma^{(m)}$ is the weak coupling approximation of the localization factor. Considering the function β of the continuous

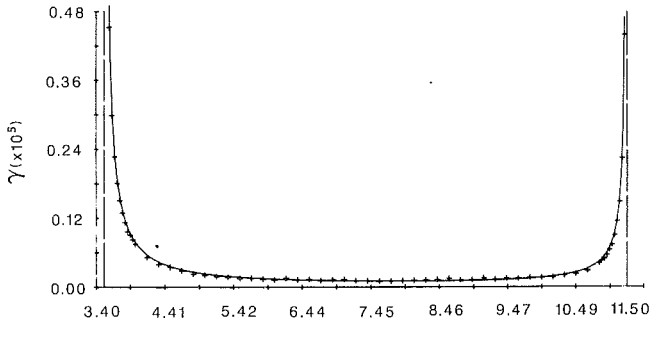

Fig. 6(*a*) First passband. (——) classical perturbation.

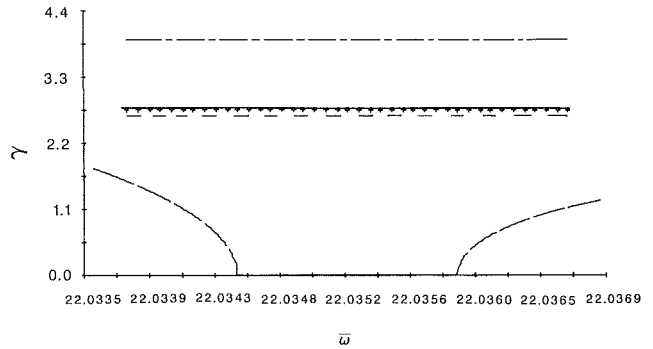

Fig. 6(*b*) Second passband. (——) multimode modified perturbation; (· ·) single-mode modified perturbation, first mode representation; (—— · ——) single-mode modified perturbation, second mode representation.

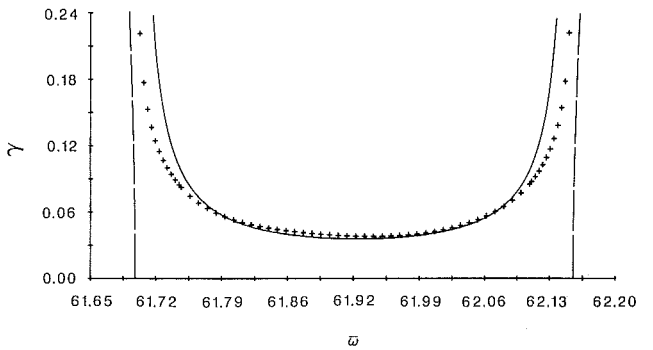

Fig. 6(*c*) Third passband. (——) classical perturbation.

Fig. 6 Localization factor in the first three frequency passbands, for $x_c = 0.78$, $\bar{R} = 15.0$ and $\sigma = 0.2$ percent. (—— ——) ordered systems; (+) Monte Carlo simulation.

disorder random variable, ϵ (by definition, $\beta(\epsilon = d\lambda^i) \equiv \beta^i$), we obtain

$$\gamma^{(m)}(\omega) = \frac{1}{2W} \int_{-W}^{W} \ln|\beta(\epsilon)|\, d\epsilon, \tag{30}$$

where the probability density function of disorder is assumed to be uniform of width $2W$ ($\sigma = W/\sqrt{3}$).

For a multimode system, we evaluate the integral (30) numerically. However, because the coupling is weak, a single-mode analysis that uses the pth mode of the nominal subsystem is often sufficient in the pth passband. Then,

$$\beta^i \simeq \frac{(1 + d\lambda^i)\lambda_p + 2R\phi_p^2 - \omega_p^2}{R\phi_p^2}, \tag{31}$$

where ω_p lies near the pth passband. This gives the one-mode approximation of the modified perturbation result, valid in the vicinity of the pth passband:

$$\gamma^{(m)}(\omega_p) \simeq -1 - \ln\left|\frac{R\phi_p^2}{\lambda_p}\right| + \frac{1+W+\frac{2R\phi_p^2}{\lambda_p}-\frac{\omega_p^2}{\lambda_p}}{2W}\ln\left|1+W+\frac{2R\phi_p^2}{\lambda_p}-\frac{\omega_p^2}{\lambda_p}\right| - \frac{1-W+\frac{2R\phi_p^2}{\lambda_p}-\frac{\omega_p^2}{\lambda_p}}{2W}\ln\left|1-W+\frac{2R\phi_p^2}{\lambda_p}-\frac{\omega_p^2}{\lambda_p}\right| \quad (32)$$

5 Perturbation and Simulation Results

The perturbation results are verified by Monte Carlo simulations for assemblies of cantilevered Euler-Bernoulli beams with random flexural rigidities. Simulations can be performed either by the wave or the modal formulation, by averaging the rate of decay in equations (13) and (15) over many realizations of disorder for assemblies of N beams. However, to offset the effect of boundary conditions, the modal scheme requires a much larger number of component beams than the wave simulation. This is particularly true when localization is weak, since the decay rate due to disorder must be orders of magnitude larger than that arising inevitably from boundary conditions. Thus, in general, wave simulations are considerably less expensive than modal ones. However, for strong localization, we observed that a modal simulation tracks the analytical result much better than a wave simulation, especially near the band edges.

To keep the computer cost reasonable, 500 realizations each with 50 random sites are considered for the modal approach. This ensures that the standard error[5] for the localization factor is consistently several orders of magnitude smaller than the mean. For the wave simulation, configurations are chosen according to the system parameters and are specified for each case considered.

Figure 5 displays the localization factor versus frequency for $\bar{R}=3.0$, $x_c=1.0$, and $\sigma=2.0$ percent. Since disorder has little effect on the attenuation in the stopbands, γ is only shown in the passbands. The modal coupling, $\bar{R}\phi_p^2/\bar{\lambda}_p$, decreases rapidly as the passband number increases, because for a cantilevered beam $\bar{\lambda}_p \simeq [(2p-1)\pi/2]^4$. The ratios of disorder to modal coupling for passbands one to four are 0.021, 0.81, 6.34, and 24.36, respectively. Therefore, we used the perturbation method for strong coupling case in the first two passbands, while we chose the weak coupling scheme for the last two. For all cases we used the full *multimode* representation of the subsystems. To validate the theoretical results, we performed wave and modal Monte Carlo simulations in the first two and last two passbands, respectively. We used the modal simulation for the third and fourth bands because we found that the wave simulation results deteriorate near the band edges. We chose a configuration of 750 realizations of 10 random sites for the wave simulation, although we observed that taking only two random sites gives accurate results as well.

The strong frequency dependence of γ in the first two passbands is readily observed in Fig. 5: Localization is maximum near the stopbands, an expected trend, and minimum near the midband. A consequence is that normal modes in the same passband can have very different degrees of localization.[6] The agreement between the theoretical and simulation results is excellent in the first passband, where localization is very weak.

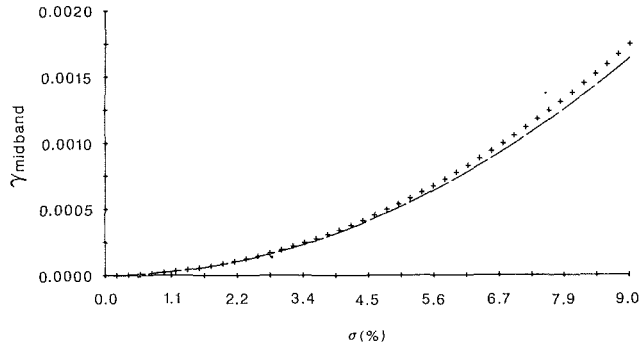

Fig. 7(*a*) First passband

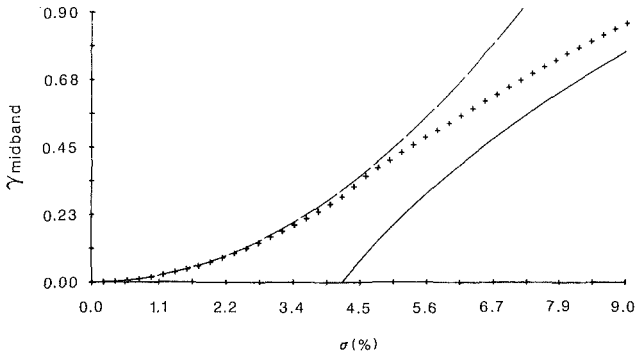

Fig. 7(*b*) Second passband

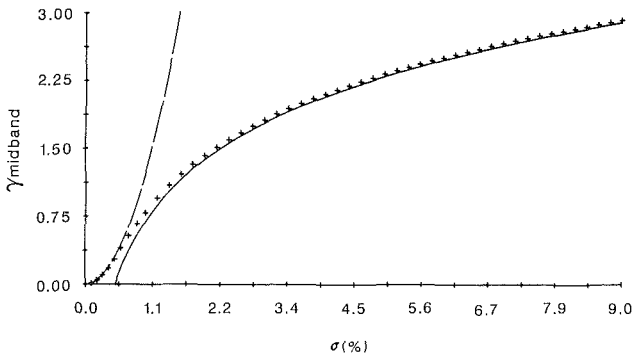

Fig. 7(*c*) Third passband

Fig. 7 Localization factor versus disorder at the first three midband frequencies, for $\bar{R}=3.0$ and $x_c=1.0$. (— —) classical perturbation; (—) modified perturbation; (+) Monte Carlo simulation.

The localization factor around midband increases approximately 1,000-fold from the first to the second passband. The agreement between simulation and perturbation is good over most of the second passband, except near the stopbands where the perturbation overpredicts the simulation; this is expected since $\gamma^{(c)} \to \infty$ at the passband edges. The agreement becomes worse in the second passband because the CPM approximation deteriorates as the modal coupling decreases. This deterioration takes place first for frequencies leading to large γ, that is, near the passband edges.

Figure 5 shows that localization becomes very strong in the third and fourth passbands. Unlike in the first and (to a lesser degree) second passbands, where γ in the stopbands is orders of magnitude larger than in the passbands, for the strong localization case the localization factors in the passbands and the stopbands have comparable magnitude. Also, contrary to the first two passbands, γ varies little with frequency in the third and fourth bands. Thus, we expect all normal modes to be strongly localized in these passbands. We also note that the

[5]The estimates of the standard deviation of γ divided by the square root of the number of realizations.

[6]Accepting the conjecture by Ishii (1973) that the forced vibration and free mode patterns are governed by the same exponential envelope at a given frequency.

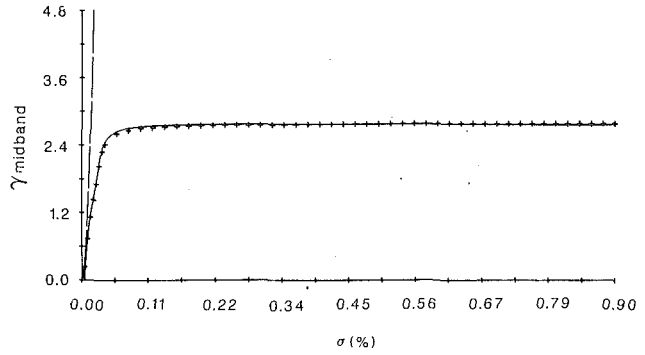

Fig. 8(*a*)

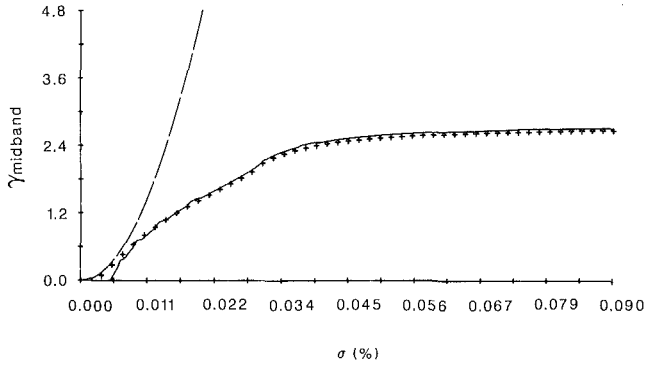

Fig. 8(*b*) Enlargement

Fig. 8 Localization factor versus disorder at the second midband frequency, for $\bar{R}=15.0$ and $x_c=0.78$. (— —) classical perturbation; (——) modified perturbation; (+) Monte Carlo simulation.

agreement between simulation and modified perturbation results is very good in the third passband. It becomes excellent in the fourth band because the modal coupling is smaller.

Finally, we found that the single-mode approximation of the MPM result, equation (32), agrees with simulation nearly as well as the multimode result in the third and fourth passbands. This confirms that the much simpler one-mode result is a valid approximation.

Figure 6 illustrates the effect of constraint location on the localization factor. The coupling spring is very close to the node of the second component mode ($\phi_2(x_c)\simeq 0$), and the static coupling is large and the disorder very small. If the constraint were at the tip, we would expect γ to be very small in the lower passbands, corresponding to weak localization. From Fig. 6, the localization factor is indeed small in passbands 1 and 3. The agreement between the wave simulation and the classical perturbation method is excellent in the first passband and good over most of the third band. Since the coupling constraint is near the node of the second mode, the corresponding modal coupling is very small ($\bar{R}\phi_2^2/\bar{\lambda}_2\simeq 0.000025$); thus, the multimode modified perturbation method is used in the second passband, and excellent agreement with the modal simulation is noted. We observe that localization in the second passband is severe, due to the location of the constraint, although it is weak in the neighboring passbands.

We found that the single-mode modified perturbation scheme ($p=2$ in equation (32)) grossly overestimates the localization factor in the second passband (this is shown in Fig. 6(*b*)), even though it gives very good results in cases of small coupling in Fig. 5. We can tentatively explain this by noting that the pth passband is nearly lost when the constraint location is near a node of the pth component mode; thus, the system practically does not vibrate in the pth mode, and the frequency range where the single-mode MPM for the $(p-1)$th passband applies is extended to encompass the pth passband. Indeed, we applied the MPM using the *first* modal representation ($p=1$ in equation (32)) for frequencies in the neighborhood of the *second* passband. Figure 6(*b*) shows that the maximum difference between the γ's obtained with MPM and simulation is less than 4 percent. This confirms our conjecture.

6 Localization Factors at Midband

The dependence of localization effects on the disorder to modal coupling ratio and the passband number is investigated by considering the midband frequencies, $(\omega_{p_m})_{p=1,\ldots,M}$, obtained from the dispersion relation for $k=\dfrac{\pi}{2}$, or $\beta^o=0$. In the strong coupling case, equation (24) gives, at midband,

$$\gamma_{p_m}^{(c)}=\frac{\sigma^2\alpha_{p_m}^2}{8R^2\phi_p^4/\lambda_p^2}. \tag{33}$$

The single-mode approximation of the localization factor at midband is given by equation (33) for $\alpha_{p_m}=1$. For weak coupling, the single-mode approximate modified perturbation scheme is used; from equations (25) and (32):

$$\gamma_{p_m}^{(m)}\simeq \ln\left|\frac{\sigma}{R\phi_p^2/\lambda_p}\right|+\ln\sqrt{3}-1. \tag{34}$$

The coefficient α_{p_m} is an explicit function of ω_{p_m}, which itself depends on R. Upon numerical examination, we found that α_{p_m} remains relatively constant when R varies, especially in the higher passbands, where it is almost equal to one. In the lower bands, where the CPM is valid, we found that α_{p_m} is a slowly increasing function of R. Thus, from equation (33), the localization factor does not vary exactly parabolically with $\sigma/(R\phi_p^2/\lambda_p)$ in the weak localization case, but increases at a slightly slower rate. Equation (34) exhibits its logarithmic variation in the strong localization case. Thus, as the disorder to coupling ratio increases from zero, the localization factor first increases nearly *parabolically*; once it reaches a large value (of the order of 0.5), its increase is more moderate, according to a *logarithmic* law.

Figure 7 displays the variation of γ in terms of the disorder strength for midband excitation with $\bar{R}=3.0$ and $x_c=1.0$. Monte Carlo simulation and multimode classical and modified perturbation results are shown. In the first passband, where weak localization occurs, the CPM tracks the numerical solution very well until $\sigma=9$ percent. In the second passband, the simulation and CPM results are in excellent agreement for $\sigma<4.5$ percent. As σ keeps increasing, the simulation diverges from the classical perturbation solution, and approaches the modified perturbation result. The Monte Carlo and the modified perturbation results are in excellent agreement in the third passband for $\sigma>1.0$ percent, corresponding to strong localization. Only for very small disorder is the CPM a good approximation in this weak coupling case. Figure 7 displays clearly the transition from parabolic to logarithmic variation (that is, from weak to strong localization). Similar results are expected if γ is plotted versus $1/\bar{R}$ instead of σ.

The dependence of γ on disorder strength is also investigated when the constraint is located near a component mode's node. Here, $x_c=0.78$, near the second mode's node. Only the second passband is considered, since in other bands the variation of γ is similar to that in Fig. 7. Figure 8 shows that for very small disorder the CPM approximates γ well, and that as disorder increases the MPM tracks the simulation result remarkably well. Interestingly, the localization factor reaches a saturation value as disorder increases to approximately 0.1 percent, and remains relatively constant thereafter. Thus, when the coupling constraint is near a node, disorder has an effect only up to a certain point, beyond which an increase in disorder strength

does not cause stronger localization. We found that this saturation value of $\gamma = 2.75$ is approximately equal to the decay factor in the stopbands adjacent to the second passband (this can be seen in Fig. 4(*b*)).

Finally, we consider the dependence of the localization factor on passband number. For a cantilevered beam, the free vibration eigenvalues increase asymptotically as $\bar{\lambda}_p \simeq [(2p-1)\pi/2]^4$, and equation (33) becomes

$$\gamma_{p_m}^{(c)} \simeq \frac{\sigma^2 \alpha_{p_m}^2 (2p-1)^8 \pi^8}{2048 \bar{R}^2 \phi_p^4}, \tag{35}$$

while equation (34) yields

$$\gamma_{p_m}^{(m)} \simeq 4 \ln |2p-1| + \ln \left| \frac{\sigma \pi^4}{16 \bar{R} \phi_p^2} \right| + \ln \sqrt{3} - 1. \tag{36}$$

For simplicity, we assume that ϕ_p is independent of p (this is true for coupling at the tip). For the case of weak localization, where the classical perturbation method applies, the localization factor varies approximately as p^8 (exactly so for a one-mode analysis), but only as $(\sigma/R)^2$. Thus, the degree of localization is much more sensitive to the passband number than to either the disorder or the static coupling strength. This implies that the transition from weak to strong localization occurs very rapidly with increasing passband number, which is observed in Fig. 5 from passband 2 to passband 3. Once the strong localization regime is reached, the degree of localization increases logarithmically with passband number, the same dependence it has on the disorder and coupling strength. This indicates that assemblies of beam-like subsystems, such as bladed-disk assemblies, are highly sensitive to irregularities, especially at high frequencies where several localization occurs.

7 Significance of Localization Effects

To illustrate confinement effects in engineering structures, consider the case $\bar{R} = 3.0$, $x_c = 1.0$, and $\sigma = 2$ percent. The simulated localization factors at the lower four midband frequencies are 0.000086, 0.068, 1.42, and 2.76, respectively. Since the vibration amplitude is governed, on the average, by $\exp(-\gamma N)$, 8100 sites are needed for the amplitude to decay by a factor of two in the first passband, but only ten sites are required in the second passband. In terms of energy, only 0.02 percent is transmitted to the third site in the third passband, and less than 0.002 percent is transmitted to the second site in the fourth passband. Recall that for a perfectly periodic (undamped) system 100 percent of the energy is transmitted. This spectacular localization is caused by a disorder of strength 2 percent only, which is difficult to avoid in engineering structures.

Our study has shown that strong modal coupling and small disorder lead to *weak* localization, characterized by very small rates of spatial decay. Typically, several thousand subsystems are needed for confinement to be significant. Few, if any, engineering structures consist of so many components. Furthermore, the effects of end conditions and damping probably conceal that of disorder when the localization factor is so small. Thus, weak localization appears to be of little importance in structural dynamics.

On the other hand, disordered assemblies with weak modal coupling experience *strong* localization, such that energy is confined to a few subsystems. Even for large static coupling and small disorder, strong localization is unavoidable at high frequencies. The placement of the coupling constraint near a node may also cause strong localization. Structural dynamicists should be fully aware of these drastic effects of small disorder.

8 Conclusions

The effects of disorder on the dynamics of assemblies of monocoupled, multimode subsystems were investigated by probabilistic perturbation methods and Monte Carlo simulations. While for an ordered assembly there are alternate frequency bands of propagation and attenuation, irregularities result in an exponential amplitude decay for all frequencies. The degree of localization depends primarily on the ratio of disorder to modal coupling: This dependence is nearly parabolic for small values of this ratio, and logarithmic for large values. Localization is strong for weak internal coupling, and the transition from weak to strong confinement occurs very rapidly with increasing passband number p (for small values, γ varies as p^8). Therefore, severe spatial attenuation is unavoidable at high frequencies.

Several fascinating issues regarding localization remain to be tackled. First, we must explore how (small) dissipation affects localization. Our goal is to identify the decay due to damping and that due to disorder in a typical structure. Second, since all engineering structures are finite, we must examine whether the "infinite" localization factors we calculate describe adequately confinement in structures with boundary conditions. For finite structures a modal analysis formulation may be more appropriate than the wave approach. Finally, we must determine whether the *average* localization factor describes the behavior of a *typical* nearly periodic structure (see the discussion in Hodges and Woodhouse, 1989). Deterministic techniques may have to be resorted to when there is considerable dispersion about the average.

Acknowledgment

This work is supported by National Science Foundation Grant No. MSM-8913196, Dynamic Systems and Control Program. Dr. Elbert L. Marsh is the grant monitor.

References

Bendiksen, O. O., 1987, "Mode Localization Phenomena in Large Space Structures," *AIAA Journal*, Vol. 25, No. 9, pp. 1241–1248.

Brillouin, L., 1953, *Wave Propagation in Periodic Structures*, 2nd ed., Dover Publications, New York.

Cha, P. D., and Pierre, C., 1989, "Eigensolution of Periodic Assemblies of Multi-Mode Component Systems," *Journal of Sound and Vibration*, Vol. 129, No. 1, pp. 168–174.

Cornwell, P. J., and Bendiksen, O. O., 1989a, "Localization of Vibration in Large Space Reflectors," *AIAA Journal*, Vol. 27, No. 2, pp. 219–226.

Cornwell, P. J., and Bendiksen, O. O., 1989b, "A Numerical Study of Vibration Localization in Disordered Cyclic Structures," *Proceedings of the 30th Structures, Structural Dynamics and Materials Conference*, Mobile, Ala., AIAA paper 89-1181-CP.

Dowell, E. H., 1972, "Free Vibrations of an Arbitrary Structure in Terms of Component Modes," ASME JOURNAL OF APPLIED MECHANICS, Vol. 39, No. 3, pp. 727–732.

Herbert, D. C., and Jones, R., 1971, "Localized States in Disordered Systems," *Journal of Physics C: Solid State Physics*, Vol. 4, pp. 1145–1161.

Hodges, C. H., 1982, "Confinement of Vibration by Structural Irregularity," *Journal of Sound and Vibration*, Vol. 82, No. 3, pp. 411–424.

Hodges, C. H., and Woodhouse, J., 1983, "Vibration Isolation from Irregularity in a Nearly Periodic Structure: Theory and Measurements," *Journal of Acoustical Society of America*, Vol. 74, No. 3, pp. 894–905.

Hodges, C. H., and Woodhouse, J., 1989, "Confinement of Vibration by One-Dimensional Disorder, I: Theory of Ensemble Averaging," *Journal of Sound and Vibration*, Vol. 130, No. 2, pp. 237–251.

Ishii, K., 1973, "Localization of Eigenstates and Transport Phenomena in the One-Dimensional Disordered System," *Supplement of the Progress of Theoretical Physics*, Vol. 53, pp. 77–138.

Kissel, G. J., 1987, "Localization in Disordered Periodic Structures," *Proceedings of the 28th Structures, Structural Dynamics and Materials Conference*, Monterey, Calif., AIAA paper 87-0819.

Kissel, G. J., 1988, "Localization in Disordered Periodic Structures," Ph.D. Dissertation, Massachusetts Institute of Technology, Cambridge, Mass.

Mead, D. J., 1975, "Wave Propagation and Natural Modes in Periodic Systems: I. Mono-Coupled Systems," *Journal of Sound and Vibration*, Vol. 40, No. 1, pp. 1–18.

Pierre, C., 1990, "Weak and Strong Vibration Localization in Disordered Structures: A Statistical Investigation," *Journal of Sound and Vibration*, Vol. 139, No. 1, pp. 111–132.

Pierre, C., and Cha, P. D., 1989, "Strong Mode Localization in Nearly Periodic Disordered Structures," *AIAA Journal*, Vol. 27, No. 2, pp. 227–241.

Pierre, C., and Dowell, E. H., 1987, "Localization of Vibrations by Structural Irregularity," *Journal of Sound and Vibration*, Vol. 114, No. 3, pp. 549–564.

Wei, S. T., and Pierre, C., 1988, "Localization Phenomena in Mistuned Assemblies with Cyclic Symmetry. Part I: Free Vibrations," *ASME Journal of Vibration, Acoustics, Stress, and Reliability in Design*, Vol. 110, No. 4, pp. 429–438.

APPENDIX A

Transfer Matrix Derivation

Consider the $M \times M$ matrix $[L]$, whose pth column is the vector of modal deflections at x_c and whose only other nonzero elements are 1's on the diagonal. This definition allows us to select a passband p of interest. For example, for $p=1$, premultiplying the first block equation in equation (5) by $[L]^{-1}$ gives, after manipulations:

$$\begin{bmatrix} w_c^{i+1} \\ 0 \\ \vdots \\ 0 \end{bmatrix} = [L]^{-1}[B^i][L]^{-T} \begin{bmatrix} w_c^i \\ \theta_2^i \\ \vdots \\ \theta_M^i \end{bmatrix} - \begin{bmatrix} w_c^{i-1} \\ 0 \\ \vdots \\ 0 \end{bmatrix} . \tag{A1}$$

Partitioning the above triple matrix product yields

$$\begin{bmatrix} w_c^{i+1} \\ \mathbf{0} \end{bmatrix} = \begin{bmatrix} E^i & \mathbf{F}^{iT} \\ \mathbf{F}^i & [G^i] \end{bmatrix} \begin{bmatrix} w_c^i \\ \overline{\boldsymbol{\Theta}}^i \end{bmatrix} - \begin{bmatrix} w_c^{i-1} \\ \mathbf{0} \end{bmatrix} \tag{A2}$$

where E^i, $\mathbf{F}^i$ and $[G^i]$ have dimensions 1×1, $(M-1) \times 1$, and $(M-1) \times (M-1)$, respectively. Eliminating $\overline{\boldsymbol{\Theta}}^i$ in equation (A2) gives equation (7), where

$$\beta^i = E^i - \mathbf{F}^{iT}[G^i]^{-1}\mathbf{F}_i \tag{A3}$$

and $[G^i]$ is nonsingular since $[B^i]$ is positive definite.

APPENDIX B

Transfer Matrix Expansion

For frequencies near the pth passband, we factor λ_p/R in $[B^i]$ to obtain a dimensionless frequency squared, ω^2/λ_p. We also factor $1/\phi_p$ in $[L]$, such that its pth diagonal element is 1. Thus,

$$[L]^{-1}[B^i][L]^{-T} = \frac{\lambda_p}{R\phi_p^2} \begin{bmatrix} E_p^i & \mathbf{F}_p^{iT} \\ \mathbf{F}_p^i & [G_p^i] \end{bmatrix} \tag{B1}$$

which yields equation (18). For small disorder to coupling ratio, we write $[B^i] = [B^o] + [b^i]$, where $[B^o]$ is given in equation (4) for $d\lambda^i = 0$ and $[b_p^i] = [\Lambda]d\lambda^i/R$. Thus,

$$\begin{bmatrix} E_p^i & \mathbf{F}_p^{iT} \\ \mathbf{F}_p^i & [G_p^i] \end{bmatrix} = \begin{bmatrix} E_p^o & \mathbf{F}_p^{oT} \\ \mathbf{F}_p^o & [G_p^o] \end{bmatrix} + d\lambda^i \begin{bmatrix} e_p & \boldsymbol{\Delta}_p^T \\ \boldsymbol{\Delta}_p & [g_p] \end{bmatrix} , \tag{B2}$$

Substituting equation (B2) into equation (A3) and expanding to the first order gives $\beta^i = \beta^o + \delta\beta^i$, where

$$\begin{cases} \beta^o = \dfrac{\lambda_p}{R\phi_p^2}\left(E_p^o - \mathbf{F}_p^{oT}[G_p^o]^{-1}\mathbf{F}_p^o\right) \quad (p=1,\ldots,m) \\ \delta\beta^i \simeq \dfrac{\lambda_p d\lambda^i}{R\phi_p^2}\left(e_p - \mathbf{F}_p^{oT}[G_p^o]^{-1}\boldsymbol{\Delta}_p\right. \\ \qquad \left. - \boldsymbol{\Delta}_p^T[G_p^o]^{-1}\mathbf{F}_p^o + \mathbf{F}_p^{oT}[G_p^o]^{-1}[g_p][G_p^o]^{-1}\mathbf{F}_p^o\right) \\ \qquad = \dfrac{\lambda_p}{R\phi_p^2}\alpha_p d\lambda^i \quad (p=1,\ldots,M) \end{cases} \tag{B3}$$

where α_p is a function of x_c and ω.

Journal of Applied Mechanics

Brief Notes

A Brief Note is a short paper that presents a specific solution of technical interest in mechanics but which does not necessarily contain new general methods or results. A Brief Note should not exceed 1500 words *or equivalent* (a typical one-column figure or table is equivalent to 250 words; a one line equation to 30 words). Brief Notes will be subject to the usual review procedures prior to publication. After approval such Notes will be published as soon as possible. The Notes should be submitted to the Technical Editor of the JOURNAL OF APPLIED MECHANICS. Discussions on the Brief Notes should be addressed to the Editorial Department, ASME, United Engineering Center, 345 East 47th Street, New York, N. Y. 10017, or to the Technical Editor of the JOURNAL OF APPLIED MECHANICS. Discussions on Brief Notes appearing in this issue will be accepted until two months after publication. Readers who need more time to prepare a Discussion should request an extension of the deadline from the Editorial Department.

On Natural Frequencies of Geometrically Imperfect, Simply-Supported Rectangular Plates Under Uniaxial Compressive Loading[1]

S. Ilanko[2] and S. M. Dickinson[3]

Introduction. The effects of geometric imperfections on the vibration behavior of biaxially compressed, simply-supported thin rectangular plates, with all edges free to move tangentially (shear free) but constrained to move with constant displacement in the direction normal to the edges, have been studied by Hui and Leissa (1983). A solution for von Karman's equations for finite deflections in terms of out-of-plane displacements and Airy stress functions was described. The compatibility equations were solved exactly, based on the assumption that the out-of-plane buckling (and/or vibration) modes were decoupled, and the Galerkin procedure was used to obtain an approximate solution for both the static and dynamic equilibrium equations. It was found that the natural frequencies increased considerably with initial geometrical imperfections as was observed subsequently by other researchers (Kapania and Yang, 1986; Ilanko and Dickinson, 1987) for similar problems.

In the present Note, a similar approach is described which is applicable to uniaxially loaded, simply-supported rectangular plates having two different sets of in-plane boundary conditions: Case (1), loaded edges subject to uniform static loading and free to move normally during vibration, with the other two edges free during both loading and vibration, and all four edges free to move tangentially at all times (that is, shear free); Case (2), as in Case (1), except that all four edges are fully tangentially restrained at all times (that is, shear diaphragm conditions). For these problems, Airy stress functions could not be obtained in exact, closed form; instead, they are taken as the summation of a series of beam functions (Bassily and Dickinson, 1977), the coefficients in the series being determined by solving the compatibility equations approximately using Galerkin's method.

Graphical results for the static deflection and fundamental frequencies of square plates, obtained using single terms for the out-of-plane displacements, are shown and agree very closely with equivalent results from a Rayleigh-Ritz displacement formulation (Ilanko and Dickinson, 1987).

Static Analysis. Consider the simply-supported geometrically imperfect plate of material having uniform thickness h, Young's modulus E, and Poisson's ratio ν with its edges lying in the xy-plane along $x = 0, a$ and $y = 0, b$. It is subject to uniform, uniaxial compressive loading of value N_x per unit width acting in the x-direction and applied along edges $x = 0, x = a$. The compatibility equation may be written in terms of Airy stress function F (Hui and Leissa, 1983)

$$\nabla^4 F = Eh[(z_{,xy})^2 - (z_{o,xy})^2 - z_{,xx}z_{,yy} + z_{o,xx}z_{o,yy}], \quad (1)$$

where the initial imperfection z_o and the static deflection under in-plane loading (both measured from the plane containing the edges of the plate) are given by

$$z_o = Z_o \sin(k\pi x/a)\sin(l\pi y/b) \quad (2a)$$

and

$$z = Z\sin(k\pi x/a)\sin(l\pi y/b). \quad (2b)$$

Substitution into equation (1) yields the equation

$$\nabla^4 F = Eh\pi^4(Z^2 - Z_o^2)k^2l^2[\cos(2k\pi x/a) + \cos(2l\pi y/b)]/(2a^2b^2). \quad (3)$$

It is convenient to express F as

$$F = F_o + F_z, \quad (4)$$

where F_o and F_z are the stress functions due to in-plane displacements and out-of-plane displacements, respectively, and F_o satisfies the equation $\nabla^4 F_o = 0$ and F_z satisfies equation (3). The function F must also satisfy the in-plane boundary conditions which are as follows:

Case (1): At $x = 0$ and $x = a$, $F_{,yy} = -N_x$ and $F_{,xy} = 0$, and at $y = 0$ and $y = b$, $F_{,xx} = F_{,xy} = 0$. These are satisfied, provided that the function F_o and F_z meet the conditions that $F_{o,yy} = -N_x$, $F_{o,xy} = F_{z,xy} = F_{z,yy} = 0$ at $x = 0$ and $x = a$, and $F_{o,xx} = F_{o,xy} = F_{z,xx} = F_{z,xy} = 0$ at $y = 0$ and $y = b$.

Case (2): At $x = 0$ and $x = a$, $F_{,yy} = -N_x$ and $F_{,xx} - \nu F_{,yy} = 0$, and at $y = 0$ and $y = b$, $F_{,xx} = F_{,yy} - \nu F_{,xx} = 0$.

[1]This work was made possible by a grant from the Canadian Natural Sciences and Engineering Research Council.

[2]Department of Mechanical Engineering, University of Canterbury, Christchurch, New Zealand.

[3]Department of Mechanical Engineering, The University of Western Ontario, London, Ontario, N6A 5B9, Canada.

Contributed by the Applied Mechanics Division of THE AMERICAN SOCIETY OF MECHANICAL ENGINEERS. Manuscript received by the ASME Applied Mechanics Division, Dec. 5, 1989; final revision, Mar. 28, 1990.

These are satisfied if $F_{o,yy} = -N_x$, $F_{o,xx} - \nu F_{o,yy} = F_{z,yy} = F_{z,xx} - \nu F_{z,yy} = 0$ at $x = 0$ and $x = a$, and $F_{o,xx} = F_{o,yy} - \nu F_{o,xx} = F_{z,xx} = F_{z,yy} - \nu F_{z,xx} = 0$ at $y = 0$ and $y = b$.

Following an analogy between the Airy stress function and the out-of-plane displacement of a thin plate (Bassily and Dickinson, 1977), the function F_z may be expressed in the form

$$F_z = \Sigma\Sigma\alpha_{pq}\phi_p(x)\psi_q(y),\ p,\ q = 1,2\ \ldots \tag{5}$$

where $\phi_p(x)$ and $\psi_q(y)$ are the characteristic functions for a flexurally vibrating clamped/clamped beam for case (1) and for a simply-supported/simply-supported beam for case (2). These functions satisfy the appropriate boundary conditions for F_z. The coefficients α_{pq} may be determined in terms of z by using $\phi_r(x)\ \psi_s(y)$ as the weighting function in a Galerkin solution of equation (3):

$$\int_{x=0}^{a}\int_{y=0}^{b} \nabla^4 F_z \phi_r(x)\psi_s(y)dxdy = (Eh\pi^4(Z^2 - Z_o^2)/(kl/ab)^2/2) \int_{x=0}^{a}\int_{y=0}^{b} [\cos(2k\pi x/a) + \cos(2l\pi y/b)]\phi_r(x)\psi_s(y)dxdy.$$

An Airy stress function F_o satisfying the boundary condition for case (1) may be written, simply, $F_o = -N_x y^2/2$, but for case (2) it is necessary to use a series for F_o. One such series is

$$F_o = (4b^2N_x/\pi^3 h)\Sigma_m(1/m^3)\phi_o(x)\sin(m\pi y/b) + \Sigma_n\Sigma_m B_{mn}\sin(m\pi x/a)\sin(n\pi y/b), \tag{6}$$

where $\phi_o(x) = 1 - \nu a^2/(4b^2) + (\nu a^2/(4b^2))\cos(2m\pi x/a)$, and $m,\ n = 1,3,5\ \ldots$. The coefficients B_{mn} are determined by solving the Galerkin equation

$$\int_{x=0}^{a}\int_{y=0}^{b} (\nabla^4 F_o)\sin(r\pi x/a)\sin(s\pi y/b)dxdy = 0 \text{ and are}$$

$$B_{mn} = -4\gamma N_x a^2[\nu mn(\gamma^4 + 8\gamma^2 + 16)/(\gamma m^2 - 4\gamma n^2) + \gamma n(4 - \nu\gamma^2)/m]/[\pi^4 h(m^2 + \gamma^2 n^2)^2], \text{ in which } \gamma = a/b.$$

The final step in the static analysis is the solution of the equilibrium equation (Hui and Leissa, 1983)

$$D\nabla^4(z - z_o) = [F_{,yy}z_{,xx} + F_{,xx}z_{,yy} - 2F_{,xy}z_{,xy}], \tag{7}$$

where D is the plate rigidity given by $D = Eh^3/12(1 - \nu^2)$. Substitution of equations (2) and (4) into equation (7) and again using Galerkin's method with the weighting function $\sin(k\pi x/a)\sin(l\pi y/b)$ leads to the equation, in nondimensional form,

$$(\mu - \mu_o) = \xi\mu N_x/N_{xc} - \zeta\mu(\mu^2 - \mu_o^2). \tag{8}$$

Here, $\mu = Z/h$, $\mu_o = Z_o/h$, N_{xc} is the critical in-plane load of a uniformly stressed, simply-supported plate corresponding to the (k, l) mode and is given by $N_{xc} = D(\pi a/k)^2[(k/a)^2 + (l/b)^2]^2$, and the coefficients ξ and ζ depend upon the case being considered.

Vibration Analysis. The dynamic out-of-plane displacement in the (m, n) mode is expressible $w(x, y, t) = W(x, y)e^{i\omega t}$, where w is measured from the static, loaded, equilibrium position, ω is the radian natural frequency, and W the maximum displacement with respect to time and is given by

$$W = H\sin(m\pi x/a)\sin(n\pi y/b).$$

The compability equation in terms of the dynamic Airy stress function f is (see Hui and Leissa, 1983)

$$\nabla^4 f = Eh(2z_{,xy}W_{,xy} - z_{,xx}W_{,yy} - z_{,yy}W_{,xx}). \tag{9}$$

As in the static analysis, the dynamic Airy stress function f can be expressed in the form

$$f = \sum_p\sum_q \beta_{pq}\phi_p(x)\psi_q(y),\ p,\ q = 1,2,3\ \ldots, \tag{10}$$

where ϕ and ψ are appropriate beam vibration characteristic functions. Here it is not necessary to consider $f = f_o + f_z$ as there is no dynamic edge loading.

Substitution for z and w into equation (9) and using Galerkin's method gives

$$\int_{x=0}^{a}\int_{y=0}^{b} \nabla^4\left(\sum_p\sum_q \beta_{pq}\phi_p\psi_q\right)\phi_r\psi_s dxdy = ZH\int_{x=0}^{a}\int_{y=0}^{b} G(x,y)\phi_r\psi_s dxdy,$$

where $G(x, y) = (Eh\pi^4/(a^2b^2))[2klmn\cos(k\pi x/a)\cos(m\pi x/a)\cos(n\pi y/b)\cos(l\pi y/b) - (k^2n^2 + l^2m^2)\sin(m\pi x/a)\sin(n\pi y/b)\sin(k\pi x/a)\sin(l\pi y/b)]$.

Finally, Galerkin's method is again used to solve the equation of motion for small amplitude flexural vibration to obtain

$$D\int_{x=0}^{a}\int_{y=0}^{b} [\nabla^4 w - (\rho h\omega^2/D)w]\sin(m\pi x/a)\sin(n\pi y/b)dxdy = \int_{x=0}^{a}\int_{y=0}^{b} [F_{,yy}W_{,xx} + F_{,xx}W_{,yy} - 2F_{,xy}W_{,xy} + f_{,yy}z_{,xx} + f_{,xx}z_{,yy} - 2f_{,xy}z_{,xy}]\sin(m\pi x/a)\sin(n\pi y/b)dxdy,$$

where ρ is the density of the plate material. After some algebra, this equation can be written in nondimensional form

$$1 - (\omega/\Omega)^2 - \xi N_x/N_{xc} + \eta\mu^2 + \delta(\mu^2 - \mu_o^2) = 0, \tag{11}$$

where Ω is the radian natural frequency of the corresponding flat, stress-free plate. In the special case where $k = m$ and $l = n$ (that is, vibration and static deflection shapes being the same), it can be shown that the coefficients $\eta = 2\zeta$ and $\delta = \zeta$.

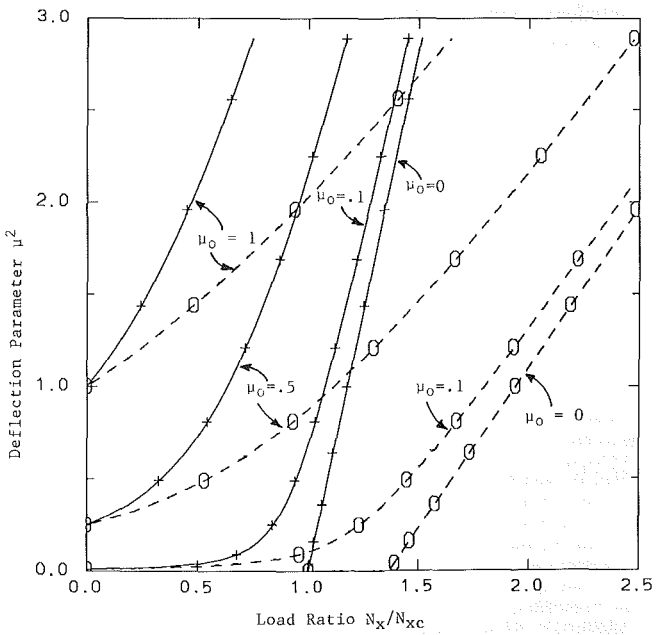

Fig. 1 Load-deflection relationship; Galerkin's Case 1 = ———, Case 2 = - - - - - - - ; Rayleigh-Ritz's Case 1 = +, Case 2 = 0

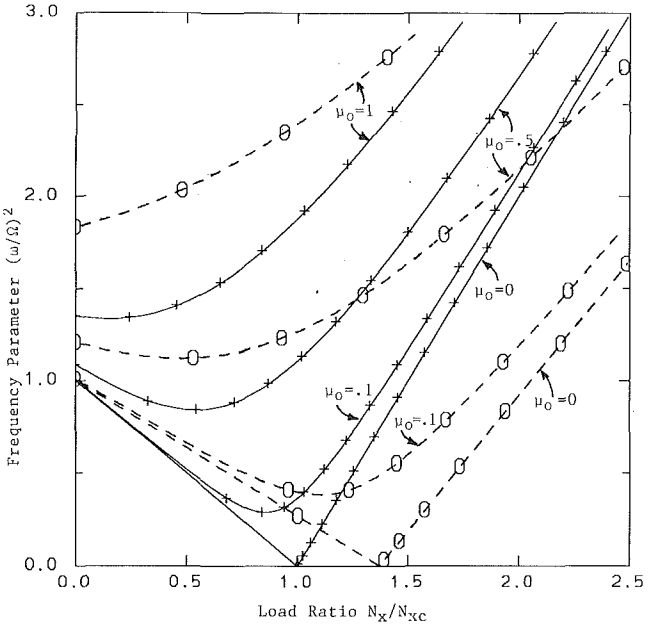

Fig. 2 Load-frequency relationship (key as for Fig. 1)

Results and Discussion. Numerical results were calculated for the static deflection and fundamental natural frequency of vibration for square plates having various degrees of initial imperfection. The imperfection and subsequent static and dynamic displacements were all taken to be of the single term form, $\sin(\pi x/a)\sin(\pi y/a)$, corresponding to the fundamental vibration and buckling mode shape, with the central displacements Z_o, Z, and H, appropriately. For the Airy stress function series (5) and (10), the first three symmetrical beam modes were taken (p, q = 1, 3, 5) and, in equation (6), the first series was summed to infinity and the double series was summed over m, n = 1, 3, 5 . . . 11. A value of 0.3 was used for Poisson's ratio.

The values calculated for ξ and ζ were, respectively, 1.000 and 0.177 for Case (1) and 0.730 and 0.418 for Case (2). These agree closely with those obtained from a Rayleigh-Ritz displacement solution (Ilanko and Dickinson, 1987), using an equivalent number of terms, which gives 1.000, 0.178, 0.731, and 0.417, respectively. The results are shown graphically in Figs. 1 and 2, where the considerable effect of the initial imperfection may be observed. The stiffening effect of the tangential edge restraint in Case (2) is also very evident in Fig. 1, where the flat-plate buckling load may be seen to have been increased by 37 percent and the square of the nondimensional central deflection, μ^2, is very significantly reduced. The effect of the tangential restraint on the natural frequency parameter $(\omega/\Omega)^2$ is rather more complicated since the frequencies tend to increase due to the in-plane stiffening effect but to decrease due to the reduced out-of-plane curvature.

References

Bassily, S. F., and Dickinson, S. M., 1977, "The Plane Stress Problem for Rectangular Regions Treated Using Functions Related to Beam Flexure," *Int. Journal of Mechanical Sciences*, Vol. 19, No. 11, pp. 639–650.

Hui, D., and Leissa, A. W., 1983, "Effects of Geometric Imperfections on Vibrations of Biaxially Compressed Rectangular Flat Plates," ASME JOURNAL OF APPLIED MECHANICS, Vol. 50, pp. 750–756.

Ilanko, S., and Dickinson, S. M., 1987, "The Vibration and Post-Buckling of Geometrically Imperfect, Simply Supported, Rectangular Plates Under Uniaxial Loading. Part I: Theoretical Approach, Part II: Experimental Investigation," *Journal of Sound and Vibration*, Vol. 118, No. 2, pp. 313–351.

Kapania, R. K., and Yang, T. Y., 1986, "Buckling, Post Buckling and Non-Linear Vibration of Imperfect Laminated Plates," Proceedings of the ASME Pressure Vessels and Piping Conference, Chicago.

Accurate Dilatation Rates for Spherical Voids in Triaxial Stress Fields

Y. Huang[4]

Introduction

In the course of a study of cavitation in elastic-plastic solids (Huang, Hutchinson, and Tvergaard, 1989), it was discovered that the well-known and widely used formula of Rice and Tracey (1969) significantly underestimates the dilatation rate of an isolated void subject to stress fields with moderate to high triaxiality. The purpose of this Note is to indicate why earlier analyses lead to underestimates and to provide accurate results.

Attention is limited to a spherical void in an infinite rigid-perfectly plastic solid characterized by the Mises yield condition, $\sigma_e = \sigma_Y$, where $\sigma_e = (3s_{ij}s_{ij}/2)^{1/2}$ with s_{ij} as the stress deviator. Remote from the void, the nonzero stresses satisfy $\sigma^\infty_{11} = \sigma^\infty_{22}$ and $\sigma^\infty_{33} - \sigma^\infty_{11} = \sigma_Y$. The nonzero strain rates in the remote field are $\dot\epsilon^\infty_{33} = -2\dot\epsilon^\infty_{11} = -2\dot\epsilon^\infty_{22} \equiv \dot\epsilon$ with $\dot\epsilon > 0$.

The Rice-Tracey high triaxiality approximation for the effect of the remote mean stress, $\sigma_m = \frac{1}{3}\sigma^\infty_{kk}$, on the dilatation rate is

$$\left(\frac{\dot V}{\dot\epsilon V}\right)_0 = 0.850 \exp\left(\frac{3\sigma_m}{2\sigma_Y}\right) \tag{1}$$

where V is the current volume of the void and $\dot V$ is the volume increment induced by the remote strain increment $\dot\epsilon$.

2 Variational Principle and Solution Method

The solution method is that suggested by Rice and Tracey (1969) and later adopted by Budiansky, Hutchinson, and Slutsky (1982). It involves minimization of the functional of the velocities

$$\Phi = \int_\Omega (s_{ij} - s^\infty_{ij})\,\dot\epsilon_{ij} d\Omega - \sigma^\infty_{ij}\int_S n_i v_j dS \tag{2}$$

where $\dot\epsilon_{ij} = \frac{1}{2}(v_{i,j} + v_{j,i})$, Ω is the infinite volume exterior to the void, S is the surface of the void, and n_i is the unit normal vector to S pointing out of the void. The solid is incompressible so the velocity field must satisfy $v_{k,k} = 0$. The deviator stress in equation (2) is that associated with $\dot\epsilon_{ij}$ through the yield condition, i.e.,

$$s_{ij} = \sigma_Y \dot\epsilon_{ij}/(3\dot\epsilon_{kl}\dot\epsilon_{kl}/2)^{1/2}. \tag{3}$$

The remote strain rate $\dot\epsilon^\infty_{ij}$ is prescribed and an additional velocity field v^*_i is defined so that

$$\dot\epsilon_{ij} = \dot\epsilon^\infty_{ij} + \dot\epsilon^*_{ij} \text{ with } \dot\epsilon^*_{ij} = \frac{1}{2}(v^*_{i,j} + v^*_{j,i}). \tag{4}$$

Among all additional fields satisfying $v^* = o(r^{-3/2})$ as $r \to \infty$, the exact field minimizes Φ.

Radial and azimuthal components, v^*_r and v^*_θ, of the axisymmetric additional field can be generated from a stream function $\chi(r,\theta)$ according to

$$v^*_r = -r^{-2}(\sin\theta)^{-1}(\chi \sin\theta)_{,\theta},\ v^*_\theta = r^{-1}\chi_{,r}. \tag{5}$$

Following Budiansky et al. (1982), we take

$$\chi(r,\theta) = A\cot\theta + \sum_{k=2,4,\ldots} P_{k,\theta}(\cos\theta) f_k(r) \tag{6}$$

where P_k is the Legendre Polynomial of degree k. The first

[4]Division of Applied Sciences, Harvard University, Cambridge, MA 02138.

Manuscript received by the ASME Applied Mechanics Division, Dec. 28, 1989; final revision, Oct. 18, 1990.

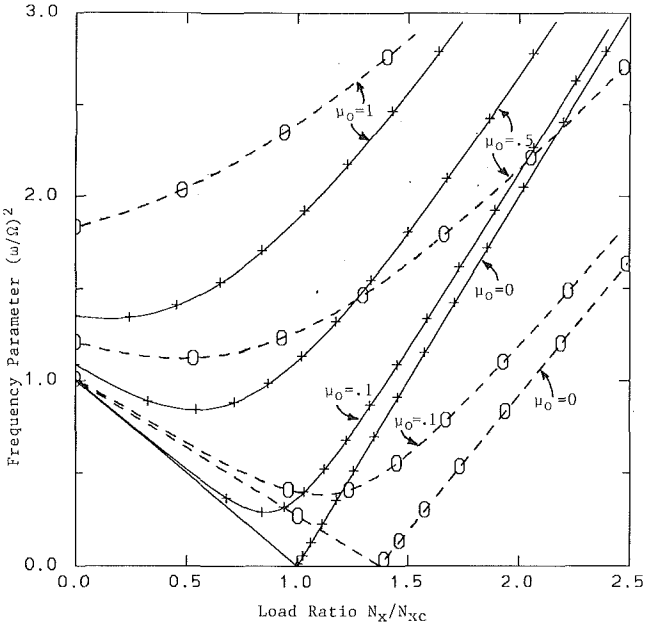

Fig. 2 Load-frequency relationship (key as for Fig. 1)

Results and Discussion. Numerical results were calculated for the static deflection and fundamental natural frequency of vibration for square plates having various degrees of initial imperfection. The imperfection and subsequent static and dynamic displacements were all taken to be of the single term form, $\sin(\pi x/a)\sin(\pi y/a)$, corresponding to the fundamental vibration and buckling mode shape, with the central displacements Z_o, Z, and H, appropriately. For the Airy stress function series (5) and (10), the first three symmetrical beam modes were taken (p, q = 1, 3, 5) and, in equation (6), the first series was summed to infinity and the double series was summed over m, n = 1, 3, 5 . . . 11. A value of 0.3 was used for Poisson's ratio.

The values calculated for ξ and ζ were, respectively, 1.000 and 0.177 for Case (1) and 0.730 and 0.418 for Case (2). These agree closely with those obtained from a Rayleigh-Ritz displacement solution (Ilanko and Dickinson, 1987), using an equivalent number of terms, which gives 1.000, 0.178, 0.731, and 0.417, respectively. The results are shown graphically in Figs. 1 and 2, where the considerable effect of the initial imperfection may be observed. The stiffening effect of the tangential edge restraint in Case (2) is also very evident in Fig. 1, where the flat-plate buckling load may be seen to have been increased by 37 percent and the square of the nondimensional central deflection, μ^2, is very significantly reduced. The effect of the tangential restraint on the natural frequency parameter $(\omega/\Omega)^2$ is rather more complicated since the frequencies tend to increase due to the in-plane stiffening effect but to decrease due to the reduced out-of-plane curvature.

References

Bassily, S. F., and Dickinson, S. M., 1977, "The Plane Stress Problem for Rectangular Regions Treated Using Functions Related to Beam Flexure," *Int. Journal of Mechanical Sciences*, Vol. 19, No. 11, pp. 639–650.

Hui, D., and Leissa, A. W., 1983, "Effects of Geometric Imperfections on Vibrations of Biaxially Compressed Rectangular Flat Plates," ASME JOURNAL OF APPLIED MECHANICS, Vol. 50, pp. 750–756.

Ilanko, S., and Dickinson, S. M., 1987, "The Vibration and Post-Buckling of Geometrically Imperfect, Simply Supported, Rectangular Plates Under Uniaxial Loading. Part I: Theoretical Approach, Part II: Experimental Investigation," *Journal of Sound and Vibration*, Vol. 118, No. 2, pp. 313–351.

Kapania, R. K., and Yang, T. Y., 1986, "Buckling, Post Buckling and Non-Linear Vibration of Imperfect Laminated Plates," Proceedings of the ASME Pressure Vessels and Piping Conference, Chicago.

Accurate Dilatation Rates for Spherical Voids in Triaxial Stress Fields

Y. Huang[4]

Introduction

In the course of a study of cavitation in elastic-plastic solids (Huang, Hutchinson, and Tvergaard, 1989), it was discovered that the well-known and widely used formula of Rice and Tracey (1969) significantly underestimates the dilatation rate of an isolated void subject to stress fields with moderate to high triaxiality. The purpose of this Note is to indicate why earlier analyses lead to underestimates and to provide accurate results.

Attention is limited to a spherical void in an infinite rigid-perfectly plastic solid characterized by the Mises yield condition, $\sigma_e = \sigma_Y$, where $\sigma_e = (3s_{ij}s_{ij}/2)^{1/2}$ with s_{ij} as the stress deviator. Remote from the void, the nonzero stresses satisfy $\sigma^\infty_{11} = \sigma^\infty_{22}$ and $\sigma^\infty_{33} - \sigma^\infty_{11} = \sigma_Y$. The nonzero strain rates in the remote field are $\dot\epsilon^\infty_{33} = -2\dot\epsilon^\infty_{11} = -2\dot\epsilon^\infty_{22} \equiv \dot\epsilon$ with $\dot\epsilon > 0$.

The Rice-Tracey high triaxiality approximation for the effect of the remote mean stress, $\sigma_m = \frac{1}{3}\sigma^\infty_{kk}$, on the dilatation rate is

$$\left(\frac{\dot V}{\dot\epsilon V}\right)_0 = 0.850 \exp\left(\frac{3\sigma_m}{2\sigma_Y}\right) \tag{1}$$

where V is the current volume of the void and $\dot V$ is the volume increment induced by the remote strain increment $\dot\epsilon$.

2 Variational Principle and Solution Method

The solution method is that suggested by Rice and Tracey (1969) and later adopted by Budiansky, Hutchinson, and Slutsky (1982). It involves minimization of the functional of the velocities

$$\Phi = \int_\Omega (s_{ij} - s^\infty_{ij})\,\dot\epsilon_{ij} d\Omega - \sigma^\infty_{ij}\int_S n_i v_j dS \tag{2}$$

where $\dot\epsilon_{ij} = \frac{1}{2}(v_{i,j} + v_{j,i})$, Ω is the infinite volume exterior to the void, S is the surface of the void, and n_i is the unit normal vector to S pointing out of the void. The solid is incompressible so the velocity field must satisfy $v_{k,k} = 0$. The deviator stress in equation (2) is that associated with $\dot\epsilon_{ij}$ through the yield condition, i.e.,

$$s_{ij} = \sigma_Y \dot\epsilon_{ij}/(3\dot\epsilon_{kl}\dot\epsilon_{kl}/2)^{1/2}. \tag{3}$$

The remote strain rate $\dot\epsilon^\infty_{ij}$ is prescribed and an additional velocity field v^*_i is defined so that

$$\dot\epsilon_{ij} = \dot\epsilon^\infty_{ij} + \dot\epsilon^*_{ij} \text{ with } \dot\epsilon^*_{ij} = \frac{1}{2}(v^*_{i,j} + v^*_{j,i}). \tag{4}$$

Among all additional fields satisfying $v^* = o(r^{-3/2})$ as $r \to \infty$, the exact field minimizes Φ.

Radial and azimuthal components, v^*_r and v^*_θ, of the axisymmetric additional field can be generated from a stream function $\chi(r,\theta)$ according to

$$v^*_r = -r^{-2}(\sin\theta)^{-1}(\chi \sin\theta)_{,\theta},\ v^*_\theta = r^{-1}\chi_{,r}. \tag{5}$$

Following Budiansky et al. (1982), we take

$$\chi(r,\theta) = A\cot\theta + \sum_{k=2,4,\ldots} P_{k,\theta}(\cos\theta) f_k(r) \tag{6}$$

where P_k is the Legendre Polynomial of degree k. The first

[4]Division of Applied Sciences, Harvard University, Cambridge, MA 02138.

Manuscript received by the ASME Applied Mechanics Division, Dec. 28, 1989; final revision, Oct. 18, 1990.

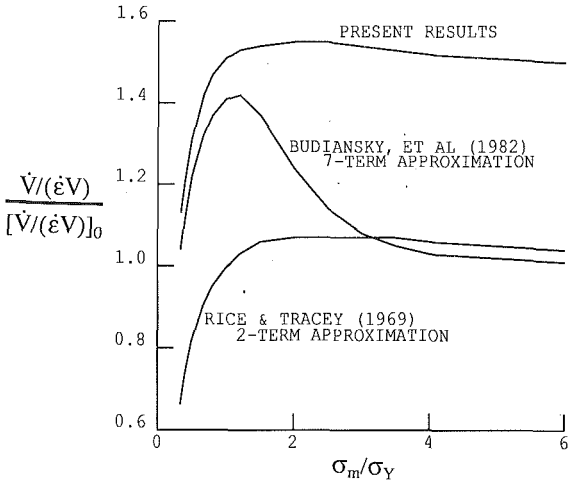

Fig. 1 Dilatation rate in a rigid-perfectly plastic solid as computed at various levels of approximation. The high triaxiality approximation $[\dot{V}/(\dot{\epsilon}\,V)]_0$ in (1) is used to normalize the results. The present results are believed to have converged.

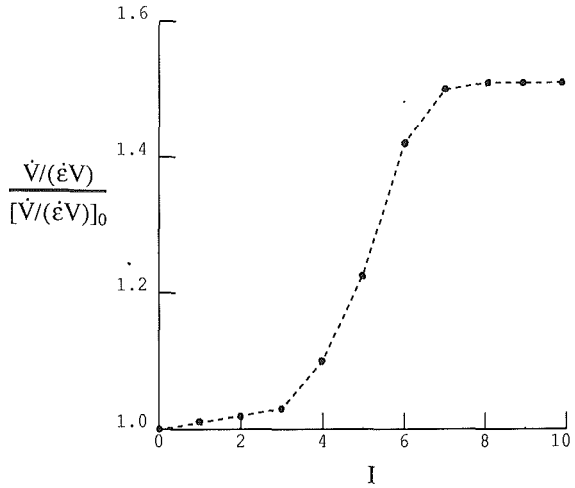

Fig. 2 Convergence study for $\sigma_m/\sigma_Y = 4$. Minimization is carried out with respect to $5I+1$ terms (A, $A_k^{(i)}$ for $k = 2,4,6,8,10$ and $i = 1,I$).

term in (6) generates the spherically symmetric contribution to the field. The amplitude A and the unknown functions $f_k(r)$ must be chosen to minimize Φ. The dilatation rate is computed using

$$\dot{V} = \int_S v_r dS = 4\pi A \tag{7}$$

involving just the spherically symmetric term. The additional terms in (6) influence the shape change of the void and the dilatation rate through their interaction with A.

3 Dilatation Rates

The high triaxiality approximation (1) was obtained by Rice and Tracey (1969) by minimizing Φ with respect to just the spherically symmetric term in (6) with amplitude A. They also investigated the accuracy of (1) by carrying out a numerical study in which they minimized Φ with respect to pairs of functions, involving A and the amplitude of a term with fixed $f_2(r)$. They found relatively little sensitivity to the particular choice of f_2. A plot of the dilatation rate, $\dot{V}/(\dot{\epsilon}\,V)$, obtained from one of their two-term numerical solutions is shown in Fig. 1, where the high triaxiality approximation (1) is used as a normalization.

Budiansky et al. (1982) let

$$f_k(r) = \sum_{i=1,2,\ldots} A_k^{(i)} r^{1-i} \tag{8}$$

and minimized Φ with respect to A and various sets of the $A_k^{(i)}$'s. Most of their calculations were carried out with the seven amplitude factors: A, $A_k^{(i)}$ with $k = 2,4$ and $i = 1,3$. The dilatation rate computed numerically using these seven terms in the minimization is also shown in Fig. 1. At very high triaxiality, the dilatation rate predicted using their choice of terms also appears to approach the high triaxiality approximation (1).

A systematic convergence study was conducted in the present work using as many as five sets of terms in the θ expansion in (6) and ten terms in each of the $f_k(r)$ for a total of 51 free amplitude factors (i.e., A and $A_k^{(i)}$ for $k = 2,4,6,8,10$ with $i = 1,10$). An example illustrating convergence with the number of terms in the expansion of the $f_k(r)$ is shown in Fig. 2. The results presented in Fig. 1 were obtained using 51 free amplitude factors and are believed to have converged. (It should also be mentioned that considerable care was taken to ensure that no error arose from the numerical integrations involved in minimizing Φ.)

As seen in Fig. 1, the high triaxiality approximation (1) underestimates the dilatation rate by about 50 percent at all triaxiality levels above $\sigma_m/\sigma_Y = 1$. A fairly good approximation for $\sigma_m/\sigma_Y \geq 1$ is clearly

$$\frac{\dot{V}}{\dot{\epsilon}\,V} = 1.28 \exp\left(\frac{3\sigma_m}{2\sigma_Y}\right). \tag{9}$$

For lower triaxiality,

$$\frac{\dot{V}}{\dot{\epsilon}\,V} = 1.28 \left(\frac{\sigma_m}{\sigma_Y}\right)^{\frac{1}{4}} \exp\left(\frac{3\sigma_m}{2\sigma_Y}\right), \quad \frac{1}{3} \leq \frac{\sigma_m}{\sigma_Y} \leq 1 \tag{10}$$

gives a reasonable fit to the present results in Fig. 1. At remote uniaxial tension, $\sigma_m/\sigma_Y = 1/3$, the error is less than 1 percent. For $1/3 \leq \sigma_m/\sigma_Y \leq 1$, the maximum error of (10) is less than 5 percent.

4 Effect of Elasticity on Dilatation Rates

Elasticity has a significant effect on the dilatation rate of an isolated void at high triaxiality. Huang et al. (1989) calculated the normalized dilatation rate of a void in an elastic-perfectly plastic solid at several levels of yield stress to Young's modulus, σ_Y/E, including the rigid-perfectly plastic limit, $\sigma_Y/E = 0$, presented in this work. The elastic-perfectly plastic solid has a cavitation limit in that the dilatation rate becomes unbounded as σ_m/σ_Y approaches a limiting value. For a Poisson's ratio of 0.3, the cavitation limit of σ_m/σ_Y is about 3.6 for $\sigma_Y/E = 0.005$, 3.9 for $\sigma_Y/E = 0.003$, and 4.7 for $\sigma_Y/E = 0.001$. The cavitation limit is unbounded as $\sigma_Y/E \to 0$. Elasticity clearly influences the dilatation rate at triaxiality levels above $\sigma_m/\sigma_Y = 2$. Further details are given in the paper by Huang et al. (1989).

Acknowledgments

The author gratefully appreciates suggestions and comments from Prof. J. W. Hutchinson. Discussions with Prof. J. R. Rice and his comments are also appreciated. This work was supported in part by the Materials Research Laboratory under Grant NSF-DMR-86-14003 and in part by Division of Applied Sciences, Harvard University.

References

Budiansky, B., Hutchinson, J. W., and Slutsky, S., 1982, "Void Growth and Collapse in Viscous Solids," *Mechanics of Solids, The Rodney Hill 60th Anniversary Volume*, H. G. Hopkins, and M. J. Sewell, eds., Pergamon Press, Oxford, pp. 13-45.

Huang, Y., Hutchinson, J. W., and Tvergaard, V., 1989, "Cavitation Instabilities in Elastic-Plastic Solids," Division of Applied Sciences, Harvard University, Report # Mech-153, to appear in *J. Mech. Phys. Solids.*

Rice, J. R., and Tracey, D. M., 1969, "On the Ductile Enlargement of Voids in Triaxial Stress Fields," *J. Mech. Phys. Solids,* Vol. 17, pp. 201-217.

A New Expression of the Energy Theorem in Discrete Mechanical Systems

René Souchet[5]

Recently, Kane and Levinson proposed testing numerical integrations by a checking function using an expression of the energy theorem involving the well-known Hamiltonian function. This paper deals with a new expression of this energy theorem that gives an alternative to the Kane-Levinson checking function.

1 Introduction

Kane and Levinson (1988) proposed to test numerical integrations of equations of motion of discrete mechanical systems by using the checking function C defined as:

$$C=H+Z,\ H=V+K_2-K_o. \tag{1}$$

In this formula, V is a potential function for given forces, K_2 and K_o are the usual homogeneous parts of the kinetic energy K, and Z is a function defined by the differential equation:

$$\dot{Z}=f(t,\ q_1,\ \ldots,\ q_n,\ u_1,\ \ldots,\ u_p), \tag{2}$$

$q=(q_1,\ \ldots,\ q_n)$ being generalized coordinates, and $u_1,\ \ldots,\ u_p$ $(p<n)$ being generalized velocities (Kane and Levinson, 1985). The function f takes into account some nonintegrable parts of both kinetic energy and dissipative forces.

However, it is possible to propose alternatives to the above function C. In order to highlight the real behavior of equation (1), we now turn to the introductory example given by Kane and Levinson (1988). Using the notations of Kane and Levinson (1988), we have the energy equation:

$$\frac{d}{dt}H-\frac{\partial}{\partial t}H=0 \tag{3}$$

where

$$V=-mgR\cos q_1,\ K_2=\frac{1}{2}mR^2{u_1}^2,\ K_o=\frac{1}{2}mR^2\Omega^2\sin^2 q_1. \tag{4}$$

We note that H depends explicitly of t, if Ω is not constant. Applying the results of Kane and Levinson (1988), we define Z by:

$$\dot{Z}=-\frac{\partial H}{\partial t}=\frac{\partial K_o}{\partial t}=mR^2\Omega\dot{\Omega}\sin^2 q_1 \tag{5}$$

so that we have

$$C=V+K_2-K_o+Z. \tag{6}$$

Now, if we develop (3), we obtain:

$$\frac{d}{dt}\{V+K_2\}-mR^2\Omega\dot{\Omega}\sin^2 q_1$$

$$-mR^2\Omega^2\dot{q}_1\sin q_1\cos q_1+mR^2\Omega\dot{\Omega}\sin^2 q_1=0$$

where two terms cancel out. Therefore, we can define a function Z_1 by

$$\dot{Z}_1=-mR^2\Omega^2u_1\sin q_1\cos q_1,\ u_1=\dot{q}_1, \tag{7}$$

so that

$$C_1=V+K_2+Z_1 \tag{8}$$

is the new checking function.

It is the purpose of this paper to show how one can directly obtain the functions Z_1 in general cases. In order to perform this work, it is necessary to briefly survey the main features of the dynamics of nonholonomic systems for both fundamental and technical reasons.

2 Kinematics

We consider a dynamical system Σ, containing rigid bodies S_α, $\alpha=1,\ldots,A$, whose configuration in a reference frame $N=\{0;x_1x_2x_3\}$ can be specified by coordinates $q=\{q_r;$ $r=1,\ldots,n\}$:

$$OP=F(t,\ q(t),\ P_o) \tag{9}$$

where P_o is the initial position of the particle actually situated in P. The velocity v of particle P in N is defined as:

$$v(P)=\sum_{r=1}^{n}\frac{\partial F}{\partial q_r}\dot{q}_r+\frac{\partial F}{\partial t}=v^q+v_t^q \tag{10}$$

$$v^q=\sum_{r=1}^{n}v_r^q\dot{q}_r,\ v_r^q=\frac{\partial F}{\partial q_r},\ v_t^q=\frac{\partial F}{\partial t} \tag{11}$$

where v_r^q and v_t^q are functions of t, q, and P, and are referred to as the holonomic partial velocities of P in N.

Following Kane's scheme (Kane and Levinson, 1985), we introduce generalized speeds u_r, $r=1,\ldots n$, in such a way that:

$$\dot{q}_s=\sum_{r=1}^{n}W_{sr}u_r+X_s,\ s=1,\ldots,n \tag{12}$$

where W_{sr} and X_s are functions of t and q. Then we can write:

$$v(P)=v^u+v_t^u,\ v^u=\sum_{r=1}^{n}v_r^u u_r, \tag{13}$$

where it is possible to have v_r^u and v_t^u from (11).

Now we suppose that Σ is a nonholonomic system, subject to $(n\text{-}p)$ constraints expressed as:

$$u_k=\sum_{r=1}^{p}A_{kr}u_r+B_k,\ k=p+1,\ldots,n, \tag{14}$$

where A_{kr} and B_k are functions of t and q. Among the relations (14), we have some motion constraints, i.e., some restrictions imposed on the positions and the velocities of rigid bodies S_α, $\alpha=1,\ldots,A$, and the constraints of rigidity for each body of the system, i.e., some relations between parameters $q_1,\ldots,q_n$ when it is made use of hybrid coordinates, e.g., Euler parameters, for rigid body motions. Using constraint relations (14), we have:

$$v(P)=V^u+V_t^u,\ V^u=\sum_{r=1}^{p}V_r^u u_r. \tag{15}$$

Following Kane (Kane and Levinson, 1985), V_r^u and V_t^u functions of t, q, and P, are referred to as the nonholonomic partial velocities of P in N.

The above decompositions are, of course, applicable to any discrete system Σ. But, when Σ is made up of rigid bodies, we can write for every particle P of the rigid body S:

$$v(P)=v(G)+\omega(S)\ \Lambda GP \tag{16}$$

where $\omega(S)$ is the angular velocity of S in N, and G is the mass center of S. Now we use the following decomposition:

$$\omega(S)=\Omega^u(S)+\Omega_t^u(S),\ \Omega^u(S)=\sum_{r=1}^{p}\Omega_r^u(S)u_r \tag{17}$$

[5] Laboratoire de Mécanique Théorique, Université de Poitiers, 86022 Poitiers, Cedex, France.

Manuscript received by the ASME Applied Mechanics Division, Mar. 26, 1990; final revision, June 15, 1990.

Huang, Y., Hutchinson, J. W., and Tvergaard, V., 1989, "Cavitation Instabilities in Elastic-Plastic Solids," Division of Applied Sciences, Harvard University, Report # Mech-153, to appear in *J. Mech. Phys. Solids.*

Rice, J. R., and Tracey, D. M., 1969, "On the Ductile Enlargement of Voids in Triaxial Stress Fields," *J. Mech. Phys. Solids,* Vol. 17, pp. 201-217.

A New Expression of the Energy Theorem in Discrete Mechanical Systems

René Souchet[5]

Recently, Kane and Levinson proposed testing numerical integrations by a checking function using an expression of the energy theorem involving the well-known Hamiltonian function. This paper deals with a new expression of this energy theorem that gives an alternative to the Kane-Levinson checking function.

1 Introduction

Kane and Levinson (1988) proposed to test numerical integrations of equations of motion of discrete mechanical systems by using the checking function C defined as:

$$C=H+Z,\ H=V+K_2-K_o. \tag{1}$$

In this formula, V is a potential function for given forces, K_2 and K_o are the usual homogeneous parts of the kinetic energy K, and Z is a function defined by the differential equation:

$$\dot{Z}=f(t,\ q_1,\ \ldots,\ q_n,\ u_1,\ \ldots,\ u_p), \tag{2}$$

$q=(q_1,\ \ldots,\ q_n)$ being generalized coordinates, and $u_1,\ \ldots,\ u_p$ $(p<n)$ being generalized velocities (Kane and Levinson, 1985). The function f takes into account some nonintegrable parts of both kinetic energy and dissipative forces.

However, it is possible to propose alternatives to the above function C. In order to highlight the real behavior of equation (1), we now turn to the introductory example given by Kane and Levinson (1988). Using the notations of Kane and Levinson (1988), we have the energy equation:

$$\frac{d}{dt}H-\frac{\partial}{\partial t}H=0 \tag{3}$$

where

$$V=-mgR\cos q_1,\ K_2=\frac{1}{2}mR^2{u_1}^2,\ K_o=\frac{1}{2}mR^2\Omega^2\sin^2 q_1. \tag{4}$$

We note that H depends explicitly of t, if Ω is not constant. Applying the results of Kane and Levinson (1988), we define Z by:

$$\dot{Z}=-\frac{\partial H}{\partial t}=\frac{\partial K_o}{\partial t}=mR^2\Omega\dot{\Omega}\sin^2 q_1 \tag{5}$$

so that we have

$$C=V+K_2-K_o+Z. \tag{6}$$

Now, if we develop (3), we obtain:

$$\frac{d}{dt}\{V+K_2\}-mR^2\Omega\dot{\Omega}\sin^2 q_1$$

$$-mR^2\Omega^2\dot{q}_1\sin q_1\cos q_1+mR^2\Omega\dot{\Omega}\sin^2 q_1=0$$

where two terms cancel out. Therefore, we can define a function Z_1 by

$$\dot{Z}_1=-mR^2\Omega^2u_1\sin q_1\cos q_1,\ u_1=\dot{q}_1, \tag{7}$$

so that

$$C_1=V+K_2+Z_1 \tag{8}$$

is the new checking function.

It is the purpose of this paper to show how one can directly obtain the functions Z_1 in general cases. In order to perform this work, it is necessary to briefly survey the main features of the dynamics of nonholonomic systems for both fundamental and technical reasons.

2 Kinematics

We consider a dynamical system Σ, containing rigid bodies S_α, $\alpha=1,\ldots,A$, whose configuration in a reference frame $N=\{0;x_1x_2x_3\}$ can be specified by coordinates $q=\{q_r;$ $r=1,\ldots,n\}$:

$$OP=F(t,\ q(t),\ P_o) \tag{9}$$

where P_o is the initial position of the particle actually situated in P. The velocity v of particle P in N is defined as:

$$v(P)=\sum_{r=1}^{n}\frac{\partial F}{\partial q_r}\dot{q}_r+\frac{\partial F}{\partial t}=v^q+v_t^q \tag{10}$$

$$v^q=\sum_{r=1}^{n}v_r^q\dot{q}_r,\ v_r^q=\frac{\partial F}{\partial q_r},\ v_t^q=\frac{\partial F}{\partial t} \tag{11}$$

where v_r^q and v_t^q are functions of t, q, and P, and are referred to as the holonomic partial velocities of P in N.

Following Kane's scheme (Kane and Levinson, 1985), we introduce generalized speeds u_r, $r=1,\ldots n$, in such a way that:

$$\dot{q}_s=\sum_{r=1}^{n}W_{sr}u_r+X_s,\ s=1,\ldots,n \tag{12}$$

where W_{sr} and X_s are functions of t and q. Then we can write:

$$v(P)=v^u+v_t^u,\ v^u=\sum_{r=1}^{n}v_r^u u_r, \tag{13}$$

where it is possible to have v_r^u and v_t^u from (11).

Now we suppose that Σ is a nonholonomic system, subject to $(n\text{-}p)$ constraints expressed as:

$$u_k=\sum_{r=1}^{p}A_{kr}u_r+B_k,\ k=p+1,\ldots,n, \tag{14}$$

where A_{kr} and B_k are functions of t and q. Among the relations (14), we have some motion constraints, i.e., some restrictions imposed on the positions and the velocities of rigid bodies S_α, $\alpha=1,\ldots,A$, and the constraints of rigidity for each body of the system, i.e., some relations between parameters $q_1,\ldots,q_n$ when it is made use of hybrid coordinates, e.g., Euler parameters, for rigid body motions. Using constraint relations (14), we have:

$$v(P)=V^u+V_t^u,\ V^u=\sum_{r=1}^{p}V_r^u u_r. \tag{15}$$

Following Kane (Kane and Levinson, 1985), V_r^u and V_t^u functions of t, q, and P, are referred to as the nonholonomic partial velocities of P in N.

The above decompositions are, of course, applicable to any discrete system Σ. But, when Σ is made up of rigid bodies, we can write for every particle P of the rigid body S:

$$v(P)=v(G)+\omega(S)\ \Lambda GP \tag{16}$$

where $\omega(S)$ is the angular velocity of S in N, and G is the mass center of S. Now we use the following decomposition:

$$\omega(S)=\Omega^u(S)+\Omega_t^u(S),\ \Omega^u(S)=\sum_{r=1}^{p}\Omega_r^u(S)u_r \tag{17}$$

[5] Laboratoire de Mécanique Théorique, Université de Poitiers, 86022 Poitiers, Cedex, France.

Manuscript received by the ASME Applied Mechanics Division, Mar. 26, 1990; final revision, June 15, 1990.

involving partial angular velocities $\Omega_r^u(S)$ and $\Omega_t^u(S)$. Specific expressions of V_r^u and V_t^u may be found as:

$$V_r^u(P) = V_r^u(G) + \Omega_r^u(S) \Lambda GP, \; V_t^u(P) = V_t^u(G) + \Omega_t^u(S) \Lambda GP \quad (18)$$

for each particle P of S.

3 Kinetics

Introducing mass distribution, we define the resultant $\mu(\Sigma)$ and the moment $\sigma(\Sigma,0)$:

$$\mu(\Sigma) = \int_\Sigma v dm, \; \sigma(\Sigma,0) = \int_\Sigma OP \Lambda v dm \quad (19)$$

If the vector v is expressed in terms of u_r, $r=1, \ldots, p$, we obtain, for $\mu(\Sigma)$ and $\sigma(\Sigma,0)$, the following expressions:

$$\mu(\Sigma) = \mu^u(\Sigma) + \mu_t^u(\Sigma), \; \mu^u(\Sigma) = \sum_{r=1}^{p} \mu_r^u(\Sigma) u_r \quad (20)$$

$$\sigma(\Sigma,0) = \sigma^u(\Sigma,0) + \sigma_t^u(\Sigma,0), \; \sigma^u(\Sigma,0) = \sum_{r=1}^{p} \sigma_r^t(\Sigma,0) u_r \quad (21)$$

with

$$\mu_r^u(\Sigma) = \int_\Sigma v_r^u dm, \; \sigma_r^u(\Sigma,0) = \int_\Sigma OP \Lambda v_r^u dm. \quad (22)$$

Since the system Σ is made up of rigid bodies S_α, $\alpha = 1, \ldots, A$, we have:

$$\mu_r^u(\Sigma) = \sum_{\alpha=1}^{A} \mu_r^u(S_\alpha), \; \sigma_r^u(\Sigma,0) = \sum_{\alpha=1}^{A} \sigma_r^u(S_\alpha,0). \quad (23)$$

So it is sufficient to derive formulae when the system is a rigid body S. In this case we have the following classical results

$$\mu(S) = mv(G), \; \sigma(S,G) = I(G)\omega(S) \quad (24)$$

where m is the mass of S, G the center of mass, and $I(G)$ the inertia tensor in G.

Next, we recall that the kinetic energy $K(\Sigma)$ can be expressed as a sum of homogeneous functions of u_r of degrees 2, 1, and 0; we use the usual form

$$K = K_2 + K_1 + K_o \quad (25)$$

where, of course, we have

$$K_2(\Sigma) = \frac{1}{2}\int_\Sigma V^u \cdot V^u dm, \; K_1(\Sigma) = \int_\Sigma V^u \cdot V_t^u dm, \; K_o(\Sigma) = \frac{1}{2}\int_\Sigma V_t^u \cdot V_t^u dm. \quad (26)$$

When Σ is composed of rigid bodies, we obtain $K(\Sigma)$ as the sum of the kinetic energy of these rigid bodies.

Finally, in practical applications, we compute kinetic energy $K(\Sigma)$ and vector fields $\{\mu(\Sigma), \sigma(\Sigma,0)\}$; then we obtain the above decompositions K_2, K_1, K_o, and μ_r^u, σ_r^u, μ_t^u, σ_t^u, from K, μ, σ, by using an identification process.

4 Equations of Motions

Classical dynamics is obtained from two main principles in a Newtonian reference frame. A first principle asserts that, for every body B, the variation of the linear momentum is due to both internal and external forces, $\phi_{(i)}$ and $\phi_{(e)}$, applied to B:

$$\frac{d}{dt}\int_B v dm = \int_B \phi_{(i)} + \int_B \phi_{(e)}. \quad (27)$$

A second principle asserts that, for every body B, the power of internal forces $\phi_{(i)}$ does not depend on reference frames, i.e.,

$$\int_B \phi_{(i)} \cdot v_1 = \int_B \phi_{(i)} \cdot v_2. \quad (28)$$

As it is known, the relations (27) and (28) are meaningful, only if both internal and external forces, $\phi_{(i)}$ and $\phi_{(e)}$ can be specified.

In fact, it is usual to write (27) and (28) in the following equivalent forms when applied to a material system Σ:

$$\int_\Sigma \gamma \cdot U dm = \int_\Sigma \phi_{(i)} \cdot U + \int_\Sigma \phi_{(e)} \cdot U \quad (29)$$

$$\int_\Sigma \phi_{(i)} \cdot V = 0 \quad (30)$$

where U is an arbitrary vector field and V an arbitrary rigid body vector field. In the dynamics of rigid bodies, the definition of internal forces for each rigid body S_α is not necessary. In fact, equations of motions for Σ are obtained by choosing in (29) vector fields, U, which are rigid body vector fields on each rigid body S_α of Σ, and the equation (30) expresses the principle of action and reaction for every pair of solids (S_α, S_β).

As an example, let us determine the Kane equations without multipliers. Taking, for U, the vector field V_r^u, we have:

$$\int_\Sigma \gamma \cdot V_r^u dm = \int_\Sigma \phi_{(i)} \cdot V_r^u + \int_\Sigma \phi_{(e)} \cdot V_r^u, \; r = 1, \ldots, p. \quad (31)$$

The right-hand side of noted $\tilde{F}_r$, the internal forces of rigid bodies, and the forces involving constraint relations between rigid bodies are noncontributing forces in $\tilde{F}_r$. The left-hand side is noted $(-\tilde{F}_r)$. Explicitly, we obtain

$$-\tilde{F}_r^* = \sum_{\alpha=1}^{A} \left\{ \frac{d}{dt}\mu(S_\alpha) \cdot V_r^u(G_\alpha) + \frac{d}{dt}\sigma(S_\alpha, G_\alpha) \cdot \Omega_r^u(S_\alpha) \right\}. \quad (32)$$

Finally, Kane equations are (Kane and Levinson, 1985):

$$\tilde{F}_r^* + \tilde{F}_r = 0, \; r = 1, \ldots, p. \quad (33)$$

In the sequel, attention is focused on an energy theorem.

5 Energy Theorem

In order to derive an energy theorem, we take, for U, the vector field V^u. We have

$$\int_\Sigma \gamma \cdot V^u dm = \sum_{r=1}^{p} \tilde{F}_r u_r, \text{ i.e., } \sum_{r=1}^{p} (\tilde{F}_r^* + \tilde{F}_r) u_r = 0. \quad (34)$$

First,

$$\int_\Sigma \gamma \cdot V^u dm = \int_\Sigma \left(\frac{d}{dt} V^u + \frac{d}{dt} V_t^u \right) \cdot V^u dm = \frac{d}{dt} K_2 + \int_\Sigma \frac{d}{dt} V_t^u \cdot V^u dm. \quad (35)$$

Now we can write

$$\sum_{r=1}^{p} \tilde{F}_r u_r = -\frac{d\Phi}{dt} + E \quad (36)$$

where the potential function Φ depends on t and q—noncontributing forces being the same in the Kane equations without multipliers. So, we obtain the following energy formula

$$\boxed{\frac{d}{dt}\{K_2(\Sigma) + \Phi\} - E + \int_\Sigma \frac{d}{dt} V_t^u \cdot V^u dm = 0} \quad (37)$$

In applications, we must be able to derive easily the integral complementary term in (37). But we have

$$\int_\Sigma \frac{d}{dt} V_t^u \cdot V^u dm = \sum_{\alpha=1}^{A} \int_{S_\alpha} \frac{d}{dt} V_t^u \cdot V^u dm. \tag{38}$$

So it is sufficient to derive formula for a rigid body S. Again, as in expressing the Kane equations we use the velocity field of S, by introducing the angular velocity. So we obtain

$$\int_S \frac{d}{dt} V_t^u \cdot V^u dm = \frac{d}{dt} V_t^u(G) \cdot \int_S V^u dm + \frac{d}{dt} \Omega_t^u(S) \cdot \int_S GP \Lambda V^u dm + \Omega_t^u(S) \cdot \int_S (\omega(S) \Lambda GP) \Lambda V^u dm. \tag{39}$$

The last term can be evaluated in the following manner:

$$\Omega_t^u(S) \cdot \int_S (\omega(S) \Lambda GP) \Lambda V^u dm$$

$$= \Omega_t^u(S) \cdot \int_S (\omega(S) \Lambda GP) \Lambda (\Omega^u(S) \Lambda GP) dm$$

$$= \Omega_t^u(S) \cdot \int_S (\Omega_t^u(S) \Lambda GP) \Lambda (\Omega^u(S) \Lambda GP) dm$$

$$= -\Omega_t^u(S) \cdot \int_S [\Omega_t^u(S) \Lambda GP) \cdot \Omega^u(S)] GP dm$$

$$= \Omega_t^u(S) \cdot \int_S [(\Omega_t^u \Lambda \Omega^u) \cdot GP] GP dm$$

$$= -\Omega_t^u(S) \cdot \{ I(S,G) (\Omega_t^u \Lambda \Omega^u) \}.$$

So, we have

$$\boxed{\int_S \frac{d}{dt} V_t^u \cdot V^u dm = \frac{d}{dt} V_t^u(G) \cdot \mu^u(S) + \frac{d}{dt} \Omega_t^u(S) \cdot \sigma^u(S,G) - (\Omega_t^u \Lambda \Omega^u) \cdot \sigma_t^u(S,G)} \tag{40}$$

It is noteworthy that the above expressions can be easily obtained from earlier calculations used in writing the Kane equations (33).

However, a different, more classical expression of the above energy formula can be given (Kane and Levinson, 1985) involving the difference $\{K_2 - K_o\}$. In fact, we have:

$$\int_\Sigma \frac{d}{dt} V_t^u \cdot V^u dm = -\frac{d}{dt} K_o + \int_\Sigma \left(\frac{d}{dt} V_t^u \right) \cdot v dm.$$

Applying the same procedure as before, we easily obtain for a rigid body(S):

$$\int_S \frac{d}{dt} V_t^u \cdot V^u dm = -\frac{d}{dt} K_o + \frac{d}{dt} V_t^u(G) \cdot \mu(S) + \frac{d}{dt} \Omega_t^u(S) \cdot \sigma(S,G). \tag{41}$$

Understanding the method used in showing this last formula (41) it appears that we have introduced supplementary terms: In practical applications these terms must disappear, as it was seen in the introductory example.

6 Examples

Next, we return to the introductory example. Since P is a simple particle, we have only

$$m \frac{d}{dt} V_t^u \cdot V^u = -mR^2 \Omega^2 \dot{q}_1 \sin q_1 \cos q_1. \tag{42}$$

So, the energy formula has directly the simplified form

$$\frac{d}{dt} \left\{ \frac{1}{2} mR^2 \dot{q}_1^2 + mgR \cos q_1 \right\} - mR^2 \Omega^2 \dot{q}_1 \sin q_1 \cos q_1 = 0. \tag{43}$$

Finally, we apply the energy formula to the second example of Kane and Levinson (1988). For the sake of brevity, we refer to the same notations and we only explicitly show the two following results:

$$\int_B \frac{d}{dt} V_t^u \cdot V^u dm = -Mr(L+q_4)\Omega^2 u_2 - \frac{2}{5} Mr(L+q_4)\Omega^2 u_2 = -\frac{7}{5} Mr(L+q_4)\Omega^2 u_2$$

$$\frac{d}{dt}(K_2 + V) - \frac{7}{5} Mr(L+q_4)\Omega^2 u_2 + \delta\{(u_1 - \Omega)u_1 + u_2^2\} = 0. \tag{44}$$

Now, following Kane and Levinson (1988), we define a function Z_1 of t that satisfies the differential equation

$$\dot{Z}_1 = \delta\{(u_1 - \Omega)u_1 + u_2^2\} - \frac{7}{5} Mr(L+q_4)\Omega^2 u_2. \tag{45}$$

Then, we have for the so-called checking function C_1:

$$C_1 = \frac{1}{2} \sigma q_4^2 + Z_1 + \frac{1}{10} Mr^2 (2u_1^2 + 7u_2^2). \tag{46}$$

Recalling the results of Kane and Levinson (1985), the above authors define the function Z by:

$$\dot{Z} = \delta\{(u_1 - \Omega)u_1 + u_2^2\} + \frac{7}{5} M\Omega\dot{\Omega}(L+q_4)^2 \tag{47}$$

so that the checking function C is

$$C = \frac{1}{2} \sigma q_4^2 + Z + \frac{1}{10} Mr^2 (2u_1^2 + 7u_2^2) - \frac{7}{10} M\Omega^2 (L+q_4)^2. \tag{48}$$

7 Conclusion

In order to test numerical integrations, Kane and Levinson have proposed an excellent method using a checking function that is obtained via the energy theorem. This function is obviously nonunique, because it involves some decomposition of the energy theorem. In this paper we have proposed to use a new form of this energy theorem, inducing an alternative checking function. Finally, we note that our alternative may be of theoretical interest, and that the question of the superiority of these checking functions is open.

References

Kane, T. R., and Levinson, D. A., 1985, *Dynamics: Theory and Applications*, McGraw-Hill, New York.

Kane, T. R., and Levinson, D. A., 1988, "A Method for Testing Numerical Integrations of Equations of Motions of Mechanical Systems," ASME JOURNAL OF APPLIED MECHANICS, Vol. 55, pp. 711–715.

A Note on the Mixed-Mode Line Spring Model for Shells

P. F. Joseph[6,7] and F. Erdogan[6,8]

Introduction

In a previous paper, a mixed-mode line spring model for the treatment of general surface crack problems in a shell was considered (Joseph and Erdogan, 1988). The objective of this Note is to append that study and modify some of the results accordingly. The questions addressed here are concerned with

[6]Department of Mechanical Engineering and Mechanics, Lehigh University, Bethlehem, PA 18015.

[7]Mem. ASME.

[8]Fellow ASME.

Manuscript received by the ASME Applied Mechanics Division, June 29, 1990; final revision, Oct. 18, 1990.

$$\int_\Sigma \frac{d}{dt} V_t^u \cdot V^u dm = \sum_{\alpha=1}^{A} \int_{S_\alpha} \frac{d}{dt} V_t^u \cdot V^u dm. \tag{38}$$

So it is sufficient to derive formula for a rigid body S. Again, as in expressing the Kane equations we use the velocity field of S, by introducing the angular velocity. So we obtain

$$\int_S \frac{d}{dt} V_t^u \cdot V^u dm = \frac{d}{dt} V_t^u(G) \cdot \int_S V^u dm + \frac{d}{dt} \Omega_t^u(S) \cdot \int_S GP \Lambda V^u dm + \Omega_t^u(S) \cdot \int_S (\omega(S) \Lambda GP) \Lambda V^u dm. \tag{39}$$

The last term can be evaluated in the following manner:

$$\begin{aligned}
&\Omega_t^u(S) \cdot \int_S (\omega(S) \Lambda GP) \Lambda V^u dm \\
&= \Omega_t^u(S) \cdot \int_S (\omega(S) \Lambda GP) \Lambda (\Omega^u(S) \Lambda GP) dm \\
&= \Omega_t^u(S) \cdot \int_S (\Omega_t^u(S) \Lambda GP) \Lambda (\Omega^u(S) \Lambda GP) dm \\
&= -\Omega_t^u(S) \cdot \int_S [\Omega_t^u(S) \Lambda GP) \cdot \Omega^u(S)] GP dm \\
&= \Omega_t^u(S) \cdot \int_S [(\Omega_t^u \Lambda \Omega^u) \cdot GP] GP dm \\
&= -\Omega_t^u(S) \cdot \{ I(S,G) (\Omega_t^u \Lambda \Omega^u) \}.
\end{aligned}$$

So, we have

$$\boxed{\int_S \frac{d}{dt} V_t^u \cdot V^u dm = \frac{d}{dt} V_t^u(G) \cdot \mu^u(S) + \frac{d}{dt} \Omega_t^u(S) \cdot \sigma^u(S,G) - (\Omega_t^u \Lambda \Omega^u) \cdot \sigma_t^u(S,G)} \tag{40}$$

It is noteworthy that the above expressions can be easily obtained from earlier calculations used in writing the Kane equations (33).

However, a different, more classical expression of the above energy formula can be given (Kane and Levinson, 1985) involving the difference $\{K_2 - K_o\}$. In fact, we have:

$$\int_\Sigma \frac{d}{dt} V_t^u \cdot V^u dm = -\frac{d}{dt} K_o + \int_\Sigma \left(\frac{d}{dt} V_t^u \right) \cdot v dm.$$

Applying the same procedure as before, we easily obtain for a rigid body(S):

$$\int_S \frac{d}{dt} V_t^u \cdot V^u dm = -\frac{d}{dt} K_o + \frac{d}{dt} V_t^u(G) \cdot \mu(S) + \frac{d}{dt} \Omega_t^u(S) \cdot \sigma(S,G). \tag{41}$$

Understanding the method used in showing this last formula (41) it appears that we have introduced supplementary terms: In practical applications these terms must disappear, as it was seen in the introductory example.

6 Examples

Next, we return to the introductory example. Since P is a simple particle, we have only

$$m \frac{d}{dt} V_t^u \cdot V^u = -mR^2 \Omega^2 \dot{q}_1 \sin q_1 \cos q_1. \tag{42}$$

So, the energy formula has directly the simplified form

$$\frac{d}{dt} \left\{ \frac{1}{2} mR^2 \dot{q}_1^2 + mgR \cos q_1 \right\} - mR^2 \Omega^2 \dot{q}_1 \sin q_1 \cos q_1 = 0. \tag{43}$$

Finally, we apply the energy formula to the second example of Kane and Levinson (1988). For the sake of brevity, we refer to the same notations and we only explicitly show the two following results:

$$\begin{aligned}
\int_B \frac{d}{dt} V_t^u \cdot V^u dm &= -Mr(L+q_4)\Omega^2 u_2 - \frac{2}{5} Mr(L+q_4)\Omega^2 u_2 \\
&= -\frac{7}{5} Mr(L+q_4)\Omega^2 u_2 \\
\frac{d}{dt}(K_2 + V) - \frac{7}{5} Mr(L+q_4)\Omega^2 u_2 + \delta\{(u_1 - \Omega)u_1 + u_2^2\} &= 0.
\end{aligned} \tag{44}$$

Now, following Kane and Levinson (1988), we define a function Z_1 of t that satisfies the differential equation

$$\dot{Z}_1 = \delta\{(u_1 - \Omega)u_1 + u_2^2\} - \frac{7}{5} Mr(L+q_4)\Omega^2 u_2. \tag{45}$$

Then, we have for the so-called checking function C_1:

$$C_1 = \frac{1}{2} \sigma q_4^2 + Z_1 + \frac{1}{10} Mr^2 (2u_1^2 + 7u_2^2). \tag{46}$$

Recalling the results of Kane and Levinson (1985), the above authors define the function Z by:

$$\dot{Z} = \delta\{(u_1 - \Omega)u_1 + u_2^2\} + \frac{7}{5} M\Omega\dot{\Omega}(L+q_4)^2 \tag{47}$$

so that the checking function C is

$$C = \frac{1}{2} \sigma q_4^2 + Z + \frac{1}{10} Mr^2 (2u_1^2 + 7u_2^2) - \frac{7}{10} M\Omega^2 (L+q_4)^2. \tag{48}$$

7 Conclusion

In order to test numerical integrations, Kane and Levinson have proposed an excellent method using a checking function that is obtained via the energy theorem. This function is obviously nonunique, because it involves some decomposition of the energy theorem. In this paper we have proposed to use a new form of this energy theorem, inducing an alternative checking function. Finally, we note that our alternative may be of theoretical interest, and that the question of the superiority of these checking functions is open.

References

Kane, T. R., and Levinson, D. A., 1985, *Dynamics: Theory and Applications*, McGraw-Hill, New York.

Kane, T. R., and Levinson, D. A., 1988, "A Method for Testing Numerical Integrations of Equations of Motions of Mechanical Systems," ASME JOURNAL OF APPLIED MECHANICS, Vol. 55, pp. 711–715.

A Note on the Mixed-Mode Line Spring Model for Shells

P. F. Joseph[6,7] and F. Erdogan[6,8]

Introduction

In a previous paper, a mixed-mode line spring model for the treatment of general surface crack problems in a shell was considered (Joseph and Erdogan, 1988). The objective of this Note is to append that study and modify some of the results accordingly. The questions addressed here are concerned with

[6]Department of Mechanical Engineering and Mechanics, Lehigh University, Bethlehem, PA 18015.

[7]Mem. ASME.

[8]Fellow ASME.

Manuscript received by the ASME Applied Mechanics Division, June 29, 1990; final revision, Oct. 18, 1990.

the rotation of the local coordinate system along the crack front in order to calculate modes II and III stress intensity factors consistent with their conventional definitions and to reexamine and modify the twisting component of the line spring model, so that for long cracks, the corresponding plane strain results are recovered. A detailed discussion of these questions may be found in a recent study (Joseph and Erdogan, 1990) where the mixed-mode surface crack problem was considered for a flat plate, and the results were compared with the existing numerical solutions given by Sorensen and Smith (1977), Simon, O'Donoghue and Atluri (1987), and Nikishkov and Atluri (1987). It was shown that the results given by the line spring model for mixed-mode problems are nearly as accurate as the similar results found for mode I problems. In this Note, after briefly discussing the two questions mentioned, the modified results are presented which should replace Figs. 6 and 7 and Tables 3–7 in the study on shells (Joseph and Erdogan, 1988).

Crack Front Curvature

Unlike the mode I problem, the three-dimensional modes II and III crack problems are always coupled. For example, in a plate containing a surface crack of finite length $2a$ and constant depth L and subjected to in-plane shear loading N_{xy}, even though the primary mode of deformation along the crack front $z=$ constant is mode III and $y=$ constant mode II, yz being the plane of the crack, the stress intensity factors corresponding to the secondary modes (k_2 along $z=$ constant and k_3 along $y=$ constant) are not zero (see Figs. 10–12, Joseph and Erdogan, 1990). Similarly, for a semi-elliptic surface crack the primary stress intensity factor would be k_3 in the central portion of the crack and k_2 near the ends. It is in the nature of the line spring model that the "stress intensity factors" k_2 and k_3 are introduced into the model in the xz-plane, x being the coordinate perpendicular to the plane of the crack. Consequently, these are the stress intensity factors calculated from the model, and are the ones given by Joseph and Erdogan (1988) for shells. On the other hand, the conventional definition of the stress intensity factors refer to the local coordinate system x', y', z' at the crack front with $x'=x$ and y' and z' being, respectively, tangent and normal to the crack front. Thus, the physically relevant stress intensity factors k_1', k_2', and k_3' may be expressed in terms of k_1, k_2, and k_3 given by the line spring model (Joseph and Erdogan, 1988) as follows:

$$k_1' = k_1,$$

$$k_2' = k_2\cos(\theta) - k_3\sin(\theta),$$

$$k_3' = k_2\sin(\theta) + k_3\cos(\theta), \qquad (1a\text{-}c)$$

where θ is the angle between z, the normal to the plate and z' the normal to the crack front.

Plane-Strain Result

In three-dimensional planar surface crack problems, under various uniform loading conditions, it is expected that as the aspect ratio a/L (or for a fixed L/h, a/h) becomes unbounded, a and L being the half crack length and the crack depth, the stress intensity factors in the center part of the crack would approach the corresponding plane-strain and antiplane shear results. Applying the line spring model to surface crack problems in plates under mode I and mixed-mode loading conditions, these two-dimensional elasticity limits seem to be recovered for all uniform loading, except the twisting moment. In preparing the paper on plates (Joseph and Erdogan, 1990) this was brought to our attention by the reviewers, and it was pointed out that similar difficulties were also observed by Desvaux (1985) in his M.S. Thesis. In shells as well as in plates with "long" surface cracks, the resistance to crack opening comes primarily from the net ligament forces, which are represented by the "line spring" terms in the integral equations. These are the algebraic terms having the coefficients γ_{ij} in equations (32)–(34) describing the shell problem (Joseph and Erdogan, 1988). There are also two secondary sources of resistance. One is the clamping effect of the crack ends. In all cases this effect reduces to zero as $h/a\to 0$. The second is the effect of the local plate or shell stiffness which, for $h/a\to 0$ approaches zero in all cases except for twisting. For small values of h/a, the Reissner theory predicts resistance of the same order coming from the line spring terms and from twisting stiffness. Note that for the classical plate theory, this resistance is infinitely large. As $h/a\to 0$ the two effects are combined, and consequently, the plane-strain results are not recovered. The Reissner plate theory appears to be too stiff in twisting for the line spring model to work. Therefore, an adjustment in the plate or the shell theory is necessary in the limit to make the line spring model compatible with the plane-strain results.

As pointed out by Joseph and Erdogan (1990), for long cracks the twisting kernel k_{55} in the shell formulation (equation (34), Joseph and Erdogan, 1988) behaves like a delta function. Since this behavior is independent of the shell curvature, the result is the same as in plates, and for $h/a\to 0$, it can be shown that

$$\lim_{a/h\to\infty} \frac{1}{\pi}\int_{-a}^{a} k_{55}(z)g_5(t_2)dt_2 = -\sqrt{10}\int_{-\infty}^{\infty}\delta(x_2-t_2)g_5(t_2)dt_2 = -\sqrt{10}g_5(x_2) \qquad (2)$$

where g_5 is the relative crack surface rotation in the yz-plane. Referring now to the integral equation (34c) associated with twisting, namely

$$\frac{1}{24\pi}\int_{-a}^{a}\frac{g_5(t_2)}{(t_2-x_2)^2}dt_2 + \frac{h}{8\pi}\left(\frac{1}{R_1}+\frac{3}{R_2}\right)\int_{-a}^{a}\frac{g_3(t_2)}{(t_2-x_2)}dt_2 + \frac{1}{\pi}\sum_{i=3}^{5}\int_{-a}^{a}k_{5i}(x_2,t_2)g_i(t_2)dt_2 - \frac{1}{\pi h(1-\nu^2)}\left[\gamma_{54}g_4(x_2)+\gamma_{54}\frac{x_2}{R_2}g_3(x_2)+\gamma_{55}\frac{h}{6}g_5(x_2)\right] = \frac{-1}{6E}\overset{\infty}{\sigma}_5, \quad (-a<x_2<a), \qquad (3)$$

and noting that all terms in (3) are normalized "force" quantities, from (2) and (3) it is seen that for $h/a\to 0$ the term involving k_{55} approaches a force quantity that is independent

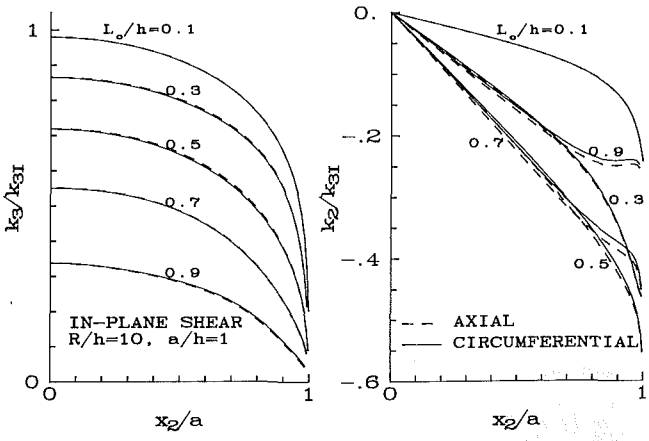

Fig. 1 The variation of the primary (mode III) and the secondary (mode II) stress intensity factors k_3' and k_2', along the crack front for a semi-elliptic surface crack on the outside of a cylinder subjected to membrane shear loading $\overset{\infty}{N}_{12}$; $\nu=0.3$, $R/h=10$, $a/h=1$

Table 1 Normalized stress intensity factor $k_3(0)/k_{3I}$ at the center of a semi-elliptic surface crack in a cylindrical shell under in-plane shear loading $\overset{\infty}{N}_{12}$; $\nu = 0.3$

	a/h=1					a/h=4				
L_o/h R/h	0.2	0.4	0.6	0.8	0.95	0.2	0.4	0.6	0.8	0.95
Outer axial crack										
5	.928	.793	.639	.456	.267	.986	.952	.887	.779	.608
10	.930	.795	.639	.453	.264	.989	.952	.883	.767	.589
20	.930	.796	.640	.452	.262	.990	.954	.882	.761	.578
50	.931	.797	.641	.452	.261	.991	.956	.883	.757	.570
→∞	.932	.799	.642	.452	.260	.993	.959	.886	.756	.565
Inner axial crack										
5	.936	.809	.655	.461	.264	.997	.977	.921	.805	.610
10	.934	.805	.649	.457	.262	.996	.972	.911	.789	.594
20	.933	.802	.646	.455	.261	.995	.968	.903	.777	.582
50	.932	.800	.644	.453	.261	.994	.964	.895	.767	.573
→∞	.932	.799	.642	.452	.260	.993	.959	.886	.756	.565
Outer circumferential crack										
5	.928	.791	.637	.456	.269	.987	.948	.884	.786	.630
10	.929	.794	.638	.453	.264	.988	.949	.879	.768	.597
20	.930	.796	.639	.452	.262	.989	.951	.879	.759	.580
50	.931	.797	.641	.452	.261	.991	.955	.881	.756	.570
→∞	.932	.799	.642	.452	.260	.993	.959	.886	.756	.565
Inner circumferential crack										
5	.937	.811	.658	.464	.265	1.000	.986	.939	.829	.633
10	.935	.806	.651	.458	.262	.998	.978	.920	.800	.602
20	.933	.803	.647	.455	.261	.996	.971	.907	.782	.585
50	.933	.801	.644	.453	.261	.995	.966	.897	.768	.574
→∞	.932	.799	.642	.452	.260	.993	.959	.886	.756	.565

Table 2 Normalized stress intensity factor $k_3(0)/k_{3I}$ at the center of a semi-elliptic surface crack in a cylindrical shell under in-plane shear loading $\overset{\infty}{N}_{12}$ and twisting moment $\overset{\infty}{M}_{12}$; $\nu = 0.3$, $R/h = 10$

	In-Plane Shear					Twisting			
L_o/h a/h	0.2	0.4	0.6	0.8	0.95	0.2	0.4	0.6	0.8
Outer axial crack									
0.5	.843	.641	.478	.311	.159	.830	.544	.130	-.942
1	.930	.795	.639	.453	.264	.925	.747	.413	-.588
2	.973	.898	.783	.617	.414	.971	.878	.662	-.079
4	.989	.952	.883	.767	.589	.989	.944	.825	.394
Inner axial crack									
0.5	.845	.645	.482	.311	.158	.833	.550	.137	-.935
1	.934	.805	.649	.457	.262	.930	.761	.435	-.561
2	.979	.916	.804	.629	.414	.979	.902	.705	-.006
4	.996	.972	.911	.789	.594	.996	.971	.880	.503
Outer circumferential crack									
0.5	.842	.641	.478	.311	.160	.830	.544	.130	-.942
1	.929	.794	.638	.453	.264	.925	.745	.411	-.591
2	.972	.896	.780	.616	.416	.970	.875	.656	-.086
4	.988	.949	.879	.768	.597	.987	.939	.817	.388
Inner circumferential crack									
0.5	.845	.646	.482	.312	.158	.833	.551	.138	-.934
1	.935	.806	.651	.458	.262	.931	.763	.439	-.555
2	.980	.919	.808	.633	.415	.980	.906	.714	.014
4	.998	.978	.920	.800	.602	.998	.978	.898	.557

of the crack length rather than vanishing, and is of the same order as the line spring terms, $\gamma_{5j}g_j$, $(j = 4,5)$. In order to remove this inconsistency, which is due to the "plate" or "shell" approximation in (3), the delta function has to be subtracted from the kernel k_{55} giving

$$\frac{1}{24\pi}\int_{-a}^{a}\frac{g_5(t_2)}{(t_2-x_2)^2}\,dt_2+\frac{h}{8\pi}\left(\frac{1}{R_1}+\frac{3}{R_2}\right)\int_{-a}^{a}\frac{g_3(t_2)}{(t_2-x_2)}\,dt_2$$
$$+\frac{1}{\pi}\sum_{i=3}^{5}\int_{-a}^{a}k_{5i}(x_2,t_2)g_i(t_2)dt_2+\sqrt{10}g_5(x_2)$$

Table 3 Normalized stress intensity factor $k_2(0)/k_{20}$ at the center of a semi-elliptic surface crack in a cylindrical shell under transverse shear loading $\overset{\infty}{V}_1$; $\nu = 0.3$, $R/h = 10$

L_o/h a/h	0.2	0.4	0.6	0.8	0.95
Outer axial crack					
0.5	.988	.883	.685	.467	.277
1	.996	.953	.851	.693	.487
2	.999	.986	.951	.878	.726
4	1.000	.997	.988	.966	.893
Inner axial crack					
0.5	.988	.883	.685	.467	.277
1	.996	.954	.852	.694	.489
2	.999	.986	.952	.881	.731
4	1.000	.997	.990	.971	.901
Outer circumferential crack					
0.5	.988	.883	.684	.466	.277
1	.996	.953	.849	.689	.483
2	.999	.985	.947	.867	.711
4	1.000	.995	.982	.949	.863
Inner circumferential crack					
0.5	.988	.883	.685	.466	.277
1	.996	.953	.851	.693	.487
2	.999	.986	.951	.878	.726
4	1.000	.996	.986	.963	.888

Table 4 Normalized stress intensity factor $k_3(0)/k_{3I}$ at the center of a semi-elliptic surface crack in a toroidal shell subjected to in-plane shear loading $\overset{\infty}{N}_{12}$; $\nu = 0.3$., $R/h = 10$, $a/h = 1$ (see Fig. 8 of Joseph and Erdogan, 1988)

		$R_i/R=1$					$R_i/R\to\infty$				
	L_o/h	0.2	0.4	0.6	0.8	0.95	0.2	0.4	0.6	0.8	0.95
	Crack Position										
A	inner	.935	.808	.653	.459	.263	.935	.806	.651	.458	.262
	outer	.929	.793	.638	.454	.266	.929	.794	.638	.453	.264
B	inner	.935	.807	.652	.459	.263	.934	.805	.649	.457	.262
	outer	.929	.793	.638	.454	.265	.930	.795	.639	.453	.264
C	inner	.932	.801	.645	.455	.262	.935	.806	.651	.458	.262
	outer	.931	.799	.643	.454	.263	.929	.794	.638	.453	.264
D	inner	.931	.799	.643	.454	.263	.934	.805	.649	.457	.262
	outer	.932	.801	.645	.455	.262	.930	.795	.639	.453	.264

$$-\frac{1}{\pi h(1-\nu^2)}\left[\gamma_{54}g_4(x_2)+\gamma_{54}\frac{x_2}{R_2}g_3(x_2)+\gamma_{55}\frac{h}{6}g_5(x_2)\right]$$
$$=\frac{-1}{6E}\overset{\infty}{\sigma}_5,\ (-a<x_2<a). \qquad (4)$$

Thus, (4) should replace (34*c*) in the system of shell equations given by Joseph and Erdogan (1988).

Results

Modes II and III stress intensity factors k_2' and k_3' given in this Note are obtained by solving the integral equations (34*a*,*b*) and (4) and by using the transformation (1). Thus, Fig. 1 given in this Note should replace Figs. 6 and 7, and Tables 1–5 should replace Tables 3–7, respectively. In these results, too, the normalizing stress intensity factors k_{3I} and k_{20} are the corresponding two-dimensional elasticity results for a plate containing an edge crack under in-plane shear N_{12}^{∞} and transverse shear V_1^{∞}, respectively.

Table 5 Normalized stress intensity factors $k_3(0)/k_{3I}$ and $k_2(0)/k_{2O}$ at the center of a semi-elliptic surface crack in a toroidal shell subjected to in-plane shear loading $\overset{\infty}{N}_{12}$ and transverse shear $\overset{\infty}{V}_1$ loading; $\nu = 0.3$., $R/h = 10$, $a/h = 2$, crack position A (see Fig. 8 of Joseph and Erdogan, 1988)

	L_o/h	0.2	0.4	0.6	0.8	0.95
Crack Position	R_i/R					
		In-Plane Shear $\overset{\infty}{N}_{12}$: $k_3(0)/k_{3I}$				
outer	1	.971	.895	.780	.618	.420
	4	.971	.896	.780	.617	.418
	7	.972	.896	.780	.617	.417
	$\to\infty$	.972	.896	.780	.616	.416
inner	1	.981	.921	.813	.638	.419
	4	.981	.920	.811	.636	.417
	7	.980	.919	.810	.635	.416
	$\to\infty$	.980	.919	.808	.633	.415
		Transverse Shear V_1: $k_2(0)/k_{2O}$				
outer	1	.999	.985	.946	.866	.710
	4	.999	.985	.946	.867	.710
	7	.999	.985	.946	.867	.711
	$\to\infty$	.999	.985	.947	.867	.711
inner	1	.999	.986	.951	.878	.726
	4	.999	.986	.951	.878	.726
	7	.999	.986	.951	.878	.726
	$\to\infty$	.999	.986	.951	.878	.726

References

Desvaux, G. J., 1985, "The Line Spring Model for Surface Flaw, an Extension to Mode II and Mode III," Master's Thesis, Department of Mechanical Engineering, Massachusetts Institute of Technology, Cambridge, Mass.

Joseph, P. F., and Erdogan, F., 1988, "A Surface Crack in Shells Under Mixing Mode Loading Conditions," ASME JOURNAL OF APPLIED MECHANICS, Vol. 55, No. 4, pp. 795-804.

Joseph, P. F., and Erdogan, F., 1990, "Surface Crack in a Plate Under Antisymmetric Loading Conditions," *International Journal of Solids and Structures*, in press.

Nikishkov, G. P., and Atluri, S. N., 1987, "Calculation of Fracture Mechanics Parameters for an Arbitrary Three-Dimensional Crack, by the 'Equivalent Domain Integral' Method," *International Journal for Numerical Methods in Engineering*, Vol. 24, pp. 1801-1821.

Simon, H. L., O'Donoghue, P. E., and Atluri, S. N., 1987, "A Finite-Element-Alternating Technique for Evaluating Mixed Mode Stress Intensity Factors for Part-Through Surface Flaws," *International Journal for Numerical Methods in Engineering*, Vol. 24, pp. 689-709.

Sorensen, D. R., and Smith, F. W., 1977, "Semielliptical Surface Cracks Subjected to Shear Loading," *Pressure Vessel Technology—Part II*, Third International Conference, Tokyo, Japan, ASME, New York, pp. 545-551.

Eigenfunction Expansion for Creeping Flow in a Partially Obstructed Flow

P. Luchini,[9,11] A. Pozzi,[10,11] and A. R. Teodori[12]

1 The Problem and its Eigenfunctions

We wish to show how an eigenfunction expansion similar to that used by Joseph (1977, 1978) and Scarpi (1981) for creeping flow in a plane duct can be constructed for the case of a duct partially filled by a porous medium. We consider a two-dimensional duct of unit width in which the porous material occupies the region $h<y<1$, y being the transverse coordinate. We assume flow in this region to be ruled by the Darcy equation $\mu\mathbf{V} = -K \operatorname{grad} p$ (μ being the viscosity of the fluid, $\mathbf{V}$ and p its velocity and pressure, and K the permeability of the porous matrix). Although better approximations involving higher derivatives of velocity could be considered (for instance, the second-order equation of Brinkman 1947), the consistent coupling conditions with the free flow region would then involve a considerable number of phenomenological coefficients which can hardly be expected to be known in practice, as discussed in some detail by Saffman (1971).

Insofar as the analysis is restricted to the Darcy approximation, the coupling conditions between the flow in the porous matrix and that in the free region may be formulated as the continuity of pressure and the two components of velocity. The problem is thus stated through the following equations and boundary conditions:

$$u_1(x, 0) = 0,\ v_1(x, 0) = 0 \qquad (y = 0) \tag{1}$$

$$\mu\Delta_2\mathbf{V}_1 = \operatorname{grad} p_1 \qquad (0 < y < h) \tag{2}$$

$$\mathbf{V}_1(x, h) = \mathbf{V}_2(x, h),\ p_1(x, h) = p_2(x, h) \qquad (y = h) \tag{3}$$

$$\mu\mathbf{V}_2 = -K \operatorname{grad} p_2 \qquad (h < y < 1) \tag{4}$$

$$v_2(x, 1) = 0 \qquad (y = 1). \tag{5}$$

It must be noted that the pressure coupling condition does not include viscous stresses as it would, for instance, at the interface between different fluids, because viscous stresses are of the same order of magnitude as the higher-order interactions of the fluid with the porous matrix that are neglected in the Darcy approximation. Pressure may be eliminated from equations (1)-(5) by introducing the streamfunctions ψ_1 and ψ_2 and the vorticity ω_1, which turn out to satisfy the equations $\Delta_2\psi_1 = \omega_1$, $\Delta_2\omega_1 = 0$, and $\Delta_2\psi_2 = 0$. The pressure coupling condition at $y = h$ then becomes $\partial\psi_2/\partial y = -K\partial\omega_1/\partial y$, the other boundary conditions being straightforward.

Having coefficients independent of x, the coupled system of equations (1)-(5) admits separable complex eigenfunctions, just as the uncoupled Stokes problem does, in which each unknown is proportional to $e^{s_n x}$, for a suitable set of complex eigenvalues for s_n. Inserting the expressions $\psi_i = Y_{i,n}(y)e^{s_n x}$ ($i = 1, 2$) and $\omega_1 = \Omega_n(y)e^{s_n x}$ into the equations and boundary conditions, we obtain a linear homogeneous system of ordinary differential equations whose solution turns out to be given by

$$\Omega_n = 2s_n \cos s_n y + A_{1,n} s_n^2 \sin s_n y \tag{6}$$

$$Y_{1,n} = y \sin s_n y + A_{1,n}(\sin s_n y - s_n y \cos s_n y) \tag{7}$$

$$Y_{2,n} = A_{2,n} \sin[s_n(1 - y)] \tag{8}$$

where $A_{1,n} = N/D$, $A_{2,n} = [(S - wC)N + hSD]/[D \sin(s_n - w)]$, $N = 2Ks_n^2 SS - s_n hC$, $D = s_n^2(hS + 2KCs_n)$, $S = \sin w$, $C = \cos w$ and $w = s_n h$.

The compatability condition of the homogeneous system, that is the dispersion equation that determines the eigenvalues s_n, is

$$s_n N\{wS \sin[s_n(1 - h)] + (S - wC)\cos[s_n(1 - h)]\} + D\{(S + wC)\sin[s_n(1 - h)] + wS\cos[s_n(1 - h)]\} = 0 \tag{9}$$

2 Series Expansion of Initial Conditions

The problems of flow in a semi-infinite, partially obstructed duct with suitable initial conditions and flow in a finite duct section with conditions at both ends can be solved by an expansion in series of eigenfunctions, if it turns out possible to represent the initial or boundary conditions as such an expansion. This is a well-known procedure for self-adjoint problems; it has been also shown to work for the Stokes problem, not

[9]Assistant Professor.

[10]Professor.

[11]Istituto di Gasdinamica, Facolta di Ingegneria, University of Naples, Naples, Italy.

[12]Associate Professor, Dipartimento di Matematica e Fisica, University of Camerino, Camerino, Italy.

Manuscript received by the ASME Applied Mechanics Division, May 26, 1989; final revision, Nov. 19, 1990.

Table 5 Normalized stress intensity factors $k_3(0)/k_{3I}$ and $k_2(0)/k_{20}$ at the center of a semi-elliptic surface crack in a toroidal shell subjected to in-plane shear loading $\overset{\infty}{N}_{12}$ and transverse shear $\overset{\infty}{V}_1$ loading; $\nu = 0.3$., $R/h = 10$, $a/h = 2$, crack position A (see Fig. 8 of Joseph and Erdogan, 1988)

	L_o/h	0.2	0.4	0.6	0.8	0.95
Crack Position	R_i/R					
		In-Plane Shear $\overset{\infty}{N}_{12}$: $k_3(0)/k_{3I}$				
outer	1	.971	.895	.780	.618	.420
	4	.971	.896	.780	.617	.418
	7	.972	.896	.780	.617	.417
	$\to\infty$	.972	.896	.780	.616	.416
inner	1	.981	.921	.813	.638	.419
	4	.981	.920	.811	.636	.417
	7	.980	.919	.810	.635	.416
	$\to\infty$	.980	.919	.808	.633	.415
		Transverse Shear V_1: $k_2(0)/k_{20}$				
outer	1	.999	.985	.946	.866	.710
	4	.999	.985	.946	.867	.710
	7	.999	.985	.946	.867	.711
	$\to\infty$	.999	.985	.947	.867	.711
inner	1	.999	.986	.951	.878	.726
	4	.999	.986	.951	.878	.726
	7	.999	.986	.951	.878	.726
	$\to\infty$	.999	.986	.951	.878	.726

References

Desvaux, G. J., 1985, "The Line Spring Model for Surface Flaw, an Extension to Mode II and Mode III," Master's Thesis, Department of Mechanical Engineering, Massachusetts Institute of Technology, Cambridge, Mass.

Joseph, P. F., and Erdogan, F., 1988, "A Surface Crack in Shells Under Mixing Mode Loading Conditions," ASME JOURNAL OF APPLIED MECHANICS, Vol. 55, No. 4, pp. 795-804.

Joseph, P. F., and Erdogan, F., 1990, "Surface Crack in a Plate Under Antisymmetric Loading Conditions," *International Journal of Solids and Structures*, in press.

Nikishkov, G. P., and Atluri, S. N., 1987, "Calculation of Fracture Mechanics Parameters for an Arbitrary Three-Dimensional Crack, by the 'Equivalent Domain Integral' Method," *International Journal for Numerical Methods in Engineering*, Vol. 24, pp. 1801-1821.

Simon, H. L., O'Donoghue, P. E., and Atluri, S. N., 1987, "A Finite-Element-Alternating Technique for Evaluating Mixed Mode Stress Intensity Factors for Part-Through Surface Flaws," *International Journal for Numerical Methods in Engineering*, Vol. 24, pp. 689-709.

Sorensen, D. R., and Smith, F. W., 1977, "Semielliptical Surface Cracks Subjected to Shear Loading," *Pressure Vessel Technology—Part II*, Third International Conference, Tokyo, Japan, ASME, New York, pp. 545-551.

Eigenfunction Expansion for Creeping Flow in a Partially Obstructed Flow

P. Luchini,[9,11] A. Pozzi,[10,11] and A. R. Teodori[12]

1 The Problem and its Eigenfunctions

We wish to show how an eigenfunction expansion similar to that used by Joseph (1977, 1978) and Scarpi (1981) for creeping flow in a plane duct can be constructed for the case of a duct partially filled by a porous medium. We consider a two-dimensional duct of unit width in which the porous material occupies the region $h<y<1$, y being the transverse coordinate. We assume flow in this region to be ruled by the Darcy equation $\mu\mathbf{V} = -K \operatorname{grad} p$ (μ being the viscosity of the fluid, $\mathbf{V}$ and p its velocity and pressure, and K the permeability of the porous matrix). Although better approximations involving higher derivatives of velocity could be considered (for instance, the second-order equation of Brinkman 1947), the consistent coupling conditions with the free flow region would then involve a considerable number of phenomenological coefficients which can hardly be expected to be known in practice, as discussed in some detail by Saffman (1971).

Insofar as the analysis is restricted to the Darcy approximation, the coupling conditions between the flow in the porous matrix and that in the free region may be formulated as the continuity of pressure and the two components of velocity. The problem is thus stated through the following equations and boundary conditions:

$$u_1(x, 0) = 0,\ v_1(x, 0) = 0 \qquad (y = 0) \tag{1}$$

$$\mu\Delta_2\mathbf{V}_1 = \operatorname{grad} p_1 \qquad (0 < y < h) \tag{2}$$

$$\mathbf{V}_1(x, h) = \mathbf{V}_2(x, h),\ p_1(x, h) = p_2(x, h) \qquad (y = h) \tag{3}$$

$$\mu\mathbf{V}_2 = -K \operatorname{grad} p_2 \qquad (h < y < 1) \tag{4}$$

$$v_2(x, 1) = 0 \qquad (y = 1). \tag{5}$$

It must be noted that the pressure coupling condition does not include viscous stresses as it would, for instance, at the interface between different fluids, because viscous stresses are of the same order of magnitude as the higher-order interactions of the fluid with the porous matrix that are neglected in the Darcy approximation. Pressure may be eliminated from equations (1)-(5) by introducing the streamfunctions ψ_1 and ψ_2 and the vorticity ω_1, which turn out to satisfy the equations $\Delta_2\psi_1 = \omega_1$, $\Delta_2\omega_1 = 0$, and $\Delta_2\psi_2 = 0$. The pressure coupling condition at $y = h$ then becomes $\partial\psi_2/\partial y = -K\partial\omega_1/\partial y$, the other boundary conditions being straightforward.

Having coefficients independent of x, the coupled system of equations (1)-(5) admits separable complex eigenfunctions, just as the uncoupled Stokes problem does, in which each unknown is proportional to $e^{s_n x}$, for a suitable set of complex eigenvalues for s_n. Inserting the expressions $\psi_i = Y_{i,n}(y)e^{s_n x}$ ($i = 1, 2$) and $\omega_1 = \Omega_n(y)e^{s_n x}$ into the equations and boundary conditions, we obtain a linear homogeneous system of ordinary differential equations whose solution turns out to be given by

$$\Omega_n = 2s_n \cos s_n y + A_{1,n} s_n^2 \sin s_n y \tag{6}$$

$$Y_{1,n} = y \sin s_n y + A_{1,n}(\sin s_n y - s_n y \cos s_n y) \tag{7}$$

$$Y_{2,n} = A_{2,n} \sin[s_n(1 - y)] \tag{8}$$

where $A_{1,n} = N/D$, $A_{2,n} = [(S - wC)N + hSD]/[D \sin(s_n - w)]$, $N = 2Ks_n^2 SS - s_n hC$, $D = s_n^2(hS + 2KCs_n)$, $S = \sin w$, $C = \cos w$ and $w = s_n h$.

The compatability condition of the homogeneous system, that is the dispersion equation that determines the eigenvalues s_n, is

$$s_n N\{wS \sin[s_n(1 - h)] + (S - wC)\cos[s_n(1 - h)]\} + D\{(S + wC)\sin[s_n(1 - h)] + wS\cos[s_n(1 - h)]\} = 0 \tag{9}$$

2 Series Expansion of Initial Conditions

The problems of flow in a semi-infinite, partially obstructed duct with suitable initial conditions and flow in a finite duct section with conditions at both ends can be solved by an expansion in series of eigenfunctions, if it turns out possible to represent the initial or boundary conditions as such an expansion. This is a well-known procedure for self-adjoint problems; it has been also shown to work for the Stokes problem, not

[9]Assistant Professor.

[10]Professor.

[11]Istituto di Gasdinamica, Facolta di Ingegneria, University of Naples, Naples, Italy.

[12]Associate Professor, Dipartimento di Matematica e Fisica, University of Camerino, Camerino, Italy.

Manuscript received by the ASME Applied Mechanics Division, May 26, 1989; final revision, Nov. 19, 1990.

self-adjoint under the usual L_2 scalar product, by introducing an ad hoc scalar product mediated by a suitable 2×2 matrix which makes the problem self-adjoint (Joseph 1977, 1978).

For the nonself-adjoint problem considered in this paper, we may apply the general procedure adopted by Van Kampen (1955) for microwave problems, which consists of explicitly determining the adjoint eigenfunctions, through the resolution of the adjoint system of differential equations, and then calculating the coefficients of the expansion from the scalar product of these adjoint eigenfunctions with the given initial conditions. Although the completeness of the eigenfunction expansion is not guaranteed for nonself-adjoint problems, and from a mathematical point of view needs to be proved case by case, we shall assume, without proof, that such an expansion exists for a physically significant problem like the one we are considering.

The solution of the adjoint system of differential equations, whose derivation we do not have enough space to discuss here, gives the three functions

$$\overline{\Omega}_n=\overline{A}_{1,n}(\sin s_n y - s_n y\cos s_n y)+\overline{B}_n y\sin s_n y \qquad (10)$$

$$\overline{Y}_{1,n}=2s_n(\overline{A}_{1,n}\sin s_n y+\overline{B}_n\cos s_n y) \qquad (11)$$

$$\overline{Y}_{2,n}=\overline{A}_{2,n}\sin s_n(1-y) \qquad (12)$$

where $\overline{A}_{1,n} = -[(S+wC)\cos(s_n-w)]/s_n^2$, $\overline{A}_{2,n} = 2(CS+w)$ and $\overline{B}_n = hS\cos(s_n-w)$. By construction these functions have the property that their scalar product with the eigenfunctions defined as

$$\int_0^h (Y_{1,n}\overline{Y}_{1,m}+\Omega_n\overline{\Omega}_m)dy + \int_h^1 Y_{2,n}\overline{Y}_{2,m}dy$$

is zero whenever $m \neq n$. Therefore, once it is assumed that an eigenfunction expansion exists, its nth coefficient can be simply determined by scalarly multiplying the initial conditions by the nth adjoint eigenfunction and dividing the result by the scalar product of the nth eigenfunction times its adjoint.

3 Test Results

The problem of flow in a partially obstructed duct, as stated previously, is characterized by the two parameters h and K, both of which have been nondimensionalized with respect to the duct width which thus becomes unity. We have calculated the 30 smallest eigenvalues, by solving equation (9) numerically by Newton iteration, and solved a test initial-value problem in the three cases $h = 0.4$, $K = 1$; $h = 0.4$, $K = 0.1$, and $h = 1$, $K = 0$, the last of which represents the already studied case of flow in a free duct. The eigenvalues turn out to be partly real and partly complex, which is not surprising since of the two problems (Laplace and biharmonic equation) of which we consider the coupling one has real and the other complex eigenvalues. The initial conditions assumed in the test were $\psi(x, 0) = \sin 2\pi y$ and $\omega(x, 0) = 0$. In all three cases the error in the representation of the initial conditions by the eigenfunction expansion decreases consistently with increasing number of terms, thus confirming the assumption that such a representation exists. Some caution is needed, however, as already noted by Joseph (1977, 1978) in connection with the free-flow problem, in dealing with the expansion for vorticity, which does not turn out to be converging in the ordinary sense at $x = 0$. This difficulty is easily circumvented, mathematically, by first summing the series for x nonzero and then letting x tend to zero; numerically, by summing the series for a nonzero x which is chosen smaller and smaller with increasing number of terms. The error in the streamfunction, whose convergence is on the contrary uniform, was of the order of a few percent with ten terms and decreased to 1-2 percent with 30 terms in the expansion.

We acknowledge the support of the Italian Ministry of Public Education.

References

Brinkman, H. C., 1947, "A Calculation of the Viscous Force Exerted by a Flowing Fluid on a Derise Swarm of Particles," *Appl. Sci. Res.*, Vol. A1, p. 27.

Joseph, D. D., 1977, "The Convergence of Biorthogonal Series for Biharmonic and Stokes Flow Edge Problems. Part I," *SIAM J. Appl. Math.*, Vol. 33, pp. 337-347.

Joseph, D. D., and Sturges, L., 1978, "The Convergence of Biorthogonal Series for Biharmonic and Stokes Problems. Part II," *SIAM J. Appl. Math.*, Vol. 34, pp. 7-26.

Saffman, P. G., 1971, "On the Boundary Condition at the Surface of a Porous Medium," *Stud. Appl. Maths.*, Vol. 50, pp. 93-101.

Scarpi, G., 1981, "The Development of a Plane Laminar Flow at Low Reynolds Numbers," *Meccanica*, Vol. 16, pp. 199-203.

Van Kampen, N. G., 1955, "On the Theory of Stationary Waves in Plasmas," *Physica*, Vol. 21, pp. 949-963.

Dynamic Response and Buckling Failure Measures for Structures With Bounded and Random Imperfections

H. E. Lindberg[13]

Comparisons between an unknown-but-bounded imperfection model and a random imperfection model show that for simple pointwise failure measures, at least, the two models give the same expressions for their measures of response, but each measure has a distinctly different interpretation. The former gives the maximum possible response for any imperfection within a specified bound. The latter gives the standard deviation of response, which, together with the statistical distribution, can be used to specify the maximum response at a specified confidence level. However, since the statistical distributions of imperfections, and hence of the response are often unknown, confidence levels are difficult to define, especially in the tail of the distribution at high confidence levels. The unknown-but-bounded model requires less information about the imperfections to come to a well-defined bound on response. It is further shown that, while the maximum possible response might seem to be a severe failure avoidance criterion, it can be less constricting than having to impose artificially high confidence levels with poorly known statistical distributions.

1 Introduction

An unknown-but-bounded imperfection model was introduced by Ben-Haim and Elishakoff (1989b) for the study of dynamic response and failure of structures under pulsed parametric loading, in particular for elastic bars under dynamic axial loads. Imperfections were taken as a series of N terms of the natural vibration (and buckling) mode shapes of the structure, with coefficients A_n specified to be bounded by an ellipsoid in N-dimensional Euclidean space. Failure was defined by several measures of response, including deflection of the bar at a particular position and time, the spatial integral of the deflection at a particular time, and the spatial integral of the square of the deflection. For each measure of failure, a formula was derived for the maximum possible response for any imperfection vector $\mathbf{A}$ within or on the ellipsoid. This work was a sequel to an earlier application of the method to imperfection sensitivity in static buckling (Ben-Haim and Elishakoff, 1989a) based on an approach developed in the field of estimation and control (Schweppe, 1973). These are all examples of convex modeling, a general set-theoretical approach to representing uncertainty, described more completely in Ben-Haim and Elishakoff (1990).

[13]Aptek, Inc., San Jose, CA 95129.

Manuscript received by the ASME Applied Mechanics Division, Sept. 5, 1989; final revision, Nov. 19, 1990.

self-adjoint under the usual L_2 scalar product, by introducing an ad hoc scalar product mediated by a suitable 2×2 matrix which makes the problem self-adjoint (Joseph 1977, 1978).

For the nonself-adjoint problem considered in this paper, we may apply the general procedure adopted by Van Kampen (1955) for microwave problems, which consists of explicitly determining the adjoint eigenfunctions, through the resolution of the adjoint system of differential equations, and then calculating the coefficients of the expansion from the scalar product of these adjoint eigenfunctions with the given initial conditions. Although the completeness of the eigenfunction expansion is not guaranteed for nonself-adjoint problems, and from a mathematical point of view needs to be proved case by case, we shall assume, without proof, that such an expansion exists for a physically significant problem like the one we are considering.

The solution of the adjoint system of differential equations, whose derivation we do not have enough space to discuss here, gives the three functions

$$\overline{\Omega}_n = \overline{A}_{1,n}(\sin s_n y - s_n y \cos s_n y) + \overline{B}_n y \sin s_n y \qquad (10)$$

$$\overline{Y}_{1,n} = 2s_n(\overline{A}_{1,n} \sin s_n y + \overline{B}_n \cos s_n y) \qquad (11)$$

$$\overline{Y}_{2,n} = \overline{A}_{2,n} \sin s_n (1-y) \qquad (12)$$

where $\overline{A}_{1,n} = -[(S+wC)\cos(s_n - w)]/s_n^2$, $\overline{A}_{2,n} = 2(CS+w)$ and $\overline{B}_n = hS\cos(s_n - w)$. By construction these functions have the property that their scalar product with the eigenfunctions defined as

$$\int_0^h (Y_{1,n}\overline{Y}_{1,m} + \Omega_n\overline{\Omega}_m)dy + \int_h^1 Y_{2,n}\overline{Y}_{2,m}dy$$

is zero whenever $m \neq n$. Therefore, once it is assumed that an eigenfunction expansion exists, its nth coefficient can be simply determined by scalarly multiplying the initial conditions by the nth adjoint eigenfunction and dividing the result by the scalar product of the nth eigenfunction times its adjoint.

3 Test Results

The problem of flow in a partially obstructed duct, as stated previously, is characterized by the two parameters h and K, both of which have been nondimensionalized with respect to the duct width which thus becomes unity. We have calculated the 30 smallest eigenvalues, by solving equation (9) numerically by Newton iteration, and solved a test initial-value problem in the three cases $h = 0.4$, $K = 1$; $h = 0.4$, $K = 0.1$, and $h = 1$, $K = 0$, the last of which represents the already studied case of flow in a free duct. The eigenvalues turn out to be partly real and partly complex, which is not surprising since of the two problems (Laplace and biharmonic equation) of which we consider the coupling one has real and the other complex eigenvalues. The initial conditions assumed in the test were $\psi(x, 0) = \sin 2\pi y$ and $\omega(x, 0) = 0$. In all three cases the error in the representation of the initial conditions by the eigenfunction expansion decreases consistently with increasing number of terms, thus confirming the assumption that such a representation exists. Some caution is needed, however, as already noted by Joseph (1977, 1978) in connection with the free-flow problem, in dealing with the expansion for vorticity, which does not turn out to be converging in the ordinary sense at $x = 0$. This difficulty is easily circumvented, mathematically, by first summing the series for x nonzero and then letting x tend to zero; numerically, by summing the series for a nonzero x which is chosen smaller and smaller with increasing number of terms. The error in the streamfunction, whose convergence is on the contrary uniform, was of the order of a few percent with ten terms and decreased to 1-2 percent with 30 terms in the expansion.

We acknowledge the support of the Italian Ministry of Public Education.

References

Brinkman, H. C., 1947, "A Calculation of the Viscous Force Exerted by a Flowing Fluid on a Derise Swarm of Particles," *Appl. Sci. Res.*, Vol. A1, p. 27.

Joseph, D. D., 1977, "The Convergence of Biorthogonal Series for Biharmonic and Stokes Flow Edge Problems. Part I," *SIAM J. Appl. Math.*, Vol. 33, pp. 337-347.

Joseph, D. D., and Sturges, L., 1978, "The Convergence of Biorthogonal Series for Biharmonic and Stokes Problems. Part II," *SIAM J. Appl. Math.*, Vol. 34, pp. 7-26.

Saffman, P. G., 1971, "On the Boundary Condition at the Surface of a Porous Medium," *Stud. Appl. Maths.*, Vol. 50, pp. 93-101.

Scarpi, G., 1981, "The Development of a Plane Laminar Flow at Low Reynolds Numbers," *Meccanica*, Vol. 16, pp. 199-203.

Van Kampen, N. G., 1955, "On the Theory of Stationary Waves in Plasmas," *Physica*, Vol. 21, pp. 949-963.

Dynamic Response and Buckling Failure Measures for Structures With Bounded and Random Imperfections

H. E. Lindberg[13]

Comparisons between an unknown-but-bounded imperfection model and a random imperfection model show that for simple pointwise failure measures, at least, the two models give the same expressions for their measures of response, but each measure has a distinctly different interpretation. The former gives the maximum possible response for any imperfection within a specified bound. The latter gives the standard deviation of response, which, together with the statistical distribution, can be used to specify the maximum response at a specified confidence level. However, since the statistical distributions of imperfections, and hence of the response are often unknown, confidence levels are difficult to define, especially in the tail of the distribution at high confidence levels. The unknown-but-bounded model requires less information about the imperfections to come to a well-defined bound on response. It is further shown that, while the maximum possible response might seem to be a severe failure avoidance criterion, it can be less constricting than having to impose artificially high confidence levels with poorly known statistical distributions.

1 Introduction

An unknown-but-bounded imperfection model was introduced by Ben-Haim and Elishakoff (1989b) for the study of dynamic response and failure of structures under pulsed parametric loading, in particular for elastic bars under dynamic axial loads. Imperfections were taken as a series of N terms of the natural vibration (and buckling) mode shapes of the structure, with coefficients A_n specified to be bounded by an ellipsoid in N-dimensional Euclidean space. Failure was defined by several measures of response, including deflection of the bar at a particular position and time, the spatial integral of the deflection at a particular time, and the spatial integral of the square of the deflection. For each measure of failure, a formula was derived for the maximum possible response for any imperfection vector $\mathbf{A}$ within or on the ellipsoid. This work was a sequel to an earlier application of the method to imperfection sensitivity in static buckling (Ben-Haim and Elishakoff, 1989a) based on an approach developed in the field of estimation and control (Schweppe, 1973). These are all examples of convex modeling, a general set-theoretical approach to representing uncertainty, described more completely in Ben-Haim and Elishakoff (1990).

[13]Aptek, Inc., San Jose, CA 95129.

Manuscript received by the ASME Applied Mechanics Division, Sept. 5, 1989; final revision, Nov. 19, 1990.

Another approach has been to specify the imperfections by a modal series with coefficients taken as random quantities having a Gaussian distribution with zero mean value and standard deviation σ_n that varies with mode number n. In early work of this type, σ_n was taken as constant to a maximum mode number N and zero thereafter, i.e., band-limited white noise. Statistics of buckle wavelengths for such imperfections were found for bars (Lindberg, 1965) and cylindrical shells (Lindberg and Herbert, 1966) under axial impact. Extension of these results to variable σ_n is straightforward. In later work, σ_n was taken to decrease with increasing n to more realistically represent imperfections measured in cylindrical shells (Arbocz, 1982; Kirkpatrick and Holmes, 1989) while also maximizing numerical efficiency in finite element calculations (Lindberg, 1988; Kirkpatrick and Holmes, 1989). Buckle shapes were calculated at a sequence of times for a few sets of random coefficients. In Lindberg (1988) the statistical distribution of peak-to-peak buckle amplitudes was calculated at a time beyond which the buckle shapes remained essentially fixed, thus giving the statistics of failure by this measure. Monte Carlo calculations for other response measures were done by Elishakoff (1978).

In the present paper, the bounded imperfection model is extended to include the mode-dependent amplitude ideas used with random imperfection model, and relationships between the two models and their respective measures of response are demonstrated which give better insight into both.

2 Bounded Imperfection Model

In the following, the derivation of the maximum possible response given by Ben-Haim and Elishakoff (1989b) is given with more complete intermediate steps and additional discussion of the nature of the imperfection bounds. The approach is similar for the other measures of response analyzed by this model, so here we consider only the deflection $u(\mathbf{x},t)$ at position vector $\mathbf{x}$ and time t. Also, this particular example allows a simple solution for its probabilistic counterpart in the next section. A general solution for the deflection is assumed to be available in modal series form:

$$u(\mathbf{x},t)=\sum_{n=1}^{N}A_n\phi_n(\mathbf{x},t)=\mathbf{A}^T\phi(\mathbf{x},t) \tag{1}$$

where $\mathbf{A}^T=\{A_1,\cdots A_N\}$ and similarly for ϕ, and $\phi_n(\mathbf{x},t)$ is defined such that $u(\mathbf{x},0)$ is the total initial imperfection shape. Thus,

$$\phi_n(\mathbf{x},t)=[1+q_n(t)]\varphi_n(\mathbf{x}) \tag{2}$$

in which $q_n(t)$ are modal response amplitudes, with initial conditions $q_n(0)=\partial q_n(0)/\partial t=0$, and $\varphi_n(\mathbf{x})$ are the mode shapes.

2.1 Unknown-But-Bounded Imperfections. Uncertainty in the initial imperfection profile is represented by allowing the imperfection vector $\mathbf{A}$ to vary on a set of values bounded by an ellipsoid:

$$Z(\theta,\mathbf{W})=\{\mathbf{A}:\quad \mathbf{A}^T\mathbf{W}\mathbf{A}\le\theta^2\} \tag{3}$$

where $\mathbf{W}$ is an $N\times N$ positive definite real symmetric matrix that specifies the shape of an ellipsoid in N-dimensional space and θ^2 is a positive number that specifies its size. The set of extreme points of the set $Z(\theta,\mathbf{W})$ is the ellipsoidal shell:

$$C(\theta,\mathbf{W})=\{\mathbf{A}:\quad \mathbf{A}^T\mathbf{W}\mathbf{A}=\theta^2\}. \tag{4}$$

Because the total displacement $u(\mathbf{x},t)$ is a linear function of the Fourier coefficients, and because $Z(\theta,\mathbf{W})$ is a convex set, the maximum $u_{\max}(\mathbf{x},t)$ occurs on the set of extreme points $C(\theta,\mathbf{W})$.

In the examples in Ben-Haim and Elishakoff (1989b), $\mathbf{W}$ was taken as the identity matrix $\mathbf{I}$, which assumes no systematic dependence of the imperfections on n. The bounding shell is then a sphere and the constraint on set $Z(\theta,\mathbf{I})$ is

$$A_1^2+A_2^2+\cdots+A_n^2+\cdots A_N^2\le\theta^2. \tag{5}$$

The nominal value of each and every coefficient A_n is zero and its range is $\pm\theta$, found by setting $A_k=0$ for $k\neq n$. The constraint shell for $\mathbf{W}=\mathbf{I}$ is

$$A_1^2+A_2^2+\cdots+A_N^2=\theta^2. \tag{6}$$

Observe that as more terms are included in the analysis, i.e., as N is increased, this constraint appears to become more severe. For example, with $N=2$ the coefficients A_1 and A_2 are constrained to the circle $A_1^2+A_2^2=\theta^2$. With $N=3$, the coefficients A_1, A_2, and A_3 are constrained to a sphere of the same radius. Thus, for nonzero A_3, $A_3=c$, the coefficients A_1 and A_2 are now constrained to a circle of smaller radius given by the cut of the plane $A_3=c$ through the sphere. However, the $N=3$ constraint still allows A_1 and A_2 to fall on the $N=2$ circle (i.e., $A_3=0$) if that happens to give greater response. An example comparison of responses from bounded and from random imperfections given in the next section shows that holding θ fixed with increasing N is analogous to (but not the same as) holding the standard deviation of the imperfection coefficients constant for all N.

The examples actually worked out are for a case in which $\mathbf{W}$ is not the identity matrix but instead specifies a known systematic dependence of the imperfection coefficients on n. Such a dependence is needed, for example, in analysis of pulse buckling under very high axial loads, in which response is dominated by modes with large values of n and hence requires large values of N. It is then essential to account explicitly for the known systematic decrease in imperfection amplitudes with increasing n. For this purpose, $\mathbf{W}$ is taken as

$$\mathbf{W}=\text{diag}\{1^p,\ 2^p,\ \cdots\ n^p,\ \cdots\ N^p\}. \tag{7}$$

The bounding ellipsoid for the set $Z(\theta,\mathbf{W})$ is then

$$A_1^2+2^pA_2^2+\cdots+n^pA_n^2+\cdots+N^pA_N^2\le\theta^2 \tag{8}$$

and the range for each A_n is from $-R_n$ to $+R_n$, where

$$R_n=\theta n^{-p/2}. \tag{9}$$

Measurements of imperfection in cylindrical shells (Arbocz, 1982) suggest that reasonable values for the exponent p are somewhat larger than 2. In Lindberg (1988) it is suggested that conservative analyses can be done with $p=1$, since this value is the separator between convergent and divergent series (as $N\to\infty$) for the power spectral density of the total initial imperfection, as shown in the next section. The measurements reported in Arbocz (1982) suggest that imperfection coefficients in low-order modes, to about $n=8$, tend to be nearly constant with n. The point here is that all such prior knowledge of the systematic variation of A_n with n, but not in specific values, must be incorporated into $\mathbf{W}$.

2.2 Maximum Response. Return now to determining the maximum deflection $u_{\max}(\mathbf{x},t)$ that can be obtained for any imperfection vector $\mathbf{A}$ in set $Z(\theta,\mathbf{W})$. Thus, from equation (1) and the convexity of the bound, we wish to maximize $\mathbf{A}^T\phi$ subject to the constraint that $\mathbf{A}$ falls on the extreme points of Z, that is, on $\mathbf{A}^T\mathbf{W}\mathbf{A}=\theta^2$. The desired maximum is found with the Hamiltonian

$$H=\mathbf{A}^T\phi+\lambda(\mathbf{A}^T\mathbf{W}\mathbf{A}-\theta^2) \tag{10}$$

in which $\mathbf{A}^T\phi$ is the function to be maximized and λ is a Lagrangian multiplier for the constraint. The extremum condition is

$$0=\frac{\partial H}{\partial\mathbf{A}}=\phi+2\lambda\mathbf{W}\mathbf{A}. \tag{11}$$

To express λ in terms of ϕ and θ, the symmetry of $\mathbf{W}$ is first used to transpose the extremum condition:

$$\phi^T=-2\lambda\mathbf{A}^T\mathbf{W}. \tag{12}$$

This expression is then post multiplied by $\mathbf{W}^{-1}$ to obtain

$$\phi^T \mathbf{W}^{-1} = -2\lambda \mathbf{A}^T. \tag{13}$$

Each side of this equation is post multiplied by the corresponding sides of the untransposed extremum condition (11) to give

$$\phi^T \mathbf{W}^{-1} \phi = 4\lambda^2 \mathbf{A}^T \mathbf{W} \mathbf{A} = 4\lambda^2 \theta^2. \tag{14}$$

The desired expression for the Lagrange multiplier is then

$$\lambda = \pm \frac{1}{2\theta} \sqrt{\phi^T \mathbf{W}^{-1} \phi}. \tag{15}$$

The extremum condition is now premultiplied by $\mathbf{A}^T$ to obtain

$$\mathbf{A}^T \phi = -2\lambda \mathbf{A}^T \mathbf{W} \mathbf{A} = \mp \theta \sqrt{\phi^T \mathbf{W}^{-1} \phi} \tag{16}$$

and hence

$$u_{\max}(\mathbf{x},t) = \theta \sqrt{\phi(\mathbf{x},t)^T \mathbf{W}^{-1} \phi(\mathbf{x},t)} \tag{17}$$

in which the signs have been dropped. The imperfection that gives this maximum response is

$$\mathbf{A}_{mr} = \frac{\theta \mathbf{W}^{-1} \phi(\mathbf{x},t)}{[\phi(\mathbf{x},t)^T \mathbf{W}^{-1} \phi(\mathbf{x},t)]^{1/2}}. \tag{18}$$

Observe that $u_{\max}$ depends directly on the imperfection amplitude parameter θ and on $\mathbf{W}$, but is independent of the vector $\mathbf{A}$ of individual imperfection coefficients. This dependence was removed by the maximization. Thus, any influence of systematic variations with n of the imperfection coefficients on maximum response must be included in the definition of $\mathbf{W}$.

With $\mathbf{W}$ from (7), the maximum response from (17) in expanded form is then

$$u_{\max}(\mathbf{x},t) = \theta \left[\sum_{n=1}^{N} \frac{1}{n^p} \phi_n^2(\mathbf{x},t) \right]^{1/2}. \tag{19}$$

2.3 Comparison to Random Imperfection Model. In the random imperfection model, the deflection is expressed by

$$u(\mathbf{x},t) = \sum_{n=1}^{N} a_n \phi_n(\mathbf{x},t) \tag{20}$$

in which the coefficients a_n are independent random variables with zero mean value and variance σ_n^2. Corresponding to the example for $\mathbf{W}$ in (7), this variance is taken as

$$\sigma_n^2 = \sigma^2 n^{-p} \tag{21}$$

where σ^2 is a positive constant. From equations (2), (20), and the independence of a_n, the variance of the initial imperfection $u(\mathbf{x},0)$ is

$$\sigma_{u0}^2 = \sigma^2 \sum_{n=1}^{N} n^{-p} \varphi_n^2(\mathbf{x}). \tag{22}$$

Since $\varphi_n^2(\mathbf{x})$ is bounded and positive, this series converges (as $N \to \infty$) in general for $p > 1$ and diverges for $p < 1$, as mentioned in the previous section.

More generally, the standard deviation of the response $u(\mathbf{x},t)$ is found by the same procedure, which gives

$$\sigma_u(\mathbf{x},t) = \sigma \left[\sum_{n=1}^{N} \frac{1}{n^p} \phi_n^2(\mathbf{x},t) \right]^{1/2}. \tag{23}$$

When this expression is compared with (19), one sees immediately that

$$u_{\max}(\mathbf{x},t) = \frac{\theta}{\sigma} \sigma_u(\mathbf{x},t). \tag{24}$$

Thus, the maximum deflection from the bounded imperfection model is proportional to the standard deviation of the deflection from the random imperfection model. Also, recall from (9) that the semi-axis range of A_n in the bounded imperfection model is $R_n = \theta n^{-p/2}$, and, from (21), the standard deviation of A_n in the random imperfection model is $\sigma_n = \sigma n^{-p/2}$. The two models therefore give the same numerical result ($\theta = \sigma$ in (24)) when the semi-range of the individual Fourier coefficients in the bounded imperfection model is equal to the standard deviation of the individual coefficients in the random imperfection model. This is a more general case of the statement made earlier that (for $p = 0$) holding θ fixed with increasing N is analogous to holding the standard deviation σ_n constant for all N.

However, it must be emphasized that the two imperfection models are distinctly different and the physical interpretation of the response measures from the two models are also different. The usefulness of the result in (24) is in problems for which the analyst does not have enough information to decide which imperfection model best describes the actual imperfections. For example, it is satisfying to know that if the statistical distribution of imperfections must be assumed, and hence the resulting statistics of response are questionable, the calculated response can also be interpreted in terms of the maximum possible response if the imperfections were bounded rather than random.

Furthermore, the constraints on loading or structural parameters, to ensure that the response is less than the maximum possible response, are comparable to the constraints to ensure a specified confidence level. In the example, the maximum possible response with bounded imperfection coefficients is equal to the standard deviation of response with random imperfections coefficients that have standard deviations equal to the semi-ranges of the bounded imperfections. The degree of conservativeness in specifying imperfection bounds (based on the same available data, the semi-range bounds will be substantially larger than the standard deviations) is comparable to the conservativeness in estimating response at confidence with poorly defined statistics (the probabilistic response at high confidence must be taken substantially larger than the standard deviation of the response).

3 Summary and Conclusions

The nonprobabilistic unknown-but-bounded model is a useful alternative in modeling uncertainty of imperfections, based on the idea of set membership and convex modeling. In application of this model, it is crucial to incorporate systematic variations of imperfections with mode number n into the definition of the matrix $\mathbf{W}$. An example is the decrease in imperfection coefficients as $n \to \infty$, required to ensure a bounded total imperfection shape. Without such variations included in $\mathbf{W}$, their influence on the calculated maximum response measures will be lost.

In the example application, the bounded and random imperfection models give the same analytical expression for their respective measures of response $u_{\max}$ and σ_u (within a multiplying constant), but each is interpreted in a different way. The response measure for the bounded imperfection model is useful in that within the specified bound one knows that no other set of imperfections results in a greater response. Interpretation of response with the random imperfection model is statistical; the maximum possible value of u is unbounded but one can associate a confidence level with the maximum being less than a multiple of σ_u. When the statistical or bounded nature of the imperfections is open to question, it is useful to know that the two measures of response have the same functional form so that interpretation of response from the two points of view can be made by simply scaling the results by a constant.

References

Arbocz, J., 1982, "The Imperfection Data Bank: A Means to Obtain Realistic Buckling Loads," *Buckling of Shells,* Proceedings of a State-of-the-Art Colloquium, New York.

Ben-Haim, Y., and Elishakoff, I., 1989a, "Non-Probabilistic Models of Uncertainty in the Nonlinear Buckling of Shells with General Imperfections: Theoretical Estimates of the Knockdown Factor," ASME JOURNAL OF APPLIED MECHANICS, Vol. 56, pp. 403-410.

Ben-Haim, Y., and Elishakoff, I., 1989b, "Dynamics and Failure of Structures Based on the Unknown-but-Bounded Imperfection Model," *Recent Advances in Impact Dynamics of Engineering Structures—1989,* D. Hui and N. Jones, eds., ASME AMD-Vol. 105, AD-Vol. 17, pp. 89-95.

Ben-Haim, Y., and Elishakoff, I., 1990, *Convex Models of Uncertainty in Applied Mechanics,* Elsevier, New York.

Elishakoff, I., 1978, "Axial Impact Buckling of a Thin Bar Via Monte Carlo Method," ASME JOURNAL OF APPLIED MECHANICS, Vol. 45, pp. 586-590.

Kirkpatrick, S. W., and Holmes, B. S., 1989, "Effect of Initial Imperfections on Dynamic Buckling of Shells," *ASCE Journal of Engineering Mechanics,* Vol. 115, No. 5, pp. 1075-1093.

Lindberg, H. E., 1965, "Impact Buckling of a Thin Bar," ASME JOURNAL OF APPLIED MECHANICS, Vol. 32, pp. 312-322.

Lindberg, H. E., and Herbert, R. E., 1966, "Dynamic Buckling of a Thin Cylindrical Shell Under Axial Impact," ASME JOURNAL OF APPLIED MECHANICS, Vol. 33, pp. 105-112.

Lindberg, H. E., 1988, "Random Imperfections for Dynamic Pulse Buckling," *ASCE Journal of Engineering Mechanics,* Vol. 114, No. 7, pp. 1144-1165.

Schweppe, F. C., 1973, *Uncertain Dynamical Systems,* Prentice-Hall, Englewood Cliffs, N.J.

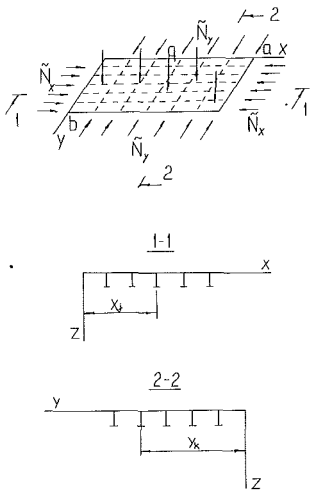

Fig. 1 Geometry of the panel; mechanical loads

Thermoelastic Problems of Reinforced Rectangular Panels

Victor Birman[14]

The static response of isotropic reinforced panels in nonuniform thermal fields is discussed. The effects of temperature on material properties are included into consideration. The governing equations formulated in the Note allow the solution both by energy methods and using equilibrium equations. The theory is applied to estimation of the effect of a uniform temperature on stability of compressed reinforced panels and to the problem of thermal bending of unstiffened plates.

Introduction

Problems of structural response of panels in thermal fields are important both for development of thermoelastic theory as well as in aerospace and nuclear engineering and in other applications. The number of investigations in this area is very large; we mention here only the classical book of Boley and Weiner (1960) dealing with the problem, and the recent review of Tauchert (1986) concentrating on thermoelasticity of plates.

Typically, the studies of thermoelastic plate problems are based on an assumption that material properties are insensitive to temperature. This approach, justified in many practical problems, becomes questionable for composite materials and new alloys operating at high temperatures resulting either from aerodynamic heating in supersonic or hypersonic flight or from a technological process. The formulations of thermoelastic problems for unstiffened composite material cylindrical shells and rectangular panels incorporating temperature-dependent material properties were presented by Ambartsumian (1970, 1974) and Tauchert (1986). The review of Noda (1986) presents a list of works on thermoelasticity of isotropic plates with temperature-dependent material properties. However, these solutions dealt only with unstiffened plates. Laminated rectangular plates with temperature-dependent properties were considered by Chen and Chen (1989). Note here also the recent results presented for beams with temperature-dependent properties by Artemian (1988) and Birman (1990).

In this Note thermoelastic problems of reinforced rectangular panels manufactured from an isotropic material are considered. Governing equations are developed, and the solutions of sample problems for reinforced and unstiffened panels are obtained.

Governing Equations

Consider a rectangular reinforced panel subject to in-plane compressive loads of intensities $\tilde{N}_x, \tilde{N}_y$, lateral distributed loading $q=q(x,y)$ and nonuniform temperature $T=T(x,y,z)$, as shown in Fig. 1. The following assumptions are used in this Note:

- materials of the stiffeners and the plate are isotropic;
- the properties of materials depend on temperature;
- materials remain in the linear elastic range;
- the strain-displacement relationships are linear.

The stiffeners are assumed to be attached to the plate so that their deformations occur without slipping. Therefore, normal strains in the plate and in the stiffeners vary linearly in the thickness direction. According to the classic approach (Baruch, 1964, 1965), the shear membrane force exists in the plate only. Torsional stiffness of the stiffeners is taken into consideration.

Strain-displacement relationships in the middle plane of the plate are:

$$\epsilon_x^o = u_{,x}$$
$$\epsilon_y^o = v_{,y} \tag{1}$$
$$\gamma_{xy}^o = u_{,y} + v_{,x}$$

where u and v are the in-plane displacements in the x and y directions, respectively, and the superscript o indicates the strains in the middle surface. The changes of curvatures and twist of the middle surface are the following functions of the lateral deflection w:

$$\kappa_x = -w_{,xx}$$
$$\kappa_y = -w_{,yy}$$
$$\kappa_{xy} = -2w_{,xy}. \tag{2}$$

The strains at the distance z from the middle surface are

$$\epsilon_x = \epsilon_x^o + z\kappa_x$$
$$\epsilon_y = -\epsilon_y^o + z\kappa_y$$
$$\gamma_{xy} = \gamma_{xy}^o + z\kappa_{xy}. \tag{3}$$

[14] University of Missouri-Rolla, Engineering Education Center, St. Louis, MO 63121. Mem. ASME.

Manuscript received by the ASME Applied Mechanics Division, Sept. 28, 1989; final revision, May, 1, 1990.

Ben-Haim, Y., and Elishakoff, I., 1989a, "Non-Probabilistic Models of Uncertainty in the Nonlinear Buckling of Shells with General Imperfections: Theoretical Estimates of the Knockdown Factor," ASME JOURNAL OF APPLIED MECHANICS, Vol. 56, pp. 403–410.

Ben-Haim, Y., and Elishakoff, I., 1989b, "Dynamics and Failure of Structures Based on the Unknown-but-Bounded Imperfection Model," *Recent Advances in Impact Dynamics of Engineering Structures—1989,* D. Hui and N. Jones, eds., ASME AMD-Vol. 105, AD-Vol. 17, pp. 89–95.

Ben-Haim, Y., and Elishakoff, I., 1990, *Convex Models of Uncertainty in Applied Mechanics,* Elsevier, New York.

Elishakoff, I., 1978, "Axial Impact Buckling of a Thin Bar Via Monte Carlo Method," ASME JOURNAL OF APPLIED MECHANICS, Vol. 45, pp. 586–590.

Kirkpatrick, S. W., and Holmes, B. S., 1989, "Effect of Initial Imperfections on Dynamic Buckling of Shells," *ASCE Journal of Engineering Mechanics,* Vol. 115, No. 5, pp. 1075–1093.

Lindberg, H. E., 1965, "Impact Buckling of a Thin Bar," ASME JOURNAL OF APPLIED MECHANICS, Vol. 32, pp. 312–322.

Lindberg, H. E., and Herbert, R. E., 1966, "Dynamic Buckling of a Thin Cylindrical Shell Under Axial Impact," ASME JOURNAL OF APPLIED MECHANICS, Vol. 33, pp. 105–112.

Lindberg, H. E., 1988, "Random Imperfections for Dynamic Pulse Buckling," *ASCE Journal of Engineering Mechanics,* Vol. 114, No. 7, pp. 1144–1165.

Schweppe, F. C., 1973, *Uncertain Dynamical Systems,* Prentice-Hall, Englewood Cliffs, N.J.

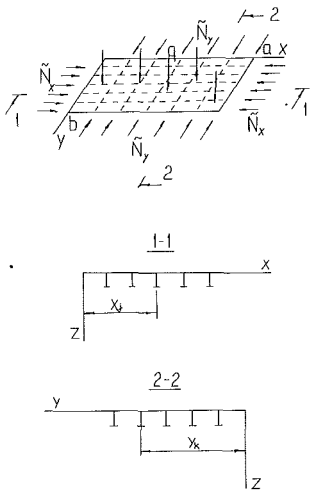

Fig. 1 Geometry of the panel; mechanical loads

Thermoelastic Problems of Reinforced Rectangular Panels

Victor Birman[14]

The static response of isotropic reinforced panels in nonuniform thermal fields is discussed. The effects of temperature on material properties are included into consideration. The governing equations formulated in the Note allow the solution both by energy methods and using equilibrium equations. The theory is applied to estimation of the effect of a uniform temperature on stability of compressed reinforced panels and to the problem of thermal bending of unstiffened plates.

Introduction

Problems of structural response of panels in thermal fields are important both for development of thermoelastic theory as well as in aerospace and nuclear engineering and in other applications. The number of investigations in this area is very large; we mention here only the classical book of Boley and Weiner (1960) dealing with the problem, and the recent review of Tauchert (1986) concentrating on thermoelasticity of plates.

Typically, the studies of thermoelastic plate problems are based on an assumption that material properties are insensitive to temperature. This approach, justified in many practical problems, becomes questionable for composite materials and new alloys operating at high temperatures resulting either from aerodynamic heating in supersonic or hypersonic flight or from a technological process. The formulations of thermoelastic problems for unstiffened composite material cylindrical shells and rectangular panels incorporating temperature-dependent material properties were presented by Ambartsumian (1970, 1974) and Tauchert (1986). The review of Noda (1986) presents a list of works on thermoelasticity of isotropic plates with temperature-dependent material properties. However, these solutions dealt only with unstiffened plates. Laminated rectangular plates with temperature-dependent properties were considered by Chen and Chen (1989). Note here also the recent results presented for beams with temperature-dependent properties by Artemian (1988) and Birman (1990).

In this Note thermoelastic problems of reinforced rectangular panels manufactured from an isotropic material are considered. Governing equations are developed, and the solutions of sample problems for reinforced and unstiffened panels are obtained.

Governing Equations

Consider a rectangular reinforced panel subject to in-plane compressive loads of intensities $\tilde{N}_x, \tilde{N}_y$, lateral distributed loading $q=q(x,y)$ and nonuniform temperature $T=T(x,y,z)$, as shown in Fig. 1. The following assumptions are used in this Note:

- materials of the stiffeners and the plate are isotropic;
- the properties of materials depend on temperature;
- materials remain in the linear elastic range;
- the strain-displacement relationships are linear.

The stiffeners are assumed to be attached to the plate so that their deformations occur without slipping. Therefore, normal strains in the plate and in the stiffeners vary linearly in the thickness direction. According to the classic approach (Baruch, 1964, 1965), the shear membrane force exists in the plate only. Torsional stiffness of the stiffeners is taken into consideration.

Strain-displacement relationships in the middle plane of the plate are:

$$\epsilon_x^o = u_{,x}$$
$$\epsilon_y^o = v_{,y} \tag{1}$$
$$\gamma_{xy}^o = u_{,y} + v_{,x}$$

where u and v are the in-plane displacements in the x and y directions, respectively, and the superscript o indicates the strains in the middle surface. The changes of curvatures and twist of the middle surface are the following functions of the lateral deflection w:

$$\kappa_x = -w_{,xx}$$
$$\kappa_y = -w_{,yy}$$
$$\kappa_{xy} = -2w_{,xy}. \tag{2}$$

The strains at the distance z from the middle surface are

$$\epsilon_x = \epsilon_x^o + z\kappa_x$$
$$\epsilon_y = -\epsilon_y^o + z\kappa_y$$
$$\gamma_{xy} = \gamma_{xy}^o + z\kappa_{xy}. \tag{3}$$

[14] University of Missouri-Rolla, Engineering Education Center, St. Louis, MO 63121. Mem. ASME.

Manuscript received by the ASME Applied Mechanics Division, Sept. 28, 1989; final revision, May, 1, 1990.

The constitutive relations for the plate are

$$\sigma_x=\frac{E}{1-\nu^2}[(\epsilon_x-\alpha T)+\nu(\epsilon_y-\alpha T)]$$

$$\sigma_y=\frac{E}{1-\nu^2}[(\epsilon_y-\alpha T)+\nu(\epsilon_x-\alpha T)]$$

$$\tau_{xy}=G\gamma_{xy}. \tag{4}$$

Equations (4) are not new; however, here we emphasize that the modulus of elasticity (E), the Poisson's ratio (ν), the shear modulus (G) and the coefficient of thermal expansion (α) are functions of temperature at the point. If the coefficients of thermal expansion depends on temperature, α is a function chosen so that the integral of this coefficient over the range of temperature is equal to αT.

The stresses in the stiffeners in the x and y directions are

$$\sigma_x^s=E_s(\epsilon_x-\alpha_s T)$$

and

$$\sigma_y^s=E_s(\epsilon_y-\alpha_s T), \tag{5}$$

respectively. The index "s" indicates a property of the stiffener. Note that $E_s=E_s(T)$ and $\alpha_s=\alpha_s(T)$.

Integration of the stresses given by (4) and (5) with respect to the thickness coordinate yields stress resultants and stress couples:

$$\begin{aligned}
N_x&=(E_1+E_{s1})\epsilon_x^o+(E_2+E_{s2})\kappa_x+E_3\epsilon_y^o+E_4\kappa_y-N_x^T\\
N_y&=(E_1+E_{s3})\epsilon_y^o+(E_2+E_{s4})\kappa_y+E_3\epsilon_x^o+E_4\kappa_x-N_y^T\\
N_{xy}&=G_1\gamma_{xy}^o+G_2\kappa_{xy}\\
M_x&=(E_2+E_{s2})\epsilon_x^o+(E_5+E_{s5})\kappa_x+E_4\epsilon_y^o+E_6\kappa_y-M_x^T\\
M_y&=(E_2+E_{s4})\epsilon_y^o+(E_5+E_{s6})\kappa_y+E_4\epsilon_x^o+E_6\kappa_x-M_y^T\\
M_{xy}&=G_2\gamma_{xy}^o+G_3\kappa_{xy}-\frac{\overline{G}_s}{2}\left[\sum_k\delta(y-y_k)J_k+\sum_j\delta(x-x_j)J_j\right]w_{,xy}.
\end{aligned} \tag{6}$$

The last term in the expression for M_{xy} includes torsional stiffness of the stiffeners. Here, J_k and J_j are torsional constants of the stiffeners in the x and y directions, respectively, and $\overline{G}_s$ is an average value of the modulus of rigidity of the stiffeners material which can be used since the effect of torsional stiffnesses is usually relatively small.

The stiffnesses of the plate (E_i) as well as the stiffnesses of the stiffeners (E_{sj}) are, in general, functions of in-plane coordinates calculated by the following formulae:

$$(E_1,E_2,E_5)=\int_{-h/2}^{h/2}(1,z,z^2)\frac{E(z)}{1-\nu^2(z)}dz$$

$$(E_3,E_4,E_6)=\int_{-h/2}^{h/2}(1,z,z^2)\frac{\nu(z)E(z)}{1-\nu^2(z)}dz$$

$$(G_1,G_2,G_3)=\int_{-h/2}^{h/2}(1,z,z^2)G(z)dz$$

$$E_{s(1,2,5)}=\sum_k\delta(y-y_k)\int_{z_k}E_s(z)\beta_k(z)(1,z,z^2)dz$$

$$E_{s(3,4,6)}=\sum_j\delta(x-x_j)\int_{z_j}E_s(z)\beta_j(z)(1,z,z^2)dz. \tag{7}$$

In (7), $\beta_k(z)$ and $\beta_j(z)$ are the widths of the stiffeners in the x and y directions, respectively, x_j and y_k are the coordinates of the stiffeners and δ is Dirac delta function.

Note that for a thermal field without a gradient in the z-direction, the stiffnesses calculated by (7) reduce to conventional stiffnesses of the theory of reinforced plates; however, they will still be functions of x and y. Thermal terms in (6) are given by:

$$N_x^T=\int_{-h/2}^{h/2}\frac{\alpha(z)E(z)T(z)}{1-\nu(z)}dz+\sum_k\delta(y-y_k)\int_{z_k}\alpha_s(z)E_s(z)\beta_k(z)Tdz$$

$$M_x^T=\int_{-h/2}^{h/2}\frac{\alpha(z)E(z)T(z)}{1-\nu(z)}zdz+\sum_k\delta(y-y_k)\int_{z_k}\alpha_s(z)E_s(z)\beta_k(z)T(z)zdz. \tag{8}$$

The terms N_y^T and M_y^T can be obtained from N_x^T and M_x^T in (8) by replacement of symbols $j\to k$, $x\to y$.

Equations of equilibrium in terms of stress resultants and stress couples are:

$$\begin{aligned}
&N_{x,x}+N_{xy,y}=0\\
&N_{xy,x}+N_{y,y}=0\\
&M_{x,xx}+2M_{xy,xy}+M_{y,yy}+(N_xw_{,x}+N_{xy}w_{,y})_{,x}\\
&\qquad+(N_{xy}w_{,x}+N_yw_{,y})_{,y}=-q.
\end{aligned} \tag{9}$$

In a geometrically linear problem, the stress resultants in the third equation (9) must be taken as

$$\begin{aligned}
N_x&=\tilde{N}_x-N_x^T\\
N_y&=\tilde{N}_y-N_y^T\\
N_{xy}&=\tilde{N}_{xy}=0
\end{aligned} \tag{10}$$

where external loads $\tilde{N}_x$ and $\tilde{N}_y$ are positive in tension.

If the temperature is uniformly distributed over the surface, i.e., $T=T(z)$, the substitution of both the constitutive relations (6) as well as the equations (10) into the equilibrium equations (9) yields

$$\begin{aligned}
&(E_1+E_{s1})u_{,xx}+G_1u_{,yy}+(E_3+G_1)v_{,xy}-(E_2+E_{s2})w_{,xxx}-(E_4+2G_2)w_{,xyy}=N_{x,x}^T\\
&(E_1+E_{s3})v_{,yy}+G_1v_{,xx}+(E_3+G_1)u_{,xy}-(E_2+E_{s4})w_{,yyy}-(E_4+2G_2)w_{,xxy}=N_{y,y}^T\\
&(E_2+E_{s2})u_{,xxx}+(E_4+2G_2)u_{,xyy}+(E_2+E_{s4})v_{,yyy}+(E_4+2G_2)v_{,xxy}-(E_5+E_{s5})w_{,xxxx}-(E_6+E_{s6})w_{,yyyy}\\
&\quad-2\left[E_6+2G_3-\frac{\overline{G}_s}{2}\left[\sum_k\delta(y-y_k)J_k+\sum_j\delta(x-x_j)J_j\right]\right]w_{,xxyy}\\
&\quad+[(\tilde{N}_x-N_x^T)w_{,x}]_{,x}+[(\tilde{N}_y-N_y^T)w_{,y}]_{,y}=-q+M_{x,xx}^T+M_{y,yy}^T.
\end{aligned} \tag{11}$$

The effect of uniformly distributed temperature on stability can be easily estimated. Consider a reinforced simply-supported panel with arbitrary in-plane boundary conditions subject to constant compressive stresses of intensity $\tilde{N}_x$. The comparison of equation (11) for the panel subject to $\tilde{N}_x$, only with these equations in the case of simultaneous action of $\tilde{N}_x$ and temperature, yields

$$[\tilde{N}_{xcr}(T)-\tilde{N}_{xcr}(0)-N_x^T]w_{,xx}-N_y^Tw_{,yy}=0 \tag{12}$$

where $\tilde{N}_{xcr}(T)$ and $\tilde{N}_{xcr}(0)$ are critical intensities of the external stresses for $T\neq 0$ and $T=0$, respectively. Note that the Poisson's effect due to resistance of the edges $y=0$, $y=b$ can be incorporated by including the terms $\nu[\tilde{N}_{xcr}(T)-\tilde{N}_{xcr}(0)w_{,yy}$. The nondimensional buckling load of the panel corresponding to m half-waves in the x-direction and the n half-waves in the y-direction is

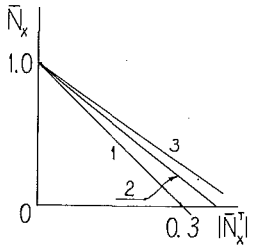

Fig. 2 Effect of uniform temperature on stability of reinforced panels: $a/b=1.5$, $\nu=0.3$, $m=n=1$, $\bar{A}_j=0$, 1: $\bar{A}_k=0$, 2: $\bar{A}_k=0.5$, 3: $\bar{A}_k=1.0$

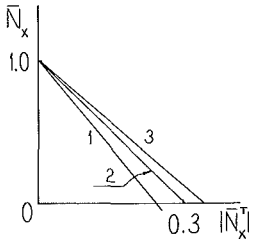

Fig. 3 Effect of uniform temperature on stability of reinforced panels: $a/b=1.5$, $\nu=0.3$, $m=n=1$, $\bar{A}_j=0.5$, 1: $\bar{A}_k=0$, 2: $\bar{A}_k=0.5$, 3: $\bar{A}_k=1.0$

$$\bar{N}_x=1+\bar{N}_x^T\left[1+\left(\frac{na}{mb}\right)^2\frac{N_y^T}{N_x^T}\right] \tag{13}$$

where

$$\bar{N}_x=\frac{\tilde{N}_{xcr}(T)}{\tilde{N}_{xcr}(0)}\quad \bar{N}_x^T=\frac{N_x^T}{\tilde{N}_{xcr}(0)}. \tag{14}$$

The nondimensional buckling loads are shown for a uniformly heated panel with closely spaced identical stiffeners in each direction in Figs. 2 and 3. In this case

$$\frac{N_y^T}{N_x^T}=\frac{1+(1-\nu)\bar{A}_j}{1+(1-\nu)\bar{A}_k}, \tag{15}$$

where $(\bar{A}_j,\ \bar{A}_k)=\left(\sum_j A_j/hl,\ \sum_k A_k/hd\right)$,

l and d being the spacings of the respective stiffeners. Figure 2 illustrates the result for panels reinforced in the x direction only. Nondimensional buckling loads for panels reinforced in both directions are shown in Fig. 3. Such figures, which are easy to generate and analyze, can be useful in the preliminary design to estimate the effect of temperature on stability of compressed panels.

Analytical Solutions of Thermoelastic Problems

Two analytical methods often used in the theory of plates and shells are those of Rayleigh-Ritz and Galerkin. The advantage of the Rayleigh-Ritz method is that the modal functions in expressions for displacements do not have to satisfy static boundary conditions. To the contrary, modal functions used in the Galerkin procedure must satisfy both kinematic and static boundary conditions. This can be rather difficult in thermoelastic problems due to the presence of thermal terms which depend on temperature and, in general, are not equal to zero at the boundaries. However, a generalized Galerkin method can be useful in thermoelastic problems: In this method static boundary conditions are included in the formulation (Tauchert, 1986). Here the solution of the problem of thermal bending of unstiffened plates with temperature-dependent material properties is considered.

Consider a rectangular plate subject to the action of a lateral load q and nonuniform temperature $T(x,y,z)$. The potential energy of such a plate is (Boley and Weiner, 1960):

$$U=\frac{1}{2}\int_{(v)}\int\int[\sigma_x\epsilon_x+\sigma_y\epsilon_y+\tau_{xy}\gamma_{xy} -\alpha T(\sigma_x+\sigma_y)]d(V)-\int_{(A)}\int qwd(A) \tag{16}$$

where (V) and (A) denote volume and area of middle surfaces, respectively. The substitution of (1)–(5) into (16) and integration in the thickness direction yields

$$\begin{aligned}U=\frac{1}{2}\int_o^a\int_o^b[&E_1u_{,x}^2-2E_2u_{,x}w_{,xx}+E_5w_{,xx}^2\\&+2E_3u_{,x}v_{,y}-2E_4u_{,x}w_{,yy}-2E_4v_{,y}w_{,xx}+2E_6w_{,xx}w_{,yy}\\&+E_1v_{,y}^2-2E_2v_{,y}w_{,yy}+E_5w_{,yy}^2+G_1u_{,y}^2+G_1v_{,x}^2+2G_1u_{,y}v_{,x}\\&+4G_3w_{,xy}^2-4G_2u_{,y}w_{,xy}-4G_2v_{,x}w_{,xy}-2N^T(u_{,x}+v_{,y}-1)\\&+2M^T(w_{,xx}+w_{,yy})-2qw]dxdy\end{aligned} \tag{17}$$

where

$$(N^T,M^T)=\int_{-h/2}^{h/2}(1,z)\frac{E(z)\alpha(z)T(z)}{1-\nu(z)}dz. \tag{18}$$

Naturally, if the plate is reinforced, the potential energy of reinforcements must be added to (17).

If displacements are represented by the series

$$\begin{aligned}u&=\sum_m\sum_n U_{mn}f_{um}(x)\phi_{un}(y)\\v&=\sum_m\sum_n V_{mn}f_{vm}(x)\phi_{vn}(y)\\w&=\sum_m\sum_n W_{mn}f_{wm}(x)\phi_{wn}(y)\end{aligned} \tag{19}$$

where U_{mn}, V_{mn}, and W_{mn} are constant coefficients and f_{im}, ϕ_{in} $(i=u,v,w)$ are the modal functions which satisfy the kinematic boundary conditions, the Rayleigh-Ritz method yields

$$\frac{\partial U}{\partial U_{mn}}=\frac{\partial U}{\partial V_{mn}}=\frac{\partial U}{\partial W_{mn}}=0. \tag{20}$$

The solution of a thermal bending problem can be obtained from the set of equations (20).

Consider, for example, a rigid simply-supported plate with the edges prevented against in-plane displacements subject to a thermal field $T=T(z)$ and to a uniform pressure q. The potential energy of such a plate is

$$\begin{aligned}U=\frac{1}{2}\int_o^a\int_o^b[&E_5(w_{,xx}^2+w_{,yy}^2)\\&+2E_6w_{,xx}w_{,yy}+4G_3w_{,xy}^2+2M^T(w_{,xx}+w_{,yy})-2qw]dxdy\end{aligned} \tag{21}$$

where the term independent of deformation has been omitted. Note that if temperature does not affect material properties, equation (21) reduces to that presented by Tauchert (1986).

Representing lateral deflections by

$$w=\sum_{m=1}^{r}\sum_{n=1}^{s}W_{mn}\sin\frac{m\pi x}{a}\sin\frac{n\pi y}{b} \tag{22}$$

and substituting (22) into (21), one obtains a set of $r\times s$ algebraic equations from which the amplitudes of harmonics in (22) can be easily evaluated:

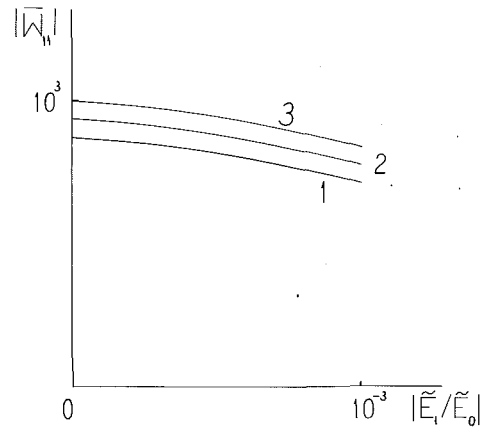

Fig. 4 Effect of sensitivity of the modulus of elasticity to temperature on deflections of unstiffened panels; $m=n=1$, curve 1: $\bar{\alpha}=0$, curve 2: $\bar{\alpha}=-0.1$, curve 3: $\bar{\alpha}=-0.2$

$$W_{mn}=\frac{16}{mn\pi^2}\left\{q+M^T\left[\left(\frac{m\pi}{a}\right)^2+\left(\frac{n\pi}{b}\right)^2\right]\right\}\left\{E_5\left[\left(\frac{m\pi}{a}\right)^4+\left(\frac{n\pi}{b}\right)^4\right]+2(E_6+2G_3)\left(\frac{m\pi}{a}\right)^2\left(\frac{n\pi}{b}\right)^2\right\}^{-1}. \quad (23)$$

In (23), m and n are odd numbers; otherwise $W_{mn}=0$.

In a particular case where

$$T(z)=T_1z+T_o$$
$$E=\tilde{E}_1T+\tilde{E}_o$$
$$\alpha=\alpha_1T+\alpha_o, \quad (24)$$

equation (23) is reduced to

$$\overline{W}_{mn}=\frac{1+\nu}{m^3n\pi^4}\left(\frac{a}{h}\right)^2\frac{2.4\overline{E}\overline{\alpha}\overline{T}+16(\overline{E}+\overline{\alpha}+\overline{T})}{1+\left(\frac{na}{mb}\right)^2} \quad (25)$$

where

$$\overline{W}_{mn}=\frac{W_{mn}}{\alpha_oT_oh} \quad \overline{E}=\frac{T_1h}{\frac{\tilde{E}_o}{\tilde{E}_1}+T_o}$$
$$\overline{\alpha}=\frac{T_1h}{\frac{\alpha_o}{\alpha_1}+T_o} \quad \overline{T}=\frac{T_1h}{T_o}. \quad (26)$$

An example illustrating bending deflections of a plate in a thermal field $T(z)=T_1z+T_o$ is shown in Fig. 4. In this example, $a/b=1.5$, $a/h=100$, and the Poisson's ratio $\nu=0.3$. The thermal field was characterized by $T_1h=-200°C$ and $T_o=150°C$. These values correspond to the surface temperatures $T(h/2)=50°C$ and $T(-h/2)=250°C$.

The relationships $E(t)$ and $\alpha(T)$ were given by (24). The modulus of elasticity usually decreases with temperature; i.e., the ratio $\tilde{E}_1/\tilde{E}_o$ is negative. The values of $\tilde{E}_1/\tilde{E}_o$ in Fig. 4 cover the range from the modulus of elasticity insensitive to temperature ($\tilde{E}_1/\tilde{E}_o=0$) to the modulus decreasing by 50 percent as temperature increases by 500°C.

The curve 1 was obtained by assumption that the coefficient of thermal expansion was independent of temperature. The curves 2 and 3 correspond to the coefficients increasing with temperature. In particular, the curve 2 was obtained for $\alpha_o/\alpha_1=1850°C$ and the curve 3 corresponded to $\alpha_o/\alpha_1=850°C$.

Note that the values of $\overline{W}$ were negative; i.e., the convex surface had a higher temperature. Thermally induced deflections decreased if the modulus of elasticity decreased with temperature. To the contrary, deflections increased if the coefficient of thermal expansion increased with temperature. Three curves in Fig. 4 are almost parallel, which means that the latter effect remains valid for materials with a range of variations of $\tilde{E}_1/\tilde{E}_o$.

Conclusions

Static thermoelastic problems of isotropic rectangular panels are considered. The effect of temperature on the elastic properties of the panel material is included in the analysis. The panels can be reinforced or unstiffened. The governing equations are formulated for stiffened panels within the framework of geometrically linear theory. These equations can be used for the solution of bending and buckling problems. As illustrations of the application of the theory, analytical solutions of the following thermoelastic problems are obtained:

- effect of uniform temperature on stability of reinforced panels, and
- thermal bending of unstiffened rectangular plates with temperature-dependent properties.

Acknowledgment

Discussions with Prof. Charles W. Bert of the University of Oklahoma and Dr. Robert W. Laurenson of McDonnell Douglas Missile Systems Company are warmly appreciated.

References

Ambartsumian, S. A., 1970, *Theory of Anisotropic Plates,* Technomic, Stamford, Conn.

Ambartsumian, S. A., 1974, *General Theory of Anisotropic Shells,* Nauka Publishers, Moscow (in Russian).

Artemian, E. G., 1988, "Vibrations of Elastic and Viscoelastic Beams in a Nonuniform Thermal Field," *Izvestiya, Akademia Nauk Armyanskoi SSR,* (in Russian) Vol. 1, pp. 13–20.

Baruch, M., 1964, "Equilibrium and Stability Equations for Stiffened Shells," *Israel Journal of Technology,* Vol. 2, pp. 117–124.

Baruch, M., 1965, "Equilibrium and Stability Equations for Discretely Stiffened Shells," *Israel Journal of Technology,* Vol. 3, pp. 138–146.

Birman, V., 1990, "Buckling and Bending of Beams Subject to a Nonuniform Thermal Field," *Mechanics Research Communications,* Vol. 17, pp. 41–45.

Boley, B. A., and Weiner, J. H., 1960, *Theory of Thermal Stresses,* John Wiley and Sons, New York.

Chen, L.-W., and Chen, L.-Y., 1989, "Thermal Buckling of Laminated Composite Plates with Temperature-Dependent Properties," *Composite Structures,* Vol. 13, pp. 275–287.

Noda, N., 1986, "Thermal Stresses in Materials with Temperature-Dependent Properties," *Thermal Stresses I,* R. B., Hetnarski, ed., Chapter 6.

Tauchert, T. R, 1986, "Thermal Stresses in Plates-Statical Problems," *Thermal Stresses I,* R. B. Hetnarski, ed., Chapter 2.

Symmetrization of Some Conservative Systems of the Second Kind

B. L. Ly[15]

1 Introduction

Certain nonself-adjoint systems have only divergence type of instability, despite the presence of the polygenic force. Pfluger's column and Greenhill's shaft are two such systems. Leipholz (1974a, 1974b) called a true divergent nonself-adjoint system which has dynamic properties very similar to those of

[15]Design and Analysis Branch, AECL-CANDU, Sheridan Park, Mississauga, Ontario L5K 1B2, Canada.

Contributed by the Applied Mechanics Division of THE AMERICAN SOCIETY OF MECHANICAL ENGINEERS. Manuscript received by the Applied Mechanics Division, July 24, 1990; final revision, Nov. 19, 1990.

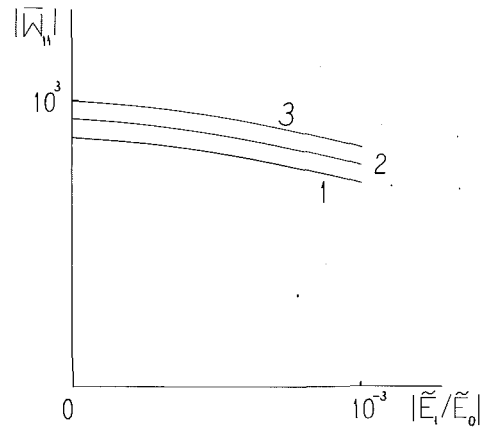

Fig. 4 Effect of sensitivity of the modulus of elasticity to temperature on deflections of unstiffened panels; $m=n=1$, curve 1: $\bar{\alpha}=0$, curve 2: $\bar{\alpha}=-0.1$, curve 3: $\bar{\alpha}=-0.2$

$$W_{mn}=\frac{16}{mn\pi^2}\left\{q+M^T\left[\left(\frac{m\pi}{a}\right)^2+\left(\frac{n\pi}{b}\right)^2\right]\right\}\left\{E_5\left[\left(\frac{m\pi}{a}\right)^4+\left(\frac{n\pi}{b}\right)^4\right]+2(E_6+2G_3)\left(\frac{m\pi}{a}\right)^2\left(\frac{n\pi}{b}\right)^2\right\}^{-1}. \quad (23)$$

In (23), m and n are odd numbers; otherwise $W_{mn}=0$.

In a particular case where

$$T(z)=T_1z+T_o$$
$$E=\tilde{E}_1T+\tilde{E}_o$$
$$\alpha=\alpha_1T+\alpha_o, \quad (24)$$

equation (23) is reduced to

$$\overline{W}_{mn}=\frac{1+\nu}{m^3n\pi^4}\left(\frac{a}{h}\right)^2\frac{2.4\overline{E}\overline{\alpha}\overline{T}+16(\overline{E}+\overline{\alpha}+\overline{T})}{1+\left(\frac{na}{mb}\right)^2} \quad (25)$$

where

$$\overline{W}_{mn}=\frac{W_{mn}}{\alpha_oT_oh} \quad \overline{E}=\frac{T_1h}{\frac{\tilde{E}_o}{\tilde{E}_1}+T_o}$$

$$\overline{\alpha}=\frac{T_1h}{\frac{\alpha_o}{\alpha_1}+T_o} \quad \overline{T}=\frac{T_1h}{T_o}. \quad (26)$$

An example illustrating bending deflections of a plate in a thermal field $T(z)=T_1z+T_o$ is shown in Fig. 4. In this example, $a/b=1.5$, $a/h=100$, and the Poisson's ratio $\nu=0.3$. The thermal field was characterized by $T_1h=-200°C$ and $T_o=150°C$. These values correspond to the surface temperatures $T(h/2)=50°C$ and $T(-h/2)=250°C$.

The relationships $E(t)$ and $\alpha(T)$ were given by (24). The modulus of elasticity usually decreases with temperature; i.e., the ratio $\tilde{E}_1/\tilde{E}_o$ is negative. The values of $\tilde{E}_1/\tilde{E}_o$ in Fig. 4 cover the range from the modulus of elasticity insensitive to temperature ($\tilde{E}_1/\tilde{E}_o=0$) to the modulus decreasing by 50 percent as temperature increases by 500°C.

The curve 1 was obtained by assumption that the coefficient of thermal expansion was independent of temperature. The curves 2 and 3 correspond to the coefficients increasing with temperature. In particular, the curve 2 was obtained for $\alpha_o/\alpha_1=1850°C$ and the curve 3 corresponded to $\alpha_o/\alpha_1=850°C$.

Note that the values of $\overline{W}$ were negative; i.e., the convex surface had a higher temperature. Thermally induced deflections decreased if the modulus of elasticity decreased with temperature. To the contrary, deflections increased if the coefficient of thermal expansion increased with temperature. Three curves in Fig. 4 are almost parallel, which means that the latter effect remains valid for materials with a range of variations of $\tilde{E}_1/\tilde{E}_o$.

Conclusions

Static thermoelastic problems of isotropic rectangular panels are considered. The effect of temperature on the elastic properties of the panel material is included in the analysis. The panels can be reinforced or unstiffened. The governing equations are formulated for stiffened panels within the framework of geometrically linear theory. These equations can be used for the solution of bending and buckling problems. As illustrations of the application of the theory, analytical solutions of the following thermoelastic problems are obtained:

- effect of uniform temperature on stability of reinforced panels, and
- thermal bending of unstiffened rectangular plates with temperature-dependent properties.

Acknowledgment

Discussions with Prof. Charles W. Bert of the University of Oklahoma and Dr. Robert W. Laurenson of McDonnell Douglas Missile Systems Company are warmly appreciated.

References

Ambartsumian, S. A., 1970, *Theory of Anisotropic Plates,* Technomic, Stamford, Conn.

Ambartsumian, S. A., 1974, *General Theory of Anisotropic Shells,* Nauka Publishers, Moscow (in Russian).

Artemian, E. G., 1988, "Vibrations of Elastic and Viscoelastic Beams in a Nonuniform Thermal Field," *Izvestiya, Akademia Nauk Armyanskoi SSR,* (in Russian) Vol. 1, pp. 13–20.

Baruch, M., 1964, "Equilibrium and Stability Equations for Stiffened Shells," *Israel Journal of Technology,* Vol. 2, pp. 117–124.

Baruch, M., 1965, "Equilibrium and Stability Equations for Discretely Stiffened Shells," *Israel Journal of Technology,* Vol. 3, pp. 138–146.

Birman, V., 1990, "Buckling and Bending of Beams Subject to a Nonuniform Thermal Field," *Mechanics Research Communications,* Vol. 17, pp. 41–45.

Boley, B. A., and Weiner, J. H., 1960, *Theory of Thermal Stresses,* John Wiley and Sons, New York.

Chen, L.-W., and Chen, L.-Y., 1989, "Thermal Buckling of Laminated Composite Plates with Temperature-Dependent Properties," *Composite Structures,* Vol. 13, pp. 275–287.

Noda, N., 1986, "Thermal Stresses in Materials with Temperature-Dependent Properties," *Thermal Stresses I,* R. B., Hetnarski, ed., Chapter 6.

Tauchert, T. R, 1986, "Thermal Stresses in Plates-Statical Problems," *Thermal Stresses I,* R. B. Hetnarski, ed., Chapter 2.

Symmetrization of Some Conservative Systems of the Second Kind

B. L. Ly[15]

1 Introduction

Certain nonself-adjoint systems have only divergence type of instability, despite the presence of the polygenic force. Pfluger's column and Greenhill's shaft are two such systems. Leipholz (1974a, 1974b) called a true divergent nonself-adjoint system which has dynamic properties very similar to those of

[15]Design and Analysis Branch, AECL-CANDU, Sheridan Park, Mississauga, Ontario L5K 1B2, Canada.

Contributed by the Applied Mechanics Division of THE AMERICAN SOCIETY OF MECHANICAL ENGINEERS. Manuscript received by the Applied Mechanics Division, July 24, 1990; final revision, Nov. 19, 1990.

a self-adjoint system a conservative system of the second kind. He showed that such a system is self-adjoint with respect to an assigned self-adjoint operator, hence self-adjoint in a generalized sense. For such a system, there exist a Lyapunov for predicting stability (Walker 1974; Leipholz 1974a) and a generalized Rayleigh quotient for determining the buckling load (Leipholz 1974a). Inman and Olsen (1988) included velocity-dependent forces in conservative systems of the second kind. They proved the generalized self-adjointness and the existence of eigenfunctions for these systems.

For certain asymmetric discrete systems, Inman (1983) showed that there exists a similarity transformation that transforms the asymmetric system into an equivalent symmetric one; i.e., one having the same eigenvalues. Here it is shown that for certain conservative systems of the second kind, an equivalent self-adjoint system can be found. In this way, a conservative system of the second kind is symmetrized, like the symmetrization of an asymmetric discrete system. As a result, stability study can be performed on the symmetrized system, which is usually easier to manage.

2 The Pfluger Column

The Pfluger column is a simply-supported column under a uniform tangential follower force. Walker (1972) generalized it to include damping and nonuniform follower force. Here, we include columns with guided ends. Stability of the generalized Pfluger column is described by the eigenvalue problem governed by the differential equation

$$-\Omega^2 w + w^{iv} + pf(x)w'' = 0,\ 0 \le x \le 1, \tag{1}$$

and the boundary conditions

$$w = w'' = 0 \tag{2a}$$

for a pinned end, or

$$w' = w''' = 0 \tag{2b}$$

for a guided end. $w(x)$ is the lateral deflection of the column, Ω is a frequency parameter, $p > 0$ is a load parameter, and $f(x)$ is a bounded function related to the distribution of the force. A guided-guided column admits a translatory isometric mode. If only the flexural modes are of interest, this column can be included in the consideration.

The operator $f(x)\partial^2$ is not self-adjoint with respect to the prescribed boundary conditions. However, the operator $-\Omega^2 + \partial^4 + pf(x)\partial^2$ is self-adjoint in a generalized sense (Leipholz, 1974) with respect to the operator ∂^2 under the boundary conditions in (2). The generalized self-adjointness implies

$$\int_0^1 (-\Omega^2 u + u^{iv} + pfu'')v''\,dx = \int_0^1 (-\Omega^2 v + v^{iv} + pfv'')u''\,dx, \tag{3}$$

where u and v are admissible functions satisfying all the boundary conditions prescribed for w.

Here, the generalized Pfluger column is shown to be a conservative system by explicitly symmetrizing it. Also, it is shown that Leipholz's generalized self-adjointness can be reduced to the classical self-adjointness.

Differentiate (1) with respect to x once and denote w' by y. Then (1) becomes

$$-\Omega^2 y + y^{iv} + p[f(x)y']' = 0. \tag{4}$$

As can be seen, the follower force now assumes the same appearance as a unidirectional loading. However, whether or not the operator in (4) is self-adjoint also depends on the boundary conditions for y.

At a pinned end of the column, $w'' = 0$ implies $y' = 0$. Also, from (1), $w = w'' = 0$ implies $w^{iv} = 0$, which in turn implies $y''' = 0$. In other words, a pinned end for w becomes a guided end for y. At a guided end of the column, $w' = 0$ implies $y = 0$ and $w''' = 0$ implies $y'' = 0$, respectively. That is to say, a guided end for w now becomes a pinned end for y. It is interesting to note from the foregoing that the boundary conditions for the systems in (1) and in (4) have a conjugate relationship between them.

The system in (4) is equivalent to that in (1), because the equation in (4) and the corresponding boundary conditions are derived from (1) and (2) via the transformation $y = w'$. Hence, the eigensolutions of (1) are also the eigensolutions of (4).

The operator in (4) is self-adjoint. It can be shown in the usual manner that

$$\int_0^1 [-\Omega^2 y + y^{iv} + p(fy')']z\,dx = \int_0^1 [-\Omega^2 z + z^{iv} + p(fz')']y\,dx. \tag{5}$$

In fact, (5) can also be derived from the generalized self-adjointness in (3) by integration by parts to obtain

$$\int_0^1 [-\Omega^2 u' + u^v + p(fu'')']v'\,dx = \int_0^1 [-\Omega^2 v' + v^v + p(fv'')']u'\,dx, \tag{6}$$

then by denoting u' by y and v' by z.

Because the operator in (4) is self-adjoint, the generalized Pfluger column can only have divergence-type of instability. Therefore, the static Euler approach can be used to study the stability. From the classical elastic stability theory, the buckling load p_{cr} has a Rayleigh quotient

$$p_{cr} = \inf_y \frac{\int_0^1 (y'')^2 dx}{\int_0^1 f(x)(y')^2 dx}, \tag{7}$$

or, in terms of w,

$$p_{cr} = \inf_w \frac{\int_0^1 (w''')^2 dx}{\int_0^1 f(x)(w'')^2 dx}. \tag{8}$$

The foregoing derivation shows that a generalized Pfluger column can be symmetrized into a self-adjoint system. Stability of the generalized Pfluger column can be studied via its equivalent self-adjoint system. The relationship between the generalized Pfluger column and its equivalent self-adjoint system is as follows:

Systems	Loading	End Conditions
generalized Pfluger column	tangential follower force	P-P P-G G-P G-G
equivalent self-adjoint system	unidirectional force	G-G G-P P-G P-P

P stands for pinned end, and G stands for guided end.

As an example, to determine the buckling load of a guided-guided column under a uniform tangential follower force, one can instead study the stability of a pinned-pinned column under its uniform self-weight. While the former is a nonconservative problem, the latter is a well-known self-adjoint problem. The critical weight of the conservative problem is equal to 18.57, so is the buckling load of the nonconservative problem.

3 The Greenhill Shaft

Greenhill's shaft is a pin-ended bar in torsion. The system is not self-adjoint except when θ, the angle between the applied torque vector and the tangent to the end of the bar, is equal to 1/2. Leipholz (1974a) studied a pure tangential torque ($\theta = 0$) and showed that the Greenhill shaft is a conservative system of the second kind. Walker (1973) considered the case $\theta \neq 1/2$ and included an axial compression and a damping force. He developed a Lyapunov functional for stability study. Here, we examine a bar in a viscoelastic medium of low density under a pure tangential torque and a pure axial torque ($\theta = 1$), respectively. We will symmetrize the systems and improve the stability boundary obtained by Walker for these two cases.

The linearized system (Bolotin, 1963) is described by the differential equation

$$\begin{bmatrix} \ddot{u}_1 \\ \ddot{u}_2 \end{bmatrix} + c\begin{bmatrix} \dot{u}_1 \\ \dot{u}_2 \end{bmatrix} + \begin{bmatrix} \partial^4 + p\partial^2 + k & L\partial^3 \\ -L\partial^3 & \partial^4 + p\partial^2 + k \end{bmatrix} \begin{bmatrix} u_1 \\ u_2 \end{bmatrix} = 0 \quad (9)$$

and the boundary conditions

$$u_1 = u_2 = 0$$
$$\begin{bmatrix} \partial^2 & \theta L\partial \\ -\theta L\partial & \partial^2 \end{bmatrix} \begin{bmatrix} u_1 \\ u_2 \end{bmatrix} = 0 \quad (10)$$

with $\theta = 0$, or $\theta = 1$, respectively. u_1 and u_2 are the deflections in the principal directions, ∂ denotes $\partial/\partial x$, L is the torque, p is the axial end compression, and c and k represent the viscoelastic medium.

Let us transform variable by denoting $z(x)e^{rt} = u_1 + iu_2$. Then, the differential equation and the boundary conditions become

$$(r^2 + cr + k)z + z^{iv} + pz'' - iLz''' = 0 \quad (11)$$

and $z = 0$

$$z'' - i\theta Lz' = 0, \quad (12)$$

respectively.

For the case of a pure tangential torque ($\theta = 0$), let us denote

$$z'' = M. \quad (13)$$

Then,

$$M = 0 \quad (14)$$

at either end, and

$$z(x) = \int_0^1 G(x,y)M(y)dy \quad (15)$$

where

$$G(x,y) = \begin{cases} x(y-1) & \text{for } 0 \le x < y \\ y(x-1) & \text{for } y < x \le 1 \end{cases}$$

is Green's influence function.

With use made of (13) and (15), the equation in (11) becomes

$$(r^2 + cr + k)\int_0^1 G(x,y)M(y)dy + M'' + pM - iLM' = 0. \quad (16)$$

We will further transform (16) by letting $M(x) = w(x)e^{\frac{iLx}{2}}$ so that

$$w(0) = w(1) = 0 \quad (17)$$

and

$$(r^2 + cr + k)\int_0^1 H(x,y)w(y)dy + w'' + \left(p + \frac{L^2}{4}\right)w = 0 \quad (18)$$

where

$$H(x,y) = G(x,y)e^{-i\frac{L}{2}(x-y)} = H^*(y,x)$$

is a symmetric kernel. As can be seen, (18) is self-adjoint. So the Greenhill shaft has been symmetrized.

For a given k and L, the critical load p_{cr} has a Rayleigh quotient

$$p_{cr} = \inf_w \frac{\int_0^1 (w')^2 dx - k\int_0^1\int_0^1 H(x,y)w(x)w(y)dxdy - \frac{L^2}{4}\int_0^1 w^2 dx}{\int_0^1 w^2 dx}$$
$$= -\frac{L^2}{4} + \inf_w \frac{\int_0^1 (w')^2 dx - k\int_0^1\int_0^1 H(x,y)w(x)w(y)dxdy}{\int_0^1 w^2 dx}. \quad (19)$$

It is noted that

$$\int_0^1\int_0^1 H(x,y)w(x)w(y)dxdy = -\int_0^1 \bar{g}'g'dx \quad (20)$$

where g is the solution of

$$g''(x) = w(x)\exp\left(\frac{iLx}{2}\right) \quad (21)$$

with

$$g(0) = g(1) = 0.$$

An estimate of p_{cr} can be obtained from (19) by assuming, for example, $w(x) = \sin\pi x$, resulting in

$$p_{cr} = -\frac{L^2}{4} + \pi^2 + \frac{k\left[\left(\pi^2 - \frac{L^2}{4}\right)\left(\pi^4 - \frac{L^4}{16}\right) - 4\pi^2L^2\left(1 + \cos\frac{L}{2}\right)\right]}{\left(\pi^2 - \frac{L^2}{4}\right)^4}. \quad (22)$$

When $k = 0$, $p_{cr} = -\frac{L^2}{4} + \pi^2$ is the necessary and sufficient condition for stability because (18) becomes

$$w'' + \left(p + \frac{L^2}{4}\right)w = 0, \; w(0) = w(1) = 0, \quad (23)$$

which describes the free vibration of a string, with $p + \frac{L^2}{4}$ playing the role of the frequency parameter. The fundamental frequency of a string is equal to $\omega^2 = \pi^2$. When $L = 0$,

$$p_{cr} = \pi^2 + \frac{k}{\pi^2}. \quad (24)$$

On the other hand, when $L = \pm 2\pi$,

$$p_{cr} = \frac{k}{8}\left(\frac{1}{3} + \frac{3}{\pi^2}\right). \tag{25}$$

Therefore $k > 0$ does increase the stability boundary, directly confirming Walker's conjecture about an increase in the upper bound on $L^2 + 4p$.

The case of a pure axial torque ($\theta = 1$) is considered next. Let (11) be integrated with respect to x twice to obtain

$$(r^2 + cr + k)\int_0^1 G(x,y)z(y)dy + z'' + pz - iLz' = a_1 + a_2 x. \tag{26}$$

The constants of integration a_1 and a_2 are found to be equal to zero, in view of the boundary conditions $z = 0$ and $z'' - iLz' = 0$. Therefore, (26) becomes

$$(r^2 + cr + k)\int_0^1 G(x,y)z(y)dy + z'' + pz - iLz' = 0. \tag{27}$$

The dependent variable needs to satisfy only the boundary conditions $z(0) = z(1) = 0$. Since (27) is the same as (16), the symmetrized system in (18) and the stability boundary in (22) also hold true for the Greenhill shaft under an axial torque. Therefore, the shaft under an axial torque and that under a tangential torque behave in a very similar manner and both have the same equivalent symmetrized system.

4 Conclusions

Some of the conservative systems of the second kind we considered here had been studied by Walker, Leipholz, and Inman and Olsen. Our objective, however, is to obtain an equivalent self-adjoint system for the nonconservative problem. Existence of the symmetrized systems confirms that certain conservative systems of the second kind indeed behave as a true conservative system. It also allows study of stability of the nonconservative problem to be carried out on the symmetrized system. In general, it is easier to study a self-adjoint problem than a nonself-adjoint problem. For example, it was shown that the buckling load of a guided-guided bar under a uniform tangential follower force can be obtained as the critical weight of a pinned-pinned column under its own weight, and that the stability of a pin-ended bar in compression and under an axial torque or a tangential torque becomes the free vibration of a string. The self-adjoint problems are simpler than the nonself-adjoint problems. In the case of a bar in torsion in a viscoelastic medium, study of the symmetrized system enables us to obtain a sharper stability boundary.

References

Bolotin, V. V., 1963, *Nonconservative Problems of the Theory of Elastic Stability*, Pergamon Press.

Inman, D. J., 1983, "Dynamics of Asymmetric Nonconservative Systems," ASME JOURNAL OF APPLIED MECHANICS, Vol. 50, No. 1, pp. 199–203.

Inman, D. J., and Olsen, C. L., 1988, "Dynamics of Symmetrizable Nonconservative Systems," ASME JOURNAL OF APPLIED MECHANICS, Vol. 55, pp. 206–212.

Leipholz, H. H. E., 1974a, "On Conservative Elastic Systems of the First and Second Kind," *Ingenieur-Archiv*, Vol. 43, pp. 255–271.

Leipholz, H. H. E., 1974b, "On a Generalization of the Concept of Self-Adjointness and of Rayleigh's Quotient," *Mechanics Research Communications*, Vol. 1, pp. 67–72.

Walker, J. A., 1972, "Liapunov Analysis of the Generalized Pfluger Problem," ASME JOURNAL OF APPLIED MECHANICS, Vol. 39, Series E, pp. 935–938.

Walker, A. J., 1973, "Stability of a Pin-Ended Bar in Torsion and Compression," ASME JOURNAL OF APPLIED MECHANICS, Vol. 40, pp. 405–409.

On the Inverse Vibration Problem With Rigid-Body Modes

Ladislav Starek[16] and Daniel J. Inman[17]

Introduction

This Note considers an alternative solution to the inverse problem for a linear lumped-parameter system with singular velocity and displacement coefficient matrices. Inverse problems for vibrating lumped-parameter nonconservative systems are concerned with constructing coefficient matrices corresponding to mass, damping, and stiffness parameters from knowledge of a systems eigenvalues and eigenvectors (referred to as spectral data). In general, knowledge of spectral data of a given system does not uniquely determine the desired coefficient matrices. However, several theories have been developed to solve the inverse problem for lumped parameter systems. Most notable is the work of Lancaster and Maroulas (1987) and that of Danek (1982, 1985). The text by Gladwell (1986) contains a general presentation of the inverse problem for undamped vibrating systems.

Lancaster and Maroulas (1987) use a matrix polynomial approach and arrive at a solution of the inverse problem which is applicable to the nonsingular case. The formulation of Lancaster and Maroulas requires complete spectral data and applies to the singular case addressed here. Danek (1987) addresses the inverse problem for nonsingular coefficient matrices using a state space approach. Danek (1982) introduces the more practical inverse problem for incomplete spectral data. This is sometimes called the *tuning problem* in Eastern Europe and is referred to as the *model correction problem* in the West (Minas and Inman, 1990) and has important implications in the modal testing and finite element industry.

The solution presented here uses a state space approach similar to Danek's to derive results equivalent to Lancaster's for the singular coefficient case and results in a formulation for using incomplete spectral data. Note that the use of the word complete in testing refers to whether or not all the spectral data is available for use in the reconstruction of the coefficient matrices. In Lancaster (1987), and as well as most theoretical treatments, the word complete refers to mathematical structure of the Jordan pair associated with a matrix polynomial.

Inverse Vibration Problem Formulation

This section introduces the class of inverse vibration problems considered. The equations of vibration are of the form of the second-order vector differential equation

$$A_1\ddot{\mathbf{q}}(t) + A_2\dot{\mathbf{q}}(t) + A_3\mathbf{q}(t) = \mathbf{f}(t) \tag{1}$$

where $\mathbf{q}(t)$ is a $n \times 1$ vector of generalized coordinates, $\dot{\mathbf{q}}(t)$ is the generalized velocity vector, $\ddot{\mathbf{q}}(t)$ is the generalized acceleration, and $\mathbf{f}(t)$ represents an $n \times 1$ vector of applied forces. The $n \times n$ real matrices A_1, A_2, and A_3 represent mass, damping, and stiffness properties of the system as well as gyroscopic, follower, and constraint damping forces (see, for instance, Huseyin, 1978, or Inman, 1989). In the problem considered

[16]Faculty of Mechanical Engineering, Slovak Technical University at Bratislava, 81231 Bratislava, Czechoslovakia.

[17]Mechanical and Aerospace Engineering, State University of New York at Buffalo, Buffalo, NY 14260. Fellow ASME.

Contributed by the Applied Mechanics Division of the American Society of Mechanical Engineers. Manuscript received by the ASME Applied Mechanics Division, Dec. 21, 1988; final revision, Jan. 18, 1991.

On the other hand, when $L = \pm 2\pi$,

$$p_{cr} = \frac{k}{8}\left(\frac{1}{3} + \frac{3}{\pi^2}\right). \tag{25}$$

Therefore $k > 0$ does increase the stability boundary, directly confirming Walker's conjecture about an increase in the upper bound on $L^2 + 4p$.

The case of a pure axial torque ($\theta = 1$) is considered next. Let (11) be integrated with respect to x twice to obtain

$$(r^2 + cr + k)\int_0^1 G(x,y)z(y)dy + z'' + pz - iLz' = a_1 + a_2 x. \tag{26}$$

The constants of integration a_1 and a_2 are found to be equal to zero, in view of the boundary conditions $z = 0$ and $z'' - iLz' = 0$. Therefore, (26) becomes

$$(r^2 + cr + k)\int_0^1 G(x,y)z(y)dy + z'' + pz - iLz' = 0. \tag{27}$$

The dependent variable needs to satisfy only the boundary conditions $z(0) = z(1) = 0$. Since (27) is the same as (16), the symmetrized system in (18) and the stability boundary in (22) also hold true for the Greenhill shaft under an axial torque. Therefore, the shaft under an axial torque and that under a tangential torque behave in a very similar manner and both have the same equivalent symmetrized system.

4 Conclusions

Some of the conservative systems of the second kind we considered here had been studied by Walker, Leipholz, and Inman and Olsen. Our objective, however, is to obtain an equivalent self-adjoint system for the nonconservative problem. Existence of the symmetrized systems confirms that certain conservative systems of the second kind indeed behave as a true conservative system. It also allows study of stability of the nonconservative problem to be carried out on the symmetrized system. In general, it is easier to study a self-adjoint problem than a nonself-adjoint problem. For example, it was shown that the buckling load of a guided-guided bar under a uniform tangential follower force can be obtained as the critical weight of a pinned-pinned column under its own weight, and that the stability of a pin-ended bar in compression and under an axial torque or a tangential torque becomes the free vibration of a string. The self-adjoint problems are simpler than the nonself-adjoint problems. In the case of a bar in torsion in a viscoelastic medium, study of the symmetrized system enables us to obtain a sharper stability boundary.

References

Bolotin, V. V., 1963, *Nonconservative Problems of the Theory of Elastic Stability*, Pergamon Press.

Inman, D. J., 1983, "Dynamics of Asymmetric Nonconservative Systems," ASME JOURNAL OF APPLIED MECHANICS, Vol. 50, No. 1, pp. 199–203.

Inman, D. J., and Olsen, C. L., 1988, "Dynamics of Symmetrizable Nonconservative Systems," ASME JOURNAL OF APPLIED MECHANICS, Vol. 55, pp. 206–212.

Leipholz, H. H. E., 1974a, "On Conservative Elastic Systems of the First and Second Kind," *Ingenieur-Archiv*, Vol. 43, pp. 255–271.

Leipholz, H. H. E., 1974b, "On a Generalization of the Concept of Self-Adjointness and of Rayleigh's Quotient," *Mechanics Research Communications*, Vol. 1, pp. 67–72.

Walker, J. A., 1972, "Liapunov Analysis of the Generalized Pfluger Problem," ASME JOURNAL OF APPLIED MECHANICS, Vol. 39, Series E, pp. 935–938.

Walker, A. J., 1973, "Stability of a Pin-Ended Bar in Torsion and Compression," ASME JOURNAL OF APPLIED MECHANICS, Vol. 40, pp. 405–409.

On the Inverse Vibration Problem With Rigid-Body Modes

Ladislav Starek[16] and Daniel J. Inman[17]

Introduction

This Note considers an alternative solution to the inverse problem for a linear lumped-parameter system with singular velocity and displacement coefficient matrices. Inverse problems for vibrating lumped-parameter nonconservative systems are concerned with constructing coefficient matrices corresponding to mass, damping, and stiffness parameters from knowledge of a systems eigenvalues and eigenvectors (referred to as spectral data). In general, knowledge of spectral data of a given system does not uniquely determine the desired coefficient matrices. However, several theories have been developed to solve the inverse problem for lumped parameter systems. Most notable is the work of Lancaster and Maroulas (1987) and that of Danek (1982, 1985). The text by Gladwell (1986) contains a general presentation of the inverse problem for undamped vibrating systems.

Lancaster and Maroulas (1987) use a matrix polynomial approach and arrive at a solution of the inverse problem which is applicable to the nonsingular case. The formulation of Lancaster and Maroulas requires complete spectral data and applies to the singular case addressed here. Danek (1987) addresses the inverse problem for nonsingular coefficient matrices using a state space approach. Danek (1982) introduces the more practical inverse problem for incomplete spectral data. This is sometimes called the *tuning problem* in Eastern Europe and is referred to as the *model correction problem* in the West (Minas and Inman, 1990) and has important implications in the modal testing and finite element industry.

The solution presented here uses a state space approach similar to Danek's to derive results equivalent to Lancaster's for the singular coefficient case and results in a formulation for using incomplete spectral data. Note that the use of the word complete in testing refers to whether or not all the spectral data is available for use in the reconstruction of the coefficient matrices. In Lancaster (1987), and as well as most theoretical treatments, the word complete refers to mathematical structure of the Jordan pair associated with a matrix polynomial.

Inverse Vibration Problem Formulation

This section introduces the class of inverse vibration problems considered. The equations of vibration are of the form of the second-order vector differential equation

$$A_1\ddot{\mathbf{q}}(t) + A_2\dot{\mathbf{q}}(t) + A_3\mathbf{q}(t) = \mathbf{f}(t) \tag{1}$$

where $\mathbf{q}(t)$ is a $n \times 1$ vector of generalized coordinates, $\dot{\mathbf{q}}(t)$ is the generalized velocity vector, $\ddot{\mathbf{q}}(t)$ is the generalized acceleration, and $\mathbf{f}(t)$ represents an $n \times 1$ vector of applied forces. The $n \times n$ real matrices A_1, A_2, and A_3 represent mass, damping, and stiffness properties of the system as well as gyroscopic, follower, and constraint damping forces (see, for instance, Huseyin, 1978, or Inman, 1989). In the problem considered

[16]Faculty of Mechanical Engineering, Slovak Technical University at Bratislava, 81231 Bratislava, Czechoslovakia.

[17]Mechanical and Aerospace Engineering, State University of New York at Buffalo, Buffalo, NY 14260. Fellow ASME.

Contributed by the Applied Mechanics Division of the American Society of Mechanical Engineers. Manuscript received by the ASME Applied Mechanics Division, Dec. 21, 1988; final revision, Jan. 18, 1991.

here, the inertia matrix A_1 is assumed to be nonsingular so that Eq. (1) may be written equivalently as

$$I\ddot{\mathbf{q}}(t)+H_2\dot{\mathbf{q}}(t)+H_3\mathbf{q}(t)=\mathbf{F}(t) \tag{2}$$

where $H_2=A_1^{-1}A_2$, $H_3=A_1^{-1}A_3$, $\mathbf{F}(t)=A_1^{-1}\mathbf{f}(t)$ and I denotes the $n\times n$ identity matrix. The matrices H_2 and H_3 are asymmetric and possibly singular to allow for rigid body motion and the possibility of semi-definite damping.

The eigenvalue problem associated with Eq. (2) determines the solution to the forward problem of calculating both the free and forced response of the system. The associated eigenvalue problem is

$$L(\lambda)\mathbf{x}=(\lambda^2+\lambda H_2+H_3)\mathbf{x}=\mathbf{0} \tag{3}$$

for nonzero vectors $\mathbf{x}$. The complex scalar λ is called an eigenvalue and $\mathbf{x}$ a right eigenvector (possibly complex) of Eq. (3). The right eigenvectors have the physical notion of mode shapes, while the eigenvalues λ contain the natural frequencies and damping ratios of the system. The matrix $L(\lambda)=\lambda^2+\lambda H_2+H_3$ is called a matrix polynomial of order 2. Since the coefficient matrices are $n\times n$, the solution of (3) yields $2n$ values of λ and $\mathbf{x}$, denoted $(\lambda_i, \mathbf{x}_i)$. The forward problem consists of calculating λ_i and $\mathbf{x}_i$ given H_2 and H_3, while the inverse problem addressed here consists of calculating the matrices H_2 and H_3 given the spectral data $(\lambda_i, \mathbf{x}_i)$, assuming the structure assigned by Eq. (3).

Also of use in the inverse problem are the left eigenvectors denoted $\mathbf{y}_i$ which satisfy

$$\mathbf{y}_i^T L(\lambda_i)=\mathbf{0}. \tag{4}$$

The vectors $\mathbf{y}_i$ and $\mathbf{x}_i$ satisfy certain orthogonality conditions. The eigenvalue problem of Eq. (3) can also be represented in state space form by defining the $2n\times 2n$ state matrix

$$A=\begin{pmatrix}0 & I\\ -H_3 & -H_2\end{pmatrix}. \tag{5}$$

The eigenvalue problem for the matrix A becomes

$$(A-\lambda_i I)\mathbf{q}_i=\mathbf{0} \tag{6}$$

where the constant nonzero vector $\mathbf{q}_i$ is related to the right eigenvector $\mathbf{x}_i$ by

$$\mathbf{q}_i=\begin{pmatrix}\mathbf{x}_i\\ \lambda\mathbf{x}_i\end{pmatrix}. \tag{7}$$

The eigenvalues of A and $L(\lambda)$ are identical. Equation (6) is the statement of the matrix eigenvalue problem. Inverse calculations based on the state space eigenvalue problem of Eq. (6) involve inversion of either a coefficient matrix or of the Jordan form, both of which may be singular in the case considered here.

An alternative form of the state matrix suggested by Danek (1982) can be employed to avoid the inversion of either a coefficient matrix or the Jordan form. This equivalent form is

$$(P-\lambda_i N)\mathbf{u}_i=\mathbf{0} \tag{8}$$

where λ_i have the same values as in (6) and $A=N^{-1}P$. Equation (8) is also known as the generalized eigenvalue problem and the $2n\times 2n$ partitioned matrices N and P are given by

$$N=\begin{pmatrix}H_2 & I\\ I & 0\end{pmatrix},\quad P=\begin{pmatrix}-H_3 & I\\ I & 0\end{pmatrix}, \tag{9}$$

respectively. Note that N is nonsingular even if H_2 is singular.

The Jordan form of the state matrix A is given by the $2n\times 2n$ block diagonal matrix J which satisfies

$$Q^{-1}AQ=J. \tag{10}$$

The blocks of J are upper triangular with the eigenvalues of A along the diagonal. The super diagonals are ones or zeros depending on the nature of the root λ_i (i.e., 1 if defective and 0 otherwise). The nonsingular matrix Q consists of the Jordan chain vectors. The vectors of the Jordan chain are generalized eigenvectors (see Ortega, 1987, for instance). For the special structure of the state matrix of Eq. (5), the matrix Q can be written as

$$\begin{bmatrix}X\\ XJ\end{bmatrix} \tag{11}$$

where X is the Jordan chain matrix associated with matrix polynomial of Eq. (3). In the case that A has all simple eigenvalues, the right eigenvectors can be used to form the matrix X.

The equivalent "Jordan" form for the eigenvalue problem of Eq. (8) is

$$NQJ=PQ \text{ or } V^TPQ=J \tag{12}$$

where

$$V^TNQ=I. \tag{13}$$

Here, J is as before and V is defined by the matrix Y to be

$$V^T=[Y^T \quad JY^T] \tag{14}$$

where Y is the matrix of elements of left eigenvectors of (3). The matrix V^T can be related to the matrix Q from the state space model by multiplying Eq. (13) from the right to get

$$Q^{-1}=V^TN. \tag{15}$$

This last expression provides a means of treating inverse calculations without explicitly calculating the inverse of Q or J.

Danek solved the problem of determining the matrices P and N given the data J and Q for the case that H_2 and H_3 are *nonsingular*. The problem addressed below is to determine H_2 and H_3 from X, Y, and J for the case when H_2 and H_3 are *singular* as well as the case when only part of X, Y, and J are known.

Solution to the Inverse Problem

In order to consider rigid-body modes it is necessary to calculate the state matrix $A=QJQ^{-1}$ without inverting the matrix Q, and hence J which is singular. Substitution of Eq. (15) into the expression for A yields

$$A=\begin{bmatrix}0 & I\\ -H_3 & -H_2\end{bmatrix}=QJV^TN. \tag{16}$$

Comparing and equating the four partitions of the matrix identity of Eq. (16) yields four matrix equations in the two unknown matrices H_2 and H_3. One of these equations (corresponding to the 1-1 block) yields an identity and the other three blocks yield

$$H_2=-XJ^2Y^T \tag{17}$$

$$H_3=(XJ^2Y^T)^2-XJ^3Y^T \tag{18}$$

$$I=XJY^T. \tag{19}$$

This last expression is a normalization condition. These matrices can now be further partitioned to solve the tuning problem and provide a direct extension of Danek (1985) to the singular coefficient case.

Consider then repartitioning X, J, and Y as

$$X=[X_1 \quad X_2],\ J=[J_1 \quad J_2] \text{ and } Y=[Y_1 \quad Y_2]. \tag{20}$$

Here, J_1 is $n\times m$ and J_2 is $(2n-m)\times(2n-m)$. With these partitions, Eqs. (17), (18), and (19) become

$$H_2=-(X_1J_1^2Y_1^T+X_2J_2^2Y_2^T) \tag{21}$$

$$H_3=(X_1J_1^2Y_1^T+X_2J_2^2Y_2^T)^2-(X_1J_1^3Y_1^T+X_2J_2^3Y_1^T) \tag{22}$$

$$I=X,J,Y^T,+X_2J_2Y_2^T. \tag{23}$$

Note that these matrices must be partitioned such that J_1 and J_2 are whole Jordan blocks.

Let the original (known) system matrices be denoted by J_0, X_0, Y_0, H_{20}, and H_{30}. Quantities of the new or tuned system

are denoted by J, X, Y, H_2, and H_3. The corrections to the original system are denoted by ΔJ, ΔX, ΔY, ΔH_2, and ΔH_3. Thus, the spectral properties of the new system are

$$J = J_0 + \Delta J,\ X = X_0 + \Delta X \text{ and } Y = Y_0 + \Delta Y. \tag{24}$$

Equation (24) provides a solution to the tuning problem when substituted into Eq. (17) and (18). That is if J_0, X_0, and Y_0 are computed from known values of H_2 and H_3, say from a finite element model, then this model can be updated, or tuned, by assigning values of ΔJ, ΔX, and ΔY to yield a new, or modified, set of coefficient matrices H_2 and H_3.

the three degree-of-freedom system with semi-definite damping and stiffness given by Eq. (2) with

$$H_2 = \begin{bmatrix} 1 & -1 & 0 \\ -1 & 2 & -1 \\ 0 & -1 & 1 \end{bmatrix} \text{ and } H_3 = \begin{bmatrix} 2 & -2 & 0 \\ -2 & 3 & -1 \\ 0 & -1 & 1 \end{bmatrix}.$$

The spectral solution of the system reveals that the matrices J and Q are defined by

$$J_{10} = \text{diag}(-1.41 \pm 1.0592i,\ -.59 \pm 1.028i),\ J_{20} = \begin{bmatrix} 0 & 1 \\ 0 & 0 \end{bmatrix}, \text{ and}$$

$$Q = \begin{bmatrix} 0.2679+0.0941i & 0.1732+0.6241i & 1 & 0 & 0.2679+0.0941i & 0.1732+0.6241i \\ -0.3305-0.3538i & 0.2462+0.1073i & 1 & 0 & -0.3305-0.3538i & 0.2462+0.1073i \\ 0.0626+0.2597i & -0.4195+0.7315i & 1 & 0 & 0.0626+0.2597i & -0.4195+0.7315i \\ -0.5197+0.2716i & -0.7443+0.1900i & 0 & 1 & -0.5197+0.2716i & -0.7443+0.1900i \\ 1. & -0.2557+0.1900i & 0 & 1 & 1. & -0.2557+0.1900i \\ -0.4803-0.2716i & 1 & 0 & 1 & -0.4803-0.2716i & 1. \end{bmatrix}$$

Partial Spectral Data

The problem of more practical interest is that if modifying H_2 and H_3 by changing only part of the spectral data (see Minas and Inman, 1990 and the references therein). In this case assume that the matrices of incomplete spectral information J_{10}, X_{10}, Y_{10} are known for the first m eigenvalues and associated eigenvectors. The remainder of the spectral properties J_{20}, X_{20}, and Y_{20} are not being changed and are unknown. The original system, according to Eqs. (21) and (22), can be written as

$$H_{20} = -(X_{10}J_{10}^2Y_{10}^T + X_{20}J_{20}^2Y_{20}^T) \tag{25}$$

$$H_{30} = (X_{10}J_{10}^2Y_{10}^T + X_{20}J_{20}^2Y_{20}^T)^2 - (X_{10}J_{10}^3Y_{10}^T + X_{20}J_{20}^3Y_{20}^T) \tag{26}$$

with the condition that

$$(X_{10}J_{10}Y_{10}^T + X_{20}J_{20}Y_{20}^T) = I. \tag{27}$$

Following Eq. (24), the new spectral matrices become $J_1 = J_{10} + \Delta J_{10}$, $X_1 = X_{10} + \Delta X_{10}$ and $Y_1 = Y_{10} + \Delta Y_{10}$, so that the system matrices become

$$H_2 = -(X_1J_1^2Y_1^T + X_{20}J_{20}^2Y_{20}^T) \tag{28}$$

$$H_3 = (X_1J_1^2Y_1^T + X_{20}J_{20}^2Y_{20}^T)^2 - (X_1J_1^3Y_1^T + X_{20}J_{20}^3Y_{20}^T) \tag{29}$$

with the condition that

$$X_1J_1Y_1^T + X_{20}J_{20}Y_{20}^T = I. \tag{30}$$

By subtracting equations (25) and (26) from (28) and (29), the expressions for H_2 and H_3 become

$$H_2 = H_{20} + \Delta H_{20} \tag{31}$$

$$H_3 = H_{30} + \Delta H_{30} \tag{32}$$

where the reconstruction associated with the changes ΔJ_{10}, ΔX_{10}, and ΔY_{10} is given by

$$\Delta H_{20} = -(X_1J_1^2Y_1^T - X_{10}J_{10}^2Y_{10}^T) \tag{33}$$

$$\Delta H_{30} = H_2^2 - H_{20}^2 - (X_1J_1^3Y_1^T - X_{10}J_{10}^3Y_{10}^T). \tag{34}$$

These formulas specify the changes in original systems due to a new partial set of spectral data. This provides a solution to the tuning problem using only a part of the spectral data for the case that the coefficient matrices are potentially singular.

Example

For the sake of illustration, the above inverse formulas are applied to a simple example. For simplicity of presentation, the matrix A_1 is taken to be the identity matrix so that $H_2 = A_2$ and $H_3 = A_3$. The example illustrates both the use of Eq. (21) and (22) as well as providing an example of the correctness of the results for a system with singular coefficients. Consider

Here, $i = \sqrt{-1}$. Let the new spectral matrix be $J_1 = \text{diag}[-1.4228 + 2.6541i,\ -0.5772 + 1.521i,\ -1.4228 - 2.6541i,\ -0.5772 - 1.521i]$ and the new matrix Q_1 is given by (11) where the matrix X is obtained from $X = [I\ 0]Q$. By using the inverse formula (21) and (22), the matrices H_2 and H_3 become

$$H_2 = \begin{bmatrix} 0.7378 & -0.8257 & 0.0879 \\ -0.8236 & 2.0869 & -1.2632 \\ 0.0858 & -1.2612 & 1.1753 \end{bmatrix}$$

and

$$H_3 = \begin{bmatrix} 3.8263 & -3.9324 & 0.1061 \\ -4.2819 & 6.4914 & -2.2095 \\ 0.4556 & -2.5590 & 2.1034 \end{bmatrix}.$$

To see that the method works, note that equation (3) with these values of H_2 and H_3 yield the Jordan matrix given by the matrix J_1.

Summary

Lancaster et al. have formulated a solution of the inverse eigenvalue problem in an abstract form resulting in formulas for calculating velocity and position coefficients from spectral data by examining second-order matrix polynomials. Danek solved a similar inverse problem by examining the generalized eigenvalue problem. The work presented here uses a combination of state space Jordan form and the equivalent Jordan form for a generalized eigenvalue problem to develop a method of calculating the matrix coefficients of velocity and displacement without calculating the inverse of the Jordan form. This yields a solution of the inverse problem for systems with rigid-body modes. An illustration of how to apply this solution to the model correction problem is also given.

The results presented here have direct application to the model correction problem for finite element models of large space structures which exhibit both asymmetric coefficient matrices and rigid-body modes.

References

Danek, O., 1982, "Nonconservative Dynamic Systems," *Strojnicky Casopis*, Vol. 33, Chapter 6, pp. 667–680 (in Czech).

Danek, O., 1985, "Tuning of Nonconservative Dynamic Systems," *Strojnicky Casopis*, Vol. 36, Chapter 2, pp. 131–137 (in Czech).

Gladwell, G. M. L., 1986, *Inverse Problem in Vibration*, Martinus Nijhoff Publishers, Dordrecht.

Huseyin, K., 1978, *Vibration and Stability of Multiple Parameter Systems*, Noordhoff International, The Netherlands.

Inman, D. J., 1989, *Vibration with Control Measurement and Stability*, Prentice-Hall, Englewood Cliffs, N. J.

Lancaster, P., and Maroulas J., 1987, "Inverse Eigenvalue Problems for Damped Vibrating Systems," *Journal of Mathematical Analysis and Applications*, Vol. 123, No. 1, pp. 238–261.

Minas, C., and Inman, D. J., 1990, "Matching Finite Element Models to Modal Data," ASME *Journal of Vibration, Acoustics, Stress, and Reliability in Design*, Vol. 112, No. 1, pp. 84–92.

Ortega, J. M., 1987, *Matrix Theory: A Second Course*, Plenum Press, New York.

An Exact Solution of Oscillatory Couette Flow in a Rotating System

B. S. Mazumder[18]

An exact solution of oscillatory Ekman boundary layer flow bounded by two horizontal flat plates, one of which is oscillating in its own plane and other at rest, is obtained. The effect of coriolis force on the resultant velocities and shear stresses for steady and unsteady flow has been studied.

Introduction

When a vast expanse of viscous fluid bounded by an infinite flat plate is rotating about an axis normal to the plate, a layer, known as Ekman Layer, is formed near the plate where the viscous and coriolis forces are of the same order of magnitude (Batchelor, 1967). The effect of uniform transverse magnetic field with or without suction was investigated by Gupta (1972a,b), Soundalgekar and Pop (1973), Mazumder et al. (1976), and others. Mazumder (1975) studied the effect of free-stream oscillations of flow of an electrically conducting fluid past an infinite plate in a rotating system. Solution was obtained for small amplitude of oscillation in the free stream using the Lighthill's technique (1954). Several investigations have been carried out on various types of flow in a rotating system such as "Poiseuille flow" by Vidyanidhu and Nigam (1967) and "plane Couette flow" by Jana and Datta (1977).

The main objective of this article is to present an exact solution to study the oscillatory flow between two parallel plates with an externally imposed pressure gradient in presence of coriolis force. In the rotating system, the top boundary wall oscillates in its own plane about a mean velocity. The study of hydrodynamic flow confined between two horizontal walls responds to oscillations in one boundary wall in a rotating system has remained untreated. The hydrodynamic and hydromagnetic flow between two parallel plates, one of which is at rest, the other oscillating in its own plane is recently studied by Vajravelu (1988) which is a particular case of the present paper.

Mathematical Formulations and Solution

Consider the flow of a viscous incompressible fluid between two parallel flat plates separated by a distance d, the lower one is at rest, the other oscillating in its own plane with a velocity $U(t)$ about a constant mean velocity U_o in the x-direction where x is taken on the lower rest plate. The z-axis is normal to the plates and the y-axis is perpendicular to the xz-plane. Since the plate $z = 0$ is infinite in extent all the physical variables, except pressure, depend on z and time t only. The equation of continuity $\nabla \cdot \mathbf{u} = 0$ gives $w = 0$, where $\mathbf{u} = (u, v, w)$. Under the assumptions of which the Navier-Stokes equations are written in a rotating frame of reference as

$$\frac{\partial u}{\partial t} = -\frac{1}{\rho}\frac{\partial p^*}{\partial x} + \nu\frac{\partial^2 u}{\partial z^2} + 2\Omega v \tag{1}$$

$$\frac{\partial v}{\partial t} = -\frac{1}{\rho}\frac{\partial p^*}{\partial y} + \nu\frac{\partial^2 v}{\partial z^2} - 2\Omega u \tag{2}$$

$$0 = -\frac{1}{\rho}\frac{\partial p^*}{\partial y} \tag{3}$$

where $(u, v, 0)$ are the velocity components along x, y, and z-directions, respectively, ν is kinematic viscosity, Ω is the constant angular velocity about z-axis normal to the plate, and p^* is the modified pressure. The boundary conditions for the velocity field are

$$u = v = 0 \text{ at } z = 0$$

$$u = U(t),\ v = 0 \text{ at } z = d. \tag{4}$$

Under the usual boundary layer approximations, eliminating the modified pressure gradients from Eqs. (1)–(4), the Navier-stokes Eqs. (1) and (2) can be rewritten as:

$$\frac{\partial u}{\partial t} = \frac{\partial U}{\partial t} + \nu\frac{\partial^2 u}{\partial z^2} + 2\Omega v \tag{5}$$

$$\frac{\partial v}{\partial t} = \nu\frac{\partial^2 v}{\partial z^2} - 2\Omega(u - U). \tag{6}$$

The oscillating velocity $U(t)$ of the plate about the mean U_o is considered in the form of:

$$U(t) = U_o[1 + 1/2\epsilon e^{i\omega t}] \tag{7}$$

where ω is the frequency of oscillation; U_o and ϵ are constants. Here, of course, only the real part contributes to the physical meaning.

Equations (5) and (6) can be written, in complex form, as

$$\frac{\partial q}{\partial t} = \nu\frac{\partial^2 q}{\partial z^2} + \frac{\partial U}{\partial t} - 2i\Omega(q - U) \tag{8}$$

and the boundary conditions (4) are

$$q = 0 \text{ at } z = 0$$

$$q = U(t) \text{ at } z = d \tag{9}$$

where $q = u + iv$.

In order to solve Eq. (8) subject to the boundary conditions (9), we look for a solution of the form

$$q(t,\eta) = U_o[q_o(\eta) + 1/2\epsilon q_1(\eta)e^{i\omega t}] \tag{10}$$

in which $\eta = z/d$, $q_0 = u_0 + iv_0$, $q_1 = u_1 + iv_1$.

Substituting Eqs. (7) and (10) in (8) and (9), and equating steady and periodic terms separately, we get

$$\frac{d^2 q_o}{d\eta^2} - 2iKq_o = -2iK$$

$$\frac{d^2 q_1}{d\eta^2} - i(\lambda + 2K)q_1 = -i(\lambda + 2K) \tag{11}$$

$$q_o = 0,\ q_1 = 0 \text{ at } \eta = 0$$

$$q_o = 1,\ q_1 = 1 \text{ at } \eta = 1 \tag{12}$$

where $K = \Omega d^2/\nu$ is the rotation parameter and $\lambda = \omega d^2/\nu$ is the frequency parameter.

Solving Eq. (11) with the conditions (12), we get

$$q_0 = 1 - \frac{\sinh[\sqrt{K}(1+i)(1-\eta)]}{\sinh[\sqrt{K}(1+i)]} \tag{13}$$

$$q_1 = 1 - \frac{\sinh[\sqrt{(K+\lambda/2)}(1+i)\,(1-\eta)]}{\sinh[\sqrt{(K+\lambda/2)}(1+i)]}. \tag{14}$$

[18]Associate Professor, Math-Stat. Division, Indian Statistical Institute, Calcutta, 700035, India. Presently at the Surface Water Section, Illinois State Water Survey, Champaign, IL 61820.

Contributed by the Applied Mechanics Division of THE AMERICAN SOCIETY OF MECHANICAL ENGINEERS. Manuscript received by the ASME Applied Mechanics Division, Oct. 20, 1989; final revision, Jan. 18, 1991.

Inman, D. J., 1989, *Vibration with Control Measurement and Stability*, Prentice-Hall, Englewood Cliffs, N. J.

Lancaster, P., and Maroulas J., 1987, "Inverse Eigenvalue Problems for Damped Vibrating Systems," *Journal of Mathematical Analysis and Applications*, Vol. 123, No. 1, pp. 238–261.

Minas, C., and Inman, D. J., 1990, "Matching Finite Element Models to Modal Data," ASME *Journal of Vibration, Acoustics, Stress, and Reliability in Design*, Vol. 112, No. 1, pp. 84–92.

Ortega, J. M., 1987, *Matrix Theory: A Second Course*, Plenum Press, New York.

An Exact Solution of Oscillatory Couette Flow in a Rotating System

B. S. Mazumder[18]

An exact solution of oscillatory Ekman boundary layer flow bounded by two horizontal flat plates, one of which is oscillating in its own plane and other at rest, is obtained. The effect of coriolis force on the resultant velocities and shear stresses for steady and unsteady flow has been studied.

Introduction

When a vast expanse of viscous fluid bounded by an infinite flat plate is rotating about an axis normal to the plate, a layer, known as Ekman Layer, is formed near the plate where the viscous and coriolis forces are of the same order of magnitude (Batchelor, 1967). The effect of uniform transverse magnetic field with or without suction was investigated by Gupta (1972a,b), Soundalgekar and Pop (1973), Mazumder et al. (1976), and others. Mazumder (1975) studied the effect of free-stream oscillations of flow of an electrically conducting fluid past an infinite plate in a rotating system. Solution was obtained for small amplitude of oscillation in the free stream using the Lighthill's technique (1954). Several investigations have been carried out on various types of flow in a rotating system such as "Poiseuille flow" by Vidyanidhu and Nigam (1967) and "plane Couette flow" by Jana and Datta (1977).

The main objective of this article is to present an exact solution to study the oscillatory flow between two parallel plates with an externally imposed pressure gradient in presence of coriolis force. In the rotating system, the top boundary wall oscillates in its own plane about a mean velocity. The study of hydrodynamic flow confined between two horizontal walls responds to oscillations in one boundary wall in a rotating system has remained untreated. The hydrodynamic and hydromagnetic flow between two parallel plates, one of which is at rest, the other oscillating in its own plane is recently studied by Vajravelu (1988) which is a particular case of the present paper.

Mathematical Formulations and Solution

Consider the flow of a viscous incompressible fluid between two parallel flat plates separated by a distance d, the lower one is at rest, the other oscillating in its own plane with a velocity $U(t)$ about a constant mean velocity U_o in the x-direction where x is taken on the lower rest plate. The z-axis is normal to the plates and the y-axis is perpendicular to the xz-plane. Since the plate $z = 0$ is infinite in extent all the physical variables, except pressure, depend on z and time t only. The equation of continuity $\nabla \cdot \mathbf{u} = 0$ gives $w = 0$, where $\mathbf{u} = (u, v, w)$. Under the assumptions of which the Navier-Stokes equations are written in a rotating frame of reference as

$$\frac{\partial u}{\partial t} = -\frac{1}{\rho}\frac{\partial p^*}{\partial x} + \nu\frac{\partial^2 u}{\partial z^2} + 2\Omega v \tag{1}$$

$$\frac{\partial v}{\partial t} = -\frac{1}{\rho}\frac{\partial p^*}{\partial y} + \nu\frac{\partial^2 v}{\partial z^2} - 2\Omega u \tag{2}$$

$$0 = -\frac{1}{\rho}\frac{\partial p^*}{\partial y} \tag{3}$$

where $(u, v, 0)$ are the velocity components along x, y, and z-directions, respectively, ν is kinematic viscosity, Ω is the constant angular velocity about z-axis normal to the plate, and p^* is the modified pressure. The boundary conditions for the velocity field are

$$u = v = 0 \text{ at } z = 0$$

$$u = U(t),\ v = 0 \text{ at } z = d. \tag{4}$$

Under the usual boundary layer approximations, eliminating the modified pressure gradients from Eqs. (1)–(4), the Navier-stokes Eqs. (1) and (2) can be rewritten as:

$$\frac{\partial u}{\partial t} = \frac{\partial U}{\partial t} + \nu\frac{\partial^2 u}{\partial z^2} + 2\Omega v \tag{5}$$

$$\frac{\partial v}{\partial t} = \nu\frac{\partial^2 v}{\partial z^2} - 2\Omega(u - U). \tag{6}$$

The oscillating velocity $U(t)$ of the plate about the mean U_o is considered in the form of:

$$U(t) = U_o[1 + 1/2\epsilon e^{i\omega t}] \tag{7}$$

where ω is the frequency of oscillation; U_o and ϵ are constants. Here, of course, only the real part contributes to the physical meaning.

Equations (5) and (6) can be written, in complex form, as

$$\frac{\partial q}{\partial t} = \nu\frac{\partial^2 q}{\partial z^2} + \frac{\partial U}{\partial t} - 2i\Omega(q - U) \tag{8}$$

and the boundary conditions (4) are

$$q = 0 \text{ at } z = 0$$

$$q = U(t) \text{ at } z = d \tag{9}$$

where $q = u + iv$.

In order to solve Eq. (8) subject to the boundary conditions (9), we look for a solution of the form

$$q(t,\eta) = U_o[q_o(\eta) + 1/2\epsilon q_1(\eta)e^{i\omega t}] \tag{10}$$

in which $\eta = z/d$, $q_0 = u_0 + iv_0$, $q_1 = u_1 + iv_1$.

Substituting Eqs. (7) and (10) in (8) and (9), and equating steady and periodic terms separately, we get

$$\frac{d^2 q_o}{d\eta^2} - 2iKq_o = -2iK$$

$$\frac{d^2 q_1}{d\eta^2} - i(\lambda + 2K)q_1 = -i(\lambda + 2K) \tag{11}$$

$$q_o = 0,\ q_1 = 0 \text{ at } \eta = 0$$

$$q_o = 1,\ q_1 = 1 \text{ at } \eta = 1 \tag{12}$$

where $K = \Omega d^2/\nu$ is the rotation parameter and $\lambda = \omega d^2/\nu$ is the frequency parameter.

Solving Eq. (11) with the conditions (12), we get

$$q_0 = 1 - \frac{\sinh[\sqrt{K}(1+i)(1-\eta)]}{\sinh[\sqrt{K}(1+i)]} \tag{13}$$

$$q_1 = 1 - \frac{\sinh[\sqrt{(K+\lambda/2)}(1+i)\,(1-\eta)]}{\sinh[\sqrt{(K+\lambda/2)}(1+i)]}. \tag{14}$$

[18]Associate Professor, Math-Stat. Division, Indian Statistical Institute, Calcutta, 700035, India. Presently at the Surface Water Section, Illinois State Water Survey, Champaign, IL 61820.

Contributed by the Applied Mechanics Division of THE AMERICAN SOCIETY OF MECHANICAL ENGINEERS. Manuscript received by the ASME Applied Mechanics Division, Oct. 20, 1989; final revision, Jan. 18, 1991.

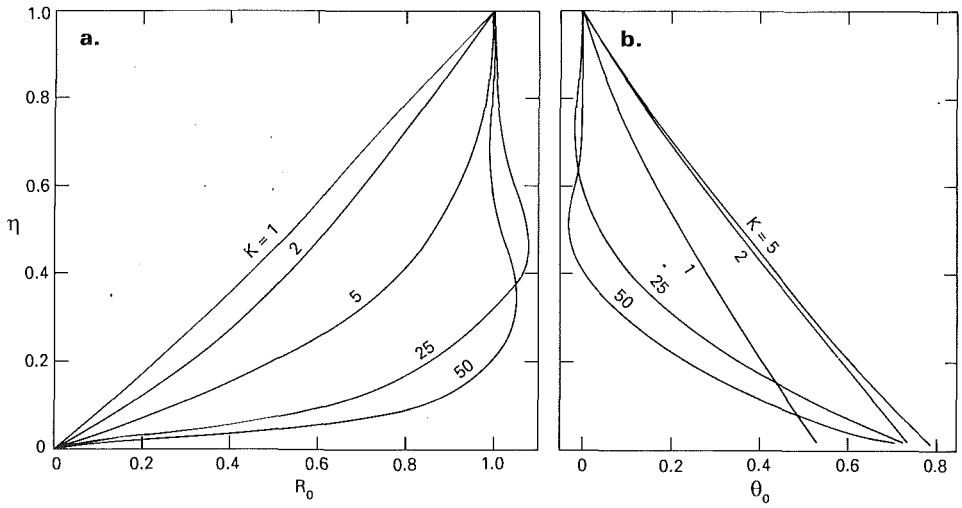

Fig. 1(*a*, *b*) Resultant velocity R_0 and phase angle θ_o due to u_o and v_o for steady flow

The solution (13) corresponds to the steady part which gives the primary u_o and secondary v_o velocity components; and the solution (14) gives the fluctuating part of the flows u_1 and v_1. Equation (10) can be rewritten as

$$q = U_0[(u_0 + iv_0) + 1/2\epsilon(u_1 + iv_1)e^{i\omega t}]. \tag{15}$$

The amplitudes and phase differences due to the primary and secondary velocities for the steady flow are given by

$$R_0 = \sqrt{(u_0^2 + v_0^2)},\ \theta_0 = \tan^{-1}(v_0/u_0), \tag{16}$$

and for unsteady flow

$$R_1 = \sqrt{(u_1^2 + v_1^2)},\ \theta_1 = \tan^{-1}(v_1/u_1). \tag{17}$$

The amplitude and phase differences of shear stresses at $\eta = 0$ due to the primary and secondary flow are given for steady flow by:

$$\tau_{0r} = \sqrt{(\tau_{0x}^2 + \tau_{0y}^2)},\ \theta_{0\tau} = \tan^{-1}(\tau_{0y}/\tau_{0x}), \tag{18}$$

and for unsteady flow

$$\tau_{1r} = \sqrt{(\tau_{1x}^2 + \tau_{1y}^2)},\ \theta_{1\tau} = \tan^{-1}(\tau_{1y}/\tau_{1x}). \tag{19}$$

The steady part of the velocity field and resultant shear stress at the plate $\eta = 0$ due to rotation has already been discussed by Jana and Datta (1976) neglecting the pressure gradients.

Discussion of Results

The resultant velocity R_0 and the phase angle θ_0 due to the primary and secondary flow for the steady part are plotted against η for various values of K in Fig. 1(*a*, *b*). It is found that the resultant velocity R_0 increases with increase in K and it becomes approximately one for large rotation in the upper half of the channel width. For large values of K, we get u_0 and v_0 from Eq. (13) as:

$$u_0 \simeq 1 - \exp\{-\sqrt{k}\eta\}\cos\sqrt{k}\eta \tag{20}$$

$$v_0 \simeq \exp\{-\sqrt{k}\eta\}\sin\sqrt{k}\eta \tag{21}$$

which represents a spiral distribution of velocity. These equations show the existence of a thin boundary layer of order $O(1/\sqrt{K})$ in the vicinity of the walls and is known as Ekman layer which decreases with increase in rotation. The phase angle θ_0 due to the primary and secondary flows increases with small rotation whereas it decreases with large rotation and is approximately zero in the upper half of the channel. The resultant shear stress at $\eta = 0$ and the phase angle due to shear stresses are given in Table 1. It is found that the resultant shear stress τ_{0r} increases with increase in rotation parameter K, but the phase angle $\theta_{0\tau}$ first increases then decreases with rotation K.

Table 1 Values of τ_{0r} and $\theta_{0\tau}$ for various K

K	τ_{0r}	$\theta_{0\tau}$
0.5	1.074350	0.313421
1.0	1.265549	0.539750
2.0	1.787115	0.748869
5.0	3.145135	0.807587
25.0	7.070535	0.785447
50.0	9.999997	0.785397

The distributions of primary and secondary velocity components of fluctuating part are shown in Fig. 2(*a*, *b*) for several values of frequency parameter λ and the rotation parameter K. From the figure, we notice that the primary velocity u_1 increases for both frequency and rotation parameters; and it becomes nearly one in the upper half of the channel for large λ and K. The secondary velocity v_1 increases with small K, whereas for large K, it decreases in the upper half and increases in the lower half of the channel. It is also seen that for large values of K there is an incipient flow reversal near the moving plate and the secondary velocity approximately becomes zero in the upper half of the channel. The resultant velocity R_1 and the phase angle θ_1, due to the primary and secondary velocities, are plotted in Fig. 3(*a*, *b*). For large values of frequency λ and rotation K, the expressions of u_1 and v_1 from the Eq. (14) can be written as:

$$u_1 \simeq 1 - \exp\{-\sqrt{(K + \lambda/2)}\eta\}\cos(K + \lambda/2)^{1/2}\eta \tag{22}$$

$$v_1 \simeq \exp\{-\sqrt{(K + \lambda/2)}\eta\}\sin(K + \lambda/2)^{1/2}\eta \tag{23}$$

which show the existence of thin Ekman boundary layer of order $O(1/(K + \lambda/2)^{1/2})$ in the vicinity of the walls and also represent a spiral distribution. The appearance of boundary layer to the lower stationary plate is due to the imposed external pressure gradient exactly in phase with the motion of the top wall, whereas boundary layer occurs next to the moving wall when no external pressure gradient is applied to the flow. It is interesting to note that the oscillatory Ekman boundary layer decreases rapidly due to the combined effect of rotation and frequency.

The shear stresses τ_{1x} and τ_{1y} due to primary and secondary flow at the plate $\eta = 0$ are shown in Fig. 4(*a*, *b*). For various values of K, the resultant shear stress τ_{1r} is also shown in Fig. 4(*a*). It is seen from the figure that the shear stresses increase with increase in λ and K, but for large rotation, both τ_{1x} and τ_{1y} are almost linear in λ. The phase angle $\theta_{1\tau}$ due to the shear stresses first increases, then decreases, with λ for small coriolis

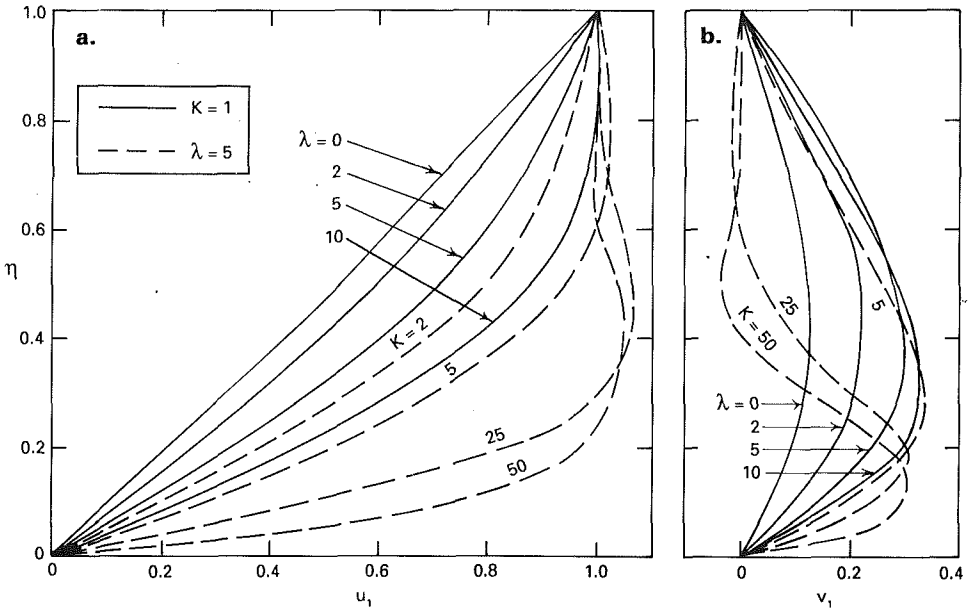

Fig. 2(*a, b*) Velocity distributions u_1 and v_1 against η

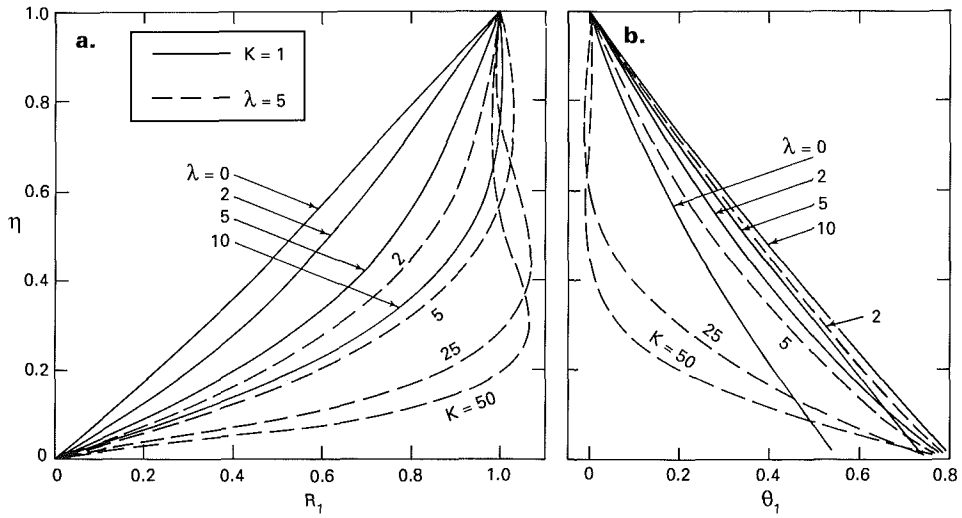

Fig. 3(*a, b*) Resultant velocity R_1 and phase angle θ_1 due to velocities u_1 and v_1 for unsteady flow

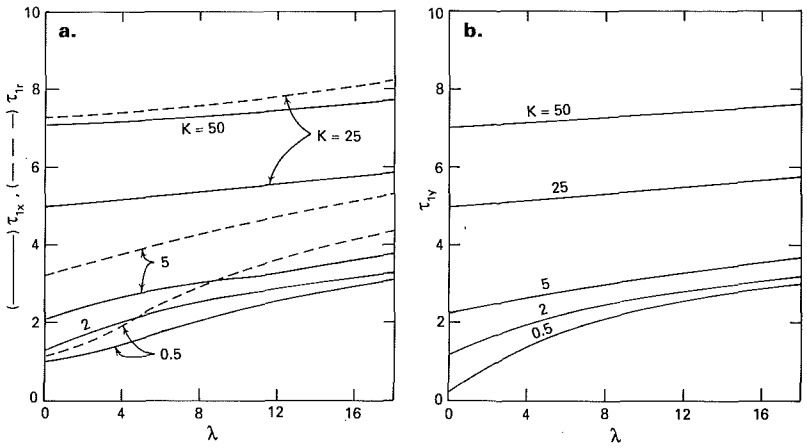

Fig. 4(*a, b*) Shear stresses at the plate $\eta = 0$ for unsteady flow

Table 2 Values of phase angle θ_{1_T} for various λ and K

λ/K	.5	1.0	2.0	5.0	25.0
0.0	.313421	.539749	.748869	.807587	.785447
1.0	.539749	.674830	.787152	.803758	.785449
2.0	.674830	.748869	.805256	.800047	.785450
3.0	.748869	.787152	.812190	.796702	.785449
5.0	.805256	.812190	.811024	.791431	.785447
10.0	.803758	.800047	.793824	.785250	.785433
16.0	.787964	.786783	.785250	.784216	.785415

force, whereas it is almost independent of λ for large coriolis force and the values are given in Table 2.

Acknowledgment

Many thanks to the anonymous referee for his helpful suggestions for improvement of the paper.

References

Batchelor, G. K., 1967, *An Introduction to Fluid Dynamics*, 1st ed., Cambridge University Press, Cambridge, U.K., p. 119.

Gupta, A. S., 1972*a*, "Ekman Layer on a Porous Plate," *Phys. Fluid*, Vol. 15, No. 5, pp. 930–931.

Gupta, A. S., 1972*b*, "Magnetohydrodynamic Ekman Layer," *Acta Mechanica*, Vol. 13, pp. 155–160.

Jana, R. N., and Datta, N., 1977, "Couette Flow and Heat Transfer in a Rotating System," *Acta Mechanica*, Vol. 26, pp. 301–306.

Lighthill, M. J., 1954, "The Response of Laminar Skin Friction and Heat Transfer to Fluctuations in a Stream Velocity," *Proc. Roy. Soc., Lond.*, Vol. A226, pp. 1–23.

Mazumder, B. S., 1975, "Oscillatory Hydromagnetic Flow of Rotating Fluid Past an Infinite Plate," Ph.D. Thesis, Indian Institute of Technology, Kharagpur, India.

Mazumder, B. S., Gupta, A. S., and Datta, N., 1976, "Flow and Heat Transfer in the Hydromagnetic Ekman Layer on a Pouous Plate with Hall Effects," *Int. Jour. Heat Mass Transfer*, Vol. 19, pp. 523–527.

Soundalgekar, V. M., and Pop, I., 1973, "On Hydromagnetic Flow in a Rotating Fluid Past an Infinite Porous Wall," *Jour. Appl. Math. and Mech. (ZAMM)*, Vol. 53, pp. 718–719.

Vajravelu, K., 1988, "An Exact Periodic Solution of a Hydromagnetic Flow in a Horizontal Channel," ASME JOURNAL OF APPLIED MECHANICS, Vol. 55, pp. 981–983.

Vidyanidhu, V., and Nigam, S. D., 1967, "Secondary Flow in a Rotating Channel," *Jour. Math. and Phys. Sci.*, Vol. 1, p. 85.

Complete Crack-Tip Shielding of the Mode III Crack in a Work-Hardening Solid

J. Weertman[19]

The crack-tip shielding stress intensity factor L *for the mode III crack in a work-hardening solid is equal to* L = −K, *where* K *is the applied stress intensity factor. That is, the crack tip is perfectly shielded. This result is shown two ways: from the dislocation shielding and from the dislocation crack extension force.*

1 Introduction

The tip of the Griffith crack in an elastic solid is not shielded because no plastic zone containing nonredundant dislocations surrounds the crack tip. The dislocations in the plastic zone around the tip of a mode III crack in an elastic perfectly plastic solid have been shown to shield perfectly (Weertman, 1986, 1989a). An argument can be made that the tip of a crack in a work-hardening solid is only partially shielded because, by varying the exponent n of the power-law work-hardening equation from 1 to 0, it is possible to change continuously from the elastic solid to the elastic perfectly plastic solid situation. Intuitively, it might be reasonable to expect that the shielding various continuously rather than changing abruptly when n is changed from a value very close to the value 1 to the elastic solid value of 1. In this Note the shielding factor for the stationary mode III crack in the work-hardening solid is found in two ways. It is shown, contrary to intuition, that the crack-tip shielding always is perfect for $0 \le n < 1$.

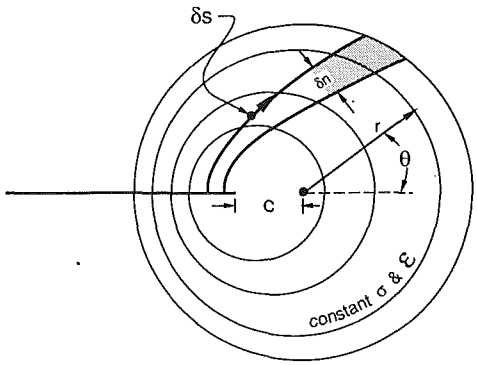

Fig. 1 Dislocation and stress trajectories and constant stress magnitude contour (from Weertman, 1989b)

Figure 1 shows the dislocation trajectories and the circular constant stress and strain magnitude contours in the plastic zone of the stationary mode III crack in a work-hardening solid. The stress magnitude σ and the strain magnitude ϵ are related by $\sigma = \sigma_0(\epsilon/\epsilon_0)^n$ where σ_0 and $\epsilon_0 = \sigma/2G$ are the yield stress and strain and G is the shear modulus. The exponent n is in the range $0 \le n \le 1$. The elastic solid has $n = 1$ and the elastic perfectly plastic solid has $n = 0$. The circular contours are centered a distance c ahead of the crack where $c = [(1-n)/(1+n)]r$ (Rice, 1967; Weertman, 1986, 1989b). The stress vector solution in the shifting center cylindrical coordinate system is $\sigma = \sigma_{yz}\mathbf{i}_x + \sigma_{xz}\mathbf{i}_y = \sigma(r)[\cos(\theta/2)\mathbf{i}_x + \sin(\theta/2)\mathbf{i}_y]$. The function $\sigma(r)$ is equal to $\sigma(r) = \sigma_0(r_0/r)^{n/(1+n)}$ where the radius of the plastic zone is $r_0 = K^2/2\pi\sigma_0^2$. In the plastic zone the nonredundant (screw) dislocation density $\mathfrak{B}(r, \theta)$, expressed as net Burgers vector per unit area, is (Weertman, 1986, 1989b)

$$\mathfrak{B} = \frac{\sigma_0}{rG}\left(\frac{r_0}{r}\right)^{\frac{n}{1+n}}\left[\frac{1-n}{(1+n)+(1-n)\cos\theta}\right]\cos\frac{\theta}{2}. \quad (1)$$

Here, r and θ are expressed in the shifting center coordinate system. The nonredundant dislocations given by this equation shield the crack tip.

2 Dislocation Crack-Tip Shielding

A shielding screw dislocation of Burgers vector b situated at a distance r_t and azimuthal angle θ_t from the crack tip reduces the stress intensity factor of the crack tip by the amount $L = -Gb(1/2\pi r_1)^{1/2}\cos(\theta_t/2)$ (Rice and Thompson, 1974; Weertman, 1984). Thus, the total shielding produced by the Eq. (1) density is

$$L = -\frac{G}{\sqrt{2\pi}}\int_{-\pi}^{\pi}\int_0^{r_0}\mathfrak{B}\frac{1}{\sqrt{r_t}}\left[\frac{(1+n)+(1-n)\cos\theta}{1+n}\right]\cos\frac{\theta}{2}\,rdrd\theta$$

$$= -\frac{1}{\pi}I(n)K, \quad (2)$$

where $I(n)$ is given by

$$I(n) = \int_{-\pi}^{\pi}\sqrt{\frac{r}{r_t}}\cos\frac{\theta}{2}\cos\frac{\theta_t}{2}\,d\theta.$$

[19]Department of Materials Science and Engineering, Department of Geological Sciences, Northwestern University, Evanston, IL 60208.

Contributed by the Applied Mechanics Division of THE AMERICAN SOCIETY OF MECHANICAL ENGINEERS. Manuscript received by the ASME Applied Mechanics Division, Jan. 2, 1991; final revision, Jan. 18, 1991.

Table 2 Values of phase angle θ_{1_T} for various λ and K

λ/K	.5	1.0	2.0	5.0	25.0
0.0	.313421	.539749	.748869	.807587	.785447
1.0	.539749	.674830	.787152	.803758	.785449
2.0	.674830	.748869	.805256	.800047	.785450
3.0	.748869	.787152	.812190	.796702	.785449
5.0	.805256	.812190	.811024	.791431	.785447
10.0	.803758	.800047	.793824	.785250	.785433
16.0	.787964	.786783	.785250	.784216	.785415

force, whereas it is almost independent of λ for large coriolis force and the values are given in Table 2.

Acknowledgment

Many thanks to the anonymous referee for his helpful suggestions for improvement of the paper.

References

Batchelor, G. K., 1967, *An Introduction to Fluid Dynamics*, 1st ed., Cambridge University Press, Cambridge, U.K., p. 119.

Gupta, A. S., 1972*a*, "Ekman Layer on a Porous Plate," *Phys. Fluid*, Vol. 15, No. 5, pp. 930–931.

Gupta, A. S., 1972*b*, "Magnetohydrodynamic Ekman Layer," *Acta Mechanica*, Vol. 13, pp. 155–160.

Jana, R. N., and Datta, N., 1977, "Couette Flow and Heat Transfer in a Rotating System," *Acta Mechanica*, Vol. 26, pp. 301–306.

Lighthill, M. J., 1954, "The Response of Laminar Skin Friction and Heat Transfer to Fluctuations in a Stream Velocity," *Proc. Roy. Soc., Lond.*, Vol. A226, pp. 1–23.

Mazumder, B. S., 1975, "Oscillatory Hydromagnetic Flow of Rotating Fluid Past an Infinite Plate," Ph.D. Thesis, Indian Institute of Technology, Kharagpur, India.

Mazumder, B. S., Gupta, A. S., and Datta, N., 1976, "Flow and Heat Transfer in the Hydromagnetic Ekman Layer on a Pouous Plate with Hall Effects," *Int. Jour. Heat Mass Transfer*, Vol. 19, pp. 523–527.

Soundalgekar, V. M., and Pop, I., 1973, "On Hydromagnetic Flow in a Rotating Fluid Past an Infinite Porous Wall," *Jour. Appl. Math. and Mech. (ZAMM)*, Vol. 53, pp. 718–719.

Vajravelu, K., 1988, "An Exact Periodic Solution of a Hydromagnetic Flow in a Horizontal Channel," ASME JOURNAL OF APPLIED MECHANICS, Vol. 55, pp. 981–983.

Vidyanidhu, V., and Nigam, S. D., 1967, "Secondary Flow in a Rotating Channel," *Jour. Math. and Phys. Sci.*, Vol. 1, p. 85.

Complete Crack-Tip Shielding of the Mode III Crack in a Work-Hardening Solid

J. Weertman[19]

The crack-tip shielding stress intensity factor L *for the mode III crack in a work-hardening solid is equal to* L = −K, *where* K *is the applied stress intensity factor. That is, the crack tip is perfectly shielded. This result is shown two ways: from the dislocation shielding and from the dislocation crack extension force.*

1 Introduction

The tip of the Griffith crack in an elastic solid is not shielded because no plastic zone containing nonredundant dislocations surrounds the crack tip. The dislocations in the plastic zone around the tip of a mode III crack in an elastic perfectly plastic solid have been shown to shield perfectly (Weertman, 1986, 1989a). An argument can be made that the tip of a crack in a work-hardening solid is only partially shielded because, by varying the exponent n of the power-law work-hardening equation from 1 to 0, it is possible to change continuously from the elastic solid to the elastic perfectly plastic solid situation. Intuitively, it might be reasonable to expect that the shielding various continuously rather than changing abruptly when n is changed from a value very close to the value 1 to the elastic solid value of 1. In this Note the shielding factor for the stationary mode III crack in the work-hardening solid is found in two ways. It is shown, contrary to intuition, that the crack-tip shielding always is perfect for $0 \le n < 1$.

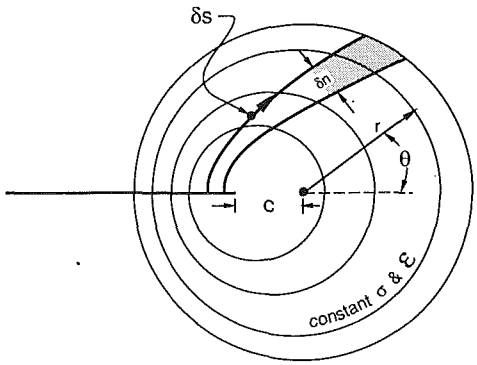

Fig. 1 Dislocation and stress trajectories and constant stress magnitude contour (from Weertman, 1989b)

Figure 1 shows the dislocation trajectories and the circular constant stress and strain magnitude contours in the plastic zone of the stationary mode III crack in a work-hardening solid. The stress magnitude σ and the strain magnitude ϵ are related by $\sigma = \sigma_0(\epsilon/\epsilon_0)^n$ where σ_0 and $\epsilon_0 = \sigma/2G$ are the yield stress and strain and G is the shear modulus. The exponent n is in the range $0 \le n \le 1$. The elastic solid has $n = 1$ and the elastic perfectly plastic solid has $n = 0$. The circular contours are centered a distance c ahead of the crack where $c = [(1-n)/(1+n)]r$ (Rice, 1967; Weertman, 1986, 1989b). The stress vector solution in the shifting center cylindrical coordinate system is $\sigma = \sigma_{yz}\mathbf{i}_x + \sigma_{xz}\mathbf{i}_y = \sigma(r)[\cos(\theta/2)\mathbf{i}_x + \sin(\theta/2)\mathbf{i}_y]$. The function $\sigma(r)$ is equal to $\sigma(r) = \sigma_0(r_0/r)^{n/(1+n)}$ where the radius of the plastic zone is $r_0 = K^2/2\pi\sigma_0{}^2$. In the plastic zone the nonredundant (screw) dislocation density $\mathfrak{B}(r, \theta)$, expressed as net Burgers vector per unit area, is (Weertman, 1986, 1989b)

$$\mathfrak{B} = \frac{\sigma_0}{rG}\left(\frac{r_0}{r}\right)^{\frac{n}{1+n}}\left[\frac{1-n}{(1+n)+(1-n)\cos\theta}\right]\cos\frac{\theta}{2}. \quad (1)$$

Here, r and θ are expressed in the shifting center coordinate system. The nonredundant dislocations given by this equation shield the crack tip.

2 Dislocation Crack-Tip Shielding

A shielding screw dislocation of Burgers vector b situated at a distance r_t and azimuthal angle θ_t from the crack tip reduces the stress intensity factor of the crack tip by the amount $L = -Gb(1/2\pi r_1)^{1/2}\cos(\theta_t/2)$ (Rice and Thompson, 1974; Weertman, 1984). Thus, the total shielding produced by the Eq. (1) density is

$$L = -\frac{G}{\sqrt{2\pi}}\int_{-\pi}^{\pi}\int_0^{r_0}\mathfrak{B}\frac{1}{\sqrt{r_t}}\left[\frac{(1+n)+(1-n)\cos\theta}{1+n}\right]\cos\frac{\theta}{2}\,rdrd\theta$$

$$= -\frac{1}{\pi}I(n)K, \quad (2)$$

where $I(n)$ is given by

$$I(n) = \int_{-\pi}^{\pi}\sqrt{\frac{r}{r_t}}\cos\frac{\theta}{2}\cos\frac{\theta_t}{2}\,d\theta.$$

[19]Department of Materials Science and Engineering, Department of Geological Sciences, Northwestern University, Evanston, IL 60208.

Contributed by the Applied Mechanics Division of THE AMERICAN SOCIETY OF MECHANICAL ENGINEERS. Manuscript received by the ASME Applied Mechanics Division, Jan. 2, 1991; final revision, Jan. 18, 1991.

Note that $r_t = [2r/(1+n)]\{\cos^2(\theta/2) + n^2\sin^2(\theta/2)\}^{1/2}$ and $\cos^2(\theta_t/2) = (1/2)\{1 + \cos\theta_t\} = (1/2)\{1 + ([\cos^2(\theta/2) - n\sin^2(\theta/2)]/[\cos^2(\theta/2) + n^2\sin^2(\theta/2)]^{1/2})\}$. The numerical integration of the integral $I(n)$ reveals that this integral has the remarkable property that, regardless of the value of n (in the range $0 \le n < 1$), $I(n) = \pi$. Thus, $L = -K$ and the crack tip is perfectly shielded.

(A reviewer questioned whether (2) is valid because L for a single dislocation is found in a linear elastic solid whereas the plastic stress-strain curve of the plastic zone is nonlinear. In (2) the smeared dislocations could be clumped into numerous discrete dislocations (a thousand "points of light") each surrounded by a linear elastic matrix. Equation (2) would give virtually the same result. This equation indeed is valid. Dislocation motion itself produces the nonlinear stress strain curve. If the solid were a nonlinear elastic one, (2) would not be valid.)

3 Dislocation Crack Extension Force

The integrated "force" (that is, the integrated product of Burgers vector and resolved stress component) directed parallel to the crack plane on all the nonredundant screw dislocations that exist on one side of the crack must equal the Eshelby-Rice J-integral-type expression $K^2/2G$ of the mode III crack. The force on a screw dislocation of Burgers vector b in this direction is given by the Peach-Koehler expression $\sigma_{yz}b$. Divide the nonredundant dislocations into two groups. One group is the "external" (to the crack plane) nonredundant dislocations that exist within the plastic zone. The other group is the "internal" (between the crack plane surfaces) nonredundant dislocations that exist on the crack plane. The integrated force F_e exerted on the external dislocations is resisted by the crystal lattice of the solid. This force, therefore, cannot produce extension of the crack tip. The net force F_i exerted on the internal dislocations is resisted by the interatomic stresses across the crack plane which resist growth of the crack. Thus, the force F_i does act to cause crack extension. The effective crack-tip stress intensity factor K_t is given by $K_t^2/2G = F_i = K^2/2G - F_e$. In the limit of a continuum solid the interatomic forces must be considered to be able to rise to an infinite value. A free surface is produced at an infinitely small separation of the crack faces. The product of infinite interatomic stress and the critical, infinitely small separation is finite and equal to twice the surface energy. Hence, the total Burgers vector of the internal dislocations just ahead of the crack is infinitely small but the net Peach-Koehler force on them can be finite (for the Griffith crack in an elastic solid) or zero. This force is F_i because the Peach-Koehler force on the internal dislocations that sit on the crack plane between the crack center and a crack tip is zero. Note that the surface traction σ_{yz} is zero across the crack faces. (A more extended discussion on the dislocation crack extension force is given in Weertman (1991).)

The net force F_e exerted on the external dislocations, which is found from an easy integration over the plastic zone of the product of the dislocation density $\mathfrak{B}$ and the shear stress component $\sigma_{yz} = \sigma_0(r_0/r)^{n/(1+n)}\cos(\theta/2)$, is

$$F_e = \sigma_0 \int_{-\pi}^{\pi}\int_0^{r_0} \mathfrak{B}\left(\frac{r_0}{r}\right)^{\frac{n}{(1+n)}}\cos\frac{\theta}{2}\, r dr d\theta = \pi r_0 \sigma_0^2 = \frac{K^2}{2G}. \quad (3)$$

Therefore, the effective stress intensity factor K_t at the crack tip is $K_t = 0$ and the effective shielding stress intensity factor is $L = -K$. Both methods of solution, therefore, give the same answer.

4 Discussion

The two calculations above for the mode III crack in a work-hardening solid show explicitly that the crack-tip shielding is perfect. This result does not mean that no stress singularity is present at the crack tip. The HRR stress singularity does exist at the tip. This stress singularity is weaker than an inverse square root of radial distance singularity. The perfect shielding implies that no crack extension force exists to start crack growth.

Acknowledgments

This research was supported by the National Science Foundation under NSF Grant DMR-86-07896.

References

Rice, J. R., 1967, "Stresses Due to a Sharp Notch in a Work Hardening Elastic Plastic Material Loaded by Longitudinal Shear," ASME JOURNAL OF APPLIED MECHANICS, Vol. 34, pp. 287–298.

Rice, J. R., and Thomson, R., 1974, "Ductile Versus Brittle Behavior of Crystals," *Philosophical Magazine*, Vol. 29, pp. 73–96.

Weertman, J., 1986, "Dislocation Emission into a Mode III Crack Tip Plastic Zone," *Scripta Metallurgica*, Vol. 20, pp. 1483–1488.

Weertman, J., 1984, "Crack Tip Stress Intensity Factor of the Double Slip Plane Crack Model: Short Cracks and Short Short-Cracks," *International Journal of Fracture*, Vol. 26, pp. 31–42.

Weertman, J., 1989a, "The Analytical Solution of a Growing Steady-State Mode III Crack in an Elastic-Perfectly Plastic Solid Through an Electrical Analogy," *Proceedings of the Royal Society*, London, Vol. A425, pp. 291–327.

Weertman, J., 1989b, "Mode III Crack Tip Plastic Zone Solution for Work Hardening Solid Using Dislocation Motion," ASME JOURNAL OF APPLIED MECHANICS, Vol. 56, pp. 976–977.

Weertman, J., 1991, "Crack Tip Plastic Zone, Dislocation Crack Tip Shielding, and the Dislocation Crack Extension Force," *Morris E. Fine Symposium*, P. K. Liaw, H. L. Marcus, J. S. Santner, and J. R. Weertman, eds., Minerals, Metals and Materials Society of the AIME, Warrendale, Penn., pp. 339–347.

Small Indentation Superimposed on a Finite Equibiaxial Stretch: Implications for Cardiac Mechanics[20]

J. D. Humphrey,[21] H. R. Halperin,[22] and F. C. P. Yin[23]

Introduction

Cardiac tissue is probably best characterized as a solid-fluid mixture exhibiting nonlinearly anisotropic, regionally heterogeneous, and perhaps incompressible behavior. Moreover, the heart has an irregular geometry and is subject to complex boundary conditions. Thus, it is difficult to rigorously study the mechanics of the heart analytically or computationally, and one must often rely on experimental methods. Unfortunately, most measurements are global in nature; as for example, measurements of intra-ventricular cavity pressure and volume. There is a need, therefore, for a reliable measurement technique for supplying regional information on cardiac mechanics.

Recent experimental data suggest that indentation tests on cardiac tissue may be useful for identifying regional differences in material behavior and estimating regional stresses in the heart (Halperin et al., 1987). Briefly, isolated, perfused cardiac tissue was subjected to in-plane biaxial stretching, with small indentations superimposed in the out-of-plane direction using a flat-ended circular punch. The data revealed that: (a) the indentation force was linearly related to the punch penetration

[20]Supported by NIH grants HL33621 and 41130.

[21]Department of Mechanical Engineering, Technology Research Center, The University of Maryland, Baltimore, MD 21228 Assoc. Mem. ASME.

[22]Department of Medicine, The Johns Hopkins Medical Institutions, Baltimore, MD 21205.

[23]Departments of Mechanical and Biomedical Engineering, The Johns Hopkins Medical Institutions, Baltimore, MD 21205. Mem. ASME.

Contributed by the Applied Mechanics Division of THE AMERICAN SOCIETY OF MECHANICAL ENGINEERS. Manuscript received by the ASME Applied Mechanics Division, July 6, 1989; final revision, Oct. 9, 1989.

Note that $r_t = [2r/(1+n)]\{\cos^2(\theta/2) + n^2\sin^2(\theta/2)\}^{1/2}$ and $\cos^2(\theta_t/2) = (1/2)\{1 + \cos\theta_t\} = (1/2)\{1 + ([\cos^2(\theta/2) - n\sin^2(\theta/2)]/[\cos^2(\theta/2) + n^2\sin^2(\theta/2)]^{1/2})\}$. The numerical integration of the integral $I(n)$ reveals that this integral has the remarkable property that, regardless of the value of n (in the range $0 \le n < 1$), $I(n) = \pi$. Thus, $L = -K$ and the crack tip is perfectly shielded.

(A reviewer questioned whether (2) is valid because L for a single dislocation is found in a linear elastic solid whereas the plastic stress-strain curve of the plastic zone is nonlinear. In (2) the smeared dislocations could be clumped into numerous discrete dislocations (a thousand "points of light") each surrounded by a linear elastic matrix. Equation (2) would give virtually the same result. This equation indeed is valid. Dislocation motion itself produces the nonlinear stress strain curve. If the solid were a nonlinear elastic one, (2) would not be valid.)

3 Dislocation Crack Extension Force

The integrated "force" (that is, the integrated product of Burgers vector and resolved stress component) directed parallel to the crack plane on all the nonredundant screw dislocations that exist on one side of the crack must equal the Eshelby-Rice J-integral-type expression $K^2/2G$ of the mode III crack. The force on a screw dislocation of Burgers vector b in this direction is given by the Peach-Koehler expression $\sigma_{yz}b$. Divide the nonredundant dislocations into two groups. One group is the "external" (to the crack plane) nonredundant dislocations that exist within the plastic zone. The other group is the "internal" (between the crack plane surfaces) nonredundant dislocations that exist on the crack plane. The integrated force F_e exerted on the external dislocations is resisted by the crystal lattice of the solid. This force, therefore, cannot produce extension of the crack tip. The net force F_i exerted on the internal dislocations is resisted by the interatomic stresses across the crack plane which resist growth of the crack. Thus, the force F_i does act to cause crack extension. The effective crack-tip stress intensity factor K_t is given by $K_t^2/2G = F_i = K^2/2G - F_e$. In the limit of a continuum solid the interatomic forces must be considered to be able to rise to an infinite value. A free surface is produced at an infinitely small separation of the crack faces. The product of infinite interatomic stress and the critical, infinitely small separation is finite and equal to twice the surface energy. Hence, the total Burgers vector of the internal dislocations just ahead of the crack is infinitely small but the net Peach-Koehler force on them can be finite (for the Griffith crack in an elastic solid) or zero. This force is F_i because the Peach-Koehler force on the internal dislocations that sit on the crack plane between the crack center and a crack tip is zero. Note that the surface traction σ_{yz} is zero across the crack faces. (A more extended discussion on the dislocation crack extension force is given in Weertman (1991).)

The net force F_e exerted on the external dislocations, which is found from an easy integration over the plastic zone of the product of the dislocation density $\mathfrak{B}$ and the shear stress component $\sigma_{yz} = \sigma_0(r_0/r)^{n/(1+n)}\cos(\theta/2)$, is

$$F_e = \sigma_0 \int_{-\pi}^{\pi}\int_0^{r_0} \mathfrak{B}\left(\frac{r_0}{r}\right)^{\frac{n}{(1+n)}}\cos\frac{\theta}{2}\, r dr d\theta = \pi r_0 \sigma_0^2 = \frac{K^2}{2G}. \quad (3)$$

Therefore, the effective stress intensity factor K_t at the crack tip is $K_t = 0$ and the effective shielding stress intensity factor is $L = -K$. Both methods of solution, therefore, give the same answer.

4 Discussion

The two calculations above for the mode III crack in a work-hardening solid show explicitly that the crack-tip shielding is perfect. This result does not mean that no stress singularity is present at the crack tip. The HRR stress singularity does exist at the tip. This stress singularity is weaker than an inverse square root of radial distance singularity. The perfect shielding implies that no crack extension force exists to start crack growth.

Acknowledgments

This research was supported by the National Science Foundation under NSF Grant DMR-86-07896.

References

Rice, J. R., 1967, "Stresses Due to a Sharp Notch in a Work Hardening Elastic Plastic Material Loaded by Longitudinal Shear," ASME JOURNAL OF APPLIED MECHANICS, Vol. 34, pp. 287–298.

Rice, J. R., and Thomson, R., 1974, "Ductile Versus Brittle Behavior of Crystals," *Philosophical Magazine*, Vol. 29, pp. 73–96.

Weertman, J., 1986, "Dislocation Emission into a Mode III Crack Tip Plastic Zone," *Scripta Metallurgica*, Vol. 20, pp. 1483–1488.

Weertman, J., 1984, "Crack Tip Stress Intensity Factor of the Double Slip Plane Crack Model: Short Cracks and Short Short-Cracks," *International Journal of Fracture*, Vol. 26, pp. 31–42.

Weertman, J., 1989a, "The Analytical Solution of a Growing Steady-State Mode III Crack in an Elastic-Perfectly Plastic Solid Through an Electrical Analogy," *Proceedings of the Royal Society*, London, Vol. A425, pp. 291–327.

Weertman, J., 1989b, "Mode III Crack Tip Plastic Zone Solution for Work Hardening Solid Using Dislocation Motion," ASME JOURNAL OF APPLIED MECHANICS, Vol. 56, pp. 976–977.

Weertman, J., 1991, "Crack Tip Plastic Zone, Dislocation Crack Tip Shielding, and the Dislocation Crack Extension Force," *Morris E. Fine Symposium*, P. K. Liaw, H. L. Marcus, J. S. Santner, and J. R. Weertman, eds., Minerals, Metals and Materials Society of the AIME, Warrendale, Penn., pp. 339–347.

Small Indentation Superimposed on a Finite Equibiaxial Stretch: Implications for Cardiac Mechanics[20]

J. D. Humphrey,[21] H. R. Halperin,[22] and F. C. P. Yin[23]

Introduction

Cardiac tissue is probably best characterized as a solid-fluid mixture exhibiting nonlinearly anisotropic, regionally heterogeneous, and perhaps incompressible behavior. Moreover, the heart has an irregular geometry and is subject to complex boundary conditions. Thus, it is difficult to rigorously study the mechanics of the heart analytically or computationally, and one must often rely on experimental methods. Unfortunately, most measurements are global in nature; as for example, measurements of intra-ventricular cavity pressure and volume. There is a need, therefore, for a reliable measurement technique for supplying regional information on cardiac mechanics.

Recent experimental data suggest that indentation tests on cardiac tissue may be useful for identifying regional differences in material behavior and estimating regional stresses in the heart (Halperin et al., 1987). Briefly, isolated, perfused cardiac tissue was subjected to in-plane biaxial stretching, with small indentations superimposed in the out-of-plane direction using a flat-ended circular punch. The data revealed that: (a) the indentation force was linearly related to the punch penetration

[20]Supported by NIH grants HL33621 and 41130.

[21]Department of Mechanical Engineering, Technology Research Center, The University of Maryland, Baltimore, MD 21228 Assoc. Mem. ASME.

[22]Department of Medicine, The Johns Hopkins Medical Institutions, Baltimore, MD 21205.

[23]Departments of Mechanical and Biomedical Engineering, The Johns Hopkins Medical Institutions, Baltimore, MD 21205. Mem. ASME.

Contributed by the Applied Mechanics Division of THE AMERICAN SOCIETY OF MECHANICAL ENGINEERS. Manuscript received by the ASME Applied Mechanics Division, July 6, 1989; final revision, Oct. 9, 1989.

depth; (b) the slope, α, of this indentation force-depth relationship increased with increasing in-plane stretch; (c) a linear relationship existed between α and an index of the in-plane normal stresses; and (d) at comparable in-plane stresses, α differed significantly for noncontracting and contracting tissue. Calling α a measure of "transverse stiffness," it was concluded that indentation tests may allow one to ". . .determine whether regional (cardiac) dysfunction is due to abnormal muscle that is not generating stress or to muscle capable of generating stress but which is abnormally loaded."

To gain additional insight into the basic mechanics of indentation experiments on cardiac tissue, we studied a related analytical problem. In this Note, we present graphical predictions for Mooney-Rivlin and exponential materials subjected to finite in-plane equibiaxial extensions and small superimposed indentations by a rigid punch. Our findings are qualitatively similar to the experimental data on cardiac tissue, and we discuss potential implications to cardiac mechanics.

Background

Small indentations superimposed on finite deformations of homogeneous and isotropic elastic half-spaces have been studied in detail (Green and Zerna, 1960; Beatty and Usmani, 1975). We employ these general results here, but restrict our attention to rigid flat-ended circular punches and hyperelastic incompressible materials. Moreover, we are interested solely in relationships between experimentally measurable quantities: the in-plane stresses and stretches, indentation force, and punch penetration depth. For completeness, we now summarize some of the relevant results from the literature.

For an initial equibiaxial finite deformation, the physical components of the deformation gradient are, $\mathbf{F} = \text{diag}\{\mu, \mu, \lambda\}$ where μ and λ are stretch ratios, and $\lambda = 1/\mu^2$ due to incompressibility. The associated in-plane components of the Cauchy stress are:

$$t_{11} = t_{22} = 2(\mu^2 - \lambda^2)(W_1 + \mu^2 W_2). \tag{1}$$

W_i are derivatives of the stored-energy function, $W(I_1, I_2)$, with respect to the invariants, I_i, of the Cauchy-Green deformation tensors; finally, $t_{33} = 0$.

For a superimposed indentation by a rigid flat-ended circular punch, the indentation force, P, is related to the punch penetration depth, e, viz.,

$$P = \alpha\, e \quad \text{where,} \quad \alpha = 4 r_o (\kappa/\eta), \tag{2}$$

r_o is the outer radius of the punch, and

$$\kappa = [(K_1 b + a)\sqrt{K_1}]/[1 + K_1] - [(K_2 b + a)\sqrt{K_2}]/[1 + K_2] \tag{3}$$

$$\eta = [K_1/(1 + K_1)] - [K_2/(1 + K_2)]. \tag{4}$$

K_1 and K_2 are roots of the following equation for K,

$$bK^2 + (a + b - c - d)K + a = 0 \tag{5}$$

with,

$$a = 2\lambda^2(W_1 + \mu^2 W_2) \tag{6a}$$

$$b = 2\mu^2(W_1 + \mu^2 W_2) \tag{6b}$$

$$c = 4\mu^2[(W_1 + \mu^2 W_2) + (\mu^2 - \lambda^2)(W_{11} + W_{22}\mu^2(\lambda^2 + \mu^2) + W_{12}(\lambda^2 + 2\mu^2)] \tag{6c}$$

$$d = 4\lambda^2[(W_1 + \mu^2 W_2) + (\lambda^2 - \mu^2)(W_{11} + 2W_{22}\mu^4 + 3W_{12}\mu^2)] \tag{6d}$$

W_{ij} $(i, j = 1, 2)$ are second derivatives of W with respect to I_i or I_j.

Results

First, consider a Mooney-Rivlin material defined by,

$$W = C_1(I_1 - 3) + C_2(I_2 - 3) \tag{7}$$

where C_1 and C_2 are material parameters. This form of $W(I_1, I_2)$ is often employed in studies of rubber elasticity, and has been assumed to describe contracting heart muscle (Hamid et al., 1986). Figure 1(*a*) illustrates the associated nearly linear stress-stretch behavior at small-to-moderate stretches ($1.0 \leq \mu \leq 1.2$). We restrict our attention to this range of stretch, which is reasonable for cardiac tissues (Humphrey and Yin, 1987).

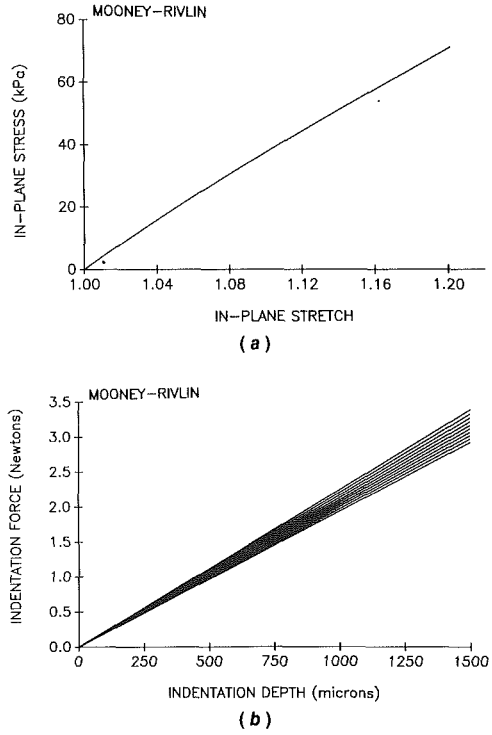

Fig. 1 (*a*) Equibiaxial stress-stretch behavior of a Mooney-Rivlin material described by Eq. (7) with C_1 = 29.5 kPa and C_2 = 5.0 kPa. These values of the constants were chosen simply to yield stresses which are comparable to those in cardiac tissue at stretches less than 20 percent; (*b*) families of indentation force versus punch penetration depth relationships. Each line corresponds to differing in-plane equibiaxial stretches, μ, from 1.0 to 1.2 in increments of 0.022. The slope increases with increasing stretch. Finally, the punch radius r_o = 0.0035 m.

From Eqs. (2)–(7) the transverse stiffness, α, for the Mooney-Rivlin material is

$$\alpha = \frac{8 r_o(\mu^9 + \mu^6 + 3\mu^3 - 1)(C_1 + C_2\mu^2)}{[\mu^4(\mu^3 + 1)]} \tag{8}$$

which, in the limit as $\mu \to 1$, becomes $(8/3)Er_o$. The Young's modulus, E, equals $6(C_1 + C_2)$, and Poisson's ratio, ν, is 0.5 due to incompressibility. Figure 1(*b*) shows the relationship between P and e for ten different in-plane equibiaxial stretches.

Next, consider an exponential material defined by,

$$W = d_1(e^{d_2(I_1 - 3)} - 1) \tag{9}$$

where d_1 and d_2 are material parameters. This form of $W(I_1, I_2)$ has been used to describe various biomaterials (Demiray, 1976; Beatty, 1987), and the associated nonlinear stress-stretch behavior is illustrated in Fig. 2(*a*). Unlike the Mooney-Rivlin material, the transverse stiffness, α, for an exponential material is not easily derived explicitly. It can, however, be determined numerically. The indentation force-depth relationship is in Fig. 2(*b*) for the same values of in-plane stretches as in Fig. 1(*b*). For equal increments in μ, the transverse stiffness of the exponential material increases markedly at higher in-plane stretches; this is in contrast to the results for the Mooney-Rivlin material wherein α increases uniformly with increasing μ.

Figure 3 shows the transverse stiffness versus the in-plane stresses and stretches for both materials. For in-plane stretches

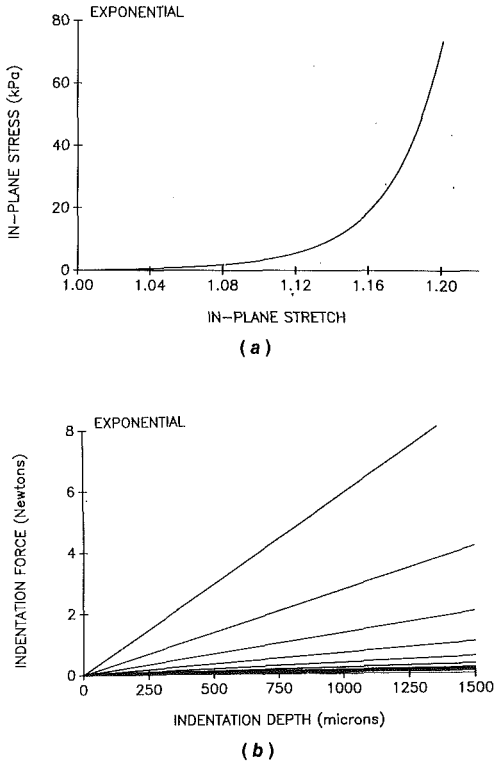

Fig. 2 (*a*) Equibiaxial stress-stretch behavior of the exponential material described by Eq. (9) with d_1 = 0.115 kPa and d_2 = 9.665. These constants are reasonable for potassium-arrested (noncontracting) cardiac tissue (Humphrey and Yin, 1987); (*b*) families of indentation force versus punch penetration depth relationships. The nomenclature is the same as in Fig. 1 and r_o = 0.0035 m.

less than 1.15, the transverse stiffness of the Mooney-Rivlin material is nearly linearly related to both in-plane stress and stretch. For $\mu > 1.15$, α is nonlinearly related to both in-plane stress and stretch. Findings for the exponential material are very different. First, except at extremely small stresses, α is nearly linearly related to the in-plane stress; second, the α versus μ relationship is highly nonlinear over the entire range of stretch.

Discussion

Indentation Force—Depth Relationships. As shown by Beatty and Usmani, a linear relationship exists between the indentation force and punch penetration depth for all homogeneous, isotropic, incompressible, hyperelastic materials indented with a rigid, flat-ended circular punch. In contrast, Green and Zerna showed that indenting the same class of materials with a rigid spherical-ended punch yields a nonlinear indentation force-depth behavior.

The linear *P-e* relationship (Eq. (2)) depends upon the indentation being small, however. Formally, this results from the requirement that the displacements and stresses induced by the punch tend to zero far away from the punch. Thus, to ensure a linear indentation force-depth behavior, one should observe certain experimental guidelines. First, the indentation should not affect the in-plane forces or deformations measured away from the punch; this is easy to check experimentally (see Fig. 6 in Halperin et al., 1987). Second, the material should be thick enough so that the punch "sees" only the deformation of the material. For example, Batra (1985) performed a finite element analysis of the indentation of slabs of rubber laying on a rigid surface, and showed that the indentation force was larger in thin layers due to the underlying rigid base. As a rule of thumb, the deformed thickness should probably be at least 20 times the indentation depth.

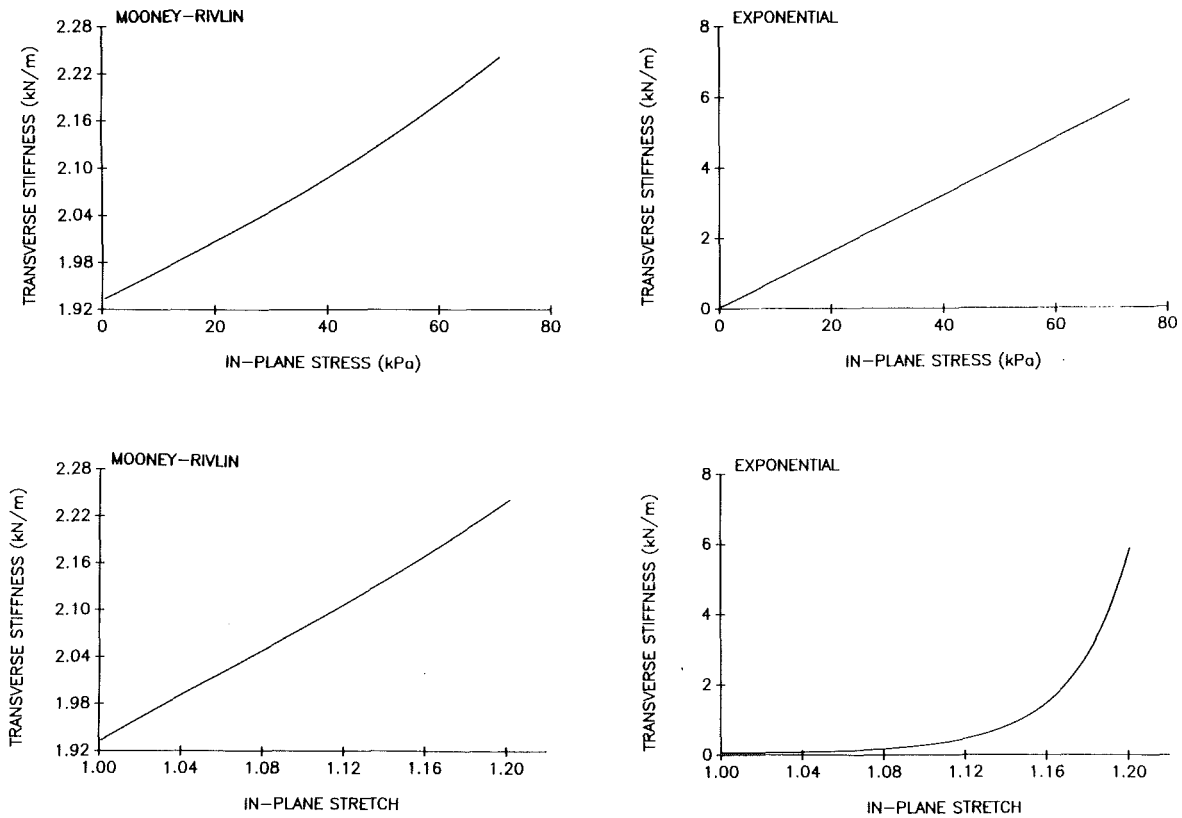

Fig. 3 (Left panels): transverse stiffness as a function of equibiaxial in-plane stress and stretch for a Mooney-Rivlin material. (Right panels): transverse stiffness as a function of equibiaxial in-plane stress and stretch for an exponential material.

Implications for Cardiac Tissue. Our findings are in close qualitative agreement with the available data on the heart. That is, both show that: (*a*) the indentation force is linearly related to the punch penetration depth; (*b*) the slope, α, of the indentation force versus depth relationship increases with increasing in-plane stretch; and (*c*) the transverse stiffness is nearly linearly related to the in-plane stress over certain ranges of stretch. New unpublished data reveal further that the transverse stiffness versus in-plane stress relation is nearly linear for both contracting and noncontracting cardiac tissue, whereas the transverse stiffness versus in-plane stretch relations appear to be nearly linear for contracting tissue but nonlinear for noncontracting tissue. Since contracting tissue appears to exhibit a nearly linear stress-stretch behavior over $1 \leq \mu \leq 1.10$ whereas noncontracting tissue exhibits a nonlinear, perhaps exponential, behavior, these new data are also consistent with our findings for Mooney-Rivlin and exponential materials.

The striking similarity between our predictions and the data on cardiac tissue must be kept in perspective, however. Although we employed constitutive relations which have been used to describe contracting (Eq. (7)) and noncontracting (Eq. (9)) cardiac tissue, and focused on physiologic ranges of in-plane stretch, the present results are based on assumptions of homogeneity, isotropy, and specific functional forms of W, none of which are strictly applicable to the heart. Thus, quantitative analysis of experiments on the heart using the present results must be approached cautiously. Nevertheless, the perhaps counterintuitive, unexpected findings in the previous experiments are qualitatively consistent with the present results.

Finally, we submit that indentation tests may be useful for distinguishing certain types of material behavior since the transverse-stiffness versus in-plane stretch behavior is qualitatively similar to the in-plane stress-stretch behavior of the material (Figs. 1–3). This observation is potentially important since the material properties of cardiac tissue can change regionally with disease, injury, and contractile state. Regional variations in material properties often affect the overall performance of the heart, and it is desirable to correlate these variations with global cardiac function. In the intact heart one cannot measure the in-plane stresses but one can perform regional indentation tests and measure in-plane strains. Thus, indentation tests may provide a tractable method to study certain aspects of regional cardiac mechanics.

References

Batra, R. C., 1985, "Quasistatic Indentation of a Rubberlike Layer by a Rigid Cylinder," *Proceedings International Conference on Finite Elements in Computational Mechanics*, T. Kant, ed., pp. 345–357.

Beatty, M. F., and Usmani, S. A., 1975, "On the Indentation of a Highly Elastic Half-Space," *Quarterly Journal of Mechanics and Applied Mathematics*, Vol. 28, pp. 47–62.

Beatty, M. F., 1987, "Topics in Finite Elasticity: Hyperelasticity of Rubber, Elastomers and Biological Tissues—with examples," *Applied Mechanics Reviews*, Vol. 40, pp. 1699–1734.

Demiray, H., 1976, "Ventricular Wall Stress," ASME JOURNAL OF APPLIED MECHANICS, Vol. 98, pp. 194–197.

Green, A. E., and Zerna, W., 1960, *Theoretical Elasticity*, Oxford University Press, U.K.

Halperin, H. R., Chew, P. H., Weisfeldt, M. L., Sagawa, K., Humphrey, J. D., and Yin, F. C. P., 1987, "Transverse Stiffness: A Method for Estimation of Myocardial Wall Stress," *Circulation Research*, Vol. 61, pp. 695–703.

Hamid, M. S., Sabbah, H. N., and Stein, P. D., 1986, "Determination of Left Ventricular Wall Stresses During Isovolumic Contraction Using Incompressible Finite Elements," *Computers and Structures*, Vol. 24, pp. 589–594.

Humphrey, J. D., and Yin, F. C. P., 1987, "On Constitutive Relations and Finite Deformations of Cardiac Tissue: I. A. Pseudostrain-Energy Function," ASME *Journal of Biomechanical Engineering*, Vol. 109, pp. 298–304.

Journal of Applied Mechanics

Book Reviews

Dynamic Stability of Suddenly Loaded Structures, by George J. Simitses. Springer-Verlag, New York, 1990. 290 pages.

REVIEWED BY R. H. PLAUT[1]

Until recently, there has been a dearth of books on the stability of structures subjected to suddenly applied loads. Happily, this situation is being remedied. Two recent books, *Dynamic Pulse Buckling* by H. E. Lindberg and A. L. Florence, and *Structural Impact* by N. Jones, concentrate on the elastic and plastic response of structures to intense loads of very short duration. They are complemented nicely by this new book written by Prof. G. J. Simitses.

Simitses considers conservative elastic systems subjected to impulse loads, step loads (i.e., suddenly applied loads with constant magnitude and infinite duration), and rectangular pulse loads (i.e., suddenly applied loads with constant magnitude and finite duration). Dynamic instability here means that the system exhibits a large-amplitude response. Throughout the book, critical values of the dynamic loads are compared to those for the case of quasi-static loading.

A "total potential energy approach" is applied, which has been developed by Simitses. (A similar method, used by C. S. Hsu and his collaborators, is also described in the book.) The energy imparted to the system by the dynamic load is compared to the potential energy of the system at all unstable equilibrium points. One can then determine lower and upper bounds on the critical loads. For one degree-of-freedom systems, these bounds are identical and exact critical loads are obtained.

Following an introductory chapter, three simple rigid-bar models are treated in Chapters 2–4. Two of them have one degree-of-freedom, while the third is a snap-through model with two degrees-of-freedom. The effect of static preloading is analyzed, and some problems are given at the ends of these chapters. For the case of rectangular pulse loading, the influence of small viscous damping is discussed in an appendix.

In Chapter 5, the application of the energy approach to continuous elastic systems is described. Impulse and step loads are considered. Simple two-bar frames are treated in Chapter 6. A step load is applied and lower bounds are obtained for various boundary conditions, eccentricities, and slenderness ratios.

Chapter 7 deals with shallow arches having a half-sine-wave initial shape. The first example is a pinned arch with the load distributed spatially in a half sine wave. Lower and upper bounds are computed for impulse, step, and rectangular pulse loads. In the second example, a clamped arch is subjected to a concentrated load at its apex, applied as an impulse or step load. The response is represented approximately as a combination of two symmetric modes and one antisymmetric mode.

Thin, shallow, clamped, spherical caps under uniform lateral pressure are treated in Chapter 8. Axiymmetric deformations are considered. Lower bounds for a two-term approximation are determined for the cases of impulse and step loading. In Chapter 9, thin cylindrical shells are analyzed. Laminated shells and stiffened shells are included, with geometric imperfections and various boundary conditions. An approximation procedure is utilized, and lower bounds on critical conditions are computed for axial step loading. Finally, conditions based on a prescribed maximum response amplitude are discussed in Chapter 10, and parametric resonance and brachistochrone problems are described in the appendices.

This book is a welcome addition in the field of structural stability. It presents an energy approach which can be used to obtain bounds on critical conditions for suddenly loaded elastic structures. The book is written clearly and covers the basic work carried out by Simitses in this area. It may be used as a textbook for part of a graduate course on dynamic stability of structures, and should be read by researchers in this field.

Introduction to Optimization of Structures, by N. V. Banichuk. Springer-Verlag, New York, 1990. 300 pages. Price: $89.00.

REVIEWED BY BHSHAN L. KARIHALOO[2]

Introduction to Optimization of Structures by Professor N. V. Banichuk is a translation of the original Russian book of the same name, published in 1986. The book is divided into two parts: Part 1 gives an introduction to the theory and techniques of optimization, whereas Part 2 demonstrates the application of theoretical concepts on several examples of beams, plates, shells, trusses, etc.

Chapter 1 gives a general overview of the optimization problem under statical and dynamical conditions, introducing the necessary objective and constraint functionals. This chapter also introduces the reader to multipurpose and multicriteria design problems. Chapters 2 and 3 give the derivation of optimality conditions using classical variational calculus. Chapters 4 and 5 are devoted to the solution of the optimization problems using several analytical and numerical approaches.

Chapters 6–8, which form Part 2 of the book, apply the optimization concepts to beams, plates, shells, trusses, etc. with a view to designing these structures, such that they use the least amount of material in fulfilling their mechanical function.

[1]Charles E. Via, Jr., Department of Civil Engineering, Virginia Polytechnic Institute and State University, Blacksburg, Virginia 24061-0105.

[2]Department of Civil and Mining Engineering, University of Sydney, New South Wales, 2006, Australia.